

Cell

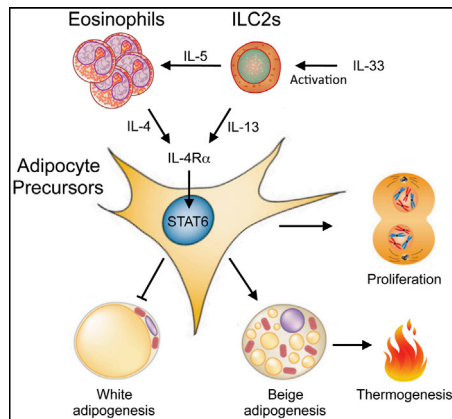
The cover art features a dark gray background with several DNA double helices. A large white helix runs vertically through the center. To its left, a red helix and a green helix run vertically. To its right, a green helix and a red helix run vertically. In the foreground, there are two large blue spheres, each with a white DNA helix wrapped around it. Below each sphere is a small blue circle with a white needle-like shape and a rainbow-colored arc, resembling a synthetic circuit component. The overall theme is synthetic biology and genetic engineering.

Volume 160
Numbers 1 and 2

January 15, 2015

www.cell.com

**Synthetic Circuits
with CRISPR**



Beiging with ILCs

PAGE 74

Type 2 innate lymphoid cells (ILC2s) are emerging as an important new class of cells in the immune system for maintaining tissue homeostasis. Lee et al. now show that IL-33-activated ILC2s directly promote the proliferation of adipocyte precursors and their subsequent commitment to the beige fat lineage, revealing a role for ILCs in metabolism and thermal homeostasis.

Immune Variation Is Environmentally Friendly

PAGE 37

Immune system properties show considerable heterogeneity among individuals. Using a system-level approach, Brodin et al. now reveal that nonheritable factors such as infections, vaccines, and nutrition largely determine the variation among individuals in the human immune system. The influence of such nonheritable factors is broad, cumulative, and becomes more significant with aging, overshadowing most heritable influences.

Cancer Genomics Meets Immunity

PAGE 48

Endogenous antitumor immunity can be exploited to treat cancer. Using large-scale data sets from solid tissue tumor biopsies, Rooney et al. explore how the genomic landscape of the tumor affects the cytolytic activity of immune cells in the tumor infiltrate. They reveal how the mutational load of the tumor shapes and is shaped by the ongoing immune response and identify key mutations that promote tumor resistance to killing by immune cells.

Dopamine Douses Inflammation

PAGE 62

The dysregulation of NLRP3 inflammasomes contributes to many inflammation-associated diseases. Yan et al. now find that dopamine and DRD1 signaling restrict NLRP3 inflammasome activation and control both neuroinflammation and peripheral inflammation by promoting NLRP3 ubiquitination and degradation.

Leptin and Insulin Unite

PAGE 88

Dodd et al. find that insulin and leptin, which are secreted after a meal, act synergistically in POMC neurons in the hypothalamus to promote browning of white fat. The increased thermogenesis capacity can promote weight loss and acts as a central homeostatic mechanism to coordinate the status of energy stores.

Beige Is the New Brown

PAGE 105

Beige fat is thought to protect against metabolic disease. McDonald et al. show that BMP signaling regulates the conversion of mesenchymal stem cells into beige adipocytes. Genetic or small-molecule-based inhibition of downstream pathway components, including a key transcription factor, leads to browning, enhanced energy expenditure, and protection against diet-induced obesity and insulin resistance in mice.

Hunger Pangs Decoded

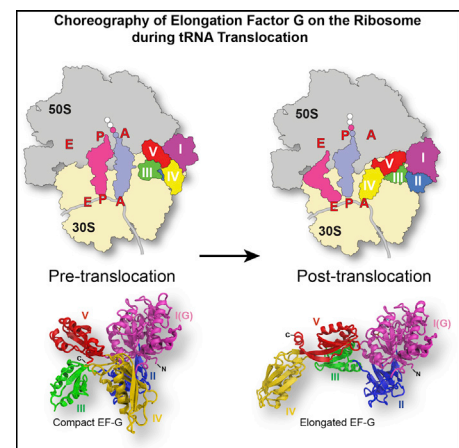
PAGE 119

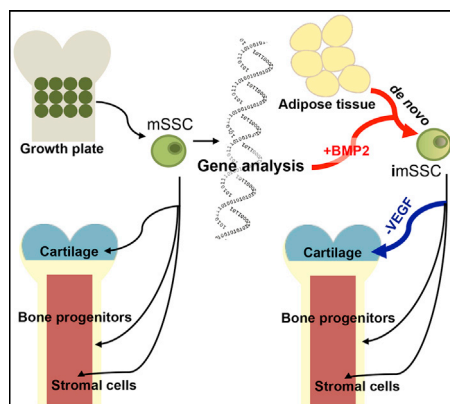
Lemieux et al. find that, in fasting worms, decreased levels of the tryptophan metabolite kynurenic acid activate NMDA receptors and trigger neuropeptide-Y and serotonin-dependent signaling, resulting in increased feeding. Replenishing kynurenic acid levels is sufficient to limit feeding, suggesting that temporal control of the levels of this metabolite can control food-dependent behavioral plasticity.

Elongation Factor Stretches Out

PAGE 219

The GTPase elongation factor G (EF-G) catalyzes the translocation of tRNA and mRNA on the ribosome after peptide bond formation. Lin et al. resolve high-resolution crystal structures, capturing the dynamic conformational states of EF-G in complex with the ribosome, and find that tRNA translocation requires a transition of EF-G from a compact to an elongated state under the regulation of the ribosomal protein S12.





Skeletal Stem Cell Identified

PAGE 285 and PAGE 269

How are skeletal tissues formed from stem cells? Chan et al. and Worthley et al. identify skeletal stem cells that generate osteoblasts, chondrocytes, and reticular marrow stromal cells, but not adipocytes. These stem cells function from development through adulthood and in bone repair. Chan et al. show that specific combinations of recombinant niche factors activate genetic programs of these cells even in nonskeletal tissues to promote de novo cartilage or bone formation. Worthley et al. also identify distinct connective tissue stem cells in the small intestine that express same marker as skeletal stem cells.

Live Long and Sulfur

PAGE 132

Dietary restriction (DR) improves health and extends life span in a variety of organisms. Hine et al. find that DR increases the systemic production of the

gas hydrogen sulfide by activating the transsulfuration pathway and confers protection from liver injury in rodents. This pathway is remarkably conserved and associated with longevity in other model systems. The findings suggest the potential for hydrogen sulfide as a hormetic compound with numerous beneficial effects.

The Two Faces of EGFR

PAGE 145

Epidermal growth factor receptor (EGFR) signaling suppresses autophagy through its kinase activity. Tan et al. report that kinase-inactivated EGFR accumulates at endosomes and cooperates with an oncoprotein and the exocyst to activate autophagy, indicating a kinase-independent role of EGFR in cancer development.

An Axonal Energy Crisis

PAGE 161

Axonal death disrupts functional connectivity of neural circuits and is a critical feature of many neurodegenerative disorders. Yang et al. delineate the core signaling pathway involved in axonal death and reveal that it is a local energy deficit that ultimately triggers breakdown of axonal structures.

Greasing the Wheels of Neurodegeneration

PAGE 177

Liu et al. show that lipid droplet accumulation in glial cells, driven by mitochondrial defects and ROS in neurons, contributes to neurodegeneration in flies, with evidence for a conserved mechanism in mice. The findings reveal an unexpected mode of crosstalk between neurons and glia in neurodegeneration and point to lipid droplets as early biomarkers and drivers of disease.

Strong Unions of Weak Units

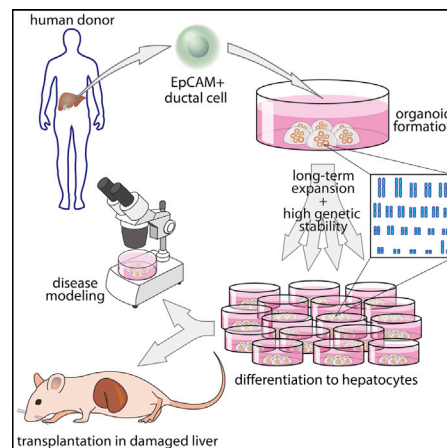
PAGE 191

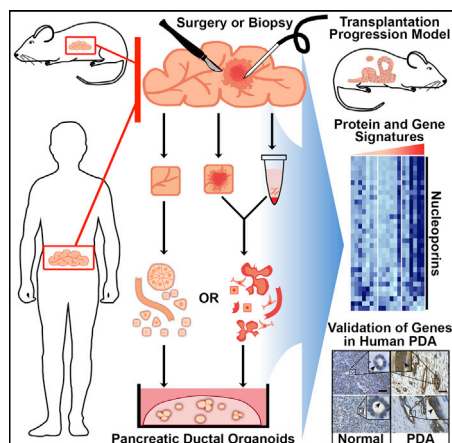
Enhancers must be regulated by the correct inputs (specificity) and function in a wide range of settings (robustness). Crocker et al. show that enhancers regulated by a subset of Hox proteins solve the specificity problem by using low-affinity binding sites and solve the robustness problem by clustering them together. These strategies are evolutionarily conserved, though the low-affinity sites themselves are not, highlighting the challenge of defining transcription factor binding sites based on sequence analysis.

Organoids DeLiver Promise

PAGE 299

The liver has a remarkable capacity for regeneration, but few models are available for expanding and preserving functional human liver cells. Huch et al. develop a culture system that allows long-term expansion of the human liver. Expanded cells are genetically stable and differentiate into functional hepatocytes in vitro and in vivo. Importantly, these cultures can be used to model and evaluate several genetic models of liver disease.





Human Pancreatic Cancer in 3D

PAGE 324

Boj et al. establish a platform for generating organoid cultures from normal and neoplastic mouse and human pancreatic tissue. Orthotopic transplantation of organoids and analyses of organoid transcriptomes and proteomes provide insights into the molecular basis of pancreatic tumorigenesis.

PRC2, Self-Disciplined

PAGE 204

In the yeast *Cryptococcus neoformans*, Dumesic et al. find that the Polycomb repressive complex 2 (PRC2) recognizes its own product, the H3K27me3 mark, to promote the specificity of H3K27me3 deposition. The findings suggest that product recognition may function to ensure the target specificity of chromatin-modifying enzymes.

Quorum Quartet

PAGE 228

Qrr sRNAs are noncoding RNAs that control quorum sensing in the bacterium *V. harveyi*. Feng et al. demonstrate that a representative Qrr deploys four different mechanisms to control target genes. One target is repressed via catalytic degradation, another through coupled degradation, and yet another through sequestration, whereas the fourth target is activated via opening of the ribosome-binding site. The distinct mechanisms are determined by differential base pairing and, in combination, enable precise dynamics of quorum-sensing outputs.

Houseguest Remodels Home

PAGE 241

Using time-lapse in vivo imaging, Tamplin et al. discover that the arrival of a hematopoietic stem cell at a perivascular niche triggers remodeling of the surrounding endothelial cells into a pocket. The stem cell then becomes anchored to a single mesenchymal stromal cell, which orients the stem cell's division plane.

Making Human Germ Cells

PAGE 253

Using human pluripotent stem cells, Irie et al. establish methods to generate human primordial germ cells (hPGC)-like cells in vitro. They find that SOX17 is a key regulator of hPGC cell fate and identify significant differences between mouse and human PGC specification, suggesting evolutionary divergence in mouse and human early development.

Invitation to an Intruder

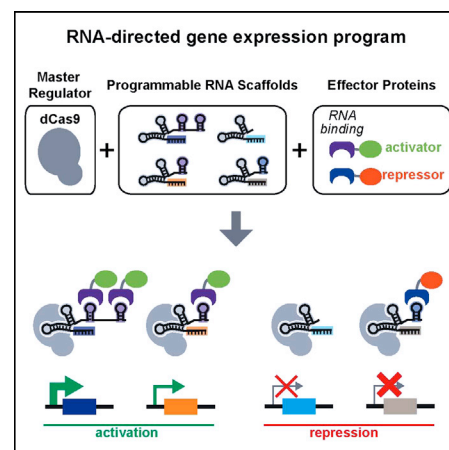
PAGE 313

To meet the extreme oxygen demand of flight muscle, *Drosophila* tracheae grow into flight muscle T-tubules, which allows them to reach mitochondria within the cytoplasm. Peterson et al. now show that a switch in localization of a tracheal chemoattractant from muscle membranes to T-tubules directs tracheal invasion, demonstrating that subcellular targeting of a chemoattractant can direct outgrowth to specific domains, even inside cells.

Multitasking CRISPR

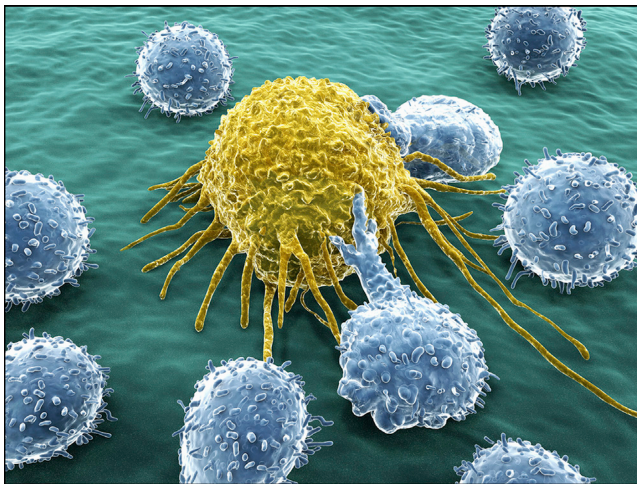
PAGE 339

A goal of synthetic biology is to engineer flexible multigene transcriptional programs. To enable this circuit engineering, Zalatan et al. generate modular CRISPR RNA scaffolds that encode both guides to target loci and domains to recruit transcriptional regulators. These allow simultaneous activation and repression of multiple different genes in eukaryotic cells, with expression of the catalytic-dead Cas9 protein acting as a single master regulatory control point.



Cancer Immunotherapy Scores Again

The use of antibodies to block pathways inhibiting the endogenous immune response to cancer, known as checkpoint blockade therapy, has stirred up a great deal of excitement among scientists, physicians, and patients alike. Clinical trials evaluating the safety and efficacy of antibodies that block the T cell inhibitory molecules CTLA-4 and PD-1 have reported success in treating subsets of patients with metastatic melanoma and renal cell carcinoma. Antibodies targeting these pathways have been approved for clinical use, and patients once unresponsive to any sort of conventional treatment have shown good and stable clinical responses—some remaining free of disease progression for many years. What types of cancer can benefit of immunotherapy and the factors that determine whether a patient will respond to treatment are now pressing questions. In the past month, seven new studies have begun to point toward the answers.



Checkpoint blockade therapy targets inhibitory pathways that keep T cells (shown in blue) from responding to tumor cells (represented in yellow). Upon release of such inhibition, the endogenous immune response can limit cancer growth (image from iStockphoto).

The first three reports expand the list of cancers that can be treated with checkpoint blockade therapy. Herbst et al. find that treatment with MPDL3280A, a monoclonal antibody specific for the PD-1 ligand (PD-L1), promotes therapeutic responses in patients with advanced non-small-cell lung cancer, renal cell cancer, and melanoma (Herbst et al. 2014), while Powles et al. show that the same antibody can be used to treat urothelial bladder cancer (Powles et al. 2014). Both groups report durable responses and low toxicity of the treatment, which is particularly important as high-grade adverse effects have limited the use of immunotherapy for cancer until now. In addition, Robert et al. provide evidence that patients with metastatic melanoma without the BRAF mutation present better responses

to immunotherapy with Nivolumab, a monoclonal antibody that blocks PD-1, than to conventional chemotherapy (Robert et al. 2014).

Thus, the list of cancers that can be targeted with immunotherapy is growing. However, only a fraction of patients treated will respond. What parameters predict a good response? Identifying biomarkers has been a long-sought goal in immunotherapy. The expression of PD-L1 in cancer cells is an obvious candidate, as it can directly turn off the immune response by inhibiting the activity of cytotoxic T cells infiltrating the tumor, but PD-L1 expression in tumor cells has had little predictive power. Analyzing samples from patients with melanoma treated with another PD-1-specific antibody, Pembrolizumab, Tumei et al. establish a set of conditions that correlates with good response to therapy (Tumei et al. 2014). These include the presence of cytotoxic T cells in the tumor, the expression of PD-L1 and PD-1 in immune cells in the tumor margin, and less complexity (in terms of antigen receptors) in the T cell population in the tumor. In support of these findings, Robert et al. and Herbst et al. also observe that PD-L1 expression in immune cells is a good biomarker of response to immunotherapy.

The finding that complexity of the T cell population in the tumor infiltrate can predict good response to checkpoint blockade therapy highlights the importance of understanding which antigens in the tumor can elicit an effective antitumor immune response. Previous studies suggested that tumors with a high load of somatic mutations are more likely to respond to immunotherapy, as in theory these tumors would have a higher diversity of neoantigens that can trigger an immune response when the CTLA-4/PD-1 inhibition is bypassed. To test this hypothesis, Snyder et al. carry out whole-exome sequencing of tumors from melanoma patients under therapy with CTLA4-specific antibodies Ipilimumab and Pembrolizumab (Snyder et al. 2014). While the data indeed show that high load of mutations correlate with responsiveness to therapy in many cases, surprisingly some tumors with a high load of somatic mutations fail to respond to checkpoint blockade. Computational analysis allows them to identify neoepitopes, antigens created by somatic mutations eliciting a T cell response, that are shared by the patients that respond to immunotherapy. It is thus possible that the nature of the mutations present in the tumor, not just the quantity, is a determining factor in responsiveness to therapy.

Identifying which mutations give rise to neoantigens that are functionally important for triggering an antitumor response has been particularly challenging. Yadav et al. attempt to facilitate the discovery of new mutant peptides by characterizing their general properties (Yadav et al. 2014). By carrying out whole-exome sequencing of two mouse tumor cell lines and comparing the data with the reference mouse exome sequences, they are able to predict candidate neoantigens in the tumor. Only a fraction of the neoantigens is predicted to bind to MHC (major histocompatibility complex) molecules, which present antigens to T cells.

An even smaller fraction binds to the MHC, as determined by mass spectrometry. The predicted mutant peptides that are immunogenic *in vivo* have solvent-exposed mutations, which are accessible to recognition by the T cell antigen receptor, as a common feature. Interestingly, these neoantigens are derived from proteins that are unlikely to contribute to tumorigenesis, confirming that passenger mutations play a significant role in shaping the immunogenicity of cancer cells. This platform could potentially be used to identify immunogenic antigens in any cancer cell type.

It is not entirely clear why the number of functionally relevant immunogenic antigens in the tumor is so low. One possibility is that mutations that give rise to highly immunogenic neoantigens are selected against during tumor growth. Indeed, Gubin *et al.* report that in a mouse model of sarcoma, resistance to immune-mediated rejection arises from loss of a major immunogenic antigen in the tumor cells (Gubin *et al.* 2014). The good news is that checkpoint blockade therapy can rescue the endogenous immune response, despite the loss of that antigen. The endogenous T cells infiltrating the tumor, once released from the inhibitory effect of CTLA-4 and PD-1, recognize neoantigens originating from two other mutations in the *Alg8* and *Lama4* genes and are thus able to reject the tumor. Importantly, vaccination of the tumor-bearing mice with these antigens also elicits tumor rejection, providing evidence that cancer vaccines can be efficacious, if the right combination of antigen and adjuvant is determined.

It is tempting to ask whether immunotherapy is evolving to become standard care for cancer patients, beyond those with advanced disease. Will it prove to be more efficacious than standard chemotherapy in cancers other than BRAF-negative melanoma? Is there a place for therapeutic regimens that combine checkpoint blockade with other strategies? While we are nowhere near having all the answers, these studies provide a wealth of data supporting the idea that somatic mutations in cancer cells are an important target of endogenous anti-tumor responses. Checkpoint blockade is effective at rescuing the anti-tumor effect and it is plausible that understanding the dynamics of the response to this therapy will also help the development of alternative and personalized approaches to treat cancer.

REFERENCES AND RECENT RELATED PAPERS

- Gubin, M.M., Zhang, X., Schuster, H., Caron, E., Ward, J.P., Noguchi, T., Ivanova, Y., Hundal, J., Arthur, C.D., Krebber, W.J., *et al.* (2014). *Nature* 515, 577–581.
- Herbst, R.S., Soria, J.C., Kowanetz, M., Fine, G.D., Hamid, O., Gordon, M.S., Sosman, J.A., McDermott, D.F., Powderly, J.D., Gettinger, S.N., *et al.* (2014). *Nature* 515, 563–567.
- Powles, T., Eder, J.P., Fine, G.D., Braithe, F.S., Loriot, Y., Cruz, C., Bellmunt, J., Burris, H.A., Petrylak, D.P., Teng, S.L., *et al.* (2014). *Nature* 515, 558–562.
- Robert, C., Long, G.V., Brady, B., Dutriaux, C., Maio, M., Mortier, L., Hassel, J.C., Rutkowski, P., McNeil, C., Kalinka-Warchoła, E., *et al.* (2014). *N. Engl. J. Med.* <http://dx.doi.org/10.1056/NEJMoa1412082>.
- Snyder, A., Makarov, V., Merghoub, T., Yuan, J., Zaretsky, J.M., Desrichard, A., Walsh, L.A., Postow, M.A., Wong, P., Ho, T.S., *et al.* (2014). *N. Engl. J. Med.* 371, 2189–2199.

Tumeh, P.C., Harview, C.L., Yearley, J.H., Shintaku, I.P., Taylor, E.J., Robert, L., Chmielowski, B., Spasic, M., Henry, G., Ciobanu, V., *et al.* (2014). *Nature* 515, 568–571.

Yadav, M., Jhunjhunwala, S., Phung, Q.T., Lupardus, P., Tanguay, J., Bumbaca, S., Franci, C., Cheung, T.K., Fritsche, J., Weinschenk, T., *et al.* (2014). *Nature* 515, 572–576.

Joao Monteiro

Max L. Birnstiel (1933–2014)

When I first met Max in Zurich in the fall of 1974, “Switzerland” seemed to be written all over him. I had just arrived from the United States, and his reserved politeness, his aversion to jokes, and his habit of neither wasting nor mincing his words all fitted the cliché of the Swiss German. My impression was reinforced when he told me that his paternal ancestors had been gunpowder manufacturers and he himself had served as an artillery officer in the Swiss Army. It was only later that I learned that about half of his genes—and all of his mitochondrial ones—came from sea-faring Portuguese who had settled in Brazil sometime in the past. The two genomes entered this world united in Bahia on July 12, 1933 when little Max was born to the Swiss merchant Max Birnstiel and his Brazilian wife Dalila Varella. When Max was five, his parents decided to move to Switzerland in order to allow Max and his brother Fritz to get a solid education. Max attended primary school and gymnasium in Zurich and then enrolled at the Swiss Federal Institute of Technology with the goal of studying biology, a subject that had fascinated him since childhood. On the advice of the botanist Albert Frey-Wyssling, he majored in physical chemistry—at that time an unorthodox *gradus ad Parnassum* for an aspiring biologist. As Max tells it, he never regretted this choice, as it taught him to look at complex biological systems with a quantitative eye. After his doctoral thesis with Frey-Wyssling, he spent 3 1/2 years at the California Institute of Technology at Pasadena, working as a postdoctoral fellow with the botanist James Bonner. This stay at one of the world’s premier scientific institutions brought him face to face with scientific giants such as Linus Pauling, George Beadle, Max Delbrück, and Renato Dulbecco and the first stirrings of the biological revolution. His postdoctoral work led to the discovery that the ribosomal RNA genes of the plant *Pisum sativum* were highly repetitive, existing in hundreds of copies. Max was never quite satisfied with his postdoctoral harvest even though it furnished the basis of some of his breakthrough discoveries

soon to come. His collaboration at Caltech with the British biologist Margaret Chipchase on ribosomal RNA genes was also fruitful in other ways: the two married in 1961.

In 1963, Conrad H. Waddington recruited the promising young Swiss to the Epigenetics Research Group at the Genetics Department of the University of Edinburgh, where Max rapidly rose through the ranks from Lecturer all the way to Professor. Inspired by his postdoctoral work on plant ribosomal RNAs, Max, his PhD students Adrian Bird and Michael Grunstein, together with team members started investigating the repetitive ribosomal RNA genes of the South African toad *Xenopus laevis*. By hybridizing total *Xenopus* DNA to the two major *Xenopus* ribosomal RNAs and subjecting the hybrids to isopycnic centrifugation in cesium chloride gradients, they purified the reiterated RNA genes as complexes with their cognate RNAs—the first gene purification ever, well before the advent of gene cloning. The ribosomal RNA genes could also be purified directly by repeated gradient centrifugation because they had an unusually high G+C content and, hence, a higher buoyant density than the bulk DNA. By today’s standards,



Max L. Birnstiel

methods for studying genes were still paltry, but Max and his team could show that the genes were located in the nucleolus in a head-to-tail tandem arrangement. By 1971, when he was promoted to professor, Max was already a major player in the new and competitive field of molecular biology.

When the University of Zürich offered him a chair in molecular biology in 1972, the OPEC oil shock had not yet rocked the West and Switzerland was still basking in the glow of financial opulence. The offer was thus very generous but came with a hitch: the university had already given one of the molecular biology chairs to Charles Weissmann, and it seemed likely that a shared institute would be too confining a habitat for two stellar and strong-willed scientists. The Solomonian solution was to split the Institute into an Institute I, headed by Charles Weissmann, and an Institute II, headed by Max Birnstiel. Max was never quite at ease with this solution, but his resources at Zurich and his growing scientific reputation allowed him to attract an impressive cast of bright young scientists, including, among others, Carmen Birchmeier, Meinrad Busslinger, Rudolf Grosschedl, Walter Schaffner, and John L. Telford.

In Zurich, Max applied improved density gradient procedures to purifying the repetitive 5S RNA genes of *Xenopus laevis* and the five clustered histone genes of the sea urchin *Psammechinus miliaris*. Never before had protein-coding genes from a multicellular organism been purified and studied in such detail. But this tour de force marked the end of an era. By 1975, gene cloning had entered the scene, rendering gene purification by physical methods obsolete.

Although by that time Max had stopped doing experiments himself, he retained an amazing experimental intuition. Walter Schaffner recounts how Max thought up an ingenious trick of injecting DNA into oocyte nuclei, which turned out to be crucial in defining DNA elements regulating gene transcription and RNA processing. Another such suggestion led to an effective method for recovering intact RNA from *Xenopus* oocytes. And

an impressive string of highly original studies, done together with his gifted collaborators, soon threw new light on the promoters of tRNA genes and the *cis*-regulatory sequences and *trans*-acting factors governing 3' end processing of mRNAs. Particularly exciting was the discovery together with Rudolf Grosschedl of a "modulator" element more than 100 nucleotides upstream of the histone H2A gene promoter. This element acted in an orientation-independent manner and was thus the first member of the "enhancers" studied later by others. In 1986, 14 years after his recruitment to Zürich, the Birnstiel laboratory went from strength to strength, showing no sign of slowing down. Always the good scientific citizen, Birnstiel also served as Chairman of the EMBO Council and organized international conferences on gene regulation that drew large audiences from all over the world. Many honors began to come his way, including foreign membership in the US National Academy of Sciences, honorary doctorates and professorships, the prestigious Naegeli Prize, and, later, medals of all stripes and colors. By the mid-1980s, Max was an admired international figure and an icon of Swiss science.

Fate had other plans, however. At the suggestion of the Austrian biochemist Peter Swetly, the US biotech pioneer Genentech and the German pharmaceutical giant Boehringer Ingelheim decided to establish a biomedical research Institute in Vienna, a city not known as a center of biomedicine. The crucial point was to find a high-profile scientist courageous enough to move to Vienna and set up a research Institute there. I had just visited Max in Zürich and sensed his eagerness for a change. When I asked him whether

he would be willing to head a new, privately funded biomedical research institute, he was immediately interested. But when he then asked "where is that institute going to be?", my reply "in Vienna" seemed to offend him and he said "no." Early the next morning, however, my phone rang—it was Max. "Is the job still available?" he asked. This tongue-in-cheek question and the enthusiastic reaction by the two founder companies opened a new chapter in Max's life and in Austrian biomedicine. Max was a perfect choice for the challenge. He accepted under the condition that the molecular biology departments of Vienna University (now the Max L. Perutz Laboratories) would move next to his new "Institute of Molecular Pathology" (IMP), which was to be erected at the site of a defunct manufacturing facility. This visionary demand spawned Austria's leading life science campus, which today houses the IMP, the Max L. Perutz Laboratories, and several biological research institutes of the Austrian Academy of Sciences, as well as biotech spin-offs. In no time, Max had recruited five first-rate young scientists as group leaders who were to shape the IMP during its crucial starting phase and beyond. Adrian Bird came from the MRC Laboratories in Edinburgh, Kim Nasmyth from the Laboratory of Molecular Biology in Cambridge, Hartmut Beug and Erwin Wagner from the European Molecular Biology Laboratory (EMBL) in Heidelberg, and Meinrad Busslinger accompanied Max from Zurich. By creating a set of core facilities, Max gave the young IMP an edge over its competitors and quickly propelled it into the top league of biomedical research centers.

At the IMP, Max continued his work on eukaryotic gene regulation but also

ventured into new areas. He searched for new cancer vaccines by transfecting murine cells by means of inactivated adenovirus particles and transferrin-poly-cation conjugates in order to generate cytokine-secreting autologous tumor cells. At work he was direct, demanding and imperial as ever, but Vienna also exposed his Brazilian heritage and the manifold layers of his complex *persona*. He had always appreciated the good things in life—wines, cigars, haute cuisine, and classical music—but now he could officially savor them with his many visitors. And he seemed to take mischievous pleasure in standing up to Austria's labyrinthine bureaucracy and mastering its mysterious titles. When he handed over the IMP directorship to Kim Nasmyth in 1996, he could look back to a period of astonishing achievement and personal happiness. After his return to Switzerland, he enjoyed traveling with his wife and children and playing classical music on his recorder. Early in 2014, he discovered a growth on his neck, which was diagnosed as an inoperable cancer. During the subsequent radiation treatment, his heart failed and he died on November 15 in a hospital near Wollerau, the Swiss village he had chosen for the final years of his eventful and brilliant life.

ACKNOWLEDGMENTS

I thank Margaret Birnstiel, Meinrad Busslinger, Rudi Grosschedl, and Walter Schaffner for helpful suggestions.

Gottfried Schatz^{1,*}

¹Universität Basel, Unterer Rebbbergweg 33, 4153 Reinach/Schweiz, Switzerland

*Correspondence: gottfried.schatz@unibas.ch

[unibas.ch](http://dx.doi.org/10.1016/j.cell.2014.12.030)

<http://dx.doi.org/10.1016/j.cell.2014.12.030>

Disentangling Inborn and Acquired Immunity in Human Twins

Jean-Laurent Casanova^{1,2,3,4,5,*} and Laurent Abel^{1,3,4}

¹St. Giles Laboratory of Human Genetics of Infectious Diseases, Rockefeller Branch, The Rockefeller University, New York, NY, USA

²Howard Hughes Medical Institute, New York, NY, USA

³Laboratory of Human Genetics of Infectious Diseases, Necker Branch, Inserm U1163, Necker Hospital for Sick Children, Paris, France

⁴Paris Descartes University, Imagine Institute, Paris, France

⁵Pediatric Hematology and Immunology Unit, Necker Hospital for Sick Children, Paris, France

*Correspondence: casanova@rockefeller.edu

<http://dx.doi.org/10.1016/j.cell.2014.12.029>

The human geneticist Archibald Garrod noted in 1931 that, “It is, of necessity, no easy matter to distinguish between immunity which is inborn and that which has been acquired” (*The Inborn Factors in Disease*). In this issue of *Cell*, Brodin et al. show that the heritability of blood counts rapidly decreases with age for the lymphoid subsets responsible for adaptive immunity, unlike cells from other hematopoietic lineages.

Twin studies were gradually introduced into human genetics between 1901 and 1924 (van Dongen et al., 2012). Comparisons of the levels of concordance and discordance of any phenotype in monozygotic (MZ) and dizygotic (DZ) twins can be used to dissociate the inborn and acquired contributions. Such studies are sometimes, incorrectly, considered to provide a clear distinction between inherited and environmental factors. However, inborn factors may not be exclusively inherited from the parental germlines, because twin fetuses may have diverged somatically, genetically, or epigenetically. Moreover, acquired factors are not necessarily induced or selected by the environment, as they can occur by natural drift in children and adults. Bearing this caveat in mind, twin studies have proved helpful in many areas of human genetics, through the estimates they provide of the respective weights of the “genetic” and “environmental” components of any physiological or pathological, qualitative or quantitative phenotype. In this issue of *Cell*, a new twin study provides evidence that this approach can have enormous immunological impact (Brodin et al., 2015).

The five broad classes of immunological diseases cover most areas of medicine. Infectious diseases and virus-induced cancers attest to an impairment of immunity to microbes, whereas allergic conditions are indicative of excessively

strong immunity to diverse stimuli. Auto-immune disorders are defined by defects in adaptive immunity to self-antigens, whereas all other types of immunological damage to self are considered to be auto-inflammatory disorders. In twin studies, these immunological conditions display variable heritability, ranging from an almost undetectable genetic component in some purely sporadic conditions to an almost total lack of environmental impact in the highly familial forms of primary immunodeficiency.

For most conditions, age at onset appears to be a good indicator of the balance between the inherited and acquired components. The genetic component has a greater weight in conditions occurring in children, adolescents, and young adults. For example, systemic lupus erythematosus, which typically strikes young women, has a stronger genetic component than rheumatoid arthritis, which affects older women (Bogdanos et al., 2012). Heritability is also strongly influenced by age in twin studies of particular conditions, such as type 1 diabetes. These results are consistent with the widely held view that pediatrics relates predominantly to the effects of germline genetics, geriatrics relates to somatic genetics, with internal medicine being a combination of the two. Children are on steeply ascending curve at the start of life, and are vulnerable to unfortunate inborn errors, whereas adults are on the

much shallower declining curve of life, vulnerable to the inevitable accumulation of somatic errors. Diseases of the elderly may be determined predominantly by somatic rather than germline variations, although these two components are mechanistically inseparable and relatively little is known about these evolutionarily recent conditions. The only long-standing, major exception to this global scheme has been infection, the highly symbolic group of environmental diseases that killed half of all children before the age of 15 years until the medical conquests derived from the germ theory of disease. However, it has recently become apparent that life-threatening primary infections of children, and even of adults, can also be caused by single-gene inborn errors of immunity.

In general terms, the patient-based discovery of the molecular genetic basis of the monogenic primary immunodeficiencies underlying increasing numbers of immunopathological phenotypes has been immensely successful (Casanova et al., 2014). Conversely, population-based studies of the molecular basis of immunological conditions lag behind estimations of heritability based on twin and other studies. This is due to both technical and intellectual challenges, resulting, in particular, in the long-term neglect of studies of rare variants by in-depth experimental approaches. Another roadblock has been the lack of genetic studies of

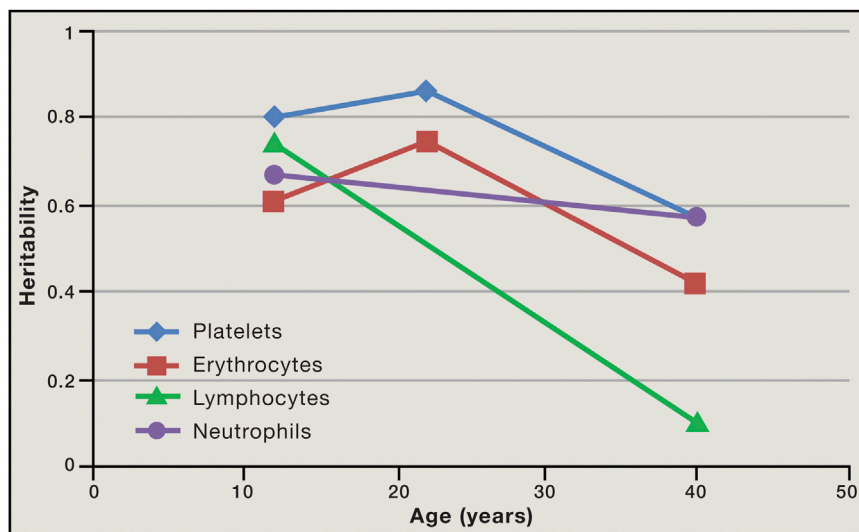


Figure 1. Variation of Heritability Values with Age for Blood Cell Counts in Human Twin Studies

The four most abundant blood cell populations are represented: (1) lymphocytes in green (>90% of which ensure adaptive immunity), (2) neutrophils in purple, (3) erythrocytes in red, and (4) platelets in blue. The data for the youngest subjects came from the study by Evans et al. (1999) on 38 MZ and 254 DZ twins at the age of 12 years. The data for subjects of intermediate ages came from the study by Whitfield and Martin (1985) on 85 MZ and 121 DZ twins aged 18–34 years (mean age: 23.1 years), which presented heritability values only for erythrocytes and platelets. The data for the oldest subjects relate to lymphocytes and neutrophils and were obtained from the study by Brodin et al. (2015) on 78 MZ and 27 DZ twins aged 8–82 years (mean age: 38), or erythrocytes and platelets, from the study by Garner et al. (2000) of 264 MZ and 511 DZ twins aged 20–80 years. Heritability value for lymphocytes estimated to be below the detection limit of 0.2 in the study of Brodin et al. were arbitrarily set to 0.1.

biological, physiological, and immunological phenotypes in “healthy” individuals, including twins (given that health is always transient and that any twin may fall ill shortly after being studied). For example, we know that environmental factors, such as HIV infection, and genetic factors, such as inherited HLA-II deficiency, can profoundly affect blood CD4 T cell counts. However, despite knowledge of the normal range for these counts and for an increasing number of other immunological measurements in each age category, the respective influences of genetic and environmental factors have rarely been studied in an unbiased manner at population level. This gap in knowledge has hindered the genetic study of immunological conditions by preventing the use of genetically determined intermediate phenotypes, which could facilitate not only genetic studies of illnesses, but also their laboratory investigation.

The remarkable paper by Brodin et al. in this issue describes a heroic attempt to compare a large number of blood immunological parameters in 78 MZ and 27

DZ twins (Brodin et al., 2015). The parameters studied include the baseline levels of 40 cytokines and 72 leukocyte subset counts, the in vitro response of eight cell types to seven cytokines, and the in vivo antibody response to influenza vaccine. The main finding of this study is that most of the phenotypes studied display very little heritability (Figure 1). Similar results were previously obtained in a family-based genome-wide association study (Orrù et al., 2013). Measurements relating to T or B cells, the two cell lineages responsible for antigen-specific adaptive immunity, account for at least three-quarters of the parameters studied and, with only a few exceptions in specific cell subsets, they display the lowest levels of heritability. Many innate myeloid and lymphoid populations were not studied. Remarkably, in a previous study including a larger number of twins (138 MZ and 254 DZ) but fewer parameters (nine leukocyte subsets), the leukocyte populations, including B and T cell subsets, displayed a much higher heritability (Figure 1) (Evans et al., 1999). However, the twins studied

were all 12 years old, whereas those studied by Brodin et al. were aged between 8 and 82 years (mean age: 38 years). Moreover, the youngest twins displayed a higher heritability for innate leukocytes, such as NK cells, neutrophils, and eosinophils. Finally, the poor heritability of the antibody response to influenza vaccine is consistent with a previous twin study, in which the heritability of antibody responses to other vaccines rapidly declined with time after vaccination (Marchant et al., 2006).

Overall, the heritability of T and B cell parameters is lower than that of the other leukocyte phenotypes currently assessed in twins and declines more rapidly with age than that of innate leukocytes. Further distinguishing the idiosyncratic homeostasis of these cells from the average hematopoietic “somatic drift,” other blood cell types, such as erythrocyte and platelet counts, the values of which are age-dependent, show an almost age-independent heritability (Figure 1) (Garner et al., 2000; Whitfield and Martin, 1985). Likewise, various circulating molecules, such as coagulation factors, metabolites, and hormones, have a high heritability at most ages studied. This apparent singularity of adaptive immunity is consistent with its unique evolution and function. Adaptive immunity in jawed vertebrates is mediated by three distinct cell lineages: α/β T, γ/δ T, and B cells. In jawless vertebrates, it is mediated by the corresponding VLRA, VLRC, and VLRB cells, which seem to recognize the same three distinctive types of antigen (Hirano et al., 2013). Adaptive immunity is unique among the physiological systems of vertebrates, not only in terms of its double emergence through convergent evolution, but also in terms of its capacity to generate an almost infinite number of cells carrying clonally distributed, antigen-specific receptors through somatic genetic recombination. It seems likely that adaptive immunity, enabling the body to recognize an almost limitless number of nonself-antigens, underwent evolutionary tinkering twice in vertebrates, to improve host defense and to ensure the survival of more individuals beyond reproductive age.

Twin studies of both biological and clinical immunophenotypes further suggest that this tremendous somatic genetic diversification provides an escape from

the germline genome, by reducing the impact of germline variation in the regulatory sequences of the genes governing T and B cell homeostasis and responses. Indeed, the genes governing the development and function of each individual lymphocyte are partly regulated by the B or T cell antigen receptor signaling pathway, and are therefore influenced in each cell by the nature of each antigen receptor, possibly accounting for the rapid loss of heritability of most adaptive parameters. The adaptive immune system can be seen as “buffering” the influence of the germline in antigen-specific cells. Of course, adaptive immunity is also controlled by the germline, as illustrated by rare inborn errors of T cells and B cells, whether protective (e.g., CCR5 deficiency protecting T cells against HIV infection) or deleterious to the host (e.g., RAG deficiency preventing the development of T and B cells). However, the tremendous diversity of antigen receptors generated by somatic recombination may globally “loosen” the germline genetic

chains of T and B cells, including common germline variations, providing us with some understanding of their negligible influence on immunological diseases. The equally tremendous spatial and temporal variety of antigenic challenges in the course of infections may leave countless somatic immunological imprints, each unique, on each individual, including identical twins. Like antigen-specific antibody titers, these various imprints may be more than a collection of scars; they may also ensure better-adapted and sustained host defense during recurrent or latent infections, at least at the population level.

REFERENCES

- Bogdanos, D.P., Smyk, D.S., Rigopoulou, E.I., Mytilinaiou, M.G., Heneghan, M.A., Selmi, C., and Gershwin, M.E. (2012). *J. Autoimmun.* 38, J156–J169.
- Brodin, P., Jojic, V., Gao, T., Bhattacharya, S., Angel, C.J.L., Furman, D., Shen-Orr, S., Dekker, C.L., Swan, G.E., Butte, A., et al. (2015). *Cell* 160, this issue, 37–47.
- Casanova, J.L., Conley, M.E., Seligman, S.J., Abel, L., and Notarangelo, L.D. (2014). *J. Exp. Med.* 211, 2137–2149.
- Evans, D.M., Frazer, I.H., and Martin, N.G. (1999). *Twin research* 2, 250–257.
- Garner, C., Tatu, T., Reittie, J.E., Littlewood, T., Darley, J., Cervino, S., Farrall, M., Kelly, P., Spector, T.D., and Thein, S.L. (2000). *Blood* 95, 342–346.
- Hirano, M., Guo, P., McCurley, N., Schorpp, M., Das, S., Boehm, T., and Cooper, M.D. (2013). *Nature* 501, 435–438.
- Marchant, A., Pihlgren, M., Goetghebuer, T., Weiss, H.A., Ota, M.O., Schlegel-Hauter, S.E., Whittle, H., Lambert, P.H., Newport, M.J., and Siegrist, C.A.; Medical Research Council Gambia Twin Study Group (2006). *J. Infect. Dis.* 193, 1598–1605.
- Orrù, V., Steri, M., Sole, G., Sidore, C., Virdis, F., Dei, M., Lai, S., Zoledziwska, M., Busonero, F., Mulas, A., et al. (2013). *Cell* 155, 242–256.
- van Dongen, J., Slagboom, P.E., Draisma, H.H., Martin, N.G., and Boomsma, D.I. (2012). *Nat. Rev. Genet.* 13, 640–653.
- Whitfield, J.B., and Martin, N.G. (1985). *Genet. Epidemiol.* 2, 133–144.

A Protein Restriction-Dependent Sulfur Code for Longevity

Hong Seok Shim¹ and Valter D. Longo^{1,2,3,*}

¹Department of Biological Sciences

²Longevity Institute, Davis School of Gerontology

University of Southern California, 3715 McClintock Avenue, Los Angeles, CA 90089, USA

³IFOM, FIRC Institute of Molecular Oncology, Via Adamello 16, 20139 Milano, Italy

*Correspondence: vlongo@usc.edu

<http://dx.doi.org/10.1016/j.cell.2014.12.027>

The restriction of proteins has recently emerged as the most important factor for the beneficial effects of calorie restriction. Hine et al. now provide strong evidence for the role of the hydrogen sulfide (H₂S) gas in the protective effects of calorie and protein restriction against ischemia/reperfusion injury (IRI) but also implicate H₂S in longevity extension in model organisms.

A severe restriction of calories (CR) from all sources is among the most effective interventions to protect cells from toxins and extend both lifespan and healthspan, but it is the reduction in protein intake (PR) that has recently emerged as the most important factor responsible for life-

span- and healthspan-extending benefits (Bruce et al., 2013; Solon-Biet et al., 2014). In fact, the TOR-S6 kinase pathway, activated directly by certain amino acids, promotes aging in all major model organisms, and deficiency in insulin-IGF-1 signaling, which is induced by

protein restriction, is implicated in lifespan extension in worms, flies, mice, and possibly humans (Fontana et al., 2010). In rodents, chronic cycles in which a normal diet is alternated with one lacking essential amino acids are sufficient to reduce IGF-1 levels and delay cognitive

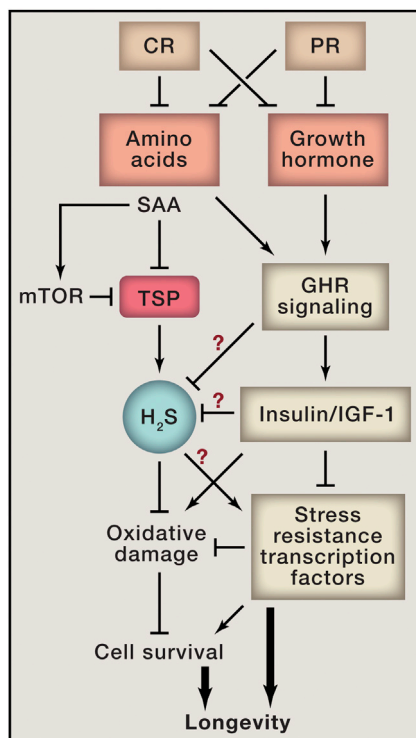


Figure 1. A Model for the Mechanisms of Calorie or Protein Restriction's Effects on Organismal Protection and Longevity

Specific sulfur amino acids activate nutrient-sensing pathways, including the insulin/IGF-1 and mTOR pathways, which accelerate the aging process in various organisms. Thus, CR, in part through protein/amino acid restriction, protects cells and organisms from stress by inhibiting insulin/IGF-1 and mTOR signaling and by switching cells to a stress-resistant mode characterized by entry into an alternative metabolic mode and H₂S generation. H₂S is important to prevent ischemia/reperfusion damage in the liver but has the potential to mediate many of the effects of CR/PR through yet poorly understood mechanisms.

decline in Alzheimer's disease models (Parrella et al., 2013), and in humans, a low protein intake is associated with reduced IGF-1 levels and a lower risk of mortality from all causes and cancer (Levine et al., 2014). Thus, the identification of the key nutrients regulating cellular protection and of the intracellular mediators of these effects is fundamental to the understanding of the mechanisms of aging. The ability of methionine deficiencies to lower IGF-1 and also protect against toxins (Miller et al., 2005) points to this essential sulfur amino acid as one of central importance in mediating the anti-aging effects of calorie restriction. In fact, methionine restriction extends life-

span in yeast, flies, and mice (Grandison et al., 2009; Miller et al., 2005; Ruckenstein et al., 2014). Thus, methionine can regulate the growth hormone-insulin-like growth factor 1 (GH-IGF-1) axis and probably the downstream mTOR-S6 kinase and PKA enzymes, as well as protective transcription factors (Figure 1). Although stress resistance transcription factors such as Msn2/4 in yeast and FOXOs in worms, flies, and mammals play essential roles in lifespan extension and can regulate both mitochondrial antioxidant enzymes and oxidative damage (Fontana et al., 2010), the underlying mechanisms connecting pro- and anti-aging pathways with stress resistance and longevity remain poorly understood.

In this issue of *Cell*, Hine and colleagues (2015) have now shed light on the mechanisms of CR-dependent protection by connecting calorie, protein, and methionine restriction to the activation of the transsulfuration pathway enzyme cystathionine γ -lyase (CGL), which is responsible for the generation of the gas hydrogen sulfide (H₂S). Restriction of all sources of calories or of only cysteine or methionine was sufficient to cause a major increase in H₂S and protection from hepatic ischemia reperfusion injury (IRI) in mice (Figure 1). This effect could be reversed by mTORC1 activation, indicating either that mTORC1 is functioning downstream of IGF-1 in this hepatic IR sensitization pathway or that cysteine and methionine can act directly to activate this kinase or upstream factors, as is well established for leucine (Sancak et al., 2008).

The demonstration that H₂S is not just a bystander but is, in fact, a mediator of the protective effects of CR came from the remarkable finding that injection of the H₂S precursor NaHS or H₂S itself in the drinking water conferred protection from the liver damage. Furthermore, CR did not protect mice lacking CGL from ischemia reperfusion injury, and CGL overexpression by adenoviral-mediated gene delivery improved the outcome after IRI. Evidence for a direct effect of H₂S on cellular stress resistance was generated by using an IRI in vitro hepatocyte model. H₂S protected a cultured hepatocyte cell line as well as primary hepatocytes during both the ischemic and reperfusion phases. To investigate

further the molecular mechanisms of H₂S-dependent stress resistance, Hine and colleagues studied the role of target mitochondrial proteins, previously shown to be sulfhydrated and protect against stress-dependent damage/death. They show that the knockdown of the sulfide quinone oxidoreductase (SQR), which transfers electrons from H₂S to coenzyme Q, reduces the ability of H₂S to protect cells from ischemia- and reperfusion-dependent damage. The hypothesis is that CR-dependent protection against ischemia could be due, in part, to the ability of H₂S to facilitate electron transport in the wake of limited nutrient supply and possibly also to the generation of sulfites or sulfates, which in bacteria can act as terminal electron acceptors for ATP production under hypoxic conditions.

In an alternative mechanism, which was not investigated in this study, H₂S could also act as a signaling molecule that can itself activate transcription factors controlling stress resistance and longevity (Figure 1). Thus, it will be interesting to determine whether H₂S could function both at the mitochondrial level to prevent oxidative damage and in the cytoplasm and nucleus to regulate enzymes and transcription factors that control cell protection and aging. In fact, the authors provide evidence for the association between H₂S and CR-dependent lifespan extension of yeast, worms, and flies independently of an ischemia-reperfusion challenge. In yeast, they show that glucose restriction induces endogenous H₂S production via the TSP from sulfur amino acids (SAAs) and that the exogenous H₂S donors, NaHS and GYY4137, added early to the culture, extended chronological longevity. In worms, the *eat-2* mutant, a genetic model of lifespan extension by CR, produced more H₂S gas, and knockdown of CBS-1, another enzyme, which promotes H₂S generation, decreased *eat-2*-mediated lifespan extension, while its overexpression extended the lifespan of wild-type controls. In flies, maximum H₂S production capacity was associated with diets that maximize lifespan.

Thus, multiple dietary-restricted regimens that promote longevity and healthspan, including single amino acid restriction, increased H₂S production in

organisms ranging from yeast to mice, indicating that generation of this gas may play a conserved protective role in many organisms, at least when generated at a specific concentration. In fact, H₂S has been traditionally regarded as a toxic gas, but recent findings indicate that it functions as a signaling molecule with potential therapeutic applications in a variety of conditions, including its remarkable ability to induce suspended animation in mice. Hine and colleagues have identified specific dietary interventions that result in the generation of protective levels of H₂S but also provided data that advance our understanding of the anti-aging mechanisms induced by CR/PR. The identification of drugs that induce the generation of protective levels of H₂S while eliminating the risk of toxic side effects could have important clinical applications for the treatment of a variety of acute conditions, such as ischemia/reperfusion and other types of damage associated with surgery. The chronic

use of drugs promoting H₂S for health-span extension could instead be much more problematic, as it is difficult to predict what the side effects caused by long-term use could be. If the effects described in model organisms are conserved in humans, protein restriction without malnutrition or the consumption of plant-based proteins with low sulfur amino acid content may represent a safer strategy to induce H₂S generation and take advantage of its protective effects.

REFERENCES

- Bruce, K.D., Hoxha, S., Carvalho, G.B., Yamada, R., Wang, H.D., Karayan, P., He, S., Brummel, T., Kapahi, P., and Ja, W.W. (2013). *Exp. Gerontol.* 48, 1129–1135.
- Fontana, L., Partridge, L., and Longo, V.D. (2010). *Science* 328, 321–326.
- Grandison, R.C., Piper, M.D., and Partridge, L. (2009). *Nature* 462, 1061–1064.
- Hine, C., Harputlugil, E., Zhang, Y., Ruckenstein, C., Lee, B.C., Brace, L., Longchamp, A., Treviño-Villarreal, J.H., Mejia, P., Ozaki, C.K., Wang, R., Gladyshev, V.N., Madeo, F., Mair, W.B., and Mitchell, J.R. (2015). *Cell* 160, this issue, 132–144.
- Levine, M.E., Suarez, J.A., Brandhorst, S., Balasubramanian, P., Cheng, C.W., Madia, F., Fontana, L., Mirisola, M.G., Guevara-Aguirre, J., Wan, J., et al. (2014). *Cell Metab.* 19, 407–417.
- Miller, R.A., Buehner, G., Chang, Y., Harper, J.M., Sigler, R., and Smith-Wheelock, M. (2005). *Aging Cell* 4, 119–125.
- Parrella, E., Maxim, T., Maialetti, F., Zhang, L., Wan, J., Wei, M., Cohen, P., Fontana, L., and Longo, V.D. (2013). *Aging Cell* 12, 257–268.
- Ruckenstein, C., Netzberger, C., Entfellner, I., Carmona-Gutierrez, D., Kickenweiz, T., Stekovic, S., Gleixner, C., Schmid, C., Klug, L., Sorgo, A.G., et al. (2014). *PLoS Genet.* 10, e1004347.
- Sancak, Y., Peterson, T.R., Shaul, Y.D., Lindquist, R.A., Thoreen, C.C., Bar-Peled, L., and Sabatini, D.M. (2008). *Science* 320, 1496–1501.
- Solon-Biet, S.M., McMahon, A.C., Ballard, J.W., Ruohonen, K., Wu, L.E., Cogger, V.C., Warren, A., Huang, X., Pichaud, N., Melvin, R.G., et al. (2014). *Cell Metab.* 19, 418–430.

Skeletal Stem Cells in Space and Time

Moustapha Kassem^{1,2,*} and Paolo Bianco^{3,*}

¹Department of Endocrinology; University Hospital of Odense, 5000 Odense C, Denmark

²The Danish Stem Cell Centre—DanStem, Panum Institute, University of Copenhagen, 2200 Copenhagen, Denmark

³Department of Molecular Medicine, Sapienza University of Rome, 00161 Rome, Italy

*Correspondence: mkassem@health.sdu.dk (M.K.), paolo.bianco@uniroma1.it (P.B.)

<http://dx.doi.org/10.1016/j.cell.2014.12.034>

The nature, biological characteristics, and contribution to organ physiology of skeletal stem cells are not completely determined. Chan et al. and Worthley et al. demonstrate that a stem cell for skeletal tissues, and a system of more restricted, downstream progenitors, can be identified in mice and demonstrate its role in skeletal tissue maintenance and regeneration.

The groundbreaking concept that bone, cartilage, marrow adipocytes, and hematopoiesis-supporting stroma could originate from a common progenitor and putative stem cell was surprising at the time when it was formulated (Owen and Friedenstein, 1988). The putative stem cell, nonhematopoietic in nature, would be found in the postnatal bone marrow stroma, generate tissues previously thought of as foreign to each other, and

support the turnover of tissues and organs that self-renew at a much slower rate compared to other tissues associated with stem cells (blood, epithelia). This concept also connected bone and bone marrow as parts of a single-organ system, implying their functional interplay. For many years, the evidence underpinning the concept has been incomplete. While multipotency of stromal progenitors has been demonstrated by in vivo transplan-

tation experiments, self-renewal, the defining property of a stem cell, has not been easily demonstrated until recently in humans (Sacchetti et al., 2007) and mice (Méndez-Ferrer et al., 2010). Meanwhile, a confusing and plethoric terminology has been introduced into the literature, which diverted and confounded the search for a skeletal stem cell and its physiological significance (Bianco et al., 2013).

Two studies in this issue of *Cell* (Chan et al., 2015; Worthley et al., 2015), using a combination of rigorous single-cell analyses and lineage tracing technologies, mark significant steps toward rectifying the course of skeletal stem cell discovery by making several important points, within and beyond skeletal physiology.

First, a stem cell for skeletal tissues, and a system of more restricted, downstream progenitors can in fact be identified and linked to defined phenotype(s) in the mouse. The system is framed conceptually, and approached experimentally, similar to the hematopoietic system.

Second, based on its assayable functions and potential, the stem cell at the top of the hierarchy is defined as a skeletal stem cell (SSC). As noted earlier (Sacchetti et al., 2007) (Bianco et al., 2013), this term clarifies, well beyond semantics, that the range of tissues that the self-renewing stromal progenitor (originally referred to as an “osteogenic” or “stromal” stem cell) (Owen and Friedenstein, 1988) can actually generate in vivo, overlaps with the range of tissues that make up the skeleton.

Third, these cells are spatially restricted, local residents of the bone/bone marrow organ. The systemic circulation is not a sizable contributor to their recruitment to locally deployed functions.

Fourth, a native skeletogenic potential is inherent to the system of progenitor/stem cells found in the skeleton, and internally regulated by bone morphogenetic protein (BMP) signaling. This is reflected in the expression of regulators and antagonists of BMP signaling within the system, highlighting potential feedback mechanisms modulating expansion or quiescence of specific cell compartments.

Fifth, in cells isolated from other tissues, an assayable skeletogenic potential is not inherent: it can only be induced de novo by BMP reprogramming. These two studies (Chan et al., 2015, Worthley et al., 2015) corroborate the classical concept of “determined” and “inducible” skeletal progenitors (Owen and Friedenstein, 1988): the former residing in the skeleton, the latter found in nonskeletal tissues; the former capable of generating skeletal tissues, in vivo and spontaneously, the latter requiring reprogramming signals in order to acquire a skeletogenic

capacity; the former operating in physiological bone formation, the latter in unwanted, ectopic bone formation in diseases such as fibrodysplasia ossificans progressiva.

A major question revolving around the concept of a SSC is how and to what extent it would contribute to postnatal physiology and adaptive changes in bone and bone marrow. Chan et al. show that SSCs (recruited locally, without significant contribution from the systemic circulation) can contribute to fracture healing. Worthley et al. show that ablation of SSCs can affect bone mass, which represents the endpoint of bone growth and a measure of skeletal health and disease. However, more studies are needed to determine in a quantitative manner the direct contribution of stem and progenitor cells to postnatal bone formation, maintenance of the skeleton, and also to fracture healing. We also need a better understanding of the mechanisms underpinning, at a tissue level, the recruitment and contribution of SSCs to the key microscopic events of lifelong bone renewal, which is important for translation of biological insight into medicine. Species specificities in patterns of bone and bone marrow remodeling, including the rate of adipogenesis in adulthood and aging, encourage efforts toward the further dissection of the system of skeletal progenitors in humans.

Both classical (Owen and Friedenstein, 1988) and recent observations (Omatsu et al., 2010; Zhou et al., 2014) support the concept of a common (stromal) progenitor for bone, cartilage, and marrow adipocytes comprised in bone as an organ. However, the lineage tracing studies of Chan et al. and Worthley et al. showing that stromal cells, osteoblasts, and chondrocytes, but not adipocytes, are clonally derived from SSCs, challenges this concept at a glance. The osteochondral-stromal clonogenic progenitors highlighted by the two studies may not coincide, in space and time, with those assayed by other studies and identified as perisinusoidal reticular cells (Sacchetti et al., 2007). Models accommodating spatially and temporally discrete cohorts of skeletal progenitors (Mizoguchi et al., 2014) need to be further explored. Indeed, in developing and growing bones, simultaneous, de novo chondrogenesis and

osteogenesis in the absence of adipogenesis occurs at specific sites distinct from bone marrow and at different developmental times. Likewise, bone and stromal cells, but hardly any adipocytes, are formed in the primary spongiosa of a growing long bone. Adipogenesis in bone marrow is a postnatal event and does not begin until specific times and at specific sites in different bones. Bone cells and adipocytes, but not chondrocytes, are generated in the marrow environment of an adult, aging or diseased bone, in a balanced fashion that implies a functional relationship (Abdallah and Kassem, 2012). Elucidating the relationship between bone and bone marrow fat will help tackling major clinically relevant issues such as osteoporosis and aging. This will also help to clarify the relationships, potential overlap, and at times apparent discrepancies, between several marker-defined populations of putative skeletal stem cells that have been proposed in multiple recent studies.

To optimize our ability to obtain specific skeletal tissues for medical application, the study by Chan et al. offers a glimpse of another facet of the biology of SSC lineages and progenitors. Chan et al. show that a homogeneous cell population inherently committed to chondrogenesis can alter its output to generate bone if cotransplanted with multipotent progenitors. Conversely, osteogenic cells can be shifted to a chondrogenic fate by blockade of vascular endothelial growth factor receptor, consistent with the avascular and hypoxic milieu of cartilage. This has two important implications: (1) commitment is flexible in the system; (2) the choir is as important as the soloist and can modulate the solo tune. Reversibility and population behavior thus emerge as two features that may be characteristic, albeit not unique, of the stromal system, resonating with conceptually comparable evidence in the human system.

The two studies by Chan et al. and Worthley et al. emphasize the relevance not only of their new data, but also of a proper concept of a skeletal stem cell per se, for proper clinical use. Confusion arising from improper conceptualization of skeletal stem cells has markedly limited clinical development of skeletal stem cell biology. New possibilities arise from these

studies for understanding and ultimately treating skeletal disorders.

REFERENCES

- Abdallah, B.M., and Kassem, M. (2012). *Bone* 50, 540–545.
- Bianco, P., Cao, X., Frenette, P.S., Mao, J.J., Robey, P.G., Simmons, P.J., and Wang, C.Y. (2013). *Nat. Med.* 19, 35–42.
- Chan, C.K.F., Seo, E.Y., Chen, J.Y., Lo, D., McArdle, A., Sinha, R., Tevlin, R., Seitla, J., Vincent-Tompkins, J., and Wearda, T. (2015). *Cell* 160, this issue, 285–298.
- Méndez-Ferrer, S., Michurina, T.V., Ferraro, F., Mazloom, A.R., Macarthur, B.D., Lira, S.A., Scadden, D.T., Ma'ayan, A., Enikolopov, G.N., and Frenette, P.S. (2010). *Nature* 466, 829–834.
- Mizoguchi, T., Pinho, S., Ahmed, J., Kunisaki, Y., Hanoun, M., Mendelson, A., Ono, N., Kronenberg, H.M., and Frenette, P.S. (2014). *Dev. Cell* 29, 340–349.
- Omatsu, Y., Sugiyama, T., Kohara, H., Kondoh, G., Fujii, N., Kohno, K., and Nagasawa, T. (2010). *Immunity* 33, 387–399.
- Owen, M., and Friedenstein, A.J. (1988). *Ciba Found. Symp.* 136, 42–60.
- Sacchetti, B., Funari, A., Michienzi, S., Di Cesare, S., Piersanti, S., Saggio, I., Tagliafico, E., Ferrari, S., Robey, P.G., Riminucci, M., and Bianco, P. (2007). *Cell* 131, 324–336.
- Worthley, D.L., Churchill, M., Compton, J.T., Taylor, Y., Rao, M., Si, Y., Levin, D., Schwartz, M.G., Uygur, A., Hayakawa, Y., et al. (2015). *Cell* 160, this issue, 269–284.
- Zhou, B.O., Yue, R., Murphy, M.M., Peyer, J.G., and Morrison, S.J. (2014). *Cell Stem Cell* 15, 154–168.

Reservoir Host Immune Responses to Emerging Zoonotic Viruses

Judith N. Mandl,^{1,7,*} Rafi Ahmed,² Luis B. Barreiro,³ Peter Daszak,⁴ Jonathan H. Epstein,⁴ Herbert W. Virgin,⁵ and Mark B. Feinberg⁶

¹Lymphocyte Biology Section, Laboratory of Systems Biology, NIAID, National Institutes of Health, Bethesda, MD 20892, USA

²Emory Vaccine Center, Emory University School of Medicine, Atlanta, GA 30322, USA

³Sainte-Justine Hospital Research Centre, Department of Pediatrics, University of Montreal, Montreal, QC H3T 1J4, Canada

⁴EcoHealth Alliance, New York, NY 10001, USA

⁵Department of Pathology & Immunology, Washington University School of Medicine, St. Louis, MO 63110, USA

⁶Merck Vaccines, Merck & Co. Inc., West Point, PA 19486, USA

⁷Present address: Department of Physiology and Complex Traits Group, McGill University, Montreal, QC H3G 0B1, Canada

*Correspondence: mandlj@niaid.nih.gov

<http://dx.doi.org/10.1016/j.cell.2014.12.003>

Zoonotic viruses, such as HIV, Ebola virus, coronaviruses, influenza A viruses, hantaviruses, or he-nipaviruses, can result in profound pathology in humans. In contrast, populations of the reservoir hosts of zoonotic pathogens often appear to tolerate these infections with little evidence of disease. Why are viruses more dangerous in one species than another? Immunological studies investigating quantitative and qualitative differences in the host-virus equilibrium in animal reservoirs will be key to answering this question, informing new approaches for treating and preventing zoonotic diseases. Integrating an understanding of host immune responses with epidemiological, ecological, and evolutionary insights into viral emergence will shed light on mechanisms that minimize fitness costs associated with viral infection, facilitate transmission to other hosts, and underlie the association of specific reservoir hosts with multiple emerging viruses. Reservoir host studies provide a rich opportunity for elucidating fundamental immunological processes and their underlying genetic basis, in the context of distinct physiological and metabolic constraints that contribute to host resistance and disease tolerance.

Introduction

Emerging infectious diseases have an enormous impact on human health (Marston et al., 2014). Viruses account for a significant proportion of emerging infections, and the majority have zoonotic origins, including ebolaviruses, human immunodeficiency virus (HIV), hantaviruses, Hendra and Nipah viruses, severe acute respiratory syndrome (SARS) coronavirus, and influenza A viruses (Jones et al., 2008; Taylor et al., 2001). Transmission can occur directly to people from live reservoir hosts (e.g., bat shedding of Nipah virus into date palm collection vessels [Luby et al., 2006]). In other instances, exposures to novel viruses have been associated with the butchering of reservoir hosts, such as bush meat in SIV or simian foamy virus transmission (Hahn et al., 2000; Wolfe et al., 2004) and, recently, in the index case of the ebolavirus outbreak in the Democratic Republic of Congo (WHO, 2014). Alternatively, transmission can be facilitated by intermediate hosts (e.g., Nipah virus infection of pigs in Malaysia resulting in pig-to-pig and pig-to-human transmission by aerosol [Parashar et al., 2000]) or can be transferred via insect vectors, as is the case for Dengue fever and West Nile virus (Mackenzie and Jeggo, 2013). Substantial growth in size and mobility of human populations, along with environmental and climate changes, and the spread of agricultural practices promoting human-animal contact has led to an increased frequency

of pathogen emergence and potential for rapid dissemination (Karesh et al., 2012). Novel viruses are being described that cause disease in humans, such as the recently identified Middle East respiratory syndrome coronavirus (MERS-CoV) associated with acute respiratory illness and renal failure (Zaki et al., 2012). Other zoonotic viruses continue to spread into new populations, as is the case for a current outbreak of Ebola virus in western Africa, where this virus was not previously documented and where it is having an unprecedented societal, economic, and public health impact (Pandey et al., 2014; WHO Ebola Response Team, 2014).

Tools to rapidly detect and sequence novel viruses have greatly improved in recent years, facilitating their detection and diagnosis in humans (Marston et al., 2014) and simplifying the identification of putative reservoir hosts. For instance, the origins of Ebola virus, although first identified in 1976, were only recently tied to bats (Biek et al., 2006; Pigott et al., 2014). These tools are enabling initiatives to monitor viruses in wildlife populations in their natural habitat before they emerge in humans and other animals (Mokili et al., 2012; Morse et al., 2012). Ecological, epidemiological, and evolutionary processes involved in the introduction and spread of pathogens in novel host populations are the subject of intensive research (Antia et al., 2003; Holmes and Drummond, 2007; Woolhouse et al., 2012). However, there

is little understanding of the within-host immunological processes underlying reservoir host-virus interactions, and this issue is rarely addressed in studies of emerging viral diseases. Yet within-host processes are ultimately critical in determining the outcome of infection, the balance between limiting infection-associated pathology and clearing the virus, and therefore the likelihood of transmission.

Upon cross-species jumps, viruses can result in severe or fatal disease in the novel, non-natural hosts, while these same viruses often appear to cause only mild infections in their reservoir hosts. Examples exist in which circulating viruses can be lethal in reservoir host populations, as is the case for rabies virus in bat populations. But even rabies virus mortality rates were recently estimated using epidemiological models as being much lower in their natural bat reservoir (~10%) than in other mammals (Blackwood et al., 2013). As we will discuss, there have been few detailed direct studies of the pathogenesis of emerging viruses in their natural wildlife hosts, and given the notorious difficulty of measuring mortality rates in wildlife populations, some reservoir host populations could be affected to a greater degree than we currently understand. Longitudinal studies may reveal fitness costs, even when the symptoms of infection are far less pronounced than what is observed in non-natural human hosts. One documented example is simian immunodeficiency virus in chimpanzees (SIVcpz), the viral precursor of HIV-1 in humans. SIVcpz leads to detectable depletion of CD4⁺ T cells and is associated with shorter life spans and reduced reproductive success of wild chimpanzees (Keele et al., 2009). Although SIVcpz infection is less pathogenic in chimpanzees than HIV-1 in humans, it is not apathogenic. Whether this is related to the more recent acquisition of SIV by chimpanzees as compared to the older association of SIV with other African nonhuman primates is still unclear (Bailes et al., 2003). In contrast, SIV infection of sooty mangabeys and African green monkeys, two natural reservoir hosts of SIV, despite a high prevalence in the wild and persistent high-level viral replication, has no detectable impact on host survival or health (Keele et al., 2009; Pandrea and Apetrei, 2010; Silvestri et al., 2003). In fact, in many cases, available observations suggest that zoonotic viruses are able to persist in natural reservoir populations for significant periods of time with no overt signs of pathology.

Different viral zoonoses affecting humans are characterized by distinct biological and clinical manifestations, with many of them displaying a significant immunopathological component. Here, we argue that elucidating the nature of immune responses in individual natural hosts may inform our understanding of how virus-host equilibria are established without substantially impacting host health. Furthermore, this may provide insight into the mechanisms of disease pathogenesis and immunity in humans. We ask whether there are fundamental immunologic properties that govern different infection outcomes of natural reservoir species compared to non-natural human hosts while acknowledging that other aspects of host physiology, behavior, or population biology may also play fundamentally important roles. Further, we examine whether there are any immunological principles underlying the association of specific reservoir host species with multiple emerging viruses. Eventually, characterizing the host-pathogen interface in key reservoir hosts may

enable us to predict which novel viruses are more likely to pose threats to human health.

Pathogenesis of Emerging Viral Infections in Humans

The pathogenic mechanisms underlying disease manifestations arising in humans infected with specific emerging viruses—whether acute or chronic in nature—are diverse, complex, and incompletely understood. Infection outcomes may vary from resolving with only mild symptoms (e.g., simian foamy virus [Wolfe et al., 2004]) to rapid developing severe disease that is either fatal or cleared (e.g., ebolaviruses), whereas others are persistent and lead to disease only after a prolonged period (e.g., HIV). The balance between protective and pathogenic immune responses is critical (Rouse and Sehrawat, 2010). A pivotal role in this balance is played by innate immune effectors that detect the presence of viral products by pattern recognition receptors, thus initiating the host response (Iwasaki, 2012). The specific cytokines, chemokines, and lipid mediators produced in response to immune activation, as well as downstream adaptive responses that themselves can modulate the innate response, can skew the relative balance between aggressive responses that rapidly clear infection and responses that minimize the extent of immunopathology. Exuberant innate immune activation can also play a direct role in precipitating host organ tissue damage (Cameron et al., 2008; Kuiken et al., 2012).

Despite a range of virus-specific mechanisms for pathogenesis, some common themes exist. In emerging viral infections causing disease in humans in whom host responses have been studied, innate immune responses are often thought to underlie severe disease manifestations. In the acute respiratory infections with SARS CoV and influenza A, excessive innate immune activation causes local tissue damage and compromises the generation of protective adaptive immune responses (Kash et al., 2006; Peiris et al., 2010). During infection with highly pathogenic influenza A viruses, production of inflammatory cytokines and chemokines responsible for the recruitment of neutrophils and mononuclear cells to the site of infection contributes to the severity of the pulmonary disease and systemic complications (Kuiken et al., 2012; Peiris et al., 2010). In addition, other mediators of inflammation, including sphingosine phosphates, also play an important role in the immunopathogenesis of influenza tissue damage and disease (Oldstone and Rosen, 2014). Specific virus strains such as H5N1 and the 1918 H1N1 viruses are particularly potent in activating high-level sustained proinflammatory cytokine production following infection (Kash et al., 2006; Peiris et al., 2010). Similarly, the pathogenesis of SARS involves infection of important cell populations in the lung, along with the elicitation of high levels of a range of inflammatory mediators (Totura and Baric, 2012). Importantly, in individuals who resolve SARS CoV infections, evidence of active innate responses wane, and effective adaptive responses develop that clear the infection. By contrast, individuals with poor outcomes exhibit persistently elevated type I interferon (IFN) production, IFN-stimulated gene (ISG) expression, and chemokine production in association with impaired antiviral antibody responses (Cameron et al., 2008; Totura and Baric, 2012).

For emerging viruses that cause hemorrhagic fever, dysregulation of the host response, the induction of inflammatory

mediators, and the impairment of adaptive immunity, in addition to direct viral damage of host tissues, are central to pathogenesis (Geisbert and Jahrling, 2004). In fatal human filovirus infections (of which Ebola virus is the best studied), antigen-presenting cells, including dendritic cells and macrophages, represent important targets for virus infection *in vivo*. High levels of proinflammatory cytokines, chemokines, and tissue factor lead to lymphocyte apoptosis, pathologic activation of coagulation cascades, and widespread compromise of vascular integrity that results in multiorgan failure and a septic shock-like syndrome (Martinez et al., 2012; Misasi and Sullivan, 2014; Zampieri et al., 2007). In infections (for instance, with West Nile virus) in which encephalitis due to viral penetration of the blood-brain barrier leads to neuropathology, inflammatory responses may be responsible for blood-brain barrier compromise (Wang et al., 2004).

In HIV infection, a persistent yet ineffective host response in the face of chronic viral replication contributes substantially to pathogenesis. Erosion of immunocompetence was initially thought to arise from active virus replication causing progressive depletion of CD4⁺ T cell populations. However, more recent evidence indicates that chronic, pleiotropic immune activation (evidenced by increased activation, proliferation, apoptosis, and dysfunction across diverse immune effector cell populations) during HIV infection is the major driver of progressive immune deficiency leading to AIDS (Moir et al., 2011). A key contributor to chronic immune activation in HIV is the ability of unrelenting virus replication to stimulate host innate immune responses and the production of type I IFNs and other proinflammatory cytokines (Miedema et al., 2013). The resulting compromised infection resistance may further amplify systemic immune activation and exacerbate its damaging effects by resulting in the expansion of the enteric virome, damaging the intestinal epithelium and leading to the translocation of intestinal bacteria, viruses, and the antigens derived from them (Branchley et al., 2006; Handedley et al., 2012).

Of note, in many instances, viral proteins produced by emerging viruses antagonize specific immune recognition mechanisms or circumvent cell-intrinsic restriction factors, thereby influencing host antiviral responses and viral replication kinetics. Given the central role of type I IFN in the direct inhibition of viral replication within cells and in the activation and execution of host innate and adaptive immune responses, it is not surprising that diverse viral gene products have been shown to specifically block the induction or the effects of the host IFN response. Ebola virus VP35 and VP24, lassa virus NP, influenza virus NS1, SARS CoV NSP1, and ORF3b are just a few examples (Ayllon and Garcia-Sastre, 2015; Hastie et al., 2012; Totura and Baric, 2012). Viral products have also been demonstrated to intercept ISGs, other immune recognition pathways, restriction factors, or production of effector molecules (Menachery et al., 2014). Features of the virion, such as the complex structure and heavy glycosylation of the HIV-1 envelope protein gp120, can make them less effective targets for elicitation of neutralizing antibody responses or structurally impervious to them when they arise (Burton et al., 2005). Moreover, the viral genome itself plays a role in the rapid evasion of adaptive immune responses, with the generation of diverse viral quasispecies that is an inherent consequence of error-prone RNA replication mechanisms

(Holmes and Drummond, 2007). Thus, the efficacy of the host response to infection depends on the complex interplay of beneficial activation of innate and adaptive immune responses, the potency and impact of viral strategies for immune evasion, and the deleterious consequences of protracted or misdirected immune responses.

Reservoir Host Infection and Disease Tolerance

A number of nonmutually exclusive hypotheses might explain why many reservoir hosts of viruses capable of causing disease in humans or other animal hosts do not show severe clinical or behavioral signs of infection (Table 1): (1) the virus is cytopathic in the nonnatural host, but not in its reservoir, (2) viral tropism differs between natural and non-natural hosts, (3) differences in the interaction between the viral genome or viral gene products and host resistance mechanisms alter the infection outcome between natural and non-natural hosts, (4) the virus confers a benefit to the host that is not conferred to humans or other animal host species, (5) interactions within the zoonotic host between the virus and other elements of the microbiome alter the pathogenesis of infection in a manner that does not apply to humans, (6) reservoir host responses control viral replication more effectively, or (7) viral infection is better tolerated by reservoir hosts even when viral loads are high. In most cases, knowledge about the features of viral infections in their reservoir hosts and immune responses elicited is incomplete, and it remains unclear which of these explanations holds for particular zoonotic viruses (Table 1). Moreover, as-yet-undiscovered mechanisms may exist which the study of reservoir hosts could reveal.

In some cases, differences in viral tropism may influence the host-virus interface, resulting in reduced pathogenesis. For instance, in the sooty mangabey, a natural host for the SIV that is the origin of HIV-2, long-lived memory T cells may be more resistant to infection due to reduced CCR5 expression (a coreceptor for SIV) such that T cell homeostasis is preserved (Paar-dini et al., 2011). Similarly, memory CD4⁺ T cells in African green monkeys downmodulate CD4 expression, rendering them resistant to SIV infection and to infection-induced dysregulation of their homeostasis (Beaumont et al., 2009).

Alternatively, the role of viral genetic functions and structural attributes in shaping the nature and consequences of host-virus interactions may be distinct in natural versus non-natural hosts. Interestingly, most studies thus far have used non-natural hosts or their cells to explore the interaction of viral products with host resistance mechanisms and impact on viral virulence. In fact, much of our current understanding of viral immune evasion and restriction factor inhibition strategies has come from studies of emerging viruses. However, although these strategies can be fit in a logical framework in the context of a pathogenic infection, it is not clear how such regulatory and structural mechanisms function or evolved within a nonpathogenic reservoir host environment, whether they promote virus persistence or limit pathologic consequences of infection, and how they impact cross-species jumps. For example, the type I IFN-inducible host cell restriction factor tetherin, identified as a cellular factor that acts to restrict the release of newly produced HIV-1 particles from the surface of human cells, is antagonized by the HIV-1 accessory protein Vpu. Of the four

Table 1. Features of Emerging Viruses in the Natural Reservoir Hosts from which They Originated

Virus ^a (Family)	Genome	Pathogenesis in Humans	Natural Host	Features of Infection and Immune Response in Natural Host				
				Virus Replication	Innate Response	Ab/B Cell	T Cell	Treg
Bas-Congo (<i>Rhabdoviridae</i>)	–ssRNA	acute hemorrhagic fever	?	?	?	?	?	?
MERS Coronavirus (<i>Coronaviridae</i>)	+ssRNA	acute pneumonia, renal failure	bats, camels	?	?	?	?	?
Chikungunya (<i>Togaviridae</i>)	+ssRNA	high fever, skin rash, arthralgia	African primates	?	?	?	?	?
Crimean-Congo hemorrhagic fever (<i>Bunyaviridae</i>)	–ssRNA	hemorrhagic fever	hares, large herbivores?	?	?	+	?	?
Ebola (<i>Filoviridae</i>)	–ssRNA	hemorrhagic fever	fruit bats	?	?	+	?	?
Hanta (<i>Bunyaviridae</i>)	–ssRNA	hemorrhagic fever with renal syndrome, cardiopulmonary syndrome	rodents, shrews, and bats	P	anti-inflammatory	+	(+)	+
Hendra and Nipah (<i>Paramyxoviridae</i>)	–ssRNA	severe acute encephalitis, respiratory disease, systemic vasculitis	fruit bats	?	?	+ T/P	?	?
Hepatitis E (<i>Hepeviridae</i>)	+ssRNA	hepatitis	pigs	?	?	?	?	?
HIV (<i>Retroviridae</i>)	–ssRNA	AIDS	African primates	P (high)	diminished chronic type I IFN	(+) (low titres)	(+)	+
Influenza A (<i>Orthomyxoviridae</i>)	–ssRNA	respiratory disease	aquatic birds	T?	variations in innate signaling pathways	+	?	?
Lassa (<i>Arenaviridae</i>)	–ssRNA	mild febrile illness but can result in hemorrhagic fever	bats? rodents	P	?	+	?	?
Lymphocytic choriomeningitis (<i>Arenaviridae</i>)	–ssRNA	mild febrile illness to meningeal symptoms; fatal in immunocompromised	rodents ^b	P, T?	?	+	?	?
Menangle (<i>Paramyxoviridae</i>)	–ssRNA	influenza-like illness and rash	fruit bats	?	?	+	?	?
SARS coronavirus (<i>Coronaviridae</i>)	+ssRNA	progressive atypical pneumonia	horseshoe bats	?	?	+	?	?
Rabies (<i>Rhabdoviridae</i>)	–ssRNA	neurological disease	bats	T?	?	+ T?	?	?
Rift Valley fever (<i>Bunyaviridae</i>)	–ssRNA	hemorrhagic fever	?	?	?	?	?	?
West Nile (<i>Flaviviridae</i>)	+ssRNA	fever, meningoencephalitis	birds?	?	?	+	?	?
Yellow fever (<i>Flaviviridae</i>)	+ssRNA	hemorrhagic fever, jaundice	African primates	T	?	+	?	?

T, transient; P, persistent; ?, unknown; +, present; –, undetectable; (+), present but weak/low compared to non-natural hosts.

^aThe list is not exhaustive but highlights representative examples of emerging viral infections. See also [Table S1](#) for a complete list of references.

^bNote that, although LCMV infection of inbred laboratory mice is an extremely well-studied pathogen-host system and a lot is known about the immunological responses during chronic and acute LCMV infections, very little is known about LCMV infection in wild rodents, circulating strains, whether virus is cleared or persistent, and how much this depends on the rodent species and virus strain in question.

groups of HIV-1 (M, N, O, and P) that arose via independent transmission events from chimpanzees, only group M viruses have become pandemic—the group shown to possess the most potent anti-tetherin activities (Sauter, 2014). Tetherin also inhibits the egress of arenavirus, filovirus, and rhabdovirus particles from infected cells, and proteins such as Ebola virus GP_{1,2} counteract the effects of tetherin (Misasi and Sullivan, 2014; Sauter, 2014). But whether these have a similar role in their reservoir hosts remains to be examined.

Innate and adaptive immune cell development and their activation thresholds are calibrated by interactions with commensals or previous pathogen encounters. Thus, it is possible that the overall microbial environment of a reservoir host species contributes to altering the outcome of a viral infection. For example, helminth infection can either reactivate herpesviruses from latency through generation of cytokines that activate or repress viral promoters (Reese et al., 2014), or it can directly inhibit T cell responses (Osborne et al., 2014). Multiple studies now indicate that the microbiome alters host responses to viral and parasite infection (Virgin, 2014). In some cases, these prolonged relationships may confer a mutualistic symbiotic advantage to the host species (Barton et al., 2007). Thus, a reservoir host may tolerate a given chronic infection and offset any fitness cost of this infection by the benefit of altered host resistance to other pathogens. However, there are as yet few studies that explore this set of issues that might distinguish the outcome of infection between a natural host and humans (Virgin, 2014; Virgin et al., 2009).

Lastly, an important set of mechanisms that determine the capacity of a reservoir host to carry a dangerous virus may be the host's ability to tolerate the damage caused by a specific pathogen or by the immune responses raised to it. This parameter, termed disease or infection tolerance, is measured as the rate of change in disease severity as a function of pathogen loads and is in contrast to host resistance mechanisms, which reduce pathogen burden (Schneider and Ayres, 2008). Interestingly, evolutionary theory predicts that, because pathogens will engage in an arms race with the host to evade resistance mechanisms but there is no selection on pathogens to evade disease tolerance mechanisms, resistance traits will be more polymorphic in a population than tolerance traits (Roy and Kirchner, 2000). We note that immune tolerance as defined by diminished immune responses to a given antigen is only one component of disease tolerance. The concept of disease tolerance was first examined in the context of selective pressures exerted by parasites and herbivores on plant evolution, and it is only recently that studies have begun to examine disease tolerance in mammalian host-parasite interactions (Råberg et al., 2007; Regoes et al., 2014) and investigate the pathways involved (Figueiredo et al., 2013; Jamieson et al., 2013; Jeney et al., 2014; Rodrigue-Gervais et al., 2014; Weber et al., 2014). Characterizing disease tolerance mechanisms is of particular importance to understanding the absence of severe disease in reservoir hosts and in the development of methods able to modulate the human response to the same virus without the risk of selecting for viral evasion mechanisms. An immunologic understanding of reservoir host species biology will include the study of all mechanisms by which the host species minimizes the overall

fitness costs to the individual or the population, attendant on carrying a given pathogen in a form that is transmissible to humans.

Disease Tolerance and Transmission of Zoonotic Viruses

Determining the kinetics of viral replication, the extent of immune control, and parameters that might impact these, such as genetic variation, hibernation, pregnancy, or stress, may provide key insights into why some viruses are more likely to make cross-species jumps and why some of these cause severe disease in humans. Indeed, for many reservoir hosts, immune responses have not been characterized beyond demonstrating seroconversion (Table 1). Further, population-level persistence of emerging pathogens in their reservoirs has primarily been investigated from an ecological perspective, and the contribution of the host response to determining population-level infection dynamics within reservoirs is unclear. Experimental studies will provide critical data to improve field ecological studies by identifying which age classes, gender, or status of individual to focus on in studying transmission events. Experimental infections will also form the basis for improving dynamic modeling of infectious diseases, which is used to assess infection risk and develop better controls to prevent spillovers (Lloyd-Smith et al., 2009). A substantial list of important biological questions remains to be answered through focused experimental studies of the interfaces between various reservoir hosts and the specific viruses they harbor (Box 1).

The extent to which immune responses limit viral replication in reservoir hosts is likely an important factor in the probability of cross-species transmission. Chronic or repeated virus shedding in infected reservoirs increases the likelihood of transmission due to the greater number of virus particles in the inoculum for each exposed individual. In addition, immunological effector mechanisms that substantially restrict virus replication will affect viral genetic diversity and evolution in ways that may impact the spillover probability and the strain structure present in the reservoir host population (Box 1). A greater viral diversity may increase the chances that at least a few viral variants are able to successfully establish an infection in the novel host. Thus, we speculate that viruses that have either chronically high virus levels or repeated transient high pathogen burdens in their natural hosts may be overrepresented among emerging viral pathogens in humans (Figure 1).

Interestingly, experimental data has suggested that, in the case of malaria infection, increased tolerance may come at the cost of reduced resistance (Råberg et al., 2007). Such a tradeoff arises if resistance and tolerance are mechanistically connected. For instance, more aggressive effector responses that result in superior pathogen replication control may also be the responses that lead to increased collateral damage. Alternatively, such a tradeoff might be observed if resistance and tolerance are energetically costly, and it is only feasible to invest resources in one of the two strategies. Moreover, attenuated immune responses may result in waning immunologic memory. For instance, anti-yellow fever virus (YFV) antibody titers following YFV vaccination declined far more rapidly

Box 1. A Checklist for Studying Emerging Viruses in Reservoir Hosts

Organism-level features of infection	Host immune system-level features of infection	Virus-level features of infection
Infection route	Is infection acute or chronic?	Virus family and genetic material used
Age at infection	Is infection cleared or controlled by immune mechanisms? If the latter, which immune mechanisms are associated with viral control?	Determinants of cell tropism (receptor, intracellular restriction factors)
Identity/range of target cells	Kinetics and magnitude of viremia, shedding of virus from mucosal surfaces	Is the virus cytopathic in reservoir host or human cells? Is it able to become latent within cells?
Tissue distribution of infection pattern and timing/duration of virus shedding	What are the innate immune receptors involved in pathogen recognition? Do the recognition mechanisms differ between humans and reservoir host species?	What is the extent of viral genetic diversity within a host, and does it bear signatures of immune selection pressure?
Symptoms of infection: any diarrhea, sneezing, coughing; any pathology, tissue destruction, mortality, weight loss, temperature changes, or behavioral changes?	What innate and adaptive immune signaling pathways are triggered downstream of recognition receptors? Magnitude, peak response, response thresholds, spatio-temporal regulation?	What is the extent of viral genetic diversity between hosts? Are there distinct strains? Is there evidence for positive selection or antigenic drift?
Any fitness cost of infection (reduction in reproductive success, changes in life expectancy)?	Magnitude and nature of innate response (DCs, macrophages, NK cells)	Can the age of the association between the virus and the reservoir host be inferred from its phylogeny?
Any life history traits that impact host response, such as metabolic rate, hibernation, seasonal stressors?	Magnitude and nature of adaptive immune cell response (T cell and B cell)	What is the role of recombination, reassortment, or other mechanisms of viral diversification? What active mechanisms of immune evasion does the virus employ (e.g., antagonists, decoys, inhibition of restriction factors)?
Does pathogen exposure history or microbiome/virome impact infection outcome?	Magnitude, duration, neutralizing capacity of antibody response	Are there structural mechanisms of immune evasion (e.g., shielded Env domains, glycosylation)?
Is there evidence for infection resistance or infection tolerance?	Is there evidence for active suppression limiting immune responses to prevent immune-mediated pathology? If so, what are the mechanisms involved?	
	If virus is persistent, are there global gene expression changes, especially during acute vs. chronic infection phase?	
	Is there persistence or exhaustion of immune responses if virus is not cleared?	
	If infection is cleared, is host protected from reinfection (with homologous vs. heterologous strains)? What immune correlates are associated with protection?	

post infection in sooty mangabeys, a primate reservoir for YFV, than in YFV-disease susceptible rhesus macaques and humans (Mandi et al., 2011). Whether a tradeoff between resistance and tolerance is a generalized phenomenon remains to be investi-

gated. A study of the rate of decline in CD4⁺ T cells across different HIV viral load set points in humans found no relationship between resistance and tolerance, although it may be the case that such a link would only become apparent over a

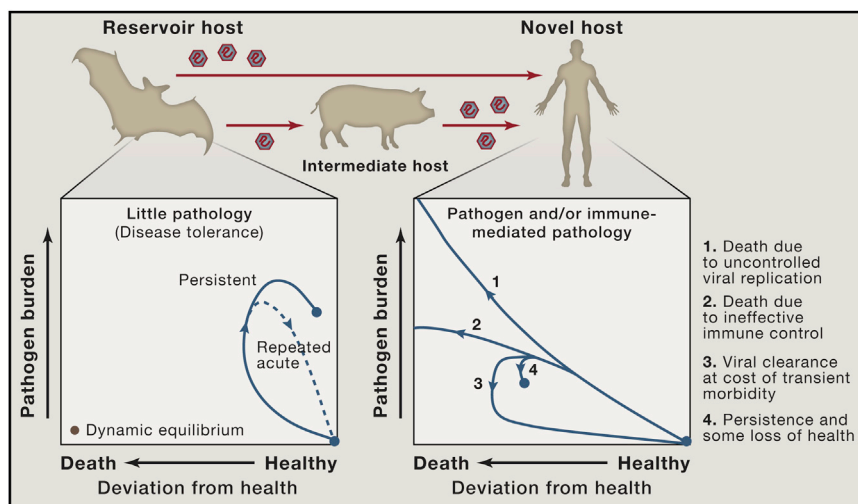


Figure 1. Reservoir Host Infection and Disease Tolerance

A feature of zoonotic infections in an individual natural host may be the tolerance of high pathogen burdens in the absence of substantial deviation from health. Phase plots (adapted from Schneider and Ayres [2008]) illustrating possible infection trajectories following infection to highlight differences between novel and reservoir hosts in the extent of viral replication, viral kinetics, and associated disease burden. Transmission of zoonotic viruses may be more likely in cases in which there are persistently high viral loads or repeated acute infections of reservoir hosts. Within a population of the reservoir host, repeated infections with a pathogen may occur as a result of waning immunological memory within individuals, circulation of diverse strains to which there is minimal cross-reactive immunity, or the introduction of new susceptible individuals (juveniles). To what extent and in which instances features of the immune response in reservoir hosts contribute to pathogen maintenance in a population is an important open question.

longer period of host-pathogen coevolution (Regoes et al., 2014).

Several examples have been described in which zoonotic viruses replicate at persistently high levels in their reservoirs. SIV establishes chronic infections in African primate species with high levels of viremia and little evidence of effective immune control (Pandrea and Apetrei, 2010; Silvestri et al., 2003). Hantavirus infections of rodent reservoirs result in persistence even in the presence of high antibody titers (Easterbrook and Klein, 2008; Schountz and Prescott, 2014). For both of these viruses, extensive within-host and between-host viral diversity has also been described in their natural hosts, and distinct strains are associated with distinct host species, suggestive of a coevolutionary history (Demma et al., 2005; Feuer et al., 1999).

In contrast, infections of wild waterfowl (*Anas platyrhynchos*) with influenza A virus were shown to be transient (Jourdain et al., 2010). Given the high prevalence of seropositivity and the presence of an enormous diversity of influenza A strains present in birds (Verhagen et al., 2012), this might be an example in which reservoir hosts previously infected with one strain are only partially protected from infection with co-circulating viral strains, but this requires further investigation. In pteropid fruit bat species, infections with Hendra and Nipah viruses are likely also transient, but few experimental infection studies have been done so far and the infection incidence is currently unknown (Halpin et al., 2011; Middleton et al., 2007). These viruses have been detected at a prevalence of around 1% or less, although seroprevalence can be as high as 60% (Breed et al., 2013; Rahman et al., 2013). Given the seasonal and synchronous breeding of these bats, it is difficult to distinguish whether there are seasonal increases in incidence due to infections of susceptible juveniles whose maternal antibodies have waned (Epstein et al., 2013), or changes in bat immunity that enable reinfections or the reactivation of low-level infections (Sohayati et al., 2011).

Clinical manifestations of infection, such as sneezing, coughing, or diarrhea, can facilitate transmission between humans

for certain zoonotic viruses where between-human secondary transmissions occur (Wolfe et al., 2007). SARS-CoV, for example, is transmitted by aerosolization and droplet infection between humans (Peiris et al., 2004), and Ebola virus spreads via contact with blood or body fluids (Dowell et al., 1999). In the absence of symptoms in disease-tolerant reservoir hosts, the routes of viral infection may be distinct from those observed in non-natural hosts. Whereas Nipah and Hendra virus is primarily respiratory in horses and pigs, transmitting oro-nasally (Geisbert et al., 2012), in bats, these viruses are shed in saliva and urine and may also be transmitted vertically (Halpin et al., 2000). For most zoonotic viruses, the transmission mode between reservoir hosts remains unknown.

Mechanisms of Disease Tolerance and Innate Immunity

Studying immune responses of reservoir hosts to their viruses provides a unique opportunity to define molecular mechanisms underlying disease tolerance and to identify therapeutic targets to prevent the dysregulated immunopathology that often characterizes infections of novel hosts. Mechanisms of disease tolerance (Schneider and Ayres, 2008) must have some degree of pathogen specificity to maintain immunocompetence. Innate immunity and mechanisms of recognizing viral invasion of cells are an important first line of host defense, and signals downstream of innate immune receptors play a key role in the magnitude of the immune response initiated (Iwasaki, 2012). Viruses can trigger endosomal, cell surface, or cytosolic innate immune receptors in a nucleic-acid-dependent manner (by their whole-genome, replication products or intermediates) or in a nucleic-acid-independent manner by virion glycoproteins or by more general changes associated with cellular stress (Iwasaki, 2012). It follows that investigating the innate immune recognition of zoonotic viruses in their reservoir hosts will provide important insight into how pathogen-specific disease tolerance is achieved.

Though innate recognition mechanisms are evolutionarily conserved, their complexity is becoming increasingly apparent. Regulatory factors are being identified that contribute to

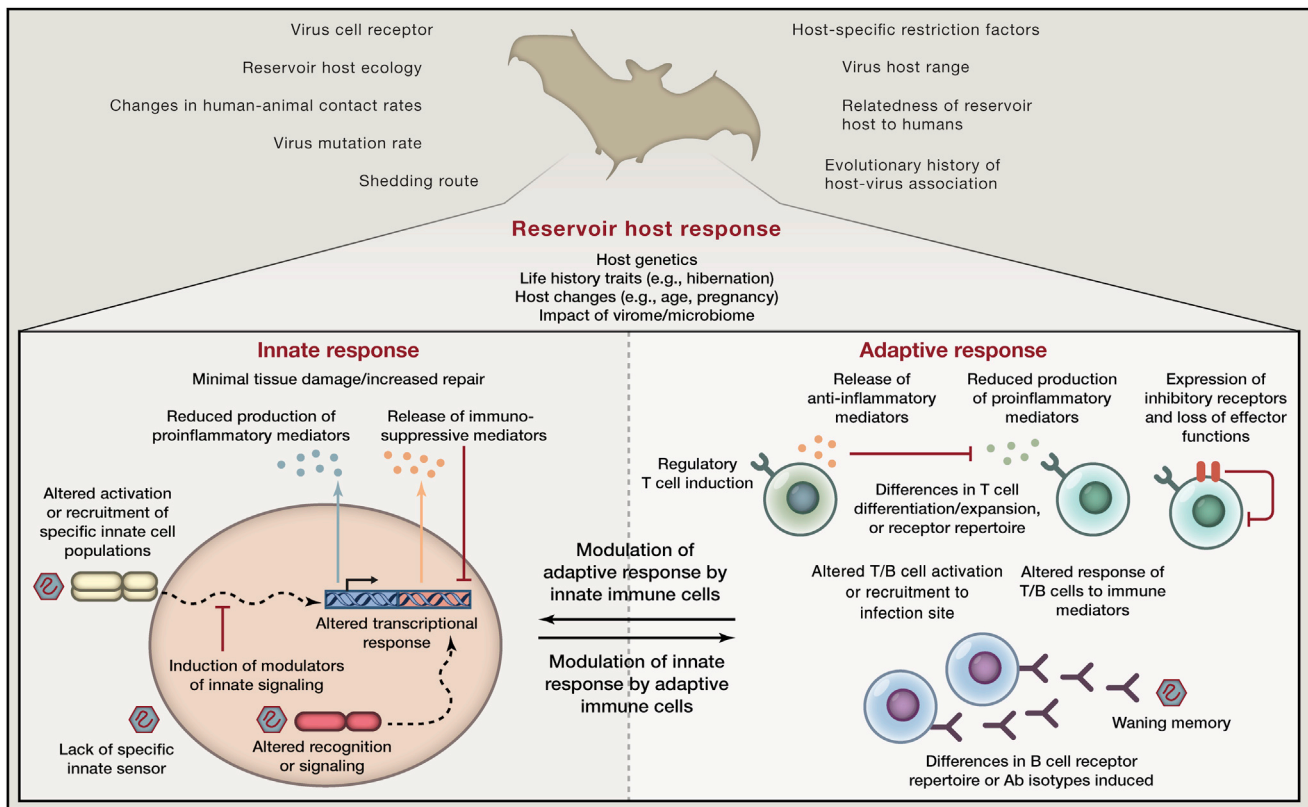


Figure 2. Differences in Immune Responses of Reservoir Hosts Impact Disease Tolerance, Infection Outcome, and the Probability of Emergence in Humans

Qualitative or quantitative aspects of innate or adaptive immune responses and their cross-talk may differ in reservoir hosts compared to novel hosts, impacting viral replication kinetics, decreasing pathology, and/or increasing the likelihood of transmission. Thus, reservoir host antiviral immunity may be one factor impacting the probability of emergence of a zoonotic virus in humans, in addition to other ecological, evolutionary, or virological risk factors.

amplifying or dampening signaling pathways downstream of innate receptors and impact the type and amount of cytokines produced (Qian and Cao, 2013). In addition, the existence of genetic heterogeneity within and between populations is emerging as an important factor contributing to host variation in innate immune responses to infection and susceptibility to disease (Lee et al., 2014; Pothlichet and Quintana-Murci, 2013). In contrast, an understanding of variation in quantitative parameters, such as measures of maximum response, half-maximal effective concentration, the dose of stimuli at which a response is initiated, the kinetics of the response, and the total magnitude of the response (by measures such as area under the curve), is still lagging behind, even in humans and mice, and may well turn out to be a critical aspect in explaining differences between hosts. Ultimately, heterogeneity in qualitative and quantitative aspects of an immune response and the selection pressure exerted by specific pathogens shapes the innate immune system of a species and thus impacts responses to future encounters with novel infectious agents (Barreiro and Quintana-Murci, 2010), as well as perhaps baseline cellular states (for which the relevant measures are not always clear). Yet, species-specific differences in responses to immune stimuli are only beginning to be described (Barreiro et al., 2010; Brinkworth et al., 2012; Seok et al., 2013).

In reservoir hosts, specific changes in innate immune recognition, innate signaling pathways, cross-talk with the adaptive immune system, or the generation and differentiation of B and T cells may play a key role in the disease tolerance to viruses that they harbor (Figure 2). Understanding which receptors, modulating factors, or deleterious molecular mediators are involved will allow us to target these in humans to alter infection outcome. For instance, blocking specific immune signaling pathways during pathogenic ebolavirus or henipavirus infection through which signaling is reduced in bat reservoir hosts upon infection may reduce tissue damage in humans. Alternatively, inhibiting specific ISGs found to be activated in non-natural hosts but that are quiescent in natural hosts may reduce downstream detrimental proinflammatory effects in infections such as HIV without preventing the antiviral effects of other ISGs induced, rather than blocking type I IFN completely (Sandler et al., 2014; Schoggins et al., 2011).

Innate immune responses can play a directly beneficial role in effecting early viral control following infection and are of fundamental importance in generating adaptive cellular and humoral immune responses required to limit virus replication. Thus, the absence of RIG-I, a sensor of viral RNA ligands, has been hypothesized to make chickens less resistant to influenza viruses

as compared to natural bird reservoirs such as ducks (Barber et al., 2010). However, specific innate immune responses may also precipitate immunopathologic consequences. For example, the absence of TLR3 leads to a reduced production of inflammatory mediators and improved survival upon infection with phlebovirus or influenza A viruses, despite similar or increased levels of viral replication (Gowen et al., 2006; Le Goffic et al., 2006). IL-17RA knockout mice infected with influenza A virus also display lower expression of inflammatory cytokines and chemokines, reduced lung inflammation, and improved survival despite having higher levels of virus replication as compared to wild-type laboratory inbred mice (Peiris et al., 2010). In addition, studies of different inbred mouse strains that are either susceptible or resistant to influenza-associated mortality have demonstrated greater activation of genes associated with inflammatory responses in susceptible mice and have begun to define the underlying genetic determinants of divergent infection outcomes (Peiris et al., 2010). Importantly, differences in responses between natural and non-natural hosts may not simply be due to the presence or absence of specific receptors or the switching on or off of specific signaling cascades. Rather, in the context of complex immune processes and cellular interactions, even small differences in the magnitude or timing of responses can substantially alter infection outcome. The use of mathematical models and careful measurements of rates of change of key response parameters may be required to ensure that such explanations are not missed.

Currently, the best-studied reservoir host responses are those of African primate species to SIV and of rodent species to hantavirus (Easterbrook and Klein, 2008; Miedema et al., 2013; Pandrea and Apetrei, 2010; Schountz and Prescott, 2014). Unlike humans infected with HIV, African primates do not develop the severe immune dysfunction and susceptibility to opportunistic infections that characterize AIDS. Pathogenic lentivirus infections in non-natural human or rhesus macaque hosts are associated with an elevated expression of ISGs and increased levels of immune activation, which includes increases in the activation and proliferation of T cells (Moir et al., 2011). During HIV infection, the majority of type I IFN production is likely due to the recognition of HIV by TLR7 expressed by pDCs (Beignon et al., 2005). However, in marked contrast to pathogenic HIV and SIV infections, an ISG expression signature is absent in sooty mangabeys during chronic SIV infection (Mandl et al., 2008). Further, chronically SIV-infected sooty mangabeys do not display elevations in aberrant T cell activation and its consequences (Silvestri et al., 2003). Whether the absence of chronic type I IFN production in sooty mangabeys is a result of reduced pDC activation by SIV or a function of actively suppressive mechanisms remains debated (Bosinger et al., 2013; Mandl et al., 2008). In African green monkeys, another reservoir host for SIV, a similar absence of an ISG expression signature during chronic SIV infection has been described (Jacquelin et al., 2009). In addition, SIV infection of African green monkeys is associated with an anti-inflammatory gene expression signature (Kornfeld et al., 2005). Interestingly, baseline cellular activation states, as measured by Ki67 on NK and T cells, are significantly lower in sooty mangabeys and African green monkey reservoir hosts than in the non-natural, AIDS-susceptible rhesus macaque host, though the rele-

vance of this for immune response parameters upon infection has not yet been explored (Mandl et al., 2008).

The situation in hantavirus-infected rodents has some notable parallels to host-virus interactions in SIV-infected primates. Rodents infected with hantavirus do not show signs of disease or of discernable fitness costs (Easterbrook and Klein, 2008; Schountz and Prescott, 2014). As in SIV-infected AGMs, induction of regulatory T cells at later stages of hantavirus infection, while resulting in viral persistence, reduces effector T cell responses and is thought to limit immunopathology (Table 1) (Easterbrook and Klein, 2008; Schountz and Prescott, 2014). Exactly how the switch from initial immune activation to a dampened response is mediated in rodents infected with hantavirus is still unclear. Specific viral proteins may interact with rodent immune pathways to limit proinflammatory responses while at the same time preventing clearance. Alternatively, or in addition, as may be the case for African primates infected with SIV, changes in innate recognition could directly lead to reduced pathology due to the reduction in the production of inflammatory mediators or due to the induction of responses that actively suppress damaging responses. Adaptive immune responses may also play a major role in modulating innate immunity in reservoir hosts. For example, cytokines secreted by activated T cells can activate or suppress innate cells, and antigen-antibody complexes impact innate cell function via Fc receptor signaling. The induction of inhibitory receptors on T cells, such as PD-1, can directly contribute to limiting T-cell-mediated pathology while preventing viral clearance (Barber et al., 2006; Frebel et al., 2012) (Figure 2). Recent data from chronically lymphocytic choriomeningitis virus (LCMV)-infected mice has highlighted that an expanded population of regulatory T cells dampens CD8⁺ T cell responses and that the depletion of regulatory T cells in conjunction with the blockade of PD-1 signaling substantially reduces viral load (Penaloza-MacMaster et al., 2014).

The innate sensors of nucleic acid engaged by a specific virus are a function of its genome. Therefore, the innate pathways important to sensing viruses with the same genomic composition or replication scheme often overlap substantially (Iwasaki, 2012). It has been hypothesized that viruses sharing cell tropism and features that result in their recognition by the same innate receptor, termed “virotypes,” will trigger the same host transcriptional response (Virgin, 2014). As a consequence of this, it is possible that changes in a discrete innate pathway predispose certain reservoir hosts to asymptotically harbor multiple viruses recognized by the same pathway if such changes increase disease tolerance to these virotypes in similar ways. Data from human studies have shown that deficiencies—in particular, innate receptor signaling molecules—can result in very defined and narrow susceptibilities to only a few specific pathogens (Al-Herz et al., 2014). Redundancies in immune recognition explain why reservoir host-pathogen associations might be very specific and thus not impair resistance to other pathogens. Sooty mangabeys, in addition to being reservoirs for SIV, are also natural hosts for yellow fever virus (YFV) and remain disease free upon infection. Studies of immune responses of sooty mangabeys to YFV have shown that, like for SIV, they mount reduced effector T cell responses following YFV infection compared to humans and macaques (Mandl et al., 2011). Both YFV and SIV

stimulate type I IFN upon recognition by TLR7, so this raises the intriguing possibility that specific changes in TLR7 signaling in sooty mangabeys impact their adaptive immune responses to these viruses.

Indeed, patterns of reservoir host and viral associations have been observed, but their biological significance is unclear, given the only very recent increase in comprehensive studies of species' viromes. For instance, bats are the reservoir of several emerging infectious agents, the majority of which are single-stranded RNA viruses, such as SARS coronavirus, MERS coronavirus, Nipah and Hendra viruses, rabies, and related lyssaviruses Menangle virus, Marburg, and Ebola viruses (Table 1). Bats may also be the ancient natural host reservoirs of the flavivirus hepatitis C (Quan et al., 2013). Is this merely a result of biases in sampling and analysis, or does the coevolution of a host with one virus of a given virotype open a window to infection with others of the same virotype? Is this a result of life history traits of bats and/or a function of species-specific variations in innate immune recognition of RNA viruses between humans and bats? Some studies have suggested that bats are disproportionately responsible for viral emergence relative to species diversity, but this conclusion and the reasons for the association of bats with zoonotic viruses remain a matter of debate (Luis et al., 2013; Olival et al., 2013). Interestingly, many viruses that cause persistent infections in humans use DNA as genomic material (Virgin et al., 2009). Is this entirely a property of these viruses or a result of a coevolution of our immune response with DNA virotypes that is different in other mammalian species with a distinct history of virus encounters? Zoonotic DNA viruses that cause disease in humans certainly exist, including monkeypox and herpes B viruses. A comparative and immune-centric understanding of virus-host relationships between virotypes and species will be required to investigate such questions. As our data set on host-virus associations increases, so will our ability to discern patterns and investigate their causes.

Reservoir Host Physiology, Metabolism, and Infection Tolerance

Studying reservoir host responses will enable us to more accurately measure the true physiological impact of emerging viruses on their coevolved host. The immune system is embedded in the complex physiology of an organism, and as such, infections and the immune responses that they elicit trigger behavioral, autonomic, endocrine, and metabolic effects. Soluble immune mediators like IL-1 and TNF α result in "sickness behavior," such as social withdrawal and decreases in food intake and motor activity in infected individuals (Dantzer et al., 2008). Specific changes in metabolism during inflammation can lead to cachexia, which is particularly well documented in *Mycobacterium tuberculosis* (once termed "consumption"), or HIV (once termed "slim disease") infections or to local changes in tissue microenvironment. In turn, metabolic processes and changes in body temperature can impact host immunity. Metabolic by-products can recruit immune cells to sites of infection, activate innate immune cells via recognition through the pattern recognition receptors, which also sense microbial products, and initiate the resolution of inflammation (Jin et al., 2013; Kominsky et al., 2010). Nutrients, metabolites, and oxygen availability within tissues can impact immune cell effector functions and immune ho-

meostasis (Pearce and Pearce, 2013; Sitkovsky and Lukashev, 2005).

It is possible that fundamental differences in reservoir host physiology and the circuitry that interfaces with the immune system are the consequence of distinct evolutionary tradeoffs between species and impact infection outcome or the resulting disease manifestations. For instance, bats have evolved unique life history traits that may have influenced their exposure to and interaction with pathogens in ways that have led to distinct virus-host detentes. Bats are capable of sustained flight and have exceptionally long lifespans despite their high metabolic rates and small body size (Wilkinson and South, 2002). Consistent with the idea that changes in energy metabolism were required to meet the extraordinary cost of flight, mitochondrial and nuclear genes involved in oxidative phosphorylation have undergone positive selection in bat lineages (Shen et al., 2010). Concomitant selection pressure on DNA damage repair pathway genes to prevent negative physiological effects of high metabolic rates caused by the release of reactive oxygen species may have had as yet undefined consequences for innate immune responses to viruses (Zhang et al., 2013). Hibernation has also been associated with altered immune cell function and reduced lymphocyte trafficking, an understanding of which could be key to explaining the devastating impact of White-nose syndrome in North American bat populations (Bouma et al., 2010; Meteyer et al., 2012).

An Experimental Toolkit for Reservoir Host Immunology

Detailed assessments of immune responses in reservoir host species have been challenging for a number of reasons. One practical constraint has been establishing colonies of reservoir host species to enable longitudinal experiments under controlled conditions. Immunological field studies, though valuable in specific instances, can be difficult to interpret given that pathogen exposure status between sampling time points is unknown and it may not always be possible to recapture the same individuals. However, keeping reservoir host colonies can require specific animal husbandry techniques, may involve training animals to accept available food sources not eaten in the wild, and can require access to special facilities to maintain the animals (such as aviaries to harbor bats or birds) and to perform infections with viruses that are often lethal to humans. Moreover, importing reservoir hosts from their country of origin can be costly, and quarantines are required to ascertain that they are free of the zoonotic pathogens dangerous to humans. The lack of experimental studies of wildlife reservoirs is also a product of our poor understanding of the true wildlife reservoirs for a number of recently emerged viruses. However, such studies, if conducted correctly, are critical to understanding pathogenesis and the risk of exposure for humans.

A second technical challenge to studies of reservoir host immunity has been the establishment of viral infection models that mimic infection in the wild and that are useful for investigating pathogen kinetics and immune responses over time in a setting where the time of infection is known and other environmental parameters can be controlled (Box 1). Extensive viral passaging in vitro, especially in cell lines that, while permissive for infection, may be quite distinct from cells infected in vivo, can

lead to the selection of viral variants that can no longer replicate effectively in the host of origin. Similarly, the use of clonal viruses can be problematic in recapitulating typical outcomes of natural infections should initiation of infection with diverse viral quasispecies be important. As such, the choice of viral inoculum can greatly influence the course of infection. For example, in studies of sooty mangabeys in which highly pathogenic SIV variants passaged in macaques were used, the infection was rapidly controlled, quite unlike the persistent high-level replication seen in natural infections (Kaur et al., 1998). Subsequent infection studies have used plasma samples harvested from SIV-infected sooty mangabeys (Mandl et al., 2008). In other instances, whether experimental infections of reservoir hosts recapitulate features of natural infection in the wild remains to be validated. Infections of bats with Nipah and Hendra viruses resulted in very few bats with detectable levels of viral replication, although in some instances seroconversion was seen nonetheless, and it is unclear whether this very low infection level mimics infections in the wild (Halpin et al., 2011; Middleton et al., 2007). Experimental rabies infections of bat reservoir hosts led to muscle weakness, paralysis, and reductions in body weight and were usually lethal (Turmelle et al., 2010), but it is difficult to extrapolate such studies to an understanding of the mortality rate of rabies in wild bat populations. In fact, epidemiological models of data gathered in field studies suggest that lethality upon rabies infection may be a far rarer outcome in wild bat populations than in the lab (Blackwood et al., 2013). Similarly, whereas LCMV infection of inbred mouse strains is one of the best-studied systems for viral immunity, surprisingly little is known about the immunologic and virologic characteristics of the host-virus interface in wild mouse species that are reservoir hosts for LCMV and other arenaviruses (Table 1) (Wade et al., 2002). Host genetic differences or small changes in the LCMV viral sequence can affect whether infections are chronic or acute (Ahmed et al., 1988). In addition, vertical transmission can lead to the establishment of a life-long viral carrier state with little adaptive immune responses raised. The dependence on the host-pathogen balance established on both strain and route of infection means that, without much information on this, it is currently difficult to extrapolate insights from laboratory experiments to infections of mice in the wild.

Notably, developing an infection model that recapitulates human disease and can be used to study host responses during pathogenic infections to perform comparative studies with natural hosts can also be challenging if laboratory mice are not susceptible to infection or are resistant to disease. In the former case, identification of the viral host cell receptor in humans can enable the development of mouse strains expressing this human protein on relevant cell types, thus enabling viral replication in mice. For instance, the expression of human dipeptidyl peptidase 4, the host cell receptor used by MERS coronavirus, in mice using adenovirus vector-mediated transduction successfully rendered mice susceptible to infection with MERS coronavirus (Zhao et al., 2014). In the case in which mice are permissive for infection but distinct host responses lead to only mild disease, the genetic traits contributing to disease susceptibility differences can be explored using a set of well-defined recombinant inbred mouse strains, the Collaborative Cross (Churchill

et al., 2004), as was recently done for Ebola virus infection (Rasmussen et al., 2014).

Investigating reservoir host immunity has also been hampered by the paucity of available immunological tools. This includes sequences of immunologically important genes, markers for cell populations of interest, and available monoclonal antibodies specific for such markers, as well as antibody tools to identify cytokines or chemokines produced by immune cell populations in vitro or in vivo. The development of such tools will be essential to increasing the kinds of questions that can be answered. Despite the difficulties that remain, recent methodological advances have enormous potential in their application to studies of immune responses of natural hosts and have opened new avenues of research.

First, there has been a rapid expansion in genomes sequenced for different reservoir host species. These sequences are themselves already informative. For instance, they allow insight into the presence or absence of specific innate receptors or cytokine mediators and provide clues as to the mechanism of B or T cell repertoire diversity generation and B cell isotypes present. Furthermore, comparative analyses can highlight genomic regions with changes of possible relevance to disease outcome upon infection and can generate hypotheses that can be tested further. A comparison between the *Pteropus alecto* and *Myotis davidii* bat genomes showed that several innate immune genes, including TLR7, were under positive selection in bat ancestors and that both species lack NK cell receptors for MHC-I, KLRs, and KIRs (Zhang et al., 2013). Genomic approaches complement the targeted sequencing of specific genes hypothesized to play a role in viral control and determination of their tissue distribution—for instance, the sequencing of specific cytokine genes in deer mice (*P. maniculatus*) reservoirs of hantavirus (Herbst et al., 2002) or interferon system genes and innate receptors in bat species (Baker et al., 2013). In addition, next-generation sequencing is rapidly emerging as a way to define the viruses that we may have to worry about as future emerging infections (Mokili et al., 2012) and when comparing the baseline microbiome or virome of different species, as well as documenting infection-related changes in their composition (Handley et al., 2012; Virgin, 2014).

Second, unbiased approaches can be used to probe both quantitative and qualitative changes in the transcriptome or proteome. The availability of reservoir host genomes or related species makes the use of microarray technology for gene expression profiling possible. Furthermore, even in the absence of a reference genome, next generation sequencing and the de novo assembly of transcripts, while computationally more challenging, now allows the assessment of gene expression. Such methods provide a promising means by which to illuminate gene expression changes—for instance, in infected versus uninfected reservoir hosts—and to allow comparisons with changes seen in infected humans. This approach has already been successfully applied to characterize responses of non-natural hosts to a number of pathogens, including infection with influenza A, SARS, and HIV (Cameron et al., 2008; Kash et al., 2006; Moir et al., 2011). Although such methods applied to bulk tissue samples may not be able to distinguish between the induction of genes from changes in cell distribution, they may identify specific

targets for further study. Eventually, the development of single-cell transcriptome analyses and computational tools to infer the presence of specific cell populations and their phenotype within bulk samples may provide additional insight when flow cytometric identification of immune cell populations using monoclonal antibodies is not possible.

Lastly, our increased understanding of the various innate immune receptors and the distinct components of pathogens that they recognize has resulted in the availability of tools with which to probe responses to specific receptor agonists *in vivo* and *in vitro*. Our knowledge of innate immunity enables us to make reasonable guesses as to which types of innate receptors might be relevant to the host-pathogen interface of particular viruses. This is particularly useful when the pathogen in question requires biosafety level 4 laboratories, thus making direct infection studies challenging. Together with the methods outlined above, it is now possible to determine which genes change their expression early on in response to the administration of, for instance, defined TLR agonists targeting the specific TLRs involved in innate recognition of the virus of interest. We can characterize specific gene circuits and their temporal regulation, comparing responses to what is seen in more well-studied species in that regard. It is also possible to measure differences in basal gene expression levels, as well as quantitative changes in response to different doses of relevant stimuli to obtain measures of the dynamic range of the response, the dose at which a response is initiated, and its duration. In addition, innate immunity can be probed in cross-sectional studies of animals, which can provide information on how infection itself can modulate immune responsiveness.

Conclusions

Given the threats to human health and economic development posed by emerging viral diseases, better understanding the nature and diversity of mechanisms responsible for the ability of reservoir hosts to tolerate viral infections and facilitate transmission to other host species is critical. Studies to date have focused primarily on viral detection and diversity, rather than on illuminating the nature of the host-virus equilibrium extant in their wild animal reservoirs. Achieving the goal of a holistic approach to understanding viral emergence will require the integration of immunological studies with investigations of animal physiology and metabolism, as well as the synthesis of such studies with epidemiological, ecological, and evolutionary insights of viral emergence. Cross-disciplinary collaborations between mechanism-targeted immunology and microbiology laboratories, veterinarians with experience in establishing colonies of wild species, and ecologists able to perform in-country field studies will be especially important in advancing our knowledge in this field. The enormous value of cross-geographical and interdisciplinary initiatives in understanding viral emergence has already been demonstrated by programs such as PREDICT, established by the U.S. Agency for International Development to detect emerging pandemic threats in partnership with local governments and scientists (Morse et al., 2012). It is also apparent in other cross-continental research teams' efforts, such as the multinational collaboration that promptly tracked the emergence and evolution of the Ebola virus variants responsible for the

ongoing outbreak in West Africa (Gire et al., 2014). The development of immunological reagents, in addition to the application of recently developed methods to define host genome sequences and to characterize patterns of host gene expression following infection or other experimental intervention, will yield valuable insights into immune responses elicited by emerging viruses in their natural hosts. Such studies may identify important pathways of pathogenesis in humans by elucidating why these infections result in such distinct infection outcomes in natural hosts and may indicate novel approaches for the treatment and prevention of zoonotic infections. They may also establish whether there are fundamental immunologic reasons—in addition to proposed behavioral, ecological, and evolutionary ones—to explain why certain animals, including bats, primates, and rodents, are most often implicated as the reservoir hosts for emerging viral zoonoses. Finally, studies of reservoir hosts stand to significantly advance our understanding of fundamental immunological processes contributing to host resistance and disease tolerance.

SUPPLEMENTAL INFORMATION

Supplemental Information includes one table and can be found with this article online at <http://dx.doi.org/10.1016/j.cell.2014.12.003>.

ACKNOWLEDGMENTS

We would like to thank Nienke Vrisekoop, Roland Regoes, and Ronald Germain for insightful comments, support, and advice during the preparation of this manuscript. We are also extremely grateful to Tony Schountz and our anonymous reviewers for their reading of the manuscript and their very thoughtful feedback. This work was supported, in part, by the Intramural Research Program of NIAID, NIH.

REFERENCES

- Ahmed, R., Simon, R.S., Matlobian, M., Kolhekar, S.R., Southern, P.J., and Freedman, D.M. (1988). Genetic analysis of *in vivo*-selected viral variants causing chronic infection: importance of mutation in the L RNA segment of lymphocytic choriomeningitis virus. *J. Virol.* 62, 3301–3308.
- Al-Herz, W., Bousfiha, A., Casanova, J.L., Chatila, T., Conley, M.E., Cunningham-Rundles, C., Etzioni, A., Franco, J.L., Gaspar, H.B., Holland, S.M., et al. (2014). Primary immunodeficiency diseases: an update on the classification from the international union of immunological societies expert committee for primary immunodeficiency. *Front. Immunol.* 5, 162.
- Antia, R., Regoes, R.R., Koella, J.C., and Bergstrom, C.T. (2003). The role of evolution in the emergence of infectious diseases. *Nature* 426, 658–661.
- Ayllon, J., and Garcia-Sastre, A. (2015). The NS1 protein: A multitasking virulence factor. *Curr. Top. Microbiol. Immunol.* 386, 73–107.
- Bailes, E., Gao, F., Bibollet-Ruche, F., Courgnaud, V., Peeters, M., Marx, P.A., Hahn, B.H., and Sharp, P.M. (2003). Hybrid origin of SIV in chimpanzees. *Science* 300, 1713.
- Baker, M.L., Schountz, T., and Wang, L.F. (2013). Antiviral immune responses of bats: a review. *Zoonoses Public Health* 60, 104–116.
- Barber, D.L., Wherry, E.J., Masopust, D., Zhu, B., Allison, J.P., Sharpe, A.H., Freeman, G.J., and Ahmed, R. (2006). Restoring function in exhausted CD8 T cells during chronic viral infection. *Nature* 439, 682–687.
- Barber, M.R., Aldridge, J.R., Jr., Webster, R.G., and Magor, K.E. (2010). Association of RIG-I with innate immunity of ducks to influenza. *Proc. Natl. Acad. Sci. USA* 107, 5913–5918.
- Barreiro, L.B., and Quintana-Murci, L. (2010). From evolutionary genetics to human immunology: how selection shapes host defence genes. *Nat. Rev. Genet.* 11, 17–30.

- Barreiro, L.B., Marioni, J.C., Blekhman, R., Stephens, M., and Gilad, Y. (2010). Functional comparison of innate immune signaling pathways in primates. *PLoS Genet.* 6, e1001249.
- Barton, E.S., White, D.W., Cathelyn, J.S., Brett-McClellan, K.A., Engle, M., Diamond, M.S., Miller, V.L., and Virgin, H.W., 4th. (2007). Herpesvirus latency confers symbiotic protection from bacterial infection. *Nature* 447, 326–329.
- Beaumier, C.M., Harris, L.D., Goldstein, S., Klatt, N.R., Whitted, S., McGinty, J., Apetrei, C., Pandrea, I., Hirsch, V.M., and Brechley, J.M. (2009). CD4 downregulation by memory CD4+ T cells in vivo renders African green monkeys resistant to progressive SIVagm infection. *Nat. Med.* 15, 879–885.
- Beignon, A.S., McKenna, K., Skoberne, M., Manches, O., DaSilva, I., Kavanagh, D.G., Larsson, M., Gorelick, R.J., Lifson, J.D., and Bhardwaj, N. (2005). Endocytosis of HIV-1 activates plasmacytoid dendritic cells via Toll-like receptor-viral RNA interactions. *J. Clin. Invest.* 115, 3265–3275.
- Biek, R., Walsh, P.D., Leroy, E.M., and Real, L.A. (2006). Recent common ancestry of Ebola Zaire virus found in a bat reservoir. *PLoS Pathog.* 2, e90.
- Blackwood, J.C., Streicker, D.G., Altizer, S., and Rohani, P. (2013). Resolving the roles of immunity, pathogenesis, and immigration for rabies persistence in vampire bats. *Proc. Natl. Acad. Sci. USA* 110, 20837–20842.
- Bosinger, S.E., Johnson, Z.P., Folkner, K.A., Patel, N., Hashempour, T., Jochims, S.P., Del Rio Estrada, P.M., Paiardini, M., Lin, R., Vanderford, T.H., et al. (2013). Intact type I Interferon production and IRF7 function in sooty mangabeys. *PLoS Pathog.* 9, e1003597.
- Bouma, H.R., Carey, H.V., and Kroese, F.G. (2010). Hibernation: the immune system at rest? *J. Leukoc. Biol.* 88, 619–624.
- Breed, A.C., Meers, J., Sendow, I., Bossart, K.N., Barr, J.A., Smith, I., Wacharapluesadee, S., Wang, L., and Field, H.E. (2013). The distribution of henipaviruses in Southeast Asia and Australasia: is Wallace's line a barrier to Nipah virus? *PLoS ONE* 8, e61316.
- Brechley, J.M., Price, D.A., Schacker, T.W., Asher, T.E., Silvestri, G., Rao, S., Kazzaz, Z., Bornstein, E., Lambotte, O., Altmann, D., et al. (2006). Microbial translocation is a cause of systemic immune activation in chronic HIV infection. *Nat. Med.* 12, 1365–1371.
- Brinkworth, J.F., Pechenkina, E.A., Silver, J., and Goyert, S.M. (2012). Innate immune responses to TLR2 and TLR4 agonists differ between baboons, chimpanzees and humans. *J. Med. Primatol.* 41, 388–393.
- Burton, D.R., Stanfield, R.L., and Wilson, I.A. (2005). Antibody vs. HIV in a clash of evolutionary titans. *Proc. Natl. Acad. Sci. USA* 102, 14943–14948.
- Cameron, M.J., Bermejo-Martin, J.F., Danesh, A., Muller, M.P., and Kelvin, D.J. (2008). Human immunopathogenesis of severe acute respiratory syndrome (SARS). *Virus Res.* 133, 13–19.
- Churchill, G.A., Airey, D.C., Allayee, H., Angel, J.M., Attie, A.D., Beatty, J., Beavis, W.D., Belknap, J.K., Bennett, B., Berrettini, W., et al.; Complex Trait Consortium (2004). The Collaborative Cross, a community resource for the genetic analysis of complex traits. *Nat. Genet.* 36, 1133–1137.
- Dantzer, R., O'Connor, J.C., Freund, G.G., Johnson, R.W., and Kelley, K.W. (2008). From inflammation to sickness and depression: when the immune system subjugates the brain. *Nat. Rev. Neurosci.* 9, 46–56.
- Demma, L.J., Logsdon, J.M., Jr., Vanderford, T.H., Feinberg, M.B., and Stappans, S.I. (2005). SIVsm quasispecies adaptation to a new simian host. *PLoS Pathog.* 1, e3.
- Dowell, S.F., Mukunu, R., Ksiazek, T.G., Khan, A.S., Rollin, P.E., and Peters, C.J. (1999). Transmission of Ebola hemorrhagic fever: a study of risk factors in family members, Kikwit, Democratic Republic of the Congo, 1995. *Commission de Lutte contre les Epidémies à Kikwit. J. Infect. Dis.* 179 (Suppl 1), S87–S91.
- Easterbrook, J.D., and Klein, S.L. (2008). Immunological mechanisms mediating hantavirus persistence in rodent reservoirs. *PLoS Pathog.* 4, e1000172.
- Epstein, J.H., Baker, M.L., Zambrana-Torrel, C., Middleton, D., Barr, J.A., Dubovi, E., Boyd, V., Pope, B., Todd, S., Crameri, G., et al. (2013). Duration of Maternal Antibodies against Canine Distemper Virus and Hendra Virus in Pteropid Bats. *PLoS ONE* 8, e67584.
- Feuer, R., Boone, J.D., Netski, D., Morzunov, S.P., and St Jeor, S.C. (1999). Temporal and spatial analysis of Sin Nombre virus quasispecies in naturally infected rodents. *J. Virol.* 73, 9544–9554.
- Figueiredo, N., Chora, A., Raquel, H., Pejanovic, N., Pereira, P., Hartleben, B., Neves-Costa, A., Moita, C., Pedrosa, D., Pinto, A., et al. (2013). Anthracyclines induce DNA damage response-mediated protection against severe sepsis. *Immunity* 39, 874–884.
- Frebel, H., Nindl, V., Schuepbach, R.A., Braunschweiler, T., Richter, K., Vogel, J., Wagner, C.A., Löffing-Cueni, D., Kurrer, M., Ludewig, B., and Oxenius, A. (2012). Programmed death 1 protects from fatal circulatory failure during systemic virus infection of mice. *J. Exp. Med.* 209, 2485–2499.
- Geisbert, T.W., and Jahrling, P.B. (2004). Exotic emerging viral diseases: progress and challenges. *Nat. Med. Suppl.* 10, S110–S121.
- Geisbert, T.W., Feldmann, H., and Broder, C.C. (2012). Animal challenge models of henipavirus infection and pathogenesis. *Curr. Top. Microbiol. Immunol.* 359, 153–177.
- Gire, S.K., Goba, A., Andersen, K.G., Sealfon, R.S., Park, D.J., Kanneh, L., Jalloh, S., Momoh, M., Fullah, M., Dudas, G., et al. (2014). Genomic surveillance elucidates Ebola virus origin and transmission during the 2014 outbreak. *Science* 345, 1369–1372.
- Gowen, B.B., Hoopes, J.D., Wong, M.H., Jung, K.H., Isakson, K.C., Alexopoulos, L., Flavell, R.A., and Sidwell, R.W. (2006). TLR3 deletion limits mortality and disease severity due to Phlebovirus infection. *J. Immunol.* 177, 6301–6307.
- Hahn, B.H., Shaw, G.M., De Cock, K.M., and Sharp, P.M. (2000). AIDS as a zoonosis: scientific and public health implications. *Science* 287, 607–614.
- Halpin, K., Young, P.L., Field, H.E., and Mackenzie, J.S. (2000). Isolation of Hendra virus from pteropid bats: a natural reservoir of Hendra virus. *J. Gen. Virol.* 81, 1927–1932.
- Halpin, K., Hyatt, A.D., Fogarty, R., Middleton, D., Bingham, J., Epstein, J.H., Rahman, S.A., Hughes, T., Smith, C., Field, H.E., and Daszak, P.; Henipavirus Ecology Research Group (2011). Pteropid bats are confirmed as the reservoir hosts of henipaviruses: a comprehensive experimental study of virus transmission. *Am. J. Trop. Med. Hyg.* 85, 946–951.
- Handley, S.A., Thackray, L.B., Zhao, G., Presti, R., Miller, A.D., Droit, L., Ab-bink, P., Maxfield, L.F., Kambal, A., Duan, E., et al. (2012). Pathogenic simian immunodeficiency virus infection is associated with expansion of the enteric virome. *Cell* 151, 253–266.
- Hastie, K.M., Bale, S., Kimberlin, C.R., and Saphire, E.O. (2012). Hiding the evidence: two strategies for innate immune evasion by hemorrhagic fever viruses. *Curr. Opin. Virol.* 2, 151–156.
- Herbst, M.M., Prescott, J., Palmer, A.D., and Schountz, T. (2002). Sequence and expression analysis of deer mouse interferon-gamma, interleukin-10, tumor necrosis factor, and lymphotoxin-alpha. *Cytokine* 17, 203–213.
- Holmes, E.C., and Drummond, A.J. (2007). The evolutionary genetics of viral emergence. *Curr. Top. Microbiol. Immunol.* 375, 51–66.
- Iwasaki, A. (2012). A virological view of innate immune recognition. *Annu. Rev. Microbiol.* 66, 177–196.
- Jacquelin, B., Mayau, V., Targat, B., Liovat, A.S., Kunkel, D., Petitjean, G., Dillies, M.A., Roques, P., Butor, C., Silvestri, G., et al. (2009). Nonpathogenic SIV infection of African green monkeys induces a strong but rapidly controlled type I IFN response. *J. Clin. Invest.* 119, 3544–3555.
- Jamieson, A.M., Pasman, L., Yu, S., Gamradt, P., Homer, R.J., Decker, T., and Medzhitov, R. (2013). Role of tissue protection in lethal respiratory viral-bacterial coinfection. *Science* 340, 1230–1234.
- Jeney, V., Ramos, S., Bergman, M.L., Bechmann, I., Tischer, J., Ferreira, A., Oliveira-Marques, V., Janse, C.J., Rebelo, S., Cardoso, S., et al. (2014). Control of disease tolerance to malaria by nitric oxide and carbon monoxide. *Cell Rep.* 8, 126–136.
- Jin, C., Henao-Mejia, J., and Flavell, R.A. (2013). Innate immune receptors: key regulators of metabolic disease progression. *Cell Metab.* 17, 873–882.

- Jones, K.E., Patel, N.G., Levy, M.A., Storeygard, A., Balk, D., Gittleman, J.L., and Daszak, P. (2008). Global trends in emerging infectious diseases. *Nature* 451, 990–993.
- Jourdain, E., Gunnarsson, G., Wahlgren, J., Latorre-Margalef, N., Bröjer, C., Sahlin, S., Svensson, L., Waldenström, J., Lundkvist, A., and Olsen, B. (2010). Influenza virus in a natural host, the mallard: experimental infection data. *PLoS ONE* 5, e8935.
- Karesh, W.B., Dobson, A., Lloyd-Smith, J.O., Lubroth, J., Dixon, M.A., Bennett, M., Aldrich, S., Harrington, T., Formenty, P., Loh, E.H., et al. (2012). Ecology of zoonoses: natural and unnatural histories. *Lancet* 380, 1936–1945.
- Kash, J.C., Tumpey, T.M., Proll, S.C., Carter, V., Perwitasari, O., Thomas, M.J., Basler, C.F., Palese, P., Taubenberger, J.K., García-Sastre, A., et al. (2006). Genomic analysis of increased host immune and cell death responses induced by 1918 influenza virus. *Nature* 443, 578–581.
- Kaur, A., Grant, R.M., Means, R.E., McClure, H., Feinberg, M., and Johnson, R.P. (1998). Diverse host responses and outcomes following simian immunodeficiency virus SIVmac239 infection in sooty mangabeys and rhesus macaques. *J. Virol.* 72, 9597–9611.
- Keele, B.F., Jones, J.H., Terio, K.A., Estes, J.D., Rudicell, R.S., Wilson, M.L., Li, Y., Learn, G.H., Beasley, T.M., Schumacher-Stankey, J., et al. (2009). Increased mortality and AIDS-like immunopathology in wild chimpanzees infected with SIVcpz. *Nature* 460, 515–519.
- Kominsky, D.J., Campbell, E.L., and Colgan, S.P. (2010). Metabolic shifts in immunity and inflammation. *J. Immunol.* 184, 4062–4068.
- Kornfeld, C., Ploquin, M.J.Y., Pandrea, I., Faye, A., Onanga, R., Apetrei, C., Poaty-Mavoungou, V., Rouquet, P., Estaquier, J., Mortara, L., et al. (2005). Antiinflammatory profiles during primary SIV infection in African green monkeys are associated with protection against AIDS. *J. Clin. Invest.* 115, 1082–1091.
- Kuiken, T., Riteau, B., Fouchier, R.A., and Rimmelzwaan, G.F. (2012). Pathogenesis of influenza virus infections: the good, the bad and the ugly. *Curr. Opin. Virol.* 2, 276–286.
- Le Goffic, R., Balloy, V., Lagranderie, M., Alexopoulou, L., Escriou, N., Flavell, R., Chignard, M., and Si-Tahar, M. (2006). Detrimental contribution of the Toll-like receptor (TLR)3 to influenza A virus-induced acute pneumonia. *PLoS Pathog.* 2, e53.
- Lee, M.N., Ye, C., Villani, A.C., Raj, T., Li, W., Eisenhaure, T.M., Imboywa, S.H., Chipendo, P.I., Ran, F.A., Slowikowski, K., et al. (2014). Common genetic variants modulate pathogen-sensing responses in human dendritic cells. *Science* 343, 1246980.
- Lloyd-Smith, J.O., George, D., Pepin, K.M., Pitzer, V.E., Pulliam, J.R., Dobson, A.P., Hudson, P.J., and Grenfell, B.T. (2009). Epidemic dynamics at the human-animal interface. *Science* 326, 1362–1367.
- Luby, S.P., Rahman, M., Hossain, M.J., Blum, L.S., Husain, M.M., Gurley, E., Khan, R., Ahmed, B.N., Rahman, S., Nahar, N., et al. (2006). Foodborne transmission of Nipah virus, Bangladesh. *Emerg. Infect. Dis.* 12, 1888–1894.
- Luis, A.D., Hayman, D.T., O'Shea, T.J., Cryan, P.M., Gilbert, A.T., Pulliam, J.R., Mills, J.N., Timonin, M.E., Willis, C.K., Cunningham, A.A., et al. (2013). A comparison of bats and rodents as reservoirs of zoonotic viruses: are bats special? *Proc. Biol. Sci.* 280, 20122753.
- Mackenzie, J.S., and Jeggo, M. (2013). Reservoirs and vectors of emerging viruses. *Curr. Opin. Virol.* 3, 170–179.
- Mandl, J.N., Barry, A.P., Vanderford, T.H., Kozyr, N., Chavan, R., Klucking, S., Barrat, F.J., Coffman, R.L., Staprans, S.I., and Feinberg, M.B. (2008). Divergent TLR7 and TLR9 signaling and type I interferon production distinguish pathogenic and nonpathogenic AIDS virus infections. *Nat. Med.* 14, 1077–1087.
- Mandl, J.N., Akondy, R., Lawson, B., Kozyr, N., Staprans, S.I., Ahmed, R., and Feinberg, M.B. (2011). Distinctive TLR7 signaling, type I IFN production, and attenuated innate and adaptive immune responses to yellow fever virus in a primate reservoir host. *J. Immunol.* 186, 6406–6416.
- Marston, H.D., Folkers, G.K., Morens, D.M., and Fauci, A.S. (2014). Emerging viral diseases: confronting threats with new technologies. *Sci. Transl. Med.* 6, 53ps10.
- Martinez, O., Leung, L.W., and Basler, C.F. (2012). The role of antigen-presenting cells in filoviral hemorrhagic fever: gaps in current knowledge. *Antiviral Res.* 93, 416–428.
- Menachery, V.D., Eisfeld, A.J., Schafer, A., Josset, L., Sims, A.C., Proll, S., Fan, S., Li, C., Neumann, G., Tilton, S.C., et al. (2014). Pathogenic influenza viruses and coronaviruses utilize similar and contrasting approaches to control interferon-stimulated gene responses. *Mbio.* 5, e01174–e01214.
- Meteyer, C.U., Barber, D., and Mandl, J.N. (2012). Pathology in euthermic bats with white nose syndrome suggests a natural manifestation of immune reconstitution inflammatory syndrome. *Virulence* 3, 583–588.
- Middleton, D.J., Morrissy, C.J., van der Heide, B.M., Russell, G.M., Braun, M.A., Westbury, H.A., Halpin, K., and Daniels, P.W. (2007). Experimental Nipah virus infection in pteropid bats (*Pteropus poliocephalus*). *J. Comp. Pathol.* 136, 266–272.
- Miedema, F., Hazenberg, M.D., Tesselaar, K., van Baarle, D., de Boer, R.J., and Borghans, J.A. (2013). Immune activation and collateral damage in AIDS pathogenesis. *Front. Immunol.* 4, 298.
- Misasi, J., and Sullivan, N.J. (2014). Camouflage and misdirection: the full-on assault of ebola virus disease. *Cell* 159, 477–486.
- Moir, S., Chun, T.W., and Fauci, A.S. (2011). Pathogenic mechanisms of HIV disease. *Annu. Rev. Pathol.* 6, 223–248.
- Mokili, J.L., Rohwer, F., and Dutilh, B.E. (2012). Metagenomics and future perspectives in virus discovery. *Curr. Opin. Virol.* 2, 63–77.
- Morse, S.S., Mazet, J.A., Woolhouse, M., Parrish, C.R., Carroll, D., Karesh, W.B., Zambrana-Torrel, C., Lipkin, W.I., and Daszak, P. (2012). Prediction and prevention of the next pandemic zoonosis. *Lancet* 380, 1956–1965.
- Oldstone, M.B., and Rosen, H. (2014). Cytokine storm plays a direct role in the morbidity and mortality from influenza virus infection and is chemically treatable with a single sphingosine-1-phosphate agonist molecule. *Curr. Top. Microbiol. Immunol.* 378, 129–147.
- Olival, K.J., Epstein, J.H., Wang, L.-F., Field, H.E., and Daszak, P. (2013). Are bats unique virus reservoirs? In *New Directions in Conservation Medicine Applied Cases of Ecological Health*, A.A. Aguirre, R.S. Ostfeld, and P. Daszak, eds. (New York: Oxford University Press), pp. 195–212.
- Osborne, L.C., Monticelli, L.A., Nice, T.J., Sutherland, T.E., Siracusa, M.C., Hepworth, M.R., Tomov, V.T., Kobuley, D., Tran, S.V., Bittiger, K., et al. (2014). Coinfection. Virus-helminth coinfection reveals a microbiota-independent mechanism of immunomodulation. *Science* 345, 578–582.
- Paiardini, M., Cervasi, B., Reyes-Aviles, E., Micci, L., Ortiz, A.M., Chahroudi, A., Vinton, C., Gordon, S.N., Bosinger, S.E., Francella, N., et al. (2011). Low levels of SIV infection in sooty mangabey central memory CD4⁺ T cells are associated with limited CCR5 expression. *Nat. Med.* 17, 830–836.
- Pandey, A., Atkins, K.E., Medlock, J., Wenzel, N., Townsend, J.P., Childs, J.E., Nyenswah, T.G., Ndeffo-Mbah, M.L., and Galvani, A.P. (2014). Strategies for containing Ebola in West Africa. *Science* 346, 991–995.
- Pandrea, I., and Apetrei, C. (2010). Where the wild things are: pathogenesis of SIV infection in African nonhuman primate hosts. *Curr. HIV/AIDS Rep.* 7, 28–36.
- Parashar, U.D., Sunn, L.M., Ong, F., Mounts, A.W., Arif, M.T., Ksiazek, T.G., Kamaluddin, M.A., Mustafa, A.N., Kaur, H., Ding, L.M., et al. (2000). Case-control study of risk factors for human infection with a new zoonotic paramyxovirus, Nipah virus, during a 1998–1999 outbreak of severe encephalitis in Malaysia. *J. Infect. Dis.* 181, 1755–1759.
- Pearce, E.L., and Pearce, E.J. (2013). Metabolic pathways in immune cell activation and quiescence. *Immunity* 38, 633–643.
- Peiris, J.S., Guan, Y., and Yuen, K.Y. (2004). Severe acute respiratory syndrome. *Nat. Med. Suppl.* 10, S88–S97.
- Peiris, J.S., Hui, K.P., and Yen, H.L. (2010). Host response to influenza virus: protection versus immunopathology. *Curr. Opin. Immunol.* 22, 475–481.

- Penaloza-MacMaster, P., Kamphorst, A.O., Wieland, A., Araki, K., Iyer, S.S., West, E.E., O'Mara, L., Yang, S., Konieczny, B.T., Sharpe, A.H., et al. (2014). Interplay between regulatory T cells and PD-1 in modulating T cell exhaustion and viral control during chronic LCMV infection. *J. Exp. Med.* 211, 1905–1918.
- Pigott, D.M., Golding, N., Mylne, A., Huang, Z., Henry, A.J., Weiss, D.J., Brady, O.J., Kraemer, M.U., Smith, D.L., Moyes, C.L., et al. (2014). Mapping the zoonotic niche of Ebola virus disease in Africa. *eLife* 3.
- Pothlichet, J., and Quintana-Murci, L. (2013). The genetics of innate immunity sensors and human disease. *Int. Rev. Immunol.* 32, 157–208.
- Qian, C., and Cao, X. (2013). Regulation of Toll-like receptor signaling pathways in innate immune responses. *Ann. N Y Acad. Sci.* 1283, 67–74.
- Quan, P.L., Firth, C., Conte, J.M., Williams, S.H., Zambrana-Torrel, C.M., Anthony, S.J., Ellison, J.A., Gilbert, A.T., Kuzmin, I.V., Niezgoda, M., et al. (2013). Bats are a major natural reservoir for hepaciviruses and pegiviruses. *Proc. Natl. Acad. Sci. USA* 110, 8194–8199.
- Råberg, L., Sim, D., and Read, A.F. (2007). Disentangling genetic variation for resistance and tolerance to infectious diseases in animals. *Science* 318, 812–814.
- Rahman, S.A., Hassan, L., Epstein, J.H., Mamat, Z.C., Yatim, A.M., Hassan, S.S., Field, H.E., Hughes, T., Westrum, J., Naim, M.S., et al.; Henipavirus Ecology Research Group (2013). Risk Factors for Nipah virus infection among pteropid bats, Peninsular Malaysia. *Emerg. Infect. Dis.* 19, 51–60.
- Rasmussen, A.L., Okumura, A., Ferris, M.T., Green, R., Feldmann, F., Kelly, S.M., Scott, D.P., Safronetz, D., Haddock, E., LaCasse, R., et al. (2014). Host genetic diversity enables Ebola hemorrhagic fever pathogenesis and resistance. *Science* 346, 987–991.
- Reese, T.A., Wakeman, B.S., Choi, H.S., Hufford, M.M., Huang, S.C., Zhang, X., Buck, M.D., Jezewski, A., Kambal, A., Liu, C.Y., et al. (2014). Coinfection. Helminth infection reactivates latent γ -herpesvirus via cytokine competition at a viral promoter. *Science* 345, 573–577.
- Regoes, R.R., McLaren, P.J., Battegay, M., Bernasconi, E., Calmy, A., Günthard, H.F., Hoffmann, M., Rauch, A., Telenti, A., and Fellay, J.; Swiss HIV Cohort Study (2014). Disentangling human tolerance and resistance against HIV. *PLoS Biol.* 12, e1001951.
- Rodrigue-Gervais, I.G., Labbé, K., Dagenais, M., Dupaul-Chicoine, J., Champagne, C., Morizot, A., Skeldon, A., Brincks, E.L., Vidal, S.M., Griffith, T.S., and Saleh, M. (2014). Cellular inhibitor of apoptosis protein cIAP2 protects against pulmonary tissue necrosis during influenza virus infection to promote host survival. *Cell Host Microbe* 15, 23–35.
- Rouse, B.T., and Sehrawat, S. (2010). Immunity and immunopathology to viruses: What decides the outcome? *Nat. Rev. Immunol.* 10, 514–526.
- Roy, B.A., and Kirchner, J.W. (2000). Evolutionary dynamics of pathogen resistance and tolerance. *Evolution* 54, 51–63.
- Sandler, N.G., Bosinger, S.E., Estes, J.D., Zhu, R.T., Tharp, G.K., Boritz, E., Levin, D., Wijeyesinghe, S., Makamdop, K.N., del Prete, G.Q., et al. (2014). Type I interferon responses in rhesus macaques prevent SIV infection and slow disease progression. *Nature* 511, 601–605.
- Sauter, D. (2014). Counteraction of the multifunctional restriction factor tetherin. *Front. Microbiol.* 5, 163.
- Schneider, D.S., and Ayres, J.S. (2008). Two ways to survive infection: what resistance and tolerance can teach us about treating infectious diseases. *Nat. Rev. Immunol.* 8, 889–895.
- Schoggins, J.W., Wilson, S.J., Panis, M., Murphy, M.Y., Jones, C.T., Bieniasz, P., and Rice, C.M. (2011). A diverse range of gene products are effectors of the type I interferon antiviral response. *Nature* 472, 481–485.
- Schountz, T., and Prescott, J. (2014). Hantavirus immunology of rodent reservoirs: current status and future directions. *Viruses* 6, 1317–1335.
- Seok, J., Warren, H.S., Cuenca, A.G., Mindrinos, M.N., Baker, H.V., Xu, W., Richards, D.R., McDonald-Smith, G.P., Gao, H., Hennessy, L., et al.; Inflammation and Host Response to Injury, Large Scale Collaborative Research Program (2013). Genomic responses in mouse models poorly mimic human inflammatory diseases. *Proc. Natl. Acad. Sci. USA* 110, 3507–3512.
- Shen, Y.Y., Liang, L., Zhu, Z.H., Zhou, W.P., Irwin, D.M., and Zhang, Y.P. (2010). Adaptive evolution of energy metabolism genes and the origin of flight in bats. *Proc. Natl. Acad. Sci. USA* 107, 8666–8671.
- Silvestri, G., Sodora, D.L., Koup, R.A., Paiardini, M., O'Neil, S.P., McClure, H.M., Staprans, S.I., and Feinberg, M.B. (2003). Nonpathogenic SIV infection of sooty mangabeys is characterized by limited bystander immunopathology despite chronic high-level viremia. *Immunity* 18, 441–452.
- Sitkovsky, M., and Lukashev, D. (2005). Regulation of immune cells by local-tissue oxygen tension: HIF1 α and adenosine receptors. *Nat. Rev. Immunol.* 5, 712–721.
- Sohayati, A.R., Hassan, L., Sharifah, S.H., Lazarus, K., Zaini, C.M., Epstein, J.H., Shamsul Naim, N., Field, H.E., Arshad, S.S., Abdul Aziz, J., and Daszak, P.; Henipavirus Ecology Research Group (2011). Evidence for Nipah virus recrudescence and serological patterns of captive Pteropus vampyrus. *Epidemiol. Infect.* 139, 1570–1579.
- Taylor, L.H., Latham, S.M., and Woolhouse, M.E.J. (2001). Risk factors for human disease emergence. *Philos. Trans. R. Soc. Lond. B Biol. Sci.* 356, 983–989.
- Totura, A.L., and Baric, R.S. (2012). SARS coronavirus pathogenesis: host innate immune responses and viral antagonism of interferon. *Curr Opin Virol* 2, 264–275.
- Turmelle, A.S., Jackson, F.R., Green, D., McCracken, G.F., and Rupprecht, C.E. (2010). Host immunity to repeated rabies virus infection in big brown bats. *J. Gen. Virol.* 91, 2360–2366.
- Verhagen, J.H., Munster, V.J., Majoor, F., Lexmond, P., Vuong, O., Stumpel, J.B., Rimmelzwaan, G.F., Osterhaus, A.D., Schutten, M., Slaterus, R., and Fouchier, R.A. (2012). Avian influenza A virus in wild birds in highly urbanized areas. *PLoS ONE* 7, e38256.
- Virgin, H.W. (2014). The virome in mammalian physiology and disease. *Cell* 157, 142–150.
- Virgin, H.W., Wherry, E.J., and Ahmed, R. (2009). Redefining chronic viral infection. *Cell* 138, 30–50.
- Wade, C.M., Kulbokas, E.J., 3rd, Kirby, A.W., Zody, M.C., Mullikin, J.C., Lander, E.S., Lindblad-Toh, K., and Daly, M.J. (2002). The mosaic structure of variation in the laboratory mouse genome. *Nature* 420, 574–578.
- Wang, T., Town, T., Alexopoulou, L., Anderson, J.F., Fikrig, E., and Flavell, R.A. (2004). Toll-like receptor 3 mediates West Nile virus entry into the brain causing lethal encephalitis. *Nat. Med.* 10, 1366–1373.
- Weber, B., Schuster, S., Zysset, D., Rihs, S., Dickgreber, N., Schürch, C., Riether, C., Siegrist, M., Schneider, C., Pawelski, H., et al. (2014). TREM-1 deficiency can attenuate disease severity without affecting pathogen clearance. *PLoS Pathog.* 10, e1003900.
- WHO (2014) (http://www.who.int/csr/don/2014_08_27_ebola/en/: World Health Organization).
- WHO Ebola Response Team (2014). Ebola virus disease in West Africa—the first 9 months of the epidemic and forward projections. *N. Engl. J. Med.* 371, 1481–1495.
- Wilkinson, G.S., and South, J.M. (2002). Life history, ecology and longevity in bats. *Aging Cell* 1, 124–131.
- Wolfe, N.D., Switzer, W.M., Carr, J.K., Bhullar, V.B., Shanmugam, V., Tamoufe, U., Prosser, A.T., Torimiro, J.N., Wright, A., Mpoudi-Ngole, E., et al. (2004). Naturally acquired simian retrovirus infections in central African hunters. *Lancet* 363, 932–937.
- Wolfe, N.D., Dunavan, C.P., and Diamond, J. (2007). Origins of major human infectious diseases. *Nature* 447, 279–283.
- Woolhouse, M., Scott, F., Hudson, Z., Howey, R., and Chase-Topping, M. (2012). Human viruses: discovery and emergence. *Philos. Trans. R. Soc. Lond. B Biol. Sci.* 367, 2864–2871.
- Zaki, A.M., van Boheemen, S., Bestebroer, T.M., Osterhaus, A.D., and Fouchier, R.A. (2012). Isolation of a novel coronavirus from a man with pneumonia in Saudi Arabia. *N. Engl. J. Med.* 367, 1814–1820.

- Zampieri, C.A., Sullivan, N.J., and Nabel, G.J. (2007). Immunopathology of highly virulent pathogens: insights from Ebola virus. *Nat. Immunol.* **8**, 1159–1164.
- Zhang, G., Cowled, C., Shi, Z., Huang, Z., Bishop-Lilly, K.A., Fang, X., Wynne, J.W., Xiong, Z., Baker, M.L., Zhao, W., et al. (2013). Comparative analysis of bat genomes provides insight into the evolution of flight and immunity. *Science* **339**, 456–460.
- Zhao, J., Li, K., Wohlford-Lenane, C., Agnihothram, S.S., Fett, C., Zhao, J., Gale, M.J., Jr., Baric, R.S., Enjuanes, L., Gallagher, T., et al. (2014). Rapid generation of a mouse model for Middle East respiratory syndrome. *Proc. Natl. Acad. Sci. USA* **111**, 4970–4975.

Variation in the Human Immune System Is Largely Driven by Non-Heritable Influences

Petter Brodin,^{1,2,3,11} Vladimir Jojic,^{4,11} Tianxiang Gao,⁴ Sanchita Bhattacharya,³ Cesar J. Lopez Angel,^{2,3} David Furman,^{2,3} Shai Shen-Orr,⁵ Cornelia L. Dekker,⁶ Gary E. Swan,⁷ Atul J. Butte,^{6,8} Holden T. Maecker,^{3,9} and Mark M. Davis^{2,3,10,*}

¹Science for Life Laboratory, Department of Medicine, Solna, Karolinska Institutet, 17121 Solna, Sweden

²Department of Microbiology and Immunology, Stanford University School of Medicine, Stanford, CA 94304, USA

³Institute of Immunity, Transplantation and Infection, Stanford University School of Medicine, Stanford, CA 94304, USA

⁴Department of Computer Science, University of North Carolina at Chapel Hill, Chapel Hill, NC 27599, USA

⁵Department of Immunology, Faculty of Medicine, Technion, Haifa 31096, Israel

⁶Department of Pediatrics, Stanford University School of Medicine, Stanford, CA 94304, USA

⁷Stanford Prevention Research Center, Department of Medicine, Stanford University School of Medicine, Stanford, CA 94304, USA

⁸Center for Pediatric Bioinformatics, Lucille Packard Children's Hospital, Stanford University, Stanford, CA 94304, USA

⁹Human Immune Monitoring Center, Stanford University School of Medicine, Stanford, CA 94304, USA

¹⁰Howard Hughes Medical Institute, Stanford University School of Medicine, Stanford, CA 94304, USA

¹¹Co-first author

*Correspondence: mmdavis@stanford.edu

<http://dx.doi.org/10.1016/j.cell.2014.12.020>

SUMMARY

There is considerable heterogeneity in immunological parameters between individuals, but its sources are largely unknown. To assess the relative contribution of heritable versus non-heritable factors, we have performed a systems-level analysis of 210 healthy twins between 8 and 82 years of age. We measured 204 different parameters, including cell population frequencies, cytokine responses, and serum proteins, and found that 77% of these are dominated (>50% of variance) and 58% almost completely determined (>80% of variance) by non-heritable influences. In addition, some of these parameters become more variable with age, suggesting the cumulative influence of environmental exposure. Similarly, the serological responses to seasonal influenza vaccination are also determined largely by non-heritable factors, likely due to repeated exposure to different strains. Lastly, in MZ twins discordant for cytomegalovirus infection, more than half of all parameters are affected. These results highlight the largely reactive and adaptive nature of the immune system in healthy individuals.

INTRODUCTION

The study of monozygotic (MZ) and dizygotic (DZ) twin pairs has provided a powerful means for separating heritable from non-heritable influences on measured traits for almost 100 years (Jablonski, 1922). Such studies have been used to study autoimmune diseases, vaccine responses (Jacobson et al., 2007), serum cytokines (de Craen et al., 2005), or the frequencies of major immune cell populations (Clementi et al., 1999; Evans et al., 2004). Most of these studies have found that both heritable

and non-heritable factors contribute to the resulting phenotype. Recent advances in technology now allow much more comprehensive surveys to be conducted across the many different components of the immune system, and thus we performed a very broad “systems-level” study in which we measured 51 serum cytokines, chemokines, and growth factors; the frequencies of 95 different immune cell subsets; and cellular responses to cytokine stimulation (Figure 1A). Our results show that these functional units of immunity vary across individuals primarily as a consequence of non-heritable factors, with a generally limited influence of heritable ones. This indicates that the immune system of healthy individuals is very much shaped by the environment and most likely by the many different microbes that an individual encounters in their lifetime.

RESULTS

A Systems-Level Analysis of the Immune System in Healthy Twins

Our study cohort was recruited from the Twin Research Registry at SRI International (Krasnow et al., 2013) in the years 2009–2011, with demographic data detailed in Table S1 (available online). The subjects were all apparently healthy, without any symptoms of disease (Experimental Procedures, “Twin Cohort”). To minimize biological variability, the time between blood sampling of each twin in a pair was kept to a minimum (Experimental Procedures, “Blood Sampling, PBMC Preparation, and Zygosity Testing”). Immunological assays were performed by the Human Immune Monitoring Center, where assays are continually benchmarked to minimize technical variability (<http://iti.stanford.edu/himc/>) (Maecker et al., 2005). However, some technical variability is inevitable, and thus we corrected for this in all of our models. We did this by analyzing aliquots of the same control sample many (>17) times to estimate the technical variance and subtracted this from our estimates of heritability (Experimental Procedures, “Correction of Model Estimates for Technical Variability”). We also analyzed longitudinal samples in an unrelated cohort over 2–5



Figure 1. Systems-Level Analysis of Healthy Human Twins
(A) Overview of data collected covering the functional units of the immune system, the cells, and proteins in circulation.
(B) Summary of all heritability estimates for 72 immune cell population frequencies as determined by flow (2009) and mass cytometry (2010–2011) (Experimental Procedures, section 3). See also Table S3.
(C) Heritability estimates of 43 serum proteins as determined by a fluorescent bead assay. See also Table S4. Error bars represent 95% confidence intervals for the heritability estimate. Gray area is heritability <0.2, our detection limit.

consecutive, yearly samplings and found that the variation was largely due to technical variability (Table S2). A total of 204 different immune measurements were included in our analyses.

Estimating Heritable and Non-Heritable Influences

Heritability for each parameter was estimated by comparing observed MZ and DZ covariance matrices to the expected

values based on a structural equation model that partitioned the observed variance into three components: heritable (A), shared (C), and unique (E) non-heritable factors. This model is based on the assumptions that: (1) heritable factors correlate perfectly between MZ twins ($r_{MZ} = 1$) but only to 50% between DZ twins ($r_{DZ} = 0.5$) and (2) that shared non-heritable influences are equally similar ($r_{MZ} = r_{DZ}$) between MZ and DZ twin pairs

([Experimental Procedures](#), “Structural Equation Modeling to Estimate Heritable and Non-Heritable Influences”). For each measurement, we subtracted the technical variance estimate from the e-component prior to normalization to correct for noise ([Experimental Procedures](#), “Correction of Model Estimates for Technical Variability”). We also corrected all measurements for the effects of age ([Dorshkind et al., 2009](#)) and gender ([Furman et al., 2014](#)) by regressing out such effects and using only residual variance for estimating heritability. Finally, we performed jackknife bootstrapping tests to obtain 95% confidence intervals ([Experimental Procedures](#), “Structural Equation Modeling to Estimate Heritable and Non-Heritable Influences”). Importantly, as our model estimates heritability by comparing MZ and DZ twins, heritable influences include genomic and shared epigenetic traits ([Bell and Spector, 2011](#)), and non-heritable influences include environmental factors and stochastic epigenetic changes ([Fraga et al., 2005](#)).

We first ran a simulation experiment to verify that our cohort size of 210 twins (78 MZ and 27 DZ pairs) would be enough to test our hypothesis that most immunological traits are explained more by non-heritable than by heritable influences. We found this to be the case, and we estimate 20% heritability to be our detection limit, under which we cannot distinguish small heritable influences from zero ([Figure S1](#)).

Most Cell Population Frequencies and Serum Proteins Are Dominated by Non-Heritable Influences

Although it is well known that the frequencies of different types of immune cells in blood often vary widely between individuals, in most cases it is not known how much of this can be attributed to heritable or non-heritable factors, respectively. To address this question, we used antibodies against cell surface markers to quantify 95 different cell subset frequencies but used the 72 most non-redundant ones and estimated the influence of heritable and non-heritable factors on their variation ([Experimental Procedures](#), “Immune Cell Phenotyping by Mass Cytometry and Flow Cytometry”). Among these, a few had very strong influences from heritable factors, especially naive, CD27⁺, and central memory CD4⁺ T cells ([Figure 1B](#) and [Table S3](#)), but for most, non-heritable influences were clearly dominant. In fact, for 61% of all cell populations, the influence of heritable factors was undetectable (<20% of the total variation) ([Figure 1B](#) and [Table S3](#)). This was true of both adaptive (T and B cells) and innate cell types (granulocytes, monocytes, and NK-cells).

Serum cytokines and chemokines also have important functions as immune mediators and biomarkers of disease ([Villeda and Wyss-Coray, 2013](#)), and thus we measured 51 serum proteins but eliminated eight that were often at or below the limits of detection ([Experimental Procedures](#), “Serum Protein Quantification”). This left 24 cytokines, 10 chemokines, 6 growth factors, and 3 other serum proteins for which we estimated the influences of heritable and non-heritable factors ([Figure 1C](#) and [Table S4](#)). Some cytokines were particularly heritable, such as IL-12p40 ([Figure 1C](#) and [Table S4](#)). Interestingly, variants in the IL12B gene that contribute to the IL-12p40 protein have been associated with immune-mediated diseases such as psoriasis ([Nair et al., 2009](#)) and asthma ([Morahan et al., 2002](#)). In the latter condition, the susceptibility locus was also associated with a

reduced serum concentration of IL-12p40 ([Morahan et al., 2002](#)). For many other measurements, such as IL-10 and a group of chemokines, the heritable influence was low ([Figure 1C](#) and [Table S4](#)).

Homeostatic Cytokine Responses Are Largely Heritable, whereas Most Other Cell Responses Are Highly Non-Heritable

Because these serum proteins often regulate immune cells, we assessed the responses of eight different cell populations stimulated in vitro with seven different cytokines for the phosphorylation of three important transcription factors, STAT1, 3, and 5, using phospho-specific antibodies in flow cytometry ([Krutzik and Nolan, 2006](#)). We performed a total of 192 different measurements but focused on the 24 baseline measurements and the 65 strongest induced responses ([Experimental Procedures](#), “Immune Cell Signaling Experiments”). Baseline measurements were generally driven by non-heritable factors, with possible minor contributions from heritable factors ([Figure 2A](#)). The important homeostatic cytokines IL-2 and IL-7, known to stimulate the proliferation and differentiation of T cells, were found to induce STAT5 phosphorylation in both CD4⁺ and CD8⁺ T cell populations, and these responses were highly heritable ([Figure 2A](#) and [Table S5](#)). In contrast, most signaling responses such as interferon-induced STAT1 phosphorylation and, in particular, the IL-6-, IL-21-, and regulatory IL-10-induced phosphorylation of STAT3, were dominated by non-heritable influences ([Figure 2A](#) and [Table S5](#)). In total, 69% of all signaling responses had no detectable heritable influence (e.g., <20%) ([Figure 2A](#) and [Table S5](#)). This lack of heritability was not related to the strength of responses or explained by a bias toward weak and variable responses ([Figure S2](#)).

Non-Heritable Influences Are Major Factors Determining Immune Variation

Taken together, these results show that variation in blood cell frequencies and functions and soluble factors is largely driven by non-heritable factors, with 58% of all measurements having <20% of their total variance explained by heritable influences ([Figure 2B](#)). There was no relationship between the absolute degree of measurement variability in the cohort and estimated heritability ([Figure S3](#)), and we could also rule out any underestimation of heritability due to the skewed ratio of MZ/DZ twin pairs in our cohort by a resampling test. In brief, by creating 1,000 synthetic data sets with uniform heritability and the same MZ/DZ ratio as in our cohort, we estimated heritability and found that none of the 1,000 data sets ever had >40% of measurements with an estimated heritability < 0.2 ($p < 0.001$) ([Figure 2C](#)), thus suggesting that the low heritability estimates obtained are not a result of study design or overall measurement variation in the cohort.

Heritable and Non-Heritable Measurements Are Interrelated in the Immune Network

Our analysis also allowed us to analyze the interrelationships between the different components of the immune system. To construct such a network model, we calculated a precision matrix derived from a Spearman correlation matrix ([Liu et al., 2012](#)).

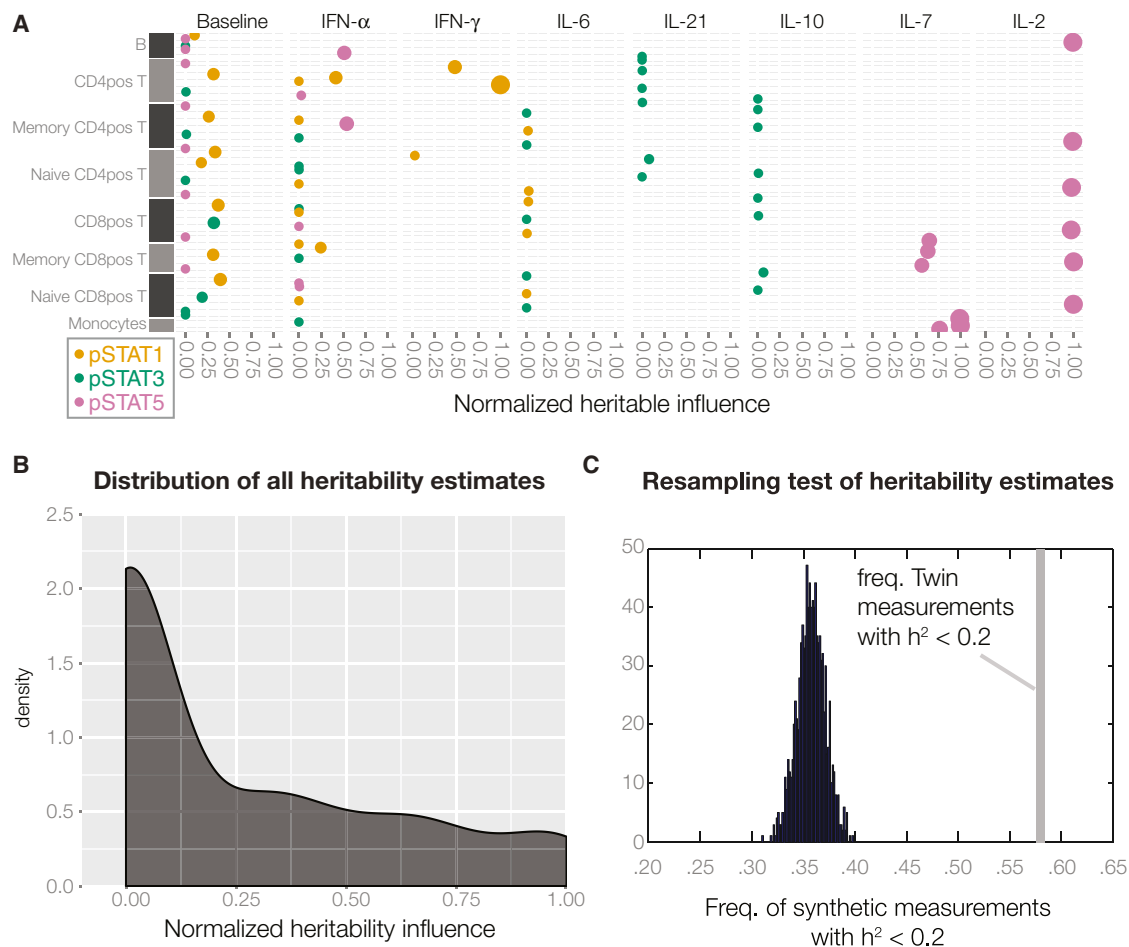


Figure 2. Heritable Factors Explain Only a Fraction of the Variation for Most Immune Measurements

(A) Heritability estimates for immune cell signaling states upon stimulation with the indicated cytokines. Only unstimulated controls and induced responses >1.5-fold are shown. See also Table S5.

(B) The overall distribution of heritability for all 204 measurements.

(C) The maximum number of measurements with heritability <0.2 across 1,000 synthetic data sets with the same MZ/DZ ratio as in our twin cohort is <40%, significantly less than our results of 58% of measurements with heritability <20% (gray bar). $p < 0.001$.

A matrix of this type captures partial correlations between variables and avoids spurious, indirect interactions that might occur in standard correlation analyses. By penalizing non-zero entries in this matrix (Friedman et al., 2008), we could pursue what is referred to as a sparse (rather than dense) network model, making it more interpretable. After removing unconnected nodes and validating the edges by a permutation test (Experimental Procedures, "Identification of Pairwise Dependencies between Measurements and the Creation of an Immune Network Model"), this model consists of 126 nodes and 142 edges (Figure 3A and Table S6). An interactive version is available online (<http://www.brodinlab.com/twins.html>). We found that heritable nodes (yellow) were generally connected to non-heritable nodes (purple) throughout the network (Figure 3A). One example shows how the weakly heritable cytokine IL-10 and CD161⁺CD45RA⁺ regulatory T cells are connected to the strongly heritable frequency of naive CD4⁺ T cells (Figure 3B). We found that all hubs in the network were dominated by non-heritable influences,

like the network as a whole, showing that heritable factors are not isolated by themselves but are buffered by connected non-heritable ones (Figure 3A and 3B). This may explain why the many gene polymorphisms found (for example, CTLA4 [Gergersen et al., 2009]) outside of the HLA locus that are associated with immune-mediated disease only explain a small fraction of the total disease risk (Todd, 2010).

With Age, Genetically Identical Twins Diverge as a Consequence of Non-Heritable Influences

As a major source of non-heritable influence is likely to be environmental, particularly microbial exposure, we reasoned that such influences would increase with time. To this end, we compared twin-twin correlations for all immune measurements between the oldest (>60 years; median, 72 years) and the youngest (<20 years; median, 13 years) MZ pairs in our cohort. Here, we also note that twins in the younger (<20 years) cohort are in most cases living together, whereas the older (>60 years) twins

Network of Immune measurements

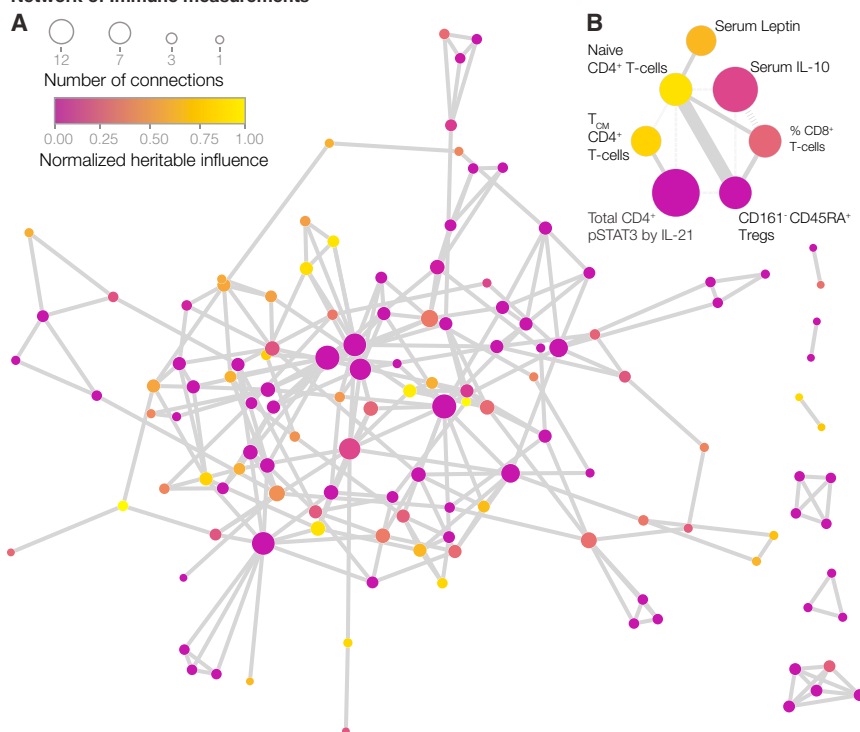


Figure 3. Network of Dependencies between Immune Measurements

(A) Undirected network model of the healthy human immune system showing 126 nodes (measurements), connected by 142 undirected edges illustrating conditional measurement dependencies. Nodes are colored by their estimated heritability and sized by their number of edges. (B) Subnetwork exemplifying direct relationships between heritable and non-heritable nodes. Solid edges represent positive relationships, and dashed edges represent negative relationships. The edge weight represents the strength of relationships. See also [Table S6](#).

have lived apart for decades, so concordance can also be a result of either shared environment and/or shared exposure, in addition to genetic similarity. For several cell population frequencies, we found much reduced correlations with age ([Figure 4A](#)). In the most striking example, the frequency of Tregs between the youngest MZ twins correlated very strongly at 0.78 but was highly uncorrelated at 0.24 between the oldest MZ twin pairs ([Figure 4A](#)). Similarly, several serum proteins showed remarkably reduced correlations between older as compared to younger MZ twins ([Figure 4B](#)). In particular, the chemokine CXCL10/IP10 showed a strong correlation (0.79) between the youngest MZ twins but was greatly reduced (0.18) in the older MZ twins ([Figure 4B](#)). Similar patterns were found for many cell signaling responses (data not shown), suggesting that this immune divergence between genetically identical twins with age is a common phenomenon, consistent with a major role for environmental exposure in driving variation, although some epigenetic changes could also contribute ([Fraga et al., 2005](#)).

Cytomegalovirus Infection Has a Broad Influence on Immune Variation

As we postulate that microbial exposure is a likely driver of immune variation with age, a particularly interesting example is cytomegalovirus (CMV), a lifelong viral infection that has striking effects on the immune phenotypes of both humans and rhesus macaques ([Sylwester et al., 2005](#)). In our twin cohort, 16 MZ pairs were discordant for CMV seropositivity, and we compared their twin-twin correlations for all measurements to those of 26 CMV concordant (negative) MZ pairs. Here, we found that the CMV discordant MZ twins showed greatly reduced correlations

for many immune cell frequencies such as effector CD8⁺ and gamma-delta T cells ([Figure 5A](#)), as compared to CMV-negative MZ twins. The same was true for cell signaling responses, especially in response to IL-10 and IL-6 stimulation ([Figure 5B](#)), as well as the concentrations of these same cytokines in serum ([Figure 5C](#)). In general, the influence of CMV was very broad, affecting 119 of all 204 measurements (58%) dispersed throughout the immune network ([Figure 5D](#)) and illustrating how at least one type of microbial exposure can dramatically modulate the overall immune profile of healthy individuals.

Antibody Responses to Seasonal Flu Vaccines in Adults Have No Detectable Heritable Component

Finally, we immunized all of the subjects with seasonal flu vaccines in the year of participation (2009, 2010, or 2011) and assessed antibody responses using a standard hemagglutination inhibition (HAI) assay ([Experimental Procedures](#), “Hemagglutination Inhibition Assays”). We were surprised to find no detectable contribution from heritable factors on any of these vaccine responses ([Table 1](#)). As pre-existing antibodies are known to influence flu vaccine responses ([Sasaki et al., 2008](#)), we excluded subjects with a pre-vaccination titer above 40 but were still unable to find any heritable influences ([Table 1](#)). Though preliminary due to a small sample size, this result suggests that responses to seasonal flu vaccines in healthy adults (median age, 44 years) are dominantly influenced by non-heritable factors, likely due to multiple previous vaccinations and/or infections involving this pathogen ([Table 1](#)).

In summary, our findings strongly suggest that a healthy human immune system adapts to non-heritable influences such as pathogens, nutritional factors, and more and that this overshadows the influences of most, although not all, heritable factors.

DISCUSSION

The vertebrate immune system consist of thousands of different components, and the application of systems biology ([Davis,](#)

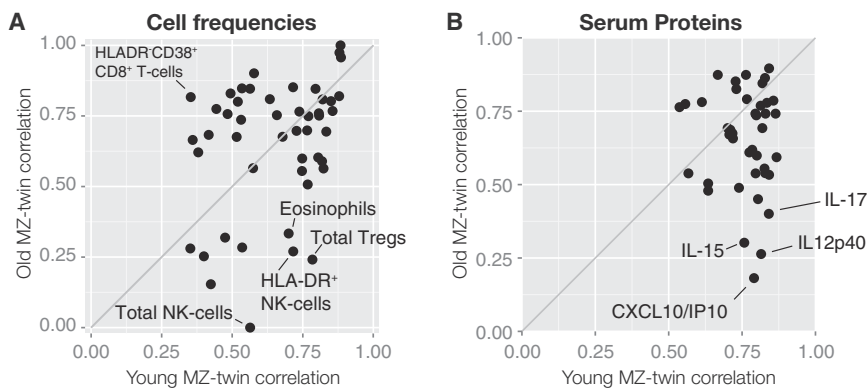


Figure 4. Increased Variability in the Immune System with Age

(A) Twin-twin correlations (Spearman's rank) for all cell frequencies within the youngest MZ twin pairs (≤ 20 years; median, 13.5; $n = 25$ pairs), and the oldest MZ twin pairs (≥ 60 years; median, 72 years; $n = 16$).

(B) Twin-twin correlations (Spearman's rank) for all serum protein concentrations within the youngest MZ twin pairs (≤ 20 years; median, 13 years; $n = 26$) and the oldest MZ twin pairs (≥ 60 years; median, 73 years; $n = 13$).

2008; Duffy et al., 2014; Li et al., 2014; Querec et al., 2009; Sekaly, 2008; Tsang et al., 2014) holds great promise as a way to understand the interactions between these during immune health and disease. Here, we combine a classical twin study approach with the most recent advances in immune monitoring technologies to assess the balance between heritable and non-heritable influences on the functional units of the immune system, namely serum proteins and cell populations. In every category, we find that non-heritable influences dominantly influence 77% of all measurements ($>50\%$ of variance) and almost exclusively drive 58% of the measurements ($>80\%$ of the variance). Because most measurements made in this study focus on the adaptive immune system, partly due to the availability of reagents, one possibility is that these low levels of heritability are related to the stochastic nature of antigen receptor recombination. Indeed, previous work has shown that there are significant differences in the immunoglobulin-sequence repertoires of MZ twins (Glanville et al., 2011). But this is unlikely, as we find low heritability estimates also for many innate immune cell frequencies (NK cells, monocytes, and granulocytes [Figure 1B]) and differences within and between CD4⁺ and CD8⁺ subsets of T cells, which share the same antigen receptor apparatus.

Although this study is not powered to completely rule out all heritable influences on any of the measurements made, the overall dominance of non-heritable factors is independent of this. The low estimates of heritable influences are also not explained by technical noise, as this is rigorously corrected for in our models (Figure S6A). We are also able to rule out that measurement variability over time is an important source of bias (Figure S6B). Therefore, the low heritability estimates for the majority of measurements cannot be explained by either technical noise or biological variability over time.

Given the concordance rates for common autoimmune diseases between 25% and 50% (Cooper et al., 1999) and the many studies finding associations between specific genetic variants and immunological traits and disorders, we were surprised to find such a dominance by non-heritable factors on these functional units of the immune system. Several large population studies have associated specific loci with white blood cell counts, showing some heritable influence though the amount of variation explained is typically low (Okada et al., 2011; Reiner et al., 2011). A recent study by Orrù et al. estimated the heritability of 272 immune cell traits from a non-twin cohort of healthy in-

dividuals on the island of Sardinia. They found that 220 of these ($\sim 81\%$) had an estimated heritability lower than 50% (Orrù et al., 2013), which is comparable to our results. Although all the most heritable subpopulations identified by Orrù et al. expressed the marker CD39, which was not analyzed in our study, a number of the cell populations gave quite similar values, although others were different, such as NKT cells and central memory CD8⁺ T cells (Table S7), possibly reflecting different environments (Bell and Spector, 2011) or a more diverse Palo Alto cohort versus a less diverse Sardinian one.

It is important to note that the twins in our cohort are healthy and without any known immunological deficiencies. Interestingly, two serious immunodeficiency syndromes are caused by defects in the genes IRAK-4 and MyD88 and are associated with invasive bacterial infections due to defects in TLR or IL-1R signaling (von Bernuth et al., 2008; Ku et al., 2007). Despite being associated with severe and often lethal infections in young children, both of these conditions improve significantly with age, starting in late childhood (von Bernuth et al., 2008; Ku et al., 2007). Although this could be explained by developmental immaturity, an alternative explanation for the improvement with age could be that these children's immune systems become more capable with greater environmental exposure.

A striking example of how broad the influence from one non-heritable factor can be is shown here for CMV, influencing 58% of all parameters measured in discordant MZ twins. These striking differences illustrate how non-heritable factors, alone or in combination, can affect the immune system broadly. We suggest that repeated environmental influences like herpes viruses and other pathogens, vaccinations, and nutritional factors cause shifts in immune cell frequencies and other parameters and, with time, outweigh most heritable factors. As an example, the life-long need to control CMV seems to cause a broad shift in the magnitude and complexity of many cell subsets (Chidrawar et al., 2009; Wills et al., 2011), and $\sim 10\%$ of all T cells in CMV⁺ individuals can be directed against this virus (Sylwester et al., 2005). The microbiome also clearly has a major influence on the immune system (Hooper et al., 2012; Mazmanian et al., 2005), and shifts in its composition might cause significant changes in the immune system. Also interesting in the context of how infectious disease exposure can shape subsequent immunity are the influenza vaccine results, in which we could not detect any heritable influence on the antibody responses to

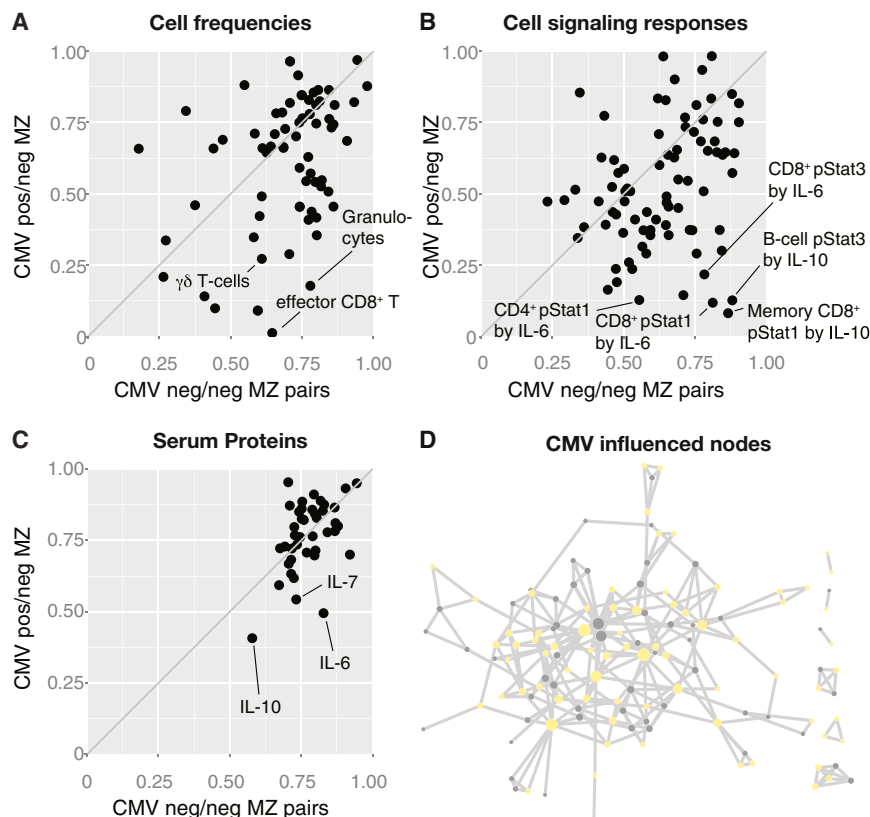


Figure 5. Broad Non-Heritable Influences in the Healthy Immune System

(A) Twin-twin correlations (Spearman's rank) for all cell frequency measurements made in CMV concordant negative (neg/neg) MZ twin pairs ($n = 26$ pairs) and CMV discordant (pos/neg) MZ twin pairs ($n = 16$ pairs). (B and C) (B) Twin-twin correlations (Spearman's rank) for cell signaling responses to cytokine stimulation and (C) serum protein measurements between CMV neg/neg and CMV pos/neg MZ twin pairs. (D) 58% of all 126 nodes in the immune network model with reduced correlations in CMV pos/neg as compared to CMV neg/neg MZ twin pairs.

influenza vaccination (Table 1). This recalls the “original antigenic sin” hypothesis (Francis, 1960), wherein it was postulated that previous encounters with influenza strains strongly impact the response to a novel strain. But our finding contrasts with other vaccine studies in twins, most often performed in very young children and involving vaccines against pathogens less frequently encountered in the population (Table 1) (Jacobson et al., 2007). Specifically, vaccines against mumps, measles, rubella (Tan et al., 2001), oral polio, tetanus, and diphtheria vaccines (Newport et al., 2004) have all been shown to be strongly heritable (Table 1) in studies with young children. The one study that we know of from adult twins is a study of hepatitis A/B vaccine responses and was conducted across a similar age range (18–65 years) as ours and reported a heritable influence of 36% for hepatitis A and 61% for hepatitis B antibody responses (Table 1). However, two other studies of hepatitis B vaccine responses performed in young children showed much higher estimates of heritability of 91% (Yan et al., 2013) and 77% (Newport et al., 2004), respectively. In addition, responses to vaccines given at birth (oral polio vaccine [OPV] and Bacillus Calmette–Guérin [BCG]) are more heritable than even those administered only 2 months later (diphtheria and tetanus) (Newport et al., 2004; O'Connor and Pollard, 2013). In addition, Evans et al. analyzed 12-year-old twins in Australia (Evans et al., 1999). Although there are only six broad categories of immune cell subsets that can be compared with our study and those of Orrù et al., it is interesting that, in all cases, the estimates of heritability in the 12-year-old twins were higher than either ours or Orrù et al., in

which the mean age is about 38 and 40 years, respectively (Table S7). These observations are consistent with our data (Figure 4), showing an increasing non-heritable influence on many variables with age, and suggest quite strongly that many if not most of the less heritable traits that we measure here in our mostly adult population may be much more heritable if measured in young children.

Before the advent of childhood vaccines, antibiotics, and improvements in human hygiene, almost half of all children younger than 5 years of age died of infectious diseases. Casanova and colleagues have proposed a genetic theory of infectious disease to account for the interindividual differences in susceptibility (Alcais et al., 2009). Our data and the vaccine studies cited here suggest that such genetic predisposition would be most pronounced in young children but that, later on, the adaptive nature of the immune system is able to overcome many defects. This is similar to the hypothesis proposed by Alcais and colleagues to explain the discrepancies in genetic lesions underlying the susceptibility to primary and secondary infections, respectively (Alcais et al., 2010). Adaptations of the immune system with time could be the result of well-known immune mechanisms, such as specific antibodies and T cells or cross-reactive immunity (Su et al., 2013), or some as yet to be defined maturational process. We would also speculate that the immune system may have feedback mechanisms that allow it to skew its mix of cell types and functional properties in order to compensate for a given individual's particular mix of gene polymorphisms and microbial exposures.

In summary, we find that, in an examination of many of the component parts of the immune system, as well as some response metrics, much of the considerable variation in human beings is driven by non-heritable influences. This variation increases with age and is likely due in large part to exposure to pathogens and other microbes, as we see for CMV discordant MZ twins and in the responses to influenza vaccination. Lastly, we expect that other complex systems in higher organisms, such as the nervous system, will also show this pronounced

Table 1. Influenza Vaccine Responses in Adults Are Determined Mainly by Non-Heritable Factors

Vaccine Response	Age at Vaccination	Heritability	Comment
Measles	1–6 years ^a	89%	(Tan et al., 2001)
Polio (oral vaccine)	<1 year	60%	(Newport et al., 2004)
H. influenzae b	<1 year	51%	(Lee et al., 2006)
Diphtheria	<1 year	49%	(Newport et al., 2004)
Rubella	1–6 years ^a	46%	(Tan et al., 2001)
Tetanus	<1 year	44%	(Newport et al., 2004)
Mumps	1–6 years ^a	39%	(Tan et al., 2001)
Combined hepatitis A/B	18–65 years	36% (HAV)/61% (HBsAg)	(Höhler et al., 2002)
Hepatitis B virus	<1 year	77%/91%	(Newport et al., 2004; Yan et al., 2013)
B/Brisbane/60/2008	12–82 years (median, 45)	0% (<20%)	
A/Cal/07/2009 (H1N1)	12–82 years (median, 44)	0% (<20%)	
A/Perth/16/2009 (H3N2)	12–82 years (median, 44)	0% (<20%)	
B/Brisbane/60/2008	13–77 years (median, 49)	0% (<20%)	Pre-vaccine titer < 40
A/Cal/07/2009 (H1N1)	12–76 years (median, 45)	0% (<20%)	Pre-vaccine titer < 40
A/Perth/16/2009 (H3N2)	12–82 years (median, 44)	0% (<20%)	Pre-vaccine titer < 40

Table of published heritability estimates for vaccine responses to various vaccines as well as the seasonal influenza vaccine responses analyzed in this study with or without the removal of subjects with a pre-vaccine antibody titer ≥ 40 .

^aVaccine responses analyzed between 2 and 18 years of age.

influence of non-heritable factors, as there is also a need (and ability) of such systems to adapt to environmental stimuli.

EXPERIMENTAL PROCEDURES

Twin Cohort

In collaboration with the Twin Research Registry at SRI International (Krasnow et al., 2013), 105 healthy twin pairs were recruited over the years 2009, 2010, and 2011. The study protocol was approved by the Stanford University Administrative Panels on Human Subjects in Medical Research, and written informed consent was obtained from all participants. We excluded anyone having received the seasonal influenza vaccine in the last 6 months, anyone with known or suspected impairment of immunologic function, with clinically significant liver disease, diabetes mellitus treated with insulin, moderate to severe renal disease, or any other chronic disorder, including autoimmune diseases or severe hypertension. We also excluded anyone who had received blood products in the last 6 months and pregnant or lactating women. The complete inclusion/exclusion criteria are available (Data S1).

Blood Sampling, PBMC Preparation, and Zygosity Testing

Blood samples were collected in heparinized vacutainer tubes by venipuncture at day 0 (and day +28 for HAI responses after seasonal influenza vaccination) at the Clinical and Translational Research Unit, Stanford University Hospital. Whole blood collected in sodium heparin tubes was either analyzed immediately using our whole-blood flow cytometry protocol below or enriched for PBMCs using 15 ml of Ficoll-Paque PLUS (GE Health Care) and frozen at -80°C overnight, transferred to liquid nitrogen, and stored until further analysis. Zygosity was determined by comparing 384 SNP loci using a discriminatory DNA polymerase and ligase assay (GoldenGate genotyping Assay, Illumina) and were performed by IGenix. Twins were considered fraternal if similarities in DNA markers were below 99.0%. Twins of the same pair were almost exclusively analyzed in the same experimental batch, irrespective of technology used in order to minimize technical variation.

Immune Cell Phenotyping by Mass Cytometry and Flow Cytometry

All experiments were performed by the Human Immune Monitoring Center at Stanford University. For years 2010 and 2011, 2 million thawed PBMCs were stained without prior resting or fixation using a panel of 26 different metal-

tagged probes to surface antigens and DNA (Data S2A). After repeated washes, cells were analyzed by mass cytometry (CyTOF, Fluidigm) with the following instrument settings: high-resolution mode analysis with cell length set to 10–75 pushes, a lower deconvolution threshold of 10, and instrument run in dual-count detection mode and noise reduction turned off. FCS3.0 files were manually analyzed using FlowJo v9.3 (TreeStar), as shown in Figure S4. Year 2009 PBMC samples were similarly processed but were instead analyzed using a set of custom-made Lyoplates (BD Biosciences) covering seven different antibody panels of fluorescently labeled antibodies (Data S2B and S2C). These samples were acquired using a LSRII flow cytometer (BD Biosciences) and were similarly analyzed manually using the same FlowJo v9.3 (TreeStar).

Immune Cell Signaling Experiments

PBMCs were thawed in warm media, washed twice, and resuspended at 0.5×10^6 viable cells/microliter. 200 μl of cells were plated per well in 96-well deep-well plates. After resting for 1 hr at 37°C , cells were stimulated by addition of 50 μl solutions of cytokines: IFN α , IFN γ , IL-6, IL-7, IL-10, IL-2, or IL-21 (Data S2D), respectively, and incubated at 37°C for 15 min. Cells were then immediately fixed in 1.6% paraformaldehyde, permeabilized with 100% cold methanol, and kept at -80°C overnight. Each well was barcoded by a unique combination of Pacific Orange and Alexa-750 dye concentrations (Invitrogen/Life Technologies), and the cells were washed with FACS buffer (PBS supplemented with 2% FBS and 0.1% sodium azide) and stained with our phospho-Flow antibody panel (Data S2E). Finally, cells were washed and resuspended in FACS buffer, and 100,000 cells per stimulation condition were collected using DIVA 6.0 software on an LSRII flow cytometer (BD Biosciences). Data analysis was performed using FlowJo v9.3 (TreeStar), as shown in Figure S5, and the mean fluorescence intensity (MFI) of the 90th percentile was used for downstream analysis. All stimulated samples were compared to unstimulated control (baseline) samples, and fold changes were calculated. Responses above 1.5 fold change as well as baseline MFI values were used for heritability estimates.

Serum Protein Quantification

Blood samples were centrifuged and stored at -80°C awaiting analysis. Human 51-plex were purchased from Affymetrix and were used according to the manufacturer's recommendations with modifications as described below. In brief, samples were mixed with antibody-linked polystyrene beads

on 96-well filter-bottom plates and incubated at room temperature for 2 hr followed by overnight incubation at 4°C. Room temperature incubation steps were performed on an orbital shaker at 500–600 rpm. Plates were vacuum filtered and washed twice with wash buffer and were then incubated with biotinylated detection antibody for 2 hr at room temperature. Samples were then filtered and washed twice as above and were resuspended in streptavidin-PE. After incubation for 40 min at room temperature, two additional vacuum washes were performed and the samples resuspended in reading buffer. Each sample was measured in duplicate. Plates were read using a Luminex 200 instrument with a lower bound of 100 beads per sample per protein. Each sample was measured in duplicate. Plates were read using a Luminex LabMap200 instrument with a lower bound of 100 beads per sample per protein per well. The Luminex LabMap200 outputs the fluorescence intensity of a given protein in a sample. For each well, we considered the median fluorescence intensity (MFI) for a serum protein as its abundance and averaged the MFI of these replicates. To ignore low-abundance proteins, only measurements with mean concentrations higher than a negative control serum were included in our analysis.

Hemagglutination Inhibition Assays

The HAI assay was performed on sera from day 0 and day 28 post influenza vaccination. Fold changes day 28/day 0 were used for analyses. In one analysis, subjects with a pre-vaccination titer of 40 or more were excluded (Table 1). Serially diluted 25 μ l aliquots of serum samples in PBS were mixed with 25 μ l aliquots of virus, corresponding to four HA units, in V-bottom 96-well plates (Nunc). These were then incubated for 15 min at room temperature. At the end of the incubation, 50 μ l of 0.5% chicken red blood cells (cRBC) were added and the plate incubated for 1 hr at room temperature, and HAI activity was read as follows: (1) positive result: hemagglutination is present, the well is hazy with no cRBC button or (2) negative result: hemagglutination is absent, the well is relatively clear with cRBC button. The HAI titer is defined as the reciprocal of dilution of the last well that inhibits hemagglutination.

Structural Equation Modeling to Estimate Heritable and Non-Heritable Influences

For all of the measurements made, a structural equation modeling approach was used to estimate heritability (Rijsdijk and Sham, 2002). This classical twin modeling approach is based on the assumption that MZ twins are genetically identical, whereas DZ twins share ~50% of their polymorphic genes and that MZ and DZ twin pairs are equally similar with respect to their shared environmental influence. The covariance matrix for each measurement made in MZ and DZ twin pairs can then be decomposed into three parameters: (1) additive genetic parameter, (2) common environmental parameter, and (3) environmental parameter unique to one twin. A linear ACE model then estimates the contribution of each of these parameters by maximum likelihood. After correcting the E-parameter for technical measurement errors, as described in detail below, all parameters were scaled as a proportion of the total variance (A+C+E). All data was corrected for age and gender prior to ACE modeling. We performed resampling tests on all heritability estimates, using a jackknife resampling approach leaving one twin pair out of the calculation in each iteration and using the mean values of all such iterations as our final estimate with 95% confidence intervals. All calculations were performed using both our own implementation of ACE fitting in MATLAB, version 8.3 and the openMX library version 1.4 running in R version 3.0.3. Both platforms were used in order to prevent any bias due to the software used.

Correction of Model Estimates for Technical Variability

For all measurements, standard samples were analyzed repeatedly (>17 times). These were either PBMC aliquots frozen at the same time and thawed for every experiment or pooled serum used as standards for Luminex and HAI assays. By calculating pooled variance estimates for these technical replicates and subtracting this from the E-component in our ACE models prior to normalization, we prevented the underestimation of heritability due to such stochastic measurement errors. This procedure overestimates the technical noise level of the actual twin samples by being collected across multiple batches, whereas twin samples compared were always analyzed within the same batch, and after correction, no relationship between technical variability and heritability

estimates is seen (Figure S6A). We also assessed the biological variability over time in an unrelated cohort by calculating coefficients of variance (CVs) from longitudinal samples drawn once yearly for 2–5 years. No relationship between longitudinal CVs and estimated heritability was found (Figure S6B).

Identification of Pairwise Dependencies between Measurements and the Creation of an Immune Network Model

To identify meaningful relationships between measurements, we used the recently developed non-paranormal SKEPTIC approach (Liu et al., 2012), with a transformed Spearman/rank correlation matrix as input. To make the network model interpretable, we pursued sparse precision matrices with a graphical lasso approach penalizing non-zero entries in the matrix (Friedman et al., 2008). A zero entry in the precision matrix encodes conditional independencies of pairs of measurements given the state of all other measurements and is less sensitive to spurious indirect connections as compared to simple correlation analyses. To validate the inferred structural relationships, two tests were performed. (1) A permutation of samples on per phenotype basis was done to obtain null distributions for entries of the precision matrix. By repeatedly producing permuted samples and running our procedure on those samples, we obtain a distribution of precision matrices that is mostly dominated by very sparse, diagonal matrices but that also has occurrences of precision matrices that have non-zero entries. The non-zero entries thus obtained were false positive, and hence we can estimate which entries obtained on the actual data exceed the size of these false positives. (2) Given relative infrequent occurrences of non-zero entries when fitting sparse precision matrices, we opted to estimate confidence intervals for each entry in the precision matrix. We deemed entries whose confidence interval contained 0 insignificant. To obtain these confidence intervals, we performed bootstrap analysis by resampling the real samples.

CMV Serology

CMV serology was determined using a commercially available ELISA kit (CMV IgG, Gold Standard Diagnostics) as per manufacturer's instructions. In brief, sera stored at -80°C were thawed to room temperature ($20\text{--}25^{\circ}\text{C}$) and diluted 1:51 in kit diluent. Diluted samples were added to wells coated with CMV antigen from strain AD169 and were incubated at room temperature for 30 min. Wells were washed and drained, followed by the addition of goat anti-human IgG antibodies labeled with calf alkaline phosphatase, and incubated at room temperature for 30 min. Wells were again washed and drained, followed by addition of p-nitrophenyl phosphate substrate, and incubated at room temperature for 30 min. After the addition of 0.5 M trisodium phosphate stop solution, the absorbance of each well at 405 nm was read and results analyzed using the manufacturer's instructions.

MZ Twin-Twin Correlations

All measurements performed in the youngest set of MZ twin pairs (<20 years) and oldest MZ twin pairs (>60 years) was extracted, and Spearman's rank correlation coefficients were calculated and compared between these independent groups for every measurement made. Similarly, CMV serologically negative/negative MZ-twin pairs were compared to CMV positive/negative (discordant twins).

SUPPLEMENTAL INFORMATION

Supplemental Information includes six figures, seven tables, and two data files and can be found with this article online at <http://dx.doi.org/10.1016/j.cell.2014.12.020>.

AUTHOR CONTRIBUTIONS

P.B. and V.J. performed all analyses. T.G. helped with the network analysis. S.B. and S.S.-O. provided input on heritability estimates. All data was generated by the Human Immune Monitoring Center under the direction of H.T.M. except for the 2009 HAI data generated by D.F. and CMV serology by C.J.L.A. G.E.S. directs the twin registry and provided input on the twin analyses, and C.L.D. was responsible for regulatory approvals, protocol design,

study conduct, and clinical data management. P.B. and M.M.D. wrote the paper with input from co-authors.

ACKNOWLEDGMENTS

The authors thank all members of the Davis and Y. Chien labs for inspiring discussions and the staff at the Human Immune Monitoring Center and the Stanford-LPCH Vaccine Program for sample collection and data generation. Thanks also to Rob Tibshirani and Chiara Sabatti for input on statistical analyses. Twins were recruited from Twin Research Registry at SRI International, Menlo Park, CA and the authors wish to thank the following individuals: Mary McElroy, Lisa Jack, Ruth Krasnow, Jill Rubin, Dina Basin, Lucia Panini, and Marty Ritchey. The Stanford-LPCH program thanks Project Manager Sally Mackey; Research Nurses Susan Swope, Tony Trela, and Cynthia Walsh; phlebotomist Michele Ugur; and CRAs Ashima Goel, Thu Quan, Kyrsten Spann, Sushil Batra, Isaac Chang, and Raquel Fleischmann. The authors also wish to thank the contributions and commitment to science provided by the twins through their ongoing participation in the Registry and various research studies. This work was supported by NIH grants U19 AI090019, U19 AI057229 and the Howard Hughes Medical Institute to M.M.D. Additional support was provided by the Wenner-Gren Foundation and Sweden-America Foundation to P.B, funds to the Twin Registry were provided through SRI's Center for Health Sciences and through grants from the NIH including DA011170, DA023063, AI090019 and ES022153. The Clinical and Translational Research Unit at Stanford University Hospital was supported by an NIH/NCRR CTSA award number UL1 RR025744.

Received: June 26, 2014

Revised: October 20, 2014

Accepted: November 14, 2014

Published: January 15, 2015

REFERENCES

- Alcaïs, A., Abel, L., and Casanova, J.-L. (2009). Human genetics of infectious diseases: between proof of principle and paradigm. *J. Clin. Invest.* **119**, 2506–2514.
- Alcaïs, A., Quintana-Murci, L., Thaler, D.S., Schurr, E., Abel, L., and Casanova, J.-L. (2010). Life-threatening infectious diseases of childhood: single-gene inborn errors of immunity? *Ann. N.Y. Acad. Sci.* **1214**, 18–33.
- Bell, J.T., and Spector, T.D. (2011). A twin approach to unraveling epigenetics. *Trends Genet.* **27**, 116–125.
- Chidrawar, S., Khan, N., Wei, W., McLarnon, A., Smith, N., Nayak, L., and Moss, P. (2009). Cytomegalovirus-seropositivity has a profound influence on the magnitude of major lymphoid subsets within healthy individuals. *Clin. Exp. Immunol.* **155**, 423–432.
- Clementi, M., Forabosco, P., Amadori, A., Zamarchi, R., De Silvestro, G., Di Gianantonio, E., Chieco-Bianchi, L., and Tenconi, R. (1999). CD4 and CD8 T lymphocyte inheritance. Evidence for major autosomal recessive genes. *Hum. Genet.* **105**, 337–342.
- Cooper, G.S., Miller, F.W., and Pandey, J.P. (1999). The role of genetic factors in autoimmune disease: implications for environmental research. *Environ. Health Perspect.* **107** (Suppl 5), 693–700.
- Davis, M.M. (2008). A prescription for human immunology. *Immunity* **29**, 835–838.
- de Craen, A.J.M., Posthuma, D., Remarque, E.J., van den Biggelaar, A.H.J., Westendorp, R.G.J., and Boomsma, D.I. (2005). Heritability estimates of innate immunity: an extended twin study. *Genes Immun.* **6**, 167–170.
- Dorshkind, K., Montecino-Rodriguez, E., and Signer, R.A.J. (2009). The ageing immune system: is it ever too old to become young again? *Nat. Rev. Immunol.* **9**, 57–62.
- Duffy, D., Rouilly, V., Libri, V., Hasan, M., Beitz, B., David, M., Urrutia, A., Bisiaux, A., Labrie, S.T., Dubois, A., et al.; Milieu Intérieur Consortium (2014). Functional analysis via standardized whole-blood stimulation systems defines the boundaries of a healthy immune response to complex stimuli. *Immunity* **40**, 436–450.
- Evans, D.M., Frazer, I.H., and Martin, N.G. (1999). Genetic and environmental causes of variation in basal levels of blood cells. *Twin Res.* **2**, 250–257.
- Evans, D.M., Zhu, G., Duffy, D.L., Frazer, I.H., Montgomery, G.W., and Martin, N.G. (2004). A major quantitative trait locus for CD4-CD8 ratio is located on chromosome 11. *Genes Immun.* **5**, 548–552.
- Fraga, M.F., Ballestar, E., Paz, M.F., Ropero, S., Setien, F., Ballestar, M.L., Heine-Suñer, D., Cigudosa, J.C., Urioste, M., Benitez, J., et al. (2005). Epigenetic differences arise during the lifetime of monozygotic twins. *Proc. Natl. Acad. Sci. USA* **102**, 10604–10609.
- Francis, T.J. (1960). On the doctrine of original antigenic sin. *Proc. Am. Philos. Soc.* **104**, 572–578.
- Friedman, J., Hastie, T., and Tibshirani, R. (2008). Sparse inverse covariance estimation with the graphical lasso. *Biostatistics* **9**, 432–441.
- Furman, D., Hejblum, B.P., Simon, N., Jojic, V., Dekker, C.L., Thiébaud, R., Tibshirani, R.J., and Davis, M.M. (2014). Systems analysis of sex differences reveals an immunosuppressive role for testosterone in the response to influenza vaccination. *Proc. Natl. Acad. Sci. USA* **111**, 869–874.
- Glanville, J., Kuo, T.C., von Büdingen, H.C., Guey, L., Berka, J., Sundar, P.D., Huerta, G., Mehta, G.R., Oksenberg, J.R., Hauser, S.L., et al. (2011). Naive antibody gene-segment frequencies are heritable and unaltered by chronic lymphocyte ablation. *Proc. Natl. Acad. Sci. USA* **108**, 20066–20071.
- Gregersen, P.K., Amos, C.I., Lee, A.T., Lu, Y., Remmers, E.F., Kastner, D.L., Seldin, M.F., Criswell, L.A., Plenge, R.M., Holers, V.M., et al. (2009). REL, encoding a member of the NF-kappaB family of transcription factors, is a newly defined risk locus for rheumatoid arthritis. *Nat. Genet.* **41**, 820–823.
- Höhler, T., Reuss, E., Evers, N., Dietrich, E., Rittner, C., Freitag, C.M., Vollmar, J., Schneider, P.M., and Fimmers, R. (2002). Differential genetic determination of immune responsiveness to hepatitis B surface antigen and to hepatitis A virus: a vaccination study in twins. *Lancet* **360**, 991–995.
- Hooper, L.V., Littman, D.R., and Macpherson, A.J. (2012). Interactions between the microbiota and the immune system. *Science* **336**, 1268–1273.
- Jablonski, W. (1922). A contribution to the heredity of refraction in human eyes. *Arch. Augenheilk.* **91**, 308–328.
- Jacobson, R.M., Ovsyannikova, I.G., Targonski, P.V., and Poland, G.A. (2007). Studies of twins in vaccinology. *Vaccine* **25**, 3160–3164.
- Krasnow, R.E., Jack, L.M., Lessov-Schlaggar, C.N., Bergen, A.W., and Swan, G.E. (2013). The Twin Research Registry at SRI International. *Twin Res. Hum. Genet.* **16**, 463–470.
- Krutzik, P.O., and Nolan, G.P. (2006). Fluorescent cell barcoding in flow cytometry allows high-throughput drug screening and signaling profiling. *Nat. Methods* **3**, 361–368.
- Ku, C.-L., von Bernuth, H., Picard, C., Zhang, S.Y., Chang, H.H., Yang, K., Chrabieh, M., Issekutz, A.C., Cunningham, C.K., Gallin, J., et al. (2007). Selective predisposition to bacterial infections in IRAK-4-deficient children: IRAK-4-dependent TLRs are otherwise redundant in protective immunity. *J. Exp. Med.* **204**, 2407–2422.
- Lee, Y.C., Newport, M.J., Goetghebuer, T., Siegrist, C.-A., Weiss, H.A., Pollard, A.J., and Marchant, A.; MRC Twin Study Group (2006). Influence of genetic and environmental factors on the immunogenicity of Hib vaccine in Gambian twins. *Vaccine* **24**, 5335–5340.
- Li, S., Roupael, N., Duraisingham, S., Romero-Steiner, S., Presnell, S., Davis, C., Schmidt, D.S., Johnson, S.E., Milton, A., Rajam, G., et al. (2014). Molecular signatures of antibody responses derived from a systems biology study of five human vaccines. *Nat. Immunol.* **15**, 195–204.
- Liu, H., Han, F., Yuan, M., Lafferty, J., and Wasserman, L. (2012). High-dimensional semiparametric Gaussian copula graphical models. *Ann. Stat.* **40**, 2293–2326.
- Maecker, H.T., Rinfret, A., D'Souza, P., Darden, J., Roig, E., Landry, C., Hayes, P., Birungi, J., Anzala, O., Garcia, M., et al. (2005). Standardization of cytokine flow cytometry assays. *BMC Immunol.* **6**, 13.

- Mazmanian, S.K., Liu, C.H., Tzianabos, A.O., and Kasper, D.L. (2005). An immunomodulatory molecule of symbiotic bacteria directs maturation of the host immune system. *Cell* 122, 107–118.
- Morahan, G., Huang, D., Wu, M., Holt, B.J., White, G.P., Kendall, G.E., Sly, P.D., and Holt, P.G. (2002). Association of IL12B promoter polymorphism with severity of atopic and non-atopic asthma in children. *Lancet* 360, 455–459.
- Nair, R.P., Duffin, K.C., Helms, C., Ding, J., Stuart, P.E., Goldgar, D., Gudjons-son, J.E., Li, Y., Tejasvi, T., Feng, B.-J., et al.; Collaborative Association Study of Psoriasis (2009). Genome-wide scan reveals association of psoriasis with IL-23 and NF-kappaB pathways. *Nat. Genet.* 41, 199–204.
- Newport, M.J., Goetghebuer, T., Weiss, H.A., Whittle, H., Siegrist, C.-A., and Marchant, A.; MRC Gambia Twin Study Group (2004). Genetic regulation of immune responses to vaccines in early life. *Genes Immun.* 5, 122–129.
- O'Connor, D., and Pollard, A.J. (2013). Characterizing vaccine responses using host genomic and transcriptomic analysis. *Clin. Infect. Dis.* 57, 860–869.
- Okada, Y., Hirota, T., Kamatani, Y., Takahashi, A., Ohmiya, H., Kumasaka, N., Higasa, K., Yamaguchi-Kabata, Y., Hosono, N., Nalls, M.A., et al. (2011). Identification of nine novel loci associated with white blood cell subtypes in a Japanese population. *PLoS Genet.* 7, e1002067.
- Orrù, V., Steri, M., Sole, G., Sidore, C., Virdis, F., Dei, M., Lai, S., Zoledziewska, M., Busonero, F., Mulas, A., et al. (2013). Genetic variants regulating immune cell levels in health and disease. *Cell* 155, 242–256.
- Querec, T.D., Akondy, R.S., Lee, E.K., Cao, W., Nakaya, H.I., Teuwen, D., Pirani, A., Germert, K., Deng, J., Marzolf, B., et al. (2009). Systems biology approach predicts immunogenicity of the yellow fever vaccine in humans. *Nat. Immunol.* 10, 116–125.
- Reiner, A.P., Lettre, G., Nalls, M.A., Ganesh, S.K., Mathias, R., Austin, M.A., Dean, E., Arepalli, S., Britton, A., Chen, Z., et al. (2011). Genome-wide association study of white blood cell count in 16,388 African Americans: the continental origins and genetic epidemiology network (COGENT). *PLoS Genet.* 7, e1002108.
- Rijsdijk, F.V., and Sham, P.C. (2002). Analytic approaches to twin data using structural equation models. *Brief. Bioinform.* 3, 119–133.
- Sasaki, S., He, X.-S., Holmes, T.H., Dekker, C.L., Kemble, G.W., Arvin, A.M., and Greenberg, H.B. (2008). Influence of prior influenza vaccination on antibody and B-cell responses. *PLoS ONE* 3, e2975.
- Sekaly, R.-P. (2008). The failed HIV Merck vaccine study: a step back or a launching point for future vaccine development? *J. Exp. Med.* 205, 7–12.
- Su, L.F., Kidd, B.A., Han, A., Kotzin, J.J., and Davis, M.M. (2013). Virus-specific CD4(+) memory-phenotype T cells are abundant in unexposed adults. *Immunity* 38, 373–383.
- Sylwester, A.W., Mitchell, B.L., Edgar, J.B., Taormina, C., Pelte, C., Ruchti, F., Sleath, P.R., Grabstein, K.H., Hosken, N.A., Kern, F., et al. (2005). Broadly targeted human cytomegalovirus-specific CD4+ and CD8+ T cells dominate the memory compartments of exposed subjects. *J. Exp. Med.* 202, 673–685.
- Tan, P.-L., Jacobson, R.M., Poland, G.A., Jacobsen, S.J., and Pankratz, V.S. (2001). Twin studies of immunogenicity—determining the genetic contribution to vaccine failure. *Vaccine* 19, 2434–2439.
- Todd, J.A. (2010). Etiology of type 1 diabetes. *Immunity* 32, 457–467.
- Tsang, J.S., Schwartzberg, P.L., Kotliarov, Y., Biancotto, A., Xie, Z., Germain, R.N., Wang, E., Olnes, M.J., Narayanan, M., Golding, H., et al.; Baylor HIPC Center; CHI Consortium (2014). Global analyses of human immune variation reveal baseline predictors of postvaccination responses. *Cell* 157, 499–513.
- Villeda, S.A., and Wyss-Coray, T. (2013). The circulatory systemic environment as a modulator of neurogenesis and brain aging. *Autoimmun. Rev.* 12, 674–677.
- von Bernuth, H., Picard, C., Jin, Z., Pankla, R., Xiao, H., Ku, C.L., Chrabieh, M., Mustapha, I.B., Ghandil, P., Camcioglu, Y., et al. (2008). Pyogenic bacterial infections in humans with MyD88 deficiency. *Science* 321, 691–696.
- Wills, M., Akbar, A., Beswick, M., Bosch, J.A., Caruso, C., Colonna-Romano, G., Dutta, A., Franceschi, C., Fülöp, T., Gkrania-Klotsas, E., et al. (2011). Report from the second cytomegalovirus and immunosenescence workshop. *Immun. Ageing* 8, 10.
- Yan, K., Cai, W., Cao, F., Sun, H., Chen, S., Xu, R., Wei, X., Shi, X., and Yan, W. (2013). Genetic effects have a dominant role on poor responses to infant vaccination to hepatitis B virus. *J. Hum. Genet.* 58, 293–297.

Molecular and Genetic Properties of Tumors Associated with Local Immune Cytolytic Activity

Michael S. Rooney,^{1,2} Sachet A. Shukla,^{1,3} Catherine J. Wu,^{1,3,4} Gad Getz,^{1,5} and Nir Hacohen^{1,4,6,*}

¹The Broad Institute, Cambridge, MA 02142, USA

²Harvard/MIT Division of Health Sciences and Technology, Cambridge, MA 02141, USA

³Department of Medical Oncology, Dana-Farber Cancer Institute, Boston, MA 02115, USA

⁴Department of Medicine, Harvard Medical School, Boston, MA 02115, USA

⁵Massachusetts General Hospital Cancer Center and Department of Pathology, Charlestown, MA 02129, USA

⁶Center for Immunology and Inflammatory Diseases and Department of Medicine, Massachusetts General Hospital, Charlestown, MA 02129, USA

*Correspondence: nhacohen@mgh.harvard.edu

<http://dx.doi.org/10.1016/j.cell.2014.12.033>

SUMMARY

How the genomic landscape of a tumor shapes and is shaped by anti-tumor immunity has not been systematically explored. Using large-scale genomic data sets of solid tissue tumor biopsies, we quantified the cytolytic activity of the local immune infiltrate and identified associated properties across 18 tumor types. The number of predicted MHC Class I-associated neoantigens was correlated with cytolytic activity and was lower than expected in colorectal and other tumors, suggesting immune-mediated elimination. We identified recurrently mutated genes that showed positive association with cytolytic activity, including beta-2-microglobulin (*B2M*), *HLA-A*, *-B* and *-C* and Caspase 8 (*CASP8*), highlighting loss of antigen presentation and blockade of extrinsic apoptosis as key strategies of resistance to cytolytic activity. Genetic amplifications were also associated with high cytolytic activity, including immunosuppressive factors such as *PDL1/2* and *ALOX12B/15B*. Our genetic findings thus provide evidence for immunoediting in tumors and uncover mechanisms of tumor-intrinsic resistance to cytolytic activity.

INTRODUCTION

With the recent success of checkpoint blockade therapy (against CTLA4 or PD1/PDL1) in inducing durable control of diverse tumors (Hinrichs and Rosenberg, 2014; Sharma et al., 2011), it has become critical to understand why some tumors are not responsive or develop resistance to therapy. Predictors of outcome have been identified in the context of spontaneous tumor immunity (Bindea et al., 2013) and immunotherapy (Herbst et al., 2014; Tumei et al., 2014; Ji et al., 2012; Snyder et al., 2014), but there remains a need for more extensive mechanistic analyses of human tumor-immune interactions.

High-dimensional data sets—such as The Cancer Genome Atlas (TCGA) that include genome-wide DNA sequencing, RNA sequencing and copy number profiles—have made it possible to dissect the factors driving malignancy with unprecedented depth. Recent analyses of TCGA data sets have linked the genomic landscape of tumors with tumor immunity, implicating neoantigen load in driving T cell responses (Brown et al., 2014) and identifying somatic mutations associated with immune infiltrates (Rutledge et al., 2013). Here, we build on this work and use the extensive TCGA data set to infer how tumors induce and adapt to immune responses.

To identify and characterize the correlates of anti-tumor immunity, we devised an RNA-based metric of immune cytolytic activity and calculated it for thousands of TCGA solid tumor samples. By correlating this metric with genetic and non-genetic findings from TCGA data, we set out to address several questions, including: does cytolytic activity vary across tumor types? Does the load of predicted neoantigens or viruses in a tumor explain the cytolytic activity? Are particular recurrent mutations in tumors associated with higher cytolytic activity, reflecting mechanisms of tumor escape from cytolytic immune activities?

RESULTS

A Metric for Immune Cytolytic Activity Based on Gene Expression in TCGA Tumors

To study immune effector activity in solid tumors, we focused on cytotoxic T cells (CTL) and natural killer cells (NK) because of their potent ability to kill tumor cells and numerous studies showing that effector T cells at the tumor site predict favorable outcome across many cancers (Pagès et al., 2005; Sato et al., 2005; Schumacher et al., 2001). Using RNA-Seq data from thousands of TCGA solid tumor biopsies, we devised a simple and quantitative measure of immune cytolytic activity (“CYT”) based on transcript levels of two key cytolytic effectors, granzyme A (*GZMA*) and perforin (*PRF1*), which are dramatically upregulated upon CD8⁺ T cell activation (Johnson et al., 2003) and during productive clinical responses to anti-CTLA-4 and anti-PD-L1 immunotherapies (Ji et al., 2012; Herbst et al., 2014). Consistent

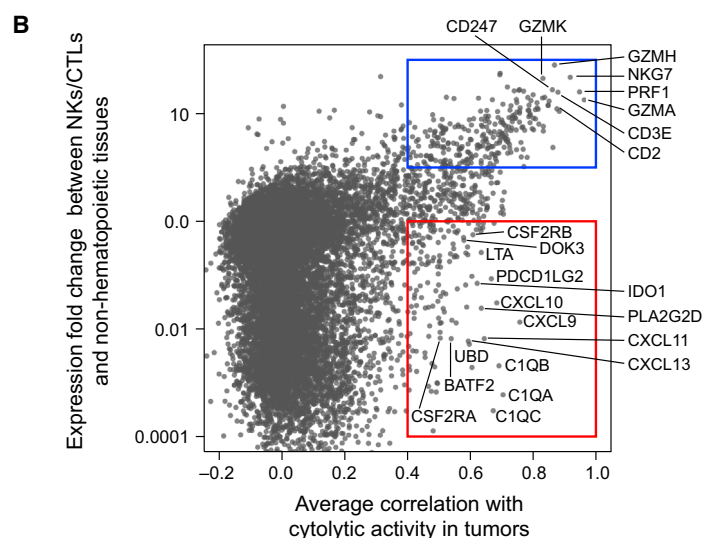
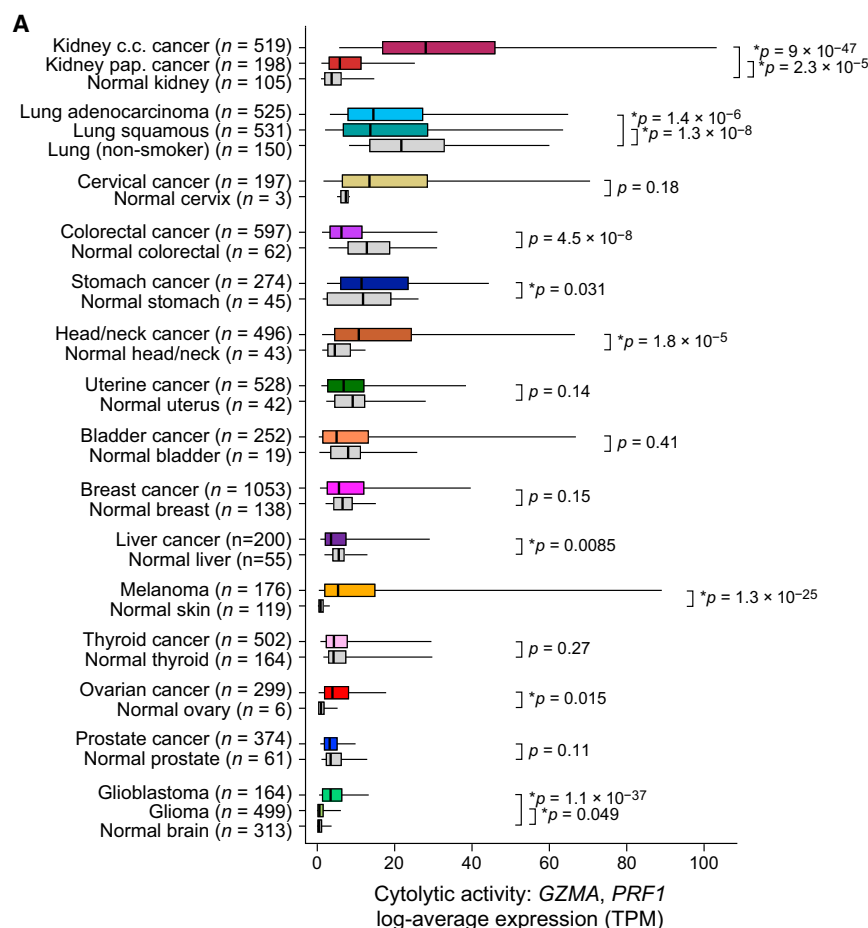


Figure 1. Immune Cytolytic Activity Varies across Tumor Types and Is Associated with Suppressive Factors

(A) Cytolytic activity (CYT), defined as the log-average (geometric mean) of *GZMA* and *PRF1* expression in transcripts per million (TPM), is shown for each of 18 TCGA tumor types and normal tissues. Normal tissue samples include TCGA controls and GTEx samples, excluding smokers for lung tissues. Boxes in box plot represent interquartile ranges and vertical lines represent 5th–95th percentile ranges, with a notch for the median. p values are unadjusted and calculated by Wilcoxon rank-sum test (comparison to relevant normal), and asterisks denote events significant at 10% FDR.

(B) The correlation of a gene with CYT across all tumor types is shown (x axis) relative to its relative expression in CTL/NK cells. Top right, genes expressed in CTL/NK cells that are associated with CYT. Bottom right, non-CTL/NK genes associated with CYT. Average Spearman correlation of expression with CYT was calculated across 18 tumor types. y axis: for each gene, median expression in NKs and CTLs divided by median expression in non-hematopoietic cells using CAGE data from Fantom5.

See also [Data S1](#) and [Table S1](#).

We found that the levels of cytolytic activity were highest in kidney clear cell carcinomas and cervical cancers, lowest in glioma and prostate cancers, and average (albeit skewed to high levels) in melanoma ([Figure 1A](#); [Table S1A](#) and [S1B](#)). Most normal tissues (from TCGA or the Genotype-Tissue Expression [GTEx] project [[GTEx Consortium, 2013](#)]) showed definitively lower (6 tissues) or equal (7 tissues) cytolytic activity compared to their corresponding tumors, but two showed definitively higher activity (lung and colon). Of note, CYT in colorectal tumors increased considerably given high microsatellite instability (MSI) ([Data S1E](#)) ([Schwitalle et al., 2008](#)). The differences in cytolytic activities across tumor types and compared to normal tissues are likely to reflect a combination of tissue- and tumor-specific mechanisms that regulate local immunity.

Cytolytic Activity Is Associated with Counter-Regulatory Immune Responses and Improved Prognosis

To determine whether cytolytic activity is associated with other immune cell types

and functions, we calculated the enrichment of 15 immune cell type and function gene sets in the same samples ([Table S1C](#); expression data from Fantom5 project [[FANTOM Consortium et al., 2014](#)]). While CYT showed moderate correlation with B cells and weak correlation with macrophages, it showed strong

with their coordinated roles, *GZMA* and *PRF1* were tightly co-expressed in TCGA samples ([Data S1A](#) and [S1B](#)) and showed CTL-specific expression in panels of human cell types ([Data S1C](#) and [S1D](#)), thus serving as highly specific markers in heterogeneous tumor samples.

correlation with: (1) CTL markers, as expected; (2) plasmacytoid dendritic cells; (3) counter-regulatory Tregs and known T cell co-inhibitory receptors, as seen in chronic inflammatory conditions (Data S1F) (Lund et al., 2008). We note that expression of the pre-defined gene sets was similarly enriched in most tumor and normal tissues, with some notable differences (Data S1G), and not typically connected to tumor stage (Data S1H and S1I). Finally, when we looked for CYT correlations with any transcript (filtering out CTL and NK genes), we found that CYT was best correlated with immunosuppressive factors (Spranger et al., 2013), such as PDL2 (*PDCD1LG2*), IDO1/2, DOK3 (Lemay et al., 2000), GM-CSF receptor (*CSF2RA*, *CSF2RB*), and the C1Q complex (Figure 1B). In addition, it was also associated with interferon-stimulated chemokines (*CXCL9*, *CLCL10*, and *CXCL11*) that attract T cells, as observed previously (Bindea et al., 2013). We conclude that tumors can differ dramatically in their infiltrate levels and composition, and that cytolytic activity is associated with counter-regulatory activities that limit the immune response.

When we used CYT and these other metrics to identify predictors of survival (controlling for tumor histology and stage), we found that high CYT (and other T cell markers) is associated with a modest but significant pan-cancer survival benefit (Data S1J). While no individual immune cell type metrics were associated with poorer prognosis, higher expression of macrophage markers relative to other markers was consistently linked with poor prognosis, while higher expression of CYT or CTL markers was correlated with improved prognosis (Data S1J).

Tumor Cytolytic Activity Is Associated with Oncogenic Viruses in Some Tumors

Viruses account for a subset of malignancies and are also known to activate high-affinity antigen-specific CTLs against non-self viral antigens. Thus, we tested for correlation of cytolytic activity levels with transcripts from oncogenic viruses—including Epstein Barr virus (EBV), hepatitis B and C (HBV and HCV), human papilloma virus (HPV), Kaposi sarcoma virus (KSV), and polyoma viruses (Table S2A).

Consistent with previous analysis of TCGA data (Tang et al., 2013), HPV infection was most abundant in cervical cancer (91%), but also frequent in head and neck cancer (12%; with more men than women, OR = 4.9; $p = 8.5 \times 10^{-4}$) and bladder cancer (2%). We also observed occasional cases in colorectal, kidney clear cell, glioma, lung squamous cell carcinoma, and uterine cancer (Figure 2A). Only stomach cancer demonstrated definitive instances of EBV infection (8%; Table S2A), which was associated with high expression of specific EBV genes *EBER-1* and *RPMS1* (Data S2A). Asian patients, known to exhibit increased rates of stomach cancer (Jemal et al., 2007), were not more likely than other stomach cancer patients to harbor EBV ($p = 0.63$). Consistent with a role for viral infection in the induction of CTLs, >2-fold increases in cytolytic activity were observed in EBV+ versus EBV− stomach cancers and HPV+ versus HPV− head and neck cancers, bladder cancers, uterine cancers and possibly cervical cancers (Figure 2B). Strikingly, all the gene sets that were most tightly associated with EBV infection in stomach cancer related to T cell activation (Table S2B).

HBV and HCV were primarily observed in liver cancer (25% and 5%, respectively), as expected, with occasional instances of HBV infection in diverse tumor types. The extra-hepatic cases did not exhibit hepatic gene expression signatures, suggesting that these are not the result of metastases (Data S2B). We also observed singleton cases of Kaposi sarcoma virus (lung squamous cell carcinoma and stomach cancer), BK polyoma (bladder cancer), and Merkel cell polyoma (ovarian cancer). While we did observe type I interferon activation and B cell infiltration for HCV+ liver cancer (Data S2C), these viruses did not show an identifiable association with cytolytic activity.

To probe indirectly for the presence of viruses, we looked for associations between CYT and two other correlates of viral infection, HLA genotype and APOBEC activity. While association with HLA genotype was not observed for a single tumor type (although there was a pan-cancer association with *HLA-A31*; Data S2D), we did detect association with high APOBEC activity in tumors with viral involvement (head and neck, cervical) and those without known viral involvement (breast, bladder) (Data S2E), suggesting potential for unknown virus infections in some tumors.

Cytolytic Cells Are Likely to Be Targeting Tumor Neoantigens

With recent studies from our group and others showing the presence of neopeptide-specific T cells in patients (Fritsch et al., 2014), we tested for CYT association with the overall rate of mutation and the rate of mutations predicted to yield a neopeptide (i.e., an expressed peptide capable of binding each patient's imputed HLA alleles) (Data S3A and S3B, Table S3). On average, 50% of non-silent mutations yielded ≥ 1 predicted neopeptide (with IC50 < 500 nM), and 39% of these impacted a substantially expressed gene (median expression ≥ 10 TPM in the given tissue type). Despite considerable inter-tumoral heterogeneity (Table S4A), both metrics exhibited significant positive association with CYT in multiple tumor types, most notably uterine cancer, breast cancer, stomach cancer, cervical cancer, and lung adenocarcinoma (Figures 3A and 3B). Consistent with a smoking etiology, lung adenocarcinomas from ever-smokers demonstrated significantly higher CYT than those from never-smokers ($p = 0.003$) (Data S3C). Melanoma mutations exhibited a likely association with CYT. Associations of mutations or neopeptides with CYT were matched by correlations for other T cell markers, but less so with interferon-responsive genes (Data S3D and S3E). These data are consistent with neopeptides driving CYT for many tumor types.

However, since the per-sample rate of neopeptide yielding mutations closely tracks with the overall rate of mutation (Spearman $\rho = 0.91$; Data S3F), CYT may be driven by mutation rate rather than neopeptides. To test a role for neopeptides, we reasoned that T cell-mediated immune surveillance would lead to elimination of immunogenic sub-clones expressing neopeptides. To quantify neopeptide depletion, we determined how the rate of predicted neopeptides generated per non-silent point mutation deviated from a null model based on the observed mutation rate of silent point mutations. We found that colorectal cancer and kidney clear cell cancer demonstrated dramatic depletions of neopeptides (Figure 3C; associated gene expression changes, Table S4B). Because neopeptide predictions are

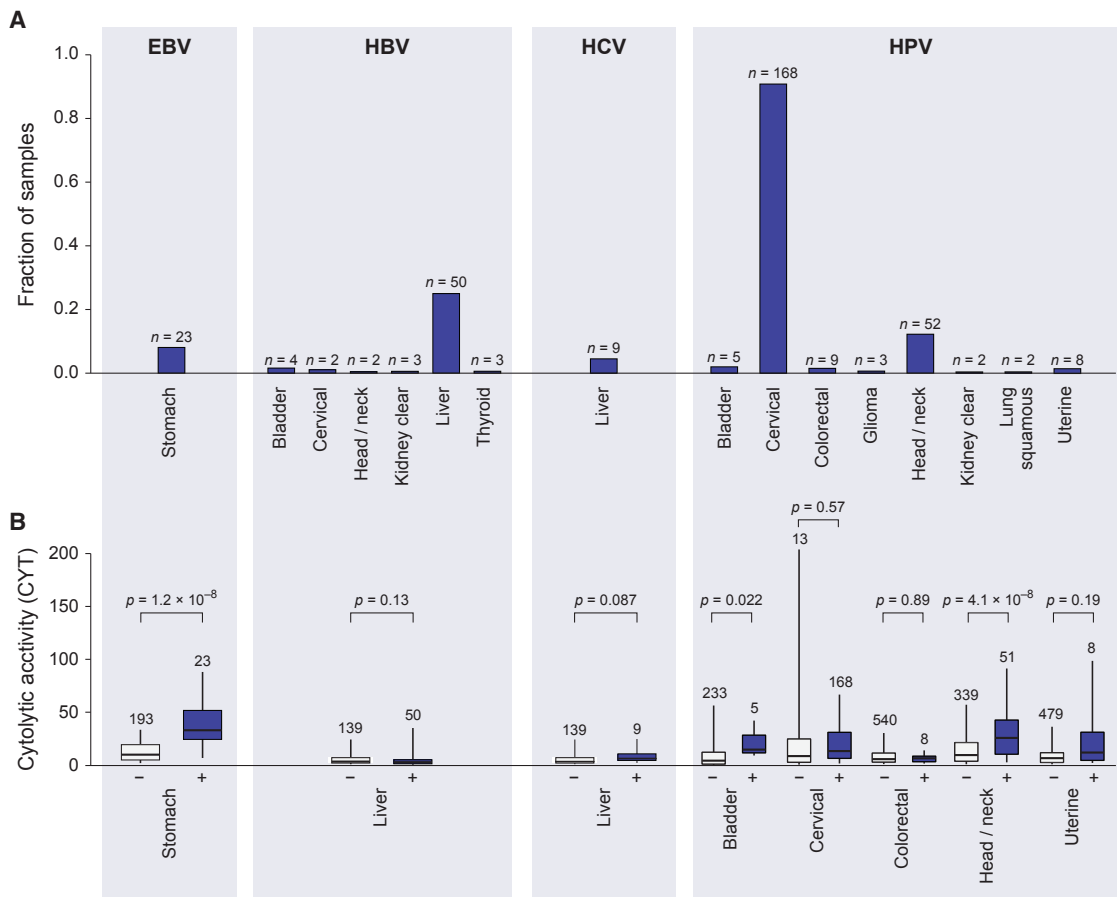


Figure 2. Viral Infection Is Tumor-Specific and Associated with Higher CYT in a Subset of Tumor Types

(A) Rates of viral infection, as defined by viral RNA-Seq read counts exceeding those observed in GTEx, for tumor types exhibiting at least one case. Isolated cases of several other viruses were also observed.

(B) Distribution of CYT in tumor samples with (+) or without (–) viral infection. In tumor types affected by multiple viruses, “negative” samples include only those negative for all viruses. Box plots as in Figure 1. p values are according to Wilcoxon rank-sum test.

See also Data S2 and Table S2.

dependent on HLA genotypes, we reasoned that random shuffling of HLA genotypes would abrogate the depletion signal (Figure S1). As expected, depletion was eliminated for colorectal cancer and kidney clear cell cancer (and we note that the residual enrichment for other tumor types may reflect degeneracy of peptide binding across HLA alleles). These findings are consistent with a model in which immune surveillance activities cull subclones expressing immunogenic antigens.

We conclude that neoepitopes are likely to be driving cytolytic activity in a number of tumors, and that the resulting antigen-specific CTLs can eliminate tumor clones harboring these neoepitopes.

Ectopic Gene Expression, Endogenous Retroviruses, and Necrosis Associated with CYT

Another potential source of tumor antigens is a unique set of genes, known as cancer testis (CT) antigens, which are not expressed in healthy tissues, except germ cells, but are aberrantly expressed in tumors and associated with antigen-specific re-

sponses in patients harboring these tumors. Ectopic expression is likely due to disturbances in genomic methylation and reactivation of stem-like expression programs that may contribute to tumorigenicity (Simpson et al., 2005). Using a set of 276 known CT genes (Almeida et al., 2009), we used GTEx to identify a subset of 60 that are transcriptionally silent in normal non-germline tissues. Ectopic expression was observed for most tumor types, especially melanoma, head and neck, lung, liver, stomach, and ovarian cancer (Data S4A; Table S4A). In no tumor type was there a clear positive association between the CYT and the count of expressed CT antigens (Data S4B). We queried individual CT antigens for correlation with CYT (Table S5A), and observed positive associations for CSAG2 in breast cancer ($p = 1.2 \times 10^{-15}$), head and neck cancer ($p = 1.9 \times 10^{-7}$), kidney clear cell cancer ($p = 9.9 \times 10^{-5}$), and other tumor types. Associations for canonical antigens, such as NY-ESO-1 (CTAG1), were less consistent. We hypothesized that T cell surveillance would lead to CT antigen silencing through chromosomal deletions, but compelling evidence for this was not observed (Data S4C).

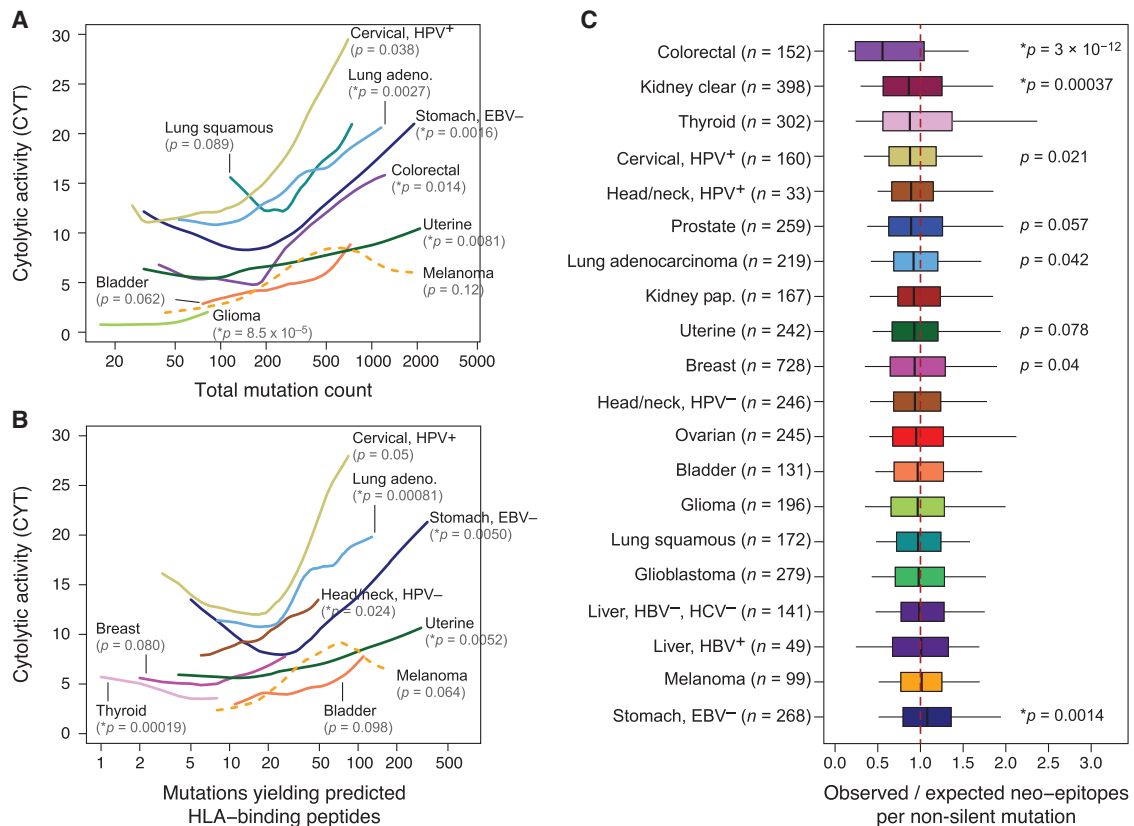


Figure 3. Count of Predicted Antigenic Mutations per Sample Is Linked with Cytolytic Activity and Selectively Depleted in Certain Tumor Types

(A) Local regression curves showing significant relationships between CYT and total mutation count in eight tumor types ($p < 0.1$, Spearman rank correlation), plus melanoma (dotted line). Curves span the 5th to 95th percentile of the mutation count variable. Colors correspond to tumor type and are the same as appear in Figure 1.

(B) Analogous to (A), but based on the count of point mutations predicted to yield an antigenic neo-epitope. Potential for antigenicity was defined based on gene expression and potential to bind the corresponding patient's imputed HLA with high affinity.

(C) For each tumor, the count of point mutations predicted to generate neo-epitopes was divided by the total count of non-silent point mutations to yield B_{obs}/N_{obs} . This observed ratio was compared to an expected ratio, B_{pred}/N_{pred} , estimated from the mutational spectra of the silent point mutations in the given sample using an empirical model (Experimental Procedures). The ratio of the observed and predicted ratios represents the relative deviation of the neo-epitope rate from expectation. p values reflect Wilcoxon rank-sum tests for deviation from 1. Asterisks denote trends significant at 10% FDR for all panels. See also Figure S1, Data S3, Table S3, and Table S4.

Endogenous retroviruses (ERVs) are another class of germ-line-encoded elements that may be re-activated in tumors, and we considered whether these might also contribute to anti-tumor immunity. TLR7 or RAG knockouts in mice develop uncontrolled ERV expression, ERV infectivity, and ERV insertion-driven tumors (Young et al., 2012; Yu et al., 2012) yet little is known about ERV-immune and ERV-cancer interactions in humans. Given reports that these elements are transcriptionally and sometimes even translationally active in humans (Boller et al., 1997; Schmitt et al., 2013), we considered the possibility that they trigger immune sensing in tumors. Therefore, we mapped TCGA RNA-Seq data to a recently published annotation of 66 expressed ERV family members (Table S5B, Data S4D) and assessed associations with cytolytic activity (Mayer et al., 2011). By comparing GTEx and TCGA tissue controls to TCGA tumor samples, we observed numerous instances of ERVs demonstrating re-activation in tumors, including one instance of an ERVH-2 element

exceeding 2,700 reads per million in a stomach adenocarcinoma (Data S4E). From these data we surprisingly discovered a conservative set of three tumor-specific endogenous retroviruses ("TSERVs") all with minimal to undetectable expression in normal tissues and elevated expression in tumor tissues (Figure 4A).

Assessing the gene expression correlates of each TSERV in the tumor type exhibiting highest expression, we observed that immune pathways were typically the most significantly enriched (Table S5C). Many ERVs, in addition to the TSERVs, demonstrated association with CYT in multiple tumor types (Figure 4B). While we cannot determine whether ERVs activate immunity or inflammation triggers ERVs (Manghera and Douville, 2013), we conclude that ERVs are highly dysregulated in tumors and speculate that they may yield tumor-specific peptide epitopes (Boller et al., 1997) or act as immunological adjuvants to activate local immunity (Yu et al., 2012).

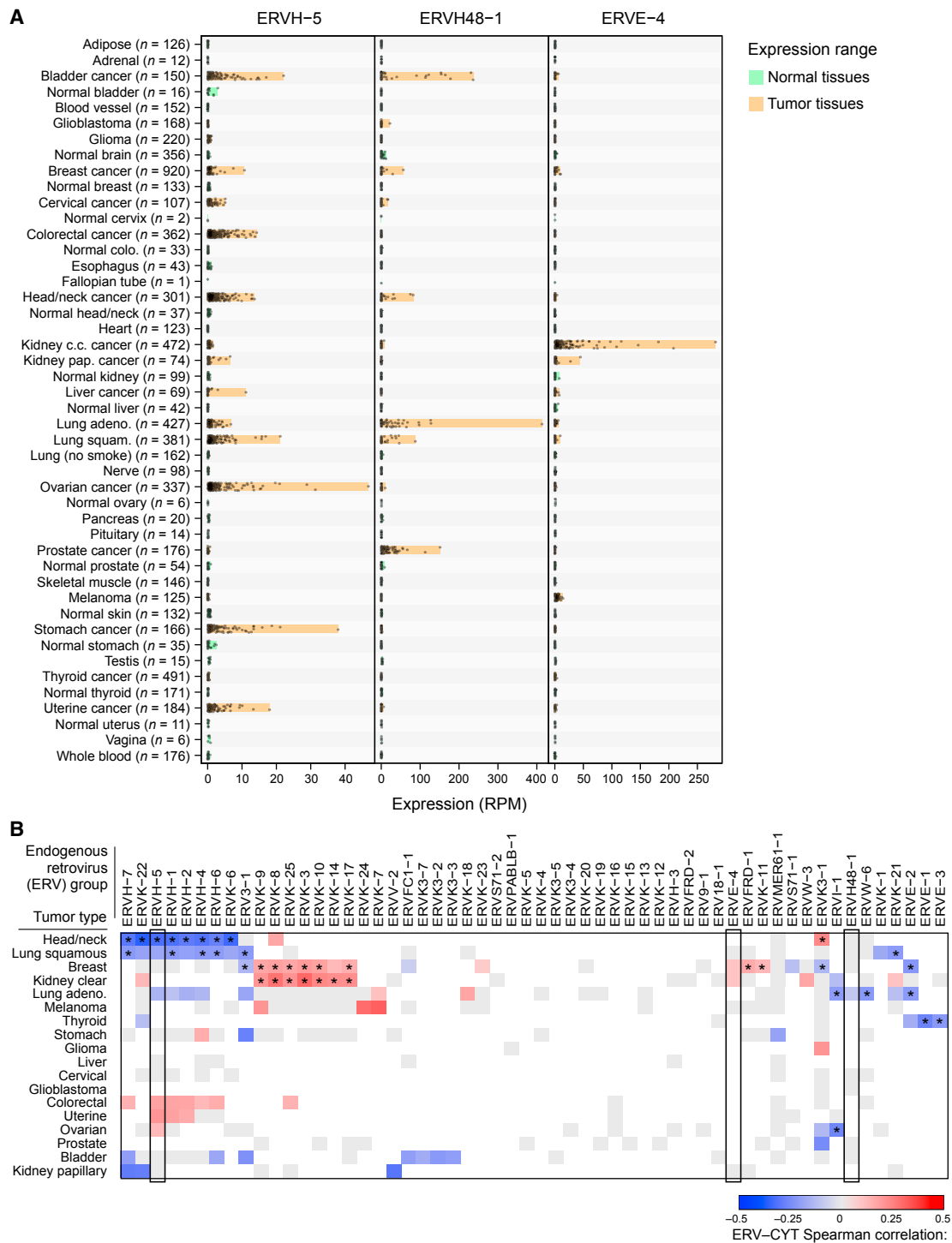


Figure 4. Endogenous Retroviruses Tied to Local Immunity

(A) RNA-Seq-derived ERV expression in reads per million (RPM) across 18 TCGA tumor types and 27 non-tumor tissue types (from TCGA and GTEx) for three elements found to be tumor-specific. The expression ranges (minimum value to maximum value) are highlighted in orange (for tumor tissues) or green (for non-tumor tissues).

(B) Spearman-rank correlations between CYT and ERV expression. Gray squares indicate non-significant association (unadjusted $p > 0.05$) and blank squares indicate no overexpression of the given ERV in the given tumor type (expression strictly below the normal tissue maximum). Asterisks (*) denote Bonferroni-significant associations (adj. $p < 0.05$).

See also [Data S4](#) and [Table S5](#).

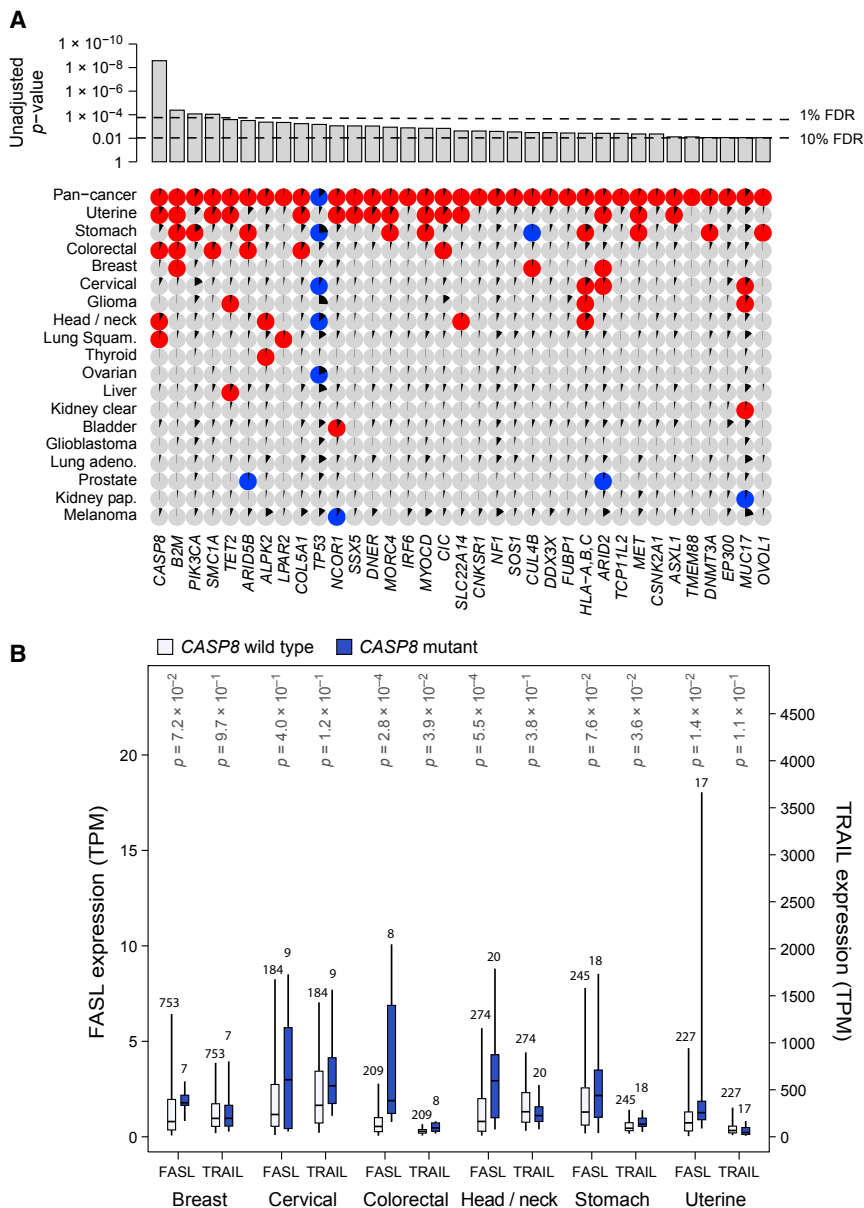


Figure 5. Gene Mutations Associated with High or Low Immune Cytolytic Activity

(A) Only genes showing pan-cancer significance (adj. $p < 0.1$, red for positive, blue for negative and gray for non-significant association) for non-silent mutation association with CYT are shown in top row. Additional rows, clustered by similarity, show independent significant (unadj. $p < 0.05$) enrichment upon sub-analysis. The black wedges represent the share of samples exhibiting mutation. Bar plot indicates unadjusted pan-cancer p values for mutational association with CYT, dashed lines indicating thresholds yielding 1% and 10% FDRs.

(B) Association between *CASP8* mutational status and *FasL* (*FASLG*) (left axis) and *TRAIL* (*TNFSF10*) (right axis) gene expression (TPM) for tumor types demonstrating at least five instances of non-synonymous *CASP8* mutation. Light and dark bars correspond to wild-type and (nonsynonymous) mutant samples, respectively. Box plots as in Figure 1. p values are calculated by Wilcoxon rank-sum test.

See also Data S5 and Table S6.

Another potential source of antigens and immunostimulatory ligands is dying cells. Thus, we explored the potential role for necrosis in driving CYT and immune infiltration in general. Rates of necrosis were highest in glioblastoma (Data S4F) and showed modest positive association ($p < 0.05$) with CYT in glioblastoma, bladder, and ovarian cancer, but notably, association with macrophage markers was consistently stronger (Data S4G).

Mutations in Specific Driver Genes Were Enriched in Tumors with Higher Cytolytic Activity

We hypothesized that high cytolytic activity could select for tumors with somatic mutations that render them resistant to immune attack. We therefore asked whether CYT is associated with mutations in 373 “driver” genes that are frequently

mutated in cancer based on analysis of TCGA exome sequencing data ($q < 0.1$ by MutSigCV [Lawrence et al., 2013]; Table S6A). Using a regression-based approach to look for pan-cancer association of these mutated genes with CYT, controlling for tumor type and background mutation rate, we found 35 genes (adj. $p < 0.1$; Figure 5A, Data S5A, Table S6B). In contrast, synonymous somatic mutations were not associated with CYT (adj. $p_{\min} = 0.09$). Of the top ten CYT-associated mutations, eight were also associated with an independent marker of CTLs (*CD8A*; 10% FDR; Data S5B), demonstrating the robustness of our CYT metric. Of the individual tumor types, uterine, stomach, and colorectal had the most associations

(15, 11, 6, respectively) while kidney clear cell and ovarian, which showed markedly higher CYT compared to normal tissue, had just one each, and lung adenocarcinoma had none. Strikingly, somatic mutations, except *TP53*, were all positively associated with CYT, consistent with a model in which tumors develop resistance mutations under selection pressure.

We note that while we predicted that cytolytic activity would have the strongest impact on the mutation landscape, we also identified gene mutations strongly associated with other immune cell types/functions (adj. $p < 0.01$; Data S5B), including *STK11* and *VHL* with reduced macrophage signature, *BRAF* with increased expression of costimulatory genes, and *AXIN2*, *SNX25* and others with the differential enrichment score of CD8+ T compared to Treg.

Higher CYT Was Associated with Mutations in Genes Involved in Antigen-Presentation, Extrinsic Apoptosis, and Innate Immune Sensing

Several themes emerged when we considered the known functions of the identified genes.

First, the most enriched gene, *CASP8* (adj. $p = 8.8 \times 10^{-7}$), is a critical player in the extrinsic apoptosis pathway and was enriched in head and neck cancer, colorectal cancer, lung squamous cell carcinoma, and uterine cancer (where it showed a maximal mutation frequency of 7.0%). The pattern of mutation was diffuse and suggested loss of function (Data S5C), a potential mechanism by which a tumor cell could evade FasL- or TRAIL-induced apoptosis. Between FasL (*FASLG*) and TRAIL (*TNFSF10*), FasL is most correlated with *CASP8* mutations and thus more consistent with such a hypothesis (Figure 5B). A study in mice indeed demonstrated that blockade of *CASP8* results in tumor escape from CTLs (Medema et al., 1999), and our result indicates that this may be a common mechanism in human tumors (that may evade CTLs or NK cells). Interestingly, four additional genes with significant but less definitive statistical enrichment also had well-established roles in regulating extrinsic apoptosis. These include, *CNKSR1* (Garimella et al., 2014), *MET* (Fan et al., 2001; Garofalo et al., 2009), *CSNK2A1* (Ravi and Bedi, 2002; Izeradjene et al., 2005; Lobet et al., 2008; Wang et al., 2006), and *PIK3CA* (Saturno et al., 2013; Song et al., 2010). *PIK3CA* mutations, which were often the well-known activating alterations E545K and H1047R (Samuels and Ericson, 2006), showed their strongest enrichment in stomach cancer, demonstrating a 20% mutation rate and a strong positive association with EBV infection ($p = 2.9 \times 10^{-10}$). As in the case of *CASP8*, mutations in each of these genes were more closely associated with FASL expression than TRAIL expression. We conclude that loss of the extrinsic apoptosis pathway may represent a general mechanism for tumors to escape immune cytolytic activity.

Second, the invariant chain of MHC Class I, *B2M*, was the next most strongly enriched gene (adj. $p = 7.1 \times 10^{-3}$), showing independently significant association in uterine, breast, colorectal cancer, and stomach cancer, which exhibited the highest rate, 5.7%. The most frequent event was the same CT dinucleotide deletion observed previously in melanoma patients relapsing from T cell-based immunotherapy (Chang et al., 2005). The MHC Class I locus itself was also significant (Table S6C; HLA-A, -B, -C mutations considered jointly, adj. $p = 5.3 \times 10^{-2}$). *HLA-A* and *HLA-B* alleles were mutated about three times as frequently as *HLA-C* alleles. No specific alleles showed strong evidence for being especially frequently mutated. The tumor types with the highest rates of HLA mutation, stomach cancer (14%), cervical cancer (12%), and head and neck cancer (11%), were also among those with frequent viral involvement. However, viral infection was not significantly associated with HLA mutation in any of them (Table S6D). Given the requirement of MHC Class I and *B2M* in presenting tumor antigens to cytotoxic CD8 T cells, we consider the enrichment of MHC Class I and *B2M* mutations in high-CYT tumors (Khong and Restifo, 2002) as an independent and strong validation of CYT as a measure of cytolytic activity. While MHC Class II genes were not significantly mutated pan-cancer, Class II gene mutations,

considered collectively, were positively associated with CYT (unadj. $p = 0.017$) with independent significance in bladder cancer (unadj. $p = 0.0084$).

Other hits included the CT antigens *MORC4* (Liggins et al., 2007) and *SSX5* (Ayyoub et al., 2004) and genes with roles in innate immune sensing, including *DDX3X* (Oshiumi et al., 2010) and *ARID2* (Yan et al., 2005). We also note that mutant *TP53* is negatively correlated with CYT, which may be explained either by a role for p53 in regulating immunity (e.g., loss of p53-regulated stress ligands that induce cytotoxicity, [Textor et al., 2011]) or from absence of viral infection (consistent with p53 mutations being anti-correlated with viral infection in stomach [$p = 2.3 \times 10^{-5}$] and head and neck cancer [$p = 2.6 \times 10^{-4}$]; Table S6D).

Because MSI-high colorectal tumors are known to be immunogenic (Kloor et al., 2010), we also considered whether MSI-high tumors were enriched for mutations in particular genes with respect to MSI-low and microsatellite stable (MSS) tumors. Mirroring the CYT analysis, *CASP8* and MHC Class I mutations were the most enriched mutations in MSI-high tumors (p adj. = 1.5×10^{-5} and 1.4×10^{-12} , respectively), with *COL5A1*, *SMC1A*, *CIC*, *ARID2*, *CNKSR1*, and *DNMT3A* also significant (adj. $p < 0.05$) (Table S6E).

Finally, we note that some candidate genes with well-known immune function (Table S6A) did not show association with CYT. However, enrichment in the expression of immune-related genes were observed in tumors with mutations in some of these genes (*TNFRSF14*, *CLEC4E*, *CD1D*, *IL32*; Table S6F).

Loci Containing Known Immune Regulators Show Copy Number Alterations Associated with CYT

We also considered the possibility that specific regions of the genome may be preferentially focally amplified or deleted (based on a data set of TCGA samples profiled with SNP6.0 arrays) in high- or low- CYT tumors. As with the point mutation analysis, we looked for pan-cancer CYT association with copy number alterations (CNAs) using regression and controlling for cancer subtype and background mutation rate (of amplifications and deletions). This approach yielded 13 significantly amplified regions (with three adjacent to each other on 6q) and one significantly deleted region (FDR = 10%) (Figure 6A, Table S7). Although CNAs include variable segments of a chromosomal region and do not typically identify causative genes, many of the identified regions harbored plausible candidates.

On chromosomes 9 and 8, we found two well-known targets of cancer immunotherapy. First, amplification of 9p23-p24.2 (Figure 6B), a region including *PDL1* (*CD274*) and *PDL2* (*PDCD1LG2*), was positively associated with CYT in lung squamous cell carcinoma, head and neck cancer, cervical cancer, stomach cancer, and colorectal cancer (Figure 6E). While tumor cells and tumor infiltrating leukocytes are known to express these ligands, our results suggest that tumor-expressed ligands affect tumor fitness in the presence of cytolytic activity. Second, a locus near 8p11.21-8p11.23 (Data S6A) showed increased probability of amplification in low-CYT tumors (pan-cancer and breast) and is adjacent to *IDO1* and *IDO2*, enzymes that degrade extracellular tryptophan and create a potent immunosuppressive microenvironment, which may explain the associated reduction in CYT (Uyttenhove et al., 2003).

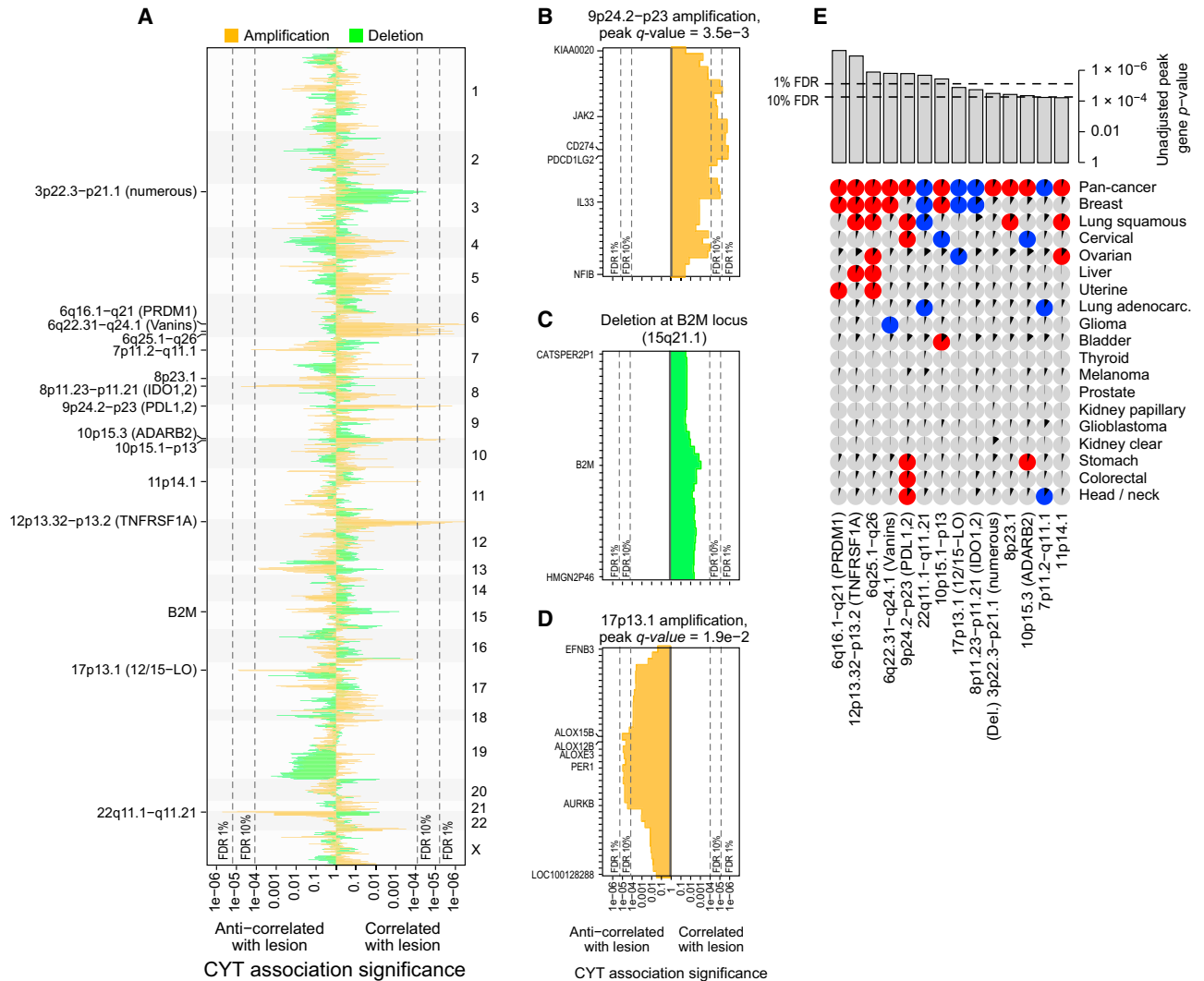


Figure 6. Amplifications and Deletions Are Associated with Cytolytic Activity in Tumors

(A) The significance of association between CYT and amplification (orange) and between CYT and deletion (green) for all genic loci. Rightward lines show unadjusted p values for instances in which the lesion was positively associated with CYT, and leftward lines show unadjusted p values for instances in which the lesion was negatively associated with CYT. Dotted lines represent the significance cutoffs yielding 1% and 10% FDRs (and also appear in parts B–E). Labels on the right side mark events significant at the 10% FDR, plus B2M. Potential driver genes appear in parentheses.

(B) Locus zoom on the 9p24.2-p23 amplification, each bar corresponding to a single gene. Labeled genes include those with driver potential or those on the locus boundary.

(C) Locus zoom on the region containing B2M, which was not genome-wide significant.

(D) Locus zoom on the 17p13.1 amplification.

(E) Significant associations between CNAs and CYT on the pan-cancer and cancer-specific level (as in Figure 5). Pan-cancer significance was defined at a 10% FDR, and significance for individual tumor types was defined at unadjusted $p < 0.05$. Positive association is indicated with red circles, negative with blue circles, and non-association with gray circles. Black wedges indicate the share of samples exhibiting the event (i.e., non-zero GISTIC score at the locus). Bar plot indicates unadjusted pan-cancer p values for CNAs, sorted by significance, with dashed lines indicating thresholds yielding 1% and 10% FDRs.

See also Data S6 and Table S7.

In addition, potential new targets were identified. These included 17p13.1, which was preferentially amplified in low-CYT tumors (Figure 6D), including breast and ovarian. The peak genes, *ALOX12B/ALOX15B* (12/15-LO) regulate immunity in many ways, including blocking the uptake of apoptotic cells by inflammatory monocytes in a manner that decreases antigen presentation to T cells (Uderhardt et al., 2012), which may

explain the observed decrease in CYT. Further supporting this model, the amplification was associated with higher necrosis in breast ($p = 0.002$) and kidney clear cell cancer ($p = 0.0002$), though not ovarian cancer. Other peaks included ones near *TNFRSF1A* and *PRDM1* (Data S6A) as well as a suggestive, but not genome-wide significant, enrichment at B2M (Figure 6C). In considering how other enrichment signatures might associate

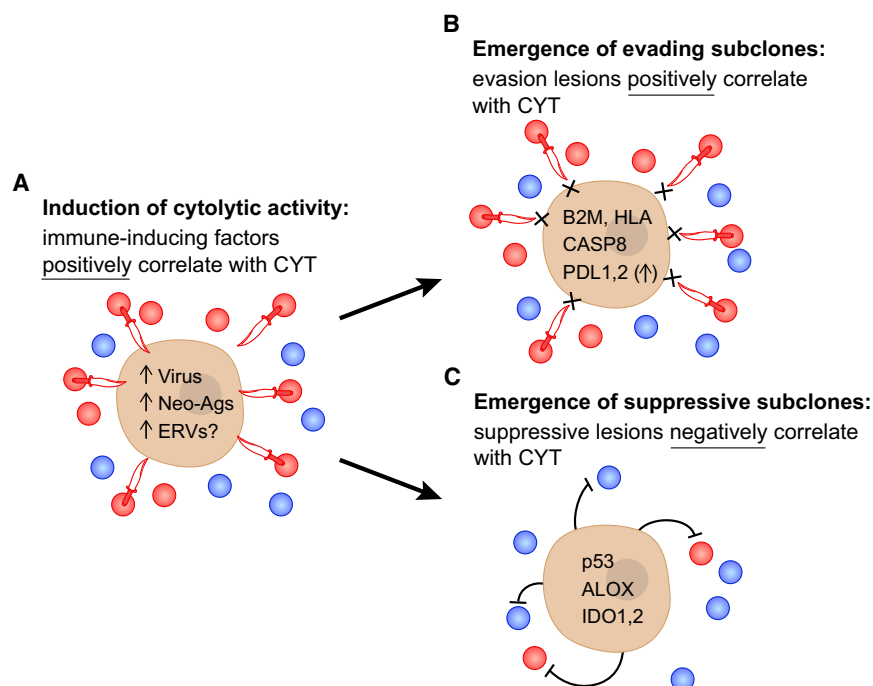


Figure 7. Proposed Model for Evolution of Tumor-Immune Associations

(A) As the tumor develops, we propose that intrinsic tumor factors—such as mutated neoantigens or viruses—induce local immune infiltrates (blue circles) that include cytolytic effector cells (expressing *GZMA/PRF1*; red circles) that kill tumors (daggers). These factors are expected to be positively correlated with CYT across tumors. (B and C) Under pressure from cytolytic immune cells, subclones with resistance mutations will grow out over time. (B) One subset of these mutations would enable tumors to evade killing, but does not impact the infiltrate, and are positively correlated with CYT (i.e., higher infiltrate samples are enriched for these mutations). (C) Another subset suppresses the immune infiltrate (i.e., lower infiltrate samples are enriched for these mutations), and is negatively correlated with CYT. Notably, p53 mutations and ALOX amplifications were also significantly negatively associated with *CD8A*, suggesting a reduction in cell numbers and not just activity. See also [Data S7](#) and [Table S8](#).

with CNAs ([Data S6B](#)), we observed a dramatic positive association between increased MHC Class I expression and amplification of the MHC Class II complex (adj. $p < 5 \times 10^{-4}$).

DISCUSSION

Based on the notion that effective natural anti-tumor immunity requires a cytolytic immune response, we quantified cytolytic activity using a simple expression metric of effector molecules that mediate cytolysis. Our analysis was designed to address which genetic and environmental factors drive tumor-associated cytolytic activity, and how this cytolytic activity selects for genetic resistance in tumors. Our results suggest that neoantigens and viruses are likely to drive cytolytic activity, and reveal known and novel mutations that enable tumors to resist immune attack.

We considered several explanations for the elevated immune cytolytic activity observed in some tumors ([Figure 7A](#)). First, we asked whether neoantigens play a role. These are a compelling set of antigens because of their absence from the thymus and thus lack of central tolerance that would normally delete cognate high-affinity T cells. Indeed, we found that neoantigen load positively associated with cytolytic activity across multiple tumor types, and that neoantigens appear to be depleted in tumors relative to their expected numbers based on the silent mutation rate, consistent with the notion of immunoediting ([Schreiber et al., 2011](#)). Second, when we analyzed CT antigens that are expressed selectively in tumors, we could not detect a positive correlation between the number of expressed CT genes and cytolytic activity. In addition, CT antigen genes were not contained within deletions associated with CYT, contrary to what would be expected if there were immune pressure on CT antigens. Although we did not uncover a role for CT antigens in spontaneous immunity (perhaps because our methods were

not optimized to detect CT depletion), we did highlight a subset of 60 CT antigens that are highly tumor-specific and may be (or are already) excellent targets for immunotherapy, including vaccines, adoptive T cell transfer, or CAR-T therapy. Third, we asked whether viruses could be inducers of immune responses. In some tumors, we observed that cytolytic activity does indeed associate with the presence of exogenous or endogenous viruses, and we expect that some viruses would trigger immunity through RNA and DNA sensors and generate immunogenic antigens for the adaptive immune response.

To learn more about how tumors adapt to attack by cytolytic immune cells, we also searched for enrichment of somatic genetic alterations in tumors with high versus low cytolytic activity. As expected, we observed enrichment of mutations in antigen presentation machinery (thus validating our cytolytic metric), including HLA and *B2M*, as well as extrinsic apoptosis genes, such as *CASP8*, that would prevent cytolytic cells from killing tumors via FasL-Fas interactions. In addition, we found cytolytic activity correlating with amplifications in regions containing genes that function in immunosuppression, such as *PDL1/2*. Most of the identified mutations—including HLA, *B2M*, and *CASP8*—were positively correlated with CYT and are likely to represent autonomous escape mechanisms ([Figure 7B](#)). In addition, we identified a smaller number of mutations that correlated negatively with cytolytic activity—including *IDO1* and *IDO2*, p53, and the ALOX locus—and may represent non-autonomous mechanisms of suppressing immunity ([Figure 7C](#)). Finally, we were surprised that CYT-associated genetic lesions represent ~10% of drivers, and these genes had largely not been studied in the context of immunity. However, given the importance of immune responses in controlling tumor progression ([Pagès et al., 2005](#)), tumors may have evolved several mechanisms of evasion.

Our approach has allowed us to positively identify the subset of tumor types that are sensitive to spontaneous cytolytic activity (Data S7, Table S8). If we consider positive correlation of HLA, *B2M*, or *CASP8* mutations with CYT as a “signature” of selection pressure by the immune system, we find that colorectal, uterine, stomach, head and neck, cervical, lung squamous, and breast tumors are most susceptible to immune elimination. If we further consider depletion of neoepitopes as an independent signature of selection, we identify colorectal as well as kidney clear cell cancer as immune-susceptible tumors. For these tumor types, we thus suggest that spontaneous tumor immunity can delete tumor cells.

For several tumor types, we did not find evidence for immunoeediting. This could be due to: insufficient power to detect associations in tumors with low rates of spontaneous immunity, non-genetic evasion mechanisms that we cannot detect, or true absence of immune cytolytic activity (perhaps for thyroid and prostate cancers, for example).

Finally, the mutations associated with cytolytic activity reveal potential genetic biomarkers for predicting outcome and candidate targets for immunotherapy. To assess the utility of these markers, one would need to genotype tumors for the 35 identified genes at clonal or subclonal levels, and test if pre-treatment or post-treatment mutations predict refractoriness or relapse in response to cytolytic immunotherapy. We predict that the presence of these mutations (assuming they do not lead to complete loss of susceptibility) indicates that re-activation of CD8 T cells would be therapeutically effective. In addition, we identified new candidates for therapeutic development, including the ALOX enzymes and their products, the PIK3CA protein that is enriched in activating mutations in high-CYT stomach cancers, and FASL which may be useful to upregulate in T cells to enhance the anti-tumor activity of adoptively transferred T cells.

Analysis of TCGA samples has revealed environmental and genetic mechanisms that impact tumor-immune interactions. While we chose to focus on cytolytic activity because of its central role in tumor elimination and the feasibility of monitoring its activity, we did not consider other tumoricidal activities (such as antibody-dependent cell-mediated cytotoxicity) because we are not aware of transcript-based markers for these activities. In addition, the CYT metric we used is transcript-based and thus may not reflect changes in cytolytic activity due to post-transcriptional regulation, and is a snapshot in time that may miss previous activity that impacted tumor growth. We anticipate that improved experimental measurements of anti-tumor immune activity will further reveal the genetic and epigenetic changes that underlie co-evolution of tumor cells and immune cells.

EXPERIMENTAL PROCEDURES

Tumor and Normal Samples and Data Sets

Analyzed samples represent untreated primary tumors, except for melanoma, which included metastases. Metastases to lymph nodes were always excluded as were patients that received neo-adjuvant therapy. Gene-level RNA-Seq expression data were accessed from GDAC Firehose (<http://gdac.broadinstitute.org>) (tumors and normals) and from the GTEx web portal (<http://www.gtexportal.org>) (normals only). RNA-Seq-based sequence data from the corresponding projects were accessed through CGHub and the

Short Read Archive (SRP012682), respectively, and used to estimate expression of endogenous and exogenous viruses. Additional gene expression data were accessed from the CCLE web portal (<http://www.broadinstitute.org/ccle/home>; Barretina et al., 2012) (Affymetrix U133+2 microarrays), Fantom5 (FANTOM Consortium et al., 2014) (cap analysis gene expression), and DMAP (Novershtern et al., 2011) and used to evaluate gene expression markers. Whole exome sequencing-derived point mutation calls were accessed from TumorPortal (Lawrence et al., 2014), Synapse workspace syn1729383 (<https://www.synapse.org/#!Synapse:syn1729383>; Kandoth et al., 2013), TCGA Data Portal (<https://tcga-data.nci.nih.gov/tcga>), GDAC Firehose (<http://gdac.broadinstitute.org/>), and the TCGA Research Network stomach adenocarcinoma publication (Cancer Genome Atlas Research Network, 2014). Whole exome sequencing-based sequence data, used to call HLA genotypes and mutations, were accessed through CGHub. GISTIC2 (Mermel et al., 2011) gene-level, zero-centered, focal copy number calls for each patient were accessed from GDAC Firehose. Clinical data for each tumor type were accessed from the TCGA public access web portal. Tables S1 and S2 catalog the TCGA and GTEx samples included in the study.

Cytolytic Activity and Other Cell Type-Specific Signatures

Cytolytic activity (CYT) was calculated as the geometric mean of *GZMA* and *PRF1* (as expressed in TPM, 0.01 offset). Marker genes for specific cell types were identified as those with expression at least 2-fold greater than observed in any other cell type (using Fantom5 and DMAP), and enrichment was calculated using ssGSEA (Barbie et al., 2009). CYT-dependent survival analyses via Cox proportional hazards were performed by separating patients into a high-CYT cohort and a low-CYT cohort, each with an identical admixture of histology-stage combinations.

Expression of Exogenous and Endogenous Retroviruses

Viral expression was quantified by mapping unmapped RNA-Seq reads (bowtie2 [Langmead and Salzberg, 2012]) to viral sequence variants deposited in GenBank and normalizing against the count of mapped reads. Positive identification required at least 300 nt of unique sequence to map to the viral genome and expression exceeding that observed in GTEx normals. To quantify the expression of endogenous retroviruses, RNA-Seq data (from TCGA and GTEx) was re-mapped (bowtie2 [Langmead and Salzberg, 2012]) to an annotation of known expressed elements (Mayer et al., 2011). For each ERV, the 95th percentile expression value was calculated per tissue type, and if this value was less than <10 TPM in all normal tissues, >10 TPM in a tumor type, and at least 5-fold higher than in all non-tumor tissues, then the ERV was deemed tumor-specific.

Tumor-Specific HLA Typing, HLA-Binding Neoepitope Prediction and CT Antigen Identification

The 4-digit HLA type for each sample was inferred using POLYSOLVER (POLYmorphic loci reSOLVER), which uses a normal tissue .bam file as input and employs a Bayesian classifier to determine genotype (unpublished, S.A.S., C.J.W., and G.G.). By comparing to matched tumor .bams, POLYSOLVER also identified HLA mutations. Neo-epitopes were predicted for each patient by defining all novel amino acid 9mers and 10mers resulting from mutation in expressed genes (median >10 TPM in the tumor type) and determining whether the predicted binding affinity to the patient's germline HLA alleles was < 500 nM using NetMHCpan (v2.4) (Nielsen et al., 2007; Rajasagi et al., 2014). A set of potential cancer testis (CT) antigens was defined by finding known CT antigens (Almeida et al., 2009) with negligible expression in GTEx normal tissues (95th percentile value < 1 TPM in all somatic tissue types).

Comparison of Expected to Observed Neoantigen Load per Tumor

To test whether the count of neo-epitopes was different from expected (ignoring the expression-based filter and excluding indels), the rate at which each mutational spectrum produces neo-epitopes was calculated empirically pan-cancer, and the silent mutations in each patient used to infer the expected ratio of neo-epitopes per non-silent mutation. This was compared to the actual ratio observed in the patient. Random shuffling of HLA genotypes among patients served as a control.

Association of CYT with Point Mutations and Amplifications/Deletions

Candidate genes were tested for non-silent point mutation association with CYT using a regression-based approach with CYT (rank-transformed) as the dependent variable, mutational status of the gene in question as the independent variable, and cancer histological subtype and the background rate of non-silent point mutations as additional control variables. Hits were defined at adj. $p < 0.1$. Candidate genes were defined by running MutSigCV (Lawrence et al., 2013) on each tumor type separately and all the tumor types collectively (adj. $p < 0.1$) and merging with a previously published result set (Lawrence et al., 2014). To assess for association between CYT and copy number alterations, a regression-based approach was likewise used, using CYT (rank-transformed) as the dependent variable, amplification, or deletion signal as the independent variable, and cancer histological subtype and the background rate of copy number alteration as additional control variables. "Peaks" were defined as contiguous regions with $p < 0.01$, and permutation testing was used to determine whether the peak score (based on the most enriched gene in the region) was truly significant (adj. $p < 0.1$).

SUPPLEMENTAL INFORMATION

Supplemental Information includes Extended Experimental Procedures, one figure, eight tables, and seven data sets and can be found with this article online at <http://dx.doi.org/10.1016/j.cell.2014.12.033>.

AUTHOR CONTRIBUTIONS

M.S.R. and N.H. conceived the project, designed analysis strategies, interpreted the results, and wrote the manuscript. M.S.R. developed and performed the computational analyses. S.S., C.J.W., and G.G. developed the tools for HLA genotyping, mutation calling, and neo-epitope prediction.

ACKNOWLEDGMENTS

We are grateful to the TCGA Research Network (<http://cancergenome.nih.gov/>), the Genotype-Tissue Expression (GTEx) Project (dbGaP phs000424.v3.p1), the FANTOM research consortium (<http://fantom.gsc.riken.jp/>), and the Broad-Novartis Cancer Cell Line Encyclopedia (<http://www.broadinstitute.org/ccle/home>) for providing the data analyzed in this manuscript. We thank Mara Rosenberg, Amaro Taylor-Weiner, Chloe Villani, Arnon Arazi, Pavan Bachireddy, and Dan-Avi Landau for their feedback and help accessing data and analysis tools and Leslie Gaffney for assistance with artwork. Funding was provided by the Blavatnik Family Foundation (N.H.), the MGH Research Scholars Program (N.H.), and the NIH Training Program in Bioinformatics and Integrative Genomics training grant (M.S.R.). G.G. is a consultant to the KEW Group.

Received: November 3, 2014

Revised: December 9, 2014

Accepted: December 24, 2014

Published: January 15, 2015

REFERENCES

- Almeida, L.G., Sakabe, N.J., deOliveira, A.R., Silva, M.C., Mundstein, A.S., Cohen, T., Chen, Y.T., Chua, R., Gurung, S., Gnjjatic, S., et al. (2009). CTdatabase: a knowledge-base of high-throughput and curated data on cancer-testis antigens. *Nucleic Acids Res.* 37 (Database issue), D816–D819.
- Ayyoub, M., Hesdorffer, C.S., Montes, M., Merlo, A., Speiser, D., Rimoldi, D., Cerottini, J.-C., Ritter, G., Scanlan, M., Old, L.J., and Valmori, D. (2004). An immunodominant SSX-2-derived epitope recognized by CD4+ T cells in association with HLA-DR. *J. Clin. Invest.* 113, 1225–1233.
- Barbie, D.A., Tamayo, P., Boehm, J.S., Kim, S.Y., Moody, S.E., Dunn, I.F., Schinzel, A.C., Sandy, P., Meylan, E., Scholl, C., et al. (2009). Systematic RNA interference reveals that oncogenic KRAS-driven cancers require TBK1. *Nature* 462, 108–112.
- Barretina, J., Caponigro, G., Stransky, N., Venkatesan, K., Margolin, A.A., Kim, S., Wilson, C.J., Lehár, J., Kryukov, G.V., Sonkin, D., et al. (2012). The Cancer Cell Line Encyclopedia enables predictive modelling of anticancer drug sensitivity. *Nature* 483, 603–607.
- Bindea, G., Mlecnik, B., Tosolini, M., Kirilovsky, A., Waldner, M., Obenauf, A.C., Angell, H., Fredriksen, T., Lafontaine, L., Berger, A., et al. (2013). Spatio-temporal dynamics of intratumoral immune cells reveal the immune landscape in human cancer. *Immunity* 39, 782–795.
- Boller, K., Janssen, O., Schuldes, H., Tönjes, R.R., and Kurth, R. (1997). Characterization of the antibody response specific for the human endogenous retrovirus HTDV/HERV-K. *J. Virol.* 71, 4581–4588.
- Brown, S.D., Warren, R.L., Gibb, E.A., Martin, S.D., Spinelli, J.J., Nelson, B.H., and Holt, R.A. (2014). Neo-antigens predicted by tumor genome meta-analysis correlate with increased patient survival. *Genome Res.* 24, 743–750.
- Cancer Genome Atlas Research Network (2014). Comprehensive molecular characterization of gastric adenocarcinoma. *Nature* 513, 202–209.
- Chang, C.C., Campoli, M., Restifo, N.P., Wang, X., and Ferrone, S. (2005). Immune selection of hot-spot beta 2-microglobulin gene mutations, HLA-A2 allospecificity loss, and antigen-processing machinery component down-regulation in melanoma cells derived from recurrent metastases following immunotherapy. *J. Immunol.* 174, 1462–1471.
- Fan, S., Ma, Y.X., Gao, M., Yuan, R.Q., Meng, Q., Goldberg, I.D., and Rosen, E.M. (2001). The multisubstrate adapter Gab1 regulates hepatocyte growth factor (scatter factor)-c-Met signaling for cell survival and DNA repair. *Mol. Cell. Biol.* 21, 4968–4984.
- FANTOM Consortium and the RIKEN PMI and CLST (DGT), Forrest, A.R., Kawaji, H., Rehli, M., Baillie, J.K., de Hoon, M.J., Haberle, V., Lassman, T., Kulakovskiy, I.V., Lizio, M., Itoh, M., et al. (2014). A promoter-level mammalian expression atlas. *Nature* 507, 462–470.
- Fritsch, E.F., Hacohen, N., and Wu, C.J. (2014). Personal neoantigen cancer vaccines: The momentum builds. *Oncimmunology* 3, e29311.
- Garimella, S.V., Gehlhaus, K., Dine, J.L., Pitt, J.J., Grandin, M., Chakka, S., Nau, M.M., Caplen, N.J., and Lipkowitz, S. (2014). Identification of novel molecular regulators of tumor necrosis factor-related apoptosis-inducing ligand (TRAIL)-induced apoptosis in breast cancer cells by RNAi screening. *Breast Cancer Res.* 16, R41.
- Garofalo, M., Di Leva, G., Romano, G., Nuovo, G., Suh, S.S., Nganheu, A., Taciccoli, C., Pichiorri, F., Alder, H., Secchiero, P., et al. (2009). miR-221&222 regulate TRAIL resistance and enhance tumorigenicity through PTEN and TIMP3 downregulation. *Cancer Cell* 16, 498–509.
- GTEx Consortium (2013). The Genotype-Tissue Expression (GTEx) project. *Nat. Genet.* 45, 580–585.
- Herbst, R.S., Soria, J.-C., Kowanetz, M., Fine, G.D., Hamid, O., Gordon, M.S., Sosman, J.A., McDermott, D.F., Powderly, J.D., Gettinger, S.N., et al. (2014). Predictive correlates of response to the anti-PD-L1 antibody MPDL3280A in cancer patients. *Nature* 515, 563–567.
- Hinrichs, C.S., and Rosenberg, S.A. (2014). Exploiting the curative potential of adoptive T-cell therapy for cancer. *Immunol. Rev.* 257, 56–71.
- Izeradjene, K., Douglas, L., Delaney, A., and Houghton, J.A. (2005). Casein kinase II (CK2) enhances death-inducing signaling complex (DISC) activity in TRAIL-induced apoptosis in human colon carcinoma cell lines. *Oncogene* 24, 2050–2058.
- Jemal, A., Siegel, R., Ward, E., Murray, T., Xu, J., and Thun, M.J. (2007). Cancer statistics, 2007. *CA Cancer J. Clin.* 57, 43–66.
- Ji, R.R., Chasalow, S.D., Wang, L., Hamid, O., Schmidt, H., Cogswell, J., Alaparthi, S., Berman, D., Jure-Kunkel, M., Siemers, N.O., et al. (2012). An immune-active tumor microenvironment favors clinical response to ipilimumab. *Cancer Immunol. Immunother.* 61, 1019–1031.
- Johnson, B.J., Costelloe, E.O., Fitzpatrick, D.R., Haanen, J.B., Schumacher, T.N., Brown, L.E., and Kelso, A. (2003). Single-cell perforin and granzyme expression reveals the anatomical localization of effector CD8+ T cells in influenza virus-infected mice. *Proc. Natl. Acad. Sci. USA* 100, 2657–2662.

- Kandoth, C., McLellan, M.D., Vandin, F., Ye, K., Niu, B., Lu, C., Xie, M., Zhang, Q., McMichael, J.F., Wyczalkowski, M.A., et al. (2013). Mutational landscape and significance across 12 major cancer types. *Nature* 502, 333–339.
- Khong, H.T., and Restifo, N.P. (2002). Natural selection of tumor variants in the generation of “tumor escape” phenotypes. *Nat. Immunol.* 3, 999–1005.
- Kloor, M., Michel, S., and von Knebel Doeberitz, M. (2010). Immune evasion of microsatellite unstable colorectal cancers. *Int. J. Cancer* 127, 1001–1010.
- Langmead, B., and Salzberg, S.L. (2012). Fast gapped-read alignment with Bowtie 2. *Nat. Methods* 9, 357–359.
- Lawrence, M.S., Stojanov, P., Polak, P., Kryukov, G.V., Cibulskis, K., Sivachenko, A., Carter, S.L., Stewart, C., Mermel, C.H., Roberts, S.A., et al. (2013). Mutational heterogeneity in cancer and the search for new cancer-associated genes. *Nature* 499, 214–218.
- Lawrence, M.S., Stojanov, P., Mermel, C.H., Robinson, J.T., Garraway, L.A., Golub, T.R., Meyerson, M., Gabriel, S.B., Lander, E.S., and Getz, G. (2014). Discovery and saturation analysis of cancer genes across 21 tumour types. *Nature* 505, 495–501.
- Lemay, S., Davidson, D., Latour, S., and Veillette, A. (2000). Dok-3, a novel adapter molecule involved in the negative regulation of immunoreceptor signaling. *Mol. Cell. Biol.* 20, 2743–2754.
- Liggins, A.P., Cooper, C.D., Lawrie, C.H., Brown, P.J., Collins, G.P., Hatton, C.S., Pulford, K., and Banham, A.H. (2007). MORC4, a novel member of the MORC family, is highly expressed in a subset of diffuse large B-cell lymphomas. *Br. J. Haematol.* 138, 479–486.
- Llobet, D., Eritja, N., Encinas, M., Llecha, N., Yeramian, A., Pallares, J., Sorolla, A., Gonzalez-Tallada, F.J., Matias-Guiu, X., and Dolcet, X. (2008). CK2 controls TRAIL and Fas sensitivity by regulating FLIP levels in endometrial carcinoma cells. *Oncogene* 27, 2513–2524.
- Lund, J.M., Hsing, L., Pham, T.T., and Rudensky, A.Y. (2008). Coordination of early protective immunity to viral infection by regulatory T cells. *Science* 320, 1220–1224.
- Manghera, M., and Douville, R.N. (2013). Endogenous retrovirus-K promoter: a landing strip for inflammatory transcription factors? *Retrovirology* 10, 16.
- Mayer, J., Blomberg, J., and Seal, R.L. (2011). A revised nomenclature for transcribed human endogenous retroviral loci. *Mob DNA* 2, 7.
- Medema, J.P., de Jong, J., van Hall, T., Melief, C.J., and Offringa, R. (1999). Immune escape of tumors in vivo by expression of cellular FLICE-inhibitory protein. *J. Exp. Med.* 190, 1033–1038.
- Mermel, C.H., Schumacher, S.E., Hill, B., Meyerson, M.L., Beroukhi, R., and Getz, G. (2011). GISTIC2.0 facilitates sensitive and confident localization of the targets of focal somatic copy-number alteration in human cancers. *Genome Biol.* 12, R41.
- Nielsen, M., Lundegaard, C., Blicher, T., Lamberth, K., Harndahl, M., Justesen, S., Røder, G., Peters, B., Sette, A., Lund, O., and Buus, S. (2007). NetMHCpan, a method for quantitative predictions of peptide binding to any HLA-A and -B locus protein of known sequence. *PLoS ONE* 2, e796.
- Novershtern, N., Subramanian, A., Lawton, L.N., Mak, R.H., Haining, W.N., McConkey, M.E., Habib, N., Yosef, N., Chang, C.Y., and Shay, T. (2011). Densely interconnected transcriptional circuits control cell states in human hematopoiesis. *Cell* 144, 296–309.
- Oshiumi, H., Sakai, K., Matsumoto, M., and Seya, T. (2010). DEAD/H BOX 3 (DDX3) helicase binds the RIG-I adaptor IPS-1 to up-regulate IFN-beta-inducing potential. *Eur. J. Immunol.* 40, 940–948.
- Pagès, F., Berger, A., Camus, M., Sanchez-Cabo, F., Costes, A., Molitor, R., Mlecnik, B., Kirilovsky, A., Nilsson, M., Damotte, D., et al. (2005). Effector memory T cells, early metastasis, and survival in colorectal cancer. *N. Engl. J. Med.* 353, 2654–2666.
- Rajasagi, M., Shukla, S.A., Fritsch, E.F., Keskin, D.B., DeLuca, D., Carmona, E., Zhang, W., Sougnez, C., Cibulskis, K., Sidney, J., et al. (2014). Systematic identification of personal tumor-specific neoantigens in chronic lymphocytic leukemia. *Blood* 124, 453–462.
- Ravi, R., and Bedi, A. (2002). Sensitization of tumor cells to Apo2 ligand/TRAIL-induced apoptosis by inhibition of casein kinase II. *Cancer Res.* 62, 4180–4185.
- Rutledge, W.C., Kong, J., Gao, J., Gutman, D.A., Cooper, L.A., Appin, C., Park, Y., Scarpace, L., Mikkelsen, T., Cohen, M.L., et al. (2013). Tumor-infiltrating lymphocytes in glioblastoma are associated with specific genomic alterations and related to transcriptional class. *Clin. Cancer Res.* 19, 4951–4960.
- Samuels, Y., and Ericson, K. (2006). Oncogenic PI3K and its role in cancer. *Curr. Opin. Oncol.* 18, 77–82.
- Sato, E., Olson, S.H., Ahn, J., Bundy, B., Nishikawa, H., Qian, F., Jungbluth, A.A., Frosina, D., Gnjatic, S., Ambrosone, C., et al. (2005). Intraepithelial CD8+ tumor-infiltrating lymphocytes and a high CD8+/regulatory T cell ratio are associated with favorable prognosis in ovarian cancer. *Proc. Natl. Acad. Sci. USA* 102, 18538–18543.
- Saturno, G., Valenti, M., De Haven Brandon, A., Thomas, G.V., Eccles, S., Clarke, P.A., and Workman, P. (2013). Combining trail with PI3 kinase or HSP90 inhibitors enhances apoptosis in colorectal cancer cells via suppression of survival signaling. *Oncotarget* 4, 1185–1198.
- Schmitt, K., Reichrath, J., Roesch, A., Meese, E., and Mayer, J. (2013). Transcriptional profiling of human endogenous retrovirus group HERV-K(HML-2) loci in melanoma. *Genome Biol. Evol.* 5, 307–328.
- Schreiber, R.D., Old, L.J., and Smyth, M.J. (2011). Cancer immunoediting: integrating immunity's roles in cancer suppression and promotion. *Science* 331, 1565–1570.
- Schumacher, K., Haensch, W., Röfzaad, C., and Schlag, P.M. (2001). Prognostic significance of activated CD8(+) T cell infiltrations within esophageal carcinomas. *Cancer Res.* 61, 3932–3936.
- Schwitalle, Y., Kloor, M., Eiermann, S., Linnebacher, M., Kienle, P., Knaebel, H.P., Tariverdian, M., Benner, A., and von Knebel Doeberitz, M. (2008). Immune response against frameshift-induced neopeptides in HNPCC patients and healthy HNPCC mutation carriers. *Gastroenterology* 134, 988–997.
- Sharma, P., Wagner, K., Wolchok, J.D., and Allison, J.P. (2011). Novel cancer immunotherapy agents with survival benefit: recent successes and next steps. *Nat. Rev. Cancer* 11, 805–812.
- Simpson, A.J., Caballero, O.L., Jungbluth, A., Chen, Y.T., and Old, L.J. (2005). Cancer/testis antigens, gametogenesis and cancer. *Nat. Rev. Cancer* 5, 615–625.
- Snyder, A., Makarov, V., Merghoub, T., Yuan, J., Zaretsky, J.M., Desrichard, A., Walsh, L.A., Postow, M.A., Wong, P., Ho, T.S., et al. (2014). Genetic basis for clinical response to CTLA-4 blockade in melanoma. *N. Engl. J. Med.* 371, 2189–2199.
- Song, J.J., Kim, J.H., Sun, B.K., Alcala, M.A., Jr., Bartlett, D.L., and Lee, Y.J. (2010). c-Cbl acts as a mediator of Src-induced activation of the PI3K-Akt signal transduction pathway during TRAIL treatment. *Cell. Signal.* 22, 377–385.
- Spranger, S., Spaapen, R.M., Zha, Y., Williams, J., Meng, Y., Ha, T.T., and Gajewski, T.F. (2013). Up-regulation of PD-L1, IDO, and Tregs in the melanoma tumor microenvironment is driven by CD8+ T cells. *Sci. transl. med.* 5, 218ra116.
- Tang, K.W., Alaei-Mahabadi, B., Samuelsson, T., Lindh, M., and Larsson, E. (2013). The landscape of viral expression and host gene fusion and adaptation in human cancer. *Nat Commun* 4, 2513.
- Textor, S., Fiegler, N., Arnold, A., Porgador, A., Hofmann, T.G., and Cerwenka, A. (2011). Human NK cells are alerted to induction of p53 in cancer cells by up-regulation of the NKG2D ligands ULBP1 and ULBP2. *Cancer Res.* 71, 5998–6009.
- Tumeh, P.C., Harview, C.L., Yearley, J.H., Shintaku, I.P., Taylor, E.J., Robert, L., Chmielowski, B., Spasic, M., Henry, G., Ciobanu, V., et al. (2014). PD-1 blockade induces responses by inhibiting adaptive immune resistance. *Nature* 515, 568–571.
- Uderhardt, S., Herrmann, M., Oskolkova, O.V., Aschermann, S., Bicker, W., Ipseiz, N., Sarter, K., Frey, B., Rothe, T., Voll, R., et al. (2012). 12/15-lipoxygenase orchestrates the clearance of apoptotic cells and maintains immunologic tolerance. *Immunity* 36, 834–846.

- Uyttenhove, C., Pilotte, L., Théate, I., Stroobant, V., Colau, D., Parmentier, N., Boon, T., and Van den Eynde, B.J. (2003). Evidence for a tumoral immune resistance mechanism based on tryptophan degradation by indoleamine 2,3-dioxygenase. *Nat. Med.* 9, 1269–1274.
- Wang, G., Ahmad, K.A., and Ahmed, K. (2006). Role of protein kinase CK2 in the regulation of tumor necrosis factor-related apoptosis inducing ligand-induced apoptosis in prostate cancer cells. *Cancer Res.* 66, 2242–2249.
- Yan, Z., Cui, K., Murray, D.M., Ling, C., Xue, Y., Gerstein, A., Parsons, R., Zhao, K., and Wang, W. (2005). PBAF chromatin-remodeling complex requires a novel specificity subunit, BAF200, to regulate expression of selective interferon-responsive genes. *Genes Dev.* 19, 1662–1667.
- Young, G.R., Eksmond, U., Salcedo, R., Alexopoulou, L., Stoye, J.P., and Kassiotis, G. (2012). Resurrection of endogenous retroviruses in antibody-deficient mice. *Nature* 491, 774–778.
- Yu, P., Lübben, W., Slomka, H., Gebler, J., Konert, M., Cai, C., Neubrandt, L., Prazeres da Costa, O., Paul, S., Dehnert, S., et al. (2012). Nucleic acid-sensing Toll-like receptors are essential for the control of endogenous retrovirus viremia and ERV-induced tumors. *Immunity* 37, 867–879.

Dopamine Controls Systemic Inflammation through Inhibition of NLRP3 Inflammasome

Yiqing Yan,^{1,4} Wei Jiang,^{1,4} Lei Liu,¹ Xiaqiong Wang,¹ Chen Ding,³ Zhigang Tian,^{1,2,*} and Rongbin Zhou^{1,2,*}

¹Institute of Immunology and the CAS Key Laboratory of Innate Immunity and Chronic Disease, School of Life Sciences and Medical Center, University of Science and Technology of China, Hefei 230027, China

²Innovation Center for Cell Biology, Hefei National Laboratory for Physical Sciences at Microscale, Hefei 230027, China

³Beijing Proteome Research Center, National Center for Protein Sciences Beijing, Beijing 102206, China

⁴Co-first author

*Correspondence: tzg@ustc.edu.cn (Z.T.), zrb1980@ustc.edu.cn (R.Z.)

<http://dx.doi.org/10.1016/j.cell.2014.11.047>

SUMMARY

Inflammasomes are involved in diverse inflammatory diseases, so the activation of inflammasomes needs to be tightly controlled to prevent excessive inflammation. However, the endogenous regulatory mechanisms of inflammasome activation are still unclear. Here, we report that the neurotransmitter dopamine (DA) inhibits NLRP3 inflammasome activation via dopamine D1 receptor (DRD1). DRD1 signaling negatively regulates NLRP3 inflammasome via a second messenger cyclic adenosine monophosphate (cAMP), which binds to NLRP3 and promotes its ubiquitination and degradation via the E3 ubiquitin ligase MARCH7. Importantly, in vivo data show that DA and DRD1 signaling prevent NLRP3 inflammasome-dependent inflammation, including neurotoxin-induced neuroinflammation, LPS-induced systemic inflammation, and monosodium urate crystal (MSU)-induced peritoneal inflammation. Taken together, our results reveal an endogenous mechanism of inflammasome regulation and suggest DRD1 as a potential target for the treatment of NLRP3 inflammasome-driven diseases.

INTRODUCTION

The NLRP3 inflammasome is a cytosolic protein complex composed of NLRP3, ASC, and caspase-1, and assembled in response to both microbial infection and endogenous “danger signal” (Davis et al., 2011; Martinon et al., 2009). The activation of NLRP3 inflammasome promotes the maturation and release of several proinflammatory cytokines, such as interleukin-1 β (IL-1 β) and IL-18, so it plays critical roles in the initiation of inflammation and the development of immune responses (Lamkanfi and Dixit, 2012; Schroder and Tschopp, 2010). However, as excessive and persistent inflammation is quite harmful, NLRP3 inflammasome has been involved in diverse inflammatory diseases, including type 2 diabetes, atherosclerosis, and gout, thus the activation of NLRP3 inflammasome should be tightly controlled (Davis et al., 2011; Lamkanfi and Dixit, 2012). Several

regulatory mechanisms have been identified to suppress NLRP3 inflammasome. Type I interferon has been shown to attenuate NLRP3 inflammasome activation via Stat1-dependent manner, while nitric oxide has been identified as another negative regulator of NLRP3 inflammasome activation (Guarda et al., 2011; Mishra et al., 2013). Recently, we have proposed that ω -3 fatty acids can negatively regulate NLRP3 inflammasome activation via G protein coupled receptor 120 (GPR120) and GPR40 (Yan et al., 2013). Although NLRP3 inflammasome has been extensively investigated, its regulatory networks, especially the endogenous mechanisms, still remain elusive.

Dopamine (DA) is a neurotransmitter, which not only can regulate behavior, movement, endocrine, cardiovascular, renal, and gastrointestinal functions, but also functions as an important molecule bridging the nervous and immune systems (Basu and Dasgupta, 2000; Beck et al., 2004; Sarkar et al., 2010). DA receptors are present in almost all immune cell subpopulations (Sarkar et al., 2010). Acting on its receptors, DA or agonists for DA receptors have been reported to modulate the activation, proliferation, and cytokine production in immune cells (Basu and Dasgupta, 2000; Sarkar et al., 2010; Torres-Rosas et al., 2014). In addition, dopamine D2 receptor (DRD2) knockout mice show remarkable inflammatory response in CNS, suggesting that DA and its downstream signaling has an antiinflammatory function (Shao et al., 2013). Consistent with this, the deficiency of DA is tightly associated with immune system abnormalities and CNS inflammation in the progression of Parkinson disease (PD) (Perry, 2012; Wüllner and Klockgether, 2003). Although the antiinflammatory effect of DA and its implication in the pathology of PD are emerging, the mechanisms are still poorly understood.

Here, we demonstrate that DA is an endogenous regulator of inflammasome activation and suggest the DRD1 as a potential target for the treatment of NLRP3 inflammasome-driven diseases.

RESULTS

DA Inhibits NLRP3 Inflammasome Activation

To determine the effect of DA on inflammasome activation, LPS-primed bone marrow-derived macrophages (BMDMs) were pretreated with DA before nigericin challenge. NLRP3-dependent caspase-1 activation and IL-1 β maturation by

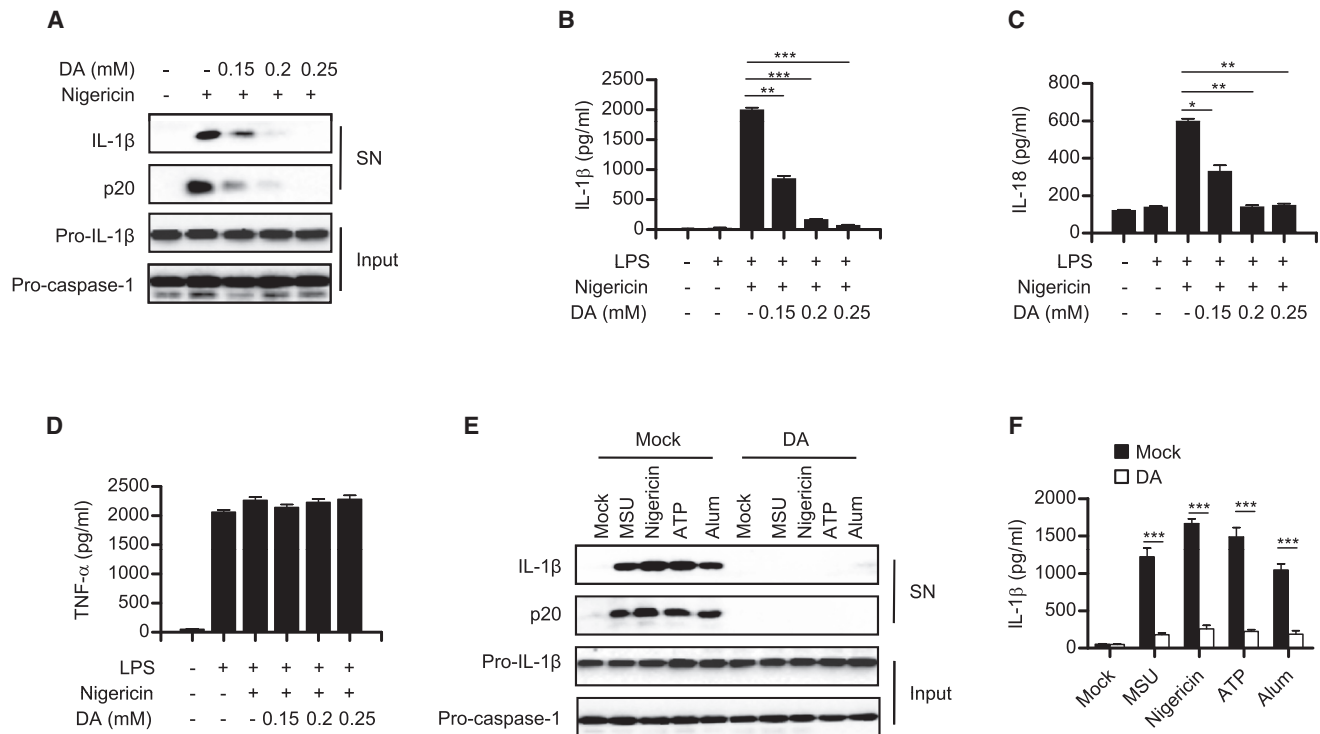


Figure 1. DA Inhibits NLRP3 Inflammasome Activation

(A) Immunoblot analysis of IL-1 β and cleaved caspase-1 (p20) in culture supernatants (SN) of LPS-primed BMDMs treated for 3 hr with various doses (above lanes) of DA and then stimulated with nigericin, and immunoblot analysis of the precursors of IL-1 β (pro-IL-1 β) and caspase-1 (pro-caspase-1) in lysates of those cells (Input).

(B–D) ELISA of IL-1 β (B), IL-18 (C), and TNF- α (D) in supernatants from LPS-primed BMDMs treated for 3 hr with various doses (above lanes) of DA and then stimulated with nigericin.

(E) Immunoblot analysis of IL-1 β and cleaved caspase-1 (p20) in culture supernatants (SN) of LPS-primed BMDMs treated for 3 hr with DA and then stimulated with MSU, nigericin, ATP, and Alum, and immunoblot analysis of the precursors of IL-1 β (pro-IL-1 β) and caspase-1 (pro-caspase-1) in lysates of those cells (Input).

(F) ELISA of IL-1 β in supernatants from LPS-primed BMDMs treated for 3 hr with DA and then stimulated with MSU, nigericin, ATP, and Alum.

Data are means \pm SEM. * p < 0.05, ** p < 0.01, *** p < 0.001.

See also Figure S1.

nigericin were indeed inhibited by DA in a dose-dependent manner (Figures 1A and 1B and Figure S1A available online). Similarly, DA also inhibited nigericin-induced production of IL-18, another NLRP3-inflammasome-dependent cytokine (Figures 1C and S1B). However, the production of TNF- α , an inflammasome-independent cytokine, was not affected by DA in this condition (Figure 1D), suggesting that DA inhibited IL-1 β production via affecting inflammasome activation. The physiological DA levels found in extracellular fluid surrounding neural synapses are ~ 1 μ M (Basu et al., 2001; Chakroborty et al., 2008), but in our study, the DA concentration required for inflammasome inhibition is over 100 μ M, which exceeds the physiological concentration of DA. We speculated that the high DA concentration needed for inflammasome inhibition might be due to the instability of DA. Actually, the half-life of DA is <2 min in plasma and is even much shorter in mouse brain tissues (Rouge-Pont et al., 2002), possibly because dopamine can be broken down into inactive metabolites by a set of enzymes, such as monoamine oxidase (MAO) and catechol-O-methyl

transferase (COMT) (Youdim et al., 2006). To test this possibility, we changed the DA treatment protocol from one single treatment with high dose to multiple treatments with low dose. The results showed that one single treatment with 45 μ M or 90 μ M DA could not inhibit nigericin-induced IL-1 β production, while treatment with 1.5 μ M or 3 μ M DA for 30 times (time interval is 5 min) inhibited nigericin-induced IL-1 β production significantly, although the total doses were identical (Figure S1C). Moreover, although DA could not inhibit nigericin-induced IL-1 β production at the doses under 10 μ M, it really could suppress IL-1 β production in the presence of MAO and COMT inhibitors at these doses (Figure S1D). In addition, the DA treatment had no effect on cell viability (Figure S1E). Taken together, these results indicate that DA has the potential to inhibit caspase-1 activation and IL-1 β secretion.

To test whether DA only affect nigericin-induced NLRP3 inflammasome activation, we examined other NLRP3 agonists. The results showed that DA could inhibit caspase-1 cleavage and IL-1 β secretion induced by all examined agonists, including

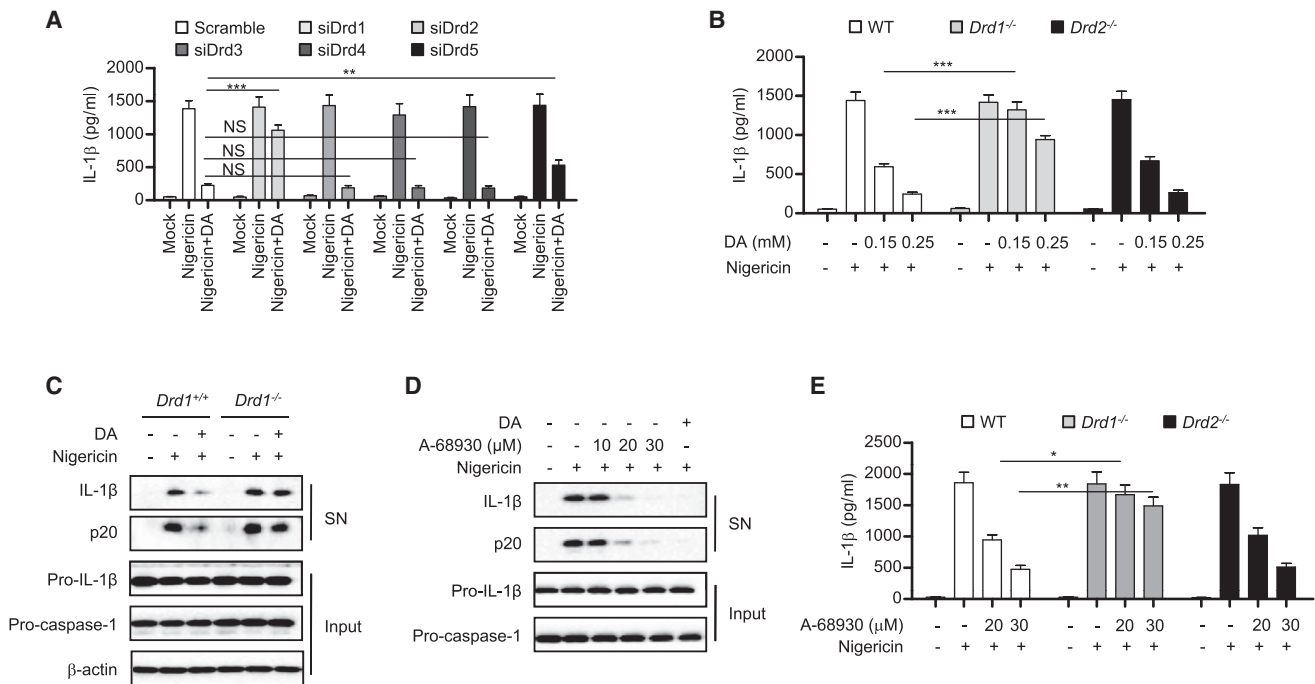


Figure 2. DA Inhibits NLRP3 Inflammasome Activation via DRD1

(A) ELISA of IL-1β in supernatants from LPS-primed BMDMs transfected with control siRNA with a scrambled sequence or *Drd1*-*Drd5*-specific siRNA as indicated, treated for 3 hr with DA and stimulated with nigericin.

(B) ELISA of IL-1β in supernatants from LPS-primed BMDMs of *Drd1*^{-/-} and *Drd2*^{-/-} mice treated for 3 hr with DA and stimulated with nigericin.

(C) Immunoblot analysis of IL-1β and cleaved caspase-1 (p20) in culture supernatants (SN) of LPS-primed BMDMs from *Drd1*^{-/-} mice treated for 3 hr with DA and then stimulated with nigericin, and immunoblot analysis of the precursors of IL-1β (pro-IL-1β), caspase-1 (pro-caspase-1) and β-actin in lysates of those cells (Input).

(D) Immunoblot analysis of IL-1β and cleaved caspase-1 (p20) in culture supernatants (SN) of LPS-primed BMDMs treated for 3 hr with various doses (above lanes) of A-68930 and then stimulated with nigericin, and immunoblot analysis of the precursors of IL-1β (pro-IL-1β) and caspase-1 (pro-caspase-1) in lysates of those cells (Input).

(E) ELISA of IL-1β in supernatants from LPS-primed BMDMs of *Drd1*^{-/-} and *Drd2*^{-/-} mice treated for 3 hr with A-68930 and then stimulated with nigericin.

Data are means ± SEM, *p < 0.05, **p < 0.01, ***p < 0.001.

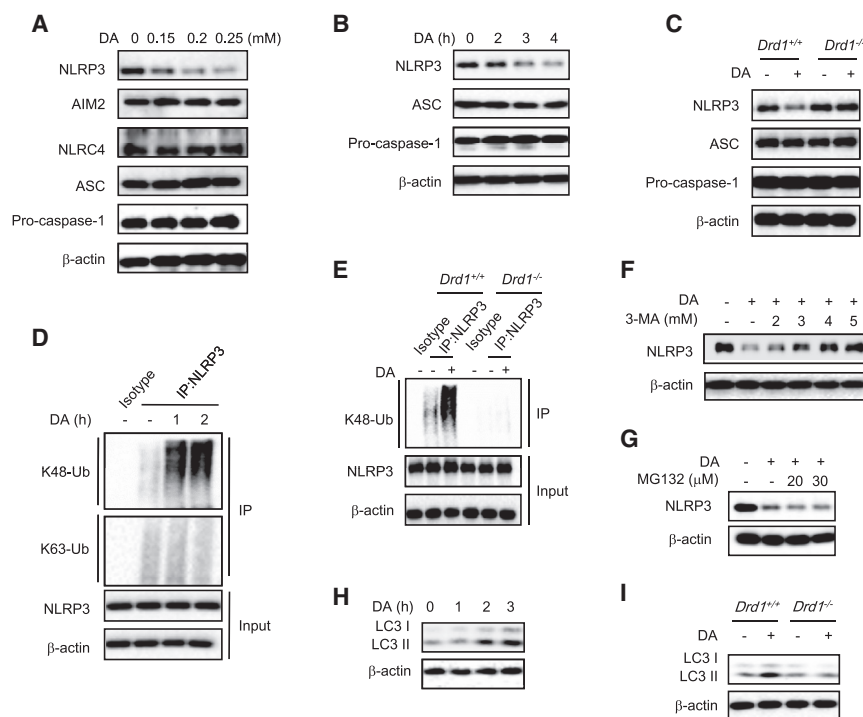
See also Figure S2.

MSU, Alum, and ATP, similar to nigericin (Figures 1E and 1F), suggesting that DA is a potent and broad inhibitor for NLRP3 inflammasome activation. Moreover, DA pretreatment had minimal effect on poly (dA:dT) transfection-induced AIM2 inflammasome activation or *Salmonella typhimurium* (*Salmonella*) infection-induced NLRC4 inflammasome activation (Figures S1F–S1I). Taken together, these results demonstrate that DA specifically inhibits NLRP3 inflammasome activation and subsequent IL-1β production.

DA Inhibits NLRP3 Inflammasome Activation via DRD1 Signaling

Next, we investigated the mechanisms underlying the inhibitory activity of DA on NLRP3 inflammasome activation. DA exerts its effects by binding to the activating receptors located on the surface of cells. There are at least five subtypes of dopamine receptors identified, termed DRD1–DRD5, and all of them can be detected in immune cells, including macrophages and dendritic cells (McKenna et al., 2002; Meredith et al., 2005; Ricci et al., 1999). To determine which receptor was involved in DA-induced

NLRP3 inflammasome inhibition, these receptors were silenced by small interfering RNA (siRNA) in BMDMs, respectively (Figures S2A and S2B). Knockdown of *Drd1* in BMDMs significantly suppressed the inhibitory effect of DA on inflammasome activation, while knockdown of *Drd2*, *Drd3*, or *Drd4* in BMDMs had no effect (Figure 2A). In addition, knockdown of *Drd5* in BMDMs had a little bit of an effect on DA-induced inflammasome inhibition (Figure 2A). These results suggest that DA inhibits NLRP3 inflammasome activation primarily through DRD1. To further confirm this, we tested the role of DA in *Drd1*^{-/-} cells. The results showed that the inhibitory effect of DA on nigericin-induced IL-1β secretion in BMDMs was inhibited completely or partially when *Drd1* was absent, depending on the doses of DA (Figures 2B and 2C). We also examined whether the agonist of DRD1 could inhibit inflammasome activation. First, we found that the agonist of DRD1 A-68930 inhibited nigericin-induced IL-1β secretion significantly, while it had no effect on cell viability, similarly to DA (Figures 2D and S2C), and the agonists of DRD2, DRD3, or DRD4 had mild or no effect on NLRP3 inflammasome activation (Figure S2D). In addition, A-68930-induced NLRP3



(H) Immunoblot analysis of LC3 and β -actin in cell lysates from LPS-primed BMDMs treated for different time points of DA (0.2 mM).

(I) Immunoblot analysis of LC3 and β -actin in cell lysates from LPS-primed BMDMs of *Drd1*^{-/-} mice treated with DA (0.2 mM) for 3 hr.

See also Figure S3.

inflammasome inhibition was not affected by DRD1 deficiency (Figure 2E).

Although our results showed that DA did not affect LPS-induced TNF- α production when macrophages were treated with DA after LPS (Figure 1D), previous results have shown that DA can inhibit some inflammasome-independent cytokine production, including TNF- α (Basu and Dasgupta, 2000). To examine the role of DRD1 signaling in inflammasome-independent cytokine production, we treated BMDMs with DA before LPS and found that DA could suppress LPS-induced TNF- α production, but the dose was higher than that needed for inflammasome inhibition (Figure S2E). In addition, the effect of DA on LPS-induced TNF- α production were significantly impaired in *Drd2*^{-/-} cells, while slightly reduced in *Drd1*^{-/-} cells, suggesting that DA inhibits LPS-induced TNF- α production primarily via DRD2 (Figure S2E). These results were consistent with a new study in which they reported that *Drd2*^{-/-} mice showed spontaneous inflammation in the brain and DRD2 can suppress the transcription and production of proinflammatory cytokines, including TNF- α (Shao et al., 2013). These results suggest that DA signals through DRD1 to inhibit inflammasome activation and signals through DRD2 to suppress the transcription proinflammatory cytokines.

DA and DRD1 Signaling Promote NLRP3 Ubiquitination and Autophagy-Mediated Degradation

Next, we asked how DA and DRD1 signaling inhibit NLRP3 inflammasome activation. Interestingly, we found that DA

Figure 3. DRD1 Signaling Promotes NLRP3 Ubiquitination and Degradation to Inhibit NLRP3 Inflammasome

(A) Immunoblot analysis of NLRP3, AIM2, NLRC4, ASC, Pro-caspase-1, and β -actin from LPS-primed BMDMs treated for 3 hr with various doses of DA.

(B) Immunoblot analysis of NLRP3, ASC, Pro-caspase-1, and β -actin from LPS-primed BMDMs treated for different time points of DA.

(C) Immunoblot analysis of NLRP3, ASC, Pro-caspase-1, and β -actin from LPS-primed BMDMs of *Drd1*^{-/-} mice treated for 3 hr of DA.

(D) LPS primed-BMDMs were treated with DA (0.2 mM). Immunoblot analysis of K48-Ub and K63-Ub proteins in cell lysates immunoprecipitated with NLRP3 antibody.

(E) LPS primed-BMDMs from *Drd1*^{-/-} mice were treated with DA (0.2 mM) for 1 hr. Immunoblot analysis of K48-Ub protein in cell lysates immunoprecipitated with NLRP3 antibody.

(F) Immunoblot analysis of NLRP3 and β -actin in cell lysates from LPS-primed BMDMs treated with different doses of 3-MA for 30 min and then stimulated with DA (0.2 mM) for 3 hr.

(G) Immunoblot analysis of NLRP3 and β -actin in cell lysates from LPS-primed BMDMs treated with different doses of MG132 for 30 min and then stimulated with DA (0.2 mM) for 3 hr.

treatment induced NLRP3 degradation in a dose- and time-dependent manner (Figures 3A and 3B). DA-induced protein degradation was specific to NLRP3, because the expression of AIM2, NLRC4, ASC, caspase-1, and pro-IL-1 β were stable in DA-treated BMDMs (Figures 3A and 3B). Similar to DA, treatment with the DRD1 agonist A-68930 also induced NLRP3 degradation in BMDMs (Figures S3A and S3B). Further study showed that DA-induced NLRP3 degradation was inhibited in *Drd1*^{-/-} macrophages (Figure 3C), suggesting that DA promotes NLRP3 degradation via DRD1 signaling. Consistent with the degradation of NLRP3, treatment with DA induced a K48-linked polyubiquitination of NLRP3 in macrophages (Figure 3D). Importantly, DA-induced NLRP3 polyubiquitination was also impaired in *Drd1*^{-/-} macrophages (Figure 3E).

We then asked whether proteasome or autophagy mediated the degradation of ubiquitinated NLRP3 protein. Our results showed that autophagy inhibitor 3-Methyladenine (3-MA) could suppress DA-induced NLRP3 degradation, while proteasome inhibitor MG132 could not (Figures 3F and 3G), suggesting that ubiquitinated NLRP3 is degraded via autophagy. Indeed, DA treatment induced EGFP-NLRP3 to form big aggregates in HEK293T cells (Figure S3C), which might explain why ubiquitinated NLRP3 is degraded by autophagy, not by proteasome. Consistent with this, DA treatment could induce autophagy in BMDMs via DRD1 signaling (Figures 3H and 3I). Importantly, DA-induced inflammasome inhibition could be rescued by autophagy inhibitor 3-MA (Figure S3D). These results suggest that autophagy mediates DA-induced NLRP3 degradation.

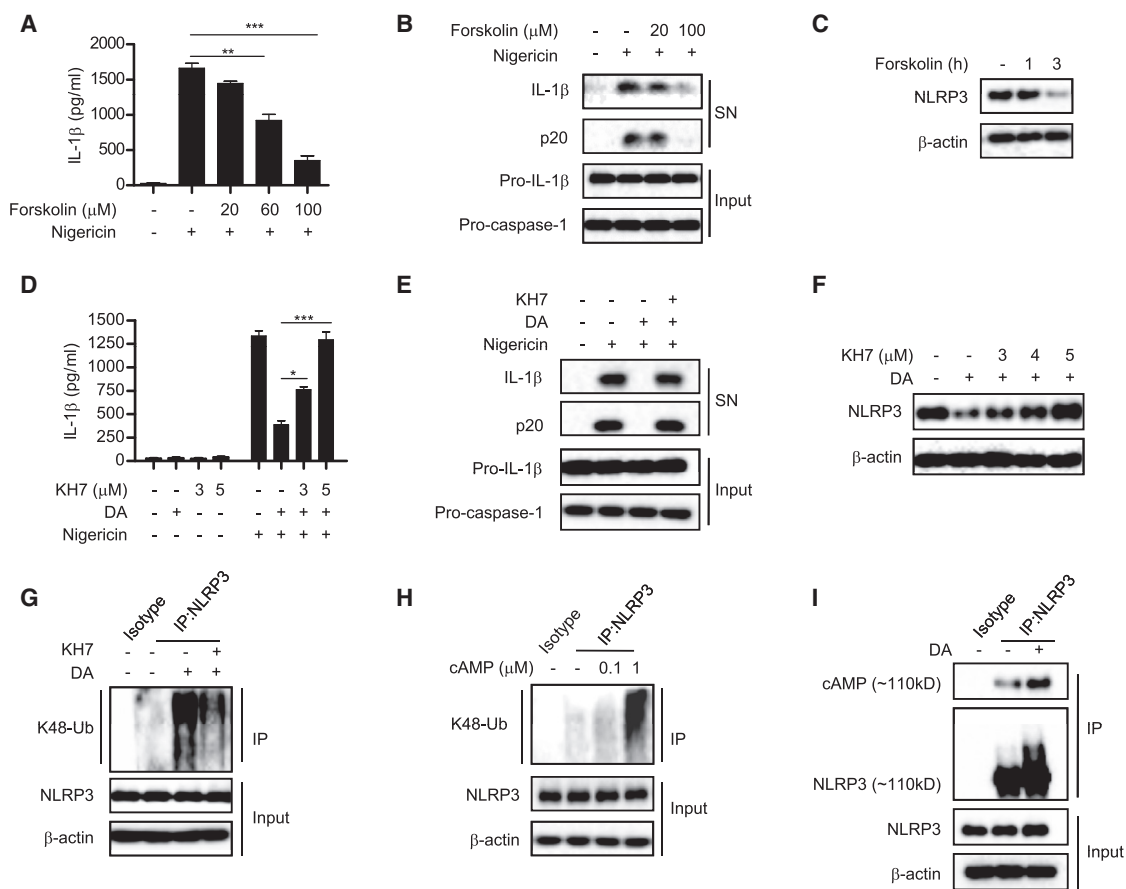


Figure 4. DRD1 Signaling Promotes NLRP3 Ubiquitination and Degradation via cAMP

(A) ELISA of IL-1 β in supernatants from LPS-primed BMDMs treated for 3 hr with forskolin and then stimulated with nigericin.

(B) Immunoblot analysis of IL-1 β and cleaved caspase-1 (p20) in culture supernatants (SN) of LPS-primed BMDMs treated for 3 hr with various doses (above lanes) of forskolin and then stimulated with nigericin, and immunoblot analysis of the precursors of IL-1 β (pro-IL-1 β) and caspase-1 (pro-caspase-1) in lysates of those cells (Input).

(C) Immunoblot analysis of NLRP3 and β -actin in cell lysates from LPS-primed BMDMs treated for different time points of forskolin (100 μ M).

(D) ELISA of IL-1 β in supernatants from LPS-primed BMDMs treated with different doses of KH7 for 30 min before 3 hr DA treatment and then stimulated with nigericin.

(E) Immunoblot analysis of IL-1 β and cleaved caspase-1 (p20) in culture supernatants (SN) of LPS-primed BMDMs treated with KH7 (5 μ M) for 30 min before 3 hr DA treatment and then stimulated with nigericin.

(F) Immunoblot analysis of NLRP3 and β -actin in cell lysates from LPS-primed BMDMs treated with different doses of KH7 for 30 min before 3 hr DA treatment.

(G) LPS-primed BMDMs were treated with KH7 (5 μ M) for 30 min before 1 hr DA treatment. Immunoblot analysis of K48-Ub protein from the cell lysates immunoprecipitated with anti-NLRP3 antibody.

(H) Lysates from LPS-primed BMDMs were treated with different doses of cAMP for 30 min. Immunoblot analysis of K48-Ub protein from the cell lysates immunoprecipitated with anti-NLRP3 antibody.

(I) LPS-primed BMDMs were treated with DA (0.2 mM) for 1 hr. Immunoblot analysis of cAMP and NLRP3 proteins from the cell lysates immunoprecipitated with anti-NLRP3 antibody.

Data are means \pm SEM, * p < 0.05, ** p < 0.01, *** p < 0.001.

See also Figure S4.

DRD1 Signaling Induces NLRP3 Ubiquitination via Cyclic AMP-Dependent Manner

We further investigated how DRD1 signaling promotes NLRP3 ubiquitination. DRD1 signaling can stimulate the activity of adenylate cyclase and the production of cyclic AMP (cAMP), which is a second messenger and is important in many biological processes (Beaulieu et al., 2004; Nishi et al., 2011). Recently, cAMP has been proposed to negatively regulate NLRP3 inflammasome

activation (Lee et al., 2012), so we examined the role of cAMP in DA-induced inflammasome inhibition. We found that the increase of the cAMP levels with adenylate cyclase (ADCY) activator forskolin inhibited NLRP3 inflammasome activation with a dose-dependent manner (Figures 4A and 4B), consistent with a previous report (Lee et al., 2012). Furthermore, forskolin treatment promoted NLRP3 degradation and ubiquitination in macrophages (Figures 4C and S4A), similar with DA treatment.

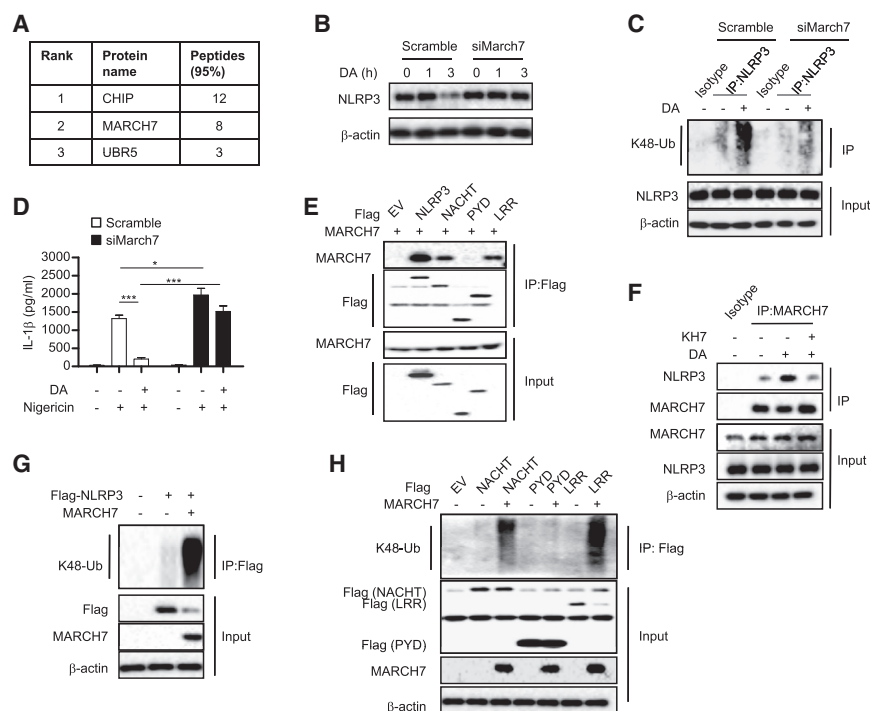


Figure 5. DRD1 Signaling Promotes NLRP3 Ubiquitination through E3 Ligase MARCH7

(A) List of E3 ligase proteins for top peptide hits identified in mass spectrometry study.

(B) Immunoblot analysis of NLRP3 and β-actin in cell lysates from LPS-primed DA-treated BMDMs transfected with siRNA against *March7*.

(C) BMDMs were transfected with siRNA against *March7*. After 48 hr, the cells were primed with LPS and then stimulated with DA (0.2 mM) for 1 hr. Immunoblot analysis of K48-Ub protein from the cell lysates immunoprecipitated with anti-NLRP3 antibody.

(D) ELISA of IL-1β in supernatants from LPS-primed DA and nigericin-treated BMDMs transfected with siRNA against *March7*.

(E) Flag-tagged NLRP3 constructs and MARCH7 construct were cotransfected in HEK293T cells. Immunoblot analysis of MARCH7 and Flag proteins in cell lysates immunoprecipitated with anti-Flag antibody. EV, empty vector.

(F) LPS primed-BMDMs were treated with KH7 (5 μM) for 30 min before 1 hr DA treatment. Immunoblot analysis of MARCH7 protein in cell lysates immunoprecipitated with anti-MARCH7 antibody. (G and H) Flag-tagged NLRP3 construct and MARCH7 construct were cotransfected in HEK293T cells. Immunoblot analysis of K48-Ub protein in cell lysates immunoprecipitated with anti-Flag antibody. Data are means ± SEM, *p < 0.05, ***p < 0.001. See also Figure S5.

Importantly, DA-induced NLRP3 inflammasome inhibition could be blocked by KH7, an ADCY inhibitor (Figures 4D and 4E), suggesting that DA-induced NLRP3 inflammasome inhibition is cAMP-dependent. Consistent with this, DA-induced NLRP3 degradation and ubiquitination could also be inhibited by KH7 (Figures 4F and 4G). Actually, cAMP also could promote NLRP3 ubiquitination in the lysates of macrophages (Figure 4H). These results indicate that the increase of cAMP in cells can promote NLRP3 ubiquitination and degradation.

Protein kinase A (PKA) and exchange protein activated by cAMP (EPAC) are the two known sensors for intracellular cAMP, so we tested whether they were involved in DA-induced NLRP3 inflammasome inhibition (Gloerich and Bos, 2010). The results showed that inhibition of PKA with H89 did not affect DA-induced NLRP3 inflammasome inhibition or DA-promoted NLRP3 degradation (Figures S4B and S4C). In addition, EPAC agonist also had no effect on NLRP3 inflammasome activation or NLRP3 degradation (Figures S4D and S4E). These results suggest that PKA and EPAC are not the downstream of cAMP to promote NLRP3 ubiquitination. Actually, when NLRP3 were immunoprecipitated and the precipitates were examined with anti-cAMP antibody, a band with the same size of NLRP3 could be detected with anti-cAMP antibody (Figure 4I), suggesting that NLRP3 can directly interact with cAMP, possibly by covalent linkage. Importantly, DA treatment promoted the interaction between cAMP and NLRP3 significantly (Figure 4I). These results indicate that DA-induced cAMP promotes NLRP3 ubiquitination and degradation via binding with NLRP3.

We then examined the role of cAMP in DA-induced autophagy. The results showed that KH7 could inhibit DA-induced autophagy, while forskolin could promote autophagy (Figures S4F and S4G), similar with DA, suggesting that DA-induced autophagy is cAMP-dependent. Similarly, DA-induced autophagy was PKA- and EPAC-independent (Figures S4H and S4I), suggesting that cAMP promotes autophagy without the involvement of its known downstream signaling. Importantly, DA-induced NLRP3 aggregation was inhibited by KH7 (Figure S4J), suggesting that cAMP promotes the formation of NLRP3 aggregates, which could trigger autophagy for its degradation.

Taken together, these results suggest that the binding of cAMP with NLRP3 promotes its ubiquitination and then the ubiquitinated NLRP3 forms aggregates, which are targeted for degradation by autophagy.

DRD1 Signaling Promotes NLRP3 Ubiquitination via E3 Ubiquitin Ligase MARCH7

To identify the E3 ligase that is responsible for DA-induced NLRP3 ubiquitination and degradation, we used mass spectrometry (MS) to identify the E3 ligases associated with NLRP3 and found that E3 ligases CHIP, MARCH7, and UBR5 had the highest number of matched peptides identified by MS in the precipitates (Figure 5A). Further studies showed that knockdown of *Chip* or *Ubr5* by using siRNA did not affect DA-induced NLRP3 degradation in BMDMs (Figures S5A–S5C). However, knockdown of *March7* could rescue DA-induced NLRP3 degradation

in BMDMs (Figures 5B and S5A). Moreover, DA-induced NLRP3 ubiquitination was also impaired when *March7* was silenced (Figure 5C). Consistent with this, the effect of DA on IL-1 β secretion depended on MARCH7 (Figure 5D). In addition, forskolin-induced NLRP3 degradation, ubiquitination, and inflammasome inhibition were also rescued by *March7* knockdown (Figures S5D–S5F). These results suggest the importance of E3 ligase MARCH7 in DRD1 signaling and cAMP-induced NLRP3 ubiquitination and inflammasome inhibition.

We further investigated how MARCH7 promoted NLRP3 ubiquitination. First, we found that overexpressed MARCH7 not only interacted with full-length NLRP3, but also interacted with NACHT or LRR domain, but not with PYD domain, in HEK293T cells (Figure 5E). Second, DA treatment could promote the endogenous interaction between NLRP3 and MARCH7 in BMDMs (Figure 5F), and this effect also depended on cAMP because KH7 could inhibit the interaction between NLRP3 and MARCH7 (Figure 5F). Importantly, overexpressed MARCH7 could promote NLRP3 ubiquitination and degradation in HEK293T cells (Figure 5G). Further studies showed that MARCH7 overexpression could promote the ubiquitination and degradation of LRR domain strongly, but could not induce the degradation of NACHT domain, although MARCH7 had some effect to enhance its ubiquitination (Figure 5H). These results suggest that LRR domain is the key region of NLRP3 for MARCH7-mediated ubiquitination and degradation.

DRD1 Signaling Prevents MPTP-Induced Neuroinflammation via Suppression of NLRP3 Inflammasome

Abundant evidence implicates that immune system abnormalities and neuroinflammation are sustaining and exacerbating reasons for the loss of the dopaminergic neurons and DA deficiency (Brochard et al., 2009; Perry, 2012; Rodrigues et al., 2013; Shao et al., 2013). NLRP3 inflammasome has been reported to be involved in the progression of several human diseases (Davis et al., 2011; Martinon et al., 2009). NLRP3 inflammasome can be activated by aggregated α -Synuclein, which has been suggested directly linked to the pathogenesis of PD (Codolo et al., 2013). To determine the role of NLRP3 inflammasome-driven neuroinflammation in the neurodegeneration of nigral dopaminergic neurons, *Nlrp3*^{−/−} mice were treated with neurotoxin 1-methyl-4-phenyl-1,2,3,6-tetrahydropyridine (MPTP). The data showed that *Nlrp3*^{−/−} mice were resistant to MPTP-induced loss of nigral dopaminergic neurons compared with their wild-type mice (Figures S6A and S6B). This difference was associated with reduced IL-1 β and IL-18 production in serum and impaired caspase-1 activation in brain tissue (Figures S6C and S6D), suggesting that dysregulation of NLRP3 inflammasome contributes to the development of MPTP-induced loss of nigral dopaminergic neurons.

We then want to know whether DA and DRD1 signaling can prevent MPTP-induced neuroinflammation and loss of neurons. In brain, the activated microglia and astrocytes have been regarded as important contributors for the progression of PD (Lucin and Wyss-Coray, 2009). Both microglia and astrocytes express NLRP3 and secrete IL-1 β via NLRP3 inflammasome-dependent manner (Alfonso-Loeches et al., 2014; Halle et al.,

2008). We first checked whether DA could inhibit inflammasome activation in microglia and astrocytes. The results showed that DA treatment could inhibit nigericin-induced IL-1 β production in both microglia and astrocytes, and the inhibitory effects of DA were impaired in *Drd1*^{−/−} cells (Figures 6A and 6B). Moreover, DRD1 signaling also induced NLRP3 degradation in microglia and astrocytes (Figures 6C and 6D). These results suggest that DA and DRD1 signaling can promote NLRP3 degradation to inhibit inflammasome activation in microglia and astrocytes. To further study the in vivo relevance of inflammasome inhibition by DA, *Drd1*^{−/−} mice were administrated with MPTP and the loss of dopaminergic neurons was examined. The results showed that *Drd1*^{−/−} mice displayed more severe loss of nigral dopaminergic neurons compared with wild-type mice when treated with MPTP (Figures 6E and 6F). Consistent with this, *Drd1*^{−/−} mice also showed more inflammasome activation by analyzing IL-1 β and IL-18 production or caspase-1 activation (Figures 6G and 6H). However, *Drd1*^{−/−}*Nlrp3*^{−/−} mice did not show more severe loss of dopaminergic neurons, IL-1 β and IL-18 production, or caspase-1 activation compared with *Drd1*^{−/−} mice (Figures S6A–S6D). Moreover, MPTP-treated *Drd1*^{−/−} mice showed more NLRP3 expression and less NLRP3 ubiquitination in the brain tissue compared with *Drd1*^{+/+} mice, suggesting that DRD1 signaling might promote NLRP3 ubiquitination in MPTP-induced neuroinflammation (Figure 6I). These results suggest that DRD1 signaling can prevent neuroinflammation via inhibition of NLRP3 inflammasome by promoting NLRP3 ubiquitination in vivo.

To further study the protective role of DRD1 signaling in neuroinflammation, *Drd1*^{+/+} or *Drd1*^{−/−} mice were treated with DRD1 agonist A-68930 before MPTP treatment. A-68930 administration resulted in a remarkable reduction of dopaminergic neuron damage, IL-1 β or IL-18 production, and caspase-1 activation in *Drd1*^{+/+} mice, but not in *Drd1*^{−/−} mice (Figures 6E–6H), indicating that activation of DRD1 signaling can protect MPTP-induced inflammasome activation and dopaminergic neuron damage in vivo.

DA and DRD1 Signaling Mitigate LPS-Induced Systemic Inflammation and MSU-Induced Peritoneal Inflammation by Inhibition of NLRP3 Inflammasome

In addition to function as neurotransmitter in the brain, DA also functions as a local chemical messenger in several periphery parts of the body, including blood, intestine, and kidney (Beaulieu and Gainetdinov, 2011). Importantly, DA is a “first line” agent for septic shock as a vasopressor over the past two decades (De Backer et al., 2010). Because septic shock is an inflammatory disorder, we asked whether DA could suppress the inflammatory responses via inhibition of NLRP3 inflammasome in septic shock. The *Nlrp3*^{+/+} or *Nlrp3*^{−/−} mice were treated with DA when challenged with LPS to induce septic shock, and the results showed that DA treatment resulted in significant reduction of serum IL-1 β or IL-18 production in *Nlrp3*^{+/+} mice but had no effect in *Nlrp3*^{−/−} mice (Figures 7A and 7B). In addition, DA treatment had only mild effect on serum TNF- α production, which was inflammasome-independent (Figure 7C). These results suggest that DA can inhibit LPS-induced NLRP3 inflammasome activation in vivo.

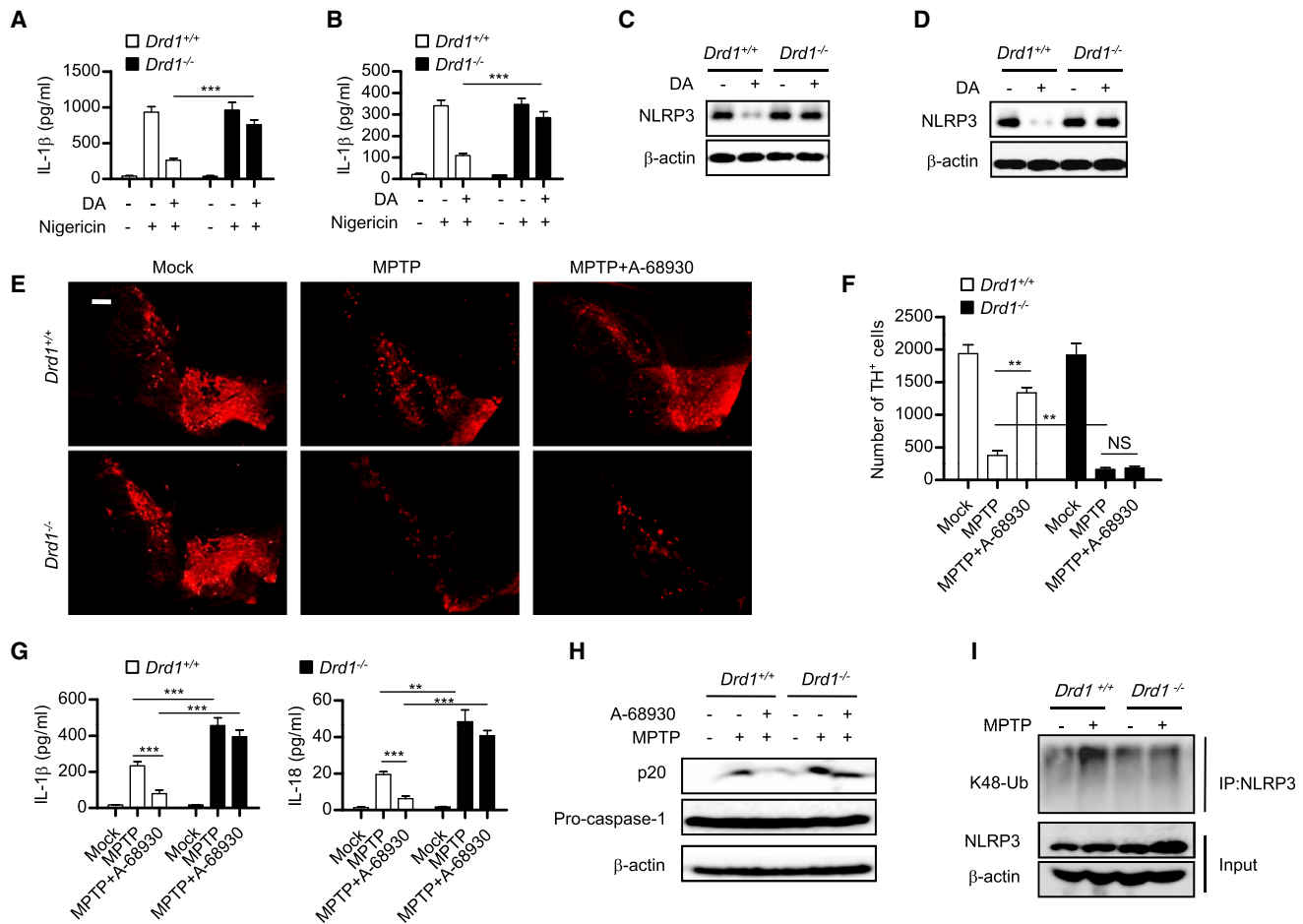


Figure 6. DRD1 Signaling Prevents Neuroinflammation via Suppression of NLRP3 Inflammasome

(A) ELISA of IL-1 β in supernatants from LPS-primed microglia of *Drd1*^{+/+} or *Drd1*^{-/-} mice treated with DA (0.2 mM) for 3 hr and stimulated with nigericin. (B) ELISA of IL-1 β in supernatants from LPS-primed astrocytes of *Drd1*^{+/+} or *Drd1*^{-/-} mice treated with DA (0.2 mM) for 3 hr and stimulated with nigericin. (C) Immunoblot analysis of NLRP3 and β -actin in cell lysates from LPS-primed microglia of *Drd1*^{+/+} or *Drd1*^{-/-} mice treated with DA (0.2 mM) for 3 hr. (D) Immunoblot analysis of NLRP3 and β -actin in cell lysates from LPS-primed astrocytes of *Drd1*^{+/+} or *Drd1*^{-/-} mice treated with DA (0.2 mM) for 3 hr. (E) Immunofluorescent histochemical staining for tyrosine hydroxylase (TH) on the ventral mesencephalon of *Drd1*^{+/+} or *Drd1*^{-/-} mice administrated with MPTP or MPTP plus A-68930. Scale bar represents 500 μ M. (F) Quantitative data of TH expression on the ventral mesencephalon of *Drd1*^{+/+} or *Drd1*^{-/-} mice administrated with MPTP or MPTP plus A-68930. (G) ELISA of IL-1 β and IL-18 in serum of *Drd1*^{+/+} or *Drd1*^{-/-} mice administrated with MPTP or MPTP plus A-68930. (H) Immunoblot analysis of caspase-1 cleavage (p20), pro-caspase-1, and β -actin of *Drd1*^{+/+} or *Drd1*^{-/-} mice administrated with MPTP or MPTP plus A-68930. (I) *Drd1*^{+/+} and *Drd1*^{-/-} mice were treated with MPTP. Immunoblot analysis of the lysates of brain tissue immunoprecipitated with anti-NLRP3 antibody. Data are means \pm SEM, **p < 0.01, ***p < 0.001.

See also Figure S6.

To determine whether DA can inhibit LPS-induced systemic inflammation via DRD1 signaling, *Drd1*^{+/+} and *Drd1*^{-/-} mice were treated with LPS, and the results showed that LPS induced more serum IL-1 β and IL-18 production, but comparable TNF- α production in *Drd1*^{-/-} mice (Figures 7D–7F). Moreover, DA treatment could suppress LPS-induced serum IL-1 β and IL-18 production in *Drd1*^{+/+} mice, but had little effect in *Drd1*^{-/-} mice (Figures 7D and 7E). Importantly, *Drd1* deletion in *Nlrp3*^{-/-} mice could not enhance LPS injection-induced serum IL-1 β and IL-18 production (Figures 7G and 7H). Consistent with DRD1 signaling-induced inhibition of NLRP3 inflammasome in vivo, DA treatment in vivo also could induce NLRP3

ubiquitination and degradation in peritoneal macrophage of *Drd1*^{+/+} mice, but not in *Drd1*^{-/-} mice (Figures S7A and S7B). In addition, treatment with autophagy inhibitor 3-MA to inhibit the degradation of NLRP3 could impair DA-induced inflammasome inhibition in LPS-treated mice (Figure S7C). These results indicate that DRD1 signaling can inhibit LPS-induced systemic inflammation via suppression of NLRP3 inflammasome activation.

To further study the protective effect of DRD1 signaling in periphery inflammation, we examined whether DRD1 signaling could suppress MSU-induced peritoneal inflammation, which is NLRP3 inflammasome-dependent (Martinon et al., 2006).

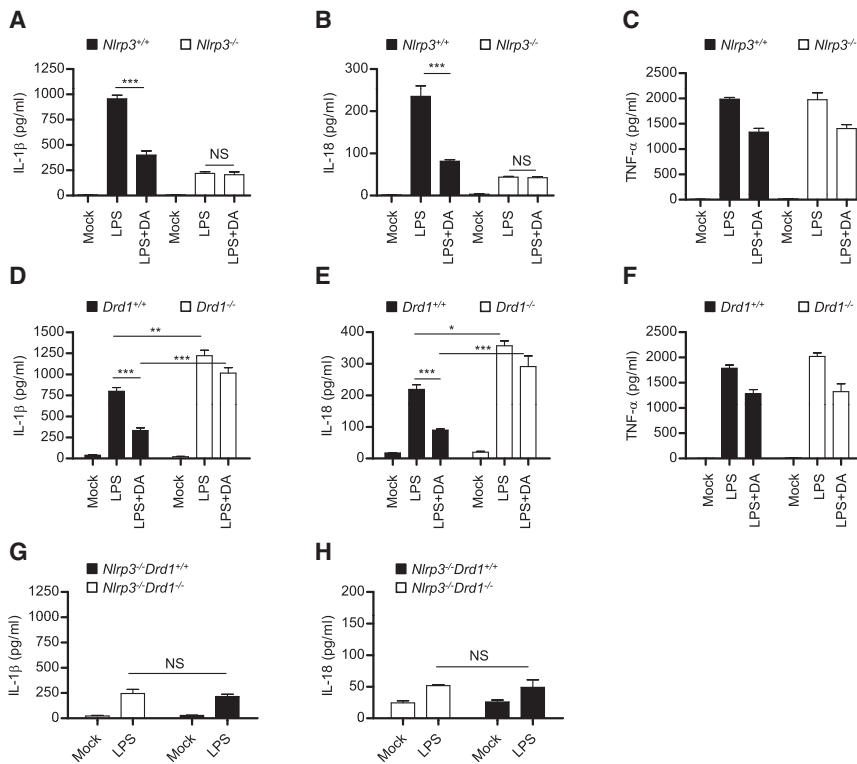


Figure 7. DRD1 Signaling Prevents LPS-Induced Systemic Inflammation and MSU-Induced Peritoneal Inflammation via Suppression of NLRP3 Inflammasome

(A–C) ELISA of IL-1β (A), IL-18 (B), and TNF-α (C) in serum of *Nlrp3*^{+/+} or *Nlrp3*^{-/-} mice intraperitoneally injected with LPS (20 mg/kg of body weight) with or without DA (50 mg/kg of body weight). (D–F) ELISA of IL-1β (D), IL-18 (E), and TNF-α (F) in serum of *Drd1*^{+/+} or *Drd1*^{-/-} mice intraperitoneally injected with LPS (20 mg/kg of body weight) with or without DA (50 mg/kg of body weight). (G and H) ELISA of IL-1β (G) and IL-18 (H) in serum of *Nlrp3*^{-/-} mice or *Nlrp3*^{-/-}*Drd1*^{-/-} mice intraperitoneally injected with LPS (20 mg/kg of body weight).

Data are means ± SEM, **p* < 0.05, ***p* < 0.01, ****p* < 0.001. NS *p* > 0.05.

See also Figure S7.

The result showed that MSU could induce more IL-1β production and recruit more neutrophils in peritoneal cavity of *Drd1*^{-/-} mice (Figures S7D and S7E). Moreover, DA treatment could inhibit MSU-induced IL-1β production and neutrophil recruitment in *Drd1*^{+/+} mice, but not in *Drd1*^{-/-} mice (Figures S7D and S7E). These results indicate that DRD1 signaling has a negative role in MSU-induced NLRP3 inflammasome activation and peritoneal inflammation in vivo.

DISCUSSION

Increasing evidence has shown that the immune system can be influenced by the nervous system and neurotransmitters (Olofsson et al., 2012; Tracey, 2009). DA not only functions as a neurotransmitter in the brain, but also functions as a local chemical messenger in several periphery parts of the body. A substantial amount of dopamine circulates in the bloodstream, but its functions are not entirely clear. Here, our results demonstrate that DA is an endogenous inhibitor of NLRP3 inflammasome activation, suggesting that DA is a potential antiinflammatory chemical, in addition to a neurotransmitter. The effect of dopamine and its agonists on immune responses including proliferation and cytokine production has been reported. Bergquist et al. (1994) reported that either DA or L-dihydroxyphenylalanine, a precursor of DA, resulted in a dose-dependent inhibition of lymphocyte proliferation and differentiation. Josefsson et al. (1996) reported that DA inhibited the ConA- or LPS-induced proliferation and cytokine production of lymphocytes. Ghosh et al. (2003) reported that DA suppressed anti-CD3-mediated proliferation and cytokine production in activated T cells. Thus, our results and previous

studies suggest that DA might play an important role in the communication between nervous system and immune system.

DA exerts its effects by binding to the activating receptors located on the surface of cells. There are at least five subtypes of dopamine receptors that have been identified, termed DRD1–DRD5,

and most of them can be detected in immune cells, including macrophages and dendritic cells (McKenna et al., 2002; Meredith et al., 2005; Ricci et al., 1999). Here, our results show that DRD1 plays a primary role and DRD5 plays a minor role, while DRD2, DRD3, and DRD4 have no roles in DA-induced NLRP3 inflammasome inhibition. The different roles of DA receptors could be explained by their different downstream signalings. Activation of D1-like receptors (DRD1 and DRD5) increases intracellular cAMP levels, while activation of D2-like receptors (DRD2, DRD3, DRD4) decreases intracellular cAMP levels (Missale et al., 1998). Consistent with this, our results demonstrate that cAMP played a critical role in DA-induced inflammasome inhibition. Taken together, our results indicate that DA can negatively regulate NLRP3 inflammasome activation via DRD1 signaling and suggest that DRD1 might be a potential target for treatment of inflammatory diseases.

NLRP3 inflammasome-mediated IL-1β production is a two-step process: a primary signal that induces pro-IL-1β and NLRP3 synthesis and a secondary signal that activates the inflammasome and the subsequent caspase-1 processing (Bauernfeind et al., 2011). NLRP3 protein expression levels have been shown to be a limiting step in inflammasome activation (Bauernfeind et al., 2009; Franchi et al., 2009). Here, we demonstrate that DA can induce the degradation of NLRP3 protein to inhibit NLRP3 inflammasome and support the recent findings that NLRP3 ubiquitination might play an important role in the regulation of inflammasome activation (Juliana et al., 2012; Py et al., 2013).

Increasing evidence imply that immune dysregulation and neuroinflammation are sustaining and exacerbating reasons for

the loss of the dopaminergic neurons in PD (Brochard et al., 2009; Perry, 2012; Rodrigues et al., 2013; Shao et al., 2013), although the precise mechanisms causing uncontrolled inflammation remain unclear. In this study, we demonstrate that NLRP3 inflammasome is involved in the MPTP-induced loss of the dopaminergic neurons. Moreover, our results show that DA and DRD1 signaling has a protective role for MPTP-induced loss of dopaminergic neurons by suppressing NLRP3 inflammasome activation. Although DRD2 was not involved in DA-induced NLRP3 inflammasome inhibition, a previous report has shown that DRD2 signaling also has a protective role in MPTP-induced loss of the dopaminergic neurons (Shao et al., 2013). It seems DRD2 signaling can affect the transcription of proinflammatory cytokines, including pro-IL-1 β , TNF- α , et al., according to Shao et al. (2013). Consistent with this, our study found that DRD2 signaling played a primary role in the inhibitory effect of DA on LPS-induced TNF- α production, while DRD1 only had a minor role. In addition, *Drd2*^{-/-} mice show spontaneous inflammation in the brain, while *Drd1*^{-/-} mice do not (Shao et al., 2013). This suggests that DRD1 only functions to suppress inflammation in “stressed” condition. These results indicate that DRD1 and DRD2 signaling exert a different role in the suppression of inflammation: DRD2 signaling inhibits the transcription proinflammatory cytokines, while DRD1 signaling inhibits the processing and secretion of IL-1 β and IL-18 via suppressing inflammasome.

DA is not only an important neurotransmitter in the brain, but also functions as a local chemical messenger in several periphery parts of the body, including blood, intestine, and kidney (Beaulieu and Gainetdinov, 2011). Our results showed that DA treatment in mice suppressed LPS-induced inflammasome-dependent cytokine production, such as IL-1 β and IL-18. More importantly, *Drd1*^{-/-} mice are susceptible to LPS-induced systemic inflammation. In addition, our results also showed that DA and DRD1 signaling could suppress MSU-induced IL-1 β production and neutrophil infiltration in peritoneal cavity. These results suggest that DA and DRD1 signaling can inhibit systemic or periphery inflammation by inhibition of NLRP3 inflammasome.

Although our results indicate that DA and DRD1 signaling can control both central and periphery inflammation in vivo by inhibition of NLRP3 inflammasome, the DA concentration required for inflammasome inhibition in vitro exceeds the reported physiological concentration of DA (Basu et al., 2001; Chakroborty et al., 2008). To address this issue, we provided results showing that multiple treatments with low dose of DA could inhibit inflammasome activation, while the single treatment with high dose (the same dose with the total dose of multiple treatments) could not. Although this is not enough to prove that the physiological dose of DA can inhibit inflammasome activation, it clearly shows that the instability of DA is an important reason for the requirement of a high dose of DA for inflammasome inhibition. In order to further find out whether the physiological dose of DA can inhibit inflammasome activation, we treated macrophages with physiological dose of DA in the presence of MAO and COMT inhibitors and found that low dose of DA could inhibit inflammasome activation in this condition. These results together suggest that the persistent treatment with physiological dose of DA can inhibit inflammasome activation in vitro. For the in vivo, although the concentration of DA is controlled by MAO and COMT, the

dopaminergic neurons can produce DA continuously so the DA levels could be maintained. In addition, we should note that it is hard to measure the levels of DA in vivo because DA is broken very fast. The reported physiological concentration of DA might be much lower than the actual concentration.

Collectively, our results demonstrate that DA and DRD1 signaling can suppress NLRP3 inflammasome activation and identify an endogenous regulatory mechanism for NLRP3 inflammasome-related inflammation. Our results also demonstrate that DA and DRD1 signaling can prevent neurotoxin-induced neuroinflammation, LPS-induced systemic inflammation, and MSU-induced peritoneal inflammation in vivo, suggesting that DA is a restrictor for the development of inflammatory diseases, and DRD1 is a potential target for the treatment for NLRP3-driven inflammatory diseases.

EXPERIMENTAL PROCEDURES

Mice

Nlrp3^{-/-}, *Drd1*^{-/-}, and *Drd2*^{-/-} mice were described previously (Drago et al., 1994; Kelly et al., 1997; Martinon et al., 2006). *Drd1*^{-/-} and *Nlrp3*^{-/-} mice were crossed to generate *Drd1*^{-/-}*Nlrp3*^{-/-} mice. All animal experiments were approved by the Ethics Committee of University of Science and Technology of China.

Cell Preparation and Stimulation

Bone-marrow macrophages were isolated and cultured as described (Yan et al., 2013). Astrocytes were prepared from the striatum of mice at P0, as described (Shao et al., 2013). Microglia were prepared from neonatal mice (age 1–3 days) as described previously (Saura et al., 2003).

For inducing inflammasome activation, 5×10^5 cells were plated in 12-well plate overnight and the medium were changed to opti-MEM in the following morning and then the cells were primed with ultra-LPS (500 ng/ml) for 3 hr. After that, the cells were stimulated as described (Yan et al., 2013).

Immunofluorescence

Confocal microscopy analyses were carried out using a Zeiss LSM700. Frozen sections were incubated with the primary antibody for tyrosine hydroxylase followed by incubation with secondary antibody conjugated with Alexa543. Sections were imaged using a cooled CCD (DP72, Olympus) on a microscope (BX53, Olympus).

siRNA-Mediated Gene Silences in BMDMs

BMDMs were plated in 12-well plates (4×10^5 cells per well) and then were transfected with 50 nM siRNA using Lipofectamine RNAiMAX (Invitrogen) according to the manufacturer's guidelines.

MPTP-Induced Neuroinflammation In Vivo

Adult mice (12 weeks) were intraperitoneally given with 20 mg/kg MPTP five times at 2 hr intervals. After 24 hr, the serum samples were collected for ELISA and the brains were dissected and processed for immunohistochemistry or immunoblotting analysis.

LPS-Induced Systemic Inflammation In Vivo

To induce in vivo cytokine secretion, adult mice (12 weeks) were injected intraperitoneally with LPS (20 mg/kg) alone or LPS plus DA (50 mg/kg). After 4 hr, the serum samples were collected and the cytokines were measured by ELISA.

Statistical Analyses

All values are expressed as the mean \pm SEM. Statistical analysis were performed with the t test for two groups or one-way ANOVA (GraphPad Software) for multiple groups. P values < 0.05 were considered significant.

See Extended Experimental Procedures for more information.

SUPPLEMENTAL INFORMATION

Supplemental Information includes Extended Experimental Procedures and seven figures and can be found with this article online at <http://dx.doi.org/10.1016/j.cell.2014.11.047>.

AUTHOR CONTRIBUTIONS

Y.Y., W.J., L.L., X.W., and C.D. performed the experiments for this work. Y.Y., W.J., and R.Z. designed the research. Y.Y., W.J., C.D., Z.T., and R.Z. wrote the manuscript. R.Z. and Z.T. supervised the project.

ACKNOWLEDGMENTS

We thank Dr. Jurg Tschopp (University of Lausanne) for providing *Nlrp3*^{−/−} mice, Dr. Jiawei Zhou (Shanghai Institutes for Biological Sciences) and Dr. Yu-qiang Ding (Tongji University School of Medicine) for providing *Drd1*^{−/−} and *Drd2*^{−/−} mice. This work was supported by National Basic Research Program of China (2014CB910800, 2013CB944904), Natural Science Foundation of China (NSFC) (81330078, 81222040), Doctoral Fund of Ministry of Education of China (20123402120001, 20123402110010), One Hundred Person Project (R.Z.), and the Fundamental Research Funds for the Central Universities (R.Z. and W.J.).

Received: May 7, 2014

Revised: September 21, 2014

Accepted: November 18, 2014

Published: January 15, 2015

REFERENCES

- Alfonso-Loeches, S., Ureña-Peralta, J.R., Morillo-Bargues, M.J., Oliver-De La Cruz, J., and Guerri, C. (2014). Role of mitochondria ROS generation in ethanol-induced NLRP3 inflammasome activation and cell death in astroglial cells. *Front. Cell. Neurosci.* 8, 216.
- Basu, S., and Dasgupta, P.S. (2000). Dopamine, a neurotransmitter, influences the immune system. *J. Neuroimmunol.* 102, 113–124.
- Basu, S., Nagy, J.A., Pal, S., Vasile, E., Eckelhoefer, I.A., Bliss, V.S., Manseau, E.J., Dasgupta, P.S., Dvorak, H.F., and Mukhopadhyay, D. (2001). The neurotransmitter dopamine inhibits angiogenesis induced by vascular permeability factor/vascular endothelial growth factor. *Nat. Med.* 7, 569–574.
- Bauernfeind, F.G., Horvath, G., Stutz, A., Alnemri, E.S., MacDonald, K., Speert, D., Fernandes-Alnemri, T., Wu, J., Monks, B.G., Fitzgerald, K.A., et al. (2009). Cutting edge: NF- κ B activating pattern recognition and cytokine receptors license NLRP3 inflammasome activation by regulating NLRP3 expression. *J. Immunol.* 183, 787–791.
- Bauernfeind, F., Ablasser, A., Bartok, E., Kim, S., Schmid-Burgk, J., Cavar, T., and Hornung, V. (2011). Inflammasomes: current understanding and open questions. *Cell. Mol. Life Sci.* 68, 765–783.
- Beaulieu, J.M., and Gainetdinov, R.R. (2011). The physiology, signaling, and pharmacology of dopamine receptors. *Pharmacol. Rev.* 63, 182–217.
- Beaulieu, J.M., Sotnikova, T.D., Yao, W.D., Kockeritz, L., Woodgett, J.R., Gainetdinov, R.R., and Caron, M.G. (2004). Lithium antagonizes dopamine-dependent behaviors mediated by an AKT/glycogen synthase kinase 3 signaling cascade. *Proc. Natl. Acad. Sci. USA* 101, 5099–5104.
- Beck, G.Ch., Brinkkoetter, P., Hanusch, C., Schulte, J., van Ackern, K., van der Woude, F.J., and Yard, B.A. (2004). Clinical review: immunomodulatory effects of dopamine in general inflammation. *Crit. Care* 8, 485–491.
- Bergquist, J., Tarkowski, A., Ekman, R., and Ewing, A. (1994). Discovery of endogenous catecholamines in lymphocytes and evidence for catecholamine regulation of lymphocyte function via an autocrine loop. *Proc. Natl. Acad. Sci. USA* 91, 12912–12916.
- Brochard, V., Combadière, B., Prigent, A., Laouar, Y., Perrin, A., Beray-Berthet, V., Bonduelle, O., Alvarez-Fischer, D., Callebaut, J., Launay, J.M., et al. (2009). Infiltration of CD4⁺ lymphocytes into the brain contributes to neurodegeneration in a mouse model of Parkinson disease. *J. Clin. Invest.* 119, 182–192.
- Chakroborty, D., Chowdhury, U.R., Sarkar, C., Baral, R., Dasgupta, P.S., and Basu, S. (2008). Dopamine regulates endothelial progenitor cell mobilization from mouse bone marrow in tumor vascularization. *J. Clin. Invest.* 118, 1380–1389.
- Codolo, G., Plotegher, N., Pozzobon, T., Brucale, M., Tessari, I., Bubacco, L., and de Bernard, M. (2013). Triggering of inflammasome by aggregated α -synuclein, an inflammatory response in synucleinopathies. *PLoS ONE* 8, e55375.
- Davis, B.K., Wen, H., and Ting, J.P. (2011). The inflammasome NLRs in immunity, inflammation, and associated diseases. *Annu. Rev. Immunol.* 29, 707–735.
- De Backer, D., Biston, P., Devriendt, J., Madl, C., Chochrad, D., Aldecoa, C., Brasseur, A., Defrance, P., Gottignies, P., and Vincent, J.L.; SOAP II Investigators (2010). Comparison of dopamine and norepinephrine in the treatment of shock. *N. Engl. J. Med.* 362, 779–789.
- Drago, J., Gerfen, C.R., Lachowicz, J.E., Steiner, H., Hollon, T.R., Love, P.E., Ooi, G.T., Grinberg, A., Lee, E.J., Huang, S.P., et al. (1994). Altered striatal function in a mutant mouse lacking D1A dopamine receptors. *Proc. Natl. Acad. Sci. USA* 91, 12564–12568.
- Franchi, L., Eigenbrod, T., and Núñez, G. (2009). Cutting edge: TNF- α mediates sensitization to ATP and silica via the NLRP3 inflammasome in the absence of microbial stimulation. *J. Immunol.* 183, 792–796.
- Ghosh, M.C., Mondal, A.C., Basu, S., Banerjee, S., Majumder, J., Bhattacharya, D., and Dasgupta, P.S. (2003). Dopamine inhibits cytokine release and expression of tyrosine kinases, Lck and Fyn in activated T cells. *Int. Immunopharmacol.* 3, 1019–1026.
- Gloerich, M., and Bos, J.L. (2010). Epac: defining a new mechanism for cAMP action. *Annu. Rev. Pharmacol. Toxicol.* 50, 355–375.
- Guarda, G., Braun, M., Staehli, F., Tardivel, A., Mattmann, C., Förster, I., Farlik, M., Decker, T., Du Pasquier, R.A., Romero, P., and Tschopp, J. (2011). Type I interferon inhibits interleukin-1 production and inflammasome activation. *Immunity* 34, 213–223.
- Halle, A., Hornung, V., Petzold, G.C., Stewart, C.R., Monks, B.G., Reinheckel, T., Fitzgerald, K.A., Latz, E., Moore, K.J., and Golenbock, D.T. (2008). The NALP3 inflammasome is involved in the innate immune response to amyloid- β . *Nat. Immunol.* 9, 857–865.
- Josefsson, E., Bergquist, J., Ekman, R., and Tarkowski, A. (1996). Catecholamines are synthesized by mouse lymphocytes and regulate function of these cells by induction of apoptosis. *Immunology* 88, 140–146.
- Juliana, C., Fernandes-Alnemri, T., Kang, S., Farias, A., Qin, F., and Alnemri, E.S. (2012). Non-transcriptional priming and deubiquitination regulate NLRP3 inflammasome activation. *J. Biol. Chem.* 287, 36617–36622.
- Kelly, M.A., Rubinstein, M., Asa, S.L., Zhang, G., Saez, C., Bunzow, J.R., Allen, R.G., Hnasko, R., Ben-Jonathan, N., Grandy, D.K., and Low, M.J. (1997). Pituitary lactotroph hyperplasia and chronic hyperprolactinemia in dopamine D2 receptor-deficient mice. *Neuron* 19, 103–113.
- Lamkanfi, M., and Dixit, V.M. (2012). Inflammasomes and their roles in health and disease. *Annu. Rev. Cell Dev. Biol.* 28, 137–161.
- Lee, G.S., Subramanian, N., Kim, A.I., Aksentjevich, I., Goldbach-Mansky, R., Sacks, D.B., Germain, R.N., Kastner, D.L., and Chae, J.J. (2012). The calcium-sensing receptor regulates the NLRP3 inflammasome through Ca²⁺ and cAMP. *Nature* 492, 123–127.
- Lucin, K.M., and Wyss-Coray, T. (2009). Immune activation in brain aging and neurodegeneration: too much or too little? *Neuron* 64, 110–122.
- Martinon, F., Pétrilli, V., Mayor, A., Tardivel, A., and Tschopp, J. (2006). Gout-associated uric acid crystals activate the NALP3 inflammasome. *Nature* 440, 237–241.
- Martinon, F., Mayor, A., and Tschopp, J. (2009). The inflammasomes: guardians of the body. *Annu. Rev. Immunol.* 27, 229–265.
- McKenna, F., McLaughlin, P.J., Lewis, B.J., Sibbring, G.C., Cummmerson, J.A., Bowen-Jones, D., and Moots, R.J. (2002). Dopamine receptor expression on

- human T- and B-lymphocytes, monocytes, neutrophils, eosinophils and NK cells: a flow cytometric study. *J. Neuroimmunol.* 132, 34–40.
- Meredith, E.J., Chamba, A., Holder, M.J., Barnes, N.M., and Gordon, J. (2005). Close encounters of the monoamine kind: immune cells betray their nervous disposition. *Immunology* 115, 289–295.
- Mishra, B.B., Rathinam, V.A., Martens, G.W., Martinot, A.J., Kornfeld, H., Fitzgerald, K.A., and Sasseti, C.M. (2013). Nitric oxide controls the immunopathology of tuberculosis by inhibiting NLRP3 inflammasome-dependent processing of IL-1 β . *Nat. Immunol.* 14, 52–60.
- Missale, C., Nash, S.R., Robinson, S.W., Jaber, M., and Caron, M.G. (1998). Dopamine receptors: from structure to function. *Physiol. Rev.* 78, 189–225.
- Nishi, A., Kuroiwa, M., and Shuto, T. (2011). Mechanisms for the modulation of dopamine d(1) receptor signaling in striatal neurons. *Front. Neuroanat.* 5, 43.
- Olofsson, P.S., Rosas-Ballina, M., Levine, Y.A., and Tracey, K.J. (2012). Rethinking inflammation: neural circuits in the regulation of immunity. *Immunol. Rev.* 248, 188–204.
- Perry, V.H. (2012). Innate inflammation in Parkinson's disease. *Cold Spring Harb. Perspect. Med.* 2, a009373.
- Py, B.F., Kim, M.S., Vakifahmetoglu-Norberg, H., and Yuan, J. (2013). Deubiquitination of NLRP3 by BRCC3 critically regulates inflammasome activity. *Mol. Cell* 49, 331–338.
- Ricci, A., Bronzetti, E., Mignini, F., Tayebati, S.K., Zaccheo, D., and Amenta, F. (1999). Dopamine D1-like receptor subtypes in human peripheral blood lymphocytes. *J. Neuroimmunol.* 96, 234–240.
- Rodrigues, M.C., Sanberg, P.R., Cruz, L.E., and Garbuzova-Davis, S. (2013). The innate and adaptive immunological aspects in neurodegenerative diseases. *J. Neuroimmunol.* 269, 1–8.
- Rouge-Pont, F., Usiello, A., Benoit-Marand, M., Gonon, F., Piazza, P.V., and Borrelli, E. (2002). Changes in extracellular dopamine induced by morphine and cocaine: crucial control by D2 receptors. *J. Neurosci.* 22, 3293–3301.
- Sarkar, C., Basu, B., Chakroborty, D., Dasgupta, P.S., and Basu, S. (2010). The immunoregulatory role of dopamine: an update. *Brain Behav. Immun.* 24, 525–528.
- Saura, J., Tusell, J.M., and Serratos, J. (2003). High-yield isolation of murine microglia by mild trypsinization. *Glia* 44, 183–189.
- Schroder, K., and Tschopp, J. (2010). The inflammasomes. *Cell* 140, 821–832.
- Shao, W., Zhang, S.Z., Tang, M., Zhang, X.H., Zhou, Z., Yin, Y.Q., Zhou, Q.B., Huang, Y.Y., Liu, Y.J., Wawrousek, E., et al. (2013). Suppression of neuroinflammation by astrocytic dopamine D2 receptors via α B-crystallin. *Nature* 494, 90–94.
- Torres-Rosas, R., Yehia, G., Peña, G., Mishra, P., del Rocio Thompson-Bonilla, M., Moreno-Eutimio, M.A., Arriaga-Pizano, L.A., Isibasi, A., and Ulloa, L. (2014). Dopamine mediates vagal modulation of the immune system by electroacupuncture. *Nat. Med.* 20, 291–295.
- Tracey, K.J. (2009). Reflex control of immunity. *Nat. Rev. Immunol.* 9, 418–428.
- Wüllner, U., and Klockgether, T. (2003). Inflammation in Parkinson's disease. *J. Neurol.* 250 (Suppl 1), I35–I38.
- Yan, Y., Jiang, W., Spinetti, T., Tardivel, A., Castillo, R., Bourquin, C., Guarda, G., Tian, Z., Tschopp, J., and Zhou, R. (2013). Omega-3 fatty acids prevent inflammation and metabolic disorder through inhibition of NLRP3 inflammasome activation. *Immunity* 38, 1154–1163.
- Youdim, M.B., Edmondson, D., and Tipton, K.F. (2006). The therapeutic potential of monoamine oxidase inhibitors. *Nat. Rev. Neurosci.* 7, 295–309.

Activated Type 2 Innate Lymphoid Cells Regulate Beige Fat Biogenesis

Min-Woo Lee,^{1,7} Justin I. Odegaard,^{1,7} Lata Mukundan,¹ Yifu Qiu,¹ Ari B. Molofsky,² Jesse C. Nussbaum,³ Karen Yun,¹ Richard M. Locksley,^{3,4,5} and Ajay Chawla^{1,6,*}

¹Cardiovascular Research Institute, University of California San Francisco, San Francisco, CA 94158-9001, USA

²Department of Laboratory Medicine, University of California San Francisco, San Francisco, CA 94143-0795, USA

³Department of Medicine, University of California, San Francisco, CA 94143-0795, USA

⁴Department of Microbiology and Immunology, University of California, San Francisco, CA 94143-0795, USA

⁵Howard Hughes Medical Institute, University of California, San Francisco, CA 94143-0795, USA

⁶Departments of Physiology and Medicine, University of California San Francisco, San Francisco, CA 94158-9001, USA

⁷Co-first author

*Correspondence: ajay.chawla@ucsf.edu

<http://dx.doi.org/10.1016/j.cell.2014.12.011>

SUMMARY

Type 2 innate lymphoid cells (ILC2s), an innate source of the type 2 cytokines interleukin (IL)-5 and -13, participate in the maintenance of tissue homeostasis. Although type 2 immunity is critically important for mediating metabolic adaptations to environmental cold, the functions of ILC2s in beige or brown fat development are poorly defined. We report here that activation of ILC2s by IL-33 is sufficient to promote the growth of functional beige fat in thermoneutral mice. Mechanistically, ILC2 activation results in the proliferation of bipotential adipocyte precursors (APs) and their subsequent commitment to the beige fat lineage. Loss- and gain-of-function studies reveal that ILC2- and eosinophil-derived type 2 cytokines stimulate signaling via the IL-4R α in PDGFR α ⁺ APs to promote beige fat biogenesis. Together, our results highlight a critical role for ILC2s and type 2 cytokines in the regulation of adipocyte precursor numbers and fate, and as a consequence, adipose tissue homeostasis.

INTRODUCTION

White adipose tissue (WAT) is a highly dynamic organ that responds to nutrient and environmental stress (Berry et al., 2014; Rosen and Spiegelman, 2006; Rosen and Spiegelman, 2014; Zeev et al., 2009). When mammals are in positive energy balance, WAT expands by hyperplasia and hypertrophy to store excess nutrients. In contrast, prolonged cold stress induces catabolic programs in WAT depots, in particular in the subcutaneous WAT (scWAT) of mice, to support thermogenesis (Harms and Seale, 2013; Wu et al., 2013). In this case, adrenergic stimulation of scWAT promotes tissue “browning” via induction of beige adipocytes that express the uncoupling protein 1 (UCP1). This de novo recruitment of beige adipocytes alleviates cold stress to restore thermal homeostasis (Nedergaard and Cannon, 2014). Despite progress in this field, the physiologic sig-

nals that regulate adipocyte precursor proliferation and their subsequent commitment to the beige adipocyte lineage remain poorly understood.

Fate mapping studies have led to the identification of progenitor or precursor cell populations that give rise to brown and beige adipocytes in adult mice. These studies have revealed that interscapular brown adipocytes arise from a mesodermal progenitor that transiently expresses the myogenic transcription factors Myf5 and Pax7 (Lepper and Fan, 2010; Seale et al., 2008). In contrast, beige adipocytes, which are found in WAT depots of mice, primarily arise from Myf5[−] PDGFR α ⁺ precursor cells (Sanchez-Gurmaches et al., 2012; Seale et al., 2008). Fate mapping studies by the Granneman laboratory have elegantly demonstrated that pharmacologic activation of the β 3-adrenergic receptor stimulates the proliferation of PDGFR α ⁺ precursor cells, which subsequently differentiate into beige adipocytes (Lee et al., 2012). Interestingly, these PDGFR α ⁺ precursor cells can also give rise to white adipocytes in the setting of dietary obesity (Berry and Rodeheffer, 2013; Hudak et al., 2014; Lee et al., 2012; Wang et al., 2014), suggesting that environmental signals likely dictate the commitment of PDGFR α ⁺ precursor cells to the beige or white adipocyte lineage.

Exposure of adult animals to environmental cold stimulates the growth of thermogenic beige fat via activation of adrenergic signaling pathways (Harms and Seale, 2013; Wu et al., 2013). In contrast to interscapular BAT, we recently reported that the scWAT relies on a hematopoietic circuit consisting of eosinophils and alternatively activated macrophages for the maintenance of its adrenergic tone. In response to environmental cold, we found that eosinophil-derived interleukin (IL)-4 induces the expression of tyrosine hydroxylase (TH), the rate-limiting enzyme in the synthesis of catecholamines, in alternatively activated macrophages (Nguyen et al., 2011; Qiu et al., 2014). Accordingly, genetic deletion of *Il4ra* or *Th* in myeloid cells significantly impaired the development of thermogenic beige fat in mice (Qiu et al., 2014). The observation that other browning factors, such as meteorin-like (METRNL) also utilize this pathway for their thermic effects (Rao et al., 2014), suggests that type 2 innate immunity might be integrally linked with the development of beige adipose tissue.

ILC2s, which are present in lymphoid and nonlymphoid tissues (Moro et al., 2010; Neill et al., 2010; Price et al., 2010),

orchestrate type 2 innate and adaptive immune responses in the setting of tissue damage, helminth infection, and allergen exposure (Koyasu and Moro, 2013; McKenzie et al., 2014; Walker et al., 2013). In these scenarios, the release of epithelial cell-derived cytokines IL-33, IL-25, and thymic stromal lymphopoietin (TSLP) results in the activation of ILC2s, which then secrete IL-5 and IL-13 to initiate type 2 immune responses (Cayrol and Girard, 2014; Licona-Limón et al., 2013). For instance, in the absence of ILC2s or IL-4/13, the allergen chitin is unable to promote recruitment of eosinophils or alternatively activated macrophages in the lungs (Van Dyken et al., 2014). In addition to their functions in immunity at mucosal sites, ILC2s have been identified in epididymal WAT (eWAT) of mice, where they sustain eosinophils and alternatively activated macrophages to promote glucose homeostasis (Molofsky et al., 2013). Since ILC2-derived IL-5 and IL-13 are critical for initiating type 2 immune responses, we asked whether these cells might also orchestrate the development of beige fat in mice.

Here, we report that administration of IL-33 results in accumulation and activation of ILC2s in the scWAT of mice to stimulate biogenesis of functional beige fat. Surprisingly, in an IL-4/13-dependent manner, IL-33 stimulates the proliferation of PDGFR α ⁺ adipocyte precursor cells, which then commit to the beige adipocyte lineage. The dependence of APs on IL-4/13 signaling for their expansion and commitment to beige adipocytes is not restricted to their pharmacological activation by IL-33 but is also observed during normal physiologic development of this tissue.

RESULTS

IL-33 Promotes Growth of Functional Beige Fat in Thermoneutral Mice

To investigate the functions of ILC2s in beige fat development, we intraperitoneally administered IL-33 to thermoneutral mice daily for 8 days to activate tissue resident ILC2s. In a dose-dependent manner, administration of IL-33 led to a robust increase in the expression of UCP1 protein in the scWAT of thermoneutral C57BL/6J mice (Figures 1A and 1B), suggesting that IL-33 stimulates the growth of beige fat. This browning of scWAT by IL-33 was comparable in magnitude to that induced by the type 2 cytokines IL-4 or IL-13 (Figure 1C), which previously have been implicated in the development of beige fat (Qiu et al., 2014; Rao et al., 2014). Histologic analysis confirmed the presence of multilocular beige adipocytes in the scWAT of mice treated with IL-33 (Figures 1D and 1E). In contrast to browning of scWAT, administration of IL-33, IL-13, or IL-4 did not alter the expression of UCP1 protein in the interscapular brown adipose tissue (BAT) of thermoneutral mice (Figure 1C). Together with our previous studies, these results demonstrate a selective role for type 2 cytokines in stimulating beige fat development.

Next, we asked whether IL-33-induced browning of scWAT contributes to whole-body energy expenditure. To test this postulate, we quantified energy expenditure in vehicle- and IL-33-treated mice at different environmental temperatures. Although energy expenditure was similar in vehicle- and IL-33-treated mice at thermoneutrality (30°C), animals treated with

IL-33 had higher energy expenditure (~13%–17%) at the cooler housing temperatures (Figures 1F and 1G), which likely reflects activation of recruited beige fat. Moreover, these results are consistent with the previous reports demonstrating that beige fat thermogenesis is stimulated by cold exposure in both mice and humans (Qiu et al., 2014; van der Lans et al., 2013; Yoneshiro et al., 2013).

Based on these results, we next investigated whether IL-33 increases energy expenditure in a UCP1-dependent manner. For these experiments, thermoneutral C57BL/6J and congenic *Ucp1*^{−/−} mice were administered IL-33 for 8 days (Figure 1A), and oxygen consumption was quantified after injection of norepinephrine (NE). Administration of NE, which activates all adrenoceptors to maximally stimulate thermogenesis (Golozubova et al., 2006), transiently increased oxygen consumption in thermoneutral C57BL/6J mice (Figure 1H). This NE-stimulated increase in metabolic rate was markedly enhanced in C57BL/6J mice that were administered IL-33 (Figure 1H). Importantly, IL-33-induced increase in oxygen consumption was completely absent in *Ucp1*^{−/−} mice (Figure 1I), indicating that IL-33-induced recruitment of beige fat is critical for increasing the total thermogenic capacity of these mice.

IL-33 Stimulates Proliferation and Commitment of Adipocyte Precursors to the Beige Fat Lineage

To uncover the mechanisms by which IL-33 promotes browning of scWAT, we characterized the immune and precursor populations present in the scWAT of mice. For these studies, we used heterozygous Red5 (*Ilf5*^{Red5/+}, R5) mice, which express tandem dimer red fluorescent protein (tdTomato) from the translation initiation site of the endogenous *Ilf5* locus (Nussbaum et al., 2013), to monitor the fate and activation of ILC2s. ILC2s residing in the scWAT of mice were identified as being Lin[−] (CD11b[−]CD4[−]CD5[−]CD11c[−]NK1.1[−])Thy1.2⁺T1/ST2⁺KLRG1⁺ cells (Figure S1A available online). In mice administered IL-33, ILC2s but not eosinophils, basophils or mast cells were the dominant source of IL-5 (Figures S1B and S1C). Furthermore, daily treatment with IL-33 for 8 days increased the numbers (~22-fold) and activation (~5.4-fold) of ILC2s in the scWAT (Figures 2A and 2B). This increase in ILC2 activation was accompanied by tissue eosinophilia and proliferation of PDGFR α ⁺ APs (~14-fold, as assessed by intracellular staining for cell proliferation antigen Ki67) (Figures 2C–2E, S2A, and S2B). Since PDGFR α ⁺ APs are bipotential cells capable of differentiating into white or beige adipocytes (Lee et al., 2012), we hypothesized that IL-33 might stimulate beige fat biogenesis by enhancing the commitment of APs to the beige fat lineage. To test this idea, we used flow cytometry to monitor the expression of beige adipocyte markers (TMEM26 and CD137) on PDGFR α ⁺ APs (Wang et al., 2014; Wu et al., 2012). We found that treatment with IL-33 increased the expression of TMEM26 and CD137 on the cell surface of PDGFR α ⁺ APs (Figures 2F, 2G, S2C, and S2D), suggesting that IL-33 enhances the growth of beige fat by altering the proliferative and differentiation potential of scWAT APs.

We next investigated the signaling pathways by which IL-33 stimulates the expansion of APs. We hypothesized that IL-33 itself or factors secreted by IL-33 activated ILC2s, such as IL-5

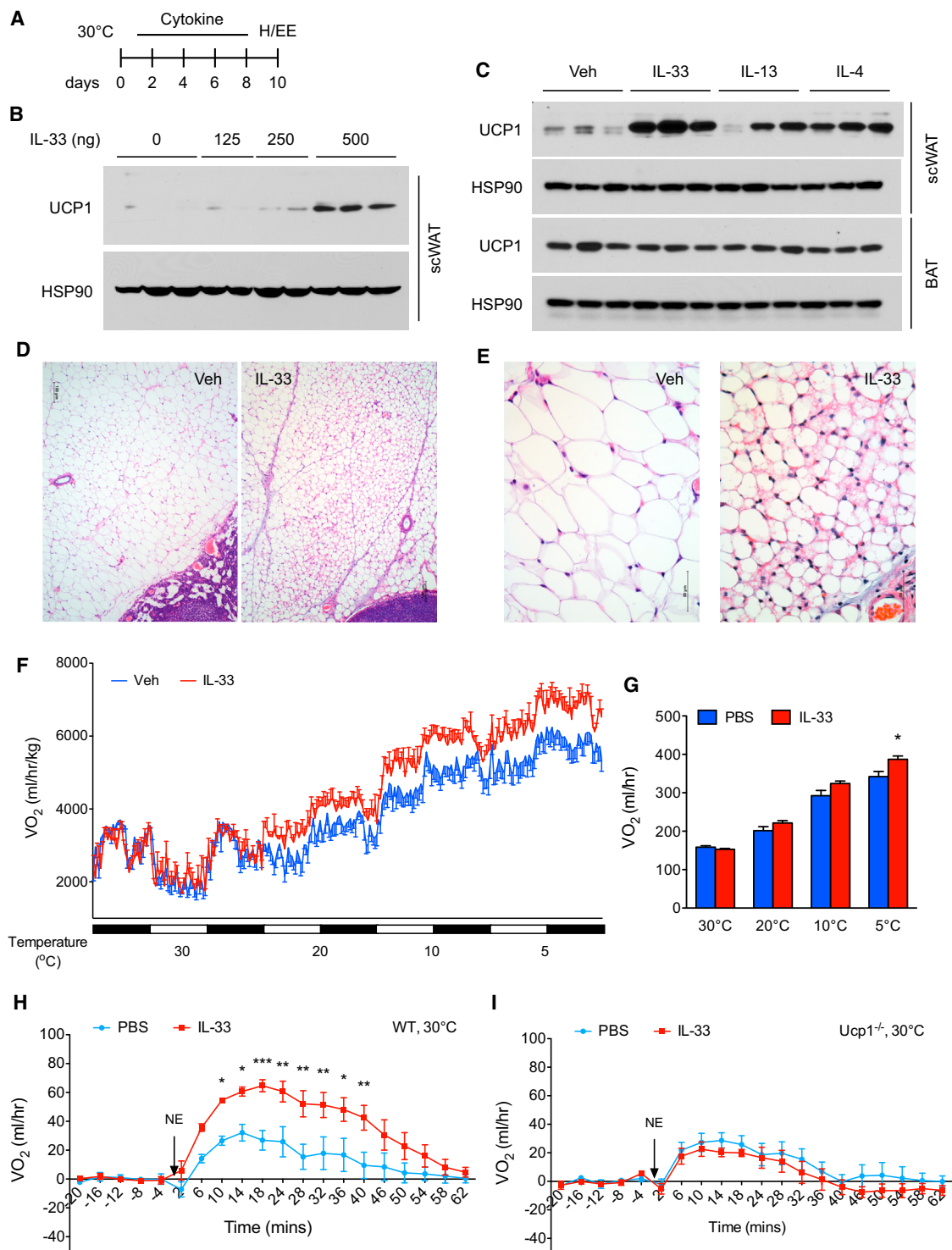


Figure 1. IL-33 Promotes Growth of Functional Beige Fat in Thermoneutral Mice

(A) Schematic for cytokine administration and metabolic analysis in thermoneutral mice.

(B) Immunoblotting for UCP1 in the scWAT of thermoneutral C57BL/6J administered various doses of IL-33 over 8 days (n = 2-3 per treatment dose).

(C) Immunoblotting for UCP1 in the scWAT and BAT of thermoneutral mice administered IL-33, IL-13, or IL-4 for 8 days (n = 3 per cytokine treatment).

(D and E) Representative sections of scWAT from thermoneutral C57BL/6J mice administered Vehicle (Veh) or IL-33 were stained with hematoxylin and eosin. (D) 100× magnification, (E) 400× magnification.

(legend continued on next page)

or IL-13 (Koyasu and Moro, 2013; McKenzie et al., 2014; Walker et al., 2013), directly stimulate the proliferation of PDGFR α ⁺ APs. Flow cytometric analysis revealed that PDGFR α ⁺ APs did not express the receptors required for signaling by IL-33 (IL1RL1) or IL-5 (IL-5R α), but they did express IL-4R α (Figures 2H–2J and S2E), which is required for both IL-13 and IL-4 signaling (Kelly-Welch et al., 2003). These observations led us to hypothesize that secretion of IL-13 by activated ILC2s or IL-4 by recruited eosinophils might support the proliferative burst of APs. We first tested the requirement for IL-5 in IL-33 stimulated AP proliferation. Albeit to a slightly lower extent than in WT mice, stimulation with IL-33 enhanced AP proliferation in R5R5 (*Il5^{Red5/Red5}*) homozygous mice (Figure S2F), which lack the eosinophil growth factor IL-5 but can secrete IL-13 upon activation (Figures S1D and S2G). Since eosinophils are an important source of IL-4 in WAT (Qiu et al., 2014; Wu et al., 2011), we next tested their requirement in IL-33-mediated AP proliferation. Figure S2H shows that IL-33 was equally efficacious in stimulating expansion of scWAT APs in eosinophil-deficient Δ dblGATA mice (Yu et al., 2002), suggesting potential redundancy between eosinophil-derived IL-4 and ILC2-derived IL-13 in mediating this response. To test this hypothesis, we asked whether IL-33 could stimulate proliferation of APs in *Il4/13*^{−/−} and *Il4ra*^{−/−} mice. Indeed, administration of IL-33 failed to increase proliferation of APs in the scWAT of *Il4/13*^{−/−} and *Il4ra*^{−/−} mice (Figures 2K and 2L). A similar requirement for type 2 cytokine signaling was observed in IL-33-mediated browning of scWAT, as monitored by the expression of UCP1 protein in the scWAT of thermoneutral WT and *Il4ra*^{−/−} mice administered IL-33 (Figure 2M). Together, these findings establish a hierarchy between ILC2s, eosinophils, and signaling via the IL-4R α in the regulation of AP biology.

To test whether the stimulatory effects of IL-33 on AP proliferation and commitment require ILC2s, we administered IL-33 to *Rag2*^{−/−} and *Rag2/Il2rg*^{−/−} mice, the latter known to lack ILC2s (Price et al., 2010). While IL-33 increased AP proliferation in *Rag2*^{−/−} mice, it failed to do so in *Rag2/Il2rg*^{−/−} mice (Figure 2N), indicating an absolute requirement for ILC2s in IL-33-mediated expansion of scWAT APs. Similarly, the induction of beige adipocyte markers, TMEM26 and CD137, by IL-33 was only observed in *Rag2*^{−/−} mice (Figures 2O, 2P, S2I, and S2J), suggesting that ILC2s are the likely target for IL-33-induced browning of scWAT.

Physiologic Expansion of Adipocyte Precursors Is Controlled by Type 2 Cytokine Signaling

Since pharmacologic activation of ILC2s promoted proliferation of adipogenic precursors in an IL-4/13-dependent manner, we next asked whether these signals might control the physiologic expansion of APs during the postnatal period. We first quantified the proliferative status of PDGFR α ⁺SCA1⁺CD45[−]CD31[−] APs in the scWAT of C57BL/6J mice at various ages (Figures

S3A and S3B). We found that proliferation of scWAT APs, as assessed by intracellular staining for the cell proliferation antigen Ki67, was age dependent (Figure 3A). Approximately 5.8% of scWAT APs stained positive for Ki67 in 4-week-old mice, which declined by 85% and 95%, respectively, in the scWAT of 8- and 12-week-old mice (Figure 3A). BrdU incorporation experiments provided independent verification for this age-associated decline in DNA synthesis and AP proliferation (Figure 3B).

We next asked whether type 2 immunity regulates this postnatal expansion of APs in the WAT. In support of our hypothesis, we observed an age-associated decline in type 2 cytokine signaling in APs, as assessed by the phosphorylation status of signal transducer and activator of transcription 6 (STAT6), which mediates the biological effects of type 2 cytokines IL-4 and IL-13 (Figure 3C) (Kelly-Welch et al., 2003). Using 4get mice, which express green fluorescent protein (GFP) from the *Il4* locus (Mohrs et al., 2001), we next asked whether the number of cells competent for IL-4 production in scWAT changes with age. Congruent with the decrease in levels of pSTAT6 (Figure 3C), the scWAT of 9-week-old mice had ~70% fewer GFP⁺ cells. This decrease in GFP⁺ cells primarily reflected a decline in the numbers of resident eosinophils (Figure S3C), which have previously been implicated in secretion of IL-4 in scWAT and eWAT (Qiu et al., 2014; Wu et al., 2011). Furthermore, this reduction in numbers of GFP⁺ eosinophils was associated with a ~70% decrease in proliferation (Ki67 positivity) and a ~50% reduction in numbers of APs present in the scWAT (Figures S3D and S3E). A similar age-associated decline in proliferation of APs was observed in the scWAT and eWAT of BALB/cJ mice (Figures S3F and S3G), suggesting that this is not a strain-specific effect. Finally, this age-associated decrease in AP proliferation was not a consequence of changes in expression of PDGFR α or IL-4R α on the cell surface of APs (Figures S3H and S3I).

Based on these results, we next asked whether loss of type 2 cells or signals affects AP proliferation and numbers in the scWAT. For these studies, we focused on 5-week-old mice because we observed robust proliferation of APs at this age in both C57BL/6J and BALB/cJ mice. Consistent with our hypothesis, Δ dblGATA mice, which lack eosinophils, had ~30% fewer APs in their scWAT with ~70% lower proliferative fraction (Figures 3E and 3F). *Il4/13*^{−/−} mice, which lack the type 2 cytokines IL-4 and IL-13, also demonstrated decreases in scWAT AP proliferation (~56%) and numbers (~70%) (Figures 3G and 3H). Similarly, deletion of the IL-4/13 signaling subunit *Il4ra* decreased the percentage of Ki67⁺ APs by ~48% and their numbers by ~52% in scWAT (Figures 3I and 3J). In aggregate, these data suggest that signaling via the IL-4R α accounts for ~50% of the proliferative capacity of APs in the scWAT of mice, prompting us to investigate the mechanisms by which type 2 immunity instructs the postnatal development and functions of this adipose depot.

(F) Cold-induced changes in oxygen consumption in thermoneutral C57BL/6J mice administered Vehicle (Veh) or IL-33 over 8 days (n = 4–5 per treatment).

(G) Oxygen consumption rate at various temperatures of C57BL/6J mice treated with Veh or IL-33 (n = 4–5 per treatment).

(H and I) Norepinephrine stimulated changes in oxygen consumption (VO₂) in conscious, thermoneutral C57BL/6J (H) and *Ucp1*^{−/−} mice that were pretreated with vehicle (Veh) or IL-33 for 8 days (n = 5 per genotype and treatment). Data are represented as mean \pm SEM.

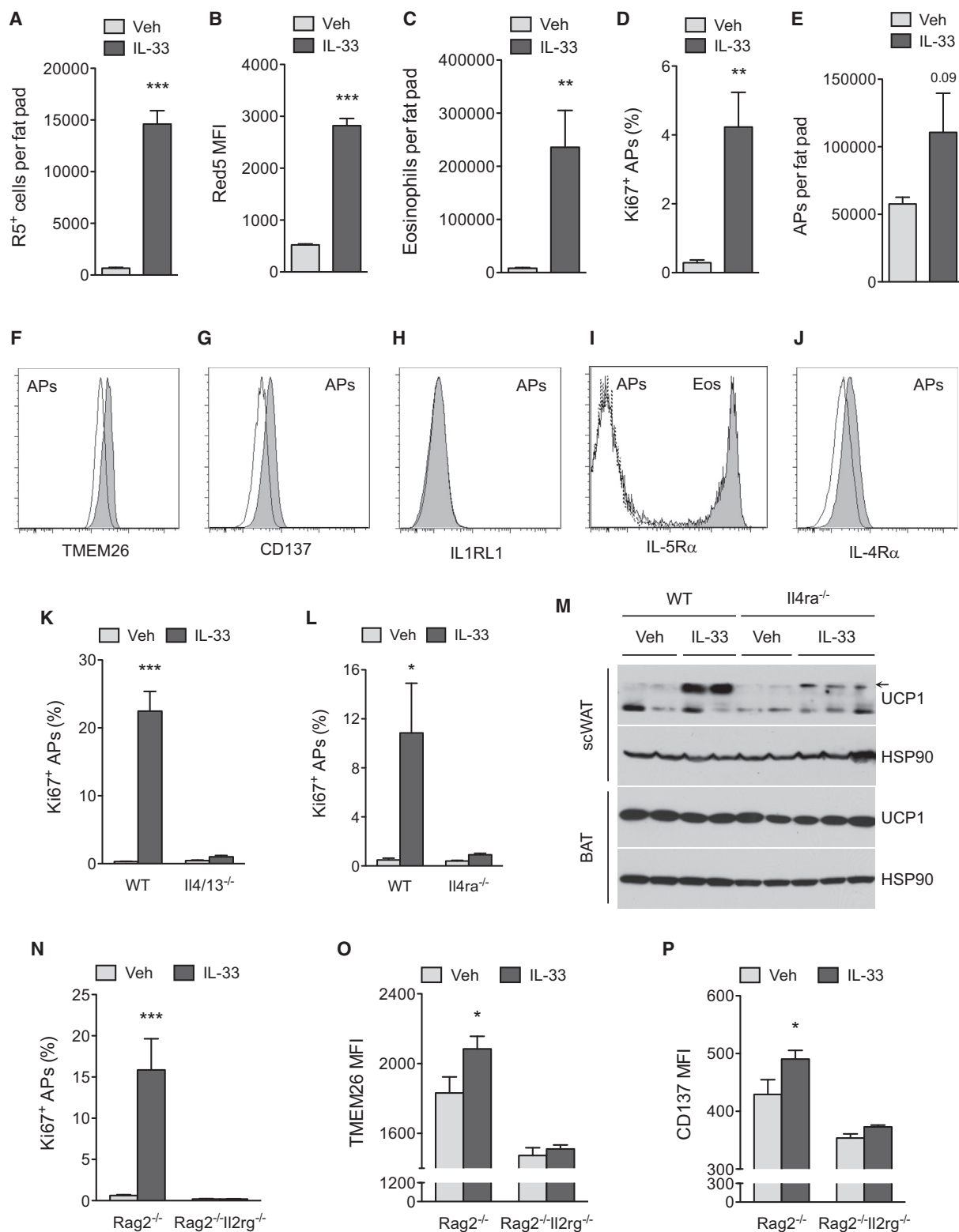


Figure 2. IL-33 Stimulates Proliferation and Commitment of Adipocyte Precursors to the Beige Fat Lineage

(A and B) Quantification of ILC2 numbers (A) and activation status (B) in the scWAT of thermoneutral, heterozygous Red5 (*Il5*^{Red5/+}) mice that were administered vehicle (Veh) or IL-33 for 8 days. Expression of IL-5 (td Tomato) from the Red5 allele was used as a marker of ILC2 activation (n = 9–10 per treatment).

(legend continued on next page)

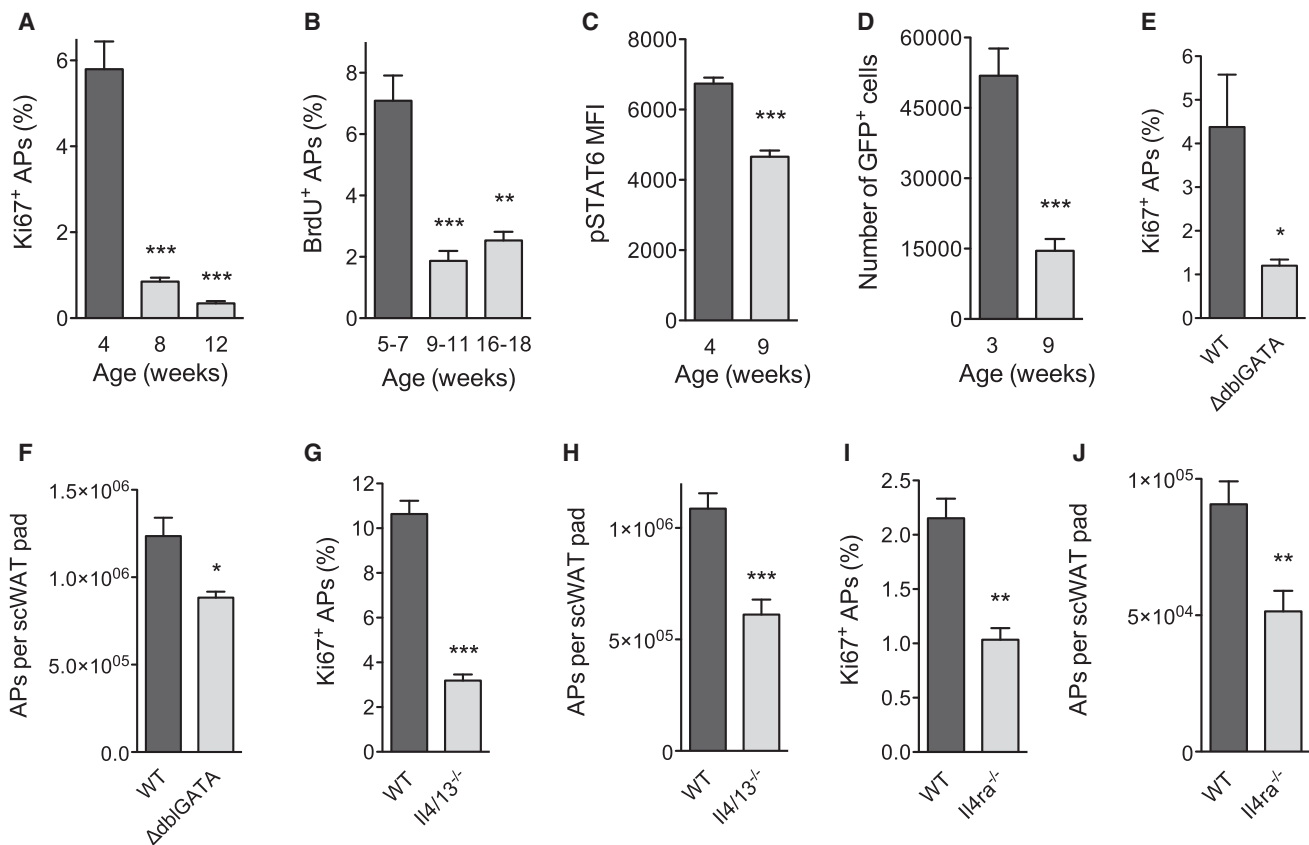


Figure 3. Type 2 Cytokine Signaling Controls Physiologic Expansion of Adipocyte Precursors

(A) Age-dependent proliferation of adipocyte precursors (APs) in the scWAT of C57BL/6J mice as assessed by intracellular staining for Ki67 (n = 4–5 per age). (B) Age-dependent incorporation of BrdU by scWAT APs in C57BL/6J mice (n = 4–5 per age). (C) Quantification of pSTAT6 levels in scWAT APs of C57BL/6J mice at different ages (n = 10–11 per age). (D) Quantification of IL-4-producing cells in the scWAT of 4-week-old mice at different ages. GFP expression marks cells competent for production of IL-4 (n = 5 per age). (E–J) Quantification of Ki67⁺ (E, G, and I) and total APs (F, H, and J) in scWAT of 5-week-old ΔdblGATA (E, F), Il4/13^{-/-} (G and H), and Il4ra^{-/-} (I and J) mice (n = 5–10 per genotype). Data are represented as mean ± SEM. See also Figure S3.

IL-4Rα Signaling in PDGFRα⁺ Cells Promotes Expansion of Adipocyte Precursors

Previous studies by the Granneman laboratory have demonstrated that pharmacologic activation of the β₃-adrenergic receptor stimulates the proliferation and differentiation of APs into beige adipocytes (Lee et al., 2012). Since we recently

demonstrated that type 2 activation of macrophages via IL-4Rα stimulates release of norepinephrine in the scWAT and eWAT of mice (Nguyen et al., 2011; Qiu et al., 2014), we next asked whether myeloid cell IL-4Rα signaling might regulate the postnatal expansion and commitment of APs to the beige adipocyte lineage. To our surprise, we found that deletion of Il4ra in

(C) Quantification of eosinophils in the scWAT of thermoneutral heterozygous Red5 (Il5^{Red5/+}) mice that were administered Veh or IL-33 for 8 days (n = 8–10 per treatment).

(D) Quantification of adipocyte precursor (AP) proliferation in the scWAT of thermoneutral Il5^{Red5/+} mice administered Veh or IL-33 for 8 days, as assessed by intracellular staining for Ki67 (D) and AP cell number per fat pad (n = 8–10 per treatment).

(F and G) Expression of beige adipocyte markers TMEM26 and CD137 on the scWAT APs of thermoneutral Il5^{Red5/+} mice administered Veh or IL-33 for 8 days (n = 8–10 per treatment). Representative histograms for TMEM26 (F) and CD137 (G) are shown; clear histogram-Veh, shaded histogram-IL-33.

(H–J) Expression of IL1RL1 (H), IL-5Rα (I), and IL-4Rα (J) on scWAT APs of mice. For IL1RL1 (H), the clear histogram represents WT APs, while the shaded histogram represents Il1rl1^{-/-} APs. For IL-5Rα (I), the dashed line histogram represents isotype, the solid line represents APs stained for IL-5Rα, and the shaded histogram represents eosinophils stained for IL-5Rα. For IL-4Rα (J), the solid line histogram represents isotype and the shaded histogram represents APs stained for IL-4Rα.

(K and L) Quantification of IL-33 induced AP proliferation in the scWAT of Il4/13^{-/-} (K) and Il4ra^{-/-} (L) mice (n = 4–8 per genotype and treatment).

(M) Immunoblotting for UCP1 in the scWAT and BAT of thermoneutral WT and Il4ra^{-/-} mice administered IL-33 for 8 days (n = 2–3 per genotype and treatment).

(N–P) Quantification of AP proliferation (N), TMEM26 (O) and CD137 (P) expression in Rag2^{-/-} and Rag2^{-/-}Il2rgc^{-/-} mice treated with IL-33 (n = 6–8 per genotype and treatment).

Data are represented as mean ± SEM. See also Figure S1 and S2.

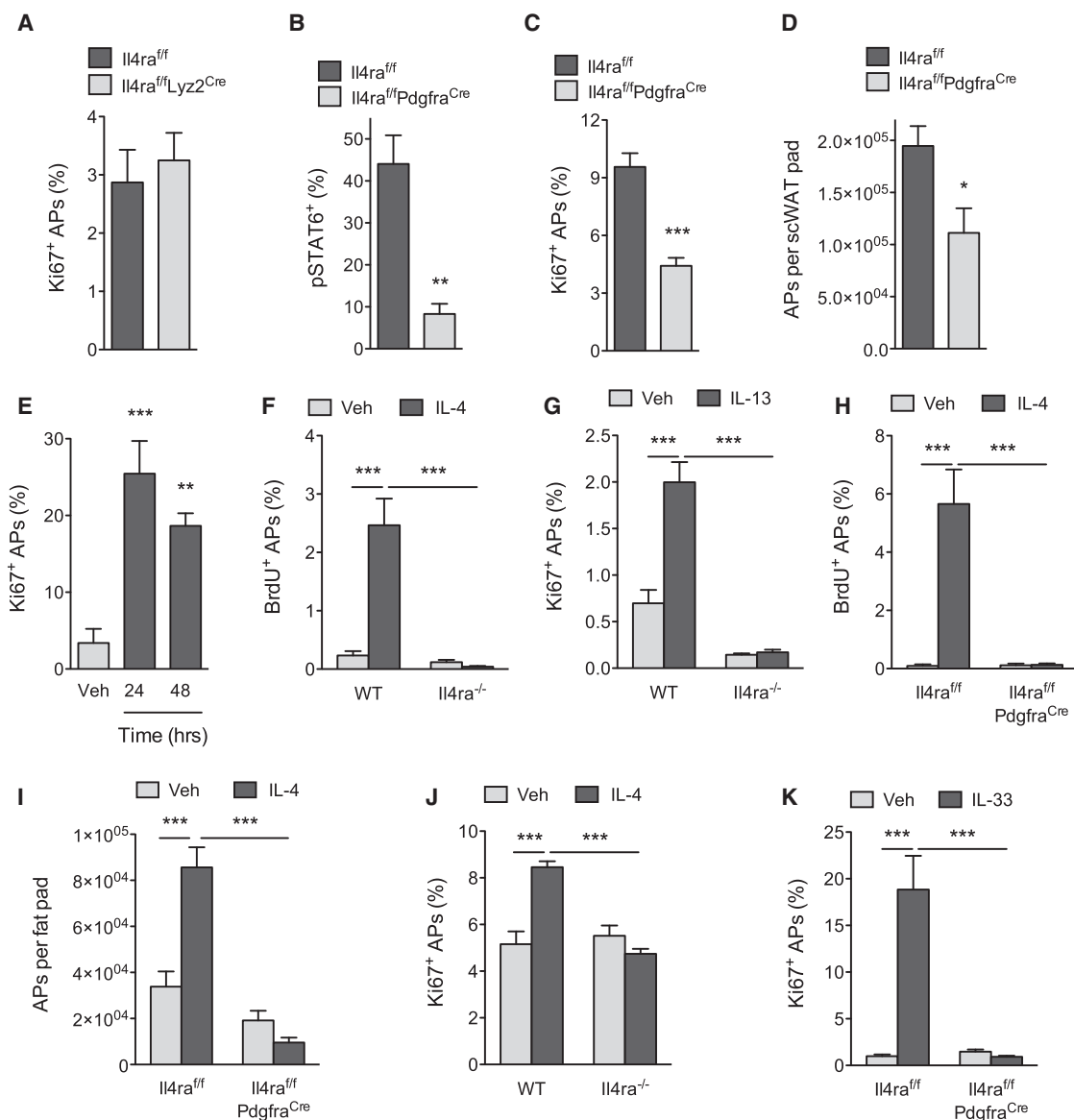


Figure 4. IL-4R α Signaling in PDGFR α ⁺ Cells Promotes Expansion of Adipocyte Precursors

(A) Quantification of scWAT adipocyte precursor (AP) proliferation in 5-week-old *Il4ra^{fl/fl}* and *Il4ra^{fl/fl}Lyz2^{Cre}* mice (n = 8–10 per genotype). (B) Analysis of IL-4-induced phosphorylation of STAT6 (pSTAT6) in scWAT APs of *Il4ra^{fl/fl}* and *Il4ra^{fl/fl}Pdgfra^{Cre}* mice (n = 3–4 per genotype). (C and D) Quantification of scWAT AP proliferation by Ki67 staining (C) and total number (D) in 5-week-old *Il4ra^{fl/fl}* and *Il4ra^{fl/fl}Pdgfra^{Cre}* mice (n = 7–12). (E) Quantification of scWAT AP proliferation by Ki67 staining in 8- to 10-week-old C57BL/6J mice at 24 and 48 hr after injection with vehicle or IL-4 (n = 5 per time point). (F and H) BrdU incorporation by the scWAT APs of wild-type and *Il4ra^{-/-}* mice (F) or *Il4ra^{fl/fl}* and *Il4ra^{fl/fl}Pdgfra^{Cre}* mice (H) 48 hr after administration of IL-4 (n = 6–8 per genotype and treatment). (G) Quantification of scWAT AP proliferation by Ki67 staining 48 hr after administration of vehicle or IL-13 (n = 6–8 per genotype and treatment). (I) Quantification of scWAT AP number in *Il4ra^{fl/fl}* and *Il4ra^{fl/fl}Pdgfra^{Cre}* mice 48 hr after administration of vehicle or IL-4 (n = 7 per genotype). (J) APs purified from wild-type and *Il4ra^{-/-}* mice were stimulated with IL-4, and cellular proliferation was quantified by intracellular staining for Ki67 48 hr later (n = 4 per genotype and treatment). (K) Quantification of scWAT AP proliferation in *Il4ra^{fl/fl}* and *Il4ra^{fl/fl}Pdgfra^{Cre}* mice 48 hr after administration of vehicle or IL-33 (n = 8–10 per genotype and treatment). Data are represented as mean \pm SEM. See also Figure S4.

myeloid cells, as in *Il4ra^{fl/fl}Lyz2^{Cre}* mice, did not significantly affect the rate of AP proliferation or expression of beige adipocyte markers in the scWAT (Figures 4A, S4A, and S4B), leading us

to hypothesize that IL-4/13 might directly stimulate AP proliferation. To address this possibility, we generated mice in which *Il4ra* was selectively deleted in PDGFR α ⁺ cells (*Il4ra^{fl/fl}Pdgfra^{Cre}*

mice). Consistent with the loss of IL-4R α expression in APs (Figure S4C), IL-4 stimulated increase in pSTAT6 was reduced by ~80% in scWAT APs, but not in the CD11b⁺ myeloid cells, of *Il4- α ^{fl/fl}Pdgfra^{Cre}* mice (Figures 4B, S4D, and S4E). Consequently, both the proliferative capacity of APs and their numbers were reduced by ~54% and ~43%, respectively, in 5-week-old *Il4- α ^{fl/fl}Pdgfra^{Cre}* mice (Figures 4C and 4D). These results indicate that the type 2 cytokines IL-4 and IL-13 play a critical role in controlling adipocyte precursor pool size by directly activating IL-4R α signaling in PDGFR α ⁺ APs.

To investigate whether pharmacological activation of IL-4R α signaling is sufficient to stimulate the proliferation of APs in scWAT, we injected 8- to 10-week-old mice with IL-4 as a complex with anti-IL4 antibody, which prolongs its biological half-life (Finkelman et al., 1993). As noted above, the rate of AP proliferation declines with age (Figures 3A and 3B); however, this was restored by the administration of IL-4 to WT mice. For instance, treatment of 8- to 10-week-old mice with IL-4 complex increased the percentage of Ki67⁺ APs by ~5.5–7.5-fold within 24–48 hr (Figure 4E). This stimulation of AP proliferation by IL-4 or IL-13 was an on-target effect of these cytokines because it required IL-4R α (Figures 4F and 4G). Furthermore, administration of IL-4 complex failed to stimulate DNA synthesis or cellular proliferation in APs of *Il4 α ^{fl/fl}Pdgfra^{Cre}* mice (Figures 4H and S4F), confirming that IL-4 stimulates the growth of APs in a cell autonomous manner. After 48 hr, the number of APs present in scWAT also increased by ~2.5-fold, demonstrating that stimulation with IL-4 is sufficient to expand the pool of PDGFR α ⁺ APs that reside within scWAT (Figures 4I and S4G). Again, this increase in AP number was dependent on cell autonomous signaling via the IL-4R α in PDGFR α ⁺ cells (Figure 4I). Purification of APs from wild-type, *Il4 α ^{-/-}*, and *Stat6^{-/-}* mice provided independent verification for the direct proliferative effects of IL-4 on APs (Figures S4H, S4I, and 4J). Finally, we tested whether IL-33-induced proliferation of APs requires cell autonomous signaling via the IL-4R α . Indeed, while IL-33 robustly induced AP proliferation (~19-fold) in the scWAT of *Il4 α ^{fl/fl}* mice, it failed to do so in *Il4 α ^{fl/fl}Pdgfra^{Cre}* mice (Figure 4K). In a similar manner, the induction of IL-4R α and beige adipocyte markers (TMEM26 and CD137) by IL-33 was absent in *Il4 α ^{fl/fl}Pdgfra^{Cre}* mice (Figures S4J–S4L). In aggregate, these results demonstrate that the IL-33/ILC2/IL-4R α signaling pathway acts directly on scWAT APs to expand the pool of beige adipogenic precursors.

IL-4 and IL-13 Direct Commitment of PDGFR α ⁺

Adipocyte Precursors to Beige Adipogenic Precursors

PDGFR α ⁺ APs present in scWAT are bipotential cells that can give rise to white or beige adipocytes (Berry et al., 2014; Lee et al., 2012), prompting us to ask whether signaling via the IL-4R α might direct the commitment of APs to either lineage. Using purified wild-type APs from the scWAT, we first investigated the effects of IL-4 on their adipogenic conversion into white adipocytes. Figures S5A–S5C show that the addition of IL-4 during the initial differentiation period inhibited the conversion of APs into white adipocytes. Since differentiated adipocytes did not express IL-4R α at any appreciable level (Figure S5C), we hypothesized that the biologic actions of type 2 cytokines might be restricted to adi-

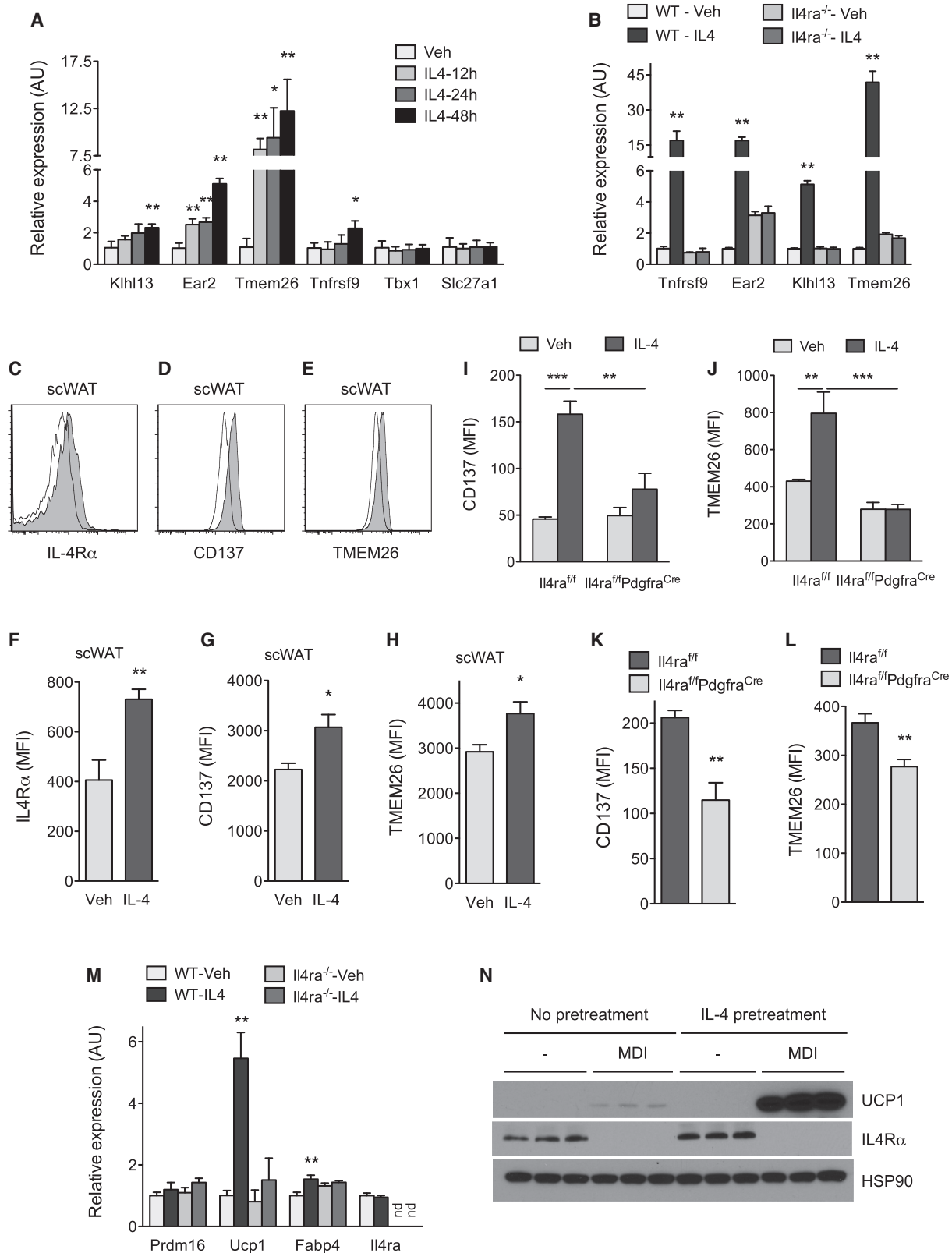
pogenic precursors. We thus asked whether, in the absence of adipogenic stimuli, treatment with IL-4 altered the fate of purified APs. Indeed, in a time-dependent manner, treatment of purified APs with IL-4 induced the expression of a number of beige adipocyte makers, including *Klh13*, *Ear2*, *Tmem26*, and *Tnfrsf9* (Figure 5A). Consistent with the distinct developmental lineages of beige and brown adipocytes (Harms and Seale, 2013), exposure to IL-4 did not alter the expression of brown fat markers in APs purified from scWAT (Figure S5D). This commitment of APs to the beige fat lineage was an on-target effect of IL-4 because it was absent in APs isolated from *Il4 α ^{-/-}* mice (Figure 5B).

We next asked whether administration of IL-4 to wild-type mice was sufficient to promote the expression of beige lineage markers in APs. Cell surface expression of IL-4R α , a known target of IL-4/STAT6 signaling (Goenka and Kaplan, 2011), and the beige precursor markers CD137 (encoded by *Tnfrsf9*) and TMEM26 were all induced in the scWAT APs upon treatment with IL-4 (Figures 5C–5H). The induction of these beige markers required intact IL-4R α signaling in PDGFR α ⁺ cells because treatment with IL-4 failed to induce expression of CD137 and TMEM26 in scWAT APs of *Il4 α ^{fl/fl}Pdgfra^{Cre}* mice (Figures 5I and 5J). Furthermore, treatment of WT mice with IL-4 was also sufficient to increase expression of beige cell markers in eWAT (Figures S6A–S6F), a tissue that is normally refractory to cold-induced browning. Consistent with these gain-of-function studies, loss of type 2 cytokine signaling, as in *ΔdblGATA*, *Il4/13^{-/-}*, and *Il4 α ^{fl/fl}Pdgfra^{Cre}* mice, decreased expression of beige precursor cell markers in scWAT APs (Figures S6G–S6J and Figures 5K and 5L).

To investigate whether the induction of beige precursor cell markers correlates with enhanced capacity for beige adipogenesis, we pretreated purified APs with IL-4 and then subjected them to beige adipogenic stimuli. Congruent with our hypothesis, we observed that IL-4 pretreated APs exhibited enhanced capacity for beige adipogenesis, as assessed by the expression of UCP1 mRNA and protein (Figures 5M and 5N). Moreover, we observed that differentiation of APs into beige adipocytes resulted in downregulation of beige adipocyte markers (*Tnfrsf9*, *Klh13*, and *Tmem26*) (Figure S6K), indicating that these markers might work better for the identification of beige adipocyte precursors rather than the differentiated beige adipocytes in WATs. Together, these in vitro and in vivo data suggest that the activation of signaling via the IL-4R α in PDGFR α ⁺ cells is both required and sufficient to promote the commitment of bipotential APs to the beige fat lineage.

IL-4R α Signaling in Adipocyte Precursors Controls Growth of Beige Fat

We next asked whether loss of IL-4R α signaling in PDGFR α ⁺ cells alters the development of beige fat in vivo. The browning of scWAT normally occurs when mice experience cold stress. Since the standard vivarium temperature of 20°C–22°C poses a significant thermal stress for young mice (Cannon and Nedergaard, 2011; Nedergaard and Cannon, 2014), due to their high ratio of body surface area to body mass, we asked whether young (5-week-old) mice exhibited browning of their scWAT. We chose this time point because it represents the peak for scWAT AP IL-4R α signaling and proliferation (Figures 3 and 4). Indeed, we found histological evidence for beige fat



(legend on next page)

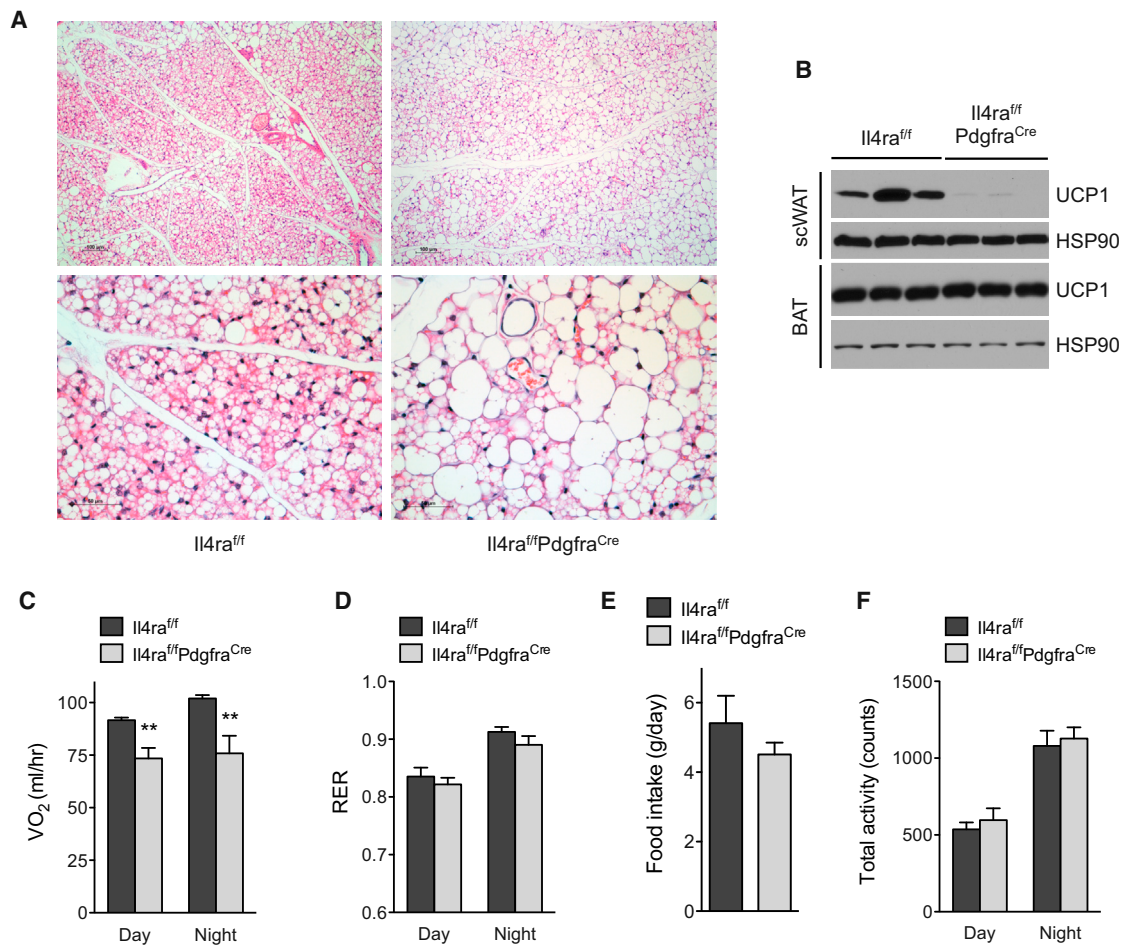


Figure 6. IL-4R α Signaling in Adipocyte Precursors Directs Growth of Beige Fat

(A) Representative sections of scWAT from 5-week-old *Il4ra^{fl/fl}* and *Il4ra^{fl/fl}/Pdgfra^{Cre}* mice were stained with hematoxylin and eosin. 100x magnification (top), 400x magnification (bottom). (B) UCP1 protein expression in scWAT and BAT of 5-week-old *Il4ra^{fl/fl}* and *Il4ra^{fl/fl}/Pdgfra^{Cre}* mice housed at 22°C (n = 3 per genotype). (C–F) Assessment of metabolic rate, food intake, and activity in 5-week-old *Il4ra^{fl/fl}* and *Il4ra^{fl/fl}/Pdgfra^{Cre}* mice housed at 22°C (n = 8 per genotype); (C) oxygen consumption (VO_2), (D) RER, (E) total activity, and (F) food intake. Data are represented as mean \pm SEM.

development in the scWAT of control (*Il4ra^{fl/fl}*) mice housed at 20°C–22°C, which was decreased in the *Il4ra^{fl/fl}/Pdgfra^{Cre}* mice (Figure 6A). Specifically, *Il4ra^{fl/fl}* mice demonstrated complete replacement of multiple adjacent central scWAT lobules

with multiloculated beige adipocytes, while beigeing in *Il4ra^{fl/fl}/Pdgfra^{Cre}* mice, in contrast, involved fewer scWAT lobules, each of which exhibited less complete beigeing (i.e., retained more cells with white adipocyte morphology). In agreement

Figure 5. IL-4 and IL-13 Direct Commitment of PDGFR α ⁺ Adipocyte Precursors to Beige Adipogenic Precursors

(A) Quantitative RT-PCR analysis of beige adipocyte precursor markers in APs purified from the scWAT of C57BL/6J stimulated with vehicle or IL-4 (n = 3 per condition and time point; data presented as mean \pm SD). (B) Quantitative RT-PCR analysis of beige adipocyte precursor markers in APs purified from Balb/cJ or *Il4ra^{-/-}* mice that were stimulated with vehicle or IL-4 for 48 hr (n = 3 per genotype and treatment; data presented as mean \pm SD). (C–E) Flow cytometric analysis of IL-4R α (C), CD137 (D) and TMEM26 (E) expression in scWAT APs of mice injected with vehicle or IL-4. Clear histogram: vehicle; shaded histogram: IL-4. (F–H) Quantification of IL-4R α , CD137, and TMEM26 expression in scWAT APs 48 hr after administration of vehicle or IL-4 (n = 5 per treatment). (I, J) Quantification of CD137 and TMEM26 expression in the scWAT APs of *Il4ra^{fl/fl}* and *Il4ra^{fl/fl}/Pdgfra^{Cre}* mice 48 hr after administration of IL-4 (n = 4–6 per genotype and treatment). (K and L) Quantification of CD137 and TMEM26 expression in the scWAT APs of 5-week-old *Il4ra^{fl/fl}* and *Il4ra^{fl/fl}/Pdgfra^{Cre}* mice (n = 8–12 per genotype). (M) Quantitative RT-PCR analysis of beige/brown adipocyte genes after in vitro differentiation of scWAT APs purified from Balb/cJ or *Il4ra^{-/-}* mice (n = 3 per genotype and treatment; data presented as mean \pm SD). (N) Immunoblot analysis for UCP1 and IL-4R α in in vitro-differentiated APs. MDI refers to stimulation of differentiation by adipogenic cocktail, (n = 3 genotype and treatment).

Unless otherwise indicated, data are represented as mean \pm SEM. See also Figure S5 and S6.

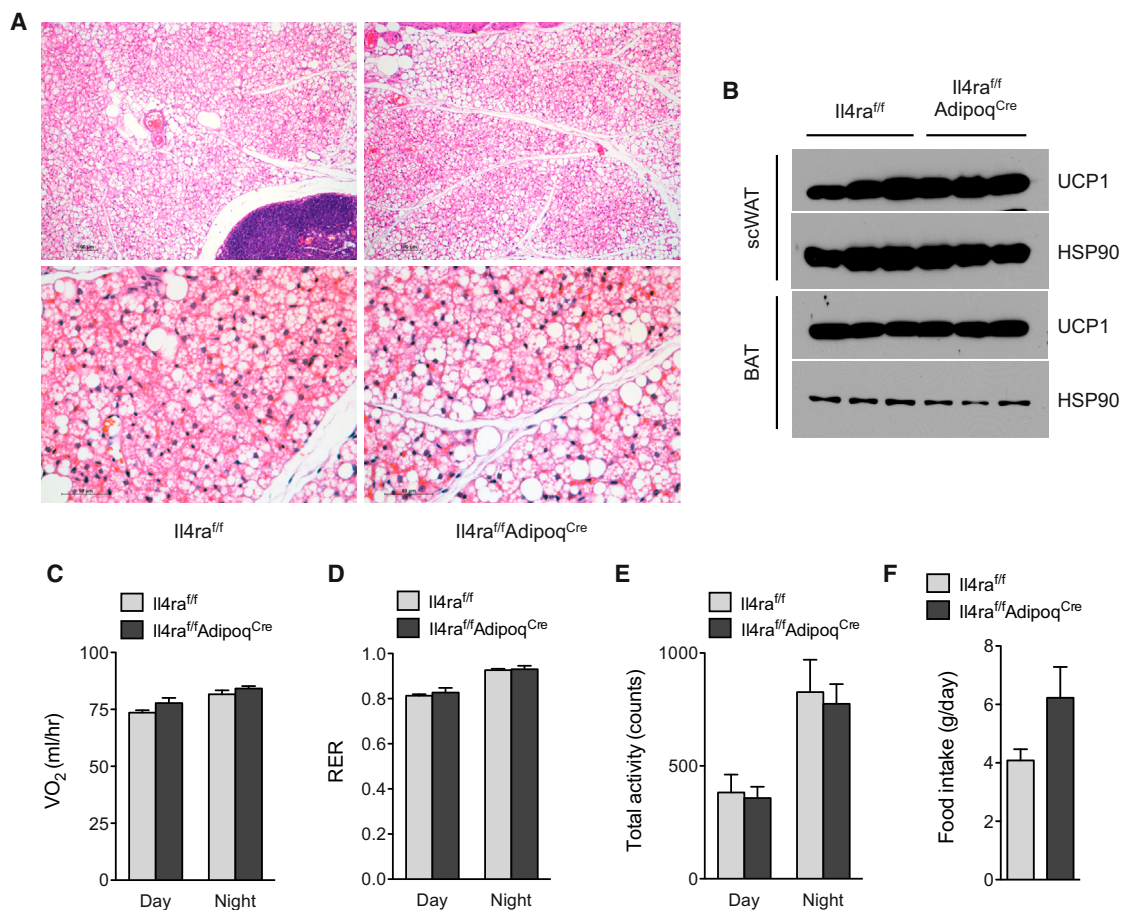


Figure 7. IL-4R α Signaling in Mature Adipocytes Is Dispensable for Growth of Beige Fat

(A) Histological analysis of scWAT of 5-week-old *Il4ra^{fl/fl}* and *Il4ra^{fl/fl}Adipoq^{Cre}* mice housed at 22°C. Representative sections were stained with hematoxylin and eosin, and images are shown at 100 \times magnification (top) and 400 \times magnification (bottom).

(B) Immunoblot analysis of UCP1 protein expression in scWAT and BAT of 5-week-old *Il4ra^{fl/fl}* and *Il4ra^{fl/fl}Adipoq^{Cre}* mice.

(C–F) Assessment of energy expenditure in 5-week-old *Il4ra^{fl/fl}* and *Il4ra^{fl/fl}Adipoq^{Cre}* mice was performed using CLAMS; (C) oxygen consumption (VO₂), (D) RER, (E) total activity, and (F) food intake. Data are represented as mean \pm SEM.

with these histological data, immunoblot analysis for UCP1 protein demonstrated its robust expression in the scWAT of *Il4ra^{fl/fl}* but not *Il4ra^{fl/fl}Pdgfra^{Cre}* mice (Figure 6B). In contrast, we did not observe significant differences among the genotypes in expression of UCP1 protein in interscapular brown adipose tissue (Figure 6B), which develops from distinct myogenic precursors (Lepper and Fan, 2010; Seale et al., 2008).

To investigate whether browning of scWAT in young mice contributed to total body energy expenditure, we studied 5-week-old mice *Il4ra^{fl/fl}* and *Il4ra^{fl/fl}Pdgfra^{Cre}* mice using the Comprehensive Lab Animal Monitoring Systems (CLAMS). Energy expenditure, as quantified by total oxygen consumption (VO₂) per mouse, was significantly lower (~20%–25%) in *Il4ra^{fl/fl}Pdgfra^{Cre}* mice in both the day and night cycle (Figure 6C). This reduction in VO₂ was unlikely to be a consequence of changes in total locomotor activity, RER, or food intake, which were similar between the two genotypes (Figure 6D–6F). Together, these results demonstrate that IL-4R α signaling in

adipocyte precursor cells is a critical regulator for the development of postnatal beige fat.

IL-4R α Signaling in Mature Adipocytes Is Dispensable for Growth of Beige Fat

Because adipogenic precursors give rise to mature adipocytes (Berry et al., 2014), it remains plausible that the metabolic phenotypes observed in *Il4ra^{fl/fl}Pdgfra^{Cre}* mice result from loss of IL-4R α signaling in mature adipocytes. To address this possibility, we generated mice in which the *Il4ra* gene was selectively deleted in differentiated adipocytes (designated *Il4ra^{fl/fl}Adipoq^{Cre}*). Consistent with its primary role in APs, deletion of *Il4ra* in mature adipocytes did not affect beige fat development as assessed histologically and by immunoblotting for UCP1 (Figures 7A, 7B and S6L). Accordingly, *Il4ra^{fl/fl}* and *Il4ra^{fl/fl}Adipoq^{Cre}* mice had similar rates of oxygen consumption, RER, total activity, and food intake (Figures 7C–7F). These findings are consistent with the observations that IL-4R α is highly expressed in adipogenic

precursors but not in mature adipocytes (Figures 5N and S5C).

DISCUSSION

We have previously demonstrated that exposure to environmental cold induces an innate type 2 response to stimulate the growth of beige fat. This efferent innate circuit consists of IL-4-secreting eosinophils and catecholamine-producing alternatively activated macrophages (Nguyen et al., 2011; Qiu et al., 2014). Here we have identified two additional components of this thermogenic circuit, which include ILC2s and PDGFR α ⁺ adipogenic precursors. Using IL-33 to pharmacologically activate ILC2s in thermoneutral mice, we were able to place ILC2s upstream of APs in the beige fat thermogenic circuit. We found that ILC2-derived IL-13 and eosinophil-derived IL-4 functionally cooperate to activate IL-4R α signaling, thus promoting the expansion and commitment of scWAT APs to the beige adipocyte lineage. Surprisingly, these browning effects of IL-4 and IL-13 were not dependent on signaling via the IL-4R α on myeloid cells but rather on PDGFR α ⁺ APs themselves. In agreement with this, both pharmacologic and physiologic expansion of beige adipocyte precursors was reduced in *Il4ra^{fl/fl}Pdgfra^{Cre}* mice. Taken together with our previous results, these findings suggest that type 2 immunity regulates two key events in the biogenesis of beige fat. First, it controls the expansion and commitment of APs to the beige fat lineage. Second, it stimulates the differentiation of beige precursor cells into beige adipocytes via myeloid cell-derived catecholamines.

Browning of WAT has principally been studied in adult rodents after prolonged exposure to cold (Nedergaard and Cannon, 2014; Wu et al., 2013). In these experimental paradigms, the housing of adult mice in cold environments (4°C–8°C for 2 days or longer) promotes the emergence of UCP1⁺ multilocular beige adipocytes. The underlying assumption here has been that prolonged cold exposure creates a mismatch between the organism's capacity for heat generation and its heat loss to the environment, necessitating the recruitment of additional thermogenic tissues to maintain thermal homeostasis (Nedergaard and Cannon, 2014; Qiu et al., 2014). Because the normal vivarium temperature of 20°C–22°C imposes a significant thermal stress on young mice, in which the ratio of body surface area to body mass is large, we reasoned that it might be a powerful stimulus for the recruitment of UCP1⁺ beige adipocytes. Indeed, we found histological evidence for browning in the scWAT of 5-week-old mice housed at 20°C–22°C. Unlike the cold-induced browning in adult mice, which is generally patchy and incomplete even within individual lobules, this “physiologic” browning of the scWAT in young mice was more widespread, involving entire adjacent lobules (Figures 6A and 7A). Thus, we suggest that, as an alternative to the classic experimental paradigm of housing adult mice at 4°C–8°C, investigations of the physiologic browning process in young mice might yield useful insights into the mechanisms that regulate beige fat biogenesis.

Although the stages of scWAT development have been studied previously (Wang et al., 2013), the physiologic signals that regulate the proliferation and/or fate of scWAT APs were unknown. Our observations that IL-33 potently stimulates prolifer-

ation of PDGFR α ⁺ APs in an IL-4/13- and IL-4R α -dependent manner (Figures 2K and 2L) led us to investigate whether type 2 cytokines might be the physiologic signals controlling the expansion of PDGFR α ⁺ APs in the scWAT. Indeed, we found that loss of type 2 cytokine signaling decreased the proliferation rate and number of PDGFR α ⁺ APs by ~50% in scWAT. Interestingly, this signaling pathway also regulated the commitment of PDGFR α ⁺ APs to the beige adipocyte precursors in a cell autonomous manner. Since the proliferation rate of PDGFR α ⁺ APs declines with age (Figures 3A and 3B), our results suggest that the activation of type 2 cytokine signaling in the early postnatal period establishes a pool of PDGFR α ⁺ beige adipocyte precursors, which are subsequently recruited by cold stress to generate beige adipocytes in the adult organism. Perhaps, these data also provide an explanation for the old observation that thermogenic adaptations to cold decline with aging (Talan et al., 1985).

Our gain- and loss-of-function studies suggest that type 2 innate immune cells have discrete roles in controlling the numbers and fate of PDGFR α ⁺ adipocyte precursors in the scWAT of mice. During physiologic development of this tissue, eosinophil-derived IL-4 seems to play a critical role in the homeostatic expansion of PDGFR α ⁺ APs into beige adipocyte precursors in young mice (Figures 3E, 3F, S6G, and S6H). However, IL-33-induced pharmacologic expansion of scWAT APs in adult animals seems to occur independently of eosinophils (Figure S2H). Since both ILC2s and signaling via the IL-4R α are required for IL-33-mediated proliferation of scWAT APs and their subsequent differentiation into beige adipocytes (Figures 2K–2P), it suggests that secretion of IL-13 by ILC2s might be a dominant mechanism by which this tissue responds to environmental stress. Thus, in the future, it will be critical to examine the requirement of and mechanisms by which ILC2s and IL-33 regulate the development of functional beige fat during cold stress.

Finally, together with previous studies, our work provides mechanistic insights into how mammals adapt and acclimatize to environmental cold. During an acute cold challenge, mice defend their core body temperature by quickly activating thermogenesis. This rapid increase in heat production, which occurs within seconds to minutes, is mediated by several thermoeffectors, including cutaneous vasoconstriction, skeletal muscle shivering, and UCP1-mediated respiration in brown adipocytes; processes that are all activated by the sympathetic nervous system (Cannon and Nedergaard, 2011; Lowell and Spiegelman, 2000). In contrast, prolonged cold stress induces cellular programs for acclimatization, such as the de novo recruitment of beige adipocytes (Harms and Seale, 2013), which occur on a longer time frame (days to weeks to months) for more stable physiologic adaptations. Although programs of acclimatization are well documented across species and are of great interest to evolutionary biologists, their mechanisms, with a few exceptions (such as changes in skin pigmentation in response to sunlight or increase in oxygen carrying capacity after living at high altitudes), are largely unknown. Through our work, we have identified the mechanism for acclimatization to environmental cold. Unlike the acute adaptations that are initiated by the sympathetic nervous system, acclimatization to environmental cold is orchestrated by type 2 immune cells (ILC2s, eosinophils, and

alternatively activated macrophages) and signals (IL-33, IL-4, and -13), which sequentially regulate the expansion, commitment, and differentiation of adipocyte precursors into beige adipocytes. Our identification of the immune system as the primary thermogenic circuit controlling the cold acclimatization process is consistent with a recent proposal that type 2 immunity co-evolved as a defensive strategy against noxious environmental stimuli (Palm et al., 2012; Profet, 1991), of which cold might be one.

EXPERIMENTAL PROCEDURES

Animal Studies

All animal studies were conducted at UCSF under an approved IACUC protocol. Mice were housed at 20°C–22°C (unless otherwise stated) in the vivarium under a 12 hr light:dark cycle. Both male and female mice of various ages were used in these studies. The following animal strains were on the BALB/cJ background: WT, *Il4/13*^{−/−}, *Il4ra*^{−/−}, *Stat6*^{−/−}, *4get*, and *4get-ΔdblGATA*, whereas WT, R5 (*Il5*^{Red5/+}), R5R5 (*Il5*^{Red5/Red5}), R5Smart13 (*Il5*^{Red5/+} *Il13*^{Smart/+}), *Il4ra*^{−/−}, *Ucp1*^{−/−}, *Il4ra*^{fl/fl}, *Il4ra*^{fl/fl} *Lyz2*^{Cre}, *Il4ra*^{fl/fl} *Pdgfra*^{Cre}, and *Il4ra*^{fl/fl} *Adipoq*^{Cre} were on the C57BL6/J background. *Rag2*^{−/−} and *Rag2*^{fl2rg}^{−/−} were purchased from Taconic. At the conclusion of experiments, tissues were harvested and snap frozen in liquid nitrogen for molecular analyses, fixed in 10% formalin for histology, or digested for flow cytometric analyses of adipocyte precursors and immune cells. For gain-of-function studies, 8- to 12-week-old mice were injected intraperitoneally with vehicle, IL-33 (0.5–1 μg, Biolegend), IL-13 (0.5 μg, Peprotech), or IL-4 (2 μg, Peprotech) that was complexed with anti-IL4 mAb (10 μg, clone 11B11). Activation of signaling via the IL-4Rα was assessed 1–2 hr after administration of recombinant IL-4 (2 μg). For the in vivo studies, cohorts of ≥ 4 mice per genotype or treatment were assembled and experiments were repeated 2–3 independent times.

Statistical Analysis

Data were analyzed using Prism (Graphpad) and are presented as mean ± SEM or mean ± SD. Statistical significance was determined using the unpaired two-tailed Student's *t* test for single variables and two-way ANOVA followed by Bonferroni posttests for multiple variables. A *p* value of < 0.05 was considered to be statistically significant and is presented as * (*p* < 0.05), ** (*p* < 0.01), or *** (*p* < 0.001).

Extended Experimental Procedures are included in the Supplemental Information.

SUPPLEMENTAL INFORMATION

Supplemental Information includes Extended Experimental Procedures, seven figures, and two tables and can be found with this article online at <http://dx.doi.org/10.1016/j.cell.2014.12.011>.

AUTHOR CONTRIBUTION

M-W.L., J.I.O., L.M., Y.Q., A.B.M., and J.C.N. designed and performed the main experiments, and K.Y. provided technical assistance for the main experiments. R.M.L. provided essential mouse lines for the completion of the studies and assisted with experimental design and manuscript preparation. M-W.L., J.I.O., L.M., Y.Q., A.B.M., J.C.N., R.M.L., and A.C. discussed and interpreted the results from the study. M-W.L., J.I.O., and A.C. conceived, supervised, and wrote the paper.

ACKNOWLEDGMENTS

We thank members of the Chawla laboratory and A. Loh for comments on the manuscript. The authors' work was supported by grants from NIH (HL076746, DK094641), American Heart Association Innovative Science Award (12PILT11840038 and 14ISA20850001), an NIH Director's Pioneer Award (DP1AR064158) to A.C. and NIH (R37AI026918, AI119944) and

HHMI to R.M.L. M-W.L. was supported by a Postdoctoral Fellowship from the Hillblom Foundation, A.B.M. by NIH K08 DK101604, and J.C.N. by NIH K08 AI113143.

Received: November 10, 2014

Revised: December 3, 2014

Accepted: December 3, 2014

Published: December 24, 2014

REFERENCES

- Berry, R., and Rodeheffer, M.S. (2013). Characterization of the adipocyte cellular lineage in vivo. *Nat. Cell Biol.* 15, 302–308.
- Berry, R., Jeffery, E., and Rodeheffer, M.S. (2014). Weighing in on adipocyte precursors. *Cell Metab.* 19, 8–20.
- Cannon, B., and Nedergaard, J. (2011). Nonshivering thermogenesis and its adequate measurement in metabolic studies. *J. Exp. Biol.* 214, 242–253.
- Cayrol, C., and Girard, J.P. (2014). IL-33: an alarmin cytokine with crucial roles in innate immunity, inflammation and allergy. *Curr. Opin. Immunol.* 31C, 31–37.
- Finkelman, F.D., Madden, K.B., Morris, S.C., Holmes, J.M., Boiani, N., Katona, I.M., and Maliszewski, C.R. (1993). Anti-cytokine antibodies as carrier proteins. Prolongation of in vivo effects of exogenous cytokines by injection of cytokine-anti-cytokine antibody complexes. *J. Immunol.* 151, 1235–1244.
- Goenka, S., and Kaplan, M.H. (2011). Transcriptional regulation by STAT6. *Immunol. Res.* 50, 87–96.
- Golozoubova, V., Cannon, B., and Nedergaard, J. (2006). UCP1 is essential for adaptive adrenergic nonshivering thermogenesis. *Am. J. Physiol. Endocrinol. Metab.* 291, E350–E357.
- Harms, M., and Seale, P. (2013). Brown and beige fat: development, function and therapeutic potential. *Nat. Med.* 19, 1252–1263.
- Hudak, C.S., Gulyaeva, O., Wang, Y., Park, S.M., Lee, L., Kang, C., and Sul, H.S. (2014). Pref-1 marks very early mesenchymal precursors required for adipose tissue development and expansion. *Cell Rep* 8, 678–687.
- Kelly-Welch, A.E., Hanson, E.M., Boothby, M.R., and Keegan, A.D. (2003). Interleukin-4 and interleukin-13 signaling connections maps. *Science* 300, 1527–1528.
- Koyasu, S., and Moro, K. (2013). Th2-type innate immune responses mediated by natural helper cells. *Ann. N.Y. Acad. Sci.* 1283, 43–49.
- Lee, Y.H., Petkova, A.P., Mottillo, E.P., and Granneman, J.G. (2012). In vivo identification of bipotential adipocyte progenitors recruited by β3-adrenoceptor activation and high-fat feeding. *Cell Metab.* 15, 480–491.
- Lepper, C., and Fan, C.M. (2010). Inducible lineage tracing of Pax7-descendant cells reveals embryonic origin of adult satellite cells. *Genesis* 48, 424–436.
- Licon-Limón, P., Kim, L.K., Palm, N.W., and Flavell, R.A. (2013). TH2, allergy and group 2 innate lymphoid cells. *Nat. Immunol.* 14, 536–542.
- Lowell, B.B., and Spiegelman, B.M. (2000). Towards a molecular understanding of adaptive thermogenesis. *Nature* 404, 652–660.
- McKenzie, A.N., Spits, H., and Eberl, G. (2014). Innate lymphoid cells in inflammation and immunity. *Immunity* 41, 366–374.
- Mohrs, M., Shinkai, K., Mohrs, K., and Locksley, R.M. (2001). Analysis of type 2 immunity in vivo with a bicistronic IL-4 reporter. *Immunity* 15, 303–311.
- Molofsky, A.B., Nussbaum, J.C., Liang, H.E., Van Dyken, S.J., Cheng, L.E., Mohapatra, A., Chawla, A., and Locksley, R.M. (2013). Innate lymphoid type 2 cells sustain visceral adipose tissue eosinophils and alternatively activated macrophages. *J. Exp. Med.* 210, 535–549.
- Moro, K., Yamada, T., Tanabe, M., Takeuchi, T., Ikawa, T., Kawamoto, H., Furusawa, J., Ohtani, M., Fujii, H., and Koyasu, S. (2010). Innate production of T(H)2 cytokines by adipose tissue-associated c-Kit(+)Sca-1(+) lymphoid cells. *Nature* 463, 540–544.
- Nedergaard, J., and Cannon, B. (2014). The browning of white adipose tissue: some burning issues. *Cell Metab.* 20, 396–407.

- Neill, D.R., Wong, S.H., Bellosi, A., Flynn, R.J., Daly, M., Langford, T.K., Bucks, C., Kane, C.M., Fallon, P.G., Pannell, R., et al. (2010). Nuocytes represent a new innate effector leukocyte that mediates type-2 immunity. *Nature* **464**, 1367–1370.
- Nguyen, K.D., Qiu, Y., Cui, X., Goh, Y.P., Mwangi, J., David, T., Mukundan, L., Brombacher, F., Locksley, R.M., and Chawla, A. (2011). Alternatively activated macrophages produce catecholamines to sustain adaptive thermogenesis. *Nature* **480**, 104–108.
- Nussbaum, J.C., Van Dyken, S.J., von Moltke, J., Cheng, L.E., Mohapatra, A., Molofsky, A.B., Thornton, E.E., Krummel, M.F., Chawla, A., Liang, H.E., and Locksley, R.M. (2013). Type 2 innate lymphoid cells control eosinophil homeostasis. *Nature* **502**, 245–248.
- Palm, N.W., Rosenstein, R.K., and Medzhitov, R. (2012). Allergic host defenses. *Nature* **484**, 465–472.
- Price, A.E., Liang, H.E., Sullivan, B.M., Reinhardt, R.L., Eisle, C.J., Erle, D.J., and Locksley, R.M. (2010). Systemically dispersed innate IL-13-expressing cells in type 2 immunity. *Proc. Natl. Acad. Sci. USA* **107**, 11489–11494.
- Profet, M. (1991). The function of allergy: immunological defense against toxins. *Q. Rev. Biol.* **66**, 23–62.
- Qiu, Y., Nguyen, K.D., Odegaard, J.I., Cui, X., Tian, X., Locksley, R.M., Palmiter, R.D., and Chawla, A. (2014). Eosinophils and type 2 cytokine signaling in macrophages orchestrate development of functional beige fat. *Cell* **157**, 1292–1308.
- Rao, R.R., Long, J.Z., White, J.P., Svensson, K.J., Lou, J., Lokurkar, I., Jedrychowski, M.P., Ruas, J.L., Wrann, C.D., Lo, J.C., et al. (2014). Meteorin-like is a hormone that regulates immune-adipose interactions to increase beige fat thermogenesis. *Cell* **157**, 1279–1291.
- Rosen, E.D., and Spiegelman, B.M. (2006). Adipocytes as regulators of energy balance and glucose homeostasis. *Nature* **444**, 847–853.
- Rosen, E.D., and Spiegelman, B.M. (2014). What we talk about when we talk about fat. *Cell* **156**, 20–44.
- Sanchez-Gurmaches, J., Hung, C.M., Sparks, C.A., Tang, Y., Li, H., and Guertin, D.A. (2012). PTEN loss in the Myf5 lineage redistributes body fat and reveals subsets of white adipocytes that arise from Myf5 precursors. *Cell Metab.* **16**, 348–362.
- Seale, P., Bjork, B., Yang, W., Kajimura, S., Chin, S., Kuang, S., Scimè, A., Devarakonda, S., Conroe, H.M., Erdjument-Bromage, H., et al. (2008). PRDM16 controls a brown fat/skeletal muscle switch. *Nature* **454**, 961–967.
- Talan, M.I., Engel, B.T., and Whitaker, J.R. (1985). A longitudinal study of tolerance to cold stress among C57BL/6J mice. *J. Gerontol.* **40**, 8–14.
- van der Lans, A.A., Hoeks, J., Brans, B., Vijgen, G.H., Visser, M.G., Vosselman, M.J., Hansen, J., Jörgensen, J.A., Wu, J., Mottaghy, F.M., et al. (2013). Cold acclimation recruits human brown fat and increases nonshivering thermogenesis. *J. Clin. Invest.* **123**, 3395–3403.
- Van Dyken, S.J., Mohapatra, A., Nussbaum, J.C., Molofsky, A.B., Thornton, E.E., Ziegler, S.F., McKenzie, A.N., Krummel, M.F., Liang, H.E., and Locksley, R.M. (2014). Chitin activates parallel immune modules that direct distinct inflammatory responses via innate lymphoid type 2 and $\gamma\delta$ T cells. *Immunity* **40**, 414–424.
- Walker, J.A., Barlow, J.L., and McKenzie, A.N. (2013). Innate lymphoid cells—how did we miss them? *Nat. Rev. Immunol.* **13**, 75–87.
- Wang, Q.A., Tao, C., Gupta, R.K., and Scherer, P.E. (2013). Tracking adipogenesis during white adipose tissue development, expansion and regeneration. *Nat. Med.* **19**, 1338–1344.
- Wang, W., Kissig, M., Rajakumari, S., Huang, L., Lim, H.W., Won, K.J., and Seale, P. (2014). Ebf2 is a selective marker of brown and beige adipogenic precursor cells. *Proc. Natl. Acad. Sci. USA* **111**, 14466–14471.
- Wu, D., Molofsky, A.B., Liang, H.E., Ricardo-Gonzalez, R.R., Jouihan, H.A., Bando, J.K., Chawla, A., and Locksley, R.M. (2011). Eosinophils sustain adipose alternatively activated macrophages associated with glucose homeostasis. *Science* **332**, 243–247.
- Wu, J., Boström, P., Sparks, L.M., Ye, L., Choi, J.H., Giang, A.H., Khandekar, M., Virtanen, K.A., Nuutila, P., Schaart, G., et al. (2012). Beige adipocytes are a distinct type of thermogenic fat cell in mouse and human. *Cell* **150**, 366–376.
- Wu, J., Cohen, P., and Spiegelman, B.M. (2013). Adaptive thermogenesis in adipocytes: is beige the new brown? *Genes Dev.* **27**, 234–250.
- Yoneshiro, T., Aita, S., Matsushita, M., Kayahara, T., Kameya, T., Kawai, Y., Iwanaga, T., and Saito, M. (2013). Recruited brown adipose tissue as an anti-obesity agent in humans. *J. Clin. Invest.* **123**, 3404–3408.
- Yu, C., Cantor, A.B., Yang, H., Browne, C., Wells, R.A., Fujiwara, Y., and Orkin, S.H. (2002). Targeted deletion of a high-affinity GATA-binding site in the GATA-1 promoter leads to selective loss of the eosinophil lineage in vivo. *J. Exp. Med.* **195**, 1387–1395.
- Zeve, D., Tang, W., and Graff, J. (2009). Fighting fat with fat: the expanding field of adipose stem cells. *Cell Stem Cell* **5**, 472–481.

Leptin and Insulin Act on POMC Neurons to Promote the Browning of White Fat

Garron T. Dodd,¹ Stephanie Decherf,¹ Kim Loh,¹ Stephanie E. Simonds,² Florian Wiede,¹ Eglantine Balland,² Troy L. Merry,¹ Heike Münzberg,³ Zhong-Yin Zhang,⁴ Barbara B. Kahn,⁵ Benjamin G. Neel,⁶ Kendra K. Bence,⁷ Zane B. Andrews,² Michael A. Cowley,² and Tony Tiganis^{1,*}

¹Department of Biochemistry and Molecular Biology, Monash University, Victoria 3800, Australia

²Department of Physiology, Monash University, Victoria 3800, Australia

³Pennington Biomedical Research Center, LSU Systems, Baton Rouge, LA 70808, USA

⁴Department of Biochemistry and Molecular Biology, Indiana University School of Medicine, Indianapolis, IN 46202, USA

⁵Division of Endocrinology, Diabetes and Metabolism, Department of Medicine, Beth Israel Deaconess Medical Center and Harvard Medical School, Boston, MA 02215, USA

⁶Campbell Family Cancer Research Institute, Ontario Cancer Institute, Princess Margaret Hospital and Department of Medical Biophysics, University of Toronto, Toronto, ON M5G 2M9, Canada

⁷Department of Animal Biology, School of Veterinary Medicine, University of Pennsylvania, Philadelphia, PA 19104, USA

*Correspondence: tony.tiganis@monash.edu

<http://dx.doi.org/10.1016/j.cell.2014.12.022>

SUMMARY

The primary task of white adipose tissue (WAT) is the storage of lipids. However, “beige” adipocytes also exist in WAT. Beige adipocytes burn fat and dissipate the energy as heat, but their abundance is diminished in obesity. Stimulating beige adipocyte development, or WAT browning, increases energy expenditure and holds potential for combating metabolic disease and obesity. Here, we report that insulin and leptin act together on hypothalamic neurons to promote WAT browning and weight loss. Deletion of the phosphatases PTP1B and TCPTP enhanced insulin and leptin signaling in proopiomelanocortin neurons and prevented diet-induced obesity by increasing WAT browning and energy expenditure. The coinfusion of insulin plus leptin into the CNS or the activation of proopiomelanocortin neurons also increased WAT browning and decreased adiposity. Our findings identify a homeostatic mechanism for coordinating the status of energy stores, as relayed by insulin and leptin, with the central control of WAT browning.

INTRODUCTION

There are two types of adipose tissue in humans, white adipose tissue (WAT) and brown adipose tissue (BAT). WAT can store vast amounts of chemical energy as triglycerides (TAGs) for utilization during periods of fasting or starvation. In contrast, BAT dissipates the chemical energy stored in TAGs as heat to preserve core temperature during hypothermia and to counteract obesity (Rosen and Spiegelman, 2014). Brown adipocytes contain a high density of mitochondria with high amounts of uncoupling protein-1 (UCP-1) allowing for the uncoupling of fatty acid oxidation from ATP production to generate heat (Rosen

and Spiegelman, 2014). Although BAT was initially considered to be present only in infants, it is now established that substantial depots of UCP-1 expressing brown-like fat can be detected in the supraspinal, supraclavicular, pericardial, and neck regions of adult humans (Cypess et al., 2009; van Marken Lichtenbelt et al., 2009; Virtanen et al., 2009). These brown-like fat depots can be induced in response to cold, but their abundance is diminished in older and obese subjects (Lee et al., 2014; Ouellet et al., 2011).

Brown-like fat is also found in rodents and is composed of beige adipocytes interspersed among white adipocytes (Rosen and Spiegelman, 2014). Under basal conditions, beige adipocytes express little to no UCP-1, but UCP-1 induction in response to cold promotes thermogenesis and energy expenditure (Rosen and Spiegelman, 2014). Interestingly, the interscapular BAT in human infants is similar to classical brown fat in rodents (Lidell et al., 2013), whereas the brown-like fat in adult humans has a molecular signature reminiscent of rodent beige fat (Lidell et al., 2013; Wu et al., 2012). Increasing WAT browning in rodents increases energy expenditure and suppresses diet-induced obesity and glucose intolerance (Seale et al., 2011). On the other hand, preventing WAT browning by deleting *Prdm16*, a transcriptional cofactor that increases UCP-1 expression, promotes obesity and severe insulin resistance (Cohen et al., 2014; Seale et al., 2011). Understanding the molecular processes governing WAT browning is highly significant, as this may identify novel approaches for increasing energy expenditure and combating obesity and the metabolic syndrome. Efforts to date have focused primarily on the role of factors that act directly on beige preadipocytes, such as irisin and FGF21 (Boström et al., 2012; Lee et al., 2014). However, there is mounting evidence that the central nervous system (CNS) control of WAT browning is also important (Plum et al., 2007; Ruan et al., 2014; Williams et al., 2014).

Leptin is produced by adipocytes and is critical for energy homeostasis and body weight control. Leptin receptors (LEPRs) are expressed in distinct regions of the brain, including the arcuate nucleus (ARC) of the hypothalamus (Myers et al.,

2008). The ARC contains two opposing neuronal populations: the appetite-suppressing proopiomelanocortin (POMC) and the orexigenic neuropeptide Y (NPY) and agouti-related peptide (AgRP)-neuropeptide-expressing neurons (Cowley et al., 2001; Elias et al., 1999). Leptin acts on POMC and NPY/AgRP neurons to suppress food intake and promote energy expenditure (Myers et al., 2008). One mechanism by which leptin increases energy expenditure is through the promotion of BAT thermogenesis. Leptin action in the hypothalamus increases sympathetic nerve activity (SNA) to BAT, increasing both UCP-1 expression and BAT activity (Commings et al., 2000; Morrison et al., 2014). Leptin signals via the LEPR to activate Janus-activated kinase (JAK)-2, which promotes signaling via effector cascades, including the phosphatidylinositol 3-kinase (PI3K)/AKT and signal transducer and activator of transcription (STAT)-3 pathways, to increase *Pomc* expression and inhibit *AgRP* expression (Myers et al., 2008). The principal role of the melanocortin system in body weight control is underscored by the marked obesity in humans and rodents with null mutations in the leptin, LEPR, or POMC genes (Coll et al., 2004).

Another peripheral factor affecting the melanocortin system is insulin (Varela and Horvath, 2012). Insulin is released from pancreatic β cells following a rise in blood glucose and acts via the insulin receptor (IR) tyrosine kinase and the PI3K/AKT pathway in liver, muscle, and fat to lower blood glucose levels (Saltiel and Kahn, 2001). Insulin also acts in the ARC on POMC and AgRP/NPY neurons to regulate whole-body glucose metabolism and elicit anorectic responses (Benoit et al., 2002; Brüning et al., 2000; Könnert et al., 2007). One prevailing view is that different POMC neurons exist and that leptin and insulin may act on distinct POMC neuronal subsets (Hill et al., 2010; Sohn et al., 2011; Williams et al., 2010).

The protein tyrosine phosphatases PTP1B (*PTPN1*) and TCPTP (*PTPN2*) regulate body weight and glucose homeostasis (Tiganis, 2013). PTP1B dephosphorylates JAK2 to suppress leptin signaling in hypothalamic neurons, including POMC neurons (Banno et al., 2010; Bence et al., 2006; Tiganis, 2013), whereas TCPTP dephosphorylates STAT3 in the hypothalamus (Loh et al., 2011). We have taken advantage of mice lacking PTP1B, TCPTP, or both phosphatases in POMC neurons to demonstrate that PTP1B and TCPTP selectively regulate leptin and insulin signaling to affect body weight, energy expenditure, and peripheral glucose homeostasis. We report that the combined inactivation of PTP1B and TCPTP and the promotion of leptin and insulin signaling in POMC neurons increases WAT browning and energy expenditure and prevents the development of diet-induced obesity. Our findings identify a mechanism in which POMC neurons integrate insulin and leptin feedback to drive WAT browning and maintain energy homeostasis.

RESULTS

Decreased Adiposity in POMC-TC Mice

Previous studies have established that PTP1B regulates leptin signaling in POMC neurons (Banno et al., 2010), but the precise

neuronal populations in which TCPTP exerts its effects remain unknown. Thus, we assessed TCPTP versus GFP expression in the hypothalamus of *Pomc*-GFP transgenic mice (Figures 1A and S1A available online). TCPTP protein was detected in $28.3\% \pm 5.9\%$ of all GFP-positive POMC neurons in the ARC with colocalization predominating in the central-caudal ARC (Figure 1B), where both LEPR- and IR-responsive POMC neurons have been detected (Williams et al., 2010). No TCPTP staining was detected in the rostral ARC (Figures 1B and S1B). TCPTP colocalization with GFP-expressing POMC neurons was confirmed by flow cytometry in papain-digested hypothalamus (Figure 1C). LEPR-responsive POMC neurons are also found in the nucleus of the solitary tract (NTS) in the hindbrain. Although TCPTP expression was evident in the NTS, the majority of TCPTP staining did not colocalize with GFP-expressing POMC neurons (Figure S1C).

Next, we examined the localization of PTP1B in POMC neurons in the ARC and its coincidence with TCPTP (Figures 1D–1F and S1A). PTP1B was detected in $74.8\% \pm 11.2\%$ of all GFP-positive POMC neurons in the ARC, with PTP1B/GFP colocalization predominating in the central-caudal ARC (Figure 1E). In contrast to TCPTP, PTP1B was also expressed in the rostral ARC (Figure S1B). Moreover, PTP1B expression in the central-caudal ARC was not restricted to medial POMC neurons, where it largely coincided with TCPTP (Figure 1F) but was also found in lateral POMC neurons, where TCPTP expression was not evident (Figures 1B, 1E, and 1F). Also, TCPTP, but not PTP1B, was expressed in a subset of medial-caudal POMC neurons (Figure 1F). Thus, TCPTP and PTP1B are found in both overlapping and distinct POMC neuronal subsets in the ARC.

To determine whether TCPTP might function in the melanocortin pathway, we crossed *Ptpn2*^{fl/fl} mice (Loh et al., 2011) with *Pomc*-Cre transgenic mice to excise *Ptpn2* (*Pomc*-Cre; *Ptpn2*^{fl/fl}; POMC-TC) in POMC-expressing neurons (Figures S1D and S1E). We compared these mice to PTP1B POMC neuronal cell-specific knockout mice (*Pomc*-Cre;*Ptpn1*^{fl/fl}; POMC-1B), generated as described previously (Banno et al., 2010). To visualize POMC cell-specific Cre-mediated recombination, we crossed POMC-TC mice to Z/EG reporter mice that express GFP after Cre-mediated recombination (Figure 1G). Z/EG;POMC-TC mice expressed GFP in the ARC and this overlapped with 92% of POMC-expressing cells (Figures 1G and 1H); no GFP staining was evident in non-POMC cells. As reported for POMC-1B mice (Banno et al., 2010), no differences were evident in the number of hypothalamic POMC neurons in POMC-TC mice (Figure 1I). POMC is expressed in the ARC, as well as the pituitary and the NTS in the hindbrain. In addition, ARC POMC neurons project to the lateral reticular nucleus in the brainstem. Consistent with this, the recombined *Ptpn2* allele ($\Delta Ptpn2$) in POMC-TC mice was evident in whole-brain, hypothalamic, pituitary, and hindbrain DNA extracts, but not in liver extracts (Figure S1D). As expected, differences in TCPTP protein were not observed in the hypothalamic extracts of POMC-TC versus control mice (Figure S1E) because POMC neurons constitute only a small proportion of the total hypothalamic cell population (Cowley et al., 2001).

Body weights were not altered in POMC-TC or POMC-1B versus floxed controls (Figures 2A, 2B, and S2A). Nevertheless,

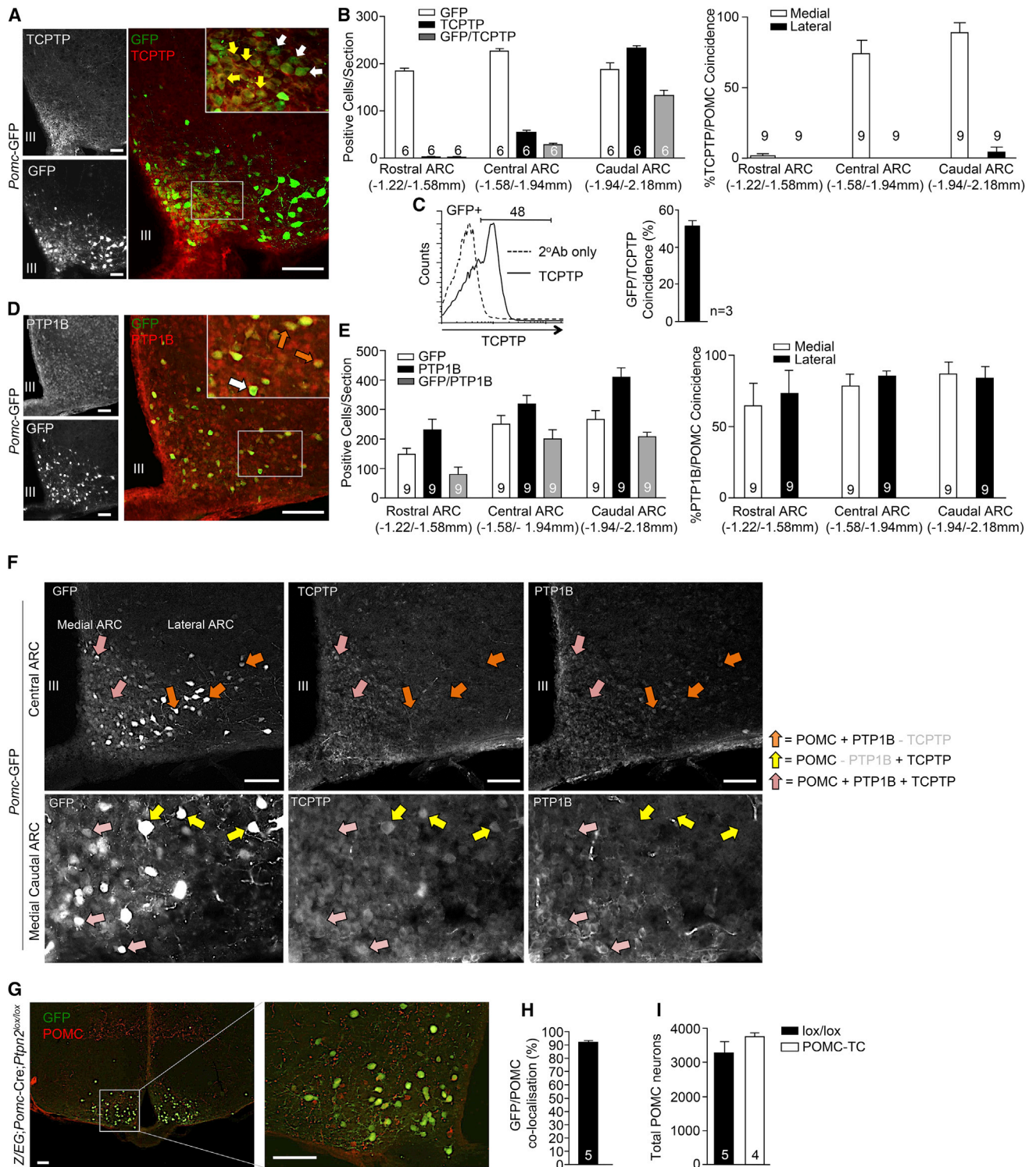


Figure 1. TCPTP and PTP1B in POMC Neurons

(A) Immunostaining for TCPTP in GFP-positive ARC POMC neurons.
 (B) Rostral-caudal immunostaining quantification of GFP- and TCPTP-expressing ARC cells.
 (C) Papain-digested hypothalami of *Pomc*-GFP mice were analyzed by flow cytometry for GFP and TCPTP.
 (D) Immunostaining for PTP1B in GFP-positive ARC POMC neurons.

(legend continued on next page)

epididymal and subcutaneous fat pad weights were decreased in POMC-TC mice and variably decreased in POMC-1B mice; only epididymal fat was significantly decreased in POMC-1B mice (Figures 2A and 2B). Dual-energy X-ray absorptiometry (DEXA) revealed that whole-body adiposity was significantly decreased in POMC-TC mice, but not in POMC-1B mice (Figures 2A and 2B). Neither bone mineral densities nor lean masses were altered (Figures 2A and 2B), and body lengths and liver weights were similar in both groups (Figures S2B and S2C). Previous studies have established that PTP1B deletion in the pituitary (*Cga-Cre;Ptpn1^{lox/lox}*) does not impact on body weight (Banno et al., 2010). Similarly, we found that TCPTP deletion in the pituitary (*Cga-Cre;Ptpn2^{lox/lox}*) did not result in overt differences in body weight or adiposity (Figures S2D–S2H). The differences in adiposity in POMC-TC and POMC-1B mice could not be ascribed to alterations in food intake, energy expenditure, or activity, and there were no differences in fuel utilization (assessed by respiratory exchange ratio, RER) in either group (Figures S2I and S2J). These findings are consistent with previous studies reporting that LEPR or IR deficiencies in POMC neurons do not alter food intake or RER (Balthasar et al., 2004; Berglund et al., 2012; Hill et al., 2010; Könnner et al., 2007).

PTP1B, but Not TCPTP, Regulates Leptin Sensitivity

The deletion of TCPTP or PTP1B in neural and glial cells by Cre-LoxP recombination using the *Nes-Cre* transgene enhances leptin sensitivity and protects mice from diet-induced obesity (DIO) (Loh et al., 2011). Accordingly, we assessed whether the decreased adiposity in chow-fed POMC-TC and POMC-1B mice might be ascribed to enhanced leptin sensitivity. POMC-TC, POMC-1B, or floxed control mice were administered leptin intraperitoneally (IP) for 3 days, and body weights and overnight food intake were recorded. Surprisingly, deletion of TCPTP in POMC neurons did not alter the leptin-mediated attenuation of food intake or decrease in body weight (Figures 2C and S2K), despite the fact that 86.5% ± 6.5% of LEPR-positive ARC POMC neurons express TCPTP (Figure S1E). In addition, plasma leptin levels (Figure 2D), leptin-induced STAT3 Y705 phosphorylation (p-STAT-3; Figures S2L and S2M), and leptin-induced hypothalamic *Pomc* expression (Figure 2G) were not altered by TCPTP deficiency, which is consistent with unaltered leptin sensitivity. As reported previously (Banno et al., 2010), PTP1B deficiency enhanced the leptin-mediated repression of body weight (Figure 2E) without overt changes in food intake (Figure S2K), reduced fed plasma leptin levels (Figure 2F), and significantly increased leptin-induced hypothalamic p-STAT-3 and *Pomc* expression (Figures 2G, S2N, and S2O); as expected, there were no differences in *Agrp* and *Npy* expression (Figure S2P). Thus, the reduced adiposity in POMC-TC mice is independent of changes in leptin sensitivity.

TCPTP, but Not PTP1B, Regulates Insulin Signaling

PTP1B and TCPTP dephosphorylate the IR and attenuate insulin signaling in the periphery (Tiganis, 2013). As the CNS effects of leptin and insulin overlap, and hypothalamic IR activation alters peripheral lipid and glucose metabolism (Marino et al., 2011; Plum et al., 2006), we monitored the effects of TCPTP versus PTP1B deficiency on hypothalamic insulin signaling. First, we determined whether PTP1B versus TCPTP deficiency in POMC neurons enhanced insulin-induced PI3K/AKT signaling in the ARC by monitoring AKT Ser-473 phosphorylation (p-AKT) by immunohistochemistry. TCPTP, but not PTP1B, deficiency enhanced p-AKT staining in the ARC in response to insulin (Figures 2H–2J). In keeping with the selective effects on p-AKT signaling, insulin-induced hypothalamic *Pomc* expression was significantly enhanced in POMC-TC, but not in POMC-1B mice (Figure 2K). To independently assess TCPTP's capacity to regulate insulin signaling in POMC neurons, we also took advantage of a highly specific TCPTP inhibitor, compound 8 (Zhang et al., 2009). This inhibitor is highly selective for TCPTP over PTP1B and intracerebroventricular (ICV) compound 8 administration enhances leptin signaling and sensitivity in wild-type mice, but not neuronal cell-specific TCPTP knockout mice (Loh et al., 2011). Compound 8 or aCSF (artificial cerebrospinal fluid) vehicle control were administered ICV into fasted C57BL/6 mice that were subsequently injected with insulin and hypothalami extracted for analysis by real-time PCR. Administration of compound 8 increased insulin-induced *Pomc* expression by ~2.5-fold (Figure 2L). Taken together, these results demonstrate that TCPTP attenuates insulin signaling in POMC neurons.

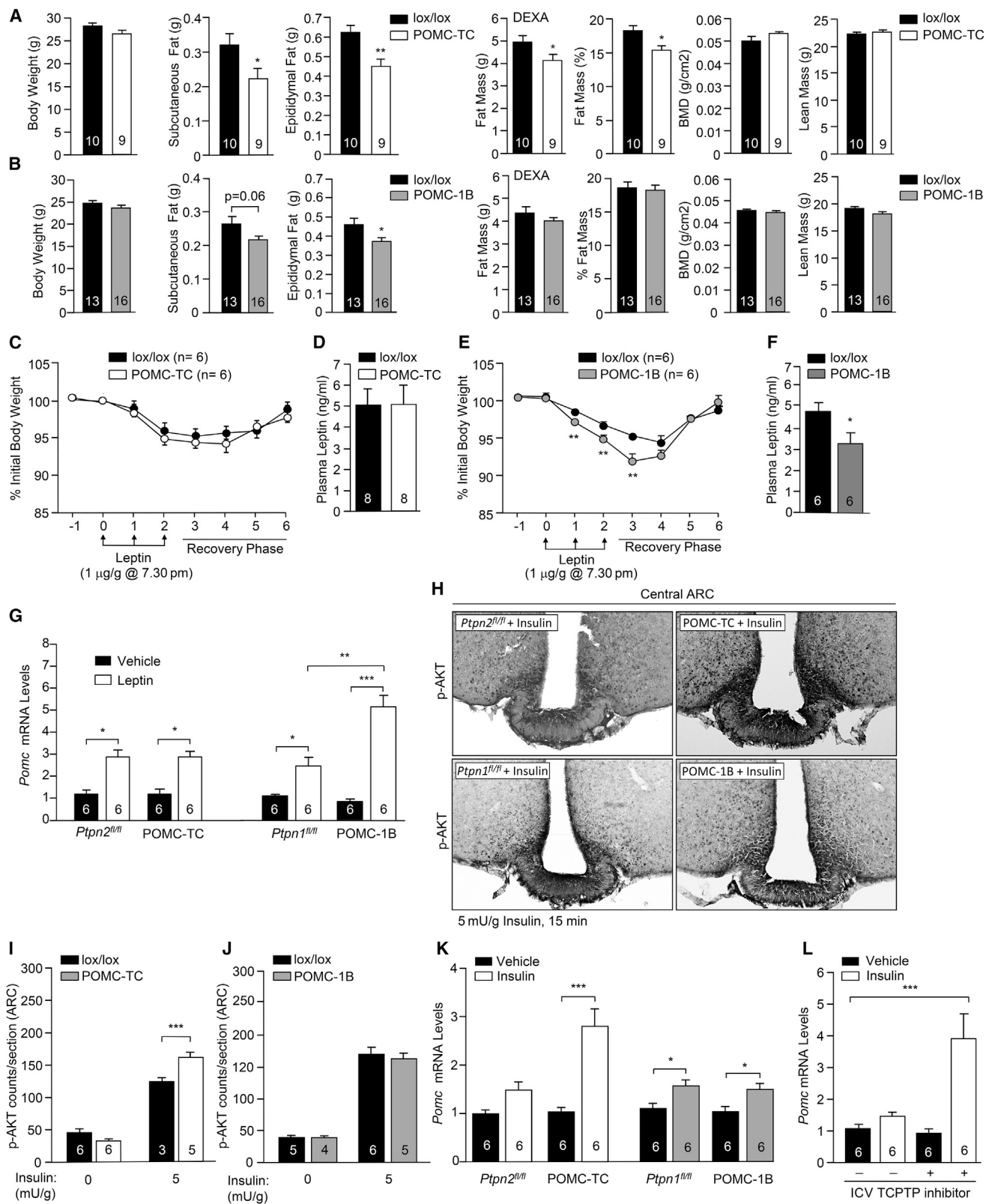
Decreased Adiposity and Increased Energy Expenditure in DKO Mice

Our results indicate that PTP1B and TCPTP differentially contribute to leptin and insulin signaling in POMC neurons. Hence, we generated POMC-TC and POMC-1B double-knockout (DKO) mice to examine whether the combined increase in IR and LEPR signaling in POMC neurons affects body weight and glucose metabolism. DKO mice had a modest reduction in body weight at 10 weeks of age, but body length, liver weight, lean mass, and bone density were unaltered (Figures 3A–3C). Differences in body weight could be explained by reduced whole-body adiposity (Figures 3B and 3C). The reduction in body weight and adiposity in DKO mice was accompanied by increased dark-phase energy expenditure without significant changes in ambulatory activity or RER or changes in food intake or feeding efficiency (Figure 3D). Furthermore, leptin sensitivity, as assessed by the effects of leptin on body weight (Figure 3E) or inferred by the reduced fed plasma leptin levels, was improved in DKO mice (Figure 3F). This was accompanied by increased leptin-induced hypothalamic *Pomc* expression in DKO mice (Figure 3G). Finally, insulin-induced

(E) Rostral-caudal immunostaining quantification of GFP- and PTP1B-expressing ARC cells.

(F) Immunostaining for PTP1B and TCPTP in GFP-positive POMC neurons in the ARC.

(G–I) (G) Immunostaining and (H and I) quantification of ARC GFP and POMC colocalization and the total number of ARC POMC neurons in *Z/EG*;POMC-TC mice. Representative images of three or more experiments are shown. Data are means ± SEM for the indicated number of mice (30 sections/mouse) or (C) experimental repeats.



(legend on next page)

hypothalamic *Pomc* expression was also increased in DKO mice (Figure 3H). These results are consistent with combined deficiencies in PTP1B and TCPTP promoting both central leptin and insulin signaling in POMC neurons to attenuate body weight/adiposity.

Increased BAT Thermogenesis and WAT Browning in DKO Mice

As the decreased adiposity and increased energy expenditure in chow-fed DKO mice could not be accounted for by changes in food intake or ambulatory activity, we examined whether DKO mice had elevated BAT thermogenesis and/or WAT browning. Although interscapular BAT mass was not altered (Figure S3A), *Ucp-1* gene expression was increased by more than 3-fold in DKO mice, which is consistent with increased BAT activity (Figure 4A); BAT *Ucp-1* expression was not altered in POMC-TC or POMC-1B mice (Figure 4A). Indeed, BAT thermogenesis, as assessed with sensors implanted below interscapular BAT, was increased during the light phase (when mice are less active) in DKO mice, but not in POMC-TC or in POMC-1B mice (Figure 4B). On the other hand, core temperature was not different from controls (Figure S3B), which is consistent with normal whole-body thermoregulation.

To determine whether WAT browning was also elevated in DKO mice, we measured *Ucp-1* gene expression in epididymal, inguinal, mesenteric, and infrarenal fat (Figure 4A). We found that *Ucp-1* expression was increased by 15- to 20-fold, specifically in inguinal WAT in DKO mice; inguinal *Ucp-1* expression was not altered in POMC-TC or POMC-1B mice (Figure 4A). Elevated *Ucp-1* mRNA in the inguinal fat of DKO mice was accompanied by increases in UCP-1 protein (Figures 4C and 4D). Inguinal fat in DKO mice had a distinct histological (hematoxylin and eosin [H&E] staining) morphology (Figure 4E), characterized by the presence of small adipocyte clusters with a multilocular lipid droplet morphology, a characteristic of brown fat (Rosen and Spiegelman, 2014). WAT browning in DKO mice also was accompanied by increased expression of *Prdm16* and *Cidea* (Figure 4F), which are found in brown and beige adipocytes, and *Tmem26* and *Cd137* (Figure 4F), which are specific to beige adipocytes (Wu et al., 2012). Previous studies have shown that cold-induced WAT browning is associated by increased angiogenesis (Xue et al., 2009). We found that angiogenesis, assessed with the angiogenesis marker CD34, was significantly elevated in inguinal WAT in DKO mice (Figures S3C and S3D). Together, these results demonstrate that the combined deletion of PTP1B and TCPTP in POMC neurons drives BAT thermogenesis and WAT browning.

SNA-Dependent WAT Browning Decreases Adiposity

To determine whether the increased WAT browning in DKO mice might be associated with SNA resulting from the combined deletion of PTP1B and TCPTP in POMC neurons, we assessed tyrosine hydroxylase (TH) expression in the inguinal fat of chow-fed DKO versus control mice. TH is the rate-limiting enzyme in catecholamine synthesis and is a marker of sympathetic innervation and was elevated in the inguinal fat of DKO mice (Figures S3E and S3F). Next, to determine whether the increased SNA was responsible for the WAT browning, we asked whether sympathetic denervation might attenuate WAT browning in DKO mice. To this end, we injected the neurotoxin 6-hydroxydopamine (6-OHDA) unilaterally into the inguinal fat area of 10 week-old DKO mice and monitored for changes in browning 2 weeks later. Unilateral sympathetic denervation dramatically reduced TH staining and attenuated WAT browning when compared with the contralateral fat pad, as assessed by gross morphology, the expression of browning genes (*Ucp-1*, *Prdm16*, *Cidea*) and histology/UCP-1 immunohistochemistry (Figures 5A–5C) without affecting BAT *Ucp-1* expression (Figure 5D). Indeed, sympathetic denervation reverted the increased inguinal WAT *Ucp-1* levels in DKO mice to levels comparable to floxed control mice (Figure 5E). These results indicate that WAT browning in DKO mice is dependent on SNA, rather than changes in metabolism or circulating factors associated with the decreased adiposity.

Next, we sought to determine the extent to which the increased SNA to inguinal fat and consequent browning may contribute to the increased energy expenditure and decreased adiposity in DKO mice. We first asked whether WAT browning and/or BAT activity might precede the decreased body weight/adiposity evident in DKO mice. Increased WAT browning was evident as early as 4 weeks of age, prior to any differences in body weight or adiposity (Figures 4C, 4E, 4F, and 4H). Moreover, the increased WAT browning in 4-week-old mice preceded changes in BAT activity, as assessed by the expression of *Ucp-1* (Figure 4G). To directly test that WAT browning decreased adiposity in DKO mice, we bilaterally denervated the inguinal fat pads of chow-fed DKO mice using 6-OHDA and measured the effect on adiposity and browning after 5 weeks. Strikingly, sympathetic denervation in DKO mice (assessed by TH staining; Figure S3G) resulted in increased weight gain and adiposity (Figures 5F, 5G, and S4A). Importantly, the increased adiposity in denervated DKO mice was accompanied by decreased WAT browning and a reduction in energy expenditure (Figures 5H and 5I), without alterations in RER or ambulatory activity (Figure S4B). Moreover, the increased weight gain occurred despite BAT

Figure 2. TCPTP and PTP1B Regulate Insulin and Leptin Signaling

(A and B) Body and WAT weights and body composition in 10-week-old POMC-TC, POMC-1B, and lox/lox mice.

(C and E) POMC-TC, POMC-1B, and lox/lox mice were administered leptin, and body weights were monitored.

(D and F) Fed plasma leptin levels in 8-week-old mice.

(G) Hypothalamic *Pomc* gene expression in mice injected IP saline or leptin (1 μ g/g, 2 hr).

(H–J) p-AKT immunostaining in mice injected IP saline or insulin (5 mU/g, 15 min).

(K) Hypothalamic *Pomc* gene expression in mice injected IP saline or insulin (0.85 mU/g, 2 hr).

(L) Hypothalamic *Pomc* gene expression in C57BL/6 mice administered saline or insulin (0.85 mU/g, IP, 2 hr), followed by aCSF or TCPTP inhibitor (1.5 μ l 0.2 nmol compound 8, ICV). Results are means \pm SEM and are representative of three independent experiments; significance was determined using (C, E, G–L) two-way ANOVA.

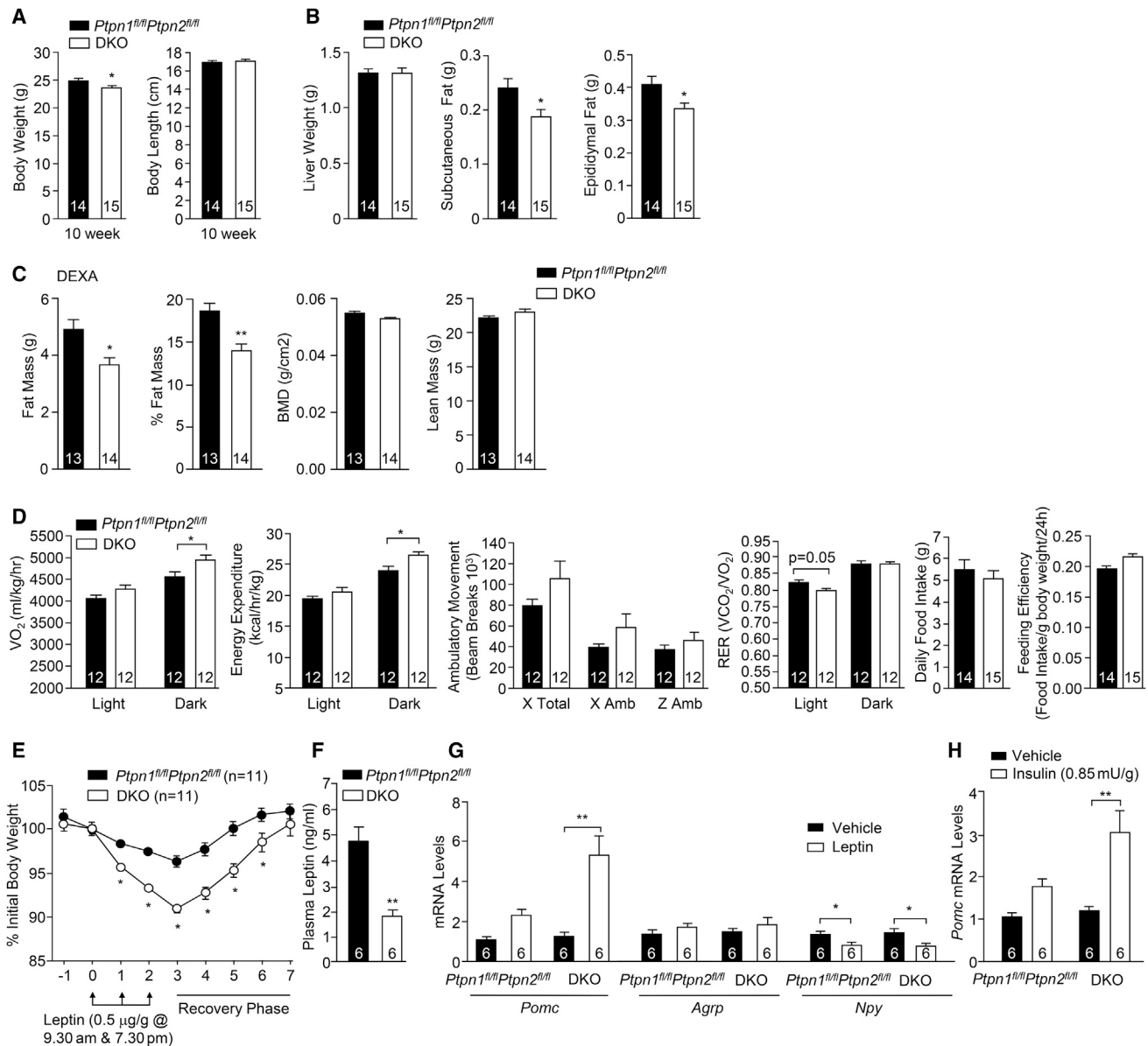


Figure 3. Decreased Adiposity and Increased Energy Expenditure in DKO Mice

(A–D) (A) Body weight and body length; (B) tissue weights; (C) body composition; and (D) oxygen consumption, energy expenditure, ambulatory activity, RER, daily food intake, and feeding efficiency in 8- to 10-week-old DKO and *Ptpn1^{fl/fl}Ptpn2^{fl/fl}* mice.

(E) Mice were administered leptin and body weights recorded.

(F) Fed plasma leptin levels in 8-week-old mice.

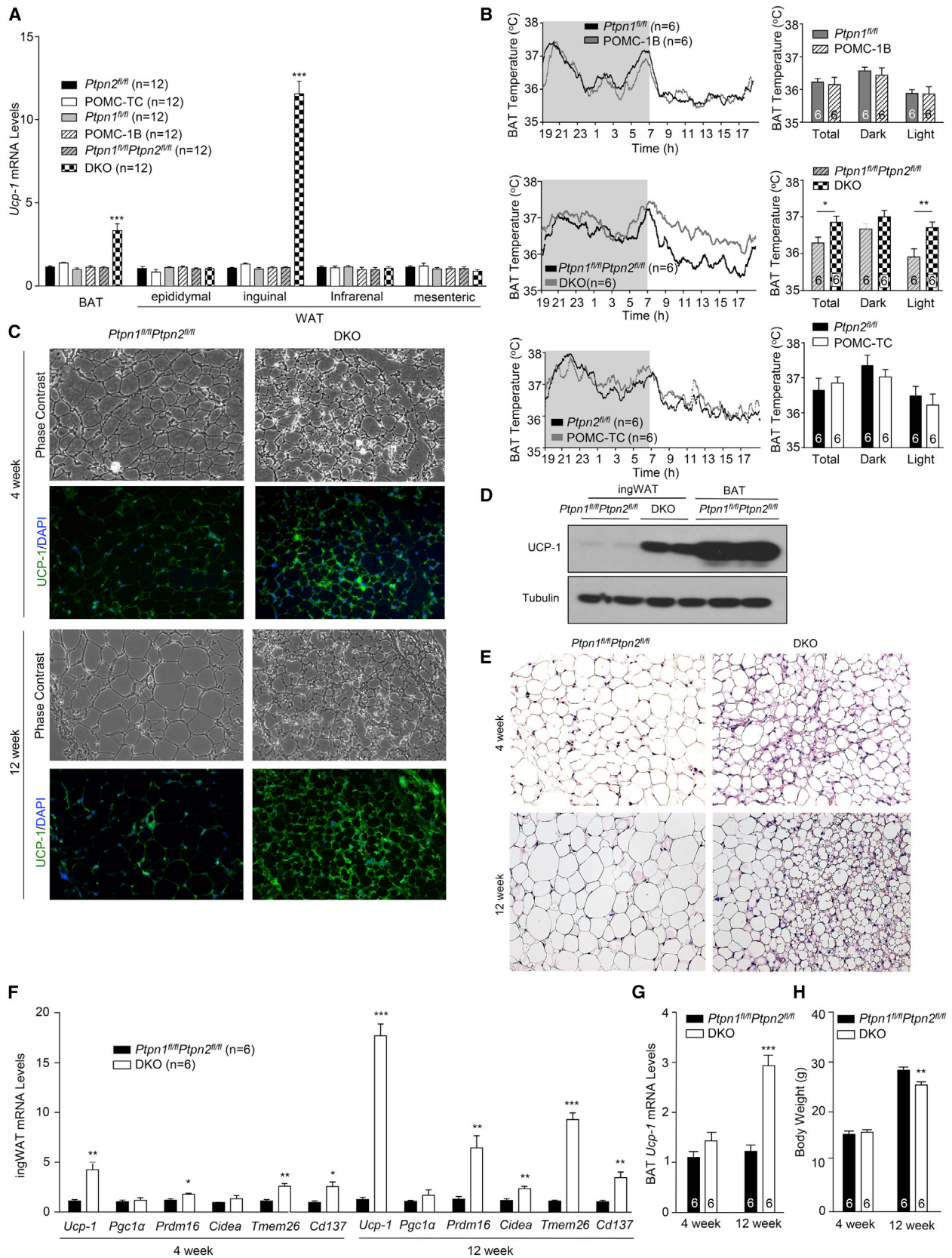
(G and H) Hypothalamic gene expression in fasted mice injected with IP saline, (G) leptin (1 μg/g), or (H) insulin. Results are means ± SEM and are representative of at least two independent experiments; significance was determined (D, E, G, and H) using two-way ANOVA.

activity remaining elevated in DKO mice (Figure 5H). Taken together, these results causally link the increased energy expenditure and decreased adiposity in DKO mice to the elevated WAT browning.

DKO Mice Are Resistant to DIO

To assess the impact of combined PTP1B and TCPTP deficiencies in POMC neurons and increased WAT browning on

DIO, we administered a high-fat diet to POMC-TC, POMC-1B, or DKO mice for 12 weeks and monitored the effects on body weight and glucose metabolism (Figures 6, S5, S6, and S7). DKO mice exhibited a significant reduction in weight gain and a marked reduction in adiposity (Figures 6A–6C and S7A). By contrast, no differences were observed in body weight, adiposity, or energy expenditure in POMC-1B or POMC-TC mice (Figures S5A–S5D and S6A–S6D). The decreased weight



(legend on next page)

gain in DKO mice was not associated with any difference in body length, lean mass, or bone density (Figures 6C and 6D), but liver weights were significantly reduced and accompanied by a marked reduction in steatosis (Figure 6E). The decreased adiposity in high-fat-fed (HFF) DKO mice was accompanied by unaltered food intake, but feeding efficiency was increased (Figure 6F), which is consistent with improved energy utilization. Moreover, HFF DKO mice exhibited increased oxygen consumption and energy expenditure, increased ambulatory activity, and increased dark-phase RER (Figure 6F). In keeping with the resistance to DIO, DKO mice had significantly greater leptin sensitivity (Figure 6G). Moreover, DKO mice exhibited a significant reduction in fasted blood glucose levels and a trend for reduced fasted insulin levels and had improved insulin and glucose tolerances (Figures 6H–6J, S7B, and S7C), consistent with overall improved glucose homeostasis. By contrast, HFF POMC-TC and POMC-1B single-mutant mice did not exhibit any differences in glucose homeostasis and leptin sensitivity (Figures S5E–S5I and S6E–S6I). These results demonstrate that the combined deletion of PTP1B and TCPTP in POMC neurons prevents the development of DIO and the associated insulin resistance, glucose intolerance, and hepatosteatosis.

The decreased adiposity in HFF DKO mice was accompanied by elevated BAT *Ucp-1* expression and increased inguinal WAT browning (Figures 6K–6M). To determine the extent to which the increased WAT browning in DKO mice prevented DIO, we bilaterally denervated (6-OHDA) the inguinal fat of DKO mice that had been HFF for 3 weeks and measured effects on adiposity, energy expenditure, and glucose homeostasis after a further 5 weeks of high-fat feeding (Figures 6N, 6O, and S7D–S7J). Bilaterally denervating inguinal fat in HFF DKO mice increased weight gain and adiposity (Figures 6N, S7D, and S7E). The increased weight gain was associated with decreased energy expenditure and RER but no alterations in ambulatory activity or food intake (Figures 6O and S7F). Moreover, the increased weight gain in the denervated HFF DKO mice was accompanied by elevated fasted blood glucose levels, glucose intolerance, insulin resistance, and hepatosteatosis (Figures S7G–S7J). These results demonstrate that the resistance to DIO in HFF DKO mice can be attributed at least in part to increased WAT browning.

Insulin and Leptin Promote WAT Browning in DKO Mice

Our studies indicate that mice lacking PTP1B or TCPTP in POMC neurons exhibit enhanced leptin or insulin signaling, respectively, and that their combined deficiency increases WAT browning and energy expenditure to decrease adiposity. Although these results are consistent with enhanced insulin and leptin signaling driving WAT browning, they do not exclude the contribution of other pathways. Moreover, they do not exclude the possibility that the combined PTP1B and TCPTP deficiency

may lead to synergistic effects on leptin-induced JAK2 activation and STAT-3 signaling, so that leptin signaling alone promotes WAT browning. To test this, we administered POMC-1B (leptin hypersensitive) or POMC-TC (insulin hypersensitive) mice either vehicle or leptin and assessed the effects on body weight, WAT browning, and BAT activity (Figures 7A and 7B). We reasoned that, if both leptin and insulin signaling are required in POMC neurons for WAT browning, then WAT browning would be greatest in the leptin-treated POMC-TC mice, as POMC-TC mice are insulin hypersensitive. On the other hand, if the exacerbation of leptin signaling by combined PTP1B and TCPTP deficiencies would be sufficient to drive browning, then this would be greatest in POMC-1B mice that are leptin hypersensitive. POMC-TC, POMC-1B, or floxed control mice were administered leptin on a daily basis for 6 days, and body weights, WAT browning, and BAT *Ucp-1* expression were assessed. POMC-1B mice exhibited the greatest decrease in body weight in response to leptin (Figure 7A). Consistent with the previously established potential for leptin to drive BAT thermogenesis, BAT *Ucp-1* was elevated in leptin-treated control mice (as compared to vehicle administered C57BL/6 mice), but this was not increased further by PTP1B or TCPTP deficiency (Figure 7B). Leptin administration also modestly increased inguinal WAT browning (Figure 7B). However, browning was greatest for leptin-treated POMC-TC mice (Figures 7B, 7C, S4C, and S4D). Thus, the enhanced insulin and leptin signaling in POMC neurons may underlie the WAT browning and consequently increased energy expenditure and decreased adiposity in DKO mice.

Insulin and Leptin Act on ARC Neurons to Drive WAT Browning

To directly assess the capacity of insulin and leptin to act synergistically in the CNS to control WAT browning, we subcutaneously implanted osmotic minipumps to ICV administer either vehicle, leptin, insulin, or leptin plus insulin into the lateral ventricle over 6 days and monitored body weight, energy expenditure, BAT activity, and WAT browning (Figures 7D–7G and S4E–S4H). We found that insulin infusion alone had no effect on food intake or body weight (Figures 7D and S4F). This is in keeping with previous studies demonstrating that the chronic ICV administration of insulin does not alter food intake or overall body weight (Koch et al., 2008). As expected, leptin decreased body weight and adiposity, and notably, this was exacerbated by the coinfusion of insulin (Figure 7D). Coinfusion of leptin and insulin did not further reduce food intake compared to leptin-only infusion (Figure S4F). To assess whether the synergistic effects of insulin and leptin on body weight may result from SNA-dependent WAT browning and/or BAT thermogenesis, we measured the expression of thermogenic genes in BAT and inguinal fat. We found (1) that BAT *Ucp-1* expression increased

Figure 4. Increased Browning in DKO Mice

(A) *Ucp-1* gene expression in BAT and WAT depots from 12-week-old POMC-1B, POMC-TC, DKO, and floxed control mice.

(B) Interscapular BAT temperature.

(C–E) Histology (H&E), immunoblotting and immunohistochemistry of inguinal WAT (ingWAT).

(F and G) IngWAT or BAT gene expression.

(H) Body weights in 4- and 12-week-old mice. Data are means \pm SEM and are representative of three independent experiments; significance was determined using (A) one-way or (F, G, and H) two-way ANOVA.

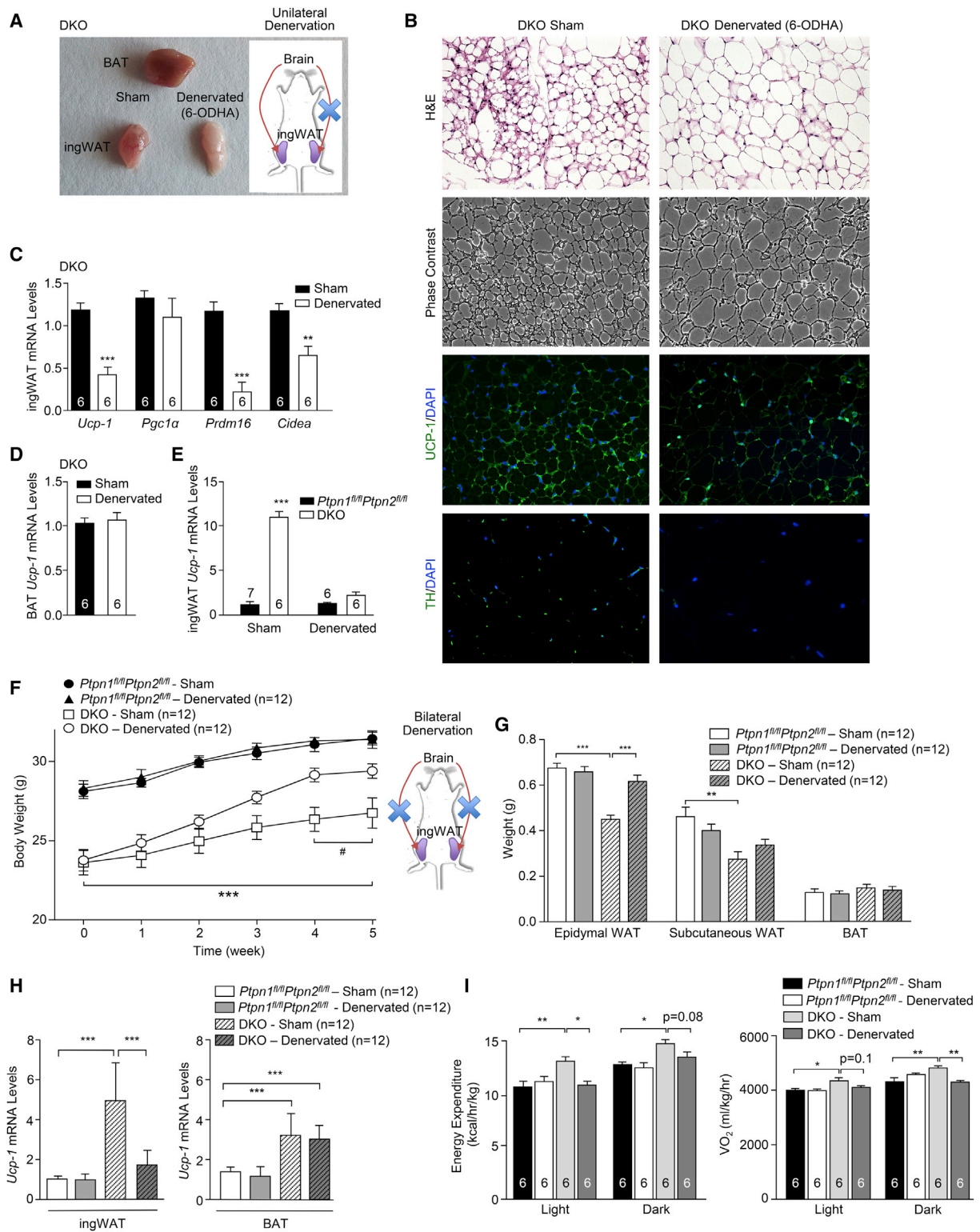


Figure 5. Denervation of DKO Inguinal WAT and Increases Body Weight

(A–D) IngWAT in 10-week-old DKO mice was unilaterally denervated (6-ODHA) and BAT and ingWAT extracted 2 weeks later for analysis. (A) Gross morphology, (B) histology/immunohistochemistry, and (C and D) gene expression; sham vehicle-administered contralateral inguinal fat pads were used as controls. (E) Contralateral sham versus denervated (6-ODHA) ingWAT from DKO versus *Ptpn1^{fl/fl}Ptpn2^{fl/fl}* mice analyzed for *Ucp-1* expression.

(legend continued on next page)

similarly in response to all treatments, but not by insulin alone (Figure 7E) and (2) that leptin, but not insulin treatment alone, resulted in a modest increase in the expression of browning genes in inguinal fat (Figure 7E). In keeping with this, leptin alone modestly increased TH and UCP-1 in inguinal fat and increased whole-body energy expenditure (Figures 7F, 7G, and S4H). However, the coinfusion of leptin and insulin resulted in a marked increase in TH staining and WAT browning (Figures 7E, 7F, S4E, S4G, and S4H). Moreover, the coinfusion of leptin plus insulin resulted in a greater increase in energy expenditure than the infusion of leptin alone (Figure 7G), which is consistent with the difference in energy expenditure being attributable to increased WAT browning.

To determine the extent to which the leptin plus insulin-induced increase in energy expenditure and weight loss may be reliant on SNA-dependent WAT browning, we bilaterally denervated (6-OHDA) the inguinal fat pads of mice that were ICV infused with leptin plus insulin. We found that the increased WAT browning (*Ucp-1* expression) and energy expenditure and decreased body weight resulting from the coinfusion of leptin and insulin were significantly attenuated by the bilateral denervation of inguinal fat (Figures 7H–7J). However, the denervation did not completely prevent the increase in energy expenditure and decrease in body weight, probably because of the sustained leptin-induced activation of BAT and the suppression of food intake (Figures 7E, 7H, and 7J).

Next, we assessed whether the effects of the ICV-administered insulin and leptin on WAT browning may be mediated via neurons in the ARC. Moreover, because both insulin and leptin can signal via PI3K to depolarize and activate POMC neurons (Cowley et al., 2001; Hill et al., 2008; Qiu et al., 2010, 2014; Rahmouni et al., 2004), we determined whether the pharmacological inhibition of PI3K could suppress WAT browning. Minipumps and intra-ARC indwelling bilateral cannulas were used to infuse vehicle, leptin plus insulin or leptin, or insulin plus the PI3K inhibitor LY294002 directly into the ARC over 6 days, and effects on body weight and WAT browning were monitored (Figures 7K–7M and S4I). The infusion of leptin/insulin directly into the ARC decreased body weight and food intake and promoted WAT browning, and these effects were attenuated by LY294002 (Figures 7K–7M and S4I). Taken together, these results demonstrate that insulin and leptin act synergistically on cells in the ARC, at least in part via PI3K, to increase WAT browning and consequent energy expenditure to decrease body weight.

ARC POMC Neurons Promote WAT Browning

We next sought to understand how leptin and insulin elicit synergistic effects on ARC cells to promote WAT browning. Previous studies have provided evidence for the existence of distinct ARC POMC neurons that are differentially responsive to insulin and leptin (Hill et al., 2010; Williams et al., 2010). To determine whether insulin and leptin may promote browning by stimulating

different POMC neurons, we administered mice insulin, leptin, or insulin plus leptin intraperitoneally and monitored for hypothalamic STAT3 Y705 or AKT Ser-473 phosphorylation by immunohistochemistry (Figures S4J–S4L). Leptin stimulation resulted in p-AKT and p-STAT-3 staining in both the ARC and DMH, whereas insulin increased p-AKT largely in the ARC (Figure S4J). Strikingly, insulin plus leptin stimulation resulted in p-AKT staining in ARC neurons that were devoid of p-STAT-3 (Figures S4J and S4K). At least a subset of the cells staining for p-AKT only also stained for POMC-derived α -MSH (Figure S4L). Thus, insulin and leptin can stimulate distinct neurons in the ARC. These results are consistent with the insulin plus leptin-mediated promotion of WAT browning resulting from the increased engagement of POMC neurons.

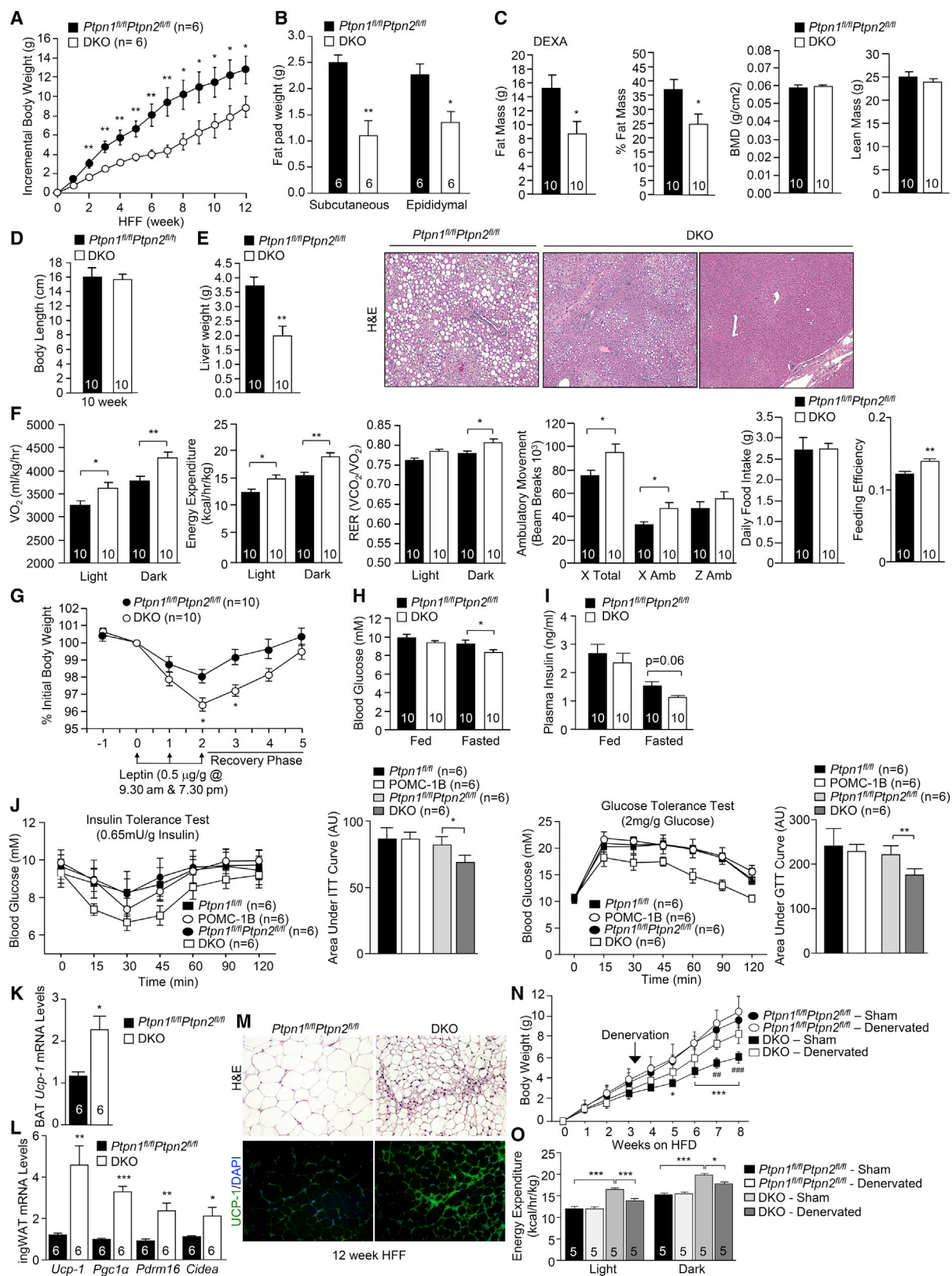
To assess whether the leptin/insulin synergy reflects the increased recruitment of POMC neurons to the melanocortin response, we sought to nonselectively activate ARC POMC neurons with the stimulatory hM3Dq DREADD (designer receptors exclusively activated by designer drugs) that is activated by clozapine-N-oxide (CNO) (Krashes et al., 2011). rAAV-hM3Dq-mCherry (capable of expressing hM3Dq-mCherry in a Cre-dependent manner) was administered into the ARC of 10-week-old *Pomc*-Cre mice that were subsequently unilaterally denervated (inguinal fat pads) with 6-OHDA. Mice were then administered vehicle or CNO to depolarize POMC neurons, and body weights and food intake were measured, and WAT browning was assessed after 14 days. CNO decreased food intake and body weight, which is consistent with POMC neuronal activation (data not shown). Postmortem analysis confirmed ARC targeting and mCherry expression in $73.1\% \pm 20.7\%$ of POMC neurons (Figures S4M and S4N). CNO administration resulted in a marked increase in WAT browning in the sham-operated contralateral inguinal fat pads, but not in the 6-OHDA denervated inguinal fat pads (Figures 7N–7P). These results demonstrate that the nonselective activation of ARC POMC neurons promotes the SNA-dependent browning of inguinal WAT. This is consistent with the synergistic actions of insulin and leptin on WAT browning, reflecting the increased engagement and activation of POMC neurons.

DISCUSSION

Our studies demonstrate that leptin and insulin act synergistically on hypothalamic POMC neurons to promote WAT browning and energy expenditure to decrease adiposity. We suggest that the engagement of insulin- and leptin-responsive POMC neurons might allow for a graded melanocortin response to regulate fat stores. Leptin would elicit immediate effects on food intake, ambulatory activity, and energy expenditure by promoting BAT activity, whereas leptin and heightened postprandial insulin would act synergistically over the longer term and engage a greater proportion of POMC neurons to promote overt WAT

(F–H) 8-week-old *Ptpr1^{fl/fl}Ptpr2^{fl/fl}* and DKO mice were sham operated or bilaterally denervated; (F) body weights and (G) WAT and BAT weights were assessed; and (H) ingWAT and BAT *Ucp-1* expression was measured.

(I) Energy expenditure and oxygen consumption in 24-week-old *Ptpr1^{fl/fl}Ptpr2^{fl/fl}* and DKO mice 5 weeks after sham or bilateral ingWAT denervations. Data are means \pm SEM and are representative of three independent experiments; significance was determined using (E and F) two-way or (G–I) one-way ANOVA. (F) * DKO v/s *Ptpr1^{fl/fl}Ptpr2^{fl/fl}*; #, denervated DKO versus sham-operated DKO.



(legend on next page)

browning and increase energy expenditure to limit weight gain. This may be a major factor contributing to the “diet-induced thermogenesis” model of body weight control, as first described by Rothwell and Stock in 1979, whose studies involved BAT cellular expansion and differentiation in rodents eating a cafeteria diet (Rothwell and Stock, 1979).

We found that TCPTP was expressed in 30%–40% and PTP1B was expressed in 70% of ARC POMC neurons and that the two phosphatases differentially contributed to leptin and insulin signaling. Previous studies have established that both phosphatases can attenuate leptin and insulin signaling in varied cell types and tissues (Tiganis, 2013). Indeed, PTP1B attenuates insulin signaling in SF-1 neurons in the VMH (Chiappini et al., 2014), whereas neuronal TCPTP deficiency promotes hypothalamic leptin signaling in vivo (Loh et al., 2011). In this study, we found that PTP1B deficiency enhanced leptin, but not insulin signaling, and TCPTP-deficiency enhanced insulin, but not leptin signaling in POMC neurons. To some degree, the differential contributions of the phosphatases may be due to their segregation in distinct POMC neurons. Such segregation is in keeping with the existence of distinct subsets of POMC neurons in the ARC (Hill et al., 2010; Sohn et al., 2011; Williams et al., 2010). However, despite a significant degree of segregation, PTP1B and TCPTP were coexpressed in medial POMC neurons in the central-caudal ARC, and TCPTP was expressed in the majority of LEPR-expressing POMC neurons. Therefore, the impact of PTP1B versus TCPTP deficiency on leptin versus insulin signaling and that of their combined deficiencies on WAT browning and energy expenditure may also be partly ascribed to functional redundancies.

Irrespective of the roles of PTP1B and TCPTP, our findings demonstrate that both insulin and leptin are required for optimal CNS-mediated WAT browning. First, leptin administration modestly increased browning in floxed control and leptin hyper-responsive POMC-1B mice, but overt WAT browning was only evident in insulin hyperresponsive POMC-TC mice. Second, leptin or insulin ICV infusion alone had little effect on browning, whereas the coinfusion of insulin and leptin strikingly enhanced browning. By contrast, BAT activity was enhanced by 2- to 3-fold in response to leptin, but not insulin, and was not enhanced further by the coinfusion of leptin and insulin. Previous studies have implicated ARC/POMC neurons and/or leptin-induced PI3K signaling in BAT thermogenesis and WAT browning (Commins et al., 2000; Plum et al., 2007; Williams et al., 2014). However, our studies provide direct evidence for POMC neuronal activation promoting SNA-dependent WAT browning and demonstrate that insulin and leptin can act synergistically

on POMC neurons to promote browning that far exceeds that achieved with leptin alone. Moreover, our studies provide evidence for the differential central control of BAT activity versus WAT browning and thus ascribe distinct physiological functions to these thermogenic tissues.

The importance of beige adipocytes to body weight control is underscored by studies overexpressing or deleting the brown adipose tissue determination factor *Prdm16* in fat (Cohen et al., 2014; Seale et al., 2011). Consistent with the importance of WAT browning for thermogenesis and energy expenditure, beige adipocytes can increase their energy uptake similar to BAT in the context of cold or β_3 -adenergetic stimulation (Bartelt et al., 2011). Also, the thermogenic capacity of mitochondria from the inguinal fat of cold-acclimated mice is one third of that of interscapular BAT (Shabalina et al., 2013). Our studies highlight the capacity of CNS-mediated WAT browning to regulate body weight and adiposity independently of BAT thermogenesis.

In humans, low brown and brown-like fat activity correlates with aging, obesity and diminishing metabolic health (Ouellet et al., 2011), but whether such decreases are causal or consequential and the basis for the decline remain unclear. Our results suggest that the diminishing brown-like fat may occur as a consequence of ARC cellular insulin and leptin resistance. Indeed, elevated hypothalamic PTP1B and TCPTP exacerbate cellular leptin resistance and DIO in mice (Loh et al., 2011). However, it remains to be established whether PTP1B and TCPTP are elevated in POMC neurons and whether this, along with other factors that promote cellular leptin/insulin resistance, such as SOCS3 (Mori et al., 2004), contribute to the diminished brown-like fat in obesity.

In summary, our findings define the complementary roles of TCPTP and PTP1B in central insulin and leptin signaling in POMC neurons and the synergistic central actions of insulin and leptin in the promotion of WAT browning. Our results suggest that browning may be the outcome of an integrated melanocortin response to peripheral factors that convey the status of both current (as conveyed by leptin) and anticipated energy reserves (as conveyed by increases in insulin) and highlight the potential for CNS-mediated WAT browning to regulate adiposity and combat obesity.

EXPERIMENTAL PROCEDURES

Mice

We maintained mice on a 12 hr light-dark cycle in a temperature-controlled high barrier facility with free access to food and water. Mice were fed a standard chow (4.6% fat) or a high-fat diet (23% fat; 45% of total energy

Figure 6. DKO Mice Are Resistant to DIO

(A–F) 8-week-old *Ptpn1^{fl/fl}Ptpn2^{fl/fl}* and DKO mice were HFF for 12 weeks, and (A) incremental body weight, (B) fat pad weight, (C) body composition, (D) body length, (E) liver weight and histology, (F) oxygen consumption, energy expenditure, ambulatory activity, RER, food intake, and feeding efficiency were assessed. (G–I) 12 week HFF mice were administered leptin, and body weights were monitored. Fed and fasted (H) blood glucose and (I) plasma insulin levels in 12 week HFF mice.

(J) Insulin and glucose tolerance tests in 12 week HFF mice.

(K–M) (K and L) BAT or ingWAT gene expression, (M) ingWAT histology, and immunohistochemistry from 12 week HFF mice.

(N and O) *Ptpn1^{fl/fl}Ptpn2^{fl/fl}* and DKO mice were HFF and either sham operated or bilaterally denervated after 3 weeks; high-fat feeding was continued for 5 weeks; and (N) incremental body weights and (O) energy expenditure were measured. Results are means \pm SEM for the indicated number of mice and are representative of three independent experiments; significance was determined using (A, B, F, G, I, J, N, and O) two-way ANOVA. (N) Asterisk (*) indicates floxed v/s DKO sham operated; pound (#), DKO sham versus DKO denervated.

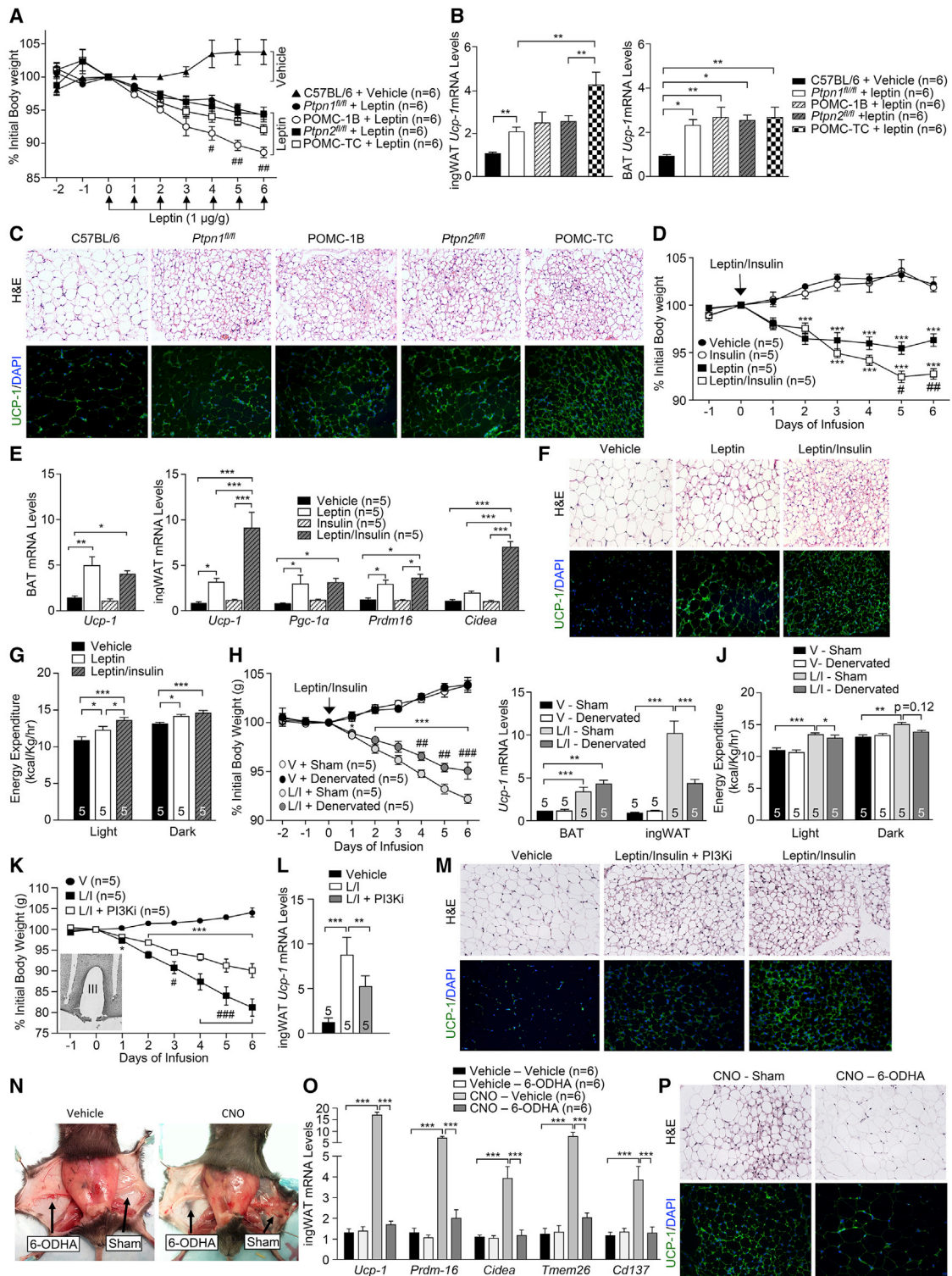


Figure 7. Leptin and Insulin Induce WAT Browning

(A–C) 8-week-old mice were administered leptin IP; (A) daily body weights were recorded; (B and C) ingWAT and BAT were extracted for (B) analysis of *Ucp-1* gene expression, (C) histology, and immunohistochemistry; C57BL/6 mice were administered vehicle as a control.

(D–G) 8-week-old C57BL/6 mice were ICV infused with vehicle, insulin (3 mU/day), leptin (4.8 µg/day), or insulin plus leptin, and (D) body weights monitored.

(E and F) BAT and ingWAT were extracted for (E) gene expression analyses, (F) histology, and immunohistochemistry, and (G) energy expenditure was assessed.

(legend continued on next page)

from fat; SF04-027; Specialty Feeds) as indicated. Experiments were approved by the Monash University School of Biomedical Sciences Animal Ethics Committee.

Immunohistochemistry

Immunohistochemistry to monitor for p-STAT3 and p-AKT in hypothalamic neurons was performed as described previously (Loh et al., 2011), and staining for TCPTP, PTP1B, eGFP, and POMC was performed as described in the [Extended Experimental Procedures](#). For inguinal WAT immunohistochemistry, tissue was formalin-fixed and processed for UCP-1, CD34, or TH immunoreactivity as described in the [Extended Experimental Procedures](#).

Metabolic Measurements

Insulin and glucose tolerance tests, leptin sensitivity, blood glucose, and plasma insulin measurements were performed as described previously (Loh et al., 2009). Activity, food intake, and energy expenditure were assessed using a Comprehensive Lab Animal Monitoring System (Columbus Instruments), and body composition was assessed by DEXA (Lunar PIXImus2; GE Healthcare).

Real-Time PCR

RNA was extracted using TRIzol reagent (Sigma), reverse transcribed, and processed for quantitative ($\Delta\Delta C_t$) real-time PCR using either TaqMan Gene Expression Assays (Applied Biosystems) or SsoAdvanced Universal SYBR Green Supermix (BioRad) as described in the [Extended Experimental Procedures](#).

BAT and Core Temperature Measurements

BAT and core temperatures and locomotor activity were measured as described previously (Enriori et al., 2011). E-Mitters (Mini Mitter Company) were implanted beneath the BAT pad between the scapulae or into the peritoneal cavity.

Sympathetic Denervation

Mice received 20 microinjections of vehicle or 6-hydroxydopamine [6-OHDA (Sigma); 1 μ l per injection, 9 mg/ml in 0.15 M NaCl containing 1% (w/v) ascorbic acid] as described previously (Chao et al., 2011) throughout the right or both inguinal fat pads.

Intracerebroventricular and Intra-ARC Infusions

For intracerebroventricular infusions, 8-week-old C57BL/6 mice were implanted with a sterile osmotic pump connector cannula (Alzet Brain Infusion Kit 3, DURECT Corp) as described in the [Extended Experimental Procedures](#). For intra-ARC infusions, mice were implanted with a bilateral cannula (Plastics One) 1.4 mm caudal of bregma, extending 5.7 mm below dura, connected to a minipump (Alzet model 1002, DURECT Corp) via PEG tubing and a Y connector. Mice received 6 day infusions of vehicle, leptin (4.8 μ g/day, Peprotech), human insulin (3 mU/day, Sigma), or leptin plus insulin. Body weights and food intake were monitored, and tissues were extracted.

DREADD

10- to 12-week-old *Pomc*-Cre mice were stereotactically injected with rAAV-hSyn-DIO-hM3D(Gq)-mCherry bilaterally into the ARC (coordinates, bregma:

anterior-posterior, -1.40 mm; dorsal-ventral, -5.80 mm; lateral, ± 0.30 mm, 200 nl/side) as described previously (Krashes et al., 2011). Two weeks after rAAV delivery, mice were unilaterally denervated with 6-OHDA. One week postdenervation, mice received daily injections of vehicle or CNO (1.5 mg/kg, IP, Sigma) for 14 days. Body weights and food intake were recorded. Mice were anaesthetized, tissues were extracted, and mice were perfused with paraformaldehyde for immunohistochemical assessment.

Statistical Analysis

Unless otherwise indicated, statistical significance was determined by a two-tailed paired Student's *t* test. *p* values < 0.05 were considered significant; * or # *p* < 0.05 , ** or ## *p* < 0.01 , and *** or ### *p* < 0.001 .

SUPPLEMENTAL INFORMATION

Supplemental Information includes Extended Experimental Procedures and seven figures and can be found with this article online at <http://dx.doi.org/10.1016/j.cell.2014.12.022>.

ACKNOWLEDGMENTS

This work was supported by the NHMRC of Australia (to T.T., Z.B.A., and M.A.C.); the NIH to B.G.N. (R37-CA49152), Z.-Y.Z. (R01-CA69202), K.K.B. (R01-DK082417), and B.B.K. (R01-DK98002); and funds from the Ontario Ministry of Health and Long Term Care and the Princess Margaret Cancer Foundation (B.G.N.).

Received: May 29, 2014

Revised: October 14, 2014

Accepted: December 10, 2014

Published: January 15, 2015

REFERENCES

- Balthasar, N., Coppari, R., McMinn, J., Liu, S.M., Lee, C.E., Tang, V., Kenny, C.D., McGovern, R.A., Chua, S.C., Jr., Elmquist, J.K., and Lowell, B.B. (2004). Leptin receptor signaling in POMC neurons is required for normal body weight homeostasis. *Neuron* 42, 983–991.
- Banno, R., Zimmer, D., De Jonghe, B.C., Atienza, M., Rak, K., Yang, W., and Bence, K.K. (2010). PTP1B and SHP2 in POMC neurons reciprocally regulate energy balance in mice. *J. Clin. Invest.* 120, 720–734.
- Bartelt, A., Bruns, O.T., Reimer, R., Hohenberg, H., Itrich, H., Peldschus, K., Kaul, M.G., Tromsdorf, U.I., Weller, H., Waurisch, C., et al. (2011). Brown adipose tissue activity controls triglyceride clearance. *Nat. Med.* 17, 200–205.
- Bence, K.K., Delibegovic, M., Xue, B., Gorgun, C.Z., Hotamisligil, G.S., Neel, B.G., and Kahn, B.B. (2006). Neuronal PTP1B regulates body weight, adiposity and leptin action. *Nat. Med.* 12, 917–924.
- Benoit, S.C., Air, E.L., Coolen, L.M., Strauss, R., Jackman, A., Clegg, D.J., Seeley, R.J., and Woods, S.C. (2002). The catabolic action of insulin in the brain is mediated by melanocortins. *J. Neurosci.* 22, 9048–9052.
- Berglund, E.D., Vianna, C.R., Donato, J., Jr., Kim, M.H., Chuang, J.C., Lee, C.E., Lauzon, D.A., Lin, P., Brule, L.J., Scott, M.M., et al. (2012). Direct leptin

(H–J) C57BL/6 mice were subjected to sham or ingWAT bilateral denervations (6-OHDA) and ICV infused with insulin + leptin. (H) Body weights, (I) BAT and ingWAT *Ucp-1* expression, and (J) energy expenditure were monitored.

(K–M) C57BL/6 mice were implanted with bilateral intra-ARC cannulas and infused with vehicle, insulin (3 mU/day) + leptin (4.8 μ g/day), or insulin + leptin + PI3K inhibitor (PI3Ki; LY294002, 5 μ g/day). (K) Daily body weights were recorded (insert: intra-ARC cannula placement) and ingWAT extracted for (L) analysis of *Ucp-1* gene expression, (M) histology, and UCP-1 immunohistochemistry.

(N–P) *Pomc*-Cre mice were bilaterally injected with rAAV-hSyn-DIO-hM3D(Gq)-mCherry into the ARC. Contralateral ingWAT depots were sham operated or denervated, and the mice were administered vehicle or CNO (1.5 mg/kg/day, IP) and ingWAT processed for (N) in situ morphology, (O) gene expression analysis, (P) histology, and immunohistochemistry.

Data are means \pm SEM and are representative of three independent experiments; significance was determined using (A, D, H, and K) two-way ANOVA with repeated measures or (B, E, G, I, J, L, and O) one-way ANOVA. In (A), the pound (#) corresponds to *Ptpn1^{fl/fl}* + Leptin versus POMC-1B + Leptin. In (D and H), the asterisk (*) corresponds to leptin(L) or L/insulin(I) versus vehicle (V), and the pound (#) L/I versus L or L/I + sham versus L/I + denervation. In (K), the asterisk (*) corresponds to L/I, or L/I + PI3Ki versus V, and the pound (#) L/I versus L/I + PI3Ki.

- action on POMC neurons regulates glucose homeostasis and hepatic insulin sensitivity in mice. *J. Clin. Invest.* **122**, 1000–1009.
- Boström, P., Wu, J., Jedrychowski, M.P., Korde, A., Ye, L., Lo, J.C., Rasbach, K.A., Boström, E.A., Choi, J.H., Long, J.Z., et al. (2012). A PGC1- α -dependent myokine that drives brown-fat-like development of white fat and thermogenesis. *Nature* **481**, 463–468.
- Brüning, J.C., Gautam, D., Burks, D.J., Gillette, J., Schubert, M., Orban, P.C., Klein, R., Krone, W., Müller-Wieland, D., and Kahn, C.R. (2000). Role of brain insulin receptor in control of body weight and reproduction. *Science* **289**, 2122–2125.
- Chao, P.T., Yang, L., Aja, S., Moran, T.H., and Bi, S. (2011). Knockdown of NPY expression in the dorsomedial hypothalamus promotes development of brown adipocytes and prevents diet-induced obesity. *Cell Metab.* **13**, 573–583.
- Chiappini, F., Catalano, K.J., Lee, J., Peroni, O.D., Lynch, J., Dhaneshwar, A.S., Wellenstein, K., Sontheimer, A., Neel, B.G., and Kahn, B.B. (2014). Ventromedial hypothalamus-specific Ptpn1 deletion exacerbates diet-induced obesity in female mice. *J. Clin. Invest.* **124**, 3781–3792.
- Cohen, P., Levy, J.D., Zhang, Y., Frontini, A., Kolodin, D.P., Svensson, K.J., Lo, J.C., Zeng, X., Ye, L., Khandekar, M.J., et al. (2014). Ablation of PRDM16 and beige adipose causes metabolic dysfunction and a subcutaneous to visceral fat switch. *Cell* **156**, 304–316.
- Coll, A.P., Farooqi, I.S., Challis, B.G., Yeo, G.S., and O'Rahilly, S. (2004). Proopiomelanocortin and energy balance: insights from human and murine genetics. *J. Clin. Endocrinol. Metab.* **89**, 2557–2562.
- Commings, S.P., Watson, P.M., Levin, N., Beiler, R.J., and Gettys, T.W. (2000). Central leptin regulates the UCP1 and ob genes in brown and white adipose tissue via different beta-adrenoceptor subtypes. *J. Biol. Chem.* **275**, 33059–33067.
- Cowley, M.A., Smart, J.L., Rubinstein, M., Cerdán, M.G., Diano, S., Horvath, T.L., Cone, R.D., and Low, M.J. (2001). Leptin activates anorexigenic POMC neurons through a neural network in the arcuate nucleus. *Nature* **411**, 480–484.
- Cypess, A.M., Lehman, S., Williams, G., Tal, I., Rodman, D., Goldfine, A.B., Kuo, F.C., Palmer, E.L., Tseng, Y.H., Doria, A., et al. (2009). Identification and importance of brown adipose tissue in adult humans. *N. Engl. J. Med.* **360**, 1509–1517.
- Elias, C.F., Aschkenasi, C., Lee, C., Kelly, J., Ahima, R.S., Bjorbaek, C., Flier, J.S., Saper, C.B., and Elmquist, J.K. (1999). Leptin differentially regulates NPY and POMC neurons projecting to the lateral hypothalamic area. *Neuron* **23**, 775–786.
- Enriori, P.J., Sinnayah, P., Simonds, S.E., Garcia Rudaz, C., and Cowley, M.A. (2011). Leptin action in the dorsomedial hypothalamus increases sympathetic tone to brown adipose tissue in spite of systemic leptin resistance. *J. Neurosci.* **31**, 12189–12197.
- Hill, J.W., Williams, K.W., Ye, C., Luo, J., Balthasar, N., Coppari, R., Cowley, M.A., Cantley, L.C., Lowell, B.B., and Elmquist, J.K. (2008). Acute effects of leptin require PI3K signaling in hypothalamic proopiomelanocortin neurons in mice. *J. Clin. Invest.* **118**, 1796–1805.
- Hill, J.W., Elias, C.F., Fukuda, M., Williams, K.W., Berglund, E.D., Holland, W.L., Cho, Y.R., Chuang, J.C., Xu, Y., Choi, M., et al. (2010). Direct insulin and leptin action on pro-opiomelanocortin neurons is required for normal glucose homeostasis and fertility. *Cell Metab.* **11**, 286–297.
- Koch, L., Wunderlich, F.T., Seibler, J., Könnner, A.C., Hampel, B., Irlenbusch, S., Brabant, G., Kahn, C.R., Schwenk, F., and Brüning, J.C. (2008). Central insulin action regulates peripheral glucose and fat metabolism in mice. *J. Clin. Invest.* **118**, 2132–2147.
- Könnner, A.C., Janoschek, R., Plum, L., Jordan, S.D., Rother, E., Ma, X., Xu, C., Enriori, P., Hampel, B., Barsh, G.S., et al. (2007). Insulin action in AgRP-expressing neurons is required for suppression of hepatic glucose production. *Cell Metab.* **5**, 438–449.
- Krashes, M.J., Koda, S., Ye, C., Rogan, S.C., Adams, A.C., Cusher, D.S., Maratos-Flier, E., Roth, B.L., and Lowell, B.B. (2011). Rapid, reversible activation of AgRP neurons drives feeding behavior in mice. *J. Clin. Invest.* **121**, 1424–1428.
- Lee, P., Linderman, J.D., Smith, S., Brychta, R.J., Wang, J., Idelson, C., Perron, R.M., Werner, C.D., Phan, G.Q., Kammula, U.S., et al. (2014). Irisin and FGF21 are cold-induced endocrine activators of brown fat function in humans. *Cell Metab.* **19**, 302–309.
- Lidell, M.E., Betz, M.J., Dahlqvist Leinhard, O., Heglund, M., Elander, L., Slawik, M., Mussack, T., Nilsson, D., Romu, T., Nuutila, P., et al. (2013). Evidence for two types of brown adipose tissue in humans. *Nat. Med.* **19**, 631–634.
- Loh, K., Deng, H., Fukushima, A., Cai, X., Boivin, B., Galic, S., Bruce, C., Shields, B.J., Skiba, B., Ooms, L.M., et al. (2009). Reactive oxygen species enhance insulin sensitivity. *Cell Metab.* **10**, 260–272.
- Loh, K., Fukushima, A., Zhang, X., Galic, S., Briggs, D., Enriori, P.J., Simonds, S., Wiede, F., Reichenbach, A., Hauser, C., et al. (2011). Elevated hypothalamic TCPTP in obesity contributes to cellular leptin resistance. *Cell Metab.* **14**, 684–699.
- Marino, J.S., Xu, Y., and Hill, J.W. (2011). Central insulin and leptin-mediated autonomic control of glucose homeostasis. *Trends Endocrinol. Metab.* **22**, 275–285.
- Mori, H., Hanada, R., Hanada, T., Aki, D., Mashima, R., Nishinakamura, H., Torisu, T., Chien, K.R., Yasukawa, H., and Yoshimura, A. (2004). Socs3 deficiency in the brain elevates leptin sensitivity and confers resistance to diet-induced obesity. *Nat. Med.* **10**, 739–743.
- Morrison, S.F., Madden, C.J., and Tupone, D. (2014). Central neural regulation of brown adipose tissue thermogenesis and energy expenditure. *Cell Metab.* **19**, 741–756.
- Myers, M.G., Cowley, M.A., and Münzberg, H. (2008). Mechanisms of leptin action and leptin resistance. *Annu. Rev. Physiol.* **70**, 537–556.
- Ouellet, V., Routhier-Labadie, A., Bellemare, W., Lakhal-Chaieb, L., Turcotte, E., Carpentier, A.C., and Richard, D. (2011). Outdoor temperature, age, sex, body mass index, and diabetic status determine the prevalence, mass, and glucose-uptake activity of 18F-FDG-detected BAT in humans. *J. Clin. Endocrinol. Metab.* **96**, 192–199.
- Plum, L., Belgardt, B.F., and Brüning, J.C. (2006). Central insulin action in energy and glucose homeostasis. *J. Clin. Invest.* **116**, 1761–1766.
- Plum, L., Rother, E., Münzberg, H., Wunderlich, F.T., Morgan, D.A., Hampel, B., Shanabrough, M., Janoschek, R., Könnner, A.C., Alber, J., et al. (2007). Enhanced leptin-stimulated PI3k activation in the CNS promotes white adipose tissue transdifferentiation. *Cell Metab.* **6**, 431–445.
- Qiu, J., Fang, Y., Rönnekleiv, O.K., and Kelly, M.J. (2010). Leptin excites proopiomelanocortin neurons via activation of TRPC channels. *J. Neurosci.* **30**, 1560–1565.
- Qiu, J., Zhang, C., Borgquist, A., Nestor, C.C., Smith, A.W., Bosch, M.A., Ku, S., Wagner, E.J., Rönnekleiv, O.K., and Kelly, M.J. (2014). Insulin excites anorexigenic proopiomelanocortin neurons via activation of canonical transient receptor potential channels. *Cell Metab.* **19**, 682–693.
- Rahmouni, K., Morgan, D.A., Morgan, G.M., Liu, X., Sigmund, C.D., Mark, A.L., and Haynes, W.G. (2004). Hypothalamic PI3K and MAPK differentially mediate regional sympathetic activation to insulin. *J. Clin. Invest.* **114**, 652–658.
- Rosen, E.D., and Spiegelman, B.M. (2014). What we talk about when we talk about fat. *Cell* **156**, 20–44.
- Rothwell, N.J., and Stock, M.J. (1979). A role for brown adipose tissue in diet-induced thermogenesis. *Nature* **281**, 31–35.
- Ruan, H.B., Dietrich, M.O., Liu, Z.W., Zimmer, M.R., Li, M.D., Singh, J.P., Zhang, K., Yin, R., Wu, J., Horvath, T.L., and Yang, X. (2014). O-GlcNAc transferase enables AgRP neurons to suppress browning of white fat. *Cell* **159**, 306–317.
- Satiel, A.R., and Kahn, C.R. (2001). Insulin signalling and the regulation of glucose and lipid metabolism. *Nature* **414**, 799–806.
- Seale, P., Conroe, H.M., Estall, J., Kajimura, S., Frontini, A., Ishibashi, J., Cohen, P., Cinti, S., and Spiegelman, B.M. (2011). Prdm16 determines the thermogenic program of subcutaneous white adipose tissue in mice. *J. Clin. Invest.* **121**, 96–105.

- Shabalina, I.G., Petrovic, N., de Jong, J.M., Kalinovich, A.V., Cannon, B., and Nedergaard, J. (2013). UCP1 in brite/beige adipose tissue mitochondria is functionally thermogenic. *Cell Rep.* 5, 1196–1203.
- Sohn, J.W., Xu, Y., Jones, J.E., Wickman, K., Williams, K.W., and Elmquist, J.K. (2011). Serotonin 2C receptor activates a distinct population of arcuate pro-opiomelanocortin neurons via TRPC channels. *Neuron* 71, 488–497.
- Tiganis, T. (2013). PTP1B and TCPTP—nonredundant phosphatases in insulin signaling and glucose homeostasis. *FEBS J.* 280, 445–458.
- van Marken Lichtenbelt, W.D., Vanhommerig, J.W., Smulders, N.M., Dros-saerts, J.M., Kemerink, G.J., Bouvy, N.D., Schrauwen, P., and Teule, G.J. (2009). Cold-activated brown adipose tissue in healthy men. *N. Engl. J. Med.* 360, 1500–1508.
- Varela, L., and Horvath, T.L. (2012). Leptin and insulin pathways in POMC and AgRP neurons that modulate energy balance and glucose homeostasis. *EMBO Rep.* 13, 1079–1086.
- Virtanen, K.A., Lidell, M.E., Orava, J., Heglind, M., Westergren, R., Niemi, T., Taittonen, M., Laine, J., Savisto, N.J., Enerbäck, S., and Nuutila, P. (2009). Functional brown adipose tissue in healthy adults. *N. Engl. J. Med.* 360, 1518–1525.
- Williams, K.W., Margatho, L.O., Lee, C.E., Choi, M., Lee, S., Scott, M.M., Elias, C.F., and Elmquist, J.K. (2010). Segregation of acute leptin and insulin effects in distinct populations of arcuate proopiomelanocortin neurons. *J. Neurosci.* 30, 2472–2479.
- Williams, K.W., Liu, T., Kong, X., Fukuda, M., Deng, Y., Berglund, E.D., Deng, Z., Gao, Y., Liu, T., Sohn, J.W., et al. (2014). Xbp1s in Pomc neurons connects ER stress with energy balance and glucose homeostasis. *Cell Metab.* 20, 471–482.
- Wu, J., Boström, P., Sparks, L.M., Ye, L., Choi, J.H., Giang, A.H., Khandekar, M., Virtanen, K.A., Nuutila, P., Schaart, G., et al. (2012). Beige adipocytes are a distinct type of thermogenic fat cell in mouse and human. *Cell* 150, 366–376.
- Xue, Y., Petrovic, N., Cao, R., Larsson, O., Lim, S., Chen, S., Feldmann, H.M., Liang, Z., Zhu, Z., Nedergaard, J., et al. (2009). Hypoxia-independent angiogenesis in adipose tissues during cold acclimation. *Cell Metab.* 9, 99–109.
- Zhang, S., Chen, L., Luo, Y., Gunawan, A., Lawrence, D.S., and Zhang, Z.Y. (2009). Acquisition of a potent and selective TC-PTP inhibitor via a stepwise fluorophore-tagged combinatorial synthesis and screening strategy. *J. Am. Chem. Soc.* 131, 13072–13079.

Myocardin-Related Transcription Factor A Regulates Conversion of Progenitors to Beige Adipocytes

Meghan E. McDonald,^{1,2} Chendi Li,^{1,2} Hejiao Bian,¹ Barbara D. Smith,¹ Matthew D. Layne,^{1,*} and Stephen R. Farmer^{1,*}

¹Department of Biochemistry, Boston University School of Medicine, Boston, MA 02118, USA

²Co-first author

*Correspondence: mlayne@bu.edu (M.D.L.), sfarmer@bu.edu (S.R.F.)

<http://dx.doi.org/10.1016/j.cell.2014.12.005>

SUMMARY

Adipose tissue is an essential regulator of metabolic homeostasis. In contrast with white adipose tissue, which stores excess energy in the form of triglycerides, brown adipose tissue is thermogenic, dissipating energy as heat via the unique expression of the mitochondrial uncoupling protein UCP1. A subset of UCP1+ adipocytes develops within white adipose tissue in response to physiological stimuli; however, the developmental origin of these “brite” or “beige” adipocytes is unclear. Here, we report the identification of a BMP7-ROCK signaling axis regulating beige adipocyte formation via control of the G-actin-regulated transcriptional coactivator myocardin-related transcription factor A, MRTFA. White adipose tissue from *MRTFA*^{-/-} mice contains more multilocular adipocytes and expresses enhanced levels of brown-selective proteins, including UCP1. *MRTFA*^{-/-} mice also show improved metabolic profiles and protection from diet-induced obesity and insulin resistance. Our study hence unravels a central pathway driving the development of physiologically functional beige adipocytes.

INTRODUCTION

Adipose tissue is an essential regulator of metabolic homeostasis and is composed of mesenchymal stem cells, vascular cells, preadipocytes, and mature fat cells. At least two types of adipocytes exist with distinct phenotypes and function. White adipocytes are morphologically distinct from brown adipocytes and store lipids in unilocular droplets. In comparison, brown adipocytes contain multilocular lipid droplets and numerous mitochondria. Whereas white adipocytes store excess energy in the form of triglycerides, brown adipocytes are thermogenic, oxidative cells that, when activated by appropriate stimuli, dissipate energy as heat (Cannon and Nedergaard, 2004). Energy release is achieved due to the activity of UCP1, a brown adipose tissue (BAT)-specific mitochondrial uncoupling protein (Nedergaard et al., 2005). Because of its unique function, enhancing BAT mass and/or activity is an attractive therapeutic

approach for individuals suffering from obesity and/or type 2 diabetes.

A distinct population of UCP1+ adipocytes develops within the white adipose tissue (WAT) of mice in response to cold exposure (Cousin et al., 1992, 1996; Guerra et al., 1998; Loncar, 1991a, 1991b), β_3 adrenergic receptor (AR) agonist treatment (Collins et al., 1997; Ghorbani and Himms-Hagen, 1997; Granneman et al., 2005; Guerra et al., 1998; Nagase et al., 1996), PPAR γ agonist administration (Petrovic et al., 2010; Vernochet et al., 2009; Wilson-Fritch et al., 2004; Xue et al., 2005), or exposure to FGF21, irisin, or cardiac natriuretic peptides (Bordicchia et al., 2012; Boström et al., 2012; Fisher et al., 2012). The developmental origins of these cells designated “brite” or “beige” adipocytes, are not well understood (Enerbäck, 2009; Ishibashi and Seale, 2010; Petrovic et al., 2010; Young et al., 1984). Current hypotheses propose that they arise from the conversion of existing white adipocytes and/or the differentiation of WAT resident progenitor cells (Himms-Hagen et al., 2000; Jimenez et al., 2003; Lee et al., 2012; Long et al., 2014; Rosenwald et al., 2013; Wang et al., 2013; Wu et al., 2012; Zingaretti et al., 2009). Lineage tracing studies revealed that interscapular BAT arises from the dermomyotome (Atit et al., 2006; Seale et al., 2008). Brown and beige adipocytes in vitro possess a distinct gene expression signature (Wu et al., 2012) suggesting divergent processes regulate prenatal development of classical BAT and postnatal formation of brite/beige adipocytes within WAT.

Discovering the origins of adipocyte progenitors is of intense interest. A population of white adipocyte progenitors resident in the adult WAT stroma were characterized by specific cell surface markers (Rodeheffer et al., 2008). PPAR γ lineage tracing studies indicated that WAT progenitors reside in the mural cell compartment of adipose vasculature (Tang et al., 2008) and at least a population of beige cells have a smooth muscle-like origin (Long et al., 2014). These observations suggest that white and beige adipocytes arise from progenitors closely associated with the vasculature. Physiological signals that regulate the fate of these progenitors, and their tissues of origin have yet to be determined.

Members of the TGF β superfamily are intimately involved in the development and maintenance of the vasculature (Jakobsen and van Meeteren, 2013; Patel-Hett and D'Amore, 2011). TGF β promotes smooth muscle differentiation and coordinates the expression of SMC genes (Hautmann et al., 1997; Li et al., 2012; Sinha et al., 2004; Wang et al., 2010). TGF β also inhibits

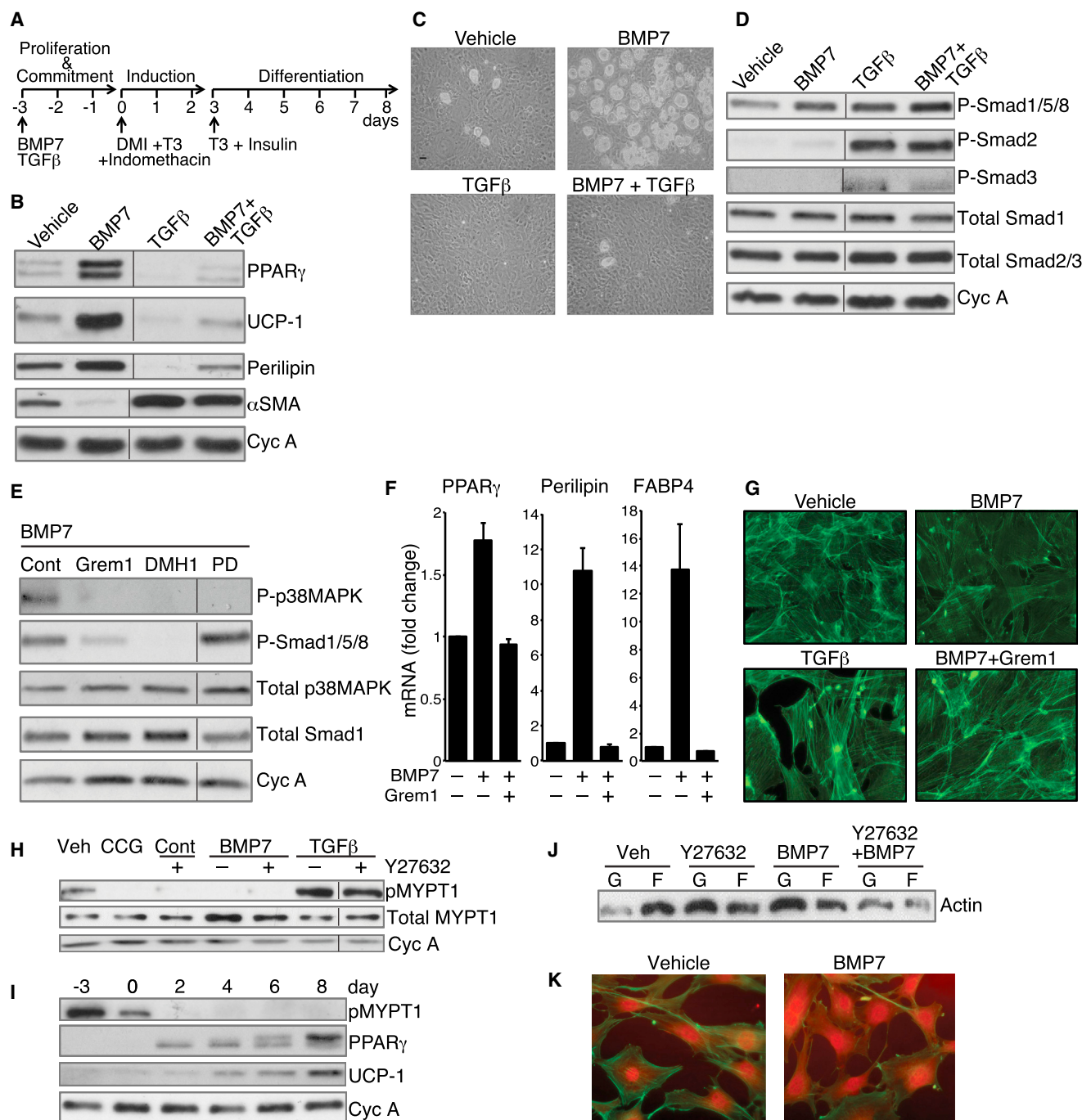


Figure 1. BMP7 and TGF β Mediate Distinct Effects on Lineage Commitment of MSCs through Alteration of ROCK Activity

(A) Differentiation protocol used for mesenchymal stem cells.

(B and C) Subconfluent C3H10T1/2 cells (B) or mouse bone marrow-derived MSCs (Life Technologies, GIBCO) (C) were exposed to BMP7 (6.3 nM) and/or TGF β 1 (1 nM) for 3 days, then induced to differentiate without BMP7 or TGF β as in (A). Differentiation of cells was assessed by western blot (B) or phase contrast microscopy (C).

(D and E) Western blot analysis of C3H10T1/2 cell proteins after a 10 min exposure to vehicle, BMP7, TGF β , or BMP7 and TGF β (D) or BMP7 alone following a 2 hr pretreatment with either 125 nM Gremlin1 or 200 nM Dorsomorphin homolog (DMH1) or 50 μ M PD169316 (E).

(F) Bone marrow MSCs were induced to differentiate in response to BMP7 as in (A) in presence or absence of Gremlin1 and RNA was subjected to qPCR analysis.

(G) Subconfluent C3H10T1/2 MSCs were exposed to TGF β 1 (1 nM) alone or BMP7 (6.3 nM) with or without Gremlin1 for 48 hr, then stained with Alexa Fluor 488 phalloidin and visualized at 40 \times magnification.

(legend continued on next page)

adipocyte differentiation via its coeffector, Smad3, which complexes with C/EBP β and represses activation of adipogenic target genes (Choy and Derynck, 2003). Interestingly, Smad3 knockout (KO) mice develop brown-like adipocytes in WAT depots and are protected from obesity, illustrating the role of the TGF β /Smad3 pathway in the negative regulation of browning of WAT (Yadav et al., 2011).

In contrast with TGF β , bone morphogenetic proteins (BMPs), promote adipocyte formation (Schulz and Tseng, 2009). Exposure of multipotent MSCs to BMP2 or BMP4 gives rise to a population of preadipocyte-like cells, which differentiate to mature adipocytes (Ahrens et al., 1993; Bowers and Lane, 2007; Tang et al., 2004; Wang et al., 1993, 2009). BMP7 initiates the commitment of MSCs to the brown adipocyte lineage (Tseng et al., 2008) by promoting the expression of the brown adipocyte factors PRDM16, PGC-1 α and UCP1, and mitochondrial biogenesis (Tseng et al., 2008). Importantly, the absence of BMP7 in mice attenuates the formation of BAT (Tseng et al., 2008); BMP7 is also able to induce the conversion of progenitors isolated from WAT, BAT, and muscle to brown-like adipocytes (Schulz et al., 2011). BMP4 and BMP8b have also been implicated in the browning of WAT and enhancing energy expenditure and insulin sensitivity (Qian et al., 2013; Whittle et al., 2012).

Additional downstream effectors of TGF β and BMPs include members of the Rho-GTPase family, which mediate the dynamic control of monomeric and filamentous actin (Moustakas and Heldin, 2008). Monomeric G-actin can regulate the nucleus-cytoplasm shuttling of serum response factor (SRF) coregulators, myocardin-related transcription factors (MRTFs) and, thereby, influence the expression of SRF target genes including smooth muscle actin (SMA) (Miralles et al., 2003; Olson and Nordheim, 2010). Several studies have reported on the involvement of Rho-GTPase in regulating the fate of MSCs (McBeath et al., 2004; Sordella et al., 2003), but there are no studies of the potential role of MRTFs. Here, we identified a BMP7-controlled signaling and transcriptional circuit involving MRTFA, which enhances the development of beige adipocytes in WAT, resulting in protection from diet-induced obesity and insulin resistance.

RESULTS

BMP7 and TGF β 1 Mediate Distinct Effects on Lineage Commitment of MSCs

To investigate the effects of BMP7 and TGF β 1 on lineage commitment, subconfluent multipotent C3H/10T1/2 MSCs were exposed to each effector for 3 days until reaching confluence and then exposed to a brown adipogenic cocktail (illustrated in Figure 1A). As anticipated, BMP7-treated cells developed into brown-like adipocytes, noted by elevated

expression of UCP1, PPAR γ , and Perilipin (Figure 1B). BMP7 also downregulated SMA in proliferating MSCs (Figure 1B). MSCs exposed to TGF β 1, however, failed to undergo adipogenesis but instead produced elevated levels of SMA, suggesting the cells committed to a smooth muscle-like lineage. Exposure to both BMP7 and TGF β 1 resulted in a mixed population of differentiated cells, as indicated by large numbers of fibroblastic cells, and to a lesser extent, Oil Red O positive adipocytes (data not shown). Heterogeneity of the population was confirmed by the abundant expression of SMA and a low level of adipocyte proteins (Figure 1B). To confirm that the effects of BMP7 and TGF β were not unique to C3H/10T1/2 MSCs, these factors also regulated the differentiation of bone marrow-derived MSCs (Figure 1C).

We next analyzed the signaling pathways activated in response to these effectors. As expected, TGF β 1 in the presence or absence of BMP7 activated the phosphorylation of SMAD2 and SMAD3. BMP7, however, stimulated the phosphorylation of SMADs 1/5/8, with negligible phosphorylation of SMADs 2 or 3 (Figure 1D). Interestingly, TGF β 1 also activated SMADs 1/5/8 indicating that BMP7-induced commitment is not mediated exclusively by activation of the SMADs, but by additional downstream effectors of the BMP receptor. In fact, BMP7 activated p38MAPK signaling (Figure S1A), which was required for BMP7-induced brown adipogenesis because treatment of the MSCs with a p38MAPK inhibitor (PD169316) suppressed UCP1 expression (Figure S1B). Inhibition of the BMP type I receptors with dorsomorphin homolog (DMH1) or inhibition of BMP7 directly with Gremlin1 (Hsu et al., 1998) attenuated the activation of SMADs 1/5/8 and p38MAPK confirming that stimulation of both pathways occurs through BMP7 and its receptor (Figure 1E). Notably, DMH1 diminished C3H/10T1/2 MSCs differentiation in a concentration-dependent manner (Figure S1C) and Gremlin1 attenuated the differentiation of bone marrow-derived MSCs in response to BMP7 (Figure 1F).

BMP7 Represses ROCK Activity and Alters Actin Dynamics in MSCs

Cells exposed to BMP7 or TGF β 1, exhibited marked changes in morphology. BMP7-treated cells exhibited a broadened shape and a less prominent actin network when compared to control cells (Figure 1G). This phenomenon is controlled by BMP activity, as it was reversed by coincubation with Gremlin1. TGF β 1, in contrast, promoted an elongated morphology and formation of actin microfilaments. We hypothesized that these changes in actin dynamics were mediated by Rho-associated protein kinase (ROCK), a major effector of the RhoA pathway (Schofield and Bernard, 2013). Following exposure of MSCs to BMP7, ROCK activity was repressed below basal levels, as assessed by a reduction in the phosphorylation of one of its targets, MYPT1 (Figure 1H). In fact, BMP7 inhibited ROCK as effectively

(H) Subconfluent C3H10T1/2 MSCs were exposed to BMP7 or TGF β with or without Y27632 (10 μ M) or CCG1423 (10 μ M) for 2 hr at which stage protein lysates were analyzed for phospho-MYPT1.

(I) Protein extracts from C3H10T1/2 MSCs at the indicated times of differentiation (as illustrated in A) were analyzed by western blot.

(J and K) Subconfluent, proliferating C3H10T1/2 MSCs were treated with Y27632 with or without BMP7 for 48 hr and levels of F-actin versus G-actin were analyzed by western blot (J) and immunofluorescence (K). Nonadjacent lanes on western blots (B, D, E, and H) are indicated by a vertical line. See also Figure S1.

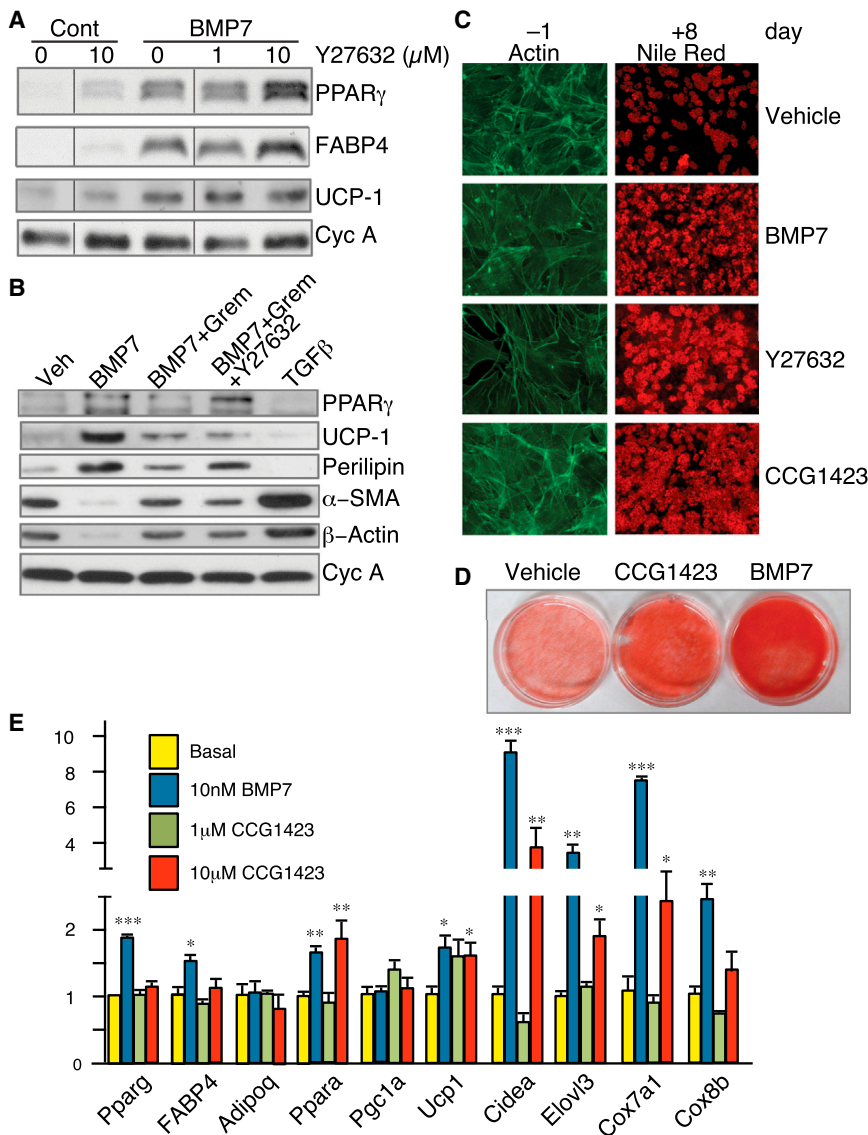


Figure 2. Inhibition of ROCK or SRF Activity Promotes Commitment to the Adipogenic Lineage

(A) C3H/10T1/2 cells were treated with the indicated concentrations of Y27632 in the presence or absence of BMP7 and induced to differentiate for 8 days and extracted proteins analyzed by western blot.

(B) C3H/10T1/2 cells were treated with Gremlin1 and/or Y27632 2 hr prior to the addition of BMP7 or TGF β , as indicated. Following adipocyte differentiation (day 8), total cellular proteins were analyzed.

(C) C3H/10T1/2 cells were exposed to either BMP7, Y27632, or CCG1423 (10 μ M) and actin filaments were analyzed after 2 days as in Figure 1G (left panels) or allowed to mature to adipocytes and stained with Nile Red (right panels).

(D) Subconfluent C3H/10T1/2 cells were treated with either CCG1423 or BMP7 for 3 days prior to induction of differentiation for 8 days, at which stage cultures were visualized following Nile Red staining.

(E) C3H/10T1/2 cells were treated with 1 μ M or 10 μ M CCG1423, or BMP7 for 3 days and induced to differentiate. Total RNA was subjected to q-PCR analysis. Nonadjacent lanes on western blots in (A) are indicated by a vertical line.

See also Figure S2.

Y27632 could mimic the effects of BMP7. Although, Y27632 alone had a modest effect on adipocyte gene expression (Figure 2A) and on the number of cells converting to Nile Red-positive adipocytes (Figure 2C), it did potentiate the action of BMP7 as revealed by enhanced expression of PPAR γ and FABP4 (Figure 2A). ROCK inhibition did not alter BMP7-induced UCP1 expression. Interestingly, ROCK inhibition partially overcame the inhibitory effect of Gremlin on adipocyte gene expression (Figure 2B,

as the ROCK-specific inhibitor, Y27632. As expected, TGF β 1 strongly induced MYPT1 phosphorylation, which was only partially inhibited by a dose of Y27632 that was sufficient to block endogenous TGF β 1 activity. Importantly, ROCK activity declined rapidly during BMP7-induced brown adipogenesis reaching undetectable levels in mature adipocytes (Figure 1I).

Coincident with modulation of the RhoA pathway are changes in the relative amounts of G-actin and F-actin. Consistent with its inhibition of ROCK, biochemical and cell staining assays revealed that BMP7 increased the G/F-actin ratio (Figures 1J and 1K). The ROCK inhibitor Y27632 similarly enhanced G-actin levels relative to F-actin (Figure 1J).

Inhibition of the ROCK/SRF Pathway Enhances Brown Adipogenesis in MSCs

The proadipogenic properties of BMP7 closely correlated with inhibition of ROCK activity, which led us to question whether

compare lanes 3 and 4) and differentiation (Figure S2) while having limited effects on UCP1 expression.

Cytoplasmic G-actin regulates SRF activity by associating with or dissociating from its coregulators, MRTFs (Posern and Treisman, 2006). When effectors activate ROCK and drive G-actin into filamentous actin (F-actin), MRTFs translocate to the nucleus and promote transcription of SRF-target genes (Olson and Nordheim, 2010). Because BMP7 inhibits ROCK, we questioned whether its proadipogenic activity involves suppression of MRTF/SRF activity. In fact, exposure of MSCs to CCG1423 (an inhibitor of SRF activity) (Evelyn et al., 2007) prior to stimulation of adipogenesis enhanced their conversion to adipocytes (Figures 2C and 2D) while inducing expression of brown adipocyte genes (Figure 2E). Importantly, unlike Y27632, CCG1423 did not alter the actin cytoskeleton, (Figure 2C, phalloidin stained cells) indicating that it blocks SRF downstream of F-actin polymerization.

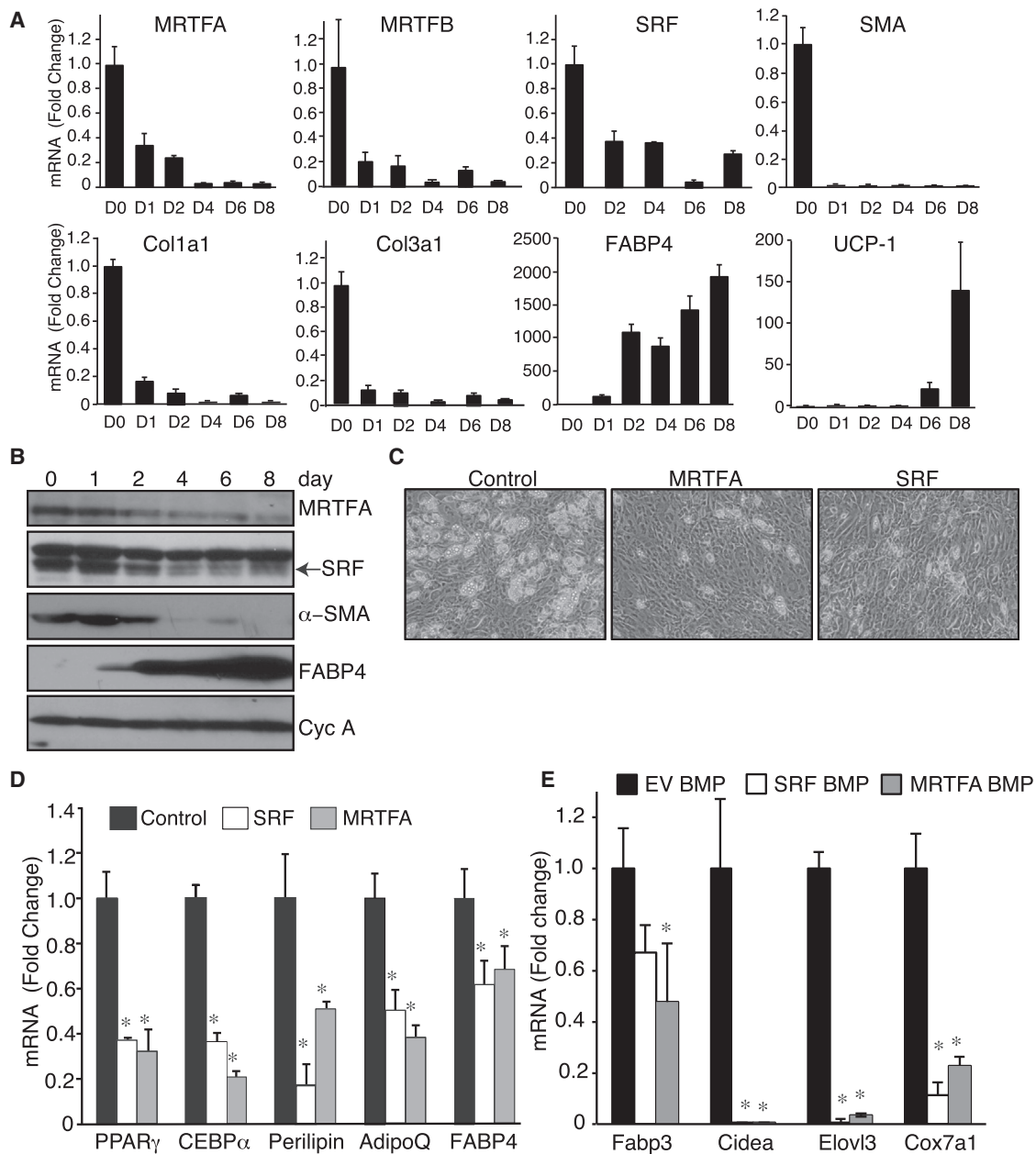


Figure 3. MRTFA and SRF Overexpression Prevent Differentiation of MSCs to Adipocytes

(A and B) qPCR and western blot analysis of indicated mRNAs (A) and proteins (B) in C3H/10T1/2 MSCs undergoing brown adipogenesis. (C) C3H/10T1/2 cell lines ectopically expressing SRF or MRTFA were induced to differentiate then visualized by phase contrast microscopy. (D and E) The cell lines (C) were differentiated in absence (D) or presence (E) of BMP7 and isolated RNA subjected to qPCR analysis. See also Figure S3.

Genetic Manipulation of MRTFA-SRF Transcriptional Activity Regulates Commitment of MSCs to an Adipogenic Lineage

Our observation that CCG1423 could mimic BMP7 suggests that MRTF/SRF antagonizes the commitment of MSCs to an adipogenic lineage. Other studies have identified SRF as an inhibitor of adipogenesis in 3T3-L1 preadipocytes (Mikkelsen et al., 2010), but little is known about its role in regulating the

fate of MSCs. Using C3H/10T1/2 MSCs, adipogenesis was accompanied by a decrease in MRTFA, MRTFB, SRF, and select SRF target genes, SMA, collagen 1 α 1, and collagen 3 α 1 (Figures 3A and 3B). The lower band in Figure 3B corresponds to SRF (Figure S3A). Cell lines were generated to ectopically express SRF or MRTFA (Luchsinger et al., 2011; Wang et al., 2012a), which resulted in reduced conversion of the MSCs to adipocytes (Figure 3C) and inhibited expression of

select white and brown adipogenic genes (Figures 3D and 3E). In addition, treatment with CCG1423 partially rescued the inhibitory effect of MRTFA or SRF on adipocyte formation (Figure S3B). Together, these results demonstrate that the ROCK-SRF pathway is an important BMP7 target and its repression facilitates adipogenesis.

Increased Production of Beige Adipocytes in WAT of MRTFA-Deficient Mice

To investigate the potential role of MRTFA/SRF in adipose development *in vivo*, we analyzed different adipose tissues in MRTFA-deficient mice (Li et al., 2006) and observed dramatic increases in multilocular adipocytes (Figure S4B) within the subcutaneous (inguinal, iWAT) fat depot of these mice compared to their wild-type (WT) littermates (Figure 4A). The epididymal (eWAT) depot of the KO mouse had few multilocular cells, but the size of the adipocytes in this depot was smaller than in the corresponding depot of WT littermates. Immunohistochemical staining of multiple tissue sections demonstrated that the multilocular adipocytes in the iWAT express UCP1 in mice maintained at room temperature, suggesting that MRTFA deficiency alters an early developmental pathway (Figure 4A). We did not detect any morphological or UCP1 expression changes in the BAT of KO mice. With maturation, iWAT from WT mice underwent hypertrophy leading to an increase in the size of individual unilocular adipocytes (Figure S4A). In contrast to WT mice, the iWAT of *MRTFA*^{-/-} mice consisted of more multilocular cells and the extent of hypertrophy with age was less pronounced (Figure S4A). Body weight also correlated with the differences in depot morphology. *MRTFA*^{-/-} mice gained less weight during 6 weeks of low fat diet and contained less overall fat mass relative to lean mass when compared to WT littermates (Figures 4B–4D and S4C). MRTFA-deficient mice also had lower fasting levels of glucose than WT mice but there were no differences in glucose measured during a GTT (Figures S4D and S4E). *MRTFA*^{-/-} mice also produced lower circulating levels of leptin and higher levels of adiponectin and insulin (Figure S4F).

RNA analysis revealed that iWAT from *MRTFA*^{-/-} mice expresses 30-fold more UCP1 mRNA relative to WT littermates (Figure 4E). No significant difference in UCP1 mRNA levels in BAT of WT and KO mice were observed, although the relative amount of UCP1 mRNA in BAT was significantly higher than in iWAT of WT littermates. Expression of other brown adipocyte mRNAs (Fabp3, Cox7a1, Elovl3, and Cox8b) were similarly higher in the iWAT of *MRTFA*^{-/-} mice compared to WT littermates. Our previous studies identified genes that are abundantly expressed in WAT relative to BAT (Vernochet et al., 2009). Importantly, one of these genes, angiotensinogen (Agt), is expressed at much lower levels in *MRTFA*^{-/-} iWAT relative to WT iWAT (Figure 4E), consistent with the enhanced development of brown-like adipocytes within iWAT of KO mice. Expression of SMA was also reduced in *MRTFA*^{-/-} iWAT compared to the WT depot. The transcription factor Tbx1 has recently been assigned as a marker of beige adipocytes (Wu et al., 2012). Importantly, Tbx1 expression was significantly higher in *MRTFA*^{-/-} iWAT compared to WT iWAT (Figure 4E) suggesting that the appearance of UCP1 positive, multilocular adipocytes in *MRTFA*^{-/-} mice is likely due to recruitment of beige progenitors.

Stromal Vascular Cells from *MRTFA*^{-/-} iWAT Undergo Beige Adipogenesis More Extensively Than WT SVF Cells

Because the mice used in this study were a total body knockout, we examined whether MRTFA represses beige adipocyte formation directly. Stromal vascular cells (SVFs) of WT and KO iWAT differentiated into adipocytes *in vitro* to approximately the same extent as judged by comparable expression of adiponectin, adipisin, and FABP4 (Figure 5A). *MRTFA*^{-/-} SVFs, however, expressed higher amounts of select BAT proteins including UCP1 and Chchd10/NDG2 (Figure 5A). Treatment of the adipocytes with forskolin (FSK) for 4 hr dramatically induced expression of UCP1 mRNA in both WT and KO cells when normalized to basal untreated levels (Figure 5B). The FSK-dependent induction of UCP1, Fabp3, Cidea, Cox7a1, and Elovl3 were significantly higher in KO versus WT adipocytes (Figure 5B). The induction of PGC-1 α mRNA, however, was similar in both WT and KO cells. A recent study suggested that some beige adipocytes have a smooth muscle-like origin; therefore, we analyzed expression of SM genes during early adipogenesis in SVF cells (Long et al., 2014). Treatment of cells with BMP7 for 48 hr resulted in a significant decrease in MRTFA, CRP2, SMA, and calponin expression (Figure 5C). In contrast, TGF β 1 enhanced SM protein expression (Figures 5C and 5D). In addition, the KO SVF cells expressed significantly lower amounts of the SM proteins under all conditions compared to WT cells (Figure 5D). These data suggest that BMP7 directs SVF progenitors to a beige adipocyte lineage rather than a SM lineage.

Treatment of mice with a β -adrenoceptor agonist such as CL316,243 results in “browning” of iWAT characterized by enhanced UCP1 expression and appearance of beige/brite adipocytes (Cousin et al., 1992; Barbatelli et al., 2010; Wu et al., 2012). We questioned, therefore, whether *MRTFA*^{-/-} mice respond differently to β -adrenergic stimulation than WT counterparts. Consistent with the earlier observations (Cousin et al., 1992), we show that WT mice induce browning of WAT depots based on more intense UCP1 staining in response to CL316,243 (Figure 6A). Importantly, *MRTFA*^{-/-} mice exhibited an enhanced response to CL316,243 than their WT littermates by producing larger regions of UCP1 positive multilocular adipocytes in iWAT (Figure 6A) and expressed higher amounts of select brown genes UCP1, Elovl3, Fabp3, Cidea, and Cox7a1 (Figure 6B) and UCP1 protein (Figure 6C).

MRTFA-Deficient Mice Are Protected from Diet-Induced Obesity and Insulin Resistance

Mice were fed a high-fat diet (HFD, fat 60 kcal%, 20 kcal% carbohydrate, protein 20 kcal%) for 6 weeks starting at 6 weeks of age. *MRTFA*^{-/-} mice gained less weight on the HFD compared to the WT littermates (Figure 7A). Body composition analysis revealed that KO mice gained less fat mass without any major change in lean mass or food intake (Figure S5B). The iWAT and eWAT of KO mice weighed less than corresponding depots in control littermates while there was no significant change in weight of BAT (Figure 7B). The weight of the liver in KO mice fed a HFD for 6 weeks was much lower than in WT littermates (Figure 7B). This difference in weight was likely due to the extensive accumulation of hepatic lipid in WT mice (Figure S5C).

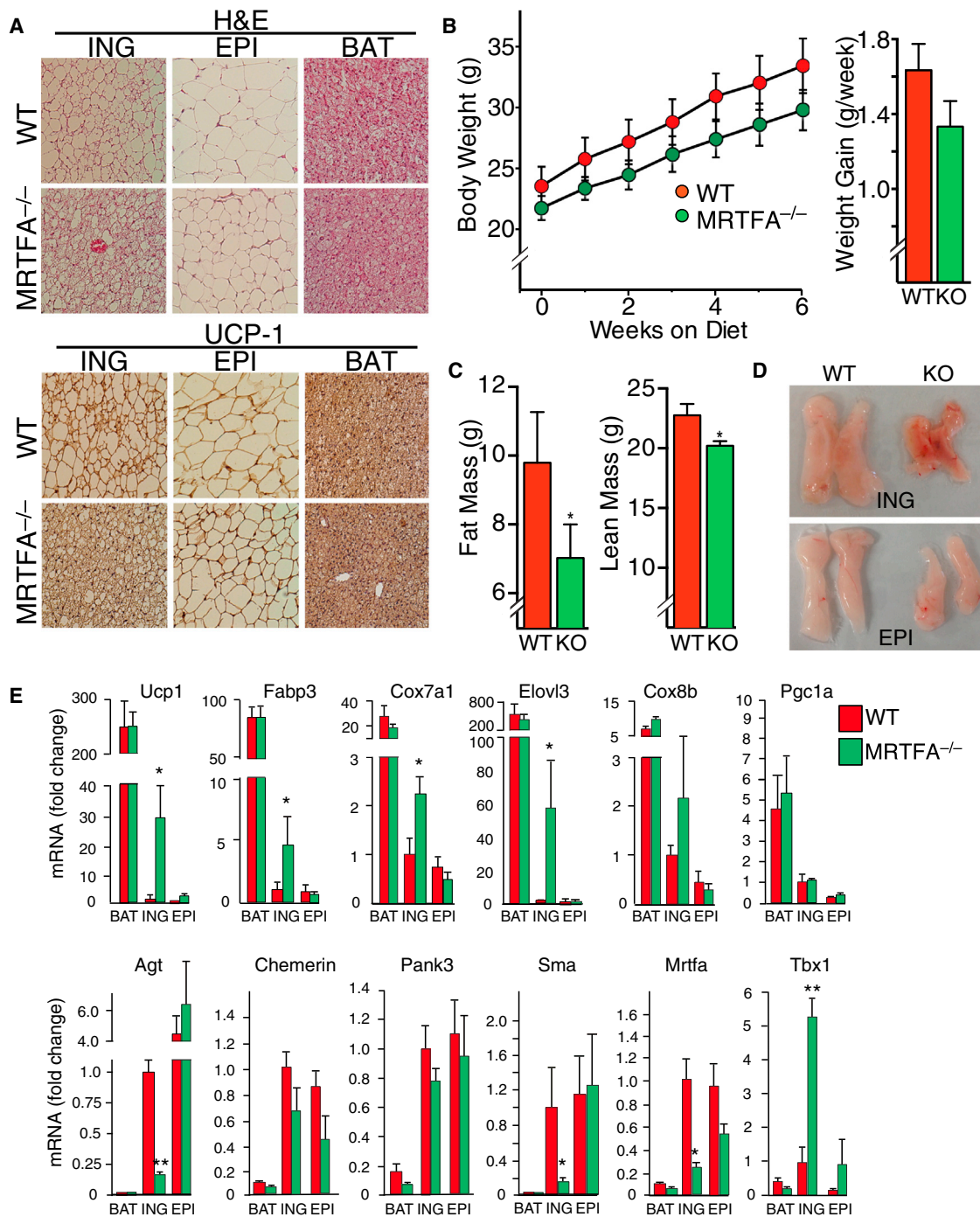


Figure 4. MRTFA Deficiency in Mice Enhances Recruitment of Beige Adipocytes to the White Adipose Depots

(A) H&E and UCP1 staining of representative sections (n = 7) of ING (Inguinal) WAT, EPI (Epididymal) WAT and BAT from 11- to 13-week-old WT and *MRTFA*^{-/-} (KO) mice on rodent diet with 10% kcal% fat.

(B) Body weight and average weight gain per week of WT and *MRTFA*^{-/-} mice on rodent diet with 10% kcal% fat (n = 5/group, *p < 0.05).

(C) Body composition determined by NMR (described in [Experimental Procedures](#)) analysis of mice from (B). Data presented mean ± SEM, n = 5/group, *p < 0.05.

(D) Gross morphology of representative ING and EPI fat pads of mice from (B).

(E) Relative mRNA levels of BAT- and WAT-enriched genes as well as other genes in WAT and BAT depots of 15-week-old WT and *MRTFA*^{-/-} mice on chow diet was analyzed by qPCR. Data presented mean ± SEM, n = 4/group, *p < 0.05, **p < 0.01.

See also [Figure S4](#).

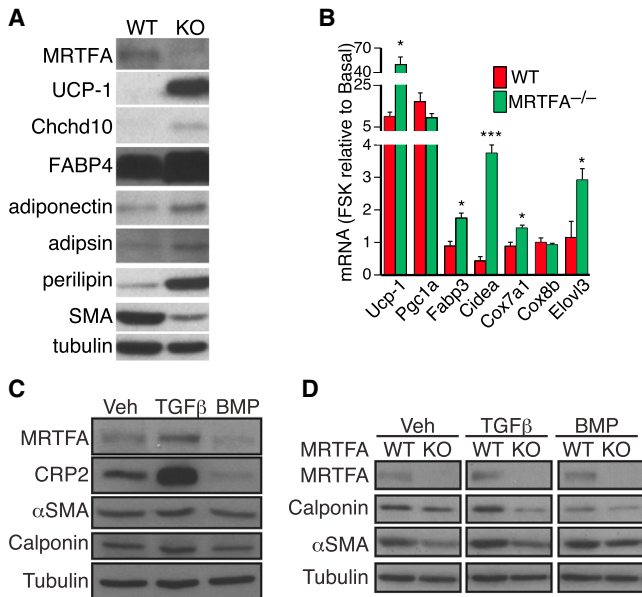


Figure 5. Cells from the Stromal Vascular Fraction of *MRTFA*^{-/-} ING WAT Express Less Smooth Muscle-like Features and Undergo Brown Adipogenesis More Extensively Than WT SVF Cells

(A) Western blot analysis on BAT- and WAT-enriched proteins of adipocytes arising from hormonal induction of stromal vascular fractions (SVFs) isolated from WT and *MRTFA*^{-/-} inguinal depots.

(B) WT and *MRTFA*^{-/-} SVC adipocytes were treated with or without forskolin (FSK) for 4 hr prior to isolation of total RNA for analysis. Values are presented as fold change in response to treatment with FSK in WT and *MRTFA*^{-/-} adipocytes.

(C and D) Subconfluent SVFs from ING and EPI WAT of WT and/or *MRTFA*^{-/-} mice were exposed to TGFβ1 or BMP7 for 2 days before reaching confluence and subjected to western blot analysis.

MRTFA^{-/-} mice had significantly lower levels of fasting glucose and exhibited enhanced glucose tolerance compared to WT littermates (Figures 7C and S5A). Additionally, KO mice had lower circulating levels of leptin (Figure S5D) consistent with them having less fat as well as higher circulating levels of adiponectin (Figure S5D). The high-fat diet also resulted in hypertrophy of individual adipocytes in the iWAT and eWAT of WT mice (Figure 7D). The corresponding depots in the KO mice showed no sign of excess lipid deposition and the iWAT still produced abundant amounts of UCP1 as well as other brown genes (Figures 7D and 7E). Importantly, KO mice were protected from diet-induced inflammation as observed by a reduction in crown-like structures in the eWAT when compared to WT littermates (Figure 7D). Taken together, these results indicate that *MRTFA* deficiency reduces HFD-induced obesity, insulin resistance, eWAT inflammation, and hepatic steatosis.

MRTFA Regulates Whole-Body Energy Expenditure

Indirect calorimetry analysis of mice following 6 weeks on high or low fat diets demonstrated that KO mice produced more heat and consumed more oxygen and carbon dioxide (Figures 7F and 7G) without any change in food intake or physical activity compared to WT animals (Figure S6). Measurement of respira-

tory exchange ratio (RER) following the 6 weeks on LFD revealed that KO mice expended significantly larger amounts of carbohydrate than WT mice during the dark period with both sets of mice switching equally to fat expenditure during the day light (Figure 7G). As expected, KO and WT mice metabolized predominantly fat throughout the entire night-day-night period on HFD (Figure 7G).

DISCUSSION

There is an urgent need for effective and safe therapeutics to address the complications arising from excessive adipose tissue expansion. Most antiobesity drugs presently available have serious side effects including depression and gastrointestinal maladies (Kang and Park, 2012). Similarly, several of the drugs that treat insulin resistance, type 2 diabetes, and cardiovascular disease, either have life threatening side effects or are minimally effective (Ahmadian et al., 2013; Stein et al., 2013). With the discovery that humans possess metabolically active brown adipose tissue (van der Lans et al., 2013), it has been suggested that increasing BAT mass and/or activity might be an effective anti-obesity therapy (Farmer, 2009). We report here on the identification of a signaling and transcriptional regulatory pathway that, when inhibited in mice, leads to “beiging” of iWAT and protection against diet-induced obesity and insulin resistance.

Various aspects of cell morphology control adipocyte differentiation (Rodríguez Fernández and Ben-Ze'ev, 1989; Spiegelman and Farmer, 1982; Spiegelman and Ginty, 1983). It has recently been shown that cell shape regulates commitment of human MSCs to an adipocyte or osteoblast fate via modulation of RhoA signaling (McBeath et al., 2004). Specifically, dominant-negative RhoA committed hMSCs to the adipogenic lineage, while constitutively active RhoA favored the osteogenic lineage. Our work demonstrates a role for RhoA signaling in controlling the fate of MSCs to an adipogenic versus smooth muscle-like lineage. Furthermore, we demonstrate that BMP7, in contrast to TGFβ suppresses ROCK and *MRTFA*/SRF activity, facilitating commitment to the adipocyte lineage. The mechanisms by which TGFβ family members control ROCK are still poorly understood. In other developmental systems, BMPs activate ROCK and BMP2 for example stimulates osteogenesis in hMSCs via ROCK-activated changes in cytoskeletal tension (Wang et al., 2012c). In fact, our report is one of very few documenting a BMP-associated suppression of the ROCK-actin-*MRTFA* signaling pathway. One potential mechanism for the suppression is a BMP-mediated inhibition of basal TGFβ1 activity, as recently reported for control of cardiac fibrosis (Wang et al., 2012b).

Modulation of *MRTFA* in MSCs highlights its role in regulating BMP7-induced adipocyte formation, but this does not necessarily exclude the participation of other actin-responsive transcription factors, including *MRTFB*. The inhibitory action of *MRTFA* appears to be mediated by its coactivation of SRF because ectopic expression of SRF also attenuates the adipogenic action of BMP7. Studies by Mikkelsen et al. (2010) showed that SRF inhibited the differentiation of 3T3-L1 preadipocytes and recently others demonstrated that MKL1 (*MRTFA*) blocks 3T3-L1 adipogenesis at a step upstream of PPARγ (Nobusue et al., 2014). The precise mechanism by which SRF controls

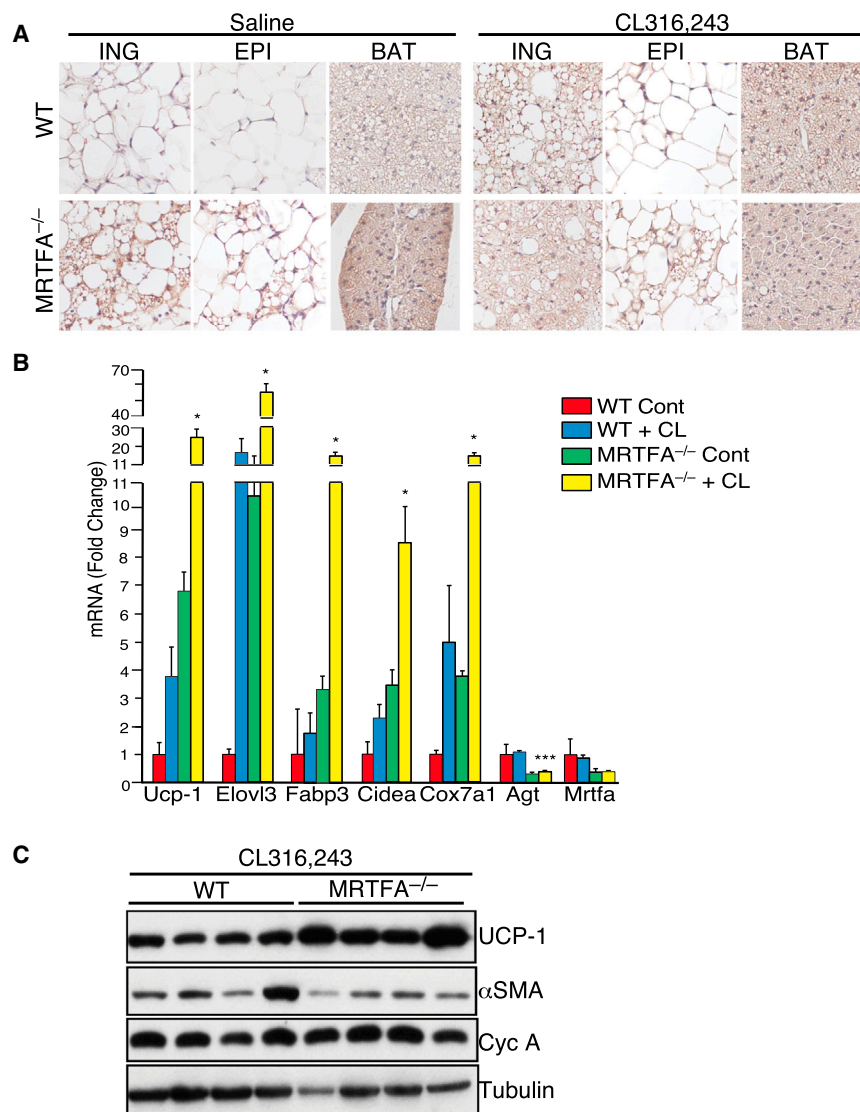


Figure 6. *MRTFA*^{-/-} Mice Are Highly Responsive to β -Adrenergic Signaling, which Enhances Beige Adipocyte Formation in ING WAT

(A) UCP1 immunohistochemistry of representative sections of BAT, ING, and EPI depots of WT and *MRTFA*^{-/-} mice following daily intraperitoneal (i.p.) injections of 1 mg/kg CL316,243 or saline for 7 days.

(B and C) mRNA and protein levels of BAT- and WAT-enriched genes as well as other genes in ING WAT of WT and *MRTFA*^{-/-} mice treated with or without CL316,243 were determined by qPCR (B) and western blot (C), respectively. Data presented mean \pm SEM, $n = 4$, * $p < 0.05$, ** $p < 0.01$.

tissues of the knockout mouse (Li et al., 2006). Interestingly, recent studies have shown a role for BMP signaling in regulating adipose formation through central as well as peripheral actions (Townsend et al., 2012; Whittle et al., 2012). The central actions of the BMPs, however, involve pathways other than the ROCK-MRTFA axis (Townsend et al., 2012; Whittle et al., 2012). Consistent with the action of MRTFA being an autonomous process, cells derived from the SVF of KO iWAT differentiate to beige adipocytes more robustly than WT cells (Figure 5). This could be due to expansion of a pool of beige progenitors in the vascular compartment of *MRTFA*^{-/-} iWAT from various sources including pericytes and/or endothelial cells. In fact, a small set of capillary endothelial cells express the adipogenic commitment factor ZFP423, suggesting a contribution of specialized endothelial cells to the adipose lineage (Gupta et al., 2010,

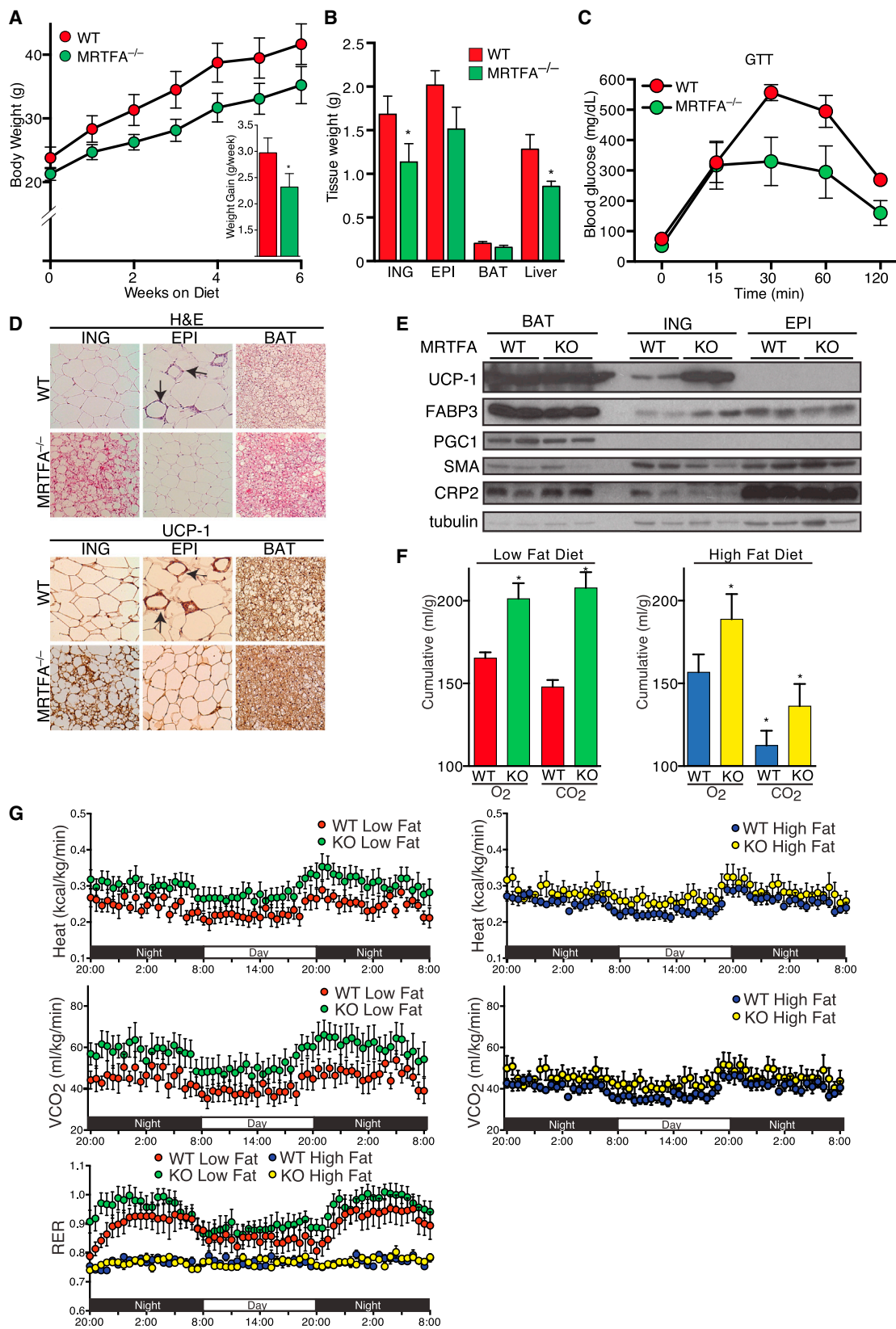
adipogenic commitment might not involve a single target gene/protein but expression of an entire program of genes coding for extracellular matrix and cytoskeleton. Such a process would facilitate extensive cell spreading, which is known to attenuate adipocyte formation (Spiegelman and Ginty, 1983).

The appearance of UCP1+ adipocytes in iWAT of KO mice suggests a role for suppression of MRTF/SRF activity in the development of beige adipocytes. Other studies have demonstrated that disruption of TGF β signaling in mice similarly enhances beige adipocyte formation in WAT (Yadav et al., 2011). The MRTFA-associated browning of iWAT likely arises through recruitment of beige progenitors, as opposed to transdifferentiation of mature white adipocytes (Barbatelli et al., 2010; Wu et al., 2012, 2013). In fact, iWAT of KO mice express high levels of Tbx1 (Figure 4E), supporting a mechanism of de novo generation of beige adipocytes.

Formation of beige adipocytes could arise from crosstalk between adipose and other organs because MRTFA is absent in all

2012). Furthermore, lineage tracing studies identified vascular endothelial cells as progenitors of both white and brown adipocytes (Tran et al., 2012). Such endothelial progenitors would need to undergo endothelial-mesenchymal transition (End-MT) prior to further adipogenic differentiation. In fact, BMP/TGF β signaling has been linked to End-MT (Maddaluno et al., 2013; Zeisberg et al., 2007), raising the possibility that MRTFA could be functioning at such an early stage of adipogenic lineage commitment.

Until recently, it was difficult to establish a role for beige adipocytes in controlling energy expenditure (EE) from the dominant role played by BAT. In fact, Shabalina et al. (2013) have argued that brite/beige adipocytes have a minimal contribution to EE because the level of UCP1 expression in these cells is too low. Cohen et al. (2014) have demonstrated that absence of beige adipocyte development in mice leads to DIO and insulin resistance without any detectable change in BAT development or activity; highlighting the potential importance of beige adipose in



(legend on next page)

energy balance. Our findings support the concept that beige adipocytes perform a physiological role because lack of MRTFA facilitated beige cell development without any significant effect on BAT activity based on minimal change in BAT mass, morphology, or UCP1 expression (Figure 4).

Our studies have uncovered a regulatory pathway that attenuates the antiadipogenic activity of MRTFA/SRF leading preferentially to beige adipocyte formation in iWAT. We suggest that this pathway directs the commitment of adipose stroma progenitors to beige adipocyte over vascular lineages. Small molecules that suppress MRTFA/SRF activity might lead to the development of effective therapeutics to combat obesity-associated comorbidities.

EXPERIMENTAL PROCEDURES

Animals

MRTFA^{+/-} mice (mixed C57BL/6J 129 genetic background) were a gift from Dr. Eric Olson, UT Southwestern Medical Center (Li et al., 2006). Mice were housed at 23°C in a 12 hr light/dark cycle with free access to normal chow. All experiments used matched littermates. Experimental procedures were approved by the Boston University Institutional Animal Care and Use Committee.

High-Fat Feeding and β -Adrenergic Stimulation

For diet studies, 4- to 6-week-old male WT and *MRTFA*^{-/-} mice were fed a diet with 10% kcal% fat (low fat diet, Research Diets, D12450B) or diet with 60% kcal% fat (high-fat diet, Research Diets, D12492) for 6 weeks. For β -adrenergic stimulation, 14-week-old male WT and *MRTFA*^{-/-} mice were intraperitoneally (i.p.) injected daily for 7 days with 1 mg/kg CL316,243 (Sigma-Aldrich) or vehicle.

Histology

Fat pads were fixed in 10% formalin, paraffin-embedded, and sectioned (7 μ m) prior to hematoxylin and eosin (H&E) staining or immunohistochemistry for UCP1 (Abcam; 1:100). Signal was detected using the Vector ABC Elite kit.

Indirect Calorimetry and Body Composition

Animals were individually housed in metabolic chambers maintained at 20°C–24°C on a 12-hr light/12 hr dark cycle. Heat, VO_2 , VCO_2 , and RER were measured continuously using CLAMS consisting of open circuit calorimeter and motion detectors. Body composition was measured by noninvasive quantitative MRI (EchoMRI700).

Glucose Tolerance Tests

Mice were fasted for 14 hr then blood glucose was measured (Bayer Contour) by tail bleeding at 0, 15, 30, 60, and 120 min after an injection of glucose (2 mg/kg body weight).

Serum Leptin and Adiponectin

Mice were euthanized, and serum, obtained from heart blood using serum separation tubes (BD), was analyzed using mouse leptin (Millipore EMD) and total and HMW adiponectin mouse adiponectin (ALPCO) ELISA kits.

Adipose Tissue Fractionation and Culture of Stromal Vascular Cells

Inguinal fat pads were dissected from male mice, digested in collagenase, filtered through a 100 μ m mesh, and centrifuged at 500 $\times g$ to isolate stromal vascular cells for differentiation as outlined for C3H/10T1/2 cells stated below.

Cell Culture

Preconfluent C3H/10T1/2 cells (ATCC) were treated with 6.3 nM rhBMP7 or 1 nM rhTGF β 1 (R&D Systems) for 3 days. The confluent cells were induced to differentiate in 10% FBS, 5 μ M dexamethasone, 0.5 mM isobutylmethylxanthine, 860 nM insulin, 1 nM 3,3,5-triiodo-L-thyronine (T3), and 125 μ M indomethacin. Two days after induction, cells were maintained in 10% FBS, insulin, and T3 for 6 days. Cells were treated with recombinant Gremlin1 (R&D) and the small molecule inhibitors Y27632, PD169316, SB341542 (Sigma), DMH1 (Tocris), or CCG1423 (Cayman) as described in the legends of Figures 1 and 2. Mouse bone marrow-derived MSCs were obtained from Life Technologies.

Plasmids and Viruses

MRTFA and SRF cDNAs (Chang et al., 2003; Luchsinger et al., 2011) were subcloned into the pMSCV retroviral vector and packaged using EcoPack cells (Clontech). Cells were incubated with viral supernatants supplemented with 10 μ g/ml polybrene and selected with hygromycin.

Gene Expression Analysis

Total RNA was isolated from cells or tissues using TRIzol reagent (Life Technologies). Gene expression was performed using an Applied Biosystems cDNA kit and Maxima SYBR Green qPCR Master Mix (Fermentas) as described (Pino et al., 2012). Primer sequences are provided in Table S1.

Western Blot Analysis

Total cellular protein was extracted and subjected to western blot analysis as described (Vernochet et al., 2009) using antibodies listed in Table S2.

Oil Red O and Nile Red Staining

Oil Red O staining was as described (Vernochet et al., 2010). Coverslips were stained with Nile Red for 20 min at room temperature.

Phalloidin/DNase I Staining

Cells on gelatin-coated coverslips were fixed in formaldehyde, permeabilized and stained in Alexa Fluor 488 Phalloidin and/or Deoxyribonuclease I Alexa Fluor 594 (Molecular Probes).

G-Actin/F-Actin Assay

Relative G-actin/F-actin ratio was assessed using the G-actin/F-actin assay kit (Cytoskeleton) according to the manufacturer's directions with minor modifications.

Figure 7. MRTFA-Deficient Mice Are Protected from Diet-Induced Obesity and Its Associated Insulin Resistance and Exhibit Altered Whole-Body Energy Expenditure

(A and B) WT and *MRTFA*^{-/-} mice, starting from 4- to 5-week-old, were fed a rodent HFD (60% kcal% fat) for 6 weeks. Body weight and weight gain were measured in weekly intervals (A), while weights of ING WAT, EPI WAT, BAT, and liver were measured at end of study (B).

(C) After 5 weeks on the HFD, mice were then i.p. injected with glucose at 2 mg/kg of body weight after fasting overnight and whole-blood glucose was measured at 15, 30, 60, and 120 min.

(D) H&E and UCP1 staining of sections of ING, EPI, and BAT depots.

(E) Western blot analysis of BAT- and WAT-enriched genes as well as other genes in WAT and BAT depots of WT and *MRTFA*^{-/-} mice were conducted as in Figure 4. Arrows point to crown-like structures. Data presented are mean \pm SEM, $n = 6$ –7/group, * $p < 0.05$, ** $p < 0.01$.

(F and G) WT and *MRTFA*^{-/-} mice on LFD or HFD for 6 weeks were housed individually in metabolic chambers for 3 days and 2 nights. Cumulative O_2 consumption and CO_2 production were measured by CLAMS (F). Traces of heat production, CO_2 production, and respiratory exchange ratio (RER) during 12 hr dark and light cycles (G). Respiratory exchange ratio (RER) were calculated by volume of carbon dioxide produced (exhaled)/volume of oxygen consumed (inhaled). Data presented are mean \pm SEM, $n = 5$ –7/group, * $p < 0.05$.

See also Figures S5 and S6.

Statistical Analysis

Results are presented as mean \pm SEM. Statistical differences were determined by a Student's two-tailed t test with equal variance or paired. Significance was considered as $p \leq 0.05$.

SUPPLEMENTAL INFORMATION

Supplemental Information includes six figures and two tables can be found with this article online at <http://dx.doi.org/10.1016/j.cell.2014.12.005>.

AUTHOR CONTRIBUTIONS

S.R.F., M.D.L., M.E.M., and C.L. conceived of the project. S.R.F., M.D.L., M.E.M., C.L., and H.B. designed the experiments. M.E.M. performed the experiments in Figures 1 and 2. C.L. performed the experiments in Figures 4, 5, 6, and 7. H.B. performed the experiments in Figure 3. B.D.S. provided scientific and technical advice. S.R.F., M.E.M., and M.D.L. wrote the manuscript. All authors edited the manuscript.

ACKNOWLEDGMENTS

We are grateful to Eric Olson, UT Southwestern Medical Center, TX for the MRTFA^{+/−} mice. We thank Tom Balon of the Mouse Phenotyping Core for his advice and assistance. This work was supported by NIH grants DK051586, DK098830 (S.R.F.), and HL078869, BNORC pilot grant P30 DK046200 (M.D.L.), and Scleroderma Foundation Research Grant (B.D.S.).

Received: November 21, 2013

Revised: September 17, 2014

Accepted: November 19, 2014

Published: January 8, 2015

REFERENCES

- Ahmadian, M., Suh, J.M., Hah, N., Liddle, C., Atkins, A.R., Downes, M., and Evans, R.M. (2013). PPAR γ signaling and metabolism: the good, the bad and the future. *Nat. Med.* 19, 557–566.
- Ahrens, M., Ankenbauer, T., Schröder, D., Hollnagel, A., Mayer, H., and Gross, G. (1993). Expression of human bone morphogenetic proteins-2 or -4 in murine mesenchymal progenitor C3H10T1/2 cells induces differentiation into distinct mesenchymal cell lineages. *DNA Cell Biol.* 12, 871–880.
- Atit, R., Sgaier, S.K., Mohamed, O.A., Taketo, M.M., Dufort, D., Joyner, A.L., Niswander, L., and Conlon, R.A. (2006). β -catenin activation is necessary and sufficient to specify the dorsal dermal fate in the mouse. *Dev. Biol.* 296, 164–176.
- Barbatelli, G., Murano, I., Madsen, L., Hao, Q., Jimenez, M., Kristiansen, K., Giacobino, J.P., De Matteis, R., and Cinti, S. (2010). The emergence of cold-induced brown adipocytes in mouse white fat depots is determined predominantly by white to brown adipocyte transdifferentiation. *Am. J. Physiol. Endocrinol. Metab.* 298, E1244–E1253.
- Bordicchia, M., Liu, D., Amri, E.Z., Ailhaud, G., Dessi-Fulgheri, P., Zhang, C., Takahashi, N., Sarzani, R., and Collins, S. (2012). Cardiac natriuretic peptides act via p38 MAPK to induce the brown fat thermogenic program in mouse and human adipocytes. *J. Clin. Invest.* 122, 1022–1036.
- Boström, P., Wu, J., Jedrychowski, M.P., Korde, A., Ye, L., Lo, J.C., Rasbach, K.A., Boström, E.A., Choi, J.H., Long, J.Z., et al. (2012). A PGC-1 α -dependent myokine that drives brown-fat-like development of white fat and thermogenesis. *Nature* 481, 463–468.
- Bowers, R.R., and Lane, M.D. (2007). A role for bone morphogenetic protein-4 in adipocyte development. *Cell Cycle* 6, 385–389.
- Cannon, B., and Nedergaard, J. (2004). Brown adipose tissue: function and physiological significance. *Physiol. Rev.* 84, 277–359.
- Chang, Y.F., Wei, J., Liu, X., Chen, Y.H., Layne, M.D., and Yet, S.F. (2003). Identification of a CAR γ -independent region of the cysteine-rich protein 2 promoter that directs expression in the developing vasculature. *Am. J. Physiol. Heart Circ. Physiol.* 285, H1675–H1683.
- Choy, L., and Derynck, R. (2003). Transforming growth factor- β inhibits adipocyte differentiation by Smad3 interacting with CCAAT/enhancer-binding protein (C/EBP) and repressing C/EBP transactivation function. *J. Biol. Chem.* 278, 9609–9619.
- Cohen, P., Levy, J.D., Zhang, Y., Frontini, A., Kolodin, D.P., Svensson, K.J., Lo, J.C., Zeng, X., Ye, L., Khandekar, M.J., et al. (2014). Ablation of PRDM16 and beige adipose causes metabolic dysfunction and a subcutaneous to visceral fat switch. *Cell* 156, 304–316.
- Collins, S., Daniel, K.W., Petro, A.E., and Surwit, R.S. (1997). Strain-specific response to β 3-adrenergic receptor agonist treatment of diet-induced obesity in mice. *Endocrinology* 138, 405–413.
- Cousin, B., Cinti, S., Morroni, M., Raimbault, S., Ricquier, D., Pénicaud, L., and Casteilla, L. (1992). Occurrence of brown adipocytes in rat white adipose tissue: molecular and morphological characterization. *J. Cell Sci.* 103, 931–942.
- Cousin, B., Bascands-Viguerie, N., Kassis, N., Nibbelink, M., Ambid, L., Casteilla, L., and Pénicaud, L. (1996). Cellular changes during cold acclimation in adipose tissues. *J. Cell. Physiol.* 167, 285–289.
- Enerbäck, S. (2009). The origins of brown adipose tissue. *N. Engl. J. Med.* 360, 2021–2023.
- Evelyn, C.R., Wade, S.M., Wang, Q., Wu, M., Iñiguez-Lluhi, J.A., Merajver, S.D., and Neubig, R.R. (2007). CCG-1423: a small-molecule inhibitor of RhoA transcriptional signaling. *Mol. Cancer Ther.* 6, 2249–2260.
- Farmer, S.R. (2009). Obesity: Be cool, lose weight. *Nature* 458, 839–840.
- Fisher, F.M., Kleiner, S., Douris, N., Fox, E.C., Mepani, R.J., Verdeguer, F., Wu, J., Kharitonov, A., Flier, J.S., Maratos-Flier, E., and Spiegelman, B.M. (2012). FGF21 regulates PGC-1 α and browning of white adipose tissues in adaptive thermogenesis. *Genes Dev.* 26, 271–281.
- Ghorbani, M., and Himms-Hagen, J. (1997). Appearance of brown adipocytes in white adipose tissue during CL 316,243-induced reversal of obesity and diabetes in Zucker fa/fa rats. *Int. J. Obes. Relat. Metab. Disord.* 21, 465–475.
- Granneman, J.G., Li, P., Zhu, Z., and Lu, Y. (2005). Metabolic and cellular plasticity in white adipose tissue I: effects of β 3-adrenergic receptor activation. *Am. J. Physiol. Endocrinol. Metab.* 289, E608–E616.
- Guerra, C., Koza, R.A., Yamashita, H., Walsh, K., and Kozak, L.P. (1998). Emergence of brown adipocytes in white fat in mice is under genetic control. Effects on body weight and adiposity. *J. Clin. Invest.* 102, 412–420.
- Gupta, R.K., Arany, Z., Seale, P., Mepani, R.J., Ye, L., Conroe, H.M., Roby, Y.A., Kulaga, H., Reed, R.R., and Spiegelman, B.M. (2010). Transcriptional control of preadipocyte determination by Zfp423. *Nature* 464, 619–623.
- Gupta, R.K., Mepani, R.J., Kleiner, S., Lo, J.C., Khandekar, M.J., Cohen, P., Frontini, A., Bhowmick, D.C., Ye, L., Cinti, S., and Spiegelman, B.M. (2012). Zfp423 expression identifies committed preadipocytes and localizes to adipose endothelial and perivascular cells. *Cell Metab.* 15, 230–239.
- Hautmann, M.B., Madsen, C.S., and Owens, G.K. (1997). A transforming growth factor β (TGF β) control element drives TGF β -induced stimulation of smooth muscle α -actin gene expression in concert with two CAR γ elements. *J. Biol. Chem.* 272, 10948–10956.
- Himms-Hagen, J., Melnyk, A., Zingaretti, M.C., Ceresi, E., Barbatelli, G., and Cinti, S. (2000). Multilocular fat cells in WAT of CL-316243-treated rats derive directly from white adipocytes. *Am. J. Physiol. Cell Physiol.* 279, C670–C681.
- Hsu, D.R., Economides, A.N., Wang, X., Eimon, P.M., and Harland, R.M. (1998). The *Xenopus* dorsalizing factor Gremlin identifies a novel family of secreted proteins that antagonize BMP activities. *Mol. Cell* 1, 673–683.
- Ishibashi, J., and Seale, P. (2010). Medicine. Beige can be slimming. *Science* 328, 1113–1114.
- Jakobsson, L., and van Meeteren, L.A. (2013). Transforming growth factor β family members in regulation of vascular function: in the light of vascular conditional knockouts. *Exp. Cell Res.* 319, 1264–1270.
- Jimenez, M., Barbatelli, G., Allevi, R., Cinti, S., Seydoux, J., Giacobino, J.P., Muzzin, P., and Preitner, F. (2003). β 3-adrenoceptor knockout in C57BL/6J mice depresses the occurrence of brown adipocytes in white fat. *Eur. J. Biochem.* 270, 699–705.

- Kang, J.G., and Park, C.Y. (2012). Anti-obesity drugs: a review about their effects and safety. *Diabetes Metab. J.* 36, 13–25.
- Lee, Y.H., Petkova, A.P., Mottillo, E.P., and Granneman, J.G. (2012). In vivo identification of bipotential adipocyte progenitors recruited by β 3-adrenoceptor activation and high-fat feeding. *Cell Metab.* 15, 480–491.
- Li, S., Chang, S., Qi, X., Richardson, J.A., and Olson, E.N. (2006). Requirement of a myocardin-related transcription factor for development of mammary myoepithelial cells. *Mol. Cell. Biol.* 26, 5797–5808.
- Li, J., Bowens, N., Cheng, L., Zhu, X., Chen, M., Hannehalli, S., Cappola, T.P., and Parmacek, M.S. (2012). Myocardin-like protein 2 regulates TGF β signaling in embryonic stem cells and the developing vasculature. *Development* 139, 3531–3542.
- Loncar, D. (1991a). Convertible adipose tissue in mice. *Cell Tissue Res.* 266, 149–161.
- Loncar, D. (1991b). Development of thermogenic adipose tissue. *Int. J. Dev. Biol.* 35, 321–333.
- Long, J.Z., Svensson, K.J., Tsai, L., Zeng, X., Roh, H.C., Kong, X., Rao, R.R., Lou, J., Lokurkar, I., Baur, W., et al. (2014). A smooth muscle-like origin for beige adipocytes. *Cell Metab.* 19, 810–820.
- Luchsinger, L.L., Patenaude, C.A., Smith, B.D., and Layne, M.D. (2011). Myocardin-related transcription factor-A complexes activate type I collagen expression in lung fibroblasts. *J. Biol. Chem.* 286, 44116–44125.
- Maddaluno, L., Rudini, N., Cuttano, R., Bravi, L., Giampietro, C., Corada, M., Ferrarini, L., Orsenigo, F., Papa, E., Boulday, G., et al. (2013). EndMT contributes to the onset and progression of cerebral cavernous malformations. *Nature* 498, 492–496.
- McBeath, R., Pirone, D.M., Nelson, C.M., Bhadriraju, K., and Chen, C.S. (2004). Cell shape, cytoskeletal tension, and RhoA regulate stem cell lineage commitment. *Dev. Cell* 6, 483–495.
- Mikkelsen, T.S., Xu, Z., Zhang, X., Wang, L., Gimble, J.M., Lander, E.S., and Rosen, E.D. (2010). Comparative epigenomic analysis of murine and human adipogenesis. *Cell* 143, 156–169.
- Miralles, F., Posern, G., Zaromytidou, A.I., and Treisman, R. (2003). Actin dynamics control SRF activity by regulation of its coactivator MAL. *Cell* 113, 329–342.
- Moustakas, A., and Heldin, C.H. (2008). Dynamic control of TGF- β signaling and its links to the cytoskeleton. *FEBS Lett.* 582, 2051–2065.
- Nagase, I., Yoshida, T., Kumamoto, K., Umekawa, T., Sakane, N., Nikami, H., Kawada, T., and Saito, M. (1996). Expression of uncoupling protein in skeletal muscle and white fat of obese mice treated with thermogenic β 3-adrenergic agonist. *J. Clin. Invest.* 97, 2898–2904.
- Nedergaard, J., Ricquier, D., and Kozak, L.P. (2005). Uncoupling proteins: current status and therapeutic prospects. *EMBO Rep.* 6, 917–921.
- Nobusue, H., Onishi, N., Shimizu, T., Sugihara, E., Oki, Y., Sumikawa, Y., Chiyoda, T., Akashi, K., Saya, H., and Kano, K. (2014). Regulation of MKL1 via actin cytoskeleton dynamics drives adipocyte differentiation. *Nat. Commun.* 5, 3368.
- Olson, E.N., and Nordheim, A. (2010). Linking actin dynamics and gene transcription to drive cellular motile functions. *Nat. Rev. Mol. Cell Biol.* 11, 353–365.
- Patel-Hett, S., and D'Amore, P.A. (2011). Signal transduction in vasculogenesis and developmental angiogenesis. *Int. J. Dev. Biol.* 55, 353–363.
- Petrovic, N., Walden, T.B., Shabalina, I.G., Timmons, J.A., Cannon, B., and Nedergaard, J. (2010). Chronic peroxisome proliferator-activated receptor γ (PPAR γ) activation of epididymally derived white adipocyte cultures reveals a population of thermogenically competent, UCP1-containing adipocytes molecularly distinct from classic brown adipocytes. *J. Biol. Chem.* 285, 7153–7164.
- Pino, E., Wang, H., McDonald, M.E., Qiang, L., and Farmer, S.R. (2012). Roles for peroxisome proliferator-activated receptor γ (PPAR γ) and PPAR γ coactivators 1 α and 1 β in regulating response of white and brown adipocytes to hypoxia. *J. Biol. Chem.* 287, 18351–18358.
- Posern, G., and Treisman, R. (2006). Actin' together: serum response factor, its cofactors and the link to signal transduction. *Trends Cell Biol.* 16, 588–596.
- Qian, S.W., Tang, Y., Li, X., Liu, Y., Zhang, Y.Y., Huang, H.Y., Xue, R.D., Yu, H.Y., Guo, L., Gao, H.D., et al. (2013). BMP4-mediated brown fat-like changes in white adipose tissue alter glucose and energy homeostasis. *Proc. Natl. Acad. Sci. USA* 110, E798–E807.
- Rodeheffer, M.S., Birsoy, K., and Friedman, J.M. (2008). Identification of white adipocyte progenitor cells in vivo. *Cell* 135, 240–249.
- Rodríguez Fernández, J.L., and Ben-Ze'ev, A. (1989). Regulation of fibronectin, integrin and cytoskeleton expression in differentiating adipocytes: inhibition by extracellular matrix and polylysine. *Differentiation* 42, 65–74.
- Rosenwald, M., Perdikari, A., Rülcke, T., and Wolfrum, C. (2013). Bi-directional interconversion of brite and white adipocytes. *Nat. Cell Biol.* 15, 659–667.
- Schofield, A.V., and Bernard, O. (2013). Rho-associated coiled-coil kinase (ROCK) signaling and disease. *Crit. Rev. Biochem. Mol. Biol.* 48, 301–316.
- Schulz, T.J., and Tseng, Y.H. (2009). Emerging role of bone morphogenetic proteins in adipogenesis and energy metabolism. *Cytokine Growth Factor Rev.* 20, 523–531.
- Schulz, T.J., Huang, T.L., Tran, T.T., Zhang, H., Townsend, K.L., Shadrach, J.L., Cerletti, M., McDougall, L.E., Giorgadze, N., Tchkonja, T., et al. (2011). Identification of inducible brown adipocyte progenitors residing in skeletal muscle and white fat. *Proc. Natl. Acad. Sci. USA* 108, 143–148.
- Seale, P., Bjork, B., Yang, W., Kajimura, S., Chin, S., Kuang, S., Scimè, A., Devarakonda, S., Conroe, H.M., Erdjument-Bromage, H., et al. (2008). PRDM16 controls a brown fat/skeletal muscle switch. *Nature* 454, 961–967.
- Shabalina, I.G., Petrovic, N., de Jong, J.M., Kalinovich, A.V., Cannon, B., and Nedergaard, J. (2013). UCP1 in brite/beige adipose tissue mitochondria is functionally thermogenic. *Cell Reports* 5, 1196–1203.
- Sinha, S., Hoofnagle, M.H., Kingston, P.A., McCanna, M.E., and Owens, G.K. (2004). Transforming growth factor- β 1 signaling contributes to development of smooth muscle cells from embryonic stem cells. *Am. J. Physiol. Cell Physiol.* 287, C1560–C1568.
- Sordella, R., Jiang, W., Chen, G.C., Curto, M., and Settlemann, J. (2003). Modulation of Rho GTPase signaling regulates a switch between adipogenesis and myogenesis. *Cell* 113, 147–158.
- Spiegelman, B.M., and Farmer, S.R. (1982). Decreases in tubulin and actin gene expression prior to morphological differentiation of 3T3 adipocytes. *Cell* 29, 53–60.
- Spiegelman, B.M., and Ginty, C.A. (1983). Fibronectin modulation of cell shape and lipogenic gene expression in 3T3-adipocytes. *Cell* 35, 657–666.
- Stein, S.A., Lamos, E.M., and Davis, S.N. (2013). A review of the efficacy and safety of oral antidiabetic drugs. *Expert Opin. Drug Saf.* 12, 153–175.
- Tang, Q.Q., Otto, T.C., and Lane, M.D. (2004). Commitment of C3H10T1/2 pluripotent stem cells to the adipocyte lineage. *Proc. Natl. Acad. Sci. USA* 101, 9607–9611.
- Tang, W., Zeve, D., Suh, J.M., Bosnakovski, D., Kyba, M., Hammer, R.E., Tallquist, M.D., and Graff, J.M. (2008). White fat progenitor cells reside in the adipose vasculature. *Science* 322, 583–586.
- Townsend, K.L., Suzuki, R., Huang, T.L., Jing, E., Schulz, T.J., Lee, K., Taniguchi, C.M., Espinoza, D.O., McDougall, L.E., Zhang, H., et al. (2012). Bone morphogenetic protein 7 (BMP7) reverses obesity and regulates appetite through a central mTOR pathway. *FASEB J.* 26, 2187–2196.
- Tran, K.V., Gealekman, O., Frontini, A., Zingaretti, M.C., Morroni, M., Giodano, A., Smorlesi, A., Perugini, J., De Matteis, R., Sbarbati, A., et al. (2012). The vascular endothelium of the adipose tissue gives rise to both white and brown fat cells. *Cell Metab.* 15, 222–229.
- Tseng, Y.H., Kokkoto, E., Schulz, T.J., Huang, T.L., Winnay, J.N., Taniguchi, C.M., Tran, T.T., Suzuki, R., Espinoza, D.O., Yamamoto, Y., et al. (2008). New role of bone morphogenetic protein 7 in brown adipogenesis and energy expenditure. *Nature* 454, 1000–1004.

- van der Lans, A.A., Hoeks, J., Brans, B., Vijgen, G.H., Visser, M.G., Vosselman, M.J., Hansen, J., Jörgensen, J.A., Wu, J., Mottaghy, F.M., et al. (2013). Cold acclimation recruits human brown fat and increases nonshivering thermogenesis. *J. Clin. Invest.* **123**, 3395–3403.
- Vernochet, C., Peres, S.B., Davis, K.E., McDonald, M.E., Qiang, L., Wang, H., Scherer, P.E., and Farmer, S.R. (2009). C/EBP α and the corepressors CtBP1 and CtBP2 regulate repression of select visceral white adipose genes during induction of the brown phenotype in white adipocytes by peroxisome proliferator-activated receptor γ agonists. *Mol. Cell. Biol.* **29**, 4714–4728.
- Vernochet, C., Davis, K.E., Scherer, P.E., and Farmer, S.R. (2010). Mechanisms regulating repression of haptoglobin production by peroxisome proliferator-activated receptor- γ ligands in adipocytes. *Endocrinology* **151**, 586–594.
- Wang, E.A., Israel, D.I., Kelly, S., and Luxenberg, D.P. (1993). Bone morphogenetic protein-2 causes commitment and differentiation in C3H10T1/2 and 3T3 cells. *Growth Factors* **9**, 57–71.
- Wang, C.J., Yang, K.D., Ko, J.Y., Huang, C.C., Huang, H.Y., and Wang, F.S. (2009). The effects of shockwave on bone healing and systemic concentrations of nitric oxide (NO), TGF- β 1, VEGF and BMP-2 in long bone non-unions. *Nitric Oxide* **20**, 298–303.
- Wang, C., Yin, S., Cen, L., Liu, Q., Liu, W., Cao, Y., and Cui, L. (2010). Differentiation of adipose-derived stem cells into contractile smooth muscle cells induced by transforming growth factor- β 1 and bone morphogenetic protein-4. *Tissue Eng. Part A* **16**, 1201–1213.
- Wang, D., Prakash, J., Nguyen, P., Davis-Dusenbery, B.N., Hill, N.S., Layne, M.D., Hata, A., and Lagna, G. (2012a). Bone morphogenetic protein signaling in vascular disease: anti-inflammatory action through myocardin-related transcription factor A. *J. Biol. Chem.* **287**, 28067–28077.
- Wang, S., Sun, A., Li, L., Zhao, G., Jia, J., Wang, K., Ge, J., and Zou, Y. (2012b). Up-regulation of BMP-2 antagonizes TGF- β 1/ROCK-enhanced cardiac fibrotic signalling through activation of Smurf1/Smad6 complex. *J. Cell. Mol. Med.* **16**, 2301–2310.
- Wang, Y.K., Yu, X., Cohen, D.M., Wozniak, M.A., Yang, M.T., Gao, L., Eyckmans, J., and Chen, C.S. (2012c). Bone morphogenetic protein-2-induced signaling and osteogenesis is regulated by cell shape, RhoA/ROCK, and cytoskeletal tension. *Stem Cells Dev.* **21**, 1176–1186.
- Wang, Q.A., Tao, C., Gupta, R.K., and Scherer, P.E. (2013). Tracking adipogenesis during white adipose tissue development, expansion and regeneration. *Nat. Med.* **19**, 1338–1344.
- Whittle, A.J., Carobbio, S., Martins, L., Slawik, M., Hondares, E., Vázquez, M.J., Morgan, D., Csikasz, R.I., Gallego, R., Rodriguez-Cuenca, S., et al. (2012). BMP8B increases brown adipose tissue thermogenesis through both central and peripheral actions. *Cell* **149**, 871–885.
- Wilson-Fritch, L., Nicoloso, S., Chouinard, M., Lazar, M.A., Chui, P.C., Leszyk, J., Straubhaar, J., Czech, M.P., and Corvera, S. (2004). Mitochondrial remodeling in adipose tissue associated with obesity and treatment with rosiglitazone. *J. Clin. Invest.* **114**, 1281–1289.
- Wu, J., Boström, P., Sparks, L.M., Ye, L., Choi, J.H., Giang, A.-H., Khandekar, M., Virtanen, K.A., Nuutila, P., Schaart, G., et al. (2012). Beige adipocytes are a distinct type of thermogenic fat cell in mouse and human. *Cell* **150**, 366–376.
- Wu, J., Cohen, P., and Spiegelman, B.M. (2013). Adaptive thermogenesis in adipocytes: is beige the new brown? *Genes Dev.* **27**, 234–250.
- Xue, B., Coulter, A., Rim, J.S., Koza, R.A., and Kozak, L.P. (2005). Transcriptional synergy and the regulation of Ucp1 during brown adipocyte induction in white fat depots. *Mol. Cell. Biol.* **25**, 8311–8322.
- Yadav, H., Quijano, C., Kamaraju, A.K., Gavrilova, O., Malek, R., Chen, W., Zervas, P., Zhigang, D., Wright, E.C., Stuelten, C., et al. (2011). Protection from obesity and diabetes by blockade of TGF- β /Smad3 signaling. *Cell Metab.* **14**, 67–79.
- Young, P., Arch, J.R., and Ashwell, M. (1984). Brown adipose tissue in the parametrial fat pad of the mouse. *FEBS Lett.* **167**, 10–14.
- Zeisberg, E.M., Potenta, S., Xie, L., Zeisberg, M., and Kalluri, R. (2007). Discovery of endothelial to mesenchymal transition as a source for carcinoma-associated fibroblasts. *Cancer Res.* **67**, 10123–10128.
- Zingaretti, M.C., Crosta, F., Vitali, A., Guerrieri, M., Frontini, A., Cannon, B., Nedergaard, J., and Cinti, S. (2009). The presence of UCP1 demonstrates that metabolically active adipose tissue in the neck of adult humans truly represents brown adipose tissue. *FASEB J.* **23**, 3113–3120.

Kynurenic Acid Is a Nutritional Cue that Enables Behavioral Plasticity

George A. Lemieux,¹ Katherine A. Cunningham,¹ Lin Lin,¹ Fahima Mayer,¹ Zena Werb,² and Kaveh Ashrafi^{1,*}

¹Department of Physiology, University of California, San Francisco, San Francisco, CA 94158-2240, USA

²Department of Anatomy, University of California, San Francisco, San Francisco, CA 94143-0452, USA

*Correspondence: kaveh.ashrafi@ucsf.edu

<http://dx.doi.org/10.1016/j.cell.2014.12.028>

SUMMARY

The kynurenine pathway of tryptophan metabolism is involved in the pathogenesis of several brain diseases, but its physiological functions remain unclear. We report that kynurenic acid, a metabolite in this pathway, functions as a regulator of food-dependent behavioral plasticity in *C. elegans*. The experience of fasting in *C. elegans* alters a variety of behaviors, including feeding rate, when food is encountered post-fast. Levels of neurally produced kynurenic acid are depleted by fasting, leading to activation of NMDA-receptor-expressing interneurons and initiation of a neuropeptide-y-like signaling axis that promotes elevated feeding through enhanced serotonin release when animals re-encounter food. Upon refeeding, kynurenic acid levels are eventually replenished, ending the elevated feeding period. Because tryptophan is an essential amino acid, these findings suggest that a physiological role of kynurenic acid is in directly linking metabolism to activity of NMDA and serotonergic circuits, which regulate a broad range of behaviors and physiologies.

INTRODUCTION

Imbalances in brain levels of metabolites derived from tryptophan degradation via the kynurenine pathway (KP) have been linked to a variety of neurodegenerative and psychiatric disorders (Schwarcz et al., 2012). Altered brain or cerebrospinal fluid levels of kynurenic acid (KynA) and/or quinolinic acid are associated with schizophrenia (Erhardt et al., 2001; Schwarcz et al., 2001), Alzheimer's, and Huntington's diseases (Beal et al., 1992; Heyes et al., 1992) and depression (Steiner et al., 2011; Erhardt et al., 2013). Genetic and pharmacological blockade of the KP ameliorates neurodegeneration and protein aggregation in diverse model organisms (Campean et al., 2011; Zwillling et al., 2011; van der Goot et al., 2012), whereas the beneficial effects of exercise on symptoms of depression have been attributed to altered peripheral KP metabolism (Agudelo et al., 2014). Despite these associations, the physiological regulation of brain levels of

KP metabolites and their normal physiological roles remain ill defined.

Several intermediates of the KP have distinct neuro- and immune-modulatory functions. For example, KynA inhibits and quinolinic acid activates glutamatergic neurotransmission (Perkins and Stone, 1982; Hilmas et al., 2001), leading to the suggestion that the associations of the KP with CNS disorders derive from modulation of glutamate excitotoxicity (Andiné et al., 1988; Carpenedo et al., 2001; Foster et al., 1984). Additionally, the serotonin-kynurenine hypothesis of depression advanced the idea that dysregulated shunting of tryptophan through the KP negatively impacts serotonin levels (Lapin and Oxenkrug, 1969). However, direct physiological evidence of KP metabolic competition limiting serotonin biosynthesis has been lacking.

C. elegans display food-related behavioral plasticity (Sengupta, 2013; Douglas et al., 2005). For example, when *C. elegans* deplete their local food source, they reduce their food intake behavior and increase their locomotory rate to forage for food, behaviors that depend on changes in serotonin signaling (Avery and Horvitz, 1990; Sawin et al., 2000; Hills et al., 2004). Upon encountering a new food source, *C. elegans* resume their ad libitum feeding and movement rates. However, if *C. elegans* experience a period of fasting before encountering food, they temporarily increase their feeding rate and slow their movement beyond the levels seen in ad-libitum-fed animals once they are back on food (Avery and Horvitz, 1990; Sawin et al., 2000). These behaviors presumably allow food-deprived animals to consume more food and rapidly recover physiologic functions post-fast. How the experience of fasting further modulates responses to food is poorly understood.

Here, we show that KynA serves as an internal gauge of nutrient availability to modulate feeding behavior in *C. elegans*. Depletion of KynA during fasting from the nervous system is required for the hyperactivation of feeding in *C. elegans* when they re-encounter food. Feeding then leads to replenishment of the KynA, ending the hyperactive feeding state. KynA depletion is sensed by neurons that express NMDA-type ionotropic glutamate receptors (NMDA-r) whose activity is communicated to serotonergic sensory neurons via a neuropeptide signaling axis. Given that many of the regulatory modules discovered in the context of *C. elegans* feeding behavior are conserved in the mammalian brain, the role of KynA as a neurally produced gauge of the peripheral metabolic state that controls serotonin signaling is likely to be well conserved.

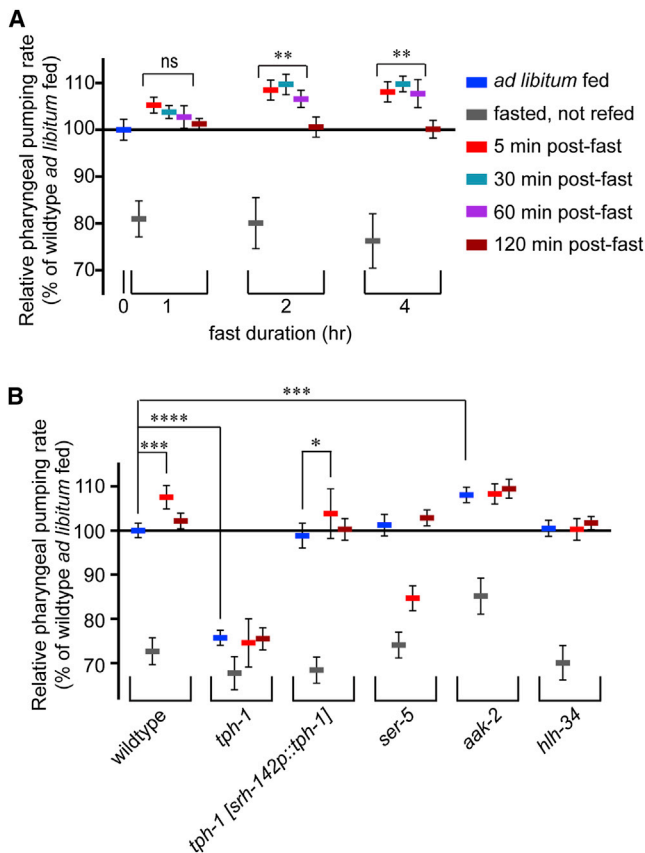


Figure 1. Post-Fast Hyperactive Feeding Requires Serotonin Signaling

(A) Animals were fasted for 1, 2, or 4 hr, and the pharyngeal pumping rate was measured before exposure to food and 5, 30, 60, and 120 min post-fast. To facilitate visualization of data pertaining to changes in pumping rate, all feeding data are presented with the x axis defining the ad-libitum-fed wild-type rate. $n = 10$ –14 animals per condition; ns, $p > 0.05$ and $**p < 0.01$ compared to ad-libitum-fed ANOVA (Dunnett).

(B) Pharyngeal pumping rates of wild-type, mutant, or transgenic animals at the indicated fasting and refeeding periods. $n = 10$ animals per condition. $*p < 0.05$, $***p < 0.001$, and $****p < 0.0001$ ANOVA (Sidak). In (A) and (B), error bars indicate 95% confidence interval (c.i.).

See also Figure S1 and Table S1.

RESULTS

Fasting Induces a Serotonin-Regulated Hyperactive Feeding State upon Food Re-exposure

C. elegans actively ingest food through regular, coordinated muscular contractions of the pharynx that concentrate, disrupt, and pump bacterial food into their intestinal lumens (Avery and You, 2012). The pharyngeal pumping rate correlates with food intake (Avery and Horvitz, 1990; Avery and You, 2012). Except for periods of developmental arrest or larval molts, when cultured on *E. coli* OP50, *C. elegans* exhibit continuous pumping with brief intermittent pauses (Avery and You, 2012; You et al., 2008). *C. elegans* change their pumping rates relative to food availability and the experience of fasting by reducing the rates when fasted, and, as we will describe in detail below, they tempo-

rarily hyperactivate it relative to the ad-libitum-fed state when they are reintroduced to food post-fast (Avery and Horvitz, 1990).

To characterize the post-fast overfeeding behavior, we subjected *C. elegans* to 1, 2, or 4 hr of fasting and measured pumping rates immediately before and after returning to ad libitum access to food for 5, 30, 60, and 120 min (Figure 1A). Each of these fast intervals caused the same extent of reduction in pumping. In turn, all fasted animals resumed rapid pumping upon returning to food. However, upon introduction of food, animals that had fasted for more than 1 hr exhibited hyperactive feeding. This hyperactive feeding state was temporary, persisting for 1 hr before subsiding to ad libitum rates that were intermediate between the depressed fasting rates and the hyperactive rate seen post-fast (Figure 1A). The extent and duration of the overfeeding were not enhanced in animals that had been fasted for 4 hr versus those fasted for 2 hr (Figure 1A). Although in absolute terms the noted changes in pumping rate are small, representing the normal physiologic range of this behavior, the pharyngeal pumping rate is a robustly quantitative trait due to its small variance.

To understand how the post-fast hyperactive feeding state is regulated, we first examined serotonin signaling. Serotonin-deficient *tph-1* mutants exhibit reduced pharyngeal pumping relative to wild-type animals (Sze et al., 2000), and restoration of *tph-1* to only the ADF neurons, a pair of serotonergic head sensory neurons, confers wild-type pumping under ad-libitum-fed conditions (Cunningham et al., 2012) and upregulated pumping in response to familiar food (Song et al., 2013). We found that serotonin deficiency also abrogates fasting-induced hyperactive feeding, which can be partially restored through reconstitution of serotonin biosynthesis in only the ADF neurons (Figure 1B and Table S1 available online). Moreover, the extent of fasting-induced hyperactive feeding was reminiscent of the effects of treatment of well-fed animals with exogenous serotonin or serotonin reuptake inhibitors (Horvitz et al., 1982; Avery and Horvitz, 1990; Srinivasan et al., 2008). Serotonin-induced hyperactive feeding is dependent on the serotonergic GPCR, SER-5, and consequent inactivation of an AMP-activated kinase (AMPK) complex encoded by *aak-2* in a pair of interneurons that selectively express the obesity-associated transcription factor, Sim-1/HLH-34 (pathway summarized in Figure S1A) (Cunningham et al., 2012). Loss-of-function mutants of *ser-5* and *hlh-34* exhibited wild-type pumping rates during the ad-libitum-fed and -fasted states but failed to hyperactivate pumping post-fast (Figure 1B). Consistent with the notion that *aak-2* mutants mimic behaviors of animals with persistently elevated serotonin signaling, their already elevated feeding was not further elevated post-fast (Figure 1B).

To determine whether the observed changes in pumping rate correlated with changes in food ingestion, we assessed the accumulation of BODIPY dye within the intestines of wild-type, *tph-1*, *ser-5*, *hlh-34*, and *aak-2* mutants cultured on the food containing the fluorescent dye. There was a direct correlation between pumping rates of these strains and the extent of BODIPY accumulation (Figure S1B).

A Kynurenine Amino Transferase Functions Upstream of Serotonin to Regulate Feeding

Our findings suggested that, in the context of feeding regulation, serotonin signaling may exist in at least three states: (1) active

signaling in well-fed wild-type animals; (2) reduced signaling upon food removal, a condition mimicked by loss of *tph-1*; and (3) a transiently elevated serotonergic state post-fast, a condition mimicked by *aak-2* mutants. To understand the transient hyperactive pumping state better, we searched for additional mutants with altered pharyngeal pumping and found that *nkat-1(ok566)* loss-of-function mutants exhibited constitutively elevated pumping rates and food ingestion (Figures 2A and S1B). Similar to *aak-2* mutants, *nkat-1* mutants reduced their pharyngeal pumping upon fasting and had elevated feeding rate post-fasting that was not attenuated with continued feeding (Figure 2A). The hyperactive feeding of *nkat-1* deficiency was suppressed in *tph-1*, *ser-5*, and *hlh-34* mutants, whereas the elevated rates of *aak-2* mutants were not further changed by *nkat-1* deficiency (Figure 2B), suggesting that *nkat-1* can function upstream of serotonergic signaling.

NKAT-1 and two other *C. elegans* proteins (NKAT-3 and TATN-1) are homologous to mammalian kynurenine aminotransferases (KATs), which act on kynurenine (Kyn), a key intermediate of the kynurenine pathway (KP). In both *C. elegans* and mammals, Kyn is derived from the irreversible catabolism of tryptophan by tryptophan 2, 3 dioxygenase (Figure 2C). Depending on which enzymes then act on Kyn, it can have three distinct proximal metabolic fates. Kynurenine mono-oxygenase and kynureninase convert Kyn into 3-hydroxy kynurenine (3-HKyn) and anthranilic acid (Ant), respectively, which are further transformed by other enzymes of the KP (Figure 2C) (van der Goot et al., 2012; Stipanuk and Caudill, 2013). Alternatively, as a substrate for KATs, kynurenine is oxidatively deaminated to form KynA, the only known biosynthetic route to this metabolite. To assess the role of KP metabolites in feeding behavior, we developed an HPLC-based assay to measure metabolite levels from whole-animal extracts. Mutants in *nkat-1* contained 50% less KynA than wild-type *C. elegans* fed ad libitum (Figure 2D). Levels of tryptophan and Kyn, the predicted substrate of *nkat-1*, were unchanged relative to wild-type animals, whereas levels of Ant were elevated in *nkat-1* mutants (Figure 2D). Other metabolites downstream of Kyn such as 3-hydroxykynurenine (3-HKyn, Figure 2C) or 3-hydroxyanthranilic acid (data not shown) were not detectable in either wild-type or *nkat-1* mutants in our assay. These findings suggested that NKAT-1 activity contributes to KynA pools and the deficiency in KAT activity may not significantly impact the organismal pool of Kyn substrate because it is 1,000-fold larger than that of KynA.

To determine whether the *nkat-1* pharyngeal pumping phenotype was related to its KynA deficiency, we supplemented the feeding media of *C. elegans* with either 0.1 or 2.5 mM KynA. These supplementations did not reduce the pharyngeal pumping rate of well-fed, wild-type animals on food (Figure 2E) but blocked the hyperactive feeding phenotype of *nkat-1* mutants (Figure 2E), indicating that a deficiency in KynA promotes hyperactive feeding.

KynA Levels Are Responsive to Fasting and Regulate Feeding

Because tryptophan is an essential amino acid in both *C. elegans* and vertebrates (van der Goot and Nollen, 2013), we suspected that nutrient status may affect the tissue pools of the KP metabo-

olites. After 2 hr of fasting, both Kyn and KynA levels declined by 70%, but the decline of the levels of Trp, a 30- to 40-fold larger pool than that of Kyn, did not attain statistical significance, and levels of Ant increased by 40% (Figure 3A). Thus, fasting promotes degradation of kynurenine and a shift from production of KynA to that of Ant. During subsequent refeeding, levels of Kyn and KynA initially remained depressed, but then the levels of KynA and Ant recovered to their pre-fast, ad-libitum-fed state by 2 hr, the same time frame when animals attenuate their hyperactive feeding post-fast. Levels of Kyn at this time point still remained depressed (Figure 3A). As summarized in Figure 3B, these data indicated that, similar to serotonin signaling, KynA levels correlate with three distinct states of feeding behavior: (1) basal ad-libitum-fed state with normal levels of KynA, (2) a fasted state resulting in depressed KynA levels, and (3) a state of depressed KynA when animals encounter food immediately post-fast and exhibit hyperactive feeding. Given ample food supplies, animals in this state eventually return to the ad libitum feeding state.

To understand the influence of KynA in mediating the plasticity between feeding states, we altered KynA levels during different nutritional states. We supplemented basal medium with 100 μ M of either Kyn (the physiological precursor to KynA), KynA, serotonin (5-HT), or 3-HKyn. These metabolite add backs were conducted during the fasting period and pharyngeal pumping rates were measured prior to and after animals were returned to food (Figure 3C). Consistent with the notion that a drop in serotonin signaling underlies the reduced feeding off of food, *C. elegans* treated with 5-HT during the 2 hr fast did not lower their feeding. Nevertheless, when these animals were returned to food (without added 5-HT), they still exhibited hyperactive feeding, indicating that the 5-HT signal of food availability is insufficient to mitigate the impact of fasting on post-fast feeding. Supplementations with KynA, but not Kyn, partially blocked the drop in pumping upon fasting (Figure 3C). Notably, both of these supplementations during the fasted state fully blocked the subsequent hyperactive state without affecting the rapid (within 1–2 min) rise in pumping from the low rates during fasting to the intermediate ad libitum rates upon exposure to food (Figures S2A and 3C). Treatment of fasting *C. elegans* with 3-HKyn, a metabolite irreversibly derived from Kyn and one that cannot be converted into KynA (Figure 2C), had no effects on feeding behavior during fasting or refeeding (Figure 3C). Metabolite measurements in fasting animals revealed that Kyn administration during fasting elevated KynA levels 3-fold over vehicle-treated animals, whereas levels of Kyn, Trp, or Ant were not significantly altered (Figure S2B).

We next examined the effects of kynurenine pathway mutations on KynA levels and feeding behavior. Under ad-libitum-fed conditions, levels of Kyn, KynA, and Ant were elevated 4- to 8-fold in *kmo-1(tm4529)* mutants relative to wild-type *C. elegans* (Figure S2C). Although subjecting the *kmo-1* mutants to a 2 hr fast caused a decline in KynA levels, these levels still far exceeded that found in ad-libitum-fed wild-type animals (Figure S2C). The *kmo-1* mutants were unable to hyperactivate their pharyngeal pumping rate post-fast (Figure 3D). However, loss of *nkat-1* resulted in constitutively hyper-activated pharyngeal pumping, even in a *kmo-1* mutant background (Figure S2D).

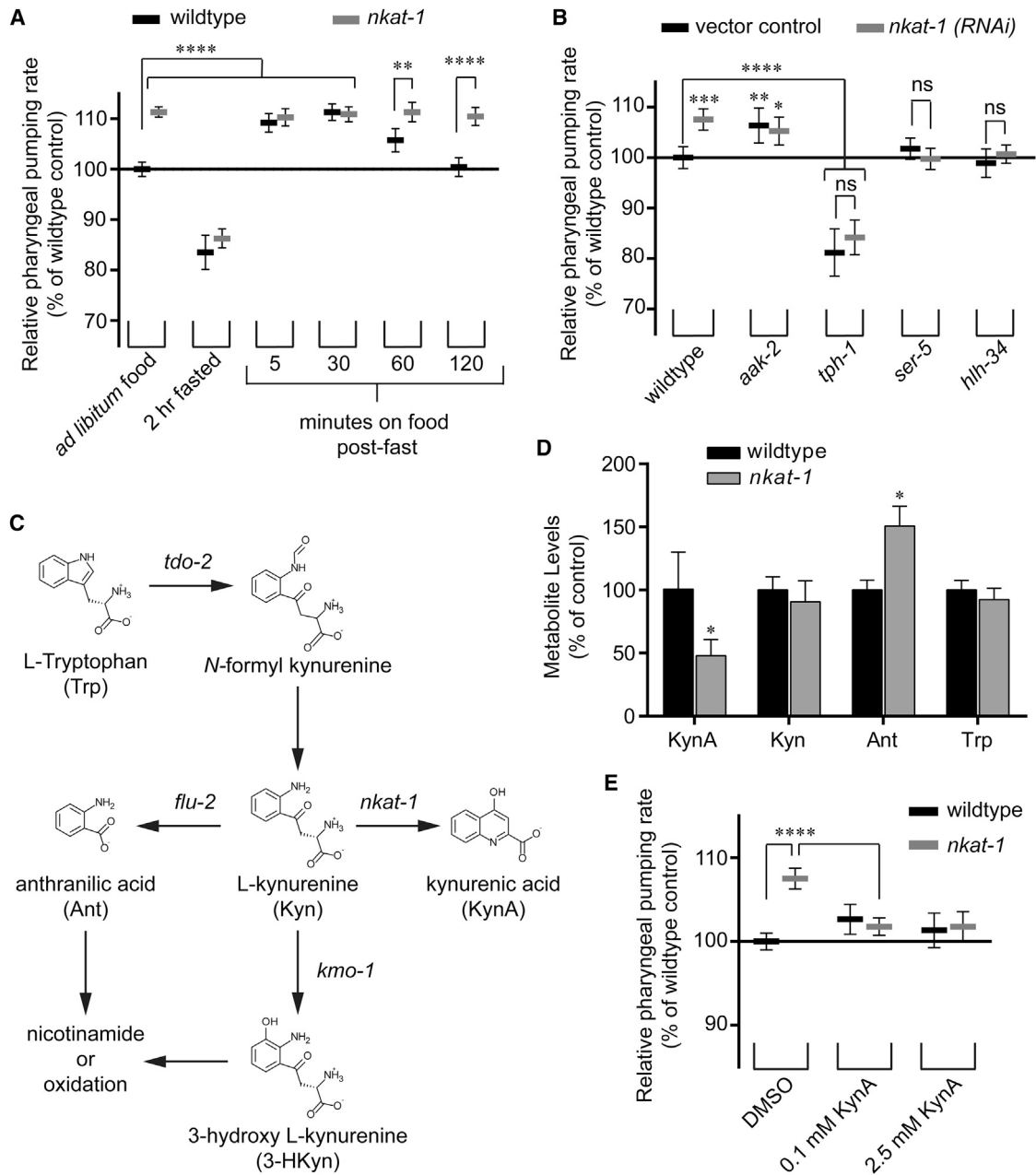


Figure 2. Mutants with Impaired KynA Production Exhibit Constitutively Hyperactive Pharyngeal Pumping that Requires Serotonin Signaling

(A) Pharyngeal pumping rates. $n = 9$ – 13 animals per condition. $**p < 0.01$ and $****p < 0.0001$ ANOVA (Tukey).

(B) Pharyngeal pumping rates of serotonin pathway mutants cultured on either vector control RNAi or *nkat-1(RNAi)* expressing *E. coli*. $n = 10$ animals per condition. ns, $p > 0.5$, $*p < 0.05$, $**p < 0.01$, $***p < 0.001$, and $****p < 0.0001$ compared to wild-type animals cultured of RNAi control vector ANOVA (Dunnett). (C) Schematic of the kynurenine pathway. *tdo-2*: tryptophan 2,3 dioxygenase; *kmo-1*: kynurenine mono-oxygenase; *flu-2*, required for kynureninase expression. (D) Comparisons of kynurenine pathway metabolite levels in wild-type versus *nkat-1* mutants. Error bars indicate SD of determinations from five cultures per genotype. $*p < 10^{-5}$ (two-tailed, t test: wild-type versus *nkat-1*).

(E) Effects of KynA supplementation on pharyngeal pumping. $n = 10$ animals per condition. $****p < 0.0001$ ANOVA (Tukey).

In (A), (B), and (E), error bars indicate 95% c.i.

Similar to *kmo-1* mutants, *flu-2(e1003)* mutants, which have low kynureninase activity and elevated Kyn and KynA levels (van der Goot et al., 2012), were unable to hyperactivate their pharyngeal pumping post-fast (Figure 3D).

Taken together, these results point to KynA as the specific metabolite whose levels determine the overfeeding behavior of animals post-fast; fasting results in a depression of KynA levels, which then permits the hyperactive feeding state when animals

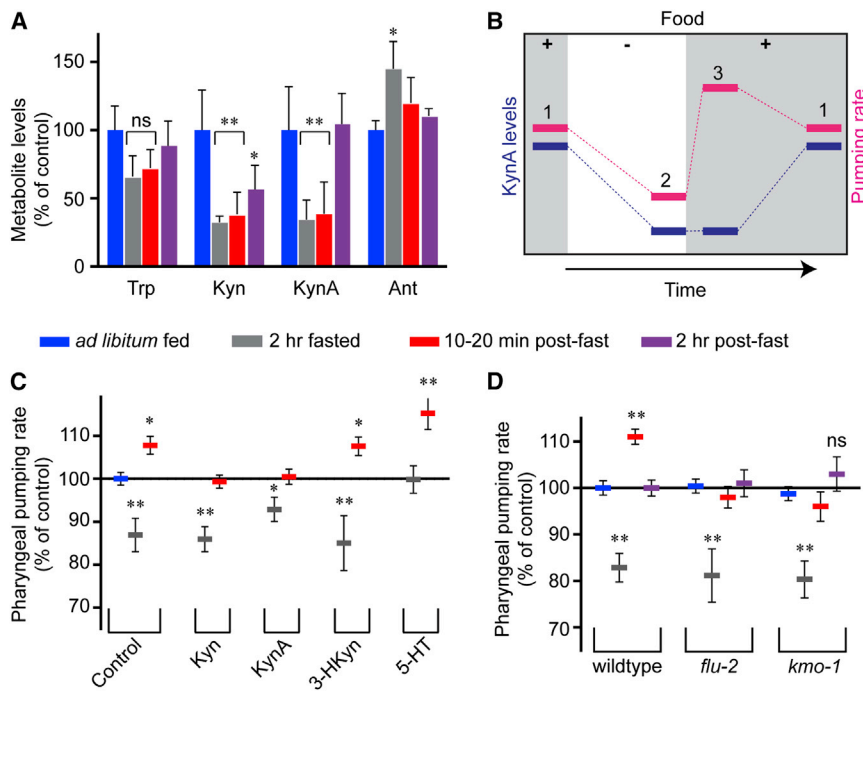


Figure 3. KynA Depletion during Fasting Is Required for Post-Fast Hyperactive Feeding

(A) Determination of tryptophan (Trp), kynurenine (Kyn), kynurenic acid (KynA), and anthranilic acid (Ant) from extracts of wild-type *C. elegans* fed ad libitum after 2 hr of fasting or after 20 min or 2 hr of post-fast feeding. For each metabolite, data are normalized to the ad-libitum-fed condition. Error bars indicate SD of three to four independent cultures. NS, $p > 0.05$, * $p < 0.05$, and ** $p < 0.0001$. ANOVA (Tukey) relative to ad libitum fed for each metabolite.

(B) Observed relationships among KynA levels, pharyngeal pumping rate, and food availability with time indicating three distinct behavioral states (1–3).

(C) Effects of metabolite supplementations on pharyngeal pumping rates of wild-type *C. elegans*. During the fasting period, animals were treated with either vehicle or 100 μ M of each of Kyn, KynA, 3-hydroxykynurenine (3-HKyn), and serotonin (5-HT). $n = 10$ –12 animals per condition. ns, $p > 0.05$, * $p < 0.01$, and ** $p < 0.0001$. ANOVA (Holm-Sidak) compared to ad-libitum-fed control.

(D) Pumping rates from wild-type and mutants at the indicated fasting and refeeding periods. $n = 12$ –14 animals per condition. ns, $p > 0.05$ and ** $p < 0.0001$. ANOVA (Holm-Sidak) compared to ad libitum fed for each mutant and wild-type control. In (C) and (D), error bars indicate 95% c.i. See also Figure S2.

are returned to food. As food is ingested, KynA levels recover, attenuating the hyperactive feeding behavior.

Localized Production of KynA in the Nervous System Regulates Feeding

To identify the tissues of origin for KynA production, we generated transgenic animals expressing a transcriptional fusion of the *nkat-1* promoter to GFP (*nkat-1p::gfp*) and observed consistent expression in head neurons with occasional weak transgene expression in the gonad and intestine (Figure 4A). To identify the precise cells in which *nkat-1p::gfp* is expressed, we generated *nkat-1p::gfp; nmr-1p::mCherry* double transgenics (Figure 4B). The *nmr-1* promoter was previously shown to be expressed in NMDA receptor expressing neurons named AVA, AVE, AVD, PVC, AVG, and RIM (Brockie et al., 2001). Based on their axonal projections and cell body positions, two of the *nkat-1p* active neurons were identified as RMDV and RIM pairs of neurons, which are directly adjacent to *nmr-1*-expressing AVA and AVD neurons, respectively. Only sporadic, weak mCherry expression could be observed in RIM. The third *nkat-1p* active neuron situated dorsal to the nerve ring with an axon projection along the dorsal nerve cord was identified as RID. Thus, with the potential exception of RIM, *nkat-1* is likely expressed in neurons that lack NMDA receptors but are in close anatomical proximity to those that do (White et al., 1986).

Reconstitution of the *nkat-1* cDNA using the *nkat-1* promoter described above, a pan-neuronal promoter (*unc-119*) or its selective expression in only the RIM and RIC interneurons using the *tdc-1* promoter, completely rescued the hyperactive pumping phenotype of *nkat-1* mutants (Figure 4C). By contrast,

nkat-1 mutants continued to exhibit hyperactive feeding when *nkat-1* cDNA was reconstituted either in the ADF serotonergic neurons using the *srh-142* promoter or when using the *nkat-3* promoter, which is robustly expressed in pharyngeal muscle, as well as in some head neurons (Figures S3A and S3B). Thus, production of KynA at specific neural locations is a critical determinant of feeding behavior.

A Neuropeptide Signaling Axis Emanating from NMDA-R-Expressing Interneurons Regulates Post-Fast Hyperactive Feeding

In mammals, KynA has been characterized as an antagonist of glutamatergic neurotransmission in particular through NMDA-gated ionotropic receptors (Perkins and Stone, 1982) and by pre-synaptic inhibition of glutamate release via antagonism of α -7 nicotinic acetylcholine receptors (Carpenedo et al., 2001). The spatial expression patterns of *nkat-1* and *nmr-1* prompted us to investigate the role of *C. elegans* NMDA-receptor (NMDA-r) in feeding behavior. The two subunits of the *C. elegans* NMDA-r are encoded by *nmr-1* and *nmr-2*, which have identical expression patterns in a few interneurons (Brockie et al., 2001). Both *nmr-1(ak4)* and *nmr-2(tm3785)* loss-of-function mutants exhibited pharyngeal pumping rates indistinguishable from wild-type animals when fed ad libitum and while fasting (Figures 5A and 5B). However, both mutants were insensitive to the feeding increasing effects of *nkat-1* deficiency (Figure 5A) and failed to exhibit post-fast hyperactive feeding (Figure 5B). Expression of the *nmr-1* cDNA under the control of the *nmr-1* promoter restored the capacity for hyperactive feeding (Figures S4A and S4B). Unlike the case of the *nkat-1* phenotypic rescue,

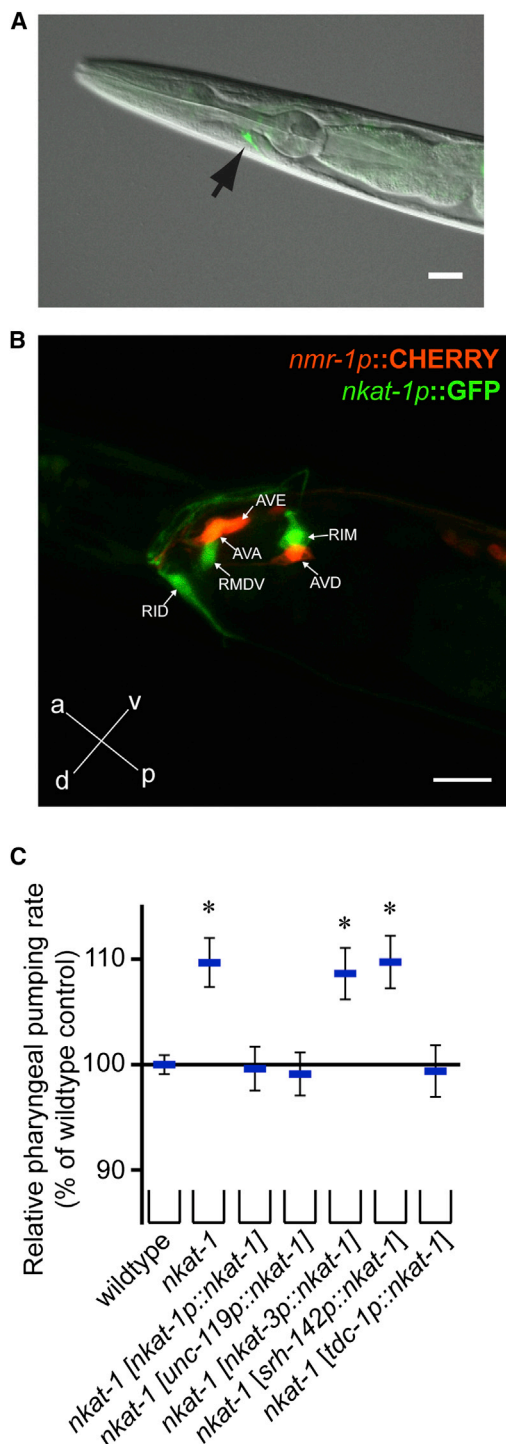


Figure 4. *nkat-1* Expression Is Limited to a Few Neurons

(A) Merged DIC and green epifluorescence image of an animal containing an *nkat-1p::gfp* transcriptional fusion. Arrow indicates a green head neuron. Scale bar, 20 μ m.

(B) Maximum intensity projection of the right lateral side of the head of a young adult animal coexpressing *nkat-1p::gfp* and *nmr-1p::mCherry* transcriptional fusions. Individual neurons are identified. Scale bar, 10 μ m.

expression of *nmr-1* cDNA in RIM and RIC using the *tdc-1* promoter or in RIM alone using the *cex-1* promoter (Cohen et al., 2009) was insufficient to rescue the hyperactive feeding defect of *nmr-1* mutants (Figures S4A and S4B). Moreover, although *nmr-1(RNAi)* suppressed the hyperactive feeding state of *nkat-1* mutants, it failed to alter the constitutive depressed pumping of serotonin deficient *tph-1* mutants or the hyperactive pumping of AMPK deficient *aak-2* mutants (Figure S4C). Collectively, our data suggested a model whereby KynA levels modulate the feeding rate by directly or indirectly antagonizing glutamatergic neurotransmission through NMDA-r and subsequent changes in serotonin signaling initiated from the ADF neurons.

To substantiate the above model, we searched for molecular links between NMDA-receptor-expressing neurons and serotonin signaling by examining neurotransmitter or neuropeptide pathways of *nmr-1*-positive neurons. The hyperactive feeding of *nkat-1*-deficient animals was unaltered in *tdc-1* mutants, which are deficient in the production of tyramine and octopamine, feeding regulatory neurotransmitters originating from the RIM and RIC interneurons, respectively (Figure 5C) (Alkema et al., 2005; Greer et al., 2008). Similarly, elevated feeding of *nkat-1*-deficient animals was not dependent on *flp-1* (an FMFRamide neuropeptide), whose expression includes *nmr-1*-positive AVA and AVE neurons and has been previously implicated in serotonin-regulated behaviors (Waggoner et al., 2000) (Figure 5C). However, loss of *flp-18*, which is expressed in AVA, RIM, and four other neurons and regulates fat metabolism, chemotaxis, and movement (Cohen et al., 2009), blocked the hyperactive feeding of *nkat-1*-deficient animals and the post-fast hyperactive feeding of wild-type animals (Figures 5C and 5D) without affecting ad libitum feeding rates. Reconstitution of *flp-18* using the *nmr-1* promoter was sufficient to rescue hyperactive feeding induced by *nkat-1* inactivation (Figure 5C) or fasting (Figure 5D), whereas reconstitutions in AIY (*ttx-3* promoter) (Altun-Gultekin et al., 2001) and in RIM alone (*cex-1* promoter) failed to do so (Figures 5C and 5D). Because the only neurons that overlap between expression patterns of *flp-18* and *nmr-1* are AVA and RIM, and RIM-specific expression of *flp-18* and *nmr-1* was insufficient to restore post-fast hyperactive feeding state to their respective mutants, AVA remains as the likely origin of the *flp-18* signal required for hyperactive feeding. Promoters for exclusive expression in AVA are not yet known.

The FLP-18 neuropeptide activates two different receptors, NPR-4 and NPR-5, that are related to the mammalian neuropeptide-Y receptor (Kubiak et al., 2008; Cohen et al., 2009). The two receptors have nonoverlapping expression with NPR-5 being expressed in select sensory neurons, including serotonergic ADF (Cohen et al., 2009). Similar to *nmr-1* and *flp-18* mutants, *npr-5* mutants have wild-type pharyngeal pumping rates when feeding ad libitum and when fasted but do not hyperactivate pharyngeal pumping in response to *nkat-1* deficiency (Figure 5E) or post-fast food encounter (Figures 5F and S4D). Transgenic expression of *npr-5* (a and b isoforms) solely in the ADF sensory neuron was

(C) Pharyngeal pumping rates of the indicated strains. Error bars indicate 95% c.i. n = 10–12 animals per condition. ****p < 0.0001 ANOVA (Dunnett) in comparison with wild-type.

See also Figure S3 and Table S1.

sufficient rescue the feeding deficiencies of *npr-5* mutants (Figures 5E and 5F). Finally, unlike its requirement in the case of *nkat-1* deficiency, loss of *npr-5* does not alter the constitutively hyperactivated feeding of *aak-2* mutants (Figure S4E). These results suggest that KynA depletion impinges on serotonin in ADF by an NMDA-r to FLP-18 to NPR-5 signaling axis.

Fasting Enhanced Activity in AVA Interneurons Is Repressed by KynA, Requires NMDA-r, and Is Independent of FLP-18

The prior results implied that the fasted state in *C. elegans* is sensed at least in part by the loss of KynA-mediated antagonism of NMDA-receptor-expressing interneurons. To measure the effect of varying KynA levels on the activity of *nmr-1*-expressing neurons, we measured calcium transients in these neurons using the intensity ratio of the fluorescent Ca^{2+} indicator GCaMP3 (Tian et al., 2009) and the Ca^{2+} -insensitive mCherry both expressed under the control of the *nmr-1* promoter. The *nmr-1p::GCaMP3*, *nmr-1p::mCherry* transgenes did not alter feeding rate of animals under any of the tested conditions (Figure S5). Because the depletion of KynA caused by fasting or genetic inactivation of *nkat-1* is a chronic condition, we measured spontaneous Ca^{2+} -induced fluorescence transients over an extended (250 s) period. The *nmr-1* promoter used to drive GCaMP3 had the most prominent expression in the AVA neurons; however, with our optical setup, we cannot rule out the acquisition GCaMP signal from both AVA and AVE. For all of our analyses, we report the total integrated signal of all the peaks in the 250 s recording window (Figures 6A and 6B). To enable comparisons of the average intensities and durations of the spontaneous, stochastic Ca^{2+} transients under different conditions, we also examined each of the 250 s recording windows for events where we could unambiguously define initiation of a spontaneous transient. We then plotted GCaMP fluorescence for the following 60 s (Figure 6A) and examined the average response of multiple such transients per condition (Figure 6C).

The total integrated change in fluorescence intensity was 2.5-fold larger in fasted wild-type animals than in fed animals (Figure 6B). Examination of the transients in the 60 s window following an initiation event indicated that the enhanced intensity observed during fasting persisted throughout the evaluation window rather than reflecting a series of short but very intense bursts of the Ca^{2+} signal (Figure 6C). Kyn or KynA supplementations reverted the elevated integrated intensity Ca^{2+} signal of fasted animals to that of ad-libitum-fed animals (Figure 6B). These supplementations did not block the initial intensity maximum of spontaneous Ca^{2+} transients in fasted animals but promoted their rapid decline to levels comparable to or below that of fed wild-type animals (Figure 6C).

Under ad-libitum-fed conditions, the total integrated fluorescence signal, as well as the size and duration of the Ca^{2+} transients of *nkat-1* mutants, was greater than those of ad-libitum-fed wild-type animals and comparable to those of fasted wild-type animals (Figures 6B and 6C). Although the total integrated intensity of GCaMP fluorescence was statistically indistinguishable between wild-type and *nmr-1* mutants during the well-fed state (Figure 6B), loss of *nmr-1* abrogated the

fasting-induced elevation of total integrated response (Figure 6B) and the persistent rise in transients (Figure 6C). These results are consistent with kynurenic acid attenuating NMDA-receptor-mediated Ca^{2+} activity in the ad-libitum-fed state, which is relieved upon fasting in wild-type animals or in animals deficient in *nkat-1* function.

We also found that the total integrated intensity (Figure 6B) and duration of Ca^{2+} transients (Figure 6C) that occur upon fasting were similar in *flp-18* mutants and wild-type animals. This suggested that the requirement for *flp-18* in post-fast hyperactive feeding is not merely an indirect outcome of inability of AVA neurons to respond to fasting in *flp-18* mutants. Although loss of *flp-18* did not alter the total integrated intensity of Ca^{2+} transients during the fed state, we noted that the intensity of these transients was more elevated relative to those of fed wild-type animals when they occurred (Figure 6C). The reasons for this are not known but may reflect a paracrine or autocrine feedback inhibitory action of FLP-18 on the activity of AVA.

KynA Levels Regulate the Amount of Secretion from ADF in Response to Food through FLP-18/NPR-5 Signaling

Because the transition from the slow-pumping fasted state to the hyperactivated post-fast state occurs within minutes (Figure S2A), we surmised that it could be driven by changes in secretion of serotonin from ADF, a process with a fast response capability (Whim and Moss, 2001). Direct observation of serotonin secretion is challenging. Both serotonin and neuropeptides such as DAF-28, an insulin-like peptide (Li et al., 2003), are secreted via dense-core vesicles. As a proxy for serotonin secretory activity, we measured the secretion of a DAF-28::mCHERRY translational fusion from ADF using a previously established assay (Kao et al., 2007; Lee et al., 2011). Depletion of KynA caused by *nkat-1* deficiency resulted in enhanced secretion of the reporter, which was completely abrogated in both *flp-18* and *npr-5* mutants (Figure 6D). Similarly, wild-type, but not *flp-18* or *npr-5* mutant, animals that had been fasted and returned to food for 20 min exhibited enhanced secretion compared to ad-libitum-fed animals (Figure 6E). Animals that had simply been fasted for 2 hr without subsequent food exposure exhibited no significant change in secretion (Figure 6E).

DISCUSSION

We have identified KynA as part of a whole-organism homeostatic feedback loop that allows animals to gauge whether they have experienced a period of fasting to alter subsequent feeding behavior (Figure 7). Because KynA is derived from tryptophan, an essential amino acid, changes in KynA levels are metabolically linked to nutritional status. Our findings suggest a model whereby fasting depletes KynA, leading to activation of NMDA-receptor-expressing neurons, which is consistent with the known role of KynA as an inhibitor of NMDA signaling. In turn, activation of these neurons initiates a neuropeptide Y-like signaling cascade, comprised of FLP-18 and its receptor NPR-5, that poises the ciliated ADF neurons for enhanced secretion of serotonin as soon as they sense the presence of

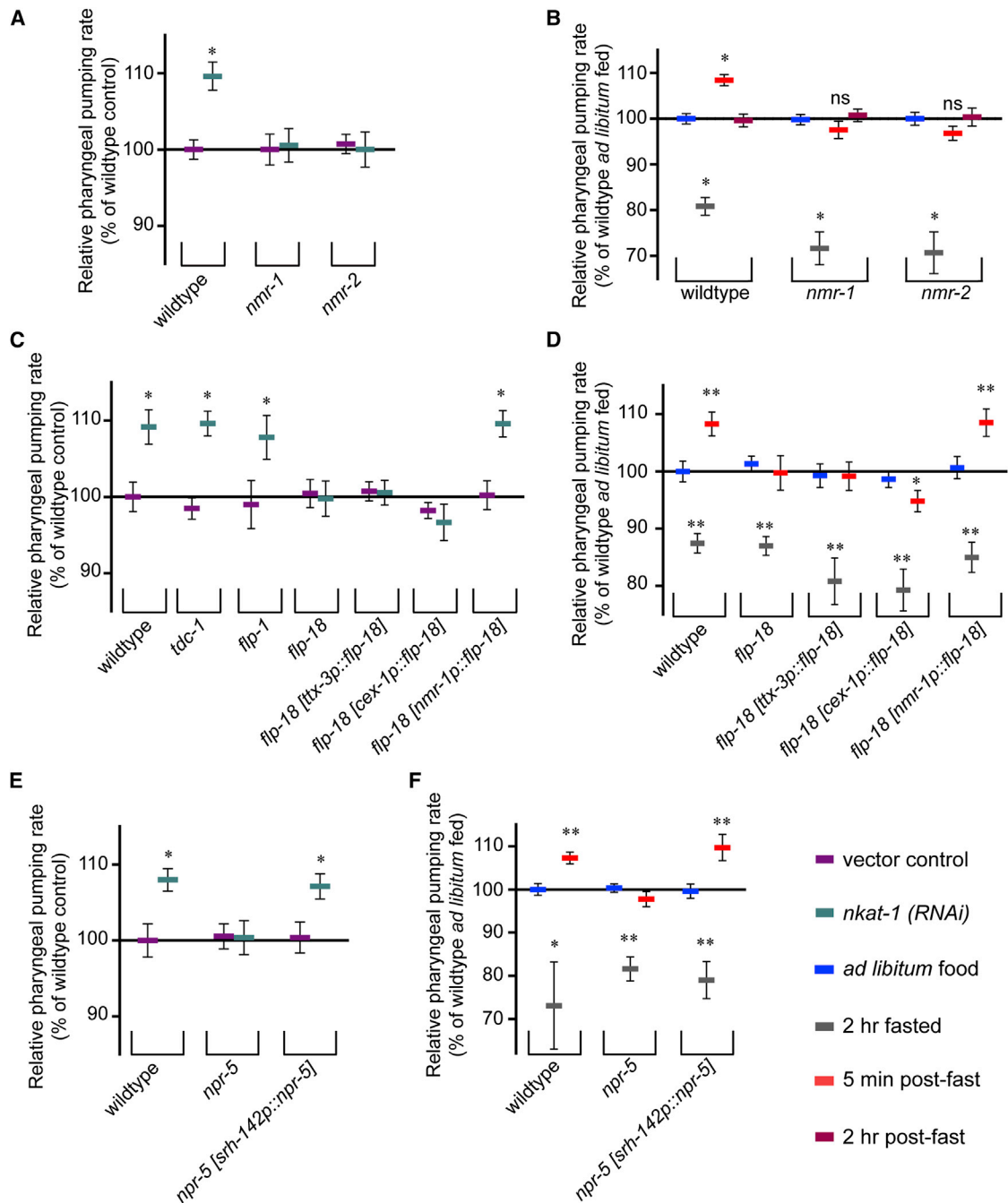


Figure 5. Hyperactive Feeding Requires an NMDA Receptor to Peptidergic Signaling Axis that Converges on a Serotonergic Sensory Neuron

(A) Pharyngeal pumping rates of wild-type, *nmr-1*, and *nmr-2* mutants cultured on either RNAi vector control or *nkat-1*(RNAi). **p* < 0.0001, ANOVA (Tukey).

(B) Pharyngeal pumping rates at the indicated fasting and refeeding periods. ns, *p* > 0.1 and **p* < 0.0001. ANOVA (Tukey) comparing fasted, post-fast animals to ad-libitum-fed controls.

(C) Pharyngeal pumping rates of the indicated strains. Animals were cultured on bacteria expressing *nkat-1*(RNAi) or RNAi vector control. **p* < 0.0001 ANOVA (Sidak) comparing vector control to *nkat-1*(RNAi) for each genotype.

(D) Pharyngeal pumping rates of wild-type, *flp-18* mutants, and *flp-18* transgenic lines used in (C) fed ad libitum, after 2 hr of fasting, and after 5 min of post-fast refeeding. **p* < 0.05 and ***p* < 0.0001. ANOVA (Tukey) comparing fasting and post-fast measurements to that of ad libitum fed for each measurement.

(E) Pharyngeal pumping rates of wild-type, *npr-5* mutants, and *npr-5* mutants expressing transgenes directing expression of *npr-5a* and *-5b* to ADF neurons. Animals were cultured on bacteria expressing either RNAi vector control or *nkat-1*(RNAi). **p* < 0.0001. ANOVA (Sidak) comparing vector control treated to *nkat-1*(RNAi) treated for each genotype.

(legend continued on next page)

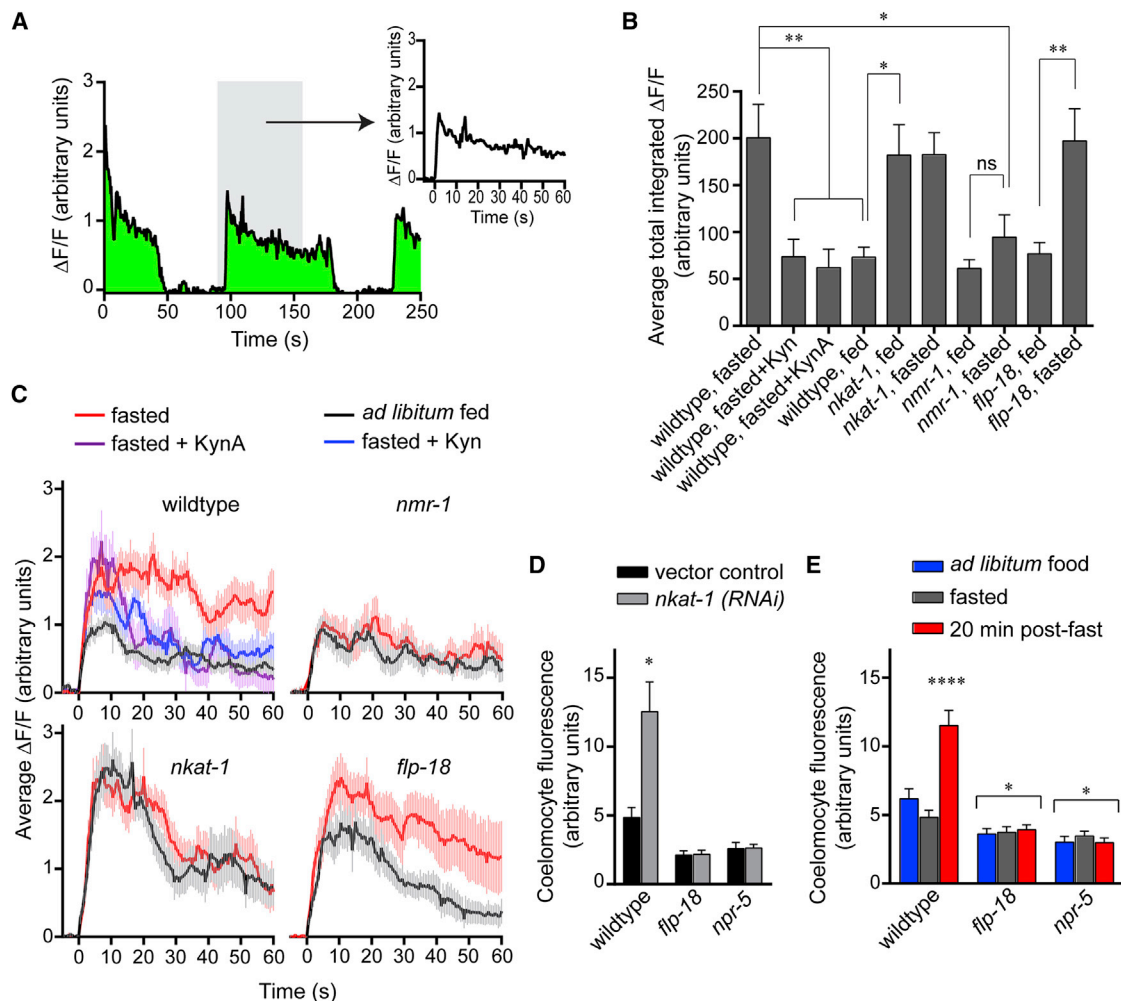


Figure 6. KynA Represses AVA Interneuron Activity and Secretion from ADF through Antagonism of the NMDA-r/FLP-18/NPR-5 Signaling Axis

(A) Sample ratiometric $\Delta F/F$ plot showing spontaneous changes over the 250 s imaging window. The area under the signal in the green shaded plot is the basis of the data in (B). The inset plot shows the portion of a spontaneous transient extracted from the 250 s imaging window aligned to a -5 to 60 s time-scale axis, which is the basis of the data shown in (C). See also Figure S5.

(B) The total integrated change in fluorescence intensity ($\Delta F/F$) over the 250 s recordings. Wild-type animals were fed ad libitum, fasted 2 hr, or fasted 2 hr in media supplemented with either 100 μ M Kyn or 100 μ M KynA. Mutants in *nkat-1*, *nmr-1*, and *flp-18* were fed ad libitum or fasted 2 hr. ns, $p > 0.8$, * $p < 0.02$, and ** $p < 0.01$; ANOVA (Sidak).

(C) Averaged spontaneous Ca^{2+} transients from each of the conditions recorded in (B). (B and C) error bars indicate SEM; $n = 10$ –12 animals per condition.

(D and E) Measurement of DAF-28::MCHERRY fluorescence in coelomocytes from transgenic animals expressing *daf-28::mCherry* in ADF neurons. Error bars indicate SEM; $n = 15$ –38 per condition.

(D) Wild-type, *flp-18*, and *npr-5* mutants expressing the transgene were cultured on bacteria expressing either *nkat-1* (RNAi) or an RNAi vector control. * $p < 0.0001$ ANOVA (Tukey) compared to RNAi vector control-treated animals.

(E) Lines used in (D) measured during ad libitum feeding after a 2 hr fast and after 20 min of post-fast refeeding. * $p < 0.05$ and **** $p < 0.0001$. ANOVA (Dunnett) comparing all measurements to wild-type, ad-libitum-fed animals.

food. The elevated serotonin signaling promotes enhanced feeding by the animals through a previously described pathway (Cunningham et al., 2012). As animals feed, the activity of

NMDA-receptor-expressing neurons is attenuated by normalizing levels of KynA, which decreases FLP-18 to NPR-5 signaling in ADF, and terminates the transiently enhanced

(F) Pharyngeal pumping rates of wild-type, *npr-5* mutants, and the *npr-5* transgenic line used in (E) fed ad libitum, after 2 hr of fasting, and after 5 min of refeeding post-fast. * $p < 0.05$ and ** $p < 0.0001$. ANOVA (Tukey) comparing fasting and post-fast measurements to that of ad libitum fed for each measurement.

In (A–F), error bars indicate 95% c.i. $n = 10$ –16 animals per condition. See also Figure S4 and Table S1.

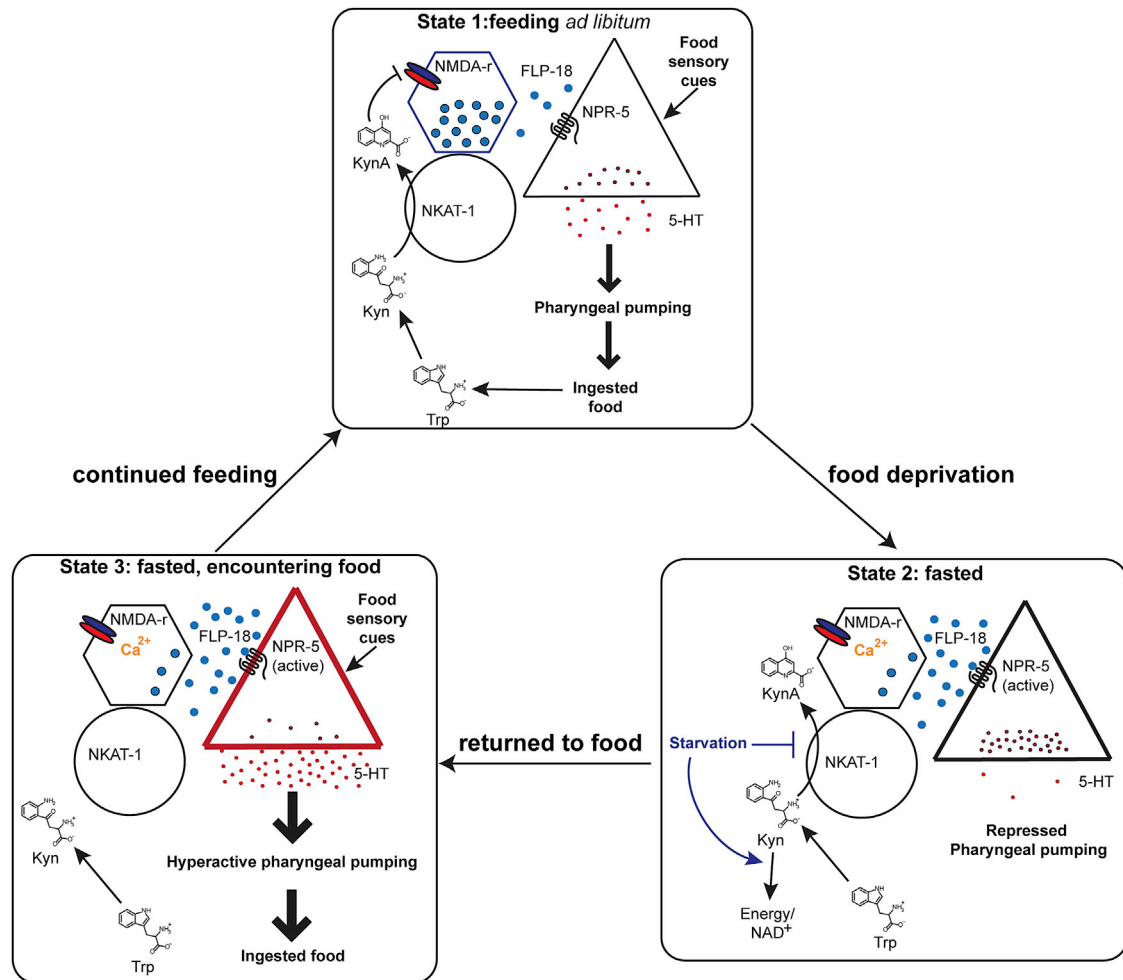


Figure 7. Model of a Neural Circuit that Integrates Food Sensory Cues with Nutritional Status to Promote Experience-Dependent Plasticity of Feeding

State 1: the activity of AVA (hexagon) is attenuated by KynA synthesized from kynurenine by NKAT-1 in RIM, RMDV, and/or RID (circle). Kynurenine is ultimately derived from ingested food. ADF (triangle) senses food cues leading to 5-HT secretion to stimulate pumping. State 2: fasting represses KynA production, causing activation of AVA neurons that promotes FLP-18/NPR-5 signaling to serotonergic ADF. In the absence of food cues, serotonin signaling from ADF is muted. State 3: when animals re-encounter food immediately post-fast, the activated NPR-5 signaling state leads to enhanced secretion from ADF when food derived sensory cues are detected. Continued feeding leads to an accumulation of KynA returning the animals to *State 1*.

serotonin signaling phase. This regulatory logic is analogous to a classical product feedback inhibition loop but one that acts on an entire neural circuit. This circuit does not simply inform the animals of the presence or absence of food but allows animals to alter behaviors in a manner that takes into account an internal nutritional cue modulated by fasting.

Although tryptophan degradation via the KP likely occurs throughout the animal (van der Goot et al., 2012), we found that the highly restricted expression pattern for *nkat-1* in the nervous system in the close spatial proximity of NMDA-receptor-expressing neurons was critical to its function in feeding behavior. Kynurenic acid is thought to antagonize glutamate signaling through binding extracellular motifs of cell-surface receptors such as the glycine coagonist site on NMDA receptors or α -7 nAChRs. Either mechanism would be consistent with our genetic data. In mammals, because it does not

cross the blood-brain barrier, KynA in the brain is synthesized by astrocytic KATs (Schwarcz et al., 2012). Therefore KynA functions cell nonautonomously. In *C. elegans*, *nkat-1* is expressed in three sets of neurons: RID, RMDV, and RIM, of which reconstitution of *nkat-1* in RIM was sufficient to confer wild-type feeding behavior to *nkat-1* mutants. The cell bodies of RMDV lie directly adjacent to those of NMDA-receptor-expressing AVA, whereas the processes of AVA and RIM are closely associated, forming several gap junctions in the nerve ring (White et al., 1986). Thus, KynA produced by NKAT-1 in RIM and RMDV is in close spatial proximity for influencing glutamate signaling in AVA and other NMDA-r-expressing neurons. A controversy in how KynA regulates mammalian glutamatergic signaling stems from the fact that the K_i of KynA for NMDA and AMPA type glutamate receptors is 10- and 100-fold higher, respectively, than the concentration of KynA measured in the bulk

extracellular space (Albuquerque and Schwarcz, 2013). However, it is possible that the concentration of KynA increases dramatically in the microscopic vicinity of a cell competent to synthesize it. Heterogeneous, localized production of KynA may differentially modulate glutamatergic signaling in different brain regions or local synaptic clusters.

Our findings suggested that FLP-18 originating from AVA neurons during the fasted state acts on the ADF food-sensing neurons via NPR-5, an ortholog of the mammalian neuropeptide-y (NPY) receptors, to increase food consumption post-fast. The AVA interneuron is also required for and its activity is correlated with initiating spontaneous reversals, a locomotory behavior that is increased in the absence of food (Gray et al., 2005; Piggott et al., 2011). Thus, AVA neurons direct two distinct functional outputs coordinated to rectify the aversive fasted state: food seeking behavior and food ingestion. This is not likely a consequence of the relatively simple nature of the *C. elegans* nervous system. For example, in mice, starvation induced activation of AgRP neurons in the hypothalamus, which also express NPY, and elicited both food-seeking behavior and elevated consumption of food through projections within the hypothalamus and to the midbrain (Betley et al., 2013). AgRP neurons also express NMDA receptors and targeted genetic ablation of NMDA receptors in AgRP neurons, attenuates the post-fast hyperphagia in mice (Liu et al., 2012). Thus, AgRP neurons represent a prime point of control in mammals upon which KynA inhibition of glutamate signaling could play a role in food-associated behaviors.

The nervous system can gauge peripheral metabolic status by direct sensation of circulating nutrients such as glucose, leucine, or lipids, as well as through indirect hormonal pathways that originate from peripheral organs and signal to the nervous system (Lam, 2010). As an indicator of nutrient status, KynA stands out because it appears to directly modulate synaptic transmission, akin to a neurotransmitter whose levels are directly tied to nutrient availability. As recently exemplified (Agudelo et al., 2014), changes in peripheral metabolism can exert effects on central KP metabolite levels. Because defects in peripheral metabolic regulation are associated with a diverse array of CNS-associated diseases (Cai et al., 2012; Mitchell et al., 2013; McElroy and Keck, 2014), KynA presents an intriguing possibility for directly linking metabolism to various neural functions. Additionally, our findings provoke a possible twist in the interpretation of the serotonin-kynurenine hypothesis of depression in that KP activation may indeed antagonize serotonin—not through direct metabolic competition for their common precursor as previously proposed (Lapin and Oxenkrug, 1969) but through the production of KynA and its antagonism of a neural circuit that, in turn, enhances serotonin release. In the case of neurodegenerative disorders, the beneficial effects of KynA have been attributed to its potential for countering glutamate toxicity (Schwarcz et al., 2012). Another possibility raised by our studies is that the effects of KynA may be due to modulation of neural circuits whose normal, physiological functions may have beneficial impacts on proteostasis and neurodegeneration. In *C. elegans*, serotonin signaling, which we show is attenuated by KynA, regulates release of systemic neuroendocrine molecules, including insulin (Cunningham et al., 2014; Liang et al.,

2006), a well-known modulator of proteostasis (Taylor et al., 2014).

EXPERIMENTAL PROCEDURES

Please see [Extended Experimental Procedures](#) for detailed procedures.

C. elegans Strains

Transgenic lines were prepared by microinjection of expression plasmids. Unless described otherwise, *C. elegans* were cultured on agar plates at 20°C on *E. coli* OP-50.

Materials

Unless described otherwise, all chemicals were purchased from Sigma. Plasmids were constructed using standard molecular biology techniques.

Pharyngeal Pumping Assay

The number of contractions of the posterior pharyngeal bulb was counted over 10 s intervals as described (Srinivasan et al., 2008). All pumping rates presented in this study are presented in tabular form in [Data S1](#).

BODIPY Uptake Assay

C. elegans were added to plates containing BODIPY (200 ng/ml) and *E. coli* for 15 min, washed off, paralyzed with NaN₃, and imaged (You et al., 2008).

Metabolite Determination

Acidified, aqueous extracts of *C. elegans* cultures were separated using an HPLC equipped with a 150 × 4.6 mm C₁₈-reversed phase column operating at flow rate of 1 ml/min. Metabolites were detected using in-line fluorescence and UV absorbance detectors. Retention times and excitation/emission data were compared to that of metabolite standards injected under the same conditions.

Metabolite Supplementation

Day 1 gravid adults were washed free of bacteria and then incubated for 2 hr in S-basal media supplemented with metabolites at 100 μM concentration. Ad libitum feeding: L4 animals were cultured for 1 day on plates containing 0.1 or 2.5 mM KynA.

Spontaneous Ca²⁺ Transients

Animals were mounted on agarose pads, immobilized with coverslips, and imaged for 250 s through a 40× objective on a microscope equipped with green and red epifluorescence filters and with a 16-bit camera acquiring 4 × 4 binned images on two channels sequentially at 2 Hz. A 6 × 6 pixel region of interest was placed over AVA, and the integrated fluorescence intensity at each time point for both the GCaMP signal and mCherry signal was measured. The Ca²⁺ signal was determined by normalizing the green channel by the red channel measurements for each time point.

Secretion Assay

The integrated fluorescence intensity from the red channel was measured in coelomocytes from animals that expressed the DAF-28::MCHERRY fusion protein from neuron-specific promoters using ImageJ.

Statistics

Two-tailed Student's *t* tests were used to calculate *p* values when comparisons were limited that between two conditions. When multiple conditions were compared per experiment, one or two-way ANOVA with appropriate post-tests was used to calculate *p* values.

SUPPLEMENTAL INFORMATION

Supplemental Information includes Extended Experimental Procedures, five figures, one data file, and one table and can be found with this article online at <http://dx.doi.org/10.1016/j.cell.2014.12.028>.

AUTHOR CONTRIBUTIONS

G.A.L., K.A.C., and K.A. designed experiments. G.A.L. and K.A.C. performed experiments. L.L. and F.M. provided technical assistance. G.A.L., K.A.C., Z.W., and K.A. analyzed data. G.A.L. and K.A. wrote the manuscript.

ACKNOWLEDGMENTS

The authors thank Shao-Yi Huang, Paul Muchowski, Steve Finkbeiner, Mihir Vohra, and Erik Johnson for helpful discussions and shared equipment and the Nikon Imaging Center at UCSF for microscope access. Some *C. elegans* strains were provided by the *Caenorhabditis* Genetics Center, funded by NIH Office of Research Infrastructure Programs (P40 OD010440), and the Mitani Lab of the National Bioresource Project of Japan for the Experimental Animal *C. elegans*. This research was supported by funds from the Program in Breakthrough Biomedical Research, UCSF Diabetes Family Fund for Innovative Patient Care, R21 ES021412 (NIEHS), R01 AG046400 (NIA), and U01 ES019458 (NCI).

Received: June 19, 2014

Revised: October 16, 2014

Accepted: December 11, 2014

Published: January 15, 2015

REFERENCES

- Agudelo, L.Z., Femenía, T., Orhan, F., Porsmyr-Palmertz, M., Gojny, M., Martínez-Redondo, V., Correia, J.C., Izadi, M., Bhat, M., Schuppe-Koistinen, I., et al. (2014). Skeletal muscle PGC-1 α 1 modulates kynurenine metabolism and mediates resilience to stress-induced depression. *Cell* 159, 33–45.
- Albuquerque, E.X., and Schwarcz, R. (2013). Kynurenic acid as an antagonist of α 7 nicotinic acetylcholine receptors in the brain: facts and challenges. *Biochem. Pharmacol.* 85, 1027–1032.
- Alkema, M.J., Hunter-Ensor, M., Ringstad, N., and Horvitz, H.R. (2005). Tyramine Functions independently of octopamine in the *Caenorhabditis elegans* nervous system. *Neuron* 46, 247–260.
- Altun-Gultekin, Z., Andachi, Y., Tsalik, E.L., Pilgrim, D., Kohara, Y., and Hobert, O. (2001). A regulatory cascade of three homeobox genes, *ceh-10*, *ttx-3* and *ceh-23*, controls cell fate specification of a defined interneuron class in *C. elegans*. *Development* 128, 1951–1969.
- Andiné, P., Lehmann, A., Ellrén, K., Wennberg, E., Kjellmer, I., Nielsen, T., and Hagberg, H. (1988). The excitatory amino acid antagonist kynurenic acid administered after hypoxic-ischemia in neonatal rats offers neuroprotection. *Neurosci. Lett.* 90, 208–212.
- Avery, L., and Horvitz, H.R. (1990). Effects of starvation and neuroactive drugs on feeding in *Caenorhabditis elegans*. *J. Exp. Zool.* 253, 263–270.
- Avery, L., and You, Y.J. (2012). *C. elegans* feeding. *WormBook*, 1–23.
- Beal, M.F., Matson, W.R., Storey, E., Milbury, P., Ryan, E.A., Ogawa, T., and Bird, E.D. (1992). Kynurenic acid concentrations are reduced in Huntington's disease cerebral cortex. *J. Neurol. Sci.* 108, 80–87.
- Betley, J.N., Cao, Z.F.H., Ritola, K.D., and Sternson, S.M. (2013). Parallel, redundant circuit organization for homeostatic control of feeding behavior. *Cell* 155, 1337–1350.
- Brockie, P.J., Mellem, J.E., Hills, T., Madsen, D.M., and Maricq, A.V. (2001). The *C. elegans* glutamate receptor subunit NMR-1 is required for slow NMDA-activated currents that regulate reversal frequency during locomotion. *Neuron* 31, 617–630.
- Cai, H., Cong, W.N., Ji, S., Rothman, S., Maudsley, S., and Martin, B. (2012). Metabolic dysfunction in Alzheimer's disease and related neurodegenerative disorders. *Curr. Alzheimer Res.* 9, 5–17.
- Campesan, S., Green, E.W., Breda, C., Sathyaikumar, K.V., Muchowski, P.J., Schwarcz, R., Kyriacou, C.P., and Giorgini, F. (2011). The kynurenine pathway modulates neurodegeneration in a *Drosophila* model of Huntington's disease. *Curr. Biol.* 21, 961–966.
- Carpenedo, R., Pittaluga, A., Cozzi, A., Attucci, S., Galli, A., Raiteri, M., and Moroni, F. (2001). Presynaptic kynurenate-sensitive receptors inhibit glutamate release. *Eur. J. Neurosci.* 13, 2141–2147.
- Cohen, M., Reale, V., Olofsson, B., Knights, A., Evans, P., and de Bono, M. (2009). Coordinated regulation of foraging and metabolism in *C. elegans* by RFamide neuropeptide signaling. *Cell Metab.* 9, 375–385.
- Cunningham, K.A., Hua, Z., Srinivasan, S., Liu, J., Lee, B.H., Edwards, R.H., and Ashrafi, K. (2012). AMP-activated kinase links serotonergic signaling to glutamate release for regulation of feeding behavior in *C. elegans*. *Cell Metab.* 16, 113–121.
- Cunningham, K.A., Bouagnon, A.D., Barros, A.G., Lin, L., Malard, L., Romano-Silva, M.A., and Ashrafi, K. (2014). Loss of a neural AMP-activated kinase mimics the effects of elevated serotonin on fat, movement, and hormonal secretions. *PLoS Genet.* 10, e1004394.
- Douglas, S.J., Dawson-Scully, K., and Sokolowski, M.B. (2005). The neurogenetics and evolution of food-related behaviour. *Trends Neurosci.* 28, 644–652.
- Erhardt, S., Blennow, K., Nordin, C., Skogh, E., Lindström, L.H., and Engberg, G. (2001). Kynurenic acid levels are elevated in the cerebrospinal fluid of patients with schizophrenia. *Neurosci. Lett.* 313, 96–98.
- Erhardt, S., Lim, C.K., Linderholm, K.R., Janelidze, S., Lindqvist, D., Samuelsson, M., Lundberg, K., Postolache, T.T., Träskman-Bendz, L., Guillemin, G.J., and Brundin, L. (2013). Connecting inflammation with glutamate agonism in suicidality. *Neuropsychopharmacology* 38, 743–752.
- Foster, A.C., Vezzani, A., French, E.D., and Schwarcz, R. (1984). Kynurenic acid blocks neurotoxicity and seizures induced in rats by the related brain metabolite quinolinic acid. *Neurosci. Lett.* 48, 273–278.
- Gray, J.M., Hill, J.J., and Bargmann, C.I. (2005). A circuit for navigation in *Caenorhabditis elegans*. *Proc. Natl. Acad. Sci. USA* 102, 3184–3191.
- Greer, E.R., Pérez, C.L., Van Gilst, M.R., Lee, B.H., and Ashrafi, K. (2008). Neural and molecular dissection of a *C. elegans* sensory circuit that regulates fat and feeding. *Cell Metab.* 8, 118–131.
- Heyes, M.P., Saito, K., Crowley, J.S., Davis, L.E., Demitrack, M.A., Der, M., Dilling, L.A., Elia, J., Kruesi, M.J.P., Lackner, A., et al. (1992). Quinolinic acid and kynurenine pathway metabolism in inflammatory and non-inflammatory neurological disease. *Brain* 115, 1249–1273.
- Hills, T., Brockie, P.J., and Maricq, A.V. (2004). Dopamine and glutamate control area-restricted search behavior in *Caenorhabditis elegans*. *J. Neurosci.* 24, 1217–1225.
- Hilmas, C., Pereira, E.F.R., Alkondon, M., Rassoulpour, A., Schwarcz, R., and Albuquerque, E.X. (2001). The brain metabolite kynurenic acid inhibits α 7 nicotinic receptor activity and increases non- α 7 nicotinic receptor expression: physiopathological implications. *J. Neurosci.* 21, 7463–7473.
- Horvitz, H.R., Chalfie, M., Trent, C., Sulston, J.E., and Evans, P.D. (1982). Serotonin and octopamine in the nematode *Caenorhabditis elegans*. *Science* 216, 1012–1014.
- Kao, G., Nordenson, C., Still, M., Rönnlund, A., Tuck, S., and Naredi, P. (2007). ASNA-1 positively regulates insulin secretion in *C. elegans* and mammalian cells. *Cell* 128, 577–587.
- Kubiak, T.M., Larsen, M.J., Bowman, J.W., Geary, T.G., and Lowery, D.E. (2008). FMRFamide-like peptides encoded on the *flp-18* precursor gene activate two isoforms of the orphan *Caenorhabditis elegans* G-protein-coupled receptor Y58G8A.4 heterologously expressed in mammalian cells. *Biopolymers* 90, 339–348.
- Lam, T.K.T. (2010). Neuronal regulation of homeostasis by nutrient sensing. *Nat. Med.* 16, 392–395.
- Lapin, I.P., and Oxenkrug, G.F. (1969). Intensification of the central serotonergic processes as a possible determinant of the thymoleptic effect. *Lancet* 1, 132–136.
- Lee, B.H., Liu, J., Wong, D., Srinivasan, S., and Ashrafi, K. (2011). Hyperactive neuroendocrine secretion causes size, feeding, and metabolic defects of *C. elegans* Bardet-Biedl syndrome mutants. *PLoS Biol.* 9, e1001219.

- Li, W., Kennedy, S.G., and Ruvkun, G. (2003). *daf-28* encodes a *C. elegans* insulin superfamily member that is regulated by environmental cues and acts in the DAF-2 signaling pathway. *Genes Dev.* 17, 844–858.
- Liang, B., Moussaif, M., Kuan, C.-J., Gargus, J.J., and Sze, J.Y. (2006). Serotonin targets the DAF-16/FOXO signaling pathway to modulate stress responses. *Cell Metab.* 4, 429–440.
- Liu, T., Kong, D., Shah, B.P., Ye, C., Koda, S., Saunders, A., Ding, J.B., Yang, Z., Sabatini, B.L., and Lowell, B.B. (2012). Fasting activation of AgRP neurons requires NMDA receptors and involves spinogenesis and increased excitatory tone. *Neuron* 73, 511–522.
- McElroy, S.L., and Keck, P.E., Jr. (2014). Metabolic syndrome in bipolar disorder: a review with a focus on bipolar depression. *J. Clin. Psychiatry* 75, 46–61.
- Mitchell, A.J., Vancampfort, D., Sweers, K., van Winkel, R., Yu, W., and De Hert, M. (2013). Prevalence of metabolic syndrome and metabolic abnormalities in schizophrenia and related disorders—a systematic review and meta-analysis. *Schizophr. Bull.* 39, 306–318.
- Perkins, M.N., and Stone, T.W. (1982). An iontophoretic investigation of the actions of convulsant kynurenes and their interaction with the endogenous excitant quinolinic acid. *Brain Res.* 247, 184–187.
- Piggott, B.J., Liu, J., Feng, Z., Wescott, S.A., and Xu, X.Z.S. (2011). The neural circuits and synaptic mechanisms underlying motor initiation in *C. elegans*. *Cell* 147, 922–933.
- Sawin, E.R., Ranganathan, R., and Horvitz, H.R. (2000). *C. elegans* locomotory rate is modulated by the environment through a dopaminergic pathway and by experience through a serotonergic pathway. *Neuron* 26, 619–631.
- Schwarcz, R., Rassoulpour, A., Wu, H.-Q., Medoff, D., Tamminga, C.A., and Roberts, R.C. (2001). Increased cortical kynurenate content in schizophrenia. *Biol. Psychiatry* 50, 521–530.
- Schwarcz, R., Bruno, J.P., Muchowski, P.J., and Wu, H.-Q. (2012). Kynurenines in the mammalian brain: when physiology meets pathology. *Nat. Rev. Neurosci.* 13, 465–477.
- Sengupta, P. (2013). The belly rules the nose: feeding state-dependent modulation of peripheral chemosensory responses. *Curr. Opin. Neurobiol.* 23, 68–75.
- Song, B.M., Faumont, S., Lockery, S., and Avery, L. (2013). Recognition of familiar food activates feeding via an endocrine serotonin signal in *Caenorhabditis elegans*. *eLife* 2, e00329.
- Srinivasan, S., Sadegh, L., Elle, I.C., Christensen, A.G.L., Faergeman, N.J., and Ashrafi, K. (2008). Serotonin regulates *C. elegans* fat and feeding through independent molecular mechanisms. *Cell Metab.* 7, 533–544.
- Steiner, J., Walter, M., Gos, T., Guillemin, G.J., Bernstein, H.-G., Sarnyai, Z., Mawrin, C., Brisch, R., Bielau, H., Meyer zu Schwabedissen, L., et al. (2011). Severe depression is associated with increased microglial quinolinic acid in subregions of the anterior cingulate gyrus: evidence for an immune-modulated glutamatergic neurotransmission? *J. Neuroinflammation* 8, 94.
- Stipanuk, M.H., and Caudill, M.A. (2013). *Biochemical, Physiological, and Molecular Aspects of Human Nutrition* (Philadelphia, PA: Elsevier Health Sciences).
- Sze, J.Y., Victor, M., Loer, C., Shi, Y., and Ruvkun, G. (2000). Food and metabolic signalling defects in a *Caenorhabditis elegans* serotonin-synthesis mutant. *Nature* 403, 560–564.
- Taylor, R.C., Berendzen, K.M., and Dillin, A. (2014). Systemic stress signalling: understanding the cell non-autonomous control of proteostasis. *Nat. Rev. Mol. Cell Biol.* 15, 211–217.
- Tian, L., Hires, S.A., Mao, T., Huber, D., Chiappe, M.E., Chalasani, S.H., Petreanu, L., Akerboom, J., McKinney, S.A., Schreiter, E.R., et al. (2009). Imaging neural activity in worms, flies and mice with improved GCaMP calcium indicators. *Nat. Methods* 6, 875–881.
- van der Goot, A.T., and Nollen, E.A.A. (2013). Tryptophan metabolism: entering the field of aging and age-related pathologies. *Trends Mol. Med.* 19, 336–344.
- van der Goot, A.T., Zhu, W., Vázquez-Manrique, R.P., Seinstra, R.I., Dettmer, K., Michels, H., Farina, F., Krijnen, J., Melki, R., Buijsman, R.C., et al. (2012). Delaying aging and the aging-associated decline in protein homeostasis by inhibition of tryptophan degradation. *Proc. Natl. Acad. Sci. USA* 109, 14912–14917.
- Waggoner, L.E., Hardaker, L.A., Golik, S., and Schafer, W.R. (2000). Effect of a neuropeptide gene on behavioral states in *Caenorhabditis elegans* egg-laying. *Genetics* 154, 1181–1192.
- Whim, M.D., and Moss, G.W.J. (2001). A novel technique that measures peptide secretion on a millisecond timescale reveals rapid changes in release. *Neuron* 30, 37–50.
- White, J.G., Southgate, E., Thomson, J.N., and Brenner, S. (1986). The structure of the nervous system of the nematode *Caenorhabditis elegans*. *Philos. Trans. R. Soc. Lond. B Biol. Sci.* 314, 1–340.
- You, Y.J., Kim, J., Raizen, D.M., and Avery, L. (2008). Insulin, cGMP, and TGF- β signals regulate food intake and quiescence in *C. elegans*: a model for satiety. *Cell Metab.* 7, 249–257.
- Zwilling, D., Huang, S.-Y., Sathyaikumar, K.V., Notarangelo, F.M., Guidetti, P., Wu, H.-Q., Lee, J., Truong, J., Andrews-Zwilling, Y., Hsieh, E.W., et al. (2011). Kynurenine 3-monooxygenase inhibition in blood ameliorates neurodegeneration. *Cell* 145, 863–874.

Endogenous Hydrogen Sulfide Production Is Essential for Dietary Restriction Benefits

Christopher Hine,¹ Eylul Harputlugil,¹ Yue Zhang,¹ Christoph Ruckenstein,⁴ Byung Cheon Lee,² Lear Brace,¹ Alban Longchamp,^{1,3} Jose H. Treviño-Villarreal,¹ Pedro Mejia,¹ C. Keith Ozaki,³ Rui Wang,⁶ Vadim N. Gladyshev,² Frank Madeo,^{4,5} William B. Mair,¹ and James R. Mitchell^{1,*}

¹Department of Genetics and Complex Diseases, Harvard School of Public Health

²Division of Genetics, Department of Medicine

³Department of Surgery and the Heart and Vascular Center

Brigham and Women's Hospital and Harvard Medical School, Boston, MA 02115, USA

⁴Institute for Molecular Biosciences, NAWI Graz, University of Graz, Graz 8010, Austria

⁵BioTechMed Graz, Humboldtstrasse 50, Graz 8010, Austria

⁶Department of Biology, Lakehead University, Thunder Bay, ON P7B 5E1, Canada

*Correspondence: jmitchel@hsph.harvard.edu

<http://dx.doi.org/10.1016/j.cell.2014.11.048>

SUMMARY

Dietary restriction (DR) without malnutrition encompasses numerous regimens with overlapping benefits including longevity and stress resistance, but unifying nutritional and molecular mechanisms remain elusive. In a mouse model of DR-mediated stress resistance, we found that sulfur amino acid (SAA) restriction increased expression of the transsulfuration pathway (TSP) enzyme cystathionine γ -lyase (CGL), resulting in increased hydrogen sulfide (H_2S) production and protection from hepatic ischemia reperfusion injury. SAA supplementation, mTORC1 activation, or chemical/genetic CGL inhibition reduced H_2S production and blocked DR-mediated stress resistance. In vitro, the mitochondrial protein SQR was required for H_2S -mediated protection during nutrient/oxygen deprivation. Finally, TSP-dependent H_2S production was observed in yeast, worm, fruit fly, and rodent models of DR-mediated longevity. Together, these data are consistent with evolutionary conservation of TSP-mediated H_2S as a mediator of DR benefits with broad implications for clinical translation.

INTRODUCTION

Dietary restriction (DR) encompasses a variety of nutritional interventions with overlapping functional benefits including increased stress resistance and extended longevity in a number of organisms across evolutionary boundaries (Fontana et al., 2010). In mammals, dietary regimens associated with these benefits are diverse, including reduced daily food intake, intermittent fasting and reduced protein or essential amino acid intake. Although common features exist among DR regimens, including reduced adiposity and improved sensitivity to growth factors, differences exist as well. Thus, whether overlapping functional benefits of DR regimens share a common underlying nutritional

and/or molecular basis remains unclear. Despite strong evidence of DR benefits in humans (Levine et al., 2014), difficulties with compliance prevent widespread clinical applications. Uncovering common mechanisms is thus of great significance for targeted dietary and/or pharmacological interventions.

Mitohormesis represents a potential unifying molecular hypothesis of DR action (Sinclair, 2005). Based on the concept of hormesis (Calabrese and Mattson, 2011), in which low-level stressors promote adaptive changes resulting in stress resistance, the mitohormesis hypothesis of DR posits that increased reactive oxygen and nitrogen species (RONS) derived from increased mitochondrial fatty acid oxidation induce mild oxidative stress, thus driving adaptive mechanisms of antioxidant protection (Tapia, 2006). SKN1/NRF2 has emerged as a candidate mediator of adaptive protection based on its activation by RONS and function as a key transcription factor in the cytoprotective phase II antioxidant and detoxification response (Hine and Mitchell, 2012). Gene targets of NRF2 include heme oxygenase-1 (HO-1), NAD(P)H dehydrogenase quinone 1 (NQO-1), glutathione transferases (GSTs), and additional genes that utilize glutathione (GSH) for resolving oxidative stress. SKN1/NRF2 in worms is required for stress resistance and longevity benefits of DR (Bishop and Guarente, 2007). In mammals, NRF2 is required for DR-mediated protection from chemically induced carcinogenesis but not for DR-mediated longevity (Pearson et al., 2008). Functionally, mitohormesis can be blocked by vitamin C, vitamin E, and/or N-acetyl cysteine (NAC), presumably due to their antioxidant capacity (Ristow and Schmeisser, 2011).

Restriction of sulfur amino acids (SAAs) methionine (Met) and cysteine (Cys) is common to numerous DR regimens across evolutionary boundaries and is thus a potential shared nutritional trigger of DR benefits. In yeast, Met restriction extends longevity (Ruckenstein et al., 2014). In flies, restriction of essential amino acids (EAAs), and in particular Met, controls DR longevity benefits (Grandison et al., 2009). Dietary Met further interacts with overall protein levels in longevity control (Lee et al., 2014). In rodents, diets lacking the nonessential amino acid (NEAA) Cys and restricted for Met (Met restriction, or MetR) extend longevity and increase hepatic stress resistance (Miller et al., 2005; Orentreich et al., 1993).

The TSP controls the conversion of Met into Cys and is required for DR-mediated lifespan extension in flies (Kabil et al., 2011a). Two key enzymes of this evolutionarily conserved pathway are cystathionine β -synthase (CBS) and cystathionine γ -lyase (CGL). Under normal physiological conditions, CBS converts serine and homocysteine, a product of Met methyl transfer, into cystathionine. Cystathionine is then converted into α -keto-butyrate and Cys by CGL (Kabil et al., 2011b). Although Cys is required for de novo synthesis of GSH, thus potentially linking TSP to NRF2-mediated antioxidant responses, the molecular mechanism underlying the genetic requirement for a functional TSP in DR-mediated benefits is unknown.

A product of the TSP with potential to mediate physiological benefits including stress resistance and extended longevity is the water and fat-soluble gas H₂S (Cuevasanta et al., 2012; Zhang et al., 2013). Although toxic at high levels, H₂S produced at low concentrations by degradation of Cys or homocysteine by CGL or CBS acts on the vasculature and the brain as a signaling molecule to reduce blood pressure (Yang et al., 2008) and prevent neurodegeneration (Paul and Snyder, 2012). Exogenous H₂S can also extend lifespan of worms (Miller and Roth, 2007) and induce suspended animation in mammals (Blackstone et al., 2005). Although diet can impact H₂S production (Predmore et al., 2010), neither the dietary requirements for increased endogenous H₂S production, nor the potential role of H₂S in the benefits of DR are currently known.

Ischemia reperfusion injury (IRI) is initiated by lack of nutrients and oxygen due to occlusion of blood flow (ischemia) followed by activation of pro-oxidation pathways and inflammatory mediators in damaged tissues upon return of blood flow (reperfusion). IRI represents a major clinical concern in controlled (tissue resection, organ transplantation) and uncontrolled settings (stroke, heart attack). Various short-term (3–14 days) DR regimens improve outcome in models of kidney, liver, and brain IRI (Harputlugil et al., 2014; Mitchell et al., 2010; Peng et al., 2012; Varendi et al., 2014). Here, we used dietary preconditioning against hepatic IRI as a model system to probe dietary and molecular mechanisms underlying protection.

RESULTS

NAC, but Not NRF2 Deficiency, Abrogates Benefits of DR against IRI

Fifty percent DR for 7 days significantly decreased body weight, percentage fat mass, serum triglycerides (TGs) (Figures 1A–1C), and blood glucose (BG) (Figure S1A available online) while increasing hepatic expression of FAO-related genes (Figure 1D) and the rate of peroxisomal FAO (Figure 1E) relative to the ad libitum (AL)-fed group. Consistent with the mitohormesis hypothesis, hepatic RONS and NRF2 target gene expression were increased (Figures 1F and 1G), and the latter blocked by NAC administration during the DR period. Total GSH was also decreased upon DR (Figure 1H).

The functional relevance of increased RONS and NRF2 activation in DR-mediated stress resistance was tested in a model of hepatic IRI. Wild-type (WT) mice were preconditioned on AL or DR regimens \pm NAC for 1 week prior to IRI. NAC treatment was halted 24 hr prior to IRI to avoid any direct antioxidant ef-

fects of this short-lived compound on outcome. Neither DR nor NAC had any significant effect on liver damage markers in serum prior to IRI (data not shown). After reperfusion, liver damage markers remained significantly lower in DR serum indicative of protection from injury (Figure 1I). NAC had no effect on outcome in the AL group, but significantly reduced protection in the DR group. Macroscopic and histological analysis of hemorrhagic necrosis in livers excised 24 hr after reperfusion (Figure 1J; Figure S1B) was consistent with serum damage markers (Figure 1I).

To test the requirement for the NRF2-dependent phase II antioxidant response, we compared NRF2 knockout (KO) mice to wild-type (WT) littermate controls. NRF2KO mice subjected to DR had decreased hepatic GSH similar to WT (Figure S1C) but failed to upregulate phase II antioxidant response genes as expected (Figure S1D). Surprisingly, benefits of DR against hepatic IRI did not require NRF2, with similar reductions in liver damage markers in serum (Figure 1K) and macroscopic evidence of hemorrhage 24 hr postreperfusion upon DR in both WT and NRF2KO mice (Figure S1E). To confirm and extend this result, we tested the requirement for NRF2 in DR-mediated protection from renal IRI. Although AL-fed NRF2KOs had slightly elevated damage and decreased renal function upon IRI relative to WT mice as reported previously (Liu et al., 2009), both gained similar benefits upon DR (Figure S1F).

Sulfur Amino Acids Control the Benefits of DR and PR

NRF2 independence of DR benefits despite abrogation by NAC is consistent either with an alternate RONS-dependent mechanism of DR-mediated protection, or an antioxidant-independent activity of NAC. NAC is also a source of Cys, and NAC supplementation to the DR group above serendipitously returned dietary Cys content close to AL levels. To separate the functional consequences of antioxidant capacity from SAA content, we supplemented restricted diets separately with either antioxidants (vitamin C and E [VitC&E]) or a 2 \times concentration of Met and Cys (2 \times Met&Cys) for 1 week prior to hepatic IRI. Following reperfusion, protection afforded by DR was maintained despite VitC&E antioxidant treatment, but abrogated by 2 \times Met&Cys (Figures 2A and 2B) without affecting food intake, weight loss, or expression of FOXO target genes (Figures S2A–S2C), consistent with the relative importance of the SAA aspect of NAC in abrogation of DR benefits.

Protein and carbohydrates are isocaloric and partially interconvertible as dietary energy sources, rendering distinctions between calorie restriction and protein/amino acid restriction upon DR challenging. To test the relative contribution of energy restriction, protein restriction (PR), and specifically SAA restriction to DR-mediated protection against hepatic IRI, we preconditioned mice on a complete or isocaloric protein-free diet fed either AL or 35% restricted \pm 2 \times Met&Cys. Following hepatic IRI, PR mice displayed significant protection from liver damage (Figures 2C and 2D) independent of total calorie intake or weight loss (Figures S2D and S2E). Importantly, 2 \times Met&Cys abrogated significant benefits of combined protein/energy restriction (Figures 2C and 2D) without affecting weight loss (Figure S2E). Because MetR regimens offering overlapping functional benefits with DR are also restricted or deficient in Cys, we also tested Cys reconstitution alone. Following reperfusion, protection observed

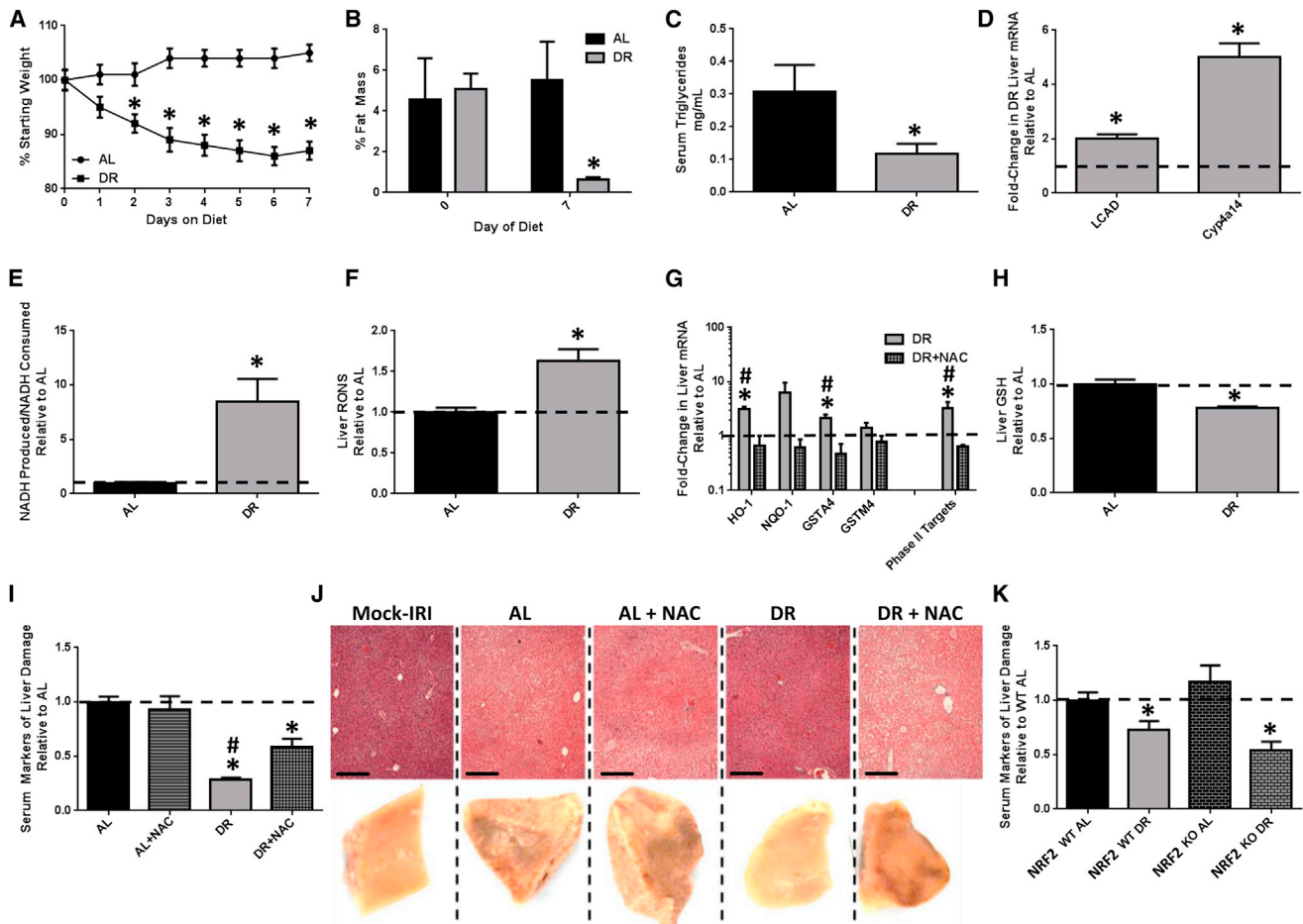


Figure 1. NAC Abrogates Benefits of DR against Acute Stress Independent of NRF2

(A–H) Effects of 1 week of 50% DR versus AL feeding \pm NAC as indicated on body weight ($n = 15$ – 17 /group, A); %fat mass ($n = 5$ /group, B); serum triglycerides ($n = 4$ – 7 /group, C); hepatic FAO-associated gene expression ($n = 3$ /group, D); peroxisomal FAO capacity in liver extracts ($n = 3$ /group, E); hepatic RONS ($n = 6$ – 8 /group, F); hepatic NRF2 target gene expression ($n = 4$ /group, G); and hepatic GSH levels ($n = 7$ /group, H).

(I and J) Combined serum markers of liver damage normalized to the average of the AL control group (I) and liver pathology from injured left liver lobes on the microscopic level stained with hematoxylin and eosin (scale bar, 250 μ m, above) and the macroscopic level (1 \times magnification, below) showing fixed tissue 24 hr after reperfusion (J) in mice ($n = 5$ – 6 /group) preconditioned as indicated before hepatic IRI or mock injury. Asterisk indicates the significance of the difference between AL and DR, and pound sign between DR and DR + NAC; $^{\#}/^{\ast}p < 0.05$.

(K) Serum markers of liver damage in WT ($n = 5$ – 6 /group) or NRF2KO ($n = 7$ – 12 /group) preconditioned as indicated. Asterisk indicates the significance of the difference between AL and DR within genotype; $^{\ast}p < 0.05$.

All error bars SEM. See also Figure S1.

in the DR group was abrogated upon 2 \times Cys supplementation (Figures 2E and 2F), consistent with PR and Cys restriction as critical aspects of DR-mediated resistance to hepatic IRI.

DR Stimulates Endogenous H₂S Production via Repression of mTORC1 and Activation of the TSP

Expression and activity of TSP genes CBS and CGL increase when Cys is low (Stipanuk and Ueki, 2011) to allow de novo synthesis from Met (Figure 3A). Hepatic CGL and CBS to a lesser degree were increased on the mRNA and protein levels upon 1 week DR (Figures 3B and 3C), and this was abrogated by 2 \times Met&Cys or NAC supplementation (Figure 3B).

A metabolomics approach was used to identify candidate TSP metabolites involved in DR-mediated protection. To facilitate

identification of potentially causative versus correlative changes, we included a genetic model that fails to gain the benefits of DR against hepatic IRI due to liver-specific genetic ablation of the mTORC1 repressor, tuberous sclerosis complex 1 (TSC1) (Hauptlugil et al., 2014) (Figure 3D; Figure S3A). GSH and taurine are two downstream metabolites with potential to protect against IRI, however neither was increased by DR specifically in WT mice (Figure 3D). A third protective TSP metabolite is hydrogen sulfide (H₂S) (Kang et al., 2009). Although not detected in our metabolomic screen, associated by-products homoserine and serine (Kabil et al., 2011b) were significantly increased upon DR in WT but not TSC1KO livers (Figure 3D).

For direct measurement of H₂S, we leveraged the specific reaction between H₂S and lead acetate to form a black precipitate

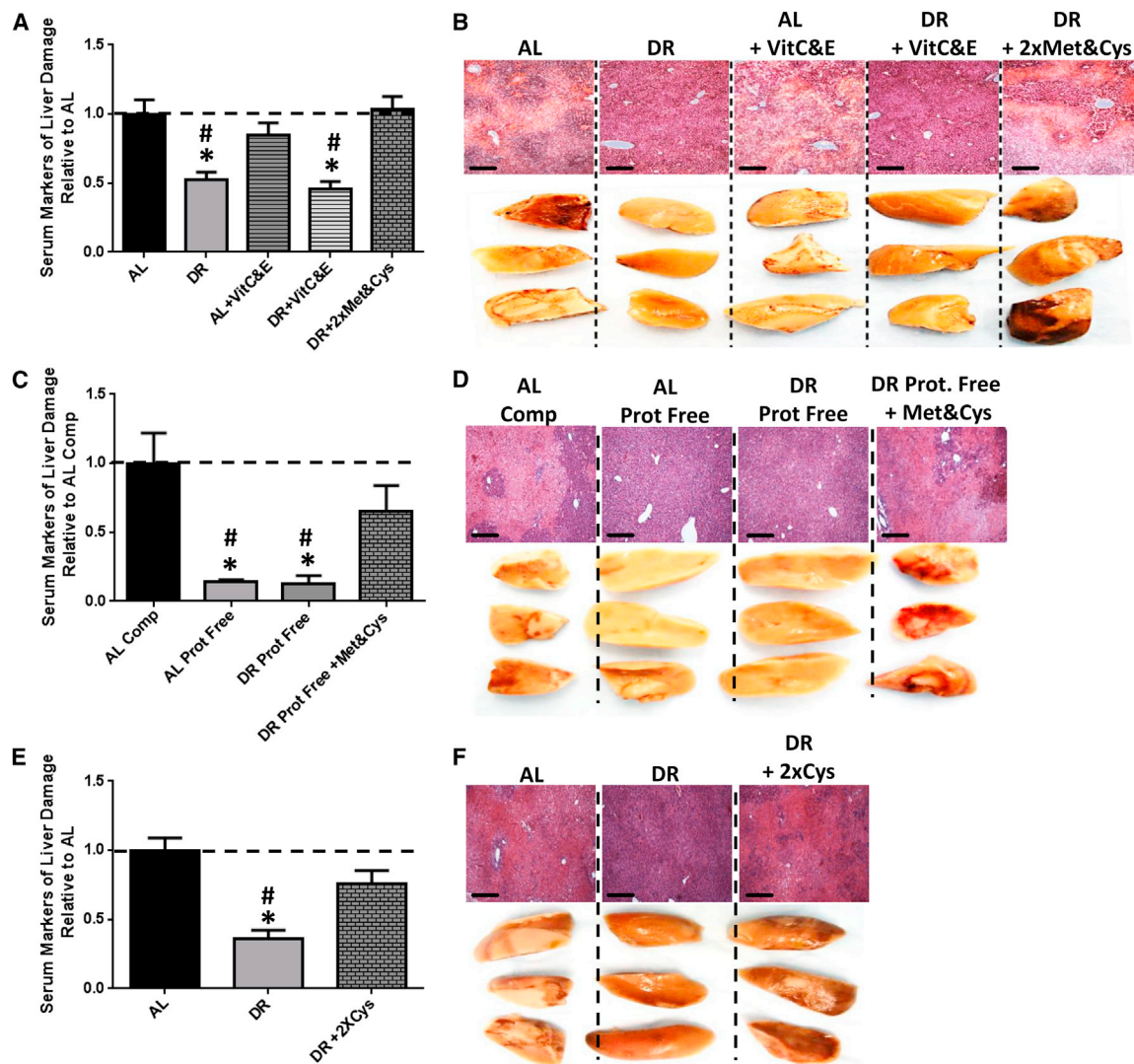


Figure 2. Sulfur Amino Acids Control the Benefits of DR and PR

(A and B) Serum markers of liver damage (A) and liver pathology after reperfusion (B) in mice ($n = 5/\text{group}$) preconditioned on complete diets fed AL or 50% DR \pm supplementation with vitamins C&E or Met&Cys as indicated. Asterisk indicates the significance of the difference versus AL and pound sign versus DR + 2 \times Met&Cys; $^{\#}/^*p < 0.05$.

(C and D) Serum markers of liver damage (C) and liver pathology after reperfusion (D) in mice ($n = 5/\text{group}$) preconditioned on complete (Comp) or protein-free (Prot. Free) diets fed AL or 35% DR with Met&Cys addition as indicated prior to hepatic IRI. Asterisk indicates the significance of the difference versus AL complete and pound sign versus DR Prot. Free + Met&Cys; $^{\#}/^*p < 0.05$.

(E and F) Serum markers of liver damage (E) and liver pathology after reperfusion (F) in mice ($n = 5/\text{group}$) preconditioned on complete diets fed AL or 50% DR with 2 \times Cys added as indicated. Asterisk indicates the significance of the difference versus AL and pound sign versus DR + 2 \times Cys; $^{\#}/^*p < 0.05$.

All error bars SEM. See also [Figure S2](#).

(lead sulfide) that can be trapped and visualized on filter paper containing lead acetate ([Figure S3B](#)). In the presence of excess CGL/CBS substrate Cys and cofactor pyridoxal-5'-phosphate (PLP), H_2S gas produced by liver extracts was greater from DR- than AL-fed mice ([Figure 3E](#)). This phenomenon was independent of NRF2 status ([Figure S3C](#)). Met&Cys add-back during DR blocked the DR-mediated increase in H_2S production capacity ([Figure 3F](#)), correlating with a loss of protection against hepatic IRI ([Figure 2A](#)) and normalization of hepatic GSH levels ([Figure S3D](#)).

Using a less specific but more easily quantifiable sulfide probe-based method calibrated against known H_2S concentrations ([Figures S3E](#) and [S3F](#)), liver extracts of DR mice displayed a 4-fold increase in H_2S production capacity compared to AL mice ([Figure 3G](#)). Endogenous hepatic H_2S levels measured by insertion of the sulfide probe into the right and median lobes of anesthetized mice were in the low micromolar range relative to the appropriate standard curve ([Figures S3G](#) and [S3H](#)), and nearly 3-fold higher in the livers of DR relative to AL-fed mice ([Figure 3H](#)).

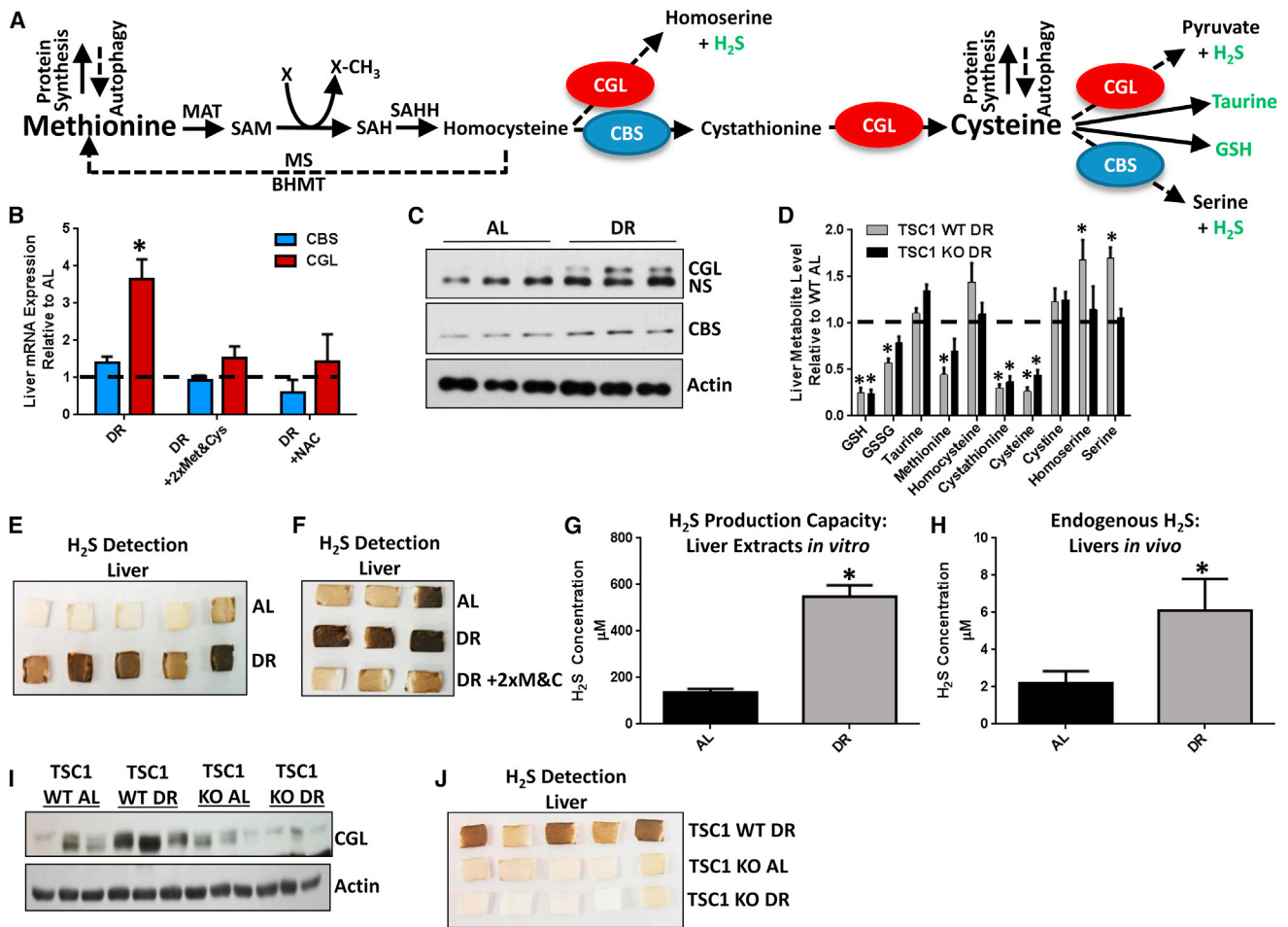


Figure 3. DR Stimulates Endogenous H₂S Production via the TSP

(A) Model of the transmethylation and TSP. Arrows trace sulfur from Met to Cys and downstream cellular processes via cystathionine beta-synthase (CBS) and cystathionine gamma-lyase (CGL). Metabolites in green (taurine, GSH and H₂S) have demonstrated potential to protect against IRI. MAT, methionine adenosyl transferase; SAM: S-adenosylmethionine; SAH, S-adenosylhomocysteine; SAHH, S-adenosylhomocysteine hydrolase; MS, methionine synthase; BHMT, betaine homocysteine methyltransferase.

(B) Hepatic CBS and CGL gene expression upon DR ± 2xMet&Cys or NAC as indicated; n = 3/group.

(C) Immunoblots of CGL, CBS, and actin in liver extracts from AL or DR mice as indicated; NS, nonspecific protein band.

(D) Liver metabolites in WT or LTsc1KO mice fed 35% DR on a protein-free diet relative to the AL-fed complete diet group; n = 5/group.

(E and F) H₂S production capacity from liver extracts of AL or DR mice (E) ± 2xMet&Cys (F) as detected by the black precipitate, lead sulfide.

(G) H₂S production capacity as in (E) but using a microsulfide probe to detect H₂S.

(H) Endogenous hepatic H₂S in mice on the indicated diet using a microsulfide probe inserted into liver lobes; n = 3 mice/group, two lobes/mouse. Asterisk indicates the significance of the difference versus AL; *p < 0.05.

(I and J) Immunoblots of liver CGL (I) and H₂S production (J) in WT and LTsc1KO mice fed AL or 35% DR on a protein-free diet.

All error bars SEM. See also Figure S3.

Consistent with a link between DR, TSP, H₂S, and protection from IRI, DR failed to increase hepatic CGL protein and H₂S production capacity in livers of TSC1KO mice (Figures 3I and 3J), suggesting that constitutive mTORC1 activation blocks DR-mediated TSP upregulation.

H₂S Is Necessary and Sufficient to Confer DR-Mediated Stress Resistance *In Vivo*

We next determined if exogenous H₂S is sufficient to confer protection in our model of hepatic IRI. AL-fed mice injected with the H₂S precursor NaHS or vehicle 30 min prior to ischemia had

decreased liver damage relative to vehicle-treated controls (Figures 4A and 4B). Similarly, noninvasive H₂S delivery in the drinking water for 1 week prior to hepatic IRI using the slow releasing/long-lived donor GYY4137 (Lee et al., 2011) (but not the fast releasing/short-lived donor NaHS) decreased liver damage without affecting animal weight, food intake, or water consumption (Figures S4A–S4D). Thus, exogenous H₂S is sufficient to protect against hepatic IRI.

A specific inhibitor of CGL, DL-propargylglycine (PAG), was employed to determine if endogenous H₂S is necessary for DR-mediated stress resistance. PAG treatment blocked hepatic

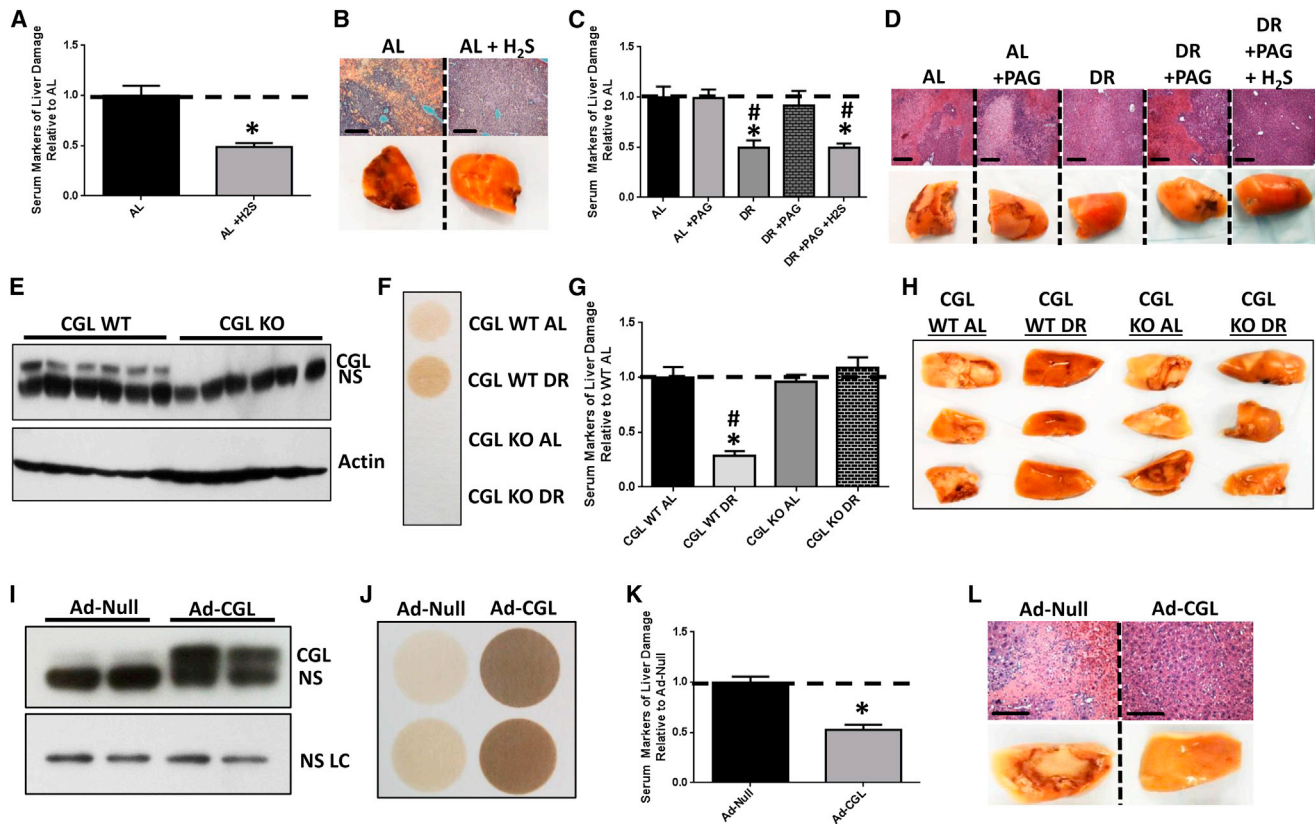


Figure 4. H₂S Is Necessary and Sufficient to Confer DR Benefits against Hepatic IRI

(A and B) Serum markers of liver damage (A) and liver pathology after reperfusion (B) in mice (n = 4–5/group) treated with vehicle or H₂S 30 min prior to surgery. Asterisk indicates the significance of the difference versus AL; *p < 0.05.

(C and D) Serum markers of liver damage (C) and liver pathology after reperfusion (D) in mice (n = 3–4/group) treated with PAG during AL or DR preconditioning with a single H₂S injection prior to surgery as indicated. Asterisk indicates the significance of the difference versus AL and pound sign versus DR + PAG; */#p < 0.05.

(E) Immunoblot of CGL in liver extracts of WT or CGLKO mice as indicated. NS, nonspecific protein.

(F) H₂S production capacity of liver extracts from WT or CGLKO mice preconditioned as indicated.

(G and H) Serum markers of liver injury (G) and liver pathology after reperfusion (H) in WT or CGLKO mice (n = 5–8/group) preconditioned as indicated. Asterisk indicates the significance of the difference versus WT AL and pound sign versus CGLKO DR; */#p < 0.05.

(I) Immunoblot of CGL in liver extracts from WT mice infected with control (Ad Null) or CGL-overexpressing (Ad-CGL) adenovirus as indicated; NS LC, nonspecific loading protein.

(J) H₂S production capacity of liver extracts of Ad-Null- or Ad-CGL-infected mice.

(K and L) Serum markers of liver damage (K) and liver pathology after reperfusion (L) in Ad-Null- or Ad-CGL-infected mice (n = 6/group). Asterisk indicates the significance of the difference versus Ad Null; *p < 0.05.

All error bars SEM. See also Figure S4.

H₂S production capacity (Figure S4E) and decreased endogenous hepatic H₂S levels upon DR (Figure S4F), consistent with the dominant role of CGL in hepatic H₂S production. PAG treatment had no effect on IRI outcome in AL mice but abrogated benefits of DR (Figures 4C and 4D). Readdition of H₂S via IP injection of 30 min prior to induction of ischemia in DR + PAG-treated mice restored protection (Figures 4C and 4D).

Two genetic models were used to test the specificity of the TSP and H₂S in protection against hepatic IRI (Figures 4E–4L). The necessity of CGL in DR-mediated benefits was tested with whole-body CGLKO mice (Yang et al., 2008). CGLKO mice responded to DR like WT mice with respect to changes in body weight, food intake, body composition, and blood glucose (Fig-

ures S4G–S4J) despite the lack of CGL protein in liver or capacity of liver extracts to produce H₂S (Figures 4E and 4F). However, whereas the absence of CGL had no apparent impact on the outcome of hepatic IRI in AL-fed mice, CGLKO mice failed to gain protection upon DR (Figures 4G and 4H). To test the sufficiency of increased TSP activity and endogenous H₂S production, CGL was overexpressed via adenoviral-mediated gene delivery (Ad-CGL). Hepatic CGL protein levels and H₂S production capacity were both significantly increased (Figures 4I and 4J) independent of body mass or food intake relative to control adenovirus (Ad Null) -infected mice (Figures S4K and S4L). Ad-CGL infection resulted in improved outcome after hepatic IRI relative to Ad-Null-infected mice (Figures 4K and 4L). Together,

these results suggest that increased TSP activity and endogenous H₂S production via CGL are sufficient and, in the case of DR, necessary for protection against the acute surgical stress of hepatic IRI.

H₂S Is Necessary and Sufficient to Confer DR-Mediated Stress Resistance In Vitro via Sulphydration and Antioxidant Properties

To determine if TSP gene expression and H₂S production can be induced in a cell-autonomous manner by SAA restriction, we cultured mouse hepatocyte-derived Hepa1-6 cells overnight in complete media or media lacking SAA (–Met&Cys). Similar to DR in vivo, SAA deprivation increased CBS and CGL expression and H₂S production capacity in vitro (Figures 5A and 5B).

To determine if exogenously added H₂S can protect cultured Hepa1-6 cells against simulated IRI, warm ischemia was simulated by replacing growth media with saline and incubating in a 37°C hypoxic chamber for up to 4 hr, and reperfusion by replacing the growth media under normoxic conditions. Addition of H₂S decreased Hepa1-6 cell damage under both normoxic and hypoxic conditions during the ischemic phase (Figure 5C) and restored MTT activity during the reperfusion phase (Figure 5D), indicating that exogenous H₂S is sufficient to induce significant protection against both nutrient/energy deprivation and hypoxia in vitro.

To assess if endogenous H₂S induced by SAA restriction afforded similar protection, primary hepatocytes were cultured ± Met&Cys overnight prior to simulated IRI. LDH release during ischemia was decreased (Figure 5E), and MTT activity during reperfusion increased in hepatocytes preconditioned in Met&Cys-deficient media (Figure 5F). Similar protection afforded by overnight preconditioning of Hepa1-6 cells in –Met&Cys media was blocked by addition of PAG during the preconditioning period and was partially rescued by exogenous addition of H₂S during ischemia (Figure S5A).

H₂S has been proposed to prevent cell damage/death under stress in part by sulphydration of target proteins (Paul and Snyder, 2012) including the mitochondrial inner membrane component sulfide quinone oxidoreductase (SQR), which allows transfer of electrons from H₂S to coenzyme Q and the electron transport chain (ETC) (Módis et al., 2013; Olson et al., 2013) (Figure 5G). To test the potential role of the SQR in H₂S-mediated protection, we partially knocked down the SQR in Hepa1-6 cells (Figure S5B) prior to simulated IRI ± exogenous H₂S. H₂S addition reduced LDH release during the ischemic phase and upon reperfusion (Figures 5H and 5I); the latter was significantly altered upon SQR knockdown (KD) (Figure 5I). Additionally, the increase in MTT activity during the reperfusion phase in the presence of H₂S was significantly reduced by SQR KD (Figure 5J). SQR KD did not significantly alter the effects of H₂S addition on nutrient/growth factor withdrawal in the absence of hypoxia (Figures 5H–5J).

Because oxidation of H₂S by SQR results in production of thiosulfate (S₂O₃^{2–}) (Hildebrandt and Grieshaber, 2008), which itself can be utilized in mammalian tissues under hypoxic conditions for further H₂S production (Olson et al., 2013), we next tested if this downstream metabolite could afford similar protection against simulated IRI in Hepa1-6 cells. Although thiosulfate

had a negative impact on LDH release upon nutrient/growth factor withdrawal under normoxia, increasing thiosulfate concentrations decreased cell damage during the ischemic phase under hypoxia (Figure S5C) and improved MTT activity during the reperfusion phase (Figure S5D). SQR KD partially blocked thiosulfate-mediated protection against simulated IRI (Figure 5K; Figure S5E), suggesting that the protective effect of thiosulfate during hypoxia can be partially attributed to its conversion to H₂S.

H₂S also has antioxidant properties (Calvert et al., 2010) that could contribute to cytoprotection independent of target protein sulphydration. At 100 μM but not 10 μM final concentration, H₂S protected Hepa1-6 cells against acute oxidative stress delivered by H₂O₂ exposure (Figures S5F and S5G). Similar protection was found with 100 μM H₂S against H₂O₂ exposure in primary smooth muscle cells (Figures S5H and S5I). Thus, H₂S protects from acute ischemic insult and oxidative stress via multiple mechanisms.

Increased Endogenous H₂S Production in Diet-Induced Longevity Extension Models across Evolutionary Boundaries

Although exogenous H₂S can extend longevity in worms, the potential role of endogenous H₂S in DR-mediated lifespan extension has not been reported. To test the hypothesis that increased endogenous H₂S is a common feature of DR regimens that lead to extended longevity across evolutionary boundaries, we measured H₂S production capacity in four different organisms subjected to species-appropriate DR longevity regimens.

Adult mice subjected to long-term MetR (Figure 6A), EOD fasting, or 20%–30% DR (Figure 6B) had increased H₂S production capacity in liver and kidney extracts compared to AL-fed complete diet controls. In mice subjected to 1 week 50% DR, kidney, spleen, and carotid artery additionally demonstrated increased H₂S production capacity (Figure S6A), whereas brain, skeletal muscle, heart, and aorta tested under the same conditions did not (Figure S6B). Nonetheless, primary smooth muscle cells prepared from aorta displayed increased H₂S production capacity upon Met&Cys depletion (Figure S6C), suggesting tissue/cell type specificity in the regulation of the TSP in response to diet. Although we failed to observe an increase in H₂S production capacity in mouse brain upon 1 week 50% DR, 3 days of water-only fasting increased H₂S production capacity (Figure S6D).

In the fruit fly *D. melanogaster*, maximal H₂S production capacity of whole-body extracts of flies subjected to varying levels of dietary protein and Met restriction (Figure 6C) correlated with maximal lifespan extension (Lee et al., 2014).

In the nematode worm *C. elegans*, the *eat-2* mutant serves as a genetic model of lifespan extension by DR due to defects in pharyngeal function resulting in decreased food intake (Lakowski and Hekimi, 1998). Extracts of *eat-2* mutants produced more H₂S than extracts of age-matched WT N2 worms (Figure 6D). To assess the genetic requirements for TSP factors in longevity extension, we performed individual RNAi-mediated KD of the two worm CGL homologs CTH-1 and CTH-2, the CBS homolog CBS-1, and a fourth worm TSP gene, CBL-1. Individual RNAi KD of CBL-1 and CBS-1 had no effect on longevity

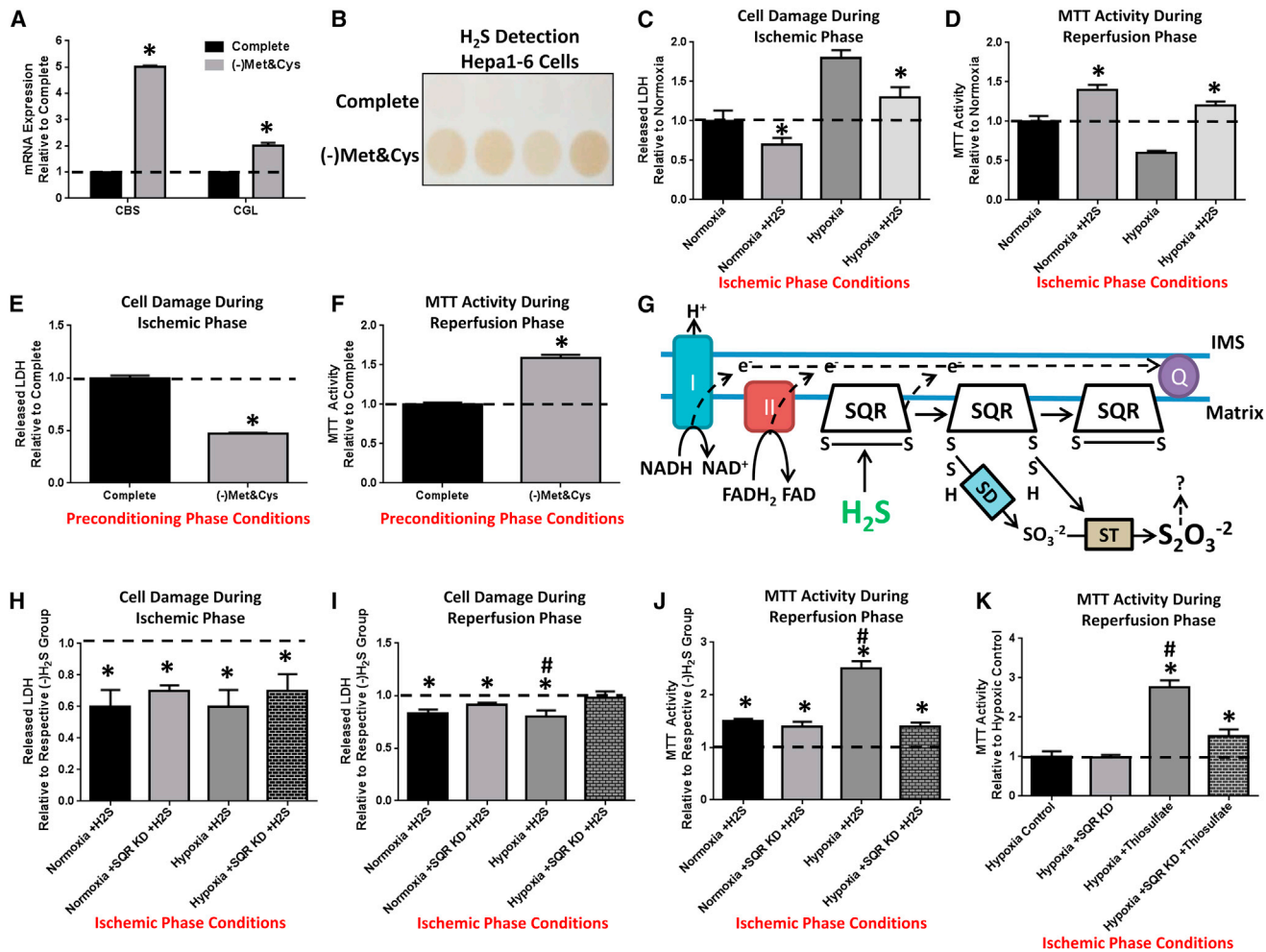


Figure 5. Mitochondrial SQR Is Required for Cytoprotective Effects of H₂S during Ischemia

(A and B) Cell-autonomous increase in TSP enzymes and H₂S production. (A) CBS and CGL gene expression in Hepa1-6 cells cultured overnight in complete or -Met&Cys media. Asterisk indicates the significance of the difference versus complete; *p < 0.05. (B) H₂S production in live Hepa1-6 cells preconditioned in complete or -Met&Cys media in quadruplicate for 16–24 hr as indicated before readdition of Cys and PLP for H₂S detection.

(C and D) Cell-autonomous effects of exogenous H₂S on simulated IRI in Hepa1-6 cells in vitro; H₂S was added during the ischemic phase and removed upon simulated reperfusion. (C) LDH release during the ischemic phase consisting of 3 hr incubation in saline (simulated nutrient/energy deprivation) under normoxic or hypoxic (simulated ischemia) conditions ± exogenous H₂S as indicated. (D) MTT activity during the reperfusion phase consisting of readdition of complete media under normoxic conditions (simulated reperfusion).

(E and F) Cell-autonomous effects of overnight Met&Cys withdrawal (preconditioning phase conditions) on simulated IRI in primary hepatocytes in vitro. LDH release (E) during simulated ischemia and MTT activity (F) upon simulated reperfusion.

(G) Schematic of H₂S oxidation to thiosulfate by SQR in mitochondria. Q, coenzyme Q; IMS, inner membrane space; I and II, complex I and II of the mitochondrial ETC; SD, sulfur dioxigenase; ST, sulfur transferase; S₂O₃²⁻, thiosulfate.

(H–J) Effects of exogenous H₂S on simulated IRI upon SQR KD in Hepa1-6 cells. LDH release during the ischemic phase (H) in saline under the indicated normoxic or hypoxic conditions ± SQR KD, and during the reperfusion phase (I) in complete media expressed relative to respective group not receiving H₂S during the ischemic phase; and MTT activity (J) during the reperfusion phase. Asterisk indicates the significance of the difference in the indicated group ± H₂S treatment; hash mark indicates the significance of the difference between control and SQR KD within a given treatment group; */#p < 0.05.

(K) Cell-autonomous effects of exogenous thiosulfate on MTT activity during the reperfusion phase following simulated IRI in Hepa1-6 cells ± SQR KD. Asterisk indicates the significance of the difference in the indicated group ± thiosulfate treatment; hash mark indicates the significance of the difference between control and SQR KD within a given treatment group; */#p < 0.05.

All error bars SEM. See also Figure S5.

(Figure S6E), but RNAi KD specifically of CBS-1 significantly decreased *eat-2* mediated lifespan extension, whereas overexpression of CBS-1 significantly extended median lifespan of WT N2 controls (Figure 6F).

Finally, DR-mediated extension of chronological lifespan in the yeast *S. cerevisiae* can be accomplished by reducing glucose in the growth media from 2% to 0.5% (Figure 6G) (Wu et al., 2013). Under these conditions, H₂S production from the

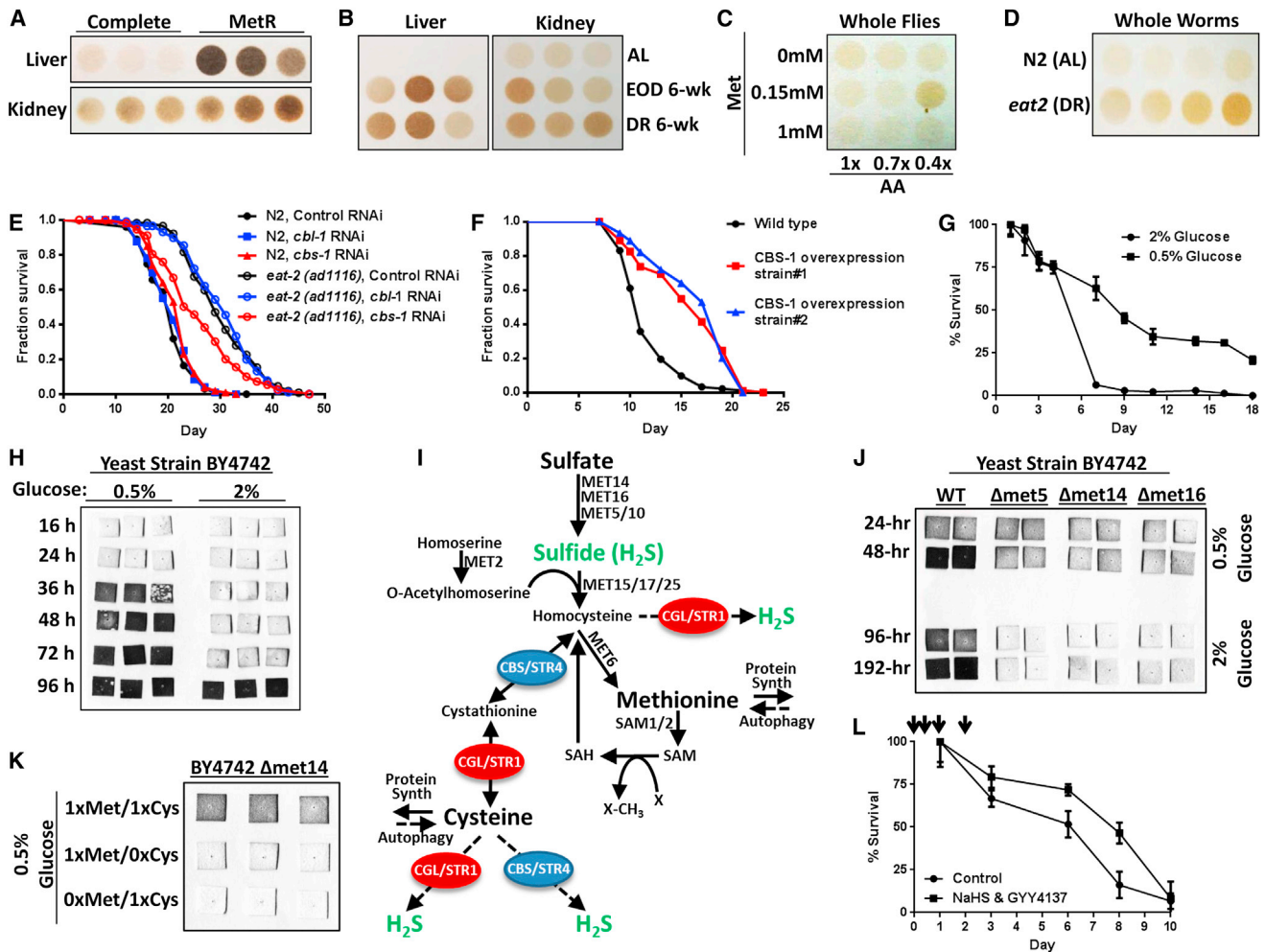


Figure 6. Increased Endogenous H_2S Production in Diet-Induced Longevity Extension Models Crosses Evolutionary Boundaries

(A and B) H_2S production capacity of liver and kidney extracts from mice with AL access to complete or MetR diets as indicated for 4 months (A) and in mice with AL, every-other-day (EOD) fasting, or 20%–30% restricted diets for 6 weeks (B). Each circle represents H_2S production from an individual animal, normalized for extract protein content.

(C) H_2S production capacity of whole-fly lysates normalized for protein content from populations subjected to the indicated dietary amino acid (AA) and Met concentrations. Maximal H_2S production capacity correlated with the optimal diet for longevity extension (0.4 × AA with 0.15 mM Met) (Lee et al., 2014).

(D) H_2S production capacity of N2 and *eat-2* whole-worm lysates in quadruplicate.

(E) Lifespan of N2 and *eat-2* worms subjected to RNAi-mediated KD of the TSP genes *cbs-1* or *cbl-1* as indicated.

(F) Lifespan analysis of WT or transgenic worms overexpressing CBS-1.

(G) Chronological lifespan of budding yeast grown in 2% or 0.5% glucose as indicated.

(H) H_2S production in yeast cultures grown in 2% or 0.5% glucose as detected by black lead sulfide accumulation on lead acetate papers inserted into the caps of the growth flasks and removed at the indicated time point.

(I) Schematic of transmethylation, TSP, and H_2S production in budding yeast.

(J) H_2S production in WT and sulfur assimilatory pathway mutant strains grown in 2% or 0.5% glucose for the indicated time.

(K) H_2S production in the *met14* sulfur assimilatory mutant grown in 0.5% glucose and the indicated relative amount of Met or Cys.

(L) Chronological lifespan in 2% glucose ± H_2S donors NaHS and GYY4137 added during early culture growth at indicated time points (arrows).

All error bars SEM. See also Figure S6.

glucose-restricted cultures was detected within 24–48 hr and continued to increase for up to 96 hr in three different yeast strains (Figure 6H; Figures S6F and S6G). As the majority of H_2S production in yeast occurs via an assimilatory pathway not present in metazoans in which extracellular sulfate is converted to sulfide by the combined enzymatic activities of MET14, MET16, and MET5/10 (Figure 6I), we next asked if

increased H_2S upon DR occurred through this assimilatory pathway or the conserved TSP pathway in yeast. Deletion of MET5, 14, or 16 resulted in inhibition of H_2S production under 2.0% glucose but did not block H_2S induction (Figure 6J) or chronological longevity extension (Figure S6H) upon glucose restriction. To further confirm Met and/or Cys, rather than inorganic sulfur, as the primary source of increased H_2S under conditions

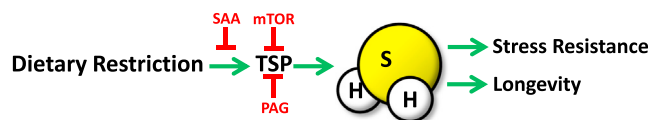


Figure 7. Model of DR-Mediated Benefits through Increased H₂S Production

DR regimens leading to extended longevity across evolutionary boundaries include PR, SAA restriction, and Cys restriction, leading to increased TSP activity via CGL and/or CBS family members, and increased endogenous H₂S production. Specific SAA addition, increased activity of the nutrient/energy sensing kinase, mechanistic target of rapamycin (mTOR), or the pharmacological agent, PAG, can block TSP upregulation and H₂S production. H₂S can readily diffuse through tissues and has pleiotropic, overlapping beneficial effects on the cellular, tissue, and organismal levels with the potential to contribute to stress resistance and longevity benefits of DR.

upon glucose restriction, we examined H₂S production in a Δ met14 line lacking a functional assimilatory pathway, with differing concentrations of Met and Cys in the media. Complete deprivation of either Met or Cys resulted in reduced H₂S production (Figure 6K). Thus, under conditions of glucose restriction, H₂S is produced from SAAs via the TSP. Because TSP-deficient CGL/STR1 and CBS/STR4 deletion strains grow abnormally in culture, it was not possible to test their requirement for increased H₂S production or extended chronological longevity under low-glucose conditions. However, exogenous H₂S donors NaHS and GYY4137 added early after inoculation were sufficient to significantly increase chronological lifespan (Figure 6L).

DISCUSSION

H₂S as Unifying Mechanism of DR Regimens and Benefits

As presented in the model in Figure 7, multiple DR regimens, including total food restriction, PR and SAA restriction/MetR, confer overlapping functional benefits in a number of diverse organisms from yeast (Johnson and Johnson, 2014) to worms (Cabreiro et al., 2013) to flies (Grandison et al., 2009; Troen et al., 2007) to rodents (Miller et al., 2005; Orentreich et al., 1993). In each of these experimental organisms, we found an increase in TSP-mediated H₂S production upon application of species-appropriate longevity regimens, ranging from EOD and MetR in mice to glucose restriction in yeast. Furthermore, in rodents and worms we demonstrated that genetic repression of TSP components blocked DR benefits, whereas overexpression could mimic benefits in the absence of any dietary intervention. In yeast, we found the TSP, rather than the assimilatory pathway, to be a major source of H₂S production upon glucose restriction. Although future studies are required to directly demonstrate the necessity of H₂S production for various DR benefits, our data demonstrate increased H₂S production via the TSP is an evolutionarily conserved response to DR from yeast to mammals with the potential to mediate multiple DR benefits including stress resistance and longevity. We note that the ability of SAA restriction to confer benefits in no way rules out other dietary triggers or downstream mechanisms of DR benefits, and that future studies will be required to determine if

benefits attributed to different DR regimens, including Trp restriction, impact the TSP or H₂S production.

Regulation of TSP Gene Expression and H₂S Production

Cys deprivation triggers increased TSP gene expression possibly via the integrated stress response through GCN2 activation, eIF2 α phosphorylation, and ATF4 stabilization (Lee et al., 2008). We confirmed the ability of DR to increase hepatic CGL expression in vivo, and Cys or NAC addback to block this induction. Whether or not GCN2 is required for this remains to be determined; however, our data suggest a role for mTORC1 in CGL regulation, because constitutive mTORC1 expression in the TSC1KO livers blocked diet-induced CGL expression.

Because the logic underlying TSP activation upon Cys deprivation is presumably to increase Cys biosynthesis, the notion that Cys degradation into H₂S increases when Cys concentrations are limiting is potentially counterintuitive. However, the in vivo source and identity of substrates for CGL or CBS-derived H₂S upon DR are not known. Free Cys released upon autophagy, rather than that produced de novo by TSP, could be a major fuel source for H₂S production. Interestingly, the benefits of MetR on longevity in yeast require autophagy (Ruckenstuhl et al., 2014), but whether autophagy plays a role in H₂S production remains to be determined.

Potential Mechanisms of H₂S Action in DR

By what mechanism(s) could endogenous H₂S give rise to pleiotropic DR benefits? We found that resistance to simulated IRI in vitro required the mitochondrial ETC component SQR. The SQR is thought to be of eubacterial origin and conserved from the early evolution of eukaryotes in an anoxic and sulfidic world (Theissen et al., 2003). H₂S could interact with SQR to lend protection against ischemia by donating electrons to the ETC via coenzyme Q, thus potentially serving as a source of electrons during ischemia. Interestingly, thiosulfate generated as a product of H₂S oxidation via SQR can undergo further chemical modification in a thioredoxin-reductase-dependent reaction using glutathione to produce sulfite and/or sulfate (Olson et al., 2013), which are used in some unicellular organisms as terminal electron acceptors for ATP production instead of oxygen, resulting in H₂S generation (Muyzer and Stams, 2008). Whether this can occur in mammalian cells remains to be explored; however, the addition of thiosulfate to hypoxic mammalian tissues results in the production of H₂S by unknown mechanisms (Olson et al., 2013).

Vasodilatory effects of H₂S could contribute to healthspan and lifespan extension in mammals by counteracting atherosclerosis, hypertension, and trauma. Exogenous H₂S protects the vasculature from oxidative damage (Yan et al., 2006), whereas a lack of CGL and/or endogenous H₂S production leads to hypertension (Yang et al., 2008). Fasting and PR protect the vasculature against intimal hyperplasia as a result of carotid focal stenosis (Mauro et al., 2014), correlating with increased H₂S production capacity upon DR in the carotid artery in vivo and vascular smooth muscle cells in vitro. Fasting protects the brain against IRI in rat models of transient middle cerebral artery occlusion (Varendi et al., 2014) and increased H₂S production capacity in mouse brain (Figure S6D). Future studies are required to address the specific role of increased TSP activity and H₂S

production in DR-mediated effects on the vasculature and other organ systems.

Clinical Significance

The use of exogenous H₂S as a DR mimetic is appealing for applications in which patient compliance with restricted food intake is an issue, but nonetheless remains challenging due to the short half-life of the gas in vivo and risks of toxicity at high levels. Modulation of endogenous H₂S production by diet offers advantages in terms of safety and continuous delivery in planned applications with brief duration, for example, in the context of preconditioning prior to elective surgery. In this context, H₂S may have pleiotropic advantages on surgical outcome, including vasodilatory and anti-inflammatory effects on the systemic level, as well as benefits against ischemic injury that may arise as part of the procedure itself or an unintended complication including heart attack or stroke.

Conclusions

H₂S was in vogue for centuries past as a cure-all before being viewed as a poisonous toxin with little or no acceptable level of exposure. Recently, H₂S has re-emerged as a potential therapeutic agent addressing numerous health issues (Zhang et al., 2013). Here, we identified DR as a trigger of increased endogenous H₂S production, and H₂S as a molecular mediator of pleiotropic DR benefits including longevity and stress resistance. These findings have broad implications for our basic understanding of DR and its potential clinical applications.

EXPERIMENTAL PROCEDURES

Additional details are provided in the [Extended Experimental Procedures](#).

Mice

All experiments were performed with the approval of the Harvard Medical Area Animal Care and Use Committee (IACUC). Eight- to 10-week-old male B6D2F1 hybrids (The Jackson Laboratory) were used for all experiments unless otherwise indicated. Male and female NRF2 KO and littermate controls on a mixed 129/C57BL/6 background (Martin et al., 1998), LTsc1KO and littermate controls on a C57BL/6 background (Harputlugil et al., 2014), and CGLKO and control mice on a mixed 129/C57BL/6 background (Yang et al., 2008) were described previously.

Preconditioning Regimens

Dietary

Mice were given AL access to food and water unless otherwise indicated. Experimental diets were based on Research Diets D12450B with approximately 18% of calories from protein (hydrolyzed casein or individual crystalline amino acids [Ajinomoto] in the proportions present in casein), 10% from fat and 72% from carbohydrate. AL food intake was monitored for several days and used to calculate 50% DR. Mice were fed daily with fresh food between 6 and 7 p.m.

Pharmacological

NAC (600 mg/kg/day total in food and drinking water) and VitC&E (1,000 and 250 mg/kg/day, respectively, in food and drinking water) supplementation was halted 16–24 hr prior to organ harvest and/or induction of IRI. NaHS (1 mM) or GYY4137 (260 μM final) was delivered in the drinking water; PAG (10 mg/kg) and NaHS (3–5 mg/kg) were administered by IP injection.

Adenoviral-Mediated Gene Delivery

CGL was overexpressed by intravenous injection of 10¹⁰ plaque-forming units of Ad-CMV-CGL (ADV-256305) or control Ad-CMV Null virus (Vector Biolabs) 7 days prior to hepatic IRI.

Cells

In vitro DR was performed in mouse Hepa1-6 cells, primary hepatocytes, or primary aortic smooth muscle cells by incubating in DMEM lacking Met and Cys (Invitrogen) with 10% dialyzed FBS for up to 20 hr.

Ischemia Reperfusion Models

In Vivo

Warm hepatic or renal IRI was induced, and damage was assessed as previously described (Peng et al., 2012). ALT, AST, and/or LDH values were normalized to the experimental control; usually the WT group fed a complete diet AL, for each time point (3, 24 hr postreperfusion) and combined into a single value per animal.

In Vitro

For simulated ischemia, growth or preconditioning media was replaced with saline to mimic nutrient/energy deprivation and placed in an airtight chamber flushed with nitrogen gas at 37°C for 4 hr. Saline supernatant was removed after simulated ischemia for LDH measurement. Reperfusion was simulated by adding back fresh complete DMEM-12320 (Invitrogen) containing 0.5 mg/ml MTT under normoxia at 37°C for an additional 3–4 hr.

Metabolic Parameters

Body composition was determined with an Echo MRI. Blood glucose was measured with an Easy Step Glucometer (Home Aide Diagnostics), serum triglycerides with a Serum Triglyceride Determination Kit (Sigma), liver RONS and GSH from left hepatic lobes normalized by wet weight using OxiSelect In Vitro Green Fluorescence ROS/RNS Assay Kit (Cell Biolabs) and the fluorimetric Glutathione Assay Kit (Sigma), and liver metabolites via mass spectrometry and normalized to total protein content. Peroxisome β-oxidation of lipids was performed on freshly harvested liver (Hu et al., 2005; Lazarow, 1981).

mRNA and Protein Analysis

Total RNA was isolated from tissues and cells using miRNeasy Mini Kit (QIAGEN) and cDNA synthesized by random hexamer priming with the Verso cDNA kit (Thermo Scientific). qRT-PCR was performed with SYBR green dye (Lonza) and TaqPro DNA polymerase (Denville). Fold changes were calculated by the ΔΔC_t method using Hprt and/or Rpl13 as standards and normalized to the experimental WT AL control. Protein expression was analyzed in tissues homogenized in passive lysis buffer (Promega), separated by SDS-PAGE, transferred to PVDF membrane (Whatman), and blotted for CGL (ab151769 Abcam), CBS (ab135626 Abcam), or actin (13E5 Cell Signaling) followed by HPRT-conjugated secondary anti-rabbit antibody (Dako).

H₂S Measurements

Lead Sulfide Method

H₂S production capacity was measured in 100 mg fresh tissue or 100–300 μg freeze-thaw homogenate in passive lysis buffer (Promega) of tissues, flies or worms, in PBS supplemented with 10 mM Cys and 10 μM-6 mM PLP. A lead acetate H₂S detection paper (Sigma; or made by soaking blotting paper [VWR] in 20 mM lead acetate [Sigma] and then vacuum drying) was placed above the liquid phase in a closed container (microcentrifuge tube or covered 96-well plate) and incubated 2–5 hr at 37°C until lead sulfide darkening of the paper occurred. In live Hepa1-6 cells in 96-well plates, growth media was supplemented with 10 mM Cys and 10 μM PLP, and a lead acetate paper placed over the plate for 2–24 hr of further incubation in a CO₂ incubator at 37°C. In live yeast culture, lead acetate papers were placed above liquid cultures at the time of inoculation.

Sulfide Probe Method

A micro-sulfide ion electrode probe (Lazar Research Laboratories) and volt meter (Jenco) were used to measure H₂S production capacity in extracts in vitro and endogenous H₂S concentrations in liver in vivo upon direct insertion into median and left lobes of anesthetized mice prior to sacrifice.

Fly Conditions

D. melanogaster were maintained as described previously (Lee et al., 2014). Flies used in the H₂S production capacity assay were held on the designated diet and transferred to fresh vials without anesthesia every 3 days until 18 days of age.

Worm Conditions

N2 and DA1116 (*eat-2(ad1116)* II.) strains were grown following standard procedures, and all lifespan experiments were carried out as previously described (Mair et al., 2011). RNAi clones were from the Ahringer RNAi library. CBS transgenic strains overexpressing the *cbs-1* isoform a (ZC373.1a) from the ubiquitous *sur-5* promoter and *unc-54* 3' UTR were generated by microinjection into gonads of young adult hermaphrodites.

Yeast Conditions

Experiments were carried out in WT strains BY4742 (MAT α his3 Δ 1 leu2 Δ 0 lys2 Δ 0 ura3 Δ 0), W303 (MAT α leu2-3,112 trp1-1 can1-100 ura3-1 ade2-1 his3-11,15), and DBY746 (MAT α leu2-3, 112 his3 Δ 1 trp1-289 ura 3-52 GAL⁺). Met deletion strains in BY4742 (*met5*, *met14*, and *met16*) were purchased from EUROSCARF. For chronological aging experiments, cells were inoculated to an OD₆₀₀ of 0.05 and grown at 28°C in SCD media, and cell survival was determined by clonogenicity at the given time points in at least three independent cultures, and values were normalized to survival on day 1. Longevity effects of exogenous H₂S were tested by adding 100 μ M GYY4137 (in DMSO) to BY4742 cultures at the time of inoculation and 5 μ M NaHS at 6, 24, and 48 hr after inoculation, with DMSO-treated BY4742 as a control.

Statistical Analyses

Data are displayed as means \pm SEM, and statistical significance was assessed in GraphPad Prism using Student's *t* tests to compare values and one-sample *t* test to compare means to a hypothetical value of 1 or 100 when data were normalized to the average value of the control group. A *p* value of 0.05 or less was deemed statistically significant.

SUPPLEMENTAL INFORMATION

Supplemental Information includes Extended Experimental Procedures and six figures and can be found with this article online at <http://dx.doi.org/10.1016/j.cell.2014.11.048>.

ACKNOWLEDGMENTS

We thank Bruce Kristal and Jaan-Olle Andressoo for critical reading of the manuscript; Silvia Dichtinger, Manmeet Gujral, and Jason Li for technical assistance; and Paul Ney for sharing the NRF2KO mice. This work was supported by grants from NIH (R01DK090629, R01AG036712) and the Glenn Foundation to J.R.M.; C.H. was supported by T32CA0093823; F.M. was supported by the Austrian Science Fund FWF (LIPOTOX, I1000, P23490-B12, and P24381-B20); W.B.M. was supported by 1R01AG044346; V.N.G. was supported by R01AG021518; C.K.O. was supported by American Heart Association 12GRNT9510001 and 12GRNT1207025; and R.W. was supported by an operating grant from the Canadian Institutes of Health Research.

Received: April 1, 2014

Revised: September 12, 2014

Accepted: November 18, 2014

Published: December 23, 2014

REFERENCES

Bishop, N.A., and Guarente, L. (2007). Two neurons mediate diet-restriction-induced longevity in *C. elegans*. *Nature* 447, 545–549.

Blackstone, E., Morrison, M., and Roth, M.B. (2005). H₂S induces a suspended animation-like state in mice. *Science* 308, 518.

Cabreiro, F., Au, C., Leung, K.Y., Vergara-Irigaray, N., Cochemé, H.M., Noori, T., Weinkove, D., Schuster, E., Greene, N.D., and Gems, D. (2013). Metformin retards aging in *C. elegans* by altering microbial folate and methionine metabolism. *Cell* 153, 228–239.

Calabrese, E.J., and Mattson, M.P. (2011). Hormesis provides a generalized quantitative estimate of biological plasticity. *J. Cell Commun. Signal.* 5, 25–38.

Calvert, J.W., Coetzee, W.A., and Lefer, D.J. (2010). Novel insights into hydrogen sulfide-mediated cytoprotection. *Antioxid. Redox Signal.* 12, 1203–1217.

Cuevasanta, E., Denicola, A., Alvarez, B., and Möller, M.N. (2012). Solubility and permeation of hydrogen sulfide in lipid membranes. *PLoS ONE* 7, e34562.

Fontana, L., Partridge, L., and Longo, V.D. (2010). Extending healthy life span—from yeast to humans. *Science* 328, 321–326.

Grandison, R.C., Piper, M.D., and Partridge, L. (2009). Amino-acid imbalance explains extension of lifespan by dietary restriction in *Drosophila*. *Nature* 462, 1061–1064.

Harputlugil, E., Hine, C., Vargas, D., Robertson, L., Manning, B.D., and Mitchell, J.R. (2014). The TSC complex is required for the benefits of dietary protein restriction on stress resistance in vivo. *Cell Reports* 8, 1160–1170.

Hildebrandt, T.M., and Grieshaber, M.K. (2008). Three enzymatic activities catalyze the oxidation of sulfide to thiosulfate in mammalian and invertebrate mitochondria. *FEBS J.* 275, 3352–3361.

Hine, C.M., and Mitchell, J.R. (2012). NRF2 and the phase II response in acute stress resistance induced by dietary restriction. *J. Clin. Exp. Pathol.* S4.

Hu, T., Foxworthy, P., Siesky, A., Ficorilli, J.V., Gao, H., Li, S., Christe, M., Ryan, T., Cao, G., Eacho, P., et al. (2005). Hepatic peroxisomal fatty acid β -oxidation is regulated by liver X receptor α . *Endocrinology* 146, 5380–5387.

Johnson, J.E., and Johnson, F.B. (2014). Methionine restriction activates the retrograde response and confers both stress tolerance and lifespan extension to yeast, mouse and human cells. *PLoS ONE* 9, e97729.

Kabil, H., Kabil, O., Banerjee, R., Harshman, L.G., and Pletcher, S.D. (2011a). Increased transsulfuration mediates longevity and dietary restriction in *Drosophila*. *Proc. Natl. Acad. Sci. USA* 108, 16831–16836.

Kabil, O., Vitvitsky, V., Xie, P., and Banerjee, R. (2011b). The quantitative significance of the transsulfuration enzymes for H₂S production in murine tissues. *Antioxid. Redox Signal.* 15, 363–372.

Kang, K., Zhao, M., Jiang, H., Tan, G., Pan, S., and Sun, X. (2009). Role of hydrogen sulfide in hepatic ischemia-reperfusion-induced injury in rats. *Liver Transpl.* 15, 1306–1314.

Lakowski, B., and Hekimi, S. (1998). The genetics of caloric restriction in *Caenorhabditis elegans*. *Proc. Natl. Acad. Sci. USA* 95, 13091–13096.

Lazarow, P.B. (1981). Assay of peroxisomal β -oxidation of fatty acids. *Methods Enzymol.* 72, 315–319.

Lee, J.I., Dominy, J.E., Jr., Sikalidis, A.K., Hirschberger, L.L., Wang, W., and Stipanuk, M.H. (2008). HepG2/C3A cells respond to cysteine deprivation by induction of the amino acid deprivation/integrated stress response pathway. *Physiol. Genomics* 33, 218–229.

Lee, Z.W., Zhou, J., Chen, C.S., Zhao, Y., Tan, C.H., Li, L., Moore, P.K., and Deng, L.W. (2011). The slow-releasing hydrogen sulfide donor, GYY4137, exhibits novel anti-cancer effects in vitro and in vivo. *PLoS ONE* 6, e21077.

Lee, B.C., Kaya, A., Ma, S., Kim, G., Geraschenko, M.V., Yim, S.H., Hu, Z., Harshman, L.G., and Gladyshev, V.N. (2014). Methionine restriction extends lifespan of *Drosophila melanogaster* under conditions of low amino-acid status. *Nat. Commun.* 5, 3592.

Levine, M.E., Suarez, J.A., Brandhorst, S., Balasubramanian, P., Cheng, C.W., Madia, F., Fontana, L., Mirisola, M.G., Guevara-Aguirre, J., Wan, J., et al. (2014). Low protein intake is associated with a major reduction in IGF-1, cancer, and overall mortality in the 65 and younger but not older population. *Cell Metab.* 19, 407–417.

Liu, M., Grigoryev, D.N., Crow, M.T., Haas, M., Yamamoto, M., Reddy, S.P., and Rabb, H. (2009). Transcription factor Nrf2 is protective during ischemic and nephrotoxic acute kidney injury in mice. *Kidney Int.* 76, 277–285.

Mair, W., Morante, I., Rodrigues, A.P., Manning, G., Montminy, M., Shaw, R.J., and Dillin, A. (2011). Lifespan extension induced by AMPK and calcineurin is mediated by CRTC-1 and CREB. *Nature* 470, 404–408.

Martin, F., van Deursen, J.M., Shvidasani, R.A., Jackson, C.W., Troutman, A.G., and Ney, P.A. (1998). Erythroid maturation and globin gene expression in mice with combined deficiency of NF-E2 and nrf-2. *Blood* 91, 3459–3466.

Mauro, C.R., Tao, M., Yu, P., Treviño-Villerreal, J.H., Longchamp, A., Kristal, B.S., Ozaki, C.K., and Mitchell, J.R. (2014). Preoperative dietary restriction

- reduces intimal hyperplasia and protects from ischemia-reperfusion injury. *J. Vasc. Surg.*
- Miller, D.L., and Roth, M.B. (2007). Hydrogen sulfide increases thermotolerance and lifespan in *Caenorhabditis elegans*. *Proc. Natl. Acad. Sci. USA* 104, 20618–20622.
- Miller, R.A., Buehner, G., Chang, Y., Harper, J.M., Sigler, R., and Smith-Wheelock, M. (2005). Methionine-deficient diet extends mouse lifespan, slows immune and lens aging, alters glucose, T4, IGF-I and insulin levels, and increases hepatocyte MIF levels and stress resistance. *Aging Cell* 4, 119–125.
- Mitchell, J.R., Verweij, M., Brand, K., van de Ven, M., Goemaere, N., van den Engel, S., Chu, T., Forrer, F., Müller, C., de Jong, M., et al. (2010). Short-term dietary restriction and fasting precondition against ischemia reperfusion injury in mice. *Aging Cell* 9, 40–53.
- Módis, K., Coletta, C., Erdélyi, K., Papapetropoulos, A., and Szabo, C. (2013). Intramitochondrial hydrogen sulfide production by 3-mercaptopyruvate sulfurtransferase maintains mitochondrial electron flow and supports cellular bioenergetics. *FASEB J.* 27, 601–611.
- Muyzer, G., and Stams, A.J. (2008). The ecology and biotechnology of sulphate-reducing bacteria. *Nat. Rev. Microbiol.* 6, 441–454.
- Olson, K.R., DeLeon, E.R., Gao, Y., Hurley, K., Sadauskas, V., Batz, C., and Stoy, G.F. (2013). Thiosulfate: a readily accessible source of hydrogen sulfide in oxygen sensing. *Am. J. Physiol. Regul. Integr. Comp. Physiol.* 305, R592–R603.
- Orentreich, N., Matias, J.R., DeFelice, A., and Zimmerman, J.A. (1993). Low methionine ingestion by rats extends life span. *J. Nutr.* 123, 269–274.
- Paul, B.D., and Snyder, S.H. (2012). H₂S signalling through protein sulfhydration and beyond. *Nat. Rev. Mol. Cell Biol.* 13, 499–507.
- Pearson, K.J., Lewis, K.N., Price, N.L., Chang, J.W., Perez, E., Cascajo, M.V., Tamashiro, K.L., Poosala, S., Csiszar, A., Ungvari, Z., et al. (2008). Nrf2 mediates cancer protection but not longevity induced by caloric restriction. *Proc. Natl. Acad. Sci. USA* 105, 2325–2330.
- Peng, W., Robertson, L., Gallinetti, J., Mejia, P., Vose, S., Charlip, A., Chu, T., and Mitchell, J.R. (2012). Surgical stress resistance induced by single amino acid deprivation requires gcn2 in mice. *Sci. Transl. Med.* 4, 118ra111.
- Predmore, B.L., Alendy, M.J., Ahmed, K.I., Leeuwenburgh, C., and Julian, D. (2010). The hydrogen sulfide signaling system: changes during aging and the benefits of caloric restriction. *Age (Dordr.)* 32, 467–481.
- Ristow, M., and Schmeisser, S. (2011). Extending life span by increasing oxidative stress. *Free Radic. Biol. Med.* 51, 327–336.
- Ruckenstuhl, C., Netzberger, C., Entfellner, I., Carmona-Gutierrez, D., Kickenweiz, T., Stekovic, S., Gleixner, C., Schmid, C., Klug, L., Sorgo, A.G., et al. (2014). Lifespan extension by methionine restriction requires autophagy-dependent vacuolar acidification. *PLoS Genet.* 10, e1004347.
- Sinclair, D.A. (2005). Toward a unified theory of caloric restriction and longevity regulation. *Mech. Ageing Dev.* 126, 987–1002.
- Stipanuk, M.H., and Ueki, I. (2011). Dealing with methionine/homocysteine sulfur: cysteine metabolism to taurine and inorganic sulfur. *J. Inher. Metab. Dis.* 34, 17–32.
- Tapia, P.C. (2006). Sublethal mitochondrial stress with an attendant stoichiometric augmentation of reactive oxygen species may precipitate many of the beneficial alterations in cellular physiology produced by caloric restriction, intermittent fasting, exercise and dietary phytonutrients: “Mitohormesis” for health and vitality. *Med. Hypotheses* 66, 832–843.
- Theissen, U., Hoffmeister, M., Grieshaber, M., and Martin, W. (2003). Single eubacterial origin of eukaryotic sulfide:quinone oxidoreductase, a mitochondrial enzyme conserved from the early evolution of eukaryotes during anoxic and sulfidic times. *Mol. Biol. Evol.* 20, 1564–1574.
- Troen, A.M., French, E.E., Roberts, J.F., Selhub, J., Ordovas, J.M., Parnell, L.D., and Lai, C.Q. (2007). Lifespan modification by glucose and methionine in *Drosophila melanogaster* fed a chemically defined diet. *Age (Dordr.)* 29, 29–39.
- Varendi, K., Airavaara, M., Anttila, J., Vose, S., Planken, A., Saarma, M., Mitchell, J.R., and Andressoo, J.O. (2014). Short-term preoperative dietary restriction is neuroprotective in a rat focal stroke model. *PLoS ONE* 9, e93911.
- Wu, Z., Liu, S.Q., and Huang, D. (2013). Dietary restriction depends on nutrient composition to extend chronological lifespan in budding yeast *Saccharomyces cerevisiae*. *PLoS ONE* 8, e64448.
- Yan, S.K., Chang, T., Wang, H., Wu, L., Wang, R., and Meng, Q.H. (2006). Effects of hydrogen sulfide on homocysteine-induced oxidative stress in vascular smooth muscle cells. *Biochem. Biophys. Res. Commun.* 351, 485–491.
- Yang, G., Wu, L., Jiang, B., Yang, W., Qi, J., Cao, K., Meng, Q., Mustafa, A.K., Mu, W., Zhang, S., et al. (2008). H₂S as a physiologic vasorelaxant: hypertension in mice with deletion of cystathionine gamma-lyase. *Science* 322, 587–590.
- Zhang, Y., Tang, Z.H., Ren, Z., Qu, S.L., Liu, M.H., Liu, L.S., and Jiang, Z.S. (2013). Hydrogen sulfide, the next potent preventive and therapeutic agent in aging and age-associated diseases. *Mol. Cell. Biol.* 33, 1104–1113.

A Kinase-Independent Role for EGF Receptor in Autophagy Initiation

Xiaojun Tan,¹ Narendra Thapa,¹ Yue Sun,¹ and Richard A. Anderson^{1,*}

¹Program in Molecular and Cellular Pharmacology, University of Wisconsin-Madison School of Medicine and Public Health, 1300 University Avenue, Madison, WI 53706, USA

*Correspondence: raanders@wisc.edu

<http://dx.doi.org/10.1016/j.cell.2014.12.006>

SUMMARY

The epidermal growth factor receptor (EGFR) is upregulated in numerous human cancers. Inhibition of EGFR signaling induces autophagy in tumor cells. Here, we report an unanticipated role for the inactive EGFR in autophagy initiation. Inactive EGFR interacts with the oncoprotein LPTM4B that is required for the endosomal accumulation of EGFR upon serum starvation. Inactive EGFR and LPTM4B stabilize each other at endosomes and recruit the exocyst subcomplex containing Sec5. We show that inactive EGFR, LPTM4B, and the Sec5 subcomplex are required for basal and starvation-induced autophagy. LPTM4B and Sec5 promote EGFR association with the autophagy inhibitor Rubicon, which in turn disassociates Beclin 1 from Rubicon to initiate autophagy. Thus, the oncoprotein LPTM4B facilitates the role of inactive EGFR in autophagy initiation. This pathway is positioned to control tumor metabolism and promote tumor cell survival upon serum deprivation or metabolic stress.

INTRODUCTION

Autophagy (macroautophagy) is a self-eating process by which part of the cytoplasm, organelles, and/or membrane are engulfed and eventually digested in lysosomes for cell homeostasis, development, and/or nutrient recycling (Feng et al., 2014). Autophagy is inducible by nutrient starvation as a mechanism to protect cells (Klionsky et al., 2012). The core machinery required for autophagosome formation consists of autophagy-related (Atg) proteins that function in a specific order (Feng et al., 2014). The Beclin 1 (Atg6 in yeast) complex containing Beclin 1, VPS34, ATG14, and VPS15 plays essential roles in phagophore nucleation and autophagy initiation and is emerging as a regulatory complex by autophagy signals (He and Levine, 2010; Matsunaga et al., 2009; Sun et al., 2009; Zhong et al., 2009). LC3 (Atg8 in yeast) is an autophagy regulator downstream of Beclin 1, and a hallmark of autophagosome formation is the conversion of the cytosolic LC3-I into the lipidated LC3-II that associates with autophagosome membranes (Kabeya et al., 2000). The exocyst also plays a role in the Beclin 1 complex assembly during autophagy initiation (Bodemann et al., 2011), but how

and where the exocyst and the autophagy complexes are regulated is not defined.

Epidermal growth factor receptor (EGFR) is a receptor tyrosine kinase that plays fundamental roles in physiology and cancers (Schlessinger, 2000). Aberrant EGFR signaling due to EGFR mutations and/or protein overexpression is associated with most epithelial cancers (Mendelsohn and Baselga, 2006). Recent studies have shown a role for EGFR signaling in autophagy suppression by activation of the PI3K/AKT/mTOR pathway or by EGFR-mediated phosphorylation and inhibition of Beclin 1 (Wei et al., 2013). Autophagy is generally thought to prevent cancer initiation but is also positioned to promote cancer cell survival upon metabolic stress (Brecht et al., 2009; White, 2012). Rapamycin, an autophagy inducer, exhibits cytotoxic effects in cancer cells treated with EGFR tyrosine kinase inhibitors (TKIs) erlotinib or gefitinib (Fung et al., 2012; Gorzalczyk et al., 2011). However, autophagy induced by EGFR TKIs or neutralizing antibody shows cytoprotective roles (Choi et al., 2013; Dragowska et al., 2013; Eimer et al., 2011; Han et al., 2011; Li and Fan, 2010; Li et al., 2010b; Sobhakumari et al., 2013; Zou et al., 2013), suggesting that EGFR TKIs (or neutralizing antibody) may induce autophagy by a mechanism distinct from rapamycin. At least some EGFR-overexpressing cells and tumors are dependent on autophagy for growth and survival (Jutten et al., 2013; Jutten and Rouschop, 2014). A gefitinib-resistant subpopulation of lung adenocarcinoma cells depend on enhanced autophagic activity, but not on EGFR signaling, for survival (Sakuma et al., 2013). The combined data suggest a kinase-independent role for EGFR in autophagy that regulates cancer cell survival.

The lysosomal-associated transmembrane protein 4B (LPTM4B) is a tetratransmembrane protein localized primarily to the late endosome and lysosome (Liu et al., 2004). LPTM4B was originally identified in hepatocellular carcinoma patients as an abnormally overexpressed protein and was later found to be upregulated in many other human cancers, including breast, lung, ovarian, and colon cancers (Kasper et al., 2005). Ectopic expression of LPTM4B transforms normal cells and promotes proliferation, migration, and invasion of cancer cells (Li et al., 2011a; Yang et al., 2010). LPTM4B is proposed to promote cancer cell proliferation by upregulating PI3K/ATK signaling (Li et al., 2010a). We have shown that LPTM4B blocks EGF-stimulated EGFR intraluminal sorting and lysosomal degradation, resulting in enhanced and prolonged EGFR signaling (X.T., Y.S., N.T., Y. Liao, A.C. Hedman, and R.A.A., unpublished data). A potential role for LPTM4B in the promotion or inhibition

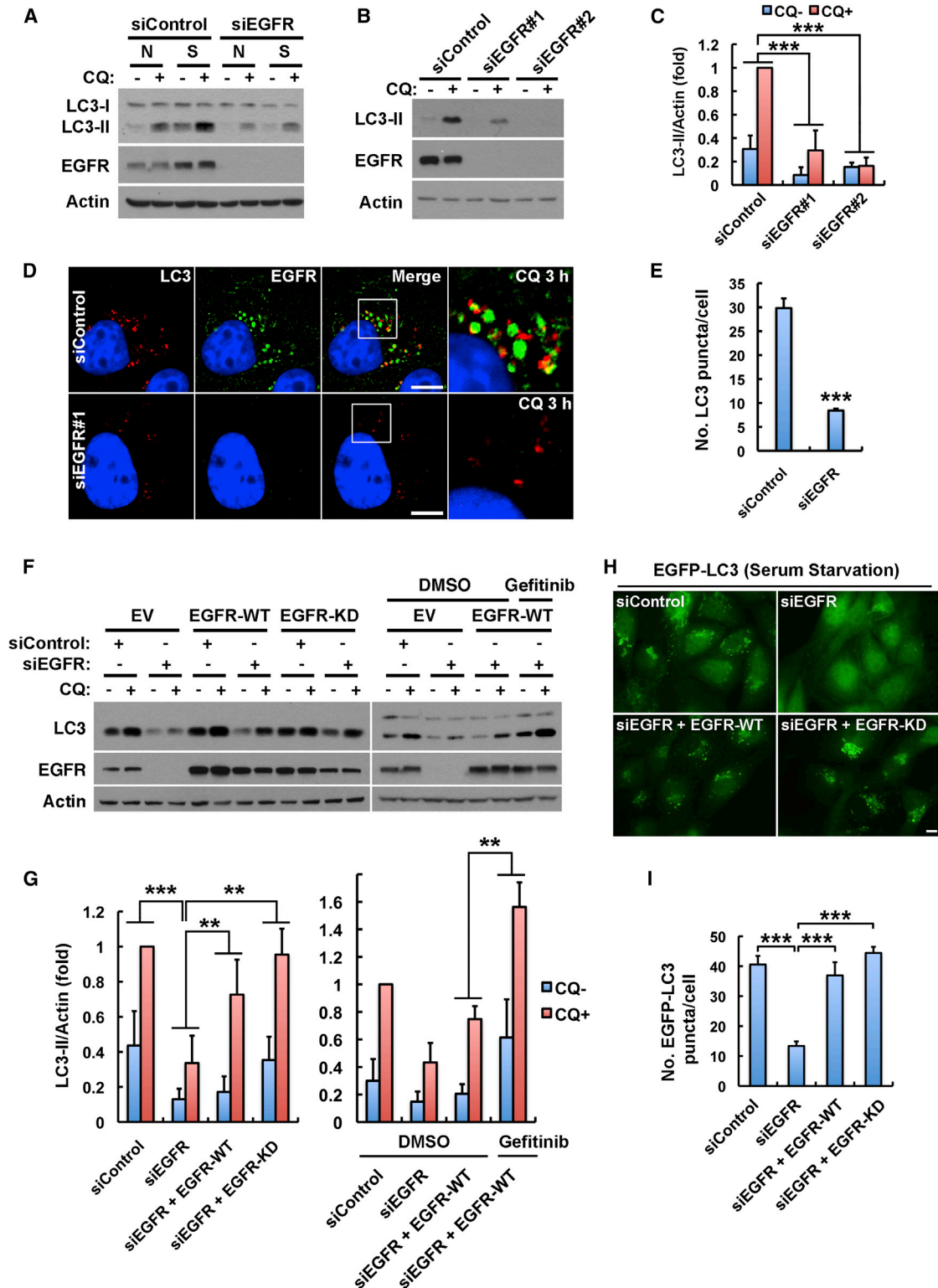


Figure 1. EGFR, but Not Its Kinase Activity, Is Required for Autophagy

(A) Knockdown of EGFR inhibits basal and serum starvation-induced LC3-II (autophagosome marker) turnover in MDA-MB-231 cells. Cells transfected with indicated siRNAs were cultured in normal medium (N) or serum-free starvation medium (S) for 24 hr and then were treated with 80 μ M chloroquine (CQ) for 2 hr to induce LC3-II accumulation. Whole-cell lysates were harvested for western blot analysis of LC3-II.

(legend continued on next page)

of autophagosome maturation has been proposed (Li et al., 2011b; Vergara-Jauregui et al., 2011).

Here, we report an unexpected role for inactive EGFR in autophagy initiation. Upon serum starvation, inactive EGFR collaborates with LAMP4B and Sec5 at endosomes to disassociate Rubicon from Beclin 1, which in turn initiates autophagy. EGFR TKIs also induce autophagy initiation, revealing that kinase-inactive EGFR functions in autophagy, and this may be a mechanism for tumor cell resistance to EGFR TKIs.

RESULTS

EGFR, but Not Its Kinase Activity, Is Required for Autophagy

EGFR TKIs induce autophagy (Han et al., 2011; Jutten and Rousschop, 2014; Li et al., 2010b), suggesting a direct role for inactive EGFR in autophagy upregulation. To test this hypothesis, we examined if EGFR is required for autophagic flux. Knockdown of EGFR inhibited basal and serum starvation-induced autophagic flux (Figure 1A), as shown by the LC3-II levels, before and after inhibition of its degradation by chloroquine. Two different EGFR small interfering RNAs (siRNAs) independently knocked down EGFR expression and inhibited autophagic flux (Figures 1B and 1C), and loss of EGFR markedly reduced endogenous LC3 puncta formation (Figures 1D and 1E), indicating a role for EGFR in autophagy initiation.

To determine whether the role for EGFR in autophagy is due to its overexpression, we tested the effects of EGFR knockdown in 7 cell lines, four of which do not overexpress EGFR (Figure S1A available online). Knockdown of EGFR inhibited autophagic flux in each cell line (Figure S1B), indicating a role in autophagy independent of receptor level. Importantly, the role for EGFR in autophagy initiation is receptor selective, as loss of PDGFRB, FGFR2, or c-Met did not suppress autophagy (Figures S1C–S1E).

Active EGFR blocks autophagy (Wei et al., 2013), and we confirmed that EGF stimulation inhibits autophagy initiation (Figure S1F); thus, we hypothesized that inactive EGFR initiates autophagy. To test this hypothesis, siRNA-resistant wild-type (WT) or K721A kinase-dead (KD) EGFR was re-expressed in cells in which endogenous EGFR was knocked down. Re-expressed

EGFR-WT is autophosphorylated and activates AKT signaling when stimulated with EGF, but EGFR-KD does not autophosphorylate or activate AKT (Figure S1G). However, re-expression of either WT or KD EGFR rescued autophagic flux in EGFR knockdown cells (Figures 1F and 1G, left panels), and treatment of EGFR-WT re-expressing cells with the EGFR TKI gefitinib enhanced the rescue of autophagy initiation (Figures 1F and 1G, right panels), indicating the role for EGFR in autophagy initiation is kinase independent. Serum starvation induced an increase in GFP-LC3 puncta (autophagosomes) (Figure S1H), and loss of EGFR strongly inhibited autophagosome formation (Figures 1H and 1I). Re-expression of either WT or KD EGFR fully rescued the starvation-induced formation of GFP-LC3 puncta in EGFR knockdown cells (Figures 1H and 1I). These combined results reveal a kinase-independent role for EGFR in basal and serum starvation-induced autophagy.

Starvation Induces Accumulation of Inactive EGFR at LAMP4B-Positive Endosomes

To explore how inactive EGFR controls autophagy, the subcellular localization of EGFR in normal and serum-starved cells was investigated. We previously showed that LAMP4B inhibits EGF-stimulated EGFR lysosomal sorting (X.T., Y.S., N.T., Y. Liao, A.C. Hedman, and R.A.A., unpublished data). Here, we show that EGFR partially colocalized with LAMP4B at endosomes in cells grown with serum (Figure 2A, top). The specificity of EGFR immunostaining was confirmed by siRNA knockdown of EGFR (Figure S2A). Surprisingly, serum-starvation enhanced EGFR accumulation at LAMP4B-positive endosomes (Figure 2A, bottom), which include both late and early endosomes (Figure S2B). Starvation-induced endosomal EGFR accumulation and EGFR-LAMP4B colocalization were observed in all cells assayed (Figures S2C–S2F). Serum starvation also induced intracellular accumulation of c-Met and FGFR2, and c-Met colocalized well with LAMP4B but FGFR2 did not (Figures S2G–S2J). However, neither FGFR2 nor c-Met was required for autophagy, indicating that this is an EGFR-selective function (Figures S1C–S1E).

EGFR translocates to endosomes upon EGF stimulation and receptor autophosphorylation/activation (Wiley, 2003). We

(B) Knockdown of EGFR by two distinct siRNAs inhibits LC3-II generation. MDA-MB-231 cells were cultured in normal medium. Unless otherwise indicated, the EGFR siRNA #1 was used in all the remaining experiments.

(C) Quantification of LC3-II levels in (B); mean + SD, $n = 3$, *** $p < 0.001$.

(D) CQ induces accumulation of LC3 puncta (autophagosomes) in control cells, but not in EGFR knockdown cells. Control or EGFR siRNA-transfected cells in normal medium were pretreated with CQ for 3 hr and fixed for immunostaining of endogenous LC3 (red) and EGFR (green). DAPI was used to stain the nuclei; boxes indicate selected regions for magnified view. Bar, 10 μ m.

(E) Quantification of LC3 puncta in (D); mean + SD, $n = 3$, *** $p < 0.001$.

(F) Left: re-expression of wild-type (WT) or the K721A kinase-dead (KD) EGFR rescues LC3-II turnover in EGFR-knockdown cells. Right: gefitinib (2 μ M) treatment enhances autophagy rescue by EGFR-WT. siRNA-resistant EGFR-WT or -KD was expressed in MDA-MB-231 cells by lentivirus-mediated infection. Endogenous EGFR was knocked down by siRNA #1, and cells were cultured in normal medium and treated with CQ for 2 hr before whole-cell lysate harvest for western analysis. EV, empty vector.

(G) Quantification of LC3-II levels in (F); mean + SD, $n = 3$, ** $p < 0.01$, *** $p < 0.001$.

(H) Representative images of serum starvation-induced EGFP-LC3 puncta in MDA-MB-231 cells treated with indicated siRNAs with or without re-expression of EGFR-WT or EGFR-KD. EGFP-LC3 was expressed by lentivirus infection and a monoclonal cell line stably expressing low levels of EGFP-LC3 was selected. Endogenous EGFR was knocked down by siRNA, and siRNA-resistant WT or KD EGFR was re-expressed using lentivirus. Cells were serum starved and fixed for fluorescence microscopy. Bar, 10 μ m.

(I) Quantification of the number of EGFP-LC3 puncta in (H); mean + SD, $n = 3$, *** $p < 0.001$.

See also Figure S1.

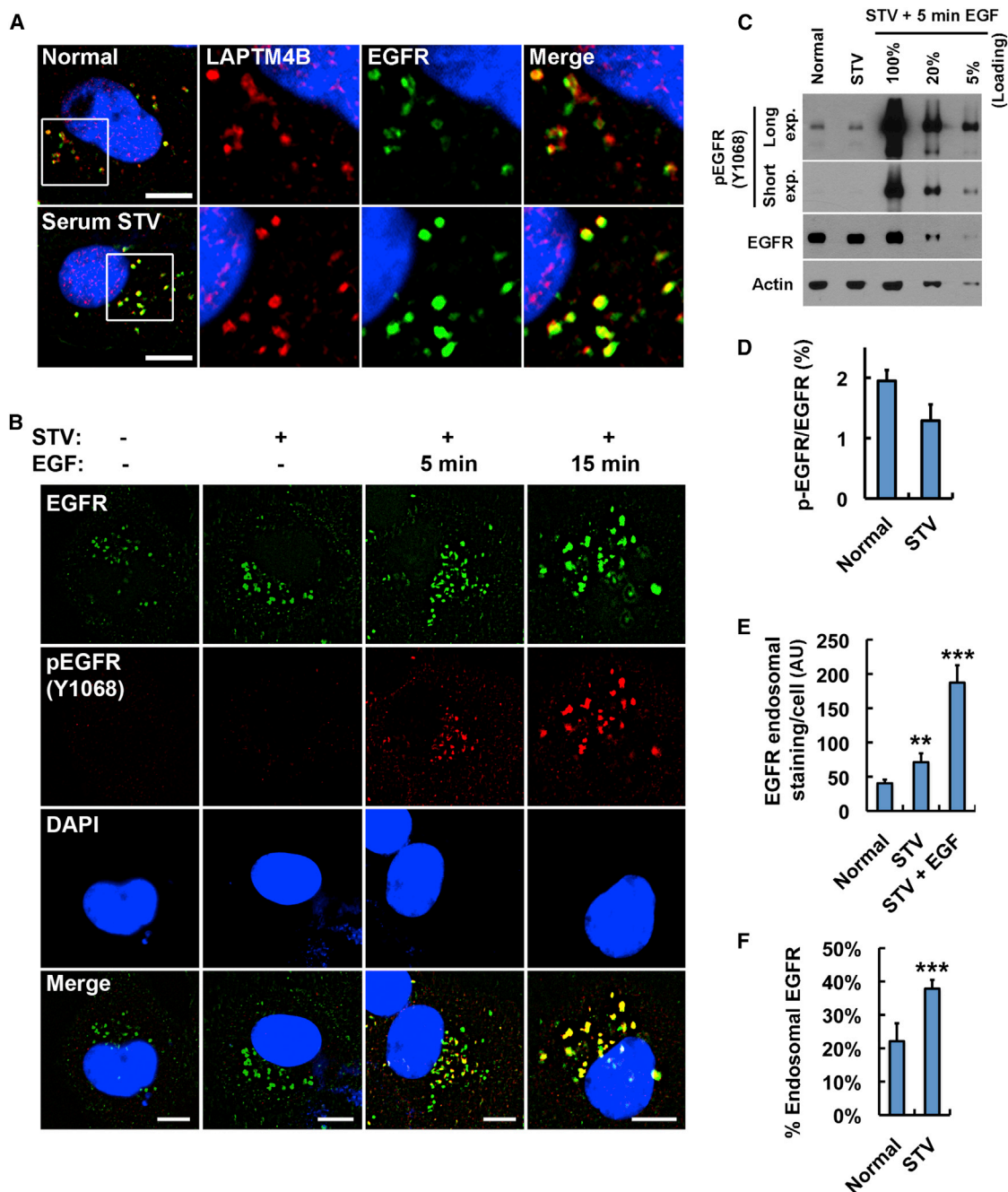


Figure 2. Serum Starvation Induces Accumulation of Inactive EGFR at LAPT4B-Positive Endosomes

(A) MDA-MB-231 cells were serum starved or not for 24 hr and fixed for costaining of endogenous EGFR (green) and LAPT4B (red). Boxes indicate regions for magnified new.

(B) MDA-MB-231 cells were serum starved (STV) or not, followed by EGF (100 ng/ml) stimulation for 5 or 15 min as indicated. Then cells were fixed for costaining of EGFR (green) and phosphor-EGFR (Y1068, red).

(C) The whole-cell lysates with or without serum starvation were analyzed by western blot to detect phosphor-EGFR (Y1068) and total EGFR. Different loadings of the lysates from MDA-MB-231 cells with 5 min EGF (100 ng/ml) stimulation after starvation were used as a standard to quantify phosphor-EGFR levels in cells without EGF stimulation.

(D) Quantification of the phosphor-EGFR (Y1068) levels in (C); mean + SD, n = 3.

(E) Quantification of endosomal EGFR staining in cells cultured in normal medium, serum-free medium (STV), or serum-free medium plus EGF (100 ng/ml, 15 min), as shown in (B); mean + SD, n = 3, **p < 0.01, ***p < 0.001.

(legend continued on next page)

therefore examined whether the EGFR accumulated at LAPTM4B-positive endosomes upon serum starvation was phosphorylated. EGF-stimulated cells were used as positive controls for phospho-EGFR staining, as shown in Figure 2B. Interestingly, in either serum grown or the starved condition, phospho-EGFR was not detected by immunofluorescence, but there was clear endosomal EGFR accumulation (Figure 2B). The endosomal staining of EGFR appears stronger than the plasma membrane staining because of the point concentration at endosomes (Figures 2A, 2B, and S2). Quantitative western blotting confirmed that less than 2% of the total EGFR was phosphorylated in cells cultured in either normal or serum starved medium, assuming that 5 min stimulation with 100 ng/ml EGF stimulated maximal EGFR phosphorylation (Figures 2C and 2D). Stimulation of cells with 100 ng/ml EGF for 15 min causes endocytosis and accumulation of over 95% of total EGFR at endosomes; we therefore calculated how much of EGFR was accumulated at endosomes in normal and starved cells by quantifying the endosomal EGFR staining in these conditions versus the EGF-stimulated (15 min) condition. This indicated that 20% or 40% of total EGFR is accumulated at endosomes in normal versus serum-starved conditions, respectively (Figures 2E and 2F). This demonstrates that in serum-grown or starved cells the endosomal EGFR is primarily unphosphorylated. Importantly, upon serum starvation, the amount of endosomal EGFR increased from 20% to 40% (Figures 2B and 2F), but the total phospho-EGFR level decreased (Figures 2C and 2D), indicating that serum starvation-induced endosomal accumulation of inactive EGFR.

Inactive EGFR and LAPTM4B Interact and Stabilize Each Other at Endosomes

The interaction between EGFR and LAPTM4B was studied to explore the mechanism for EGFR endosomal localization. EGFR was coimmunoprecipitated specifically with LAPTM4B, but not with other LAPTM members (Figure S3A). Serum starvation increased EGFR endosomal accumulation (Figure 2) and enhanced the LAPTM4B-EGFR association (Figure 3A), whereas EGF stimulation reduced the interaction (Figure 3B), indicating that LAPTM4B preferentially interacts with inactive EGFR. This was confirmed using the EGFR-KD mutant that has much stronger interaction with LAPTM4B compared with EGFR-WT (Figure 3C). EGF stimulation did not affect the LAPTM4B interaction with EGFR-KD (Figure 3D) that is not activated by EGF (Figure S1G). As serum starvation also induces endosomal accumulation of other receptors, LAPTM4B interaction with PDGFRB, FGFR2, and c-Met was tested. These receptors also coimmunoprecipitated with LAPTM4B (Figure S3B), but none of these interactions were enhanced upon serum starvation (Figure S3C), indicating that the serum starvation promoted EGFR-LAPTM4B interaction is selective.

As LAPTM4B is an endosomal protein (Shao et al., 2003; Ver-garauregui et al., 2011), we determined whether LAPTM4B could modulate EGFR endosomal accumulation. MDA-MB-231

cells express variable amounts of LAPTM4B, and in cells with low LAPTM4B, there was less endosomal EGFR (Figure S3D, arrowhead), suggesting LAPTM4B modulation of EGFR localization. Strikingly, upon knockdown of LAPTM4B, EGFR endosomal accumulation was lost, but EGFR targeting was fully rescued by re-expression of siRNA-resistant LAPTM4B (Figure 3E). Loss of LAPTM4B also resulted in a loss of endosomal EGFR in A431 and HeLa cells, indicating that this was independent of cell type (Figures S3E and S3F). To confirm that LAPTM4B mediates endosomal accumulation of inactive EGFR, cells stably expressing C terminally Flag-tagged WT or KD EGFR were generated. Both WT and KD EGFR had endosomal localization, but this was disrupted by loss of LAPTM4B (Figure 3F), demonstrating that LAPTM4B is required for the endosomal accumulation of inactive EGFR. Though c-Met and FGFR2 also accumulate at endosomes upon serum starvation, LAPTM4B knockdown reduced the endosomal localization of c-Met, but not of FGFR2 (Figures S3G and S3H). Interestingly, whereas c-Met localization appears to be impacted by LAPTM4B, c-Met was not required for autophagy initiation (Figures S1C–S1E).

To further explore LAPTM4B regulation of EGFR endosome accumulation, a biotinylation assay was used to quantify the amount of cell-surface EGFR. This demonstrated that although the total EGFR level was reduced in LAPTM4B knockdown cells, the level of EGFR at the cell surface was not affected (Figure 3G), consistent with a specific loss of endosomal EGFR in LAPTM4B knockdown cells. This indicates that LAPTM4B mediates endosomal EGFR accumulation by stabilizing inactive EGFR at endosomes. Likewise, inactive EGFR also stabilizes LAPTM4B at endosomes, as knockdown of EGFR caused a loss of endosomal LAPTM4B staining, and re-expression of either WT or KD EGFR rescued LAPTM4B staining at endosomes (Figure 3H).

Importantly, the endosomal localization of EGFR or LAPTM4B is not dependent on Hrs or TSG101 (Figure S3I), both of which are essential for the ESCRT-mediated EGFR intraluminal sorting upon ligand stimulation (Sorkin and Goh, 2008). This indicates that the pathway-mediating accumulation of inactive EGFR at LAPTM4B-positive endosomes is different from that for ligand stimulated EGFR endosomal sorting.

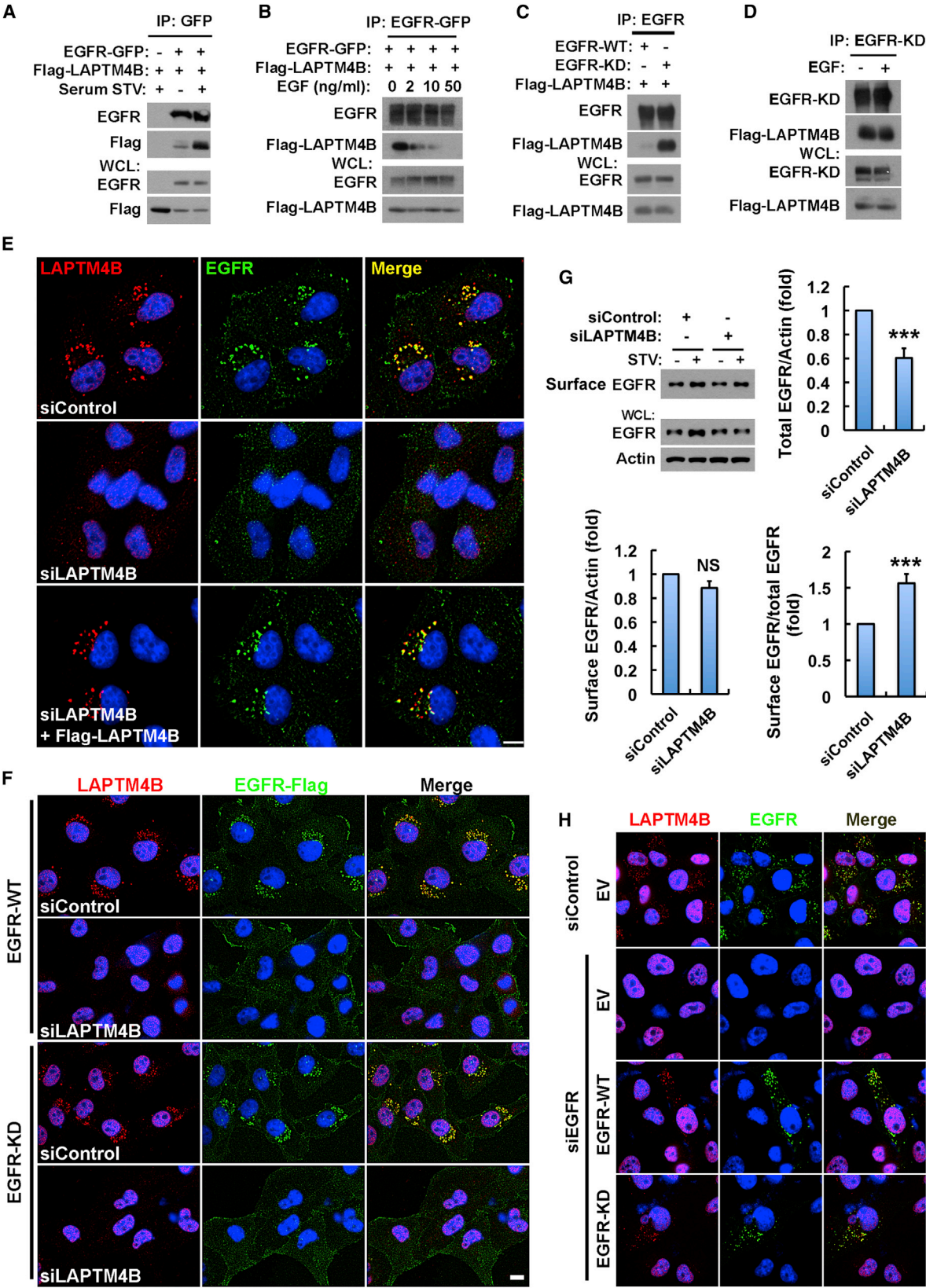
LAPTM4B Is Required for Basal and Serum Starvation-Induced Autophagy

The data suggest that EGFR-dependent autophagy initiation may be linked to LAPTM4B-mediated EGFR endosomal localization. To determine if LAPTM4B is required for autophagy, different siRNAs were used to knockdown LAPTM4B, and LC3-II turnover was quantified. Both LAPTM4B siRNAs knocked down LAPTM4B expression and inhibited basal autophagic flux (Figures 4A–4C). The chloroquine-induced accumulation of endogenous LC3 puncta was also strongly inhibited in LAPTM4B siRNA-treated cells (Figures 4D and 4E), phenocopying that of EGFR knockdown. Similarly, starvation-induced formation of the GFP-LC3 puncta was markedly decreased upon loss of

(F) Quantification of the relative amount of endosomal EGFR staining in cells cultured in normal medium or serum-free medium (STV) normalized to the amount of endosomal EGFR staining in cells in serum-free medium plus EGF (100 ng/ml, 15 min); mean + SD, n = 3, ***p < 0.001.

DAPI was used to stain the nuclei; pEGFR, phosphor-EGFR (Y1068). Bar, 10 μ m.

See also Figure S2.



(legend on next page)

LAPTM4B (Figures 4F and 4G). Consistently, ectopic expression of LAPTM4B increased LC3-II turnover (Figures S4A and S4B), as well as basal GFP-LC3 puncta formation (Figure S4C), and re-expression of siRNA-resistant LAPTM4B rescued starvation-induced GFP-LC3 puncta formation in LAPTM4B knockdown cells (Figure S4D). Significantly, knockdown of EGFR and LAPTM4B together did not further inhibit LC3-II turnover compared to the single knockdown of either protein (Figures S4E and S4F), suggesting that LAPTM4B and EGFR function in the same pathway.

To explore if EGFR and LAPTM4B have mechanisms independent of each other for autophagy initiation, we examined autophagic turnover in cells with knockdown of one protein and overexpression of the other. Interestingly, overexpression of EGFR largely rescued autophagy in LAPTM4B knockdown cells (Figures S4G and S4H), whereas overexpression of LAPTM4B weakly, if at all, rescued autophagy in EGFR knockdown cells (Figures S4I and S4J). This suggests that LAPTM4B is a cofactor for EGFR-driven autophagy initiation.

Inactive EGFR and LAPTM4B Interact with the Exocyst for Autophagy Initiation

The data indicate that serum starvation promotes the assembly of an endosomal EGFR-LAPTM4B complex that regulates autophagy initiation. Recently, exocyst complexes have been implicated in starvation-induced autophagy (Bodemann et al., 2011). A proteomic screen demonstrated that exocyst subunits interact with the EGFR complex (Foerster et al., 2013); we therefore explored if LAPTM4B and inactive EGFR interact with exocyst complex to modulate autophagy. As shown in Figures 5A and 5B, LAPTM4B and EGFR interact with multiple subunits of the exocyst complex. Sec8 is a core subunit of the exocyst and in endogenous coimmunoprecipitation (coIP), Sec8 associated with LAPTM4B and EGFR (Figure 5C). Exo70 also interacted with LAPTM4B and EGFR and localized to subdomains of LAPTM4B-positive endosomes (Figure 5D), and a fraction of endosomes were positive for EGFR, LAPTM4B, and Exo70 (Figure 5E).

As LAPTM4B selectively interacts with inactive EGFR, we determined if exocyst subunits interact similarly. Strikingly, Sec5 interacted with EGFR-KD much more strongly than with EGFR-WT (Figures 5F and 5H). Sec6 and Sec8 also associated

with EGFR-KD more strongly (Figures 5G, 5H, and S5A), but Exo70 and Exo84 did not (Figures 5H, S5B, and S5C), demonstrating that inactive EGFR selectively associates with the Sec5 exocyst subcomplex.

To determine if the Sec5 subcomplex modulates autophagy, Sec5 was knocked down, and this strongly inhibited basal LC3 turnover (Figures 5I and 5J) and serum starvation-induced GFP-LC3 puncta formation (Figures 5K and 5L), indicating that Sec5 is required for basal and serum starvation-induced autophagy initiation. This was unexpected as Sec5 has inhibitory roles in amino acid starvation-induced autophagy (Bodemann et al., 2011). Sec6, Sec8, and Exo70 also interacted with LAPTM4B and EGFR (Figures 5A and 5B), and all were required for autophagic turnover in MDA-MB-231 cells (Figures S5D–S5F).

EGFR, LAPTM4B, and Sec5 Regulate Rubicon Disassociation from the Beclin 1 Complex

Beclin 1 is a core subunit of the autophagy initiation complex involved in phagophore formation (He and Levine, 2010). To investigate how inactive EGFR may modulate the Beclin 1 complex, changes in the Beclin 1 interactome (He and Levine, 2010) upon serum starvation were explored. Although serum starvation-induced strong autophagosome formation and autophagic flux in cells (Figures 1A and S1H), only the association between Beclin 1 and the autophagy inhibitor Rubicon was reduced, whereas the Beclin 1 association with VPS34 or ATG14 was not affected by serum starvation (Figures 6A and 6E). Importantly, serum starvation strongly stimulated autophagy in control cells, but in Rubicon knockdown cells, basal autophagy is dramatically enhanced, and serum starvation does not further induce autophagy (Figure S6), signifying that the disassociation of Rubicon from Beclin 1 is a major mechanism for serum starvation induced autophagy. EGFR, LAPTM4B, and Sec5 appear to have a collaborative role in autophagy initiation, as loss of any of these components blocked autophagy (Figures 1, 4, and 5) and inhibited Rubicon disassociation from Beclin 1 (Figures 6B–6E).

Rubicon strongly and selectively associates with EGFR-KD (Figure 6F), and consistently, serum starvation significantly enhanced the coIP of EGFR with overexpressed or endogenous Rubicon (Figures 6G and 6H), suggesting that inactive EGFR regulates autophagy by interacting with Rubicon. To determine if the

Figure 3. Inactive EGFR and LAPTM4B Interact and Stabilize Each Other at Endosomes

- (A) coIP of EGFR-GFP with Flag-LAPTM4B in HEK293 cells cultured in normal or serum-free medium.
- (B) coIP of EGFR-GFP with Flag-LAPTM4B in HEK293 cells cultured in serum-free medium with 0, 2, 10, or 50 ng/ml EGF treatment (30 min).
- (C) coIP of wild-type (WT) or kinase-dead (KD) EGFR with Flag-LAPTM4B in HEK293 cells in normal medium.
- (D) coIP of EGFR-KD with Flag-LAPTM4B in HEK293 cells cultured in serum-free medium with or without 50 ng/ml EGF treatment (30 min).
- (E) LAPTM4B is required for the endosomal accumulation of endogenous EGFR. MDA-MB-231 cells were treated with control or LAPTM4B siRNA, and after 48 hr, the siRNA-resistant LAPTM4B was re-expressed via transient transfection. Cells were serum starved and fixed for costaining of LAPTM4B (red) and EGFR (green).
- (F) Ectopically expressed wild-type (WT) and kinase-dead (KD) EGFR depend on LAPTM4B for endosomal accumulation. MDA-MB-231 cells stably expressing C terminally Flag-tagged EGFR-WT or -KD were treated with control or LAPTM4B siRNA, serum starved, and fixed for costaining of Flag (green) and endogenous LAPTM4B (red).
- (G) Control and LAPTM4B knockdown cells were surface biotinylated, and surface and total EGFR levels were analyzed by western blot (top left). Quantification of total EGFR levels (top right), cell-surface EGFR levels (bottom left), and the relative amounts of cell-surface EGFR (bottom right) in serum-starved control and LAPTM4B knockdown cells; mean + SD, n = 3; ***p < 0.001; ns, not significant.
- (H) Inactive EGFR stabilizes endosomal LAPTM4B. MDA-MB-231 cells were transfected with control or EGFR siRNA, and after 48 hr cells, they were transfected with empty vector (EV) or siRNA-resistant EGFR-WT or -KD and starved overnight, followed by fixing and costaining of EGFR (green) and LAPTM4B (red). WCL, whole-cell lysate; STV, serum starvation. Bar, 10 μ m. DAPI was used to stain the nuclei.

See also Figure S3.

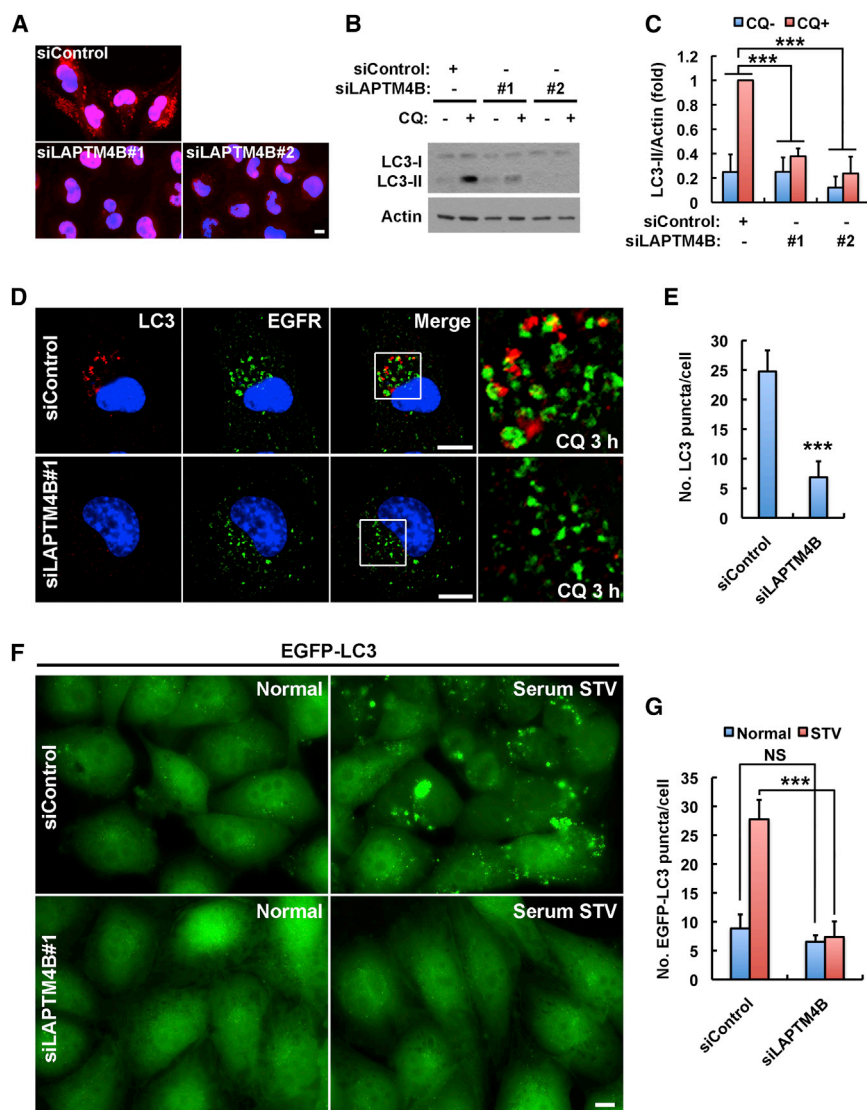


Figure 4. LAPTMB4B Is Required for Basal and Serum Starvation-Induced Autophagy

(A) Immunofluorescence images showing the knockdown efficiency of two distinct LAPTMB4B siRNAs. Nuclear staining is nonspecific.

(B) Knockdown of LAPTMB4B by two distinct siRNAs suppresses LC3-II turnover in MDA-MB-231 cells cultured in normal medium. CQ, chloroquine.

(C) Quantification of LC3-II in (B); mean + SD, $n = 3$, *** $p < 0.001$.

(D) Knockdown of LAPTMB4B results in a loss of chloroquine (CQ)-induced accumulation of endogenous LC3 puncta. Note: different from Figure 3E, some EGFR intracellular puncta were observed here in LAPTMB4B knockdown cells because of chloroquine treatment that blocked basal EGFR lysosomal degradation. Boxes are selected regions for magnified view.

(E) Quantification of the number of LC3 puncta in (D); mean + SD, $n = 3$, *** $p < 0.001$.

(F) Knockdown of LAPTMB4B causes a loss of serum starvation-induced EGFP-LC3 puncta formation. MDA-MB-231 cells stably expressing low levels of EGFP-LC3 as described in Figure 1H were treated with control or LAPTMB4B siRNA and serum starved or not before fixing for microscopy.

(G) Quantification of the number of EGFP-LC3 puncta in (F); mean + SD, $n = 3$; ns, not significant; *** $p < 0.001$.

Bar, 10 μ m. DAPI was used to stain the nuclei.

See also Figure S4.

promotes disassociation of Rubicon from the Beclin 1 complex, which in turn initiates autophagy.

Erlotinib and Gefitinib Induce a Sec5-Dependent Role for Inactive EGFR in Autophagy Initiation

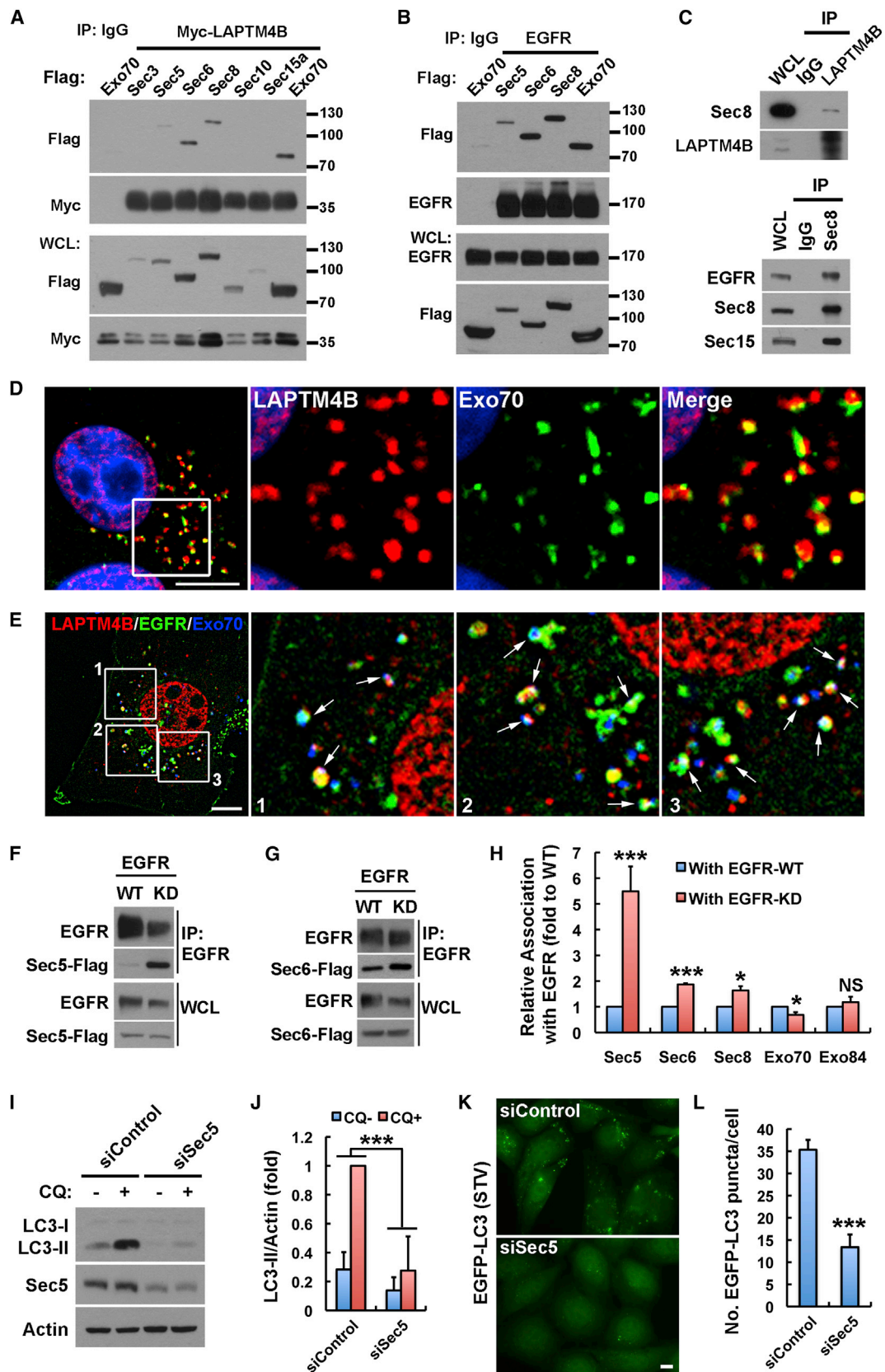
The EGFR TKIs erlotinib and gefitinib induce autophagy in multiple cancer cell

lines, and the underlying mechanisms have been linked to the inhibition of the downstream PI3K/AKT/mTOR pathway and/or the inhibition of EGFR-mediated Beclin 1 phosphorylation (Dragowska et al., 2013; Jutten and Rouschop, 2014; Sobhakumari et al., 2013; Wei et al., 2013). The role for inactive EGFR in autophagy initiation suggests that EGFR TKIs may induce a direct role for EGFR in autophagy. At clinically relevant concentrations (Baselga et al., 2002; Soulieres et al., 2004), erlotinib or gefitinib stimulated autophagic activity comparable to that induced by serum starvation or rapamycin (Figures 7A, S7A, and S7B). Further, TKI-induced autophagy is EGFR dependent as loss of EGFR strongly suppressed gefitinib-induced autophagy (Figures 7B and 7C). TKIs downregulated phosphorylation of EGFR, but not of Akt (Figure 7D), consistent with a direct role for inactive EGFR, but not for Akt/mTOR inactivation, in the EGFR TKI-induced autophagy.

As erlotinib and gefitinib inhibit EGFR kinase activity, we investigated whether the EGFR-LAPTMB4B-Sec5 pathway is required

EGFR C-tail (EGFR-CT) could modulate the Rubicon-Beclin 1 interaction in vitro, the Beclin 1 complex was purified by immunoprecipitation (IP) and incubated with purified glutathione S-transferase (GST) or EGFR-CT. As shown in Figures 6I and 6J, incubation with EGFR-CT efficiently disassociated Rubicon from Beclin 1 in vitro. The EGFR-CT lacks the kinase domain and is not phosphorylated, consistent with the concept that the inactive EGFR functions as a nonphosphorylated receptor in autophagy initiation and removes Rubicon from the Beclin 1 complex.

LAPTMB4B is overexpressed in most epithelial cancers, and increased LAPTMB4B expression enhanced the EGFR interaction with Rubicon and Sec5 (Figure 6K). Sec5 has been shown to associate with Rubicon (Bodemmann et al., 2011), and the knockdown of either LAPTMB4B or Sec5 diminished the Rubicon interaction with EGFR (Figures 6L and 6M), indicating that LAPTMB4B and Sec5 facilitate the Rubicon interaction with inactive EGFR. Thus, the endosomal inactive EGFR, with LAPTMB4B and Sec5,



(legend on next page)

for autophagy initiation. Erlotinib and gefitinib inhibited the interaction between EGFR and LAPTM4B (Figures 7E and 7I) but still stimulated accumulation of EGFR at endosomes (Figures 7F and S7C), similar to serum starvation (Figure 2). The EGFR interactions with Sec5, Sec6, and Rubicon were all enhanced by erlotinib or gefitinib (Figures 7G–7I and S7D). As with serum starvation, erlotinib or gefitinib also promoted Rubicon disassociation from the Beclin 1 complex (Figure 7J), indicating that erlotinib and gefitinib induce a LAPTM4B-independent role for EGFR in Rubicon regulation. Finally and consistently, whereas Sec5 and LAPTM4B were required for basal autophagy (Figures 7K and 7L, left), loss of Sec5, but not of LAPTM4B, inhibited the gefitinib- (or erlotinib-; not shown) stimulated LC3-II turnover (Figures 7K and 7L, right). Together, these results reveal that the EGFR TKIs, erlotinib and gefitinib, stimulate a direct role for inactive EGFR in autophagy initiation that is dependent on Sec5 but is independent of LAPTM4B.

Together, the data suggest a model that serum starvation induces LAPTM4B-dependent EGFR accumulation at endosomes, where inactive EGFR synergizes with LAPTM4B and Sec5 in stimulating autophagy initiation independently of its tyrosine kinase activity by facilitating the disassociation of Rubicon from Beclin 1 (Figure 7M, top). Similarly, EGFR TKIs induce LAPTM4B-independent accumulation of EGFR at endosomes, where EGFR associates with Sec5 and Rubicon to release Beclin 1 for autophagy initiation (Figure 7M, bottom).

DISCUSSION

Autophagy is activated in many cancers and facilitates cancer cell survival in stressed conditions (Brech et al., 2009; White, 2012). EGFR plays crucial roles in many epithelial cancers, and its signaling has been linked to prosurvival, proliferative, and prometastatic functions of cancer cells (Mendelsohn and Baselga, 2006). There are multiple links of EGFR to autophagy: (1) EGFR signaling activates the PI3K/AKT/mTOR pathway that inhibits autophagy; (2) activated EGFR directly phosphorylates and inhibits Beclin 1, a key component in autophagy initiation; and (3) EGFR TKIs upregulate autophagy in many cancer cells (Jutten and Rouschop, 2014; Li and Fan, 2010; Wei et al., 2013). These studies all support a role for EGFR signaling in autophagy suppression.

Our data reveal a direct and unexpected role for inactive EGFR in autophagy initiation. Upon serum starvation, inactive EGFR

forms a complex with LAPTM4B at endosomes, where it recruits the Sec5 exocyst subcomplex. This EGFR complex binds the autophagy inhibitor Rubicon, resulting in its disassociation from Beclin 1, releasing the Rubicon-free Beclin 1 complex to initiate autophagy (Figure 7M, top). These results establish the concept that whereas in nutrient-rich conditions activated EGFR suppresses autophagy and promotes cancer cell proliferation and survival through agonist stimulated EGFR signaling, in metabolically stressed conditions inactive EGFR alternatively facilitates cancer cell survival by activating autophagy. Consistent with our findings, kinase-independent roles for EGFR in cancer cell survival have been reported (Coker et al., 1994; Ewald et al., 2003; Weihua et al., 2008), and cancer cells expressing EGFR have been shown to depend on autophagy for survival and growth (Jutten et al., 2013; Jutten and Rouschop, 2014; Sakuma et al., 2013).

In clinical treatments, the EGFR TKIs erlotinib and gefitinib are effective in non-small-cell lung cancers (NSCLCs) that have activating mutations in EGFR, but show no effects in most solid tumors with WT EGFR (Mendelsohn and Baselga, 2006; Paez et al., 2004). Recent studies have shown that treatment with EGFR TKIs increased autophagy with cytoprotective effects in many cancer cells (Dragowska et al., 2013; Eimer et al., 2011; Gorzalczyk et al., 2011; Han et al., 2011; Jutten and Rouschop, 2014; Li et al., 2013; Sakuma et al., 2013; Sobhakumari et al., 2013; Zou et al., 2013). EGFR TKIs activate autophagy by blocking the role for active EGFR in autophagy suppression in lung cancer cells with activating EGFR mutations (Wei et al., 2013), but the mechanism by which the EGFR TKIs induce autophagy in cancer cells with WT EGFR was not defined. We show that EGFR TKIs induce a direct role for inactivated EGFR in autophagy initiation. EGFR TKIs mimic serum starvation and trigger endosomal accumulation of inactive EGFR that gains enhanced interaction with the Sec5 exocyst subcomplex and Rubicon, releasing Beclin 1 to initiate autophagy (Figure 7M, bottom). Thus, though EGFR TKIs block the cellular functions mediated by EGFR kinase signaling, they activate a role for inactive EGFR in autophagy that could potentially provide a survival advantage and TKI resistance in WT EGFR-expressing cancers. In fact, there is in vitro and in vivo evidence that cotargeting EGFR and autophagy is a promising strategy to overcome TKI resistance of cancer cells with WT EGFR, even when these cancer cells carry a different oncogenic factor like *K-Ras* or *p53*

Figure 5. Inactive EGFR and LAPTM4B Interact with Exocyst for Autophagy Initiation

(A and B) colP of LAPTM4B or EGFR with different exocyst subunits in HEK293 cells cotransfected with indicated proteins.

(C) Endogenous colP of Sec8 with LAPTM4B or EGFR in MDA-MB-231 cells.

(D) Colocalization of LAPTM4B and Exo70-Flag. MDA-MB-231 cells were fixed and stained with anti-LAPTM4B (red) and anti-Flag (green). DAPI was used to stain the nuclei.

(E) Colocalization of LAPTM4B (red), EGFR-GFP (green), and Exo70-Flag (blue) in MDA-MB-231 cells.

(F and G) colP of EGFR-WT or -KD with Sec5 or Sec6 in HEK293 cells cotransfected with indicated proteins.

(H) Quantification of the relative amounts of different exocyst subunits coimmunoprecipitated with EGFR-WT or -KD; mean + SD, $n \geq 3$; ns, not significant; * $p < 0.05$; *** $p < 0.001$.

(I) Knockdown of Sec5 suppresses LC3-II turnover in MDA-MB-231 cells cultured in normal medium.

(J) Quantification of LC3-II levels in (I); mean + SD, $n = 3$; *** $p < 0.001$.

(K) Knockdown of Sec5 suppresses serum starvation-induced EGFP-LC3 puncta formation in MDA-MB-231 cells.

(L) Quantification of the number of EGFP-LC3 puncta in (K); mean + SD, $n = 3$; *** $p < 0.001$.

Boxes are selected regions for magnified new. Bar, 10 μm .

See also Figure S5.

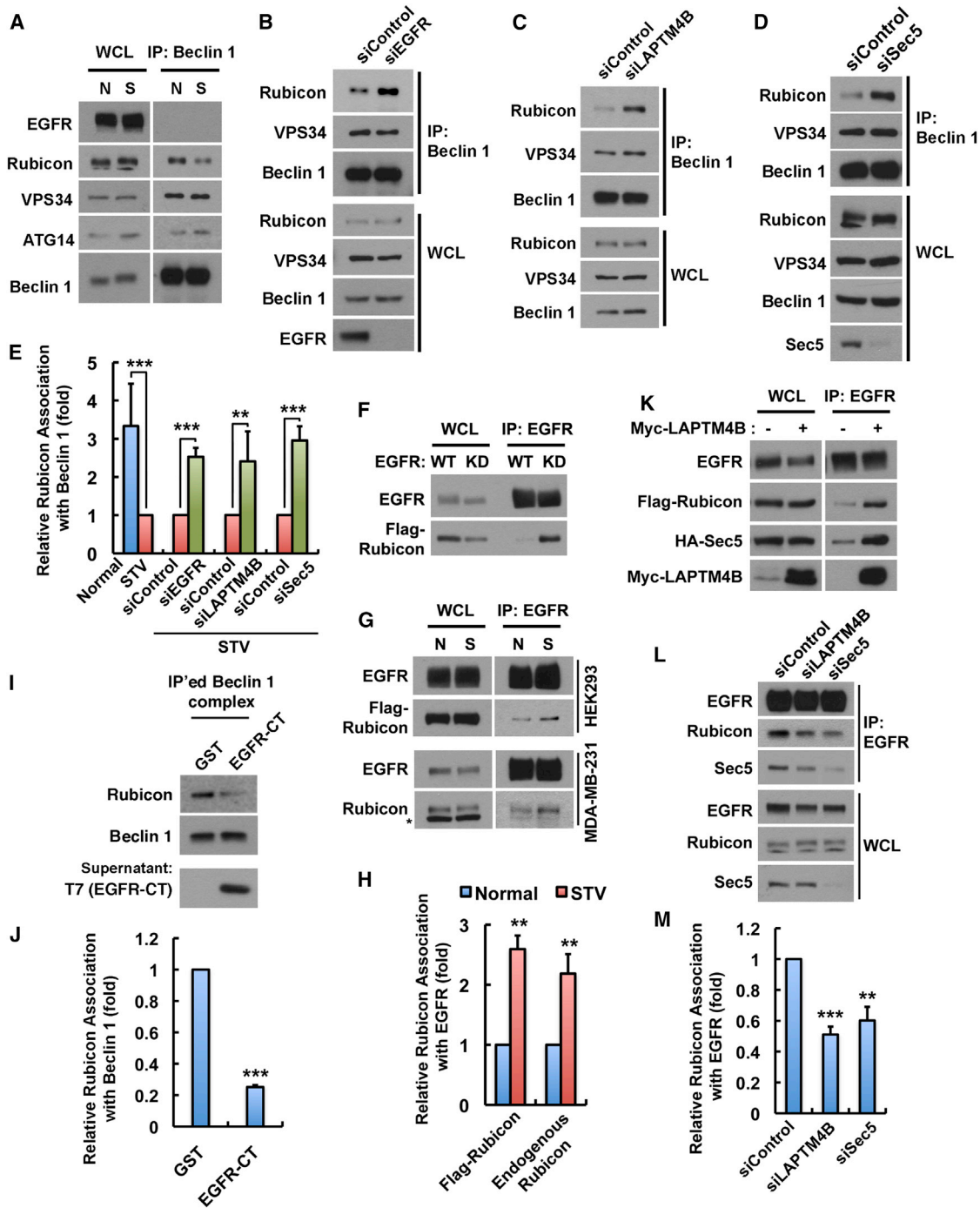


Figure 6. EGFR, LAPT4B, and Sec5 Regulate Rubicon Disassociation from the Beclin 1 Complex

(A) colP of Beclin 1 with ATG14, VPS34, and Rubicon in normal (N) and serum-starved (S) MDA-MB-231 cells.

(B–D) colP of Beclin 1 with VPS34 and Rubicon in serum-starved MDA-MB-231 cells pretreated with indicated siRNAs.

(E) Quantification of relative Rubicon association with Beclin 1 in (A–D); mean + SD, n = 3; **p < 0.01; ***p < 0.001.

(F) colP of Rubicon with EGFR-WT or -KD in HEK293 cells cotransfected with indicated proteins.

(G) colP of EGFR with Flag-Rubicon or endogenous Rubicon in normal (N) and serum-starved (S) conditions. Asterisk indicates a nonspecific band.

(H) Quantification of relative Rubicon association with EGFR in (G); mean + SD, n = 3; **p < 0.01.

(I) Endogenous Beclin 1 complex was immunoprecipitated from MDA-MB-231 cells using anti-Beclin 1. The beads with immunocomplex were washed, divided into equal volumes, and then incubated with purified GST or EGFR-C tail (EGFR-CT; amino acids 959–1186) for 20 min at room temperature. Changes of Rubicon association with Beclin 1 after the incubation were analyzed by western blot.

(legend continued on next page)

mutation (Choi et al., 2013; Dragowska et al., 2013; Jutten and Rouschop, 2014; Zou et al., 2013). For example, while erlotinib or hydroxychloroquine (HCQ; a clinically available autophagy inhibitor) alone show no antitumor activity in xenografts derived from H460 NSCLC cells expressing WT EGFR but mutant K-Ras, combination of the two drugs resulted in dramatic inhibition of tumor growth (Zou et al., 2013). A recent clinical trial has confirmed the safety and tolerance for cotreatment of erlotinib with HCQ (Goldberg et al., 2012), and additional trials combining HCQ with erlotinib or gefitinib are ongoing for the treatment of NSCLC.

EGFR and/or LAPTM4B are overexpressed in the majority of human cancers and contribute to cancer cell survival and proliferation (Kasper et al., 2005; Shao et al., 2003). The results presented here highlight the roles for the oncoprotein LAPTM4B in EGFR-mediated cell survival functions. We have previously shown that LAPTM4B promotes active EGFR signaling by blocking EGF-stimulated EGFR intraluminal sorting and lysosomal degradation (X.T., Y.S., N.T., Y. Liao, A.C. Hedman, and R.A.A., unpublished data). In the EGF-stimulated condition, LAPTM4B has a weak interaction with EGFR, but it inhibits the function of Hrs, a key subunit of the endosomal sorting complex required for transport-0 (ESCRT-0), through enhancing the ubiquitination of Hrs by the E3 ubiquitin ligase Nedd4 (X.T., Y.S., N.T., Y. Liao, A.C. Hedman, and R.A.A., unpublished data). Here, we show that upon serum starvation, LAPTM4B senses EGFR inactivation at endosomes and selectively forms a complex with inactive EGFR to initiate autophagy. In both conditions, LAPTM4B facilitates the prosurvival functions of EGFR in cancer cells. The lack of a requirement for LAPTM4B in EGFR-TKIs-induced autophagy is not surprising, as LAPTM4B appears to be a cofactor for EGFR-driven autophagy, and the effects of LAPTM4B knockdown on autophagy can be largely compensated by EGFR overexpression (Figures S4G and S4H). Importantly, in chemotherapies, LAPTM4B appears to increase drug resistance by multiple mechanisms (Li et al., 2010a, 2010c). Thus, although LAPTM4B is not required for the erlotinib/gefitinib-induced EGFR functions in autophagy initiation, it may enhance EGFR-TKI resistance through other pathways. This supports LAPTM4B as a therapeutic target for EGFR-positive cancers or a combined target for anti-EGFR therapies.

Multivesicular endosomes (MVEs) and autophagosomes are closely related as in mammalian cells autophagosomes often fuse with endosomes to form amphisomes before the final formation of autolysosomes (Fader and Colombo, 2009; Lamb et al., 2013). Therefore, endosomes have an established role in autophagosome maturation. Our results demonstrate that the endosome-localized inactive EGFR and LAPTM4B play pivotal roles in autophagy initiation. This emphasizes the importance of endosomes not only as canonical degradative compartments of the autophagosome content but also as signaling

organelles that activate the autophagy pathway. The EGFR-mediated Rubicon-Beclin 1 disassociation may occur at the endosomal surface, but the Beclin 1 complex functions in autophagosomal membrane nucleation at the endoplasmic reticulum (ER) (Hamasaki et al., 2013; Lamb et al., 2013). This suggests that the phagophore initiation sites at ER are in close proximity to endosomal Beclin 1-releasing sites. In support of this, LC3 puncta were observed adjacent to EGFR-positive endosomes (Figures 1D and 4D, top panels), suggesting that autophagosomes are formed at the ER close to EGFR-positive endosomes. Consistently, there are tight associations between the ER network and endosomes through ER-endosome contacts in mammalian cells (Eden et al., 2010; Friedman et al., 2013; Helle et al., 2013). Although most studies have focused on the roles for ER, mitochondria and Golgi in phagophore initiation, the ER-endosome contact sites are positioned to play key roles. In this case, autophagosome maturation could be coupled, as autophagosomes would be formed close to endosomes.

In summary, this study identifies a key role for inactive EGFR in autophagy initiation in cells with WT EGFR gene in both serum starved and EGFR TKIs-treated cells. It provides insights into the mechanistic regulation of cancer cell survival by EGFR expression in metabolically stressed tumors and suggests a basis for EGFR TKI resistance in the treatments of tumors without EGFR mutations.

EXPERIMENTAL PROCEDURES

Cell Culture, Transfection, Plasmids, siRNA, Antibodies, and Reagents

MDA-MB-231, HeLa, A431, and HEK293 cells were cultured in Dulbecco's modified Eagle's medium (DMEM) (Corning) with 10% fetal bovine serum (FBS) (Invitrogen). Transfection of plasmids and siRNA oligonucleotides was carried out using Lipofectamine 2000 and Lipofectamine RNAiMax (Invitrogen), respectively, following the manufacturer's instructions. For serum starvation, cells were washed with DMEM twice and cultured in DMEM without FBS for the indicated time periods. A detailed description of reagents, DNA plasmids, antibody origins, siRNA sequences, and cell treatments is included in the [Extended Experimental Procedures](#).

Immunofluorescence Microscopy

Immunostaining of tagged and endogenous proteins was performed using standard procedures. Cells on glass coverslips were washed, fixed, permeabilized, blocked, and stained with indicated antibodies. Cells were mounted using Vectashield and visualized with a Nikon TE2000-U microscope. Colocalization quantification was performed using the Coloc 2 plugin for Fiji (ImageJ). See the [Extended Experimental Procedures](#) for details.

CoIP and Western Blotting Assays

Immunoprecipitation of indicated proteins was performed using nondenaturing cell extracts. Immunocomplex and whole-cell lysates were analyzed by SDS-PAGE, followed by immunoblotting with indicated antibodies. See the [Extended Experimental Procedures](#) for details.

(J) Quantification of relative Rubicon association with Beclin 1 in (I); mean + SD, n = 5; ***p < 0.001.

(K) LAPTM4B overexpression facilitates EGFR coIP with Rubicon and Sec5 in HEK293 cells.

(L) Knockdown of LAPTM4B or Sec5 diminishes Rubicon coIP with EGFR in serum-starved MDA-MB-231 cells.

(M) Quantification of relative Rubicon association with EGFR in (L); mean + SD, n = 3; **p < 0.01; ***p < 0.001.

N, normal medium with serum; S, STV, serum-free starvation medium; WCL, whole-cell lysate.

See also [Figure S6](#).

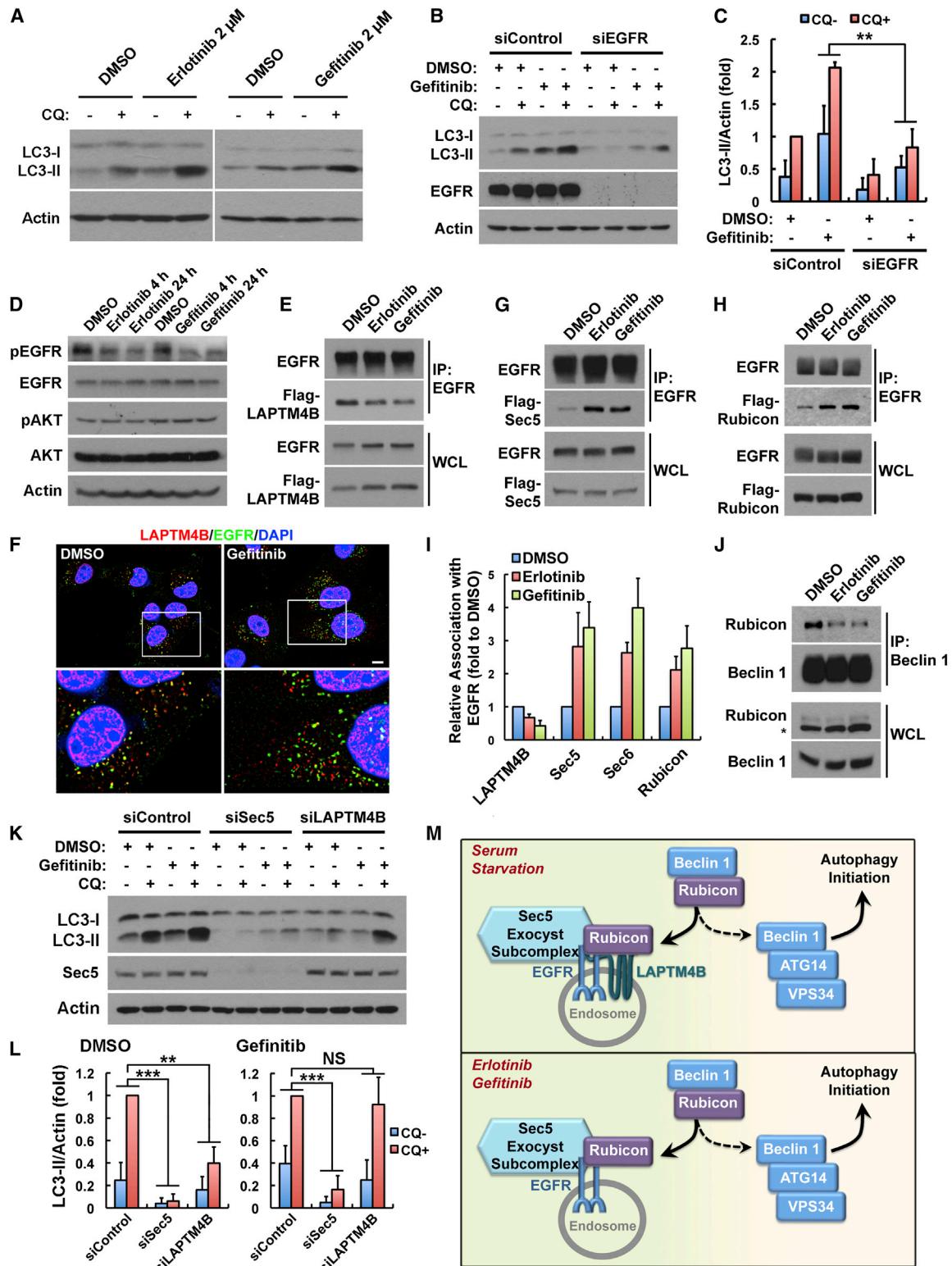


Figure 7. Erlotinib and Gefitinib Induce a Sec5-Dependent Role for Inactive EGFR in Autophagy Initiation

(A) The EGFR TKIs, erlotinib and gefitinib, induce autophagy in MDA-MB-231 cells. Cells were treated with DMSO or 2 μ M of erlotinib or gefitinib for 24 hr, followed by 2 hr of 80 μ M chloroquine (CQ) treatment as indicated, and whole-cell lysates were analyzed for LC3 levels.

(legend continued on next page)

Autophagy Assays

Autophagy was analyzed by (1) Western blotting detection of LC3-II turnover in the presence and absence of autophagy inhibitor chloroquine, (2) quantifying chloroquine-induced accumulation of endogenous LC3 puncta, and (3) quantifying of the number of EGFP-LC3 puncta in cells stably expressing low levels of EGFP-LC3 using fluorescence microscopy. See the [Extended Experimental Procedures](#) for details.

Biotinylation Assay

Cells were surface biotinylated and harvested for purification of biotinylated proteins using streptavidin affinity gel. Whole-cell lysates and purified biotinylated proteins were analyzed by immunoblotting. See the [Extended Experimental Procedures](#) for details.

SUPPLEMENTAL INFORMATION

Supplemental Information includes Extended Experimental Procedures and seven figures and can be found with this article online at <http://dx.doi.org/10.1016/j.cell.2014.12.006>.

AUTHOR CONTRIBUTIONS

X.T. and R.A.A. conceived the study. X.T., N.T., Y.S., and R.A.A. designed the experiments. X.T., N.T., and Y.S. performed the experiments. X.T. and R.A.A. wrote the manuscript.

ACKNOWLEDGMENTS

We thank M.A. White (University of Texas South Western) for sharing reagents, S.J. Parsons (University of Virginia) for the EGFR-K721A construct, R. Zhou (Peking University) for the LAPTM4B construct, R. Puertollano (NIH) for the LAPTM4A construct, Paul Bertics (University of Wisconsin-Madison) for the EGFR-GFP construct, J.E. Ladbury (University of Texas MD Anderson Cancer Center) for the FGFR2-GFP construct, H. Band (University of Nebraska Medical Center) for the PDGFRB-GFP construct, and D. Wheeler (University of Wisconsin-Madison) for the c-Met-GFP construct. We thank Drs. Randall Kimple, Alan Rapraeger, and Paul Lambert from University of Wisconsin-Madison and Drs. Andrew C. Hedman, Weimin Li, and Suyong Choi in the laboratory for extensive comments on the manuscript, research discussions, and reagents. This work is supported by NIH grants (CA104708 and GM057549) (to R.A.A.), a Howard Hughes Medical Institute International Student Research Fellowship

(59107631) (to X.T.), and an American Heart Association (AHA) Scientist Development Grant (12SDG11950022) (to Y.S.).

Received: May 12, 2014

Revised: September 21, 2014

Accepted: November 19, 2014

Published: January 15, 2015

REFERENCES

- Baselga, J., Rischin, D., Ranson, M., Calvert, H., Raymond, E., Kieback, D.G., Kaye, S.B., Gianni, L., Harris, A., Bjork, T., et al. (2002). Phase I safety, pharmacokinetic, and pharmacodynamic trial of ZD1839, a selective oral epidermal growth factor receptor tyrosine kinase inhibitor, in patients with five selected solid tumor types. *J. Clin. Oncol.* **20**, 4292–4302.
- Bodemann, B.O., Orvedahl, A., Cheng, T., Ram, R.R., Ou, Y.H., Formstecher, E., Maiti, M., Hazelett, C.C., Wauson, E.M., Balakireva, M., et al. (2011). RalB and the exocyst mediate the cellular starvation response by direct activation of autophagosome assembly. *Cell* **144**, 253–267.
- Brech, A., Ahlquist, T., Lothe, R.A., and Stenmark, H. (2009). Autophagy in tumour suppression and promotion. *Mol. Oncol.* **3**, 366–375.
- Choi, H.S., Jeong, E.H., Lee, T.G., Kim, S.Y., Kim, H.R., and Kim, C.H. (2013). Autophagy inhibition with monensin enhances cell cycle arrest and apoptosis induced by mTOR or epidermal growth factor receptor inhibitors in lung cancer cells. *Tuberc. Respir. Dis. (Seoul)* **75**, 9–17.
- Coker, K.J., Staros, J.V., and Guyer, C.A. (1994). A kinase-negative epidermal growth factor receptor that retains the capacity to stimulate DNA synthesis. *Proc. Natl. Acad. Sci. USA* **91**, 6967–6971.
- Dragowska, W.H., Weppeler, S.A., Wang, J.C., Wong, L.Y., Kapanen, A.I., Rawji, J.S., Warburton, C., Qadir, M.A., Donohue, E., Roberge, M., et al. (2013). Induction of autophagy is an early response to gefitinib and a potential therapeutic target in breast cancer. *PLoS ONE* **8**, e76503.
- Eden, E.R., White, I.J., Tsapara, A., and Futter, C.E. (2010). Membrane contacts between endosomes and ER provide sites for PTP1B-epidermal growth factor receptor interaction. *Nat. Cell Biol.* **12**, 267–272.
- Eimer, S., Belaud-Rotureau, M.A., Airiau, K., Jeanneteau, M., Laharanne, E., Véron, N., Vital, A., Loiseau, H., Merlio, J.P., and Belloc, F. (2011). Autophagy inhibition cooperates with erlotinib to induce glioblastoma cell death. *Cancer Biol. Ther.* **11**, 1017–1027.

(B) Knockdown of EGFR blocks gefitinib-induced autophagy in MDA-MB-231 cells. Control or EGFR knockdown cells were treated with DMSO or 2 μ M gefitinib for 24 hr, followed by 2 hr of CQ treatment as indicated.

(C) Quantification of LC3-II levels in (B); mean \pm SD, $n = 3$; ** $p < 0.01$.

(D) Erlotinib and gefitinib inhibit EGFR, but not Akt phosphorylation, in MDA-MB-231 cells. Cells were treated with DMSO or 2 μ M of erlotinib or gefitinib for 4 hr or 24 hr, followed by whole-cell lysate harvest and western blot analysis of indicated proteins. Specific antibodies recognizing pEGFR (Y1068) and pAkt (S473) were used.

(E) Erlotinib and gefitinib inhibit EGFR association with LAPTM4B. HEK293 cells cotransfected with EGFR and Flag-LAPTM4B were treated with DMSO or 2 μ M erlotinib or gefitinib for 2 hr and whole-cell lysates were harvested for coIP assay.

(F) Gefitinib treatment stimulates EGFR accumulation at endosomes. MDA-MB-231 cells treated with DMSO or 2 μ M of gefitinib for 24 hr were fixed for costaining of endogenous LAPTM4B (red) and EGFR (green). Bar, 10 μ m.

(G and H) Erlotinib and gefitinib (2 μ M) treatment enhances EGFR association with Sec5 and Rubicon in HEK293 cells cotransfected with EGFR and Sec5 or Rubicon.

(I) Quantification of relative EGFR association with indicated proteins in (E), (G), and (H); mean \pm SD, $n = 3$.

(J) Erlotinib/gefitinib (2 μ M) induces disassociation of Rubicon from Beclin 1 in MDA-MB-231 cells. Asterisk indicates a nonspecific band.

(K) Gefitinib-induced autophagy requires Sec5, but not LAPTM4B. MDA-MB-231 cells were transfected with indicated siRNAs and treated with DMSO or 2 μ M gefitinib for 24 hr, followed with or without 2 hr of CQ treatment. Whole-cell lysates were harvested for western blot analysis of LC3-II.

(L) Quantification of LC3-II levels in (K); mean \pm SD, $n = 3$; ** $p < 0.01$; *** $p < 0.001$; ns, not significant.

(M) A model for the role of inactive EGFR in autophagy initiation. Serum starvation enhances EGFR interaction with LAPTM4B, resulting in increased accumulation of inactive EGFR at endosomes, where EGFR also gains stronger interaction with Sec5. LAPTM4B and Sec5 facilitate Rubicon association with EGFR, which promotes the release of Beclin 1 from Rubicon for autophagy initiation. The EGFR TKIs, erlotinib and gefitinib, stimulate LAPTM4B-independent EGFR accumulation at endosomes, where EGFR still gains enhanced Sec5 and Rubicon interaction so as to release Rubicon-free Beclin 1 for autophagy initiation.

WCL, whole-cell lysate.

See also [Figure S7](#).

- Ewald, J.A., Wilkinson, J.C., Guyer, C.A., and Staros, J.V. (2003). Ligand- and kinase activity-independent cell survival mediated by the epidermal growth factor receptor expressed in 32D cells. *Exp. Cell Res.* 282, 121–131.
- Fader, C.M., and Colombo, M.I. (2009). Autophagy and multivesicular bodies: two closely related partners. *Cell Death Differ.* 16, 70–78.
- Feng, Y., He, D., Yao, Z., and Klionsky, D.J. (2014). The machinery of macroautophagy. *Cell Res.* 24, 24–41.
- Foerster, S., Kacprowski, T., Dhople, V.M., Hammer, E., Herzog, S., Saafan, H., Bien-Möller, S., Albrecht, M., Völker, U., and Ritter, C.A. (2013). Characterization of the EGFR interactome reveals associated protein complex networks and intracellular receptor dynamics. *Proteomics* 13, 3131–3144.
- Friedman, J.R., Dibenedetto, J.R., West, M., Rowland, A.A., and Voeltz, G.K. (2013). Endoplasmic reticulum-endosome contact increases as endosomes traffic and mature. *Mol. Biol. Cell* 24, 1030–1040.
- Fung, C., Chen, X., Grandis, J.R., and Duvvuri, U. (2012). EGFR tyrosine kinase inhibition induces autophagy in cancer cells. *Cancer Biol. Ther.* 13, 1417–1424.
- Goldberg, S.B., Supko, J.G., Neal, J.W., Muzikansky, A., Digumarthy, S., Fidas, P., Temel, J.S., Heist, R.S., Shaw, A.T., McCarthy, P.O., et al. (2012). A phase I study of erlotinib and hydroxychloroquine in advanced non-small-cell lung cancer. *J. Thorac. Oncol.* 7, 1602–1608.
- Gorzalczany, Y., Gilad, Y., Amihai, D., Hammel, I., Sagi-Eisenberg, R., and Merimsky, O. (2011). Combining an EGFR directed tyrosine kinase inhibitor with autophagy-inducing drugs: a beneficial strategy to combat non-small cell lung cancer. *Cancer Lett.* 310, 207–215.
- Hamasaki, M., Furuta, N., Matsuda, A., Nezu, A., Yamamoto, A., Fujita, N., Oomori, H., Noda, T., Haraguchi, T., Hiraoka, Y., et al. (2013). Autophagosomes form at ER-mitochondria contact sites. *Nature* 495, 389–393.
- Han, W., Pan, H., Chen, Y., Sun, J., Wang, Y., Li, J., Ge, W., Feng, L., Lin, X., Wang, X., et al. (2011). EGFR tyrosine kinase inhibitors activate autophagy as a cytoprotective response in human lung cancer cells. *PLoS ONE* 6, e18691.
- He, C., and Levine, B. (2010). The Beclin 1 interactome. *Curr. Opin. Cell Biol.* 22, 140–149.
- Helle, S.C., Kanfer, G., Kolar, K., Lang, A., Michel, A.H., and Kornmann, B. (2013). Organization and function of membrane contact sites. *Biochim. Biophys. Acta* 1833, 2526–2541.
- Jutten, B., and Rouschop, K.M. (2014). EGFR signaling and autophagy dependence for growth, survival, and therapy resistance. *Cell Cycle* 13, 42–51.
- Jutten, B., Keulers, T.G., Schaaf, M.B., Savelkoul, K., Theys, J., Span, P.N., Vooijs, M.A., Bussink, J., and Rouschop, K.M. (2013). EGFR overexpressing cells and tumors are dependent on autophagy for growth and survival. *Radiother. Oncol.* 108, 479–483.
- Kabeya, Y., Mizushima, N., Ueno, T., Yamamoto, A., Kirisako, T., Noda, T., Kominami, E., Ohsumi, Y., and Yoshimori, T. (2000). LC3, a mammalian homologue of yeast Apg8p, is localized in autophagosome membranes after processing. *EMBO J.* 19, 5720–5728.
- Kasper, G., Vogel, A., Klamann, I., Gröne, J., Petersen, I., Weber, B., Castañón-Vélez, E., Staub, E., and Mennerich, D. (2005). The human LAPTM4b transcript is upregulated in various types of solid tumours and seems to play a dual functional role during tumour progression. *Cancer Lett.* 224, 93–103.
- Klionsky, D.J., Abdalla, F.C., Abeliovich, H., Abraham, R.T., Acevedo-Arozena, A., Adeli, K., Agholme, L., Agnello, M., Agostinis, P., Aguirre-Ghisso, J.A., et al. (2012). Guidelines for the use and interpretation of assays for monitoring autophagy. *Autophagy* 8, 445–544.
- Lamb, C.A., Yoshimori, T., and Tooze, S.A. (2013). The autophagosome: origins unknown, biogenesis complex. *Nat. Rev. Mol. Cell Biol.* 14, 759–774.
- Li, X., and Fan, Z. (2010). The epidermal growth factor receptor antibody cetuximab induces autophagy in cancer cells by downregulating HIF-1 α and Bcl-2 and activating the beclin 1/hVps34 complex. *Cancer Res.* 70, 5942–5952.
- Li, L., Wei, X.H., Pan, Y.P., Li, H.C., Yang, H., He, Q.H., Pang, Y., Shan, Y., Xiong, F.X., Shao, G.Z., and Zhou, R.L. (2010a). LAPTM4B: a novel cancer-associated gene motivates multidrug resistance through efflux and activating PI3K/AKT signaling. *Oncogene* 29, 5785–5795.
- Li, X., Lu, Y., Pan, T., and Fan, Z. (2010b). Roles of autophagy in cetuximab-mediated cancer therapy against EGFR. *Autophagy* 6, 1066–1077.
- Li, Y., Zou, L., Li, Q., Haibe-Kains, B., Tian, R., Li, Y., Desmedt, C., Sotiriou, C., Szallasi, Z., Iglehart, J.D., et al. (2010c). Amplification of LAPTM4B and YWHAZ contributes to chemotherapy resistance and recurrence of breast cancer. *Nat. Med.* 16, 214–218.
- Li, L., Shan, Y., Yang, H., Zhang, S., Lin, M., Zhu, P., Chen, X.Y., Yi, J., McNutt, M.A., Shao, G.Z., and Zhou, R.L. (2011a). Upregulation of LAPTM4B-35 promotes malignant transformation and tumorigenesis in L02 human liver cell line. *Anat. Rec. (Hoboken)* 294, 1135–1142.
- Li, Y., Zhang, Q., Tian, R., Wang, Q., Zhao, J.J., Iglehart, J.D., Wang, Z.C., and Richardson, A.L. (2011b). Lysosomal transmembrane protein LAPTM4B promotes autophagy and tolerance to metabolic stress in cancer cells. *Cancer Res.* 71, 7481–7489.
- Li, Y.Y., Lam, S.K., Mak, J.C., Zheng, C.Y., and Ho, J.C. (2013). Erlotinib-induced autophagy in epidermal growth factor receptor mutated non-small cell lung cancer. *Lung Cancer* 81, 354–361.
- Liu, X.R., Zhou, R.L., Zhang, Q.Y., Zhang, Y., Jin, Y.Y., Lin, M., Rui, J.A., and Ye, D.X. (2004). Structure analysis and expressions of a novel tetratransmembrane protein, lysosoma-associated protein transmembrane 4 beta associated with hepatocellular carcinoma. *World J. Gastroenterol.* 10, 1555–1559.
- Matsunaga, K., Saitoh, T., Tabata, K., Omori, H., Satoh, T., Kurotori, N., Maejima, I., Shirahama-Noda, K., Ichimura, T., Isobe, T., et al. (2009). Two Beclin 1-binding proteins, Atg14L and Rubicon, reciprocally regulate autophagy at different stages. *Nat. Cell Biol.* 11, 385–396.
- Mendelsohn, J., and Baselga, J. (2006). Epidermal growth factor receptor targeting in cancer. *Semin. Oncol.* 33, 369–385.
- Paez, J.G., Jänne, P.A., Lee, J.C., Tracy, S., Greulich, H., Gabriel, S., Herman, P., Kaye, F.J., Lindeman, N., Boggon, T.J., et al. (2004). EGFR mutations in lung cancer: correlation with clinical response to gefitinib therapy. *Science* 304, 1497–1500.
- Sakuma, Y., Matsukuma, S., Nakamura, Y., Yoshihara, M., Koizume, S., Sekiguchi, H., Saito, H., Nakayama, H., Kameda, Y., Yokose, T., et al. (2013). Enhanced autophagy is required for survival in EGFR-independent EGFR-mutant lung adenocarcinoma cells. *Lab. Invest.* 93, 1137–1146.
- Schlessinger, J. (2000). Cell signaling by receptor tyrosine kinases. *Cell* 103, 211–225.
- Shao, G.Z., Zhou, R.L., Zhang, Q.Y., Zhang, Y., Liu, J.J., Rui, J.A., Wei, X., and Ye, D.X. (2003). Molecular cloning and characterization of LAPTM4B, a novel gene upregulated in hepatocellular carcinoma. *Oncogene* 22, 5060–5069.
- Sobhakumari, A., Schickling, B.M., Love-Homan, L., Raeburn, A., Fletcher, E.V., Case, A.J., Domann, F.E., Miller, F.J.J., Jr., and Simons, A.L. (2013). NOX4 mediates cytoprotective autophagy induced by the EGFR inhibitor erlotinib in head and neck cancer cells. *Toxicol. Appl. Pharmacol.* 272, 736–745.
- Sorkin, A., and Goh, L.K. (2008). Endocytosis and intracellular trafficking of ErbBs. *Exp. Cell Res.* 314, 3093–3106.
- Soulieres, D., Senzer, N.N., Vokes, E.E., Hidalgo, M., Agarwala, S.S., and Siu, L.L. (2004). Multicenter phase II study of erlotinib, an oral epidermal growth factor receptor tyrosine kinase inhibitor, in patients with recurrent or metastatic squamous cell cancer of the head and neck. *J. Clin. Oncol.* 22, 77–85.
- Sun, Q., Fan, W., and Zhong, Q. (2009). Regulation of Beclin 1 in autophagy. *Autophagy* 5, 713–716.
- Vergarajauregui, S., Martina, J.A., and Puertollano, R. (2011). LAPTM4s regulate lysosomal function and interact with mucolipin 1: new clues for understanding mucopolipidosis type IV. *J. Cell Sci.* 124, 459–468.
- Wei, Y., Zou, Z., Becker, N., Anderson, M., Sumpter, R., Xiao, G., Kinch, L., Koduru, P., Christudass, C.S., Veltri, R.W., et al. (2013). EGFR-mediated Beclin 1 phosphorylation in autophagy suppression, tumor progression, and tumor chemoresistance. *Cell* 154, 1269–1284.
- Weihua, Z., Tsan, R., Huang, W.C., Wu, Q., Chiu, C.H., Fidler, I.J., and Hung, M.C. (2008). Survival of cancer cells is maintained by EGFR independent of its kinase activity. *Cancer Cell* 13, 385–393.

- White, E. (2012). Deconvoluting the context-dependent role for autophagy in cancer. *Nat. Rev. Cancer* 12, 401–410.
- Wiley, H.S. (2003). Trafficking of the ErbB receptors and its influence on signaling. *Exp. Cell Res.* 284, 78–88.
- Yang, H., Xiong, F., Wei, X., Yang, Y., McNutt, M.A., and Zhou, R. (2010). Overexpression of LAPTM4B-35 promotes growth and metastasis of hepatocellular carcinoma in vitro and in vivo. *Cancer Lett.* 294, 236–244.
- Zhong, Y., Wang, Q., Li, X., Yan, Y., Backer, J., Chait, B., Heintz, N., and Yue, Z. (2009). Distinct regulation of autophagic activity by Atg14L and Rubicon associated with Beclin 1-phosphatidylinositol-3-kinase complex. *Nat. Cell Biol.* 11, 468–476.
- Zou, Y., Ling, Y.H., Sironi, J., Schwartz, E.L., Perez-Soler, R., and Piperdi, B. (2013). The autophagy inhibitor chloroquine overcomes the innate resistance of wild-type EGFR non-small-cell lung cancer cells to erlotinib. *J. Thorac. Oncol.* 8, 693–702.

Pathological Axonal Death through a MAPK Cascade that Triggers a Local Energy Deficit

Jing Yang,¹ Zhu hao Wu,¹ Nicolas Renier,¹ David J. Simon,¹ Kunihiro Uryu,² David S. Park,³ Peter A. Greer,⁴ Cathy Tournier,⁵ Roger J. Davis,⁶ and Marc Tessier-Lavigne^{1,*}

¹Laboratory of Brain Development and Repair, The Rockefeller University, New York, NY 10065, USA

²Electron Microscopy Resource Center, The Rockefeller University, New York, NY 10065, USA

³University of Ottawa Brain and Mind Research Institute, University of Ottawa, Canada

⁴Queen's University Cancer Research Institute, Kingston, Ontario, Canada

⁵University of Manchester, Oxford Road, Manchester M13 9PT, UK

⁶Howard Hughes Medical Institute, University of Massachusetts Medical School, Worcester, MA 01605, USA

*Correspondence: marctl@rockefeller.edu

<http://dx.doi.org/10.1016/j.cell.2014.11.053>

SUMMARY

Axonal death disrupts functional connectivity of neural circuits and is a critical feature of many neurodegenerative disorders. Pathological axon degeneration often occurs independently of known programmed death pathways, but the underlying molecular mechanisms remain largely unknown. Using traumatic injury as a model, we systematically investigate mitogen-activated protein kinase (MAPK) families and delineate a MAPK cascade that represents the early degenerative response to axonal injury. The adaptor protein Sarm1 is required for activation of this MAPK cascade, and this Sarm1-MAPK pathway disrupts axonal energy homeostasis, leading to ATP depletion before physical breakdown of damaged axons. The protective cytoNmnat1/Wld^s protein inhibits activation of this MAPK cascade. Further, MKK4, a key component in the Sarm1-MAPK pathway, is antagonized by AKT signaling, which modulates the degenerative response by limiting activation of downstream JNK signaling. Our results reveal a regulatory mechanism that integrates distinct signals to instruct pathological axon degeneration.

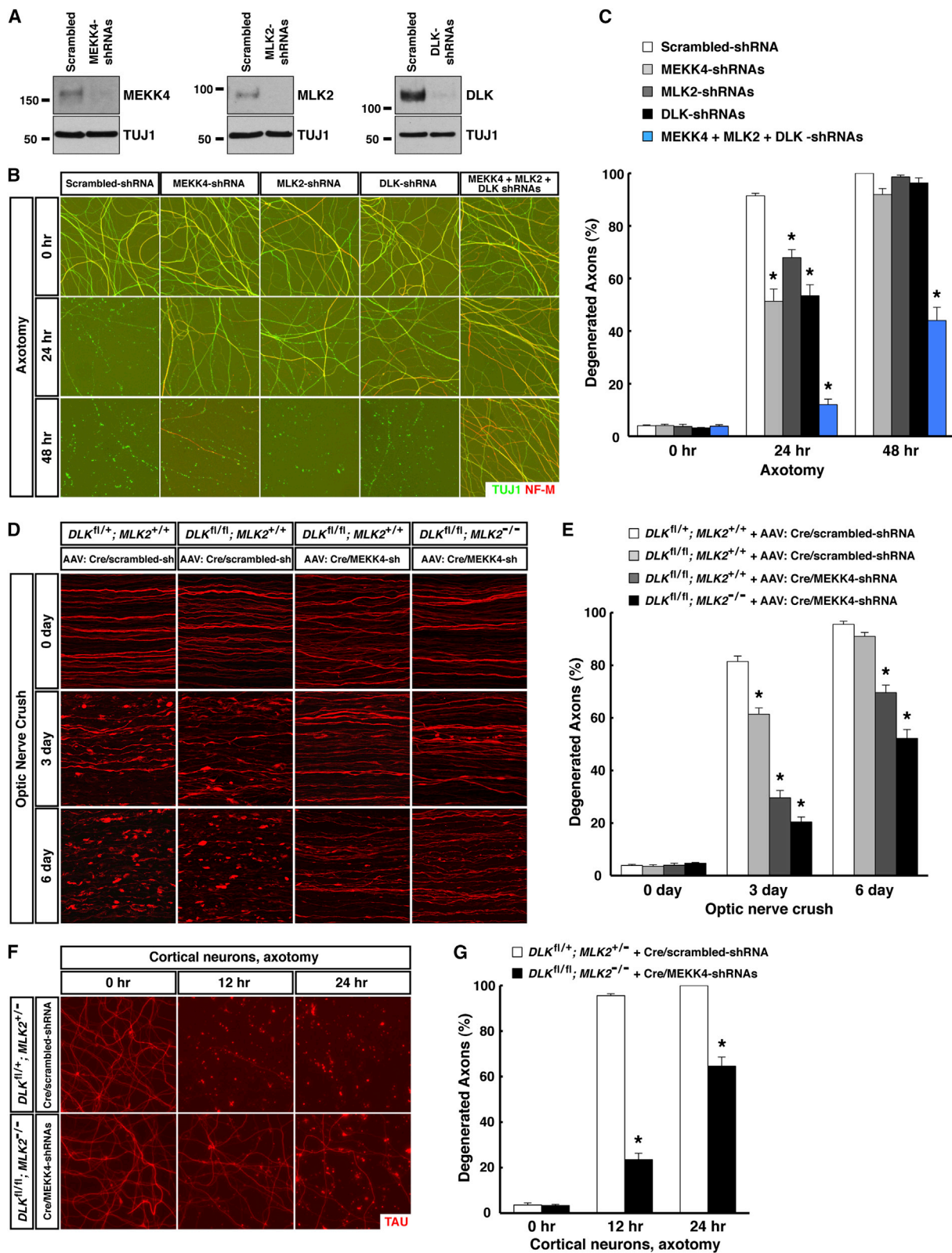
INTRODUCTION

Axons connect neurons with their innervating targets, forming the intricate neural circuits underlying perception, motility, cognition, and memory. However, the enormous distance axons can span (e.g., over a meter for certain axons in humans) creates a challenge for maintaining their structural and functional integrity. In fact, axonal death has been observed as a key pathological feature in many neurodegenerative disorders including traumatic injury, Alzheimer's disease, Parkinson's disease, glaucoma, multiple sclerosis, and amyotrophic lateral sclerosis (Conforti et al., 2014; Wang et al., 2012).

A common form of pathological axonal death is observed in segments distal to a site of traumatic injury, a process known as Wallerian degeneration. The discovery of the Wallerian Degeneration Slow mouse (*Wld^s*) and characterization of the *Wld^s* protein, whose gain-of-function can dramatically prolong axonal survival after injury, has suggested that death of injured axons is not simply due to loss of trophic support from neuronal cell bodies, but is instead triggered by an intrinsic signal(s) in axons. The *Wld^s* protein can suppress axon degeneration in many neurodegeneration models besides traumatic injury (Conforti et al., 2014; Wang et al., 2012), suggesting that a common mechanism might regulate axonal death in different neurodegenerative conditions.

Despite morphological similarities to cells undergoing apoptosis, including membrane blebbing and cytoskeletal fragmentation, axon degeneration under pathological conditions often does not involve the classic apoptotic pathway. For instance, genetic deletion of apoptotic regulators like BAX and caspases has no effect on Wallerian degeneration (Simon et al., 2012; Whitmore et al., 2003). In addition, at least during traumatic injury, axon degeneration also appears independent of the necroptotic pathway, since treatment with necroptosis inhibitors or lentiviral-shRNA knockdown of signaling components of necroptosis pathway like RIP3 and MLKL do not protect axons (data not shown). Therefore, axonal death in traumatic injury, as well as in neurodegeneration more broadly, likely represents a yet-to-be-characterized death program critical for human diseases. In-depth understanding of this degeneration program should illuminate neurodegenerative diseases and reveal novel therapeutic targets to battle them.

Our colleagues and we recently showed that loss-of-function of the adaptor protein Sarm1 significantly delays degeneration of injured axons (Gerdtts et al., 2013; Osterloh et al., 2012). Despite this breakthrough, signaling components in the Sarm1-mediated degenerative response are largely unknown. Previous studies have described roles for Sarm1 or its *C. elegans* ortholog *tir-1* in neural development (Chen et al., 2011; Chuang and Bargmann, 2005), stress responses (Couil-lault et al., 2004; Kurz et al., 2007), and non-apoptotic cell death (Blum et al., 2012). While the identity of signaling components



(legend on next page)

varies in different settings, a MAPK cascade downstream of *Sarm1/tir-1* has been observed in each case, suggesting potential conservation of the *Sarm1*-MAPK signaling axis. In addition, genetic deletion of the mouse MAPK kinase kinase (MAPKKK) member *DLK* transiently delayed, though to a significantly lesser extent than in *Wld^s* mice, the degeneration of injured axons in sciatic nerves in vivo and in cultured sensory neurons in vitro (Miller et al., 2009; Shin et al., 2012), and protection in vitro was also seen with a pharmacological inhibitor of MAPKs of the JNK family (Chen et al., 2012; Miller et al., 2009). Weak protection of injured axons was also reported with deletion of the *DLK* homolog *Wallenda* in *Drosophila* in some neurons (Miller et al., 2009), though not others (Osterloh et al., 2012; Xiong and Collins, 2012).

These observations prompted us to systematically investigate MAPK family members, and we delineate a MAPK cascade that is central in axon degeneration under pathological conditions. This cascade represents the early degenerative response, and *Sarm1* is required for its activation after injury. Activation of the *Sarm1*-MAPK pathway in turn disrupts local energy homeostasis in injured axons, leading to ATP depletion before activation of calpains and breakdown of axonal structures. We find that a cytosolic version of *Nmnat1* (nicotinamide mononucleotide adenylyltransferase 1, an enzyme in the NAD^+ synthesis pathway), which mimics the functional moiety of the *Wld^s* protein (Sasaki et al., 2009), inhibits activation of this MAPK pathway. Furthermore, *MKK4*, a central component in the pathway, is antagonized by AKT signaling, which modulates the early degenerative response by limiting activation of downstream JNKs. Our results reveal that distinct signals can converge onto a central MAPK pathway that triggers local energy deficit to promote pathological axon degeneration—a regulatory mechanism with potentially broad implications in neurodegenerative disorders.

RESULTS

Fluorescence-Labeling Approach to Examine Axons Undergoing Degeneration

To facilitate in vivo analysis of injury-induced axon degeneration, we established an approach to examine the axons of retinal ganglion cells (RGCs) undergoing degeneration in mouse optic nerves. RGCs were sparsely labeled with the *TdTomato* fluorescent protein via intravitreal delivery of adeno-associated virus 2 (AAV2). Degeneration of *TdTomato*-positive RGC axons was visualized at different time points following traumatic

injury (optic nerve crush). Across experiments, 70% to 80% of *TdTomato*-positive axons showed large swellings and/or fragmentation and were scored as degenerated 3 days after injury, and all axons had fragmented by 6 days (Figures S1A and S1B). This approach gave equivalent results to electron microscopic analysis (Figures S1C and S1D), i.e., about 80% of all RGC axons underwent demyelination and/or cytoskeletal destruction at 3 days, with complete breakdown of axonal structures by 6 days.

To validate this approach further, we examined the cytosolic version of *Nmnat1* (cytoNmnat1). As expected, in a transgenic mouse line expressing cytoNmnat1 driven by the prion protein promoter (PrP) (Sasaki et al., 2009), most *TdTomato*-positive axons remained intact 6 days after injury (Figures S1A and S1B). Transduction of wild-type axons with a virus expressing *TdTomato*-P2A-cytoNmnat1 (*TdTomato* and cytoNmnat1 proteins linked by a porcine teschovirus-derived self-cleaving 2A peptide) similarly resulted in robust protection, with over 60% of *TdTomato*-positive axons being intact at 6 days (Figures S1A and S1B). Of note, the protection level observed with *TdTomato*-P2A-cytoNmnat1 was modestly weaker than that in cytoNmnat1-transgenic mice, even though the level of cytoNmnat1 protein expressed by AAV2 was higher than by the transgene (Figure S1E). We attribute this to the fact that, in *TdTomato*-P2A-cytoNmnat1 optic nerves, unlabeled RGC axons (>99% of all axons) still degenerated normally as shown by electron microscopy (Figures S1C and S1D). There was profound activation of microglia and astrocytes in *TdTomato*-P2A-cytoNmnat1 nerves, but not in cytoNmnat1-transgenic nerves (Figure S1F), and it seems possible that this inflammatory response might secondarily influence axonal survival.

Further confirming the effectiveness of our approach, we found that RGC axons of wild-type mice transduced with *TdTomato*/*Sarm1*-shRNA (*TdTomato* together with a specific shRNA targeting *Sarm1*) virus were highly resistant to degeneration after nerve injury, in contrast to those transduced with control *TdTomato*/scrambled-shRNA virus (Figures S2D and S2E), consistent with the fact that *Sarm1* mRNA is expressed in RGCs (Figure S2A) and degeneration of injured RGC axons was largely blocked in *Sarm1*^{-/-} mice (Figures S2B and S2C).

Finally, degeneration of traumatically-injured axons depends on calpain activation as it can be delayed by expression of the endogenous calpain inhibitor calpastatin (Yang et al., 2013). Confirming this, RGC axons of *CAPNS1*^{flox/flox} mice transduced with a *TdTomato*-P2A-Cre virus, which results in disruption of both calpain-1 and calpain-2 activity through deletion of their

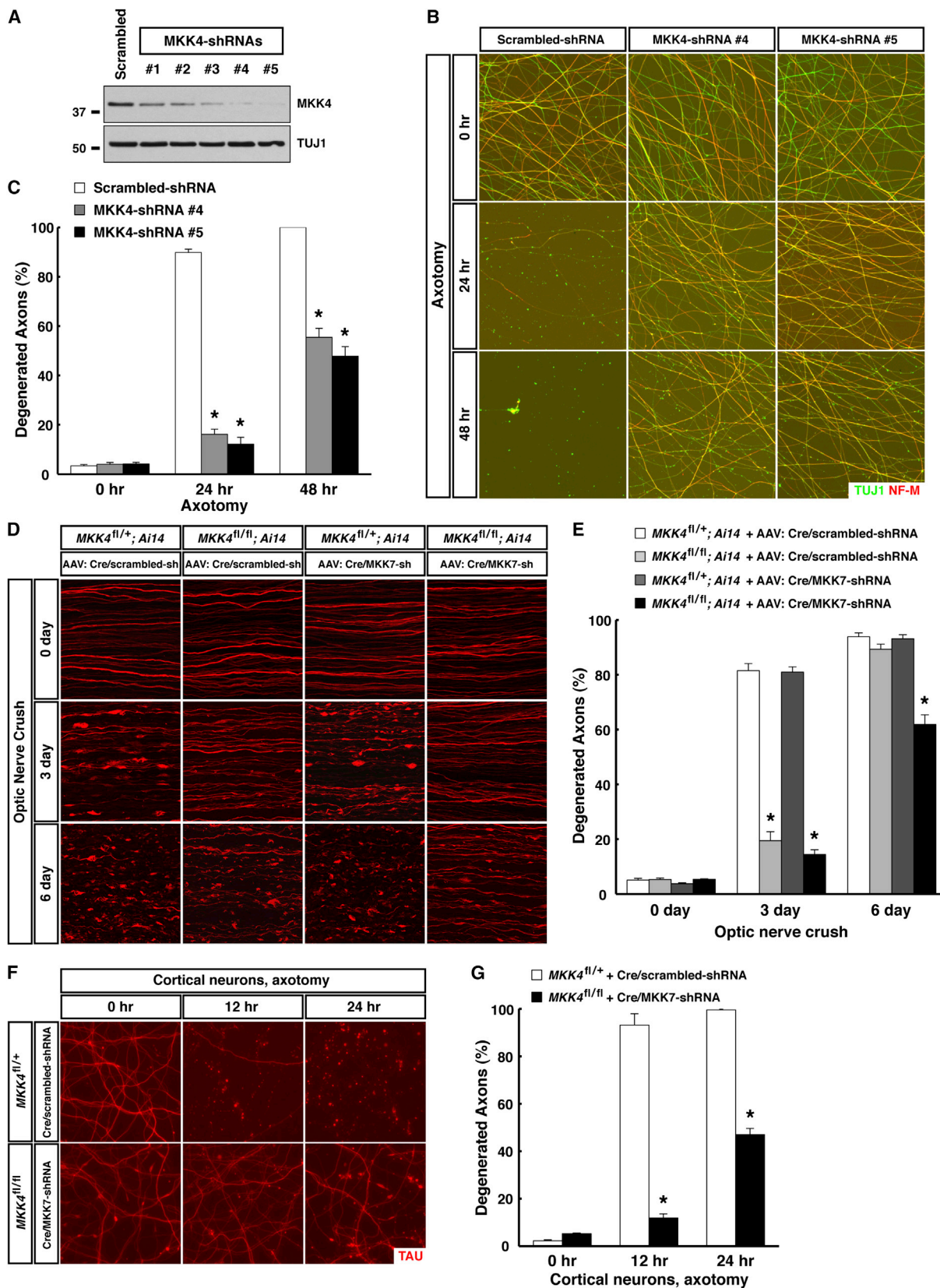
Figure 1. MEKK4/MLK2/DLK Function as the Predominant MAPKKs in Axon Degeneration Following Traumatic Injury

(A to C) MEKK4/MLK2/DLK regulate degeneration of injured sensory axons. Cultures of embryonic DRG neurons were subjected to lentiviral-shRNA knockdown of MEKK4, MLK2 and DLK, individually or in combination. The efficiency of lentiviral-shRNAs was examined by immunoblot analysis of axonal proteins harvested from each condition (A). Axon degeneration at indicated time points following axotomy was visualized by immunostaining (B), and degeneration was quantified (C), n = 3 for each condition.

(D and E) MEKK4/MLK2/DLK regulate degeneration of injured RGC axons in vivo. RGCs of the mice with indicated genotypes were transduced with *TdTomato* virus together with either Cre/scrambled-shRNA or Cre/MEKK4-shRNA. Degeneration of *TdTomato*-positive axons was visualized at indicated time points after optic nerve crush (D), and degeneration was quantified (E), n = 4 for each condition.

(F and G) MEKK4/MLK2/DLK regulate degeneration of injured cortical axons. Cultures of embryonic cortical neurons with indicated genotypes were transduced with lentivirus expressing Cre together with scrambled-shRNA or MEKK4-shRNAs. Axon degeneration at indicated time points following axotomy was visualized by immunostaining (F), and degeneration was quantified (G), n = 3 for each condition. Values are presented as mean ± SEM; *p < 0.01.

See also Figure S3 and Table S1.



(legend on next page)

common small subunit (Tan et al., 2006), showed significantly delayed degeneration compared to those of wild-type mice (Figures S2F and S2G). Together, our results show that this labeling approach can provide effective cell-autonomous manipulation of signaling components involved in axon degeneration.

A Central MAPK Pathway in Axon Degeneration after Traumatic Injury

Sarm1 was recently shown to regulate axon degeneration after traumatic injury (Gerdtts et al., 2013; Osterloh et al., 2012). As mentioned, in other biological processes Sarm1 and its ortholog *tir-1* were linked to MAPK signaling, and prior genetic analyses implicated the MAPKKK member DLK as a weak regulator in degeneration of injured axons (Miller et al., 2009; Osterloh et al., 2012; Shin et al., 2012), prompting us to investigate the function of MAPK families more systematically.

There are 23 members of the MAPKKK family in mouse. Using cultured sensory neurons, we found that the highly specific inhibitor PLX-4720 for three MAPKKs, A-raf, B-raf, and C-raf, did not offer protection after axotomy (data not shown). We therefore performed lentiviral-shRNA knockdown screening of the remaining 20 MAPKKK members (Table S1) and observed that knockdown of each of three MAPKKK members, MEKK4, MLK2, and DLK, in sensory axons partially protected (Figures 1A to 1C). Moreover, MEKK4/MLK2/DLK function additively, as knockdown of any two produced a stronger phenotype (data not shown), and knockdown of all three resulted in the strongest protection, with about 60% of axons intact 48 hr after axotomy (Figures 1A to 1C). In parallel, we examined expression of mRNAs for the 23 MAPKKK members in adult mouse retina (Figure S3A). Many show no or very low expression (e.g., *MAP3K15*), but a few are strongly expressed (e.g., *B-raf*). Importantly, MEKK4, MLK2, and DLK mRNAs are all expressed in RGCs. In functional analyses, we found that RGC axons in *DLK^{flox/flox}* mice transduced by viral delivery of Cre together with a control scrambled-shRNA (Cre/scrambled-shRNA) showed a modest delay of degeneration compared to *DLK^{flox/+}* mice 3 days, but not 6 days, after injury (Figures 1D and 1E), in line with the transient protection of injured axons in mouse sciatic nerve after *DLK* deletion (Shin et al., 2012). Greater protection was seen after further knockdown of MEKK4 in RGC axons of *DLK^{flox/flox}* mice with a Cre/MEKK4-shRNA virus, and even more with *MLK2* deletion through delivery of that virus into *DLK^{flox/flox}; MLK2^{-/-}* mice, with 50% of TdTomato-positive axons remaining intact 6 days after injury (Figures 1D and 1E). Although we cannot rule out that other MAPKKs might exert a minor role, our results identify

MEKK4/MLK2/DLK as the predominant MAPKKs regulating this degeneration process.

We next explored the seven members of MAPK kinase (MAPKK) family. Inhibition of MEK1/MEK2 with the highly specific inhibitor PD-0325901 failed to protect sensory axons after injury in vitro (data not shown). We therefore screened lentiviral-shRNAs against the other five MAPKK members (Table S1). Knockdown of MKK4 (also known as SEK1) led to strong protection of injured sensory axons, i.e., with either of the two most efficient shRNAs, axon degeneration was almost completely suppressed at 24 hr, and about 50% of injured axons persisted even at 48 hr (Figures 2A to 2C). In parallel, we examined expression of six MAPKK members in adult mouse retina, and found that mRNAs for all six, including MKK4, are expressed in RGCs (Figure S3B). To determine the function of MKK4 in vivo, RGC axons of *MKK4^{flox/flox}* mice were transduced with a Cre/scrambled-shRNA virus. TdTomato-positive axons were dramatically protected against degeneration compared to those in *MKK4^{flox/+}* mice 3 days after injury (Figures 2D and 2E). However, RGC axons in *MKK4^{flox/flox}* mice still exhibited significant degeneration at 6 days, raising the possibility that other MAPKKs might contribute. Indeed, further knockdown of MKK7 in RGC axons of *MKK4^{flox/flox}* mice using a Cre/MKK7-shRNA virus led to significant enhancement of protection, i.e., over 40% of TdTomato-positive axons were intact at 6 days (Figures 2D and 2E). Of note, transduction of RGC axons of *MKK4^{flox/+}* mice with the Cre/MKK7-shRNA virus did not offer protection (Figures 2D and 2E), and shRNA knockdown of MKK3 or MKK6 failed to enhance protection in *MKK4^{flox/flox}* mice (data not shown). These results identify MKK4 as the predominant MAPKK in axon degeneration after injury, with MKK7 exerting a moderate redundant function.

MKK4 activates MAPK members of the JNK and p38 families, whereas MKK7 only activates JNK family members (Weston and Davis, 2007). mRNAs of all three JNKs and two p38s (p38alpha and p38delta) are expressed in RGCs in adult mouse retina (Figure S4A). In vitro treatment of injured RGC axons with a JNK inhibitor but not a p38 inhibitor delayed degeneration (Figures S4C and S4D), consistent with previous reports (Chen et al., 2012; Miller et al., 2009). As well, in the lentiviral-shRNA screening of 13 MAPK family members (Table S1), knockdown of JNK3 significantly protected sensory axons in vitro, i.e., degeneration was strongly suppressed 24 hr after axotomy with either of the two most efficient shRNAs, and a sizable fraction of injured axons still remained intact at 48 hr with the most efficient shRNA (Figures 3A to 3C). Consistent with the in vitro

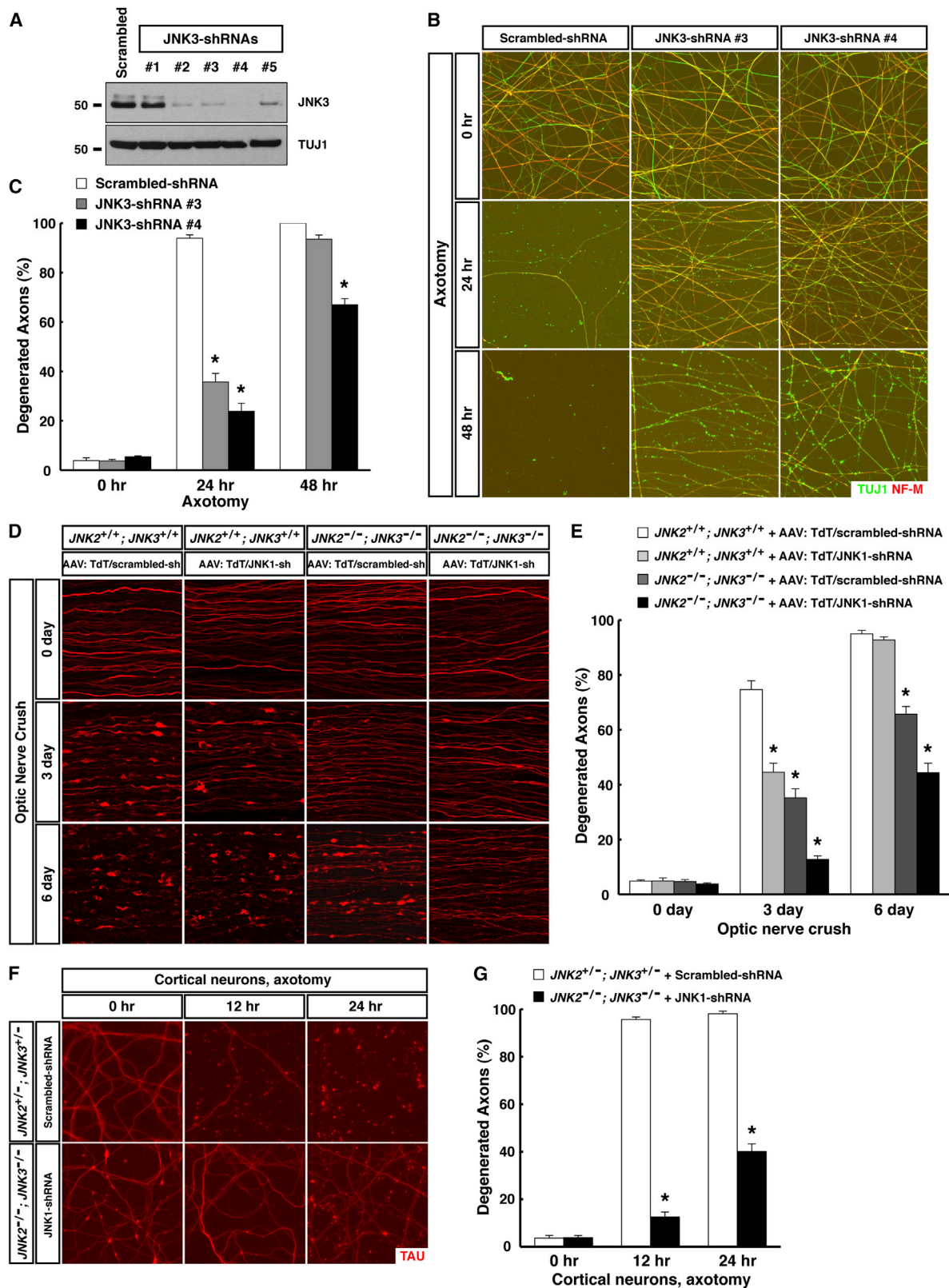
Figure 2. MKK4 Functions as the Predominant MAPKK Assisted by MKK7 in Axon Degeneration Following Traumatic Injury

(A to C) MKK4 regulates degeneration of injured sensory axons. Cultures of embryonic DRG neurons were subjected to lentiviral-shRNA knockdown of MKK4. Efficiency of lentiviral-shRNAs was examined by immunoblot analysis of axonal proteins harvested from each condition (A). Degeneration of axons transduced with the two most efficient lentiviral-shRNAs was visualized by immunostaining at indicated time points after axotomy (B), and degeneration was quantified (C), $n = 3$ for each condition.

(D and E) MKK4 functions with MKK7 to regulate degeneration of injured RGC axons in vivo. RGCs of the mice with indicated genotypes were transduced with Cre/scrambled-shRNA or Cre/MKK7-shRNA virus. *Ai14* represents the *Rosa26-CAG-LSL-TdTomato* reporter. Degeneration of TdTomato-positive axons was visualized at indicated time points after optic nerve crush (D), and degeneration was quantified (E), $n = 4$ for each condition.

(F and G) MKK4/MKK7 regulate degeneration of injured cortical axons. Cultures of embryonic cortical neurons with indicated genotypes were transduced with lentivirus expressing Cre together with scrambled-shRNA or MKK7-shRNA. Axon degeneration at indicated time points following axotomy was visualized by immunostaining (F), and degeneration was quantified (G), $n = 3$ for each condition. Values are presented as mean \pm SEM; * $p < 0.01$.

See also Figure S3 and Table S1.



(legend on next page)

results, degeneration of RGC axons was significantly delayed 6 days after injury in *JNK3*^{-/-} mice, and the protection level was greater in *JNK2*^{-/-}; *JNK3*^{-/-} mice, while there was no effect in *JNK2*^{-/-} mice alone (Figures S4E and S4F). Further, shRNA-knockdown of JNK1 in wild-type RGC axons inhibited degeneration after injury (Figures 3D and 3E). More importantly, survival of RGC axons in *JNK2*^{-/-}; *JNK3*^{-/-} mice was enhanced by shRNA-knockdown of JNK1, with about 60% of TdTomato-positive axons being intact at 6 days (Figures 3D and 3E). Therefore, JNK1/JNK2/JNK3 function to regulate the degeneration of injured axons, with JNK1 and JNK3 playing predominant roles.

MAPK signaling can be modulated by various scaffold proteins, including the JIPs (JNK-interacting proteins) (Morrison and Davis, 2003). mRNAs of three JIPs are expressed in adult mouse RGCs (Figure S4B). Knockdown of JIP3 in wild-type RGCs with a TdTomato/JIP3-shRNA virus protected their axons at 3 days, though not 6 days, after injury (Figures S4G and S4H, data not shown), whereas shRNA-knockdown of JIP1 or JIP2 did not (data not shown), showing specific involvement of JIP3 in this process.

Thus, using sensory neurons and RGCs as models, we delineate a MAPK cascade comprising three MAPKKs (MEKK4/MLK2/DLK), two MAPKKs (MKK4/MKK7), three MAPKs (JNK1/JNK2/JNK3), and the scaffold protein JIP3, as a central pathway in axon degeneration after traumatic injury. This MAPK cascade is also critical for the degeneration of injured cortical axons, as combinatorial depletion of MEKK4/MLK2/DLK (Figures 1F and 1G), MKK4/MKK7 (Figures 2F and 2G), or JNK1/JNK2/JNK3 (Figures 3F and 3G) in cultured cortical neurons all strongly protected against injury, with the protective level comparable to that in *Sarm1*^{-/-} cortical neurons (Osterloh et al., 2012).

The MAPK Cascade Functions Downstream of Sarm1 as the Early Degenerative Response to Axonal Injury

We next examined activation of this MAPK pathway after axonal injury. Ser257/Thr261 phosphorylation of MKK4, which reflects activity of upstream MAPKKs, was evident as little as 5 min after optic nerve injury. MKK4 activation peaked between 15 to 30 min, then returned to baseline between 2 to 4 hr (Figures 4A and S5A). This signaling represents the early degenerative response, occurring days before physical breakdown of axons, as assessed by proteolysis of cytoskeletal components starting around 48 hr (e.g., α -internexin, Figure 4A).

MKK4 activation in injured optic nerves was specific to RGC axons. When we transduced RGCs of *MKK4*^{flox/flox} mice with a saturating amount of Cre virus, which depleted MKK4 protein

in over 90% of RGCs (Figure S5C) and decreased total MKK4 protein in optic nerves, this in turn eliminated MKK4 phosphorylation on Ser257/Thr261 in injured nerves (Figures 4B and S5B). Deletion of MKK4 in RGC axons also largely diminished activation of downstream JNKs (Figure 4B). To determine the physiological role of MKK4 phosphorylation on Ser257/Thr261 in degeneration, we depleted endogenous MKK4 protein in RGCs of *MKK4*^{flox/flox} mice with Cre, and concurrently delivered into these cells wild-type MKK4 or the MKK4(S257A/T261A) mutant. After nerve injury, RGC axons of *MKK4*^{flox/flox} mice transduced with the Cre-P2A-MKK4(WT) virus degenerated normally (Figures 7E and 7F). In contrast, RGC axons transduced with the Cre-P2A-MKK4(S257A/T261A) virus exhibited strong reduction of degeneration at 3 days (Figures S5D and S5E) similar to that seen in *MKK4*^{flox/flox} mice transduced with the Cre virus (Figures 2D and 2E), showing that MKK4(S257A/T261A) failed to rescue the function of endogenous MKK4. Moreover, MKK4(S257A/T261A) had a dominant-negative effect, since RGC axons of wild-type mice transduced with the Cre-P2A-MKK4(S257A/T261A) virus showed delayed degeneration 3 days after injury (Figures S5D and S5E).

We also studied MKK4 activation in an in vitro degeneration model, which allows us to obtain preparations of axonal proteins excluding neuronal cell bodies and non-neuronal cells, and therefore to focus on axon-specific events (Yang et al., 2013). Similar to our in vivo data, MKK4 phosphorylation on Ser257/Thr261 occurred during the early degenerative response in vitro, peaking around 10 to 15 min after axotomy (Figures 6A and 6B), but hours before proteolysis of cytoskeletal proteins (e.g., α II-spectrin). In addition, treatment of RGC axons in vitro with the JNK inhibitor during the first 1 hr after injury was sufficient to suppress degeneration (data not shown), similar to a previous observation implying an early role of JNK signaling in the degeneration of injured sensory axons (Miller et al., 2009).

Supporting the hypothesis of an evolutionarily conserved Sarm1-MAPK signaling axis, early activation of MKK4 and downstream JNKs in injured optic nerves was abolished in *Sarm1*^{-/-} mice (Figures 4C and S5B). Similarly, MKK4 phosphorylation on Ser257/Thr261 was absent in *Sarm1*^{-/-} sensory axons in the in vitro model (Figure 6H). To further determine the genetic interaction between Sarm1 and the MAPK cascade, we examined additivity of the protective effects afforded by depletion of Sarm1 or MKK4/MKK7. Combinatorial depletion of MKK4/MKK7 in sensory axons resulted in strong protection until 48 hr after axotomy, but most injured axons eventually degenerated at 96 hr (Figures 4E and 4F). While shRNA knockdown of

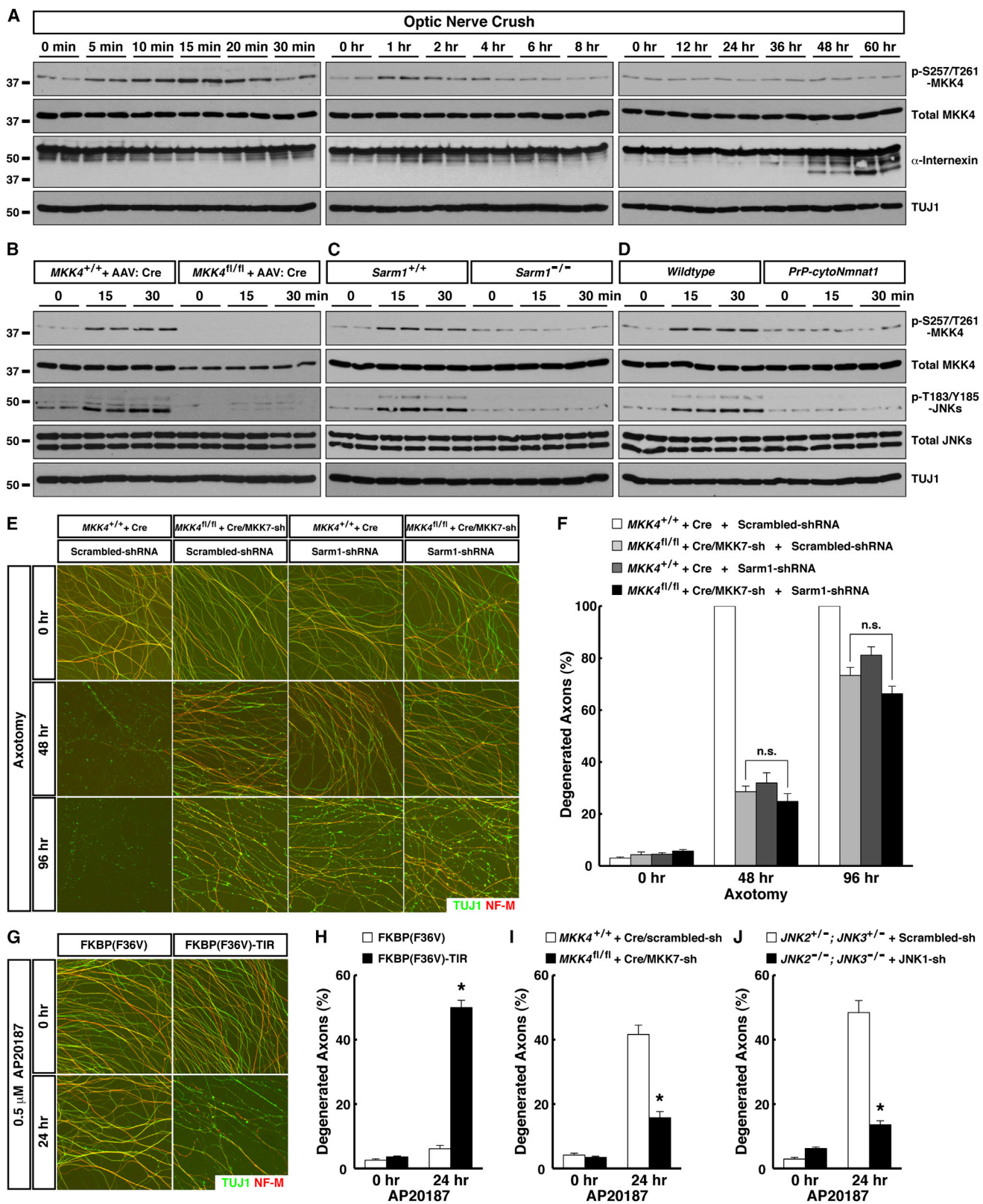
Figure 3. JNK1 and JNK3 Function as the Predominant MAPKs Assisted by JNK2 in Axon Degeneration after Traumatic Injury

(A to C) JNK3 regulates degeneration of injured sensory axons. Cultures of embryonic DRG neurons were subjected to lentiviral-shRNA knockdown of JNK3. Efficiency of lentiviral-shRNAs was examined by immunoblot analysis of axonal proteins harvested from each condition (A). Degeneration of axons transduced with the two most efficient lentiviral-shRNAs was visualized by immunostaining at indicated time points after axotomy (B), and degeneration was quantified (C), *n* = 3 for each condition.

(D and E) JNK1 and JNK3 function as the predominant MAPKs in regulating degeneration of injured RGC axons in vivo. RGCs of the mice with indicated genotypes were transduced with TdTomato/scrambled-shRNA or TdTomato/JNK1-shRNA virus. Degeneration of TdTomato-positive axons was visualized at indicated time points after optic nerve crush (D), and degeneration was quantified (E), *n* = 4 for each condition.

(F and G) JNK1/JNK2/JNK3 regulate degeneration of injured cortical axons. Cultures of embryonic cortical neurons with indicated genotypes were transduced with lentivirus expressing scrambled-shRNA or JNK1-shRNA. Axon degeneration at indicated time points following axotomy was visualized by immunostaining (F), and degeneration was quantified (G), *n* = 3 for each condition. Values are presented as mean \pm SEM; **p* < 0.01.

See also Figure S4 and Table S1.



(legend on next page)

Sarm1 gave rise to a similar protection, Sarm1-shRNA did not further potentiate protection by MKK4/MKK7 depletion (Figures 4E and 4F). Similarly, though *Sarm1*^{-/-} sensory axons were highly resistant to degeneration, the majority degenerated 96 hr after axotomy (Figures S5F and S5G). shRNA knockdown of MKK4/MKK7 also strongly protected, but failed to further extend survival of *Sarm1*^{-/-} axons. The non-additivity of protective effects implies that Sarm1 and the MAPK cascade reside in the same genetic pathway.

Domain analyses of Sarm1 or its ortholog *tir-1* have indicated that the SAM domains mainly function in protein dimerization, which enables the C-terminal TIR domain to activate downstream signaling. The N-terminal ARM domain exerts an auto-inhibitory role, because Sarm1 or TIR-1 without the ARM domain appears constitutively active (Chuang and Bargmann, 2005; Gerdtts et al., 2013). Consistent with this, expression of a Sarm1 mutant lacking the N-terminal ARM domain led to axon degeneration about 4 to 6 days after viral transduction (data not shown). To control the pro-degenerative Sarm1 signal in a temporally-defined manner, we fused the Sarm1 TIR-domain to FKBP(F36V), which could be dimerized by the cell-permeable chemical AP20187. Treatment of sensory neurons expressing FKBP(F36V)-TIR with AP20187 induced degeneration of distal axons (Figures 4G and 4H), which appears independent of the apoptotic pathway since it was not affected by genetic deletion of caspase-9 or overexpression of Bcl-xl (data not shown). Importantly, axons of neurons expressing FKBP(F36V)-TIR showed rapid MKK4 phosphorylation on Ser257/Thr261 in response to AP20187 (Figures S5H and S5I), and their degeneration was largely blocked by combinatorial depletion of MKK4/MKK7 or JNK1/JNK2/JNK3 (Figures 4I and 4J). Although care must be taken in interpreting the effect of Sarm1 gain-of-function, especially as FKBP(F36V)-TIR dimerization also led to atrophy and death of neuronal cell bodies similar to that observed with constitutively-active Sarm1 (Gerdtts et al., 2013; Summers et al., 2014), the results nonetheless further support the model that Sarm1 functions upstream of the MAPK cascade.

The axonal protective function of the Wld^s protein has been known for decades, but its underlying mechanism remains elusive. To determine its relationship to MAPK signaling, we examined activation of the pathway in cytoNmnat1-transgenic mice. Early activation of MKK4 and downstream JNKs in injured optic nerves in vivo was suppressed in these mice (Figures 4D

and S5B), and MKK4 phosphorylation on Ser257/Thr261 was absent from their sensory axons after axonal injury in vitro (Figure 6I), suggesting that cytoNmnat1/Wld^s might protect by inhibiting the MAPK pathway.

The Sarm1-MAPK Pathway Triggers Local Energy Deficit Leading to Morphological Degeneration

Activation of the Sarm1-MAPK pathway occurs minutes after injury, but hours or even days before breakdown of axonal structures, prompting us to explore the connection between these processes. A previous study reported a decrease of ATP level in injured axons that could be inhibited by the Wld^s protein (Wang et al., 2005), but the relevance of ATP depletion was questioned by other studies (Press and Milbrandt, 2008; Summers et al., 2014). Of note, the original measurement of ATP levels was carried out with axonal samples (Wang et al., 2005), but in later studies was done with whole neuronal cultures including cell bodies, and we reasoned that this difference might explain the discrepancy. Taking advantage of our in vitro axonal enrichment method and also a newly-devised luciferase-based ATP measurement method (instead of classic HPLC), we followed ATP levels exclusively in axons after injury. Consistent with the original study (Wang et al., 2005), there was continuous depletion of axonal ATP in injured sensory axons, which preceded proteolysis of cytoskeletal proteins and morphological degeneration (Figures 5A and 5B, and data not shown). That study also showed that ATP levels in axons could be rescued by metabolic fuel such as methyl-pyruvate (a cell-permeable form of pyruvate) provided prior to injury (Wang et al., 2005). We extended that finding by treating injured axons with methyl-pyruvate 2 hr post-axotomy, i.e., after the early activation of Sarm1-MAPK pathway in this in vitro model (Figures 6A and 6B), and observed that it could also significantly delay the ATP depletion (Figure 5C). Because calpain activation is responsible for proteolysis of cytoskeletal components and physical breakdown of axonal structures (Figures S2F and S2G) (Yang et al., 2013), we examined the relationship between this local energy deficit and calpain activation. Methyl-pyruvate treatment, which delayed ATP depletion, strongly suppressed calpain-mediated proteolysis of cytoskeletal proteins (Figure 5D) as well as morphological degeneration of injured axons (Figure 5E and Figure 5F). To further confirm that calpains function downstream of ATP depletion, we treated injured axons 2 hr post-axotomy with calpain

Figure 4. Sarm1 Is Required for Activation of the MAPK Cascade as an Early Response to Axonal Injury

(A to D) Nerve samples were harvested at indicated time points after optic nerve crush for immunoblot analysis (two mice per time point). (A) Activation of the MAPK cascade represents an early response to axonal injury. (B) MKK4 functions as the predominant MAPKK for activation of downstream JNKs. RGCs of wild-type or *MKK4*^{flax/flax} mice were subjected to saturated transduction of Cre virus for 6 weeks prior to optic nerve crush. (C) Sarm1 is required for activation of the MAPK cascade. (D) Activation of the MAPK cascade is suppressed by the cytoNmnat1 transgene.

(E and F) Sarm1 and MKK4/MKK7 function in the same genetic pathway. Cultures of sensory neurons with indicated genotypes were transduced with lentivirus expressing scrambled-shRNA or Sarm1-shRNA. Axon degeneration at indicated time points following axotomy was visualized by immunostaining (E), and degeneration was quantified (F), n = 3 for each condition.

(G and H) Induced dimerization of the Sarm1 TIR-domain causes axon degeneration. Cultures of sensory neurons were transduced with lentivirus expressing FKBP(F36V) or FKBP(F36V)-TIR. Axon degeneration at 24 hr after treatment with 0.5 μ M AP20187 was visualized by immunostaining (G), and degeneration was quantified (H), n = 3 for each condition.

(I and J) Axon degeneration induced by the Sarm1 TIR-domain requires the MAPK cascade. Cultures of sensory neurons with indicated genotypes were transduced with lentivirus expressing FKBP(F36V)-TIR. Axon degeneration at 24 hr after treatment with 0.5 μ M AP20187 was quantified, n = 3 for each condition. Values are presented as mean \pm SEM; *p < 0.01; n.s., not significant.

See also Figure S5.

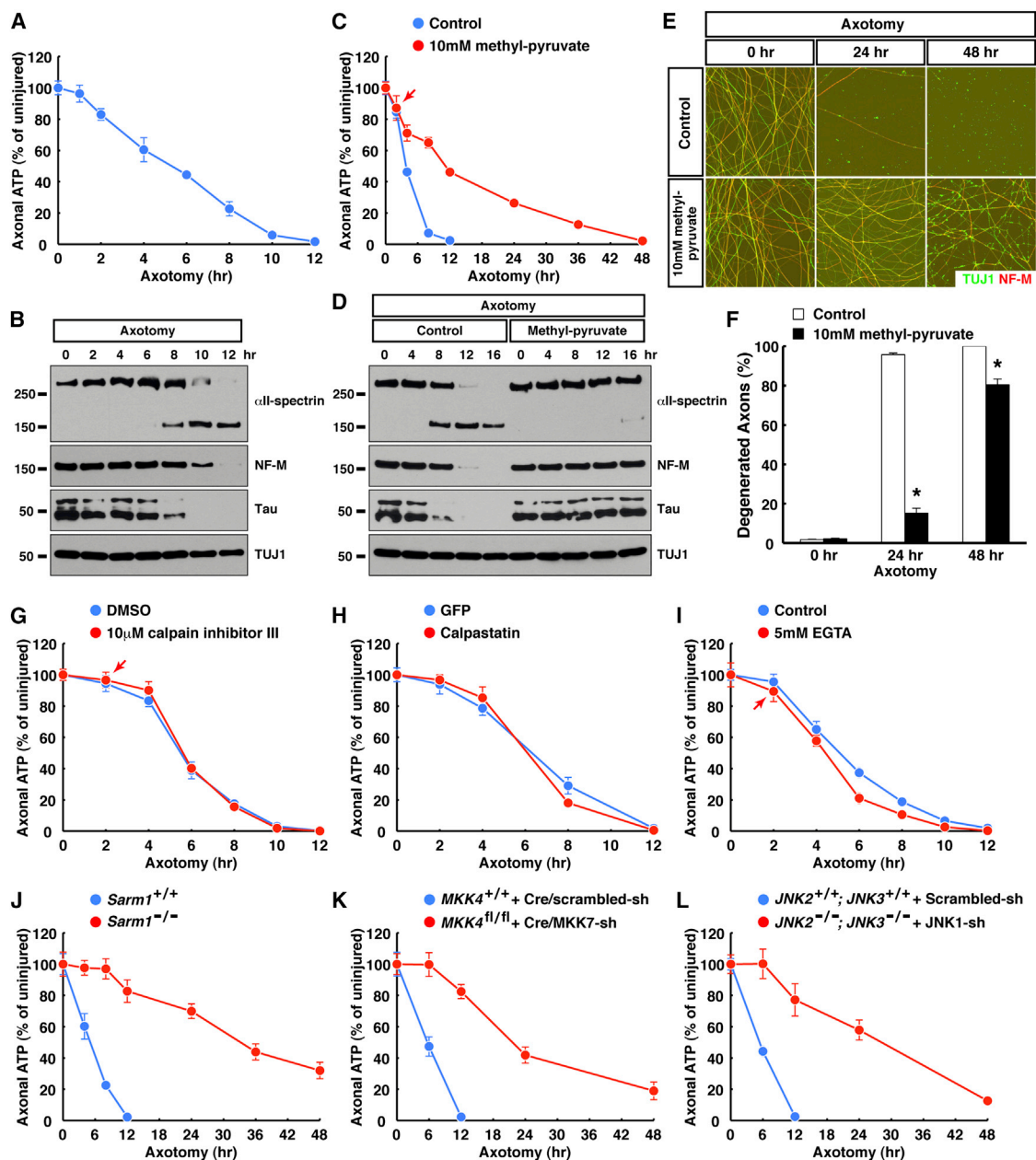


Figure 5. The Sarm1-MAPK Pathway Triggers an Axonal Energy Deficit Following Traumatic Injury

(A and B) Energy deficit precedes calpain activation in injured axons. Axonal ATP levels of cultured sensory neurons were measured at indicated time points after axotomy (A, $n = 6$ for each condition), and in parallel, axonal proteins were harvested for immunoblot analysis (B).

(C to F) Energy deficit is causative to calpain activation and morphological degeneration. Cultures of sensory neurons were provided with 10 mM methyl-pyruvate as metabolic fuel 2 hr post-axotomy. At indicated time points, axonal ATP levels were measured (C, $n = 6$ for each condition), axonal proteins were harvested for immunoblot analysis (D), axon degeneration was visualized by immunostaining (E), and the degeneration was quantified (F, $n = 4$ for each condition).

(G to I) Calpains function downstream of axonal energy deficit. Cultures of sensory neurons were treated with 10 μM calpain inhibitor III (G, $n = 6$ for each condition) or 5 mM EGTA (I, $n = 6$ for each condition) 2 hr post-axotomy, or were transduced with lentivirus expressing calpastatin (H, $n = 4$ for each condition). Axonal ATP levels were measured at indicated time points.

(J to L) The Sarm1-MAPK pathway triggers local energy deficit following axonal injury. Axonal ATP levels of cultured sensory neurons with indicated genotypes were measured at indicated time points after axotomy, $n = 4$ for each condition. Values are presented as mean \pm SEM; * $p < 0.01$.

See also Figure S6.

inhibitor III, which is relatively selective to calpains (Yang et al., 2013), or transduced the neurons with lentivirus expressing the endogenous specific calpain inhibitor calpastatin. Both methods strongly inhibited calpain activation and morphological degeneration (Yang et al., 2013), but neither ameliorated the energy deficit in injured axons (Figure 5G and 5H). Similarly, treatment of injured axons 2 hr post-axotomy with EGTA to chelate Ca^{2+} that is essential for calpain activation—a manipulation that also protects axons (data not shown)—also failed to rescue axonal ATP levels (Figure 5I). The results together argue that the local energy deficit in axons precedes, and is causative to, calpain activation and morphological degeneration after injury.

Importantly, the first detectable change of axonal ATP levels occurred around 2 hr post-axotomy (e.g., Figure 1A), after the early activation of the Sarm1-MAPK pathway (Figure 6A and 6B), and depletion of Sarm1, MKK4/MKK7, or JNK1/JNK2/JNK3, which suppressed morphological degeneration as reported above, all dramatically preserved ATP levels in injured axons (Figure 5J to 5L), even better than methyl-pyruvate treatment. The same was also true in sympathetic (i.e., superior cervical ganglion) axons: injury triggered ATP depletion in these axons that preceded proteolysis of cytoskeletal proteins and morphological degeneration (data not shown); this energy deficit was not affected by calpain inhibition (Figure S6A), but was significantly delayed by deletion of Sarm1 (Figure S6B) or inhibition of JNKs (Figure S6C). Together, our results support the model that the Sarm1-MAPK pathway triggers a local energy deficit in injured axons, which leads to calpain activation and morphological degeneration.

Pro-Degenerative Function of MKK4 Is Antagonized by AKT

While studying the phosphorylation status of Sarm1-MAPK components in injured axons, we unexpectedly found that MKK4 was also phosphorylated on Ser78. This phosphorylation increased significantly around 1 to 5 min after injury, even preceding phosphorylation on Ser257/Thr261 (Figures 6A and 6B). The sequence surrounding Ser78 residue of mouse MKK4 is an authentic target for AKT, and phosphorylation of Ser78 can inhibit MKK4 activity (Park et al., 2002). Two selective AKT inhibitors, i.e., the allosteric inhibitor MK-2206 and the ATP-competitive inhibitor GDC-0068, both significantly reduced MKK4 phosphorylation on Ser78 in axons after injury (Figure 6C), though as expected from their distinct mechanisms, MK-2206 decreased while GDC-0068 increased AKT phosphorylation on Thr308 and Ser473, residues critical for AKT activation (Figure 6C and data not shown). We noted that phosphorylation on Thr308 and Ser473 appeared constant in injured axons and only started to decrease when degeneration began (Figures 6A and 6C). However, there was enhanced interaction between AKT and MKK4 in axons immediately after injury (Figure 6D), temporally correlating with increased MKK4 phosphorylation on Ser78 (Figures 6A and 6B).

We explored how these two distinct phosphorylation events regulate MKK4 activity toward downstream JNKs. MKK4 was expressed in cultured cells with DLK (whose overexpression is self-activating, and thus mimics activation of the MAPK cascade) or myrAKT1 (a constitutively-active form of AKT1

that mimics AKT signaling). As expected, DLK significantly increased MKK4 phosphorylation on Ser257/Thr261, and myrAKT1 enhanced MKK4 phosphorylation on Ser78 (Figure 6E). Notably, AKT-mediated Ser78 phosphorylation did not affect the level of Ser257/Thr261 phosphorylation induced by DLK, and vice versa. Moreover, when phospho-S257/T261-MKK4 was specifically enriched using the p-S257/T261-MKK4 antibody, Ser78 phosphorylation was retained in the immunoprecipitated sample (Figure 6E). The results suggest that the two phosphorylation events are biochemically independent. Next, MKK4 expressed with DLK or myrAKT1 was immunoaffinity purified and subjected to a kinase assay using recombinant JNK3(K55R) as the substrate. While MKK4 activated by DLK had strong activity in phosphorylating JNK3, MKK4 expressed with DLK and AKT1 together exhibited little activity, even though the two samples had similar levels of Ser257/Thr261 phosphorylation (Figure 6F). This Ser78 phosphorylation-mediated inhibition of MKK4 activity correlated with a decrease of direct interaction between MKK4 and the JNK substrate in a protein pull-down assay (Figure 6G), in line with the fact that a major JNK-binding site of MKK4 is adjacent to the Ser78 residue (Ho et al., 2003). The AKT-mediated inhibitory effects were abolished with the MKK4(S78A) mutant protein (Figures 6F and 6G). These results show that while Ser257/Thr261 phosphorylation of MKK4 activates its kinase activity toward JNK, Ser78 phosphorylation of MKK4 can block its interaction with the JNK substrate.

Interestingly, unlike Ser257/Thr261 phosphorylation, MKK4 phosphorylation on Ser78 was not affected in injured sensory axons from *Sarm1*^{-/-} (Figures 6H and S6D) or cytoNmnat1-transgenic (Figures 6I and S6D) mice. Moreover, AKT inhibition did not have a significant effect on MKK4 phosphorylation on Ser257/Thr261 after injury (Figure 6C). The results suggest that AKT signaling targets MKK4 in a Sarm1-independent manner.

The finding that AKT-mediated Ser78 phosphorylation can suppress Ser257/Thr261-phosphorylated MKK4 activity toward JNKs raised the possibility that it might promote axonal survival. Indeed, transient inhibition of AKT in the first 1 hr after injury significantly accelerated degeneration of RGC axons in vitro (Figure S6G and S7H). In vivo, MKK4 phosphorylation on Ser78 was present in optic nerves and transiently increased after injury (Figure 7A), and was dramatically reduced following deletion of MKK4 in RGCs of *MKK4*^{flox/flox} mice with the Cre virus (Figure 7A). Supporting involvement of AKT signaling, mRNAs of all three AKT members are expressed in RGCs (Figure 7B). To determine its physiological relevance, we depleted endogenous MKK4 protein in RGCs of *MKK4*^{flox/flox} mice with Cre, and concurrently delivered either wild-type MKK4 or the MKK4(S78A) mutant, which were expressed at levels comparable to endogenous MKK4 both in cultured cells (Figure S6E) and in optic nerves (Figure 7C). After nerve injury, *MKK4*^{flox/flox} mice transduced with the Cre-P2A-MKK4(WT) virus showed a similar level of JNK activation as in wild-type mice, whereas those transduced with the Cre-P2A-MKK4(S78A) virus exhibited significantly stronger JNK activation (Figures 7C and 7D). In the latter case, RGC axons underwent accelerated degeneration, i.e., while the vast majority of TdTomato-positive axons were intact in wild-type mice or in the Cre-P2A-MKK4(WT) condition 48 hr

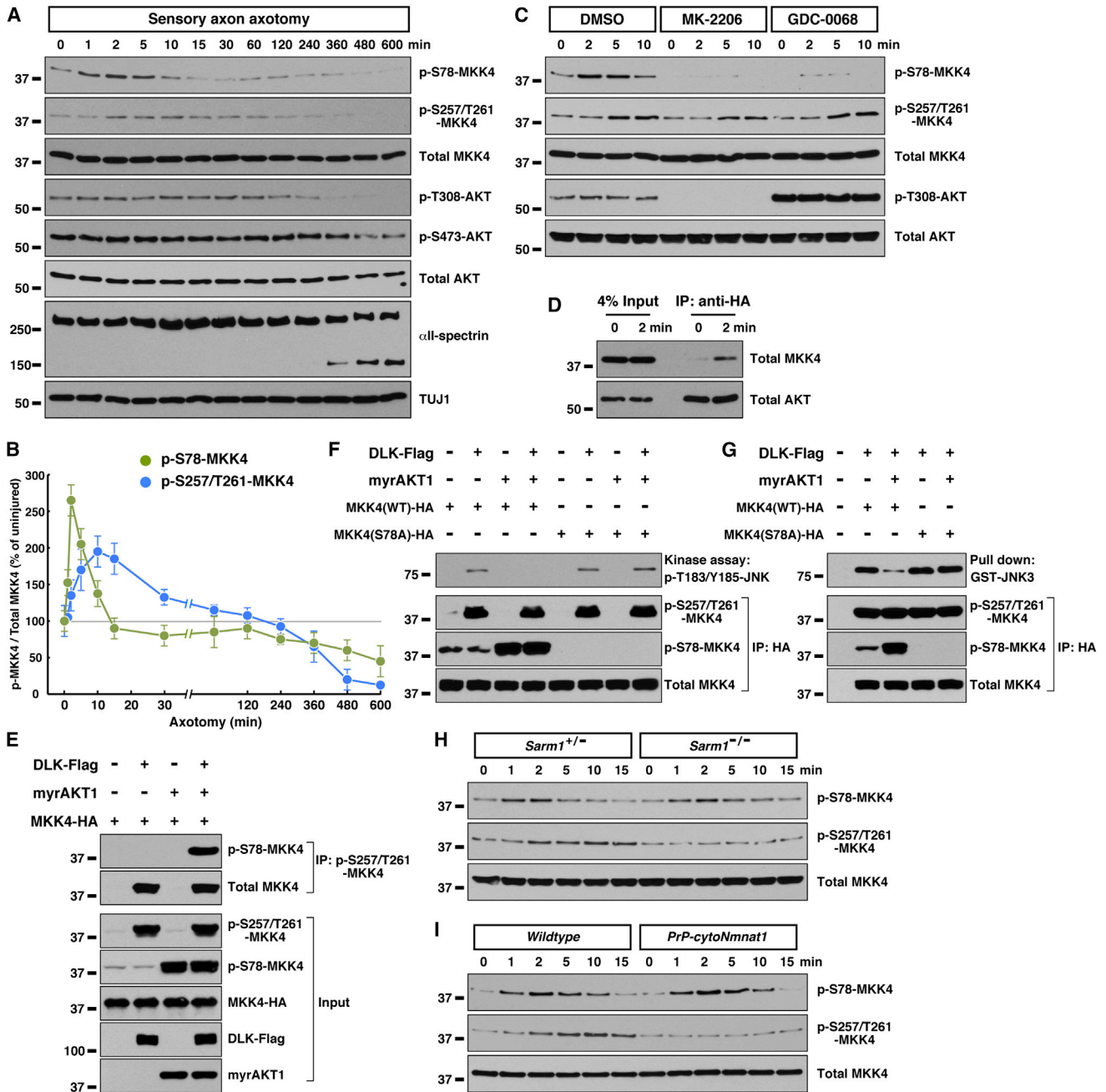


Figure 6. Sarm1-Independent Regulation of MKK4 by AKT Signaling in the Early Response to Axonal Injury

(A and B) Two temporally distinct MKK4 phosphorylation events in response to axonal injury. Axonal proteins of cultured sensory neurons were harvested at indicated time points after axotomy for immunoblot analysis (A), and MKK4 phosphorylation on Ser78 or Ser257/Thr261 was quantified (B). Values are presented as mean \pm SD.

(C) Inhibition of AKT signaling abolishes MKK4 phosphorylation on Ser78 in injured axons. Cultures of sensory neurons were treated with 5 μ M MK-2206 or 5 μ M GDC-0068 for 1 hr prior to axotomy. Axonal proteins harvested at indicated time points after axotomy were subjected to immunoblot analysis.

(D) Axonal injury promotes interaction between AKT and MKK4. Cultures of sensory neurons were transduced with lentivirus expressing AKT1 with a C-terminal HA-tag, and axonal proteins were subjected to anti-HA immunoprecipitation.

(E) Ser257/Thr261 and Ser78 phosphorylation can occur simultaneously on MKK4. HEK293 cells were transfected with plasmids expressing MKK4, together with DLK or myrAKT1. Ser257/Thr261-phosphorylated MKK4 was immunoprecipitated by p-S257/T261-MKK4 specific antibody.

(legend continued on next page)

after injury, over 60% of axons in the Cre-P2A-MKK4(S78A) condition had already degenerated, and their degeneration was completed by 72 hr (Figures 7E and 7F). Consistent with Ser257/Thr261 and Ser78 phosphorylation being independent events, *MKK4^{flox/flox}* mice transduced with the Cre-P2A-MKK4(WT) or Cre-P2A-MKK4(S78A) viruses exhibited similar levels of Ser257/Thr261 phosphorylation after injury (Figures 7C and S6F). Our results demonstrate that MKK4 is regulated by two distinct phosphorylation events in the early response to axonal injury, and Ser78 phosphorylation mediated by a Sarm1-independent AKT signal modulates the degeneration process by limiting activation of downstream JNKs.

Involvement of the Sarm1-MAPK Pathway in Other Axonal Insults

So far our study has focused on axon degeneration in models of traumatic injury. To determine whether the Sarm1-MAPK pathway participates in other types of axonal insult, we examined toxic effects of vincristine, a common chemotherapy drug, and rotenone, a mitochondrial poison. Consistent with a previous report (Gerdtz et al., 2013), *Sarm1*^{-/-} sensory axons were resistant to vincristine toxicity. In addition, we observed that combinatorial depletion of components at each level of the MAPK cascade resulted in significant protection (Figure S7A). Moreover, vincristine-damaged axons also exhibited local energy deficit before morphological degeneration in a Sarm1-dependent manner (Figure S7B). Similarly, depletion of *Sarm1* or components at each level of the MAPK cascade all protected rotenone-damaged sensory axons against degeneration (Figure S7C), and rotenone-induced ATP depletion was partially blocked in *Sarm1*^{-/-} axons (Figure S7D).

DISCUSSION

Although axonal death has been increasingly recognized as a key pathological feature of neurodegenerative disorders, the molecular mechanisms underlying the degeneration program have been poorly characterized. In this study, we delineate a MAPK cascade regulating pathological axon degeneration. Our genetic analyses show that this MAPK cascade operates downstream of Sarm1, and likely represents the major downstream signal mediated by Sarm1. Its pivotal role appears not to have been fully appreciated because of the significant redundancy at each level of the cascade. Interestingly, Sarm1-MAPK signaling triggers a local energy deficit in injured axons, which serves as the key functional link between the early degenerative response of the Sarm1-MAPK pathway and the late phase of morphological degeneration. Because the low level of cytosolic Ca^{2+} in axons is maintained by Ca^{2+} -ATPases and $\text{Na}^{+}/\text{Ca}^{2+}$ -exchangers, both of which directly or indirectly depend on a constant energy input, it appears plausible that energy deficit in

injured axons could result in gradual accumulation of cytosolic Ca^{2+} which eventually activates calpains. Given the essential role of ATP in cellular processes, this energy deficit might also disrupt other vital functions in axons, which together with calpain activation would lead to final breakdown of injured axons.

Various studies have supported the possibility that axon degeneration in different pathological conditions could be under a common regulatory mechanism. Therefore, the Sarm1-MAPK pathway could play a critical role following axonal insults besides traumatic injury. Indeed, our results with vincristine and rotenone support that the signaling pathway from Sarm1 to the MAPK cascade to axonal ATP depletion and to calpain-mediated breakdown of axonal structures could be a common mechanism in different types of pathological axon degeneration. In this context, it is interesting to note that JNK3 has been implicated in the degeneration process in models of ischemic stroke (Kuan et al., 2003), Huntington's disease (Morfini et al., 2009), and Alzheimer's disease (Yoon et al., 2012), and a role for DLK has also been reported in excitotoxicity-induced degeneration (Pozniak et al., 2013). However, given the diversity of MAPK family members, especially the MAPKKs, it will be important to determine whether additional MAPK member(s) are involved in other types of axonal insults.

Future studies will also help elucidate the biochemical mechanism underlying Sarm1-mediated activation of the MAPK cascade. In our initial studies we were unable to detect a direct physical interaction between Sarm1, or its individual domains, with components in the MAPK cascade (data not shown). In addition, it will be critical to understand how the Sarm1-MAPK pathway triggers local energy deficit in response to axonal insults. Two pieces of evidence suggest that Sarm1-MAPK signaling may disrupt a step(s) in glycolysis in axons: ATP depletion in wild-type injured axons can be ameliorated by the glycolysis end-product pyruvate (Figure 5C), and *Sarm1*^{-/-} axons can maintain a fraction of their original ATP level even with ATP production from mitochondria completely blocked by rotenone (Figure S7D). Of note, our findings on ATP depletion are consistent with a previous report that examined axonal ATP (Wang et al., 2005), but contrast with some others that examined ATP levels in whole neuronal cultures, which included both axons and cell bodies (Press and Milbrandt, 2008; Summers et al., 2014). Because ATP measurements in this study were all performed with pure axonal samples in absence of neuronal cell bodies, our results provide a more direct insight into axon-specific signaling events.

The protective cytoNmnat1/Wld^s protein can inhibit activation of the MAPK cascade upon injury. The mechanism underlying cytoNmnat1/Wld^s protective effect has been under debate, and our finding opens an avenue to understanding how it intersects with MAPK activation, either by altering nucleotide metabolism or by additional mechanism(s). Since cytoNmnat1/Wld^s

(F and G) Ser78 phosphorylation inhibits MKK4 kinase activity toward JNK. HEK293 cells were transfected with plasmids expressing MKK4 or MKK4(S78A) mutant with C-terminal HA-tag, together with DLK or myrAKT1. MKK4 proteins were immunoaffinity-purified, then subjected to kinase assay (F) or pull-down assay (G) with recombinant GST-JNK3(K55R).

(H and I) MKK4 phosphorylation on Ser78 is independent of Sarm1 (H) or cytoNmnat1 (I). Axonal proteins of cultured sensory neurons with indicated genotypes were harvested at indicated time points after axotomy for immunoblot analysis.

See also Figure S6.

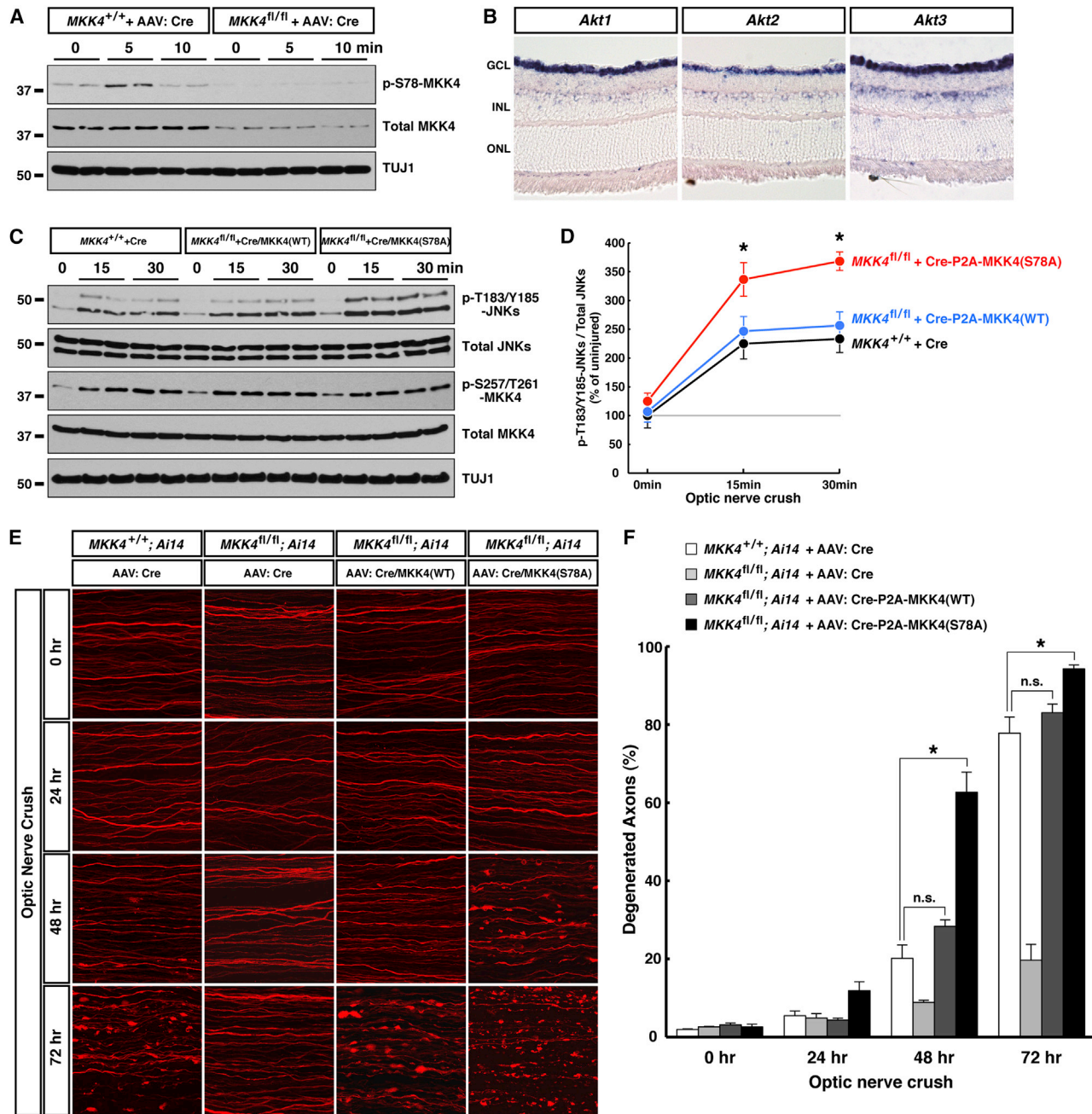


Figure 7. Antagonism of Pro-Degenerative Function of MKK4 by AKT Modulates the Early Response to Axonal Injury

(A) MKK4 phosphorylation on Ser78 in the early response to axonal injury in vivo. RGCs of wild-type or *MKK4*^{fl/fl} mice were subjected to saturated transduction of Cre virus. Nerve samples were harvested at indicated time points after optic nerve crush for immunoblot analysis.

(B) mRNA expression of the 3 members of the AKT family in adult mouse retina was determined by in situ hybridization. GCL, ganglion cell layer; INL, inner nuclear layer; ONL, outer nuclear layer.

(C and D) MKK4 phosphorylation on Ser78 limits activation of downstream JNKs. RGCs of wild-type or *MKK4*^{fl/fl} mice were subjected to saturated transduction of indicated virus. Nerve samples were harvested at indicated time points after optic nerve crush for immunoblot analysis (C), and JNK phosphorylation on Thr183/Tyr185 was quantified (D, $n = 3$ for each condition). Values are presented as mean \pm SD.

(E and F) MKK4 phosphorylation on Ser78 modulates degeneration of injured RGC axons in vivo. RGCs of mice with indicated genotypes were transduced with indicated viruses. Degeneration of TdTomato-positive axons was visualized at indicated time points after optic nerve crush (E), and degeneration was quantified (F), $n = 3$ for each condition. *Ai14* is the *Rosa26-CAG-LSL-TdTomato* reporter. Values are presented as mean \pm SEM. * $p < 0.01$; n.s., not significant.

See also Figure S6.

inhibits axon degeneration in many models of neurodegeneration, it will also be exciting to determine whether its protective effects in other degenerative paradigms rely on inhibition of the MAPK pathway identified here.

It remains possible that AKT signaling also functions through other targets to modulate axon degeneration. For instance, a previous study reported that AKT could protect injured axons by inhibiting GSK3 β (Wakatsuki et al., 2011), although we found that pharmacological inhibition of GSK3 in injured RGC axons failed to significantly protect at least in vitro (Figures S6I and S6J). With our finding that MKK4 is subject to the two temporally-distinct phosphorylation events, it is tempting to speculate that activation of these two antagonizing signals could enable pro-survival AKT to act immediately following injury to suppress the MAPK degenerative response, allowing axons to repair themselves if possible. Only when damage is irreversible would the Sarm1-MAPK pathway instruct the destruction of injured axons. Such a balance could represent an important checkpoint to prevent inappropriate initiation of axon degeneration. It will be of particular interest to explore whether reduction of AKT signaling in axons, resulting in loss of this antagonistic mechanism, contributes to axon degeneration in any disease condition.

In summary, our study demonstrates that distinct upstream signals can converge onto a central MAPK pathway that triggers local energy deficit to promote pathological axon degeneration (Figure S7E), a regulatory mechanism with potentially broad implications in neurodegenerative disease.

EXPERIMENTAL PROCEDURES

Intravitreal Injection and Optic Nerve Injury

All surgical procedures in mice were performed in compliance with the protocol approved by the IACUC of the Rockefeller University. RGCs were transduced by AAV2 (2×10^3 transduction units for sparse labeling; 1×10^7 transduction units for saturated labeling) delivered via intravitreal injection. After 3 to 6 weeks, optic nerve crush was performed about 1 mm distal from the eyeball. For visualization of TdTomato-labeled axons, nerve segments about 2 mm proximal to the optic chiasm were scanned by confocal microscopy. For biochemical analysis, nerve segments starting immediately distal to the injury site up to the optic chiasm were dissected and homogenized in 150 μ l Urea/SDS buffer (50 mM Tris-Cl [pH 6.8], 8 M urea, 10% SDS, 10 mM sodium EDTA, and 50 mM DTT). Ten microgram of total protein for each nerve sample was subjected to immunoblot analysis.

Neuronal Cultures and Analyses on Axonal Preparations

For RGC explant cultures, mouse retinas were dissected at post-natal day 1, cut into 200 to 300 μ m square explants, and cultured in growth factor-free medium (Neurobasal medium supplemented with 2% B-27, 2 mM glutamine, 100 U/ml penicillin, 100 μ g/ml streptomycin, 0.5% methyl-cellulose, and 0.75% glucose) with the RGC layer facing toward the culture surface coated with poly-D-lysine/N-cadherin/fibronectin. Cultures of mouse embryonic DRG neurons, embryonic cortical neurons, and post-natal SCG neurons were as described (Osterloh et al., 2012). For biochemical analysis of axonal samples, neuronal cell bodies and proximal axons were removed as described (Yang et al., 2013). Axons were immediately quenched in 100% methanol pre-cooled to -20°C , then dissolved in Urea/SDS buffer. One microgram of total protein for each condition pooled from 3 to 6 wells of cultures was subjected to immunoblot analysis. For measurement of axonal ATP levels, neuronal cell bodies and proximal axons were removed, and axons were lysed and subjected to ATP measurement with the ATPlite Luminescence Assay System (PerkinElmer). Four to six wells of cultures were included for each condition, and results are presented as mean \pm SEM.

Quantification of Axon Degeneration

TdTomato-labeled axons in optic nerves or immunostained axons in cultures were scored as degenerated with any sign of swelling and/or fragmentation. Axons observed by electron microscopy in optic nerves were scored as degenerated with any sign of demyelination and/or destruction of axoplasm. Degeneration was quantified as the percentage of all axons scored as degenerated. Results are presented as mean \pm SEM, and p value was calculated using a two-way ANOVA post hoc test.

In Situ Hybridization

Retinas from 8-week-old mice were dissected for 12 μ m sagittal cryosections, and sections were hybridized with digoxigenin-labeled antisense or sense RNA probes (sequences available on request). Hybridized probes were detected by alkaline phosphatase-conjugated anti-digoxigenin antibody (Roche) and revealed by chromogenic substrate NBT/BCIP (Roche).

Experimental procedures including lentivirus production and transduction, adeno-associated virus production, and electron microscopy have been previously described (Yang et al., 2013). The lentiviral-shRNA constructs from The RNAi Consortium used in the study are listed in Table S1.

Information including antibodies and chemicals, and detailed procedures for animal surgeries, neuronal cultures, immunohistochemistry, in situ hybridization, kinase assay, and quantification methods are in Extended Experimental Procedures.

SUPPLEMENTAL INFORMATION

Supplemental Information includes Extended Experimental Procedures, seven figures, and one table and can be found with this article online at <http://dx.doi.org/10.1016/j.cell.2014.11.053>.

ACKNOWLEDGMENTS

We thank the members of Tessier-Lavigne lab for discussion and suggestions. This work was supported by NIH grant 1R01NS08313-01A1 to M.T.-L.

Received: May 29, 2014

Revised: September 12, 2014

Accepted: November 20, 2014

Published: January 15, 2015

REFERENCES

- Blum, E.S., Abraham, M.C., Yoshimura, S., Lu, Y., and Shaham, S. (2012). Control of nonapoptotic developmental cell death in *Caenorhabditis elegans* by a polyglutamine-repeat protein. *Science* 335, 970–973.
- Chen, C.Y., Lin, C.W., Chang, C.Y., Jiang, S.T., and Hsueh, Y.P. (2011). Sarm1, a negative regulator of innate immunity, interacts with syndecan-2 and regulates neuronal morphology. *J. Cell Biol.* 193, 769–784.
- Chen, M., Maloney, J.A., Kallop, D.Y., Atwal, J.K., Tam, S.J., Baer, K., Kissel, H., Kaminker, J.S., Lewcock, J.W., Weimer, R.M., and Watts, R.J. (2012). Spatially coordinated kinase signaling regulates local axon degeneration. *J. Neurosci.* 32, 13439–13453.
- Chuang, C.F., and Bargmann, C.I. (2005). A Toll-interleukin 1 repeat protein at the synapse specifies asymmetric odorant receptor expression via ASK1 MAPKKK signaling. *Genes Dev.* 19, 270–281.
- Conforti, L., Gilley, J., and Coleman, M.P. (2014). Wallerian degeneration: an emerging axon death pathway linking injury and disease. *Nat. Rev. Neurosci.* 15, 394–409.
- Couillault, C., Pujol, N., Reboul, J., Sabatier, L., Guichou, J.F., Kohara, Y., and Ewbank, J.J. (2004). TLR-independent control of innate immunity in *Caenorhabditis elegans* by the TIR domain adaptor protein TIR-1, an ortholog of human SARM. *Nat. Immunol.* 5, 488–494.
- Gerdts, J., Summers, D.W., Sasaki, Y., DiAntonio, A., and Milbrandt, J. (2013). Sarm1-mediated axon degeneration requires both SAM and TIR interactions. *J. Neurosci.* 33, 13569–13580.

- Ho, D.T., Bardwell, A.J., Abdollahi, M., and Bardwell, L. (2003). A docking site in MKK4 mediates high affinity binding to JNK MAPKs and competes with similar docking sites in JNK substrates. *J. Biol. Chem.* 278, 32662–32672.
- Kuan, C.Y., Whitmarsh, A.J., Yang, D.D., Liao, G., Schloemer, A.J., Dong, C., Bao, J., Banasiak, K.J., Haddad, G.G., Flavell, R.A., et al. (2003). A critical role of neural-specific JNK3 for ischemic apoptosis. *Proc. Natl. Acad. Sci. USA* 100, 15184–15189.
- Kurz, C.L., Shapira, M., Chen, K., Baillie, D.L., and Tan, M.W. (2007). *Caenorhabditis elegans* ppg-5 is involved in resistance to bacterial infection and heavy metal and its regulation requires TIR-1 and a p38 map kinase cascade. *Biochem. Biophys. Res. Commun.* 363, 438–443.
- Miller, B.R., Press, C., Daniels, R.W., Sasaki, Y., Milbrandt, J., and DiAntonio, A. (2009). A dual leucine kinase-dependent axon self-destruction program promotes Wallerian degeneration. *Nat. Neurosci.* 12, 387–389.
- Morfini, G.A., You, Y.M., Pollema, S.L., Kaminska, A., Liu, K., Yoshioka, K., Björklom, B., Coffey, E.T., Bagnato, C., Han, D., et al. (2009). Pathogenic huntingtin inhibits fast axonal transport by activating JNK3 and phosphorylating kinesin. *Nat. Neurosci.* 12, 864–871.
- Morrison, D.K., and Davis, R.J. (2003). Regulation of MAP kinase signaling modules by scaffold proteins in mammals. *Annu. Rev. Cell Dev. Biol.* 19, 91–118.
- Osterloh, J.M., Yang, J., Rooney, T.M., Fox, A.N., Adalbert, R., Powell, E.H., Sheehan, A.E., Avery, M.A., Hackett, R., Logan, M.A., et al. (2012). dSarm/Sarm1 is required for activation of an injury-induced axon death pathway. *Science* 337, 481–484.
- Park, H.S., Kim, M.S., Huh, S.H., Park, J., Chung, J., Kang, S.S., and Choi, E.J. (2002). Akt (protein kinase B) negatively regulates SEK1 by means of protein phosphorylation. *J. Biol. Chem.* 277, 2573–2578.
- Pozniak, C.D., Sengupta Ghosh, A., Gogineni, A., Hanson, J.E., Lee, S.H., Larson, J.L., Solanoy, H., Bustos, D., Li, H., Ngu, H., et al. (2013). Dual leucine zipper kinase is required for excitotoxicity-induced neuronal degeneration. *J. Exp. Med.* 210, 2553–2567.
- Press, C., and Milbrandt, J. (2008). Nmnat delays axonal degeneration caused by mitochondrial and oxidative stress. *J. Neurosci.* 28, 4861–4871.
- Sasaki, Y., Vohra, B.P., Baloh, R.H., and Milbrandt, J. (2009). Transgenic mice expressing the Nmnat1 protein manifest robust delay in axonal degeneration in vivo. *J. Neurosci.* 29, 6526–6534.
- Shin, J.E., Cho, Y., Beirowski, B., Milbrandt, J., Cavalli, V., and DiAntonio, A. (2012). Dual leucine zipper kinase is required for retrograde injury signaling and axonal regeneration. *Neuron* 74, 1015–1022.
- Simon, D.J., Weimer, R.M., McLaughlin, T., Kallop, D., Stanger, K., Yang, J., O'Leary, D.D., Hannoush, R.N., and Tessier-Lavigne, M. (2012). A caspase cascade regulating developmental axon degeneration. *J. Neurosci.* 32, 17540–17553.
- Summers, D.W., DiAntonio, A., and Milbrandt, J. (2014). Mitochondrial dysfunction induces Sarm1-dependent cell death in sensory neurons. *J. Neurosci.* 34, 9338–9350.
- Tan, Y., Dourdin, N., Wu, C., De Veyra, T., Elce, J.S., and Greer, P.A. (2006). Conditional disruption of ubiquitous calpains in the mouse. *Genesis* 44, 297–303.
- Wakatsuki, S., Saitoh, F., and Araki, T. (2011). ZNRF1 promotes Wallerian degeneration by degrading AKT to induce GSK3B-dependent CRMP2 phosphorylation. *Nat. Cell Biol.* 13, 1415–1423.
- Wang, J., Zhai, Q., Chen, Y., Lin, E., Gu, W., McBurney, M.W., and He, Z. (2005). A local mechanism mediates NAD-dependent protection of axon degeneration. *J. Cell Biol.* 170, 349–355.
- Wang, J.T., Medress, Z.A., and Barres, B.A. (2012). Axon degeneration: molecular mechanisms of a self-destruction pathway. *J. Cell Biol.* 196, 7–18.
- Weston, C.R., and Davis, R.J. (2007). The JNK signal transduction pathway. *Curr. Opin. Cell Biol.* 19, 142–149.
- Whitmore, A.V., Lindsten, T., Raff, M.C., and Thompson, C.B. (2003). The pro-apoptotic proteins Bax and Bak are not involved in Wallerian degeneration. *Cell Death Differ.* 10, 260–261.
- Xiong, X., and Collins, C.A. (2012). A conditioning lesion protects axons from degeneration via the Wallenda/DLK MAP kinase signaling cascade. *J. Neurosci.* 32, 610–615.
- Yang, J., Weimer, R.M., Kallop, D., Olsen, O., Wu, Z., Renier, N., Uryu, K., and Tessier-Lavigne, M. (2013). Regulation of axon degeneration after injury and in development by the endogenous calpain inhibitor calpastatin. *Neuron* 80, 1175–1189.
- Yoon, S.O., Park, D.J., Ryu, J.C., Ozer, H.G., Tep, C., Shin, Y.J., Lim, T.H., Pastorino, L., Kunwar, A.J., Walton, J.C., et al. (2012). JNK3 perpetuates metabolic stress induced by A β peptides. *Neuron* 75, 824–837.

Glial Lipid Droplets and ROS Induced by Mitochondrial Defects Promote Neurodegeneration

Lucy Liu,¹ Ke Zhang,^{2,10} Hector Sandoval,³ Shinya Yamamoto,^{3,4,5} Manish Jaiswal,^{3,6} Elisenda Sanz,⁷ Zhihong Li,³ Jessica Hui,⁸ Brett H. Graham,³ Albert Quintana,^{7,8,9} and Hugo J. Bellen^{1,2,3,4,5,6,*}

¹Department of Neuroscience, Baylor College of Medicine, Houston, TX 77030, USA

²Structural and Computational Biology & Molecular Biophysics Graduate Program, Baylor College of Medicine, Houston, TX 77030, USA

³Department of Molecular and Human Genetics, Baylor College of Medicine, Houston, TX 77030, USA

⁴Program in Developmental Biology, Baylor College of Medicine, Houston, TX 77030, USA

⁵Jan and Dan Duncan Neurological Research Institute at Texas Children's Hospital, Houston, TX 77030, USA

⁶Howard Hughes Medical Institute, Baylor College of Medicine, Houston, TX 77030, USA

⁷Center for Integrative Brain Research, Seattle Children's Research Institute, Seattle, WA 98101, USA

⁸Center for Developmental Therapeutics, University of Washington, Seattle, WA, 98195, USA

⁹Department of Pediatrics, University of Washington, Seattle, WA, 98195, USA

¹⁰Present address: Department of Neurology, Johns Hopkins University School of Medicine, Baltimore, MD 21205, USA

*Correspondence: hbellen@bcm.edu

<http://dx.doi.org/10.1016/j.cell.2014.12.019>

SUMMARY

Reactive oxygen species (ROS) and mitochondrial defects in neurons are implicated in neurodegenerative disease. Here, we find that a key consequence of ROS and neuronal mitochondrial dysfunction is the accumulation of lipid droplets (LD) in glia. In *Drosophila*, ROS triggers c-Jun-N-terminal Kinase (JNK) and Sterol Regulatory Element Binding Protein (SREBP) activity in neurons leading to LD accumulation in glia prior to or at the onset of neurodegeneration. The accumulated lipids are peroxidated in the presence of ROS. Reducing LD accumulation in glia and lipid peroxidation via targeted lipase overexpression and/or lowering ROS significantly delays the onset of neurodegeneration. Furthermore, a similar pathway leads to glial LD accumulation in *Ndufs4* mutant mice with neuronal mitochondrial defects, suggesting that LD accumulation following mitochondrial dysfunction is an evolutionarily conserved phenomenon, and represents an early, transient indicator and promoter of neurodegenerative disease.

INTRODUCTION

Many neurodegenerative diseases are characterized by a gradual demise of neurons, coupled with a reduction in antioxidant capacity and/or an increase in oxidative stress (Turner et al., 2009; Gilgun-Sherki et al., 2001; Lin and Beal, 2006; Keller et al., 2005). Oxidative stress may result from impaired mitochondrial function and/or glutamate excitotoxicity and causes DNA and protein damage as well as lipid peroxidation (Niki, 2009; Reed, 2011). These stresses promote damage to neurons and glia and contribute to the demise of neurons (Barnham et al.,

2004; Listenberger et al., 2003). In the cell, complexes I and III of the mitochondrial electron transport chain are the major contributors of free radicals and ROS (Beal, 2007). Importantly, signs of oxidative stress precede the neurological signs of neurodegeneration (ND) in disease models (Praticò et al., 2001; Keller et al., 2005; Xie et al., 2013).

Lipid droplets (LDs) are dynamic organelles that emerge from the endoplasmic reticulum (ER) membrane and serve as a site of triglyceride and cholesterol storage. Under normal conditions, LDs are mostly found in liver and adipose tissues and actively respond to cellular signaling (Murphy, 2001; Farese and Walther, 2009). One important regulator of LD biogenesis is sterol regulatory element binding protein (SREBP), a highly conserved, membrane-bound, basic helix-loop-helix leucine zipper transcription factor that is crucial for lipid homeostasis (Horton et al., 2002). SREBP regulates lipogenesis and responds to levels of sterols in mammals and palmitate in *Drosophila*, respectively (Shao and Espenshade, 2012; Dobrosotskaya et al., 2002). Importantly, *Drosophila* SREBP mutants are auxotrophs, and SREBP levels are critical in larval stages (Kunte et al., 2006). Inactive SREBP is a transmembrane protein located in the ER membrane which relocates to the Golgi upon activation where it forms a complex with SREBP-cleavage activating protein (SCAP) (Horton et al., 2002). In the Golgi, SREBP is cleaved by site-1 and site-2 proteases to generate active SREBP. Active SREBP is then translocated into the nucleus and promotes transcription of genes involved in lipid metabolism (Shao and Espenshade, 2012). Although SREBP expressed in the gut responds to levels of circulating lipids and cholesterol, the blood-brain-barrier prevents lipids from entering the brain in mammals and de novo lipogenesis is critical for nervous system function (Camargo et al., 2009). Though the *Drosophila* nervous system can incorporate lipids from the gut, brain triacylglycerol levels are protected under stress and starvation (Palm et al., 2012; Cheng et al., 2011).

Cells other than adipocytes can form LDs as a response to cellular inflammation and stress (Santos and Schulze, 2012). In

cancer cells, LDs are hypothesized to be an important source of energy for proliferation and may serve a protective role under conditions of hypoxia and cellular stress by gathering free fatty acids to protect cells against lipotoxicity (Bozza and Viola, 2010). However, ND has typically not been associated with LD formation in the nervous system, although few mouse mutants have been documented to have LDs in the brain (Mato et al., 1999; Hulshagen et al., 2008; Wang et al., 2002). Finally, lipid metabolism defects have been implicated in some forms of ALS (Ilieva et al., 2009; Turner et al., 2009; Praticò et al., 2001), but not other neurodegenerative diseases.

In this study, we document that ROS induced LD accumulation presages ND in several *Drosophila* mutants affecting mitochondrial function. We describe a ROS-activated pathway in neurons, which induces LD formation in glia in a cell non-autonomous fashion. Reducing LD accumulation is sufficient to delay ND. Finally, we find that the LD accumulation also occurs in mice with mitochondrial dysfunction, suggesting that LD formation upon oxidative stress is an evolutionarily conserved phenomenon.

RESULTS

Mitochondrial Mutants Exhibit Lipid Droplet Accumulation in Glia

We previously performed forward genetic mosaic screens of essential genes in the *Drosophila* visual system to uncover genes that cause ND of photoreceptors (Yamamoto et al., 2014). While characterizing the phenotypes by transmission electron microscopy (TEM) in the retina and brain, we found structures reminiscent of LDs. In *Drosophila*, photoreceptors (neurons) project their axons directly into the brain and form synapses with post-synaptic neurons. Pigment cells (glia) ensheath the photoreceptor cell body in the retina and epithelial glia ensheath their axonal terminals (Edwards and Meinertzhagen, 2010). We found that three different mutants, *sicily* (Zhang et al., 2013), *Aats-met* (Bayat et al., 2012), and *Marf* (Sandoval et al., 2014) exhibit abundant LD accumulations in pigment (Figures 1A–1C) and epithelial glia (Figures S1A–S1C).

These three fly genes play important but distinct roles in mitochondrial biology and mutations in the human homologs cause neurological diseases. *sicily* is the homolog of the human nuclear encoded mitochondrial gene *NDUFAF6* (*C8orf38*). Its loss leads to an early onset neurodegenerative disease known as Leigh syndrome (Pagliarini et al., 2008). *sicily* functions as a chaperone for Complex I proteins and its loss leads to severe mitochondrial dysfunction (Zhang et al., 2013; McKenzie et al., 2011). *Marf* encodes the *Drosophila* homolog of the mitochondrial fusion GTPase, Mitofusin 1 and 2 (Debattisti and Scorrano, 2013). Mutations in *MFN2* cause Charcot-Marie-Tooth disease type 2A2 (CMT2-A2), an autosomal dominant adult onset peripheral neuropathy (Kijima et al., 2005) as well as Hereditary motor and sensory neuropathy VI (HMSN6) (Del Bo et al., 2008). Lastly, *Aats-met* is the *Drosophila* homolog of mitochondrial methionyl-tRNA synthetase 2, or *MARS2*. Proteins encoded by these genes mediate the transfer of methionine to their cognate tRNA in the mitochondria matrix. Mutations in *MARS2* lead to a disease known as autosomal

recessive spastic ataxia with leukoencephalopathy (ARSAL) (Thiffault et al., 2006; Bayat et al., 2012).

Transmission electron micrographs of 1-day-old wild-type retinal clones show the stereotypical organization of photoreceptors in each ommatidium (Figure 1A a). Each ommatidium is separated by thin pigment cells (Figures 1A a and 1B, pseudo-colored in blue). Loss of *sicily*, *Aats-met* or *Marf* leads to an accumulation of LDs (arrow) in glia (Figures 1A a–d and 1C), which is not observed in controls. Importantly, LDs are not observed in photoreceptors. In addition to the retina, LDs also accumulate in the epithelial glia of the lamina (Figure S1A a–d, S1B, and S1C). In summary, LD-like structures are present in cells that function as glia but not in neurons.

To determine whether the structures seen in Figure 1 are indeed LDs, we created large mutant clones in the visual system by *GMR-hid* (Stowers and Schwarz, 1999) and observed LD accumulation in the glia in *sicily*, *Marf*, and *Aats-met* mutants using Nile Red (Figure 1D a–d) and BODIPY^{493/503} (Figure S1D), (Greenspan et al., 1985; Pavlopoulos et al., 1990). The rhabdomeres (dashed white) are also labeled and serve as reference point for each ommatidium. *sicily*, *Aats-met* and *Marf* clones show LD accumulation in the area where the glia are located, whereas control animals do not show staining (Figure 1E). In summary, mutations in genes involved in three separate mitochondrial processes, Complex I activity, fusion, and protein translation, exhibit LD accumulations in the glia of newly eclosed adults prior to the onset of ND. However, not all mitochondrial mutations cause LD accumulation (see below).

The morphology of *sicily*, *Aats-met*, and *Marf* photoreceptors is mostly normal or only mildly affected at day 1 based on TEM (Figure 1A). They begin to degenerate several days after eclosion and the process occurs faster in *sicily* and *Marf* mutants than in *Aats-met* mutant clones (Figure S1E) as revealed by fluorescently conjugated phalloidin labeling of actin rich rhabdomeres. Elongated or diffuse rhabdomeres are characteristic for mutants that cause a progressive photoreceptor degeneration (Xiong and Bellen, 2013).

Lipid Droplets Accumulate Transiently in Glia

Next, we sought to characterize the temporal nature of the LD accumulation phenotype. One-day-old *sicily*, *Aats-met* and *Marf* clones exhibit approximately 10 LD per ommatidium. Upon aging, we noticed a significant decrease in the number of LD in the mutant clones (Figures S2A a–i, j–l and S2B), indicating that LD accumulation occurs prior to or concurrent with the onset of ND and is a transient phenomenon (Figure S2C).

Increased ROS Correlates with Increased LD Accumulation

Since *sicily*, *Aats-met*, and *Marf* affect mitochondrial function, we sought to investigate the potential link between LD accumulation and mitochondrial dysfunction for other nuclear encoded mitochondrial genes. We knocked down *ND42*, a CI subunit that is chaperoned by *sicily* (Zhang et al., 2013) and *parkin*, an E3 ubiquitin ligase involved in mitochondrial clearance using RNAi. Whole-eye knockdown of both *ND42* and *parkin* leads to LD accumulation (Figure S3A a and b and Figure 1E). However,

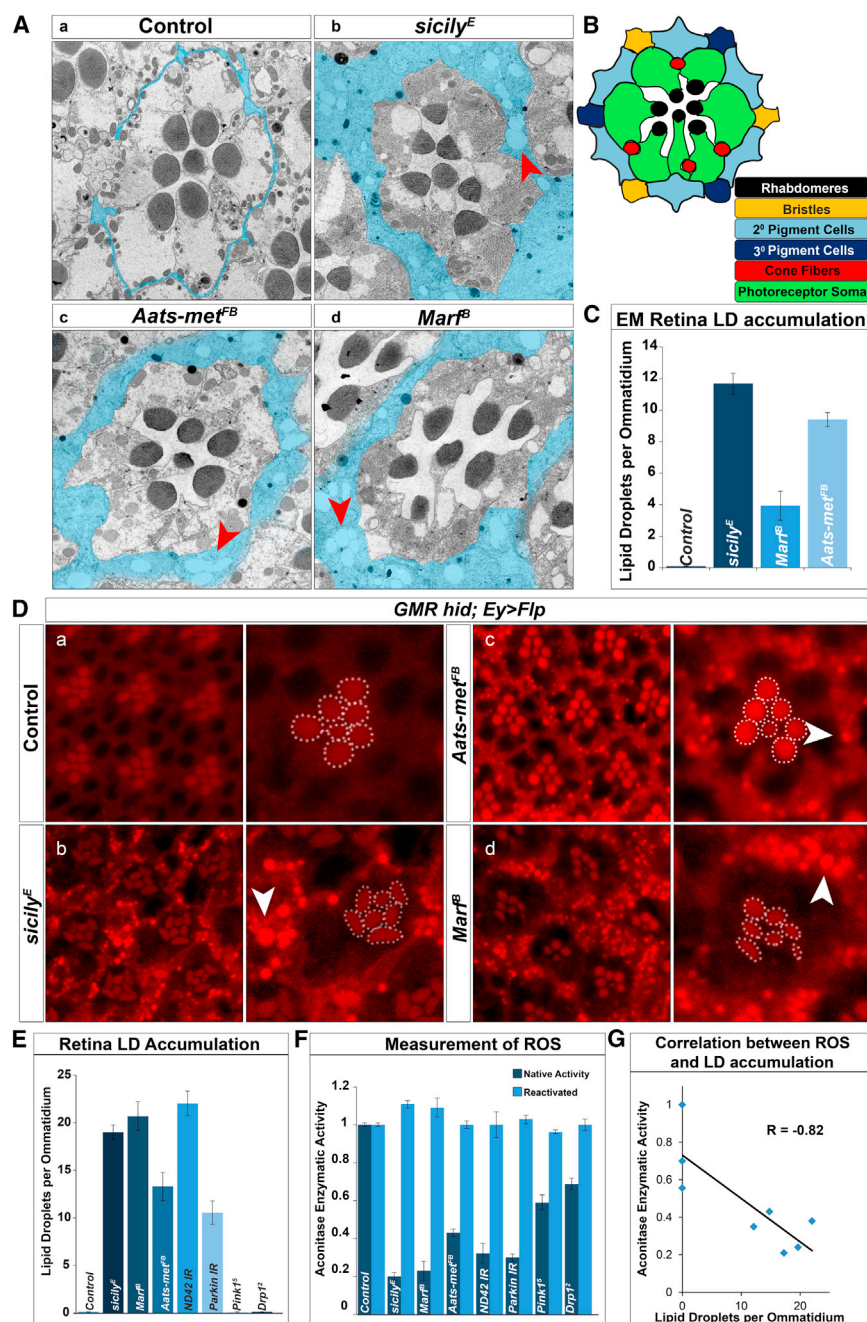


Figure 1. LD Accumulate in Glia of Mitochondrial Mutants with Elevated Levels of Reactive Oxygen Species

TEM of a single ommatidium of 1-day-old flies. (A) a, Pigment cells that surround the photoreceptors are typically very thin (blue) in wild-type eyes (*y w FRT19A* clones). They are vastly expanded in b, *sicily*, c, *Aats-met*, and d, *Marf* mutants and contain numerous LD (red arrowhead). (B) Schematic of a single ommatidium in cross-section. (C) Quantification of retina LD per ommatidium. (D) a–d, Nile Red stained whole-mount retina show LD accumulation (white arrowhead) in *sicily*, *Marf*, and *Aats-met* mutant clones of 1-day-old flies, but not in controls (*y w FRT19A* clones). Rhabdomeres outlined in white. Abnormal rhabdomere morphology can be seen in *sicily* and *Marf* mutant clones. (E) Quantification of LD per ommatidium of (D). A minimum of 16 eyes were stained and approximately 36 ommatidia were quantified. (F) Aconitase activity is used to measure ROS - before and after enzymatic reactivation with reducing agents. RNAis were driven by the ubiquitously expressed *daughterless[da]-GAL4*. (G) Correlation between aconitase enzymatic activity and LD per ommatidium. R = correlation coefficient. Data are represented as mean \pm SEM. See also Figures S1, S2, and S3.

mine whether increased ROS production and subsequent oxidative stress may promote LD formation, we measured aconitase enzymatic activity in third instar larvae (Yan et al., 1997). Enzymatic activity for aconitase is less than 50% of wild-type activity in all three mutants as well as *ND42* and *parkin* RNAi knockdown, documenting the presence of high levels of ROS and possibly a threshold effect. Moreover, aconitase activity is less affected (more than 50% of wild-type activity) in *Drp1²* and *Pink1⁵* mutants (Figure 1F). As shown in Figure 1G, there is a strong correlation between decreased aconitase enzymatic activity and the number of LD per ommatidium ($R = -0.82$). These data suggest that ROS may play a role in LD accumulation.

escapers of *Pink1⁵* (which encodes a mitochondrial kinase; Clark et al., 2006) do not exhibit LD accumulation (Figure S3A c and Figure 1E). In addition, retinal clones of *Drp1²*, which encodes a protein involved in mitochondria fission (Verstreken et al., 2005), also do not result in LD accumulation (Figure S3A d and Figure 1E). The presence of LD accumulations in a subset of mitochondrial mutants suggests that the loss of these genes share a common pathway.

Previously, we noticed elevated levels of reactive oxygen species (ROS) in *sicily*, *Marf*, and *Aats-met* mutants (Zhang et al., 2013; Bayat et al., 2012; Sandoval et al., 2014). To deter-

mined whether increased ROS production and subsequent oxidative stress may promote LD formation, we measured aconitase enzymatic activity in third instar larvae (Yan et al., 1997). Enzymatic activity for aconitase is less than 50% of wild-type activity in all three mutants as well as *ND42* and *parkin* RNAi knockdown, documenting the presence of high levels of ROS and possibly a threshold effect. Moreover, aconitase activity is less affected (more than 50% of wild-type activity) in *Drp1²* and *Pink1⁵* mutants (Figure 1F). As shown in Figure 1G, there is a strong correlation between decreased aconitase enzymatic activity and the number of LD per ommatidium ($R = -0.82$). These data suggest that ROS may play a role in LD accumulation.

Reducing ROS Ameliorates Lipid Droplet Accumulation

To establish a causative relationship between ROS and LD accumulation, we employed pharmacologic and genetic methods to reduce ROS and assessed LD. N-acetyl cysteine amide (AD4) is a blood-brain-barrier penetrating antioxidant that can decrease oxidative stress in vitro and in vivo (Schimmel et al., 2011; Amer et al., 2008). We administered AD4 via fly food at concentrations of 20 μ g/ml and 40 μ g/ml (Bayat et al., 2012).

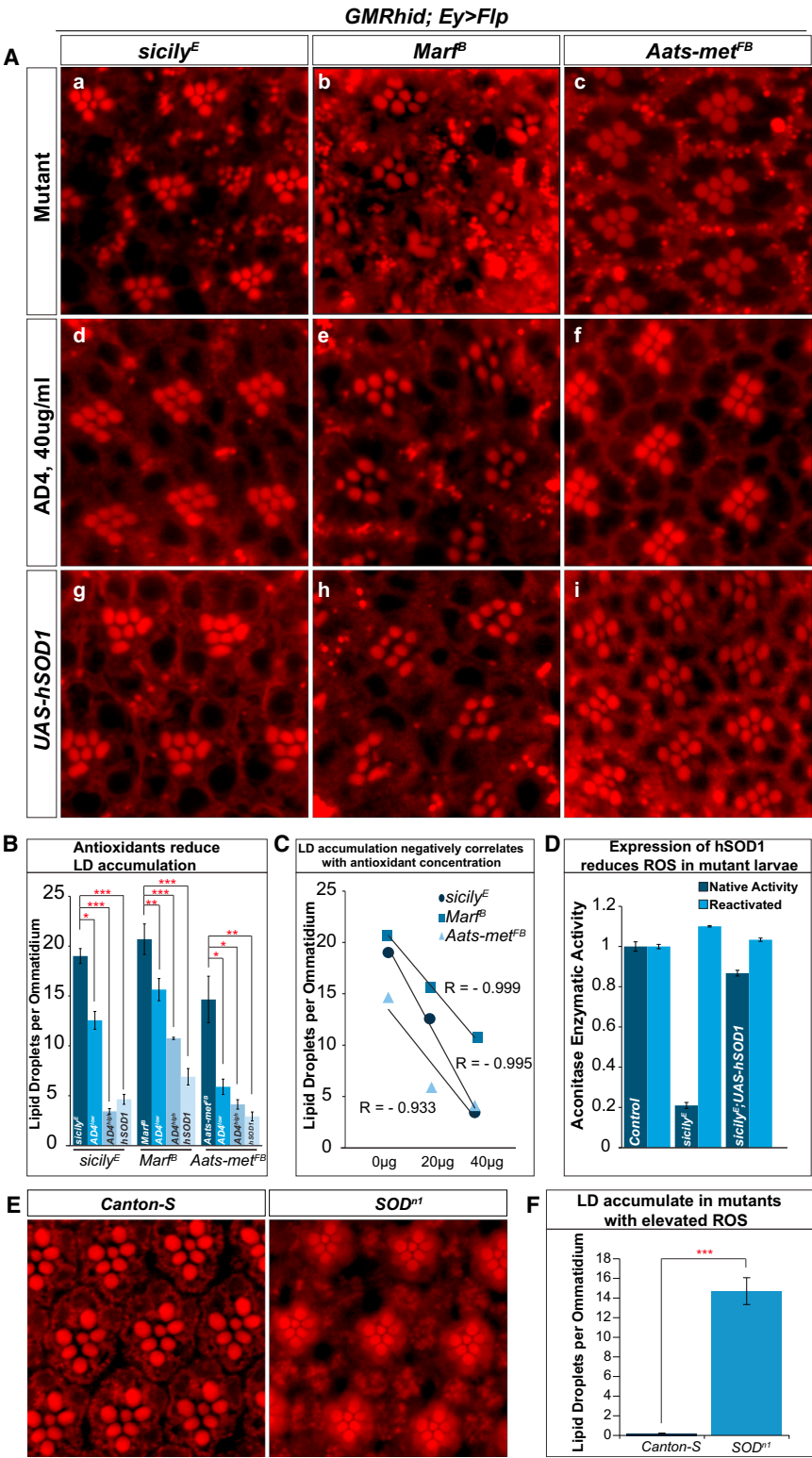


Figure 2. Antioxidants Reduce LD Accumulation in Mutant Retinas

(A) a–c, Nile Red stains of 1-day-old *sicily*, *Marf*, and *Aats-met* mutant retinas reveal LD accumulation. d–f, Animals fed with AD4 at 40 $\mu\text{g/ml}$ (AD4^{high} in quantification) reduces the number of LD. Notice the partial restoration of rhabdomere integrity in *Marf* mutants. g–i, Suppressing ROS by overexpression of a copy of *hSOD1* (*eyeless[ey]-Gal4, UAS-Flp*) also reduces LD accumulations. (B) Quantification of the data presented in (A) and animals with mutant clones raised on food supplemented with 20 $\mu\text{g/ml}$ (AD4^{low}) of AD4 the show a reduction of LD accumulation. (C) Linear regressions show a negative correlation between the numbers of LD accumulated and the amount of supplemented AD4. (D) Expression of *hSOD1* with *da-Gal4* in *sicily* mutants significantly suppresses the loss of aconitase activity and hence ROS. (E) Nile Red staining of wild-type (Canton-S) flies show no LD accumulation whereas staining of *SOD^{nt}* mutant escapers reveal high levels of LD accumulation. (F) Quantification of *SOD^{nt}* LD accumulation. Data are represented as mean \pm SEM. Significance was calculated compared to controls using t tests (* $p < 0.05$, ** $p < 0.005$, *** $p < 0.0005$).

tion, we overexpressed human copper-zinc superoxide dismutase (hSOD1), a conserved antioxidative enzyme that has been shown to rescue or extend *Drosophila* lifespan (Parkes et al., 1998). Overexpression of hSOD1 in mutant larvae reduces ROS levels (Figure 2D) and considerably suppresses the LD accumulations in glia (Figure 2A g–i). To further determine whether the presence of ROS causes LD accumulation, we assessed LD accumulation in *SOD* mutant flies. *SOD^{nt}* mutant (Sun et al., 2012) glia also exhibit LD accumulations, similar in levels to what we observe in *Aats-met* clones (Figures 2E and 2F and 2B). In summary, these results provide compelling evidence that removing ROS reduces LD accumulation and increasing ROS induces LD accumulation.

Elevated ROS Promotes JNK/SREBP Activation and Reducing JNK/SREBP Activity Suppresses LD Accumulation

Prolonged increase of ROS triggers a stress response that is mediated by c-Jun-N-terminal Kinase (JNK) signaling in

Compared to mutants raised in standard fly food (Figure 2A a–c), animals raised on AD4 food (Figure 2A d–f) show a dose-dependent reduction in LD accumulation (Figures 2B and 2C). In addition, both *Drosophila* and mammals. JNK activates the transcription of downstream genes, including its own inhibitor, JNK phosphatase. In *Drosophila*, JNK phosphatase is encoded by *puckered*

(*puc*), whose expression is used as readout for JNK activity (Martín-Blanco et al., 1998). ROS can suppress JNK phosphatase activity and therefore allows sustained JNK activation (Kamata et al., 2005).

Given the presence of LD, we assessed SREBP activity. To determine whether JNK and SREBP are involved in the LD accumulation observed in *sicily*, *Aats-met* and *Marf* clones, we removed a copy of either JNK or SREBP in each mutant background. Removal of a single copy of either JNK or SREBP is sufficient to ameliorate the LD accumulation in all three mutants (Figures 3A and 3B). In addition, visual system (*ey-GAL4*) knock-down of JNK in the *sicily* and *Marf* mutant background also significantly reduces LD accumulation (Figures 3A and 3B). Furthermore, JNK may be upstream of SREBP as the LD accumulations caused by overexpressing JNK with a neuronal driver in SREBP hemizygous (*SREBP*^{189/+}) flies is strongly suppressed (Figure S6C and quantified in Figure S6D) (Kunte et al., 2006).

To determine the extent of JNK upregulation in these mutants, we first performed quantitative RT-PCR in all three mutant larvae and observed an upregulation of *puc* (Figure 3C), suggesting JNK activation. To determine whether JNK is elevated, we used brain lysates from mutant larvae and immunoblotted against total JNK and phosphorylated JNK (pJNK) and found both to be elevated (Figure S4C). To further document a persistent elevation of JNK, we performed immunoblots for total JNK in adult heads with mutant eye clones. Although most of the brain is wild-type, much of the visual system is mutant. *sicily*, *Aats-met*, and *Marf* mutants exhibit elevated levels of total JNK (Figure 3D), yet only an estimated 40% of the loaded tissue is homozygous mutant. These data indicate that JNK activation correlates with ROS levels.

To test whether SREBP is upregulated in these mutants, we immunoblotted protein extracted from mutant larvae and observed a ~five-fold increase in level of active/cleaved SREBP (Figure S4C). Mutants that do not exhibit LD accumulation do not exhibit elevated levels (*Pink1*⁵) or modest increases of SREBP (*Drp1*²) (Figure S4D). Furthermore, we observe an upregulation of active SREBP as well as an upregulation of Acetyl CoA carboxylase (ACC) in adult heads with mutant clones (Figure 3D), whose transcription levels are directly regulated by SREBP (Seegmiller et al., 2002). JNK is necessary for the activation of SREBP (Figure 3D). Moreover, reducing ROS by overexpressing *hSOD1* in *sicily* mutant larvae decreases the levels of JNK and active SREBP (Figure S4E). Finally, reducing ROS with AD4 reduces levels of active SREBP in mutant larvae (Figure S4C). Our results therefore strongly indicate that ROS stimulates the activation of JNK and SREBP and this axis directly contributes to the LD accumulation phenotype in the nervous system.

Neuronal but Not Glial Mitochondrial Dysfunction Induces Cell Non-Autonomous LD Accumulation in Glia

To determine the cell specific defects that lead to LD accumulation, we knocked down *Marf*, *Aats-met*, and *ND42* expression with RNAi lines driven by a neuronal driver or pigment glia driver (Bao et al., 2010). To demonstrate that the glial driver is able to reduce the expression of genes in pigment cells we crossed it to an RNAi against the *white* gene. As shown in Figure S5, the *54C-GAL4* driver efficiently reduces pigment levels.

Neuronal expression of RNAi against *Marf*, *Aats-met* and *ND42* causes significant LD accumulation in glia but not neurons (Figure 4A a–c and Figure 4B). However, RNAi in glia for these genes does not result in LD accumulation (Figure 4A d–f and Figure 4B). Hence, neuronal knockdown of *Marf*, *Aats-met* and *ND42* is sufficient to lead to LD accumulation in glia.

To assess if overexpression of JNK or SREBP is sufficient to induce LD accumulation, we overexpressed JNK, Hemipterous (the *Drosophila* JNK Kinase), or full-length SREBP using neuronal or glia specific drivers. As shown in Figure 4C, neuronal expression of JNK or SREBP leads to glial cell specific LD accumulation, whereas glial cell specific expression did not. Activation of JNK is required for the LD accumulation phenotype as overexpression of JNKK also leads to LD accumulation. In summary, activation of JNK or SREBP in neurons is sufficient to cause LD in glia.

It is interesting to note that neuronal overexpression of JNK or SREBP alone does not cause ND upon aging (Figure S5B) and LDs are retained in aged animals (data not shown). These data show that glial LD accumulation is not sufficient to cause ND, and additional insults are likely to be required.

Neuronal knockdown of *Marf*, *Aats-met*, and *ND42* leads to LD accumulation in glia. To assess whether a reduction in ROS or JNK in neurons alone is sufficient to reduce LD accumulation in glia, we expressed *Marf* RNAi under the control of the photoreceptor specific Rhodopsin (Rh1) promoter (*Rh-Marf* RNAi). *Rh-Marf* RNAi leads to LD accumulation in glia, but expression of *hSOD1* or reduction of JNK (RNAi) using a neuronal driver, significantly reduce LD accumulation. However, when we reduce JNK in glia, LDs are retained (Figures S7A and S7B). Hence, elevated ROS and JNK activation in neurons is sufficient and necessary to cause LD accumulation in glia, providing compelling evidence that this neuronal pathway plays a critical role in LD accumulation.

Reduction of LDs Delays Neurodegeneration

To assay ND in various genetic backgrounds, we assessed degeneration as previously mentioned. Upon aging, mutant flies exhibit a significant loss of f-actin staining in rhabdomeres when compared to day 1 (Figure 5A a–f). To assay whether reduction of the levels of ROS, JNK, or SREBP suppress LD as well as ND, we analyzed the rhabdomere phenotypes of flies fed with 40 µg/ml of AD4, overexpressing *hSOD1*, or lacking one copy of *JNK* or *SREBP*, by phalloidin staining (Figure 5A g–r). These animals contain significantly more intact rhabdomeres when aged compared to mutants alone (Figure 5B). These data show that suppression of ROS/JNK/SREBP suppress LD formation and delays ND.

To determine whether reducing LD by ectopic expression of lipases are protective in ND, we expressed two different lipases in mutant clones and assessed ND: *Lipase 4* (*Lip4*), homolog of human acid lipases, functions in starvation mediated lipolysis, and *brummer*, homolog of adipocyte triglyceride lipase (ATGL), localizes to the LD surface, and acts in lipolysis (Grönke et al., 2005). When we expressed the lipases in mutant clones, the expression of either lipase partially restores the shape, density, and number of identifiable rhabdomeres (Figure 5A s–x, and 5C), indicating that reducing LD accumulation partially alleviates ND. This was confirmed by TEM (Figure S5C).

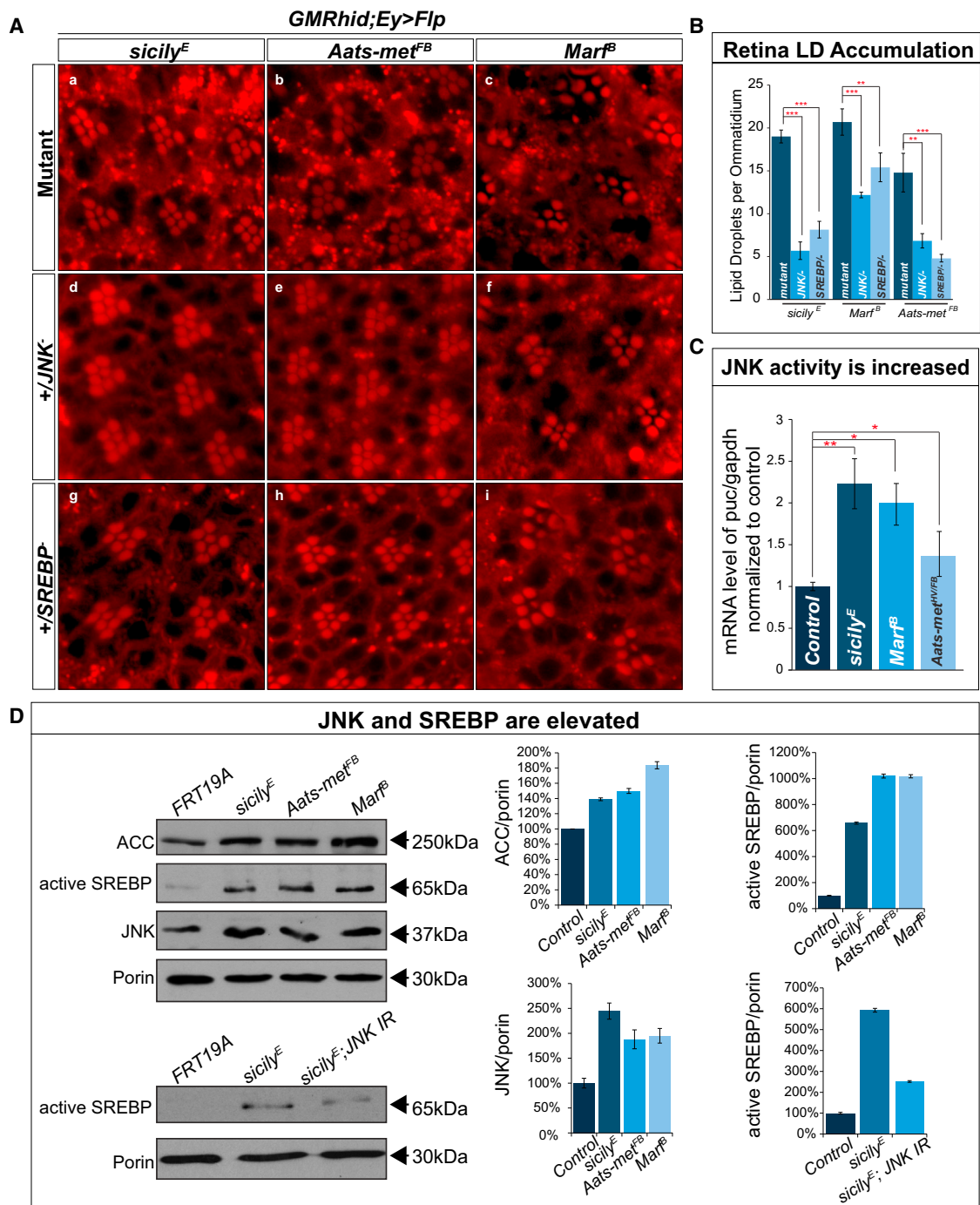


Figure 3. ROS Leads to Aberrant Activation of JNK and SREBP and Reducing JNK or SREBP in Mutants Reduces LD Accumulation

(A) a–c, *sicily^E*, *Aats-met* and *Marf* mutant clones exhibit high levels of LD accumulation but when one copy of JNK (d–f) or SREBP (g–i) is removed, LD accumulation is significantly reduced.

(B) Quantification of retinas in (A).

(C) qRT-PCR quantification of *puc* mRNA shows a significant upregulation of *puc* mRNA in all three mutant larvae compared to control (*y w FRT19A*).

(D) Immunoblot of *sicily^E*, *Aats-met* and *Marf* heads with mutant eye clones show an increase in ACC, total JNK and active SREBP when compared to control (*y w FRT19A*). Knockdown of JNK in the *sicily^E* mutant background (heads), reduces active SREBP levels compared to heads with mutant visual systems.

Data are represented as mean \pm SEM. Significance was calculated compared to controls and immunoblots were normalized to loading control (porin). (* $p < 0.05$, ** $p < 0.005$, *** $p < 0.0005$). See also Figure S4.

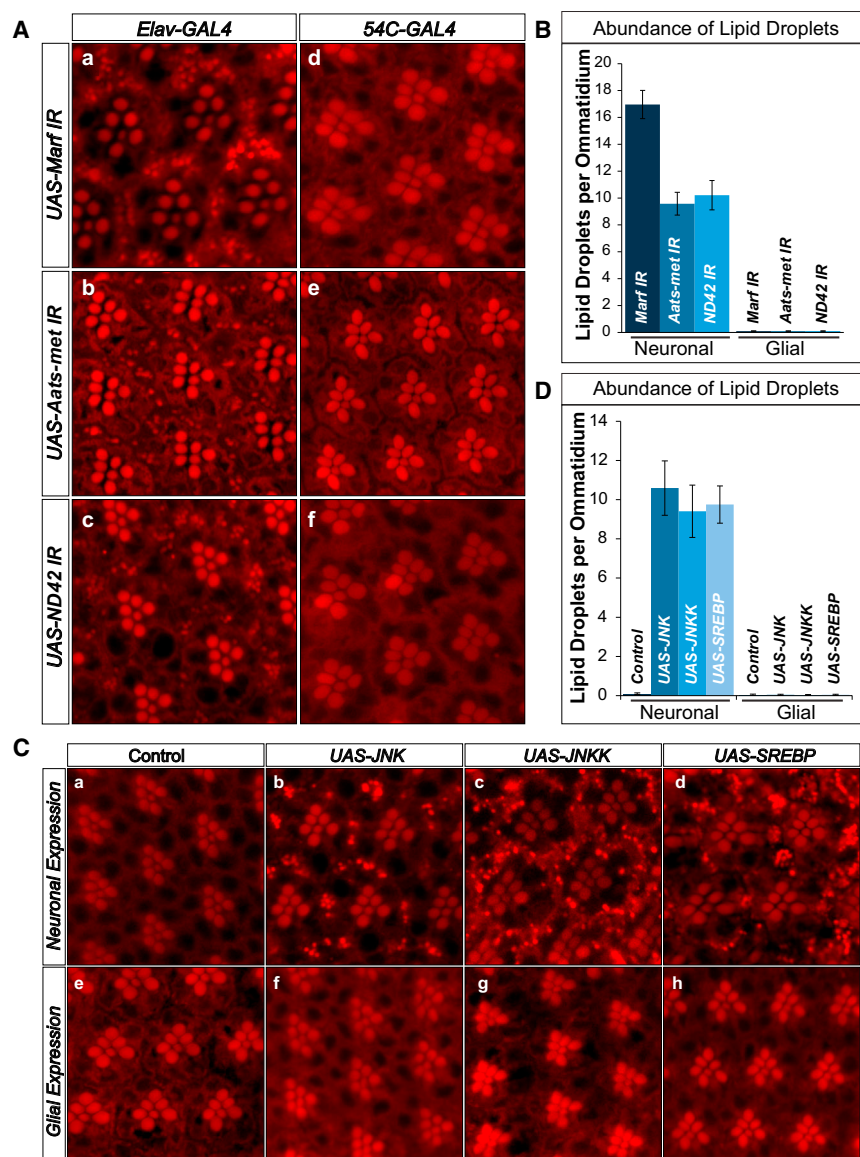


Figure 4. Photoreceptor Neurons, but Not Glia, Induce LD Accumulation Cell Non-Autonomously

(A) a–c, Nile Red stains show that neuronal knockdown (*elav-GAL4*) of *Marf*, *Aats-met*, and *ND42* result in LD accumulation in the glia. d–f, Glial (*54C-GAL4*) knockdown of *Marf*, *Aats-met*, and *ND42* does not result in LD accumulation.

(B) Quantification of (A).

(C) a and e, Control (white) do not exhibit LD accumulation. b–d, Overexpression of JNK, JNKK and SREBP in the neurons (*elav-GAL4*) leads to LD accumulation in the glia. e–h, However, overexpression of JNK, JNKK and SREBP in the glia (*54C-GAL4*) does not result in LD accumulation.

(D) Quantification of LD abundance.

Data are represented as mean \pm SEM. See also Figure S5.

in glia lowers LD accumulation and delays ND (Figures 6B d–l and Figures S6G and S6H). In summary, reducing lipid load in neurons or glia reduces LD accumulation (Figures 6D and 6E) and delays ND. Note that with *elav-GAL4* or *Rh* promoter driven knockdowns of *ND42* or *Marf*, the onset of ND is significantly delayed compared to the ND observed in mutant clones. Finally, reducing lipid load in both cell types seems more potent in delaying ND than reducing lipid load in each cell type separately.

Since LD formation alone is not sufficient to induce ND (Figures 4C and S5B), and since levels of ROS are elevated in mutants, we explored whether accumulated lipids are peroxidized. Lipids can be peroxidized in presence of ROS and mediate cellular stress (Niki, 2009; Reed, 2011). To visualize peroxidized lipids, staining with BODIPY 581/591 C11 revealed an abundance of peroxidized

Lipid Peroxidation in Glial Cells Affects the Demise of Neurons

LD accumulation occurs early and disappears by the time the features of ND become more apparent (Figure S2C). To demonstrate that the lipases reduce the formation of LD, we assessed the loss of LD upon overexpression of lipases in the eye at day 1. Overexpression of the lipases significantly reduces LD formation (Figures 6A a–i and 6C). To assess the specific cellular requirements, we determined whether LD accumulation in glia induced by knockdown of *Marf*, *Aats-met* or *ND42* (Figure 4) is suppressed by co-expression with *Lip4* in neurons. Neuronal expression of *Lip4* suppresses LD accumulation in glia (Figures 6B a–c and quantified in 6D) and ND (Figures S6E and S6F).

Is expressing lipases in glia sufficient to reduce LD and delay ND? A knockdown of *Marf* and *ND42* (*Rh-ND42 RNAi* and *Rh-Marf RNAi*) in neurons and overexpression of *Lip4* or *brummer*

lipids when compared to controls that do not exhibit LD accumulations (Figure 6F). Furthermore, as neuronal overexpression of SREBP leads to LD accumulation but not ND, we assessed lipid peroxidation in animals overexpressing SREBP and observed no difference compared to controls (Figure 6G). Finally, neuronal knockdown of *ND42* results in LD accumulation and peroxidized lipids. However, this peroxidation is reduced when lipases are expressed neuronally (Figure 6H). Hence, these data show that LD accumulation alone is insufficient to cause ND, and ROS is required in conjunction with LD accumulation to promote ND.

Ndufs4^{-/-} Mice Exhibit Glial LD Accumulation and Neurodegeneration that Is Significantly Ameliorated with Presymptomatic Antioxidant Treatment

We hypothesized that mitochondrial defects in vertebrates may also lead to LD accumulation in glia, as mitochondrial genes as

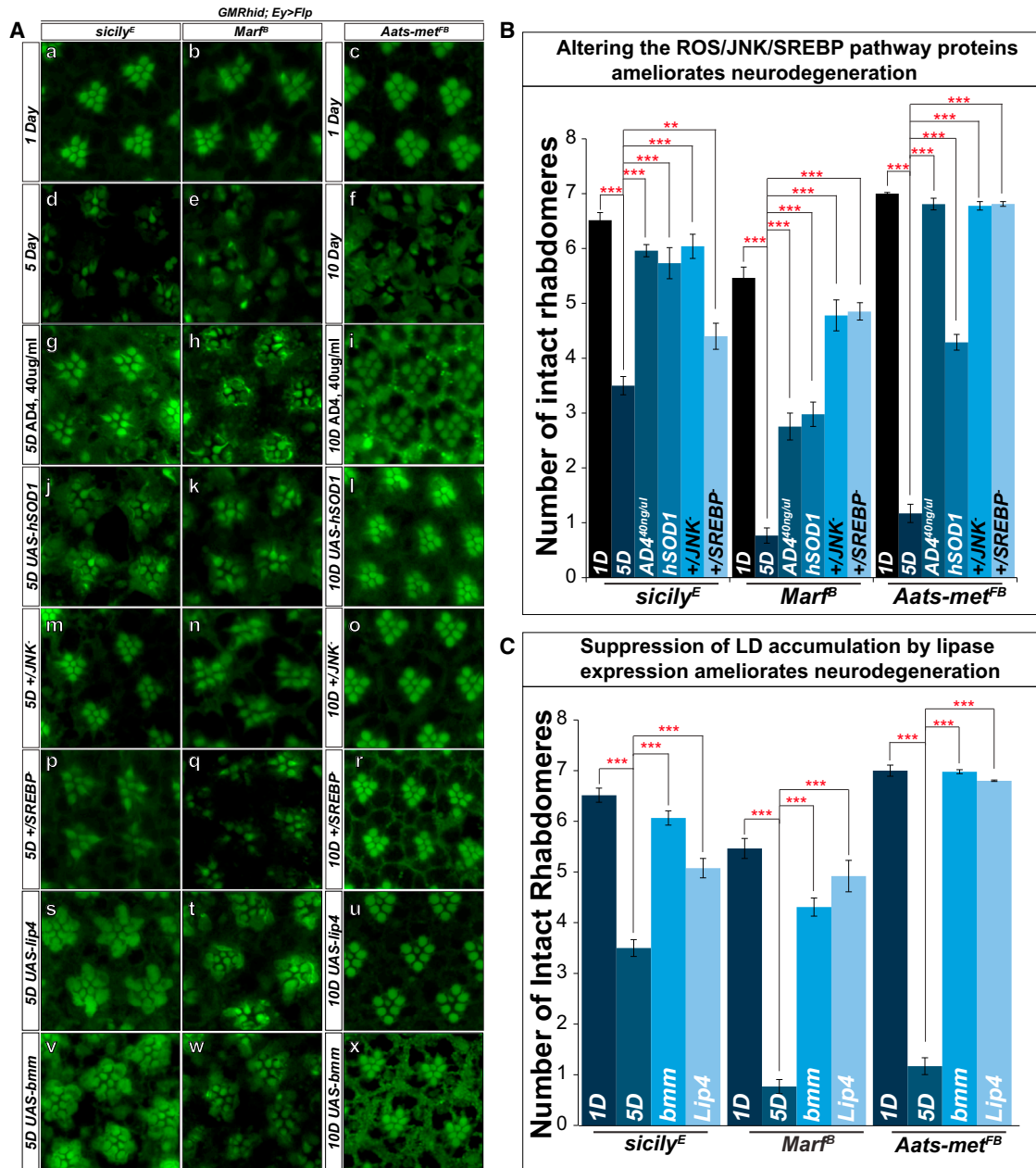


Figure 5. Reduction of LD Accumulation Restores Rhabdomere Integrity and Partially Suppresses Neurodegeneration

(A) a–c, Phalloidin staining of whole-mount retina of 1-day-old *sicily*, *Marf*, and *Aats-met* mutant clones exhibit mostly intact rhabdomeres at this early stage. d–f, Upon aging, *sicily* (5d), *Marf* (5d), and *Aats-met* (10d) mutant clones show obvious signs of degeneration. g–i, animals fed with 40 μ g/ml of AD4 exhibit more intact rhabdomeres after aging for all three mutants. j–l, Reducing LD accumulation by overexpression of *hSOD1*, or m–r, one copy of JNK or SREBP all partially restore rhabdomere integrity after aging based on phalloidin staining. s–x, The expression of lipases (*brummer* and *Lip4*) in the mutant background also delays degeneration compared to mutant clones alone.

(B) Quantification of rhabdomere numbers after aging show that expression of *hSOD1*, feeding AD4 and removing one copy of JNK or SREBP restores rhabdomere integrity.

(C) Quantification of rhabdomere numbers after aging shows that expression of both *brummer* and *Lip4* significantly restore the number of photoreceptors in all three mutant backgrounds. Data are represented as mean \pm SEM. Significance was calculated compared to controls ($p < 0.05$, $**p < 0.005$, $***p < 0.0005$). See also Figure S6.

well as JNK and SREBP are conserved. A mouse model has been generated which permits modeling of Leigh syndrome by removing a mitochondrial Complex I subunit, *Ndufs4* (Quintana

et al., 2012; Quintana et al., 2010; Kruse et al., 2008). Mutant *Ndufs4* mice develop normally but exhibit signs of encephalomyopathy at postnatal day 30 (P30) and eventually die from

breathing defects around P50. These mice develop brain lesions similar to those in Leigh syndrome patients. The KO animals also exhibit reduced activity in Complex I and oxidative stress (Quintana et al., 2012; Assouline et al., 2012).

To determine whether LD accumulate in *Ndufs4* KO mice (*Ndufs4*^{-/-}), we systematically profiled the brain with neutral lipid stains (20 μ m coronal sections from the olfactory bulb to the brain stem) of presymptomatic (P23), mid (P35) and late-stage (>P50) mice along with gender and age-matched controls. We observed an abundance of LD in the olfactory bulb (OB) and vestibular nucleus (VN) of P23 brain slices (Figures 7A a–d and S7C). We also observed mild LD accumulation in the periaqueductal gray, cerebellum, dorsal motor nucleus, vagus and abducens nuclei of mutant brains that are not observed in controls (data not shown). As quantified in Figures 7B and 7C, there is an abundance of LDs in the VN of presymptomatic brains but LDs progressively disappear in P34 and P50 mice. We also observed lesions at P34 and >P50 in the areas where LDs accumulated at P23 (Figures S7A and S7B). Aside from the VN, LDs also accumulate in the OB of presymptomatic animals. However, unlike in the VN, accumulations in the OB persist throughout the lifespan of these mice, perhaps of newborn neurons in this region (Ming and Song, 2011). Interestingly, the areas of the brain with LD accumulation at P23 (VN and the OB) do not exhibit other obvious pathological phenotypes at this time. However, at P34, and especially at P50, the VN and the OB are the main affected regions by lesions and gliosis previously described in Quintana et al. (2012). These data show that LD accumulation precede physical and histological evidence of ND in mice. In addition, triglyceride (TAG) levels in OB of early-, mid- and late-stage *Ndufs4*^{-/-} mice progressively increase (Figure 7D). No differences in TAG levels were observed in the brainstem, a small portion of which corresponds to the VN (data not shown).

To determine the cellular specificity of this LD accumulation, we stained for neutral lipids and glial markers. In the OB and VN, LD co-localize with the astrocyte and microglia markers (Figure 7A e–h). However, LD are rarely seen at P34 and >P50 mice, when there are obvious pathological signs, such as reactive astrocytes and activated microglia. Hence, LDs accumulate in glia prior to the onset of the physical signs of ND in the mutants.

We also assessed JNK activation in the OB of WT and P34 *Ndufs4*^{-/-} mice (Figure 7E); a stage at which the highest level of LD is observed in this area (Figure 7C). Levels of pJNK are increased in the OB of *Ndufs4*^{-/-} mice (Figure 7E), suggesting activation of JNK. Finally, neuronal knockdown of fly *Ndufs4* (CG12203) via RNAi in neurons also causes LD accumulations in glia, consistent with our observations in mice (Figures 7F and 7G).

As the levels of ROS, JNK and LD are elevated, we tested whether AD4 can delay ND in *Ndufs4*^{-/-} mice. KOs were injected intraperitoneally with 150 mg/kg/day from P21 to P28. This short treatment leads to a delay in onset and reduction in severity of clinical signs throughout the lifespan of treated mice (Figure 7H). By P30, the treated KO mice have a significantly delayed latency to fall in the rotarod assay compared to saline treated KO mice (Figure 7I). Thus, a brief administration of AD4 is sufficient to delay the onset of ND and motor defects in *Ndufs4*^{-/-} mice, arguing that increased ROS plays a role in the pathogenesis.

DISCUSSION

Here, we show that neuronal mitochondrial defects that lead to elevated levels of ROS, induce activation of JNK and SREBP, which in turn elevate lipid synthesis in neurons and formation of LD in glial cells. These LDs contribute to and promote ND through elevated levels of lipid peroxidation. LDs form in glia prior to or at the onset of the appearance of obvious degenerative histological features in *Drosophila* and mice. Reducing the number and size of LD pharmacologically or genetically delays ND in the fly. To our knowledge, this is the first indication that SREBP, lipid droplet biogenesis, and lipid metabolism play a role in the pathogenesis of several neurodegenerative diseases.

A growing body of evidence points to the importance of glial health and function in nervous system energy metabolism and homeostasis (Bélanger et al., 2011). Nevertheless, given the number and prevalence of different types of neurodegenerative diseases, very few reports have documented the presence of LDs in either neuron or glia in patients and in animal models. LD accumulation in the brain has been reported in cells that line the ventricles in the globus pallidus and substantia nigra in mutant mice lacking both subunits of the liver X receptor (Wang et al., 2002), apolipoprotein E (Mato et al., 1999), or a peroxisomal biogenesis factor (Pex5) (Hulshagen et al., 2008). In addition, in vitro studies using immortalized cell lines and explants show that LD may form and accumulate in glia under conditions of nutrient deprivation or lipopolysaccharide induced stress (Cabodevilla et al., 2013; Bozza and Viola, 2010). However, LDs have not been shown to play an active role in neurodegenerative processes. Furthermore, LD accumulation has not been reported in patients with or animal models of Leigh syndrome (*NDUFS4/Ndufs4*, *NDUFAF6/sicily*), CMT-2A2 or HMSN6 (*MFN2/Marf*), and ARSAL (*MARS2/Aats-met*) (Assouline et al., 2012; McKenzie et al., 2011; Pagliarini et al., 2008; Boaretto et al., 2010; Bayat et al., 2012; Thiffault et al., 2006). The lack of neuropathological reports of LDs in animal models or in patients with ND may be attributed to the fact that LD accumulation is transient and mostly occur during presymptomatic stages of the disease.

Although these genes/mutants are implicated in very different mitochondrial processes, they exhibit a common phenotype of elevated levels of ROS, leading to LD accumulation. Similar morphological changes of glia have been reported under stress conditions (Boche et al., 2013; Pekny and Nilsson, 2005). Interestingly, mid- and late-stage *Ndufs4*^{-/-} mice exhibit CNS lesions in the same brain regions where the LD accumulate in early stage animals, showing a strong correlative relationship. Similarly, LD accumulation in *Drosophila* mutants occurs prior to or at the onset of physical signs of ND. Importantly, the delivery of AD4 is able to significantly ameliorate LD accumulation in *Drosophila* and delay the onset of ND in flies and mice. Hence, the molecular mechanisms underlying these phenotypes are likely to be conserved between these species and potentially also in higher organisms.

In the clinical setting, the prescription of antioxidants toward treatment of neurodegenerative diseases has been tested repeatedly on patients with neurodegenerative disorders (Gala-sko et al., 2012; Gilgun-Sherki et al., 2001; Gandhi and Abramov,

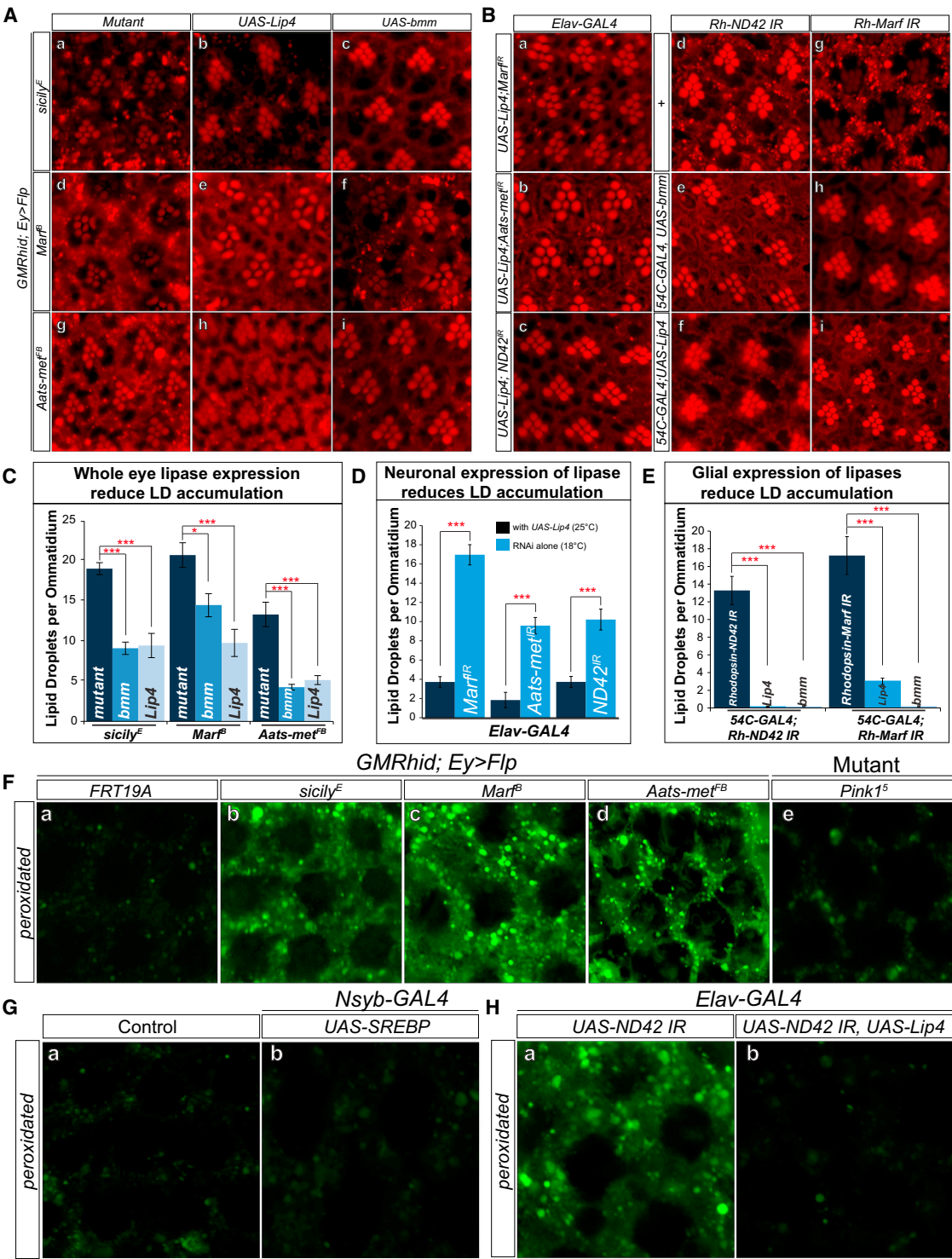


Figure 6. Lipid Peroxidation in Glial Cells Affects the Demise of Neurons
(A) a–i, Nile Red staining of whole-mount retina show that overexpression of *brummer* and *Lip4* in the visual system reduces LD accumulations in *sicily*, *Marf*, and *Aats-met* mutant clones.
(B) a–c, Neuronal expression of lipases and knockdown of *Marf*, *Aats-met* and *sicily* also reduces LD accumulation in the glia. Flies with *elav-GAL4* mediated knockdown of the RNAis alone were raised at 18°C (efficient RNAi leads to high percentage of death) and flies expressing *Lip4* and RNAi were raised at 25°C. d–i, *Rh-ND42* and *Marf* RNAi in the neurons results in glial LD accumulation. Expression of *brummer* and *Lip4* in the glia (*54C-GAL4*) reduces the formation of LD accumulation.

(legend continued on next page)

2012), without compelling results. The LD accumulation phenotype in our mutants occurs prior to histopathological and physical signs of ND. A brief period of AD4 delivery prior to the onset of symptoms in mutant mice is effective in delaying onset of clinical signs. Thus, therapy with an effective antioxidant that penetrates the blood-brain barrier should be started early and sustained over long periods. In addition, pharmacological manipulation of JNK or lipid levels in the brain may serve as a potential therapy to delay the onset of ND. However, similar to antioxidant treatment, this may need to be administered at an early stage. Hence, early identification of potential ROS related neurological disease based on genetic/genomic diagnosis or by biomarkers may be critical. Since LD accumulation is one of the earliest presymptomatic changes that occurs in the nervous system, detection of LD itself or changes in neurometabolism may be a promising biomarker.

In summary, we provide evidence for the role of altered lipid metabolism and a neuron-glia interplay that promotes ND. In some mitochondrial mutants, we observe an upregulation of SREBP as well as lipid biogenesis and glial LD formation. The accumulation of LD is not sufficient to promote the ND process itself. However, in the presence of ROS the accumulated lipids are peroxidated and promote ND, possibly by promoting the release of lipids from LD, elevating the cytoplasmic load, and causing a progressive loss of LD. Hence, the synergistic effects of increased lipid synthesis and/or LD accumulation in combination with elevated ROS and lipid peroxidation promote ND. Finally, we show that LD accumulation occurs at the onset or precedes ND in flies and mice, suggesting that LD and changes in lipid metabolism in the nervous system may be a promising biomarker to identify brain regions susceptible to but not yet exhibiting symptoms of ND.

EXPERIMENTAL PROCEDURES

Lipid Droplet Staining

For whole-mount staining of fly retinas, heads were dissected in cold PBS and fixed in 3.7% formaldehyde for 1 hr. Subsequently, the retinas were dissected and fixed for an additional 30 min. Retinas were rinsed several times with 1× PBS and incubated for 10 min at 1:1,000 dilution of PBS with 1 mg/ml Nile Red (Sigma) or BODIPY^{493/503} (Life Technologies). Subsequently, tissues were rinsed with PBS and immediately mounted with Vectashield (Vector Labs) for same-day imaging. Images were obtained with a Zeiss LSM 510 microscope.

For LD staining in the CNS, mice were perfused transcardially with 4% paraformaldehyde. Brains were extracted and post-fixed in the same fixative overnight at 4°C and then dehydrated in sucrose. They were then embedded in OCT (Tissue-Tek) and cryosectioned at 20 μm per slice. Slides were submerged in 1× PBS for 10 min and then incubated for 10 min in Nile Red/BODIPY as above. Subsequently, the slides were washed twice with 1×

PBS and immediately covered with Vectashield mounting medium with DAPI (Vector Labs) for same-day imaging.

Lipid Peroxidation

Procedures with C11-BODIPY^{581/591} were adapted for tissue staining instead of cell culture as described in (Drummen et al., 2002). BODIPY was solubilized in 50 μl DMSO and was added to a final concentration of 20 μM in BSA. For live tissue staining of mutant retinas, whole flies were pinned to Sylgard silicone elastomer plates and submerged with 1% BSA and BODIPY. Tungsten needles were used to slice the cuticle around the eye for optimal dye penetration. Plates were incubated for 30 min at 37°C and subsequently rinsed with 1× PBS before the retinas were sliced out, mounted with Vectashield, and imaged immediately.

Tissue Triglyceride Quantification

Triglyceride levels in OB samples (n = 6 for WT mice, n = 3 for each *Ndufs4* mice group) were determined using the PicoProbe Triglyceride Quantification Assay Kit (Abcam) according to manufacturer's directions. Wild-type mice included age-matched controls.

AD4 Administration

Control and KO mice were administered i.p. daily for 7 days with either saline (CT SAL, n = 11; KO SAL, n = 7) or 150 mg/kg AD4 (KO AD4, n = 6) from day P21 until P28.

SUPPLEMENTAL INFORMATION

Supplemental Information includes Extended Experimental Procedures and seven figures and can be found with this article online at <http://dx.doi.org/10.1016/j.cell.2014.12.019>.

AUTHOR CONTRIBUTION

L.L., K.Z., and H.J.B. conceived and designed the project. L.L. conducted the lipid stainings, genetic interaction studies and analyzed the data. L.L., K.Z. and H.S. prepared samples for TEM. L.L., K.Z., Z.L., H.S., and B.H.G. performed the mitochondria assays. L.L., E.S., J.H., A.Q. designed or performed, the mouse biochemical, behavioral, and drug studies. K.Z., H.S., S.Y., and M.J. performed the screen that isolated the mutants. L.L. and H.J.B. wrote the manuscript.

ACKNOWLEDGMENTS

We thank Karen Schulze, Richard Palmiter, Bertrand Mollereau, and Kartik Venkatachalam for comments; Robert Rawson (SREBP antibody), Ronald Kühnlein (UAS-bmm), the Bloomington Drosophila Stock Center, the Vienna Drosophila RNAi center, and the TRIP at Harvard Medical School (NIH/NIGMS R01-GM084947) for providing stocks and reagents; Ching-On Wong for help with westerns; and Lita Duraine for TEM. Confocal microscopy was supported by the BCM Intellectual and Developmental Disabilities Research Center (NIH/NICHHD P30 HD024064). H.S. was supported by NIH 5R01GM067858, NIH T32 NS043124-11 and the Research Education and Career Horizon Institutional Research and Academic Career Development Award Fellowship 5K12GM084897. L.L. was supported by the Neuroscience graduate program training grant (5T32GM008507-18) from 2011 to 2012. S.Y. is supported by the Jan and Dan Duncan Neurological

(C) Quantification of (A).

(D) Quantification of (B a–c). Significance was calculated compared to Figure 4A a–c.

(E) Quantification of (B d–i).

(F) a and e. Measurement of peroxidated lipids shows basal level of peroxidated lipids in control (*FRT19A*) clones and *pink1⁵* mutant retinas. b–d, 1-day-old mutant clones exhibit elevated levels of peroxidated lipids.

(G) Neuronal overexpression of SREBP does not result in elevated levels of peroxidated lipids compared to control (UAS-SREBP).

(H) Neuronal RNAi knockdown of *ND42* results in elevated levels of peroxidated lipids, which is rescued with neuronal expression of lipase. Data are represented as mean ± SEM. Significance was calculated compared to controls. (**p* < 0.05, ***p* < 0.005, ****p* < 0.0005). See also Figure S6.

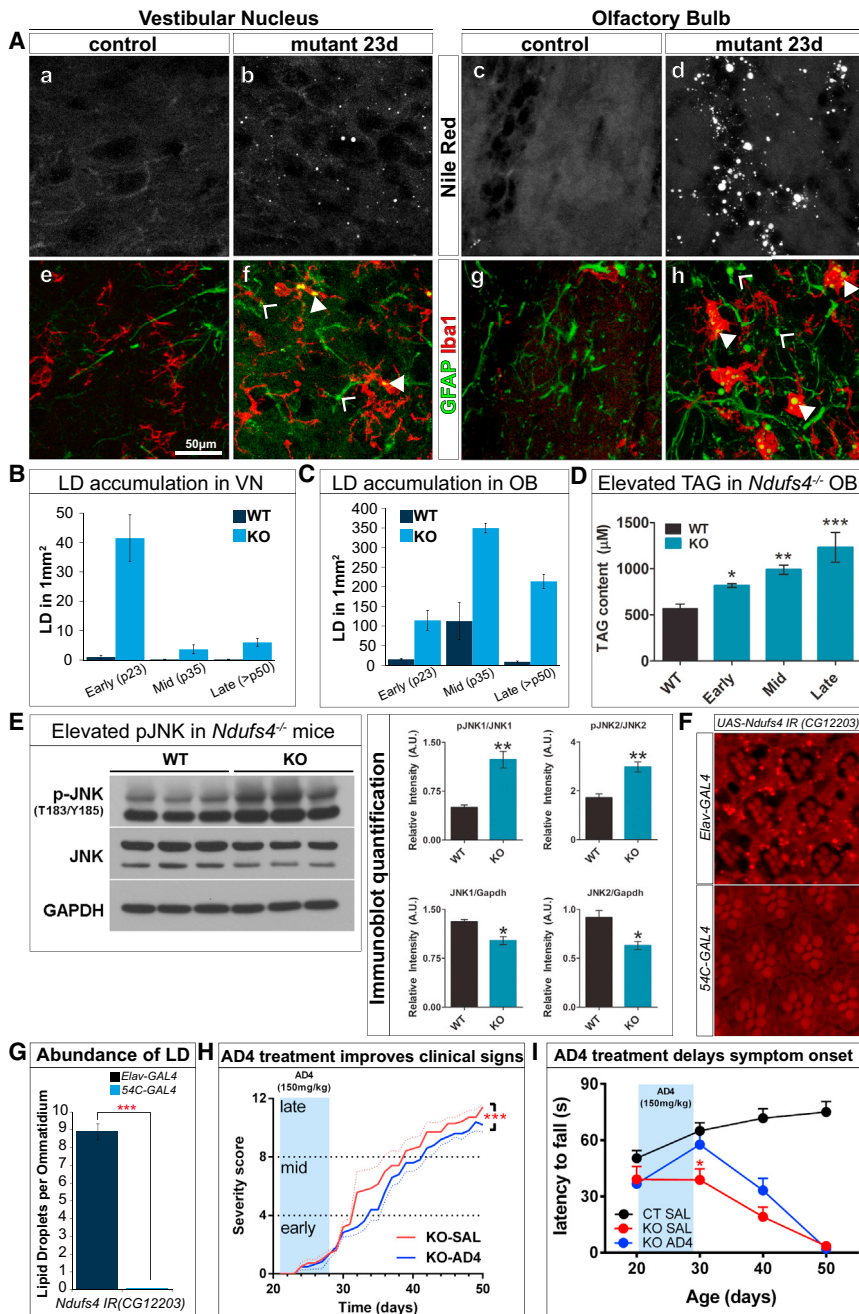


Figure 7. LD Accumulation Is Present in the Astrocytes and Microglia of *Ndufs4*^{-/-} Mice Prior to Neurodegeneration

(A) a–d 20 μ m coronal cryosections reveal LD accumulation in the VN and OB of *Ndufs4*^{-/-} mice compared to control (C57Bl/6). e–h LD accumulates in the astrocytes and microglia of the VN and OB shown by colocalization with the astrocyte marker, GFAP and the microglia marker, Iba1. (B) LD accumulation in the VN is high in the P23 mutants but decreases in number in the P34 and >P50 mutants. (C) In the OB, LD accumulation occurs in the P23 mutants and increases in number in the P34 and >P50 animals. (D) *Ndufs4*^{-/-} exhibit elevated triglyceride (TAG) levels in the OB in an age-dependent manner. (E) pJNK is increased in the mutants. Right panels show the quantification of the immunoblots. (F) Neuronal knockdown of *dNdufs4* (CG12203) leads to LD accumulation in the glia, while glial knockdown results in no LD accumulation. (* $p < 0.05$, ** $p < 0.005$, *** $p < 0.0005$). (G) Quantification of F. (H and I) 7 day administration of AD4 in P21 animals via IP injection at 150 mg/kg shows treated mutant animals with improved clinical signs (body weight loss, hypotonia, ataxia, piloerection, clamping, gasping, paralysis, tremor) upon aging (H) and performing at a comparable level as control while mutants treated with saline show progressive decline in motor performance (I). (* $p < 0.05$ KO SAL versus KO AD4, two-way ANOVA). See also Figure S7.

Research Institute at Texas Children's Hospital. We acknowledge support of the NW Mitochondrial Research Guild to A.Q. We acknowledge support of the NIH (1RC4GM096355), the Robert A. and Renee E. Belfer Family Foundation, the Huffington Foundation and Target ALS to H.J.B. S.Y. is supported by the Jan and Dan Duncan Neurological Research Institute at Texas Children's Hospital. H.J.B. is an Investigator of the Howard Hughes Medical Institute.

Received: April 11, 2014
Revised: September 22, 2014
Accepted: November 19, 2014
Published: January 15, 2015

REFERENCES

- Amer, J., Atlas, D., and Fibach, E. (2008). N-acetylcysteine amide (AD4) attenuates oxidative stress in beta-thalassemia blood cells. *Biochim. Biophys. Acta* 1780, 249–255.
- Assouline, Z., Jambou, M., Rio, M., Bole-Feysot, C., de Lonlay, P., Barnerias, C., Desguerre, I., Bonnemaïn, C., Guillermet, C., Steffann, J., et al. (2012). A constant and similar assembly defect of mitochondrial respiratory chain complex I allows rapid identification of NDUFS4 mutations in patients with Leigh syndrome. *Biochim. Biophys. Acta* 1822, 1062–1069.

- Bao, S., Fischbach, K.F., Corbin, V., and Cagan, R.L. (2010). Preferential adhesion maintains separation of ommatidia in the *Drosophila* eye. *Dev. Biol.* **344**, 948–956.
- Barnham, K.J., Masters, C.L., and Bush, A.I. (2004). Neurodegenerative diseases and oxidative stress. *Nat. Rev. Drug Discov.* **3**, 205–214.
- Bayat, V., Thiffault, I., Jaiswal, M., Tétreault, M., Donti, T., Sasarman, F., Bernard, G., Demers-Lamarche, J., Dicaire, M.J., Mathieu, J., et al. (2012). Mutations in the mitochondrial methionyl-tRNA synthetase cause a neurodegenerative phenotype in flies and a recessive ataxia (ARSAL) in humans. *PLoS Biol.* **10**, e1001288.
- Beal, M.F. (2007). Mitochondria and neurodegeneration. *Novartis Found. Symp.* **287**, 183–192, discussion 192–196.
- Bélanger, M., Allaman, I., and Magistretti, P.J. (2011). Brain energy metabolism: focus on astrocyte-neuron metabolic cooperation. *Cell Metab.* **14**, 724–738.
- Boaretto, F., Vettori, A., Casarin, A., Vazza, G., Muglia, M., Rossetto, M.G., Cavallaro, T., Rizzuto, N., Carelli, V., Salviati, L., et al. (2010). Severe CMT type 2 with fatal encephalopathy associated with a novel MFN2 splicing mutation. *Neurology* **74**, 1919–1921.
- Boche, D., Perry, V.H., and Nicoll, J.A. (2013). Review: activation patterns of microglia and their identification in the human brain. *Neuropathol. Appl. Neurobiol.* **39**, 3–18.
- Bozza, P.T., and Viola, J.P. (2010). Lipid droplets in inflammation and cancer. *Prostaglandins Leukot. Essent. Fatty Acids* **82**, 243–250.
- Cabodevilla, A.G., Sánchez-Caballero, L., Nintou, E., Boiadjeva, V.G., Picatoste, F., Gubern, A., and Claro, E. (2013). Cell survival during complete nutrient deprivation depends on lipid droplet-fueled β -oxidation of fatty acids. *J. Biol. Chem.* **288**, 27777–27788.
- Camargo, N., Smit, A.B., and Verheijen, M.H. (2009). SREBPs: SREBP function in glia-neuron interactions. *FEBS J.* **276**, 628–636.
- Cheng, L.Y., Bailey, A.P., Leever, S.J., Ragan, T.J., Driscoll, P.C., and Gould, A.P. (2011). Anaplastic lymphoma kinase spares organ growth during nutrient restriction in *Drosophila*. *Cell* **146**, 435–447.
- Clark, I.E., Dodson, M.W., Jiang, C., Cao, J.H., Huh, J.R., Seol, J.H., Yoo, S.J., Hay, B.A., and Guo, M. (2006). *Drosophila* pink1 is required for mitochondrial function and interacts genetically with parkin. *Nature* **441**, 1162–1166.
- Debattisti, V., and Scorrano, L. (2013). *D. melanogaster*, mitochondria and neurodegeneration: small model organism, big discoveries. *Mol. Cell. Neurosci.* **55**, 77–86.
- Del Bo, R., Moggio, M., Rango, M., Bonato, S., D'Angelo, M.G., Ghezzi, S., Airoldi, G., Bassi, M.T., Guglieri, M., Napoli, L., et al. (2008). Mutated mitofusin 2 presents with intrafamilial variability and brain mitochondrial dysfunction. *Neurology* **71**, 1959–1966.
- Dobrosotskaya, I.Y., Seigmiller, A.C., Brown, M.S., Goldstein, J.L., and Rawson, R.B. (2002). Regulation of SREBP processing and membrane lipid production by phospholipids in *Drosophila*. *Science* **296**, 879–883.
- Drummen, G.P., van Liebergen, L.C., Op den Kamp, J.A., and Post, J.A. (2002). C11-BODIPY(581/591), an oxidation-sensitive fluorescent lipid peroxidation probe: (micro)spectroscopic characterization and validation of methodology. *Free Radic. Biol. Med.* **33**, 473–490.
- Edwards, T.N., and Meinertzhagen, I.A. (2010). The functional organisation of glia in the adult brain of *Drosophila* and other insects. *Prog. Neurobiol.* **90**, 471–497.
- Farese, R.V., Jr., and Walther, T.C. (2009). Lipid droplets finally get a little R-E-S-P-E-C-T. *Cell* **139**, 855–860.
- Galasko, D.R., Peskind, E., Clark, C.M., Quinn, J.F., Ringman, J.M., Jicha, G.A., Cotman, C., Cottrell, B., Montine, T.J., Thomas, R.G., and Aisen, P.; Alzheimer's Disease Cooperative Study (2012). Antioxidants for Alzheimer disease: a randomized clinical trial with cerebrospinal fluid biomarker measures. *Arch. Neurol.* **69**, 836–841.
- Gandhi, S., and Abramov, A.Y. (2012). Mechanism of oxidative stress in neurodegeneration. *Oxid. Med. Cell. Longev.* **2012**, 428010.
- Gilgun-Sherki, Y., Melamed, E., and Offen, D. (2001). Oxidative stress induced-neurodegenerative diseases: the need for antioxidants that penetrate the blood brain barrier. *Neuropharmacology* **40**, 959–975.
- Greenspan, P., Mayer, E.P., and Fowler, S.D. (1985). Nile red: a selective fluorescent stain for intracellular lipid droplets. *J. Cell Biol.* **100**, 965–973.
- Grönke, S., Mildner, A., Fellert, S., Tennagels, N., Petry, S., Müller, G., Jäckle, H., and Kühnlein, R.P. (2005). Brummer lipase is an evolutionary conserved fat storage regulator in *Drosophila*. *Cell Metab.* **1**, 323–330.
- Horton, J.D., Goldstein, J.L., and Brown, M.S. (2002). SREBPs: activators of the complete program of cholesterol and fatty acid synthesis in the liver. *J. Clin. Invest.* **109**, 1125–1131.
- Hulshagen, L., Krysko, O., Bottelbergs, A., Huyghe, S., Klein, R., Van Veldhoven, P.P., De Deyn, P.P., D'Hooge, R., Hartmann, D., and Baes, M. (2008). Absence of functional peroxisomes from mouse CNS causes dysmyelination and axon degeneration. *J. Neurosci.* **28**, 4015–4027.
- Ilieva, H., Polymenidou, M., and Cleveland, D.W. (2009). Non-cell autonomous toxicity in neurodegenerative disorders: ALS and beyond. *J. Cell Biol.* **187**, 761–772.
- Kamata, H., Honda, S., Maeda, S., Chang, L., Hirata, H., and Karin, M. (2005). Reactive oxygen species promote TNF α -induced death and sustained JNK activation by inhibiting MAP kinase phosphatases. *Cell* **120**, 649–661.
- Keller, J.N., Schmitt, F.A., Scheff, S.W., Ding, Q., Chen, Q., Butterfield, D.A., and Markesbery, W.R. (2005). Evidence of increased oxidative damage in subjects with mild cognitive impairment. *Neurology* **64**, 1152–1156.
- Kijima, K., Numakura, C., Izumino, H., Umetsu, K., Nezu, A., Shiiki, T., Ogawa, M., Ishizaki, Y., Kitamura, T., Shozawa, Y., and Hayasaka, K. (2005). Mitochondrial GTPase mitofusin 2 mutation in Charcot-Marie-Tooth neuropathy type 2A. *Hum. Genet.* **116**, 23–27.
- Kruse, S.E., Watt, W.C., Marcinek, D.J., Kapur, R.P., Schenkman, K.A., and Palmiter, R.D. (2008). Mice with mitochondrial complex I deficiency develop a fatal encephalomyopathy. *Cell Metab.* **7**, 312–320.
- Kunte, A.S., Matthews, K.A., and Rawson, R.B. (2006). Fatty acid auxotrophy in *Drosophila* larvae lacking SREBP. *Cell Metab.* **3**, 439–448.
- Lin, M.T., and Beal, M.F. (2006). Mitochondrial dysfunction and oxidative stress in neurodegenerative diseases. *Nature* **443**, 787–795.
- Listenberger, L.L., Han, X., Lewis, S.E., Cases, S., Farese, R.V., Jr., Ory, D.S., and Schaffer, J.E. (2003). Triglyceride accumulation protects against fatty acid-induced lipotoxicity. *Proc. Natl. Acad. Sci. USA* **100**, 3077–3082.
- Martin-Blanco, E., Gampel, A., Ring, J., Virdee, K., Kirov, N., Tolkovsky, A.M., and Martinez-Arias, A. (1998). puckered encodes a phosphatase that mediates a feedback loop regulating JNK activity during dorsal closure in *Drosophila*. *Genes Dev.* **12**, 557–570.
- Mato, M., Ookawara, S., Mashiko, T., Sakamoto, A., Mato, T.K., Maeda, N., and Kodama, T. (1999). Regional difference of lipid distribution in brain of apolipoprotein E deficient mice. *Anat. Rec.* **256**, 165–176.
- McKenzie, M., Tucker, E.J., Compton, A.G., Lazarou, M., George, C., Thorburn, D.R., and Ryan, M.T. (2011). Mutations in the gene encoding C8orf38 block complex I assembly by inhibiting production of the mitochondria-encoded subunit ND1. *J. Mol. Biol.* **414**, 413–426.
- Ming, G.L., and Song, H. (2011). Adult neurogenesis in the mammalian brain: significant answers and significant questions. *Neuron* **70**, 687–702.
- Murphy, D.J. (2001). The biogenesis and functions of lipid bodies in animals, plants and microorganisms. *Prog. Lipid Res.* **40**, 325–438.
- Niki, E. (2009). Lipid peroxidation: physiological levels and dual biological effects. *Free Radic. Biol. Med.* **47**, 469–484.
- Pagliarini, D.J., Calvo, S.E., Chang, B., Sheth, S.A., Vafai, S.B., Ong, S.E., Walford, G.A., Sugiana, C., Boneh, A., Chen, W.K., et al. (2008). A mitochondrial protein compendium elucidates complex I disease biology. *Cell* **134**, 112–123.
- Palm, W., Sampaio, J.L., Brankatschk, M., Carvalho, M., Mahmoud, A., Shevchenko, A., and Eaton, S. (2012). Lipoproteins in *Drosophila melanogaster*—assembly, function, and influence on tissue lipid composition. *PLoS Genet.* **8**, e1002828.

- Parkes, T.L., Elia, A.J., Dickinson, D., Hilliker, A.J., Phillips, J.P., and Boulianne, G.L. (1998). Extension of *Drosophila* lifespan by overexpression of human SOD1 in motoneurons. *Nat. Genet.* **19**, 171–174.
- Pavlopoulos, T.G., Boyer, J.H., Shah, M., Thangaraj, K., and Soong, M.L. (1990). Laser action from 2,6,8-position trisubstituted 1,3,5,7-tetramethylpyromethene-BF(2) complexes: part 1. *Appl. Opt.* **29**, 3885–3886.
- Pekny, M., and Nilsson, M. (2005). Astrocyte activation and reactive gliosis. *Glia* **50**, 427–434.
- Praticò, D., Uryu, K., Leight, S., Trojanowski, J.Q., and Lee, V.M. (2001). Increased lipid peroxidation precedes amyloid plaque formation in an animal model of Alzheimer amyloidosis. *J. Neurosci.* **21**, 4183–4187.
- Quintana, A., Kruse, S.E., Kapur, R.P., Sanz, E., and Palmiter, R.D. (2010). Complex I deficiency due to loss of Ndufs4 in the brain results in progressive encephalopathy resembling Leigh syndrome. *Proc. Natl. Acad. Sci. USA* **107**, 10996–11001.
- Quintana, A., Zanella, S., Koch, H., Kruse, S.E., Lee, D., Ramirez, J.M., and Palmiter, R.D. (2012). Fatal breathing dysfunction in a mouse model of Leigh syndrome. *J. Clin. Invest.* **122**, 2359–2368.
- Reed, T.T. (2011). Lipid peroxidation and neurodegenerative disease. *Free Radic. Biol. Med.* **51**, 1302–1319.
- Sandoval, H., Yao, C.K., Chen, K., Jaiswal, M., Danti, T., Lin, Y.Q., Bayat, V., Xiong, B., Zhang, K., David, G., Charng, W.L., Yamamoto, S., Duraine, L., Graham, B.H., and Bellen, H.J. (2014). Mitochondrial fusion but not fission regulates larval growth and synaptic development through steroid hormone production. *Elife* **3**, 03558.
- Santos, C.R., and Schulze, A. (2012). Lipid metabolism in cancer. *FEBS J.* **279**, 2610–2623.
- Schimmel, A.M., Abraham, L., Cox, D., Sene, A., Kraus, C., Dace, D.S., Ercal, N., and Apte, R.S. (2011). N-acetylcysteine amide (NACA) prevents retinal degeneration by up-regulating reduced glutathione production and reversing lipid peroxidation. *Am. J. Pathol.* **178**, 2032–2043.
- Seegmiller, A.C., Dobrosotskaya, I., Goldstein, J.L., Ho, Y.K., Brown, M.S., and Rawson, R.B. (2002). The SREBP pathway in *Drosophila*: regulation by palmitate, not sterols. *Dev. Cell* **2**, 229–238.
- Shao, W., and Espenshade, P.J. (2012). Expanding roles for SREBP in metabolism. *Cell Metab.* **16**, 414–419.
- Stowers, R.S., and Schwarz, T.L. (1999). A genetic method for generating *Drosophila* eyes composed exclusively of mitotic clones of a single genotype. *Genetics* **152**, 1631–1639.
- Sun, X., Komatsu, T., Lim, J., Laslo, M., Yoltz, J., Wang, C., Poirier, L., Alberico, T., and Zou, S. (2012). Nutrient-dependent requirement for SOD1 in lifespan extension by protein restriction in *Drosophila melanogaster*. *Aging Cell* **11**, 783–793.
- Thiffault, I., Rioux, M.F., Tetreault, M., Jarry, J., Loiseleur, L., Poirier, J., Gros-Louis, F., Mathieu, J., Vanasse, M., Rouleau, G.A., et al. (2006). A new autosomal recessive spastic ataxia associated with frequent white matter changes maps to 2q33–34. *Brain* **129**, 2332–2340.
- Turner, M.R., Kiernan, M.C., Leigh, P.N., and Talbot, K. (2009). Biomarkers in amyotrophic lateral sclerosis. *Lancet Neurol.* **8**, 94–109.
- Verstreken, P., Ly, C.V., Venken, K.J., Koh, T.W., Zhou, Y., and Bellen, H.J. (2005). Synaptic mitochondria are critical for mobilization of reserve pool vesicles at *Drosophila* neuromuscular junctions. *Neuron* **47**, 365–378.
- Wang, L., Schuster, G.U., Hultenby, K., Zhang, Q., Andersson, S., and Gustafsson, J.A. (2002). Liver X receptors in the central nervous system: from lipid homeostasis to neuronal degeneration. *Proc. Natl. Acad. Sci. USA* **99**, 13878–13883.
- Xie, H., Hou, S., Jiang, J., Sekutowicz, M., Kelly, J., and Bacskaï, B.J. (2013). Rapid cell death is preceded by amyloid plaque-mediated oxidative stress. *Proc. Natl. Acad. Sci. USA* **110**, 7904–7909.
- Xiong, B., and Bellen, H.J. (2013). Rhodopsin homeostasis and retinal degeneration: lessons from the fly. *Trends Neurosci.* **36**, 652–660.
- Yamamoto, S., Jaiswal, M., Charng, W.L., Gambin, T., Karaca, E., Mirzaa, G., Wiszniewski, W., Sandoval, H., Haelterman, N.A., Xiong, B., et al. (2014). A *Drosophila* genetic resource of mutants to study mechanisms underlying human genetic diseases. *Cell* **159**, 200–214.
- Yan, L.J., Levine, R.L., and Sohal, R.S. (1997). Oxidative damage during aging targets mitochondrial aconitase. *Proc. Natl. Acad. Sci. USA* **94**, 11168–11172.
- Zhang, K., Li, Z., Jaiswal, M., Bayat, V., Xiong, B., Sandoval, H., Charng, W.L., David, G., Haueter, C., Yamamoto, S., et al. (2013). The C8ORF38 homologue Sicily is a cytosolic chaperone for a mitochondrial complex I subunit. *J. Cell Biol.* **200**, 807–820.

Low Affinity Binding Site Clusters Confer Hox Specificity and Regulatory Robustness

Justin Crocker,¹ Namiko Abe,² Lucrezia Rinaldi,² Alistair P. McGregor,³ Nicolás Frankel,⁴ Shu Wang,⁵ Ahmad Alsawadi,^{6,7} Philippe Valenti,^{6,7} Serge Plaza,^{6,7} François Payre,^{6,7} Richard S. Mann,^{2,*} and David L. Stern^{1,*}

¹Janelia Research Campus, Howard Hughes Medical Institute, 19700 Helix Drive, Ashburn, VA 20147, USA

²Columbia University Medical Center, 701 West 168th Street, HHSC 1104, New York, NY 10032, USA

³Department of Biological and Medical Sciences, Oxford Brookes University, Gypsy Lane, Oxford OX3 0BP, UK

⁴Departamento de Ecología, Genética y Evolución, IEGEBA-CONICET, Facultad, de Ciencias Exactas y Naturales, Universidad de Buenos Aires, Ciudad, Universitaria, Pabellón 2, 1428 Buenos Aires, Argentina

⁵New Jersey Neuroscience Institute, 65 James Street, Edison, NJ 08820, USA

⁶Centre de Biologie du Développement, Université de Toulouse, UPS, 31062 Cedex 9, France

⁷CNRS, UMR5547, Centre de Biologie du Développement, Toulouse, 31062 Cedex 9, France

*Correspondence: rsm10@columbia.edu (R.S.M.), sternd@janelia.hhmi.org (D.L.S.)

<http://dx.doi.org/10.1016/j.cell.2014.11.041>

SUMMARY

In animals, Hox transcription factors define regional identity in distinct anatomical domains. How Hox genes encode this specificity is a paradox, because different Hox proteins bind with high affinity in vitro to similar DNA sequences. Here, we demonstrate that the Hox protein Ultrabithorax (Ubx) in complex with its cofactor Extradenticle (Exd) bound specifically to clusters of very low affinity sites in enhancers of the *shavenbaby* gene of *Drosophila*. These low affinity sites conferred specificity for Ubx binding in vivo, but multiple clustered sites were required for robust expression when embryos developed in variable environments. Although most individual Ubx binding sites are not evolutionarily conserved, the overall enhancer architecture—clusters of low affinity binding sites—is maintained and required for enhancer function. Natural selection therefore works at the level of the enhancer, requiring a particular density of low affinity Ubx sites to confer both specific and robust expression.

INTRODUCTION

Diversity along the anterior-posterior axis of animals results from differential expression of Hox transcription factors, which regulate different sets of target genes to determine the features specific to each anatomical region (McGinnis and Krumlauf, 1992). For example, in *Drosophila*, *Sex combs reduced* (*Scr*) determines anterior thoracic segments (Struhl, 1982; Wakimoto and Kaufman, 1981), whereas *Ultrabithorax* (*Ubx*) and *abdominal A* (*abdA*) specify thoracic and abdominal segments (Lewis, 1978; Sánchez-Herrero et al., 1985).

Hox protein specificity is paradoxical, because all Hox proteins have similar DNA binding domains (the homeodomain),

particularly for residues that contact DNA directly (Akam, 1989; McGinnis and Krumlauf, 1992). As a result, all Hox proteins bind similar DNA sequences with high affinity (Berger et al., 2008; Mann et al., 2009; Noyes et al., 2008). In principle, one solution to this paradox is that sequences outside of the homeodomain, which have diverged among Hox proteins, allow interactions with a diversity of cofactors to confer specificity. However, only two cofactors, the homeodomain proteins Extradenticle/Pbx (Exd) and Homothorax/MEIS (Hth) (Moens and Selleri, 2006), are known to interact with Hox proteins (Chan et al., 1994; Chang et al., 1995; Mann et al., 2009). Exd dimerizes with Hox proteins and Hth facilitates nuclear localization and DNA binding of Exd (Pai et al., 1998; Rieckhof et al., 1997; Ryoo et al., 1999). Thus, Hox specificity is unlikely to arise from interactions with a diversity of cofactors.

However, Hox protein structure is altered when bound to DNA with Exd, resulting in increased binding site specificity of Hox-Hth-Exd complexes in comparison with Hox monomers (Joshi et al., 2007; Slattery et al., 2011). In vivo support for this latent specificity model came from studies of artificial enhancers containing multimerized Hox-Exd binding sites (Ryoo and Mann, 1999). Therefore, it is not clear whether this mechanism is sufficient to account for the high degree of regulatory specificity exhibited by Hox proteins on native enhancers.

One clue that may inform the Hox specificity paradox is that many enhancers, including Hox-regulated enhancers, contain multiple binding sites for the same transcription factor (Arnone and Davidson, 1997; Gotea et al., 2010; Lifanov et al., 2003; Ochoa-Espinosa et al., 2005; Papatsenko et al., 2002; Stanojevic et al., 1991). These so-called homotypic binding site clusters are widespread, but the functions of clustered binding sites are understood in only a few cases. For example, homotypic clusters can fine-tune the response to graded transcription factors levels (Driever et al., 1989; Gaudet and Mango, 2002; Jiang and Levine, 1993; Rowan et al., 2010; Struhl et al., 1989), control the timing of enhancer activation (Gaudet and Mango, 2002), or determine whether binding results in repression or activation (Ramos and Barolo, 2013). However, elimination of individual binding sites

in homotypic clusters often has little or no effect on enhancer activity (Doniger et al., 2005; Driever and Nüsslein-Volhard, 1989; Hersch and Carroll, 2005; Saramäki et al., 2006; Stanojevic et al., 1991), suggesting that there may be additional reasons for the widespread existence of homotypic binding site clusters.

To gain insight into the Hox specificity paradox, we asked how Hox factors regulate native enhancers to achieve a specific pattern of epidermal trichomes along the anterior-posterior axis of *Drosophila* larvae. Trichome patterns display strong differences between adjacent segments in a Hox-dependent manner (Lewis, 1978; Sánchez-Herrero et al., 1985). Because *shavenbaby* (*svb*) is the master control gene for trichome development (Chanut-Delalande et al., 2006; Delon et al., 2003; Payre et al., 1999), we examined whether and how Hox factors regulate *svb*. We found that *svb* enhancers are directly regulated by Ubx and that they solve the Hox specificity paradox by employing clusters of low affinity Ubx-Exd binding sites. Specificity is encoded by low affinity sites and homotypic clusters of these sites provide regulatory robustness. This overall architecture—homotypic clusters of low affinity binding sites—is evolutionarily conserved and may provide a general mechanism to reconcile the need for both enhancer specificity and robustness.

RESULTS

Ubx Positively Regulates *svb* Expression

In wild-type embryos of *Drosophila melanogaster*, cells of the ventral first abdominal segment (A1) differentiate a row of stout trichomes (Figure 1B). These trichomes were lost in the absence of Ubx (Figure 1D). Reciprocally, ectopic expression of Ubx using a heat shock inducible promoter (*HS:Ubx*) caused production of ectopic trichomes in thoracic segments (Figure 1F) (González-Reyes and Morata, 1990; Mann and Hogness, 1990). Because *svb* controls trichome development (Chanut-Delalande et al., 2006), we tested whether Ubx regulates *svb* expression. In wild-type embryos, *svb* was expressed strongly in cells of A1 and other abdominal segments that generate ventral trichomes and only weakly in the third thoracic segment (Figure 1A). In the absence of Ubx, *svb* expression was reduced in segment A1 (Figure 1C), consistent with the loss of the A1 trichomes in these larvae (Figure 1D). When we expressed Ubx ubiquitously, *svb* was upregulated in thoracic segments in a pattern similar to *svb* expression in segment A1 (Figure 1E). These results indicate that Ubx is required for expression of *svb* in the cells that generate A1 trichomes and that Ubx is sufficient to induce ectopic expression of *svb* when misexpressed in thoracic segments.

Ubx Controls Multiple *svb* Enhancers

To determine how Ubx regulates *svb* expression, we examined the effects of altered Ubx expression on two *svb* enhancers, called E and 7, that drive ventral stripes of expression (Figure 1G) (Frankel et al., 2010, 2011; McGregor et al., 2007). Through systematic functional dissection, we identified a 292 bp region of E, called E3N, and a 1,056 bp region of 7, called 7H (Figure S1 available online; Table S1), that each drove expression that accurately recapitulated the ventral patterns generated by the larger regions from which they were derived.

In wild-type embryos, E3N and 7H reporter genes were expressed in ventral rows of segments A1–A8 (Figures 1H and 1I). In embryos that lacked Ubx, E3N and 7H reporter gene expression was lost in the A1 segment (Figures 1J and 1K) and reduced in A2–A8 segments (Figures 1H–1K), consistent with the reduction in trichome numbers caused by loss of Ubx function (Lewis, 1978). Ectopic Ubx caused ectopic expression of E3N and 7H in thoracic segments and increased expression in abdominal segments (Figures 1L and 1M). In response to all manipulations of Ubx function, the expression patterns driven by E3N and 7H were similar to endogenous *svb* expression (Figures 1A–1F and 1H–1M). Therefore, these two enhancers respond to Ubx and, at least in part, capture the regulatory inputs of Hox genes to establish the anterior-posterior pattern of *svb* expression and trichomes.

Hox proteins bind DNA with Exd and Hth (Mann et al., 2009) and embryos lacking either *hth* or *exd* display homeotic transformations of trichome patterns (Jürgens et al., 1984; Peifer and Wieschaus, 1990; Rieckhof et al., 1997). To test if the Exd-Hth complex contributes to Ubx regulation of *svb* expression, we assayed expression of the E3N and 7H enhancers in embryos homozygous for a strongly hypomorphic *hth* allele, *hth*^{P2}, which cannot facilitate nuclear localization of Exd (Noro et al., 2006; Rieckhof et al., 1997). E3N and 7H expression was abrogated in *hth*^{P2} embryos (Figures 1N and 1O), suggesting that Ubx requires Exd and Hth for activation of these *svb* enhancers.

The loss of E3N and 7H activity in abdominal segments in *hth*^{P2} embryos suggests that multiple Hox genes activate these enhancers. While Ubx specifies the trichomes in A1, it acts together with *abdA* to specify trichomes in more posterior segments (Lewis, 1978). Ubx and AbdA have similar DNA-binding specificities in complex with Exd (Karch et al., 1990; Slattery et al., 2011) and either Ubx or *abdA* is sufficient to drive *svb* expression in ventral abdominal stripes (Coiffier et al., 2008). Accordingly, we found that embryos deficient for Ubx and *abdA* expressed neither E3N nor 7H in abdominal stripes (see below), indicating that both Ubx and AbdA activate the E3N and 7H *svb* enhancers.

Ubx Regulates the E3N and 7H Enhancers Directly through Multiple Low Affinity Binding Sites

To determine whether E3N and 7H are *svb* enhancers, first we examined genome-wide Ubx and Hth chromatin immunoprecipitation data (Choo et al., 2011). These data revealed in vivo binding of Ubx and Hth at the E3N and 7H regions, as well as at other *svb* enhancer regions (Figure S1). These results suggest that Ubx may regulate the E3N and 7H *svb* enhancers directly, which we tested further below.

Surprisingly, the DNA sequences of E3N and 7H contained no Hox-Exd sites that match those previously identified by systematic evolution of ligands by exponential enrichment sequencing (SELEX-seq) (Slattery et al., 2011). Therefore, we systematically searched for Ubx binding sites in E3N using electrophoretic mobility shift assays (EMSAs) of overlapping DNA fragments (Figures 2A and S2; Table S2). Ubx showed concentration-dependent binding to E3N1 and E3N2 fragments, but only when in complex with both Hth and Exd (Figures 2C, S2B, and S2C). These fragments bound Ubx-Exd in complex with either full-length Hth (Hth^{FL}) or with Hth^{HM}, similar to a naturally

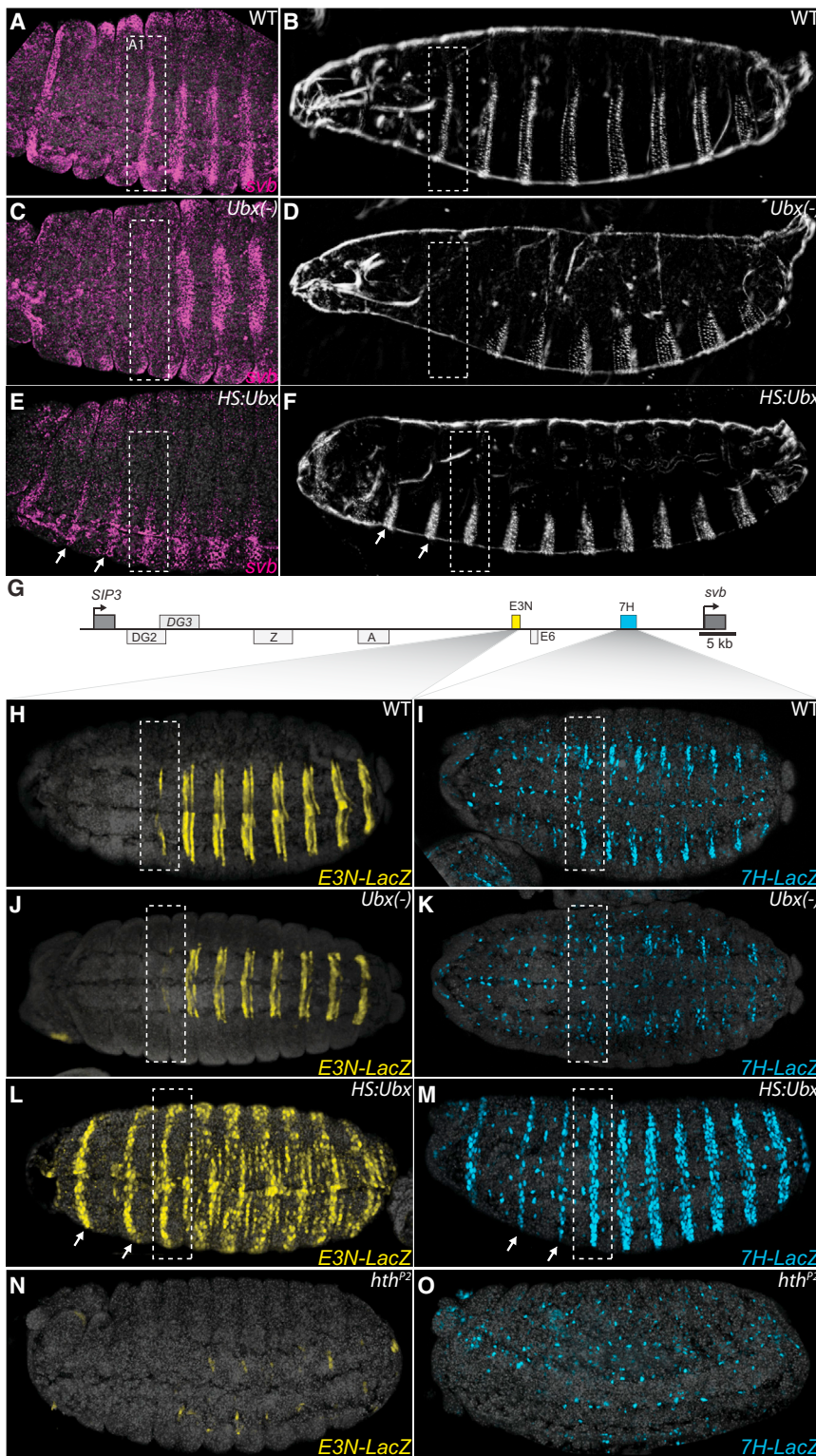


Figure 1. Ubx Is Necessary and Sufficient for *svb* Expression

(A–F) Embryos stained with fluorescent *svb* mRNA probe and larval cuticle preps (B, D, and F) of the indicated genotypes. Loss of *Ubx* function transformed segment A1 into a thoracic segment that lacks *svb* expression (C) and larval trichomes (D), highlighted with bounding boxes. Ubiquitous expression of *Ubx* protein resulted in homeotic transformations of thoracic segments (arrows) into segments resembling segment A1 (E and F).

(G) Schematic of the *svb* upstream *cis*-regulatory region, indicating embryonic enhancers. The ventral enhancers *E3N* and *7H* are highlighted in yellow and blue boxes, respectively. See also Figure S1.

(H–O) Expression of *E3N::lacZ* or *7H::lacZ* reporter constructs (I, K, M, and O). *Ubx* was necessary for *E3N* and *7H* reporter expression in segment A1 (J and K) and sufficient for their expression in thoracic segments when expressed ubiquitously (L and M).

(N and O) In *hth*^{P2} mutant embryos, activity of both the *E3N* and *7H* enhancers was lost.

See also Table S1.

absence of *Ubx* (Figures S2B and S2C). Thus, despite the absence of predicted *Ubx* binding sites in *E3*, these data revealed binding of *Ubx*-*Exd*-*Hth* trimers—hereafter abbreviated as *Ubx*-*Exd* for simplicity—to several regions of this enhancer.

To identify the *Ubx*-*Exd* binding sites in the *E3N* subregions, we systematically tested binding of *Ubx*-*Exd* to oligonucleotides mutated at each 5'-AT dinucleotide pair (Figure S3) and found that most of the *Ubx*-*Exd* binding activity came from three sites (Figure 2C). Mutation of each of two binding sites in *E3N1* reduced *Ubx*-*Exd* binding and mutation of both together abolished *Ubx*-*Exd* binding (Figure 2C, see also Figure S3). In the *E3N2* fragment, we found a third site that, when mutated, abolished *Ubx*-*Exd* binding (Figures S3P and S3Q). Mutation of an additional site located near the 5' end of *E3N1* also reduced *Ubx*-*Exd* binding, suggesting that this region may contain another low affinity *Ubx*-*Exd* binding site (Figures S2 and S3D). The *Ubx*-*Exd* binding sites in *E3N* show variable levels of evolutionary conservation and only site 3 is conserved across all sequenced *Drosophila* species.

occurring isoform of *Hth* that lacks a homeodomain but that can translocate *Exd* to the nucleus (Ryoo et al., 1999). Neither *Hth*^{HM}-*Exd* nor *Hth*^{FL}-*Exd* bound to these *E3N* subfragments in the

We next tested, *in vivo*, the role of *Ubx*-*Exd* sites identified *in vitro* by generating transgenic constructs with all possible combinations of the three sites mutated (Figure 2). Mutation of

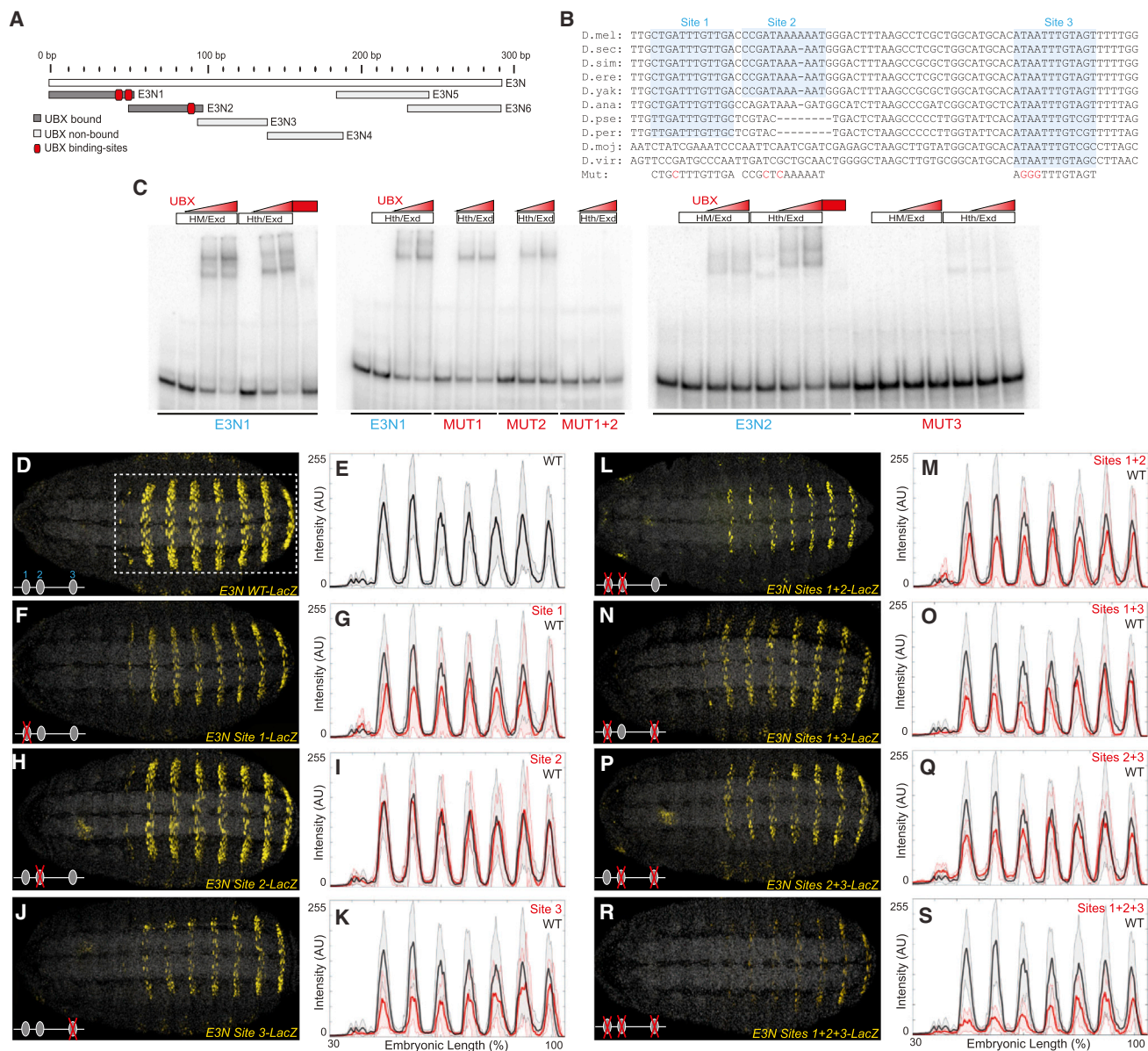


Figure 2. The *svb* *E3N* Enhancer Contains a Cluster of Ubx-Exd Binding Sites

(A) A schematic of the regions tested for their ability to bind Ubx-Exd, assayed via EMSAs. See also Figures S2 and S3.

(B) Sequence alignment for the region of the *E3N* enhancer containing the three Ubx-Exd sites, labeled and highlighted. Dashes indicate gaps in the aligned sequence. Mutations of the Ubx-Exd binding sites are shown (Mut).

(C) Ubx-Hth-Exd bound specifically to each of the three sites, as demonstrated with EMSAs. In this and the following figures, Hth and HM refer to the full-length (Hth^{FL}) and homeodomainless (Hth^{HM}) isoforms of Hth, respectively.

(D–S) Expression of *E3N::lacZ* reporter constructs with Ubx-Exd sites altered as indicated (B), juxtaposed with plots of average expression in the region outlined in (D) ($n = 10$ for each genotype). In all plots, the black and red lines denote expression driven by the wild-type and modified enhancers, respectively. Shaded areas indicate ± 1 SD. AU, arbitrary units of fluorescence intensity.

See also Figures S4 and S5 and Tables S1 and S2.

either site 1 or site 3 reduced the expression levels driven by *E3N* (Figures 2F, 2G, 2J, and 2K). Mutation of site 2 had no detectable effect on *E3N* expression (Figures 2H and 2I), including when combined with either site 1 or site 3 mutations (Figures 2L, 2M, 2P, and 2Q). However, when both site 1 and site 3 were mutated, the *E3N* enhancer still drove weak expression, which was

reduced further upon knockout of site 2 (Figures 2N, 2O, 2R, and 2S). Thus, all three Ubx-Exd sites in the *E3N* enhancer are functional in vivo.

We obtained very similar results for Ubx binding to the *7H* enhancer. In vitro assays identified three low affinity Ubx-Exd binding sites in *7H* (Figures S4A and S4B). Individual mutation

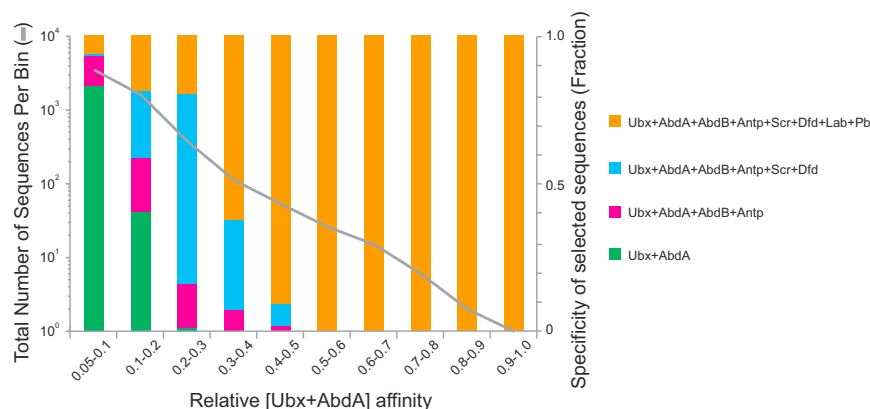


Figure 3. Inverse Correlation between Sequence Affinity and Specificity

The proportion of 12mer sequences bound by various Hox-Exd complexes versus relative affinity of these 12mers for Ubx/AbdA-Exd is shown as colored bars (specificity groups). The number of 12mers in each affinity bin is plotted as a gray line. Average relative affinities of 12mers were calculated for four pairs of Hox-Exd complexes with similar binding profiles: (1) Labial and Pb, (2) Dfd and Scr, (3) AbdB and Antp, and (4) Ubx and AbdA. Sequences specific for Ubx/AbdA-Exd (green bars) are more prevalent in lower affinity bins than in higher affinity bins.

of each of the three Ubx-Exd binding sites did not modify the activity of *7H* in embryos, either qualitatively (Figures S4C, S4G, S4K, and S4O) or quantitatively (Figures S4D, S4H, S4L, and S4P). In contrast, simultaneous mutation of sites 1 and 2, or sites 2 and 3, decreased *7H* activity (Figures S4E–S4N) and mutation of all three sites almost completely abrogated *7H* expression (Figures S4Q and S4R). Collectively, these results indicate that, as observed for *E3N*, the *7H* *svb* enhancer uses at least three low affinity Ubx-Exd sites to drive expression along the AP axis of embryos. The absence of Ubx-Exd sites in *E3N* or *7H* that match those detected by SELEX-seq (Slattery et al., 2011) implies that these sites have very low affinity for Ubx-Exd (see below).

In addition to Ubx, the *E3N* and *7H* enhancers are regulated in vivo by abdA (Figure S5). Therefore, we tested whether the Ubx-Exd sites we identified could also bind AbdA-Hth-Exd (AbdA-Exd). In vitro, AbdA-Exd bound to the same *E3N* and *7H* binding sites as Ubx-Exd did, and binding was abrogated when these sites were mutated (Figure S5). Thus, Ubx-Exd and AbdA-Exd directly regulate the *E3N* and *7H* enhancers through the same binding sites.

Taken together, these data show that both the *E3N* and *7H* *svb* enhancers contain clusters of low affinity Ubx/AbdA-Exd binding sites that are required to drive *svb* expression in ventral abdominal stripes. They further indicate that these sites mediate the action of Ubx in segment A1 and Ubx plus AbdA in segments A2–A8.

Proper Regulation of a *svb* Enhancer Requires Low Affinity Ubx Binding Sites

While our in vivo assays demonstrated that all of the Hox-Exd sites in *E3N* and *7H* are required for proper function, it is not clear why these enhancers employ low affinity rather than higher affinity binding sites. We hypothesized that the low affinity of these binding sites may be part of the solution to the Hox specificity paradox. To explore this idea, we analyzed previously published data in which the DNA sequence preferences of all *Drosophila* Hox-Exd complexes were measured using SELEX-seq, resulting in relative affinity scores from 0.03 to 1 (Slattery et al., 2011). Using these data, we asked if there was any correlation between affinity and specificity. For example, do sequences with low affinity versus high affinity for Ubx-Exd display preference

for Ubx-Exd compared to other Hox-Exd complexes? The results of this analysis were striking; only sequences with a relative affinity lower than 0.3 bound Ubx/AbdA-Exd specifically compared to the other Hox-Exd complexes (Figure 3). Moreover, as the relative affinity for Ubx/AbdA-Exd decreased, the number of sequences that bound specifically to Ubx/AbdA-Exd increased (Figure 3). These data imply that Hox-Exd complexes display, at least in vitro, a tradeoff between binding affinity and specificity.

To test whether this affinity-specificity tradeoff holds in vivo, we generated *E3N* transgenic variants in which we varied the affinity of the Ubx-Exd binding sites according to the relative affinities predicted by SELEX-seq (Figure 4A) (Slattery et al., 2011). Although none of the binding sites found in the native *svb* enhancer were identified by SELEX-seq, we estimate (based on the core 8-mer) that they have relative affinities <0.03 (Slattery et al., 2011). Every mutation that increased the affinity of Ubx-Exd sites resulted in qualitative or quantitative changes in *E3N* enhancer expression (Figure 4). For example, converting either native sites 1 or 2 to high-affinity sites (scores of 0.87 or 0.79, respectively) resulted in increased expression in the normal domain of *E3N* and ectopic expression anteriorly and dorsally (Figures 4C and 4D). Replacing site 3 in *E3N* with the highest affinity site (score of 1.0) also resulted in ectopic expression in anterior segments and in the intestine (Figure 4B). We further explored the functional consequences of gradually increasing the affinity of a Hox-Exd binding site by replacing site 3 with sites that have a range of relative affinities, from 0.06 to 0.72. A small increase in affinity to 0.06 resulted in higher levels of *E3N* expression within its normal expression domain (Figures 4H and 4I). Increasing the affinity to 0.25, 0.65, and 0.72 altered levels of expression in the normal domains of *E3N* and induced ectopic expression in anterior segments (white arrows in Figures 4E–4G).

We also observed strong position effects of a high affinity site, similar to observations in a previous study (Swanson et al., 2010). Placing the highest affinity site 5' of the *E3N* enhancer resulted in ectopic expression in anterior segments, but decreased expression in the normal domain (Figure S6B). In contrast, placing this site inside the enhancer increased expression in the normal domain and generated ectopic expression in multiple regions (Figure S6C). We cannot rule out the possibility, however, that

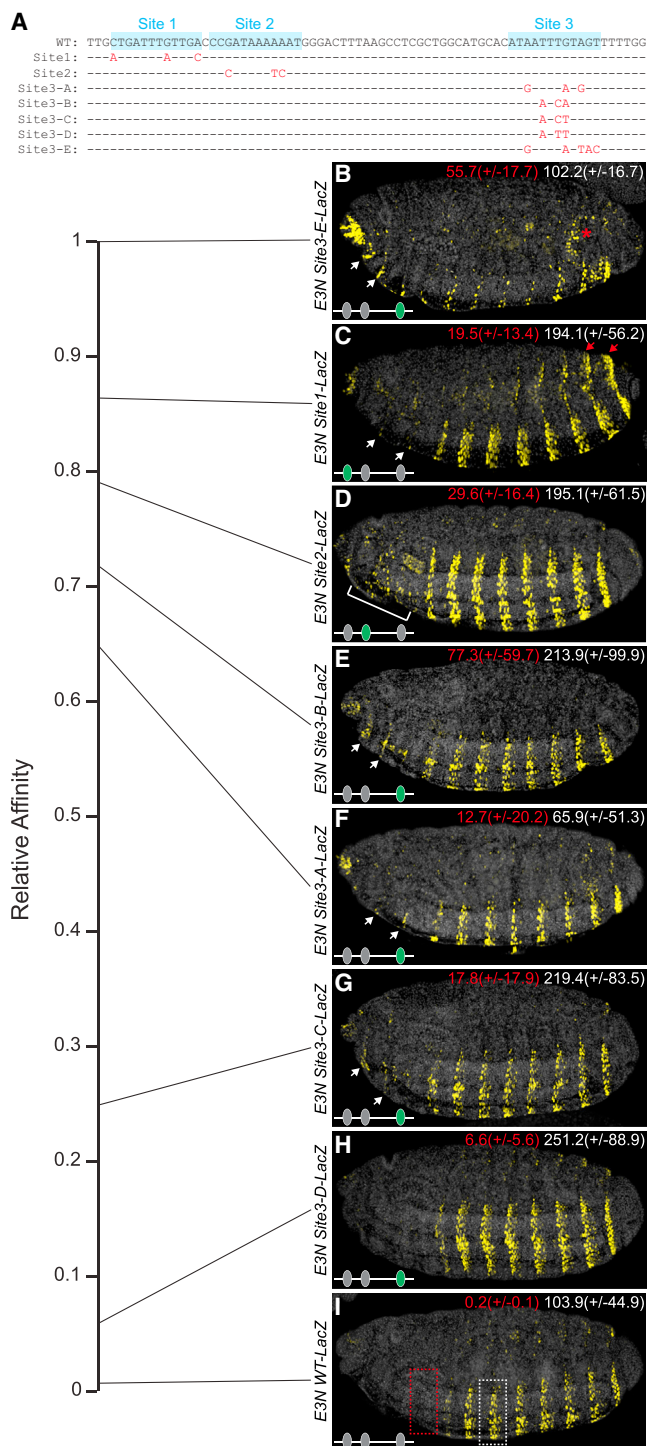


Figure 4. Conversion of Low Affinity Ubx-Exd Binding Sites to Higher Affinity Sites Results in Ectopic Expression

(A) Aligned E3N sequences from wild-type and mutated sequences. Dashes and red letters indicate unaltered and modified sequence, respectively.

(B–I) Embryos carrying E3N::lacZ constructs, with Ubx-Exd sites altered as indicated in (A). The numbers in the top right of each panel indicate the average levels of expression in the regions outlined in (I) ($n = 10$ for each genotype), measured in arbitrary units of fluorescence intensity. Numbers in parentheses

these position-dependent effects resulted from the creation or destruction of binding sites for additional factors.

Taken together, these results indicate that Hox-Exd sites with higher affinity than the native sites alter the specificity of the *svb* enhancer, demonstrating that the affinity-specificity tradeoff that was inferred from in vitro data also pertains in vivo.

High Affinity Hox Binding Sites Decreased the Specificity of Enhancer Function

Replacement of native sites with high affinity sites caused ectopic expression mostly outside of the domains of *Ubx* and *abdA* expression (Figure S5), suggesting that these high affinity sites bound transcription factors other than *Ubx* and *AbdA*. Indeed, in embryos deficient for *Ubx*, the E3N enhancers with high affinity binding sites showed the expected reduction of expression in A1 (where *Ubx* is the only Hox gene active), but they also continued to drive ectopic expression in anterior segments (Figures 5A–5D).

Sex comb reduced (*Scr*) was an attractive candidate for driving some of the ectopic anterior expression of *svb* enhancers carrying high-affinity sites. *Scr* is expressed in anterior segments (Kuroiwa et al., 1985) and SELEX-seq data indicated that *Scr*-Exd can bind to high-affinity *Ubx*/Exd binding sites (Slattery et al., 2011). When assayed on the E3N *svb* enhancer, *Scr*-Exd showed little or no in vitro binding to the native E3N sites, but it bound to the high affinity sites even more strongly than *Ubx*-Exd bound to the native sites (Figure 5E). In vivo, uniform expression of *Scr* produced no obvious changes in the expression of wild-type E3N (Figures 5F and 5G), but drove ectopic expression of E3N variants that carried one high-affinity site (Figures 5H–5K). Thus, replacing low affinity *Ubx*/Exd sites with high-affinity sites enabled the E3N enhancer to respond to *Scr*. In addition to *Scr*, it is likely that other homeodomain transcription factors bind and activate the E3N enhancers carrying high-affinity sites to generate their broad domains of ectopic expression.

Together, our results indicate that the native low affinity *Ubx*/Exd binding sites in the E3N enhancer confer specificity for *Ubx*-Exd and *AbdA*-Exd over other Hox proteins, such as *Scr*, and probably over additional homeodomain factors.

Clusters of HOX Binding Sites Confer Robustness to Genetic and Environmental Variability

As discussed earlier, some of the *Ubx*/Exd binding sites in the E3N and 7H enhancers can be mutated with minimal effects on reporter gene expression (Figures 2 and S4). It is not clear, therefore, why these enhancers contain multiple Hox binding sites. We wondered if the multiple, apparently redundant, *Ubx*-Exd binding sites within individual *svb* enhancers contribute to transcriptional robustness, in the same way that multiple enhancers of *svb* confer robustness in the face of environmental and genetic variation (Frankel et al., 2010).

indicate ± 1 SD. White arrows and brackets denote expression in domains anterior to segment A1 (B–G). The red asterisk marks ectopic staining in the intestine; red arrows indicate ectopic dorsal and lateral expression (C). See also Figure S6 and Table S1.

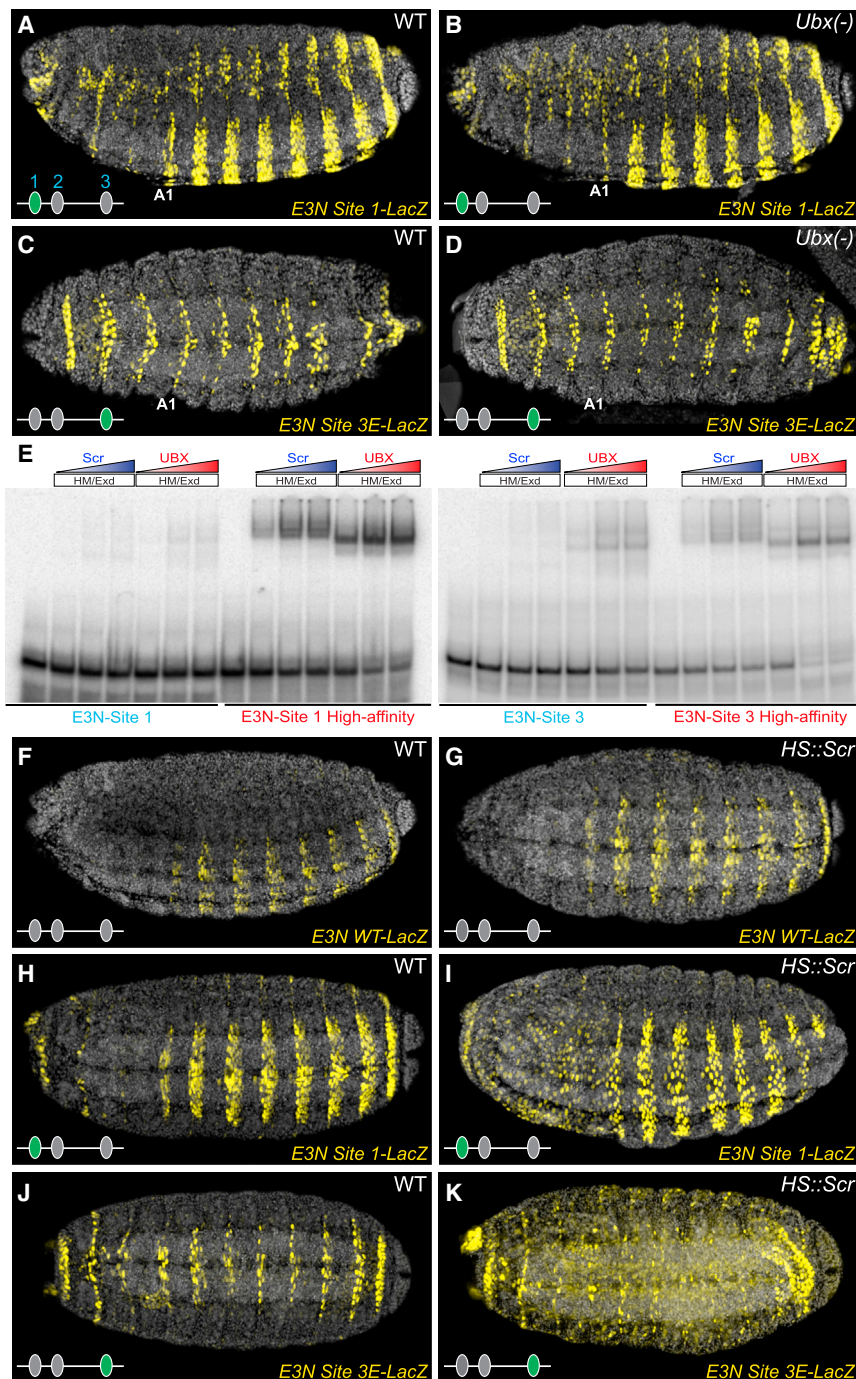


Figure 5. Low Affinity Ubx-Exd Binding Sites Provide High Ubx-Exd Specificity

(A–D) Embryos carrying *E3N::lacZ* constructs, with Ubx-Exd sites altered as indicated in (Figure 4A). In embryos deficient for Ubx, *E3N::lacZ* with high affinity sites drove extensive ectopic expression (B and D).

(E) Scr-Exd did not bind to wild-type *E3N* Ubx-Exd sites in vitro, as demonstrated with EMSAs. However, both Scr-Exd and Ubx-Exd bound to high-affinity Ubx-Exd sites.

(F–K) Ubiquitous expression of Scr (*hs::Scr*) did not alter expression of the wild-type *E3N::lacZ* (G), but caused ectopic expression of *E3N::lacZ* carrying high-affinity Ubx-Exd sites (I and K).

See also Tables S1 and S2.

results indicate that *E3N* requires multiple sites to confer robustness when *Ubx* dose is perturbed. The reduced activity of these *E3N* enhancers in *Ubx* heterozygotes also provides further evidence that the Ubx-Exd binding sites respond to Ubx in vivo.

Next, we assayed the effects of environmental variation on enhancer activity by exploiting the fact that *svb* enhancers driving a *svb* cDNA in *svb* null embryos provide a sensitive and quantitative readout of enhancer function (Frankel et al., 2010, 2011). We reared embryos at 17°C and 32°C, temperature extremes that are still compatible with normal development (Powsner, 1935). In embryos carrying the wild-type *E3N::svb* rescue construct, trichome numbers were relatively invariant to temperature extremes (Figure 6C'). In contrast, enhancers containing a single mutated Ubx/Exd binding site showed reduced rescue of trichomes at extreme temperatures (Figure 6C'). Furthermore, the simultaneous mutation of site 1 and 2 abrogated trichome rescue at extreme temperatures, while other double or triple combinations led to no rescue (Figure 6C').

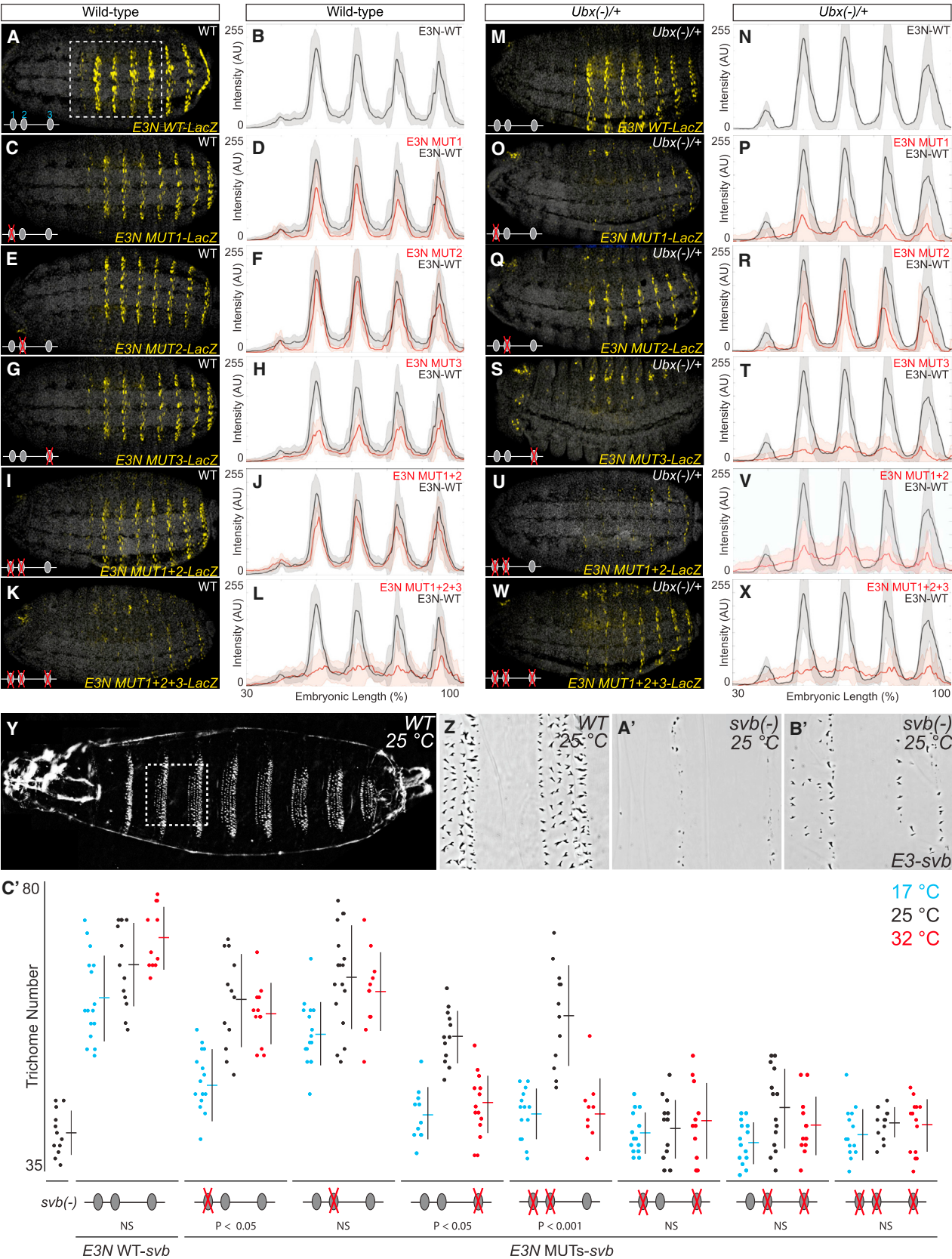
These results indicate that multiple Ubx-Exd binding sites are required for

To test this hypothesis, first we examined the effects of altered levels of Ubx on the expression of *E3N* enhancers. The wild-type *E3N* enhancer drove normal expression in embryos heterozygous for an *Ubx* null mutation (Figures 6A, 6B, 6M, and 6N). In contrast, all *E3N* enhancers that contained single mutations in the Ubx-Exd binding sites drove dramatically lower levels of expression in *Ubx* heterozygotes, compared to wild-type embryos (Figures 6C–6T). Similar effects were observed for most combinations of the mutations (Figures 6I, 6J, 6U, and 6V). These

normal enhancer function and to cope with variable genetic backgrounds and environments, similar to conditions faced by flies in the wild.

Ubx Binds a Cluster of Low Affinity Binding Sites in the Orthologous *E3N* Enhancer from a Distantly Related Species

We wondered whether the enhancer architecture discovered for *E3N* and *7H*, with homotypic clusters of low affinity Hox-Exd



(legend on next page)

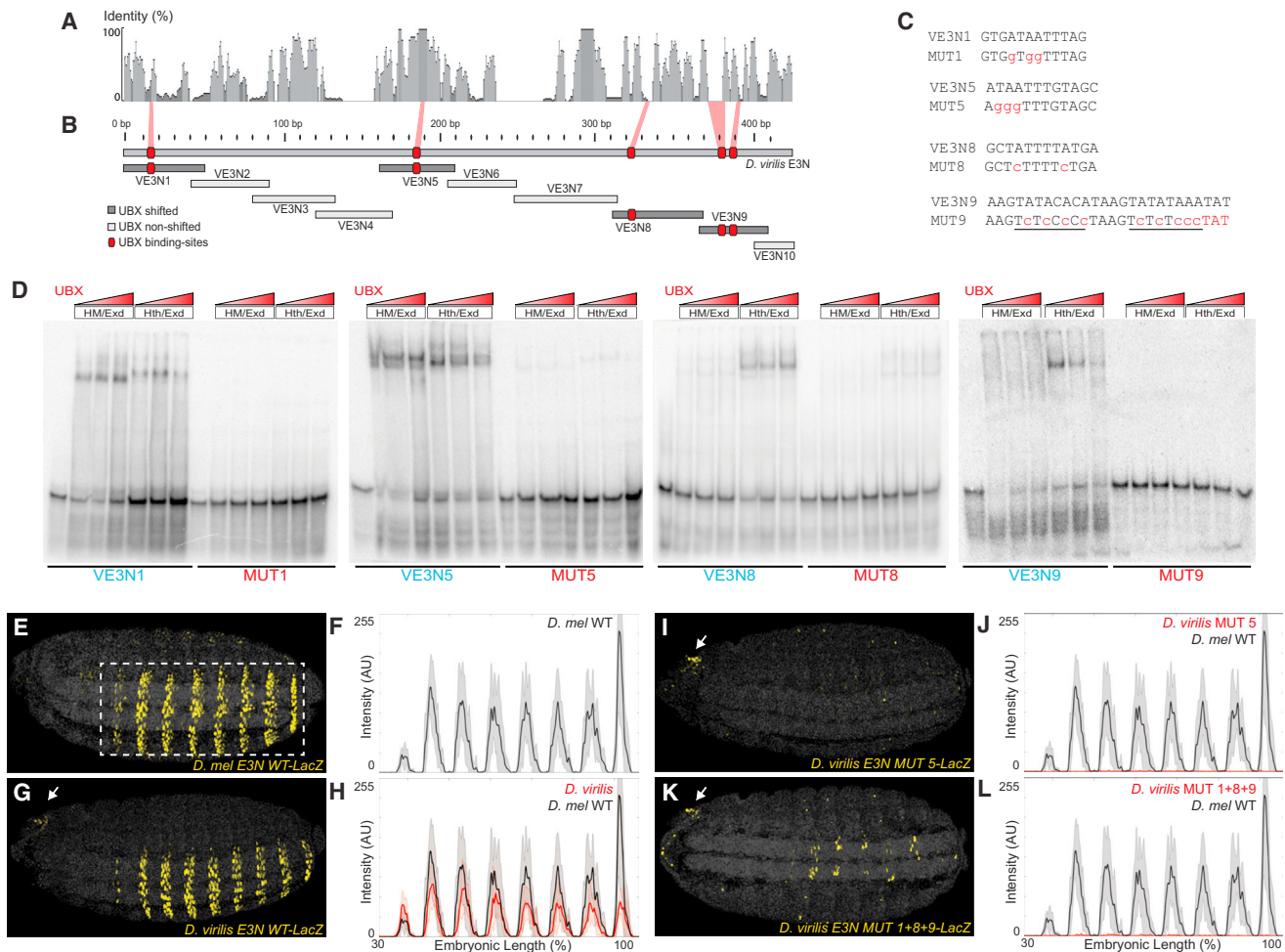


Figure 7. Multiple Low Affinity Poorly Conserved Ubx-Exd Binding Sites Regulate the *Drosophila virilis* E3N Enhancer

(A) Sequence conservation over a 10 bp sliding window for a sequence alignment of the E3N region from ten *Drosophila* species.
 (B) Regions tested for the ability to bind Ubx-Exd, assayed via EMSAs (see also Figure S7). The positions of the Ubx-Exd sites are indicated with red boxes.
 (C) E3N Ubx-Exd binding-site sequences aligned with site-specific mutations indicated in lowercase, red letters.
 (D) Ubx-Hth^{FL}-Exd and Ubx-Hth^{HM}-Exd bound five sites in the *D. virilis* E3N enhancer, as demonstrated with EMSAs (see also Figure S7). This binding was reduced when the sites were mutated (MUT).
 (E–L) Embryos carrying E3N::LacZ constructs, with Ubx-Exd sites altered as indicated in (C), juxtaposed with plots of average expression (n = 10 for each genotype). Black lines denote expression driven by the *D. melanogaster* and *D. virilis* enhancers, respectively.
 See also Tables S1 and S2.

sites, is an evolutionarily conserved feature of *svb* enhancers. Because the large-scale *cis*-regulatory landscape of *svb* has been well conserved in *Drosophila virilis* (Frankel et al., 2012), we examined this question by focusing on the E3N region of *D. virilis*.

Drosophila melanogaster and *D. virilis* last shared a common ancestor ~40 mya and the E3N region displays little sequence conservation between these species (Figure 7A). We thus employed EMSAs to identify, in an unbiased manner, all of the Ubx-Exd binding sites putatively present in the *D. virilis* E3N

Figure 6. The *svb* E3N Enhancer Contains a Cluster of Ubx-Exd Binding Sites that Confer Robustness against Environmental and Genetic Variation

(A–X) Wild-type (A–L) and Ubx heterozygote (M–X) embryos carrying E3N::LacZ constructs with Ubx-Exd sites altered as indicated in Figure 2B, juxtaposed with plots of average expression in the region outlined in (D) (n = 10 for each genotype). Shaded bounding areas indicate ± 1 SD. AU, arbitrary units of fluorescence intensity.
 (Y–B') Cuticle preps showing that the E3N::*svb* transgene (B') in a *svb* null mutant background rescued a subset of the wild-type trichome pattern (cf. Y–A').
 (C') The number of trichomes in the larval A2 segment for the corresponding genotypes. The error bars indicate ± 1 SD. Significance values are sequential Bonferroni test p values, to control the type I error rate, from separate ANOVA tests for each genotype.
 See also Table S1.

orthologous region (*VE3N*). We found that four fragments—*VE3N1*, *VE3N2*, *VE3N5*, and *VE3N9*—bound Ubx-Exd in vitro (Figures 7B–7D). Comprehensive mutagenesis of these fragments revealed five Ubx-Exd binding sites (Figures 7B, 7C, and S7). One of these sites is evolutionarily conserved and four sites display no sequence conservation to *D. melanogaster* and only weak conservation to closely related species (Figure 7A). As observed for *D. melanogaster*, none of the Ubx-Exd binding sites of *VE3N* were detected by SELEX-seq, indicating that they are low affinity sites.

We next tested whether these Ubx-Exd sites function in vivo by generating transgenic *D. melanogaster* lines that contained either the wild-type or mutated *D. virilis* *VE3N* enhancers. The wild-type *VE3N* enhancer drove lower levels of expression than did its *D. melanogaster* *E3N* counterpart (Figures 7E–7H), a result observed often in tests of orthologous enhancers (Crocker et al., 2008; Ludwig et al., 1998). Mutation of the conserved site present in *VE3N* resulted in the loss of reporter expression (Figures 7I and 7J). To test if only this site was required for *VE3N* expression, we mutated the four nonconserved sites, leaving the conserved site intact. This reporter also displayed very little *VE3N* activity (Figures 7K and 7L). Therefore, multiple Ubx-Exd binding sites, at least some of which are poorly conserved, contribute to the proper regulation of the *D. virilis* *VE3N* enhancer.

Taken together, these results indicate that clustering of low affinity Ubx-Exd sites is an evolutionarily conserved strategy used by *svb* enhancers, although many of the individual binding sites are not conserved across species.

DISCUSSION

We have demonstrated that the Hox protein Ubx regulates separate enhancers of the *svb* gene by binding, with its cofactors Exd and Hth, to clusters of low affinity binding sites. Combining in vitro and in vivo assays, we provided experimental demonstration of an affinity-specificity tradeoff for Hox proteins, such that enhancers that integrate Hox inputs to drive regionalized expression are unlikely to utilize high affinity Hox binding sites. Forced to utilize low affinity sites, enhancers have evolved to contain multiple binding sites to ensure regulatory robustness to genetic and environmental variations. Most individual Ubx-Exd sites have evolved rapidly, but evolution has conserved overall enhancer architecture, with clusters of low affinity sites.

Homotypic clusters of transcription factor binding sites are pervasive in animal genomes (Arnone and Davidson, 1997; Gotea et al., 2010; Lifanov et al., 2003; Ochoa-Espinosa et al., 2005; Papatsenko et al., 2002; Stanojevic et al., 1991) and several models have been proposed to explain their existence (Doniger et al., 2005; Giorgetti et al., 2010; He et al., 2012; Segal et al., 2008). Our results provide experimental evidence that homotypic clusters of Hox binding sites can confer robustness to enhancers. This may reflect a more widespread phenomenon. Although many enhancers contain homotypic clusters with low affinity sites, previous studies have rarely detected changes in expression by deleting individual binding sites (Doniger and Fay, 2007; Driever and Nüsslein-Volhard, 1989; Estella et al., 2008; Giorgianni and Mann, 2011; Hersh and Carroll, 2005; Sar-

amäki et al., 2006; Stanojevic et al., 1991). However, these mutated enhancers have not been tested in variable environments. It is possible that many of these clustered sites confer regulatory robustness.

It is useful to compare our results with previous studies that have demonstrated specific regulatory functions for homotypic clusters. For example, clustered binding sites in an enhancer of the *Drosophila hunchback* gene mediate cooperative DNA binding by Bicoid, which provides threshold-dependent enhancer activity (Driever et al., 1989; Lebrecht et al., 2005; Struhl et al., 1989). In other cases, clusters of homotypic binding sites act in a noncooperative manner to allow enhancers to respond in a graded fashion (Giorgetti et al., 2010), for example to determine expression levels in response to transcription factor concentrations (Driever et al., 1989; Gaudet and Mango, 2002; Rowan et al., 2010). It is worth noting that in these cases, where homotypic clusters mediate specific linear or nonlinear outputs, enhancers are bound by transcription factors that belong to small paralogous families: e.g., two paralogs for Msn2 (Hasan et al., 2002); three for p53 (Belyi et al., 2010); two for Dorsal (Silverman and Maniatis, 2001); and five for NFκB (Silverman and Maniatis, 2001). In contrast, there are 84 homeodomain-containing proteins encoded in the *Drosophila* genome, many with overlapping specificities (Berger et al., 2008; Noyes et al., 2008). Therefore, in previously described examples of homotypic clusters, binding affinity may not be a strong constraint on specificity.

For the Hox regulated *svb* enhancers, low affinity Ubx/AbdA-Exd binding sites enable specificity, while the clustering of low affinity sites confers phenotypic robustness. This is a fundamentally different constraint on clustered binding sites than observed in all previous examples. The affinity-specificity tradeoff, initially supported by our computational analysis of in vitro data, was confirmed in vivo by progressively increasing the affinity of the Ubx-Exd binding sites. While replacement of low affinity sites with higher affinity sites always quantitatively altered enhancer activity, either positively or negatively, most higher affinity sites generated strong ectopic expression. As we show, this ectopic expression is driven, at least in part, by gaining the binding of additional Hox proteins, which are normally not involved in the regulation of these enhancers. Other studies have performed replacement of low affinity sites with higher affinity sites and, in some cases, they have also observed ectopic expression (Busser et al., 2012; Driever et al., 1989; Gaudet and Mango, 2002; Jiang and Levine, 1993; Peterson et al., 2012; Ramos and Barolo, 2013; Scardigli et al., 2003; Stewart-Ornstein et al., 2013; Struhl et al., 1989). These altered patterns of expression may reflect increased sensitivity of enhancers to the same transcription factor that binds to the wild-type enhancer (Jiang and Levine, 1993). We observed a similar effect for Ubx and AbdA-dependent upregulation of *svb* enhancers in the cells in which they are normally expressed. In addition, however, we found that sites with higher affinity resulted in a reduced specificity, due to the binding of additional homeodomain proteins, such as Scr, to *svb* enhancers. Our computational analyses suggest that this affinity-specificity tradeoff is a fundamental property of Hox proteins and would therefore influence the architecture of enhancers that must generate specific outputs in response to Hox factors. We suggest that transcription factors

that belong to other large paralog groups may exhibit a similar affinity-specificity tradeoff and that enhancers regulated by these factors may also exploit clusters of low affinity sites.

Our results help to explain previous difficulties with bioinformatic prediction of functional Hox binding sites, because low affinity sites are difficult to detect reliably. Indeed, the low affinity sites that implement Hox regulation within *svb* enhancers share little similarity with canonical Hox or Hox-Exd binding sites. Consequently, a very large number of seemingly disparate DNA sequences can confer low affinity binding for Hox proteins. If Hox-Exd sites are often clustered in the genome, then signals from genome-wide chromatin immunoprecipitation sequencing (ChIP-seq) will reflect binding to the entire cluster (as we observed) and the signals associated with individual low affinity sites may be difficult to discern from noise. Identification of important low affinity sites will require a change in computational approaches to analyzing genome-wide data. Currently, it is de rigueur to apply an arbitrary threshold to genome-wide data and then to analyze only signals above this threshold. This approach is likely to bias detection toward high affinity sites, whose functions may be distinct from those of clusters of low affinity sites.

Our findings provide insight into how different Hox proteins regulate specific target genes to generate phenotypic diversity across the anterior-posterior axis. One unanswered question is how the many low affinity DNA sequences, which appear to share little in common, are bound by the same Hox-Exd complex with apparently similar affinity. It is possible that variations in DNA shape (deviations from the structure of canonical B-DNA) influence Hox-Exd binding to low affinity sites (Dror et al., 2014; Joshi et al., 2007; Rohs et al., 2009). It remains unclear if very different sequences can adopt similar shapes, or whether instead the Hox-Exd complex can recognize a range of shapes. Resolution of this question will require structural studies of Hox-Exd complexes bound to a range of low affinity DNA sequences and quantitative analysis of their binding dynamics in vivo.

EXPERIMENTAL PROCEDURES

Fly Strains and Transgenic Constructs

DNA fragments were cloned into the reporter constructs *placZattB* and *pHSPattB GFP* and the *pRSQsvb* rescue construct (Frankel et al., 2011) (see Table S1). Mutations were introduced using site-directed mutagenesis (Genescript). Plasmids were integrated into the *attP2* landing site by Rainbow Transgenic Flies. Additional strains used were: *svb^{FR9}/FM7c twi::GFP* (Delon et al., 2003); *HS::Ubx-1; Ubx¹; hth^{P2}* (Noro et al., 2006); and *Ubx¹abdA^{D24}AbdB^{D18}* (Bloomington stock 1108).

Embryo Staining and Cuticles

Stage 15/16 embryos were collected, fixed, and stained using standard protocols with mouse anti-βGal (1:1,000, Promega) and anti-mouse AlexaFluor (1:500, Invitrogen) antibodies. Cuticles were prepared following standard protocols, imaged with phase-contrast microscopy, and ventral trichomes in larval A2 segments were counted.

Image Analysis

Embryos carrying reporter constructs were imaged on a Leica SPE Confocal Microscope. Sum projections of confocal stacks were assembled, images were scaled, background was subtracted using a 50-pixel rolling-ball radius and plot profiles of fluorescence intensity were analyzed using ImageJ software (<http://rsb.info.nih.gov/ij>). Data from the plot profiles were analyzed further in MATLAB (<http://www.mathworks.com>) (Crocker and Stern, 2013).

In Vitro Affinity-Specificity Tradeoff Calculations

Average relative affinities of 12mers from SELEX-seq data (Slattery et al., 2011) were calculated for four pairs of Hox-Exd complexes that share similar binding preferences: (1) Labial and Pb, (2) Dfd and Scr, (3) Antp and AbdB, and (4) Ubx and AbdA. Specificity groups (colored bars in Figure 3) were defined as having an average relative affinity ≥ 0.05 for bound complexes and <0.03 for unbound complexes. The proportion and total number of sequences in each specificity group were calculated for ten bins based on their Ubx/AbdA-Exd relative affinities.

DNA Alignments

Multiple sequence alignments were performed using Geneious (<http://www.geneious.com>) with MUSCLE alignment algorithms (anchor optimized).

Protein Purification and EMSAs

Ubx (isoform IVa), *abdA*, *Hth^{HM}-Exd*, and *Hth^{FL}-Exd* constructs, protein purification, and EMSA conditions were described previously (Lelli et al., 2011). Further experimental details are provided in Table S2.

SUPPLEMENTAL INFORMATION

Supplemental Information includes seven figures and two tables and can be found with this article online at <http://dx.doi.org/10.1016/j.cell.2014.11.041>.

AUTHOR CONTRIBUTIONS

The experimental plan was conceived by J.C., N.A., R.S.M., and D.L.S. Most in vivo assays were performed by J.C. All in vitro assays and computational analysis were performed by N.A., assisted by L.R. and R.S.M. A.P.M., A.A., P.V., S.P., F.P., and D.L.S. defined the minimal enhancer elements. N.F. and S.W. performed some in vivo assays. J.C. assembled all figures. J.C., R.S.M., and D.L.S. wrote the paper, with input from N.A., A.P.M., N.F., S.W., S.P., and, especially, from F.P.

ACKNOWLEDGMENTS

We thank A. Sterling for technical assistance with EMSA experiments, A. Lemire and V. FitzPatrick for bioinformatics assistance, E. Preger for use of her 7::GFP reporter construct, and J. Cande, Y. Ding, A. Lemire, J. Mast, E. Preger, and T. Shirangi for helpful discussions. This work was supported in part by NIH grant GM054510 to R.S.M. and ANR grant (ChronoNet) to F.P.

Received: June 5, 2014

Revised: September 11, 2014

Accepted: November 13, 2014

Published: December 31, 2014

REFERENCES

- Akam, M. (1989). Hox and HOM: homologous gene clusters in insects and vertebrates. *Cell* 57, 347–349.
- Arnold, M.I., and Davidson, E.H. (1997). The hardwiring of development: organization and function of genomic regulatory systems. *Development* 124, 1851–1864.
- Belyi, V.A., Ak, P., Markert, E., Wang, H., Hu, W., Puzio-Kuter, A., and Levine, A.J. (2010). The origins and evolution of the p53 family of genes. *Cold Spring Harb. Perspect. Biol.* 2, a001198.
- Berger, M.F., Badis, G., Gehrke, A.R., Talukder, S., Philippakis, A.A., Peña-Castillo, L., Alleyne, T.M., Mnaimneh, S., Botvinnik, O.B., Chan, E.T., et al. (2008). Variation in homeodomain DNA binding revealed by high-resolution analysis of sequence preferences. *Cell* 133, 1266–1276.
- Busser, B.W., Shokri, L., Jaeger, S.A., Gisselbrecht, S.S., Singhania, A., Berger, M.F., Zhou, B., Bulyk, M.L., and Michelson, A.M. (2012). Molecular mechanism underlying the regulatory specificity of a Drosophila homeodomain protein that specifies myoblast identity. *Development* 139, 1164–1174.

- Chan, S.-K.K., Jaffe, L., Capovilla, M., Botas, J., and Mann, R.S. (1994). The DNA binding specificity of Ultrabithorax is modulated by cooperative interactions with extradenticle, another homeoprotein. *Cell* 78, 603–615.
- Chang, C.P., Shen, W.F., Rozenfeld, S., Lawrence, H.J., Largman, C., and Cleary, M.L. (1995). Pbx proteins display hexapeptide-dependent cooperative DNA binding with a subset of Hox proteins. *Genes Dev.* 9, 663–674.
- Chanut-Delalande, H., Fernandes, I., Roch, F., Payre, F., and Plaza, S. (2006). Shavenbaby couples patterning to epidermal cell shape control. *PLoS Biol.* 4, e290.
- Choo, S.W., White, R., and Russell, S. (2011). Genome-wide analysis of the binding of the Hox protein Ultrabithorax and the Hox cofactor Homothorax in *Drosophila*. *PLoS ONE* 6, e14778.
- Coiffier, D., Charroux, B., and Kerridge, S. (2008). Common functions of central and posterior Hox genes for the repression of head in the trunk of *Drosophila*. *Development* 135, 291–300.
- Crocker, J., and Stern, D.L. (2013). TALE-mediated modulation of transcriptional enhancers in vivo. *Nat. Methods* 10, 762–767.
- Crocker, J., Tamori, Y., and Erives, A. (2008). Evolution acts on enhancer organization to fine-tune gradient threshold readouts. *PLoS Biol.* 6, e263.
- Delon, I., Chanut-Delalande, H., and Payre, F. (2003). The Ovo/Shavenbaby transcription factor specifies actin remodelling during epidermal differentiation in *Drosophila*. *Mech. Dev.* 120, 747–758.
- Doniger, S.W., and Fay, J.C. (2007). Frequent gain and loss of functional transcription factor binding sites. *PLoS Comput. Biol.* 3, e99.
- Doniger, S.W., Huh, J., and Fay, J.C. (2005). Identification of functional transcription factor binding sites using closely related *Saccharomyces* species. *Genome Res.* 15, 701–709.
- Driever, W., and Nüsslein-Volhard, C. (1989). The bicoid protein is a positive regulator of hunchback transcription in the early *Drosophila* embryo. *Nature* 337, 138–143.
- Driever, W., Thoma, G., and Nüsslein-Volhard, C. (1989). Determination of spatial domains of zygotic gene expression in the *Drosophila* embryo by the affinity of binding sites for the bicoid morphogen. *Nature* 340, 363–367.
- Dror, I., Zhou, T., Mandel-Gutfreund, Y., and Rohs, R. (2014). Covariation between homeodomain transcription factors and the shape of their DNA binding sites. *Nucleic Acids Res.* 42, 430–441.
- Estella, C., McKay, D.J., and Mann, R.S. (2008). Molecular integration of wingless, decapentaplegic, and autoregulatory inputs into Distalless during *Drosophila* leg development. *Dev. Cell* 14, 86–96.
- Frankel, N., Davis, G.K., Vargas, D., Wang, S., Payre, F., and Stern, D.L. (2010). Phenotypic robustness conferred by apparently redundant transcriptional enhancers. *Nature* 466, 490–493.
- Frankel, N., Erezylmaz, D.F., McGregor, A.P., Wang, S., Payre, F., and Stern, D.L. (2011). Morphological evolution caused by many subtle-effect substitutions in regulatory DNA. *Nature* 474, 598–603.
- Frankel, N., Wang, S., and Stern, D.L. (2012). Conserved regulatory architecture underlies parallel genetic changes and convergent phenotypic evolution. *Proc. Natl. Acad. Sci. USA* 109, 20975–20979.
- Gaudet, J., and Mango, S.E. (2002). Regulation of organogenesis by the *Caenorhabditis elegans* FoxA protein PHA-4. *Science* 295, 821–825.
- Giorgetti, L., Siggers, T., Tiana, G., Caprara, G., Notarbartolo, S., Corona, T., Pasparakis, M., Milani, P., Bulyk, M.L., and Natoli, G. (2010). Noncooperative interactions between transcription factors and clustered DNA binding sites enable graded transcriptional responses to environmental inputs. *Mol. Cell* 37, 418–428.
- Giorgianni, M.W., and Mann, R.S. (2011). Establishment of medial fates along the proximodistal axis of the *Drosophila* leg through direct activation of dachshund by Distalless. *Dev. Cell* 20, 455–468.
- González-Reyes, A., and Morata, G. (1990). The developmental effect of overexpressing a Ubx product in *Drosophila* embryos is dependent on its interactions with other homeotic products. *Cell* 61, 515–522.
- Gotea, V., Visel, A., Westlund, J.M., Nobrega, M.A., Pennacchio, L.A., and Ovcharenko, I. (2010). Homotypic clusters of transcription factor binding sites are a key component of human promoters and enhancers. *Genome Res.* 20, 565–577.
- Hasan, R., Leroy, C., Isnard, A.-D., Labarre, J., Boy-Marcotte, E., and Toledano, M.B. (2002). The control of the yeast H₂O₂ response by the Msn2/4 transcription factors. *Mol. Microbiol.* 45, 233–241.
- He, X., Duque, T.S.P.C., and Sinha, S. (2012). Evolutionary origins of transcription factor binding site clusters. *Mol. Biol. Evol.* 29, 1059–1070.
- Hersh, B.M., and Carroll, S.B. (2005). Direct regulation of knot gene expression by Ultrabithorax and the evolution of cis-regulatory elements in *Drosophila*. *Development* 132, 1567–1577.
- Jiang, J., and Levine, M. (1993). Binding affinities and cooperative interactions with bHLH activators delimit threshold responses to the dorsal gradient morphogen. *Cell* 72, 741–752.
- Joshi, R., Passner, J.M., Rohs, R., Jain, R., Sosinsky, A., Crickmore, M.A., Jacob, V., Aggarwal, A.K., Honig, B., and Mann, R.S. (2007). Functional specificity of a Hox protein mediated by the recognition of minor groove structure. *Cell* 131, 530–543.
- Jürgens, G., Wieschaus, E., Nüsslein-Volhard, C., and Kluding, H. (1984). Mutations affecting the pattern of the larval cuticle in *Drosophila melanogaster*. II. Zygotic loci on the third chromosome. *Roux Arch. Dev. Biol.* 193, 283–295.
- Karch, F., Bender, W., and Weiffenbach, B. (1990). abdA expression in *Drosophila* embryos. *Genes Dev.* 4, 1573–1587.
- Kuroiwa, A., Kloter, U., Baumgartner, P., and Gehring, W.J. (1985). Cloning of the homeotic Sex combs reduced gene in *Drosophila* and in situ localization of its transcripts. *EMBO J.* 4 (13B), 3757–3764.
- Lebrecht, D., Foehr, M., Smith, E., Lopes, F.J.P., Vanario-Alonso, C.E., Reinitz, J., Burz, D.S., and Hanes, S.D. (2005). Bicoid cooperative DNA binding is critical for embryonic patterning in *Drosophila*. *Proc. Natl. Acad. Sci. USA* 102, 13176–13181.
- Lelli, K.M., Noro, B., and Mann, R.S. (2011). Variable motif utilization in homeotic selector (Hox)-cofactor complex formation controls specificity. *Proc. Natl. Acad. Sci. USA* 108, 21122–21127.
- Lewis, E.B. (1978). A gene complex controlling segmentation in *Drosophila*. *Nature* 276, 565–570.
- Lifanov, A.P., Makeev, V.J., Nazina, A.G., and Papatsenko, D.A. (2003). Homotypic regulatory clusters in *Drosophila*. *Genome Res.* 13, 579–588.
- Ludwig, M.Z., Patel, N.H., and Kreitman, M. (1998). Functional analysis of eve stripe 2 enhancer evolution in *Drosophila*: rules governing conservation and change. *Development* 125, 949–958.
- Mann, R.S., and Hogness, D.S. (1990). Functional dissection of Ultrabithorax proteins in *D. melanogaster*. *Cell* 60, 597–610.
- Mann, R.S., Lelli, K.M., and Joshi, R. (2009). Hox specificity unique roles for cofactors and collaborators. *Curr. Top. Dev. Biol.* 88, 63–101.
- McGinnis, W., and Krumlauf, R. (1992). Homeobox genes and axial patterning. *Cell* 68, 283–302.
- McGregor, A.P., Orgogozo, V., Delon, I., Zanet, J., Srinivasan, D.G., Payre, F., and Stern, D.L. (2007). Morphological evolution through multiple cis-regulatory mutations at a single gene. *Nature* 448, 587–590.
- Moens, C.B., and Selleri, L. (2006). Hox cofactors in vertebrate development. *Dev. Biol.* 291, 193–206.
- Noro, B., Culi, J., McKay, D.J., Zhang, W., and Mann, R.S. (2006). Distinct functions of homeodomain-containing and homeodomain-less isoforms encoded by homothorax. *Genes Dev.* 20, 1636–1650.
- Noyes, M.B., Christensen, R.G., Wakabayashi, A., Stormo, G.D., Brodsky, M.H., and Wolfe, S.A. (2008). Analysis of homeodomain specificities allows the family-wide prediction of preferred recognition sites. *Cell* 133, 1277–1289.
- Ochoa-Espinosa, A., Yucel, G., Kaplan, L., Pare, A., Pura, N., Oberstein, A., Papatsenko, D., and Small, S. (2005). The role of binding site cluster strength in Bicoid-dependent patterning in *Drosophila*. *Proc. Natl. Acad. Sci. USA* 102, 4960–4965.

- Pai, C.Y., Kuo, T.S., Jaw, T.J., Kurant, E., Chen, C.T., Bessarab, D.A., Salzberg, A., and Sun, Y.H. (1998). The Homothorax homeoprotein activates the nuclear localization of another homeoprotein, extradenticle, and suppresses eye development in *Drosophila*. *Genes Dev.* 12, 435–446.
- Papatsenko, D.A., Makeev, V.J., Lifanov, A.P., Régnier, M., Nazina, A.G., and Desplan, C. (2002). Extraction of functional binding sites from unique regulatory regions: the *Drosophila* early developmental enhancers. *Genome Res.* 12, 470–481.
- Payre, F., Vincent, A., and Carreno, S. (1999). *ovo/svb* integrates Wingless and DER pathways to control epidermis differentiation. *Nature* 400, 271–275.
- Peifer, M., and Wieschaus, E. (1990). Mutations in the *Drosophila* gene *extradenticle* affect the way specific homeo domain proteins regulate segmental identity. *Genes Dev.* 4, 1209–1223.
- Peterson, K.A., Nishii, Y., Ma, W., Vedenko, A., Shokri, L., Zhang, X., McFarlane, M., Baizabal, J.M., Junker, J.P., van Oudenaarden, A., et al. (2012). Neural-specific Sox2 input and differential Gli-binding affinity provide context and positional information in Shh-directed neural patterning. *Genes Dev.* 26, 2802–2816.
- Powsner, L. (1935). The effects of temperature on the durations of the developmental stages of *Drosophila melanogaster*. *Physiol. Zool.* 8, 474–520.
- Ramos, A.I., and Barolo, S. (2013). Low-affinity transcription factor binding sites shape morphogen responses and enhancer evolution. *Philos. Trans. R. Soc. Lond. B Biol. Sci.* 368, 20130018.
- Rieckhof, G.E., Casares, F., Ryoo, H.D., Abu-Shaar, M., and Mann, R.S. (1997). Nuclear translocation of extradenticle requires homothorax, which encodes an extradenticle-related homeodomain protein. *Cell* 91, 171–183.
- Rohs, R., West, S.M., Sosinsky, A., Liu, P., Mann, R.S., and Honig, B. (2009). The role of DNA shape in protein-DNA recognition. *Nature* 461, 1248–1253.
- Rowan, S., Siggers, T., Lachke, S.A., Yue, Y., Bulyk, M.L., and Maas, R.L. (2010). Precise temporal control of the eye regulatory gene *Pax6* via enhancer-binding site affinity. *Genes Dev.* 24, 980–985.
- Ryoo, H.D., and Mann, R.S. (1999). The control of trunk Hox specificity and activity by *Extradenticle*. *Genes Dev.* 13, 1704–1716.
- Ryoo, H.D., Marty, T., Casares, F., Affolter, M., and Mann, R.S. (1999). Regulation of Hox target genes by a DNA bound Homothorax/Hox/Extradenticle complex. *Development* 126, 5137–5148.
- Sánchez-Herrero, E., Vernós, I., Marco, R., and Morata, G. (1985). Genetic organization of *Drosophila bithorax* complex. *Nature* 313, 108–113.
- Saramäki, A., Banwell, C.M., Campbell, M.J., and Carlberg, C. (2006). Regulation of the human p21(waf1/cip1) gene promoter via multiple binding sites for p53 and the vitamin D3 receptor. *Nucleic Acids Res.* 34, 543–554.
- Scardigli, R., Bäumer, N., Gruss, P., Guillemot, F., and Le Roux, I. (2003). Direct and concentration-dependent regulation of the proneural gene *Neurogenin2* by *Pax6*. *Development* 130, 3269–3281.
- Segal, E., Raveh-Sadka, T., Schroeder, M., Unnerstall, U., and Gaul, U. (2008). Predicting expression patterns from regulatory sequence in *Drosophila* segmentation. *Nature* 451, 535–540.
- Silverman, N., and Maniatis, T. (2001). NF-kappaB signaling pathways in mammalian and insect innate immunity. *Genes Dev.* 15, 2321–2342.
- Slattery, M., Riley, T., Liu, P., Abe, N., Gomez-Alcala, P., Dror, I., Zhou, T., Rohs, R., Honig, B., Bussemaker, H.J., and Mann, R.S. (2011). Cofactor binding evokes latent differences in DNA binding specificity between Hox proteins. *Cell* 147, 1270–1282.
- Stanojevic, D., Small, S., and Levine, M. (1991). Regulation of a segmentation stripe by overlapping activators and repressors in the *Drosophila* embryo. *Science* 254, 1385–1387.
- Stewart-Ornstein, J., Nelson, C., DeRisi, J., Weissman, J.S., and El-Samad, H. (2013). *Msn2* coordinates a stoichiometric gene expression program. *Curr. Biol.* 23, 2336–2345.
- Struhl, G. (1982). Genes controlling segmental specification in the *Drosophila* thorax. *Proc. Natl. Acad. Sci. USA* 79, 7380–7384.
- Struhl, G., Struhl, K., and Macdonald, P.M. (1989). The gradient morphogen bicoid is a concentration-dependent transcriptional activator. *Cell* 57, 1259–1273.
- Swanson, C.I., Evans, N.C., and Barolo, S. (2010). Structural rules and complex regulatory circuitry constrain expression of a Notch- and EGFR-regulated eye enhancer. *Dev. Cell* 18, 359–370.
- Wakimoto, B.T., and Kaufman, T.C. (1981). Analysis of larval segmentation in lethal genotypes associated with the antennapedia gene complex in *Drosophila melanogaster*. *Dev. Biol.* 81, 51–64.

Product Binding Enforces the Genomic Specificity of a Yeast Polycomb Repressive Complex

Phillip A. Dumesic,¹ Christina M. Homer,¹ James J. Moresco,² Lindsey R. Pack,³ Erin K. Shanle,⁴ Scott M. Coyle,¹ Brian D. Strahl,⁴ Danica G. Fujimori,³ John R. Yates III,² and Hiten D. Madhani^{1,*}

¹Department of Biochemistry and Biophysics, University of California, San Francisco, San Francisco, CA 94158, USA

²Department of Chemical Physiology, The Scripps Research Institute, La Jolla, CA 92037, USA

³Department of Cellular and Molecular Pharmacology, University of California, San Francisco, CA 94158, USA

⁴Department of Biochemistry and Biophysics, University of North Carolina School of Medicine, Chapel Hill, NC 27599, USA

*Correspondence: hitenmadhani@gmail.com

<http://dx.doi.org/10.1016/j.cell.2014.11.039>

SUMMARY

We characterize the Polycomb system that assembles repressive subtelomeric domains of H3K27 methylation (H3K27me) in the yeast *Cryptococcus neoformans*. Purification of this PRC2-like protein complex reveals orthologs of animal PRC2 components as well as a chromodomain-containing subunit, Ccc1, which recognizes H3K27me. Whereas removal of either the EZH or EED ortholog eliminates H3K27me, disruption of mark recognition by Ccc1 causes H3K27me to redistribute. Strikingly, the resulting pattern of H3K27me coincides with domains of heterochromatin marked by H3K9me. Indeed, additional removal of the *C. neoformans* H3K9 methyltransferase Ctr4 results in loss of both H3K9me and the redistributed H3K27me marks. These findings indicate that the anchoring of a chromatin-modifying complex to its product suppresses its attraction to a different chromatin type, explaining how enzymes that act on histones, which often harbor product recognition modules, may deposit distinct chromatin domains despite sharing a highly abundant and largely identical substrate—the nucleosome.

INTRODUCTION

The Polycomb (Pc) system plays critical roles in eukaryotic biology by triggering the deposition of facultative heterochromatin. This type of chromatin is associated with two conserved protein complexes: PRC2, whose catalytic subunit (EZH2 in mammals and E(z) in *Drosophila*) is a histone H3 lysine 27 methyltransferase; and PRC1, which mediates chromatin compaction and histone H2A ubiquitylation (Simon and Kingston, 2009). PRC1 also contains a chromodomain protein, CBX/Pc, which recognizes H3K27 methylation (H3K27me). First identified in *Drosophila* as a mechanism responsible for epigenetic memory of developmental gene expression states, the Polycomb system is now appreciated to play key roles in mammalian development

as well (Aloia et al., 2013; Steffen and Ringrose, 2014). Diverse additional biological roles have been ascribed to the system in other contexts, ranging from the control of DNA elimination in ciliates to the coupling of flowering and cold exposure in plants (Chalker et al., 2013; Song et al., 2012). Significantly, Polycomb plays a widespread role in human cancers. Redistribution of H3K27me domains has been observed in cancer genomes (Bender et al., 2013; Popovic et al., 2014), as have mutations in Polycomb system components including EZH2, the H3K27 demethylase KDM6A/Utx, and in histone genes at the lysine 27 residue itself (Plass et al., 2013). These findings have driven efforts to develop chemotherapeutics aimed at the Polycomb system.

The appropriate functioning of facultative heterochromatin requires its restricted deposition at the proper genomic sites. In *Drosophila*, DNA sequence elements called Polycomb response elements are bound by specific DNA-binding proteins that themselves recruit PRC2 (Simon and Kingston, 2013). In mammals, however, analogous elements have yet to be identified. PRC2 localization and activity have been suggested to instead be controlled by a diverse set of inputs including DNA-binding proteins, DNA GC content, noncoding RNAs, nucleosome spacing, and numerous histone posttranslational modifications (Klose et al., 2013; Margueron and Reinberg, 2011; Simon and Kingston, 2013). Further complicating the picture, recent studies have shown that H2A ubiquitylation can recruit PRC2 in order to promote H3K27me, thereby challenging the model that PRC2 recruitment acts upstream of PRC1 (Blackledge et al., 2014; Cooper et al., 2014). Thus, the mechanisms that establish H3K27me domains remain highly enigmatic.

A tractable yeast Polycomb system would enhance investigations of this evolutionarily conserved mechanism. Unfortunately, genes encoding PRC2 components were lost during the evolution of highly developed yeast systems such as *S. cerevisiae* and *S. pombe* (Shaver et al., 2010), precluding either from serving as such a model. Here, we identify and characterize a PRC2 complex in a budding yeast, *Cryptococcus neoformans*, and describe a function for H3K27me recognition in the accurate assembly of this type of heterochromatin. We show that the *C. neoformans* EZH2 ortholog acts to deposit H3K27me₃ in subtelomeric regions, silencing gene expression across large domains. This activity requires a PRC2-like complex whose

subunits include orthologs of metazoan PRC2 components as well as a chromodomain protein that binds specifically to H3K27me marks. Disruption of this binding activity reconfigures the genomic landscape of H3K27me₃ to one that strikingly coincides with sites of H3K9me₂ heterochromatin. Indeed, we find that this redistribution is entirely dependent on the Ctr4 histone methyltransferase that deposits H3K9me₂. These results indicate that the binding of PRC2 to its product restrains a latent attraction toward signals that emanate from H3K9me₂ domains. Chromodomain-mediated recognition of H3K27me thereby limits the commingling of two distinct types of repressive chromatin. As many chromatin-modifying complexes contain product recognition modules, the principle uncovered here may broadly contribute to the fidelity of genome-regulating enzymes that act upon a highly abundant and grossly identical substrate—the nucleosome.

RESULTS

Subtelomeric Domains Are Repressed by Methylation of Histone H3 on Lysine 27

PRC2 component orthologs have been identified in protists, filamentous fungi, and algae, and in some cases have been linked to repressive H3K27 methylation (Connolly et al., 2013; Jamieson et al., 2013; Liu et al., 2007; Shaver et al., 2010). Because the human fungal pathogen *C. neoformans* encodes genes for such orthologs (Shaver et al., 2010), we investigated the potential for H3K27me in this organism. However, the amino acid sequence of histone H3 in *Cryptococcus* contains an insertion of two amino acids following residue 28 as well as flanking substitutions that are not present in other model eukaryotes, precluding the use of commercial antibodies (Figure 1A). We therefore purified specific antibodies from rabbit polyclonal antiserum raised against a synthetic H3K27me₃ peptide that corresponded to the predicted *Cryptococcus* sequence (Extended Experimental Procedures). Dot blot analysis demonstrated that the purified antibody does not cross-react with H3K27me₂, H3K9me_{2/3}, or unmodified H3K27 peptides (Figure S1A).

Use of the H3K27me₃ antibody for ChIP-seq revealed the presence of this mark in broad domains at every subtelomeric region of the 14 *C. neoformans* chromosomes (Figures 1B and S1B). Although subtelomeres are enriched in repetitive sequences, the H3K27me₃ distribution is similar when ChIP-seq analysis is restricted to unique sequences (Figure S1C). Because we observed minimal signal in other regions of the genome (Figure S1B), we focused our analysis on subtelomeres by generating metatelope plots: all 28 chromosome ends were aligned, after which their average H3K27me₃ signal was calculated as a function of chromosomal position and normalized to that of a whole-cell extract (WCE) sample (Figure 1C). Subtelomeric H3K27me₃ domains have an average size of 41 kb (Table S1). Importantly, these domains are not observed in cells lacking the putative H3K27 methyltransferase Ezh2 (Figures 1B and 1C).

Given the conserved role of Polycomb in repressing transcription, we examined the effect of H3K27me₃ domains on gene expression in *C. neoformans*. When grown in rich media, cells lacking Ezh2 show widespread gene derepression, as determined by RNA-seq: 75 transcripts increase in expression >3-

fold as compared to wild-type cells, whereas no transcript except that of *EZH2* itself decreases >3-fold. Most derepressed loci (71%) are within the 41 kb subtelomeric regions identified by H3K27me₃ ChIP-seq, despite the fact that these regions make up only 5% of the genome (Figure 1D). In fact, when all genome-wide sites of H3K27me₃ signal are assessed (Figure S1D), most sites lie in subtelomeric regions and no sites greater than 50 kb from a chromosome end are associated with transcript derepression. Thus, the nonsubtelomeric transcripts repressed by Ezh2 are unlikely to be directly regulated by H3K27me₃.

Our findings indicate that H3K27me₃ in *C. neoformans* depends on the presence of the *EZH2* gene product. To test the functional importance of this histone residue, we incorporated a K27A mutation into histone H3, which is encoded by a single-copy gene in *C. neoformans*. Cells harboring the *h3-K27A* mutation show subtelomeric transcript derepression as much as 60-fold, as assessed by RT-qPCR analysis of five transcripts identified by RNA-seq to be elevated in *ezh2Δ* cells (Figure 1E). The phenotype of an *h3-K27A ezh2Δ* double mutant is indistinguishable from that of each single mutant, suggesting that Ezh2, in its gene silencing role, acts via H3K27. Next, we generated strains that encoded Ezh2 SET domain mutations predicted to eliminate its catalytic activity (Tan et al., 2014). These mutations, which have little (681-689Δ) or no (Y721A) effect on Ezh2 protein levels, recapitulate the high degree of subtelomeric transcript derepression seen in *ezh2Δ* cells (Figures 1F and 1G). Our results support a model in which Ezh2 deposits broad domains of repressive subtelomeric H3K27me₃.

A Yeast PRC2-like Complex

The activity of metazoan EZH2 is controlled extensively by inputs from the other PRC2 subunits (O'Meara and Simon, 2012). To determine whether a similar regulatory logic might exist in *C. neoformans*, we investigated the protein-interaction partners of Ezh2 in this system. We generated cells expressing CBP-2xFLAG-tagged Ezh2 from its normal chromosomal site, then isolated it by tandem affinity purification and identified its copurifying proteins by mass spectrometry. This purification yielded Ezh2 itself as well as four additional proteins, two of which are orthologs of metazoan PRC2 components (Figures 2A, 2B, and see below). We subsequently tagged and affinity-purified each of these four proteins: Eed1, Msl1, Bnd1, and Ccc1 (Figures 2A and 2B). Purifications of these proteins consistently yielded the original five Ezh2-associated proteins, suggesting the existence of a core PRC2-like protein complex (Figure 2C). The other proteins in the interaction network, which associated with only a subset of the core PRC2 components, may represent more loosely associated factors. Alternatively, these proteins may interact with individual PRC2 components in PRC2-independent contexts.

The members of the putative PRC2-like complex include orthologs of metazoan PRC2 components as well as additional factors (Figure 2D and Extended Experimental Procedures). Ezh2 is the H3K27 methyltransferase and Eed1 is an ortholog of EED/ESC, a WD40 repeat protein that binds directly to EZH2/E(z) and stimulates EZH2/E(z) activity. Msl1 is a fungal ortholog of RbAp46/48/Nurf55, a WD repeat protein that associates with

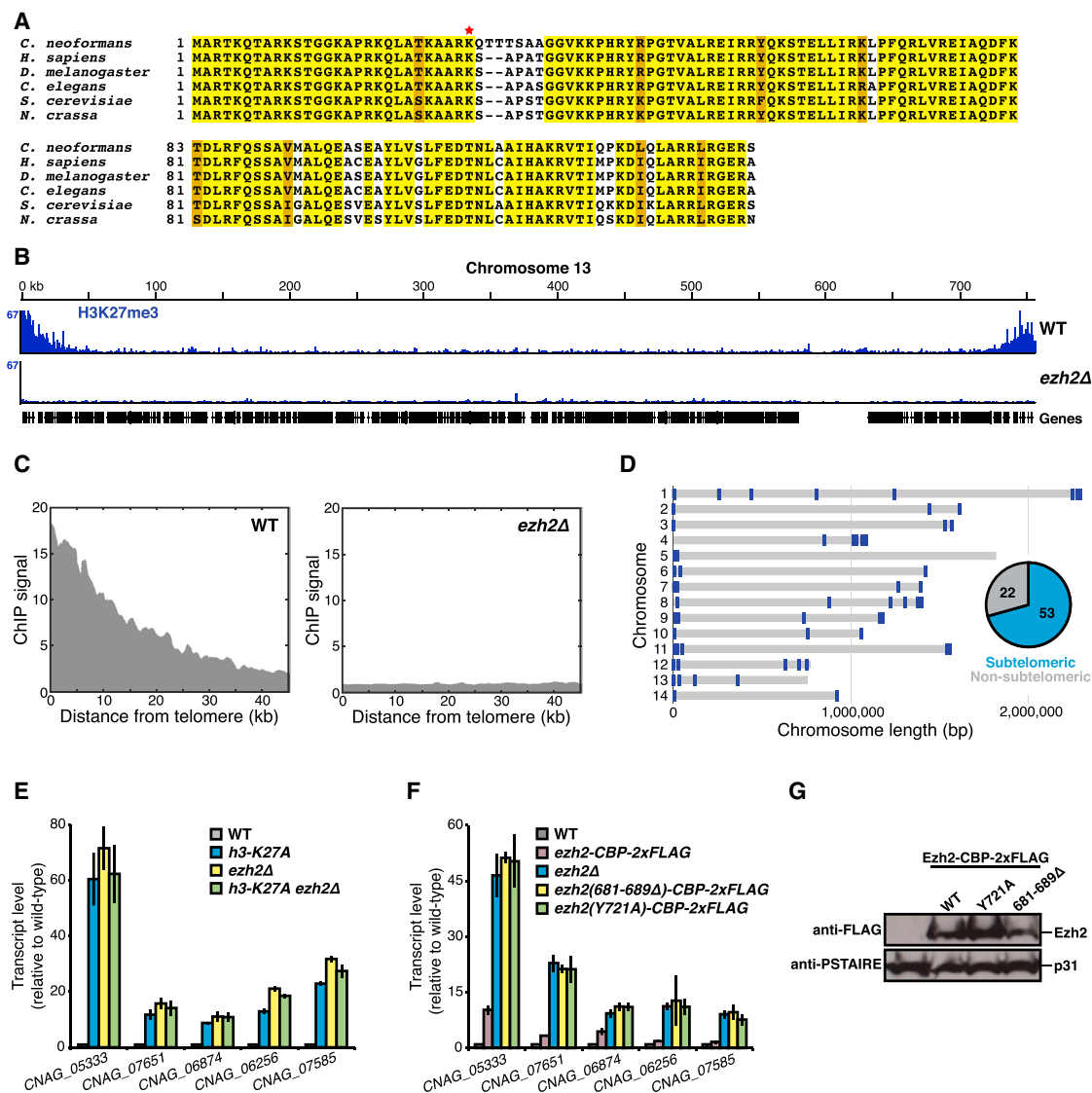


Figure 1. *C. neoformans* Ezh2 Deposits Broad, Subtelomeric Domains of Repressive H3K27me3 Heterochromatin

(A) Alignment of histone H3 protein sequences in eukaryotic model systems. Red star indicates lysine 27, a substrate of Ezh2.

(B) ChIP-seq traces of H3K27me3 signal across the representative chromosome 13 in wild-type or *ezh2Δ* cells. Other chromosomes are shown in Figure S1B.

(C) Average subtelomeric H3K27me3 signal, as measured by ChIP-seq. ChIP signal at all 28 subtelomeric regions was averaged, normalized to a WCE sample, and plotted as a function of distance from chromosome end.

(D) Chromosomal location of transcripts whose levels are elevated >3-fold in the absence of Ezh2, as assessed by RNA-seq. The proportion of these loci within the 41 kb subtelomeric H3K27me3 domains is indicated.

(E) Transcript levels of five Ezh2 target genes in the context of histone H3 or Ezh2 mutations, as assessed by RT-qPCR and normalized to 18S rRNA levels. Error bars represent SD.

(F) Transcript levels of five Ezh2 target genes in the context of Ezh2 SET domain mutations, as assessed by RT-qPCR and normalized to 18S rRNA levels. Error bars represent SD.

(G) Expression level of Ezh2 SET domain mutants, as assessed by immunoblot using the antibodies indicated at left. p31 serves as a loading control.

See also Figure S1 and Table S1.

PRC2 but is not required for EZH2/E(z) activity and has additional roles in other chromatin-modifying complexes. The remaining components of *C. neoformans* PRC2 are two factors with no clear orthologs in higher eukaryotes: Bnd1, a big protein with no domains; and Ccc1, a protein that contains a chromodomain and a coiled coil region. Like some other single-celled eukary-

otes, *C. neoformans* does not appear to encode an ortholog of the metazoan PRC2 component SUZ12/Su(z)12 in its genome (Shaver et al., 2010).

We used a yeast two-hybrid assay in order to assess pairwise interactions between PRC2 components when expressed in *S. cerevisiae*. We observed that each component interacts with

at least one other complex member, supporting the associations identified by tandem affinity purification (Figure S2A and Table S2). These interactions include one between Eed1 and Ezh2, whose metazoan orthologs bind one another directly in PRC2. Furthermore, two PRC2 components—Bnd1 and Ccc1—display self-interaction, raising the possibility of physical interactions that bridge multiple PRC2 complexes.

To assess the functional roles of each PRC2 subunit, we generated strains lacking each individual factor and tested their ability to silence Ezh2 target loci. Every knockout strain shows derepression of subtelomeric transcripts, as determined by RT-qPCR (Figure 2E). However, their phenotypes differ quantitatively. Cells lacking Ezh2, Eed1, or Bnd1 display equivalent, maximal phenotypes. In contrast, loss of Ccc1 causes a less severe phenotype in which some Ezh2 targets are fully derepressed and others are only partially derepressed. Msl1 mutants display the most minor phenotype: at all tested loci, this protein is only partially required for silencing, consistent with the relatively minor contribution of its ortholog, RbAp46/48/Nurf55, to PRC2-mediated silencing in mammals (O'Meara and Simon, 2012). The physical interactions among the PRC2 components, together with the phenotypes of their corresponding knockouts, suggest that they functionally cooperate, with the individual subunits contributing distinct and separable activities in gene silencing.

Several lines of evidence suggest that Msl1 and Ccc1 play additional roles independent of PRC2. First, Msl1 and Ccc1 physically associate not only with PRC2 components but also with members of the chromatin assembly factor (CAF) complex and multiple histone deacetylase (HDAC) complexes (Figure 2B). Metazoan Msl1 orthologs are involved in similar interactions (Suganuma et al., 2008). Second, both *msl1Δ* and *ccc1Δ* strains exhibit a growth defect, whereas strains lacking any of the other PRC2 components—*ezh2Δ*, *eed1Δ*, and *bnd1Δ*—do not (Table S3). Third, cells lacking Msl1 or Ccc1 demonstrate more widespread gene expression changes than do cells lacking Ezh2, as measured by RNA-seq (Figure 2F). Specifically, Msl1 is required for silencing of approximately half of the Ezh2 target genes, and additionally represses 225 other loci, whereas Ccc1 silences approximately half of the Ezh2 target genes as well as 65 other loci, most of which are coregulated by Msl1.

We tested whether the PRC2-independent factors associated with Msl1 and Ccc1 are involved in repressing PRC2 target loci. We were able to generate knockout strains for a subset of these factors, which we tested by RT-qPCR for their ability to silence subtelomeric transcripts. Loss of Cac2 (of the CAF complex) has no effect on subtelomeric transcript levels, nor does loss of Eza1, Nop1, Hat1, or CNA04786 (Figure S2B). A strain lacking Rpd3 (of the Rpd3S and Rpd3L HDAC complexes) displays derepression of a subset of subtelomeric loci, but does not phenocopy the PRC2 component gene knockouts. Notably, however, deletion of the gene encoding an ortholog of *S. pombe* Ctr3 leads to a full derepression of subtelomeric genes (Figure S2C), implicating this Class II HDAC ortholog in PRC2 action. Notably, HDAC activity cooperates with PRC2 in metazoan systems, where it removes antagonistic marks such as H3K27 acetylation (Reynolds et al., 2012; Tie et al., 2009).

Together, these data point to the *C. neoformans* PRC2 as a five-protein functional core complex that mediates H3K27me3-dependent gene silencing and shares structural and functional similarities with the metazoan PRC2.

Dissection of PRC2 Function Reveals Subunit Specialization

Having determined that PRC2 components play varying roles in subtelomeric gene repression, we investigated their respective functions in the formation of H3K27me3 domains. We used H3K27me3 ChIP-seq to examine a knockout from each phenotypic group: *ezh2Δ* cells display the maximal transcript derepression phenotype, whereas *ccc1Δ* and *msl1Δ* cells represent two partial phenotypes at the Ezh2 target genes, with the *msl1Δ* phenotype being the more minor of the two. As seen before, *ezh2Δ* cells lack all detectable H3K27me3 signal (Figures 3A and 3B). In contrast, and consistent with its minor transcript phenotype, the *msl1Δ* strain shows only a minor reduction in its subtelomeric H3K27me3 domains: ChIP enrichment is slightly reduced, as is their average size (35 kb versus 41 kb in wild-type, Table S1). Cells lacking Ccc1 have an intermediate phenotype in which subtelomeric H3K27me3 signal is reduced but not eliminated, with small domains (14 kb) still detectable. While these data do not rule out downstream roles for Msl1 and Ccc1, they suggest that these PRC2 components contribute to subtelomeric gene silencing by enabling the formation of appropriately-positioned H3K27me3 domains.

Further examination of the ChIP-seq data revealed a remarkable feature of *ccc1Δ* cells: whereas H3K27me3 signal is reduced at its normal subtelomeric locations, signal is increased at an ectopic site—the centromeres (Figure 3A). Centromeres have not been extensively studied in *C. neoformans*, but consist largely of transposon-derived repeats and correspond to a single broad region on each chromosome that lacks open reading frames (Janbon et al., 2014). H3K27me3 signal is increased at all 14 centromeres in *ccc1Δ* cells, and for some centromeres becomes comparable in magnitude to subtelomeric signal on the same chromosome. To systematically examine centromeric H3K27me3, we generated meta-centromere plots: all centromeres were aligned at their midpoints, after which their average H3K27me3 signal was calculated as a function of chromosomal position and normalized to that of a WCE sample (Figure 3C). Our analysis revealed an increase in centromeric H3K27me3 signal in *ccc1Δ* cells, but not in *msl1Δ* cells.

To quantify the extent of ectopic H3K27me3 deposition, we compared the density of H3K27me3 ChIP-seq signal at its proper sites—subtelomeres—versus centromeres (Figure 3D). As expected, wild-type cells exhibit subtelomeric signal but negligible centromeric signal, whereas *msl1Δ* cells display diminished subtelomeric signal. In contrast, *ccc1Δ* cells show not only a reduction in subtelomeric signal, but also a dramatic increase in centromeric signal (Figure 3D). These findings indicate that multiple PRC2 components are required for the proper spatial distribution of H3K27me3, with Ccc1 specifically being required to prevent an ectopic redistribution of this chromatin mark.

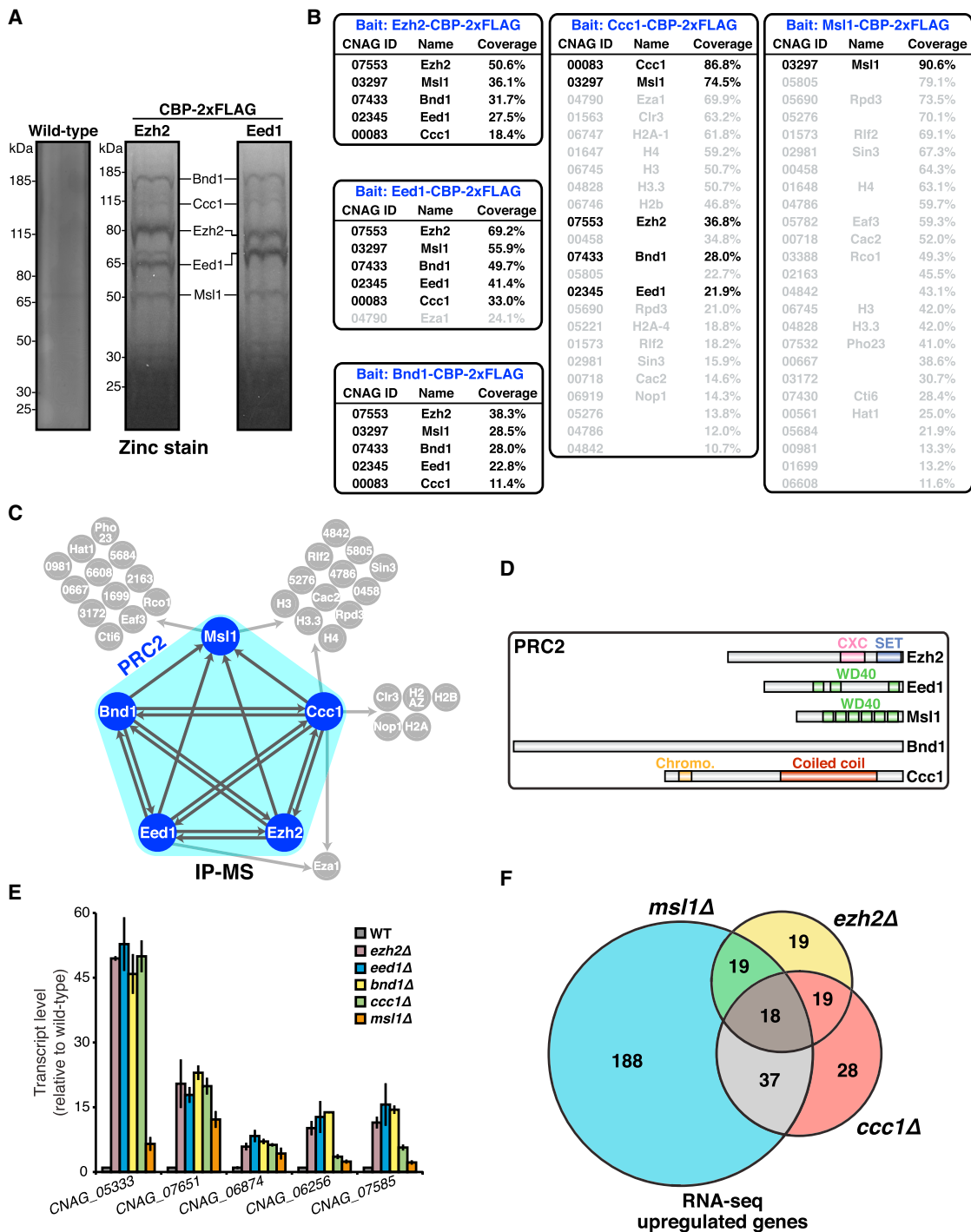


Figure 2. Purification and Functional Characterization of Ezh2-Associated Proteins

(A) Tandem affinity purifications were performed from wild-type (untagged) cells or cells expressing CBP-2xFLAG-tagged Ezh2 or Eed1. Purified protein was resolved by PAGE and visualized by zinc stain. Proteins identified by mass spectrometry analysis of the Ezh2 purification are labeled.

(B) Protein interaction partners of Ezh2 and of each of its associated proteins. Each bait protein was purified by tandem affinity purification and its protein interaction partners were determined by mass spectrometry. Likely contaminants and proteins with <10% sequence coverage have been excluded. Subunits of the putative PRC2 complex are indicated in black type.

(C) Protein interaction network of Ezh2-associated proteins. Each protein shaded in blue was used as bait for a separate IP-MS experiment, and arrows point to its respective associated proteins.

(D) Predicted protein domains of PRC2 subunits.

(legend continued on next page)

Ccc1 Chromodomain Binds H3K27me and Prevents Its Ectopic Deposition

To determine the mechanism by which Ccc1 enforces the correct genomic localization of H3K27me₃, we examined its chromodomain, a protein motif that can bind directly to histone methyl-lysine residues (Eissenberg, 2012). First, we recombinantly expressed a truncated fragment of Ccc1 that contains its chromodomain (Figures 4A and S3A). We then tested its capacity to bind histone modifications by using a peptide array representing 384 different histone modification combinations. We observed binding to only eight peptides on the array (Figure 4B). Strikingly, each peptide contains either a H3K27me₂ or H3K27me₃ modification, implying that the Ccc1 chromodomain is a specific reader of these PRC2-deposited marks. These results were somewhat surprising because the bound peptides correspond to the human H3 sequence, which differs from the *C. neoformans* sequence at residues downstream of K27. The downstream residues may therefore be less important for binding, consistent with the fact that the Pc chromodomain binds histone H3 primarily via interactions with residues upstream of H3K27me₃ (Min et al., 2003). Nonetheless, we confirmed Ccc1 chromodomain binding to the *C. neoformans* H3K27me_{2/3} sequence using fluorescence polarization. Chromodomain binding to a fluorescently labeled, human H3K27me₃ peptide was competed with increasing amounts of unlabeled *Cryptococcus* H3K27 peptides (Figure 4C). H3K27me₂ and me₃ peptides compete with apparent affinities of 119 and 28 μ M, respectively, while we observed no competition with the unmodified peptide.

To test the importance of the Ccc1 chromodomain in vivo, we generated *ccc1* mutations predicted to disrupt its aromatic cage residues, which mediate methyl-lysine recognition (Eissenberg, 2012). Based on sequence alignment to structurally characterized chromodomains in other systems (Extended Experimental Procedures), two aromatic cage residues in Ccc1 could be identified, which we individually mutated. Strains containing these mutations express Ccc1 at normal levels but show subtelomeric transcript derepression to the same extent as does the *ccc1 Δ* strain (Figures 4D and 4E). Using RNA-seq, we observed that the *ccc1-W52A* aromatic cage mutation causes derepression of a set of genes wholly within the set derepressed in *ezh2 Δ* cells, whereas the *ccc1 Δ* mutant derepresses additional genes (Figure 4F). Thus, the chromodomain mutations appear to separate the Polycomb functions of Ccc1 from its PRC2-independent functions. Consistent with this view, the *ccc1 Δ* strain exhibits a growth defect, whereas the *ccc1-W52A* and *ezh2 Δ* strains do not (Table S3).

We examined the effect of Ccc1 chromodomain mutations on H3K27me₃. ChIP-seq revealed that *ccc1-W52A* cells, like *ccc1 Δ* cells, display reduced subtelomeric H3K27me₃ domain magnitude and size (13 and 14 kb, respectively, as compared to 41 kb in wild-type) (Figure 4G and Table S1). Furthermore, both

the chromodomain mutant and knockout cells show a gain of H3K27me₃ at centromeres (Figures 4H and 4I). In the context of the H3K27me₃ redistribution in *ccc1-W52A* cells, the total cellular level of this histone mark does not decrease, as assessed by immunoblot (Figure S3B).

These findings demonstrate that the Ccc1 chromodomain recognizes specific histone modifications—H3K27me_{2/3}—and suggest that this activity anchors PRC2 to its product in order to maintain the genome-wide distribution of Polycomb heterochromatin. Consistent with such a role for Ccc1, the *ccc1-W52A* mutation reduces the association of PRC2 with subtelomeric chromatin, as assessed by ChIP of Ezh2 (Figure S3C). At centromeric chromatin, PRC2 association is not detected above background in either wild-type or *ccc1-W52A* cells, indicating that this association is below the limit of detection or that PRC2 is not stably bound to centromeres despite its evident enzymatic action there.

H3K9me₂ Heterochromatin Localizes Primarily to Centromeres

Because centromeres are the predominant site of ectopic H3K27me₃ in *ccc1* mutants, we hypothesized that PRC2 might be recruited to these improper sites by constitutive heterochromatin, which decorates centromeres in other systems (Grewal and Jia, 2007). To determine the distribution of constitutive heterochromatin in *C. neoformans*, we performed ChIP-seq using an antibody against an associated histone mark: H3K9me₂. As expected, wild-type cells exhibit signal primarily at centromeres (Figures 5A and 5C). They also display some H3K9me₂ near chromosome ends, but these domains are considerably smaller than those of H3K27me₃ (13 kb versus 41 kb) (Figure 5B and Table S1). Quantification of subtelomeric versus centromeric ChIP-seq signal density confirmed this complementary relationship, with H3K9me₂ density greatest at centromeres and H3K27me₃ greatest at subtelomeres (Figure 5D). Importantly, H3K9me₂ signal is eliminated in cells lacking Ctr4, the *C. neoformans* ortholog of the H3K9 methyltransferase SUV39H/Su(var)3-9 (Figures 5A–5D). Consistent with a repressive function for H3K9me₂, loss of Ctr4 results in an approximately 6-fold increase in centromeric transcript levels, as assessed by RNA-seq (Figure S4A).

We next tested whether either type of heterochromatin requires the presence of the other. Cells lacking Ezh2 have no H3K27me₃, but exhibit normal H3K9me₂, indicating that constitutive heterochromatin does not depend on PRC2 (Figures 5A–5D). Cells lacking Ctr4 have no detectable H3K9me₂, but exhibit, if anything, a slight increase in total amount of subtelomeric H3K27me₃. In addition, these cells contain a total cellular level of H3K27me₃ similar to that of wild-type cells, as assessed by immunoblot (Figure S4B). Thus, there is no requirement for Ctr4 during the assembly of H3K27me₃ domains in otherwise wild-type cells.

(E) Transcript level of Ezh2 target genes in the context of PRC2 subunit mutations, as assessed by RT-qPCR and normalized to 18S rRNA levels. Error bars represent SD.

(F) Venn diagram of genes upregulated >3-fold in *msl1 Δ* , *ezh2 Δ* , and *ccc1 Δ* strains, as determined by RNA-seq. See also Figure S2 and Tables S2 and S3.

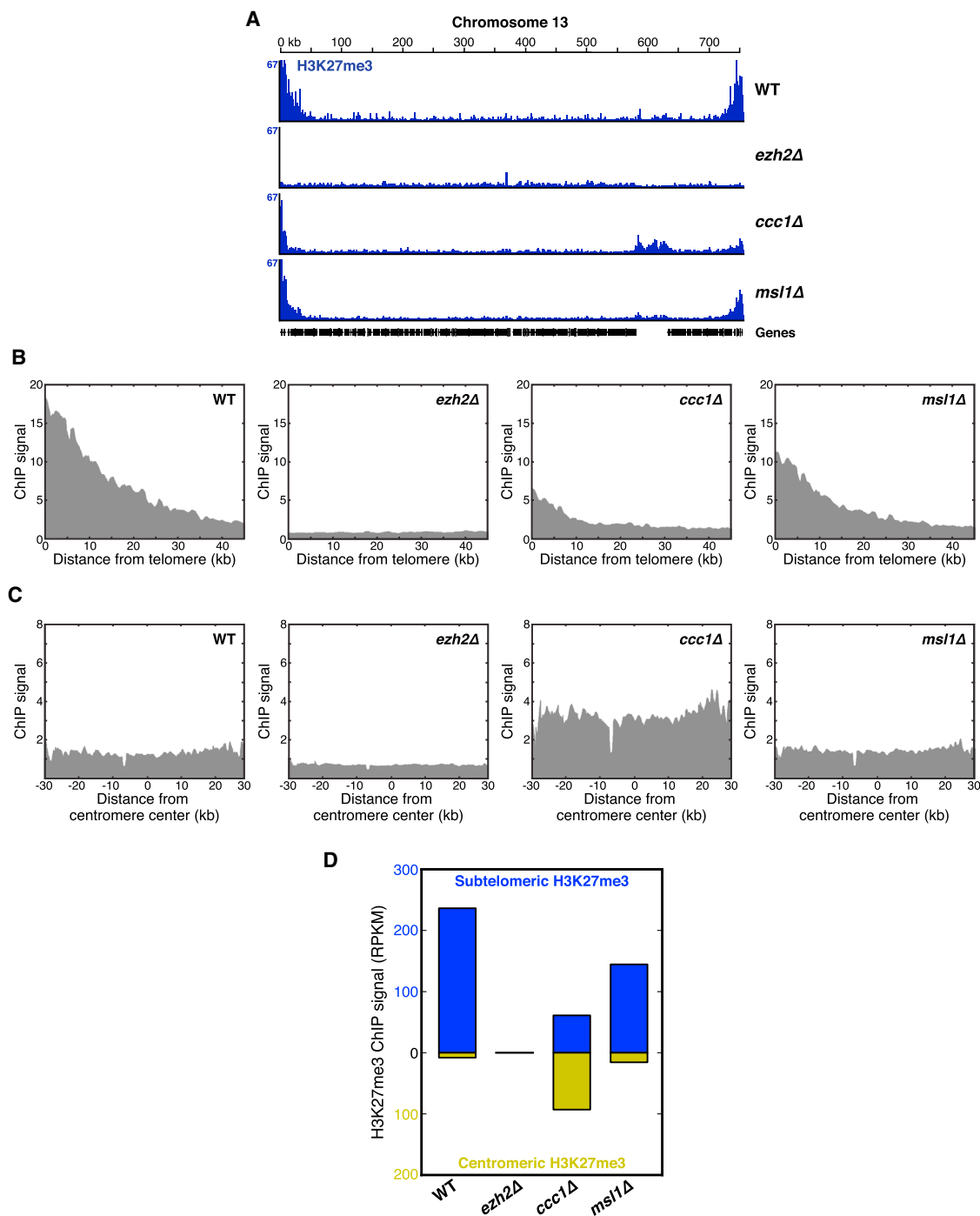


Figure 3. PRC2 Subunits Are Required for the Proper Spatial Deposition of H3K27me3 Heterochromatin

(A) ChIP-seq traces of H3K27me3 signal across chromosome 13 in wild-type cells or cells lacking individual PRC2 components. The gene-poor region near 600 kb corresponds to the centromere.

(B) Average subtelomeric H3K27me3 signal, as measured by ChIP-seq.

(C) Average centromeric H3K27me3 signal, as measured by ChIP-seq.

(D) H3K27me3 at subtelomeric versus centromeric regions, as measured by ChIP-seq. Density (RPKM) of signal above background is reported for subtelomeric regions (blue bar) and centromeric regions (green bar).

H3K9me2 Heterochromatin Directs H3K27me3 Deposition in *ccc1-W52A* Cells

Because the H3K9me2 pattern in wild-type cells coincides with the sites to which H3K27me3 is redistributed in *ccc1* mutants, we tested the hypothesis that the former recruits the latter. First, we used ChIP-seq to measure the genome-wide H3K27me3 distribution in *ccc1-W52A* mutants, *clr4Δ* mutants, and double-mutant cells. As seen before, *ccc1-W52A* mutants show reduced subtelomeric H3K27me3 signal and an emergence of ectopic signal in centromeres (Figures 6A–6D). Remarkably, the loss of Clr4 in the context of *ccc1-W52A* causes a complete loss of centromeric H3K27me3 signal (Figures 6A–6D). Thus, the ectopic redistribution of H3K27me3 in the context of *ccc1-W52A* requires Clr4, which itself deposits H3K9me2. Similarly, the subtelomeric H3K27me3 signal, which is not Clr4-dependent in a wild-type background, becomes Clr4-dependent in the context of *ccc1-W52A* (Figures 6B, 6D, and S5). ChIP-qPCR validation confirms that centromeric and telomeric H3K27me3 is, in the context of *ccc1-W52A*, dependent on H3K9me2 (Figures 6E and S6A). These results suggest that, when the Ccc1 chromodomain is disrupted, H3K9me2 guides the genome-wide deposition of H3K27me3. In further support of this conclusion, the average size of subtelomeric H3K27me3 domains is distinct from that of H3K9me2 domains in wild-type cells (41 kb for H3K27me3 versus 13 kb for H3K9me2) but becomes similar in the context of *ccc1-W52A* (13 kb versus 9 kb), consistent with a collapse of H3K27me3 onto sites of H3K9me2 when Ccc1 is mutated (Table S1).

We considered what features of PRC2 might enable it to respond to signals that emanate from constitutive heterochromatin. In higher eukaryotes, the EED/Esc WD40 domains contain a pocket that can bind methyl-lysine side chains (Margueron et al., 2009; Xu et al., 2010). This interaction stimulates the methyltransferase activity of EZH2/E(z) and is required for recruitment of PRC2 to its target loci (Margueron et al., 2009). However, the pocket in EED/Esc is not specific for H3K27me3: it can bind several different histone tail methyl-lysine residues, with silenced gene marks (such as H3K27me3 and H3K9me3) tending to bind EED/Esc with higher affinity and to activate PRC2 more strongly than do active gene marks (such as H3K4me3 and H3K36me3) (Margueron et al., 2009; Xu et al., 2010). These findings suggested the possibility that the yeast Eed1 might promote ectopic H3K27me3 in the *ccc1-W52A* mutant.

To test this hypothesis, we first recombinantly expressed full-length *C. neoformans* Eed1 in *E. coli* and tested its ability to bind histone tail peptides using an in-solution peptide pull-down assay. GST-Eed1 interacts with peptides corresponding to the first 20 residues of histone H3, with a modest (but consistent) preference for the repressive marks H3K9me1/2/3 (Figure S6B). In contrast, the activation-associated marks H3K4me3 and polyacetylated H3 cause, respectively, a reduction or elimination of Eed1 binding, further consistent with the idea that Eed1 prefers an H3K9me heterochromatin signature (Figure S6B). Next, we generated a *C. neoformans* strains in which a conserved tyrosine residue in the putative Eed1 methyl-lysine binding pocket is mutated. We observed that this single amino acid replacement of Eed1, which is expressed at normal levels in cells, significantly reduces the ectopic, Clr4-dependent H3K27me3 induced by

Ccc1-W52A (Figures S6C and S6D). The Eed1-Y134A mutation has a significantly weaker effect on the eutopic, Clr4-independent H3K27me3 observed at subtelomeric regions in otherwise wild-type cells harboring a functional Ccc1 protein (Figure S6E). Thus, direct sensing of H3K9me2 and other histone marks by Eed1 may be in part responsible for the aberrant H3K27 trimethylation in Ccc1 chromodomain mutants.

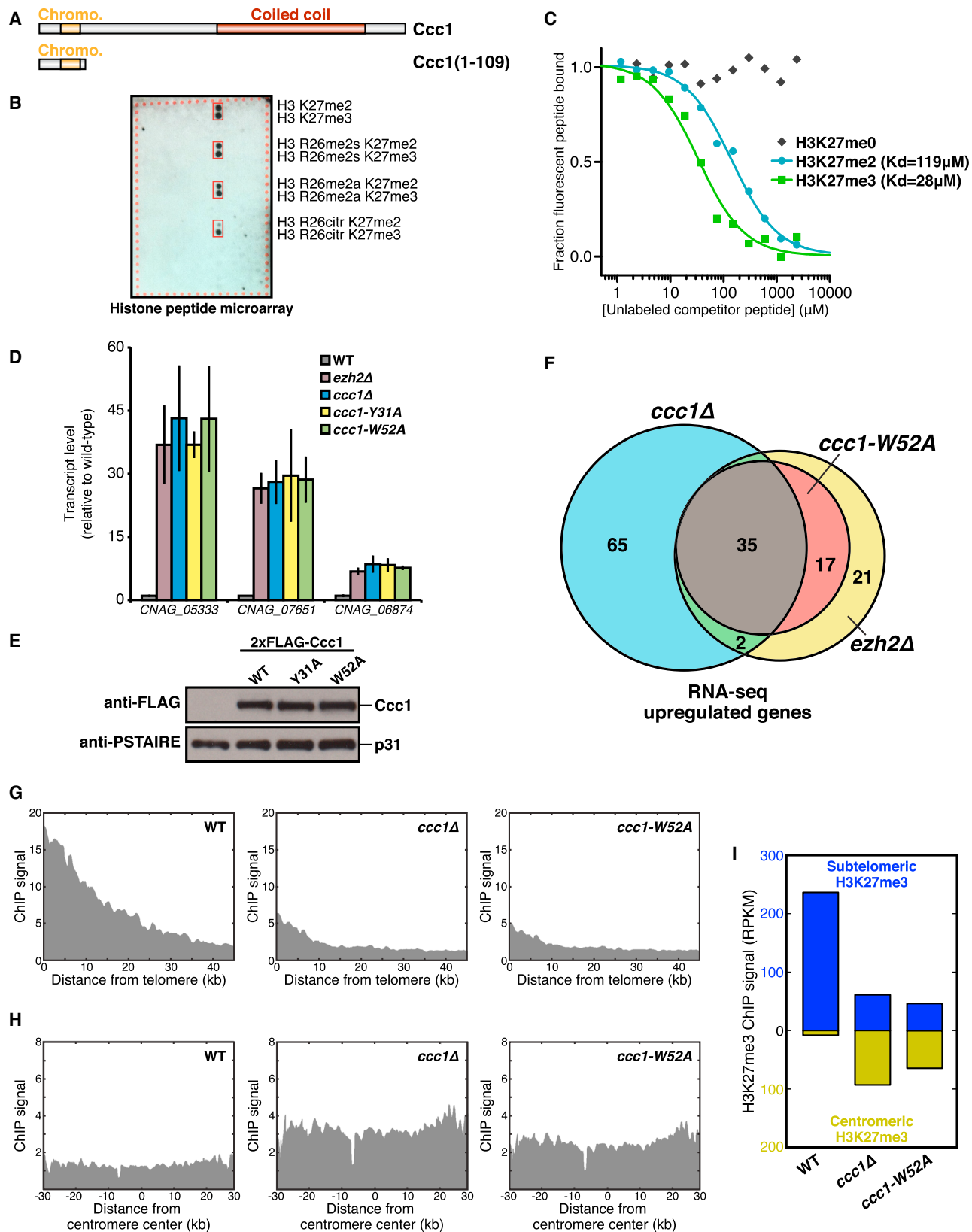
DISCUSSION

The Polycomb system is central to animal and plant development and plays a key role in human disease. Despite the importance of these chromatin regulators, how they guide the establishment and inheritance of repressive H3K27me domains remains poorly understood. In this paper, we describe the Polycomb system of a budding yeast, *C. neoformans*. We identify a PRC2-like complex that mediates all genome-wide H3K27me3 via its catalytic Ezh2 subunit. Our genetic and biochemical dissection of the other PRC2 components reveals distinct roles for different subunits. Most strikingly, our results demonstrate that product recognition by a chromodomain subunit masks a latent promiscuity of PRC2 by which it is attracted to centromeric H3K9me2 domains, where H3K27me3 is not normally deposited. As chromatin-modifying enzymes typically contain product recognition modules, these findings have general implications.

H3K27me3 and PRC2 in a Budding Yeast

In contrast to *S. cerevisiae* and *S. pombe*, the human fungal pathogen *C. neoformans* encodes an ortholog not only of the H3K9 methyltransferase Clr4 but also of the H3K27 methyltransferase EZH2/E(z). By generating modification-specific antibodies, we found that H3K27me3 is deposited by the EZH2/E(z) ortholog across subtelomeric domains that repress the expression of underlying genes and noncoding transcripts. Polycomb heterochromatin may therefore have a specialized role in the regulation of subtelomeres, which in fungi are enriched for rapidly-evolving genes involved in niche adaptation and specialized metabolic functions (Brown et al., 2010; Chow et al., 2012). Consistent with this idea, the 41 kb average size of subtelomeric H3K27me3 domains closely matches a computational prediction of *C. neoformans* subtelomere size based on enrichment for metabolism-related gene products (~40 kb) (Chow et al., 2012). Intriguingly, subtelomeric genes in other pathogenic fungi are silenced by domains of repressive chromatin and respond to environmental changes during the process of host infection, raising the possibility that Polycomb heterochromatin could contribute to the pathogenicity of *C. neoformans* (Domergue et al., 2005; De Las Peñas et al., 2003; McDonagh et al., 2008).

We found that H3K9me2 domains also repress transcript levels, but are deposited at largely spatially distinct locations, analogous to the distinct patterns of these two chromatin types in metazoans (Filion et al., 2010; Kharchenko et al., 2011; Rosenfeld et al., 2009). H3K9me2 domains are found primarily at centromeres, consistent with their broadly conserved roles in centromere function and chromosome segregation (Grewal and Jia, 2007). We also observed small regions of H3K9me2 deposition at subtelomeres. These are approximately 25% the size of the H3K27me3 domains with which they overlap. Both



(legend on next page)

the H3K27me3 and H3K9me2 domains exhibit a distinctive shape: their ChIP enrichments are greatest at the chromosome termini, and taper off toward the chromosome interior. The spread of the two types of marks is evidently mutually independent, because neither chromatin mark depends on the other for its proper distribution.

In higher eukaryotes, EZH2/E(z) activity is extensively regulated by its protein interaction partners within PRC2 (O'Meara and Simon, 2012). Our biochemical purifications of PRC2/E(z) protein orthologs in *Cryptococcus* suggest the existence of a PRC2-like core complex of at least five components, all of which functionally contribute to the formation of H3K27me3 domains of the proper size and location. Three of these components—Ezh2, Eed1, and Msl1—are clear orthologs of mammalian PRC2 components, whereas two others—Bnd1 and Ccc1—appear to be fungal-specific proteins, although they may have functions analogous to those of other mammalian PRC2 and/or PRC1 components.

We identified additional chromatin-related proteins in purifications of particular PRC2 components. Among these is a class II histone deacetylase homolog, Clr3, whose removal caused subtelomeric gene derepression. Analogously, the mammalian NuRD complex, which contains a Clr3-related histone deacetylase, has recently been shown to facilitate PRC2 recruitment in embryonic stem cells (Reynolds et al., 2012).

Product Recognition Suppresses Latent Promiscuity of the PRC2 Complex

One subunit of the *C. neoformans* PRC2 complex, Ccc1, harbors a chromodomain, a protein motif that typically binds to histone tails in a manner dependent on methylation of a specific lysine residue. Indeed, our biochemical studies demonstrated that this domain binds PRC2 reaction products—H3K27me2/3—but not other histone tail modifications. Remarkably, mutation of the Ccc1 chromodomain at residues responsible for methyl-lysine recognition causes a genome-wide redistribution of H3K27me3: the subtelomeric H3K27me3 domains shrink in size and ectopic H3K27me3 domains arise at centromeres. Strikingly, this altered H3K27me3 distribution coincides with the genomic sites of H3K9me2 heterochromatin. This observation led us to hypothesize that the Ccc1 chromodomain suppresses a latent attraction of PRC2 to signals from H3K9me2 heterochromatin. Indeed, we found that the ectopic deposition

of H3K27me3 at centromeres in the context of Ccc1 chromodomain disruption is completely suppressed by removal of the H3K9 methyltransferase Clr4. These findings demonstrate a role for product recognition in ensuring the fidelity of a chromatin-modifying complex by suppressing the influence of inappropriate signals (Figure 7).

Although we suspect that multiple features make heterochromatin attractive to PRC2, our analysis of a conserved tyrosine residue in Eed1 predicted to be involved in methyl-lysine binding suggests that H3K9me2 may be one such inappropriate signal (Margueron et al., 2009; Xu et al., 2010). Further detailed mechanistic tests of this model will require reconstitution of an active *C. neoformans* complex in vitro. In human EED, methyl-lysine binding specificity is remarkably broad (Margueron et al., 2009), raising the possibility that PRC2 complexes may be generally susceptible to aberrant recruitment. Additional inputs are known to impact PRC2, which include histone modifications, chromatin density, noncoding RNA, and posttranslational modification of EZH2/E(z) itself (O'Meara and Simon, 2012). As many of these features are found in H3K9me-marked heterochromatin, they likely also serve as latent “attractants” for PRC2. Because removal of Clr4 does not reduce H3K27me3 in otherwise wild-type cells (but reduces H3K27me3 in *ccc1* mutant cells), an important additional conclusion is that product recognition by Ccc1 is required not only to shield PRC2 from inappropriate signals but also for the assembly of H3K27me3 domains per se, perhaps by facilitating spread of the H3K27me3 mark.

H3K27me-specific chromodomains in other eukaryotes may also act to promote the fidelity of chromatin transactions. In higher eukaryotes, Polycomb repressive complex 1 (PRC1) includes the eponymous Polycomb protein, which contains an H3K27me-specific chromodomain that is thought in some settings to guide the complex to sites where PRC2 has been active, thereby positioning PRC1 to repress transcription (Sparmann and van Lohuizen, 2006). The ability of PRC1 and PRC2 components to physically interact raises the possibility that PRC1 might also provide product recognition activity for PRC2, analogous to the role of Ccc1 (Cao et al., 2014; Poux et al., 2001). However, intriguing recent work on animal Polycomb systems raises additional possibilities. In particular, several studies have demonstrated that a modification catalyzed by PRC1—H2A monoubiquitylation (H2AUb)—can recruit PRC2 in vivo, changing the view that PRC2 acts strictly upstream of PRC1

Figure 4. The Ccc1 Chromodomain Binds H3K27me2/3 and Is Required for Proper Spatial Positioning of H3K27me3 Heterochromatin

- (A) Predicted domains of full-length Ccc1 and of the truncated construct Ccc1(1-109) that was expressed recombinantly.
- (B) Binding of Ccc1 chromodomain to a modified histone peptide array, detected by chemiluminescence using an anti-GST antibody. The eight bound peptides are labeled at right.
- (C) Binding of Ccc1 chromodomain to methylated or unmethylated H3K27 peptides, as assessed by fluorescence polarization binding assay. Ccc1(1-109) was bound to a fluorescently-labeled H3K27me3 peptide, and this labeled peptide was competed off with increasing concentrations of unlabeled *C. neoformans* H3K27me0/2/3.
- (D) Transcript level of Ezh2 target genes in the context of Ccc1 chromodomain mutations, as assessed by RT-qPCR and normalized to 18S rRNA levels. Error bars represent SD.
- (E) Expression level of Ccc1 chromodomain mutants, as assessed by immunoblot using the antibodies indicated at left. p31 serves as a loading control.
- (F) Venn diagram of genes upregulated >3-fold in *ccc1Δ*, *ccc1-W52A*, and *ezh2Δ* strains, as determined by RNA-seq.
- (G) Average subtelomeric H3K27me3 signal, as measured by ChIP-seq.
- (H) Average centromeric H3K27me3 signal, as measured by ChIP-seq.
- (I) H3K27me3 at subtelomeric versus centromeric regions, as measured by ChIP-seq.

See also Figure S3.

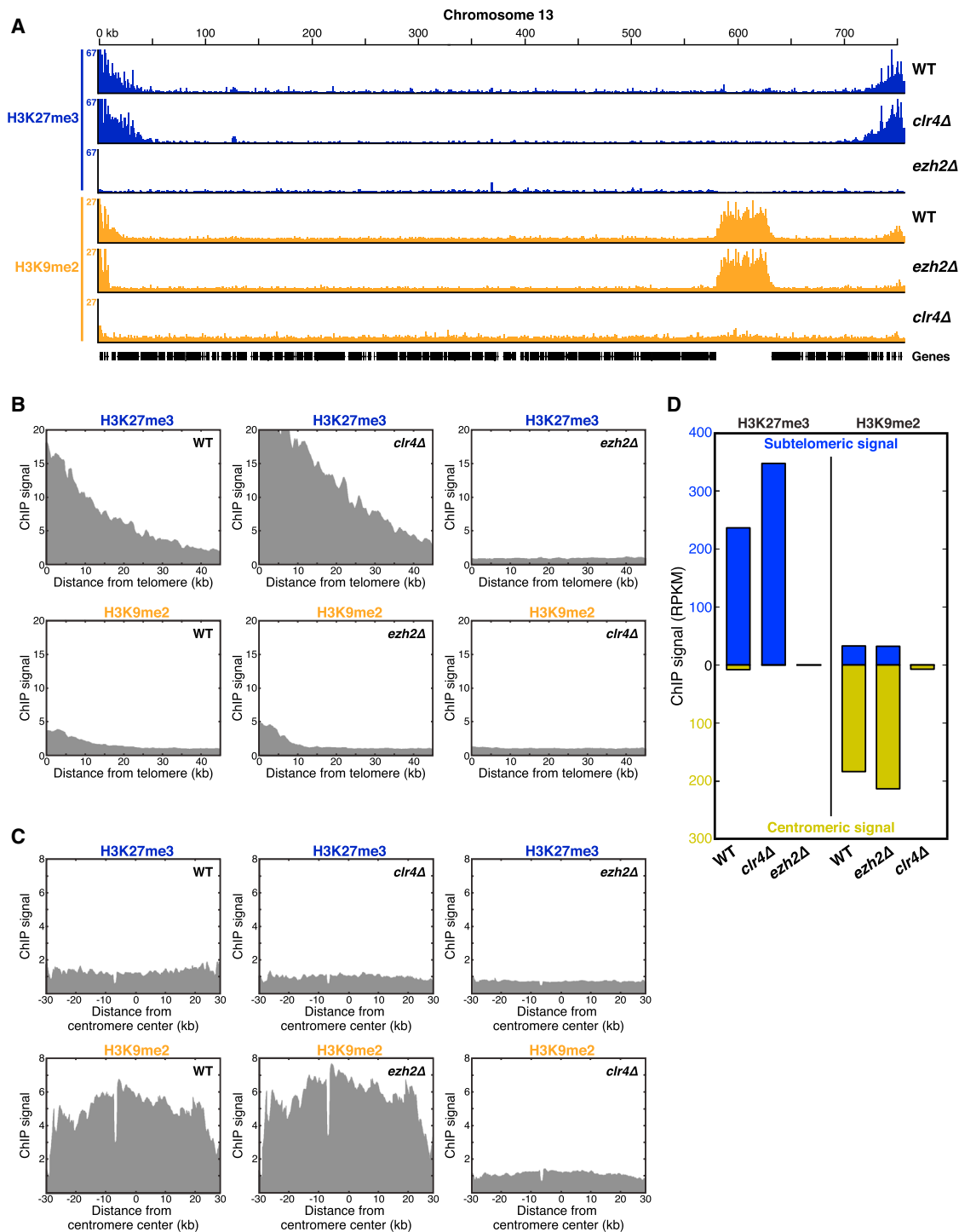


Figure 5. H3K9me2 Heterochromatin Decorates Centromeres and Small Subtelomeric Regions in *C. neoformans*

(A) ChIP-seq traces of H3K27me3 signal (blue) and H3K9me2 signal (orange) across chromosome 13 in wild-type cells or cells lacking Clr4 or Ezh2, the methyltransferases for H3K9 and H3K27, respectively.

(B) Average subtelomeric H3K27me3 and H3K9me2 signal, as measured by ChIP-seq.

(C) Average centromeric H3K27me3 and H3K9me2 signal, as measured by ChIP-seq.

(D) H3K27me3 and H3K9me2 at subtelomeric versus centromeric regions, as measured by ChIP-seq.

See also Figure S4.

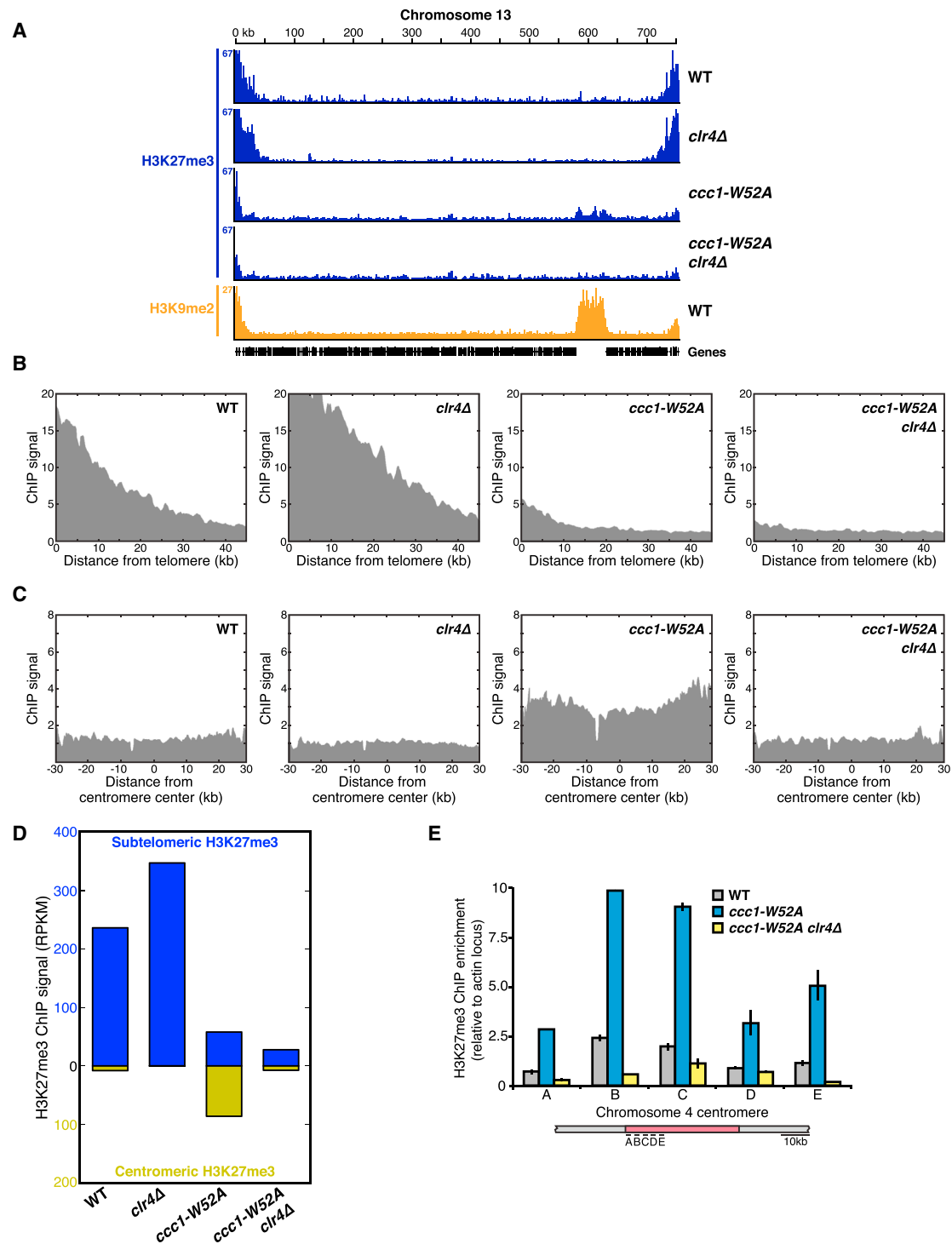


Figure 6. Constitutive Heterochromatin Instructs H3K27me3 in the *ccc1-W52A* Mutant

(A) ChIP-seq traces of H3K27me3 signal (blue) and H3K9me2 signal (orange) across chromosome 13.

(B) Average subtelomeric H3K27me3 signal, as measured by ChIP-seq.

(C) Average centromeric H3K27me3 signal, as measured by ChIP-seq.

(D) H3K27me3 at subtelomeric versus centromeric regions, as measured by ChIP-seq.

(E) H3K27me3 enrichment at five centromeric loci (below) in the context of Ccc1 chromodomain mutations, as assessed by ChIP-qPCR. Signal was normalized to WCE and plotted relative to signal at the euchromatic actin locus. Error bars represent SD.

See also Figures S5 and S6.

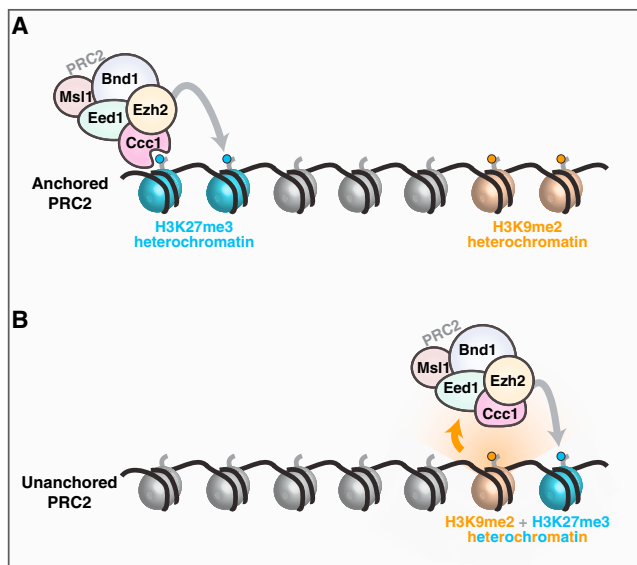


Figure 7. Model for the Role of Product Recognition by *C. neoformans* PRC2

(A) In wild-type cells, PRC2 deposits repressive H3K27me3 at subtelomeres. The Ccc1 subunit of PRC2 binds H3K27me3 via its chromodomain, thereby anchoring PRC2 to its product. In this context, subtelomeric H3K27me3 does not depend on the presence of H3K9me2, and these two chromatin types are largely distinct in location.

(B) In the context of the *ccc1-W52A* mutant, PRC2 lacks product recognition activity and is not anchored to H3K27me3 by Ccc1. In this setting, H3K27me3 is redistributed to sites of H3K9me2, including centromeres, and this redistribution depends on the presence of Ctr4. Thus, unanchored PRC2 inappropriately responds to signals from another chromatin type, H3K9me2 heterochromatin, which causes ectopic redistribution of H3K27me3. These signals may include direct H3K9me2 binding by Eed1 (orange arrow) as well as recognition of the other features of heterochromatin such as its nucleosome density and its specific patterns of additional histone modifications (orange ray).

(Blackledge et al., 2014; Cooper et al., 2014). In this scenario, PRC2 would not directly recognize its own product, but would rather bind a modification deposited by an enzyme, PRC1, that itself had previously been recruited by the PRC2 product. Such a mechanism could have a functional impact equivalent to that described here: the tethering of PRC2 to the sites of its product. A situation more directly analogous to the yeast system may occur in plants, where a chromodomain protein called LHP1 binds to both the RbAp46/48/Nurf55 ortholog as well as to H3K27me2/3, thereby linking PRC2 to its product (Derkacheva et al., 2013). Assessing the potential role of product recognition in the fidelity of animal and plant Polycomb systems will require generation of specific mutations that disrupt product recognition (be it H3K27me or H2AUb) and assessment of their impact on the fidelity of chromatin modification via genome-wide ChIP studies.

Given our results, it is notable that there are some hints in higher eukaryotes that Polycomb systems may interact with constitutive heterochromatin, both in normal or pathologic contexts. For example, although H3K27me and H3K9me repressive chromatin domains are generally separated in these organisms, overlap at a subset of targets has been observed in some cell

types (Bilodeau et al., 2009; Mozzetta et al., 2014; Wang et al., 2008), suggesting potential functional interaction. Such interactions may contribute to pathology as well: coincident H3K27me and H3K9me deposition at the INK4/ARF locus, a key tumor suppressor, is associated with spontaneous transformation of mesenchymal stem cells, raising the possibility that the reconfiguration of H3K27me patterns could be oncogenic (Zheng et al., 2013).

In contrast to many other enzyme classes, chromatin-modifying complexes typically harbor product recognition modules, either encoded within the same polypeptide as the enzymatic domain or on an associated protein. This attribute can be important for the local spread of a modification and has been hypothesized to assist in positive feedback as well as epigenetic inheritance of chromatin states across cell division (Collins et al., 2008; Hansen et al., 2008; Hassan et al., 2002; Klein et al., 2014; Lan et al., 2007; Liou et al., 2005; Margueron et al., 2009; Zhang et al., 2008; Zhu and Reinberg, 2011). Our findings demonstrate a conceptually distinct (but not mutually exclusive) role for product recognition: to anchor a chromatin-modifying complex to its target, thereby preventing its aberrant recruitment by signals from a distinct type of chromatin. Because nucleosomes exist at high copy-number, with a concentration of ~ 0.1 mM in mammalian interphase nuclei (Hihara et al., 2012), chromatin-modifying complexes likely operate in an environment that is rich in off-target substrates. Thus, fidelity-enhancing mechanisms of the type described here are likely to be an important, underexplored aspect of chromatin-based genome regulation.

EXPERIMENTAL PROCEDURES

Yeast Strains

Yeast strains used in this study are listed in Table S4. All *C. neoformans* strains were derived from strain H99 using published procedures (Chun and Madhani, 2010).

Tandem Affinity Protein Purification

C. neoformans strains encoding CBP-2xFLAG-tagged proteins expressed from their endogenous promoters were grown to log phase, harvested, and snap frozen. Frozen cells were lysed in a coffee grinder and tagged proteins were purified using anti-FLAG M2 (Sigma) resin, after which they were eluted using 3xFLAG peptide (Sigma). A second purification step was performed using calmodulin resin (Stratagene), after which the bound protein was eluted using 3 mM EGTA and analyzed by zinc stain (Pierce) or mass spectrometry as described in Table S5 and elsewhere (Dumesic et al., 2013).

RNA Isolation and Expression Profiling

Total RNA was isolated using TRIzol (Invitrogen). For RT-qPCR, RNA was treated with DNaseI (Roche) and then Superscript III (Invitrogen) to generate cDNA. PCR primers are listed in Table S6. For RNA-seq, mRNA was isolated from total RNA using the Oligotex mRNA mini kit (QIAGEN) and two biological replicate sequencing libraries were prepared for each genotype using the NEBNext Ultra Directional RNA Library Prep Kit (New England Biolabs) as described in Extended Experimental Procedures.

Chromatin Immunoprecipitation

C. neoformans cultures were crosslinked with formaldehyde and lysate was generated using a Mini-Beadbeater (Biospec Products), from which DNA was isolated and sheared in a Bioruptor waterbath sonicator (Diagenode). Antibodies against H3K27me3 (generated in this study) and H3K9me2 (ab1220, Abcam) were used for immunoprecipitation. The resulting DNA was analyzed by qPCR using primers listed in Table S6 or by high throughput

sequencing (1–3 replicates per genotype) as described in [Extended Experimental Procedures](#). Meta-telomeres (or meta-centromeres) were generated by aligning all such regions in the genome, calculating average sequencing read coverage, and normalizing both to a WCE sample as well as for differences in total read count between samples.

Recombinant Protein Expression and Binding Assays

Codon-optimized vectors were expressed in *E. coli*. Purified GST-tagged Ccc1 chromodomain was bound to a Modified histone peptide array (Active Motif) and detected by chemiluminescence using anti-GST antibodies. To measure dissociation constants, the binding of recombinant Ccc1 chromodomain to a fluorescent H3K27me3 peptide was competed using increasing concentrations of unlabeled H3K27me0/2/3 peptide, with binding measured by fluorescence polarization.

ACCESSION NUMBERS

ChIP-seq and RNA-seq data were deposited in the Gene Expression Omnibus under accession number GSE61550.

SUPPLEMENTAL INFORMATION

Supplemental Information includes Extended Experimental Procedures, six figures, and eight tables and can be found with this article online at <http://dx.doi.org/10.1016/j.cell.2014.11.039>.

AUTHOR CONTRIBUTIONS

P.A.D. and H.D.M. designed the study. P.A.D. performed experiments shown in [Figures 1, 2, 3, 4, 5, 6, S1, S2, S3, S4, S5, and S6](#). C.M.H. performed bioinformatic analyses in [Figures 1, 2, 3, 4, 5, 6, S1, S4, and S5](#). J.J.M. and J.R.Y. performed mass spectrometry analyses shown in [Figure 2](#). L.R.P. and D.G.F. provided protocols and reagents for peptide binding assays shown in [Figure 4](#). E.K.S. and B.D.S. performed recombinant protein expression and pull-down assay shown in [Figure S6B](#) and provided protocols and advice for antibody production. S.M.C. provided protocols and assistance in recombinant protein expression. P.A.D. and H.D.M. wrote the manuscript. All authors contributed to editing the manuscript.

ACKNOWLEDGMENTS

We thank members of the Madhani lab for helpful discussions, N. Nguyen for media preparation, Krzysztof Krajewski and the University of North Carolina High-Throughput Peptide Synthesis and Arraying Facility for histone peptide production, and Geeta Narlikar for critical reading of the manuscript. Mass spectrometry experiments were supported by the National Center for Research Resources (5P41RR011823-17), the National Institute of General Medical Sciences (8 P41 GM103533-17), and the National Institute on Aging (R01AG027463-04).

Received: July 3, 2014

Revised: September 30, 2014

Accepted: November 12, 2014

Published: December 18, 2014

REFERENCES

Aloia, L., Di Stefano, B., and Di Croce, L. (2013). Polycomb complexes in stem cells and embryonic development. *Development* **140**, 2525–2534.

Bender, S., Tang, Y., Lindroth, A.M., Hovestadt, V., Jones, D.T.W., Kool, M., Zapatka, M., Northcott, P.A., Sturm, D., Wang, W., et al. (2013). Reduced H3K27me3 and DNA hypomethylation are major drivers of gene expression in K27M mutant pediatric high-grade gliomas. *Cancer Cell* **24**, 660–672.

Bilodeau, S., Kagey, M.H., Frampton, G.M., Rahl, P.B., and Young, R.A. (2009). SetDB1 contributes to repression of genes encoding developmental regulators and maintenance of ES cell state. *Genes Dev.* **23**, 2484–2489.

Blackledge, N.P., Farcas, A.M., Kondo, T., King, H.W., McGouran, J.F., Hanssen, L.L.P., Ito, S., Cooper, S., Kondo, K., Koseki, Y., et al. (2014). Variant PRC1 complex-dependent H2A ubiquitylation drives PRC2 recruitment and polycomb domain formation. *Cell* **157**, 1445–1459.

Brown, C.A., Murray, A.W., and Verstrepen, K.J. (2010). Rapid expansion and functional divergence of subtelomeric gene families in yeasts. *Curr. Biol.* **20**, 895–903.

Cao, Q., Wang, X., Zhao, M., Yang, R., Malik, R., Qiao, Y., Poliakov, A., Yocum, A.K., Li, Y., Chen, W., et al. (2014). The central role of EED in the orchestration of polycomb group complexes. *Nat. Commun.* **5**, 3127.

Chalker, D.L., Meyer, E., and Mochizuki, K. (2013). Epigenetics of ciliates. *Cold Spring Harb. Perspect. Biol.* **5**, a017764–a017764.

Chow, E.W.L., Morrow, C.A., Djordjevic, J.T., Wood, I.A., and Fraser, J.A. (2012). Microevolution of *Cryptococcus neoformans* driven by massive tandem gene amplification. *Mol. Biol. Evol.* **29**, 1987–2000.

Chun, C.D., and Madhani, H.D. (2010). Applying genetics and molecular biology to the study of the human pathogen *Cryptococcus neoformans*. *Methods Enzymol.* **470**, 797–831.

Collins, R.E., Northrop, J.P., Horton, J.R., Lee, D.Y., Zhang, X., Stallcup, M.R., and Cheng, X. (2008). The ankyrin repeats of G9a and GLP histone methyltransferases are mono- and dimethyllysine binding modules. *Nat. Struct. Mol. Biol.* **15**, 245–250.

Connolly, L.R., Smith, K.M., and Freitag, M. (2013). The *Fusarium graminearum* histone H3 K27 methyltransferase KMT6 regulates development and expression of secondary metabolite gene clusters. *PLoS Genet.* **9**, e1003916.

Cooper, S., Dienstbier, M., Hassan, R., Schermelleh, L., Sharif, J., Blackledge, N.P., De Marco, V., Elderkin, S., Koseki, H., Klose, R., et al. (2014). Targeting polycomb to pericentric heterochromatin in embryonic stem cells reveals a role for H2AK119u1 in PRC2 recruitment. *Cell Rep* **7**, 1456–1470.

De Las Peñas, A., Pan, S.J., Castaño, I., Alder, J., Cregg, R., and Cormack, B.P. (2003). Virulence-related surface glycoproteins in the yeast pathogen *Candida glabrata* are encoded in subtelomeric clusters and subject to RAP1- and SIR-dependent transcriptional silencing. *Genes Dev.* **17**, 2245–2258.

Derkacheva, M., Steinbach, Y., Wildhaber, T., Mozgová, I., Mahrez, W., Nanni, P., Bischof, S., Grisse, W., and Hennig, L. (2013). Arabidopsis MSI1 connects LHP1 to PRC2 complexes. *EMBO J.* **32**, 2073–2085.

Domergue, R., Castaño, I., De Las Peñas, A., Zupancic, M., Lockett, V., Hebel, J.R., Johnson, D., and Cormack, B.P. (2005). Nicotinic acid limitation regulates silencing of *Candida* adhesins during UTI. *Science* **308**, 866–870.

Dumesic, P.A., Natarajan, P., Chen, C., Drinnenberg, I.A., Schiller, B.J., Thompson, J., Moresco, J.J., Yates, J.R., 3rd, Bartel, D.P., and Madhani, H.D. (2013). Stalled spliceosomes are a signal for RNAi-mediated genome defense. *Cell* **152**, 957–968.

Eisenberg, J.C. (2012). Structural biology of the chromodomain: form and function. *Gene* **496**, 69–78.

Filion, G.J., van Bommel, J.G., Braunschweig, U., Talhout, W., Kind, J., Ward, L.D., Brugman, W., de Castro, I.J., Kerkhoven, R.M., Bussemaker, H.J., and van Steensel, B. (2010). Systematic protein location mapping reveals five principal chromatin types in *Drosophila* cells. *Cell* **143**, 212–224.

Grewal, S.I.S., and Jia, S. (2007). Heterochromatin revisited. *Nat. Rev. Genet.* **8**, 35–46.

Hansen, K.H., Bracken, A.P., Pasini, D., Dietrich, N., Gehani, S.S., Monrad, A., Rappasilber, J., Lerdrup, M., and Helin, K. (2008). A model for transmission of the H3K27me3 epigenetic mark. *Nat. Cell Biol.* **10**, 1291–1300.

Hassan, A.H., Prochasson, P., Neely, K.E., Galasinski, S.C., Chandy, M., Carrozza, M.J., and Workman, J.L. (2002). Function and selectivity of bromodomains in anchoring chromatin-modifying complexes to promoter nucleosomes. *Cell* **111**, 369–379.

- Hihara, S., Pack, C.-G., Kaizu, K., Tani, T., Hanafusa, T., Nozaki, T., Takemoto, S., Yoshimi, T., Yokota, H., Imamoto, N., et al. (2012). Local nucleosome dynamics facilitate chromatin accessibility in living mammalian cells. *Cell Rep* 2, 1645–1656.
- Jamieson, K., Rountree, M.R., Lewis, Z.A., Stajich, J.E., and Selker, E.U. (2013). Regional control of histone H3 lysine 27 methylation in *Neurospora*. *Proc. Natl. Acad. Sci. USA* 110, 6027–6032.
- Janbon, G., Ormerod, K.L., Paulet, D., Byrnes, E.J., 3rd, Yadav, V., Chatterjee, G., Mullapudi, N., Hon, C.-C., Billmyre, R.B., Brunel, F., et al. (2014). Analysis of the genome and transcriptome of *Cryptococcus neoformans* var. *grubii* reveals complex RNA expression and microevolution leading to virulence attenuation. *PLoS Genet.* 10, e1004261.
- Kharchenko, P.V., Alekseyenko, A.A., Schwartz, Y.B., Minoda, A., Riddle, N.C., Ernst, J., Sabo, P.J., Larschan, E., Gorchakov, A.A., Gu, T., et al. (2011). Comprehensive analysis of the chromatin landscape in *Drosophila melanogaster*. *Nature* 471, 480–485.
- Klein, B.J., Piao, L., Xi, Y., Rincon-Arango, H., Rothbart, S.B., Peng, D., Wen, H., Larson, C., Zhang, X., Zheng, X., et al. (2014). The histone-H3K4-specific demethylase KDM5B binds to its substrate and product through distinct PHD fingers. *Cell Rep.* 6, 325–335.
- Klose, R.J., Cooper, S., Farcas, A.M., Blackledge, N.P., and Brockdorff, N. (2013). Chromatin sampling—an emerging perspective on targeting polycomb repressor proteins. *PLoS Genet.* 9, e1003717.
- Lan, F., Collins, R.E., De Cegli, R., Alpatov, R., Horton, J.R., Shi, X., Gozani, O., Cheng, X., and Shi, Y. (2007). Recognition of unmethylated histone H3 lysine 4 links BHC80 to LSD1-mediated gene repression. *Nature* 448, 718–722.
- Liou, G.-G., Tanny, J.C., Kruger, R.G., Walz, T., and Moazed, D. (2005). Assembly of the SIR complex and its regulation by O-acetyl-ADP-ribose, a product of NAD-dependent histone deacetylation. *Cell* 121, 515–527.
- Liu, Y., Taverna, S.D., Muratore, T.L., Shabanowitz, J., Hunt, D.F., and Allis, C.D. (2007). RNAi-dependent H3K27 methylation is required for heterochromatin formation and DNA elimination in *Tetrahymena*. *Genes Dev.* 21, 1530–1545.
- Margueron, R., and Reinberg, D. (2011). The Polycomb complex PRC2 and its mark in life. *Nature* 469, 343–349.
- Margueron, R., Justin, N., Ohno, K., Sharpe, M.L., Son, J., Drury, W.J., 3rd, Voigt, P., Martin, S.R., Taylor, W.R., De Marco, V., et al. (2009). Role of the polycomb protein EED in the propagation of repressive histone marks. *Nature* 461, 762–767.
- McDonagh, A., Fedorova, N.D., Crabtree, J., Yu, Y., Kim, S., Chen, D., Loss, O., Cairns, T., Goldman, G., Armstrong-James, D., et al. (2008). Sub-telomere directed gene expression during initiation of invasive aspergillosis. *PLoS Pathog.* 4, e1000154.
- Min, J., Zhang, Y., and Xu, R.-M. (2003). Structural basis for specific binding of Polycomb chromodomain to histone H3 methylated at Lys 27. *Genes Dev.* 17, 1823–1828.
- Mozzetta, C., Pontis, J., Fritsch, L., Robin, P., Portoso, M., Proux, C., Margueron, R., and Ait-Si-Ali, S. (2014). The histone H3 lysine 9 methyltransferases G9a and GLP regulate polycomb repressive complex 2-mediated gene silencing. *Mol. Cell* 53, 277–289.
- O'Meara, M.M., and Simon, J.A. (2012). Inner workings and regulatory inputs that control Polycomb repressive complex 2. *Chromosoma* 121, 221–234.
- Plass, C., Pfister, S.M., Lindroth, A.M., Bogatyrova, O., Claus, R., and Lichter, P. (2013). Mutations in regulators of the epigenome and their connections to global chromatin patterns in cancer. *Nat. Rev. Genet.* 14, 765–780.
- Popovic, R., Martinez-Garcia, E., Giannopoulou, E.G., Zhang, Q., Zhang, Q., Ezponda, T., Shah, M.Y., Zheng, Y., Will, C.M., Small, E.C., et al. (2014). Histone methyltransferase MMSET/NSD2 alters EZH2 binding and reprograms the myeloma epigenome through global and focal changes in H3K36 and H3K27 methylation. *PLoS Genet.* 10, e1004566.
- Poux, S., Melfi, R., and Pirrotta, V. (2001). Establishment of Polycomb silencing requires a transient interaction between PC and ESC. *Genes Dev.* 15, 2509–2514.
- Reynolds, N., Salmon-Divon, M., Dvinge, H., Hynes-Allen, A., Balasooriya, G., Leaford, D., Behrens, A., Bertone, P., and Hendrich, B. (2012). NuRD-mediated deacetylation of H3K27 facilitates recruitment of Polycomb Repressive Complex 2 to direct gene repression. *EMBO J.* 31, 593–605.
- Rosenfeld, J.A., Wang, Z., Schones, D.E., Zhao, K., DeSalle, R., and Zhang, M.Q. (2009). Determination of enriched histone modifications in non-genic portions of the human genome. *BMC Genomics* 10, 143.
- Shaver, S., Casas-Mollano, J.A., Cerny, R.L., and Cerutti, H. (2010). Origin of the polycomb repressive complex 2 and gene silencing by an E(z) homolog in the unicellular alga *Chlamydomonas*. *Epigenetics* 5, 301–312.
- Simon, J.A., and Kingston, R.E. (2009). Mechanisms of polycomb gene silencing: knowns and unknowns. *Nat. Rev. Mol. Cell Biol.* 10, 697–708.
- Simon, J.A., and Kingston, R.E. (2013). Occupying chromatin: Polycomb mechanisms for getting to genomic targets, stopping transcriptional traffic, and staying put. *Mol. Cell* 49, 808–824.
- Song, J., Angel, A., Howard, M., and Dean, C. (2012). Vernalization - a cold-induced epigenetic switch. *J. Cell Sci.* 125, 3723–3731.
- Sparmann, A., and van Lohuizen, M. (2006). Polycomb silencers control cell fate, development and cancer. *Nat. Rev. Cancer* 6, 846–856.
- Steffen, P.A., and Ringrose, L. (2014). What are memories made of? How Polycomb and Trithorax proteins mediate epigenetic memory. *Nat. Rev. Mol. Cell Biol.* 15, 340–356.
- Suganuma, T., Pattenden, S.G., and Workman, J.L. (2008). Diverse functions of WD40 repeat proteins in histone recognition. *Genes Dev.* 22, 1265–1268.
- Tan, J.-Z., Yan, Y., Wang, X.-X., Jiang, Y., and Xu, H.E. (2014). EZH2: biology, disease, and structure-based drug discovery. *Acta Pharmacol. Sin.* 35, 161–174.
- Tie, F., Banerjee, R., Stratton, C.A., Prasad-Sinha, J., Stepanik, V., Zlobin, A., Diaz, M.O., Scacheri, P.C., and Harte, P.J. (2009). CBP-mediated acetylation of histone H3 lysine 27 antagonizes *Drosophila* Polycomb silencing. *Development* 136, 3131–3141.
- Wang, Z., Zang, C., Rosenfeld, J.A., Schones, D.E., Barski, A., Cuddapah, S., Cui, K., Roh, T.-Y., Peng, W., Zhang, M.Q., and Zhao, K. (2008). Combinatorial patterns of histone acetylations and methylations in the human genome. *Nat. Genet.* 40, 897–903.
- Xu, C., Bian, C., Yang, W., Galka, M., Ouyang, H., Chen, C., Qiu, W., Liu, H., Jones, A.E., MacKenzie, F., et al. (2010). Binding of different histone marks differentially regulates the activity and specificity of polycomb repressive complex 2 (PRC2). *Proc. Natl. Acad. Sci. USA* 107, 19266–19271.
- Zhang, K., Mosch, K., Fischle, W., and Grewal, S.I.S. (2008). Roles of the Clr4 methyltransferase complex in nucleation, spreading and maintenance of heterochromatin. *Nat. Struct. Mol. Biol.* 15, 381–388.
- Zheng, Y., He, L., Wan, Y., and Song, J. (2013). H3K9me-enhanced DNA hypermethylation of the p16INK4a gene: an epigenetic signature for spontaneous transformation of rat mesenchymal stem cells. *Stem Cells Dev.* 22, 256–267.
- Zhu, B., and Reinberg, D. (2011). Epigenetic inheritance: uncontested? *Cell Res.* 21, 435–441.

Conformational Changes of Elongation Factor G on the Ribosome during tRNA Translocation

Jinzhong Lin,^{1,4} Matthieu G. Gagnon,^{1,3,4} David Bulkley,^{1,2,5} and Thomas A. Steitz^{1,2,3,*}

¹Department of Molecular Biophysics and Biochemistry, Yale University, New Haven, CT 06520-8114, USA

²Department of Chemistry, Yale University, New Haven, CT 06520-8107, USA

³Howard Hughes Medical Institute, Yale University, New Haven, CT 06520-8114, USA

⁴Co-first author

⁵Present address: Department of Biochemistry and Biophysics, University of California San Francisco School of Medicine, San Francisco, CA 94158-2517, USA

*Correspondence: thomas.steitz@yale.edu

<http://dx.doi.org/10.1016/j.cell.2014.11.049>

SUMMARY

The universally conserved GTPase elongation factor G (EF-G) catalyzes the translocation of tRNA and mRNA on the ribosome after peptide bond formation. Despite numerous studies suggesting that EF-G undergoes extensive conformational rearrangements during translocation, high-resolution structures exist for essentially only one conformation of EF-G in complex with the ribosome. Here, we report four atomic-resolution crystal structures of EF-G bound to the ribosome programmed in the pre- and posttranslocational states and to the ribosome trapped by the antibiotic dityromycin. We observe a previously unseen conformation of EF-G in the pretranslocation complex, which is independently captured by dityromycin on the ribosome. Our structures provide insights into the conformational space that EF-G samples on the ribosome and reveal that tRNA translocation on the ribosome is facilitated by a structural transition of EF-G from a compact to an elongated conformation, which can be prevented by the antibiotic dityromycin.

INTRODUCTION

Translation of the genetic code requires a codon-by-codon movement of mRNA and its associated tRNAs through the ribosome, a process catalyzed by the guanosine triphosphatase (GTPase) elongation factor G (EF-G) (Voorhees and Ramakrishnan, 2013). After each codon is decoded in the ribosome and peptide bond formation has occurred, the ribosome in the pretranslocational (PRE) state fluctuates between two conformations (Blanchard et al., 2004; Cornish et al., 2008; Fei et al., 2008; Munro et al., 2007) through a ratchet-like movement of the 30S ribosomal subunit with respect to the 50S subunit (Frank and Agrawal, 2000): a nonrotated form with tRNAs in the classical A/A and P/P states and a rotated form in which the CCA acceptor

ends of tRNAs have moved from the A and P sites to the P and E sites on the 50S subunit, taking the hybrid A/P and P/E positions, respectively. EF-G in complex with guanosine triphosphate (GTP) engages the PRE ribosome in both states, but binding to the nonrotated PRE ribosome is immediately followed by the ratchet-like movement of the ribosome into the rotated state (Chen et al., 2011, 2013a; Ermolenko and Noller, 2011; Holtkamp et al., 2014; Spiegel et al., 2007). In the next step, which is facilitated by the conformational changes of EF-G and concomitant GTP hydrolysis, the anticodon ends of tRNAs are translocated inside the ribosome via an intermediate step that involves swiveling of the 30S subunit head domain (Guo and Noller, 2012; Zhou et al., 2014), resulting in a posttranslocational (POST) state of the ribosome in which the mRNA has been moved by one codon.

The structures of ribosome complexes with EF-G determined by cryoelectron microscopy (cryo-EM) (Agrawal et al., 1998; Connell et al., 2007; Frank and Agrawal, 2000; Ramrath et al., 2013; Ratje et al., 2010; Valle et al., 2003) and X-ray crystallography (Chen et al., 2013b; Gao et al., 2009; Pulk and Cate, 2013; Tourigny et al., 2013; Zhou et al., 2013, 2014) have shown that EF-G binds to the ribosome mainly through interactions between its G domain (domain I) and the 50S subunit. These structures, however, represent either a POST state of the ribosome (Gao et al., 2009) or a state in transit during tRNA translocation (Chen et al., 2013b; Ramrath et al., 2013; Tourigny et al., 2013; Zhou et al., 2013, 2014) and exhibit an elongated form of EF-G with its domain IV projecting into the decoding center of the ribosome, where the anticodon end of the A-site tRNA would be bound.

How EF-G binds a PRE ribosome and which position domain IV of EF-G takes to avoid collision with the A-site tRNA before translocation have remained an enigma in the field. Recently, a cryo-EM reconstruction of EF-G on the rotated PRE ribosome exhibited small conformational changes of EF-G compared to the one in the POST complex (Brilot et al., 2013), but the whole EF-G moves as a result of the G-domain rotating around the sarcin-ricin loop (SRL) such that domain IV is positioned next to the A-site tRNA. While the structure provides a snapshot of EF-G bound to the rotated PRE ribosome, the earlier event of EF-G sampling and binding to the nonrotated PRE ribosome remains to be determined. Meanwhile, several lines of evidence suggest

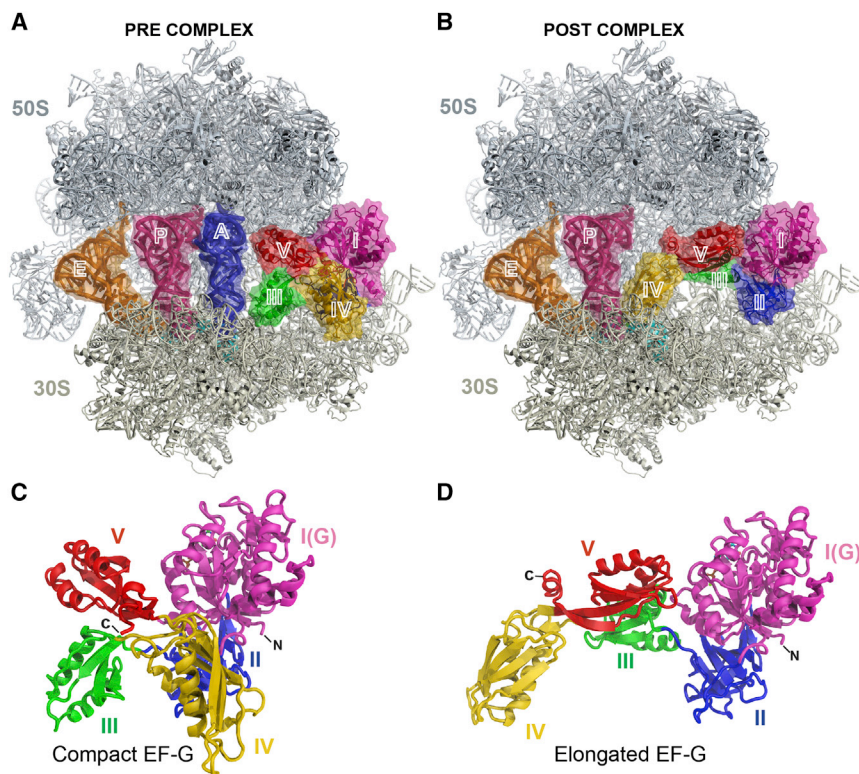


Figure 1. The Structures of EF-G Bound to the Pre- and Posttranslocation Ribosome

(A and B) Overview of EF-G bound to the PRE (A) and the POST (B) ribosome. Shown are the 50S (gray) and the 30S (ivory) subunits, the A site (blue), P site (pink), and E site (orange) tRNAs, mRNA (cyan), and EF-G with its five domains colored differently.

(C and D) Cartoon representations of EF-G shown in the compact conformation (C) from the PRE complex and the elongated conformation (D) from the POST complex. Domains of EF-G are colored and labeled as in (A) and (B).

See also [Figure S1](#), [Table S1](#), and [Movie S1](#).

that a large-scale conformational change of EF-G occurs during translocation ([Agrawal et al., 1999](#); [Bulkley et al., 2014](#); [Munro et al., 2010](#); [Salsi et al., 2014](#); [Stark et al., 2000](#); [Wang et al., 2007](#)), including a recent study of the antibiotic dityromycin ([Bulkley et al., 2014](#)). Dityromycin was shown to block EF-G-mediated tRNA translocation without affecting the binding of EF-G to the ribosome ([Brandt et al., 2006, 2012](#)). The crystal structure of dityromycin in complex with the ribosome shows that dityromycin binds to ribosomal protein S12 ([Bulkley et al., 2014](#)), a position that would severely overlap with domain III of EF-G in the elongated form, thereby indicating the necessity for substantial domain rearrangements in EF-G on the PRE ribosome.

We have now determined the atomic resolution structures of EF-G bound to the ribosome in both the PRE and the POST states, as well as of an EF-G-ribosome complex trapped by the antibiotic dityromycin. We captured a new compact conformation of EF-G in the PRE complex that is also trapped by dityromycin. Together with the elongated form of EF-G in the POST complex, our structures reveal a conformational space that EF-G samples on the ribosome and suggest that tRNA translocation is accompanied by a structural transition of EF-G from a compact to an elongated conformation, which can be blocked by the antibiotic dityromycin.

RESULTS

Crystallization of the L9-GTPase Fusion Protein with the Ribosome

To crystallize EF-G with the ribosome in different stages of translocation, we used a newly developed strategy that entails a

fusion of the N-terminal domain (NTD) of ribosomal protein L9 to the N terminus of EF-G ([Figure S1](#) available online). By varying the length of the linker between the L9-NTD and EF-G, one construct of L9-EF-G crystallized with the ribosome lacking the endogenous L9 under the same condition and in the same space group as the wild-type ribosome ([Blaha et al., 2009](#)). Using this strategy, we first determined the structure of EF-G bound to the ribosome in the POST state. The structure of the POST complex shows

that EF-G binds to the ribosome in the same manner as seen in the previously determined structure ([Figures 1B, 1D, and 2A](#)) ([Gao et al., 2009](#)), whereas the NTD of L9, which is fused to the N terminus of EF-G, binds to its canonical site on the neighboring ribosome ([Figure S1](#)). This indicates that the chimeric fusion does not interfere with the conformation of EF-G. Importantly, this method allows us to crystallize EF-G with the ribosome in the PRE state revealing drastic conformational changes. We have applied this strategy successfully in a recent study of elongation factor 4 bound to a clockwise-ratcheted ribosome ([Gagnon et al., 2014](#)), showing this crystallization strategy to be an excellent tool to study the structures of GTPases on the ribosome in different functional states, especially when only weak or transient interactions are involved.

Structure of a PRE Ribosome in Complex with EF-G

When regular aminoacyl-tRNAs were placed in the ribosomal P and A sites to prepare a PRE ribosome, the resultant structure of the complex always displayed a posttranslocated ribosome, suggesting that the system is capable of active translocation. In order to lock the ribosome in the PRE state, we have taken advantage of nonhydrolyzable aminoacyl-tRNA analogs ([Voorhees et al., 2009](#)) to prevent deaminoacylation of the P-site-bound tRNA and its subsequent movement into the E site. Accordingly, we prepared a PRE ribosome with nonhydrolyzable fMet-NH-tRNA^{fMet} in the P site and Phe-NH-tRNA^{Phe} in the A site. This complex was then cocrystallized with EF-G.

Crystals obtained using this approach diffracted to 2.8 Å resolution, and after molecular replacement using an empty ribosome as the search model, we observed well-resolved electron

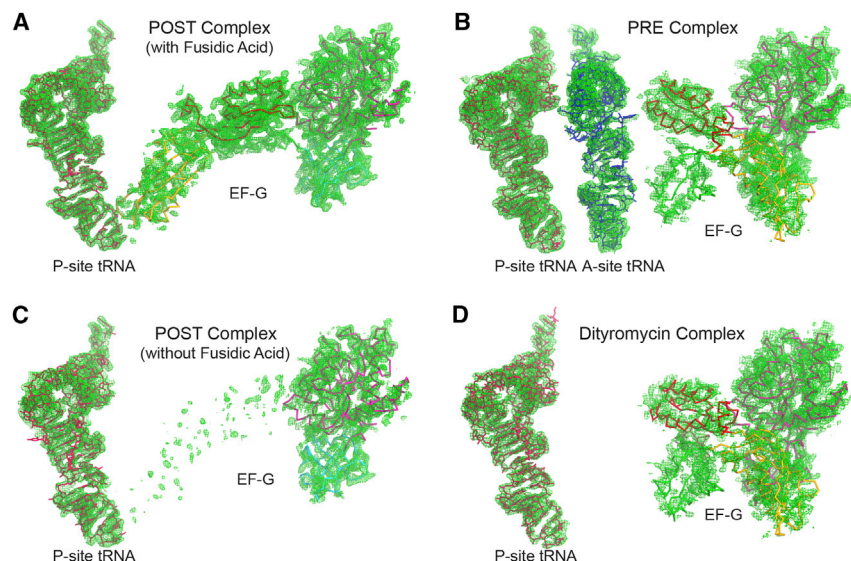


Figure 2. Partial Electron Density for the POST and the PRE Complexes

(A–D) Unbiased $F_{\text{obs}} - F_{\text{calc}}$ difference Fourier map of EF-G and the P-site tRNA in the POST complex in the presence of fusidic acid (A), EF-G and the A- and P-site tRNAs in the PRE complex (B), EF-G and the P-site tRNA in the POST complex in the absence of fusidic acid (C), and EF-G and the P-site tRNA in the dityromycin complex (D). All maps are contoured at 2.5σ obtained after initial refinement with an empty ribosome as a starting model. Domains of EF-G are colored as in Figure 1. See also Table S1.

density for mRNA, tRNAs in the A, P, and E sites, and domains I, II, and V of EF-G. Unexpectedly, the orientation for domain V of EF-G had to be inverted to fit into the electron density compared with the POST complex (Figure 2B). Additional density was confined to regions near domains I and II of EF-G, which was unambiguously assigned to domains III and IV after refinement. As expected for a ribosome with an aminoacyl-tRNA in the P site (Valle et al., 2003), the ribosome is in the nonrotated state with tRNAs in the classical P/P and A/A positions. Whereas domains I and II of EF-G bind to the ribosome in the same manner as they do in previously determined complexes (Gao et al., 2009; Tourigny et al., 2013), domains III–V undergo dramatic conformational changes, resulting in a structure of EF-G bound to the ribosome that has not been previously observed (Figures 1A and 1C; Movie S1).

EF-G in a Compact Conformation

Instead of exhibiting the usual elongated shape seen in previous structures, EF-G in the PRE complex adopts a compact conformation in which domain IV is in close proximity to domains I and II. A superimposition of domain I from the PRE and the POST complexes reveals that domains III–V move as a relatively rigid entity, swiveling around the center of domain V, such that domain V remains in the same position but flips by $\sim 180^\circ$ with a simultaneous $\sim 90^\circ$ self-rotation (Figure 3A; Movies S1 and S2). As a result, the tip of domain IV swivels by ~ 100 Å between the two conformations with a 90° self-rotation, a possibility that was not previously anticipated for EF-G. These movements are concomitant with a swing of domain III, which disengages from its interactions with domain I near the catalytic site and moves outward by ~ 50 Å (Figure 3A). It appears that the rearrangement of domains III–V relies on the loop connecting domains II and III, which is able to turn 90° between the two conformations of EF-G (Figure 3A). Overall, the two relatively rigid entities in the EF-G structure, domains I–II and domains III–V, are loosely connected through a flexible loop without apparent interaction in the compact conformation, and as a result, the catalytic site is fully

exposed, and switches I and II are both disordered (Figures 3B and 3C).

Interactions between the Compact EF-G and the Ribosome

Although domains I and II of EF-G interact with the ribosome in essentially the same

manner in both the PRE and the POST complexes, the interfaces between domains III–V and the ribosome are significantly different. Instead of occupying its usual binding position in the intersubunit cleft of the ribosome between proteins S12 and L14, domain III moves to the opposite side of ribosomal protein S12 in the PRE complex, being positioned close to the A-site tRNA and h34 in the 30S head (Figure 4B). Domain IV hangs over the 30S shoulder with its tip pointing toward protein S4 in the PRE complex, in contrast with the POST complex, where domain IV reaches into the A site (Figure 4C). Strikingly, the position of domain IV is similar to the interpretation made of a previous low-resolution cryo-EM reconstruction (Stark et al., 2000), in which the antibiotic thiostrepton was used to trap EF-G on the PRE ribosome. Domain V is positioned in the vicinity of the same elements of the ribosome in both the PRE and the POST complexes (Figure 4D), but the backward folding of EF-G in the PRE complex makes domain V more distant from these elements, such that helices H43/44 in the stalk base become mobile and the nucleotides at the tips of H43/44 and the SRL are more exposed in the PRE complex (Figure 5). Interestingly, the new interface between domain V and the stalk base in the PRE complex may allow the binding of the antibiotic thiostrepton to the stalk base (Figure S2), suggesting the prior cryo-EM structure (Stark et al., 2000) may have captured a similar compact conformation of EF-G.

EF-G Has Two Superdomains that Are Loosely Connected

The compact EF-G reveals a hinge joint that divides EF-G into two superdomains: domains I–II and domains III–V. To explore the interdomain flexibility of EF-G, we redetermined the structure of the POST complex in the absence of fusidic acid. We observed well-resolved density for domains I, II, and GDP, which bind tightly to the ribosome. However, domains III–V become flexible as shown by their residual density, which is only strong enough to indicate that EF-G is in the elongated conformation (Figure 2C). Soaking fusidic acid into the crystal restores density for all domains of EF-G (Figure 2A). These observations confirm

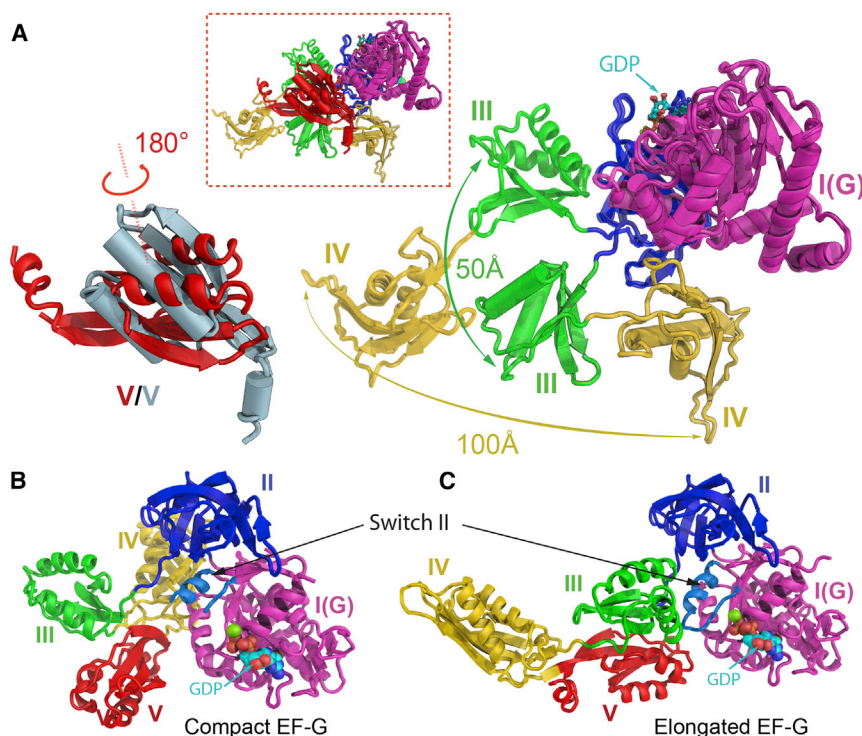


Figure 3. Comparison of the EF-G Structures in the Elongated and the Compact Conformations

(A) Inset is a superimposition of the structures of the elongated and the compact EF-G through domain I. Helices in the compact EF-G are displayed as cylinders. Lower right is a close-up view of the movements of domains III and IV. For clarity, conformational change of domain V is displayed separately in the lower left, where the one from the compact EF-G is colored in light blue. The GDP nucleotide is shown as spheres.

(B and C) Structures of the compact (B) and the elongated (C) EF-G viewed from the catalytic site. The switch II is colored in light blue as indicated. The switch I loop is disordered and not shown in both complexes.

See also [Movie S2](#).

that EF-G favors the elongated conformation (Czworkowski and Moore, 1997), while harboring an intrinsic flexibility between the two relatively independent superdomains that are connected through a hinge. In the compact EF-G conformation, the absence of interaction between the superdomains (Figure 3C) strongly suggests that its binding partner, the PRE ribosome, stabilizes EF-G in a compact form.

Dityromycin Traps a Compact Form of EF-G on the Ribosome

The newly characterized antibiotic dityromycin/GE82832 targets ribosomal protein S12 and traps EF-G in a pretranslocational state (Bulkley et al., 2014). To investigate the conformation of EF-G on the ribosome trapped by dityromycin, we determined a structure of EF-G bound to the ribosome in the presence of dityromycin (Figure 6A). The ribosome was programmed in the POST state to remove the structural constraints imposed by the A-site tRNA on the conformation of EF-G. Remarkably, EF-G adopts the same compact form on the ribosome in response to the binding of dityromycin instead of the one observed in the POST complex (Figures 6B and 6C; [Movie S2](#)). Our structure shows that the binding position of dityromycin on protein S12 does not interfere with domain III of EF-G in the compact conformation, while it would clash with domain III when EF-G is in the elongated conformation.

DISCUSSION

EF-G Exhibits a Great Degree of Conformational Flexibility on the Ribosome

This study unveils a compact conformation of EF-G on the ribosome, suggesting that EF-G is far more flexible than previously

thought. The transient nature of this conformation may account for the fact that it has eluded direct observation for decades despite extensive studies involving various techniques. EF-G favors the elongated conformation in solution through weak association between two superdomains, regardless of the identity of the bound nucleotide (Czworkowski and Moore, 1997; Czworkowski et al., 1994). Our structures show that this weak association breaks as a result of EF-G binding to the PRE ribosome. It is notable that the interface between the two superdomains in EF-G is not strengthened by the binding of GTP when EF-G is off the ribosome, because switches I and II remain disordered in both states (Hansson et al., 2005; Ticu et al., 2009). This suggests that the flexibility of EF-G is minimally influenced by the bound nucleotide.

A Pretranslocation Complex of the Ribosome with EF-G

It has been a challenge to obtain the structural conformation of EF-G-GTP on a pretranslocation ribosome because of its transient existence and the difficulty in preparing a homogenous sample of the PRE ribosome that is deficient in tRNA translocation upon EF-G binding (Figure 7, steps A and B). Although the antibiotic viomycin can prevent translocation by keeping the PRE ribosome in the rotated state, considerable conformational heterogeneity still exists (Brilot et al., 2013; Stanley et al., 2010). In this study, we found the placement of nonhydrolyzable aminoacyl-tRNA in the P site to be effective in stalling the ribosome in the PRE state albeit before peptidyl transfer. Such ribosomes are essentially identical to the authentic PRE ribosome (after peptidyl transfer) in the nonrotated state. However, we found only in the presence of the GDP nucleotide, and not of GTP, does EF-G crystalize with the nonrotated ribosome under our experimental conditions. This is likely because of the unstable binding of domains I and II of EF-G on the nonrotated ribosome in the presence of GTP as confirmed by a recent crystal structure (Pulk and Cate, 2013). It has been established that EF-G bound with GTP engages the PRE ribosome. Therefore, in the bona fide

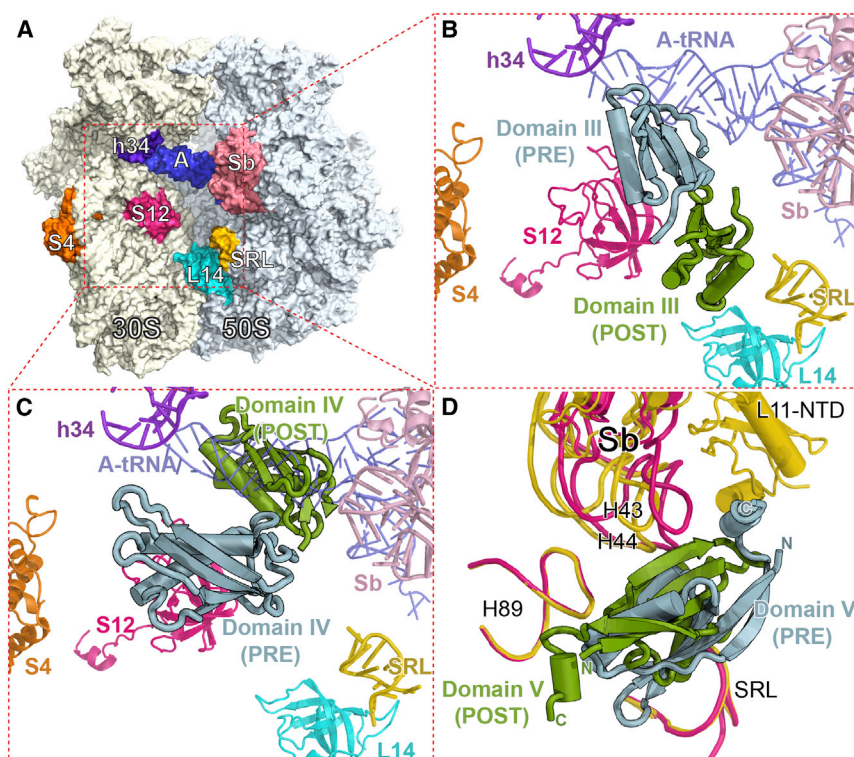


Figure 4. Interfaces between Domains III, IV, and V of EF-G and the Ribosome in the PRE and the POST Complexes

(A) Overview of the ribosome showing the orientation of the insets (B) and (C). Elements of the ribosome are indicated and colored differently. (B and C) Positions of domains III (B) and IV (C) on the ribosome in the two complex structures. (D) Surroundings of domain V in the two complex structures. Helix 43/44, L11-NTD in the stalk base (Sb), helix 89, and the sarcin-ricin loop (SRL) are shown in yellow in the POST complex and pink in the PRE complex. The L11-NTD in the PRE complex is not visible.

PRE complex, GTP instead of GDP associates with EF-G (Figure 7, steps C and D), although minor positional adjustments of domains I and II of EF-G should be anticipated (Gao et al., 2009; Pulk and Cate, 2013; Tourigny et al., 2013).

Our PRE complex addresses the long-standing puzzle of how EF-G avoids a collision with the A-site tRNA before promoting its translocation: domain IV simply folds backward through an interdomain joint. Such a conformational change is consistent with the movement of domain IV with respect to ribosomal protein S12 revealed by a recent single-molecule fluorescence resonance energy transfer (smFRET) study (Salsi et al., 2014). Evidently, the compact conformation of EF-G on the nonrotated ribosome displays the extreme end of the conformational

space at which domain IV reaches its closest proximity to domain II (Figure 7, step C). It is likely that domain IV could freely move next to the anticodon stem loop of the A-site tRNA following the rotating motion of the 30S subunit, thereby adopting a conformation similar to that seen in a recent cryo-EM structure of EF-G bound to the rotated PRE ribosome (Brilot et al., 2013) (Figure 7, steps C–E). Therefore, EF-G may not necessarily adopt the fully compact form when engaging the rotated PRE ribosome unless the ribosome is locked in the PRE state (Figure 7, step D). Interestingly, a smFRET study observed fluctuations of FRET between the C terminus of EF-G and the A-site tRNA to zero after EF-G-GTP binds to the viomycin-trapped PRE ribosome (Munro et al., 2010); part of the fluctuations was attributed to the conformational changes of EF-G on the ribosome. We reason that EF-G-GTP can sporadically sample the fully compact conformation on the rotated PRE ribosome. Our dityromycin complex further confirms the flexibility of EF-G and the existence of its compact form on the ribosome.

Although it is debatable whether the antibiotic thiostrepton inhibits EF-G turnover on the ribosome (Rodnina et al., 1999) or binding to the ribosome (Walter et al., 2012), our data suggest

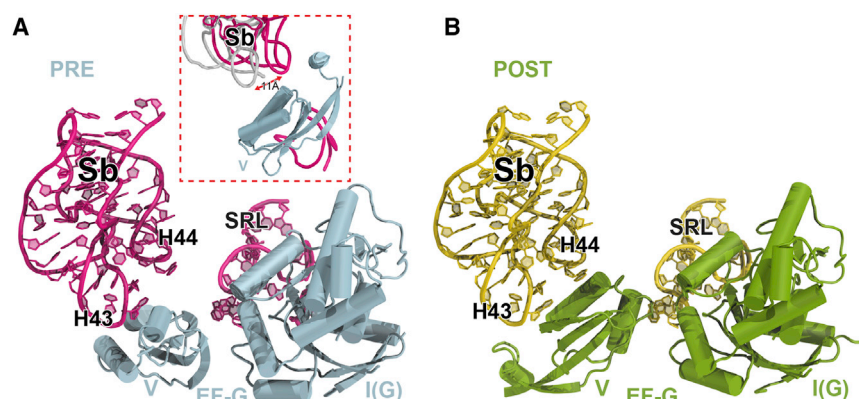


Figure 5. Contacts between Domain V of EF-G, the Stalk Base, and the Sarcin-Ricin Loop

(A and B) Nucleotides at the tips of H43, H44, and the SRL are exposed in the PRE complex and are in close contacts with domain V in the POST complex. Positions of Sb from the two copies in the crystal of the PRE complex shown in the inset of (A) demonstrate that Sb becomes flexible in the PRE state. See also Figure S2 and Movie S2.

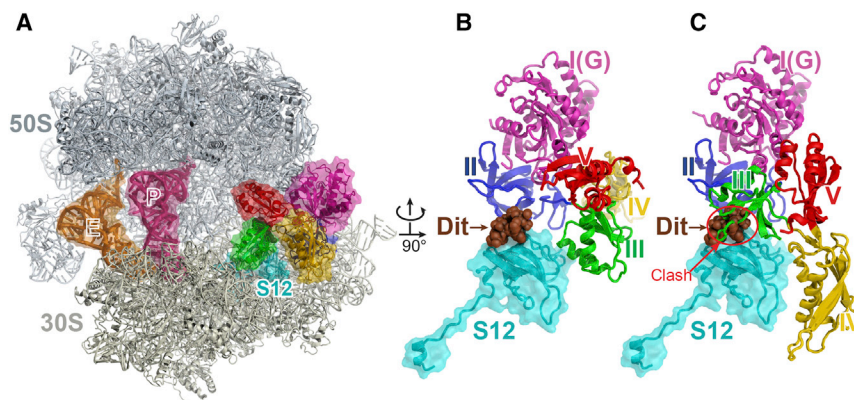


Figure 6. The Structure of EF-G Bound to the Ribosome Trapped by the Antibiotic Dityromycin

(A) Overview of the structure of the complex. The components are colored in the same scheme as in Figure 1, except that here ribosomal protein S12, instead of mRNA, is shown in cyan. Dityromycin (Dit) binds to protein S12 located behind EF-G. (B) Close-up of EF-G, S12, and dityromycin (brown). (C) Model of EF-G from the POST complex on the ribosome showing the steric collision between domain III and dityromycin. See also Movie S2.

that it may be able to coexist with a compact EF-G on the ribosome, thereby supporting the previous cryo-EM study (Stark et al., 2000). However, the close proximity of thiostrepton to domain V of EF-G and the SRL may interfere with stable binding of EF-G to the ribosome.

Insights into EF-G-Mediated tRNA Translocation

A comparison of the structures of our PRE and POST complexes immediately suggests that tRNA translocation is associated with a structural transition of EF-G from the compact to the previously observed elongated form (Figure 7; Movie S2). The path of domain IV movement merges with that of the anticodon stem loop of the A-site tRNA, in which the A-site tRNA travels into the P site, and domain IV enters the vacated A site. Single-molecule studies have suggested that conformational changes of EF-G are coordinated with the ribosome during translocation (Chen et al., 2013b; Munro et al., 2010). Our work offers clues

into the communication between EF-G and the ribosome during translocation. The structural transition of EF-G involves domain III passing over ribosomal protein S12 to approach the GTP-binding pocket in domain I (Figure 4B). Protein S12 seems to pose a steric restriction on the path of domain III in the non-rotated PRE complex, which could be presumably lifted by the rotation of the 30S subunit. On the other hand, dityromycin binding on top of protein S12 completely blocks the path taken by domain III, thereby preventing a structural transition of EF-G and inhibiting tRNA translocation (Figure 7, steps C–E; Movie S2). Interestingly, removal of S12 from the ribosome stimulates spontaneous translocation (Cukras et al., 2003), underlining the significance of the interaction between S12 and EF-G during translocation. Domain V flips underneath the stalk base (H43 and H44) during the conformational change of EF-G. Consistent with chemical probing data (Bowen et al., 2005; Wilson and Nechifor, 2004), our structures show that the stalk base, which

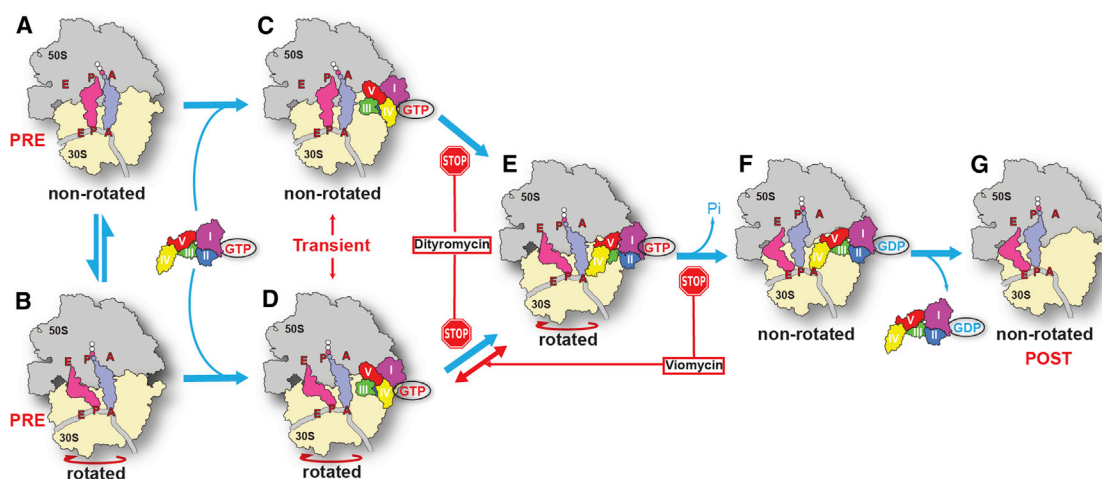


Figure 7. Conformational Changes of EF-G on the Ribosome

EF-G in complex with GTP transiently folds into a compact conformation, from an elongated conformation in the ribosome-free state, after engaging the ribosome in the pretranslocational state to avoid a collision with the A-site tRNA (steps A–D). Rotation of the 30S subunit enables domain IV moving next to the A-site tRNA, a step that can be blocked by the antibiotic dityromycin (steps C–E). Further conformational changes of EF-G with concomitant GTP hydrolysis facilitate tRNA translocation (steps E and F). This process involves swiveling of the 30S head domain (Ramrath et al., 2013), which is not shown here. The antibiotic viomycin prevents translocation by locking the ribosome in the rotated state, while not affecting the initial conformational changes of EF-G (Munro et al., 2010). tRNA translocation is completed by dissociation of EF-G in complex with GDP from the ribosome (steps F and G).

is mobile in the PRE complex, is stabilized by domain V in the POST complex. This may account for the different FRET states observed between the G' subdomain of EF-G and protein L11 in the stalk base (Wang et al., 2007). As part of the GTPase-associated center on the ribosome, the stalk (through its bound protein L12) may stimulate GTP hydrolysis (Mohr et al., 2002) or control the timing of phosphate release (Savelsbergh et al., 2005) by sensing the orientation of domain V. Considering that the swivel of the 30S head domain effectively translocates the anticodon ends of the tRNAs (Guo and Noller, 2012; Ramrath et al., 2013; Zhou et al., 2014) and the critical role of domain IV in translocation (Rodnina et al., 1997), we speculate that an interaction between domain IV and the 30S head may be essential for translocation. In support of this proposal, h34 in the 30S head, which slightly overlaps with the path taken by domain IV during the transformation of EF-G (Figure 4C), was found to be protected during translocation (Matassova et al., 2001). It is generally accepted that GTP hydrolysis in EF-G precedes tRNA translocation (Pan et al., 2007; Savelsbergh et al., 2003), but how exactly these two processes are coupled remains less understood. To activate the catalytic center, domain III of EF-G needs to be positioned next to domain I to close the GTP binding pocket (Chen et al., 2013b; Martemyanov and Gudkov, 2000; Pulk and Cate, 2013), which would require EF-G to form at least a partially extended conformation (Figure 7, step E). This suggests that the earlier stage of conformational change of EF-G is independent of GTP hydrolysis (Salsi et al., 2014). Energy from GTP hydrolysis could be harnessed to promote further conformational changes of EF-G to the fully elongated conformation with domain IV reaching into the A site (Figure 7, step F). Such a process, coupled with a swivel of the 30S head, would result in translocation of the anticodon ends of tRNAs in the ribosome.

EXPERIMENTAL PROCEDURES

Additional details can be found online in the [Extended Experimental Procedures](#).

Preparation of the L9-EF-G Protein Fusions and the *Thermus thermophilus* Mutant Ribosomes Lacking L9

The N-terminal domain (74 residues) of ribosomal protein L9 was fused to the N terminus of EF-G with varying lengths of the linker between L9 and EF-G, as previously described (Gagnon et al., 2014). The *Escherichia coli* BL21 (DE3) Star (Invitrogen) cells were transformed with each construct, and expression of the protein fusion was induced when the absorbance reached ~ 2.0 at 600 nm.

Before lysis, cells with the overexpressed protein fusion were resuspended at 4°C in a buffer containing 20 mM Tris-HCl (pH 8.0), 50 mM NaCl, and 1 mM β -mercaptoethanol. Pure L9-EF-G fusion protein was obtained after multiple purification steps, including hydrophobic interaction, anion exchange, and size-exclusion chromatography. The purified fractions containing the L9-EF-G fusion were concentrated to ~ 100 μ M in a buffer containing 10 mM Tris-HCl (pH 7.5), 200 mM KCl, 10 mM $\text{Mg}(\text{CH}_3\text{COO})_2$, and 1 mM β -mercaptoethanol.

The *Thermus thermophilus* 70S ribosomes lacking L9 were prepared from the same mutant *T. thermophilus* 70S:L9₁₋₅₈ strain used in the previous study (Gagnon et al., 2014).

Complex Formation and Crystallization

The complexes were formed as previously described with some modifications (Gagnon et al., 2012). The POST complex was formed by incubating ribo-

somes with mRNA and a P-site fMet-tRNA^{fMet}. Thereafter, the L9-EF-G fusion protein was added together with the GDP nucleotide. The PRE complex was formed as described above, except that fMet-NH-tRNA^{fMet} and Phe-NH-tRNA^{Phe} were used. For the dityromycin-containing complex, a P-site Phe-tRNA^{Phe} and dityromycin were used during complex formation.

Ribosome crystals were grown at room temperature in sitting drop trays. All complexes grew in the presence of the L9-EF-G fusion connecting residues 1–74 of ribosomal protein L9 and residues 8–691 of EF-G. The crystals were cryoprotected and frozen in a liquid nitrogen stream before plunging in liquid nitrogen.

Data Collection

X-ray diffraction data were collected at the beamlines X25 at Brookhaven National Laboratory and 24-ID-C at the Advanced Photon Source at Argonne National Laboratory using 0.2° or 0.3° oscillations. Data were integrated and scaled with the XDS program package (Kabsch, 1993).

Molecular Replacement, Model Building, and Structure Refinement

Molecular replacement was performed using PHASER (McCoy et al., 2007). Two 70S ribosomes were found per asymmetric unit of the crystal. EF-G, mRNA, and tRNAs in the A, P, or E sites were built into the $F_{\text{obs}} - F_{\text{calc}}$ electron density map using Coot (Emsley and Cowtan, 2004), and the structures were refined in PHENIX (Adams et al., 2002). The E-site tRNA in all complexes comes from the excess of tRNAs in the sample preparation. In the POST complex, domains III, IV, and V of EF-G were only resolved when the crystals were soaked with fusidic acid. The final refinement statistics for all the complexes are provided in Table S1. Figures 1, 2, 3, 4, 5, and 6 were generated using PyMOL (DeLano, 2006).

ACCESSION NUMBERS

The Protein Data Bank accession numbers for the atomic coordinates and structure factors reported in this paper are 4WPO (PRE complex), 4WQF (POST complex with fusidic acid), 4WQY (POST complex without fusidic acid), and 4WQU (Dityromycin complex).

SUPPLEMENTAL INFORMATION

Supplemental Information includes Extended Experimental Procedures, two figures, one table, and two movies and can be found with this article online at <http://dx.doi.org/10.1016/j.cell.2014.11.049>.

AUTHOR CONTRIBUTIONS

J.L., M.G.G., D.B., and T.A.S. conceived the project. J.L. and M.G.G. designed and performed all experiments. D.B. contributed to the purification of ribosomes. J.L., M.G.G., and T.A.S. analyzed the data and wrote the manuscript.

ACKNOWLEDGMENTS

We thank P. Moore, S. Seetharaman, Y. Polikanov, I. Lomakin, and A. Innis for their valuable discussions and critical reading of the manuscript. We thank R. Grodzicki and Y. Polikanov for preparing tRNAs. The antibiotic dityromycin was kindly provided by the Gualerzi laboratory at the University of Camerino, Italy. We also thank the staff of the Advanced Photon Source beamline 24-ID and the National Synchrotron Light Source beamline X25 for help during data collection and the Center for Structural Biology facility at Yale University for computational support. This work was supported by an NIH grant (GM022778).

Received: July 2, 2014

Revised: September 9, 2014

Accepted: November 21, 2014

Published: January 15, 2015

REFERENCES

- Adams, P.D., Grosse-Kunstleve, R.W., Hung, L.W., Ioerger, T.R., McCoy, A.J., Moriarty, N.W., Read, R.J., Sacchettini, J.C., Sauter, N.K., and Terwilliger, T.C. (2002). PHENIX: building new software for automated crystallographic structure determination. *Acta Crystallogr. D Biol. Crystallogr.* **58**, 1948–1954.
- Agrawal, R.K., Penczek, P., Grassucci, R.A., and Frank, J. (1998). Visualization of elongation factor G on the *Escherichia coli* 70S ribosome: the mechanism of translocation. *Proc. Natl. Acad. Sci. USA* **95**, 6134–6138.
- Agrawal, R.K., Heagle, A.B., Penczek, P., Grassucci, R.A., and Frank, J. (1999). EF-G-dependent GTP hydrolysis induces translocation accompanied by large conformational changes in the 70S ribosome. *Nat. Struct. Biol.* **6**, 643–647.
- Blaha, G., Stanley, R.E., and Steitz, T.A. (2009). Formation of the first peptide bond: the structure of EF-P bound to the 70S ribosome. *Science* **325**, 966–970.
- Blanchard, S.C., Kim, H.D., Gonzalez, R.L., Jr., Puglisi, J.D., and Chu, S. (2004). tRNA dynamics on the ribosome during translation. *Proc. Natl. Acad. Sci. USA* **101**, 12893–12898.
- Bowen, W.S., Van Dyke, N., Murgola, E.J., Lodmell, J.S., and Hill, W.E. (2005). Interaction of thiostrepton and elongation factor-G with the ribosomal protein L11-binding domain. *J. Biol. Chem.* **280**, 2934–2943.
- Brandi, L., Fabbretti, A., Di Stefano, M., Lazzarini, A., Abbondi, M., and Gualerzi, C.O. (2006). Characterization of GE82832, a peptide inhibitor of translocation interacting with bacterial 30S ribosomal subunits. *RNA* **12**, 1262–1270.
- Brandi, L., Maffioli, S., Donadio, S., Quaglia, F., Sette, M., Milón, P., Gualerzi, C.O., and Fabbretti, A. (2012). Structural and functional characterization of the bacterial translocation inhibitor GE82832. *FEBS Lett.* **586**, 3373–3378.
- Brilot, A.F., Korostelev, A.A., Ermolenko, D.N., and Grigorieff, N. (2013). Structure of the ribosome with elongation factor G trapped in the pretranslocation state. *Proc. Natl. Acad. Sci. USA* **110**, 20994–20999.
- Bulkley, D., Brandi, L., Polikanov, Y.S., Fabbretti, A., O'Connor, M., Gualerzi, C.O., and Steitz, T.A. (2014). The antibiotics dityromycin and GE82832 bind protein S12 and block EF-G-catalyzed translocation. *Cell Reports* **6**, 357–365.
- Chen, C., Stevens, B., Kaur, J., Cabral, D., Liu, H., Wang, Y., Zhang, H., Rosenblum, G., Smilansky, Z., Goldman, Y.E., and Cooperman, B.S. (2011). Single-molecule fluorescence measurements of ribosomal translocation dynamics. *Mol. Cell* **42**, 367–377.
- Chen, J., Petrov, A., Tsai, A., O'Leary, S.E., and Puglisi, J.D. (2013a). Coordinated conformational and compositional dynamics drive ribosome translocation. *Nat. Struct. Mol. Biol.* **20**, 718–727.
- Chen, Y., Feng, S., Kumar, V., Ero, R., and Gao, Y.G. (2013b). Structure of EF-G-ribosome complex in a pretranslocation state. *Nat. Struct. Mol. Biol.* **20**, 1077–1084.
- Connell, S.R., Takemoto, C., Wilson, D.N., Wang, H., Murayama, K., Terada, T., Shirouzu, M., Rost, M., Schüler, M., Giesebrecht, J., et al. (2007). Structural basis for interaction of the ribosome with the switch regions of GTP-bound elongation factors. *Mol. Cell* **25**, 751–764.
- Cornish, P.V., Ermolenko, D.N., Noller, H.F., and Ha, T. (2008). Spontaneous intersubunit rotation in single ribosomes. *Mol. Cell* **30**, 578–588.
- Cukras, A.R., Southworth, D.R., Brunelle, J.L., Culver, G.M., and Green, R. (2003). Ribosomal proteins S12 and S13 function as control elements for translocation of the mRNA:tRNA complex. *Mol. Cell* **12**, 321–328.
- Czworkowski, J., and Moore, P.B. (1997). The conformational properties of elongation factor G and the mechanism of translocation. *Biochemistry* **36**, 10327–10334.
- Czworkowski, J., Wang, J., Steitz, T.A., and Moore, P.B. (1994). The crystal structure of elongation factor G complexed with GDP, at 2.7 Å resolution. *EMBO J.* **13**, 3661–3668.
- DeLano, W.L. (2006). The PyMOL molecular graphics system. <http://www.pymol.org>.
- Emsley, P., and Cowtan, K. (2004). Coot: model-building tools for molecular graphics. *Acta Crystallogr. D Biol. Crystallogr.* **60**, 2126–2132.
- Ermolenko, D.N., and Noller, H.F. (2011). mRNA translocation occurs during the second step of ribosomal intersubunit rotation. *Nat. Struct. Mol. Biol.* **18**, 457–462.
- Fei, J., Kosuri, P., MacDougall, D.D., and Gonzalez, R.L., Jr. (2008). Coupling of ribosomal L1 stalk and tRNA dynamics during translation elongation. *Mol. Cell* **30**, 348–359.
- Frank, J., and Agrawal, R.K. (2000). A ratchet-like inter-subunit reorganization of the ribosome during translocation. *Nature* **406**, 318–322.
- Gagnon, M.G., Seetharaman, S.V., Bulkley, D., and Steitz, T.A. (2012). Structural basis for the rescue of stalled ribosomes: structure of YaeJ bound to the ribosome. *Science* **335**, 1370–1372.
- Gagnon, M.G., Lin, J., Bulkley, D., and Steitz, T.A. (2014). Crystal structure of elongation factor 4 bound to a clockwise ratcheted ribosome. *Science* **345**, 684–687.
- Gao, Y.G., Selmer, M., Dunham, C.M., Weixlbaumer, A., Kelley, A.C., and Ramakrishnan, V. (2009). The structure of the ribosome with elongation factor G trapped in the posttranslocational state. *Science* **326**, 694–699.
- Guo, Z., and Noller, H.F. (2012). Rotation of the head of the 30S ribosomal subunit during mRNA translocation. *Proc. Natl. Acad. Sci. USA* **109**, 20391–20394.
- Hansson, S., Singh, R., Gudkov, A.T., Liljas, A., and Logan, D.T. (2005). Crystal structure of a mutant elongation factor G trapped with a GTP analogue. *FEBS Lett.* **579**, 4492–4497.
- Holtkamp, W., Cunha, C.E., Peske, F., Konevega, A.L., Wintermeyer, W., and Rodnina, M.V. (2014). GTP hydrolysis by EF-G synchronizes tRNA movement on small and large ribosomal subunits. *EMBO J.* **33**, 1073–1085.
- Kabsch, W. (1993). Automatic processing of rotation diffraction data from crystals of initially unknown symmetry and cell constants. *J. Appl. Cryst.* **26**, 795–800.
- Martemyanov, K.A., and Gudkov, A.T. (2000). Domain III of elongation factor G from *Thermus thermophilus* is essential for induction of GTP hydrolysis on the ribosome. *J. Biol. Chem.* **275**, 35820–35824.
- Matassova, A.B., Rodnina, M.V., and Wintermeyer, W. (2001). Elongation factor G-induced structural change in helix 34 of 16S rRNA related to translocation on the ribosome. *RNA* **7**, 1879–1885.
- McCoy, A.J., Grosse-Kunstleve, R.W., Adams, P.D., Winn, M.D., Storoni, L.C., and Read, R.J. (2007). Phaser crystallographic software. *J. Appl. Cryst.* **40**, 658–674.
- Mohr, D., Wintermeyer, W., and Rodnina, M.V. (2002). GTPase activation of elongation factors Tu and G on the ribosome. *Biochemistry* **41**, 12520–12528.
- Munro, J.B., Altman, R.B., O'Connor, N., and Blanchard, S.C. (2007). Identification of two distinct hybrid state intermediates on the ribosome. *Mol. Cell* **25**, 505–517.
- Munro, J.B., Wasserman, M.R., Altman, R.B., Wang, L., and Blanchard, S.C. (2010). Correlated conformational events in EF-G and the ribosome regulate translocation. *Nat. Struct. Mol. Biol.* **17**, 1470–1477.
- Pan, D., Kirillov, S.V., and Cooperman, B.S. (2007). Kinetically competent intermediates in the translocation step of protein synthesis. *Mol. Cell* **25**, 519–529.
- Pulk, A., and Cate, J.H. (2013). Control of ribosomal subunit rotation by elongation factor G. *Science* **340**, 1235970.
- Ramrath, D.J., Lancaster, L., Sprink, T., Mielke, T., Loerke, J., Noller, H.F., and Spahn, C.M. (2013). Visualization of two transfer RNAs trapped in transit during elongation factor G-mediated translocation. *Proc. Natl. Acad. Sci. USA* **110**, 20964–20969.
- Ratje, A.H., Loerke, J., Mikolajka, A., Brünner, M., Hildebrand, P.W., Starosta, A.L., Dönhöfer, A., Connell, S.R., Fucini, P., Mielke, T., et al. (2010). Head swivel on the ribosome facilitates translocation by means of intra-subunit tRNA hybrid sites. *Nature* **468**, 713–716.
- Rodnina, M.V., Savelsbergh, A., Katunin, V.I., and Wintermeyer, W. (1997). Hydrolysis of GTP by elongation factor G drives tRNA movement on the ribosome. *Nature* **385**, 37–41.

- Rodnina, M.V., Savelsbergh, A., Matassova, N.B., Katunin, V.I., Semenov, Y.P., and Wintermeyer, W. (1999). Thiostrepton inhibits the turnover but not the GTPase of elongation factor G on the ribosome. *Proc. Natl. Acad. Sci. USA* **96**, 9586–9590.
- Salsi, E., Farah, E., Dann, J., and Ermolenko, D.N. (2014). Following movement of domain IV of elongation factor G during ribosomal translocation. *Proc. Natl. Acad. Sci. USA* **111**, 15060–15065.
- Savelsbergh, A., Katunin, V.I., Mohr, D., Peske, F., Rodnina, M.V., and Wintermeyer, W. (2003). An elongation factor G-induced ribosome rearrangement precedes tRNA-mRNA translocation. *Mol. Cell* **11**, 1517–1523.
- Savelsbergh, A., Mohr, D., Kothe, U., Wintermeyer, W., and Rodnina, M.V. (2005). Control of phosphate release from elongation factor G by ribosomal protein L7/12. *EMBO J.* **24**, 4316–4323.
- Spiegel, P.C., Ermolenko, D.N., and Noller, H.F. (2007). Elongation factor G stabilizes the hybrid-state conformation of the 70S ribosome. *RNA* **13**, 1473–1482.
- Stanley, R.E., Blaha, G., Grodzicki, R.L., Strickler, M.D., and Steitz, T.A. (2010). The structures of the anti-tuberculosis antibiotics viomycin and capreomycin bound to the 70S ribosome. *Nat. Struct. Mol. Biol.* **17**, 289–293.
- Stark, H., Rodnina, M.V., Wieden, H.J., van Heel, M., and Wintermeyer, W. (2000). Large-scale movement of elongation factor G and extensive conformational change of the ribosome during translocation. *Cell* **100**, 301–309.
- Ticu, C., Nechifor, R., Nguyen, B., Desrosiers, M., and Wilson, K.S. (2009). Conformational changes in switch I of EF-G drive its directional cycling on and off the ribosome. *EMBO J.* **28**, 2053–2065.
- Tourigny, D.S., Fernández, I.S., Kelley, A.C., and Ramakrishnan, V. (2013). Elongation factor G bound to the ribosome in an intermediate state of translocation. *Science* **340**, 1235490.
- Valle, M., Zavialov, A., Sengupta, J., Rawat, U., Ehrenberg, M., and Frank, J. (2003). Locking and unlocking of ribosomal motions. *Cell* **114**, 123–134.
- Voorhees, R.M., and Ramakrishnan, V. (2013). Structural basis of the translational elongation cycle. *Annu. Rev. Biochem.* **82**, 203–236.
- Voorhees, R.M., Weixlbaumer, A., Loakes, D., Kelley, A.C., and Ramakrishnan, V. (2009). Insights into substrate stabilization from snapshots of the peptidyl transferase center of the intact 70S ribosome. *Nat. Struct. Mol. Biol.* **16**, 528–533.
- Walter, J.D., Hunter, M., Cobb, M., Traeger, G., and Spiegel, P.C. (2012). Thiostrepton inhibits stable 70S ribosome binding and ribosome-dependent GTPase activation of elongation factor G and elongation factor 4. *Nucleic Acids Res.* **40**, 360–370.
- Wang, Y., Qin, H., Kudaravalli, R.D., Kirillov, S.V., Dempsey, G.T., Pan, D., Cooperman, B.S., and Goldman, Y.E. (2007). Single-molecule structural dynamics of EF-G–ribosome interaction during translocation. *Biochemistry* **46**, 10767–10775.
- Wilson, K.S., and Nechifor, R. (2004). Interactions of translational factor EF-G with the bacterial ribosome before and after mRNA translocation. *J. Mol. Biol.* **337**, 15–30.
- Zhou, J., Lancaster, L., Donohue, J.P., and Noller, H.F. (2013). Crystal structures of EF-G-ribosome complexes trapped in intermediate states of translocation. *Science* **340**, 1236086.
- Zhou, J., Lancaster, L., Donohue, J.P., and Noller, H.F. (2014). How the ribosome hands the A-site tRNA to the P site during EF-G-catalyzed translocation. *Science* **345**, 1188–1191.

A Qrr Noncoding RNA Deploys Four Different Regulatory Mechanisms to Optimize Quorum-Sensing Dynamics

Lihui Feng,¹ Steven T. Rutherford,^{1,4} Kai Papenfort,¹ John D. Bagert,³ Julia C. van Kessel,^{1,5} David A. Tirrell,³ Ned S. Wingreen,^{1,*} and Bonnie L. Bassler^{1,2,*}

¹Department of Molecular Biology, Princeton University, Princeton, NJ 08544, USA

²Howard Hughes Medical Institute, Chevy Chase, MD 20815, USA

³Division of Chemistry and Chemical Engineering, California Institute of Technology, Pasadena, CA 91125, USA

⁴Present address: Genentech, San Francisco, CA 94080, USA

⁵Present address: Department of Molecular and Cellular Biochemistry, Indiana University, Bloomington, IN 47405, USA

*Correspondence: wingreen@princeton.edu (N.S.W.), bbassler@princeton.edu (B.L.B.)

<http://dx.doi.org/10.1016/j.cell.2014.11.051>

SUMMARY

Quorum sensing is a cell-cell communication process that bacteria use to transition between individual and social lifestyles. In vibrios, homologous small RNAs called the Qrr sRNAs function at the center of quorum-sensing pathways. The Qrr sRNAs regulate multiple mRNA targets including those encoding the quorum-sensing regulatory components *luxR*, *luxO*, *luxM*, and *aphA*. We show that a representative Qrr, Qrr3, uses four distinct mechanisms to control its particular targets: the Qrr3 sRNA represses *luxR* through catalytic degradation, represses *luxM* through coupled degradation, represses *luxO* through sequestration, and activates *aphA* by revealing the ribosome binding site while the sRNA itself is degraded. Qrr3 forms different base-pairing interactions with each mRNA target, and the particular pairing strategy determines which regulatory mechanism occurs. Combined mathematical modeling and experiments show that the specific Qrr regulatory mechanism employed governs the potency, dynamics, and competition of target mRNA regulation, which in turn, defines the overall quorum-sensing response.

INTRODUCTION

Small regulatory RNAs (sRNAs) act as core regulators in many bacterial signal transduction cascades (Waters and Storz, 2009). Bacterial sRNAs function by several mechanisms. Here, we focus on *trans*-encoded Hfq-binding sRNAs. This class of sRNAs can act positively or negatively, and noncontiguous base-pairing with mRNA targets is employed. In the case of negative regulation, *trans*-encoded sRNAs base pair near the ribosome binding site of the mRNA target, leading to ribosome occlusion (Altuvia et al., 1998; Kawamoto et al., 2006; Møller et al., 2002; Udekwi et al., 2005). In most cases, occlusion is associated with RNase E recruitment and degradation of the

mRNA (Massé et al., 2003; Prévost et al., 2011). In the case of positive regulation, *trans*-encoded sRNAs perform anti-anti-sense base-pairing with the mRNA target (Fröhlich and Vogel, 2009; Majdalani et al., 1998). Binding reveals the ribosome binding site and promotes stabilization of the mRNA target and, in turn, gene expression (McCullen et al., 2010). The RNA chaperone Hfq mediates the interactions between *trans*-encoded sRNAs and their mRNA targets and protects the sRNAs from RNase E-mediated degradation (Vogel and Luisi, 2011; Kawamoto et al., 2006). Hfq is thought to be limiting, leading to competition between different sRNA-mRNA pairs for its chaperone function (Fender et al., 2010; Hussein and Lim, 2011; Moon and Gottesman, 2011).

The implications of *trans*-encoded sRNA regulation at the systems level depend on the fate of the sRNA. First, sRNAs can undergo coupled degradation in which both the sRNA and the mRNA target are degraded following base-pairing. The RyhB sRNA exemplifies this mode of regulation (Massé et al., 2003). Second, sRNAs can act catalytically, in which the target mRNA is degraded but the sRNA is not. Thus, the sRNA is available to be recycled. One such example is the MicM (ChiX) sRNA, which acts catalytically on the mRNA target *ybfM* (*chiP*) (Overgaard et al., 2009). Third, sRNAs can also act by sequestering their targets. An example of this type of regulation occurs between the sRNA Spot42 and its mRNA target *galK*. In this case, Spot42 specifically blocks the ribosome binding site of *galK*, but no mRNA degradation occurs (Møller et al., 2002). Finally, the fates of sRNAs that act as activators have not been well characterized. In theory, activating sRNAs can be degraded, recycled, or sequestered.

The quorum regulatory RNAs (Qrr) sRNAs are Hfq-dependent *trans*-encoded sRNAs that control vibrio quorum sensing (Lenz et al., 2004). Quorum sensing is a cell-cell communication process that bacteria use to monitor changes in cell-population density and control collective behaviors such as biofilm formation and virulence factor production. Quorum sensing involves production, detection, and population-wide response to extracellular signal molecules called autoinducers (Rutherford and Bassler, 2012). In vibrio quorum-sensing circuits, several nearly identical Qrr sRNAs control multiple target mRNAs, and the Qrr

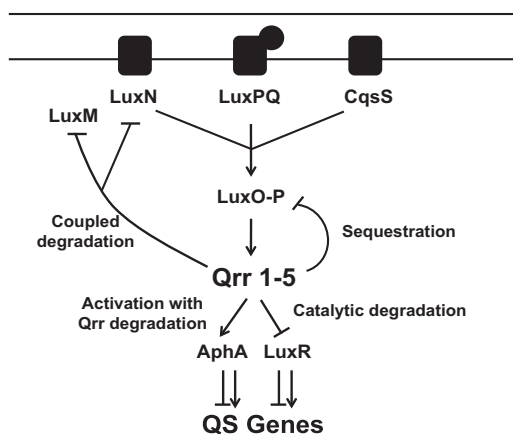


Figure 1. Schematic for How a *V. harveyi* Quorum-Sensing Qrr sRNA Uses Four Regulatory Mechanisms to Control Target mRNAs

At low cell density, the three quorum-sensing receptors LuxN, LuxPQ, and CqsS transfer phosphate through LuxU (not shown) to LuxO. Phosphorylated LuxO activates transcription of genes encoding five sRNAs called Qrr1–Qrr5. Using Qrr3 as the representative quorum-sensing regulatory sRNA, we show that the Qrr sRNA catalytically represses the high-cell-density master regulator *luxR*. The Qrr sRNA represses *luxO* through sequestration. The Qrr sRNA represses the *luxMN* operon through coupled degradation (*luxM* encodes the synthase that produces the ligand for LuxN). The Qrr sRNA also activates translation of the low-cell-density master regulator *aphA*; base-pairing with the *aphA* mRNA leads to Qrr degradation.

sRNAs act as both positive and negative regulators. These features enable us to exploit this set of sRNAs and their particular mRNA targets to dissect pairing regimes, target preferences, and modes of regulation. The Qrr sRNAs positively control the production of the low-cell-density master regulator AphA and they repress the production of the high-cell-density master regulator LuxR (Rutherford et al., 2011; Tu and Bassler, 2007). The Qrr sRNAs feed back to repress the genes encoding one of the quorum-sensing synthase-receptor pairs, LuxMN, and the gene encoding the transcription factor LuxO (Teng et al., 2011; Tu et al., 2010). The Qrr sRNAs also posttranscriptionally regulate sixteen genes outside of the quorum-sensing circuit (Shao et al., 2013).

In the present study, we show that a representative Qrr sRNA, Qrr3, uses four distinct mechanisms to regulate four different target mRNAs. The Qrr3 sRNA undergoes coupled degradation when it pairs with *luxM* mRNA, it uses sequestration to control *luxO* mRNA, it catalytically represses *luxR* mRNA, and it activates *aphA* mRNA expression while the Qrr3 sRNA itself is degraded. The mRNA targets that reduce Qrr sRNA stability (*luxM* and *aphA*) do so by remodeling the 5′-most stem-loop of the Qrr sRNA. mRNA targets that sequester the Qrr sRNA (*luxO*) presumably do so via tight binding to the Qrr sRNA. Indeed, we demonstrate that a particular regulatory mechanism can be converted into a different one by altering the base-pairing position or binding strength. The different sRNA-target mRNA interaction mechanisms result in distinct regulatory strength and dynamical behaviors of the mRNA targets in vivo. Furthermore, the particular regulatory mechanism used for mRNA target regulation is critical for properly timed quorum-sensing responses.

RESULTS

The Qrr3 sRNA Uses Distinct Mechanisms to Regulate Different mRNA Targets

There are 20 known targets of the *Vibrio harveyi* Qrr sRNAs (Shao et al., 2013), four of which, *luxM*, *luxO*, *luxR*, and *aphA*, are members of the quorum-sensing regulatory circuit and are the focus of this work (Figure 1). Little is known about how the five Qrr sRNAs choose among their mRNA targets in vivo. To investigate Qrr target preferences, we developed a competition assay in *Escherichia coli*. We constructed a dual reporter system on a single plasmid that encodes (1) an isopropyl β-D-1-thiogalactopyranoside (IPTG)-inducible 5′UTR-GFP fusion to a Qrr-repressed mRNA target (the Qrr “target” in all assays), and (2) an arabinose inducible 5′UTR-mCherry fusion to a different Qrr-controlled mRNA target (the Qrr “competitor”). We transformed this dual reporter plasmid along with a second plasmid encoding anhydrotetracycline-inducible Qrr3 into *E. coli* (Figure S1A available online; Tables S1, S2, and S3). The five Qrr sRNAs are similar in sequence and secondary structure and they share most of the target mRNAs (Shao et al., 2013; Tu and Bassler, 2007). We arbitrarily chose Qrr3 to use in these assays.

To monitor Qrr preference, we first measured GFP fluorescence from the target mRNA in the absence of both Qrr3 and competitor mRNA to determine the basal expression level of the mRNA target. Next, we measured target GFP fluorescence when Qrr3 was induced to determine the level of target mRNA repression by Qrr3. Finally, we measured GFP fluorescence from the target mRNA when Qrr3 was induced and, additionally, the competitor mRNA was induced to different levels. This third measurement allowed us to assess the ability of different competitor mRNAs to compete with the target mRNA for regulation by Qrr3. Our expectation was that, in the case of a Qrr3 repressed target mRNA, if competition occurred, the target mRNA-GFP fluorescence should increase when we induced expression of the competitor mRNA because the amount of Qrr3 available to regulate the target mRNA would decrease. By contrast, if the target mRNA-GFP level did not change when we induced expression of the competitor mRNA, we would infer that the competitor mRNA did not compete with the target mRNA for regulation by Qrr3.

Our dual reporter system allowed us to simultaneously measure mCherry production from the competitor mRNA. A change in mCherry level following induction of Qrr3 was useful to verify that the competitor was indeed being regulated by Qrr3. We also determined the expression level and the half-life of Qrr3 in the absence and presence of the mRNA targets. Likewise, we measured the expression level of the target mRNAs in the absence and presence of Qrr3. These final measurements allowed us to discover the fates of Qrr3 and the target mRNA, and thus the mechanism used by Qrr3 to control each target—catalytic, coupled degradation, sequestration, or mRNA activation with concomitant sRNA degradation.

Using this strategy, we first investigated whether *luxM* mRNA competes with *luxR* mRNA for regulation by Qrr3. As a control, we show that, in the absence of Qrr3, increasing the *luxM*-mCherry production does not significantly alter LuxR-GFP production (Figure 2A, open circles). When Qrr3 is present, LuxR-GFP is

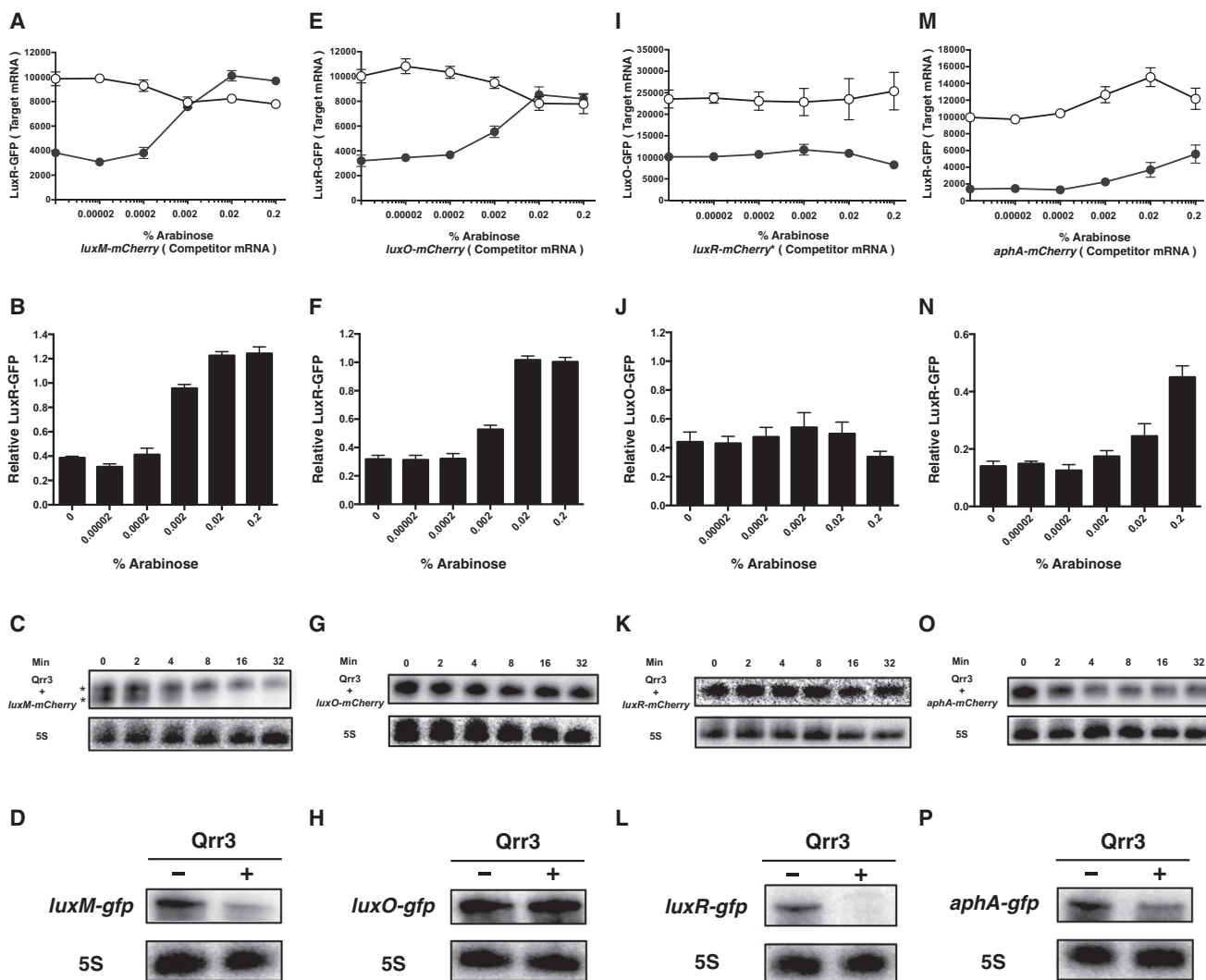


Figure 2. mRNAs Have Different Abilities to Compete for Qrr sRNA Regulation

(A, E, I, and M) Competition between different Qrr sRNA target mRNAs. Fluorescence from a plasmid-borne *luxR-gfp* (A, E, and M) or *luxO-gfp* (I) translational fusion was measured in *E. coli*. Experiments were performed in the absence of Qrr3 (open circles) and in the presence of Qrr3 (filled circles). Arabinose was added to drive production of the competitor mRNA *luxM-mCherry* (A), *luxO-mCherry* (E), *luxR-mCherry** (I), and *aphA-mCherry* (M). Means and SEM for triplicate cultures are shown.

(B, F, J, and N) Quantification of the fractional expression of LuxR-GFP (B, F, and N) or LuxO-GFP (J) from (A), (E), (M), and (I), respectively. GFP fluorescence in the presence of Qrr3 was normalized to that in its absence. Means and SEM for triplicate cultures are shown.

(C, G, K, and O) Half-life of Qrr3 in the presence of *luxM-mCherry* (C), *luxO-mCherry* (G), *luxR-mCherry* (K), and *aphA-mCherry* (O).

(D, H, L, and P) Northern blots of *luxM-gfp* (D), *luxO-gfp* (H), *luxR-gfp* (L), and *aphA-gfp* (P) translational fusions in the absence (–) and presence (+) of Qrr3. For all Northern blots, results are representative of two independent experiments and 5S rRNA was used as the loading control.

See also Figures S1, S2, and S3.

repressed 2.5-fold in the absence of *luxM-mCherry* (Figures 2A, filled circles, and 2B; no arabinose). Inducing *luxM-mCherry* expression causes an increase in LuxR-GFP (Figures 2A, filled circles, and 2B). This result shows that *luxM* mRNA successfully competes with *luxR* mRNA for regulation by Qrr3. We confirmed that in the absence of Qrr3, increasing the arabinose inducer results in increasing production of *luxM-mCherry* (Figure S1B, open circles). At low arabinose concentration and thus low *luxM-mCherry* levels, LuxM-mCherry is repressed 2.5-fold in the presence of Qrr3 (Figure S1C). By contrast, at high arabinose,

and thus high *luxM-mCherry* levels, neither LuxM-mCherry nor LuxR-GFP is repressed by Qrr3 (Figures 2B and S1C). Presumably, under the latter condition, Qrr3 is saturated by the competitor mRNA or degraded. In analogous experiments, we measured the ability of *luxM-mCherry* to compete with *luxO-gfp* and with *luxM-gfp* for regulation by Qrr3 and obtained similar results (Figures S2A and S2B). Thus, *luxM* mRNA can successfully compete for regulation by Qrr3 against *luxM* (itself), *luxO*, and *luxR* mRNA.

To assess what becomes of Qrr3 when regulating the *luxM-mCherry* target mRNA, we measured Qrr3 levels in the absence

and presence of *luxM-mCherry* mRNA. When no *luxM-mCherry* mRNA is present, Qrr3 appears as one band on a Northern blot (Figure S3A, left lane). In the presence of *luxM-mCherry* mRNA, two Qrr3 bands appear, suggesting that Qrr3 is processed (Figure S3A, right lane). In the absence of any mRNA target, the Qrr3 half-life is over 32 min (Figure S3B). In the presence of *luxM-mCherry* mRNA, the half-lives of both Qrr3 RNA bands decrease, with the processed Qrr3 product exhibiting the most dramatic decline (to $t_{1/2} < 8$ min, Figure 2C). Together, these data explain how *luxM* mRNA competes with *luxR* mRNA for regulation by Qrr3: the presence of *luxM* mRNA causes Qrr3 degradation, decreasing the amount of Qrr3 available to regulate *luxR* mRNA. We also examined what becomes of the *luxM* mRNA during regulation by Qrr3. We used *gfp* fusions to measure target mRNA levels. Both the *luxM-gfp* mRNA (Figure 2D) and the LuxM-GFP protein (Figure S1D) decreased in the presence of Qrr3, indicating that *luxM* mRNA is degraded during regulation. We therefore conclude that Qrr3 regulates *luxM* mRNA through a coupled degradation mechanism: when base-paired, both the *luxM* mRNA target and the Qrr3 sRNA are subject to degradation.

We next investigated whether *luxO* mRNA can compete with other mRNA targets for Qrr3 regulation. We again used *luxR-gfp* mRNA as the “target” for which we show data, but we note that the results are the same when *luxM-gfp* or *luxO-gfp* mRNAs act as the “target” (data not shown). Figures 2E, 2F, S1E, and S1F show that *luxO* mRNA can indeed compete with *luxR* mRNA for Qrr3 regulation, similar to what we found above when *luxM-mCherry* acts as the competitor. However, unlike when *luxM-mCherry* was the competitor, the level and half-life of Qrr3 are identical in the absence and presence of *luxO-mCherry* competitor mRNA (Figures 2G, S3B, and S3C) and no processed Qrr3 RNA band was detected (Figures 2G and S3C). Furthermore, the presence of Qrr3 does not alter *luxO-gfp* mRNA levels (Figure 2H), however, LuxO-GFP protein production is repressed ~15-fold in the presence of Qrr3 (Figure S1G). Based on these data, we propose that Qrr3 and *luxO* mRNA sequester one another when base-paired.

We likewise tested whether *luxR* mRNA could act as a competitor. Induction of high *luxR-mCherry* caused significant reductions in target-GFP levels even in the absence of Qrr3 suggesting that high levels of the LuxR-mCherry protein are toxic. To circumvent this problem, we introduced a stop codon in *mCherry* to abolish mCherry protein production. We call this construct *luxR-mCherry**. When the *luxR-mCherry** mRNA is the competitor, it does not affect Qrr regulation of *luxO-gfp* (Figures 2I and 2J) or *luxR-gfp* (Figures S2C and S2D). Importantly, Figures S1H and S1I show that the *luxR-mCherry** construct is induced by arabinose and is fully repressed by Qrr3. Thus, even though *luxR-mCherry** is capable of interacting with Qrr3, it cannot compete with *luxO-gfp* mRNA or *luxR-gfp* mRNA for Qrr-regulation. To eliminate the possibility that this lack of competition is due to the *mCherry** mutation, we inserted the same stop codon into the *luxM-mCherry* construct. We call this *luxM-mCherry**. *luxM-mCherry** mRNA remains fully capable of competing for Qrr regulation against *luxO-gfp* mRNA (Figures S2E and S2F) and *luxR-gfp* mRNA (Figures S2G and S2H). As controls, we show that the *luxR-mCherry** mRNA is expressed at levels comparable to the *luxM-mCherry*, *luxO-mCherry* and

*luxM-mCherry** mRNAs (Figure S2I). Thus, we conclude that *luxR* mRNA does not compete with other mRNA targets for Qrr regulation. Figures 2K and S3D show that *luxR* mRNA does not affect Qrr stability because both the Qrr3 level and its half-life are identical in the absence and presence of *luxR-mCherry* mRNA (or *luxR-mCherry** mRNA; data not shown). By contrast, the level of *luxR-gfp* mRNA decreased in the presence of Qrr3 (Figure 2L), and Qrr3 repressed LuxR-GFP protein production (Figure S1J). These data indicate that Qrr3 causes degradation of *luxR* mRNA. However, the Qrr itself is not degraded and is thus available to regulate other targets. Therefore, we propose that Qrr3 acts catalytically on *luxR* mRNA.

Finally, the Qrr sRNAs posttranscriptionally activate AphA production by base-pairing to *aphA* mRNA (Rutherford et al., 2011; Shao and Bassler, 2012). To test if an activated target can compete for Qrr regulation, we performed our competition assay using *luxR-gfp* as the target mRNA and *aphA-mCherry* as the competitor mRNA. The endogenous expression level of *aphA-mCherry* mRNA is much lower than other competitor mRNA targets (data not shown). We therefore introduced an additional plasmid carrying the identical arabinose inducible *aphA-mCherry* construct into *E. coli* to boost *aphA-mCherry* mRNA levels. Figures 2M and 2N show that *aphA* can compete for regulation by Qrr3. Specifically, Qrr repression of LuxR-GFP decreased from 7-fold to 2-fold (Figure 2N). AphA-mCherry was activated by Qrr3, indicating that *aphA* is regulated by Qrr3 during the competition (Figures S1K and S1L). Qrr3 levels declined and the Qrr3 stability dramatically decreased when *aphA-mCherry* mRNA was present (Figures 2O, S3E, and S3F). Notably, Qrr3 levels reached a plateau after 4 min. We suspect that during the first 4 min there exists *aphA-mCherry*, which fosters Qrr3 degradation. However, after 4 min, there is likely little or no *aphA-mCherry* mRNA remaining to promote Qrr3 degradation. Thus, the Qrr3 level remains stable from that point onward. We also measured what becomes of the *aphA-gfp* mRNA in the absence and presence of Qrr3. Although AphA-GFP protein production is activated ~2.5-fold by Qrr3 (Figure S1M), the full-length *aphA-gfp* mRNA decreased ~2.5-fold in the presence of Qrr3 (Figure 2P). We suggest that when Qrr3 pairs with the *aphA* mRNA, *aphA* translation is activated while Qrr3 is destabilized. The fate of the *aphA* mRNA is unclear and is under investigation.

Together, the above experiments demonstrate that Qrr3 uses four different mechanisms to regulate its mRNA targets: Qrr3 represses *luxM* mRNA through coupled degradation, *luxR* mRNA through catalytic degradation, *luxO* mRNA through sequestration, and Qrr3 activates *aphA* mRNA translation while the Qrr is itself degraded (Figure 1).

mRNA Pairing to Particular sRNA Stem-Loops Dictates the Qrr sRNA Half-Life

We considered what features of the Qrr-mRNA pairs dictate the Qrr fate. *luxM* base pairs with the first and second stem-loops (SL1+SL2) of the Qrr, *aphA* base pairs with SL1, and *luxR* and *luxO* base pair with SL2 (Figures 3A1–3A5) (Rutherford et al., 2011; Shao and Bassler, 2012; Teng et al., 2011; Tu and Bassler, 2007; Tu et al., 2010). 5' stem-loops commonly protect mRNAs from RppH- and RNase E-mediated degradation (Belasco, 2010). We have previously shown that this same

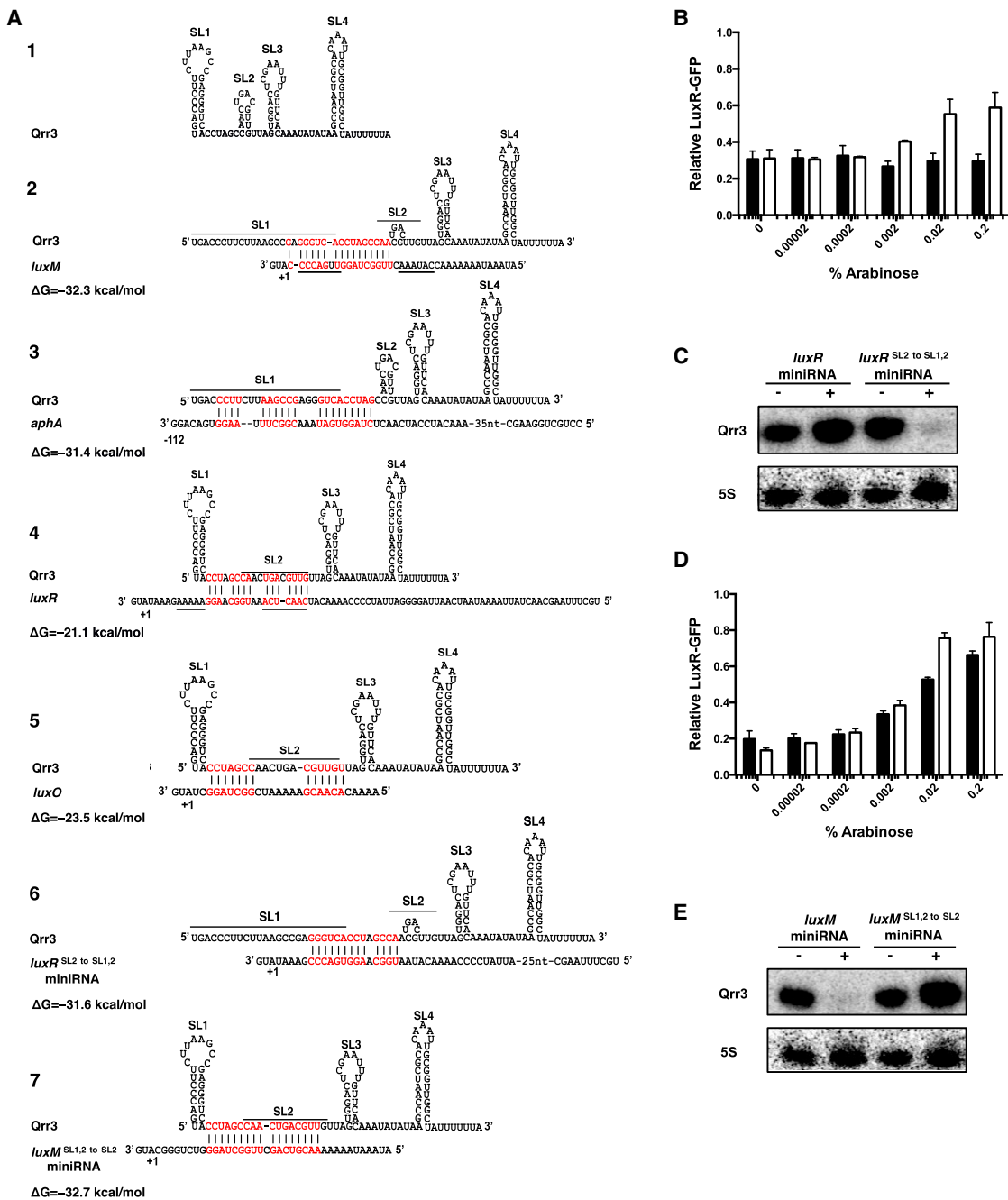


Figure 3. Base-Pairing to the 5' Stem-Loop of Qrr3 Leads to Qrr Degradation

(A) Predicted secondary structure of Qrr3 and base-pairing patterns with the target mRNAs. The four predicted stem-loops of Qrr3 are labeled SL1, SL2, SL3, and SL4. Melted loops are shown with overlines. Base-pairing patterns and energies for Qrr3 and target mRNAs were predicted by RNAhybrid (<http://bibiserv.techfak.uni-bielefeld.de/rnahybrid/>). Nucleotides involved in base-pairing are labeled red. Nucleotides mutated to make the miniRNAs (see [Extended Experimental Procedures](#)) are shown with underlines. Translational start sites are denoted +1.

(B) Competition for Qrr3 regulation between the *luxR* miniRNA (black bars) or the *luxR*^{SL2 to SL1,2} miniRNA (white bars) and *luxR-gfp*.

(C) Northern blot showing Qrr3 levels in the absence (–) and presence (+) of the *luxR* miniRNA or the *luxR*^{SL2 to SL1,2} miniRNA.

(D) Competition between the *luxM* miniRNA (black bars) or the *luxM*^{SL1,2 to SL2} miniRNA (white bars) for Qrr3 regulation of *luxR-gfp*.

(E) Northern blot showing *Qrr3* levels in the absence (–) and presence (+) of the *luxM* miniRNA or the *luxM*^{SL1,2 to SL2} miniRNA. For (B) and (D), means and SEM for triplicate cultures are shown. Normalization as in Figure 2. For (C) and (E), results are representative of two independent experiments.

See also [Figures S3](#) and [S4](#).

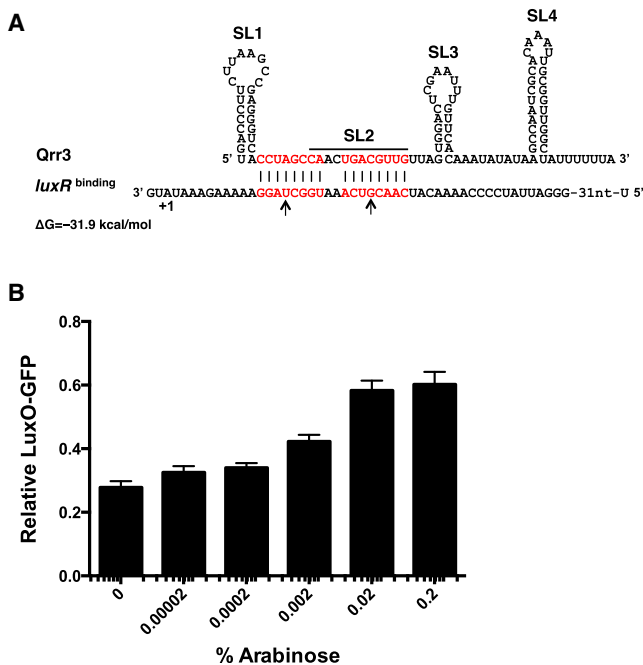


Figure 4. The Binding Strength of the Qrr sRNA-Target mRNA Pair Determines Sequestration versus Catalytic Degradation

(A) Base-pairing between Qrr3 and *luxR*^{binding} mRNA. Designations as in Figure 3A. Mutated nucleotides are labeled with arrows. (B) Competition between *luxR*^{binding}-*mCherry*^{*} and *luxO-gfp* for Qrr3 regulation. *luxR*^{binding}-*mCherry*^{*} was driven by the arabinose promoter. Means and SEM for triplicate cultures are shown. Normalization as in Figure 2.

mechanism is also used to protect the Qrr sRNAs from degradation. Deletion of SL1 or mutations that disrupt SL1 base-pairing destabilize the Qrr sRNAs, and mutations that restore SL1 base-pairing restore Qrr stability in *E. coli* (Shao et al., 2013) and in vivo in *V. harveyi* (Figure S3G). We wondered whether base-pairing to the target mRNA, if it leads to melting of SL1, causes Qrr degradation. To test this possibility, we constructed miniRNAs containing only the 5'UTRs of selected mRNA targets linked to transcription terminators. We used miniRNAs to eliminate ribosome-mediated mRNA stabilization effects. Using the above competition assay, we found that the *luxR* miniRNA does not affect Qrr3 repression of *luxR-gfp*, which is consistent with a catalytic regulatory mechanism (Figure 3B, black bars). However, shifting the Qrr3-*luxR* base-pairing from SL2 to SL1+SL2 (Figure 3A6) confers competition capability to the *luxR* SL2 to SL1,2 miniRNA (Figure 3B, white bars). The presence of the *luxR* miniRNA did not affect the level of Qrr3, however, the presence of the *luxR* SL2 to SL1,2 miniRNA caused a decrease in Qrr3 level (Figure 3C).

We also constructed a *luxM* miniRNA and found that it competes with *luxR-gfp* for Qrr regulation identically to the full-length *luxM-mCherry* mRNA fusion (Figure 3D, black bars). Qrr3 was degraded in the presence of the *luxM* miniRNA as shown by its decreased expression level (Figure 3E). A construct that retains the number of base-pairing nucleotides but moves the base-pairing region from SL1+SL2 to SL2 eliminated the ability of the *luxM* SL1,2 to SL2 miniRNA to induce Qrr degradation (Figures 3A7 and 3E).

Together, these data suggest that pairing to, and presumably remodeling of SL1 causes Qrr degradation, while pairing to SL2 does not. As controls, we show that the *luxR*, *luxR* SL2 to SL1,2, *luxM*, and *luxM* SL1,2 to SL2 miniRNAs are expressed (Figures S4A and S4C, respectively), regulated by Qrr3 (Figures S4B and S4D, respectively), and the *luxR* SL2 to SL1,2 and *luxM* SL1,2 to SL2 miniRNAs behave identically to the *luxR* SL2 to SL1,2 and *luxM* SL1,2 to SL2 mRNAs, respectively (Figure S4E).

To map the processing site in the Qrr sRNA when base-paired to *luxM*, we expressed steady-state levels of Qrr3, induced target mRNA expression, and monitored the dynamics of Qrr decay. Consistent with *luxM* mRNA being controlled by coupled degradation and *luxR* mRNA being controlled by a catalytic mechanism, a Qrr sRNA degradation product appeared within ten minutes of induction of *luxM* mRNA (Figure S3H) whereas Qrr3 was not degraded following *luxR* mRNA induction (Figure S3H). Primer extension analysis revealed that processing occurred in the Qrr SL1 region after nucleotides C (position 5), U (position 7), and U (position 8) (Figure S3I, red arrows), suggesting that opening the SL1 structure makes the RNase cleavage sites accessible.

We did not observe processing of the Qrr sRNA when *aphA* was expressed (Figures 2O, S3E, and S3F) presumably because the cleavage sites are involved in base-pairing to the *aphA* mRNA (Figure 3A3). This arrangement likely shields the sites from cleavage. We wondered whether partial opening of SL1 in a way that does not reveal the cleavage sites is sufficient to induce Qrr degradation. We constructed mutations (GAC to CUG at positions 2 to 4) to partially open SL1 (Figure S3J) and mimic when *aphA* is base-paired. We call this construct Qrr3mut. The Qrr3mut sRNA is unstable (Figure S3J) compared to wild-type Qrr3 (Figure S2B) and degraded without an apparent cleavage product.

The Qrr-mRNA Base-Pairing Strength Determines Whether an mRNA Target Will Sequester the Qrr sRNA

The *luxM* SL1,2 to SL2 miniRNA does not induce Qrr degradation (Figure 3E). Yet, unlike the *luxR* miniRNA, the *luxM* SL1,2 to SL2 miniRNA is capable of competing with *luxR-gfp* mRNA for Qrr regulation (Figure 3D, white bars). These data suggest that the *luxM* SL1,2 to SL2 miniRNA competes for Qrr regulation by sequestering the Qrr sRNA. Comparison of the predicted binding energies of *luxM* SL1,2 to SL2 miniRNA, *luxR* mRNA, and *luxR* miniRNA (the base pairing region in the *luxR* mRNA and the *luxR* miniRNA is identical) to Qrr3 reveals that the Qrr3-*luxM* SL1,2 to SL2 miniRNA duplex (−32.7 kcal/mol) is more stable than the Qrr3-*luxR* mRNA (or *luxR* miniRNA) duplex (−21.1 kcal/mol) (Figures 3A7 and 3A4). We wondered whether mRNA targets that bind strongly to SL2 of Qrr3 sequester the Qrr sRNA, whereas targets with lower binding energy are catalytically degraded. If so, this could explain why some targets can compete for Qrr regulation while others cannot. To test this hypothesis, we introduced two point mutations into the *luxR-mCherry*^{*} mRNA 5'UTR to increase its strength of binding to Qrr3 (−31.9 kcal/mol) (Figure 4A). We call this construct *luxR*^{binding}-*mCherry*^{*}. Indeed, *luxR*^{binding}-*mCherry*^{*} gains the capability to compete with *luxO-gfp* mRNA for Qrr regulation (Figure 4B, compare to Figure 2J). As a control, we show that the *luxR*^{binding}-*mCherry*^{*} mRNA is made at levels comparable to that of *luxR-mCherry*^{*} mRNA (Figure S2I). We suggest that the base-pairing strength between an mRNA target

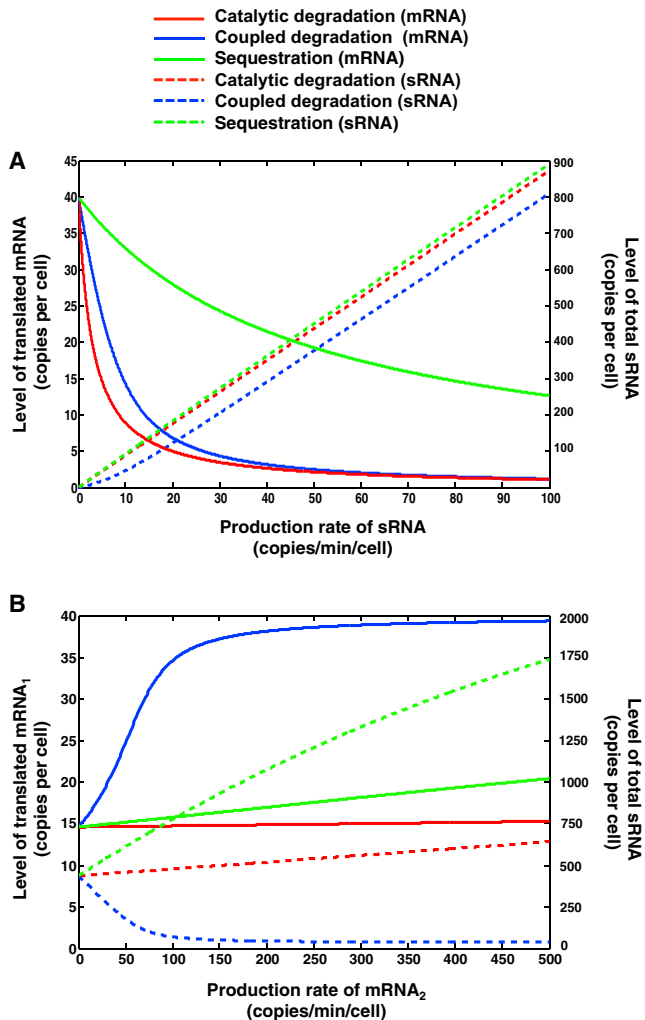


Figure 5. Modeling the Strength and Competition Capacity of the Different sRNA Regulatory Mechanisms

(A) The levels of translated mRNA (solid curves) and total sRNA (dashed curves) plotted against the production rate of the sRNA, based on Equations S1, S2, S3, S4, S5, and S6.

(B) The levels of translated mRNA₁ (solid curves) and total sRNA (dashed curves) are plotted against the production rate of the competitor mRNA₂ based on Equations S1, S2, S3, S4, S5, and S6. In (A) and (B), three different regulatory mechanisms are explored: catalytic degradation (red), coupled degradation (blue), and sequestration (green).

and the Qrr sRNA governs whether an mRNA target will sequester the Qrr sRNA and thus compete for its regulation against other target mRNAs.

The Different Qrr Regulatory Mechanisms Govern Competition and Potency of Target Control

We used mathematical modeling to explore the consequences of the distinct sRNA-mRNA interaction modes on the different RNA species and the underlying biological process being regulated. This initial modeling effort is focused on sRNA-mediated repression because sRNA-directed activation is not yet well characterized. Based on experimental evidence from previous

studies, we assume that Hfq protein complexes are always close to saturated by sRNAs and mRNAs (Hussein and Lim, 2011; Moon and Gottesman, 2011), but that individual sRNA and mRNA molecules actively cycle on and off of Hfq complexes (Fender et al., 2010; Wagner, 2013).

We first modeled the scenario of a single species of sRNA (e.g., a single Qrr) specifically regulating a single type of mRNA target, in the presence of a background of noncognate sRNAs and mRNAs (see Supplemental Information and Table S4). In Figure 5A, we show as solid curves the copy number of mRNA molecules available for translation, which are the free mRNA molecules and the mRNA molecules bound to Hfq with noncognate sRNAs, versus the production rate of the sRNA. We find that an mRNA target regulated by catalytic degradation (red) is the most efficiently repressed by the sRNA, followed by an mRNA regulated by coupled degradation (blue). An mRNA controlled by sequestration (green) exhibits only moderate repression by the sRNA. Moreover, mRNA targets that are regulated by coupled degradation decrease the total sRNA level (dashed blue curve). Specifically, the total sRNA level remains suppressed by coupled degradation until sRNA production exceeds the expected threshold of ~ 7.5 copies/min/cell and then increases linearly. (The threshold occurs where the sRNA production rate/the sRNA degradation rate in the sRNA-Hfq-mRNA complex equals the mRNA production rate/the mRNA degradation rate in the sRNA-Hfq-mRNA complex). This threshold-linear behavior of total sRNA does not occur in the cases of regulation by catalytic degradation or sequestration (red and green dashed curves, respectively).

We next modeled the scenario in which competition occurs between different mRNA targets for sRNA regulation (see Supplemental Information). In our system, we have one target mRNA (mRNA₁) and one competitor mRNA (mRNA₂). Our modeling results show that coupled degradation supplies the most efficient competition: the level of translated mRNA₁ increases with the production rate of mRNA₂ (Figure 5B, solid blue curve), followed by sequestration (Figure 5B, solid green curve). Catalytic degradation provides only minimal competition (Figure 5B, solid red curve). This result is in good qualitative agreement with our experimental data in which *luxM* and *luxO* mRNAs compete for Qrr regulation and *luxO* mRNA is nearly incapable of competing for Qrr regulation. We also examined the total sRNA level when we increased the production rate of the competitor mRNA₂ (Figure 5B, dashed curves). As expected, coupled degradation results in a significant decrease in sRNA level (Figure 5B, dashed blue curve). The increase of the total sRNA level in the case of sequestration is due to the sequestering mRNA₂ partially protecting the sRNA from degradation (Figure 5B, dashed green curve).

The Different Qrr Regulatory Mechanisms Govern the Dynamics of Target mRNA Expression

To examine the effect of different regulatory mechanisms on the dynamics of target regulation, we modeled a situation in which sRNA production is induced at time zero and then terminated after 2 hr. We found that when sRNA production is induced (Figure 6A, dashed curves), catalytic degradation and coupled degradation provide the most rapid mRNA and protein

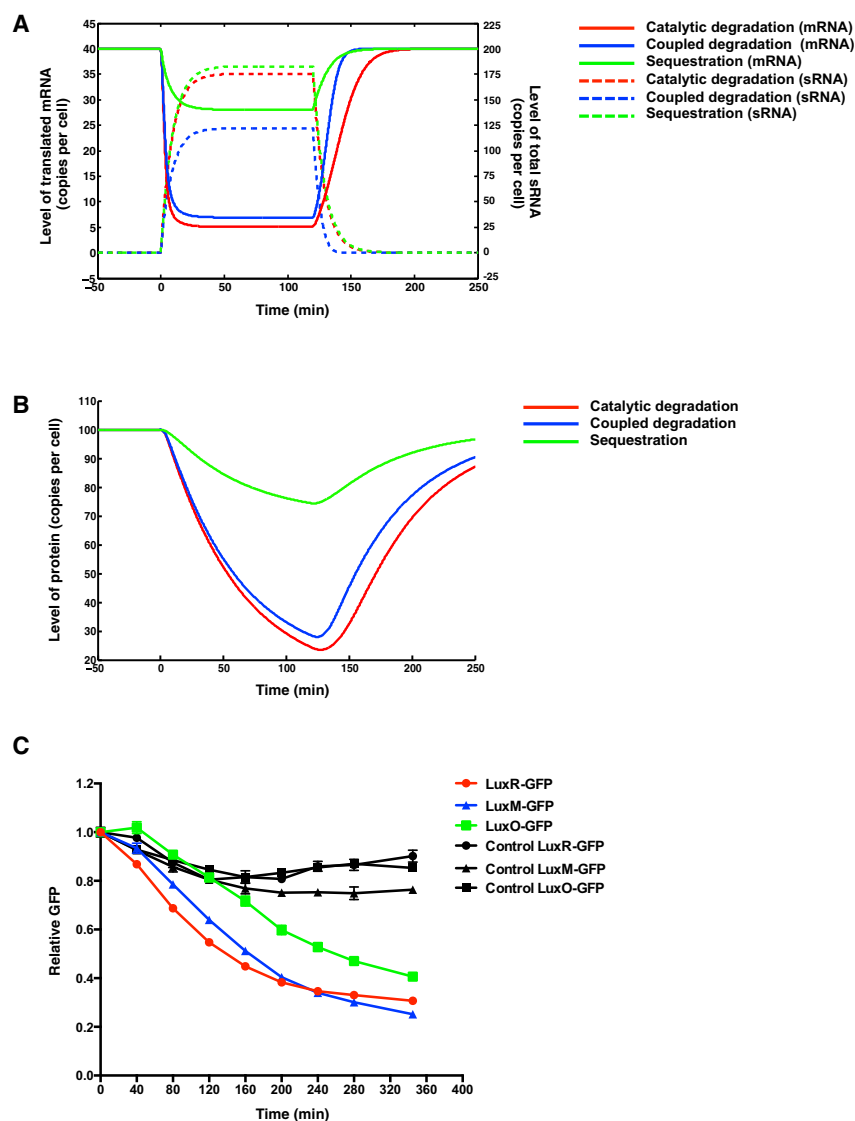


Figure 6. mRNA Target Dynamics Provided by the Different sRNA Regulatory Mechanisms

(A) The levels of translated mRNA (solid curves) and total sRNA (dashed curves) are plotted over time based on Equations S1, S2, S3, S4, S5, and S6.

(B) The level of regulated protein is plotted over time based on Equations S1, S2, S3, S4, S5, S6, and S9. sRNA production is induced at time zero and is terminated at 120 min. Three different regulatory mechanisms are explored: catalytic degradation (red), coupled degradation (blue), and sequestration (green).

(C) Repression of target mRNAs following Qrr sRNA induction. GFP fluorescence at each time-point was normalized to mCherry fluorescence, and the relative normalized GFP levels are plotted. The results are LuxR-GFP: red and black (control) circles, LuxM-GFP: blue and black (control) triangles, LuxO-GFP: green and black (control) squares. Means and SEM from three independent cultures are shown. See also Figure S5.

more rapidly to changes in Qrr levels than do *luxM* and *luxO* mRNAs. To test the predictions of the model, we constructed three *V. harveyi* strains that report on target mRNA levels by integrating a *luxR*, a *luxM*, or a *luxO* 5'UTR translational GFP fusion under a constitutive promoter onto the chromosome. We used *mCherry* oriented in the opposite direction to normalize for cellular protein (Long et al., 2009). We measured GFP and mCherry fluorescence after we induced Qrr production by adding a quorum-sensing antagonist (see Experimental Procedures) (Shao et al., 2013). Figure 6C shows that the LuxR-GFP protein is indeed the most rapid to respond to Qrr changes, followed by the LuxM-GFP protein, and finally the LuxO-GFP protein. As a control, we measured LuxR-GFP, LuxM-GFP, and LuxO-GFP levels in *V. harveyi* strain lacking all five Qrr sRNAs; GFP did not significantly change following addition of the antagonist.

GFP protein. As a control, we measured LuxR-GFP, LuxM-GFP, and LuxO-GFP levels in *V. harveyi* strain lacking all five Qrr sRNAs; GFP did not significantly change following addition of the antagonist.

The Different Qrr Regulatory Mechanisms Are Critical for Quorum-Sensing Circuit Dynamics

Our data and model show that the particular Qrr sRNA mechanism used to regulate each mRNA target dictates the level and dynamics of the target's expression. We expect that these dynamics specify the quorum-sensing response timing in vivo. To investigate this notion, we measured the in vivo dynamical changes of individual quorum-sensing components that occurred in response to alterations in Qrr levels. We measured the mRNA levels and the rates of protein synthesis (see Extended Experimental Procedures and Table S5) of LuxR, LuxO, LuxM, and AphA over a 90 min time period following termination of Qrr production. As controls, we show that the levels of

response, while sequestration confers the slowest response (Figures 6A, solid curves, and 6B; Supplemental Information). By contrast, when sRNA production is terminated, catalytic degradation yields the slowest recovery. As expected, sequestration affects the translated mRNA level but it does not affect the total mRNA level. Catalytic degradation and coupled degradation affect both mRNA translation and overall target mRNA levels (Figure S5). In all cases, repression of mRNA is rapid (~10 min) (Figure 6A, solid curves), whereas repression of protein is slow—approaching steady state only after hours—due to the slow dilution rate of protein (Figure 6B). These predictions are in agreement with existing experimental data (Papenfort et al., 2013; Vanderpool and Gottesman, 2004).

With respect to the mRNA targets studied here, the model predicts that *luxR* mRNA will be the most sensitive to changes in Qrr levels because it is controlled by catalytic degradation. Thus, during the high-cell-density to low-cell-density transition, when the Qrr sRNAs are produced, *luxR* mRNA should respond

Qrr1-4 decreased following autoinducer addition (Figure S6A). Qrr5 is not produced under our experimental conditions, so we did not measure it (Tu and Bassler, 2007). Figure 7A shows that, following the addition of the autoinducer, *luxR* mRNA increased ~14-fold and the rate of LuxR protein synthesis increased ~25-fold; *luxO* mRNA does not change within 90 min, however, the rate of LuxO protein production increased 2-fold; *luxM* mRNA increased ~3-fold (we were unable to detect the LuxM protein, likely because the *luxM* gene is partially deleted in this locked strain); *aphA* mRNA decreased ~20-fold and AphA protein synthesis decreased ~4- to 6-fold. These results confirm our prediction that catalytically regulated targets (e.g., *luxR*) undergo larger dynamic range changes than do targets regulated by coupled degradation (e.g., *luxM*). Sequestered targets such as *luxO* are the most weakly regulated.

We next explored how important the specific mechanism is for the quorum-sensing response. We altered the regulatory mechanism by which a particular mRNA target (*luxR*) is controlled and tested the effects on overall quorum-sensing dynamics. To accompany the experiment, we modeled an internal segment of the circuit in which phosphorylated LuxO activates the production of the Qrr sRNAs and the Qrr sRNAs catalytically repress *luxR* mRNA, whereas they sequester *luxO* mRNA (Figure 7B).

The subcircuit equations correspond to those used for one Qrr with two mRNA targets (Supplemental Information), with Qrr production assumed to be proportional to the level of phosphorylated LuxO. The kinetic equation for the Qrr sRNA is therefore:

$$\begin{aligned} \frac{d[\text{Qrr}]_{\text{total}}}{dt} = & \Gamma_{\text{Qrr}}[\text{LuxO} \sim \text{P}] - \gamma_{\text{Qrr}}[\text{Qrr}]_{\text{free}} \\ & - \gamma_{\text{Qrr:mRNA}_0}[\text{Qrr} : \text{Hfq} : \text{mRNA}_0] \\ & - \gamma_{\text{Qrr:luxO}}[\text{Qrr} : \text{Hfq} : \text{luxO}_m] \\ & - \gamma_{\text{Qrr:luxR}}[\text{Qrr} : \text{Hfq} : \text{luxR}_m]. \end{aligned} \quad (\text{Equation 1})$$

We added two kinetic equations for LuxO and LuxR protein:

$$\frac{d[\text{LuxO}_p]}{dt} = \Gamma_{\text{LuxO}_p}[\text{luxO}_m] - \gamma_{\text{LuxO}_p}[\text{LuxO}_p] \quad (\text{Equation 2})$$

$$\frac{d[\text{LuxR}_p]}{dt} = \Gamma_{\text{LuxR}_p}[\text{luxR}_m] - \gamma_{\text{LuxR}_p}[\text{LuxR}_p]. \quad (\text{Equation 3})$$

Using these equations, we explored three possible mechanisms for *luxR* regulation: catalytic degradation, coupled degradation, and sequestration. Our choice of parameters is based on the RNA copy numbers we measured (Figure S7) and previous measurement of LuxR protein copy number (Teng et al., 2010) (see Supplemental Information).

In Figure 7C, we plot the prediction for LuxR protein copy number per cell versus the phosphorylated fraction of LuxO ($[\text{LuxO} \sim \text{P}]/[\text{LuxO}]$). The ratio $[\text{LuxO} \sim \text{P}]/[\text{LuxO}]$ is low in the high-cell-density state and high in the low-cell-density state. Within the model, the catalytic mechanism yields the most efficient repression of LuxR protein, followed by coupled degradation, while sequestration does not achieve the experimentally observed level of LuxR repression. Can sequestration adequately repress LuxR if we allow increased Qrr production?

We found that in order to achieve ~10-fold repression of LuxR, the Qrr production rate must be increased ~100-fold (Figure 7C, black curve). Under this condition, LuxO protein is repressed at low cell density to the unrealistically low level of fewer than five copies per cell (Figure 7D, black curve). In effect, converting regulation of LuxR from catalytic degradation to sequestration would require rewiring of much of the quorum-sensing network to achieve the same dynamics. Thus, the modeling results suggest that the particular Qrr sRNA mechanisms used to regulate specific quorum-sensing mRNA targets can be crucial for the integrated operation of the quorum-sensing circuit.

To experimentally validate the prediction from the model, we replaced the 5'UTR of *luxR* with that of *luxM* or *luxO* on the chromosome of a *V. harveyi* strain containing only Qrr3. We note that the levels of LuxR protein produced from the three endogenous 5'UTRs are different. Different levels of LuxR feedback on quorum-sensing circuit components would complicate our analysis (Chatterjee et al., 1996; Tu et al., 2008), thus we isolated LuxR production from feedback by introducing a mutation in LuxR (LuxR R17C) that eliminates DNA binding (van Kessel et al., 2013). Figure 7E shows that *luxR* mRNA regulated by a catalytic (red curve) or coupled degradation (blue curve) mechanism increases from low cell density to high cell density, although coupled degradation provides a smaller dynamic range (~3.5-fold) for *luxR* mRNA than catalytic degradation (~10-fold). *luxR* mRNA regulated by sequestration (green curve) shows no increase during growth, which agrees with our prediction. Over the course of the experiment, Qrr3 levels decrease from low cell density to high cell density and the levels of Qrr3 in the three strains are comparable (Figure S6B). These results show that the regulatory mechanism used for a particular target mRNA (*luxR* in this case) determines the precise timing and amplitude of the quorum-sensing response.

DISCUSSION

sRNAs are ubiquitous regulators in bacterial genetic circuits, primarily functioning to control growth rate and stress responses (Gottesman, 2004). Several well-characterized bacterial sRNAs, such as Spot42, RyhB, RybB, and the Qrr sRNAs each control multiple target mRNAs (Beisel and Storz, 2011; Massé and Gottesman, 2002; Papenfort et al., 2010; Shao et al., 2013; Storz et al., 2011). Here, we use the Qrr3 sRNA to show that a single sRNA can regulate its different targets by distinct mechanisms. The particular mechanism used is defined by the base-pairing strategy the Qrr sRNA employs for the particular mRNA target. Specifically, mRNA targets that base pair with the first stem-loop of the Qrr sRNA cause Qrr degradation, and these targets include both repressed (*luxM*) and activated (*aphA*) targets. mRNA targets that base pair with the second stem-loop of the Qrr sRNA do not cause Qrr degradation. Rather, they sequester the Qrr sRNA if the binding is strong (*luxO*), and they are catalytically regulated if binding is weak (*luxR*). Our combined mathematical modeling and experiments show that the regulatory mechanism used determines the potency of regulation, competition capability, and the temporal dynamics of each target mRNA. These distinct mechanisms are crucial to drive the overall quorum-sensing circuit dynamics.

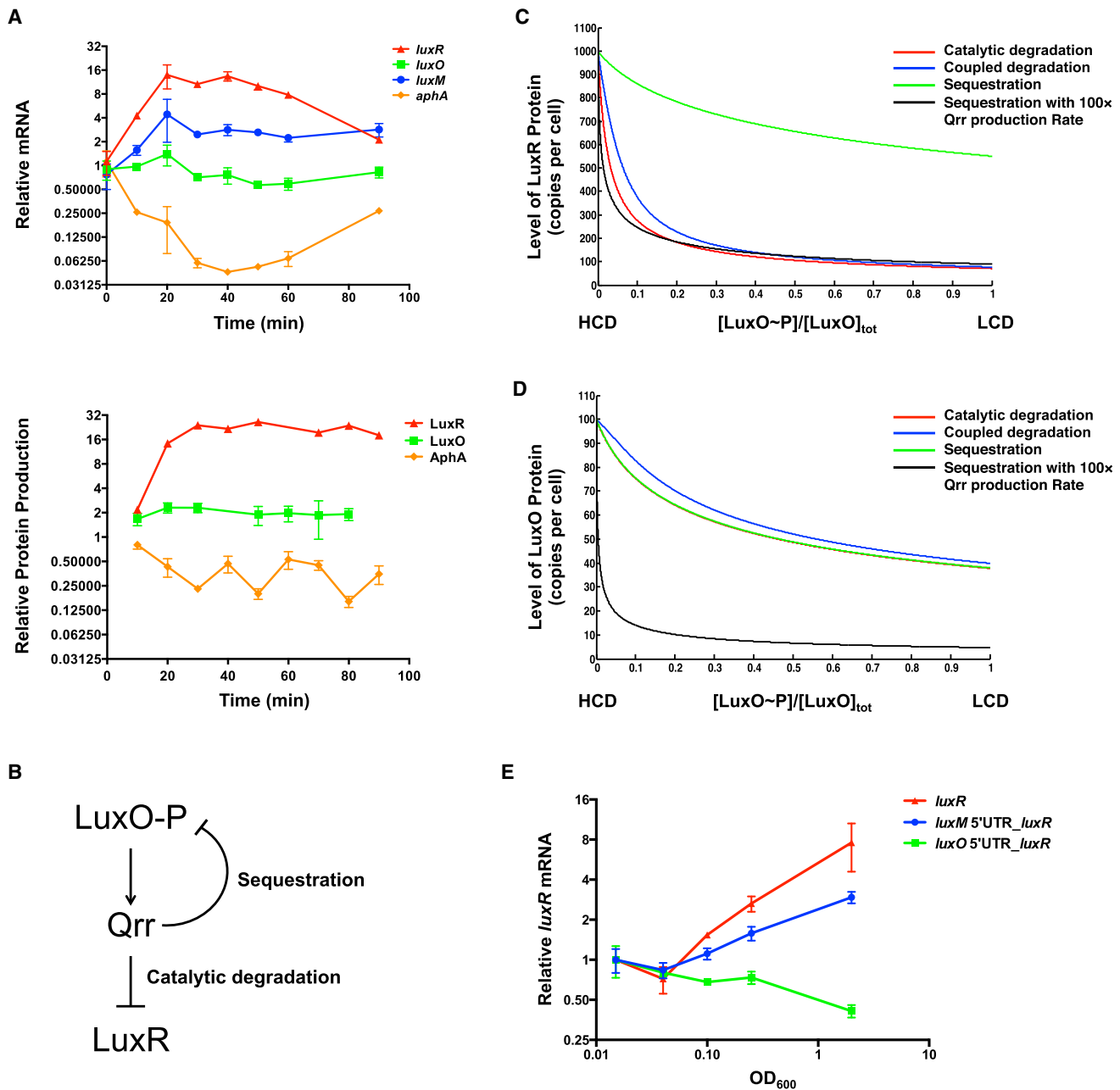


Figure 7. Particular Qrr Regulatory Mechanisms Are Crucial for Proper Quorum-Sensing Dynamics

(A) qRT-PCR and BONCAT of *luxR*, *luxO*, *luxM*, and *aphA* following addition of AI-1 to TL25. Data were normalized to the first time-point in the RNA measurement. Means and SEM from three independent cultures are shown. Relative protein synthesis rates were measured by BONCAT (Supplemental Information) and the evidence for each quantification is provided in Table S5.

(B) Simplified quorum-sensing circuit used for mathematical modeling.

(C and D) LuxR (C) and LuxO (D) protein copy number plotted against the ratio of phosphorylated LuxO to total LuxO protein, based on Equations 1, 2, 3, S1, S2, S3, S4, S5, and S6. In (C) and (D), *luxR* mRNA is regulated by catalytic degradation (red), coupled degradation (blue), or sequestration (green). The black curve shows the case when *luxR* mRNA is regulated by sequestration but the Qrr production rate is increased 100-fold.

(E) qRT-PCR of *luxR* mRNA from *luxR* R17C (red), *luxM* 5'UTR-*luxR* R17C (blue), and *luxO* 5'UTR-*luxR* R17C (green) over growth. Data from each strain were normalized to the first time-point ($\text{OD}_{600} = 0.015$) and plotted against OD_{600} . Means and SEM from four independent cultures are shown.

See also Figures S6 and S7 and Table S5.

In terms of deployment of this set of regulatory mechanisms, we suspect that mRNA targets that require complete and immediate repression will likely be regulated either catalytically or by coupled degradation. Growth and stress response mRNAs are good candidates for these modes of sRNA regulation (Beisel and Storz, 2011; Massé and Gottesman, 2002; Vanderpool and Gottesman, 2004). Catalytic degradation, because it does not alter the total sRNA pool, could be the superior mode of regulation when a target mRNA exists in high copy numbers and requires a large dynamic range for function, or when a target mRNA needs to be fully repressed even under conditions of low sRNA levels. The MicM (ChiX) target *ybfM* (*chiP*) fits this scenario. *ybfM* (*chiP*) is completely silenced by MicM (ChiX) in the absence of chitooligosaccharide inducers (Figuroa-Bossi et al., 2009; Overgaard et al., 2009).

The coupled degradation mechanism is notable because it provides a threshold-linear response: regulation depends on the relative sRNA to mRNA ratio (Levine et al., 2007). Specifically, in the low sRNA:target mRNA regime, mRNA repression is not efficient because the sRNA is degraded following base-pairing and this greatly reduces the sRNA pool. Thus, coupled degradation is an excellent mechanism for rapidly turning over and thus eliminating the sRNA pool once the response is complete. Good examples for this case include the sRNAs RyhB and MicM (ChiX) (Figuroa-Bossi et al., 2009; Massé et al., 2003; Overgaard et al., 2009; Plumbbridge et al., 2014).

Sequestration is an excellent mechanism for regulation of target mRNAs that require modulation rather than dramatic on-off changes. In this case, the mRNA levels are not significantly affected by sRNA regulation, which has the advantage of fine-tuning target expression levels. One example to consider is the sRNA Spot42 and its target *galK*. Spot42-directed repression of *galK* by sequestration presumably fine-tunes the relative levels of the galactose catabolism proteins for optimal carbon utilization (Møller et al., 2002). We hypothesize that the propensity for a target mRNA to sequester an sRNA depends on both the binding strength of the sRNA-mRNA pair and the degradation rate of the target mRNA upon pairing. Strong sequestration will occur if the target mRNA binds tightly to the sRNA but the target mRNA is not degraded efficiently. This is the case for the *luxO*-Qrr pair.

Finally, we show that the Qrr sRNA is degraded following activation of the *aphA* mRNA. We hypothesize that this mode of action generates a negative feedback loop that has the advantage of preventing overexpression of the target mRNA when the sRNA level is low. Specifically, because the sRNA is degraded during regulation, it cannot be reused. Thus, when the sRNA:target mRNA ratio is low, the degree of target mRNA activation is limited by the concentration of the sRNA.

Here, we rationalize the Qrr sRNAs use of particular regulatory mechanisms for the particular quorum-sensing target mRNAs. First, regarding *luxR* mRNA: LuxR is the master quorum-sensing regulator that, at high cell density, controls the bulk of genes in the quorum-sensing regulon (~600 genes in *V. harveyi*) (Rutherford et al., 2011). Our measurements of *luxR* mRNA and LuxR protein copy numbers indicate that *luxR* exists in high copy numbers (at least 40 mRNA copies and ~600 protein dimers per cell) at high cell density, presumably due to the requirement

for LuxR dimers to bind their 115 DNA promoter sites (van Kessel et al., 2013; Teng et al., 2010). However, this high LuxR concentration presents a conundrum for the cell when it needs to, essentially instantaneously, transition to the low-cell-density mode upon, for example, excretion from the host or exit from a biofilm. Repression of *luxR* mRNA via a Qrr catalytic mechanism should be the most effective means to rapidly decrease high levels of LuxR protein to reset the quorum-sensing genetic program. Regarding *luxO* mRNA, which is controlled by a Qrr feedback-sequestration mechanism: the Qrr-to-*luxO* feedback loop acts as a rheostat to moderately adjust Qrr levels (Tu et al., 2010). We argue that using sequestration to regulate *luxO* mRNA prevents dramatic spikes and valleys in Qrr levels, while simultaneously buffering LuxO protein levels from valleys and spikes due to noise associated with fluctuations in Qrr levels. With respect to the use of coupled degradation to regulate *luxM* mRNA: we propose that the *luxM* mRNA and seven other target mRNAs that are able to base-pair with SL1 of the Qrr sRNAs (Shao et al., 2013) are exploited to control Qrr turnover in order to set the appropriate concentration of the total Qrr sRNA pool under different quorum-sensing states. This feature is important for when the cells initiate the high-cell-density program and they need to eliminate the Qrr sRNAs. Finally, as we discussed above, activation of *aphA* with concomitant degradation of the Qrr sRNAs may prevent overproduction of the AphA protein. Our finding that AphA protein production changes only 4- to 6-fold supports this hypothesis (Figure 7A). AphA fine-tunes quorum-sensing gene expression at low cell density (van Kessel et al., 2012). Keeping AphA levels in check may be critical for its subtle function. Indeed, AphA feeds back to repress Qrr transcription, which further guarantees tight control of AphA levels (Rutherford et al., 2011).

We predict that the regulatory mechanisms we discovered between Qrr3 and the target mRNAs are conserved across all five Qrr sRNAs based on their highly similar secondary structures and sequences (Tu and Bassler, 2007). The caveat is that Qrr1 lacks nine nucleotides in the first stem-loop, which makes it unable to regulate certain targets, such as *aphA* (Shao and Bassler, 2012). The five Qrr sRNAs are expressed at different levels and with somewhat different timing (Tu and Bassler, 2007). Thus, how the in vivo competition occurs between all five Qrr sRNAs and all 20 mRNA targets to provide a robust quorum-sensing response remains to be defined. Nonetheless, embedding the capacity for multiple regulatory mechanisms into a single sRNA is an evolutionarily economical method to endow a biological circuit with diverse dynamic behaviors. The principles underpinning the regulatory mechanisms we discovered here could be employed by other natural systems or to engineer synthetic sRNAs with numerous functions.

EXPERIMENTAL PROCEDURES

Strains, plasmids, and oligonucleotides used in this study are listed in Tables S1, S2, and S3. Detailed protocols are described in Extended Experimental Procedures.

Competition Assay

Overnight cultures (Table S1) were diluted 1,000-fold into fresh M9 minimal medium containing 0.5% glycerol, appropriate antibiotics, 0.2 mM IPTG,

0 or 3 ng ml⁻¹ anhydrotetracycline (aTc; Clontech), and varying amounts of arabinose. GFP and mCherry fluorescence were measured following 10 hr of growth using fluorescence-activated cell sorting (FACS) (BD Biosciences FACSria cell sorter).

RNA Expression and Half-Life

Qrr3 and target mRNAs were induced for 10 hr and measured by Northern blot to determine expression. Rifampicin (250 µg ml⁻¹) was added to stop transcription followed by collection of RNA at different time points to determine half-life.

V. harveyi GFP Assay

Overnight cultures of *V. harveyi* strains LF1838, LF1845, LF1848, LF2328, LF2332, and LF2335 were diluted to OD₆₀₀ = 0.0002 into fresh AB medium containing 1 µM AI-1 and grown for 6.5 hr. 3-oxo-C12-HSL (100 µM; Sigma) (LuxN/AI-1 antagonist) was added to cultures. GFP and mCherry fluorescence were measured every 40 min thereafter using FACS.

Quantitative RT-PCR of luxR mRNA

Overnight cultures of *V. harveyi* strains LF2269, LF2246, and LF2254 were diluted into fresh LM medium to OD₆₀₀ = 0.005 and grown for 6 hr to OD₆₀₀ = 2.0. Cultures were diluted again into fresh LM medium to OD₆₀₀ = 0.005. Total RNA was collected at 45, 90, 135, 180, and 345 min after the dilution. Total RNA (4 µg) was used for cDNA synthesis and quantitative RT-PCR (qRT-PCR) was performed as described in [Supplemental Information](#).

qRT-PCR and Proteomics

Overnight cultures of *V. harveyi* strain TL25 were diluted 1:1,000-fold into fresh LM medium and grown to mid-log phase. Cultures were divided in half, and one aliquot was treated with 10 µM AI-1. Total RNA was collected from both samples at 0, 10, 20, 30, 40, 50, 60, and 90 min thereafter. Total RNA (4 µg) was used for cDNA synthesis and qRT-PCR was performed as described in [Supplemental Information](#). Proteomics was performed as described in [Supplemental Information](#).

SUPPLEMENTAL INFORMATION

Supplemental Information includes Extended Experimental Procedures, seven figures, and five tables and can be found with this article online at <http://dx.doi.org/10.1016/j.cell.2014.11.051>.

AUTHOR CONTRIBUTIONS

L.F., S.T.R., K.P., J.D.B., J.C.V.K., D.A.T., N.S.W., and B.L.B. designed the experiments. L.F., K.P., J.D.B., and J.C.V.K. performed the experiments. L.F., K.P., J.D.B., N.S.W., and B.L.B. analyzed the data. L.F., N.S.W., and B.L.B. wrote the paper.

ACKNOWLEDGMENTS

We thank Terence Hwa for generously providing the BW-RI strain and the pZA31-lucNB and pZE12G plasmids. We are indebted to members of the B.L.B. and N.S.W. laboratories for insightful discussions and suggestions. This work was supported by the Howard Hughes Medical Institute, NIH grant 5R01GM065859 and National Science Foundation (NSF) grant MCB-0343821 to B.L.B., NIH grant R01GM082938 to N.S.W., and NIH grant R01GM062523 and the Institute for Collaborative Biotechnologies through grant W911NF-09-0001 from the U.S. Army Research Office to D.A.T. K.P. is supported by a postdoctoral fellowship from the Human Frontiers in Science Program (HFSP). S.T.R. was supported by NIH fellowship F32AI085922. J.C.V.K. is supported by funds from Indiana University.

Received: May 2, 2014

Revised: September 20, 2014

Accepted: November 14, 2014

Published: January 8, 2015

REFERENCES

- Altuvia, S., Zhang, A., Argaman, L., Tiwari, A., and Storz, G. (1998). The *Escherichia coli* OxyS regulatory RNA represses *fhlA* translation by blocking ribosome binding. *EMBO J.* 17, 6069–6075.
- Beisel, C.L., and Storz, G. (2011). The base-pairing RNA spot 42 participates in a multioutput feedforward loop to help enact catabolite repression in *Escherichia coli*. *Mol. Cell* 41, 286–297.
- Belasco, J.G. (2010). All things must pass: contrasts and commonalities in eukaryotic and bacterial mRNA decay. *Nat. Rev. Mol. Cell Biol.* 11, 467–478.
- Chatterjee, J., Miyamoto, C.M., and Meighen, E.A. (1996). Autoregulation of *luxR*: the *Vibrio harveyi* lux-operon activator functions as a repressor. *Mol. Microbiol.* 20, 415–425.
- Fender, A., Elf, J., Hampel, K., Zimmermann, B., and Wagner, E.G.H. (2010). RNAs actively cycle on the Sm-like protein Hfq. *Genes Dev.* 24, 2621–2626.
- Figueroa-Bossi, N., Valentini, M., Malleret, L., Fiorini, F., and Bossi, L. (2009). Caught at its own game: regulatory small RNA inactivated by an inducible transcript mimicking its target. *Genes Dev.* 23, 2004–2015.
- Fröhlich, K.S., and Vogel, J. (2009). Activation of gene expression by small RNA. *Curr. Opin. Microbiol.* 12, 674–682.
- Gottesman, S. (2004). The small RNA regulators of *Escherichia coli*: roles and mechanisms*. *Annu. Rev. Microbiol.* 58, 303–328.
- Hussein, R., and Lim, H.N. (2011). Disruption of small RNA signaling caused by competition for Hfq. *Proc. Natl. Acad. Sci. USA* 108, 1110–1115.
- Kawamoto, H., Koide, Y., Morita, T., and Aiba, H. (2006). Base-pairing requirement for RNA silencing by a bacterial small RNA and acceleration of duplex formation by Hfq. *Mol. Microbiol.* 61, 1013–1022.
- Lenz, D.H., Mok, K.C., Lilley, B.N., Kulkarni, R.V., Wingreen, N.S., and Bassler, B.L. (2004). The small RNA chaperone Hfq and multiple small RNAs control quorum sensing in *Vibrio harveyi* and *Vibrio cholerae*. *Cell* 118, 69–82.
- Levine, E., Zhang, Z., Kuhlman, T., and Hwa, T. (2007). Quantitative characteristics of gene regulation by small RNA. *PLoS Biol.* 5, e229.
- Long, T., Tu, K.C., Wang, Y., Mehta, P., Ong, N.P., Bassler, B.L., and Wingreen, N.S. (2009). Quantifying the integration of quorum-sensing signals with single-cell resolution. *PLoS Biol.* 7, e1000068.
- Majdalani, N., Cunniff, C., Sledjeski, D., Elliott, T., and Gottesman, S. (1998). DsrA RNA regulates translation of RpoS message by an anti-antisense mechanism, independent of its action as an antisilencer of transcription. *Proc. Natl. Acad. Sci. USA* 95, 12462–12467.
- Massé, E., and Gottesman, S. (2002). A small RNA regulates the expression of genes involved in iron metabolism in *Escherichia coli*. *Proc. Natl. Acad. Sci. USA* 99, 4620–4625.
- Massé, E., Escorcia, F.E., and Gottesman, S. (2003). Coupled degradation of a small regulatory RNA and its mRNA targets in *Escherichia coli*. *Genes Dev.* 17, 2374–2383.
- McCullen, C.A., Benhammou, J.N., Majdalani, N., and Gottesman, S. (2010). Mechanism of positive regulation by DsrA and RprA small noncoding RNAs: pairing increases translation and protects rpoS mRNA from degradation. *J. Bacteriol.* 192, 5559–5571.
- Møller, T., Franch, T., Udesen, C., Gerdes, K., and Valentin-Hansen, P. (2002). Spot 42 RNA mediates discoordinate expression of the *E. coli* galactose operon. *Genes Dev.* 16, 1696–1706.
- Moon, K., and Gottesman, S. (2011). Competition among Hfq-binding small RNAs in *Escherichia coli*. *Mol. Microbiol.* 82, 1545–1562.
- Overgaard, M., Johansen, J., Møller-Jensen, J., and Valentin-Hansen, P. (2009). Switching off small RNA regulation with trap-mRNA. *Mol. Microbiol.* 73, 790–800.
- Papenfort, K., Bouvier, M., Mika, F., Sharma, C.M., and Vogel, J. (2010). Evidence for an autonomous 5' target recognition domain in an Hfq-associated small RNA. *Proc. Natl. Acad. Sci. USA* 107, 20435–20440.

- Papenfort, K., Sun, Y., Miyakoshi, M., Vanderpool, C.K., and Vogel, J. (2013). Small RNA-mediated activation of sugar phosphatase mRNA regulates glucose homeostasis. *Cell* 153, 426–437.
- Plumbridge, J., Bossi, L., Oberto, J., Wade, J.T., and Figueroa-Bossi, N. (2014). Interplay of transcriptional and small RNA-dependent control mechanisms regulates chitosugar uptake in *Escherichia coli* and *Salmonella*. *Mol. Microbiol.* 92, 648–658.
- Prévost, K., Desnoyers, G., Jacques, J.-F., Lavoie, F., and Massé, E. (2011). Small RNA-induced mRNA degradation achieved through both translation block and activated cleavage. *Genes Dev.* 25, 385–396.
- Rutherford, S.T., and Bassler, B.L. (2012). Bacterial quorum sensing: its role in virulence and possibilities for its control. *Cold Spring Harb. Perspect. Med.* 2, 1–25.
- Rutherford, S.T., van Kessel, J.C., Shao, Y., and Bassler, B.L. (2011). AphA and LuxR/HapR reciprocally control quorum sensing in vibrios. *Genes Dev.* 25, 397–408.
- Shao, Y., and Bassler, B.L. (2012). Quorum-sensing non-coding small RNAs use unique pairing regions to differentially control mRNA targets. *Mol. Microbiol.* 83, 599–611.
- Shao, Y., Feng, L., Rutherford, S.T., Papenfort, K., and Bassler, B.L. (2013). Functional determinants of the quorum-sensing non-coding RNAs and their roles in target regulation. *EMBO J.* 32, 2158–2171.
- Storz, G., Vogel, J., and Wassarman, K.M. (2011). Regulation by small RNAs in bacteria: expanding frontiers. *Mol. Cell* 43, 880–891.
- Teng, S.-W., Wang, Y., Tu, K.C., Long, T., Mehta, P., Wingreen, N.S., Bassler, B.L., and Ong, N.P. (2010). Measurement of the copy number of the master quorum-sensing regulator of a bacterial cell. *Biophys. J.* 98, 2024–2031.
- Teng, S.-W., Schaffer, J.N., Tu, K.C., Mehta, P., Lu, W., Ong, N.P., Bassler, B.L., and Wingreen, N.S. (2011). Active regulation of receptor ratios controls integration of quorum-sensing signals in *Vibrio harveyi*. *Mol. Syst. Biol.* 7, 491.
- Tu, K.C., and Bassler, B.L. (2007). Multiple small RNAs act additively to integrate sensory information and control quorum sensing in *Vibrio harveyi*. *Genes Dev.* 21, 221–233.
- Tu, K.C., Waters, C.M., Svenningsen, S.L., and Bassler, B.L. (2008). A small-RNA-mediated negative feedback loop controls quorum-sensing dynamics in *Vibrio harveyi*. *Mol. Microbiol.* 70, 896–907.
- Tu, K.C., Long, T., Svenningsen, S.L., Wingreen, N.S., and Bassler, B.L. (2010). Negative feedback loops involving small regulatory RNAs precisely control the *Vibrio harveyi* quorum-sensing response. *Mol. Cell* 37, 567–579.
- Udekwi, K.I., Darfeuille, F., Vogel, J., Reimegård, J., Holmqvist, E., and Wagner, E.G.H. (2005). Hfq-dependent regulation of OmpA synthesis is mediated by an antisense RNA. *Genes Dev.* 19, 2355–2366.
- van Kessel, J.C., Rutherford, S.T., Shao, Y., Utria, A.F., and Bassler, B.L. (2012). The master regulators AphA and LuxR control the *Vibrio harveyi* quorum-sensing regulon: analysis of their individual and combined effects. *J. Bacteriol.* 195, 436–443.
- van Kessel, J.C., Ulrich, L.E., Zhulin, I.B., and Bassler, B.L. (2013). Analysis of activator and repressor functions reveals the requirements for transcriptional control by LuxR, the master regulator of quorum sensing in *Vibrio harveyi*. *MBio.* 4, e00378-13.
- Vanderpool, C.K., and Gottesman, S. (2004). Involvement of a novel transcriptional activator and small RNA in post-transcriptional regulation of the glucose phosphoenolpyruvate phosphotransferase system. *Mol. Microbiol.* 54, 1076–1089.
- Vogel, J., and Luisi, B.F. (2011). Hfq and its constellation of RNA. *Nat. Rev. Microbiol.* 9, 578–589.
- Wagner, E.G.H. (2013). Cycling of RNAs on Hfq. *RNA Biol.* 10, 619–626.
- Waters, L.S., and Storz, G. (2009). Regulatory RNAs in bacteria. *Cell* 136, 615–628.

Hematopoietic Stem Cell Arrival Triggers Dynamic Remodeling of the Perivascular Niche

Owen J. Tamplin,^{1,6} Ellen M. Durand,^{1,2,6} Logan A. Carr,¹ Sarah J. Childs,³ Elliott J. Hagedorn,¹ Pulin Li,^{1,4,7} Amanda D. Yzaguirre,⁵ Nancy A. Speck,⁵ and Leonard I. Zon^{1,2,4,*}

¹Stem Cell Program and Division of Hematology/Oncology, Boston Children's Hospital and Dana Farber Cancer Institute, Howard Hughes Medical Institute, Harvard Stem Cell Institute, Harvard Medical School, Boston, MA 02115, USA

²Biological and Biomedical Sciences, Harvard University, Cambridge, MA 02138, USA

³Biochemistry and Molecular Biology, Alberta Children's Hospital Research Institute, University of Calgary, Calgary, AB T2N 4N1, Canada

⁴Chemical Biology Program, Harvard University, Cambridge, MA 02138, USA

⁵Abramson Family Cancer Research Institute and Department of Cell and Developmental Biology, Perelman School of Medicine, University of Pennsylvania, Philadelphia, PA 19104, USA

⁶Co-first author

⁷Present address: Howard Hughes Medical Institute, Division of Biology and Biological Engineering, California Institute of Technology, Pasadena, CA 91125, USA

*Correspondence: zon@enders.tch.harvard.edu

<http://dx.doi.org/10.1016/j.cell.2014.12.032>

SUMMARY

Hematopoietic stem and progenitor cells (HSPCs) can reconstitute and sustain the entire blood system. We generated a highly specific transgenic reporter of HSPCs in zebrafish. This allowed us to perform high-resolution live imaging on endogenous HSPCs not currently possible in mammalian bone marrow. Using this system, we have uncovered distinct interactions between single HSPCs and their niche. When an HSPC arrives in the perivascular niche, a group of endothelial cells remodel to form a surrounding pocket. This structure appears conserved in mouse fetal liver. Correlative light and electron microscopy revealed that endothelial cells surround a single HSPC attached to a single mesenchymal stromal cell. Live imaging showed that mesenchymal stromal cells anchor HSPCs and orient their divisions. A chemical genetic screen found that the compound lycorine promotes HSPC-niche interactions during development and ultimately expands the stem cell pool into adulthood. Our studies provide evidence for dynamic niche interactions upon stem cell colonization.

INTRODUCTION

Hematopoietic stem and progenitor cells (HSPCs) self-renew and give rise to all blood cell types. Definitive HSPCs arise from the hemogenic endothelium of the dorsal aorta (DA) (Bertrand et al., 2010; Boisset et al., 2010; Kissa and Herbomel, 2010), are released into circulation, and then seed an intermediate hematopoietic niche before colonizing the adult marrow. In mammals, this intermediate tissue is the fetal liver (FL), and in ze-

brafish, it is the caudal hematopoietic tissue (CHT), a vascular plexus in the ventral tail of the embryo (Murayama et al., 2006; Orkin and Zon, 2008). After rapid expansion in the intermediate niche, HSPCs will leave and go on to seed the adult marrow, which in mammals is bone and in zebrafish is kidney (Traver et al., 2003).

The adult niche is a complex microenvironment that maintains and regulates HSPCs throughout life. The bone marrow contains a complex network of sinusoidal vessels that act as an interface between circulation and the niche. Most HSPCs are proximal to these vessels and are considered to be in a perivascular niche (Kiel et al., 2005; Nombela-Arrieta et al., 2013). Studies have shown that endothelial cells (ECs) have distinct properties that enable them to support and expand associated HSPCs (Butler et al., 2010; Hooper et al., 2009). However, the perivascular niche is not limited to ECs, and many other cell types also play a role, including mesenchymal stromal cells, osteoblasts, arterioles, and sympathetic nerves (Morrison and Scadden, 2014). Stromal cells are likely heterogeneous throughout the bone marrow and provide HSPC maintenance factors such as CXCL12 and KITLG (Ding and Morrison, 2013; Ding et al., 2012; Greenbaum et al., 2013; Méndez-Ferrer et al., 2010; Sugiyama et al., 2006). HSPCs in the bone marrow have been observed in a number of elegant studies (Köhler et al., 2009; Lo Celso et al., 2009; Xie et al., 2009). Primarily, these studies used multiphoton intravital microscopy to locate transplanted HSPCs in surgically accessed bone or bone explants. A high-resolution and dynamic live view of the physical interactions between endogenous cell types in the niche has not been achieved.

We have developed a transgenic zebrafish line to observe the migration and behavior of endogenous HSPCs. Conserved hematopoietic regulatory genes have led to the development of HSPC transgenic reporter lines, although none of these are entirely specific (Lin et al., 2005; North et al., 2007). To establish a more specific HSPC line, we utilized a regulatory element from the first intron of the mouse *Runx1* locus (+23 kb downstream of

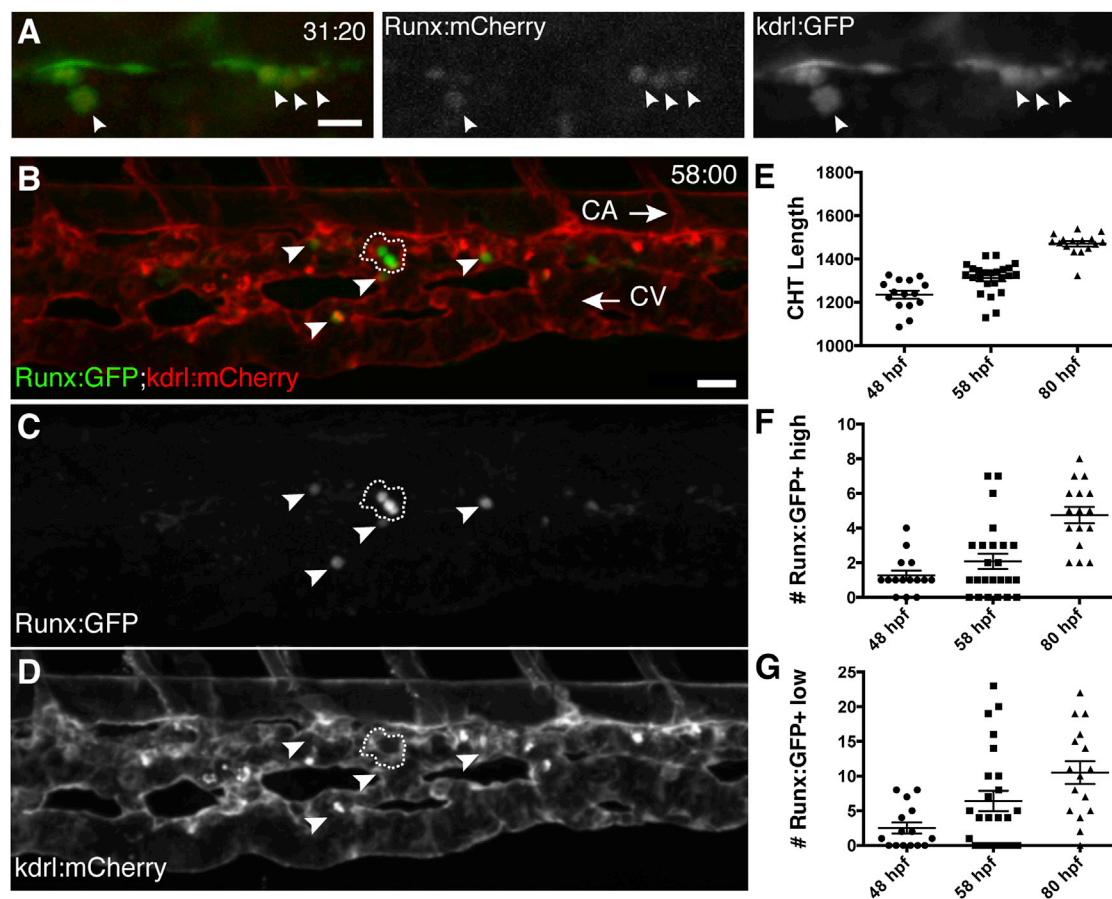


Figure 1. A Transgenic Zebrafish Line that Specifically Marks HSPCs

(A) Single frame of time-lapse (hr post fertilization:min) showing Runx:mCherry+ HSPCs (arrowheads, red nuclei) budding from kdrl:GFP+ hemogenic endothelium of DA (green). See [Movie S1](#).

(B–D) CHT is colonized by Runx:GFP+ HSPCs (green) that are closely associated with kdrl:mCherry+ ECs (red). Caudal artery (CA) is dorsal to CHT, caudal vein (CV) is ventral, and circulation runs posterior (right arrow) and anterior (left arrow), respectively. Cluster of three Runx:GFP+ high cells outlined with dashed line and four Runx:GFP+ low cells indicated with arrowheads. 58 hpf embryo.

(E–G) Runx:GFP+ high and low cells quantified, with CHT length as indicator of stage (anterior from cloaca to posterior limit of CA).

Note: confocal images are 3D rendered depth or max projections of 20–30 μm z stacks. Scale bars, (A) 15 μm ; (B) 25 μm . Error bars show mean \pm SEM. See also [Figure S1](#).

the P1 promoter) to drive expression of a marker ([Nottingham et al., 2007](#)). The Runx1+23 enhancer from mouse marks definitive HSPC in the zebrafish in all sites of definitive hematopoiesis and has been confirmed by long-term transplantation.

The ability to track endogenous HSPCs in the live embryo allowed us to observe dynamic interactions with the niche. We discovered a cellular behavior that involves triggered remodeling of perivascular ECs upon arrival of an HSPC in a new site of hematopoiesis. We also show that mesenchymal stromal cells can anchor and orient the division plane of an HSPC. Using correlative light and electron microscopy, we reveal the high-resolution ultrastructure of a single HSPC in the perivascular niche after live tracking and lodgement. Lastly, we used a chemical genetic approach to modulate the HSPC-niche interactions observed in the embryo. These interactions lead to long-term changes in the size of the stem cell pool into adulthood. Our studies suggest that the niche reacts to the arrival of stem cells.

RESULTS

Establishment of a Highly Specific HSPC Transgenic Zebrafish Line

To observe and study endogenous HSPCs, we established transgenic zebrafish lines with the mouse Runx1+23 enhancer driving either cytoplasmic EGFP (Runx:GFP) or nuclear localized NLS-mCherry (Runx:mCherry). These two lines were crossed to demonstrate that the green and red fluorescent proteins marked mostly the same cell populations, with the Runx:mCherry line showing broader expression in progenitors ([Figures S1A and S1B](#) available online). Time-lapse live imaging showed that Runx+ cells emerge from the hemogenic endothelium of the DA ([Figure 1A](#) and [Movie S1](#)). Intercrossing the Runx:mCherry line with *cmyb:EGFP* and *cd41:EGFP* lines showed that Runx+ cells marked an overlapping population in all major hematopoietic sites of the embryo, including the DA, CHT, thymus,

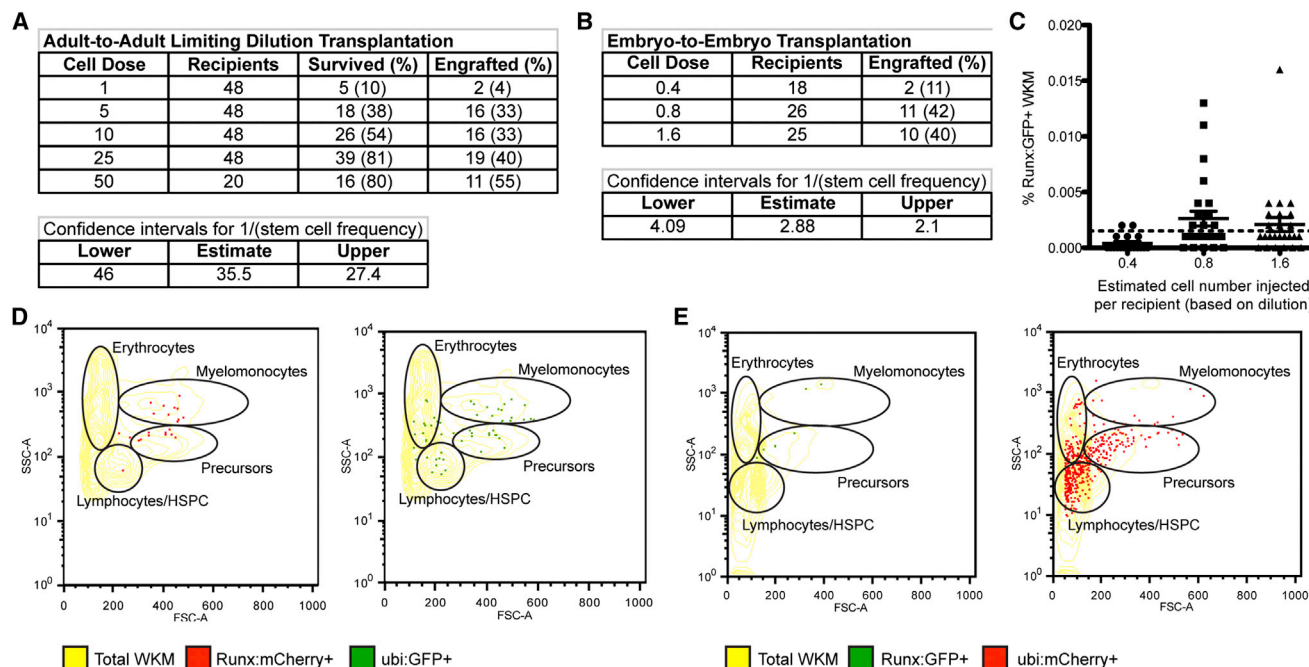


Figure 2. Functional HSPCs Are Highly Purified Using a Single Transgenic Marker

(A and B) Summary of results from (A) adult-to-adult and (B) embryo-to-embryo limiting dilution transplantation experiments.

(C) Embryo-to-embryo transplantation recipients with engraftment of Runx:GFP⁺ cells in kidney marrow at 3 months (above background; >0.001%).

(D and E) Representative kidney marrow flow cytometry analysis of (D) adult-to-adult transplantation recipient with Runx:mCherry⁺ HSPCs and ubi:GFP⁺ lineages and (E) embryo-to-embryo transplantation recipient with Runx:GFP⁺ HSPCs and ubi:mCherry⁺ lineages.

Error bars show mean \pm SEM. See also Figure S2.

and kidney (Figures S1C–S1I; data not shown). We detected Runx⁺ cells in the adult kidney marrow using flow cytometry and immunohistochemistry (Figures S1J–S1L).

Next, we followed newly born HSPCs as they colonized the CHT niche. We quantified the number of Runx:GFP⁺ cells in the CHT at different developmental stages. We found there were an average of 1, 2, or 5 Runx:GFP⁺ high cells (and 2, 6, or 10 Runx:GFP⁺ low cells) in the CHT at 48, 58, and 80 hr post-fertilization (hpf), respectively (Figures 1B–1G). Cell numbers in the Runx:mCherry⁺ line were comparable, except for greater expansion of Runx:mCherry⁺ low cells from 72 hpf (Figures S1A and S1B). Looking at Runx:GFP⁺ cells in the CHT together with a vascular reporter, we found that HSPCs were closely associated with ECs of the caudal vein plexus (Figures 1B–1D). Both cell numbers and localization of Runx:GFP⁺ cells are consistent with previous lineage-tracing experiments of HSPC from the hemogenic endothelium to the CHT (Kissa et al., 2008).

The Functional Stem Cell Characteristics of Runx⁺ HSPCs in the Zebrafish

To assess the functional characteristics of cells in the Runx⁺ pool, we performed limiting dilution transplantation as a standard assay to determine hematopoietic stem cell content. We purified Runx:mCherry⁺ cells from the kidney marrow of adult transgenic donors. These donors also carried the ubiquitous ubi:GFP transgene (Mosimann et al., 2011) so that multilineage contribution could be assessed if the Runx:mCherry HSPC

enhancer was downregulated upon differentiation. Sorted double-positive cells were diluted in a range between 1 and 50 then transplanted into irradiated recipients (Figure 2A). Survival rates improved in recipients that received a greater number of donor HSPCs, and at 3 months posttransplantation, the kidney marrow of recipients was dissected for flow cytometry analysis. Runx:mCherry⁺ cells were present in the kidney marrow and had contributed ubi:GFP⁺ progeny to all lineages (Figures 2A and 2D). Statistical analysis of engraftment over a range of cell doses estimated a stem cell frequency of ~ 1 in 35 (Figure 2A) (Hu and Smyth, 2009). We consider this to be an underestimate because the donors and recipients were not immune matched; previous work from our lab showed that immune matching can improve hematopoietic transplantation in zebrafish (de Jong et al., 2011). The Runx⁺ cell pool can be sorted with a single transgenic marker, and no additional labeling of cell-surface markers, to a purity that is within the range of the well-characterized KSL (c-Kit⁺ Sca-1⁺ Lin[−]) population in mouse (Osawa et al., 1996). Based on the ability of a small number of adult Runx⁺ cells to engraft long-term, self-renew, and produce all lineages, we have demonstrated that there is substantial stem cell content within this pool of cells.

We also wanted to evaluate the stem cell characteristics of the Runx⁺ population in the embryo. Studies have shown that hematopoietic stem cells isolated from different tissues of the mouse embryo have the capacity to contribute to hematopoiesis when transplanted into recipient embryos (Fleischman and

Mintz, 1979) or adults (Medvinsky and Dzierzak, 1996; Müller et al., 1994). Based on a previous approach (Traver et al., 2003), we have further developed an HSPC embryo-to-embryo transplantation assay in zebrafish. Runx+ cells were sorted from a pool of 3 days post fertilization (dpf) double transgenic Runx+ and ubi+ donor embryos because sufficient cell numbers could be collected at that stage. Only one to two cells were injected into the circulation of a wild-type recipient embryo at 2 dpf. A dilution series established the number of cells injected for each experiment. At 2 dpf, the CHT is being colonized by endogenous HSPCs, but the thymus has not formed, allowing introduction of exogenous cells without the possibility of immune rejection. Recipient embryos are then raised to adulthood, and their kidney marrow is analyzed by flow cytometry for engraftment at 3–5 months. We scored engraftment as any detectable Runx+ cells above background (Figures 2B and 2C). This rationale was chosen because approximately one donor HSPC will be competing with endogenous stem cells in an unconditioned wild-type recipient embryo—there is no precedent to predict chimerism in this scenario. The transplanted cells must seed the CHT, migrate to the kidney, and persist into adulthood, where they will self-renew and contribute to all lineages.

We identified recipients with Runx+ HSPCs and ubi+ progeny in the kidney marrow, as well as some that had ubi+ cells in the peripheral blood (Figure 2E; data not shown). Statistical analysis estimated the stem cell frequency of the Runx+ population in the 3 dpf embryo to be $\sim 1/2.88$ cells (Figure 2B). These results were representative of three independent experiments—two with Runx:GFP;ubi:mCherry double-transgenic lines and a third with the opposite Runx:mCherry;ubi:GFP transgenic combination (Figure S2). Together, our limiting dilution adult and embryo transplantation assays demonstrate the Runx+ populations contain functional stem cells based on long-term multilineage engraftment. Our data also suggest that some Runx+ cells are progenitors based on (1) overlap with transgenic reporters that mark both stem and progenitor cells (cmyb:EGFP and cd41:EGFP; Figure S1); (2) a Runx+ low population that appears to expand from Runx+ high cells (Figures 1 and S1; data not shown); (3) flow cytometry analysis of adult kidney marrow that shows Runx+ cells in gates that contain progenitors (Figures 2D, 2E, and S2C). There are no antibodies available in zebrafish to further purify these populations or to distinguish between a stem and progenitor cell, so we will operationally define engrafting Runx+ cells as HSPCs in this study.

Dynamic Visualization of Stem Cell Colonization of the CHT Niche

To directly observe the interaction of HSPCs with surrounding ECs during CHT colonization, we performed time-lapse live imaging with spinning-disk confocal microscopy. We were able to routinely acquire image series with high temporal resolution (1–2 min per two-channel confocal z stack) for up to 16 continuous hours. A wide-field image was acquired using a 20 \times objective because the rare lodgement of a single HSPC could occur anywhere in the length of the CHT (Figure 1B). We observed HSPC arrival in the CHT via circulation, followed by adherence to endothelial walls (Figure S3A and Movie S2). Next, cells underwent rapid extravasation to the abluminal side of the endothelial

wall (<5 min; Figure S3A). Once HSPCs lodged in the CHT, we made a striking observation: a small group of ECs actually remodeled around a single HSPC to form a stem cell pocket, which we call “endothelial cuddling” (Figures 3A and S3B and Movie S2). Within the 12–16 hr limit of time-lapse acquisition, an HSPC would make one of three cell division decisions: (1) symmetric (defined as two daughter cells that remain in the pocket); (2) asymmetric (defined as one daughter cell remaining in the pocket and the other migrating out); (3) or no division. In this example, the division is asymmetrical, with one daughter cell crawling out of the endothelial niche and the other remaining (Figure S3C and Movie S2).

After HSPC lodgement in the CHT, we used higher magnification (40 \times –60 \times) to better detail the close association and contact of surrounding ECs (Figure 3B). To quantify the number of surrounding ECs, we briefly fixed and stained embryos with a nuclear dye and then imaged using scanning confocal microscopy (Figure 3C). The ECs in contact with a single HSPC were outlined with membrane-bound mCherry, and their nuclei were counted. In each structure, we typically observed 5–6 ECs surrounding a single HSPC. Time-lapse live imaging of endogenous Runx+ HSPCs in the embryo has revealed striking interactions with perivascular ECs in the niche microenvironment.

Endothelial Niche Remodeling Is Conserved in Mammalian Fetal Liver

We sought to establish whether the distinct endothelial niche structure identified in the zebrafish CHT was also found in mammals. The equivalent tissue is the FL, as it is the first tissue colonized by definitive HSPCs from the DA. The FL is an intermediate site of hematopoiesis where HSPCs expand before leaving to colonize the adult marrow, and it produces the majority of blood during development (Morrison et al., 1995; Sánchez et al., 1996). To examine the earliest stages of FL colonization, we dissected E11.5 FLs from Ly6a-GFP (Sca-1) mice, which have GFP+ HSPC (Ma et al., 2002). Together with HSPC marker Runx1 and EC marker VE-cadherin (Cdh5), we found Ly6a-GFP+/Runx1+ HSPCs in one of three compartments in the FL (Figures 4A–4C and Movie S3A–C): (1) an abluminal space with no EC contact, (2) adherent to ECs on one side, or (3) inside an EC pocket. The similarity of a single HSPC surrounded by a small group of ECs in both the mouse FL and zebrafish CHT (compare Figures 3B and 4C) suggests that this is a conserved cellular structure that forms during stem cell lodgement in hematopoietic niches.

The identification of a potentially conserved HSPC-endothelial niche structure raised the possibility that HSPCs also trigger a dynamic remodeling of ECs during colonization of the FL. The FL tissue in mouse is not directly accessible to confocal microscopy, so we instead applied a protocol for live imaging of embryo explants (Boisset et al., 2010). We dissected wild-type and Ly6a-GFP E11.5 FLs, soaked the explant FL in fluorescently conjugated Kit (c-kit) and Pecam1 (CD31) antibodies, and then immediately performed live imaging for up to 4 hr. With the caveat that the marker profile of early E11.5 FL HSPCs has not been well defined and that many c-kit+ cells in the FL are progenitors, we have observed hematopoietic and EC interactions that are strikingly similar to those in the zebrafish CHT (compare

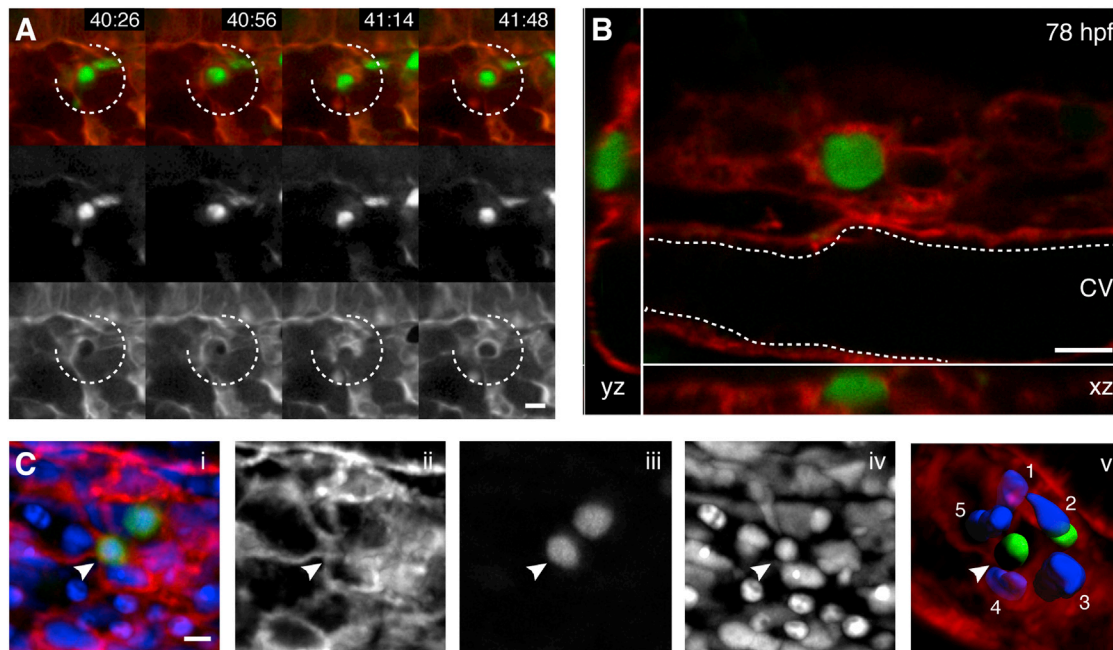


Figure 3. Endothelial Cells in the Perivascular Niche Remodel to Surround a Single HSPC

(A) Four frames from time-lapse [Movie S2](#) 40–42 hpf (hr post fertilization:min). Upper row is a merge of Runx:GFP+ HSPC (green, middle row) and kdrl:RFP ECs (red, lower row). A group of surrounding ECs (broken circle) remodel around a single HSPC soon after its arrival.
(B) Higher magnification (60 \times) live image of single Runx:GFP+ HSPC surrounded by kdrl:mCherry ECs at 78 hpf (orthogonal views).
(C) 3D rendered projection of scanning confocal image from fixed 80 hpf embryo. (i) merge, (ii) kdrl:mCherry ECs, (iii) Runx:GFP+ HSPCs, (iv) DRAQ5 nuclei, and (v) kdrl:mCherry projection with 3D modeled green HSPCs and five blue surrounding EC nuclei (arrowhead indicates HSPC in EC surround).
All views: dorsal up, ventral down. Scale bars, 10 μ m. See also [Figure S3](#).

[Figures 3A and 4D](#)). We observed c-kit⁺ hematopoietic cells adhered to the sinusoidal network of CD31⁺ ECs ([Figures 4D, 4E, and S4](#)). We followed a c-kit⁺ cell attached to the sinusoid as it migrated into and was surrounded by a small group of ECs ([Figure 4D and Movie S4](#)). Tracking a Ly6a-GFP⁺/c-kit⁺ cell in another explant, we observed one cell division ([Figure 4E](#)). Intriguingly, the daughter cell proximal to the sinusoid remained surrounded by ECs, whereas the daughter cell distal to the sinusoid migrated away into the abluminal space ([Figure 4E and Movie S5](#)). In another time-lapse sequence, a c-kit⁺ cell was observed undergoing discrete steps toward lodgement—adherence, extravasation, abluminal migration, and endothelial niche remodeling ([Figures S4A–S4C](#)). Even though FL explants have been removed from circulation and are imaged ex vivo, our live-imaging data strongly suggest an evolutionary conserved process of dynamic EC remodeling around a single hematopoietic cell in a site of hematopoiesis.

Stem Cell Divisions Are Oriented Relative to Mesenchymal Stromal Cells

To further understand the interaction of HSPCs with the perivascular niche, we identified a cxcl12a:DsRed2 transgenic line that allowed us to observe mesenchymal stromal cells in the CHT ([Glass et al., 2011](#)). These are likely the “fibroblastic reticular cells” that were previously described in the CHT ([Murayama et al., 2006](#)) and similar to the “CXCL12-abundant reticular” cells

in the perivascular bone marrow niche ([Sugiyama et al., 2006](#)). By combining cxcl12a:DsRed2 and kdrl:GFP transgenic lines, we could see that mesenchymal stromal and endothelial cells are closely associated in the CHT, with cxcl12a⁺ cells distributed in abluminal spaces that underlie kdrl⁺ ECs ([Figure 5A](#)). We then crossed the Runx:GFP and cxcl12a:DsRed2 transgenic lines to observe HSPCs together with mesenchymal stromal cells. Most of the HSPCs in the CHT were lodged next to a stromal cell ([Figure 5C](#)). To quantify the proximity of these two cell types within 3D confocal z stacks, the distance between a Runx⁺ HSPC and its nearest cxcl12a⁺ stromal cell was measured ([Figures 5B and 5C](#)). This analysis showed that 60% of HSPCs are in direct contact with a cxcl12a⁺ cell and that 85% are ≤ 3 microns away. We performed time-lapse live imaging of CHT colonization in these double-transgenic embryos and similarly found that arrival and expansion of most HSPCs occurred in close proximity to stromal cells (data not shown). When we tracked HSPCs attached to stromal cells over time, we observed that a significant majority of divisions had a distinct orientation: one daughter cell remained joined and was proximal to the stromal cell, and the other daughter cell was distal and displaced away from the niche ([Figures 5D–5F and Movie S6](#)). These data suggest that the cxcl12a⁺ stromal cell might orient the division plane of the HSPC by providing a polarizing signal. Together, this work shows that cxcl12a⁺ stromal cells dynamically interact with HSPCs in the CHT niche.

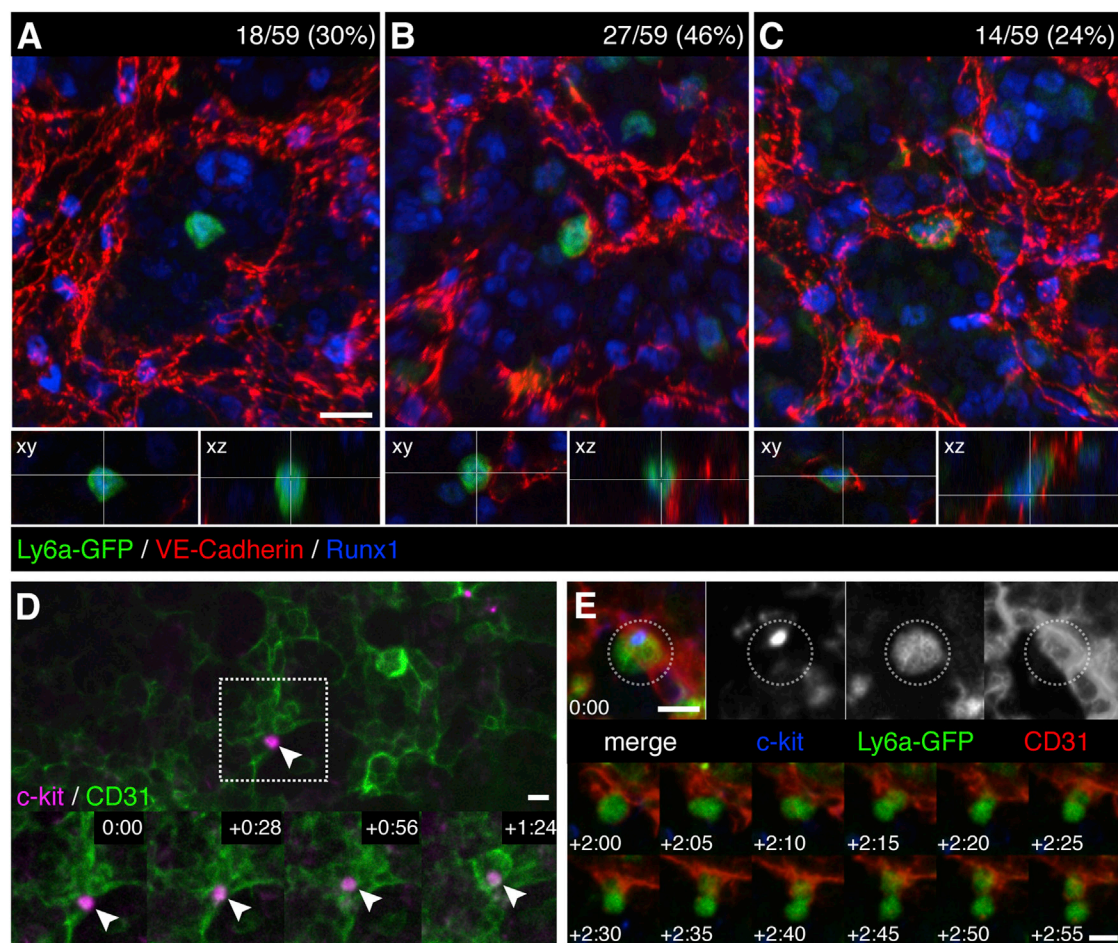


Figure 4. Endothelial Cells Surround HSPCs in the Fetal Liver Microenvironment

(A–C) FLs from E11.5 Ly6a-GFP mice were fixed and stained for immunofluorescence with anti-VE-Cadherin (red), anti-Runx1 (blue), and anti-GFP (green) antibodies. We scored 59 Ly6a-GFP+/Runx1+ cells from 3 FLs and identified 3 different HSPC-EC configurations: (A) abluminal with no contact between HSPC and ECs (18/59; 30%); (B) EC contact on one side of the HSPC (27/59; 46%); and (C) HSPC surrounded on all sides with ECs (14/59; 24%). See [Movie S3](#).

(D) c-kit+ cell (magenta) adhered to CD31+ ECs (green) in one lobe of an E11.5 FL (arrowhead). White box marks details below. Time-lapse frames show in <90 min the HSPC migrates into a field of ECs. Soon after, ECs surround HSPC to form niche. See also [Movie S4](#).

(E) c-kit+(blue)/Ly6a-GFP+(green) HSPC adhered to abluminal side of CD31+ EC (red). Following this cell >2 hr (1 frame/5 min) shows a division with distal and proximal daughters relative to sinusoid; the latter remains in an endothelial surround. See also [Movie S5](#). Confocal images: 3D rendered depth projection (A, B, C, and E), orthogonal view (A, B, and C below), maximum projection (D) of z stack.

Scale bars, 10 μ m. See also [Figure S4](#).

High-Resolution Ultrastructure of an Endogenous HSPC in the Perivascular Niche

We wanted to reveal the high-resolution architecture and cellular interactions of a single rare HSPC in the perivascular niche. To do this, we used correlative light and electron microscopy ([Mironov and Beznoussenko, 2009](#)). First, to confirm that an HSPC was lodged in the CHT, we performed time-lapse live imaging of Runx:GFP;kdr:mCherry embryos as above ([Figure 3A](#)). Imaging multiple stage-matched embryos in parallel, we confirmed that 1–2 HSPCs per embryo had not only migrated to the CHT but had also lodged and triggered an EC remodeling event that was stable for more than 6 hr ([Figures 6A and 6B](#)). These same embryos were then fixed and embedded for electron microscopy (EM). Serial block face

scanning EM captured large sections of the CHT at high resolution ([Figure 6C](#); XY, 10 nm/pixel; Z, 100 nm/slice). Based on a number of cellular and anatomical markers (e.g., vessels, melanocytes, and somites), the position of the lodged HSPC in time-lapse could be correlated with EM serial sections ([Figures S5A and S5B](#); data not shown). In summary, we tracked a single cell in an embryo by time-lapse live imaging, processed that same embryo for serial block face scanning EM, and then identified the single cell in a high-resolution 3D reconstruction of the EM sections.

3D reconstruction of EM scans shows that the HSPC lodges in a region just adjacent to the caudal artery ([Figures 6C and S5E](#)). As predicted from our confocal microscopy analysis ([Figure 3C](#)), a pocket of at least five ECs surrounds the HSPC ([Figures 6C and](#)

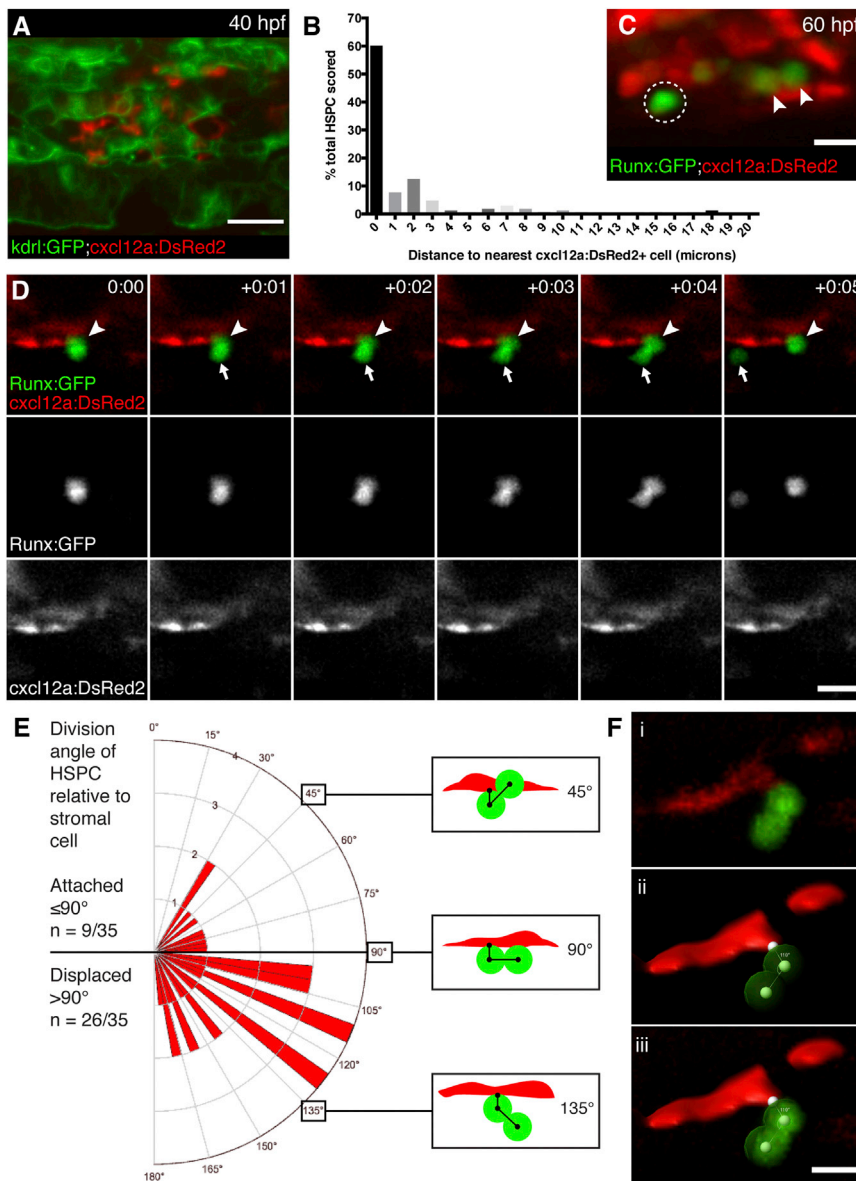


Figure 5. HSPCs Are Anchored to Perivascular Stromal Cells during Cell Divisions

(A) cxcl12a:DsRed2+ stromal cells (red) underlie kdr1:GFP+ ECs (green). 40 hpf embryo.

(B) Percentage of HSPCs in CHT scored by distance to nearest stromal cell (n = 168 total cells from 25 embryos).

(C) Detail of Runx:GFP+ HSPCs (green) in proximity to cxcl12a:DsRed2+ stromal cells (red). Arrowheads mark HSPCs in contact with stromal cell. Circle marks HSPC with 2 μ m gap between it and stromal cell. 60 hpf embryo.

(D) Six frames selected from time-lapse Movie S6 (hr:min). Top row is a merge of Runx:GFP+ HSPC (green, middle row) and cxcl12a:DsRed2+ stromal cells (red, lower row). Proximal HSPC anchored to stromal cell (arrowhead) divides and releases distal daughter cell into circulation (arrow).

(E) Rose diagram showing division plane of HSPC oriented relative to stromal cell. Majority of divisions result in displaced daughter cell (n = 26/35 cell divisions from 22 embryos; 95% confidence interval 0.567–0.875; mean division angle of 110°). Diagrams show HSPCs dividing over stromal cell surface (45°), perpendicular to stromal cell (90°), or displaced away from stromal cell (135°). Angles may be affected by release into flow of circulation.

(F) 3D models used to measure HSPC divisions relative to stromal cells. (i) Volume rendered confocal image. (ii) 3D model showing angle measurement between attachment point on stromal cell surface and center points of proximal and distal HSPCs (example shown is 110°). (iii) Overlay of confocal image and 3D model.

Scale bars, (A) 25 μ m; (C and F) 10 μ m; (D) 15 μ m.

S5E). Our EM scans showed the details of cellular interactions between HSPCs and ECs. Regarding the endothelial cells, one example showed the HSPC partially wrapped by an EC (Figures 6E and 6F). In another example, only one region of the HSPC was attached to an EC (Figures S5G and S5H). In other sections, an EC would only contact the HSPC with a small protrusion or not contact it at all, lying opposite an extracellular space (Figures 6D and S5F; data not shown). Regarding the mesenchymal stromal cells, in one case, we found two stromal cells in proximity to the HSPC, but only one is in direct contact in a narrow region near the midpoint of the cell (Figures 6D, 6G, and 6H). This reveals the actual anchored attachment of HSPC to stromal cell that was suggested by our confocal microscopy (Figures 5B–5F). In addition, a previously unidentified cell type, a fibroblastic cell with melanophore inclusions, was found within the perivascular

niche and tightly wrapped around the HSPC (Figures 6D, 6I, and 6J and Movie S7). The melanophore inclusions suggest a cell of neural crest origin, as such cells have been found in the adult marrow (Isen et al., 2014; Méndez-Ferrer et al., 2010). The combined technology of time-lapse confocal imaging and electron microscopy has shown that perivascular

A Chemical Genetic Screen to Discover Small-Molecule Regulators of CHT Niche Colonization

Next, we wanted to modulate the interactions between HSPC and perivascular niche to test their functional significance. We decided to use a chemical genetic approach so that we could perturb the embryo with small molecules during a discrete window of CHT colonization (48–72 hpf; Figure S6A). Hits were scored if they increased or decreased hematopoietic progenitor markers *cmyb* and *runx1* with activities that were similar to control compounds (Figures S6B–S6E; data not shown). We used (\pm)11,12-epoxyeicosatrienoic acid (EET) as a control because it was identified by our lab as a strong positive regulator of HSPC (P.L. and L.I.Z.,

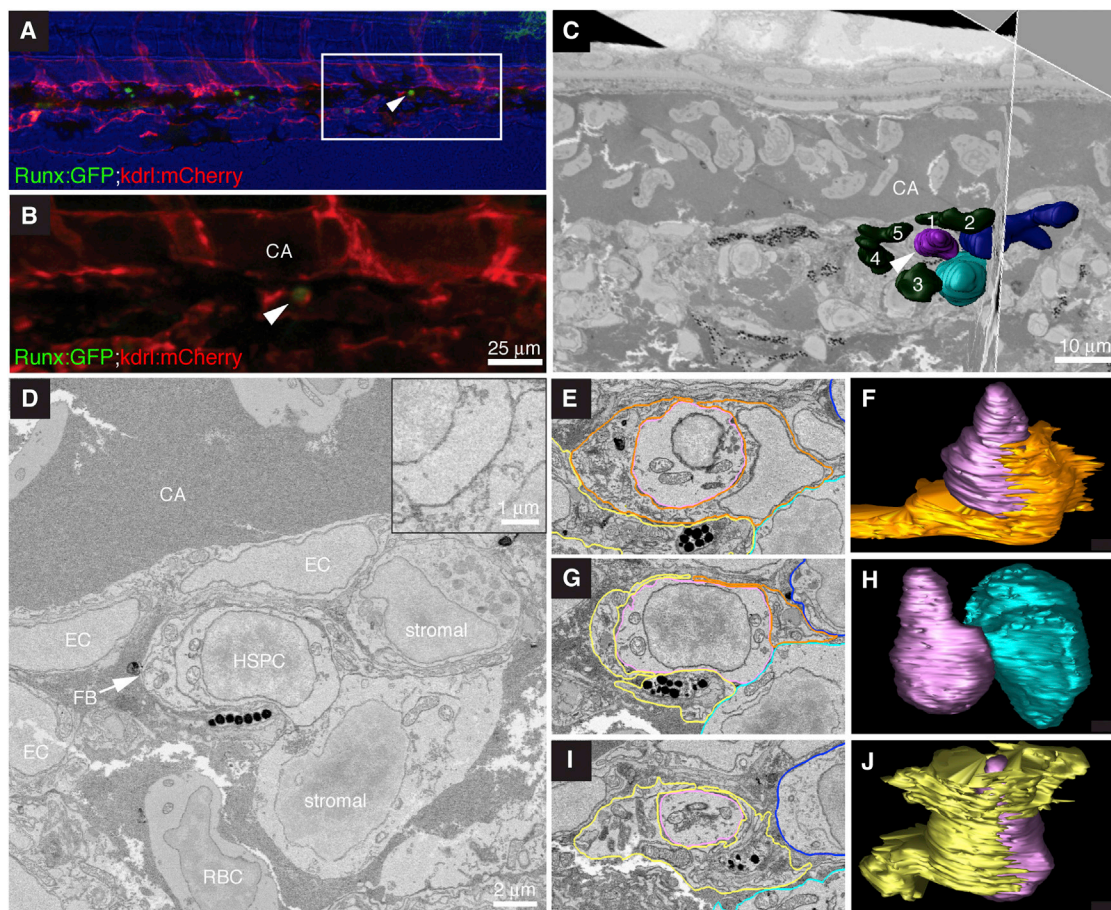


Figure 6. High-Resolution Electron Microscopy of Endogenous HSPC in the Perivascular Niche

(A) Last frame of CHT time lapse (60 hpf). Arrowhead marks HSPC lodged >6 hr. Runx:GFP (green), kdrl:mCherry (red), bright field (blue). Anterior left, posterior right, dorsal top, ventral bottom.

(B) Detail of region in (A) marked by box.

(C) Single section and orthogonal slice from serial block face EM scans. Lodged HSPC (purple, arrowhead), surrounding EC nuclei (green, numbered), and stromal cells (dark and light blue).

(D) High-resolution EM of HSPC lodged in perivascular niche ventral to DA. The HSPC is in direct contact with one stromal cell (see higher-magnification inset).

(E–J) Selected sections (left) through niche with cell membrane traces used to build 3D models (right).

(E) In this section, the HSPC (purple) is mostly surrounded by EC (orange). Portions of fibroblastic (yellow) and stromal (light and dark blue) cells are visible.

(F) About half of the HSPC surface is wrapped by EC.

(G) The HSPC directly contacts the stromal cell. Portions of the fibroblastic cell, EC, and second stromal cell are visible.

(H) Only the midsection of the HSPC contacts the stromal cell.

(I) The fibroblastic cell surrounds the HSPC. Portions of two stromal cells are visible.

(J) Most of the HSPC surface is wrapped by the fibroblastic cell.

Scale bars, (B) 25 μ m; (C) 10 μ m; (D) 2 μ m; and inset, 1 μ m. See also [Figure S5](#) and [Movie S7](#).

unpublished data). We tested the CXCR4 antagonist, AMD3100, as a potential inhibitor of CHT colonization because *cxcr4a/b* and *cxcl12a/b* genes are expressed in the CHT ([Figure S6K](#)), as is the *cxcl12a* transgenic reporter ([Figure 5](#)). After treating embryos with a range of AMD3100 doses, we observed dose-dependent reduction of HSPC markers in the CHT ([Figure S6F](#)). Following these results, we screened ~2,400 known bioactive compounds and identified 40 individual compounds that increased and 107 that decreased CHT hematopoiesis.

We tested a subset of our chemical screen hits by adding individual compounds to the media of Runx:GFP;kdrl:mCherry em-

bryos during time-lapse imaging to directly observe the behavior of HSPCs as they colonize the CHT. Validation of our approach came from one of our positive hits for increased CHT hematopoiesis, SB-431542 ([Figures S6D](#) and [S6G–S6J](#)), a selective inhibitor of transforming growth factor (TGF)- β type I receptors, and, most potently, ALK5/TGFBR1 ([Inman et al., 2002](#)). When added during time-lapse imaging, a small number of newly arrived HSPCs in the CHT would undergo a greater number of divisions ([Figures S6H–S6J](#)), which was never observed in control-treated embryos. We measured these differences by performing lineage tree analysis of HSPCs during parallel time-lapse movies

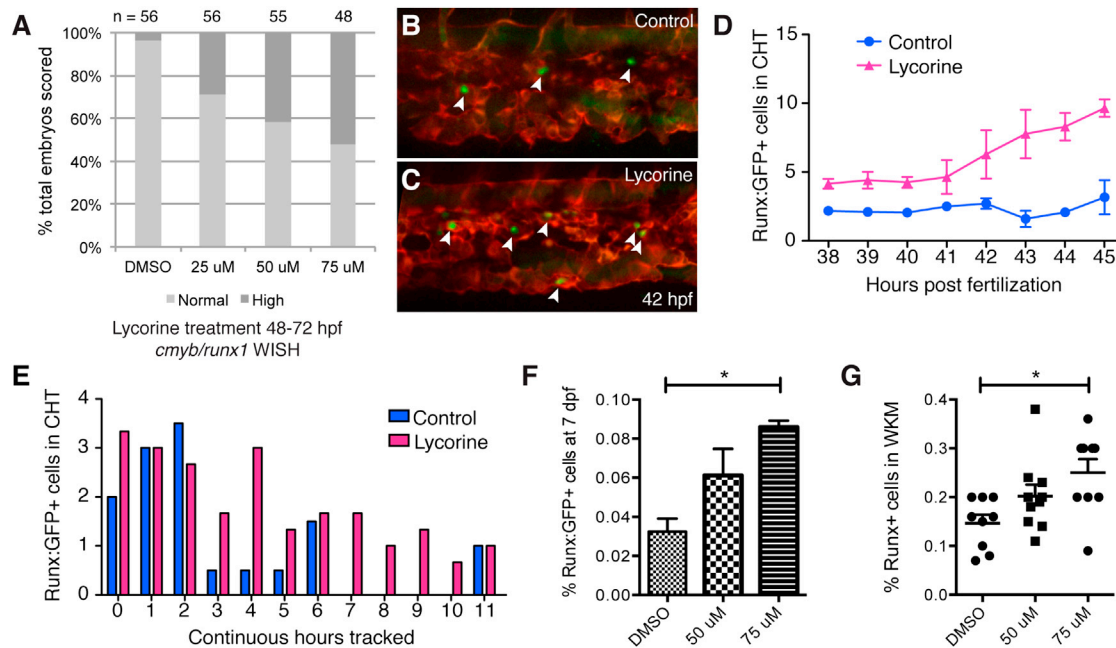


Figure 7. Modulating HSPC Niche Colonization with Lycorine Has Long-Term Effects on the Stem Cell Pool

(A) Lycorine treatment dose-dependently increases the percentage of embryos with high *cmyb/runx1* expression levels, as shown in Figure S6E (linear regression of Y [response] on X [dose] is significant: $r^2 = 0.146607$, $p = 6.46 \times 10^{-9}$). (B and C) Stage-matched frames from parallel time-lapse movies show more HSPCs (arrowheads) with (C) 25 μ M lycorine treatment than (B) DMSO-treated controls (42 hpf, Runx:GFP;kdrl:RFP). (D) HSPCs counted in each frame and then averaged each hour. Five movies imaged in parallel: $n = 2$ controls and $n = 3$ lycorine treated. (E) HSPCs in the same embryos were scored for continuous hours tracked in CHT. Longer median time HSPCs spent in CHT of lycorine-treated embryos was significant (1.67 hr; Wilcoxon signed-rank test, $p = 0.01$; HSPC counts normalized because treatment group was $n = 3$ and control group was $n = 2$). (F and G) Pools of Runx:GFP+ embryos treated with lycorine from 2–3 dpf and washed off had significantly increased HSPC at (F) 7 dpf (DMSO versus 75 μ M, $p = 0.0004$; flow cytometry analysis of four independent pools per dose) and (G) 4 months (DMSO versus 75 μ M, $p = 0.006$). Error bars show mean \pm SEM. See also Figure S6.

(i.e., control and treated stage-matched embryos imaged side by side). HSPCs in control-treated embryos would undergo 0–1 divisions, whereas rare HSPCs in SB-431542-treated embryos would divide 2–3 times. These data illustrate that inhibition of TGF- β receptor signaling using the chemical SB-431542 expands HSPC populations by increasing cell divisions. This is consistent with previously published in vitro and in vivo data that showed TGF- β signal negatively regulates HSPC proliferation (Soma et al., 1996; Yamazaki et al., 2011). Directly visualizing the effect of SB-431542 on HSPCs has demonstrated that we can rapidly identify cellular response to a specific signal in the endogenous niche.

HSPC-Niche Interactions in the Embryo Have a Long-Term Effect on the Stem Cell Pool

A second compound we identified in our screen was lycorine, a natural alkaloid extracted from the Amaryllidaceae plant family that dose-dependently increased *cmyb* and *runx1* in the CHT (Figures 7A and S6E). This drug does not have a defined target or mechanism of action but is a candidate anti-inflammatory and anti-cancer drug (Kang et al., 2012; Lamoral-Theys et al., 2009). Running parallel time-lapse movies, we observed more HSPCs lodged in the CHT in lycorine-treated embryos compared to controls (Figures 7B and 7C). Over time, lycorine

treatment dramatically increased HSPC number in the CHT (Figure 7D). We also scored the total amount of time each HSPC was resident in the CHT during the time lapse and found that lycorine treatment produced a significant shift toward longer durations spent in the niche (Figure 7E).

To better understand the molecular changes that occur during lycorine treatment and how this positively regulates HSPC-niche interactions in the embryo, we treated Runx:GFP;kdrl:RFP embryos from 2–3 dpf and then sorted Runx+ HSPCs and kdrl+ ECs for whole-genome microarray analysis (GEO accession number GSE56015). Lycorine treatment induces significant gene expression changes that suggest altered adhesive properties of ECs and a changed activation state of HSPCs (Table S1A). These changes are possibly related to inflammatory pathways (e.g., TNF, IL1B, and INFG) that could alter the interaction between ECs and HSPCs within the CHT niche (Table S1B).

Lastly, we wanted to determine whether there was long-term functional significance for these changes in embryonic HSPC-niche interactions. Pools of Runx:GFP+ embryos were treated with lycorine from 2–3 dpf then washed off and examined at later time points. Strikingly, transient lycorine treatment during CHT colonization had a sustained effect on the total number of HSPCs. At 7 dpf, after colonization and early expansion in the kidney, lycorine-treated embryos had a significantly higher

number of Runx:GFP+ HSPCs (Figure 7F). We then followed treated embryos into adulthood. After 4 months, analysis of whole-kidney marrow (WKM) showed a significant increase in the percentage of Runx:GFP+ HSPCs (Figure 7G). Using a chemical genetic screening approach, we found a single compound, lycorine, that increased HSPC lodgement during development and ultimately led to a sustained increase in the size of the stem cell pool into adulthood.

DISCUSSION

The ability to follow endogenous HSPCs in the live zebrafish embryo has allowed us to directly observe cellular behaviors during lodgement in the perivascular niche. Current technology has not visualized similar events in the mammalian bone marrow. We watched as HSPCs attached to the endothelial wall of a vessel, underwent extravasation, migrated into the abluminal space, and then triggered a striking endothelial remodeling event (Figure S3D). Live imaging of mouse FL explants revealed comparable interactions between hematopoietic cells and sinusoidal ECs, suggesting that these steps toward HSPC lodgement are conserved (Figure S4D). Correlative light and electron microscopy allowed us to identify a single lodged HSPC in the perivascular niche that we could then resolve at very high resolution. This confirmed our initial observations made by confocal microscopy and also revealed new detailed cellular interactions. Perivascular niche cells can contact a single stem cell by wrapping, firm attachment, and extension of projections. Other niche cells stay close to the stem cell but keep their distance across small extracellular spaces. Together, our data are beginning to reveal the spatial relationships between a stem cell and its niche.

Our finding that HSPC arrival triggers cellular changes in the local perivascular niche raises interesting questions about what constitutes a hematopoietic stem cell niche. Rather than a static number of niches that can be either cleared or filled (Schofield, 1978), our results are suggestive of basic niche components that create a permissive environment for an arriving stem cell. Once attracted to these general locations in the marrow, the stem cell will move out of circulation and lodge in its new surroundings. The rapid remodeling of endothelial cells around a stem cell may provide a mechanism to retain and protect these new arrivals. The formation of a pocket by endothelial cells could effectively increase the concentration of local growth factors and signaling molecules and maintain more productive stem cell interactions of HSPCs with stromal cells. We observed that the division plane of HSPCs is often oriented relative to attached stromal cells. Future studies should investigate the potential for plasticity in terms of location and the number of sites where stem cells can reside. Our study focused on the hematopoietic microenvironment in the zebrafish CHT and mouse FL. These are intermediate niches required to rapidly expand the stem cell pool. With continual advancements in imaging technology, we hope to soon be able to resolve similar cellular dynamics in the adult marrow.

EXPERIMENTAL PROCEDURES

All animals were handled according to approved Institutional Animal Care and Use Committee (IACUC) of Boston Children's Hospital protocols.

Transgenic Zebrafish Lines

To generate the Runx transgenic lines, the Runx1 +23 enhancer (Nottingham et al., 2007) and mouse β -globin minimal promoter were PCR amplified from C57/BL6 mouse genomic DNA. MultiSite Gateway Cloning (Invitrogen) was used to assemble constructs for injection into embryos using Tol2 transgenesis. See also the [Extended Experimental Procedures](#).

Imaging

Transgenic zebrafish lines were crossed, and staged embryos were selected by fluorescence microscopy. Zebrafish embryos were mounted for live imaging in glass bottom dishes or multiwell plates with 1% LMP agarose and covered with E3 media and tricaine as described (Bertrand et al., 2010). Zebrafish embryos were imaged in an incubated chamber at 28.5°C. Mouse embryos were dissected and staged at E11–E11.5 by counting >42 somite pairs. FL explants were imaged at 37°C with humidified CO₂ and in culture media as previously described (Boisset et al., 2010). Live confocal microscopy was performed using a Yokogawa spinning disk and Nikon inverted Ti microscope. Multiple embryos were imaged within a 1–5 min interval using a moving XY stage, as well as acquisition of z stacks through the entire CHT in multiple fluorescent channels. Fixed transgenic zebrafish embryos were scanned using a Nikon C2si confocal NiE upright microscope. Fixed mouse FLs were scanned using a Zeiss LSM 710 confocal microscope. See also the [Extended Experimental Procedures](#).

Image Analysis

Image processing and rendering was done using Fluorender, Imaris (Bitplane), NIS-elements (Nikon), Volocity (PerkinElmer), and ImageJ/Fiji. See also the [Extended Experimental Procedures](#).

Adult-to-Adult HSPC Transplantation

WKM from 3 month Runx:mCherry;ubi:GFP fish was isolated and sorted by fluorescence-activated cell sorting (FACS). Double-positive cells were transplanted into irradiated casper recipients (n = 20–48 recipients per cell dose), along with untreated helper marrow at the following ratios: 1:20,000; 5:20,000; 10:20,000; 25:20,000; and 50:20,000. At 3 months posttransplant, WKM from recipient fish was collected and analyzed by flow cytometry to detect chimerism levels of mCherry and GFP-positive cells in the marrow. We confirmed multilineage reconstitution by observing differentiated GFP-positive cells in multiple cell populations, as determined by forward and side scatter profiles (Traver et al., 2003). Stem cell frequency was determined using ELDA software (confidence interval = 0.95; [Hu and Smyth, 2009]).

Embryo-to-Embryo HSPC Transplantation

Double-positive transgenic embryos were finely chopped and dissociated using Liberase (Roche). Cell suspensions were filtered, and mCherry+/GFP+ cells were collected using a FACS Aria cell sorter (BD Biosciences). Collected cells were resuspended in PBS at an estimated concentration of 400 cells/microliter and 1, 2, or 4 nanoliters were injected directly into the circulation of wild-type 2 dpf embryos. Based on these dilutions, the estimated cell numbers were 0.4, 0.8, and 1.6, respectively. Approximately 30 embryos were injected per dose, and 12–26 embryos per group survived to adulthood (3–5 months). WKM was analyzed for percentage of engrafted Runx+ cells using a LSR II flow cytometer (BD Biosciences). Any recipients with positive cells detected above background (> 0.001% of WKM) were scored as engrafted. Flow cytometry data were analyzed using FACS Diva and FlowJo software. See also the [Extended Experimental Procedures](#).

Serial Block Face Scanning Electron Microscopy and 3D Reconstructions

Immediately at the end of live imaging time-lapse acquisition, 60 hpf embryos were fixed in 2.5% glutaraldehyde and 4% paraformaldehyde in a 0.1 M sodium cacodylate buffer. Samples were submitted to Renovo Neural Inc. (Cleveland, USA) for further processing and serial block face scanning electron microscopy. Images were imported into the program IMOD 4.5 then aligned and reconstructed using dual-axis tomography. Cells were manually outlined and 3D reconstructions were generated. See also the [Extended Experimental Procedures](#).

Chemical Screening

Embryos were treated from 48–72 hpf with individual library chemicals (~2,400 bioactives) by placement directly in 96-well receiver plates containing small molecules diluted in E3/1% DMSO (average final concentration of library compounds was ~30 μ M). After treatment and before fixation, we checked for secondary defects (e.g., no circulation, toxicity, or developmental delay). We performed whole-mount in situ hybridization with HSPC markers *cmyb* and *runx1* and scored for expression levels in the CHT. See also the [Extended Experimental Procedures](#).

Microarrays

Runx:GFP;kdrl:RFP embryos were treated from 48–72 hpf with E3/1% DMSO or E3/1%DMSO/75 μ M Lycorine (~100–150 embryos per group). Embryos were dissociated and sorted as above. Three populations were collected: GFP+ HSPC (~1,000–2,000 cells/experiment), RFP+ EC (~10,000–20,000/experiment), and negative cells (~100,000 cells/experiment; total embryo as a comparator population). In total, 18 samples were collected: 3 biological replicates \times 2 treatment conditions \times 3 cell populations. Cells were sorted directly in Trizol LS. Total RNA was amplified and hybridized to Affymetrix Zebrafish GeneChip ZebGene-1_0-st microarrays. See also the [Extended Experimental Procedures](#).

ACCESSION NUMBERS

The GEO accession number for the microarray data reported in this paper is GSE56015.

SUPPLEMENTAL INFORMATION

Supplemental Information includes Extended Experimental Procedures, six figures, one table, and seven movies and can be found with this article online at <http://dx.doi.org/10.1016/j.cell.2014.12.032>.

AUTHOR CONTRIBUTIONS

O.J.T. designed and performed transgenic, imaging, and chemical screening experiments. E.M.D. designed and performed transplantation and flow cytometry experiments. O.J.T. wrote the manuscript. L.A.C., E.J.H., and P.L. performed experiments. S.J.C. performed analysis and reconstruction of EM data. A.D.Y. and N.A.S. designed and performed fetal liver experiments. L.I.Z. designed experiments, edited the manuscript, and supervised the project.

ACKNOWLEDGMENTS

We thank the following for their support and contributions: L. Cameron for confocal imaging (Dana Farber Cancer Institute); T. Schlaeger, S. Datta, and P.D. Manos for chemical screening (Boston Children's Hospital [BCH]); R. Mathieu for flow cytometry (BCH); L. Bu and A. Hill for confocal imaging (BCH); H.A. Feldman and W. London for statistical analysis (BCH); T.P. Ward and Y. Zhou for computer support (BCH); J. Hutchinson, O.M. Hofmann, and W.A. Hide for microarray analysis (Harvard School of Public Health); M. Ericsson and E.J. Benecchi for conventional electron microscopy (Harvard Medical School); A. Roholt for serial block face scanning EM (Renovo Neural, Cleveland, USA); T. Fuerstenhaupt for guidance in EM tomographic reconstructions (University of Calgary); and T. Bowman for immunohistochemistry (Brigham and Women's Hospital). We thank T.V. Bowman, J.R. Perlin, and C.K. Kaufman for critical reading of this manuscript. This work was supported by HHMI and NIH grants R01 HL04880, 5P30 DK49216, 5R01 DK53298, 5U01 HL10001-05, and R24 DK092760 (to L.I.Z.); R01 HL091724 and U01HL100405 (to N.A.S.); and 1F31HL120615 (to A.D.Y.). O.J.T. was supported by the American Society of Hematology, Canadian Institutes of Health Research (CIHR), and Heart and Stroke Foundation of Canada. S.J.C. was supported by CIHR (MOP-97787) and Alberta Innovates Health Solutions. E.J.H. was supported by a Helen Hay Whitney Foundation Fellowship. L.I.Z. is a founder and stockholder of Fate Therapeutics, Inc. and Scholar Rock and is a scientific advisor for Stemgent.

Received: April 16, 2014

Revised: October 8, 2014

Accepted: December 24, 2014

Published: January 15, 2015

REFERENCES

- Bertrand, J.Y., Chi, N.C., Santoso, B., Teng, S., Stainier, D.Y.R., and Traver, D. (2010). Haematopoietic stem cells derive directly from aortic endothelium during development. *Nature* **464**, 108–111.
- Boisset, J.-C., van Cappellen, W., Andrieu-Soler, C., Galjart, N., Dzierzak, E., and Robin, C. (2010). In vivo imaging of haematopoietic cells emerging from the mouse aortic endothelium. *Nature* **464**, 116–120.
- Butler, J.M., Nolan, D.J., Vertes, E.L., Varnum-Finney, B., Kobayashi, H., Hooper, A.T., Seandel, M., Shido, K., White, I.A., Kobayashi, M., et al. (2010). Endothelial cells are essential for the self-renewal and repopulation of Notch-dependent hematopoietic stem cells. *Cell Stem Cell* **6**, 251–264.
- de Jong, J.L.O., Burns, C.E., Chen, A.T., Pugach, E., Mayhall, E.A., Smith, A.C.H., Feldman, H.A., Zhou, Y., and Zon, L.I. (2011). Characterization of immune-matched hematopoietic transplantation in zebrafish. *Blood* **117**, 4234–4242.
- Ding, L., and Morrison, S.J. (2013). Haematopoietic stem cells and early lymphoid progenitors occupy distinct bone marrow niches. *Nature* **495**, 231–235.
- Ding, L., Saunders, T.L., Enikolopov, G., and Morrison, S.J. (2012). Endothelial and perivascular cells maintain haematopoietic stem cells. *Nature* **481**, 457–462.
- Fleischman, R.A., and Mintz, B. (1979). Prevention of genetic anemias in mice by microinjection of normal hematopoietic stem cells into the fetal placenta. *Proc. Natl. Acad. Sci. USA* **76**, 5736–5740.
- Glass, T.J., Lund, T.C., Patrinostr, X., Tolar, J., Bowman, T.V., Zon, L.I., and Blazar, B.R. (2011). Stromal cell-derived factor-1 and hematopoietic cell homing in an adult zebrafish model of hematopoietic cell transplantation. *Blood* **118**, 766–774.
- Greenbaum, A., Hsu, Y.-M.S., Day, R.B., Schuettelpelz, L.G., Christopher, M.J., Borgerding, J.N., Nagasawa, T., and Link, D.C. (2013). CXCL12 in early mesenchymal progenitors is required for haematopoietic stem-cell maintenance. *Nature* **495**, 227–230.
- Hooper, A.T., Butler, J.M., Nolan, D.J., Kranz, A., Iida, K., Kobayashi, M., Kopp, H.-G., Shido, K., Petit, I., Yanger, K., et al. (2009). Engraftment and reconstitution of hematopoiesis is dependent on VEGFR2-mediated regeneration of sinusoidal endothelial cells. *Cell Stem Cell* **4**, 263–274.
- Hu, Y., and Smyth, G.K. (2009). ELDA: extreme limiting dilution analysis for comparing depleted and enriched populations in stem cell and other assays. *J. Immunol. Methods* **347**, 70–78.
- Inman, G.J., Nicolás, F.J., Callahan, J.F., Harling, J.D., Gaster, L.M., Reith, A.D., Laping, N.J., and Hill, C.S. (2002). SB-431542 is a potent and specific inhibitor of transforming growth factor-beta superfamily type I activin receptor-like kinase (ALK) receptors ALK4, ALK5, and ALK7. *Mol. Pharmacol.* **62**, 65–74.
- Isern, J., García-García, A., Martín, A.M., Arranz, L., Martín-Pérez, D., Torroja, C., Sánchez-Cabo, F., and Méndez-Ferrer, S. (2014). The neural crest is a source of mesenchymal stem cells with specialized hematopoietic stem cell niche function. *eLife* **3**, e03696.
- Kang, J., Zhang, Y., Cao, X., Fan, J., Li, G., Wang, Q., Diao, Y., Zhao, Z., Luo, L., and Yin, Z. (2012). Lycorine inhibits lipopolysaccharide-induced iNOS and COX-2 up-regulation in RAW264.7 cells through suppressing P38 and STATs activation and increases the survival rate of mice after LPS challenge. *Int. Immunopharmacol.* **12**, 249–256.
- Kiel, M.J., Yilmaz, O.H., Iwashita, T., Yilmaz, O.H., Terhorst, C., and Morrison, S.J. (2005). SLAM family receptors distinguish hematopoietic stem and progenitor cells and reveal endothelial niches for stem cells. *Cell* **121**, 1109–1121.
- Kissa, K., and Herbomel, P. (2010). Blood stem cells emerge from aortic endothelium by a novel type of cell transition. *Nature* **464**, 112–115.

- Kissa, K., Murayama, E., Zapata, A., Cortés, A., Perret, E., Machu, C., and Herbomel, P. (2008). Live imaging of emerging hematopoietic stem cells and early thymus colonization. *Blood* 111, 1147–1156.
- Köhler, A., Schmithorst, V., Filippi, M.-D., Ryan, M.A., Daria, D., Gunzer, M., and Geiger, H. (2009). Altered cellular dynamics and endosteal location of aged early hematopoietic progenitor cells revealed by time-lapse intravital imaging in long bones. *Blood* 114, 290–298.
- Lamoral-Theys, D., Andolfi, A., Van Goietsenoven, G., Cimmino, A., Le Calvé, B., Wauthoz, N., Mégalliz, V., Gras, T., Bruyère, C., Dubois, J., et al. (2009). Lycorine, the main phenanthridine Amaryllidaceae alkaloid, exhibits significant antitumor activity in cancer cells that display resistance to proapoptotic stimuli: an investigation of structure-activity relationship and mechanistic insight. *J. Med. Chem.* 52, 6244–6256.
- Lin, H.-F., Traver, D., Zhu, H., Dooley, K., Paw, B.H., Zon, L.I., and Handin, R.I. (2005). Analysis of thrombocyte development in CD41-GFP transgenic zebrafish. *Blood* 106, 3803–3810.
- Lo Celso, C., Fleming, H.E., Wu, J.W., Zhao, C.X., Miake-Lye, S., Fujisaki, J., Côté, D., Rowe, D.W., Lin, C.P., and Scadden, D.T. (2009). Live-animal tracking of individual haematopoietic stem/progenitor cells in their niche. *Nature* 457, 92–96.
- Ma, X., Robin, C., Ottersbach, K., and Dzierzak, E. (2002). The Ly-6A (Sca-1) GFP transgene is expressed in all adult mouse hematopoietic stem cells. *Stem Cells* 20, 514–521.
- Medvinsky, A., and Dzierzak, E. (1996). Definitive hematopoiesis is autonomously initiated by the AGM region. *Cell* 86, 897–906.
- Méndez-Ferrer, S., Michurina, T.V., Ferraro, F., Mazloom, A.R., Macarthur, B.D., Lira, S.A., Scadden, D.T., Ma'ayan, A., Enikolopov, G.N., and Frenette, P.S. (2010). Mesenchymal and haematopoietic stem cells form a unique bone marrow niche. *Nature* 466, 829–834.
- Mironov, A.A., and Beznoussenko, G.V. (2009). Correlative microscopy: a potent tool for the study of rare or unique cellular and tissue events. *J. Microsc.* 235, 308–321.
- Morrison, S.J., and Scadden, D.T. (2014). The bone marrow niche for haematopoietic stem cells. *Nature* 505, 327–334.
- Morrison, S.J., Hemmati, H.D., Wandycz, A.M., and Weissman, I.L. (1995). The purification and characterization of fetal liver hematopoietic stem cells. *Proc. Natl. Acad. Sci. USA* 92, 10302–10306.
- Mosimann, C., Kaufman, C.K., Li, P., Pugach, E.K., Tamplin, O.J., and Zon, L.I. (2011). Ubiquitous transgene expression and Cre-based recombination driven by the ubiquitin promoter in zebrafish. *Development* 138, 169–177.
- Müller, A.M., Medvinsky, A., Strouboulis, J., Grosveld, F., and Dzierzak, E. (1994). Development of hematopoietic stem cell activity in the mouse embryo. *Immunity* 1, 291–301.
- Murayama, E., Kissa, K., Zapata, A., Mordelet, E., Briolat, V., Lin, H.-F., Handin, R.I., and Herbomel, P. (2006). Tracing hematopoietic precursor migration to successive hematopoietic organs during zebrafish development. *Immunity* 25, 963–975.
- Nombela-Arrieta, C., Pivarnik, G., Winkel, B., Canty, K.J., Harley, B., Mahoney, J.E., Park, S.Y., Lu, J., Protopopov, A., and Silberstein, L.E. (2013). Quantitative imaging of haematopoietic stem and progenitor cell localization and hypoxic status in the bone marrow microenvironment. *Nat. Cell Biol.* 15, 533–543.
- North, T.E., Goessling, W., Walkley, C.R., Lengerke, C., Kopani, K.R., Lord, A.M., Weber, G.J., Bowman, T.V., Jang, I.-H., Grosser, T., et al. (2007). Prostaglandin E2 regulates vertebrate hematopoietic stem cell homeostasis. *Nature* 447, 1007–1011.
- Nottingham, W.T., Jarratt, A., Burgess, M., Speck, C.L., Cheng, J.-F., Prabhakar, S., Rubin, E.M., Li, P.-S., Sloane-Stanley, J., Kong-A-San, J., and de Bruijn, M.F. (2007). Runx1-mediated hematopoietic stem-cell emergence is controlled by a Gata/Ets/SCL-regulated enhancer. *Blood* 110, 4188–4197.
- Orkin, S.H., and Zon, L.I. (2008). Hematopoiesis: an evolving paradigm for stem cell biology. *Cell* 132, 631–644.
- Osawa, M., Nakamura, K., Nishi, N., Takahashi, N., Tokumoto, Y., Inoue, H., and Nakauchi, H. (1996). In vivo self-renewal of c-Kit⁺ Sca-1⁺ Lin^(low/-) hematopoietic stem cells. *J. Immunol.* 156, 3207–3214.
- Sánchez, M.J., Holmes, A., Miles, C., and Dzierzak, E. (1996). Characterization of the first definitive hematopoietic stem cells in the AGM and liver of the mouse embryo. *Immunity* 5, 513–525.
- Schofield, R. (1978). The relationship between the spleen colony-forming cell and the haematopoietic stem cell. *Blood Cells* 4, 7–25.
- Soma, T., Yu, J.M., and Dunbar, C.E. (1996). Maintenance of murine long-term repopulating stem cells in ex vivo culture is affected by modulation of transforming growth factor-beta but not macrophage inflammatory protein-1 alpha activities. *Blood* 87, 4561–4567.
- Sugiyama, T., Kohara, H., Noda, M., and Nagasawa, T. (2006). Maintenance of the hematopoietic stem cell pool by CXCL12-CXCR4 chemokine signaling in bone marrow stromal cell niches. *Immunity* 25, 977–988.
- Traver, D., Paw, B.H., Poss, K.D., Penberthy, W.T., Lin, S., and Zon, L.I. (2003). Transplantation and in vivo imaging of multilineage engraftment in zebrafish bloodless mutants. *Nat. Immunol.* 4, 1238–1246.
- Xie, Y., Yin, T., Wiegand, W., He, X.C., Miller, D., Stark, D., Perko, K., Alexander, R., Schwartz, J., Grindley, J.C., et al. (2009). Detection of functional haematopoietic stem cell niche using real-time imaging. *Nature* 457, 97–101.
- Yamazaki, S., Ema, H., Karlsson, G., Yamaguchi, T., Miyoshi, H., Shioda, S., Taketo, M.M., Karlsson, S., Iwama, A., and Nakauchi, H. (2011). Nonmyelinating Schwann cells maintain hematopoietic stem cell hibernation in the bone marrow niche. *Cell* 147, 1146–1158.

SOX17 Is a Critical Specifier of Human Primordial Germ Cell Fate

Naoko Irie,^{1,2,3,5} Leehee Weinberger,^{4,5} Walfred W.C. Tang,^{1,2,3,5} Toshihiro Kobayashi,^{1,2,3} Sergey Viukov,⁴ Yair S. Manor,⁴ Sabine Dietmann,³ Jacob H. Hanna,^{4,6,*} and M. Azim Surani^{1,2,3,6,*}

¹Wellcome Trust Cancer Research UK Gurdon Institute, Tennis Court Road, University of Cambridge, Cambridge CB2 1QN, UK

²Department of Physiology, Development and Neuroscience, Downing Street, University of Cambridge, Cambridge CB2 3EG, UK

³Wellcome Trust-Medical Research Council Stem Cell Institute, Tennis Court Road, University of Cambridge, Cambridge CB2 3EG, UK

⁴The Department of Molecular Genetics, Weizmann Institute of Science, Rehovot 76100, Israel

⁵Co-first author

⁶Co-senior author

*Correspondence: jacob.hanna@weizmann.ac.il (J.H.H.), a.surani@gurdon.cam.ac.uk (M.A.S.)

<http://dx.doi.org/10.1016/j.cell.2014.12.013>

This is an open access article under the CC BY license (<http://creativecommons.org/licenses/by/3.0/>).

SUMMARY

Specification of primordial germ cells (PGCs) marks the beginning of the totipotent state. However, without a tractable experimental model, the mechanism of human PGC (hPGC) specification remains unclear. Here, we demonstrate specification of hPGC-like cells (hPGCLCs) from germline competent pluripotent stem cells. The characteristics of hPGCLCs are consistent with the embryonic hPGCs and a germline seminoma that share a CD38 cell-surface marker, which collectively defines likely progression of the early human germline. Remarkably, SOX17 is the key regulator of hPGC-like fate, whereas BLIMP1 represses endodermal and other somatic genes during specification of hPGCLCs. Notable mechanistic differences between mouse and human PGC specification could be attributed to their divergent embryonic development and pluripotent states, which might affect other early cell-fate decisions. We have established a foundation for future studies on resetting of the epigenome in hPGCLCs and hPGCs for totipotency and the transmission of genetic and epigenetic information.

INTRODUCTION

Primordial germ cells (PGCs) are the precursors of sperm and eggs, which generate the totipotent state. The genetic basis of mammalian PGC specification was first established in mice (Saitou et al., 2002; Ohinata et al., 2005; Hayashi et al., 2007), which are specified from postimplantation epiblast cells on embryonic day (E)6.25 in response to bone morphogenetic protein 4 (BMP4) (Lawson et al., 1999). Subsequently, ~35 founder PGCs are detected at E7.25. Similar studies on human PGCs (hPGCs) would require E9–E16 embryos, which is not practicable. However, embryonic hPGCs at approximately week 5 to 10 of development, which correspond to mouse PGCs at E10.5–E13.5, can in principle be examined (Leitch et al., 2013). These cells retain charac-

teristic of PGCs while they undergo resetting of the epigenome and global DNA demethylation (Hackett et al., 2012).

In mice, BMP4 induces expression of BLIMP1 (encoded by *Prdm1*) and PRDM14 in the postimplantation epiblast at E6.25; together with AP2 γ (encoded by *Tfap2c*), a direct target of BLIMP1, they induce PGC fate (Magnúsdóttir et al., 2013; Nakaki et al., 2013). The tripartite genetic network acts combinatorially to repress somatic genes, induce expression of PGC genes, such as *Nanos3*, reinduce pluripotency genes, and initiate the epigenetic program (Hackett et al., 2013; Magnúsdóttir and Surani, 2014). PGC-like cells (PGCLCs) can also be induced in vitro from naive pluripotent mouse embryonic stem cells (mESCs) after they acquire competence for germ cell fate after ~48 hr culture in basic fibroblast growth factor (bFGF) and Activin A (Hayashi et al., 2011). These competent cells acquire PGC-like fate in response to either BMP4 signal or directly to *Blimp1*, *Prdm14*, and *Tfap2c*, which is similar to PGCs in vivo (Magnúsdóttir et al., 2013; Nakaki et al., 2013).

Human PGCLCs (hPGCLCs) have been generated at a low frequency by spontaneous differentiation of human ESCs (hESC) in vitro (Gkoutela et al., 2013; Kee et al., 2009), but systematic studies to characterize and identify the key regulators of hPGCs remain to be elucidated. Because there are evident differences between the regulation of mouse and human pluripotent ESCs (Hackett and Surani, 2014; Nichols and Smith, 2009) and during their early postimplantation development (de Fellici, 2013; De Miguel et al., 2010; Irie et al., 2014), this might affect the mechanism and the role of the key regulators of hPGCLC specification (Imamura et al., 2014; Pera, 2013). Once the mechanism of hPGCLC specification is established, it could provide insights on the progression of the early human germline with reference to embryonic hPGCs and seminomas that originate from human germ cells in vivo and retain key characteristics of the lineage (Looijenga et al., 2014).

We have developed a robust approach for hPGCLC specification from germ cell competent hESCs/hiPSCs (Gafni et al., 2013). We show that SOX17, a critical transcription factor for endoderm lineages, is the earliest marker of hPGCLCs and is in fact the key regulator of hPGCLC fate, which is not the case in mice (Hara et al., 2009; Kanai-Azuma et al., 2002). BLIMP1 is downstream of SOX17, and it represses endodermal and other somatic genes

during hPGCLC specification. Comparisons among hPGCLCs, embryonic hPGCs, and a seminoma indicate likely progression of the early human germline. These cells also exhibit CD38 cell surface marker, which is shared by cells with germ cell characteristics. We anticipate that genome editing approaches with our robust in vitro model for hPGCLC specification, combined with patient-specific human-induced pluripotent stem cells (hiPSCs), will lead to major advances in human germ cell biology, including on the unique germline-specific epigenetic program with potential consequences for subsequent generations.

RESULTS

Generation of hPGCLCs from Embryonic Stem Cells

First, we generated three independent hESC lines (WIS2 and LIS1 male hESC and WIBR3 female hESC line) (Gafni et al., 2013) with a NANOS3-mCherry knockin reporter (Figure S1A available online), a highly conserved PGC-specific gene (Gkoutela et al., 2013; Julaton and Reijo Pera, 2011). These hESCs maintained in bFGF and responded to BMP2/BMP4 with ~0%–5% NANOS3-mCherry positive putative hPGCLCs at day 4 (see Figure 7A). Like hESC, mouse epiblast stem cells (mEpiSC) also respond poorly to specification of PGCLCs (Hayashi and Surani, 2009). In contrast, epiblast-like cells (EpiLCs) derived from naive mESCs have a significant potential for germ cell fate (Hayashi et al., 2011). However, the approach used for mouse ESCs did not confer competence for germline fate on hESCs.

Next, we tested hESC-NANOS3-mCherry cells that were maintained in four-inhibitor-containing medium with LIF, bFGF, and TGF β (adopted and modified from NHSM conditions; see Experimental Procedures), henceforth called “4i” medium, which endows the cells with a distinct pluripotent state (Gafni et al., 2013). These hESCs were then cultured for 2 days in bFGF, TGF β , and 1% KSR medium, and thereafter, 2,000–4,000 cells were cultured in low-attachment well in the presence of BMP2 or BMP4, LIF, stem cell factor (SCF), epidermal growth factor (EGF), and Rho-kinase (ROCK) inhibitor to induce hPGCLCs (Hayashi et al., 2011; Watanabe et al., 2007) (Figure 1A). These cells aggregated to form embryoid bodies (henceforth called embryoids) and responded within 3 days with significant expression of NANOS3-mCherry and tissue-nonspecific alkaline phosphatase (TNAP), a PGC and pluripotency marker in humans and mice (Figure 1B). The intensity of the NANOS3-mCherry reporter increased progressively until day 4–5, resulting in ~27% of NANOS3/TNAP double-positive putative hPGCLCs (Figures 1B and S1B). Similar to mice, hPGCLCs do not proliferate significantly after 5 days under these conditions (Hayashi et al., 2011). The response was highly reproducible in three independent male and female NANOS3-mCherry hESC lines. Both BMP2 and/or BMP4 (with LIF, SCF, and EGF) were effective in inducing hPGCLC (Figure S1C) in a dose-dependent manner in the range of 50–500 ng/ml (Figures S1D and S1E).

The NANOS3/TNAP double-positive putative hPGCLCs also expressed key PGC genes, including *NANOS3*, *BLIMP1*, *TFAP2C*, *STELLA*, *TNAP*, *KIT*, *OCT4*, and *NANOG*, as well as *PRDM14*, albeit with reduced levels compared to hESC (Figure 1C). Remarkably, *SOX17* was significantly upregulated,

whereas *SOX2* was downregulated in the putative hPGCLCs that reflects their expression in embryonic hPGCs and seminomas (de Jong et al., 2008; see Figure 2), which is not the case in mouse PGCs. Immunofluorescence confirmed that NANOS3-mCherry expression coincided with OCT4, NANOG, and TFAP2C in day 4 embryoids (Figures 1D and S1F), as did OCT4 with BLIMP1 (Figure S1F). This suggests that the NANOS3-mCherry-positive cells are very likely nascent germ cells.

RNA-Seq Analysis of hPGCLCs: Comparison with hPGCs and Seminoma

We carried out RNA sequencing (RNA-seq) on NANOS3/TNAP double-positive cells from day 4 embryoids and compared them with the gonadal hPGCs from week 7 male human embryos (Carnegie stage 18/19), which are equivalent to mouse ~E12.5–E13.5 PGCs (Leitch et al., 2013). These hPGCs retain key characteristics of earlier hPGCs but, consistent with their more advanced state, expresses later germ cell markers such as *VASA* and *DAZL*. We also included TCam-2, a human seminoma that originates from the germline in vivo (Looijenga et al., 2014).

Unsupervised hierarchical clustering of global gene expression showed that the hPGCLCs clustered with hPGCs and TCam-2, whereas 4i hESCs and preinduced cells (4i hESCs treated with bFGF and TGF β for 2 days) clustered together in another branch away from gonadal somatic cells (soma) (Figure 2A). Consistently, hPGCs were globally more related to hPGCLCs (Pearson correlation coefficient [r] = 0.85) and TCam-2 (r = 0.818) than to 4i hESCs (r = 0.799) and preinduced cells (r = 0.773) (Figure S2A).

A heat map of mRNA expression revealed that hPGCLCs and gonadal hPGCs shared expression of early PGCs (*BLIMP1*, *TFAP2C*, *DND1*, *NANOS3*, *UTF1*, *ITGB3*, and *KIT*) and pluripotency genes (*TNAP*, *OCT4*, *NANOG*, *PRDM14*, and *LIN28A*) but with a notable lack of *SOX2* expression (Figure 2C). Early mesoderm marker *T* was detected in hPGCLCs (Figure 2C), as in mouse early PGCs (Aramaki et al., 2013). Interestingly, expression of two endodermal genes, *SOX17* and *GATA4*, was detected in hPGCLCs, embryonic hPGCs, and TCam-2, which are absent in the mouse germline. Notably, we identified CD38 expression in hPGCLCs/hPGCs and TCam-2, but not in hESCs or soma (Figures 2C and see also Figures 3A–3C). Overall, hPGCLCs indeed have germ cell characteristics consistent with hPGCs. Late germ cell markers, however, including *DAZL*, *VASA*, and *MAEL*, were only detected in hPGCs (Figure 2C). TCam-2 gene expression was similar to hPGCLCs, albeit with lower expression levels of *NANOS3*, *ITGB3*, and *T* and upregulation of a few somatic genes, e.g., *HAND1* and *RUNX1*. Immunofluorescence analysis validated the expression of BLIMP1, TFAP2C, and OCT4 in hPGCLCs/hPGCs and TCam-2 (Figures 2E–2H). Interestingly, PRDM14 showed nuclear localization in the majority of hPGCLCs but was predominantly enriched in the cytoplasm of hPGCs (Figure 2F). Importantly, although *SOX2* was undetectable, there was significant expression of *SOX17* in hPGCLCs, hPGCs, and TCam-2 (Figures 2G and 2H).

Given the similarities of hPGCLCs, hPGCs, and TCam-2, a three-way Venn diagram was plotted to investigate their relationships (Figure 2D). Out of 972 highly upregulated genes

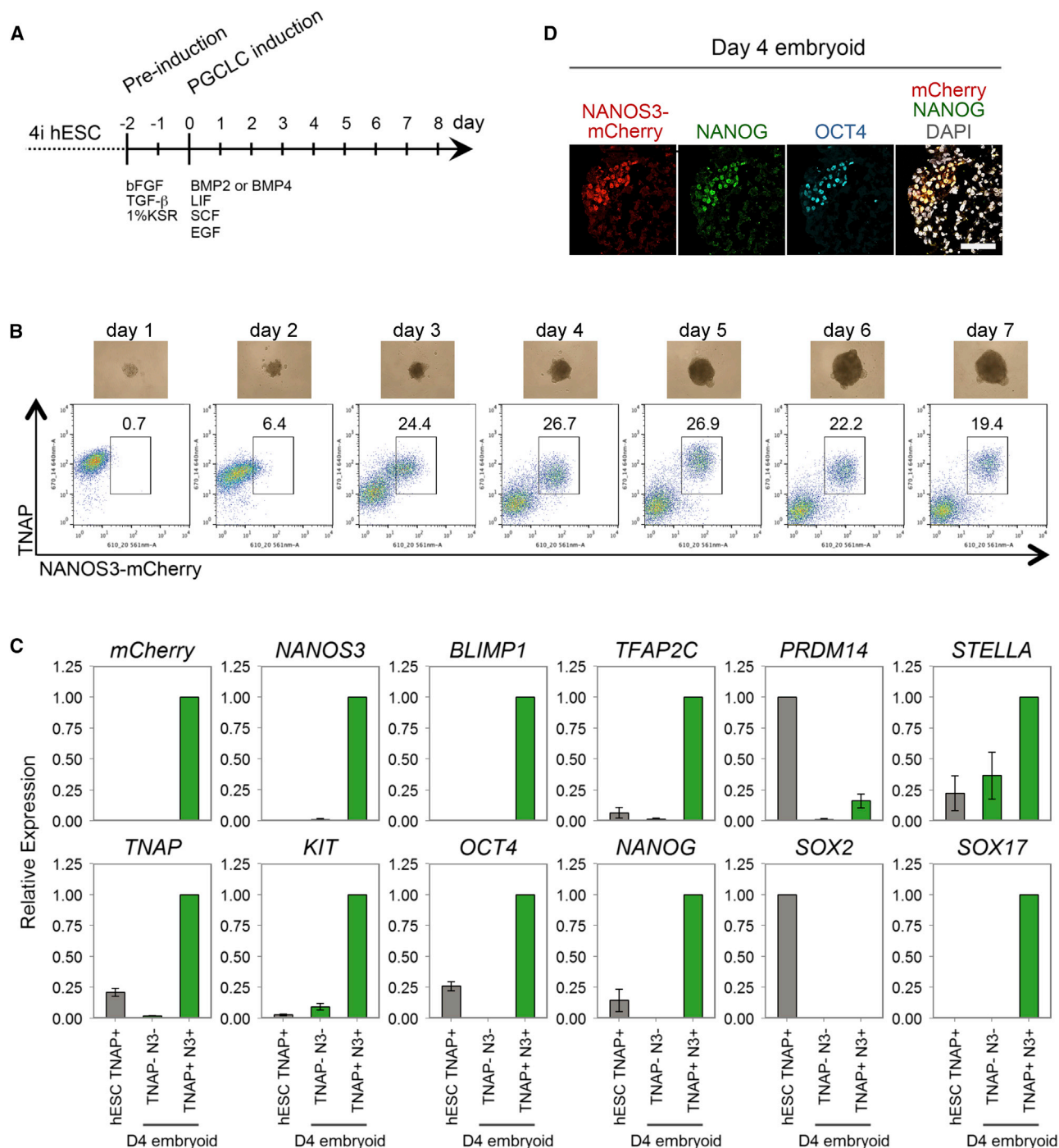


Figure 1. Specification of hPGCLCs from Human Embryonic Stem Cells

(A) Schematic protocol for hPGCLCs specification from hESCs.

(B) Development of day 1–7 embryos derived from WIS2-NANOS3-mCherry hESCs. Top row: images of embryos. Bottom row: FACS analysis of the dissociated embryos with anti-TNAP-Alexa Fluor 647 and NANOS3-mCherry to detect hPGCLCs.

(C) Expression analysis by RT-qPCR of TNAP-positive 4i hESCs (hESC TNAP+), TNAP/NANOS3-mCherry-positive hPGCLCs (TNAP+N3+), and the remaining cells (TNAP-N3-) of day 4 embryos (D4 embryo). Relative expression levels are shown with normalization to β -ACTIN. Error bars indicate mean \pm SD from three independent biological replicates.

(D) Immunofluorescence of a day 4 embryo showing coexpression of NANOS3-mCherry, NANOG, and OCT4 in hPGCLCs. Scale bar, 66 μ m.

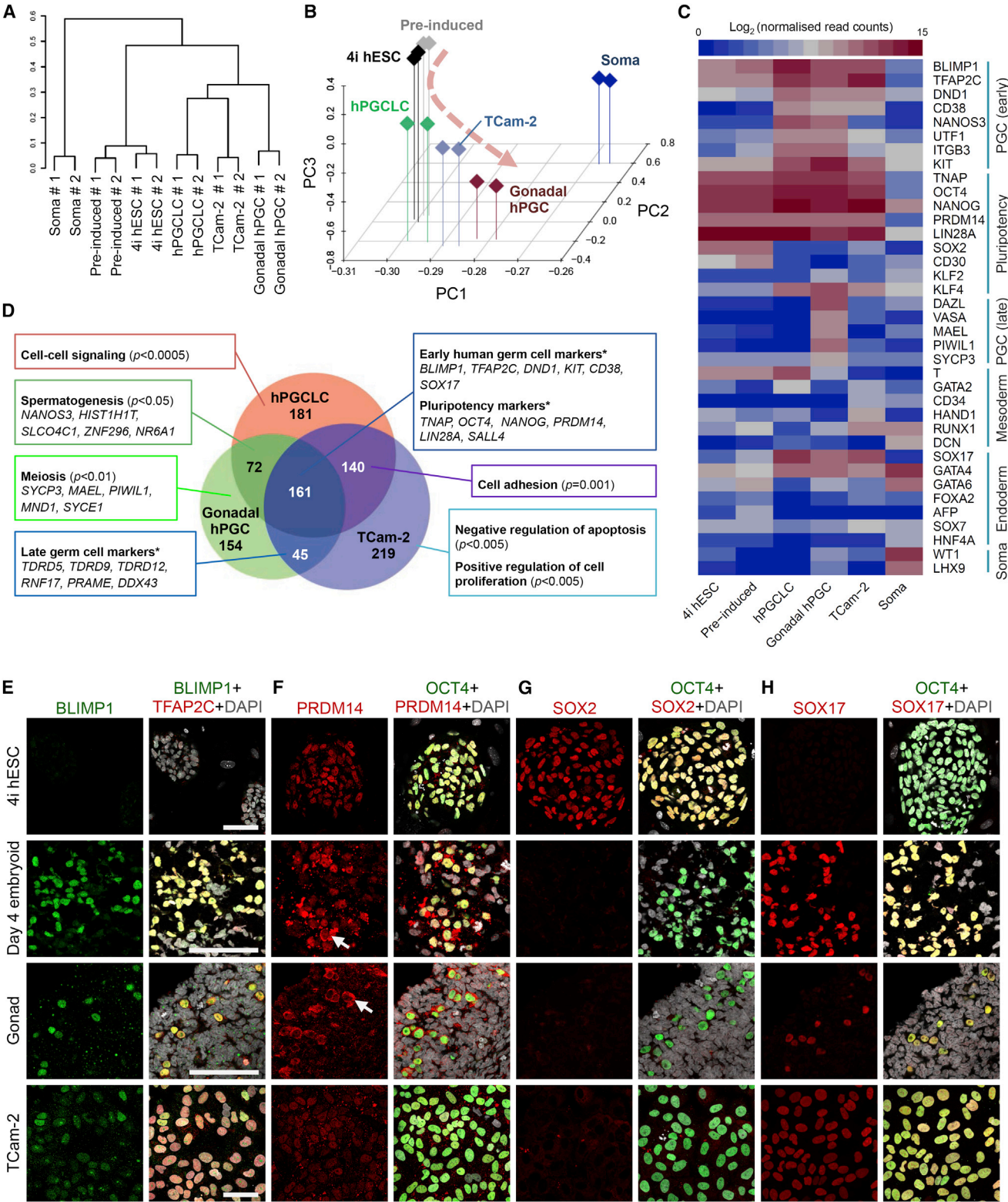


Figure 2. hPGCLC Shares Transcriptional Profile with Human Embryonic PGCs and TCam-2 Seminoma

(A) Unsupervised hierarchical clustering (UHC) of gene expression in 4i hESC, preinduced cells (Pre-induced), day 4 hPGCLCs (hPGCLC), gonadal hPGC, TCam-2, and gonadal somatic cell (Soma). RNA-seq was performed on two biological replicates (#1 and #2) for each cell type.

(B) PCA of RNA-seq data. Arrowline indicates potential germline progression from 4i hESC to hPGCLC and gonadal hPGC.

(legend continued on next page)

compared to soma (Table S1), the three germline-related cell types shared expression of 161 genes, including pluripotency and germline-specific genes: *BLIMP1*, *TFAP2C*, *CD38*, *SOX17*, *OCT4*, and *NANOG* (Figure 2D). Gene ontology (GO biological process) analysis revealed (Table S1) that hPGCLCs from male cell line and male gonadal hPGCs were commonly enriched in “spermatogenesis” genes—for example, *NANOS3* and *HIST1H1T*—whereas meiosis-related *SYCP3*, *MAEL*, and *PIWIL1* genes were upregulated only in embryonic hPGCs (Figures 2C and 2D). Interestingly, TCam-2 and hPGCs revealed expression of a number of late germ cell markers, including Tudor-domain-containing *TDRD5*, *TDRD9*, and *TDRD12* genes, which have been implicated in PIWI-interacting RNA biogenesis pathway (Shoji et al., 2009) (Figure 2D). As expected, TCam-2 showed characteristics associated with cancer cells, including genes that promote cell proliferation with suppression of apoptosis genes (Figure 2D). Altogether, hPGCLCs, TCam-2, and hPGCs share key germ cell characteristics and expressed the core germ cell genes, including *CD38*, whereas the differentially expressed genes reflected their corresponding stages of development and cell identity.

Principal component analysis (PCA) further illustrates the relationships between the different cell types. PCA reduces dimensionality of whole-genome expression data by transforming into principal components (PCs), in which the variance within the dataset is maximal. A three-dimensional (3D) PCA plot of the first three PCs showed that the 4i hESC, soma, and hPGC-related cells (hPGCLCs, gonadal hPGCs, and TCam-2) settled at three discrete positions (Figure 2B). In particular, hPGCLCs, TCam-2, and gonadal hPGCs aligned together at the lower extreme of PC2, whereas 4i hESCs and preinduced cells formed a distinct cluster with medium PC2 scores and soma at the upper extreme (Figures 2B and S2B). The relative contributions (weights) of key germ cell, pluripotency, and gonadal somatic genes to PC2 and PC3 were plotted as two-dimensional (2D) loading plot alongside a corresponding 2D PCA plot (Figure S2B). Indeed, the weights of germ cell, pluripotency, and somatic genes highly overlap with the position of germ-cell-related cell types, hESCs, and soma, respectively. Germ-cell-related genes, such as *SOX17*, *CD38*, and *NANOS3* loaded heavily for lower extreme of PC2, where hPGCLCs, TCam-2, and gonadal hPGCs were aligned. There was a clear difference in weights of early germ cell genes (commonly expressed in hPGCLCs, TCam-2, and gonadal hPGCs—for example, *BLIMP1* and *TFAP2C*) and late germ cell genes (expressed only in gonadal hPGCs or TCam-2—for example, *VASA* and *DAZL*) on PC3, with the latter weighing more heavily toward low PC3 scores (Figure S2B). Notably, decreasing scores of PC3 reflected potential progression of germ cell development from hPGCLCs toward gonadal

hPGCs, whereas TCam-2 aligned between hPGCLCs and gonadal hPGCs (Figures 2B and S2B).

Taken together, hPGCLCs demonstrate germ cell characteristics that are apparently en route to hPGCs, whereas our objective analysis placed TCam-2 in an intermediate position, which reflects their origin from hPGCs in vivo. Notably, hPGCLCs evidently represent the earliest stages of the human germ cell lineage, indicating that our in vitro model provides an important opportunity to explore the mechanism of hPGC specification, which is otherwise not possible because E9–E14 postimplantation human embryos are excluded from investigations. TCam-2 and other seminomas might, however, also serve as important in vitro models of human germ cell biology (Looijenga et al., 2014; Schafer et al., 2011).

CD38: A Core Marker of Human Germ-Cell-Related Cells and Initiation of the Epigenetic Program

CD38, an established cell-surface glycoprotein on leukocytes, is a prognostic marker of leukemia (Malavasi et al., 2008). Surprisingly, we detected CD38 expression in hPGCLCs, gonadal hPGCs, and TCam-2, but not in hESCs or gonadal somatic cells (Figure 2C). Indeed, fluorescence-activated cell sorting (FACS) analysis showed that CD38 is present on all the TNAP-positive embryonic hPGCs and on TCam-2 with some heterogeneity (Figures 3B and 3C). Although CD38 is absent on hESCs, ~50% of the NANOS3-mCherry-positive hPGCLCs were CD38 positive on day 4 (Figure 3A), which increased to ~70% by day 5 (Figure 3A). Interestingly, the NANOS3-mCherry/CD38 cells had higher expression of *NANOS3*, *BLIMP1*, *SOX17*, *OCT4*, and *NANOG* (Figure 3D). By contrast, hESCs and embryonic carcinoma cells exhibit *CD30* (also known as *TNFRSF8*) and *SOX2* (Figures 3D and 2G) (Pallesen and Hamilton-Dutoit, 1988). Thus, CD38 and CD30 could potentially be used as additional markers of germ cell tumors in vivo (Figure 7D).

The RNA-seq of hPGCLC also revealed gene expression changes that indicate initiation of the epigenetic program with downregulation of *UHRF1*, *DNMT3A*, and *DNMT3B* and upregulation of *TET1* and *TET2* (Figure S3D). Notably, we found a significant increase in 5-hydroxymethylcytosine (5hmC) in hPGCLCs, which is consistent with an increase in the expression of *TET1*, an enzyme that converts 5-methylcytosine (5mC) to 5hmC (Figures 3E–3G), together with a small but significant decline in 5mC (Figures 3G and S3A). This indicates that, as in the mouse PGCs, loss of 5mC might be coupled with the conversion of 5mC to 5hmC (Hackett et al., 2013). At the same time, we detected a decline in the expression of de novo DNA methyltransferase 3A (*DNMT3A*) and *UHRF1* in hPGCLCs compared to the neighboring somatic cells in the embryoids (Figures 3G, S3B, and S3C). *UHRF1* targets *DNMT1* to replication foci to

(C) Heat map of gene expression of key PGC-associated genes (early and late) and of pluripotency, mesoderm, endoderm, and gonadal somatic (Soma) markers. (D) Venn diagram illustrates common and differentially expressed genes. Significantly upregulated genes in hPGCLC, gonadal hPGC, and TCam-2 (with log2 (fold change) > 3 and adjusted p value < 0.05 versus gonadal Soma, respectively) were compared. Representative genes that were exclusive to each category are indicated. Text boxes indicate gene ontology biological processes (BP) terms that were significantly enriched as indicated by p values. Asterisk denotes custom categories absent from BP annotation.

(E–H) Immunofluorescence analysis for (E) *BLIMP1*, (F) *PRDM14*, (G) *SOX2*, and (H) *SOX17* on 4i hESCs (top row), day 4 hPGCLC embryoids (second row), human week 7 male gonad (third row), and TCam-2 (bottom row). Samples were counterstained with *TFAP2C* or *OCT4* to identify hPGCLCs in embryoids and hPGCs in embryonic gonad. Arrows indicate cytoplasmic enrichment of *PRDM14* (F). Scale bars, 70 μ m.

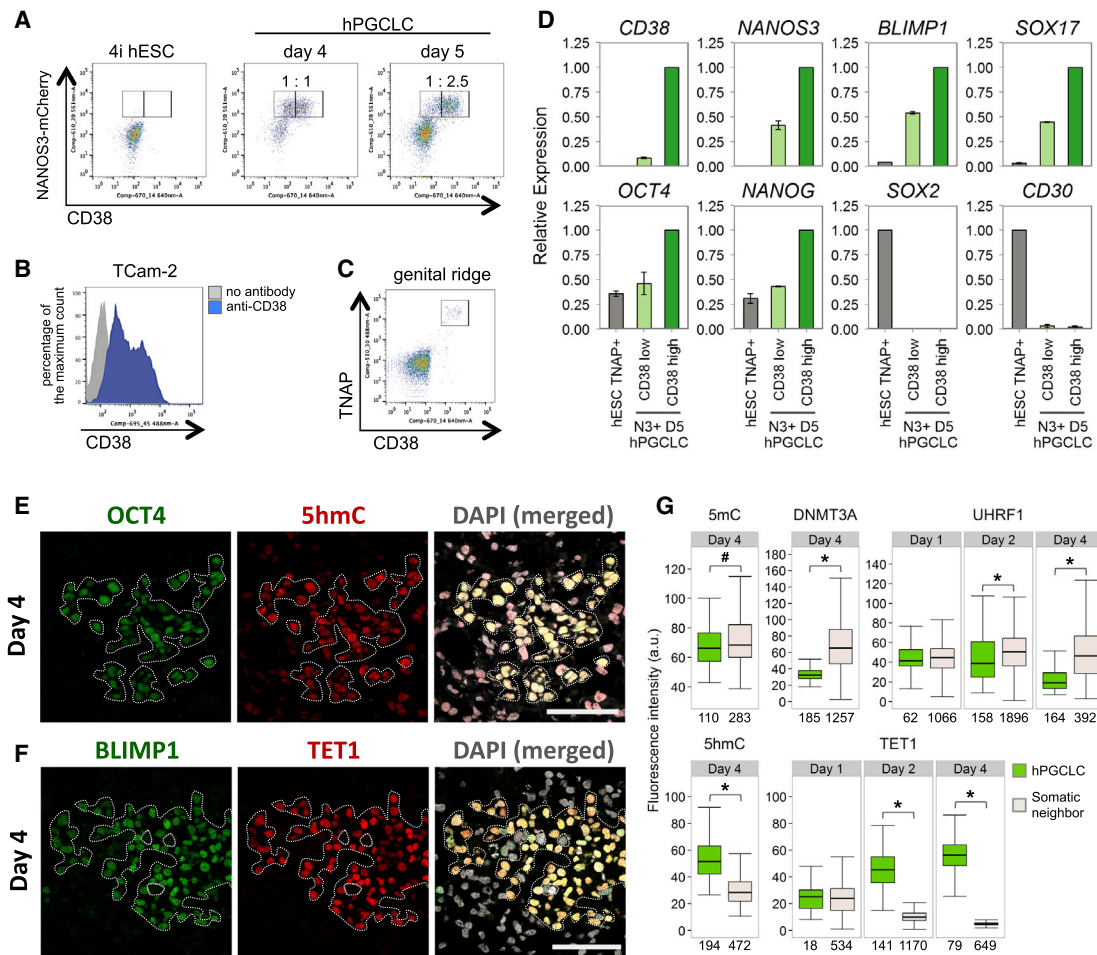


Figure 3. CD38 Expression in Human Germ-Cell-Related Cells and Epigenetic Changes in hPGCLCs

(A) FACS analysis of NANOS3-mCherry and CD38 on WIS2-NANOS3-mCherry cell line cultured in 4i medium and on day 4 and 5 embryoids following hPGCLC induction. Ratios of CD38 low and high expression in the NANOS3-mCherry-positive cells are indicated.

(B) FACS histogram of CD38 low and high populations in Tcam-2.

(C) FACS analysis of CD38 and TNAP on genital ridges isolated from a week 6 human embryo.

(D) Expression analysis by RT-qPCR for FACS-sorted TNAP-positive 4i hESCs (TNAP+ hESC) and CD38 low or high/NANOS3-mCherry day 5 hPGCLCs. Relative expression levels are shown with normalization to β -ACTIN. Error bars indicate mean \pm SD from two independent biological replicates.

(E and F) Immunofluorescence analysis for 5hmC (E) and TET1 (F) on day 4 embryoids cryosection. OCT4 or BLIMP1 were used to identify hPGCLCs (highlighted). Scale bars, 50 μ m.

(G) Quantification of immunofluorescence intensity of various epigenetic marks/modifiers in hPGCLCs and somatic neighbors in day 1–4 embryoids (see also Figures S3A–S3C). For UHRF1, only KI-67-positive (proliferating) cells were used for quantification. Numbers below each box denotes number of cells analyzed. Black central line represents the median, boxes and whiskers represent the 25th and 75th, and 2.5th and 97.5th percentiles, respectively. Wilcoxon signed-rank test was used to test for statistical significance. #p < 0.05; *p < 0.0001.

confer maintenance of DNA methylation (Liu et al., 2013). The repression of UHRF1 in proliferating (KI-67-positive) hPGCLCs would allow DNA-replication-coupled loss of 5mC, which is analogous to the observations on the early mouse germline.

Taken together, day 4 hPGCLCs, which are the nascent human germ cells, already showed evidence for the initiation of epigenetic changes and DNA demethylation that are comparable to E8 mouse PGCs (Hackett et al., 2013). Notably, we also found that PRMT5, an arginine methyltransferase that was ubiquitously but weakly present in the cytoplasm of day 1 and 2 embryoids, showed enhanced expression in the nucleus of

day 4–8 hPGCLCs (Figure S3E). This is a shared characteristic with ~E8 mouse PGCs, hPGCs, and Tcam-2 seminoma (Eckert et al., 2008). The translocation of PRMT5 to the nucleus is important for the suppression of transposable elements at the onset of DNA demethylation (Kim et al., 2014).

Sequential Gene Expression during hPGCLC Specification in Embryoids

Having established similarities between hPGCLCs and the authentic hPGCs, we set out to investigate the mechanism of hPGCLC specification. First, for establishing the precise

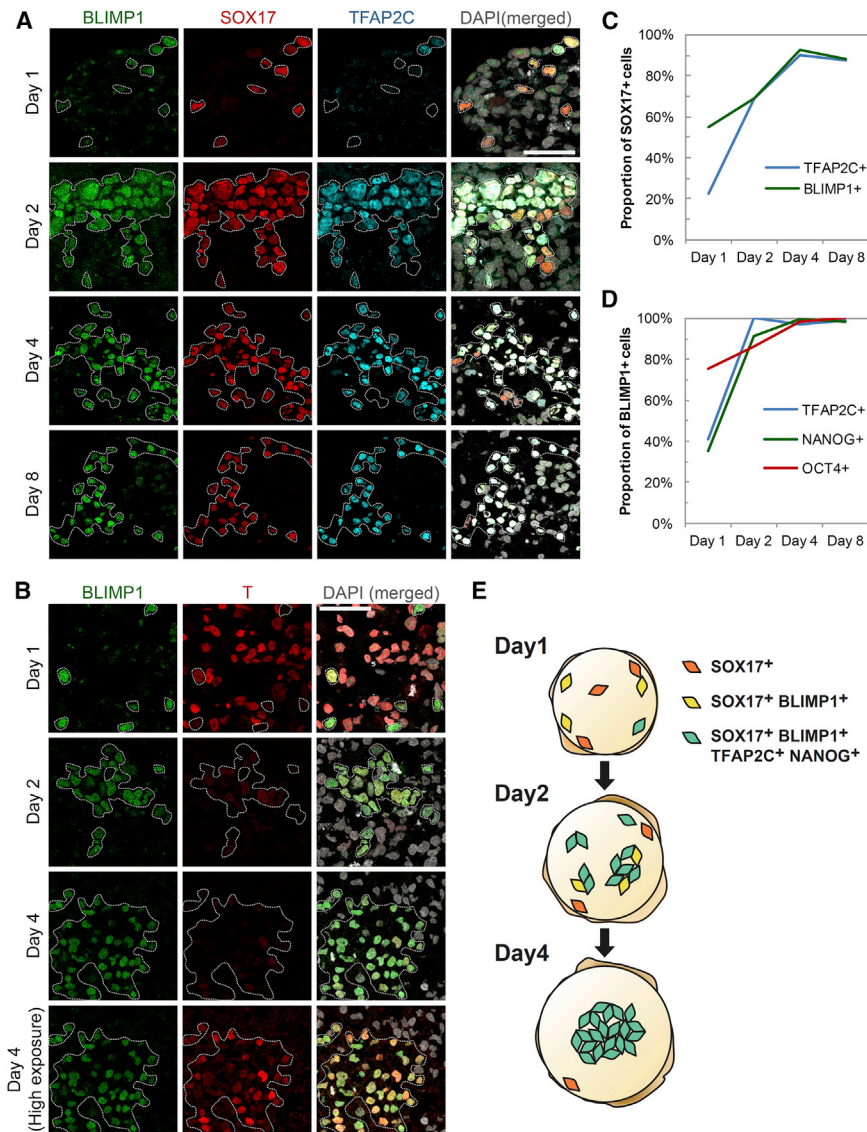


Figure 4. Sequential Expression of Germ-Cell-Related Transcription Factors in Single Cells during hPGCLC Specification

(A and B) Immunofluorescence analysis for (A) BLIMP1, SOX17, and TFAP2C and (B) BLIMP1 and T in cryosections of day 1–8 embryoids after hPGCLC induction. Bottom row in (B) shows high exposure (digital) image of T, indicating low but specific expression in hPGCLC. SOX17-positive or BLIMP1-positive cells are highlighted. Scale bars, 50 μ m.

(C) Percentage of SOX17-positive (+) cells in day 1–8 embryoids that were also TFAP2C+ or BLIMP1+. Corresponds to data in Figure 4A.

(D) Percentage of BLIMP1-positive (+) cells in day 1–8 embryoids that were TFAP2C+, NANOG+, or OCT4+. Corresponds to data in Figures 4A, S4A, and S4B.

(E) Summary model for dynamics of hPGCLC specification in embryoids. SOX17-positive cells are first scattered in day 1 embryoids. They gain expression of BLIMP1, TFAP2C, and NANOG sequentially and form a cluster from day 2 onward until the formation of nascent hPGCLC.

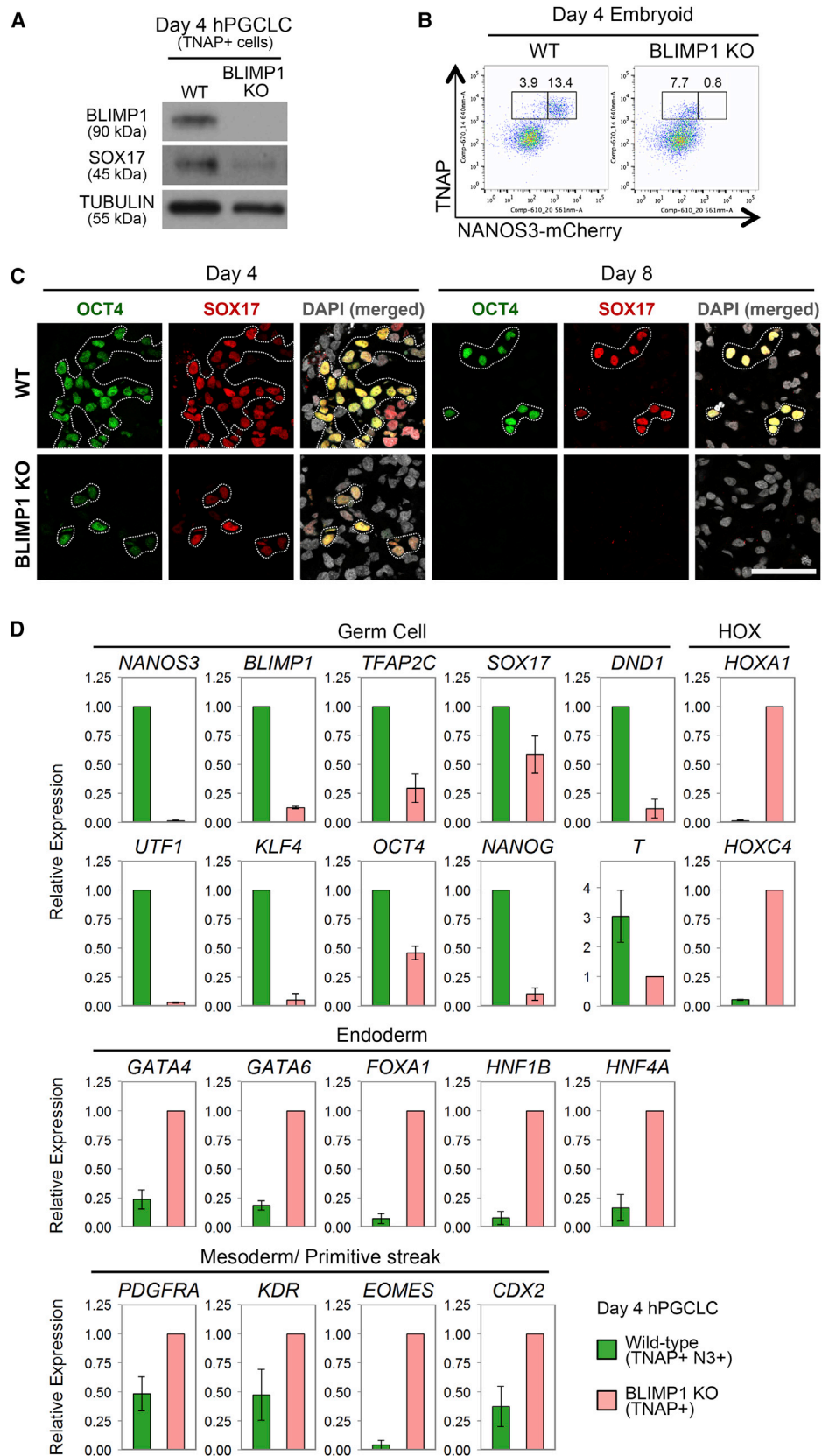
Expression of T is of particular interest, as it signifies competence for germ cell fate in mice, and BMPs can induce it in hESCs (Bernardo et al., 2011; Yu et al., 2011). Notably, expression of T was high in the majority of cells on day 1, except for most of the BLIMP1+ cells (Figure 4B). By day 2, however, T was dramatically downregulated in most cells, although now the BLIMP1+ nascent hPGCLC retained low T expression, which persisted until at least day 4 (Figure 4B), consistent with the T transcripts detected by RNA-seq (Figure 2C). It is possible that BMP signaling may initially enhance expression of T in the embryoids (Bernardo et al., 2011), and it is from this population

sequence of expression of the key hPGC-related genes at the resolution of single cells, we performed systematic time course analysis by immunofluorescence on day 1–8 embryoids after hPGCLC differentiation.

On day 1, we first detected SOX17 in a few widely scattered cells throughout the embryoids (Figures 4A and 4E). Among the SOX17-positive (+) cells, 55% were also BLIMP1+, and 22% were TFAP2C+ (Figures 4A and 4C). However, all BLIMP1+ cells coexpressed SOX17, suggesting that SOX17 is upregulated before BLIMP1. The proportion of BLIMP1+ and TFAP2C+ cells increased to ~70% on day 2 and to ~90% on days 4–8 (Figures 4A and 4C). These triple-positive cells likely represent specified hPGCLCs, as they also coexpressed other key hPGC genes. However, ~10% of single SOX17+ cells failed to undergo hPGCLC specification but persisted in day 4–8 embryoids. These may be aberrant cells or else may belong to other lineages.

that hPGCLCs are specified, which reflects the events during mouse PGC induction (Aramaki et al., 2013).

Expression of OCT4 was low but widespread in the day 1 embryoids, including 75% of the BLIMP1+ cells (Figures S4B and 4D). Although the overall OCT4 expression declined dramatically in day 2 embryoids, it was strongly expressed in ~86% of the BLIMP1+ cells. Subsequently, all BLIMP1+ cells became highly OCT4+ by day 4. By contrast, NANOG was expressed in ~35% of BLIMP1+ cells on day 1, but it was generally absent in other cells in the embryoids (Figures 4D and S4A). Thereafter, NANOG was also rapidly upregulated in the majority of BLIMP1+ cells by day 2–4. The upregulation of key pluripotency genes, such as OCT4 and NANOG, is also reminiscent of their re-expression in mouse PGCs (Magnúsdóttir et al., 2013). Although NANOS3-mCherry expression was weakly detected in 24% of OCT4+ cells at day 2 (Figure S4C), it was detected in all OCT4+ cells on day 4, confirming their PGCLC identity.



(legend on next page)

PRDM14 is a key regulator of pluripotency in mouse and human ESCs (Chia et al., 2010; Grabole et al., 2013; Ma et al., 2011; Yamaji et al., 2013) and is a key regulator of mouse PGC specification (Yamaji et al., 2008). PRDM14 was generally down-regulated in day 1–2 embryoids but was detectable in the nucleus of most BLIMP1+ cells by day 4 (Figure S4A). Notably, in a minority of BLIMP1/NANOG-positive hPGCLCs at day 8, PRDM14 was enriched in the cytoplasm (Figure S4A), which was the case in most of the gonadal hPGCs (Figure 2F). This is in marked contrast to the persistent nuclear PRDM14 expression in mouse PGCs (Grabole et al., 2013).

The SOX17/BLIMP1 double-positive cells were initially distributed randomly in day 1 embryoids (Figure 4A) but were then loosely organized in clusters and often a single cluster in day 2 embryoids. By day 4, generally one and occasionally two tight clusters of hPGCLCs were observed either at the core or periphery of each embryoid (Figure 4E). Cumulative observations suggest that SOX17/BLIMP1 might be among the key regulators of hPGCLC specification. Although OCT4 and NANOG were detected between days 1 and 2 in conjunction with NANOS3-mCherry and other PGC-specific genes from days 2–4, PRDM14 was upregulated more gradually in hPGCLCs and was subsequently detected in the cytoplasm of embryonic hPGCs. Following the early expression of SOX17 and BLIMP1 in hPGCLCs, these two transcription factors were also detected in embryonic hPGCs in vivo, as well as in Tcam-2 (Figures 2E and 2H). These observations suggest that SOX17-BLIMP1 might be among the critical determinant of hPGC specification and maintenance.

Role of BLIMP1 during hPGCLC Specification

BLIMP1 is the first and key regulator of mouse PGC, and loss of function abrogates PGC fate (Ohinata et al., 2005; Vincent et al., 2005). However, BLIMP1 expression is apparently downstream of SOX17 in hPGCLCs (Figures 4A and 4C). We examined its mechanistic role by generating *BLIMP1* knockout (KO) NANOS3-mCherry hESC line (Figure S5A). These cells showed loss of BLIMP1 by western blot (Figure 5A) and immunofluorescence (Figure S5B) on day 4 of hPGCLCs induction. Notably, there was also a loss of NANOS3-mCherry-positive cells, together with a significant reduction of NANOG, OCT4, and TFAP2C expression on day 4 (Figures 5C and S5B), indicating a failure of hPGCLC specification, and all of these cells disappeared by day 8 (Figure 5C). However, we detected ~8% of TNAP-positive cells in day 4 embryoids (Figure 5B). This observation is highly reminiscent of the effects of *Blimp1* mutation on mouse PGC specification (Ohinata et al., 2005).

We isolated and characterized the TNAP-positive cells by FACS and confirmed loss of *BLIMP1*, except for low expression

of mutant transcripts (Figure 5D). These cells also showed loss of *NANOS3*, *UTF1*, and *KLF4* and reduced expression of *TFAP2C*, *DND1*, *OCT4*, *NANOG*, and *T* (Figures 5D and S5B). In addition, they showed prominent upregulation of mesodermal/primitive streak and *HOX* genes, as well as endodermal genes, including *GATA4*, *GATA6*, *FOXA1*, *HNF1 β* , and *HNF4 α* (Figure 5D). By contrast, endodermal genes were not upregulated in *Blimp1* mutant mouse PGCs (Kurimoto et al., 2008; Vincent et al., 2005). This suggests that BLIMP1 probably suppresses endoderm and other somatic genes, which might otherwise be induced by SOX17 and BMP signaling during hPGCLCs specification (Figure 6H). Loss of *BLIMP1* and *TFAP2C* also caused upregulation of *HOX* genes in Tcam-2 (Weber et al., 2010). This suggests that one of the roles of BLIMP1 is to continually suppress the somatic program during human germline development.

SOX17 Is the Key Regulator of hPGCLCs, which Acts Upstream of BLIMP1

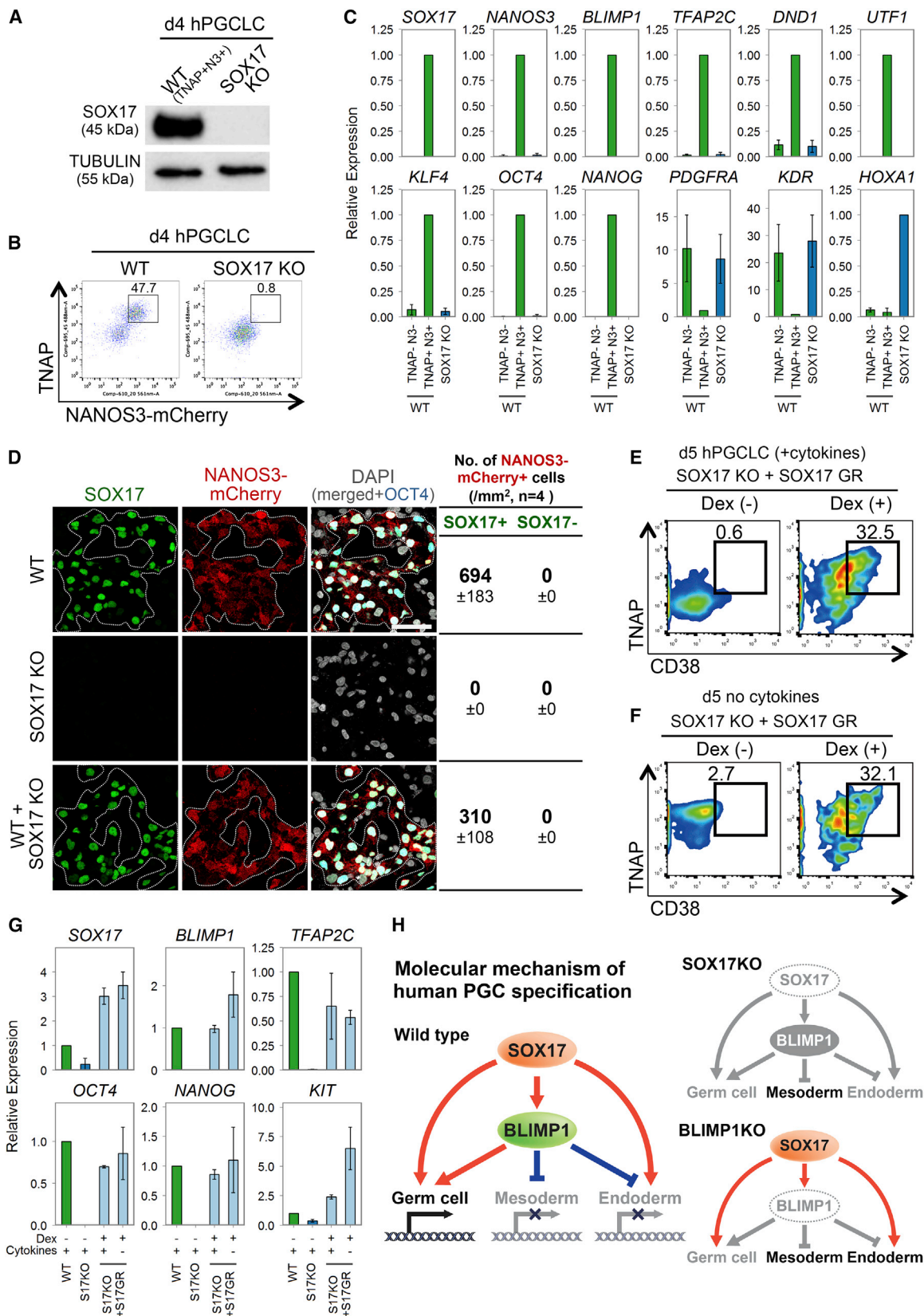
Expression of SOX17 among T-positive cells prior to BLIMP1 apparently marks the onset of hPGCLC specification, which is a key difference between the specification of human and mouse germline fate (see Figure 4). Notably, SOX17 and BLIMP1 are also expressed in the authentic in vivo hPGCs and in Tcam-2 (de Jong et al., 2008) (Figure 2). Knockdown of SOX17 in Tcam-2, which exhibits key germ cell characteristics (Looijenga et al., 2014) (Figure 2), induced repression of the pluripotency genes *NANOG*, as well as of the PGC-genes *BLIMP1*, *NANOS3*, *TFAP2C*, *STELLA*, and *KIT* (Figure S6A). This suggests that SOX17 might be important for regulating the established germline gene expression network.

We addressed the role of SOX17 during hPGCLC specification by generating *SOX17* KO NANOS3-mCherry hESC line (Figure S6B) and validated absence of SOX17 expression in day 4 embryoids from mutant cells by western blot and immunofluorescence (Figures 6A and S6C). Notably, we did not detect any NANOS3-mCherry or TNAP-positive cells in the embryoids from *SOX17* mutant cells (Figure 6B). Further, RT-qPCR analysis of day 4 *SOX17* null embryoids showed absence of *NANOS3*, *TFAP2C*, *DND1*, *UTF1*, *KLF4*, *OCT4*, *NANOG*, and, importantly, *BLIMP1* (Figure 6C). Instead, there was upregulation of mesodermal genes *PDGFRA*, *KDR*, and *HOXA1* (Figure 6C). Although a few *TFAP2C*-positive cells were detected on day 4, they were BLIMP1 negative and most likely belong to other lineages (Figure S6C).

To determine whether SOX17 acts cell autonomously, we mixed wild-type NANOS3-mCherry hESCs with the *SOX17* null hESCs in 1:1 ratio during induction of hPGCLCs by cytokines.

Figure 5. Role of BLIMP1 in hPGCLC Specification

- (A) Western blot analysis of BLIMP1 and SOX17 in TNAP-positive (TNAP+) cells sorted from wild-type (WT) and BLIMP1 knockout (BLIMP1 KO) day 4 embryoids after hPGCLC induction. TUBULIN was used as loading control.
- (B) FACS analysis of TNAP and NANOS3-mCherry on WT and BLIMP1 knockout (BLIMP1 KO) day 4 embryoids.
- (C) Immunofluorescence for OCT4 and SOX17 in cryosections of WT and BLIMP1 KO day 4 and 8 embryoids. OCT4-positive cells are highlighted. Scale bar, 50 μ m.
- (D) Expression analysis by RT-qPCR for WT TNAP/NANOS3-mCherry double-positive cells (WT; TNAP+N3+) and BLIMP1 KO TNAP single-positive cells (BLIMP1 KO; TNAP+) sorted from day 4 embryoids. Relative expression levels are shown with normalization to β -ACTIN. Error bars indicate mean \pm SD from two independent biological replicates.



(legend on next page)

All NANOS3-mCherry positive cells detected by immunofluorescence on day 4 were SOX17 positive (Figure 6D), indicating that SOX17 null hESCs did not undergo hPGCLC specification even in the presence of wild-type cells. The overall number of NANOS3-mCherry-positive cells in the embryoid with mixed cells was about half of that in the control consisting of wild-type cells only (Figure S6D), suggesting that SOX17 null cells did not affect PGCLC induction from wild-type cells. Thus, SOX17 null cells have intrinsic defect for hPGCLC specification.

To determine the competency of the SOX17 null hESCs, we transfected an inducible SOX17 fusion construct with human glucocorticoid receptor ligand-binding domain (GR) into the SOX17 null hESCs. This would allow dexamethasone (Dex) to activate the SOX17-GR and induce translocation of SOX17 fusion protein from the cytoplasm into the nucleus (Brocard et al., 1998). After 5 days of induction with cytokines and Dex in the SOX17 null SOX17-GR hESCs, expression of germ cell genes *BLIMP1*, *TFAP2C*, *OCT4*, *NANOG*, and *KIT* and the TNAP/CD38-positive population was restored (Figures 6E and 6G). This demonstrates that SOX17 null hESCs maintain competency for hPGCLC specification. Strikingly, activation of SOX17 alone in the absence of cytokines was sufficient to induce germ cell genes and TNAP/CD38-positive cells from 4i hESCs (Figures 6F and 6G). Taken together, SOX17 is indispensable and sufficient for hPGCLC gene induction from competent hESCs, and it acts upstream of BLIMP1 and other genes to initiate the human germ cell transcriptional network (Figure 6H). Interestingly, loss of SOX17 in TCam-2 also causes a repression of germ-cell- and pluripotency-associated genes (Figure S6A). This suggests that SOX17 might also be important for the maintenance of the germ cell state because it is also highly expressed in embryonic hPGCs.

Specification of hPGCLCs from Germ-Cell-Competent hESC/hiPSCs

Because gene expression of hESCs in 4i medium resembles that of hESC after preinduction for 2 days in bFGF/TGF β (Figures 2A, 2B, and S2A), we decided to investigate hPGCLC induction directly in hESCs maintained in 4i medium (Figure 1A). Indeed, hPGCLCs could be induced directly from 4i hESCs

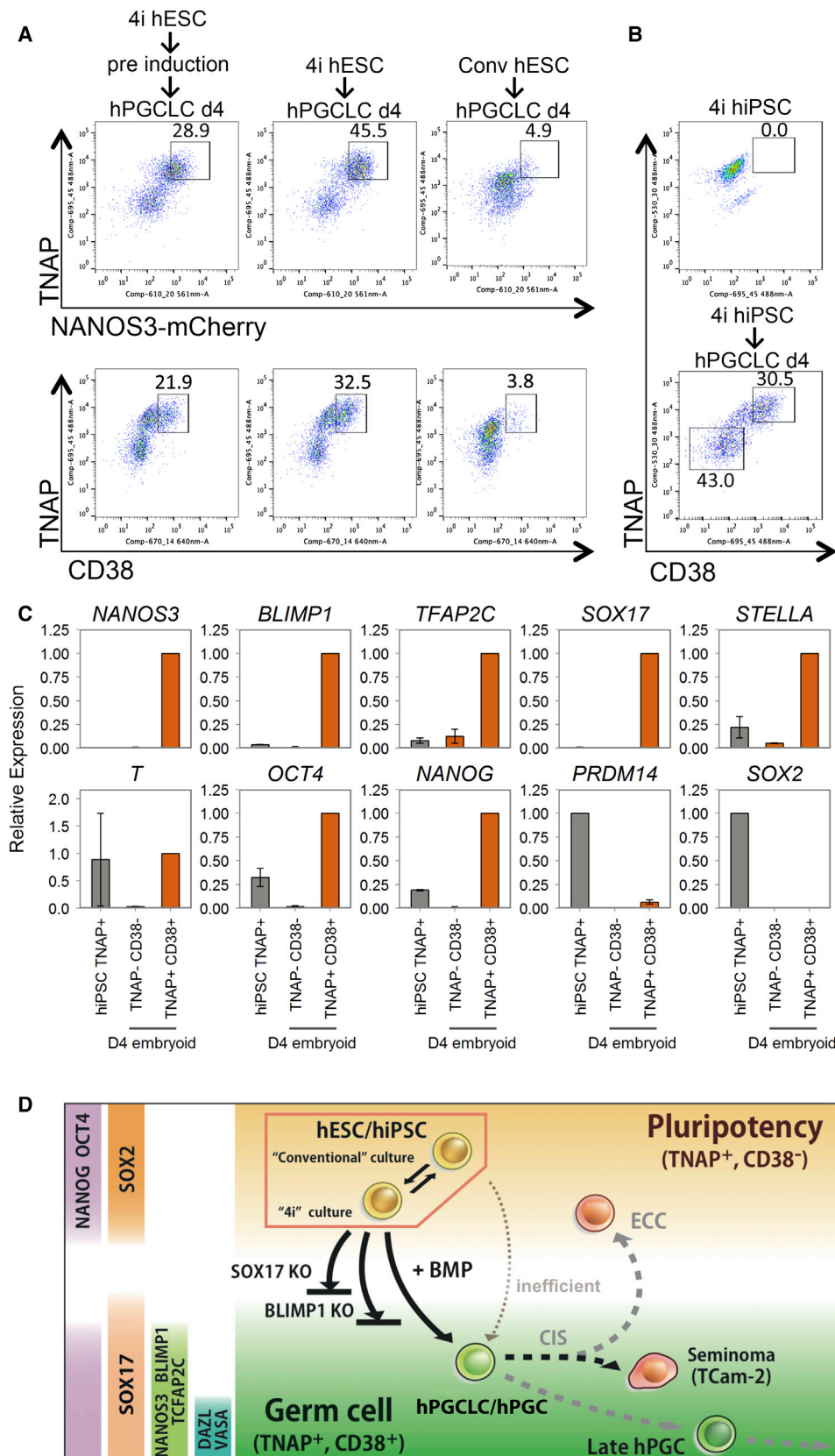
with apparent enhanced response resulting in ~46% hPGCLCs (Figure 7A). These hPGCLCs showed a slightly higher intensity of NANOS3/TNAP by FACS, and a greater proportion of them were CD38 positive (Figure 7A). Notably, cells maintained for more than 2 weeks in the conventional hESC medium, regardless of whether they were initially maintained in 4i medium, showed a significantly lower numbers of hPGCLCs (~5%) with a reduced intensity of NANOS3-mCherry/TNAP and CD38 expression (Figure 7A). This demonstrates that hESCs in 4i medium are highly competent for the hPGCLC fate. Importantly, the competent state is conferred reversibly because it is gained and lost in 4i and conventional culture conditions, respectively.

Global gene expression analysis indicated overall similarities between hESCs in the conventional medium versus those in “4i” medium ($r = 0.923$) but with notable differences (Figure S7A). Although these cells showed similar expression levels of core pluripotency factors *OCT4*, *NANOG*, and *SOX2*, 4i hESCs had higher expression of mesoderm and gastrulation genes, including *T*, *RUNX1*, and *PDGFRA* (Figures S7B and S7C and Table S2). Furthermore, OCT4-positive cells in 4i hESCs had varying levels of T protein, possibly due to inhibition of GSK3 β (Chen et al., 2013), which is not the case in hESC cultured in conventional condition (Figure S7D). These differences might be relevant for the mechanism of competence of ESCs for PGCLC, which merits further investigation.

We also asked whether hiPSCs could be used to generate and isolate hPGCLCs using the combination of surface markers CD38 with TNAP (Figures 2C and 3A–3D). Using FX71.1 hiPSCs (see Experimental Procedures) maintained in 4i medium for >2 weeks that lack CD38 expression, we detected ~31% of TNAP/CD38 double-positive cells after 4 days in response to cytokines (Figure 7B). TNAP/CD38 double-positive hPGCLCs showed expression of *NANOS3*, *BLIMP1*, *TFAP2C*, *SOX17*, *STELLA*, *T*, *OCT4*, *NANOG*, and *PRDM14*, but not of *SOX2* (Figure 7C). Similar results were obtained with another hiPSC line (C1, Gafni et al., 2013). Thus, hPGCLC specification could be induced efficiently and directly in hiPSCs that are maintained in the 4i medium, which could be used for disease modeling using patient-derived iPSCs.

Figure 6. Role of SOX17 in hPGCLC Specification

- (A) Western blot analysis of SOX17 expression of WT day 4 TNAP/NANOS3-mCherry-positive hPGCLCs (WT, TNAP+N3+), and whole SOX17 knockout day 4 embryoids. TUBULIN was used as loading control.
- (B) FACS analysis of TNAP and NANOS3-mCherry on WT and SOX17 KO day 4 embryoids.
- (C) RT-qPCR analysis of TNAP/NANOS3-mCherry FACS-sorted WT double-negative (TNAP-N3-) or -positive (TNAP+N3+) cells sorted from day 4 embryoids and whole SOX17 KO embryoids (SOX17 KO). Relative expression levels are shown with normalization to β -ACTIN. Error bars indicate mean \pm SD from two independent biological replicates.
- (D) Immunofluorescence of day 4 embryoids derived from WT, SOX17 knockout (SOX17 KO), and from 1 to 1 mixture of WT and SOX17 KO 4i hESCs. The number of NANOS3-mCherry+ cells with or without SOX17 expression is shown. Quantification was based on seven to nine confocal images from four independent embryoids of each condition. Scale bars, 50 μ m.
- (E and F) FACS analysis of TNAP and CD38 on day 5 embryoids derived from SOX17 knockout 4i hESCs containing SOX17 fusion construct with human glucocorticoid receptor ligand-binding domain (SOX17 KO+ SOX17 GR). Embryoids were derived in the presence (E) or absence (F) of cytokines with (Dex+) or without (Dex-) addition of dexamethasone.
- (G) RT-qPCR analysis of day 5 hPGCLC derived from WT and SOX17 KO (S17KO) and SOX17 KO + SOX17-GR (S17KO+S17GR) hESCs with (+) or without (–) dexamethasone (Dex) and in the presence (+) or absence (–) of cytokines. FACS-sorted NANOS3-mCherry/TNAP double-positive cells or whole embryoids (for S17KO) were used. Relative expression levels are shown with normalization to *GAPDH*. Error bars indicate mean \pm SD from two biological replicates.
- (H) Model for establishment of hPGC transcription network by SOX17 and BLIMP1. SOX17 induces germ cell genes and, potentially, endoderm gene. Expression of BLIMP1, downstream of SOX17, suppresses endodermal genes, as well as mesodermal genes. As a result, the SOX17-BLIMP1 axis initiates hPGC program from competent cells upon induction by BMP signaling. The hPGC specification gene network is abrogated in the absence of SOX17 or BLIMP1.



(legend on next page)

DISCUSSION

Specification of hPGCLCs from germ cell competent hESC/hiPSC provides a unique mechanistic view of the establishment of the human germline (Figure 7D). Notably, SOX17 is the key regulator of hPGCLC specification, whereas BLIMP1 represses endodermal and other somatic genes during hPGCLC specification. This was unexpected because the primary role of SOX17 is in the endoderm (D'Amour et al., 2005; Kanai-Azuma et al., 2002) and because *Sox17* has no detectable role in the specification of mouse PGCs (Hara et al., 2009; Kanai-Azuma et al., 2002). A comparison among hPGCLCs, embryonic hPGCs, and Tcam-2 seminoma (Looijenga et al., 2014; Schafer et al., 2011) also establishes the likely progression of the early human germline (Figure 2B).

During hPGCLC specification from hESCs, SOX17 was first detected in a few scattered cells in day 1 embryoids, which showed expression of T. The nascent hPGCLCs subsequently form a few or a single cluster in day 4–8 embryoids. SOX17 is indeed essential for hPGCLC specification, and this gene alone is sufficient to induce germ cell genes in the SOX17 mutant cells, with or without cytokines from 4i hESCs. SOX17 acts cell autonomously, and the presence of mutant cells in embryoids had no effect on hPGCLC specification from wild-type cells. It will be of interest to see how SOX17, with or without BLIMP1, determines cell fates between germ cell, hematopoietic, and endodermal lineages (Nakajima-Takagi et al., 2013; Clarke et al., 2013).

Expression of BLIMP1 is intimately associated with SOX17 during hPGCLC specification. BLIMP1 represses somatic genes, including mesendodermal genes, which might allow SOX17 to function as the regulator of hPGCLCs specification. A mutation in BLIMP1 abrogates hPGCLC specification but without completely abolishing SOX17 expression. However, TNAP-positive cells were detected, in which PGC-specific genes were repressed but some endodermal and other somatic genes were upregulated. This suggests that BLIMP1 might repress them during hPGCLC specification, but not excluding its wider role in hPGCLC specification in conjunction with SOX17. In mice, BLIMP1 also represses somatic genes in PGCs (Ohinata et al., 2005; Vincent et al., 2005), but it is also a key determinant of PGC specification, together with PRDM14 and TFAP2C (Magnúsdóttir et al., 2013).

Although PRDM14 is critical for mouse PGC specification, its expression during hPGCLC specification is delayed and significantly diminished in hPGCs and is very low in Tcam-2 compared to hESCs. PRDM14 is crucial for maintaining pluripotency in human and mouse ESCs, although different signaling molecules

regulate its expression, and the genomic targets in ESCs also differ in the two species (Chia et al., 2010; Grabole et al., 2013; Ma et al., 2011; Yamaji et al., 2013). The rapid downregulation and delayed re-expression of PRDM14 at the onset of hPGCLC induction (Figures 2F and S4A) may allow exit of pluripotency from 4i hESC en route to germ cell differentiation. Interestingly, the human and mouse PRDM14 proteins have diverged, which might result in functional differences. There is expression of SOX2 in mouse PGCs, which is apparently regulated by PRDM14 (Grabole et al., 2013), whereas SOX2 is repressed in human hPGCLCs/hPGCs. BLIMP1 also apparently represses SOX2 during spontaneous differentiation of hPGCLCs from hESCs (Lin et al., 2014). By contrast, KLF4 is expressed in hPGCLCs/hPGCs (Figure 2C), but not in mouse PGCs (Kurimoto et al., 2008). The precise significance of the repression and expression of pluripotency genes, including NANOG, remains to be elucidated.

Germ cell neoplasia or carcinoma in situ (CIS) (Skakkebaek, 1972) can generate embryonal carcinoma cells that resemble hESCs or seminomas such as Tcam-2 that inherit key characteristics of germ cells (Looijenga et al., 2014; Schafer et al., 2011). Tcam-2 expresses *SOX17*, *BLIMP1*, *TFAP2C*, *KIT*, and *DND1* with low levels of *SOX2* and *PRDM14*. Knockdown of SOX17 in Tcam-2 induces repression of germ cell and pluripotency genes (Figure S6A), whereas knockdown of BLIMP1 and TFAP2C induced upregulation of somatic genes (Weber et al., 2010). These observations suggest that SOX17 and BLIMP1 might also be important for the maintenance of the early human germline. We found that CD38 is a marker of all human germline-related cells, including seminomas. Distinction between seminoma and embryonal carcinoma could therefore be made by the expression of SOX17/CD38 and SOX2/CD30, respectively (de Jong et al., 2008). Furthermore, CD38/TNAP are reliable markers for the isolation of hPGCLCs derived from hESC/hiPSC without any reporters.

The hPGCLCs also showed early signs of DNA demethylation, which is consistent with the germline-specific epigenetic program. The striking upregulation of 5hmC concomitantly with TET1 suggests that, similar to mouse, conversion of 5mC to 5hmC may contribute to DNA demethylation in hPGC (Hackett et al., 2013). Furthermore, repression of UHRF1 and DNMT3A in hPGCLCs would promote DNA-replication-coupled loss of 5mC. Indeed, there was a small but significant decline in 5mC in hPGCLCs, a trend that could lead to a significant loss of 5mC with further proliferation of hPGCLCs. Furthermore, we detected upregulation and translocation of PRMT5 to the nucleus in hPGCLC, which occurs with the onset of global DNA

Figure 7. Induction and Isolation of hPGCLCs from Competent hiPSCs/hESCs

(A) FACS analysis of TNAP and NANOS3-mCherry (top) and TNAP and CD38 (bottom) on day 4 embryoids induced from 4i hESCs after preinduction (left), directly without preinduction (middle) or from conventional hESCs (right, Conv hESC).

(B) FACS analysis of TNAP and CD38 in 4i hiPSCs (top) and day 4 embryoids derived from 4i hiPSCs after direct induction (bottom).

(C) Expression analysis by RT-qPCR on TNAP-positive hiPSCs (iPSC TNAP+), TNAP/CD38 double-negative (TNAP–CD38–) population and TNAP/CD38 double-positive population (TNAP+CD38+) on day 4 after hPGCLC induction. Relative expression levels are shown with normalization to β -ACTIN. Error bars indicate mean \pm SD from two independent biological replicates.

(D) Overview of human germline development. hESCs in 4i reversibly attains competence for germ cell fate. Exposure of 4i cells to cytokines containing BMPs results in strong induction of hPGCLCs following expression of SOX17–BLIMP1, which are among the key regulators of germ cell fate. SOX17 and BLIMP1 are detected in in vivo gonadal hPGC and Tcam-2 seminoma, indicating a likely progression of early human germ cell lineage. CD38, a cell-surface glycoprotein, is shared by all cells with germ cell characteristics, but not by hESC. Loss of SOX17 or BLIMP1 abrogates hPGCLC specification.

demethylation to repress transposable elements (Kim et al., 2014). Detailed analysis of the transcriptome and epigenome, together with the targets of SOX17 in hPGCLCs/hPGCs, should provide insights on the mechanism of how the epigenome is reset in the early human germline and potentially on the inheritance and consequences of transgenerational epigenetic inheritance (Heard and Martienssen, 2014).

This study shows that changes in pluripotent cell states can be induced by environmental factors with respect to gain and loss of competence for germ cell fate in hESCs in the 4i culture (Gafni et al., 2013). This competence for hPGCLCs is reversibly maintained and progressively lost in conventional culture conditions. Notably, hESCs in 4i medium show a slight upregulation of T together with HAND1 compared to conventional hESCs (Figure S7), with putative posterior primitive streak-like feature (Mendjan et al., 2014). This might explain why hESC in 4i are highly competent for hPGCLC fate. Because MAPK inhibitors may also alter the epigenetic state of pluripotent cells (Gafni et al., 2013), the precise molecular basis for competence for PGC fate remains to be elucidated in both mouse and human. Nonetheless, hESC/hiPSC can reversibly gain competence for hPGCLC specification in 4i medium, which provides a model for advances in human germ cell biology.

Mouse is the primary model organism for early mammalian development, pluripotency, and the regulation of cell fates. Post-implantation rodent embryos develop as egg cylinders with an overlying extraembryonic ectoderm, which is the source of signals, including BMP4, whereas postimplantation epiblast embryonic disc in humans is typical of many mammalian species (Barrios et al., 2013; de Fellici, 2013; Irie et al., 2014). These differences may affect the source, duration, and the nature of signaling molecules that regulate competence for cell fates in vivo. The evolutionary divergence in the pluripotent states in mouse and human might also result in differences in the mechanism of germline specification and, potentially, other cell fate decisions. If so, mechanisms of early cell fate decisions in mice cannot be safely or wholly extrapolated to specification events during early human development.

EXPERIMENTAL PROCEDURES

hESC/iPSC Culture and hPGCLC Differentiation

4i hESCs (WIS2: 46XY; WIBR3: 46XX; LIS1, 46XY) and iPSCs (FX71.1; a fragile X male patient-derived iPSC line, C1 female iPSC line) were grown in conditions adapted and modified from previously described WIS-NHSC conditions (Gafni et al., 2013). 4i cells were grown on irradiated mouse embryonic fibroblasts (MEFs) (GlobalStem) in knockout DMEM supplemented with 20% knockout serum replacement (KSR), 2 mM L-glutamine, 0.1 mM nonessential amino acids, 0.1 mM 2-mercaptoethanol (all GIBCO), 20 ng/ml human LIF (Stem Cell Institute [SCI]), 8 ng/ml bFGF (SCI), 1 ng/ml TGF- β 1 (PeproTech), 3 μ M CHIR99021 (Miltenyi Biotec), 1 μ M PD0325901 (Miltenyi Biotec), 5 μ M SB203580 (TOCRIS bioscience), and 5 μ M SP600125 (TOCRIS bioscience). Cells were passaged every 3 to 5 days using TrypLE Express (GIBCO). 10 μ M of ROCK inhibitor (Y-27632, TOCRIS bioscience) was used for 24 hr after the passage.

To preinduce, 4i hESCs were dissociated with TrypLE Express and filtered with 50 μ m cell filter (PERTEC), and 4×10^5 cells/12-well were plated on vitronectin/gelatin-coated plates (Gafni et al., 2013) in N2B27 medium (Ying et al., 2008) with 1% KSR, 10 ng/ml bFGF (SCI), 1 ng/ml TGF- β 1 (PeproTech), or 20 ng/ml Activin A (SCI) and 10 μ M ROCK inhibitor. Medium was changed on day 1. After 2 days of preinduction, the cells are dissociated with TrypLE

and plated to ultra-low cell attachment U-bottom 96-well plates (Corning, 7007) at a density of 2,000–4,000 cells/well in 200 μ l PGCLC medium. PGCLC medium is composed of Glasgow's MEM (GMEM, GIBCO), 15% KSR, 0.1 mM nonessential amino acids, 0.1 mM 2-mercaptoethanol, 100 U/ml Penicillin-0.1 mg/ml Streptomycin, 2 mM L-Glutamine, 1 mM Sodium pyruvate, and the following cytokines: 500 ng/ml BMP4 (R&D Systems) or BMP2 (SCI), 1 μ g/ml human LIF (SCI), 100 ng/ml SCF (R&D Systems), 50 ng/ml EGF (R&D Systems), and 10 μ M ROCK inhibitor.

Conventional hESCs/hiPSCs were maintained on irradiated MEFs (GlobalStem) in DMEM/F12+GlutaMAX supplemented with 20% KSR, 0.1 mM nonessential amino acids, 0.1 mM 2-mercaptoethanol (all GIBCO), and 10–20 ng/ml of bFGF (SCI). Media were replaced every day. Cells were passaged every 4 to 6 days using 1 mg/ml of Dispase (GIBCO), and 10 μ M ROCK inhibitor (Y-27632, TOCRIS bioscience) was added for 24 hr after the passage.

ACCESSION NUMBERS

The NCBI GEO accession number for the RNA-seq data reported in this paper is GSE60138.

SUPPLEMENTAL INFORMATION

Supplemental Information includes Extended Experimental Procedures, seven figures, and three tables and can be found with this article online at <http://dx.doi.org/10.1016/j.cell.2014.12.013>.

AUTHOR CONTRIBUTIONS

The study was conceived and designed by N.I., L.W., J.H.H., and M.A.S. The NANOS3-mCherry reporter hESC lines and the BLIMP1 and SOX17 knockout hESCs were generated by L.W. and S.V. hESC growth conditions were developed by L.W. and J.H.H. The PGCLC induction experiments were performed by N.I. and L.W. W.W.C.T. collected human embryos and performed immunofluorescence, RNA-seq, and bioinformatics analysis, together with S.D. and Y.M. Experiments on Tcam-2, including the knockdowns, exogenous SOX17 expression experiments, and western blot analysis, were performed by T.K. The study was supervised by M.A.S. and J.H.H. The manuscript was written by N.I., W.W.C.T., J.H.H., and M.A.S. with input from most authors.

ACKNOWLEDGMENTS

We thank Rick Livesey and his lab for help with the culture of hESCs; Sohei Kitazawa and Janet Shipley for the Tcam-2 cells; Nigel Miller and Andy Riddell for cell sorting; Roger Barker, Xiaoling He, and Pam Tyers for collection of human embryos; and Charles Bradshaw for help with bioinformatics. We thank members of the Surani and Hanna labs for important discussions and technical help. N.I. is supported by Grant-in-Aid for fellows of the JSPS and by BIRAX (the Britain Israel Research and Academic Exchange Partnership) initiative, who provided a project grant to J.H.H. and M.A.S. J.H.H. is supported by Ilana and Pascal Mantoux, the Kimmel Award, ERC (StG-2011-281906), Helmsley Charitable Trust, ISF (Bikura, Morasha, ICORE), ICRF, the Abisch Frenkel Foundation, the Fritz Thyssen Stiftung, Erica and Robert Drake, Benozio Endowment fund, and the Flight Attendant Medical Research Institute (FAMRI). J.H.H. is a New York Stem Cell Foundation Robertson Investigator. W.C.T. is supported by Croucher Foundation and Cambridge Trust; M.A.S. is supported by HFSP and a Wellcome Trust Investigator Award.

Received: August 8, 2014

Revised: November 13, 2014

Accepted: December 4, 2014

Published: December 24, 2014

REFERENCES

Aramaki, S., Hayashi, K., Kurimoto, K., Ohta, H., Yabuta, Y., Iwanari, H., Mochizuki, Y., Hamakubo, T., Kato, Y., Shirahige, K., and Saitou, M. (2013).

- A mesodermal factor, T, specifies mouse germ cell fate by directly activating germline determinants. *Dev. Cell* 27, 516–529.
- Barrios, F., Irie, N., and Surani, M.A. (2013). Perceiving signals, building networks, reprogramming germ cell fate. *Int. J. Dev. Biol.* 57, 123–132.
- Bernardo, A.S., Faial, T., Gardner, L., Niakan, K.K., Ortmann, D., Senner, C.E., Callery, E.M., Trotter, M.W., Hemberger, M., Smith, J.C., et al. (2011). BRACHYURY and CDX2 mediate BMP-induced differentiation of human and mouse pluripotent stem cells into embryonic and extraembryonic lineages. *Cell Stem Cell* 9, 144–155.
- Brocard, J., Feil, R., Chambon, P., and Metzger, D. (1998). A chimeric Cre recombinase inducible by synthetic, but not by natural ligands of the glucocorticoid receptor. *Nucleic Acids Res.* 26, 4086–4090.
- Chen, Y., Blair, K., and Smith, A. (2013). Robust self-renewal of rat embryonic stem cells requires fine-tuning of glycogen synthase kinase-3 inhibition. *Stem Cell Reports* 1, 209–217.
- Chia, N.Y., Chan, Y.S., Feng, B., Lu, X., Orlov, Y.L., Moreau, D., Kumar, P., Yang, L., Jiang, J., Lau, M.S., et al. (2010). A genome-wide RNAi screen reveals determinants of human embryonic stem cell identity. *Nature* 468, 316–320.
- Clarke, R.L., Yzaguirre, A.D., Yashiro-Ohtani, Y., Bondue, A., Blanpain, C., Pear, W.S., Speck, N.A., and Keller, G. (2013). The expression of Sox17 identifies and regulates haemogenic endothelium. *Nat. Cell Biol.* 15, 502–510.
- D'Amour, K.A., Agulnick, A.D., Eliazer, S., Kelly, O.G., Kroon, E., and Baetge, E.E. (2005). Efficient differentiation of human embryonic stem cells to definitive endoderm. *Nat. Biotechnol.* 23, 1534–1541.
- de Fellici, M. (2013). Origin, migration, and proliferation of human primordial germ cells. In *Oogenesis*, G. Coticchio, D.F. Albertini, and L. De Santis, eds. (London: Springer-Verlag), pp. 19–37.
- de Jong, J., Stoop, H., Gillis, A.J., van Gurp, R.J., van de Geijn, G.J., Boer, M., Hersmus, R., Saunders, P.T., Anderson, R.A., Oosterhuis, J.W., and Looijenga, L.H. (2008). Differential expression of SOX17 and SOX2 in germ cells and stem cells has biological and clinical implications. *J. Pathol.* 215, 21–30.
- De Miguel, M.P., Fuentes-Julián, S., and Alcaina, Y. (2010). Pluripotent stem cells: origin, maintenance and induction. *Stem Cell Rev.* 6, 633–649.
- Eckert, D., Biermann, K., Nettersheim, D., Gillis, A.J., Steger, K., Jäck, H.M., Müller, A.M., Looijenga, L.H., and Schorle, H. (2008). Expression of BLIMP1/PRMT5 and concurrent histone H2A/H4 arginine 3 dimethylation in fetal germ cells, CIS/IGCNU and germ cell tumors. *BMC Dev. Biol.* 8, 106.
- Gafni, O., Weinberger, L., Mansour, A.A., Manor, Y.S., Chomsky, E., Ben-Yosef, D., Kalma, Y., Viukov, S., Maza, I., Zviran, A., et al. (2013). Derivation of novel human ground state naive pluripotent stem cells. *Nature* 504, 282–286.
- Gkoutela, S., Li, Z., Vincent, J.J., Zhang, K.X., Chen, A., Pellegrini, M., and Clark, A.T. (2013). The ontogeny of cKIT+ human primordial germ cells proves to be a resource for human germ line reprogramming, imprint erasure and in vitro differentiation. *Nat. Cell Biol.* 15, 113–122.
- Grabole, N., Tischler, J., Hackett, J.A., Kim, S., Tang, F., Leitch, H.G., Magnúsdóttir, E., and Surani, M.A. (2013). Prdm14 promotes germline fate and naive pluripotency by repressing FGF signalling and DNA methylation. *EMBO Rep.* 14, 629–637.
- Hackett, J.A., and Surani, M.A. (2014). Regulatory principles of pluripotency: from the ground state up. *Cell Stem Cell* 15, 416–430.
- Hackett, J.A., Zyllicz, J.J., and Surani, M.A. (2012). Parallel mechanisms of epigenetic reprogramming in the germline. *Trends Genet.* 28, 164–174.
- Hackett, J.A., Sengupta, R., Zyllicz, J.J., Murakami, K., Lee, C., Down, T.A., and Surani, M.A. (2013). Germline DNA demethylation dynamics and imprint erasure through 5-hydroxymethylcytosine. *Science* 339, 448–452.
- Hara, K., Kanai-Azuma, M., Uemura, M., Shitara, H., Taya, C., Yonekawa, H., Kawakami, H., Tsunekawa, N., Kurohmaru, M., and Kanai, Y. (2009). Evidence for crucial role of hindgut expansion in directing proper migration of primordial germ cells in mouse early embryogenesis. *Dev. Biol.* 330, 427–439.
- Hayashi, K., and Surani, M.A. (2009). Self-renewing epiblast stem cells exhibit continual delineation of germ cells with epigenetic reprogramming in vitro. *Development* 136, 3549–3556.
- Hayashi, K., de Sousa Lopes, S.M.C., and Surani, M.A. (2007). Germ cell specification in mice. *Science* 316, 394–396.
- Hayashi, K., Ohta, H., Kurimoto, K., Aramaki, S., and Saitou, M. (2011). Reconstitution of the mouse germ cell specification pathway in culture by pluripotent stem cells. *Cell* 146, 519–532.
- Heard, E., and Martienssen, R.A. (2014). Transgenerational epigenetic inheritance: myths and mechanisms. *Cell* 157, 95–109.
- Imamura, M., Hikabe, O., Lin, Z.Y., and Okano, H. (2014). Generation of germ cells in vitro in the era of induced pluripotent stem cells. *Mol. Reprod. Dev.* 81, 2–19.
- Irie, N., Tang, W.W., and Azim Surani, M. (2014). Germ cell specification and pluripotency in mammals: a perspective from early embryogenesis. *Reprod. Med. Biol.* 13, 203–215.
- Julatón, V.T., and Reijo Pera, R.A. (2011). NANOS3 function in human germ cell development. *Hum. Mol. Genet.* 20, 2238–2250.
- Kanai-Azuma, M., Kanai, Y., Gad, J.M., Tajima, Y., Taya, C., Kurohmaru, M., Sanai, Y., Yonekawa, H., Yazaki, K., Tam, P.P., and Hayashi, Y. (2002). Depletion of definitive gut endoderm in Sox17-null mutant mice. *Development* 129, 2367–2379.
- Kee, K., Angeles, V.T., Flores, M., Nguyen, H.N., and Reijo Pera, R.A. (2009). Human DAZL, DAZ and BOULE genes modulate primordial germ-cell and haploid gamete formation. *Nature* 462, 222–225.
- Kim, S., Günesdogan, U., Zyllicz, J.J., Hackett, J.A., Cougot, D., Bao, S., Lee, C., Dietmann, S., Allen, G.E., Sengupta, R., and Surani, M.A. (2014). PRMT5 Protects Genomic Integrity during Global DNA Demethylation in Primordial Germ Cells and Preimplantation Embryos. *Mol. Cell* 56, 564–579.
- Kurimoto, K., Yabuta, Y., Ohinata, Y., Shigeta, M., Yamanaka, K., and Saitou, M. (2008). Complex genome-wide transcription dynamics orchestrated by Blimp1 for the specification of the germ cell lineage in mice. *Genes Dev.* 22, 1617–1635.
- Lawson, K.A., Dunn, N.R., Roelen, B.A., Zeinstra, L.M., Davis, A.M., Wright, C.V., Korving, J.P., and Hogan, B.L. (1999). Bmp4 is required for the generation of primordial germ cells in the mouse embryo. *Genes Dev.* 13, 424–436.
- Leitch, H.G., Tang, W.W., and Surani, M.A. (2013). Primordial germ-cell development and epigenetic reprogramming in mammals. *Curr. Top. Dev. Biol.* 104, 149–187.
- Lin, I.Y., Chiu, F.L., Yeang, C.H., Chen, H.F., Chuang, C.Y., Yang, S.Y., Hou, P.S., Sintupisut, N., Ho, H.N., Kuo, H.C., and Lin, K.I. (2014). Suppression of the SOX2 neural effector gene by PRDM1 promotes human germ cell fate in embryonic stem cells. *Stem Cell Reports* 2, 189–204.
- Liu, X., Gao, Q., Li, P., Zhao, Q., Zhang, J., Li, J., Koseki, H., and Wong, J. (2013). UHRF1 targets DNMT1 for DNA methylation through cooperative binding of hemi-methylated DNA and methylated H3K9. *Nat. Commun.* 4, 1563.
- Looijenga, L.H., Stoop, H., and Biermann, K. (2014). Testicular cancer: biology and biomarkers. *Virchows Arch.* 464, 301–313.
- Ma, Z., Swigut, T., Valouev, A., Rada-Iglesias, A., and Wysocka, J. (2011). Sequence-specific regulator Prdm14 safeguards mouse ESCs from entering extraembryonic endoderm fates. *Nat. Struct. Mol. Biol.* 18, 120–127.
- Magnúsdóttir, E., and Surani, M.A. (2014). How to make a primordial germ cell. *Development* 141, 245–252.
- Magnúsdóttir, E., Dietmann, S., Murakami, K., Günesdogan, U., Tang, F., Bao, S., Diamanti, E., Lao, K., Gottgens, B., and Azim Surani, M. (2013). A tripartite transcription factor network regulates primordial germ cell specification in mice. *Nat. Cell Biol.* 15, 905–915.
- Malavasi, F., Deaglio, S., Funaro, A., Ferrero, E., Horenstein, A.L., Ortolan, E., Vaisitti, T., and Aydin, S. (2008). Evolution and function of the ADP ribosyl cyclase/CD38 gene family in physiology and pathology. *Physiol. Rev.* 88, 841–886.

- Mendjan, S., Mascetti, V.L., Ortmann, D., Ortiz, M., Karjosukarso, D.W., Ng, Y., Moreau, T., and Pedersen, R.A. (2014). NANOG and CDX2 pattern distinct subtypes of human mesoderm during exit from pluripotency. *Cell Stem Cell* 15, 310–325.
- Nakajima-Takagi, Y., Osawa, M., Oshima, M., Takagi, H., Miyagi, S., Endoh, M., Endo, T.A., Takayama, N., Eto, K., Toyoda, T., et al. (2013). Role of SOX17 in hematopoietic development from human embryonic stem cells. *Blood* 121, 447–458.
- Nakaki, F., Hayashi, K., Ohta, H., Kurimoto, K., Yabuta, Y., and Saitou, M. (2013). Induction of mouse germ-cell fate by transcription factors in vitro. *Nature* 501, 222–226.
- Nichols, J., and Smith, A. (2009). Naive and primed pluripotent states. *Cell Stem Cell* 4, 487–492.
- Ohinata, Y., Payer, B., O'Carroll, D., Ancelin, K., Ono, Y., Sano, M., Barton, S.C., Obukhanych, T., Nussenzweig, M., Tarakhovsky, A., et al. (2005). Blimp1 is a critical determinant of the germ cell lineage in mice. *Nature* 436, 207–213.
- Pallesen, G., and Hamilton-Dutoit, S.J. (1988). Ki-1 (CD30) antigen is regularly expressed by tumor cells of embryonal carcinoma. *Am. J. Pathol.* 133, 446–450.
- Pera, R.A. (2013). Status of human germ cell differentiation from pluripotent stem cells. *Reprod. Fertil. Dev.* 25, 396–404.
- Saitou, M., Barton, S.C., and Surani, M.A. (2002). A molecular programme for the specification of germ cell fate in mice. *Nature* 418, 293–300.
- Schafer, S., Anschlag, J., Nettersheim, D., Haas, N., Pawig, L., and Schorle, H. (2011). The role of BLIMP1 and its putative downstream target TFAP2C in germ cell development and germ cell tumours. *Int. J. Androl.* 34, e152–e158, discussion e158–e159.
- Shoji, M., Tanaka, T., Hosokawa, M., Reuter, M., Stark, A., Kato, Y., Kondoh, G., Okawa, K., Chujo, T., Suzuki, T., et al. (2009). The TDRD9-MIWI2 complex is essential for piRNA-mediated retrotransposon silencing in the mouse male germline. *Dev. Cell* 17, 775–787.
- Skakkebaek, N.E. (1972). Possible carcinoma-in-situ of the testis. *Lancet* 2, 516–517.
- Vincent, S.D., Dunn, N.R., Sciammas, R., Shapiro-Shalef, M., Davis, M.M., Calame, K., Bikoff, E.K., and Robertson, E.J. (2005). The zinc finger transcriptional repressor Blimp1/Prdm1 is dispensable for early axis formation but is required for specification of primordial germ cells in the mouse. *Development* 132, 1315–1325.
- Watanabe, K., Ueno, M., Kamiya, D., Nishiyama, A., Matsumura, M., Wataya, T., Takahashi, J.B., Nishikawa, S., Nishikawa, S., Muguruma, K., and Sasai, Y. (2007). A ROCK inhibitor permits survival of dissociated human embryonic stem cells. *Nat. Biotechnol.* 25, 681–686.
- Weber, S., Eckert, D., Nettersheim, D., Gillis, A.J., Schäfer, S., Kuckenberger, P., Ehlermann, J., Werling, U., Biermann, K., Looijenga, L.H., and Schorle, H. (2010). Critical function of AP-2 gamma/TFAP2C in mouse embryonic germ cell maintenance. *Biol. Reprod.* 82, 214–223.
- Yamaji, M., Seki, Y., Kurimoto, K., Yabuta, Y., Yuasa, M., Shigeta, M., Yamana, K., Ohinata, Y., and Saitou, M. (2008). Critical function of Prdm14 for the establishment of the germ cell lineage in mice. *Nat. Genet.* 40, 1016–1022.
- Yamaji, M., Ueda, J., Hayashi, K., Ohta, H., Yabuta, Y., Kurimoto, K., Nakato, R., Yamada, Y., Shirahige, K., and Saitou, M. (2013). PRDM14 ensures naive pluripotency through dual regulation of signaling and epigenetic pathways in mouse embryonic stem cells. *Cell Stem Cell* 12, 368–382.
- Ying, Q.-L., Wray, J., Nichols, J., Battle-Morera, L., Doble, B., Woodgett, J., Cohen, P., and Smith, A. (2008). The ground state of embryonic stem cell self-renewal. *Nature* 453, 519–523.
- Yu, P., Pan, G., Yu, J., and Thomson, J.A. (2011). FGF2 sustains NANOG and switches the outcome of BMP4-induced human embryonic stem cell differentiation. *Cell Stem Cell* 8, 326–334.

Gremlin 1 Identifies a Skeletal Stem Cell with Bone, Cartilage, and Reticular Stromal Potential

Daniel L. Worthley,^{1,2,3,4} Michael Churchill,¹ Jocelyn T. Compton,⁵ Yagnesh Tailor,¹ Meenakshi Rao,⁶ Yiling Si,¹ Daniel Levin,⁷ Matthew G. Schwartz,⁸ Aysu Uygur,⁸ Yoku Hayakawa,¹ Stefanie Gross,⁹ Bernhard W. Renz,¹ Wanda Setlik,¹⁰ Ashley N. Martinez,⁵ Xiaowei Chen,¹ Saqib Nizami,⁵ Heon Goo Lee,⁵ H. Paco Kang,⁵ Jon-Michael Caldwell,⁵ Samuel Asfaha,¹ C. Benedikt Westphalen,^{1,11} Trevor Graham,¹² Guangchun Jin,¹ Karan Nagar,¹ Hongshan Wang,¹ Mazen A. Kheirbek,¹³ Alka Kolhe,¹ Jared Carpenter,¹ Mark Glaire,¹ Abhinav Nair,¹ Simon Renders,¹ Nicholas Manieri,¹⁴ Sureshkumar Muthupalani,¹⁵ James G. Fox,¹⁵ Maximilian Reichert,¹⁶ Andrew S. Giraud,⁴ Robert F. Schwabe,¹ Jean-Phillipe Pradere,^{1,17} Katherine Walton,¹⁸ Ajay Prakash,¹⁸ Deborah Gumucio,¹⁸ Anil K. Rustgi,¹⁶ Thaddeus S. Stappenbeck,¹⁴ Richard A. Friedman,¹⁹ Michael D. Gershon,¹⁰ Peter Sims,²⁰ Tracy Grikscheit,⁷ Francis Y. Lee,⁵ Gerard Karsenty,⁹ Siddhartha Mukherjee,^{1,21,*} and Timothy C. Wang^{1,21,*}

¹Department of Medicine and Irving Cancer Research Center, Columbia University, New York, NY 10032, USA

²Department of Medicine, University of Adelaide, SA, 5005, Australia

³Cancer theme, South Australian Health and Medical Research Institute, SA, 5001, Australia

⁴Murdoch Children's Research Institute, Royal Children's Hospital, Vic., 3052, Australia

⁵Department of Orthopedic Surgery, Columbia University Medical Center, New York, NY 10032, USA

⁶Department of Pediatrics, Columbia University, New York, NY 10032, USA

⁷Children's Hospital Los Angeles, Saban Research Institute, Keck School of Medicine of the University of Southern California, Los Angeles, CA 90027, USA

⁸Department of Genetics, Harvard Medical School, Boston, MA 02114, USA

⁹Department of Genetics and Development, Columbia University, New York, NY 10032, USA

¹⁰Department of Pathology and Cell Biology, Columbia University, New York, NY 10032, USA

¹¹Department of Internal Medicine III, University Hospital Munich, Ludwig-Maximilians-University Munich - Campus Großhadern, Munich 81377, Germany

¹²Barts Cancer Institute, Barts and the London School of Medicine and Dentistry, Queen Mary University of London, London EC1M 6BQ, UK

¹³Department of Psychiatry, Columbia University, New York, NY 10032, USA

¹⁴Department of Pathology and Immunology, Washington University, St. Louis, MO 63110, USA

¹⁵Division of Comparative Medicine, Massachusetts Institute of Technology, Cambridge, MA 02139, USA

¹⁶Division of Gastroenterology, Departments of Medicine and Genetics, Abramson Cancer Center, University of Pennsylvania Perelman School of Medicine, Philadelphia, PA 19104, USA

¹⁷Institut National de la Santé et de la Recherche Médicale (INSERM), Université Paul Sabatier, Institut des Maladies Métaboliques et Cardiovasculaires (I2MC)- UMR1048, Toulouse 31432, France

¹⁸Department of Cell and Developmental Biology, University of Michigan, Ann Arbor, MI 48109, USA

¹⁹Herbert Irving Comprehensive Cancer Center Biomedical Informatics Shared Resource and Department of Biomedical Informatics, Columbia University, New York, NY 10032, USA

²⁰Department of Systems Biology, Columbia University, NY, 10032, USA

²¹Co-senior authors

*Correspondence: sm3252@columbia.edu (S.M.), tcw21@columbia.edu (T.C.W.)

<http://dx.doi.org/10.1016/j.cell.2014.11.042>

SUMMARY

The stem cells that maintain and repair the postnatal skeleton remain undefined. One model suggests that perisinusoidal mesenchymal stem cells (MSCs) give rise to osteoblasts, chondrocytes, marrow stromal cells, and adipocytes, although the existence of these cells has not been proven through fate-mapping experiments. We demonstrate here that expression of the bone morphogenetic protein (BMP) antagonist gremlin 1 defines a population of osteochondroreticular (OCR) stem cells in the bone marrow. OCR stem cells self-renew and generate osteoblasts, chondrocytes, and reticular marrow stromal cells, but not adipocytes. OCR stem cells

are concentrated within the metaphysis of long bones not in the perisinusoidal space and are needed for bone development, bone remodeling, and fracture repair. *Gremlin 1* expression also identifies intestinal reticular stem cells (iRSCs) that are cells of origin for the periepithelial intestinal mesenchymal sheath. *Gremlin 1* expression identifies distinct connective tissue stem cells in both the bone (OCR stem cells) and the intestine (iRSCs).

INTRODUCTION

Long bones consist of a cortex supported by an internal framework of trabecular bone. The trabecular bone and the adjacent cartilaginous growth plates contain the cellular progenitors

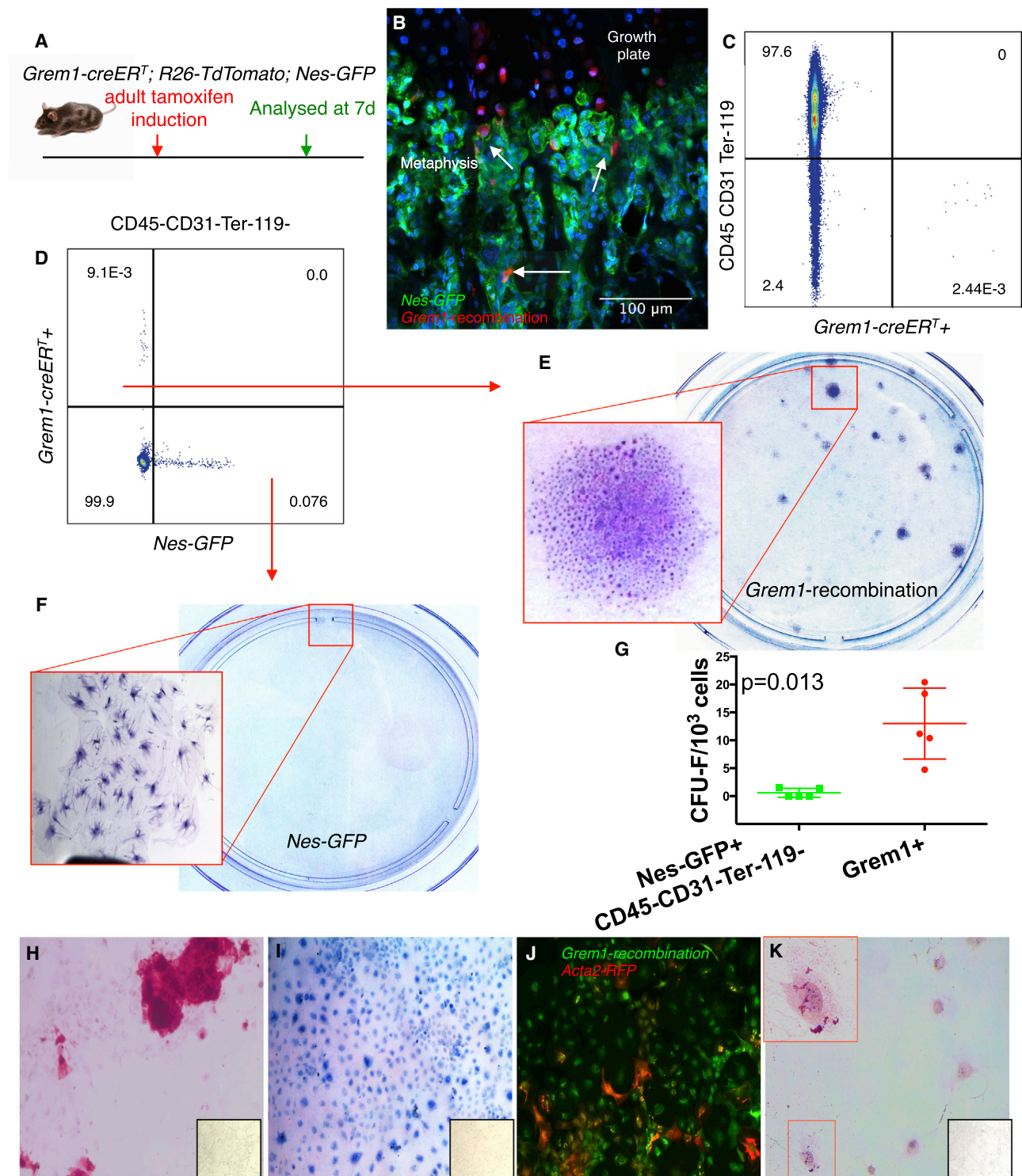


Figure 1. *Grem1* Identifies Rare Adult Multipotent Mesenchymal Stromal Cells

(A) Protocol and (B) *Grem1-creERT^T; R26-LSL-TdTomato; Nes-GFP* mouse femur, showing that metaphyseal Nes-GFP⁺ (green) and *Grem1*⁺ cells (red, white arrows) are distinct.

(C) Adult *Grem1-creERT^T; R26-LSL-TdTomato* bone marrow cells are rare and mesenchymal (CD45⁻CD31⁻Ter-119⁻).

(D–G) Adult *Grem1-creERT^T; R26-LSL-TdTomato; Nes-GFP* mice: *Grem1* and mesenchymal Nes-GFP cells do not overlap, and clonogenicity is greater in the *Grem1*⁺ versus the mesenchymal Nes-GFP⁺ cells (CD45⁻CD31⁻Ter-119⁻). (E and F) 10 cm cell culture dish; (G) n = 5, data shown with mean \pm SD, p = 0.013.

(legend continued on next page)

necessary for postnatal bone growth. The prevailing model for the development, growth, and repair of long bones proposes two phases. First, cartilage cells lay down a matrix that forms a “scaffold” for bone formation. Osteoblasts then invade this matrix and lay down the mineralized parts of bone (Kronenberg, 2003). Although this process—termed “endochondral ossification”—has been known for decades, it remains unclear whether postnatal bones are grown and repaired by osteoblasts and chondrocytes already committed to their respective lineages, or whether there are specialized multipotent cells that determine postnatal growth and repair.

The mesenchymal stem cell (MSC) model suggests that a self-renewing stem cell exists within the bone marrow that gives rise to mature osteoblasts, chondrocytes, adipocytes, and marrow stromal cells required for skeletal development, homeostasis, and repair. A prime candidate for the endogenous MSC has been the mesenchymal cells that surround the bone marrow sinusoids (Bianco et al., 2013). Perisinusoidal mesenchymal cells are marked by nestin (*Nes*)-GFP (Méndez-Ferrer et al., 2010) and leptin receptor (*Lepr*)-cre (Ding et al., 2012; Mizoguchi et al., 2014; Zhou et al., 2014) in mice and by CD146 in humans (Sacchetti et al., 2007).

Recently, perisinusoidal mesenchymal cells expressing *Lepr* were found to include multipotent, colony-forming unit-fibroblasts (CFU-Fs) (Zhou et al., 2014). Lineage-tracing studies revealed that this perisinusoidal population also contained cells with in vivo osteogenic and adipogenic potential; however, these cells gave rise to osteo-adipogenic lineages exclusively in adult animals (>8 weeks of age) and not during development or bone growth (Ding et al., 2012; Mizoguchi et al., 2014; Zhou et al., 2014). Furthermore, *Lepr*-expressing perisinusoidal cells never contributed to normal developing chondrocytes, the major cell lineage generating the cartilaginous matrix required for endochondral ossification (Ding et al., 2012; Mizoguchi et al., 2014; Zhou et al., 2014). Thus, perisinusoidal MSCs do not fulfill all of the characteristics expected of a skeletal MSC. In addition, putative MSC markers such as *Nes* (Méndez-Ferrer et al., 2010) have failed to prove that single MSCs have in vivo postnatal multipotentiality and self-renewal. Together, these data raise the prospect that another complementary postnatal skeletal stem cell may exist.

We developed an inducible *Cre* transgenic line marking a skeletal stem cell. In doing so, we discovered the osteochondroreticular (OCR) stem cell. We also provide evidence indicating that analogous connective tissue stem cells, intestinal reticular stem cells (iRSCs), exist in the small intestine.

RESULTS

Generating a Specific Marker of Skeletal Stem Cells

To select a specific MSC marker in the bone and intestine, we considered human gene-expression arrays from bone marrow, intestine, and peritumoral mesenchyme (Delorme et al., 2009;

Kosinski et al., 2007; Sneddon et al., 2006). Gremlin 1 (*Grem1*), identified from these studies, is a secreted antagonist of bone morphogenetic protein (Bmp) -2, -4, and -7 and a VEGFR2 agonist (Hsu et al., 1998; Mitola et al., 2010). *Grem1* is important in normal skeletal and renal development and homeostasis (Canalis et al., 2012; Khokha et al., 2003; Michos et al., 2004). Furthermore, overexpression of *Grem1* interrupts normal intestinal function and has been linked to intestinal cancer (Jaeger et al., 2012).

We previously found that *Grem1* expression identified the most clonogenic fraction of marrow stromal cultures (Quante et al., 2011). In the present study, we confirmed that expression of *Grem1* was increased in undifferentiated mesenchymal cultures compared to endogenous bone marrow mesenchyme (Figures S1A–S1C available online).

To extend these findings in vivo, we generated a tamoxifen-inducible BAC transgenic *creER^T* line specific for *Grem1* expression (*Grem1-creER^T*, Figures S1D–S1F, Table S1A). The *Grem1-creER^T* BAC transgenic line was crossed to different reporters (such as *R26-LSL-TdTomato* and *R26-LSL-ZsGreen*) and the *R26-LSL-diphtheria toxin subunit A* (*DTA*) line to allow lineage tracing and functional ablation of specific mesenchymal cells, respectively (See Tables S1B and S1C for summary of transgenic lines).

Grem1⁺ Cells Are Distinct from, and More Clonogenic than, *Nes*-GFP⁺ MSCs

Tamoxifen induction of adult *Grem1-creER^T*; *R26-LSL-TdTomato* mice (Figure 1A) resulted in recombination in and expression of the TdTomato reporter (red fluorescent protein) in a rare and exclusively mesenchymal population of bone marrow cells (0.0025% of all single, live, nucleated cells after collagenase digestion [95% confidence interval (CI) 0.0022–0.0028]). In this experiment and elsewhere in the paper, we defined skeletal mesenchyme as triple negative for CD45^{Ter-119}CD31⁺ in enzymatically digested bone and bone marrow cells. CD45 characterizes most hematopoietic cells with the exception of maturing erythroid cells, which are marked by Ter-119. CD31 was used to exclude endothelial cells (Park et al., 2012) (Table S1D). The CD45-negative, Ter-119-negative, and CD31-negative fraction of bone marrow defines the nonendothelial, nonhematopoietic compartment that contains putative skeletal stem cells. Many *Grem1-creER^T* cells, identified by a recombined fluorescent reporter gene shortly after tamoxifen administration (hereafter referred to as *Grem1*⁺ cells), were immediately adjacent to the growth plate and trabecular bone (Figures 1B, 1C, and 5B).

To determine the overlap between *Grem1*⁺ and other reported CFU-F populations, we crossed *Grem1-creER^T* to *Nes-GFP*; *R26-LSL-TdTomato* (*Grem1*⁺ cells and their progeny were red, and *Nes-GFP*-expressing cells were green) and to *Acta2-RFP*; *R26-LSL-ZsGreen* (*Grem1*⁺ cells and their progeny were green, and *Acta2-RFP*-expressing cells were red) (Grcevic et al., 2012; Méndez-Ferrer et al., 2010). Adult *Grem1*⁺ cells

(H–K) *Grem1*⁺ cells from *Grem1-creER^T*; *R26-LSL-ZsGreen*; *Acta2-RFP* mice could be clonally expanded in vitro and differentiated into bone (H) (alizarin red), cartilage (I) (toluidine blue), and myofibroblasts (J) (*Grem1*⁺ green-derived cells with coexpression of *Acta2* [red]), but very limited adipogenesis (oil red) (K). Lower right insets show equivalent stain in a control marrow culture.

In all graphs, the data are shown with the mean ± SD.

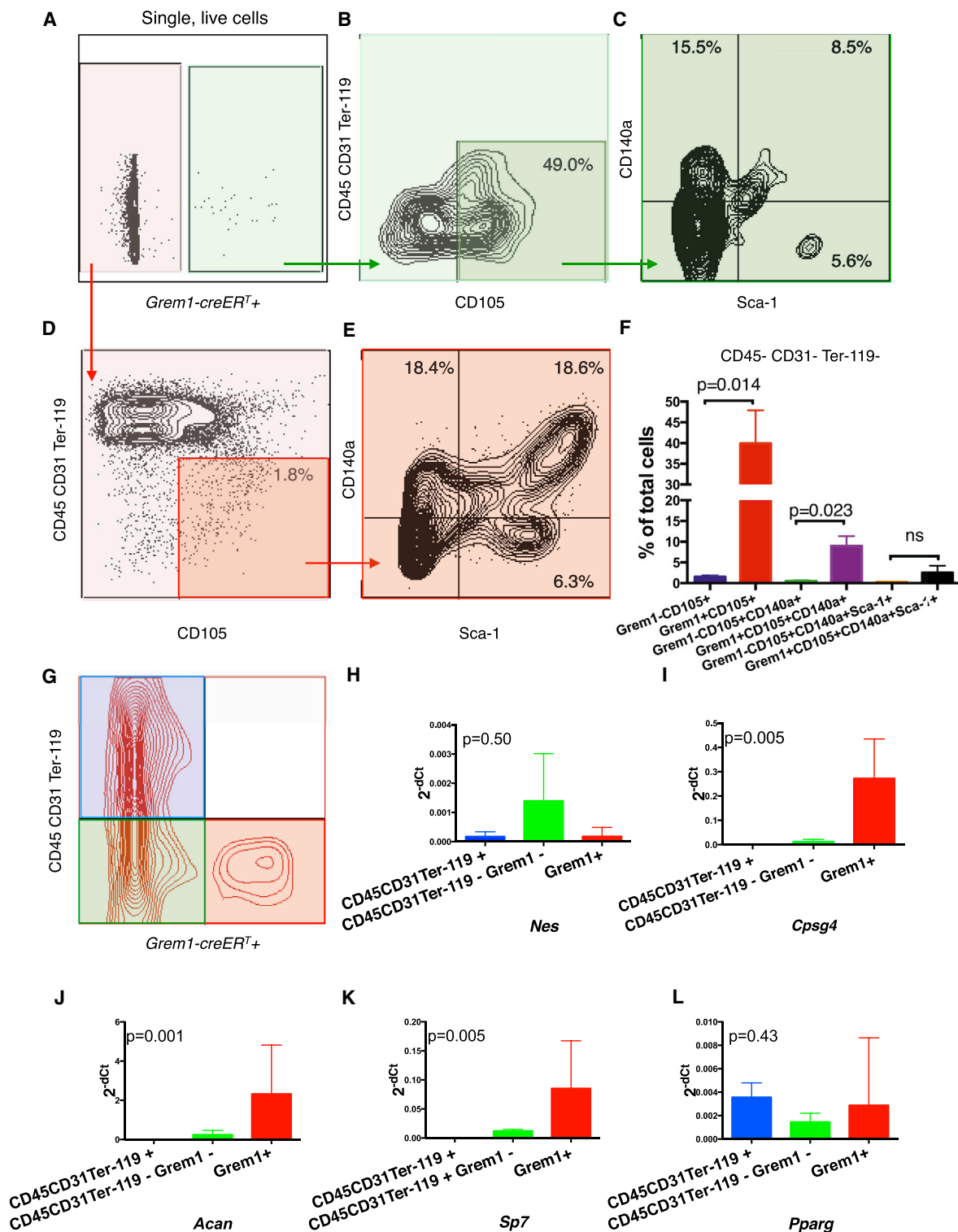


Figure 2. *Grem1*⁺ Cells Are Enriched for CD105 Bone Marrow Cells with Upregulated Osteochondral versus Adipogenic Gene Expression (A–F) *n* = 3, *Grem1*⁺ cells from adult, collagenase-digested whole bone and bone marrow were compared to the *Grem1*-negative population. On average, 40% (95% CI 20%–60%) of all *Grem1* cells were CD45⁻CD31⁻Ter-119⁻CD105⁺ compared to only 1.8% of *Grem1*-negative cells (F, *p* = 0.014). (C) *Grem1*⁺ cells, however, were not further enriched for other MSC markers CD140a and Sca-1. *Grem1*⁺ and *Grem1*-negative cells were compared across the increasingly specific immunophenotypes; data shown with mean ± SD.

(legend continued on next page)

did not express *Nes-GFP* (Figures 1B and 1D), and only a minority of *Grem1*⁺ cells expressed *Acta2-RFP* (mean 5.9% of *Grem1*⁺ were *Acta2*⁺; Figure S2A). The *Grem1*⁺ population was more clonogenic than *Nes-GFP* or *Acta2-RFP* cells, even after depletion of contaminating nonmesenchymal lineages (Figures 1D–1G and S2B). *Grem1*⁺ CFU-Fs did not initially express *Acta2-RFP*, but during culture, the *Grem1*⁺ progeny differentiated into *Acta2-RFP*-expressing myofibroblasts (these cells were yellow, expressing both *ZsGreen* and *Acta2-RFP*; Figure S2C). Importantly, the proportion of CFU-Fs was diminished within the *Grem1*⁺ descendants expressing *Acta2-RFP*, suggesting that *Acta2* expression marks a more differentiated cell less capable of clonogenic growth (Figure S2D). *Grem1*⁺ cells, however, never gave rise to *Nes-GFP*-expressing cells, either in adherent culture or in vivo (10 months tracing after adult tamoxifen induction of *Grem1-creER^T;R26-LSL-TdTomato;Nes-GFP* mice; Figure S2E).

For the clonal differentiation experiments (Figure 1), adult *Grem1-creER^T;R26-LSL-ZsGreen;Acta2-RFP* and *Grem1-creER^T;R26-LSL-TdTomato* mice were administered tamoxifen by oral gavage at 6–8 weeks of age. Bones were processed as described (see Experimental Procedures), and the fluorescent *Grem1*⁺ cells were sorted by fluorescence-activated cell sorting (FACS) and plated at clonal density < 2,500 cells/10 cm dish. Clones (i.e., isolated clusters of > 50 cells at 10–14 days) were harvested using a cloning cylinder and expanded into individual wells for differentiation. We evaluated 19 clones after in vitro differentiation. Single clones gave rise to osteoblasts (defined by alizarin red [Figure 1H] or alkaline phosphatase staining in 84% of clones, [Figures S2F and S2G]), chondrocytes (100% of clones confirmed by toluidine blue staining), and myofibroblasts on the basis of coexpression of the *Acta2-RFP* transgene (100%, Figures 1H–1J). In contrast, the *Grem1*⁺ cell-derived clones showed little capacity for adipocytic differentiation (defined by oil red staining, Figure 1K, 0 of 19 single clones). Polyclonal cultures from sorted *Grem1*⁺ cells also failed to differentiate into adipocytes.

A substantial proportion (40%) of *Grem1*⁺ cells, in addition to being triple negative for CD45⁺Ter-119⁺CD31⁺, were also positive for CD105, a well-established marker of bone marrow CFU-Fs (Park et al., 2012). In contrast, less than 2% of the *Grem1*-negative cells were CD45⁺CD31⁺Ter-119⁺CD105⁺. *Grem1*⁺ cells, however, expressed lower levels of CD140a and Sca-1 (Figures 2A–2F). The *Grem1*⁺ population was enriched for CD45⁺CD31⁺Ter-119⁺CD105⁺ cells, a subpopulation previously reported to contain all mouse bone marrow CFU-Fs (Park et al., 2012). It followed that *Grem1*⁺ cells were also enriched for CFU-Fs compared to *Grem1*-negative fractions (Data S1A and S1B). It is worth noting that we used standard adherent cell culture conditions (α MEM with 10% FBS), whereas other studies have used 20% FBS, hypoxic conditions, and a

ROCK inhibitor, which enhance the recovery of CFU-Fs (Zhou et al., 2014). Thus, the exact CFU-F efficiencies reported in our study may not be directly comparable to other reports.

Gene-expression microarray of *Grem1*⁺ versus *Grem1*-negative mesenchymal (CD45⁺CD31⁺Ter-119⁺) cells revealed 1,426 differentially expressed genes (false discovery rate [FDR] < 0.05). The *Grem1*⁺ population had significantly higher expression of many osteoblast (*Sp7*), chondrocyte (*Acan*), pericytic (*Cpsg4*, *Fap*), and putative stem cell genes (*Klf4*), all of which were confirmed by qPCR (Figures 2G–2M, Table S1E, and Data S1C and S1E). *Grem1*⁺ cells did not differentially express *Nes* (Figure 2H) or other genes typical of the perisinusoidal mesenchymal niche (Table S1E).

To determine the signaling pathways that were activated in the *Grem1*⁺ cells, we investigated candidate pathways previously reported to be relevant in MSC differentiation, such as the BMP, TGF- β , FGF/PDGF, and VEGF pathways (Gerber et al., 1999; Ng et al., 2008). Although all of these pathways were statistically significant (<2.2 $\times 10^{-16}$ by the χ^2 test), only the genes in the Bmp-activating pathway were consistently increased. *Bmp2*, *Bmp5*, *Bmp6*, the Bmp receptor *Acvr1*, and the BMP signaling target gene *Id2* were all upregulated in *Grem1*⁺ versus *Grem1*-negative mesenchymal cells (Data S1F and Table S1F). To support the role of BMP signaling in the *Grem1*⁺ population, we performed qPCR on 23 clones derived from *Grem1*⁺ bone marrow cells. *Id2* was expressed in 100% of clones, and *Bmp2* was expressed in 91% of clones. Furthermore, using flow cytometry, pSmad1,5, a marker of BMP signaling, was detected in 37.5% of *Grem1*⁺ versus 5.8% of *Grem1*-negative freshly sorted cells (Data S1G, $p = 0.004$). In contrast, genes identified in the TGF- β , FGF/PDGF, and VEGF pathways were found to be both activators and repressors and so did not generate a coherent signal constituting pathway activation (Data S1F, S1H, and S1I).

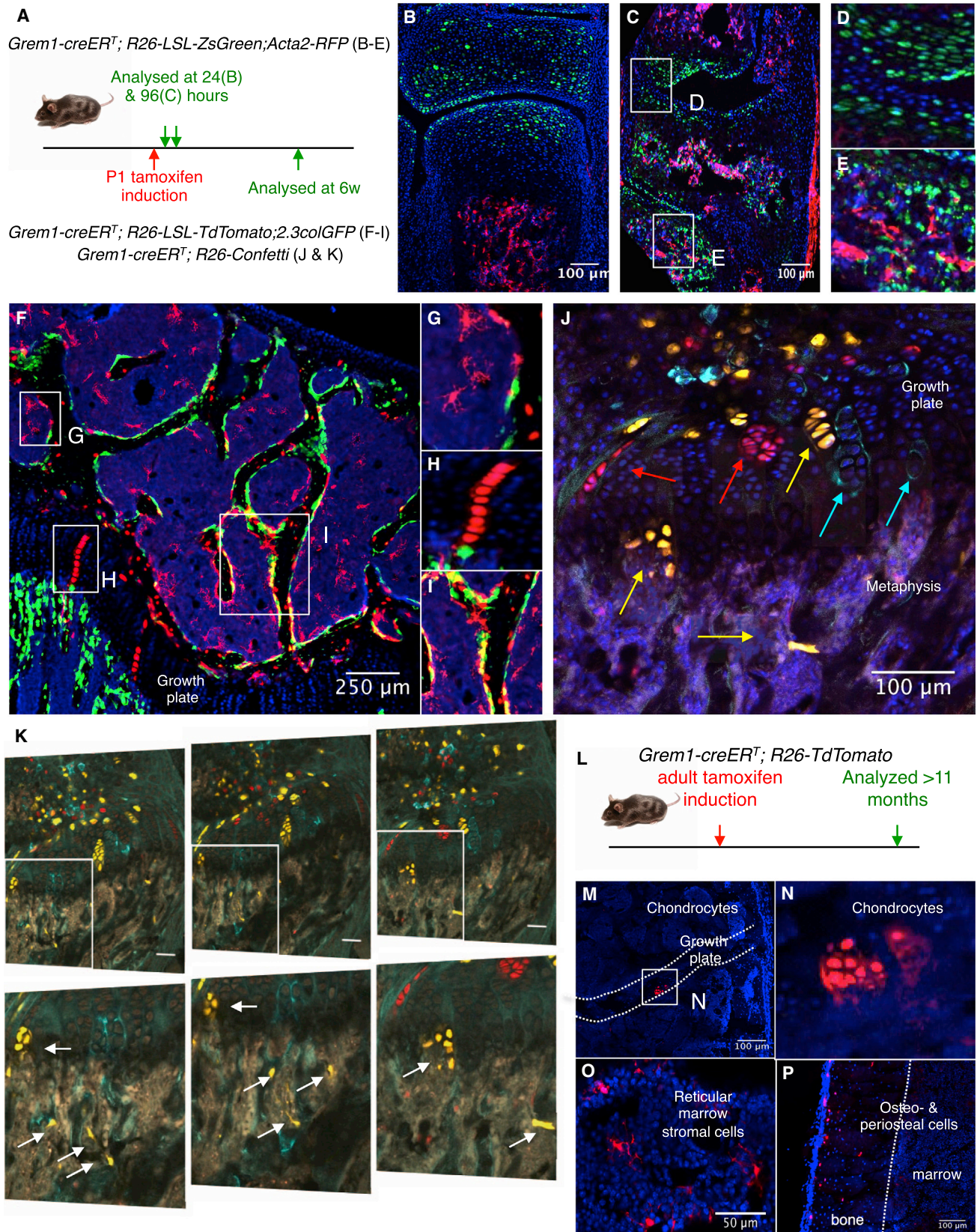
We also used an unbiased analysis in which all differentially expressed genes in *Grem1*⁺ versus *Grem1*-negative cells ($\text{fdr} < 0.05$) were evaluated against the KEGG and Reactome databases. Pathways with a gamma $\text{fdr} < 0.05$ are included in Table S1G (KEGG) and Table S1H (Reactome). The top 3 significant KEGG pathways, the ECM-receptor interaction, PI3K-Akt signaling, and focal adhesion pathways, were all activated according to PathwayGuide's statistical criterion. Differentially expressed genes from these pathways are given in Tables S1I–S1K. Many of the genes upregulated in these pathways are involved in differentiation into bone and cartilage and include the following: chondroadherin, cartilage oligomeric matrix protein, fibroblast growth factors, collagens, integrins, and cyclins. Taken together, BMP signaling along with ECM-receptor interaction, PI3K-Akt signaling, and focal adhesion pathways were all significantly activated in the *Grem1*⁺ cells and are likely to be important either in determining or as a consequence of the *Grem1*⁺ cells' osteochondral lineage potential.

(G) Microarray was performed to compare the *Grem1*⁺ (red) to the nonrecombined stromal (CD45⁺CD31⁺Ter-119⁺) population (green); in qPCR, we also sorted and evaluated the CD45⁺CD31⁺Ter-119⁺ population (blue) that did not contain any recombined cells.

(H) *Grem1*⁺ cells were not enriched for *Nes* expression.

(I–L) qPCR confirmation of microarray revealed that *Grem1*⁺ cells had increased expression of pericytic (*Cpsg4*; I) and osteochondral genes (*Acan* and *Sp7*; J and K) but no association with the adipogenic differentiation gene *Pparg* (L).

In all graphs, the data are shown with the mean \pm SD.



(legend on next page)

The expression profile of *Grem1*⁺ cells was enriched for genes implicated in bone and cartilage, rather than adipocytic, differentiation (Data S1J; Tables S1L–S1N). Furthermore, *Grem1*⁺ cells, and their derivative clones, expressed active inhibitors of adipogenesis (e.g., *Nr2f2*; Data S1K; Xu et al., 2008). The exact molecular explanation for the more restricted mesenchymal repertoire of *Grem1*⁺ cells, however, remains to be confirmed.

Further qPCR analysis of 23 *Grem1*⁺ cell-derived clones confirmed the mesenchymal homogeneity of *Grem1* cells and their derivative clones (Data S1L). Interestingly, 100% of the *Grem1*⁺ clones expressed both *Nes* and *Grem1*, and *Grem1* transcripts were also detectable within polyclonal *Nes*-GFP cultures. Thus, endogenous *Grem1* and *Nes* expression are not as mutually exclusive as their respective transgenes in vivo. Finally, *GREM1* is also expressed in human MSCs. We examined three distinct human MSC lines derived from normal bone marrow, normal synovium, or inflamed synovium. All lines expressed *GREM1* (Data S1M).

***Grem1* Cells Are Endogenous OCR Stem Cells**

Grem1-creERT⁺;R26-LSL-ZsGreen;Acta2-RFP mice were induced with perinatal tamoxifen (postnatal day [P] 1, Figure 3A). In these mice, all *Grem1*⁺ cells and their subsequent progeny were labeled by green fluorescence, and any cells expressing *Acta2* were marked by red fluorescence. Twenty-four hours after P1 induction, *Grem1*⁺ (green) cells were present within the primitive mesenchyme and the primary spongiosa of the femur. In contrast, the *Acta2*-expressing (red) stromal cells were localized within the bone marrow (Figure 3B). By P5, *Grem1*⁺ cells had differentiated into columns of chondrocytes (Figures 3C and 3D, green) as well as spindle-shaped stromal cells immediately inferior to the developing growth plate (Figures 3C and 3E).

By using *Grem1-creERT⁺;R26-LSL-TdTomato;2.3colGFP* mice, one can track *Grem1*⁺ cells and their progeny by red fluorescence, and osteoblasts are marked by green fluorescence. The *2.3colGFP* mouse is a transgenic line in which GFP expression, driven by a short 2.3 kb promoter element from the rat collagen 1a1 gene, has been used to identify committed osteoblasts (Kalajzic et al., 2002). After 6 weeks, the P1-labeled *Grem1*⁺ cells had differentiated into reticular marrow stromal cells (red), chondrocytes (red), and osteoblasts (yellow), all concentrated within the peritrabecular bone area (Figures 3F–3I). Many of the reticular marrow stromal cells anatomically spanned perivascular and endosteal regions and were CD105⁺ by immunostaining (Figure S3A). As early as 4 weeks (P28) following P1 induction,

Grem1⁺ cells give rise to approximately 64% of the bone and 50% of the chondrocytes within the metaphysis and epiphysis, albeit with little contribution to diaphyseal bone (Figure S3B).

To prove that the fluorescent cells represented clonal populations, we generated *Grem1-creERT⁺;R26-Confetti* mice and again induced at P1. Single-color clones of chondrocytes and marrow stromal cells were present by 6 weeks, confirming single-cell multipotentiality (Figures 3J and 3K). Our Monte Carlo simulation confirmed that the majority (>90%) of patches of adjacent identically colored cells (“clones”) were likely to be monoclonal in origin (see Experimental Procedures).

Approximately 12 months after adult (6–8 weeks, Figure 3L) tamoxifen induction of *Grem1-creERT⁺;R26-LSL-TdTomato* mice (and *Grem1-creERT⁺;R26-LSL-ZsGreen*, mice), we found that *Grem1*⁺ cells had differentiated into columns of chondrocytes (Figures 3M and 3N), articular cartilage (Figure S3C), reticular marrow stromal cells (Figure 3O), periosteal cells (Figure 3P), diaphyseal osteoblasts (Figure S3D), and osteocytes (Figure 3P). No adipocytes, either in the femurs (Figure S3E) or in the vertebral bodies (Figure S3F), were derived from adult *Grem1*⁺ cells, even at 1 year after tamoxifen induction. Fluorescently labeled *Grem1*⁺ cells harvested from the bone marrow after 1 year could still self-renew in vitro. The harvested *Grem1*⁺ cells in culture formed large colonies, which were clonally expanded (using cloning cylinders) to prove that they retained clonal in vitro multipotentiality, even 12 months after adult tamoxifen induction (Figure S3G). Again, in vitro differentiation was skewed to osteoblast and chondrocyte (Figures S3G–S3J), with little in vitro adipogenesis (Figure S3H). These results indicate that expression of *Grem1* also identified adult multipotent stem cells.

To confirm that *Grem1*⁺ cells were functional, postnatal skeletal stem cells, we generated *Grem1-creERT⁺;R26-LSL-ZsGreen;R26-LSL-DTA* mice and *Grem1-creERT⁺;R26-LSL-ZsGreen* littermate and related controls. In these mice, Cre-mediated excision of a STOP signal leads to the expression of the Diphtheria toxin (DTA) and thus ablation of *Grem1*-expressing cells. We administered four daily doses of 2 mg subcutaneous tamoxifen starting at P9 and measured total body and left femoral bone volume by microcomputed tomography (CT) at P23 (Quantum FX Micro-CT, Perkin-Elmer; Figures S4A–S4C). *Grem1* cells were incompletely ablated, although reduced, as assessed by the proportion of *ZsGreen*-expressing cells in the bone marrow (Figure S4A). The DTA⁺ mice were significantly smaller than the controls (Figure S4B). There was a significant difference in femoral volume between the groups and a trend toward reduced total bone volume in the DTA versus the control mice (Figure S4C).

Figure 3. Endogenous *Grem1* Cells Self-Renew and Lineage Trace Bone, Cartilage, and Stroma

(A) Protocol.

(B–E) P1 induction in *Grem1-creERT⁺;R26-LSL-ZsGreen;Acta2-RFP* mice. (B) At 24 hr after tamoxifen, *Grem1* recombined (green) only within the primary spongiosa of long bones distinct from the *Acta2-RFP* (red) cells in the marrow. But, over the following 96 hr (C), the *Grem1* cells began organizing into chondrocytic columns (D) and differentiated into stromal cells that invade the bone marrow (E) intertwined with *Acta2*-positive (red) cells.

(F–I) *Grem1-creERT⁺;R26-LSL-TdTomato;2.3colGFP* mice induced at P1, examined at 6 weeks, show that the *Grem1*⁺ cells generate reticular marrow stromal cells (G), chondrocytes in the epiphyseal plate (H), osteoblasts (*2.3colGFP*⁺, thus yellow) in the trabecular bone (I).

(J) *Grem1-creERT⁺;R26-Confetti* P1 induction, examined at 6 weeks, revealed clonal populations of chondrocytes, and (K) serial sections confirm mixed clones, yellow clone shown, of chondrocytes and marrow stromal cells, low- and higher-power (inset) images.

(L–P) Adult induction in *Grem1-creERT⁺;R26-LSL-TdTomato* analyzed 11 months after adult induction (L). *Grem1*⁺ cells had generated chondrocytes (M and N), reticular marrow stromal cells (O), and bone and periosteal cells (red) (P).

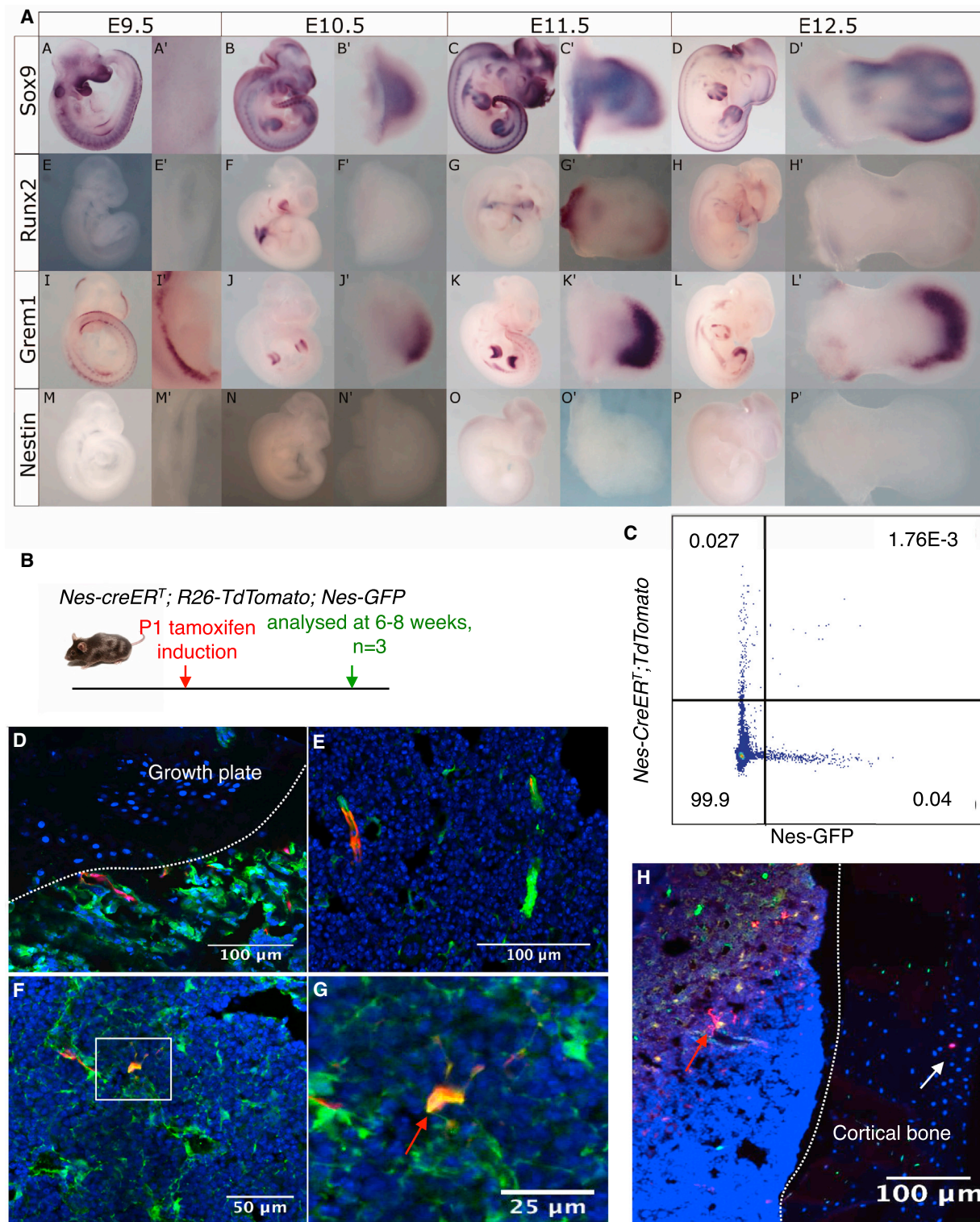


Figure 4. *Nes-GFP* Cells Make Little Contribution to Skeletal Tissues during Early Life

(A) Whole-mount in situ hybridization on mouse embryos at E9.5, E10.5, E11.5 and E12.5. These embryos were evaluated for *Sox9*, *Runx2*, *Grem1*, and *Nes* expression. *Nes-creERT⁺; R26-LSL-TdTomato; Nes-GFP* mice (n = 3) were generated to lineage trace from *Nes-GFP*-positive cells throughout the bone marrow. These mice were induced at P1 and examined 6–8 weeks after.

(B) Protocol.

(legend continued on next page)

We noted that the major site of *Grem1*-driven recombination at P23, after P9 induction, was within the femoral epiphysis (nearly 60% of the epiphyseal bone was labeled). Therefore, we examined anatomically comparable sections in *Grem1* DTA versus control mice and measured the fraction of mineralized bone in the femoral epiphysis. Here too, the trabecular bone fraction was significantly reduced in DTA mice versus control mice (Figure S4D). This suggested a functional role of *Grem1*⁺ cells in postnatal skeletogenesis. We acknowledge, however, that ablation of extra-skeletal *Grem1*⁺ cells may have indirectly contributed, at least in part, to the impaired skeletogenesis.

We measured the expression of *Grem1*, *Nes*, *Runx2*, and *Sox9* by whole-mount in situ hybridization during the earliest stages of hindlimb bud development, i.e., embryonic day (E) 9.5, E10.5, E11.5, and E12.5 (Figure 4A). *Grem1* was expressed at the onset of hindlimb development, E9.5. *Nes* was not expressed within the hindlimb at these stages. To confirm that *Grem1* marked a multipotent mesenchymal stem/progenitor cell during development, we administered tamoxifen to pregnant *Grem1-creERT*; *R26-LSL-TdTomato* dams at E13.5. Consistent with the in situ hybridization findings, *Grem1* was expressed within much of the primitive hindlimb mesenchyme within the embryos and gave rise to almost all of the cells within the primitive mesenchyme and the primary spongiosa by E21 (Figures S4E and S4F).

Taken together, these results confirm that *Grem1* expression marked a new, endogenous skeletal stem cell, in development and adulthood, which lacked any significant capacity for adipogenesis. As a result, it does not meet the minimal criteria for MSCs (Dominici et al., 2006). Thus, we named these *Grem1*⁺ stem cells as osteochondroreticular “OCR stem cells” in reference to the earlier concept of the osteochondroprogenitor (Ducy et al., 1997).

Perisinusoidal *Nes-GFP*⁺ Cells May Not Be Skeletal Stem Cells during Early Life

The previously published *Nes-cre* and *Nes-creERT* lines may not reliably identify the perisinusoidal *Nes-GFP* cells that are purported to be endogenous MSCs (Ding et al., 2012; Méndez-Ferrer et al., 2010). Thus, we used a different transgenic *Nes-creERT* line in an attempt to better understand the lineage potential of *Nes-GFP*⁺ perisinusoidal MSCs (Dranovsky et al., 2011). Compared to previously reported *Nes* reporter mouse lines, the transgenic *Nes-creERT* line used here had a different *Nes* regulatory sequence directing the expression of *creERT* (Dranovsky et al., 2011). Following P1 tamoxifen induction of *Nes-creERT*; *R26-LSL-TdTomato*; *Nes-GFP* mice (Figure 4B), *Nes-creERT* recombined *R26-LSL-TdTomato* in approximately 4% of all bone marrow *Nes-GFP* cells by 6–8 weeks (Figure 4C). This included metaphyseal (Figure 4D), periarterial (Figure 4E), and perisinusoidal *Nes-GFP* cells (Figures 4F–4H). In keeping with previous perisinusoidal lineage-tracing studies, this *Nes-creERT* line did not generate cartilage or trabecular bone by 6–8 weeks (Ding et al., 2012; Mizoguchi et al., 2014). The only os-

teochondral cells that were traced consisted of rare, isolated osteocytes embedded within the diaphyseal cortical bone (Figure 4H). Our findings suggest that perisinusoidal cells, labeled by *Nes-GFP*, may not be the principal skeletal stem cells during development or early postnatal life (Ding et al., 2012; Mizoguchi et al., 2014; Zhou et al., 2014). It is quite possible, however, that the endogenous *Nes* gene or other *Nes*-transgenic lines could be expressed in postnatal skeletal stem/progenitor cells, but that these cells were not captured by our lineage-tracing strategy in young (<8-week-old) mice.

Grem1⁺ OCR Stem Cells Contribute to Fracture Repair

Do adult *Grem1* OCR stem cells respond to skeletal injury? Adult *Grem1*⁺ cells do not overlap with *2.3colGFP*⁺ osteoblasts. *Grem1*⁺ cells are, however, adjacent to osteoblasts in vivo and during early adherent bone marrow stromal culture (Figures 5B and 5C). Surgical fracture with internal fixation of the femur in *Grem1-creERT*; *R26-LSL-TdTomato*; *2.3colGFP* mice (performed 1 week after adult induction with tamoxifen) (Figures 5A and 5D) resulted in *Grem1*⁺ OCR stem cell expansion and differentiation into *2.3colGFP*-positive (and osteocalcin-positive, Figure S5D) osteoblasts and *2.3colGFP*-negative, *Sox9*⁺ chondrocytes within the fracture callus (Figures 5E–5H and S5A–S5C). The *Grem1*⁺ OCR stem cell lineage, as defined by red fluorescence, contributed approximately 28% of osteoblasts (red and *2.3colGFP* green) and 14% of chondrocytes (defined by *Sox9* immunostaining and/or by hematoxylin and eosin staining [H&E] on serial sections) within the fracture callus.

Next, we tested whether *Grem1*⁺ cells could be transplanted into the fracture site. We harvested and expanded a clonal population of *Grem1*⁺ OCR stem cells. This clone, mixed with hydrogel, was applied to the fracture site at the time of injury and engrafted into the callus of the recipient wild-type mice (Figures 5I and 5J). The transplanted cells differentiated into osteoblasts (alkaline phosphatase-expressing) within the fracture callus (Figure 5K). OCR stem cells self-renewed within the callus and were recovered from the recipient animals and rapidly expanded again in fracture callus cultures (Figure 5L). The *Grem1*⁺ OCR stem cells cultured from the fracture callus and expanded in vitro could be serially transplanted into a second fracture (Figure S5E). Thus, *Grem1* expression identifies developmental and adult, both physiological and reactive, endogenous OCR stem cells amenable to serial transplantation.

Grem1 Expression also Defines a New iRSC

Could *Grem1* also mark extramedullary connective tissue stem cells? The small intestine was selected as our extramedullary organ of interest because the gut is known to contain multipotent mesenchymal stromal cells (Powell et al., 2011). It is worth emphasizing that we searched for a connective tissue stem cell within the lamina propria and not for an epithelial stem cell, such as that previously identified by *Lgr5* expression (Barker et al., 2007). Furthermore, the small intestine does not contain

(C) By flow cytometry, approximately 4% of *Nes-GFP*-positive cells recombined (that is, were both green and red).

(D–H) This specific *Nes-CreERT* transgenic line recombined in all typical *Nes-GFP* populations, including perivascular cells immediately inferior to the growth plate (D), in periarterial cells (E), and in perisinusoidal *Nes-GFP*-positive cells (red arrows, F–H). The only osteochondral lineage tracing found were isolated osteocytes throughout the diaphyseal bone (H, white arrow).

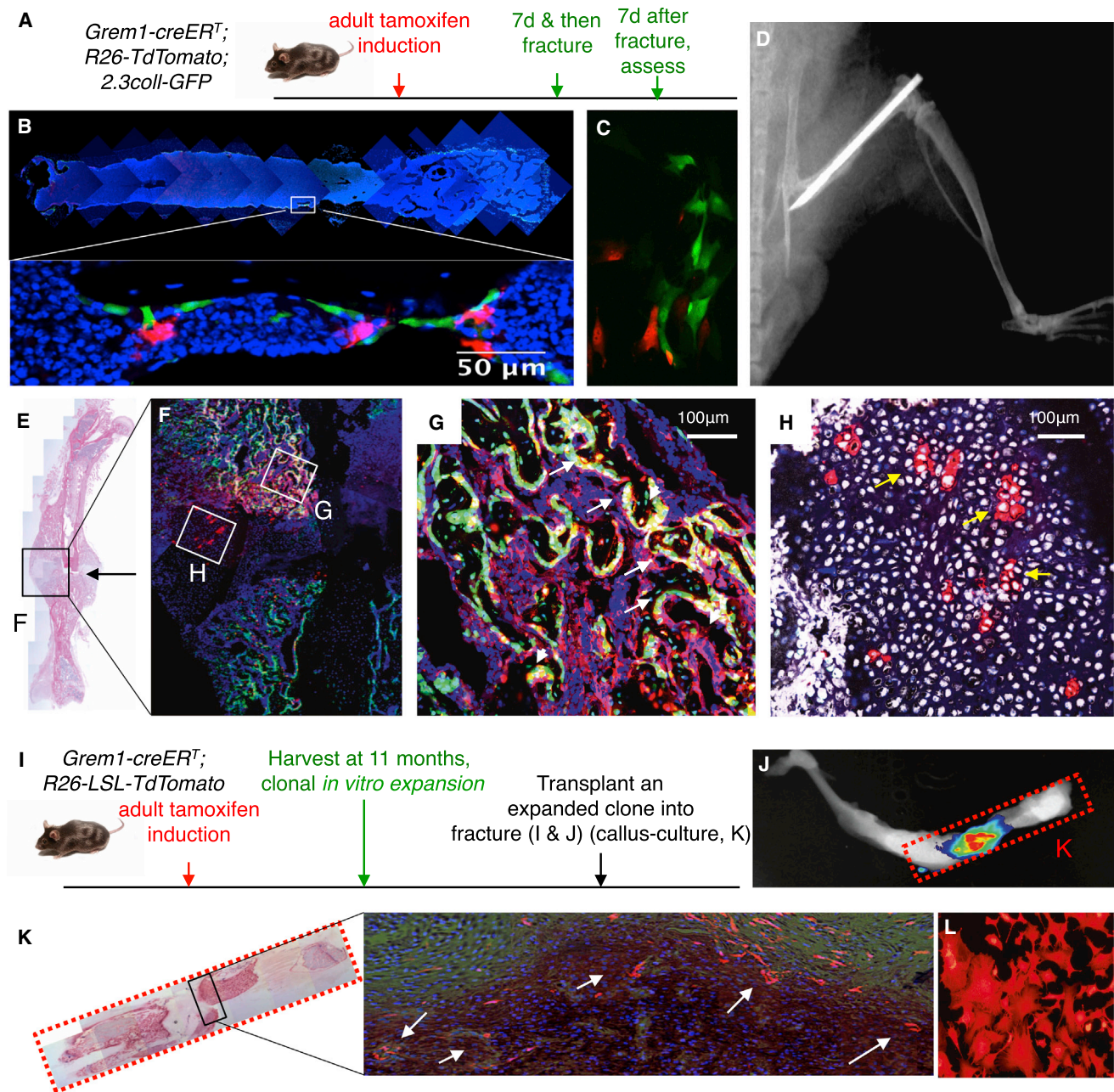


Figure 5. Adult *Grem1* Cells, Both Endogenous and Transplanted, Differentiate into Osteochondral Fracture Callus

(A) Protocol.

(B and C) *Grem1-creERT*; *R26-LSL-TdTomato*; *2.3collGFP* mice adult induction: *Grem1*⁺ (red) cells were not osteoblasts (green) but were adjacent to each other in situ (B) and during the first week of adherent bone marrow stromal culture (C).

(D) is an X-ray of the femoral osteotomy and internal fixation of the bone.

(E) and (F) show the serial histology and fluorescent microscopy sections from the resulting fracture callus after the osteotomy.

(G) and (H) are magnified from areas shown in (F). *Grem1*⁺ cells (red) stream into the fracture site and differentiate into either osteoblasts (G, yellow cells, white arrows) or Sox9⁺ (white, nuclear stain) chondrocytes (yellow arrows) (H).

(I) A *Grem1*⁺ clone, after adult induction, was expanded in vitro. An osteotomy with internal fixation was performed in wild-type mice, at which point 500×10^6 clonal cells (red) were irrigated into the surgical field. Seven days later, the *Grem1* clone had engrafted (J), the site of injury was identified by TdTomato fluorescence imaging, and recombined cells (fluorescent red) differentiated into osteoblastic cells (K) (alkaline phosphatase positive cells, red-brown, white arrows) in the callus (sequential fluorescence microscopy and ALP staining performed on the same slide).

(L) Callus culture was performed, and the recombined *Grem1* cells were easily recovered in vitro and serially transplanted into a secondary fracture (Figure S5E).

bone and cartilage, and thus we were not expecting to find a bona fide OCR stem cell. Rather, we were interested in testing for an organ-relevant connective tissue stem cell, sharing *Grem1* expression and the defining stem cell characteristics of self-renewal and multipotentiality. The connective tissue immediately beneath the intestinal epithelium is a mesenchymal sheath that invests the entire intestinal gland (Powell et al., 2011). Adult *Grem1* recombination (24 hr after 6 mg of tamoxifen by oral gavage, *Grem1-creER^T;R26-mT/mG*) identified single cells (*Grem1*⁺ = green) immediately beneath the epithelium at the junction between the small-intestinal crypt and villus, a region known as the intestinal isthmus (Figures 6A and 6B). In situ hybridization confirmed *Grem1* expression within periepithelial isthmus cells, and these cells were also positive in the *Grem1-LacZ* knockin line (Data S2A–S2F) (Khokha et al., 2003).

Single periepithelial *Grem1* cells divided slowly (BrdU incorporation over 1 month of continuous dosing; Data S2G). Over time, the fluorescently tagged *Grem1*⁺ cells gave rise to reticular, periepithelial mesenchymal lineages throughout both the crypt and villus sheaths (Figures 6B–6E). The *Grem1*⁺ cells differentiated into both *Acta2*-positive myofibroblasts (Figure 6F) and *Acta2*-negative, but *Ng2*-positive, stromal cells (Data S2H). *Grem1* cells gave rise to an intricate reticular network of cells that invested the entire gland (Figures 6B–6E, Movie S1). The *Grem1* lineage was distinct from the closely associated s100b (Data S2I) and *Nes-GFP* positive periepithelial glial sheath (Data S2J) (Belkind-Gerson et al., 2013). The *Grem1*⁺ cell lineage was intimately related to the overlying intestinal epithelium (Figures 6G and Data S2K). After 6 to 9 months, intestinal *Grem1* cells had expanded to give rise to the mesenchymal sheath subjacent to the *Lgr5*⁺ crypt base columnar stem cell zone (Figures 6B, 6C, and 6E) (Barker et al., 2007). After 12 months, the cells had also renewed the periepithelial mesenchymal sheath to the tip of the villi (Figure 6B). The *Grem1*⁺ cells at the isthmus self-renewed so that their fluorescently tagged lineage persisted across the entire crypt-villus axis for at least 2 years after adult tamoxifen induction (Data S2L). Perinatal induction at P1 led to accelerated intestinal mesenchymal tracing (at 6 weeks), providing further proof of the clonality of the *Grem1* lineage within the mesenchymal sheath (*Grem1-creER^T;R26-Confetti* mice; Data S2M). The *Grem1* lineage also identified small-intestinal CFU-Fs (Data S2N). Similar patterns of lineage tracing were evident throughout the entire gastrointestinal tract, including the stomach (Data S2O). *Grem1* also identified a progenitor population within the skin (Data S2O). The exact nature of these cells, however, requires further study.

Extending the concept of connective tissue stem cells to extramedullary mesenchyme, however, requires that the model be rigorously validated in vivo. We adapted a protocol for generating tissue-engineered small intestines (TESIs) to test whether *Grem1*⁺ intestinal mesenchymal cells could be transplanted to generate the small-intestinal, periepithelial mesenchymal sheath within the recipient's TESI graft (Levin et al., 2013). *Grem1-creER^T;R26-LSL-TdTomato* donor small-intestinal organoid units were transplanted into the omentum of recipient wild-type mice. Only one or two *Grem1*⁺ cells were present within the harvested donor units (Figure 6H), but they were able to expand and restore the intestinal mesenchymal sheath in the

TESI (Figures 6I and Data S2P). Thus, small-intestinal *Grem1*⁺ cells self-renew and clonally generate multiple distinct, compartment-relevant mesenchymal lineages and can be transplanted to recapitulate the periepithelial mesenchymal sheath, confirming that they are connective tissue stem cells. In this context, we refer to them as iRSCs. We use this term, iRSCs, to reflect their morphology and the reticular network formed by these cells and in reference to their *Grem1*-expressing reticular counterparts in the bone marrow.

DISCUSSION

Despite intensive investigation, the identity of an endogenous “skeletal stem cell” has remained elusive. We generated an inducible *Cre* line, driven by the enhancer elements of the BMP antagonist *Grem1*, to identify and lineage trace rare skeletal stem cells in vivo. Adult *Grem1* OCR stem cells were found beside the growth plate and the trabecular bone, where they generated and maintained articular and growth plate cartilage, bone and reticular marrow stromal cells, but not fat. Adult *Grem1* OCR stem cells did not overlap with perisinusoidal *Nes-GFP* MSCs, appear to be more clonogenic in vitro than *Nes-GFP* MSCs, and make a far greater contribution to early postnatal skeletogenesis than traditional perisinusoidal MSCs (Ding et al., 2012; Zhou et al., 2014). This study complements the existing, perisinusoidal MSC model of postnatal skeletogenesis (Figure 7) (Bianco et al., 2013). We have also identified *Grem1*-expressing, reticular stem cells in the small intestine, the iRSCs, that self-renew to maintain the multilineage periepithelial, mesenchymal sheath. The iRSCs are distinct from, but analogous to, their *Grem1*-expressing OCR stem cells in the bone. Each has an organ-appropriate mesenchymal repertoire, but these *Grem1*-expressing stem cells are united by their capacity for self-renewal, multipotentiality, and continued functionality following transplantation.

Bone and cartilage could develop from a population of dedicated and committed postnatal progenitors (as with pancreatic beta cells). Alternatively, they could arise from a multipotent stem cell capable of generating bone, cartilage, and accessory elements, such as adipocytes and pericytes. A third model, which we favor, suggests that discrete stem cells make temporal and lineage-specific contributions to skeletal development and maintenance (Takashima et al., 2007). That is, the OCR stem cell is a substantial skeletal stem cell in development and early postnatal life, but over time, the perisinusoidal MSC increases its contribution to skeletal homeostasis, such that ultimately adult mesenchymal tissues are maintained from two separate, but complementary, stem cell pools (Figure 7).

Perisinusoidal *Nes-GFP* MSCs fulfill the in vitro criteria of MSCs (Méndez-Ferrer et al., 2010); however, they make little endogenous contribution to skeletogenesis, at least during early life (Figure 4) (Ding et al., 2012; Mizoguchi et al., 2014; Zhou et al., 2014). In contrast, OCR stem cells are most active during development, giving rise to trabecular bone, cartilage, and reticular marrow stromal cells. Although it was reported that all adult bone marrow CFU-Fs are *Nes-GFP*⁺ (Méndez-Ferrer et al., 2010), *Grem1* OCR stem cells are negative for *Nes-GFP* and yet are clonogenic (Figures 1D–1G). We believe that this

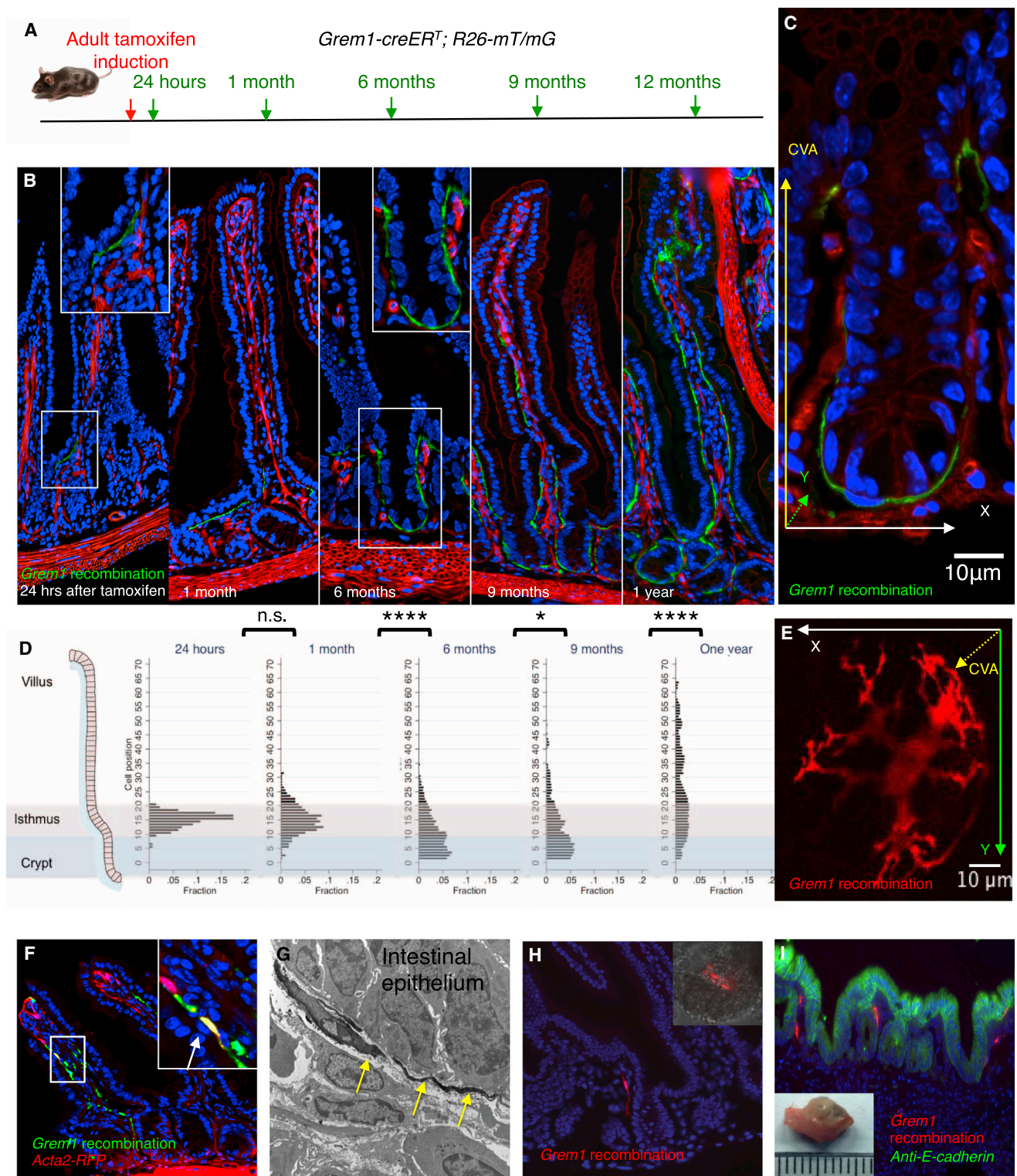


Figure 6. *Grem1* Expression Identifies iRSCs

(A) Protocol.

(B and C) *Grem1-creERT⁺; R26-mT/mG* adult induction identifies rare, single cells at the junction of the crypt and villus in the small intestine (green = *Grem1-creERT⁺*, red = *Grem1-creERT⁻*). Over 1 year, *Grem1⁺* cells expand to renew the entire periepipithelial mesenchymal sheath. By 6 months, they are

(legend continued on next page)

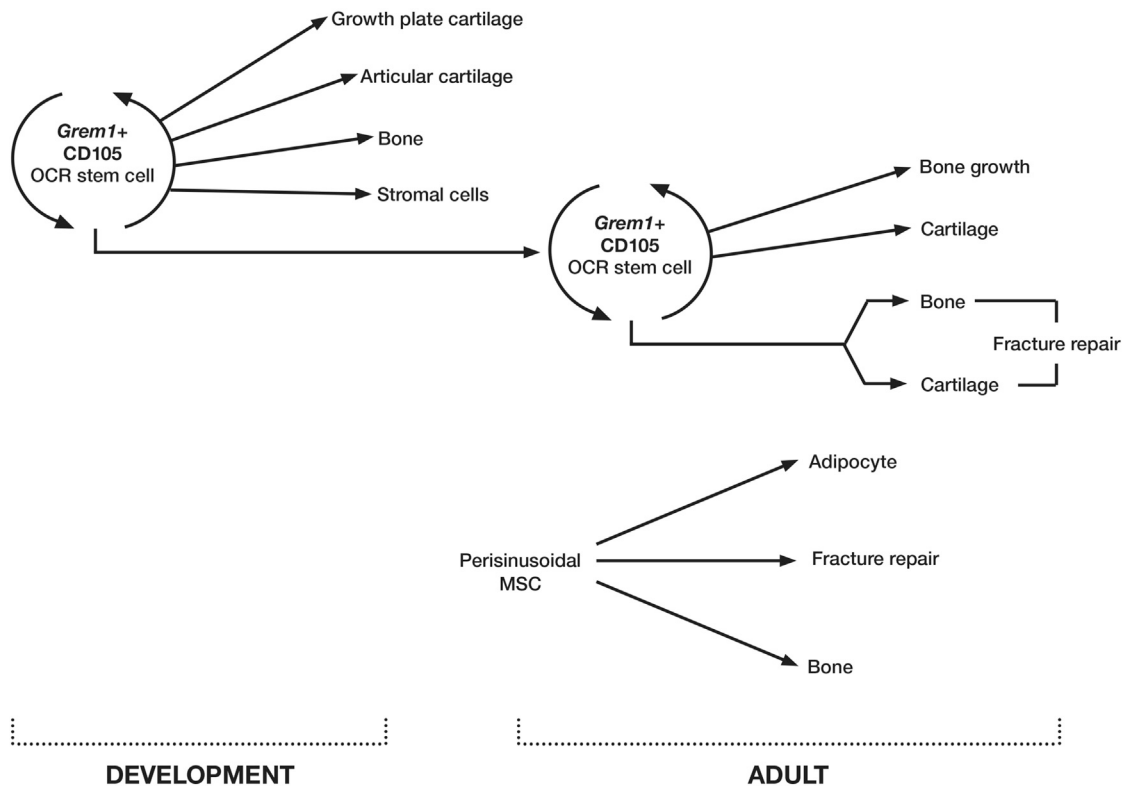


Figure 7. A Model in which the OCR Stem Cell and the Perisinusoidal MSC Make a Complementary Contribution to Skeletal Development, Adult Homeostasis, and Repair

discrepancy may arise from differences in our isolation and culture of the bone marrow. Bone marrow *Nes-GFP* cells were originally isolated by bone flush without reported collagenase digestion (Méndez-Ferrer et al., 2010), which enhances the yield of CFU-Fs (Morikawa et al., 2009). Enzymatic digestion was essential for liberating *Grem1*⁺ cells from the bone and bone marrow. There were also differences in our mesenchymal sorting strategy. We classified CD45[−]CD31[−]Ter-119[−] triple-negative cells as bone marrow mesenchyme, as previously reported (Park et al., 2012), whereas in the original *Nes-GFP* MSC study, CD45[−] alone was used as the mesenchymal arbiter (Méndez-Ferrer et al., 2010). This may have resulted in some CD31⁺ endothelial cells being collected, and given that *Nes-GFP*

is expressed in bone marrow endothelium (Ono et al., 2014), it is conceivable that the mesenchymal *Nes-GFP* population we evaluated (CD45[−]CD31[−]Ter-119[−]*Nes-GFP*⁺) was different from that evaluated previously (Méndez-Ferrer et al., 2010).

Developmentally, *Nes-GFP*⁺ and *Lepr-cre*⁺ perisinusoidal MSCs and *Grem1*⁺ OCR stem cells could represent different cells within a common lineage. Although this remains a possibility, we note that *Grem1*⁺ cells do not give rise to *Nes-GFP* cells, even 10 months after tamoxifen induction. Similarly, P1 induction of *Nes-creER*^T, or constitutive lineage tracing of *Lepr*⁺ cells using the *Lepr-cre* (Zhou et al., 2014), did not lead to significant genetic recombination of trabecular bone or cartilage in early life. In contrast, trabecular bone and cartilage are clearly derived from

immediately beneath the intestinal stem cells at the crypt base (B and C). Axes are provided to indicate the longitudinal and circumferential axes (x and y), and “CVA” to designate the crypt-villus, or radial, axis.

(D) The mesenchymal expansion was plotted relative to the adjacent epithelial position; 20 well-orientated crypt-villus columns were quantified per mouse. n = 3–5 mice at each time point; Kruskal-Wallis analysis (p < 0.0001) and post-hoc pairwise Mann-Whitney tests, corrected for multiple comparisons, revealed significant differences (****p ≤ 0.0001, *p ≤ 0.05).

(E) The sheath was comprised of a reticulated population of stellate cells with long processes that encircled the entire intestinal gland. This cell encapsulated the very base of the intestinal crypt, similar to the position of the cell identified in (C).

(F) The *Grem1*⁺ population self-renewed and was multipotent, generating both *Acta2* positive (yellow cell, white arrow) and negative fibroblastic lineages.

(G) Transmission electron microscopy: the *Grem1* lineage (yellow arrows) is immediately beneath the epithelial cells.

(H) Tissue engineering: representative images from n = 8 small-intestinal organoid unit transplants. Small intestines were harvested from 3-week-old, tamoxifen-induced donor mice. In the donor intestines, prior to harvest, there were single *Grem1*⁺ cells (red) near the isthmus of the intestinal gland. After digestion of the donor intestines into organoid units, rare *Grem1*⁺ mesenchymal cells (red) were found within individual organoid units (inset).

(I) Four weeks after transplantation, TESs develop, with the periepipithelial mesenchymal sheath recapitulated from the donor *Grem1*⁺ cells (red). E-cadherin staining (green) was used to identify the epithelium.

Grem1⁺ cells. Thus, based on our data, and those of others (Ding et al., 2012; Mizoguchi et al., 2014; Zhou et al., 2014), we conclude that there are at least two skeletogenic stem cells contributing to postnatal bone (Figure 7). Remarkably, only OCR stem cells appear to generate articular and growth-plate cartilage during development, and the contribution of perisinusoidal MSCs is modest until later adulthood, at which point the perisinusoidal MSCs are ultimately capable of generating fat, bone, and cartilage, particularly following injury (Figure 7) (Zhou et al., 2014). We propose that the OCR stem cell is vital in skeletogenesis, whereas the traditional perisinusoidal MSCs gradually increase their skeletal contribution over time. Traditional MSCs appear to partner with OCR stem cells to repair bone in the event of fracture, but this may again depend on the developmental stage at which the injury occurs (Figure 7).

In contrast to perisinusoidal MSCs, the *Grem1* OCR stem cells did not generate adipocytes *in vivo* or *in vitro*. Thus, although the *Grem1*⁺ cell is multipotent (giving rise to osteoblasts, chondrocytes, and reticular marrow stromal cells) and a bone fide stem cell, it is not the usual origin of adipocytes, at least under the conditions examined. The relative ascendancy of perisinusoidal MSCs in later adulthood could potentially explain the increasing adipogenesis evident in the bone marrow in later life.

Our selected marker, *Grem1*, is a BMP antagonist that is especially important for skeletal patterning and contributes to postnatal skeletal homeostasis (Bénazet et al., 2009; Canalis et al., 2012; Khokha et al., 2003). BMP signaling in skeletogenesis expands primitive mesenchymal cells, laying the foundation for subsequent endochondral ossification (Kronenberg, 2003). Despite expression of the BMP antagonist *Grem1*, BMP signaling was elevated in OCR stem cells compared to the *Grem1*-negative mesenchymal cells. Increased BMP signaling is consistent with the location of OCR stem cells, which is immediately adjacent to the BMP-producing growth plate, and our microarray and qPCR data suggest that OCR stem cells also produce Bmps that may act in an autocrine fashion (Kronenberg, 2003).

Researchers have harvested MSC-like cells from many different adult organs (Crisan et al., 2008). In the small intestine, single *Grem1*⁺ iRSCs immediately subjacent to the epithelium at the junction between the small-intestinal crypt and villus (the intestinal isthmus) undergo slow division, to ultimately generate the entire periepithelial sheath of the crypt and villus, forming a closely connected mesenchymal network. In adulthood, this process takes about one year, during which time the *Grem1* iRSCs give rise to both *Acta2*-positive myofibroblasts and *Acta2*-negative periepithelial fibroblasts, thus establishing their endogenous self-renewal and compartment-specific multipotentiality.

The *Grem1*⁺ iRSC is a different cell from the *Grem1*⁺ OCR stem cell, with discrete functions and distinct lineage potential, namely periepithelial mesenchyme rather than bone and cartilage. Nevertheless, it shares with the *Grem1* OCR stem cell a stellate morphology, relative quiescence, and most importantly the properties of endogenous self-renewal and mesenchymal multipotentiality.

The stem cell responsible for developing bone and cartilage *in vivo*, the OCR stem cell, appears to show great promise for

skeletal tissue engineering, particularly for conditions such as osteoarthritis, osteoporosis, and fracture. *Grem1* OCR stem cells could be harvested from a donor animal, expanded *in vitro*, and transplanted, both directly and serially, into the femurs of fractured recipient animals, resulting in osteochondral differentiation in the callus. Future studies will be needed to compare the ability of *Grem1*⁺ cells to heal skeletal diseases relative to those of other mesenchymal progenitor populations. Our discovery of analogous iRSCs is also likely to be important in intestinal replacement and repair and may inform mesenchymal hierarchy in other complicated connective tissues, including the tumor microenvironment.

Taken together, our findings confirm the existence and relevance of bone, cartilage, and reticular stromal stem cells and present a paradigm shift in understanding the diverse origins of connective tissues in health, aging, and disease.

EXPERIMENTAL PROCEDURES

Mice

We used the following lines: *Nes-GFP* (Mignone et al., 2004), *Nes-CreER^{T2}* (Dranovsky et al., 2011), *Grem1-LacZ* (Khokha et al., 2003), *Acta2-RFP* (Magness et al., 2004), *R26-LSL-ZsGreen* (Madisen et al., 2010), *R26-LSL-TdTomato* (Madisen et al., 2010), *R26-LSL-mT/mG* (Muzumdar et al., 2007), *2.3ColGFP* (Kalajic et al., 2002), *R26-LSL-Confetti* (Snippert et al., 2010), and *R26-LSL-DTA* (Voehringer et al., 2008) (Table S1B). The *R26-LSL-mT/mG* was used in the intestine to better appreciate intestinal architecture, but for the bone marrow, either the *R26-LSL-ZsGreen* or the *R26-LSL-TdTomato* was used to enable the addition of a second reporter, such as *Nes-GFP*, *2.3colGFP* or *Acta2-RFP*. We generated the *Grem1-CreER^T* transgenic by BAC recombineering (clone RP24-317C19), as previously described (Sharan et al., 2009). The recombineering primers amplified the *CreER^T*-pA-fnf cassette with 60 bp homology arms upstream and downstream of the *Grem1* translational start site in exon 2 (Table S1A). We generated three founder lines. Line 3 displayed the greatest recombination following adult tamoxifen induction, and it was backcrossed six generations to C57BL/6J. All experiments were performed according to the guidelines of the Institute of Comparative Medicine at Columbia University.

Marrow Stromal Cell Isolation

Long bones of the arms and legs were harvested and gently disrupted using a mortar and pestle, in PBS with 2% FBS and 1 mM EDTA. The bone and all of the liberated bone marrow were collected and digested in 0.25% collagenase type I (Worthington, Lakewood, NJ, USA, LS004196) in PBS with 20% FBS, for cell culture or flow cytometry.

Clonal In Vitro Bone Marrow MSC Culture, Clonogenicity Assays, and Differentiation

Marrow stromal cells were plated at clonal density and cultured for 14 days in α MEM + 10% defined MSC FBS + 1% penicillin/streptomycin. The total number of colonies, defined as ≥ 50 cells, were stained with Giemsa. The number of clones were reported as (CFU-Fs)/1,000 cells plated. For differentiation, single recombined clones were isolated using cloning cylinders and then expanded and split for differentiation using Invitrogen StemPro differentiation products into adipocytes, chondrocytes, and osteoblasts. All *in vitro* differentiation reported in this study is clonal.

Fracture Studies

Adult *Grem1-creER^T;R26-LSL-TdTomato;2.3ColGFP* mice were induced with tamoxifen with a 1 week washout period before fracture. Unilateral femoral osteotomy was internally fixed by an angiocatheter. Femurs were harvested at 7 days. For the fracture transplantation, a single *Grem1*-derived clone (after adult *in vivo* induction) was expanded *in vitro* and then 500×10^6 cells were mixed with a HyStem-C(TM) Hydrogel Kit (Glycosan) and injected

around the fracture sites of the recipient wild-type mice. The fractured bones were harvested at 7 days. Some of the fracture callus was recultured to recover the donor *Grem1*⁺ cells. The fractures were imaged by X-ray and a Kodak In Vivo Multispectral Imaging System FX (carestream Health) specific for TdTomato fluorescence.

Tissue-Engineered Small Intestines

Organoid units were harvested from 3-week-old, P1 tamoxifen-induced *Grem1-creERT;R26-LSL-TdTomato* donor mice and transplanted into 8 wild-type adult C57BL/6 mice. The procedure was otherwise performed as previously described (Levin et al., 2013) with the TESIs harvested at 4 weeks post-implantation for analysis.

SUPPLEMENTAL INFORMATION

Supplemental Information includes Extended Experimental Procedures, five figures, one table, two data files, and one movie and can be found with this article online at <http://dx.doi.org/10.1016/j.cell.2014.11.042>.

AUTHOR CONTRIBUTIONS

D.L.W., T.C.W., S.M., G.K., and F.Y.L.: study concept and design; analysis and interpretation of data; writing and revising the manuscript. All other authors contributed to the acquisition and interpretation of data and review of the manuscript.

ACKNOWLEDGMENTS

Thank you to Dr. Liza Phillips. Thank you to all members of the Wang laboratory at Columbia University. Thank you to Professor David Callen, Dr. Miao Yang, and Dr. Laura Vrbanc at the University of Adelaide. Thank you to Dr. Lei Ding for his advice and assistance. Thank you to Dr. Grigori Enikolopov (Cold Spring Harbor Laboratory) and Dr. Rene Hen (Columbia University) for sharing their transgenic mice. Thank you to Dr. Victor Lin for his transgenic advice and to Dr. Brian Eyden for his advice regarding intestinal mesenchymal cells. We are grateful for the following funding: from the NIH to T.C.W. (NIH 5U54 CA126513), to S.M. (R01 RHL115145A), to F.Y.L. from the Robert Carroll and Jane Chace Carroll Laboratories and also the NIH (NIH AR056246 and EB006834), to A.K.R. from the American Cancer Society, and to D.L.W. from the NH&MRC and Menzies Foundation, Cancer Council SA's Beat Cancer Project on behalf of its donors and the State Government of South Australia through the Department of Health, Gastroenterological Society of Australia, the American Gastroenterological Association, the American Association for Cancer Research, the Royal Australasian College of Physicians, and the Ines Mandl Postdoctoral research fellowship Columbia University.

Received: May 27, 2014

Revised: September 9, 2014

Accepted: November 12, 2014

Published: January 15, 2015

REFERENCES

Barker, N., van Es, J.H., Kuipers, J., Kujala, P., van den Born, M., Cozijnsen, M., Haegebarth, A., Korving, J., Begthel, H., Peters, P.J., and Clevers, H. (2007). Identification of stem cells in small intestine and colon by marker gene *Lgr5*. *Nature* 449, 1003–1007.

Belkind-Gerson, J., Carreon-Rodriguez, A., Benedict, L.A., Steiger, C., Pieretti, A., Nagy, N., Dietrich, J., and Goldstein, A.M. (2013). Nestin-expressing cells in the gut give rise to enteric neurons and glial cells. *Neurogastroenterol. Motil.* 25, 61.e7.

Bénazet, J.-D., Bischofberger, M., Tiecke, E., Gonçalves, A., Martin, J.F., Zuniga, A., Naef, F., and Zeller, R. (2009). A self-regulatory system of interlinked signaling feedback loops controls mouse limb patterning. *Science* 323, 1050–1053.

Bianco, P., Cao, X., Frenette, P.S., Mao, J.J., Robey, P.G., Simmons, P.J., and Wang, C.Y. (2013). The meaning, the sense and the significance: translating the science of mesenchymal stem cells into medicine. *Nat. Med.* 19, 35–42.

Canalis, E., Parker, K., and Zanotti, S. (2012). Gremlin1 is required for skeletal development and postnatal skeletal homeostasis. *J. Cell. Physiol.* 227, 269–277.

Crisan, M., Yap, S., Casteilla, L., Chen, C.-W., Corselli, M., Park, T.S., Andriolo, G., Sun, B., Zheng, B., Zhang, L., et al. (2008). A perivascular origin for mesenchymal stem cells in multiple human organs. *Cell Stem Cell* 3, 301–313.

Delorme, B., Ringe, J., Pontikoglou, C., Gaillard, J., Langonné, A., Sensebé, L., Noël, D., Jorgensen, C., Häupl, T., and Charbord, P. (2009). Specific lineage-priming of bone marrow mesenchymal stem cells provides the molecular framework for their plasticity. *Stem Cells* 27, 1142–1151.

Ding, L., Saunders, T.L., Enikolopov, G., and Morrison, S.J. (2012). Endothelial and perivascular cells maintain haematopoietic stem cells. *Nature* 481, 457–462.

Dominici, M., Le Blanc, K., Mueller, I., Slaper-Cortenbach, I., Marini, F., Krause, D., Deans, R., Keating, A., Prockop, D.J., and Horwitz, E. (2006). Minimal criteria for defining multipotent mesenchymal stromal cells. The International Society for Cellular Therapy position statement. *Cytotherapy* 8, 315–317.

Dranovsky, A., Picchini, A.M., Moadel, T., Sisti, A.C., Yamada, A., Kimura, S., Leonardo, E.D., and Hen, R. (2011). Experience dictates stem cell fate in the adult hippocampus. *Neuron* 70, 908–923.

Ducy, P., Zhang, R., Geoffroy, V., Ridall, A.L., and Karsenty, G. (1997). *Osf2/Cbfa1*: a transcriptional activator of osteoblast differentiation. *Cell* 89, 747–754.

Gerber, H.P., Vu, T.H., Ryan, A.M., Kowalski, J., Werb, Z., and Ferrara, N. (1999). VEGF couples hypertrophic cartilage remodeling, ossification and angiogenesis during endochondral bone formation. *Nat. Med.* 5, 623–628.

Grcevic, D., Pejda, S., Matthews, B.G., Repic, D., Wang, L., Li, H., Kronenberg, M.S., Jiang, X., Maye, P., Adams, D.J., et al. (2012). In vivo fate mapping identifies mesenchymal progenitor cells. *Stem Cells* 30, 187–196.

Hsu, D.R., Economides, A.N., Wang, X., Eimon, P.M., and Harland, R.M. (1998). The Xenopus dorsalizing factor Gremlin identifies a novel family of secreted proteins that antagonize BMP activities. *Mol. Cell* 1, 673–683.

Jaeger, E., Leedham, S., Lewis, A., Segditsas, S., Becker, M., Cuadrado, P.R., Davis, H., Kaur, K., Heinemann, K., Howarth, K., et al. (2012). Hereditary mixed polyposis syndrome is caused by a 40-kb upstream duplication that leads to increased and ectopic expression of the BMP antagonist GREM1. *Nat. Genet.* 44, 699–703.

Kalajzic, I., Kalajzic, Z., Kaliterna, M., Gronowicz, G., Clark, S.H., Lichtler, A.C., and Rowe, D. (2002). Use of type I collagen green fluorescent protein transgenes to identify subpopulations of cells at different stages of the osteoblast lineage. *J. Bone Miner. Res.* 17, 15–25.

Khokha, M.K., Hsu, D., Brunet, L.J., Dionne, M.S., and Harland, R.M. (2003). Gremlin is the BMP antagonist required for maintenance of Shh and Fgf signals during limb patterning. *Nat. Genet.* 34, 303–307.

Kosinski, C., Li, V.S.W., Chan, A.S.Y., Zhang, J., Ho, C., Tsui, W.Y., Chan, T.L., Mifflin, R.C., Powell, D.W., Yuen, S.T., et al. (2007). Gene expression patterns of human colon tops and basal crypts and BMP antagonists as intestinal stem cell niche factors. *Proc. Natl. Acad. Sci. USA* 104, 15418–15423.

Kronenberg, H.M. (2003). Developmental regulation of the growth plate. *Nature* 423, 332–336.

Levin, D.E., Sala, F.G., Barthel, E.R., Speer, A.L., Hou, X., Torashima, Y., and Grikscheit, T.C. (2013). A “living bioreactor” for the production of tissue-engineered small intestine. *Methods Mol. Biol.* 1001, 299–309.

Madisen, L., Zwingman, T.A., Sunken, S.M., Oh, S.W., Zariwala, H.A., Gu, H., Ng, L.L., Palmiter, R.D., Hawrylycz, M.J., Jones, A.R., et al. (2010). A robust and high-throughput Cre reporting and characterization system for the whole mouse brain. *Nat. Neurosci.* 13, 133–140.

- Magness, S.T., Batailler, R., Yang, L., and Brenner, D.A. (2004). A dual reporter gene transgenic mouse demonstrates heterogeneity in hepatic fibrogenic cell populations. *Hepatology* 40, 1151–1159.
- Méndez-Ferrer, S., Michurina, T.V., Ferraro, F., Mazloom, A.R., Macarthur, B.D., Lira, S.A., Scadden, D.T., Ma'ayan, A., Enikolopov, G.N., and Frenette, P.S. (2010). Mesenchymal and haematopoietic stem cells form a unique bone marrow niche. *Nature* 466, 829–834.
- Michos, O., Panman, L., Vintersten, K., Beier, K., Zeller, R., and Zuniga, A. (2004). Gremlin-mediated BMP antagonism induces the epithelial-mesenchymal feedback signaling controlling metanephric kidney and limb organogenesis. *Development* 131, 3401–3410.
- Mignone, J.L.J., Kukekov, V.V., Chiang, A.-S.A., Steindler, D.D., and Enikolopov, G.G. (2004). Neural stem and progenitor cells in nestin-GFP transgenic mice. *J. Comp. Neurol.* 469, 311–324.
- Mitola, S., Ravelli, C., Moroni, E., Salvi, V., Leali, D., Ballmer-Hofer, K., Zampataro, L., and Presta, M. (2010). Gremlin is a novel agonist of the major proangiogenic receptor VEGFR2. *Blood* 116, 3677–3680.
- Mizoguchi, T., Pinho, S., Ahmed, J., Kunisaki, Y., Hanoun, M., Mendelson, A., Ono, N., Kronenberg, H.M., and Frenette, P.S. (2014). Osterix marks distinct waves of primitive and definitive stromal progenitors during bone marrow development. *Dev. Cell* 29, 340–349.
- Morikawa, S., Mabuchi, Y., Kubota, Y., Nagai, Y., Niibe, K., Hiratsu, E., Suzuki, S., Miyauchi-Hara, C., Nagoshi, N., Sunabori, T., et al. (2009). Prospective identification, isolation, and systemic transplantation of multipotent mesenchymal stem cells in murine bone marrow. *J. Exp. Med.* 206, 2483–2496.
- Muzumdar, M.D., Tasic, B., Miyamichi, K., Li, L., and Luo, L. (2007). A global double-fluorescent Cre reporter mouse. *Genesis* 45, 593–605.
- Ng, F., Boucher, S., Koh, S., Sastry, K.S., Chase, L., Lakshminpathy, U., Choong, C., Yang, Z., Vemuri, M.C., Rao, M.S., and Tanavde, V. (2008). PDGF, TGF-beta, and FGF signaling is important for differentiation and growth of mesenchymal stem cells (MSCs): transcriptional profiling can identify markers and signaling pathways important in differentiation of MSCs into adipogenic, chondrogenic, and osteogenic lineages. *Blood* 112, 295–307.
- Ono, N., Ono, W., Mizoguchi, T., Nagasawa, T., Frenette, P.S., and Kronenberg, H.M. (2014). Vasculature-associated cells expressing nestin in developing bones encompass early cells in the osteoblast and endothelial lineage. *Dev. Cell* 29, 330–339.
- Park, D., Spencer, J.A., Koh, B.I., Kobayashi, T., Fujisaki, J., Clemens, T.L., Lin, C.P., Kronenberg, H.M., and Scadden, D.T. (2012). Endogenous bone marrow MSCs are dynamic, fate-restricted participants in bone maintenance and regeneration. *Cell Stem Cell* 10, 259–272.
- Powell, D.W., Pinchuk, I.V., Saada, J.I., Chen, X., and Mifflin, R.C. (2011). Mesenchymal cells of the intestinal lamina propria. *Annu. Rev. Physiol.* 73, 213–237.
- Quante, M., Tu, S.P., Tomita, H., Gonda, T., Wang, S.S.W., Takashi, S., Baik, G.H., Shibata, W., Diprete, B., Betz, K.S., et al. (2011). Bone marrow-derived myofibroblasts contribute to the mesenchymal stem cell niche and promote tumor growth. *Cancer Cell* 19, 257–272.
- Sacchetti, B., Funari, A., Michienzi, S., Di Cesare, S., Piersanti, S., Saggio, I., Tagliafico, E., Ferrari, S., Robey, P.G., Riminucci, M., and Bianco, P. (2007). Self-renewing osteoprogenitors in bone marrow sinusoids can organize a hematopoietic microenvironment. *Cell* 131, 324–336.
- Sharan, S.K., Thomason, L.C., Kuznetsov, S.G., and Court, D.L. (2009). Recombineering: a homologous recombination-based method of genetic engineering. *Nat. Protoc.* 4, 206–223.
- Sneddon, J.B., Zhen, H.H., Montgomery, K., van de Rijn, M., Tward, A.D., West, R., Gladstone, H., Chang, H.Y., Morganroth, G.S., Oro, A.E., and Brown, P.O. (2006). Bone morphogenetic protein antagonist gremlin 1 is widely expressed by cancer-associated stromal cells and can promote tumor cell proliferation. *Proc. Natl. Acad. Sci. USA* 103, 14842–14847.
- Snippert, H.J., van der Flier, L.G., Sato, T., van Es, J.H., van den Born, M., Kroon-Veenboer, C., Barker, N., Klein, A.M., van Rheenen, J., Simons, B.D., and Clevers, H. (2010). Intestinal crypt homeostasis results from neutral competition between symmetrically dividing Lgr5 stem cells. *Cell* 143, 134–144.
- Takashima, Y., Era, T., Nakao, K., Kondo, S., Kasuga, M., Smith, A.G., and Nishikawa, S. (2007). Neuroepithelial cells supply an initial transient wave of MSC differentiation. *Cell* 129, 1377–1388.
- Voehringer, D., Liang, H.E., and Locksley, R.M. (2008). Homeostasis and effector function of lymphopenia-induced “memory-like” T cells in constitutively T cell-depleted mice. *J. Immunol.* 180, 4742–4753.
- Zhou, B.O., Yue, R., Murphy, M.M., Peyer, J.G., and Morrison, S.J. (2014). Leptin-receptor-expressing mesenchymal stromal cells represent the main source of bone formed by adult bone marrow. *Cell Stem Cell* 15, 154–168.

Identification and Specification of the Mouse Skeletal Stem Cell

Charles K.F. Chan,^{1,4,6,*} Eun Young Seo,^{1,4,6} James Y. Chen,^{2,6} David Lo,^{1,4,6} Adrian McArdle,^{1,4} Rahul Sinha,^{2,4} Ruth Tevlin,^{1,4} Jun Seita,^{2,4} Justin Vincent-Tompkins,² Taylor Wearda,^{1,4} Wan-Jin Lu,^{2,4} Kshemendra Senarath-Yapa,¹ Michael T. Chung,¹ Owen Marecic,¹ Misha Tran,¹ Kelley S. Yan,³ Rosalind Upton,² Graham G. Walmsley,^{1,4} Andrew S. Lee,² Debashis Sahoo,^{2,4,5} Calvin J. Kuo,³ Irving L. Weissman,^{2,4,7} and Michael T. Longaker^{1,4,7,*}

¹Department of Surgery

²Departments of Pathology and Developmental Biology

³Stanford Cancer Institute

⁴Institute for Stem Cell Biology and Regenerative Medicine

Stanford University, 450 Serra Mall, Palo Alto, CA 94305, USA

⁵Department of Pediatrics, University of California, San Diego, 9500 Gilman Drive, La Jolla, CA 92093, USA

⁶Co-first author

⁷Co-senior author

*Correspondence: chazchan@stanford.edu (C.K.F.C.), longaker@stanford.edu (M.T.L.)

<http://dx.doi.org/10.1016/j.cell.2014.12.002>

SUMMARY

How are skeletal tissues derived from skeletal stem cells? Here, we map bone, cartilage, and stromal development from a population of highly pure, post-natal skeletal stem cells (*mouse skeletal stem cells*, mSSCs) to their downstream progenitors of bone, cartilage, and stromal tissue. We then investigated the transcriptome of the stem/progenitor cells for unique gene-expression patterns that would indicate potential regulators of mSSC lineage commitment. We demonstrate that mSSC niche factors can be potent inducers of osteogenesis, and several specific combinations of recombinant mSSC niche factors can activate mSSC genetic programs in situ, even in nonskeletal tissues, resulting in *de novo* formation of cartilage or bone and bone marrow stroma. Inducing mSSC formation with soluble factors and subsequently regulating the mSSC niche to specify its differentiation toward bone, cartilage, or stromal cells could represent a paradigm shift in the therapeutic regeneration of skeletal tissues.

INTRODUCTION

Stem cell regulation in the skeletal system, as compared to the hematopoietic system, remains relatively unexplored. Pioneering studies by Friedenstein et al. established the presence of colony-forming skeletogenic cells, but only recently have efforts begun to identify and isolate bone, cartilage, and stromal progenitors for rigorous functional characterization (Bianco, 2011; Chan et al., 2013; Friedenstein et al., 1987; Méndez-Ferrer et al., 2010; Morrison et al., 2006; Park et al., 2012). In addition, the bone marrow is a favored site of prostate and breast cancer metastasis, and the characteristics of the bone stroma support-

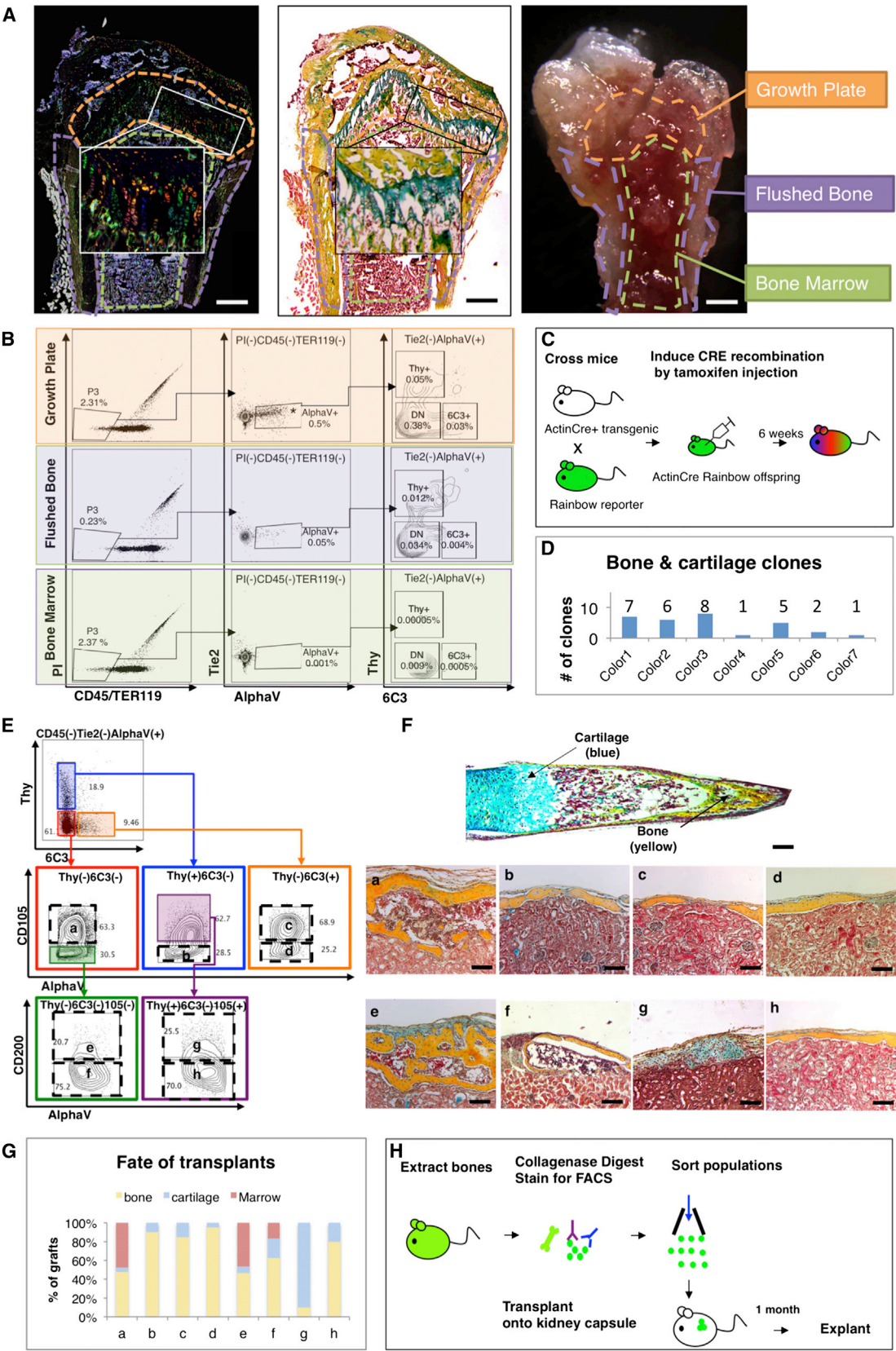
ing metastatic stem cell niches are largely uncharted. Another important challenge in tissue regeneration is the limited capacity to (re)generate cartilage, which is deficient in many diseases (e.g., osteoarthritis, connective tissue disorders) (Burr, 2004; Kilic et al., 2014).

We hypothesized that the skeletal system follows a program similar to that of hematopoiesis, with a multipotent stem cell generating various lineages in a niche that regulates differentiation. Thus we sought to (1) identify a multipotent skeletal stem cell and map its relationship to its lineage-committed progeny and (2) identify cells and factors in the skeletal stem cell niche that regulate its activity.

RESULTS

Identification of the Skeletal Stem Cell, Its Progeny, and Their Lineage Relationships Bone and Cartilage Are Derived from Clonal, Lineage-Restricted Progenitors

We used a “Rainbow mouse” (Ueno and Weissman, 2006) model to evaluate clonal-lineage relationships in vivo to determine whether mesenchymal tissues in bone—including stroma, fat, bone, cartilage, and muscle—share a common progenitor (Rinkevich et al., 2011) (see *Experimental Procedures*). To visualize clonal patterns within all tissues, we crossed Rainbow mice with mice harboring a tamoxifen (TMX)-inducible ubiquitously expressed Cre under the actin promoter (Actin-Cre-ERT) (Figure 1C). Six weeks after this recombinase activation, clonal regions could be detected as uniformly labeled areas of a distinct color (Figures S1A and S1B). Using this system, we observe clonal regions in the bone, particularly at the growth plate, that encompass bone, cartilage, and stromal tissue but not hematopoietic, adipose, or muscle tissue at all time points studied (Figures 1A, 1C–1D, and S1D). These data indicate that bone, cartilage, and stromal tissue are clonally derived in vivo from lineage-restricted stem and progenitor cells that do not also give rise to muscle and fat, at least at the time points examined (Figure S1).



(legend on next page)

Purified Cartilage, Bone, and Stromal Progenitor Cells Are Heterogeneous and Lineage Restricted

As we had observed a high frequency of clonal regions in the growth plate during our Rainbow clonal analysis, we isolated cells from the femoral growth plates by enzymatic and mechanical dissociation and analyzed them by fluorescence-activated cell sorting (FACS) for differential expression of CD45, Ter-119, Tie2, and AlphaV integrin. These surface markers correspond to those present on hematopoietic (CD45, Ter-119), vascular and hematopoietic (Tie2), and osteoblastic (AlphaV integrin) cells. We found that the growth plate had a high frequency of cells that were CD45⁻Ter-119⁻Tie2⁻AlphaV⁺, hereafter referred to as [AlphaV⁺]. Based on subsequent microarray analysis of [AlphaV⁺] showing differential expression of CD105, Thy, 6C3, and CD200, we fractionated this population into eight subpopulations (Figures 1B and 1E) (Seita et al., 2012).

To evaluate the intrinsic ability of the eight subpopulations to give rise to skeletal tissue, we isolated cells of each subpopulation from the long bones, ribs, and sternum of GFP⁺ mice (Figure 1E) and transplanted them beneath the renal capsules of immunodeficient mice (Figure 1H). Four weeks after transplantation, we explanted the GFP-labeled kidney grafts and processed the tissues for histological analysis to determine developmental outcome (Figure 1F). The eight subpopulations exhibited different developmental fates (Figures 1F and 1G): three followed a pattern of endochondral ossification (grafts consisting of bone, cartilage, and marrow) (Figures 1F and 1G: populations a, e, f); four gave rise to primarily bone with minimal cartilage and no marrow (Figures 1F and 1G: populations b, c, d, h); and one gave rise to predominantly cartilage with minimal bone and no marrow (Figures 1F and 1G: population g). Unlike the eight subpopulations of [AlphaV⁺], the CD45⁺Ter-119⁺ and Tie2⁺ subsets did not form bone, cartilage, or stroma (Figure S4), further emphasizing the existence of distinct progenitors of bone, cartilage, and stromal tissue. These results indicate that the skeletogenic progenitors are diverse, with distinct cell-surface marker profiles and skeletal tissue fates, similar to the diverse hematopoietic progenitor cells that generate various differentiated blood cells.

Identification of a Postnatal Skeletal Stem Cell

We hypothesized that skeletogenesis may proceed through a developmental hierarchy of lineage-restricted progenitors as occurs in hematopoiesis. We observed that the [CD45⁻Ter-119⁻Tie2⁻AlphaV⁺Thy⁻6C3⁻CD105⁻CD200⁺] subpopulation generates all of the other (seven) subpopulations through a sequence of stages both in vitro and in vivo, beginning with generation of two multipotent progenitor cell types: first, the [CD45⁻Ter-119⁻Tie2⁻AlphaV⁺Thy⁻6C3⁻CD105⁻CD200⁻] cell population, hereafter referred to as the pre-BCSP (*pre*-bone cartilage and stromal progenitor); and the [CD45⁻Ter-119⁻Tie2⁻AlphaV⁺Thy⁻6C3⁻CD105⁺] cell population, which we previously described as the BCSP (bone, cartilage, and stromal progenitor) (Chan et al., 2013). The [CD45⁻Ter-119⁻Tie2⁻AlphaV⁺Thy⁻6C3⁻CD105⁻CD200⁺] subpopulation generates in vitro and in vivo all of the other (seven) subpopulations in a linear fashion. In vitro, freshly sorted cells were cultured for 25 days, at which point they were refractionated by FACS (Figure 2A (i), Figures 2Bi and 2Bii), and subsequently transplanted beneath the renal capsule (Figures 2Ai and 2Biii). In vivo, the purified cells were transplanted beneath the renal capsule and explanted 1 month later for FACS analysis (Figures 2Aii, 2Ci, and 2Cii) or immunohistochemistry (Figure 2Ciii). These data demonstrate that the [CD45⁻Ter-119⁻Tie2⁻AlphaV⁺Thy⁻6C3⁻CD105⁻CD200⁺] subpopulation generates all of the other (seven) subpopulations in a linear fashion both in vitro and in vivo.

Single sorted cells from the [CD45⁻Ter-119⁻AlphaV⁺Thy⁻6C3⁻CD105⁻CD200⁺] subpopulation also generated all of the other subpopulations in a linear fashion both in vitro and in vivo (Figures 2D and 2E). In vitro: Individual [CD45⁻Ter-119⁻Tie2⁻AlphaV⁺Thy⁻6C3⁻CD105⁻CD200⁺] cells were plated and cultured for 14 days (Figure 2Ei). FACS analysis of the resultant primary colonies showed that they contained clones of the original cell and all other (seven) subpopulations of [AlphaV⁺] (Figure 2Eiv: *middle panel FACS plot*). These colonies contained both cartilage and bone tissue when examined by immunohistochemistry (Figure 2Eiii). Furthermore, when a single freshly sorted [CD45⁻Ter-119⁻Tie2⁻AlphaV⁺Thy⁻6C3⁻CD105⁻CD200⁺] cell isolated from the primary colony was again plated

Figure 1. Bone and Cartilage Are Derived from Clonal, Lineage-Restricted Progenitors

(A) Micrographs: 6-week-old Rainbow Actin-Cre-ERT mouse femur, following TMX induction at P3, shows clonal expansion at the growth plate. Fluorescent microscopy (left), pentachrome stain (middle), and dissection microscope (right). Scale bar: 500 μ m. Representative of 10 replicates.

(B) FACS plots: cells isolated from three different parts of the femur illustrate that [AlphaV⁺] is most prevalent in the growth plate (uppermost horizontal panel in the middle) ($p < 0.001$, ANOVA, $n = 3$). DN = double negative, negative for Thy and 6C3 surface expression.

(C) Scheme of experiment: Actin-Cre-ERT transgenic mouse was crossed with Rainbow reporter gene mouse. Cre recombination of offspring was induced by TMX induction on E15, P3, and postnatal week 6. Bones were harvested 6 weeks post-induction.

(D) Graphic representation illustrating different numbers of clones present, which span the bone and cartilage. Representative of sections with ten mice. See also Figure S1.

(E) FACS gating strategy for isolation of eight distinct skeletal tissue subpopulations obtained from the [AlphaV⁺] subset. a = BCSP, b = BLSP, c = 6C3, d = HEC, e = mSSC, f = pre-BCSP, g = PCP, h = Thy. Representative of 50 replicates.

(F) P3 Femur stained with Movat's pentachrome (top). Sections stained with pentachrome of tissue grafts following cell transplant beneath the renal capsule (bottom). Populations e (mSSC), f (pre-BCSP), and a (BCSP) can reconstruct entire bone, consisting of bone, cartilage, and a functional marrow cavity. Populations b (BLSP), c (6C3), d (HEC), and h (Thy) formed bone with minimal cartilage. Population g (PCP) formed cartilage with a minimum of bone. Scale bar: 200 μ m. Representative of 3–20 experiments.

(G) Graph depicting the percentage tissue composition (bone [yellow], marrow [red], and cartilage [blue]) of each of the explanted grafts a to h. Representative of 3–20 experiments.

(H) Scheme of experiment: 20,000 cells of each subpopulation of [AlphaV⁺] were isolated from the long bones of GFP-labeled P3 mice using FACS. Purified GFP⁺ cells were then transplanted beneath the kidney capsules of recipient mice. One month later, the grafts were explanted.

See also Figures S1, S3, S4, and S6.

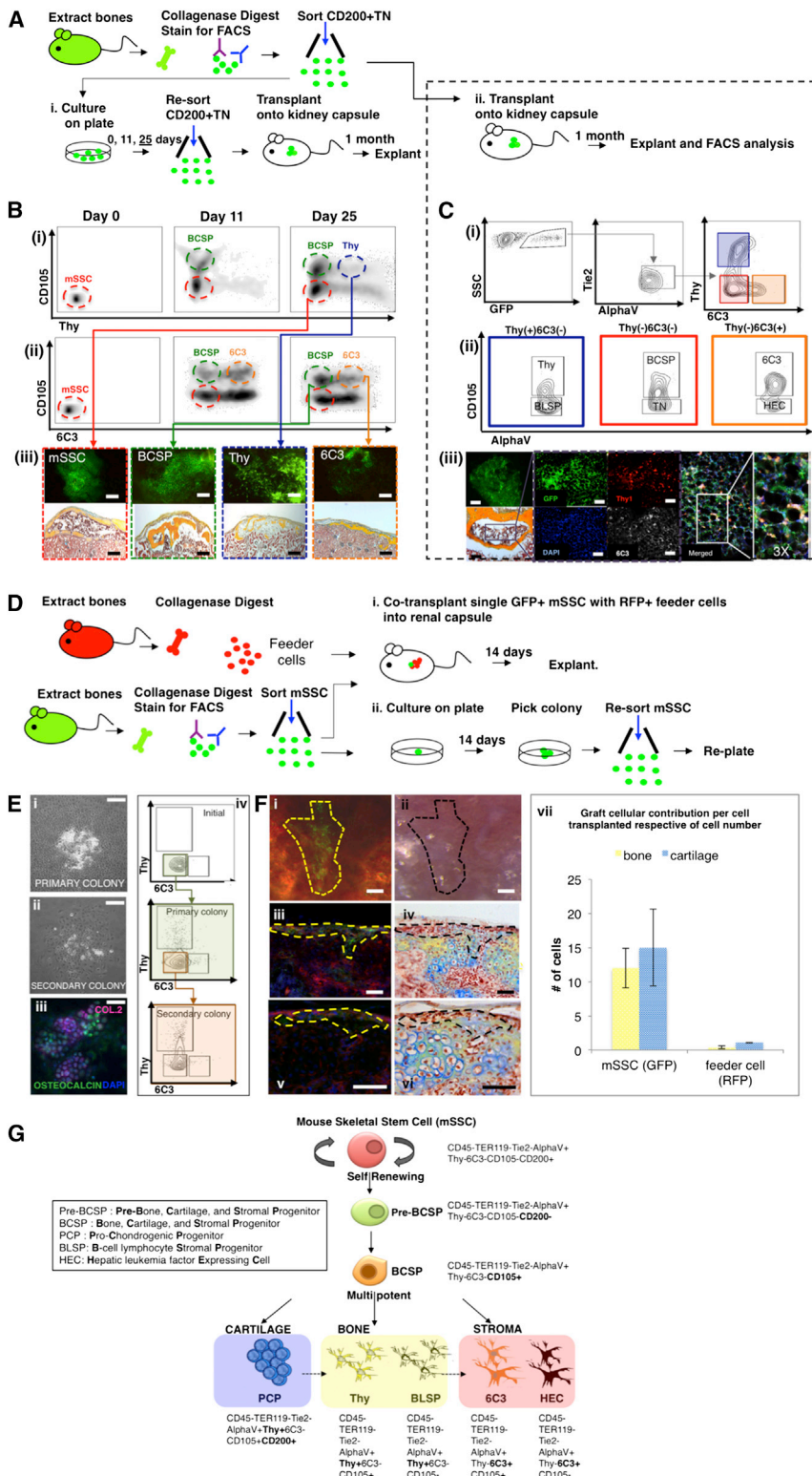


Figure 2. Identification of the mSSC

(A) Scheme of experiment: CD200⁺TN [CD45⁺Ter-119⁻Tie2⁺AlphaV⁺Thy⁻6C3⁻CD105⁻CD200⁺] cells were isolated from femora of GFP⁺ mice at P3. (i) Purified mSSCs were seeded and harvested on days 0, 11, 25 for FACS analysis. On day 25 following refractionation of the cells by FACS, 20,000 cells of each subset (mSSC, BCSP, Thy, 6C3) were transplanted beneath the kidney capsules of recipient mice. The grafts were explanted 1 month later. (ii) Purified GFP-labeled mSSCs were also directly transplanted beneath the kidney capsules of recipient mice. One month post-transplantation, the grafts were explanted.

(B) FACS analysis of cultured mSSCs on days 0, 11, and 25 in culture (i, ii). Transplanted mSSCs (red box) and BCSPs (green box) formed bone, cartilage, and a marrow cavity. Thy (blue box) and 6C3 (orange box) formed bone only, without a marrow cavity (iii). Scale bar: 500 μ m (iii, upper panel), 200 μ m (iii, lower panel). Representative of three replicates/subpopulation.

(C) (i, ii) FACS analysis of explanted kidney capsule grafts, in which highly purified populations of GFP-labeled [CD45⁺Ter-119⁻Tie2⁺AlphaV⁺Thy⁻6C3⁻CD105⁻CD200⁺] (mSSC) cells were transplanted beneath the kidney capsule: graft consisted of seven downstream subpopulations (blue, red, and orange boxes). Bright-field micrograph of pentachrome-stained explant (iii, far lower left) demonstrates that mSSCs are capable of generating bone, cartilage, and marrow. Immunostained explant (purple box, high magnification) shows that mSSCs are capable of generating cells that express Thy and 6C3 (iii, middle; Thy = red, 6C3 = white). Merged image (iii, extreme right). Fluorescent image of GFP⁺ graft (iii, far upper left). Scale bar: 500 μ m (iii, upper panel), 100 μ m (iii, lower panel), 50 μ m (iii). Representative of three replicates per transplanted subpopulation.

(D) Scheme of experiment: Unsorted cells from the long bones of RFP⁺ P3 mice served as feeder cells. Cells from the long bones of P3 GFP⁺ mice were isolated following mechanical and enzymatic dissociation, and mSSCs were obtained following FACS. (i) A single GFP-labeled mSSC was co-transplanted with 5,000 RFP⁺ feeder cells beneath the renal capsule of immunodeficient mice. (ii) A single purified GFP-labeled mSSC was plated per well of a 96-well culture dish. Following 14 days, formed colonies were counted, harvested, and re-sorted using FACS, and a single purified GFP-labeled mSSC was again plated per well of a 96-well culture dish, and the assay repeated.

(E) In vitro, colony formation assays were performed by plating a single mSSC in each well of a 96-well culture dish. (i) Representative micrograph of a primary colony depicted at 14 days post-plating. (ii) Passaging of primary colonies resulted in the formation of secondary colonies with similar morphologies to those of primary colonies. (iii) Primary colonies stained positive for anti-collagen 2 (purple), anti-osteocalcin (green), and DAPI

(blue) following immunofluorescent staining. (iv) Vertical panel on right depicts FACS analysis of initial mSSC cells isolated (top), subsequent primary colony (middle), and secondary colony cell (bottom). Scale bar: 500 μ m (i, ii), 100 μ m (iii). Representative of ten assays.

(F) Microscopy of explanted grafts (as per Figure 2Di). The extent of the in vivo colony formation from GFP-labeled mSSCs is outlined by a yellow broken line (i, iii, v) or black broken line (ii, iv, vi). Clonally expanded, GFP-labeled mSSCs are seen as green cells (fluorescent image, i, iii, v). Corresponding bright-field

(legend continued on next page)

and cultured for 14 days, the resultant secondary colony contained clones of the original cell and all other subpopulations (Figure 2Eii) on FACS analysis (Figure 2Eiv: bottom panel FACS plot). These results demonstrate that the in vitro self-renewal of a single [CD45⁺Ter-119⁺Tie2⁺AlphaV⁺Thy⁺6C3⁺CD105⁺CD200⁺] cell maintained the skeletogenic properties of freshly isolated [CD45⁺Ter-119⁺Tie2⁺AlphaV⁺Thy⁺6C3⁺CD105⁺CD200⁺] cells. In vivo: When transplanted individually, [CD45⁺Ter-119⁺Tie2⁺AlphaV⁺Thy⁺6C3⁺CD105⁺CD200⁺] cells did not engraft efficiently beneath the renal capsule, perhaps reflecting their need for a supportive niche. Thus, we cotransplanted a single GFP-labeled [CD45⁺Ter-119⁺Tie2⁺AlphaV⁺Thy⁺6C3⁺CD105⁺CD200⁺] cell with 5,000 unsorted, RFP-labeled cells isolated from the long bones to simulate a niche (Figure 2Di). Two weeks after transplantation, we explanted the grafts for immunohistochemical analysis. The GFP-labeled transplanted cells (Figures 2Fi and 2Fii) differentiated into both chondrocytes and osteocytes in vivo (Figures 2Fiv, 2Fvi, and 2Fvii), consistent with in vitro properties (Figure 2Eiii). These data indicate that the [CD45⁺Ter-119⁺Tie2⁺AlphaV⁺Thy⁺6C3⁺CD105⁺CD200⁺] population possesses definitive stem cell-like characteristics of self-renewal and multipotency. We therefore conclude that the [CD45⁺Ter-119⁺Tie2⁺AlphaV⁺Thy⁺6C3⁺CD105⁺CD200⁺] cell population represents a mouse skeletal stem cell (mSSC) population in postnatal skeletal tissues (Figure 2G), and that the seven other subpopulations of [AlphaV⁺] are mSSC progeny.

Based on the analyses described above, we defined a lineage tree of skeletal stem/progenitor cells (Figure 2G). The mSSC initiates skeletogenesis by producing a hierarchy of increasingly fate-limited progenitors. The multipotent and self-renewing mSSC first gives rise to multipotent progenitors, pre-BCSPs and BCSPs. These cells then produce the following oligolineage progenitors: pro-chondrogenic progenitors (PCPs) [CD45⁺Ter-119⁺Tie2⁺AlphaV⁺Thy⁺6C3⁺CD105⁺CD200⁺]; the Thy subpopulation, [CD45⁺Ter-119⁺Tie2⁺AlphaV⁺Thy⁺6C3⁺CD105⁺], hereafter referred to as Thy; B cell lymphocyte stromal progenitors, BLSPs [CD45⁺Ter-119⁺AlphaV⁺Thy⁺6C3⁺CD105⁺]; the 6C3 subpopulation, [CD45⁺Ter-119⁺AlphaV⁺Thy⁺6C3⁺CD105⁺], hereafter referred to as 6C3; and the hepatic leukemia factor-expressing cell, HEC [CD45⁺Ter-119⁺AlphaV⁺Thy⁺6C3⁺CD105⁺] (Figure 2G). mSSC-derived lineages include cell types that we have previously characterized, which possess distinct hematopoietic supportive capabilities (Chan et al., 2013) (Figures S2A and S2B).

Identification of Factors that Regulate Skeletal Stem and Progenitor Cell Activity and Differentiation Downstream Skeletal Progenitors Regulate mSSC Activity

Once we had isolated the mSSC, we focused on identifying the cells that make up the mSSC niche, the microenvironment that

supports and regulates stem cell activity. We first conducted microarray gene-expression analyses of freshly sorted mSSC/pre-BCSP and five downstream progenitor populations [(1) BCSP; (2) Thy; (3) 6C3; (4) BLSP; and (5) HEC] to identify receptors to signaling pathways that may regulate activity of the mSSC and its progeny (Figures 3D and 3E).

To interpret the gene-expression profiles of these cells, we used the Gene Expression Commons (Seita et al., 2012), a platform that normalizes microarray data against a large collection of publicly available microarray data from the National Center for Biotechnology Information Gene Expression Omnibus. From this analysis, it is apparent that mSSC and its progeny differentially express receptors involved in transforming growth factor, TGF (specifically bone morphogenetic protein [BMP]) and Wnt signaling pathways, and cognate morphogens of these pathways, including BMP2, TGF- β 3, and Wnt3a (Figures 3D and 3E). These results suggest that paracrine and/or autocrine signaling among mSSCs and their progeny may positively regulate their own expansion (Figure 3F). Furthermore, single cell RNA sequencing revealed coexpression of BMP2 and its receptor (BMPRIa) in 28% of mSSCs (Figures 3A–3C and S5), supporting potential for autocrine and/or paracrine signaling in the mSSCs.

In support of transcriptional data, the addition of exogenous recombinant BMP2 to culture media rapidly induced expansion of isolated mSSC, whereas supplementation of media with either exogenous recombinant TGF- β or tumor necrosis factor alpha (TNF- α) did not (Figures 3G and 3H). In addition, proliferation of mSSC in vitro was markedly inhibited by addition of recombinant gremlin 2 (an antagonist of BMP2 signaling) protein to culture media, in contrast to control. Progeny of the mSSCs express antagonists of the BMP2 signaling pathway, such as Gremlin 2 and Noggin (Figure 3I), suggesting the presence of a potential negative feedback mechanism to control mSSC proliferation by more differentiated progeny. Specifically, Thy expresses Gremlin 2, and both Thy and BLSP express Noggin. This is consistent with Thy and BLSP subpopulations acting in a negative feedback loop to inhibit BMP2-induced proliferation of the mSSC, further supporting a regulatory role for paracrine signaling among mSSCs and their progeny.

Shifting Fates: Cartilage to Bone

Our next step was to comprehend signaling pathways that could play a role in directing the differentiation of skeletal stem/progenitor cells. Specifically, we wished to direct osteogenesis to chondrogenesis, as this is directly related to a large unmet clinical need for cartilage (Bhumiratana et al., 2014; Jo et al., 2014; Makris et al., 2014; Mollon et al., 2013). We asked whether mSSC-derived stroma could influence fate commitment of skeletal progenitor cells (Figure 2G). We observed that the skeletal subsets with the immunophenotype [CD45⁺Ter-119⁺AlphaV⁺Thy⁺6C3⁺CD105⁺CD200⁺] (Figure 1F: population g) isolated

micrographs are shown (ii, iv, vi). Fluorescent imaging of transverse sections of grafts are shown (iii, v). Corresponding bright-field micrographs of pentachrome-stained sections demonstrate that clonally expanded cells are fated into bone (yellow) and cartilage (blue) (iv, vi). Graph (vii) is representative of the contribution by GFP or RFP cells (per cell transplanted) to bone or cartilage formation (mean \pm SEM). Scale bar: 200 μ m (i–vi). Representative of five transplants of each assay. (G) Schematic representation of the skeletal stem cell lineage tree. The mSSC occupies the apex of this hierarchical tree and is multipotent and capable of self-renewal and differentiation into more lineage-restricted progenitor cells (pre-BCSP and BCSP). The mSSCs, pre-BCSPs, and BCSPs are capable of giving rise to bone, cartilage, and hematopoietic supportive stroma. The immunophenotype of each cell is shown.

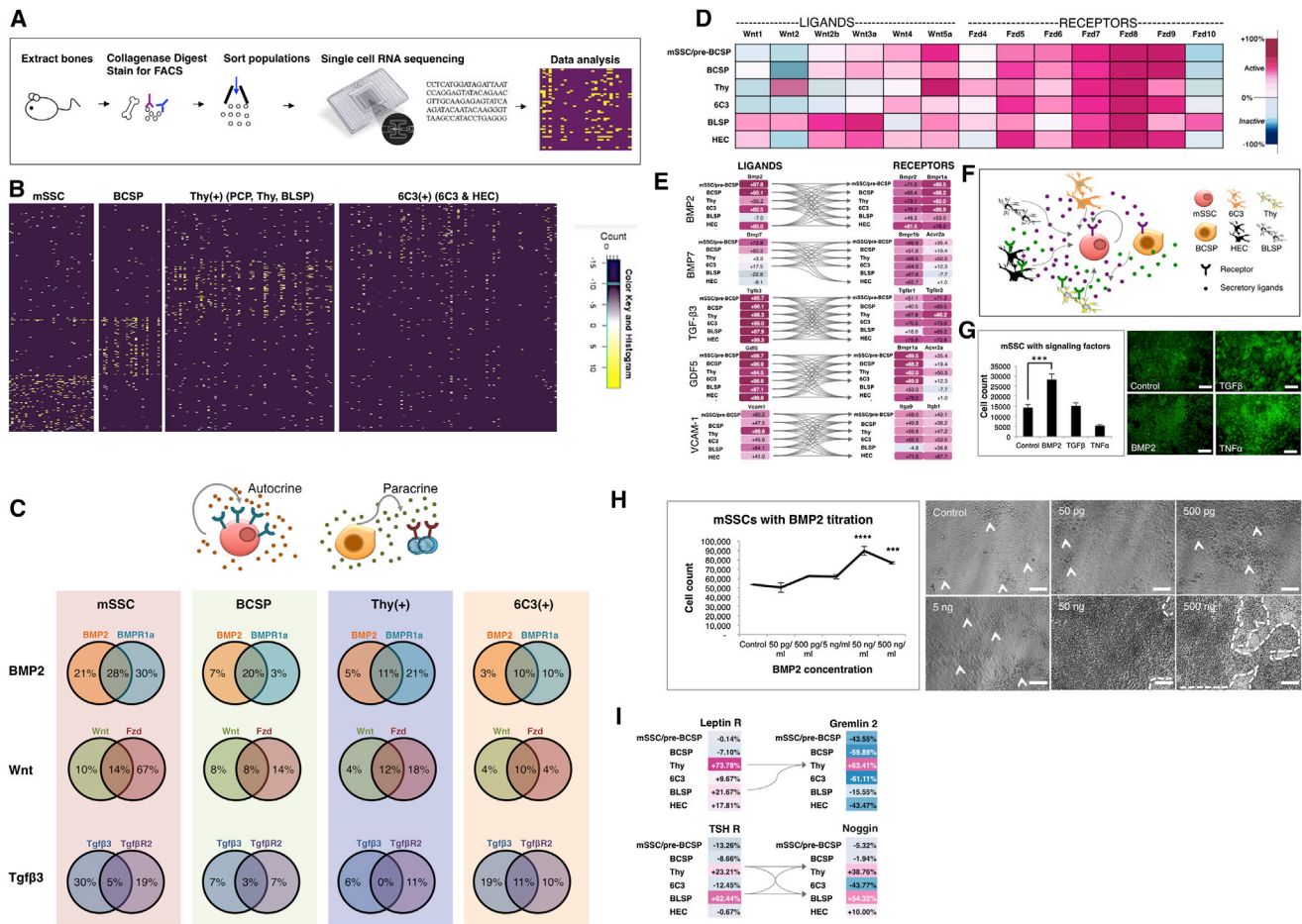


Figure 3. The mSSC Niche Is Composed of Other Skeletal-Lineage Cells

(A) Scheme of experiment: Long bones of P3 mice were harvested as previously described. The cell suspension was sorted by FACS to obtain mSSC; BCSP; Thy⁺, which encompasses the PCP, Thy, and BLSP subsets; and 6C3⁺, which encompasses 6C3 and HEC. Cell subpopulations were prepared for single-cell RNA sequencing.

(B) Hierarchical clustering of single-cell RNA-sequencing data demonstrates four molecularly distinct patterns of single-cell transcriptional expression between mSSC, BCSP, Thy⁺, and 6C3⁺.

(C) Percentage transcriptional expression of morphogen (left circle in each Venn diagram), receptor (right circle in each Venn diagram), or both (overlapping central portion of the Venn diagram) on single-cell RNA sequencing. Note that the percentage denotes the percentage of cells within each subset (mSSC, BCSP, Thy⁺, and 6C3⁺), which express the relevant gene sequence. (Top) The patterns show the potential for paracrine (right) and autocrine (left) signaling.

(D) Gene-expression levels of Wnt-associated genes in skeletal populations as determined using the Gene Expression Commons analysis platform. The range of transcriptional expression is illustrated by a color change as depicted on the extreme right of the figure (i.e., dark purple correlates to high expression, whereas dark blue correlates to low expression). Heatmap shows high expression of both Wnt ligands (*Wnt3a*, *Wnt4*, *Wnt5a*) and receptors (*Fzd5-9*), demonstrating that Wnt signaling may be actively involved in skeletal progenitor function. *Fzd* = frizzled receptor. These data were compiled in triplicate, with 10,000 cells of each subset analyzed in each sample.

(E) Ligand-receptor interaction maps demonstrate that the skeletal stem/progenitor cells can act as their own niche and signal through each other to promote skeletogenesis. Gene-expression analysis of microarray data extracted from skeletal subsets show ligands in the left column and cognate receptors in the right column. The connecting arrows indicate possible ligand-receptor interaction pathways. Note: GDF = growth and differentiation factor, VCAM-1 = vascular cell adhesion molecule-1. Data were compiled from triplicate samples, with 10,000 cells of each subset analyzed in each sample.

(F) Diagram illustrating potential signaling pathways influencing activity of skeletal stem/progenitor cells. Paracrine and/or autocrine signaling may occur in the skeletal stem cell niche and regulate cell activity and maintenance.

(G) Fluorescent micrographs illustrate colony morphology of mSSCs post-culture with morphogen (BMP2/TGF-β/TNF-α) supplementation/control (right). Graph shows the number of mSSCs present following culture for 14 days under the different conditions (left). rhBMP2 supplementation was associated with significant amplification of the mSSC populations in vitro (bottom left) in comparison to control, nonsupplemented media (top left) (mean ± SEM, *p* < 0.01, *t* test, *n* = 3). Supplementation with TGF-β or TNF-α resulted in altered colony morphology (upper and lower right). These results show that niche signaling can influence mSSC proliferation. Scale bar: 200 μm.

(H) Graph illustrates the effect of rhBMP2 titration on mSSC proliferation in culture (left). The effect of BMP2 was significantly greater than control at each of the following concentrations: 50 ng/ml (mean ± SEM, *p* < 0.001, ANOVA), 500 ng/ml (mean ± SEM, *p* < 0.01, ANOVA). Phase images illustrate the colonies of cells

(legend continued on next page)

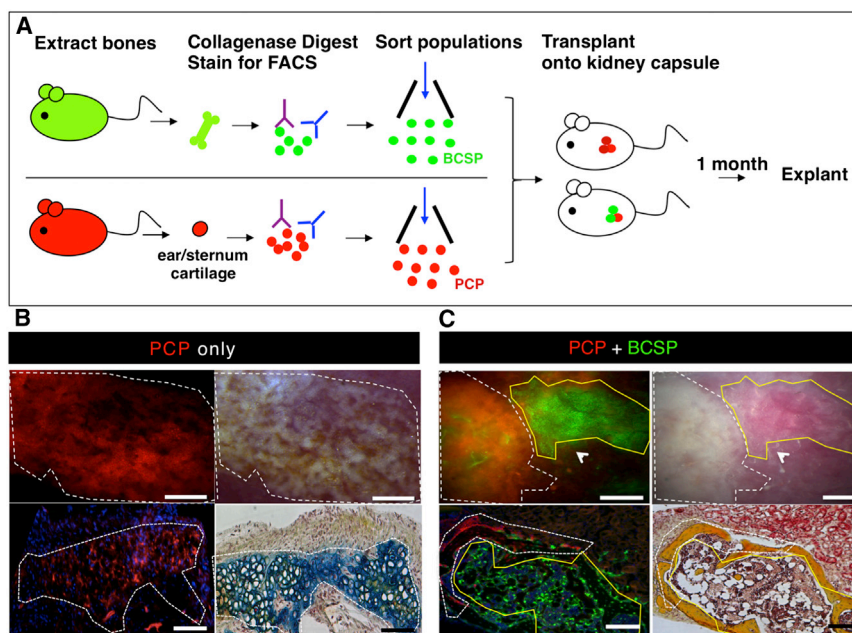


Figure 4. Shifting Fates: Cartilage to Bone

(A) Scheme of experiment: BCSPs were isolated from femora of GFP⁺ mice at P3, and PCPs were isolated from ears/sternum of RFP⁺ adult mice following mechanical and enzymatic digestion and subsequent FACS fractionation. Purified GFP⁺ BCSP and RFP⁺ PCP were cotransplanted beneath the kidney capsules of immunodeficient recipient mice. RFP⁺ PCP transplant served as a control. One month after transplantation, all grafts were removed for analysis.

(B) Microscopy of explanted grafts 1 month following transplantation of 20,000 RFP⁺ PCP cells (see Figure 4A). The white dotted line outlines the extent of the graft formed. Fluorescence micrograph of explanted graft demonstrate the presence of an RFP⁺ graft (upper left). Corresponding bright-field micrograph is shown in upper right panel. Transverse section stained with Movat's pentachrome demonstrates that RFP-labeled PCP cells form cartilage (blue stain) (lower right). Scale bar: 500 μ m (upper panel), 200 μ m (lower panel). Representative of four replicates.

(C) Microscopy of explanted grafts following cotransplantation of 20,000 RFP-labeled PCP cells with 20,000 GFP-labeled BCSPs (as detailed in Figure 4A). The grafts, which formed, are outlined

by a white dotted line (indicating RFP⁺ portion) and a yellow solid line (indicating GFP⁺ portion) (upper left). A corresponding bright-field micrograph is shown in the upper right panel. A transverse section stained with Movat's pentachrome shows that both RFP-labeled PCPs and GFP-labeled BCSPs form bone (yellow stain) (lower right). Scale bar: 500 μ m (upper panel), 200 μ m (lower panel). Representative of five replicates.

from RFP⁺ mice are directed primarily toward cartilage formation when transplanted in isolation beneath the renal capsule of nonfluorescent mice; thus, we designated this cell the PCP (Figures 4A and 4B). However, when RFP-labeled PCPs (Figure 2G) are cotransplanted with GFP-labeled BCSPs, they differentiate into bone but not cartilage (Figure 4C).

Shifting Fates: Bone to Cartilage

Having observed that signaling from cotransplanted BCSP could divert cartilage-fated cells toward bone formation, we next sought to identify factors that could, conversely, selectively promote mSSCs to cartilage rather than bone fates. Emerging evidence indicates that increased VEGF expression can spur resting chondrocytes to re-enter a hypertrophic state and resume endochondral ossification (Saito et al., 2010; Street et al., 2002). Thus, we aimed to determine whether inhibition of mSSCs by blocking VEGF-dependent ossification (Figure 5A). We administered adenoviral vectors encoding a soluble ligand-binding ectodomain (ECD) of the VEGFR1 receptor (Ad sVEGFR1) intravenously, leading to potent systemic VEGF antagonism (Wei et al., 2013). Adenovirus encoding a control

immunoglobulin IgG2 α Fc domain served as control treatment. One day later, we transplanted either intact embryonic day (E) 14.5 pre-osteogenic fetal femora or freshly sorted mSSCs under the renal capsules of these mice and then explanted the tissue 3 weeks later (Figure 5A). The grafts from the Ad sVEGFR1-treated mice contained predominantly cartilaginous tissue (Figure 5B, right). In contrast, the grafts from the control Ad Fc animals evidenced endochondral ossification and formation of a marrow cavity surrounded by cortical bone (Figure 5B, left). These results suggest that VEGF blockade may promote chondrogenesis at the expense of osteogenesis (Figure 5C).

BMP Pathway Manipulation Can Induce De Novo Formation of the mSSC in Extraskeletal Locations

We next investigated whether other tissue types contain cells that are osteo-inducible or harbor dormant mSSCs that can be activated to undergo osteogenesis. As we observed that BMP2 can expand mSSC in vitro (Figures 3G and 3H), we tested BMP2 as an agent that may induce such osteogenesis. We placed collagen sponges containing recombinant BMP2 into subcutaneous extraskeletal sites. Harvest of the collagen sponges 4 weeks after placement revealed abundant osseous

derived from the mSSCs (indicated by arrowhead in control, 50 pg/ml, 500 pg/ml, 5 ng/ml and by a broken line in 50 ng/ml and 500 ng/ml) (right). Scale bar: 500 μ m, n = 3.

(I) Ligand-receptor interaction maps show gene-expression levels of BMP antagonists gremlin 2 and Noggin (right top and bottom, respectively). There is increased expression of the receptors for the systemic hormones leptin and thyroid-stimulating hormone (TSH) on the same subpopulations of downstream progenitors Thy and BLSP (left top and bottom), which express BMP antagonists. Viewing the left and right panels in unison, the ligand-cognate receptor interaction graph shows that signaling through systemic hormones leptin and TSH receptors may produce inhibitory signals for mSSC expansion by BMP2 antagonism (via gremlin 2, noggin) and subsequent osteogenesis in skeletal stromal populations. Arrows illustrate the potential receptor-ligand interactions. Data were compiled from triplicate samples, with 10,000 cells of each subset analyzed in each sample.

See also Figures S2 and S5.

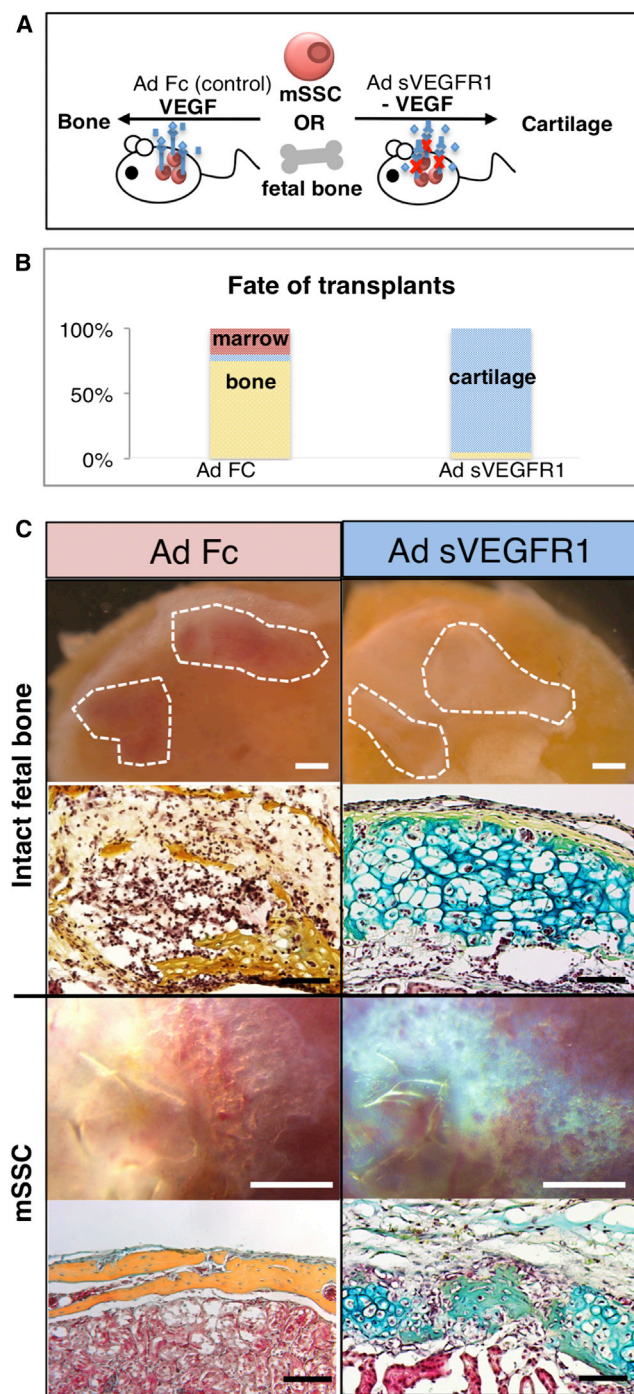


Figure 5. Shifting Fates: Bone to Cartilage

(A) Scheme of experiment: mSSCs were isolated from P3 mice as described previously. Either intact pre-osteogenic femora isolated from E14.5 mice or 20,000 mSSCs were then transplanted beneath the kidney capsules of recipient mice with/without systemic inhibition of VEGF signaling. For inhibition of VEGF signaling, adenoviral vectors encoding soluble VEGFR1 ectodomain (Ad sVEGFR1) were delivered intravenously to the recipient mice 24 hr prior to cell transplantation, leading to systemic release of this potent antagonist of VEGF signaling. Ad Fc encoding an immunoglobulin Fc fragment was served as a negative control. Grafts were explanted 3 weeks later.

osteoids replete with marrow (Figures 6A–6C). Furthermore, FACS analysis of cells within the marrow of the induced osteoids revealed that hematopoietic stem cell (HSC) engraftment also occurs in the osteoids (Figure 6B). By FACS analysis, we determined that mSSCs are normally not detectable or are exceedingly rare in subcutaneous adipose tissue (Figure 6C, right panel). In contrast, mSSCs are plentiful in BMP2-induced osteoids 10 days after implantation, whereas ossification is still proceeding (Figure 6C, left panel).

To determine whether BMP2 induced skeletal transformation of in situ cells or migration of circulating skeletal progenitors recruited from bone tissue, we used a parabiont model (Figure 6D). We surgically fused actin-GFP transgenic mice to non-GFP congenic mice such that they established a shared circulatory system (Conboy et al., 2013). Two weeks after parabiosis, after confirmation of chimerism, we implanted collagen sponges containing recombinant BMP2 into the inguinal fat pad of the non-GFP parabiont. Ten days after implantation, we explanted the sponge and surrounding tissue and performed mechanical and chemical dissociation to isolate the constituent cells. We assayed the contribution of the GFP-labeled cells to ectopic bone formation in the non-GFP mouse by FACS analysis to determine whether circulating cells contributed to ectopic bone development. The tissue of the explants contained abundant GFP-labeled cells at harvest, but GFP-labeled cells in the graft were solely CD45⁺ hematopoietic cells (Figure 6D, left panel, top and bottom) and not skeletal progenitors (Figure 6D, FACS plots, mSSC cell population shown on far right). The skeletal progenitor population present in the explanted tissue was entirely GFP negative, suggesting that circulating cells did not contribute to BMP2-induced ectopic bone. These data indicate that BMP2-induced osteogenesis involves local cell response that is sufficient to induce mSSC formation in the subcutaneous fat pads, leading to formation of ectopic bone that can support hematopoiesis.

We next wished to determine which cell types could undergo BMP2-mediated reprogramming to mSSC in these extraskeletal sites. We, therefore, conducted FACS analysis of suspended cells isolated from the kidney and the subcutaneous adipose tissue and looked for markers that could distinguish cell types common to both of these extraskeletal organs. We found that both kidney and adipose tissue contain high numbers of Tie2 (Arai et al., 2004; De Palma et al., 2005; Heldin and Westermark, 1999). Using a specific Tie2Cre × MTMG reporter mouse, which genetically labels cells that expressed Tie2 with GFP and other cells with RFP, we again inserted collagen sponges containing

(B) Graphic representation of the fate of the mSSC/fetal bone transplants in the presence of Ad sVEGFR1 or Ad Fc control. Cartilaginous fate is promoted in the presence of systemic VEGF antagonism ($n = 5$, ANOVA, $p < 0.001$).

(C) Explanted grafts are shown in the first and third rows from the top of the panel (control, Ad Fc in left panel, and Ad sVEGFR1 in the right panel). Representative sections stained with Movat's pentachrome are shown in the second and fourth rows from the top of the panel (top two rows: intact fetal bone, bottom two rows: mSSC). VEGF signaling inhibition resulted in the formation of cartilage (blue stain) (right), with the Ad Fc group forming bone (yellow stain) (left). Scale bar: 500 μ m (intact fetal bone, top), 100 μ m (intact fetal bone, bottom), 500 μ m (mSSC, top), 200 μ m (mSSC, bottom). Representative of five replicates per assay.

recombinant BMP2 into the inguinal fat pad and harvested the implanted tissue 1 month later (Figure 6E). FACS analysis revealed that BMP2-derived ossicles clearly incorporated GFP-positive Tie2-derived osteocytes with visible canaliculi (Figure 6F, high-magnification inset) and Tie2-negative RFP-labeled osteocytes (Figure 6F), suggesting that both Tie2-positive and Tie2-negative lineages underwent BMP2-induced skeletal reprogramming. These data suggest that a variety of cell types could potentially be induced by BMP2 to initiate formation of mSSC.

Codelivery of BMP2 and VEGF Inhibitor Is Sufficient to Induce De Novo Formation of Cartilage in Adipose Tissue

Although bone itself possesses regenerative ability, the capacity for regeneration in other skeletal tissue (e.g., cartilage) is very low. As BMP2 induction could stimulate mSSC expansion and formation (Figures 3G, 3H, and 6C), we speculated that the mSSC-inducing capacity of BMP2 could be coupled with VEGF blockade to direct de novo cartilage formation. To test this possibility, we implanted BMP2-treated collagen sponges into the adipose tissue of mice that had either been treated 24 hr earlier with intravenous Ad sVEGFR1 as in Figure 5 or included soluble VEGFR1 ECD (50 μ g) directly in the collagen sponge (Figure 7A). One month later, the tissues were explanted. BMP2 alone generated bone tissue with a marrow cavity (Figure 7B, left panel). However, BMP2 with either systemic or local VEGF inhibition resulted in predominant cartilage formation (Figure 7B, right panel). The induced cartilage contained a similar frequency of PCPs to that seen in natural cartilage (Figure 7C). As native adipose tissue normally does not undergo chondrogenesis, the induced cartilage likely derives from BMP2-induced mSSCs that were shifted toward cartilage fate by the action of VEGF blockade.

Translational Implications of Skeletal Stem Cell Biology

We next investigated the role of mSSCs in skeletal repair. Highlighting their potential regenerative capabilities, we find that the mSSC number is significantly higher in the callus of a fractured femur than in the uninjured femur (Figures S6A and S6B). Interestingly, mSSCs isolated from a fracture callus also demonstrate enhanced osteogenic capacity (in comparison to uninjured) *in vitro* (Figure S6C, left panel) and *in vivo* (Figure S6C, right panel). As it is well known that irradiation results in osteopenia and reduced fracture healing (Mitchell and Logan, 1998), we asked whether the skeletal response to irradiation is linked to depletion of mSSC activity. When mice were irradiated 12 hr prior to fracture induction, we noted a significant reduction in mSSC expansion at 1 week following fracture in comparison to nonirradiated femora 1 week post-fracture (Figure S6D), echoing previous observations (Galloway et al., 2009).

DISCUSSION

Identifying Postnatal Skeletal Stem/Progenitor Cells and Defining the Lineage Tree

The mSSC lineage map we present consists of eight different cellular subpopulations with distinct skeletogenic properties and encompasses subpopulations that have characteristics of described skeletogenic cell types identified by lineage tracing

(Bianco, 2014; Méndez-Ferrer et al., 2010; Park et al., 2012; Zhou et al., 2014). For example, the Thy subtype selectively expresses high levels of CXCL12, leptin receptor, and nestin, which are characteristics of CXCL12-abundant reticular cells, leptin receptor-expressing cells (LepR⁺), and Nestin-expressing mesenchymal stem cells, respectively. We also find that both Nestin-cre- and MX1-cre-labeled populations overlap with the mSSC population (Figure S3) (Chan et al., 2013).

Signals Controlling mSSC and Progenitor Activity

Mechanistically, mSSC expansion and self-renewal must be tightly controlled, evidenced by the expression of numerous cognate receptors to signaling molecules belonging to most of the known signaling pathways, including Hedgehog, BMP, FGF, and Notch. Both BMP2 and 4 are expressed by mSSCs and most mSSC-derived subsets, where they likely mediate survival and expansion via both autocrine and paracrine loops. Conversely, downstream progeny of mSSCs, such as Thy and BLSP populations, express noggin and/or gremlin 2, which antagonize BMP signaling. This suggests that mSSCs and some of their progeny form a portion of their own niche, maintaining critical levels of prosurvival factors such as BMP2 but also controlling skeletal growth by antagonizing BMP signaling. In addition, mSSCs are dramatically amplified in fracture callus, implying that extrinsic signals generated in the regenerative environment could locally activate these cells (Figure S6).

Directing Skeletal Progenitor Fate Determination from Bone to Cartilage

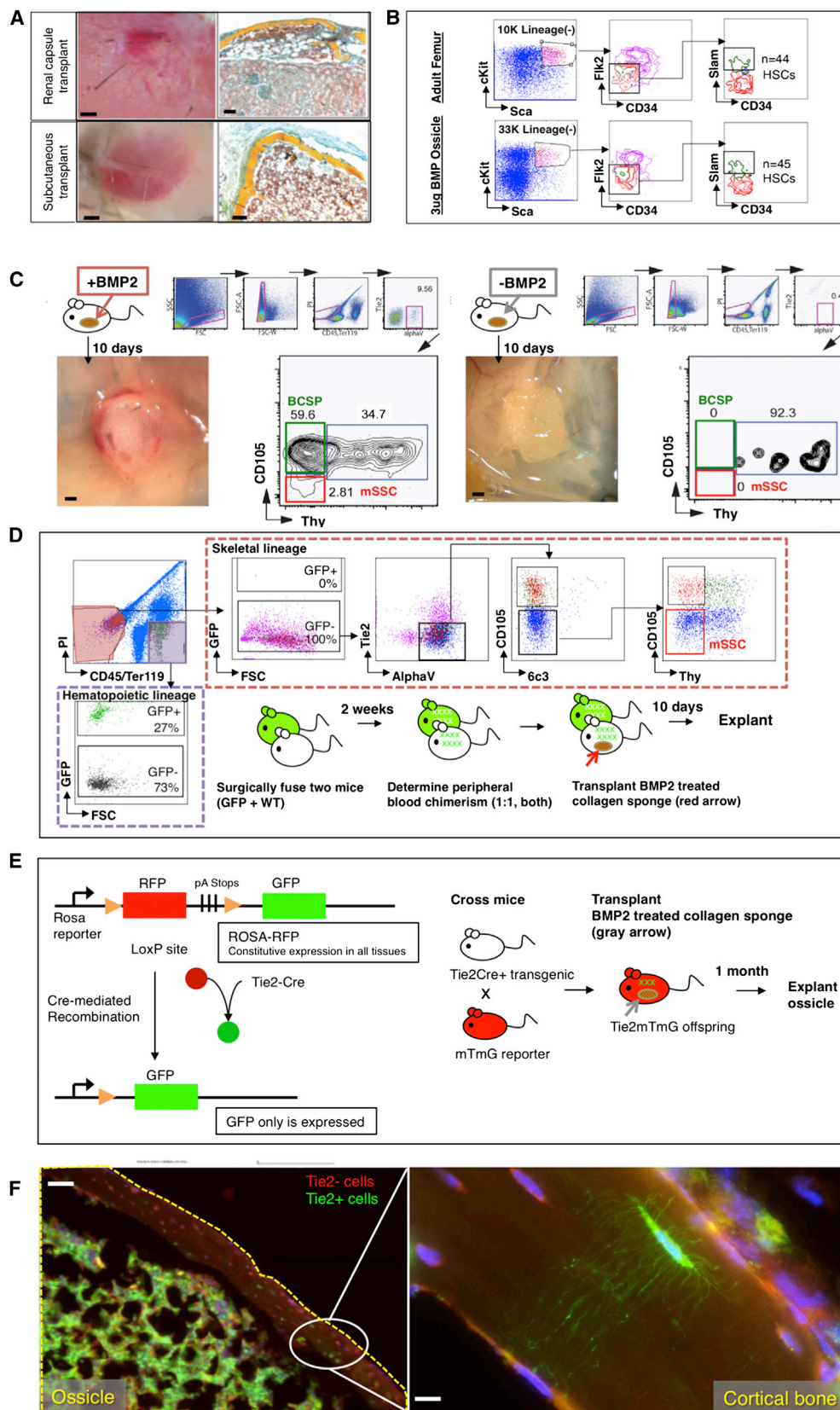
Antagonistic signaling between mSSC-derived skeletal subsets also appears to be a key mechanism in skeletal subset lineage commitment, particularly to either a bone or cartilage fate. When we antagonized VEGF signaling in early skeletal progenitors, bone fates were inhibited in favor of cartilage fates. These results echo previous reports, which suggest that VEGF acts as an essential chondrogenic regulator (Carlevaro et al., 2000; Gerber et al., 1999; Harper and Klagsbrun, 1999).

Directing Skeletal Progenitor Fate Determination from Cartilage to Bone

Paracrine signaling among skeletal subsets may also participate in determining bone versus cartilage formation, specifically in favoring bone. Altered signaling in a particular subpopulation can direct the skeletal fate of other subpopulations in the micro-environment. It is possible that pathological conditions involving calcification of cartilaginous tissues, such as osteoarthritis, could stem from defects in the mSSC niche, leading to aberrant signaling that promotes osteogenesis.

Hematopoietic and Skeletal Stem Cell Homeostasis May Be Closely Related

At a transcriptional level, mSSC-generated progeny express numerous cytokines necessary for HSC maintenance and hematopoiesis, including Kit ligand and stromal-derived factor (Figure S2C). We also find evidence that stem and progenitor cells of the hematopoietic system may reciprocally regulate skeletal progenitors (Figures S2A, S2B, and S2D). We conducted gene-expression analysis of multiple hematopoietic stem and



(legend on next page)

progenitor subsets and found that hematopoietic progenitors express myriad factors associated with skeletogenesis, including *BMP2*, *BMP7*, and *Wnt3a*. As previously shown, the cognate receptors of these factors are highly expressed by mSSCs and their progeny (Figures 3D and 3E). Intriguingly, although mSSC-generated progeny, such as Thy and BLSP, selectively express receptors to circulating systemic hormones, such as leptin and thyroid-stimulating hormone, these receptors are not highly expressed in HSCs or hematopoietic subsets (Figure S2D; data not shown; Seita et al., 2012), thus, suggesting that mSSC-derived stromal cells may link systemic endocrine regulation to both skeletal and hematopoietic systems.

Altering Extraskelatal Niche Signaling to Induce Osteogenesis and Chondrogenesis

Modulating niche signaling can stimulate tissue growth by inducing proliferation of stem cells, as we have observed with skeletal stem cells and as described in the hematopoietic system (Calvi et al., 2003). Niche interactions may also play significant roles in maintaining lineage commitment, for instance, high levels of BMP2 signaling can dominate local adipose signaling and re-specify resident Tie2⁺ and Tie2⁻ subsets to undergo osteogenesis. Niche interactions can also determine the fate of the mSSC. By implanting BMP2-treated collagen sponges in concert with systemic or local application of soluble VEGF receptor, we demonstrate that cartilage can be induced to form entirely by manipulation of local signaling pathways in extraskelatal tissue.

Conclusion

Inducing mSSC formation with soluble factors and subsequently regulating the mSSC niche to specify its differentiation toward bone, cartilage, or stromal cells could represent a paradigm shift in the therapeutic regeneration of skeletal tissues. This therapeutic modality could also extend to the codependent hematopoietic system even when resident levels of endogenous mSSCs

have been depleted by disease or aging. The challenge now is to understand how intrinsic and extrinsic signals guide mSSCs to regulate skeletal shape and patterning at the single-cell level.

EXPERIMENTAL PROCEDURES

Detailed experimental procedures are described in the [Extended Experimental Procedures](#).

Mice

C57BL6, Rag-2/gamma(c)KO, C57BL/6-Tg(CAG-EGFP)10sb/J, Mx1Cre, and mTmG were bred in our laboratory. Rosa-Tomato Red RFP and Tie2Cre mice were obtained from Jackson. "Rainbow" mice were bred with mice harboring a TMX-inducible ubiquitously expressed Cre under the promoter of the actin gene. Mice were bred at our animal facility according to NIH guidelines. Protocols were approved by the institutional review board.

Isolation and Transplantation of Adult and Fetal Skeletal Progenitors

Skeletal tissues were dissected from postnatal day (P) 3 GFP-labeled mice and dissociated by mechanical and enzymatic dissociation. Total dissociated cells were stained with fluorochrome-conjugated antibodies for fractionation by FACS. Sorted and unsorted skeletal progenitors were then injected under the renal capsule of immunodeficient mice.

Transcriptional Expression Profiling

Microarray analyses was performed on mSSC/pre-BCSPs, BCSPs, Thy⁺, 6C3⁺, HEC, and BLSPs. RNA was isolated, twice amplified, streptavidin-labeled, fragmented, and hybridized to Affymetrix 430-2.0 arrays. Raw microarray data were submitted to Gene Expression Commons (<http://gexc.stanford.edu>). Heatmaps representing fold change of gene expression were generated in Gene Expression Commons.

Histological Analysis of Endochondral Ossification

Representative sections were stained with H&E, Movat's modified pentachrome, or alizarin red stains depending on requirement.

Immunofluorescence

Briefly, specimens were treated with a blocking reagent, then probed with monoclonal antibody at 4°C overnight. Specimens were washed, probed

Figure 6. Manipulation of the BMP Pathway Can Induce De Novo Formation of the mSSCs in Extraskelatal Regions

(A) Collagen sponges containing 3 μ g of lyophilized rhBMP2 were placed into extraskelatal sites in C57BL6 wild-type mice. One month later, the graft was explanted for analysis. Bright-field images of explants are shown, with renal capsule transplants shown above and subcutaneous transplants shown below (left). Transverse sections stained with Movat's pentachrome demonstrate that induced osseous osteoids formed a marrow cavity (red stain) (right). Scale bar: 500 μ m (left), 200 μ m (right). Representative of five replicates.

(B) FACS analysis of cells within the induced osteoid marrow reveals that circulating SlamF1-positive HSC engraftment occurs in the osteoids (bottom row) similar to that which occurs naturally in "normal" adult femurs (top row). Representative of three replicates.

(C) (Left) Following explantation of rhBMP2-laced collagen sponges at day 10 post-extraskelatal placement, FACS analysis of constituent cell populations present within the graft revealed that mSSC (red box on FACS plot) and BCSP (green box on FACS plot) are readily detectable in the rhBMP2-treated explants. (Right) In contrast, FACS analysis of adipose tissue in the absence of BMP2 does not detect either mSSC (red box on FACS plot) or BCSP (green box on FACS plot). Scale bar: 500 μ m. Representative of three replicates.

(D) A parabiosis model of GFP⁺ and non-GFP mouse shows that circulating skeletal progenitor cells did not contribute to BMP2-induced ectopic bones. A GFP⁺ mouse was parabiosed to a non-GFP mouse. Two weeks later, a collagen sponge containing 3 μ g of lyophilized rhBMP2 was transplanted into the inguinal fat pad of the non-GFP mouse. Ten days later, the tissue was explanted and isolated the constituent cell populations of the ectopic bone tissue as described previously. The contribution of the GFP-labeled cells to ectopic bone formation in the non-GFP mouse was analyzed by FACS (broken red line; GFP⁺ = circulating cells, and nonfluorescent = local cells). GFP-labeled cells contributing to the graft were solely CD45⁺ hematopoietic cells (extreme left panel, broken purple line) and not consistent of the skeletal progenitor population (horizontal upper panel, mSSCs shown in red box on FACS plot). Representative of three replicates.

(E) (Left) Diagram of reporter gene mouse model shows that Tie2 expression leads to GFP expression. Tie2⁺ cells turn green, but Tie2⁻ cells remain red. (Right) Scheme of experiment: In order to determine the cell types, which could undergo BMP2-mediated reprogramming to mSSCs in extraskelatal sites, we implemented a Tie2Cre \times MTMG reporter mouse and placed a collagen sponge containing rhBMP2 into the subcutaneous inguinal fat pad. The ossicle was explanted 1 month later for histological analysis.

(F) Fluorescent micrographs: BMP2-derived ossicles (yellow broken line) clearly incorporate both GFP⁺ Tie2⁺-derived osteocytes with visible canaliculi and Tie2⁻ RFP-labeled osteocytes. Area denoted by white oval is shown at higher magnification in the box on the extreme right, showing the presence of GFP⁺ Tie2⁺ canaliculi in the presence of RFP⁺ Tie2⁻ cells. Scale bar: 500 μ m (left), 50 μ m (right). Representative of three replicates.

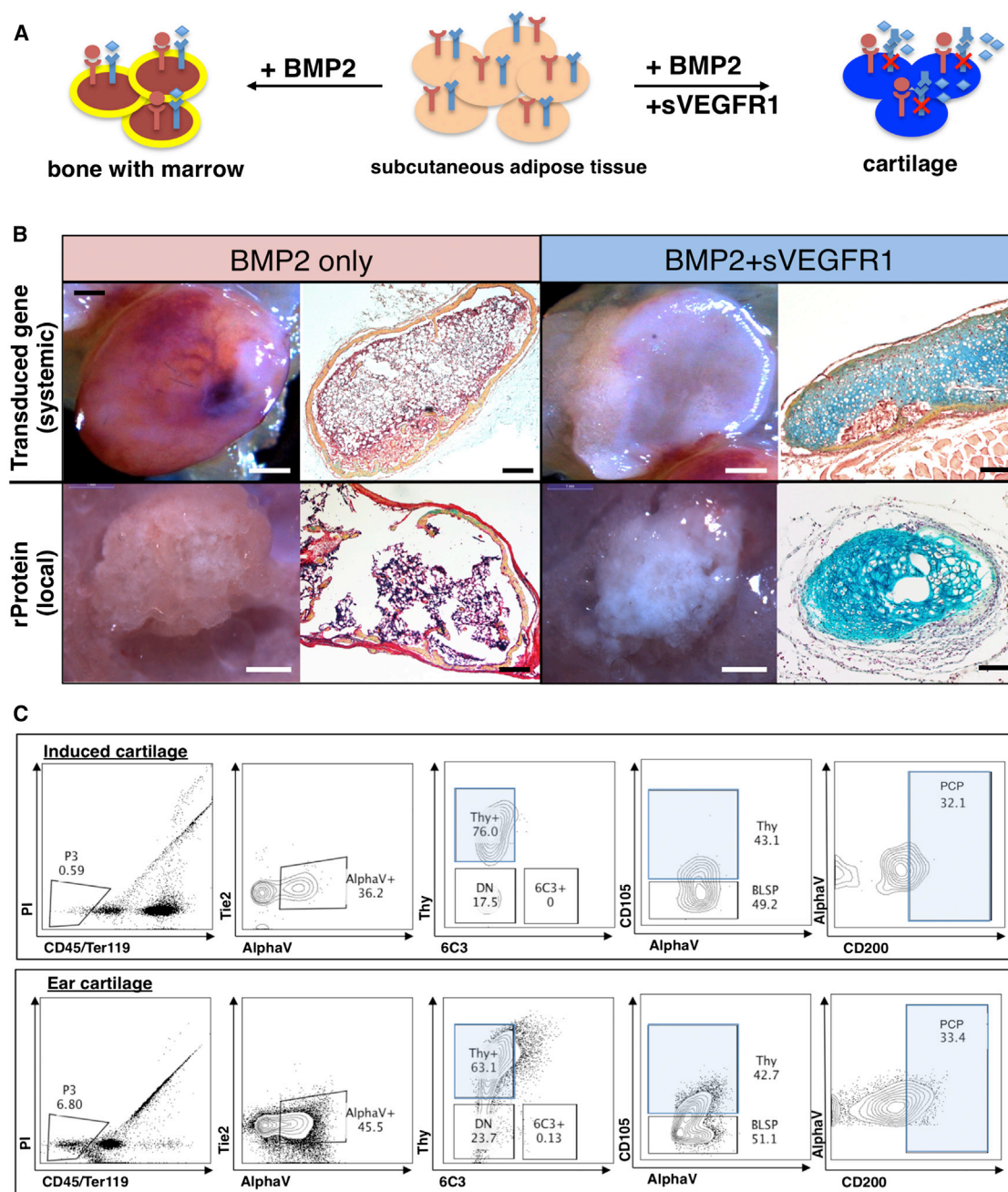


Figure 7. Codelivery of BMP2 and VEGF Inhibitor Is Sufficient to Induce De Novo Formation of Cartilage in Adipose Tissue

(A) Scheme of experiment: codelivery of BMP2 and soluble VEGFR1 in adipose tissue. BMP2 and inhibition of VEGF signaling leads to cartilage formation. BMP2 alone leads to bone formation.

(B) Fate of subcutaneous collagen sponge implants containing BMP2 without (two panels on left) or with VEGF blockade (two panels on right). One month after placement of collagen sponges, the grafts were explanted for analysis. Bright-field images of grafts (left) are shown alongside representative sections stained with Movat's pentachrome (right). The codelivery of BMP2 and sVEGFR1 resulted in the formation of blue staining cartilage (extreme right panels, top and bottom). The result following systemic VEGF blockade is shown in the top series on the right, whereas the result of local VEGF blockade is shown in the bottom series on the right. Scale bar (panels moving from right to left): 1 mm, 200 μ m, 1 mm, 200 μ m. Representative of four replicates.

(C) FACS plot analysis of the constituent cells of the induced cartilage (top horizontal panel) (experimental scheme as shown in Figure 7A) versus those of freshly isolated cells from ear cartilage of age-matched mice (bottom horizontal panel) demonstrates that PCPs are found in similar frequency in the induced and natural cartilage tissue. Representative of the assay performed in triplicate.

with alexa-dye-conjugated antibodies, washed, and imaged with an inverted microscope.

Cell Culture

Skeletal progenitors were cultured in MEM α medium with 10% FCS, 1% penicillin-streptomycin under low O₂ (2% atmospheric oxygen, 7.5%CO₂) conditions. For mSSC colony-forming assays, single cells were sorted into each well of a 96-well plate and cultured for 2 weeks.

Parabiosis

Age- and sex-matched congenic GFP and non-GFP mice were sutured together along the dorsal-dorsal and ventral-ventral folds of the skin flaps. Two weeks later, blood chimerism was assessed by FACS.

In Vivo Osteo-induction with BMP2

rhBMP2 was resuspended in sterile filtered buffer and applied to a collagen sponge. Sponge was lyophilized and transplanted subcutaneously into anesthetized mice.

Inhibition of VEGF Signaling

To study systemic inhibition of VEGF signaling, 10⁹ pfu units of adenoviral vectors encoding the soluble murine VEGFR1 ectodomain (Ad sVEGFR1) was injected intravenously to the designated recipient mice 24 hr prior to transplantation, leading to hepatic infection and secretion of this potent antagonist of VEGF signaling into the circulation. For negative control, adenovirus encoding a murine IgG2 α Fc immunoglobulin fragment was used (Ad Fc). These reagents are described elsewhere (Wei et al., 2013).

Local VEGF inhibition: 50 μ g of soluble VEGFR1 was lyophilized together with recombinant BMP2 in a collagen sponge, which was then inserted into subcutaneous fat.

Single-Cell RNA Sequencing

This was performed as previously described (Treutlein et al., 2014).

Mouse Femoral Fracture \pm Hindlimb Irradiation

An incision was made from the groin crease to the knee of the right femur. A medullary rod was placed via the intercondylar fossa. A bicortical transverse mid-diaphyseal fracture was created, and the skin incision closed with nylon sutures, and the mice received post-operative analgesia. The callus was harvested, and constituent cells isolated by mechanical and enzymatic dissociation and subsequent FACS fractionation. C57BL6 hindlimbs received a single dose of 800 rads (8Gy) to bilateral hind limbs. Surgical placement of fracture was performed 12 hr post-irradiation.

ACCESSION NUMBERS

The NIH GEO accession number for the microarray data reported in this paper is GSE64447. Normalized data can also be accessed through Gene Expression Commons, "Public Bone Progenitors Model."

SUPPLEMENTAL INFORMATION

Supplemental Information includes Extended Experimental Procedures and six supplemental figures and can be found with this article online at <http://dx.doi.org/10.1016/j.cell.2014.12.002>.

AUTHOR CONTRIBUTIONS

C.K.F.C., I.L.W., and M.T.L. conceived the overall project strategy; C.K.F.C., E.Y.S., J.Y.C., D.L., A.M., R.T., J.V.-T., T.W., W.-J.L., K.S.-Y., M.T.C., O.M., M.T., R.U., G.G.W., and A.S.L. designed, performed, and interpreted data, contributed to the writing and editing of manuscript, and prepared figures. R.S., E.Y.S., and D.S. performed single-cell RNA-sequencing/analysis; J.S. provided new algorithms for transcriptional analysis. C.K. and K.S.Y. designed and contributed reagents for vascular signaling manipulation. I.L.W. and M.T.L. edited the manuscript and supervised the laboratory.

ACKNOWLEDGMENTS

We would like to acknowledge Seth Karten for his critical help in editing the manuscript; Christopher Duldulao and Tejaswitha Naik for technical assistance; Shirley Kantoff, Libuse Jerabek, and Terry Storm for laboratory management; Aaron McCarty, Joel Dollaga, and Felix Manuel for animal care; Patty Lovelace and Jennifer Ho in the Shared FACS Facility in the Lokey Stem Cell Institute; Steve Quake, Norma Neff, Sopheak Sim, and Gary Mantalas for critical help while performing single-cell RNA sequencing; and Natalia Kosovilka and Michael Eckart at Stanford PAN Facility for help with microarray analysis. The authors would like to acknowledge ongoing support for this work: Virginia and D.K. Ludwig Fund for Cancer Research, National Institutes of Health (NIH) Grants U01HL099999, R01 CA86065, and R01 HL058770 (to I.L.W.); R01 DE021683, R21 DE024230, R01 DE019434, R02 DE020771, U01 HL099776, and R21 DE019274 (to M.T.L.); and 1R01CA158528, 1R01NS064517, and 2U01DK085527-06 (to C.J.K.); Siebel Fellowship from Thomas and Stacey Siebel Foundation and Prostate Cancer Foundation Young Investigator Award (to C.K.F.C.); CIRM TR1-01249, the Oak Foundation, the Hagey Laboratory for Pediatric Regenerative Medicine, the Gunn/Olivier Research Fund, Stinehart-Reed Fund (to M.T.L.); the Stanford Medical Scientist Training Program, NIH-T32GM007365 (to J.Y.C.); Stanford University Transplant and Tissue Engineering Center of Excellence Fellowship (to A.M. and R.T.); the Plastic Surgery Foundation/Plastic Surgery Research Council Pilot Grant and the American Society of Maxillofacial Surgeons Research Grant (to R.T.); Burroughs Wellcome Career Award for Medical Scientists, K08 DK096048 01 (to K.S.Y.); Stanford Developmental Cancer Research Award (to D.S.); the Stanford Medical Scientist Training Program, NIGMS training grant GM07365 (to G.G.W.); and the Anonymous Donor Skeletal Stem Cell Research Fund (to E.Y.S., C.K.F.C., and M.T.L.). The content is solely the responsibility of the authors and does not necessarily represent the official views of the NIH.

Received: May 26, 2014

Revised: September 22, 2014

Accepted: November 25, 2014

Published: January 15, 2015

REFERENCES

- Arai, F., Hirao, A., Ohmura, M., Sato, H., Matsuoka, S., Takubo, K., Ito, K., Koh, G.Y., and Suda, T. (2004). Tie2/angiopoietin-1 signaling regulates hematopoietic stem cell quiescence in the bone marrow niche. *Cell* 118, 149–161.
- Bhumirata, S., Eton, R.E., Oungoulian, S.R., Wan, L.Q., Ateshian, G.A., and Vunjak-Novakovic, G. (2014). Large, stratified, and mechanically functional human cartilage grown in vitro by mesenchymal condensation. *Proc. Natl. Acad. Sci. USA* 111, 6940–6945.
- Bianco, P. (2011). Bone and the hematopoietic niche: a tale of two stem cells. *Blood* 117, 5281–5288.
- Bianco, P. (2014). "Mesenchymal" stem cells. *Annu. Rev. Cell Dev. Biol.* 30, 677–704.
- Burr, D.B. (2004). The importance of subchondral bone in the progression of osteoarthritis. *J. Rheumatol. Suppl.* 70, 77–80.
- Calvi, L.M., Adams, G.B., Weibrecht, K.W., Weber, J.M., Olson, D.P., Knight, M.C., Martin, R.P., Schipani, E., Divieti, P., Bringham, F.R., et al. (2003). Osteoblastic cells regulate the haematopoietic stem cell niche. *Nature* 425, 841–846.
- Carlevaro, M.F., Cermelli, S., Cancedda, R., and Descalzi Cancedda, F. (2000). Vascular endothelial growth factor (VEGF) in cartilage neovascularization and chondrocyte differentiation: auto-paracrine role during endochondral bone formation. *J. Cell Sci.* 113, 59–69.
- Conboy, M.J., Conboy, I.M., and Rando, T.A. (2013). Heterochronic parabiosis: historical perspective and methodological considerations for studies of aging and longevity. *Aging Cell* 12, 525–530.
- Chan, C.K., Lindau, P., Jiang, W., Chen, J.Y., Zhang, L.F., Chen, C.C., Seita, J., Sahoo, D., Kim, J.B., Lee, A., et al. (2013). Clonal precursor of bone, cartilage,

- and hematopoietic niche stromal cells. *Proc. Natl. Acad. Sci. USA* 110, 12643–12648.
- De Palma, M., Venneri, M.A., Galli, R., Sergi Sergi, L., Politi, L.S., Sampaolesi, M., and Naldini, L. (2005). Tie2 identifies a hematopoietic lineage of proangiogenic monocytes required for tumor vessel formation and a mesenchymal population of pericyte progenitors. *Cancer Cell* 8, 211–226.
- Friedenstein, A.J., Chailakhyan, R.K., and Gerasimov, U.V. (1987). Bone marrow osteogenic stem cells: in vitro cultivation and transplantation in diffusion chambers. *Cell Tissue Kinet.* 20, 263–272.
- Galloway, J.L., Delgado, I., Ros, M.A., and Tabin, C.J. (2009). A reevaluation of X-irradiation-induced phocomelia and proximodistal limb patterning. *Nature* 460, 400–404.
- Gerber, H.P., Vu, T.H., Ryan, A.M., Kowalski, J., Werb, Z., and Ferrara, N. (1999). VEGF couples hypertrophic cartilage remodeling, ossification and angiogenesis during endochondral bone formation. *Nat. Med.* 5, 623–628.
- Harper, J., and Klagsbrun, M. (1999). Cartilage to bone—angiogenesis leads the way. *Nat. Med.* 5, 617–618.
- Heldin, C.H., and Westermark, B. (1999). Mechanism of action and in vivo role of platelet-derived growth factor. *Physiol. Rev.* 79, 1283–1316.
- Jo, C.H., Lee, Y.G., Shin, W.H., Kim, H., Chai, J.W., Jeong, E.C., Kim, J.E., Shim, H., Shin, J.S., Shin, I.S., et al. (2014). Intra-articular injection of mesenchymal stem cells for the treatment of osteoarthritis of the knee: a proof-of-concept clinical trial. *Stem Cells* 32, 1254–1266.
- Kilic, G., Kilic, E., Akgul, O., and Ozgocmen, S. (2014). Decreased femoral cartilage thickness in patients with systemic sclerosis. *Am. J. Med. Sci.* 347, 382–386.
- Makris, E.A., Gomoll, A.H., Malizos, K.N., Hu, J.C., and Athanasiou, K.A. (2014). Repair and tissue engineering techniques for articular cartilage. *Nat. Rev. Rheumatology*. Published online September 23, 2014. <http://dx.doi.org/10.1038/nrrheum.2014.157>.
- Méndez-Ferrer, S., Michurina, T.V., Ferraro, F., Mazloom, A.R., Macarthur, B.D., Lira, S.A., Scadden, D.T., Ma'ayan, A., Enikolopov, G.N., and Frenette, P.S. (2010). Mesenchymal and haematopoietic stem cells form a unique bone marrow niche. *Nature* 466, 829–834.
- Mitchell, M.J., and Logan, P.M. (1998). Radiation-induced changes in bone. *Radiographics* 18, 1125–1136, quiz 1242–1243.
- Mollon, B., Kandel, R., Chahal, J., and Theodoropoulos, J. (2013). The clinical status of cartilage tissue regeneration in humans. *Osteoarthritis and cartilage / OARS. Osteoarthritis Research Society* 21, 1824–1833.
- Morrison, J.I., Löff, S., He, P., and Simon, A. (2006). Salamander limb regeneration involves the activation of a multipotent skeletal muscle satellite cell population. *J. Cell Biol.* 172, 433–440.
- Park, D., Spencer, J.A., Koh, B.I., Kobayashi, T., Fujisaki, J., Clemens, T.L., Lin, C.P., Kronenberg, H.M., and Scadden, D.T. (2012). Endogenous bone marrow MSCs are dynamic, fate-restricted participants in bone maintenance and regeneration. *Cell Stem Cell* 10, 259–272.
- Rinkevich, Y., Lindau, P., Ueno, H., Longaker, M.T., and Weissman, I.L. (2011). Germ-layer and lineage-restricted stem/progenitors regenerate the mouse digit tip. *Nature* 476, 409–413.
- Saito, T., Fukai, A., Mabuchi, A., Ikeda, T., Yano, F., Ohba, S., Nishida, N., Akune, T., Yoshimura, N., Nakagawa, T., et al. (2010). Transcriptional regulation of endochondral ossification by HIF-2alpha during skeletal growth and osteoarthritis development. *Nat. Med.* 16, 678–686.
- Seita, J., Sahoo, D., Rossi, D.J., Bhattacharya, D., Serwold, T., Inlay, M.A., Ehrlich, L.I., Fathman, J.W., Dill, D.L., and Weissman, I.L. (2012). Gene Expression Commons: an open platform for absolute gene expression profiling. *PLoS ONE* 7, e40321.
- Street, J., Bao, M., deGuzman, L., Bunting, S., Peale, F.V., Jr., Ferrara, N., Steinmetz, H., Hoeffel, J., Cleland, J.L., Daugherty, A., et al. (2002). Vascular endothelial growth factor stimulates bone repair by promoting angiogenesis and bone turnover. *Proc. Natl. Acad. Sci. USA* 99, 9656–9661.
- Treutlein, B., Brownfield, D.G., Wu, A.R., Neff, N.F., Mantalas, G.L., Espinoza, F.H., Desai, T.J., Krasnow, M.A., and Quake, S.R. (2014). Reconstructing lineage hierarchies of the distal lung epithelium using single-cell RNA-seq. *Nature* 509, 371–375.
- Ueno, H., and Weissman, I.L. (2006). Clonal analysis of mouse development reveals a polyclonal origin for yolk sac blood islands. *Dev. Cell* 11, 519–533.
- Wei, K., Pieciewicz, S.M., McGinnis, L.M., Taniguchi, C.M., Wiegand, S.J., Anderson, K., Chan, C.W., Mulligan, K.X., Kuo, D., Yuan, J., et al. (2013). A liver Hif-2α-Irs2 pathway sensitizes hepatic insulin signaling and is modulated by Vegf inhibition. *Nat. Med.* 19, 1331–1337.
- Zhou, B.O., Yue, R., Murphy, M.M., Peyer, J.G., and Morrison, S.J. (2014). Leptin-receptor-expressing mesenchymal stromal cells represent the main source of bone formed by adult bone marrow. *Cell Stem Cell* 15, 154–168.

Long-Term Culture of Genome-Stable Bipotent Stem Cells from Adult Human Liver

Meritzell Huch,^{1,9,10,*} Helmuth Gehart,^{1,9} Ruben van Boxtel,^{1,9} Karien Hamer,¹ Francis Blokzijl,¹ Monique M.A. Verstegen,² Ewa Ellis,⁷ Martien van Wenum,³ Sabine A. Fuchs,⁴ Joep de Ligt,¹ Marc van de Wetering,^{1,8} Nobuo Sasaki,¹ Susanne J. Boers,⁴ Hans Kemperman,⁵ Jeroen de Jonge,² Jan N.M. Ijzermans,² Edward E.S. Nieuwenhuis,⁴ Ruurdte Hoekstra,³ Stephen Strom,⁶ Robert R.G. Vries,^{1,8} Luc J.W. van der Laan,² Edwin Cuppen,¹ and Hans Clevers^{1,*}

¹Hubrecht Institute-KNAW, University Medical Centre Utrecht, CancerGenomics.nl, Uppsalalaan 8, 3584 CT Utrecht, the Netherlands

²Department of Surgery, Erasmus MC-University Medical Center, Postbus 2040, 3000 CA Rotterdam, the Netherlands

³Surgical Laboratory, Tytgat Institute for Liver and Intestinal Research, Academic Medical Center, Meibergdreef 9, 1105 AZ Amsterdam, the Netherlands

⁴Division of Pediatric Gastroenterology, Wilhelmina Children's Hospital, University Medical Center Utrecht, Lundlaan 6, 3584 EA Utrecht, the Netherlands

⁵Department of Clinical Chemistry and Haematology, University Medical Center Utrecht, Lundlaan 6, 3584 EA Utrecht, the Netherlands

⁶Division of Pathology, Department of Laboratory Medicine, Karolinska Institute, Alfred Nobels Alle 8, F 56 141-86 Stockholm, Sweden

⁷Unit for Transplantation Surgery, Department of CLINTEC, Karolinska Institute, Karolinska University Hospital Huddinge, Hälsovägen, Flemingsberg, SE-141 86 Stockholm, Sweden

⁸Hubrecht Organoid Technology (HUB), Uppsalalaan 8, 3584CT, Utrecht, the Netherlands

⁹Co-first author

¹⁰Present address: Wellcome Trust/Cancer Research UK Gurdon Institute, Wellcome Trust/MRC Stem Cell Institute and Department of Physiology, Development and Neuroscience, University of Cambridge, Tennis Court Road, CB2 1QN Cambridge, UK

*Correspondence: m.huch@gurdon.cam.ac.uk (M.H.), h.clevers@hubrecht.eu (H.C.)

<http://dx.doi.org/10.1016/j.cell.2014.11.050>

This is an open access article under the CC BY license (<http://creativecommons.org/licenses/by/3.0/>).

SUMMARY

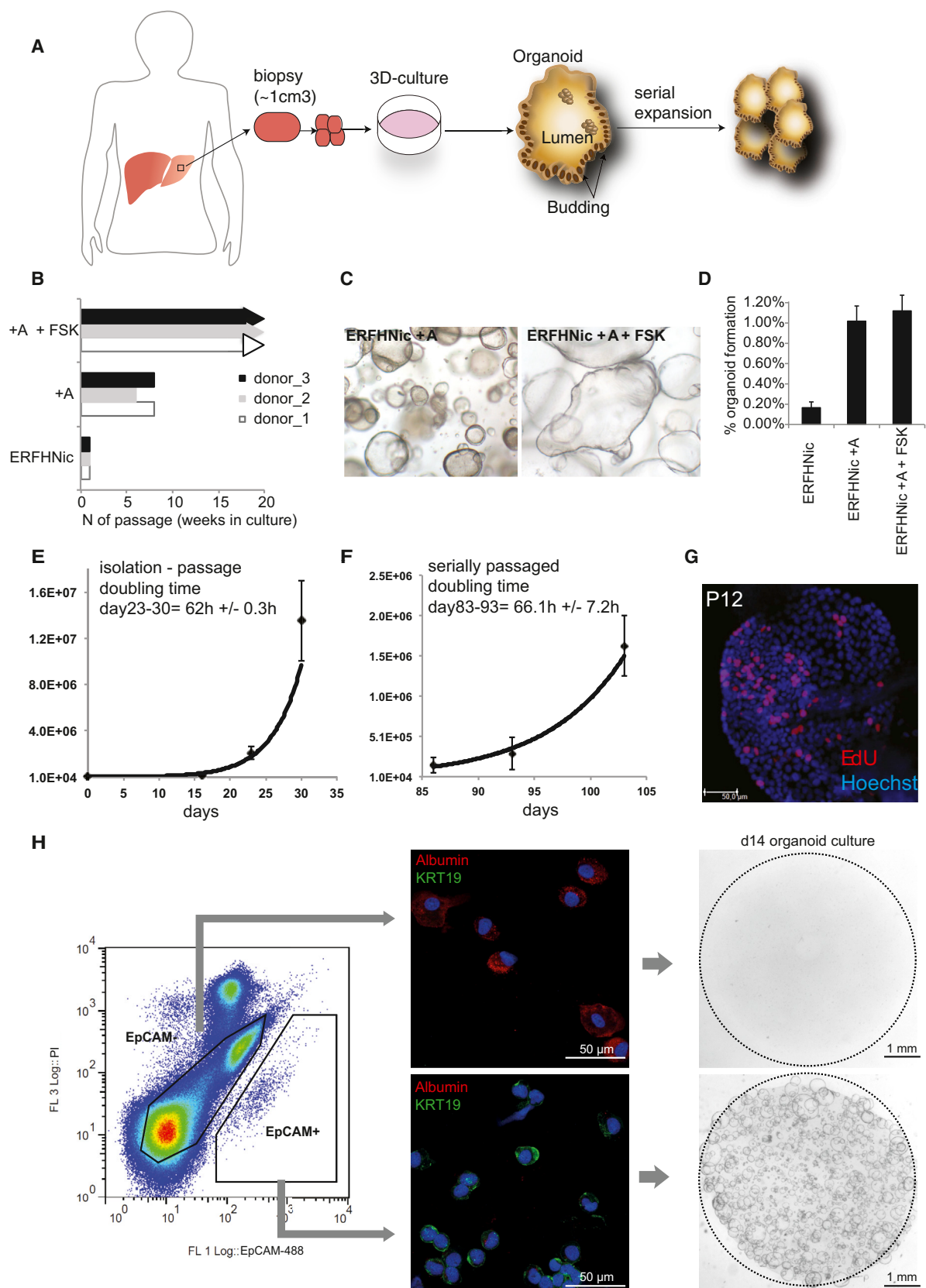
Despite the enormous replication potential of the human liver, there are currently no culture systems available that sustain hepatocyte replication and/or function in vitro. We have shown previously that single mouse *Lgr5*⁺ liver stem cells can be expanded as epithelial organoids in vitro and can be differentiated into functional hepatocytes in vitro and in vivo. We now describe conditions allowing long-term expansion of adult bile duct-derived bipotent progenitor cells from human liver. The expanded cells are highly stable at the chromosome and structural level, while single base changes occur at very low rates. The cells can readily be converted into functional hepatocytes in vitro and upon transplantation in vivo. Organoids from α 1-antitrypsin deficiency and Alagille syndrome patients mirror the in vivo pathology. Clonal long-term expansion of primary adult liver stem cells opens up experimental avenues for disease modeling, toxicology studies, regenerative medicine, and gene therapy.

INTRODUCTION

The liver is mainly composed of two epithelial cell types, hepatocytes and ductal cells. Hepatocytes synthesize essential serum proteins, control metabolism, and detoxify a wide variety of endogenous and exogenous molecules (Duncan

et al., 2009). Despite their considerable replication capacity in vivo (Michalopoulos, 2014), hepatocytes have resisted long-term expansion in culture (Mitaka, 1998). Indeed, a recent study describes a human liver hepatocyte culture system for a period of ~1 week with only 10-fold expansion (Shan et al., 2013). As an alternative, human embryonic stem (hES) cells and human induced pluripotent stem (hiPS) cells have been differentiated toward hepatocyte-like cells. However, recent reports imply that genetic and epigenetic aberrations occur during the derivation and reprogramming processes (Liang and Zhang, 2013; Pera, 2011; Lund et al., 2012). These range from chromosomal abnormalities (Laurent et al., 2011), “de novo” copy number variations (CNVs) (Hussein et al., 2011), and point mutations in protein-coding regions (Gore et al., 2011). Such changes may complicate their use for regenerative medicine purposes (Bayart and Cohen-Haguenaer, 2013).

We have recently described a culture system that allows the long-term expansion (>1 year) of single mouse adult intestine (Sato et al., 2009), stomach (Barker et al., 2010), liver (Huch et al., 2013b), and pancreas (Huch et al., 2013a) stem cells. *Lgr5*, the receptor for the Wnt agonists R-spondins (Carmon et al., 2011; de Lau et al., 2011), marks adult stem cells in these mouse tissues (Barker et al., 2007, 2010; Huch et al., 2013a, 2013b). These cultures remain committed to their tissue of origin. We have recently adapted the technology to allow culturing of human intestinal stem cells (Jung et al., 2011; Sato et al., 2011) and have shown that patient-derived intestinal organoids recapitulate the pathology of hereditary intestinal diseases (Bigorgne et al., 2014; Dekkers et al., 2013; Wiegerinck et al., 2014). Here, we pursue the establishment of an organoid culture system for human liver.



(legend on next page)

RESULTS

Optimization of Human Liver Stem Cell Culture

Our defined mouse liver medium (ERFHNic [Huch et al., 2013b]) supported the growth of human liver cells only for 2–3 weeks (Figure 1A and 1B and Figure S1A, top, available online). Gene expression profiles of human liver cultures that were maintained for 2 weeks in “mouse liver medium” revealed highly active Tgf- β signaling. Tgf- β target genes such as *CTGF*, *PLAT*, *TIMP1*, and *TIMP2* were highly expressed, whereas Tgf- β sequestrators (*LTBP2* and *LTBP3*) and Smad4 inhibitors (*SMURF1* and *SMURF2*) (Massagué et al., 2005) were virtually absent (Figure S1B). Tgf- β signaling induces growth arrest and epithelial-to-mesenchymal transition (Xu et al., 2009). Specific inhibition of Tgf- β receptors Alk4/5/7 by the small molecule inhibitor A8301 downregulated *CTGF*, *TIMP2*, and *PLAT* (Figure S1C), extended the time in culture (~6–7 weeks, six to seven splits) (Figure 1B), and enhanced colony-forming efficiency (Figure 1D). Still, the cultures eventually deteriorated (Figures 1B and 1C, left). Expression of the stem cell marker *LGR5* decreased over time, whereas differentiation markers such as Albumin (*ALB*) or *CYP3A4* were upregulated (data not shown), indicating that our conditions were promoting differentiation.

We then tested additional compounds to induce proliferation and/or *LGR5* expression (Table S1). Proliferating bile-duct progenitor cells occur both during homeostasis (Furuyama et al., 2011) and after damage (Dorrell et al., 2011; Huch et al., 2013b; Shin et al., 2011). As Forskolin (FSK), a cAMP pathway agonist, induces proliferation of biliary duct cells in vivo (Francis et al., 2004), we asked whether cAMP would support the human liver cultures.

FSK addition upregulated *LGR5* and the ductal marker *KRT19*, whereas *ALB* and *CYP3A4* decreased (Figure S1D). Colony-forming efficiency was essentially unchanged (Figure 1D), yet the cultures expanded as budding organoids for many months in culture (>6 months) at a weekly split ratio of 1:4–1:6 (Figures 1B and 1C, right). Similar results were observed with other cAMP agonists (8-Br-cAMP, Cholera toxin or NKH477) (Figure S1E). Removal of cAMP agonists resulted in rapid deterioration (Figures S1F and S1G). Similarly, removal of the Wnt agonist R-spo or blocking Wnt secretion by porcupine inhibition (IWP-2) resulted in rapid loss of the cultures (Figures S1F–S1H). This

effect was rescued by exogenous addition of Wnt (Figure S1H). Twelve additional healthy human donor liver biopsies were cultured in the improved medium, with a consistent doubling time of ~60 hr, independent of the age of the culture (Figures 1E and 1F and Table S2). EdU incorporation confirmed that the cells maintained their proliferative state in vitro (Figure 1G) for >3 months. Cultures could be readily frozen and thawed (data not shown). Thus, Wnt signals, cAMP activation, and Tgf- β inhibition were essential for long-term expansion.

Organoids Originate from Ductal cells

Collagenase perfusion of donor livers yields high numbers of fresh, viable, and functional human hepatocytes (Gramignoli et al., 2012) (Figure S2A). We employed EpCAM to differentially sort hepatocytes (EpCAM[−]) from ductal EpCAM⁺ ductal cells (Figures 1H, S2B, and S2C) (Schmelzer et al., 2007; Yoon et al., 2011). Although hepatocytes formed no organoids, EpCAM⁺ bile duct cells developed into organoids with a striking efficiency of 28.4% \pm 3.2% (Figures 1H, S2D, and S2E). Crude liver cell preparations grew into organoid structures with an efficiency that equaled the number of EpCAM⁺ cells (Figures S2F and S2G). In our culture system, ductal cells rather than hepatocytes initiate organoids.

Clonal Organoids Are Genetically Stable

Organoids cultured for 3 months maintained normal chromosome numbers (Figures 3A and S4A). From two donors, we obtained biopsy samples, which we dissociated and cultured in bulk for 7 days. Subsequently, we isolated single cells and established two independent clonal lines for each of the two livers (cultures A and B). After 3 months of expanding these cultures, a second cloning step was performed. We could thus determine all genomic variation accumulated in a single cell during life, derivation, and 3 months of culture (Figures 2A and 2B).

We observed 720–1,424 base substitutions per cultures, of which 63–139 were introduced during the 3 months culture (Figure 2C). Therefore, the majority of the base substitutions identified had been incorporated in vivo (during life) or introduced during organoid derivation, but not during culture. How do these numbers compare to published data? iPS cells contain 1,058–1,808 de novo base substitutions (determined at passage numbers between 15 and 25) compared to their parental somatic

Figure 1. Growing Liver Organoids from Ductal Cells

3,000 or 10,000 human primary liver cells were seeded per well in a 48-well plate in different culture conditions, as indicated.

(A) Scheme of the experimental protocol.

(B) Mouse liver culture medium (ERFHNic) or medium supplemented with A8301 (A) or A8301 and Forskolin (FSK). The cultures were split every week 7–10 days at a ratio of 1:4–1:6 dilution. Supplementing with A8301 and FSK significantly increased the expansion efficiency to grow for >18 passages at a split ratio of 1:4–1:6 every 7–10 days for >5 months. Experiments were performed in triplicate. Each bar indicates a different donor.

(C) DIC images of organoids treated with mouse liver medium with A8301 and with (right) or without (left) FSK. Magnification, 4 \times .

(D) Percentage of colony formation efficiency in the presence or absence of A8301 and/or FSK. Experiments were performed in triplicate and for five donors. Results are expressed as mean \pm SEM of five independent experiments.

(E–G) Expansion rates, in vitro growth curves, and EdU incorporation were analyzed at early and late passages in EM. (E and F) Graphs illustrate the number of cells counted per well at each passage from P1–P4 (E) to P16–P18 (F). Results are expressed as mean \pm SEM of three independent cultures. The doubling time was calculated as described in the Extended Experimental Procedures. (G) EdU incorporation was still detected at late passages.

(H) Human liver cell suspensions were separated into EpCAM⁺ ductal cells and larger EpCAM[−] hepatocytes (for exact gating strategy, see Figure S2C). Identity of the populations was confirmed by staining for Albumin and KRT19. Sorted cells were grown for 14 days. Organoids were exclusively derived from EpCAM⁺ ductal cells.

See also Figures S1 and S2.

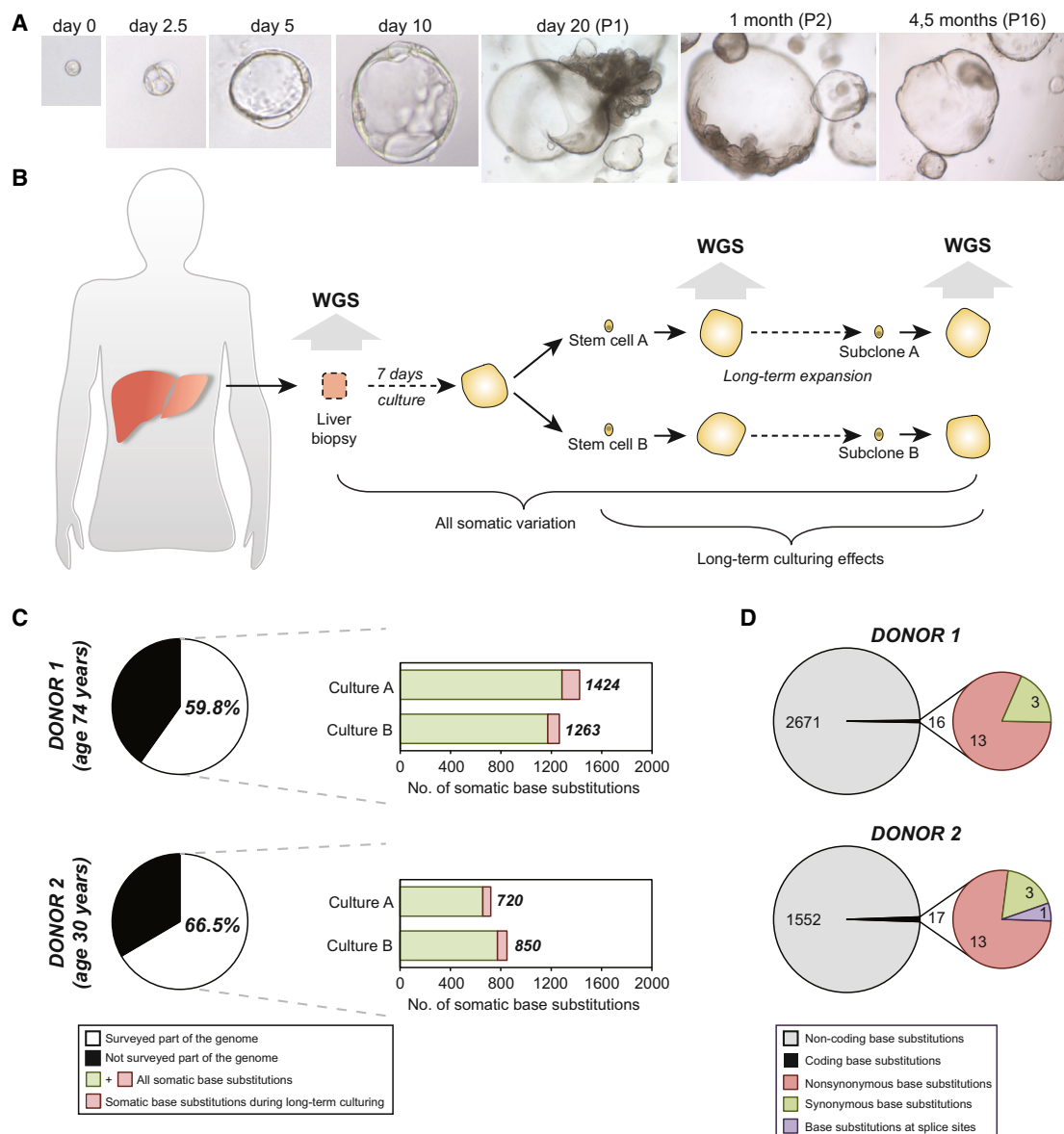


Figure 2. Human Organoids Are Genetically Stable in Culture

(A) Clonal cultures were obtained by seeding sorted cells at one cell per well. DIC images at magnifications: 40× (days 0–10), 4× (day 20 onward).

(B) Schematic overview of the experimental setup. Two independent donor liver biopsies were cultured for 1 week. Single cells were then clonally expanded to obtain two independent organoid cultures per donor (cultures A and B). After long-term expansion, a second clonal expansion step was performed. The resulting organoid cultures were subjected to WGS analysis. To obtain all somatic variation, variants were filtered for presence in the original biopsy. To determine the effect of long-term culturing on genomic stability, somatic variation was filtered for presence in earlier passages.

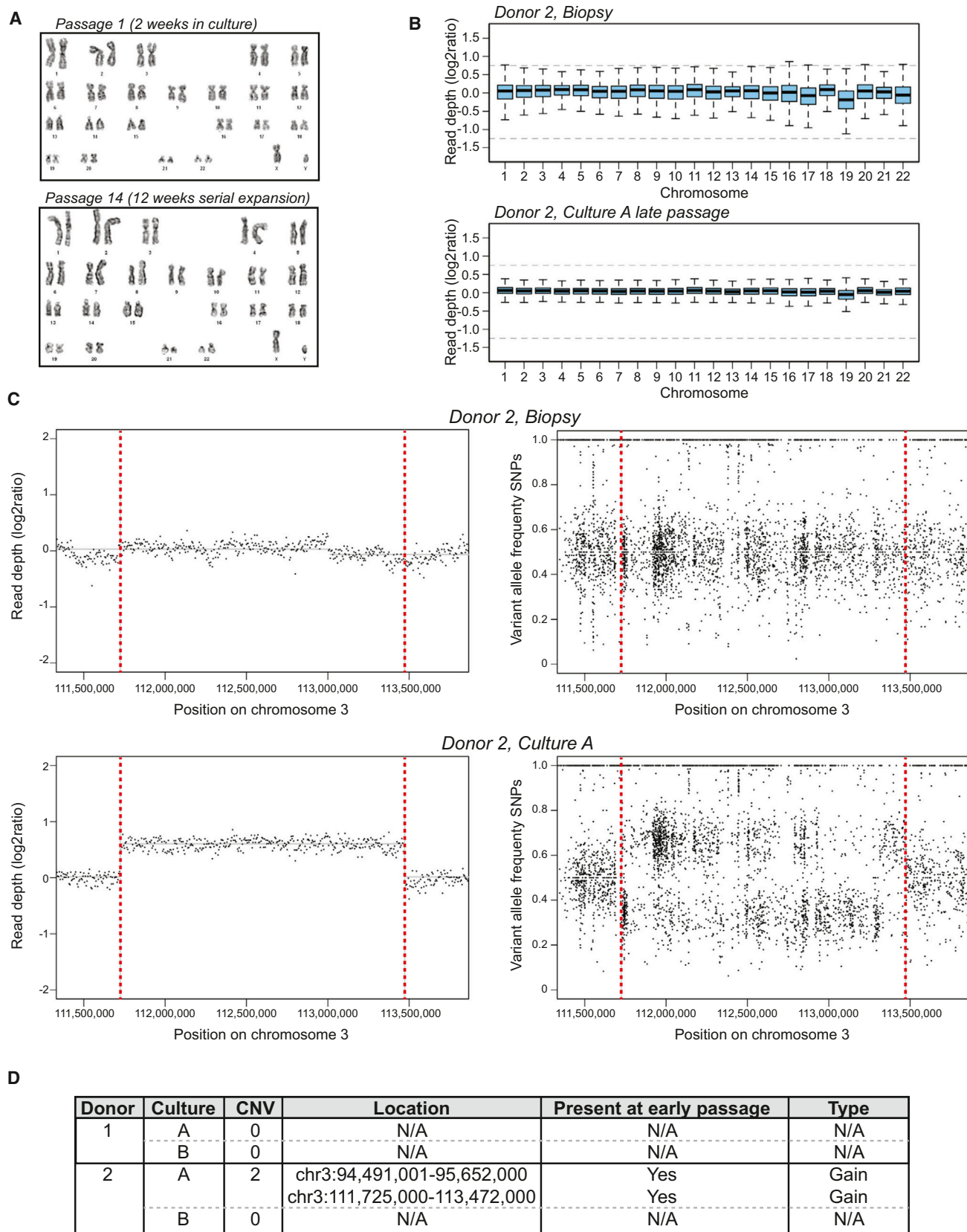
(C) The pie chart indicates the percentage of the genome that was surveyed per donor. The right panels indicate the absolute numbers of base substitution observed in the surveyed part of the genome. Indicated are the total number of somatic base substitutions per culture and the number induced by long-term culturing.

(D) Left panels indicate the total number of somatic base substitutions per donor, and the right panel indicates those affecting protein-coding DNA.

See also Figure S3.

cells (Cheng et al., 2012). Of note, the numbers from these studies do not include the variation acquired in vivo in the parental somatic cells. Thus, 3 months of in vitro expansion of liver organoids introduces 10-fold fewer base substitutions than iPS cell reprogramming. Of the total number of base substi-

tutions, only few were located in protein-coding DNA (seven to nine base substitutions per culture; Figures 2D and S3). With the exception of one synonymous mutation in culture A from donor 2 (Table S3), all mutations were already present in the early passage clonal cultures, indicating that they were not



(legend on next page)

incorporated during the 3 months of expansion. None of the mutated genes occurs in COSMIC databases (Table S3). In iPS cells, an average of six base substitutions per line affect protein-coding DNA (Cheng et al., 2012; Gore et al., 2011).

Next, we searched for structural aberrations in the WGS data. We did not observe any gross chromosomal aberrations (Figure 3B). We observed two copy number variants (CNVs), heterozygous gains, in one of the liver organoid cultures (Figures 3C). In the other cultures, we did not detect any CNV (Figures 3D and S4B–S4D). Moreover, these two CNVs were already present in the early passage cultures and therefore did not result from long-term culturing. ES cell cultures routinely show abnormal karyotypes (Baker et al., 2007), and iPS cells can harbor considerable numbers of somatic CNVs (Hussein et al., 2011; Laurent et al., 2011; Martins-Taylor et al., 2011; Mayshar et al., 2010; Abyzov et al., 2012).

Differentiation into Functional Hepatocytes In Vitro and upon Transplantation

The stem cell markers *PROM1* and *LGR5*, as well as ductal (*SOX9*, *OC2*) and hepatocyte markers (*HNF4a*) were readily expressed (Figures 4A, S5A, and S5B). Histologically, liver organoids displayed a duct-like phenotype presenting either as: (1) a single-layered epithelium, expressing the cytokeratin markers *KRT19* and *KRT7*, or (2) a pseudo-stratified epithelium with non-polarized E-Cadherin⁺ HNF4a⁺ and some KRT7⁺ cells (Figures 4B–4D). *SOX9* (Figure 4E) and *EPHB2* (Figure 4F) were detectable in almost all cells, whereas *LGR5* was detectable within the *EPHB2*⁺ population (Figure 4F). The organoids failed to express markers of mature hepatocytes, such as Albumin or CYP3A4 (Figures 4A and 5C, EM bars). Therefore, we defined a human differentiation medium (DM) (Table S1). Removal of the growth stimuli R-spo and FSK resulted in upregulation of Albumin and CYP3A4 (Figure S5C). To this medium, we then added the Notch inhibitor DAPT (Huch et al., 2013b), FGF19 (Wu et al., 2011), and dexamethasone (Rashid et al., 2010) (Figure S5D). BMP7 reportedly accelerates hepatocyte proliferation in vivo (Sugimoto et al., 2007). Addition of BMP7 slightly facilitated the expression of hepatocyte markers *ALB* and *CYP3A4* even during expansion medium (data not shown). Therefore, 5–7 days prior to the start of differentiation, we added 25 ng/ml BMP7 to the expansion medium (EM) (Figure 5A). When cultured in this differentiation medium (DM), the cells acquired pronounced hepatocyte morphologies, including polygonal cell shapes (Figure 5B). Gene expression profiles revealed high

levels of hepatocyte markers such as *ALB*, cytochromes, Apolipoproteins (*APOB*), and complement factors (*C3*) (Figures 5C, 5D, and S5E). Cells with high levels of *ALB* and *MRP4* were detected by immunofluorescence (Figure 5B). Similar results were obtained with cultures derived from EpCAM⁺-sorted ductal cells (Figures S5F and S5G). Immunohistochemical analysis indicated that the cells accumulate glycogen (Figure 6A) and take up LDL (Figure 6B). Albumin was secreted into the medium (Figure 6C). The cultures exhibited similar CYP3A4 activity as fresh isolated hepatocytes (Figure 6D, compare to Figure S2A). Differentiated organoids hydroxylated midazolam, another indication of functional CYP3A3/4/5 activity (Wandel et al., 1994), and glucuronidated hydroxy-midazolam, thereby showing evidence of both phase I and II detoxifying reactions (Figure 6E). Bile acid salts were readily secreted into the medium (Figure 6F). Finally, the organoids detoxified ammonia at similar levels to HepaRG cells (Figure 6G). In all cases, the expanded human liver organoids showed stronger hepatocyte functions when compared to the standard/reference cell line HepG2 cells (Figure 6).

To test the ability of the organoids to engraft as functional hepatocytes in vivo, we treated Balb/c nude mice with CCl₄-retroretrosine to induce acute liver damage. This treatment allows engraftment of hepatocytes (Guo et al., 2002; Schmelzer et al., 2007). Using human-specific antibodies (Figure S6A), we initially detected *KRT19*-positive, ductal-like cells at 2 hr and 2 days after transplantation, distributed throughout the liver parenchyma (Figure S6B). At later time points, we observed *ALB*⁺, *KRT19*[−] human cells as singlets/doublets or, more rarely, in larger hepatocyte foci (Figures 6H and S6C). Of note, our damage model provides no stimulus for expansion of the transplant after engraftment. Human Albumin and α -1-antitrypsin were found in serum of recipient mice within 7–14 days (Figures 6I, S6D, and S6E) at a level that remained stable for more than 60 days in five out of six mice and for more than 120 days in two out of five animals. Although transplantation of primary human hepatocytes initially yielded higher levels of human Albumin (Figure 6I), the levels approximated those of transplanted organoids within a month.

Patient Organoids Model Disease Pathogenesis

α 1-antitrypsin (A1AT) deficiency is an inherited disorder that predisposes to chronic obstructive pulmonary disease and chronic liver disease (Stoller and Aboussouan, 2005). A1AT is secreted from the liver to protect the lung against proteolytic damage from neutrophil elastase. The most frequent mutation is the

Figure 3. Structural Variation in Human Liver Organoids

- (A) Representative karyotyping image of organoids cultured for 16 days (P1) and 90 days (P14), illustrating a normal chromosomal count ($n = 46$). No major chromosomal aberrations were observed in any of the samples analyzed ($n = 15$). Detailed chromosomal counts for different donors are shown in Figure S4.
- (B) Read-depth analysis of whole-genome sequencing data over the different chromosomes for the biopsy (top) and organoid culture A (bottom) that were derived from donor 2. Read depth was corrected for GC content and normalized for genome coverage. Gray dotted lines indicate \log_2 values associated with a gain or deletion.
- (C) Copy number analysis of a region at chromosome 3 found to harbor a heterozygous gain in culture A of donor 2. Left panels indicate read-depth analysis of the indicated region in 5 kb bins, corrected for GC content and normalized for genome coverage, of the biopsy (top) and organoid culture (bottom). Right panels show the variant allele frequencies of informative nonreference single-nucleotide polymorphisms (SNPs) in the indicated region for the biopsy (top) and organoid culture (bottom).
- (D) Summary of copy number analysis of the different organoid cultures of the two donors. Somatic CNVs were exclusively observed in culture A derived from donor 2 and were already present in the parental culture. See also Figure S4.

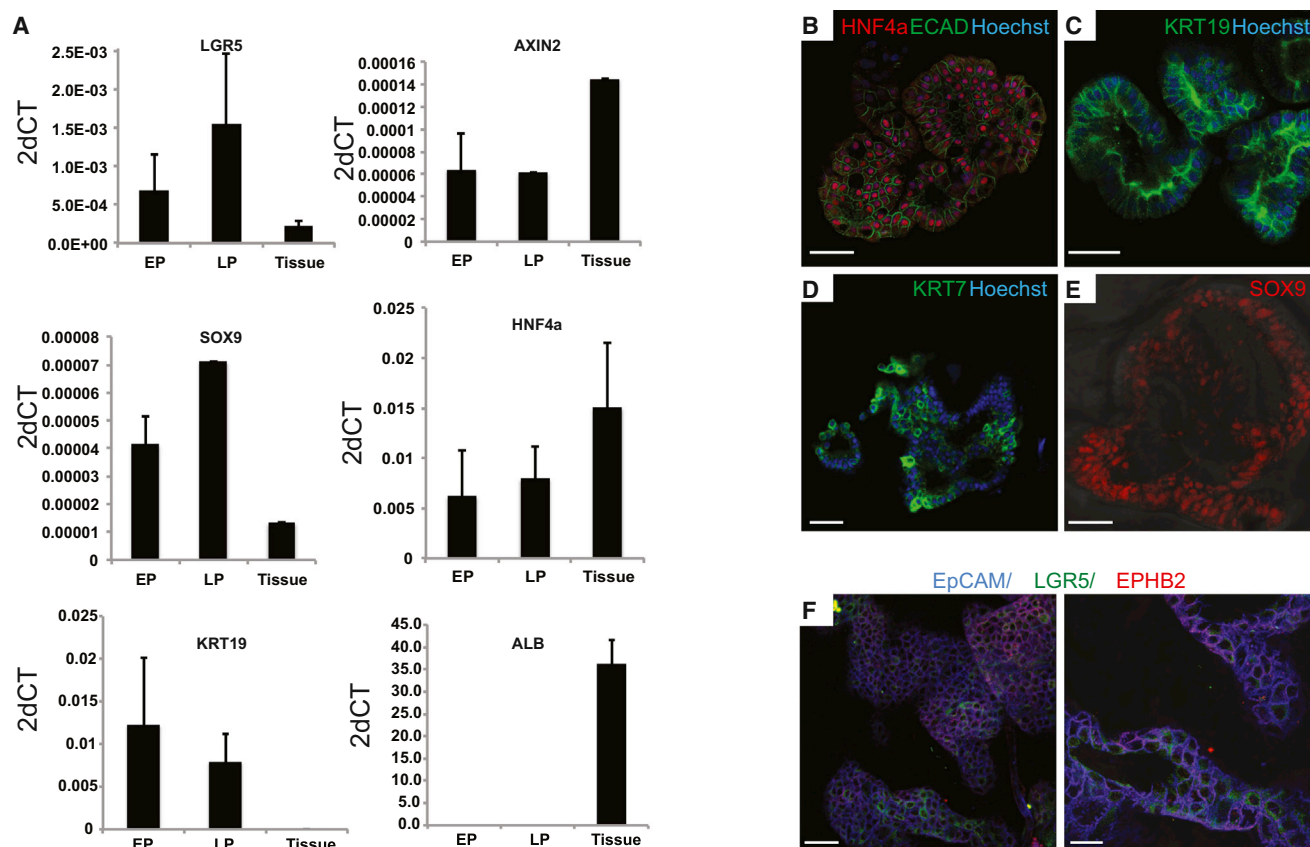


Figure 4. Marker Expression of Human Liver Organoids

(A and B) Gene expression was analyzed by RT-PCR (A) and immunofluorescence (B) in human liver cultures grown in EM.

(A) Gene expression was analyzed at early (EP) and late (LP) passages. Human liver cultures expressed progenitor (*LGR5*, *SOX9*), ductal (*KRT19*, *SOX9*), and hepatocyte (*HNF4A*) markers, but no albumin (*ALB*). Results are indicated as 2-dCt ($2^{\Delta\Delta CT}$). Values represent mean \pm SEM of three independent experiments in five independent donor-derived cultures. $2^{\Delta\Delta CT}$ were calculated using the housekeeping gene *GAPDH* as reference gene. Tissue, whole-liver lysate.

(B–F) Confocal images stained for ECAD and the hepatocyte marker HNF4 (B) and the ductal markers (*KRT19* [C], *KRT7* [D], and *SOX9* [E]). Nuclei were counterstained with Hoechst. (F) Confocal image stained for EPCAM (blue). The stem cell marker Lgr5 (green) was restricted to a subset of the cells staining for the Wnt target gene EPHB2 (red). Scale bars, 50 μ m (B–E and F, left); 25 μ m (F, right).

See also Figure S5.

Z allele (Glu342Lys) of the *SERPINA1* gene, which causes accumulation of misfolded A1AT in hepatocytes. The ZZ mutant phenotype is characterized by a \sim 80% reduction of the protein in plasma, which subsequently causes lung emphysema (Stoller and Aboussouan, 2005). Biopsies from three patients diagnosed with A1AT deficiency (Table S2 and Figure S7A) were subjected to histological characterization, RNA, and DNA isolation and expansion in culture. Organoids were grown for >4 months in culture and behaved normally. Gene expression analysis demonstrated that the cells differentiated normally in DM (Figure S7B). Functional tests revealed that the differentiated cells from A1AT patients secreted high levels of Albumin and take up LDL similar to that of healthy donor-derived organoid cultures (Figures 7B–7D). In A1AT deficiency, the molecular pathogenesis of the liver disease relates to the aggregation of the protein within the endoplasmic reticulum of hepatocytes (Lawless et al., 2008). A1AT protein aggregates were readily observed within the cells of the differentiated organoids (Figure 7H), similar to what was

found in the original biopsy (Figure 7G). A1AT ELISA confirmed reduced protein secretion (Figure 7I) (Table S2 indicates the A1AT secretion per patient), and supernatants from differentiated mutant organoids showed reduced ability to block elastase activity (Figure 7J). Protein misfolding is one of the primary causes that drive hepatocytes apoptosis in PiZZ individuals (Lawless et al., 2008). Differentiated liver organoids from A1AT-D patients mimicked the in vivo situation and showed signs of ER stress, such as phosphorylation of eIF2 α (Figure 7K) and increased apoptosis in the differentiated state (Figures S7C and S7D).

Using a biopsy from an Alagille syndrome (AGS) patient, we tested whether structural defects of the biliary tree can also be modeled. AGS is caused by mutations in the Notch-signaling pathway, which results in partial to complete biliary atresia (Kamath et al., 2013). Patient organoids resembled their healthy counterparts in the undifferentiated state. However, upon differentiation to the biliary fate by withdrawal of R-spondin,

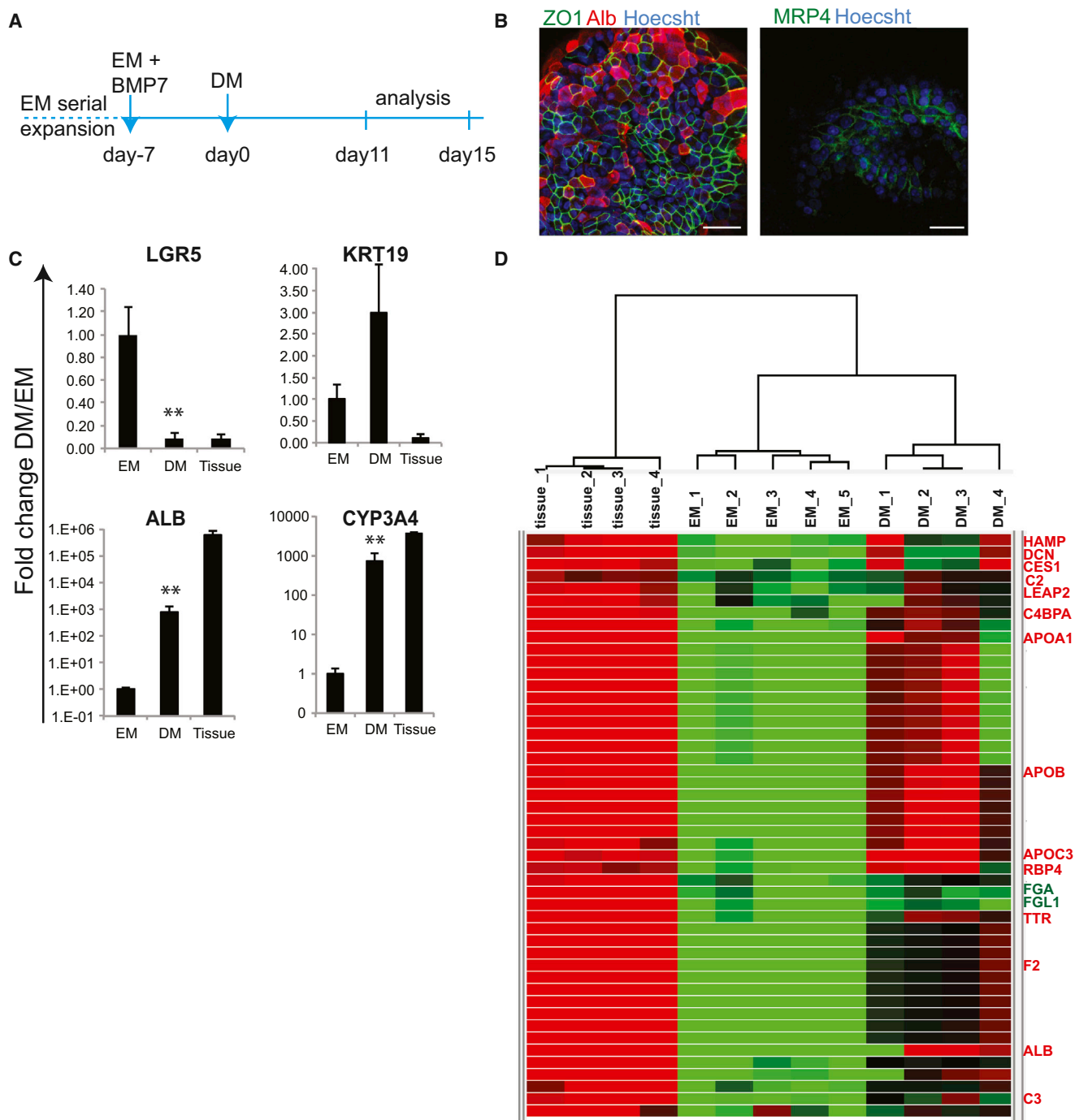


Figure 5. Differentiation of Organoids into Hepatocytes

Human liver cultures expanded for >1 month were transferred to DM.

(A) Experimental strategy.

(B and C) Expression of hepatocyte genes determined by immunofluorescence (B) or qPCR (C) after 11 days. (B) Immunofluorescence for albumin (ALB, red) and ZO-1 (green). Scale bar: 25 μ m, left; 30 μ m, right. (C) qPCR analysis for albumin and cytochrome p450 3A4. Graphs indicate mean \pm SEM of three independent experiments for three independent donors. Tissue: whole lysate from human liver. ** $p < 0.01$ when comparing EM versus DM.

(D) Whole-genome transcriptome analysis of human liver cultures grown in EM or after being cultured 11 days in DM. Heat map indicates cluster of genes highly expressed in liver tissue and in differentiated organoids. Of note, this cluster contains genes essential for liver function, as indicated in red. Green, downregulated; red, upregulated.

See also Figure S5.

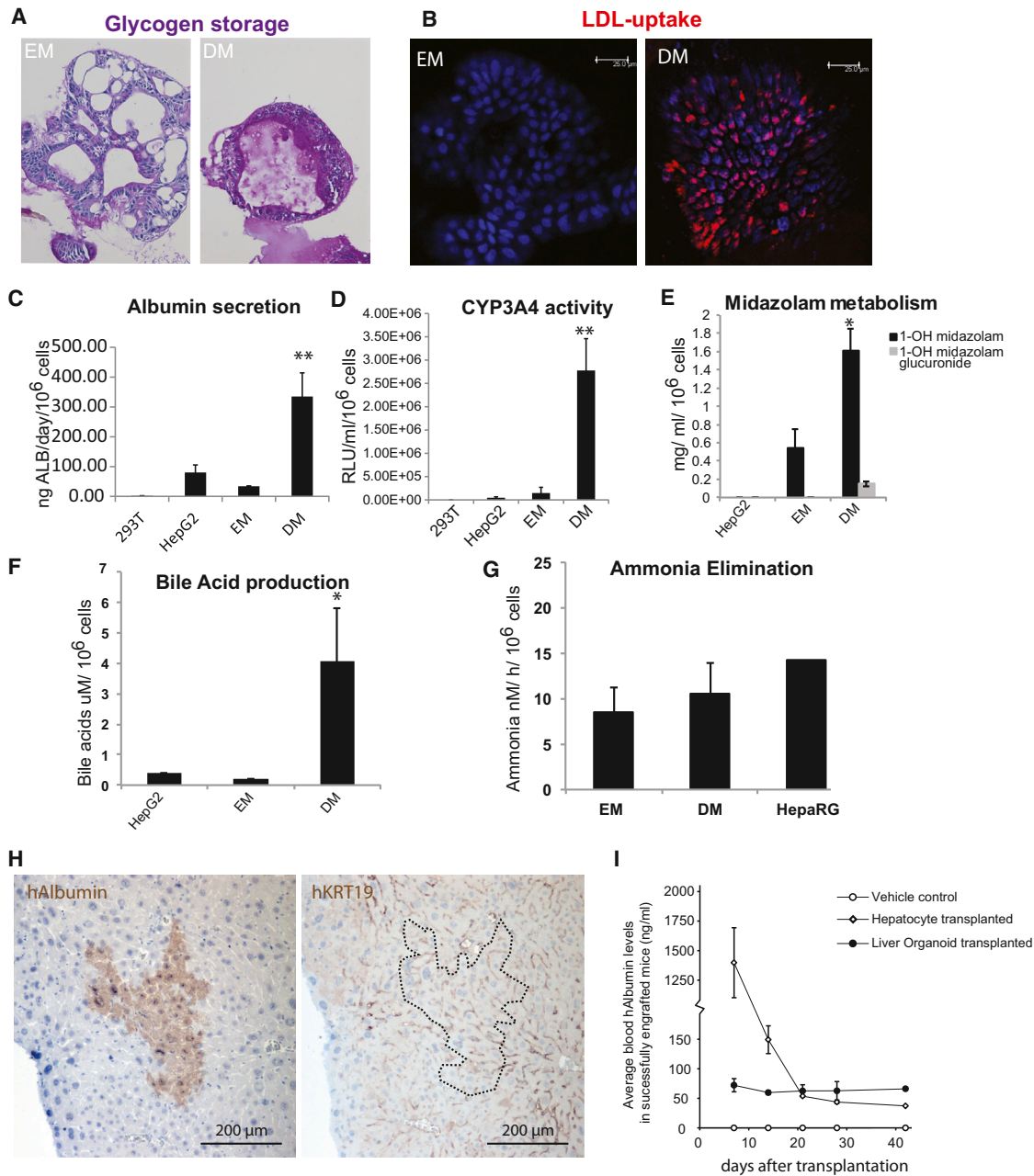


Figure 6. Liver Cultures Exhibit Hepatocyte Functions In Vitro and In Vivo

(A) Glycogen accumulation was determined by PAS (Periodic-Acid Schiff) staining in organoids grown in EM or DM for 11 days. PAS staining (pink) was exclusively observed after differentiation (DM), indicating the capacity to accumulate glycogen. Magnification, 10 \times .

(B) LDL uptake was analyzed using Dil-ac-LDL fluorescent substrate (red) after EM (left) or DM (right) culture for 11 days. Only cultures maintained in DM incorporated the substrate (red). Nuclei were counterstained with DRAQ5. Scale bar, 25 μ m.

(C) Albumin production during 24 hr was measured in supernatant. Results are expressed as mean \pm SEM of two independent experiments in four independent donor-derived cultures.

(D) CYP3A4 activity was measured in cultures kept in DM for 11 days. Results are expressed as RLU per ml per million cells. HEK293T cells and HepG2 cells were used as negative and positive controls, respectively. Note that DM organoids upon DM exhibit similar the CYP3A4 activity as freshly isolated hepatocytes (see Figure S2A). Triplicates for each condition were analyzed. Results are shown as mean \pm SEM of two independent experiments in four independent donor-derived cultures.

(E) Midazolam metabolism is performed exclusively by functional CYP3A3/4/5 enzymes. Three different organoid cultures from two different donors and HepG2 cells were cultured for 11 days as described. Midazolam was added to the medium (5 μ M), and after 24 hr, concentrations of 1-OH midazolam and 1-OH

(legend continued on next page)

Nicotinamide, TGF β i, and FSK, AGS patient organoids failed to upregulate biliary markers such as *KRT19* and *KRT7* (Figure S7E). Staining for KRT19 revealed that biliary cells were scarce and unable to integrate into the epithelium. Rather, they rounded up and underwent apoptosis in the organoid lumen (Figure S7F). In AGS mouse models, *JAGGED-1/NOTCH2* is dispensable for biliary lineage specification but is required for biliary morphogenesis (Geisler et al., 2008; McCright et al., 2002). Thus, AGS liver organoids constitute the first human 3D model system to study Alagille syndrome.

DISCUSSION

Liver diseases (ranging from genetic inherited disorders to viral hepatitis, liver cancer, and obesity-related fatty liver disease) account for the twelfth-leading cause of death in the United States (Heron, 2012). Failure in the management of liver diseases can be attributed to the shortage of donor livers (Vilarinho and Lifton, 2012) as well as to our poor understanding of the mechanisms behind liver pathology. The value of any cultured cell as a disease model or as a source for cell therapy transplantation depends on the fidelity and robustness of its expansion potential as well as its ability to maintain a normal genetic and epigenetic status (Pera, 2011). The possibility of differentiating hESC or reprogrammed fibroblasts (iPS) into almost any differentiated cell type, from neurons to hepatocytes, has allowed modeling of many human genetic diseases, including A1AT-D (Rashid et al., 2010). However, the genetic instability of cultured stem cells raises concerns regarding their safe use in cell therapy transplantation (Bayart and Cohen-Haguenauer, 2013).

Here, we show that primary human bile duct cells can readily be expanded in vitro as bipotent stem cells into 3D organoids. These cells differentiate into functional hepatocyte cells in vitro and generate bona fide hepatocytes upon transplantation. Extensive analysis of the genetic stability of cultured organoids in vitro demonstrates that the expanded cells preserve their genetic integrity over months in culture. These results agree with our previous observations in the mouse (Huch et al., 2013b) yet are in striking contrast to recent publications in which, utilizing several lineage tracing approaches, ductal/resident stem cells have been described as not contributing to mouse liver regeneration (Schaub et al., 2014; Yanger et al., 2014; Yanger et al., 2013). Our results resemble what has been elegantly shown in zebrafish and rat models: in the event of an almost complete hepatocyte loss or blockage of hepatocyte proliferation, biliary epithelial cells convert into hepatocytes (Choi et al., 2014) (Michalopoulos, 2014). Our data are further corroborated in human fulminant hepatic failure, in which, upon

80% loss of hepatocyte compartment, huge numbers of proliferating EpCAM⁺ biliary epithelial cells are observed (Hattoum et al., 2013).

Organoids from A1AT-deficiency patients can be expanded in vitro and mimic the in vivo pathology. Similarly, organoids from an Alagille syndrome patient reproduce the structural duct defects present in the biliary tree of these patients. Repair by homologous recombination using CRISPR/Cas9 technology is feasible in organoid cultures, as we recently demonstrated in colon stem cells of cystic fibrosis patients (Schwank et al., 2013). A variety of monogenic hereditary diseases affect the liver specifically, and these should all be amenable to a comparable in vitro approach of gene repair in clonal liver progenitor cells. Overall, our results open up the avenue to start testing human liver material expanded in vitro as an alternative cell source for studies of human liver regeneration, human liver disease mechanism, cell therapy transplantation, toxicology studies, or drug testing.

EXPERIMENTAL PROCEDURES

Human Liver Organoid Culture

Liver biopsies (0.5–1 cm³) were obtained from donor and explant livers during liver transplantation performed at the Erasmus MC, Rotterdam. The Medical Ethical Council of the Erasmus Medical Center approved the use of this material for research purposes, and informed consent was provided from all patients. For EpCAM sorting experiments and hepatocyte isolation, primary human liver tissue was obtained with informed consent and approval by the Regional Ethics Board, from the CLINTEC division of Karolinska institute (Dnr: 2010/678-31/3) (Jorns et al., 2014). Liver cells were isolated from human liver biopsies (0.5–1 cm³) by collagenase-accutase digestion, as described in the Extended Experimental Procedures. The different fractions were mixed and washed with cold Advanced DMEM/F12 and spun at 300–400 $\times g$ for 5 min. The cell pellet was mixed with Matrigel (BD Biosciences) or reduced growth factor BME 2 (Basement Membrane Extract, Type 2, Pathclear), and 3,000–10,000 cells were seeded per well in a 48-well/plate. Non-attaching plates were used (Greiner). After Matrigel or BME had solidified, culture medium was added. Culture media was based on AdDMEM/F12 (Invitrogen) supplemented with 1% N2 and 1% B27 (both from GIBCO), 1.25 mM N-Acetylcysteine (Sigma), 10 nM gastrin (Sigma), and the growth factors: 50 ng/ml EGF (Peprotech), 10% RSPO1 conditioned media (homemade), 100 ng/ml FGF10 (Peprotech), 25 ng/ml HGF (Peprotech), 10 mM Nicotinamide (Sigma), 5 μ M A83.01 (Tocris), and 10 μ M FSK (Tocris). For the establishment of the culture, the first 3 days after isolation, the medium was supplemented with 25 ng/ml Noggin (Peprotech), 30% Wnt CM (homemade prepared as described in Barker et al. [2010]), and 10 μ M (Y27632, Sigma Aldrich) or hES cell cloning recovery solution (Stemgent). Then, the medium was changed into a medium without Noggin, Wnt, Y27632, hES cell cloning recovery solution. After 10–14 days, organoids were removed from the Matrigel or BME, mechanically dissociated into small fragments, and transferred to fresh matrix. Passage was performed in a 1:4–1:8 split ratio once every 7–10 days for at least 6 months. To prepare frozen stocks, organoid

midazolam glucuronide were determined. Duplicates for each condition and donor were analyzed. Results are shown as mean \pm SEM of two independent experiments.

(F) Bile acid production shown as \pm SEM of two independent experiments in two independent donor-derived cultures. Duplicates for each condition and donor were analyzed.

(G) Ammonia elimination, shown as \pm SEM of $n = 3$ independent experiments in two independent donor-derived cultures, given as nM/h/million cells.

(H) Retrorsine/ CCl_4 -treated Balb/c nude mice were transplanted with $1\text{--}2 \times 10^6$ human liver organoid cells and were sacrificed after 120 days. The presence of foci of human Albumin⁺/KRT19⁺ hepatocytes demonstrates engraftment and differentiation in mouse liver.

(I) Serum levels of human Albumin after transplantation. Results are shown as \pm SEM of two vehicle control animals, two primary hepatocyte transplanted mice, and six human liver organoid transplanted animals.

** $p < 0.01$ and * $p < 0.05$ when comparing EM versus DM. See also Figures S5 and S6.

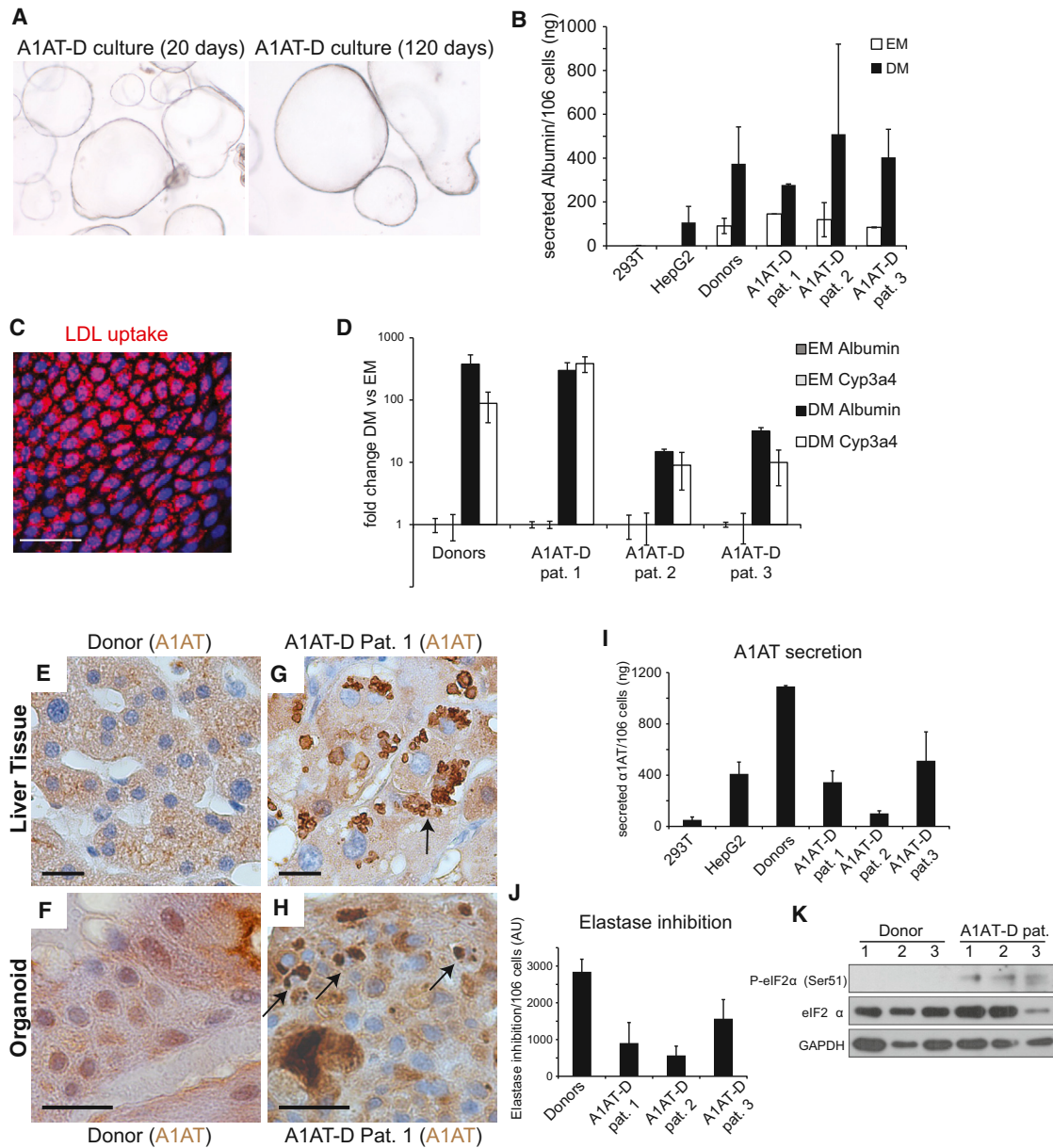


Figure 7. Human A1AT Deficiency Liver Cultures as an In Vitro Disease Model

(A) A1AT-deficiency patient-derived liver organoids at passage 2 and passage 11 (4 \times magnification).

(B) Albumin secretion in supernatant from donor and A1AT-deficient patient organoids in EM or after 11 days in DM. Results are expressed as mean \pm SEM of two independent experiments.

(C) A1AT-deficient organoids were differentiated for 11 days and incubated with Dil-Ac-LDL. Fluorescence microscopy shows robust LDL uptake in patient organoids. Scale bar, 50 μ m.

(D) Fold induction of Albumin and CYP3A4 mRNA levels after 11 days of differentiation of donor and A1AT-deficient organoids. Results are expressed as mean \pm SEM of two independent experiments.

(E–H) Immunohistochemistry for A1AT on liver tissue (E and G) and liver-derived organoids from a healthy donor (F) and a representative A1AT deficiency patient (H). Arrows indicate A1AT protein aggregates in patient-derived liver tissue (G) and organoids (H). Scale bar, 20 μ m.

(I) ELISA measurement of A1AT secretion in supernatants from donor and patient organoids after 11 days of differentiation. Results are expressed as mean \pm SEM of two independent experiments.

(J) Enzymatic measurement of elastase inhibition by supernatants of differentiated donor and patient-derived organoids. Results are expressed as mean \pm SEM of two independent experiments.

(K) Western blot of lysates from donor and A1AT deficiency patient organoids after 11 days of differentiation. Increased eIF2 α phosphorylation at Ser51 was detected in the three patients. Representative image is shown. Pat, patient.

See also Figure S7.

cultures were dissociated and mixed with recovery cell culture freezing medium (GIBCO) and frozen following standard procedures. When required, the cultures were thawed using standard thawing procedures and cultured as described above. For the first 3 days after thawing, the culture medium was supplemented with Y-27632 (10 μ M).

Growth curves and expansion ratios were performed and calculated as described in the [Extended Experimental Procedures](#).

Isolation of EpCAM+ Cells and Single-Cell Culture

Cell suspensions prepared as described in the [Extended Experimental Procedures](#) were stained with anti-human CD326 (EpCAM), sorted on a MoFlo (Dako Cytomation) sorter, and cultured as described above with medium supplemented with Y-27632 (10 μ M, Sigma Aldrich) for the first 4 days. Passage was performed in split ratios of 1:4–1:8 once per week.

For clonogenic assays, single-cell suspensions were sorted using FSC and pulse width to discriminate single cells. Propidium iodide staining was used to label dead cells and FSC: pulse-width gating to exclude cell doublets (MoFlow, Dako). Sorted cells were embedded in Matrigel and seeded in 96-well plates at a ratio of 1 cell/well. Cells were cultured as described above.

Hepatocyte Differentiation and In Vitro Functional Studies

Liver organoids were seeded and kept 7–10 days under the liver medium explained above (EM, expansion medium) supplemented with BMP7 (25 ng/ml). Then, the cultures were split and seeded accordingly in this EM supplemented with BMP7 for at least 2–4 days. Then, medium was changed to the differentiation medium (DM): AdDMEM/F12 medium supplemented with 1% N2 and 1% B27 and containing EGF (50 ng/ml), gastrin (10 nM, Sigma), HGF (25 ng/ml), FGF19 (100 ng/ml), A8301 (500 nM), DAPT (10 μ M), BMP7 (25 ng/ml), and dexamethasone (30 μ M). Differentiation medium was changed every 2–3 days for a period of 11–13 days.

To assess hepatocyte function, culture medium was collected 24 hr after the last medium change. Functional studies were performed in the collected supernatant or in whole organoids, as described in the [Extended Experimental Procedures](#).

Transplantation

We used a modified version of the protocol used by Guo et al. ([Guo et al., 2002](#)). In short, female BALB/c nude mice (around 7 weeks of age) were pre-treated with two injections of 70 mg/kg Retrovirus (Sigma) at 30 and 14 days before transplantation. One day prior to transplantation, mice received 0.5 ml/kg CCl4 and 50 mg/animal anti-asialo GM1 (Wako Pure Chemical Industries) via IP injection. Furthermore, animals received 7.5 μ g/ml FK506 in drinking water until the end of the experiment due to the reported positive effects on liver regeneration ([He et al., 2010](#)). On the day of transplantation, mice were anaesthetized, and suspensions of $1\text{--}2 \times 10^6$ human liver organoid cells derived from four independent donors (p6–p10) or fresh isolated hepatocytes (two donors) were injected intrasplenically. Transplanted mice received weekly injections of 50 mg/animal anti-asialo GM1 (Wako Pure Chemical Industries) to deplete NK cells. To monitor the transplantation state, blood samples were taken in regular intervals from the tail vein and were analyzed for the presence of human albumin and human α 1-antitrypsin using respective human specific ELISAs (Assaypro).

Karyotyping and Genetic Stability Analysis

Organoid cultures in exponential growing phase were incubated for 16 hr with 0.05 μ g/ml colcemid (GIBCO). Then, cultures were dissociated into single cells using TrypLE express (GIBCO) and processed using standard karyotyping protocols.

DNA libraries for WGS analysis were generated from 1 μ g of genomic DNA using standard protocols (Illumina). The libraries were sequenced with paired-end (2 \times 100 bp) runs using Illumina HiSeq 2500 sequencers to a minimal depth of 30 \times base coverage (average depth of \sim 36.9 \times base coverage). As a reference sample, liver biopsies were sequenced to equal depth for the different donors. Analysis of the sequence reads, calling of CNVs, and base substitutions are described in detail in the [Extended Experimental Procedures](#). The data for the whole-genome sequencing were deposited to the EMBL European Nucleotide Archive with accession number ERP005929.

Immunohistochemistry, Immunofluorescence, and Image Analysis

Tissues and organoids were fixed o/n with formalin or 4% PFA, respectively, and stained and imaged as described in the [Extended Experimental Procedures](#).

A1AT-D Functional Experiments

Elastase inhibition assay and detection of phosphorylated eIF2 α were performed as described in the [Extended Experimental Procedures](#).

Microarray

For the expression analysis of human liver cultures, total RNA was isolated from liver biopsies or from organoid cultures grown in our defined medium, using QIAGEN RNeasy kit following the manufacturer's instructions. Five hundred ng of total RNA were labeled with low RNA Input Linear Amp kit (Agilent Technologies). Universal human reference RNA (Agilent) was differentially labeled and hybridized to the tissue or cultured samples. A 4X 44 K Agilent whole human genome dual color microarray (G4122F) was used. Labeling, hybridization, and washing were performed according to Agilent guidelines. Microarray signal and background information were retrieved using Feature Extraction software (V.9.5.3, Agilent Technologies). Hierarchical clustering analysis was performed in whole-liver tissue or organoid arrays. A cut-off of 3-fold differentially expressed was used for the clustering analysis.

Data Analysis

All values are represented as mean \pm SEM. Man-Whitney nonparametric test was used. $p < 0.05$ was considered statistically significant. In all cases, data from at least three independent experiments was used. All calculations were performed using SPSS package.

ACCESSION NUMBERS

The data for the whole-genome sequencing of clonal organoid cultures has been deposited to the EMBL European Nucleotide Archive under accession number ERP005929. The gene expression data reported in this paper has been deposited at the GEO repository with accession number GSE63859.

SUPPLEMENTAL INFORMATION

Supplemental Information includes Extended Experimental Procedures, seven figures, and five tables and can be found with this article online at <http://dx.doi.org/10.1016/j.cell.2014.11.050>.

AUTHOR CONTRIBUTIONS

M.H., H.G., and H.C. designed and, together with K.H., performed and analyzed experiments. M.H. designed and developed and, with K.H., performed all experiments and analyzed all data that characterized the human liver culture system. M.H., R.v.B., E.C., and H.C. designed the genetic studies. M.H. and H.G. designed and M.H., H.G., and K.H. performed A1AT experiments. H.G. and H.C. designed and H.G. and K.H. performed ductal origin, transplantation, and AGS experiments. R.v.B. performed the genetic stability studies, supervised the next-gen sequencing, and set up the filtering pipeline. F.B. adjusted and applied pipeline. J.d.L. performed the CNV analysis. M.H., M.v.W., R.H., S.A.F., S.J.B., and H.K. performed functional in vitro experiments and analyzed the data. M.v.d.W. and N.S. performed FACS. M.M.A.V., J.N.M.I., S.S., E.E. and L.J.W.v.d.L. provided Ethical Approval, human liver donor biopsies, isolated hepatocytes, and patient material. E.E.S.N. and R.R.G.V. provided METC. R.R.G.V. provided helpful discussions. M.H., H.G., R.v.B., E.C., and H.C. wrote the manuscript. All authors commented on the manuscript.

ACKNOWLEDGMENTS

We thank The Hubrecht Imaging Center for imaging assistance and the Genome Diagnostics laboratory of the UMC-Utrecht for help with the karyotype analysis. We also thank Lara Elshove, Herold Metselaar, Petra de Ruiter,

and the Erasmus MC liver explantation student team for liver biopsies. The Rspo cell line was kindly provided by Calvin Kuo. This work was supported by grants to M.H., H.G., and K.H. (EU/232814 Stem Cell Mark), H.G. (SNF early Postdoc Mobility and EMBO Long-Term fellowship), R.v.B. (NWO/ZonMW 116.005.002), E.C. (NWO/ZonMW Zenith 93512003), and H.C. (The United European Gastroenterology Federation (UEGF) Research Prize 2010, EU/232814-StemCellMark and NWO/116002008). M.H. is a Wellcome Trust Sir Henry Dale Fellow and is jointly funded by the Wellcome Trust and the Royal Society (grant number 104151/Z/14/Z).

Received: May 23, 2014

Revised: September 21, 2014

Accepted: November 21, 2014

Published: December 18, 2014

REFERENCES

- Abyzov, A., Mariani, J., Palejev, D., Zhang, Y., Haney, M.S., Tomasini, L., Ferlandino, A.F., Rosenberg Belmaker, L.A., Szekely, A., Wilson, M., et al. (2012). Somatic copy number mosaicism in human skin revealed by induced pluripotent stem cells. *Nature* 492, 438–442.
- Baker, D.E., Harrison, N.J., Maltby, E., Smith, K., Moore, H.D., Shaw, P.J., Heath, P.R., Holden, H., and Andrews, P.W. (2007). Adaptation to culture of human embryonic stem cells and oncogenesis in vivo. *Nat. Biotechnol.* 25, 207–215.
- Barker, N., van Es, J.H., Kuipers, J., Kujala, P., van den Born, M., Cozijnsen, M., Haegebarth, A., Korving, J., Begthel, H., Peters, P.J., and Clevers, H. (2007). Identification of stem cells in small intestine and colon by marker gene Lgr5. *Nature* 449, 1003–1007.
- Barker, N., Huch, M., Kujala, P., van de Wetering, M., Snippert, H.J., van Es, J.H., Sato, T., Stange, D.E., Begthel, H., van den Born, M., et al. (2010). Lgr5(+ve) stem cells drive self-renewal in the stomach and build long-lived gastric units in vitro. *Cell Stem Cell* 6, 25–36.
- Bayart, E., and Cohen-Haguener, O. (2013). Technological overview of iPS induction from human adult somatic cells. *Curr. Gene Ther.* 13, 73–92.
- Bigorgne, A.E., Farin, H.F., Lemoine, R., Mahlaoui, N., Lambert, N., Gil, M., Schulz, A., Philippet, P., Schlessner, P., Abrahamsen, T.G., et al. (2014). TTC7A mutations disrupt intestinal epithelial apicobasal polarity. *J. Clin. Invest.* 124, 328–337.
- Carmon, K.S., Gong, X., Lin, Q., Thomas, A., and Liu, Q. (2011). R-spondins function as ligands of the orphan receptors LGR4 and LGR5 to regulate Wnt/beta-catenin signaling. *Proc. Natl. Acad. Sci. USA* 108, 11452–11457.
- Cheng, L., Hansen, N.F., Zhao, L., Du, Y., Zou, C., Donovan, F.X., Chou, B.K., Zhou, G., Li, S., Dowey, S.N., et al.; NISC Comparative Sequencing Program (2012). Low incidence of DNA sequence variation in human induced pluripotent stem cells generated by nonintegrating plasmid expression. *Cell Stem Cell* 10, 337–344.
- Choi, T.Y., Ninov, N., Stainier, D.Y., and Shin, D. (2014). Extensive conversion of hepatic biliary epithelial cells to hepatocytes after near total loss of hepatocytes in zebrafish. *Gastroenterology* 146, 776–788.
- de Lau, W., Barker, N., Low, T.Y., Koo, B.K., Li, V.S., Teunissen, H., Kujala, P., Haegebarth, A., Peters, P.J., van de Wetering, M., et al. (2011). Lgr5 homologues associate with Wnt receptors and mediate R-spondin signalling. *Nature* 476, 293–297.
- Dekkers, J.F., Wiegerinck, C.L., de Jonge, H.R., Bronsveld, I., Janssens, H.M., de Winter-de Groot, K.M., Brandsma, A.M., de Jong, N.W., Bijvelds, M.J., Scholte, B.J., et al. (2013). A functional CFTR assay using primary cystic fibrosis intestinal organoids. *Nat. Med.* 19, 939–945.
- Dorrell, C., Erker, L., Schug, J., Kopp, J.L., Canaday, P.S., Fox, A.J., Smirnova, O., Duncan, A.W., Finegold, M.J., Sander, M., et al. (2011). Prospective isolation of a bipotential clonogenic liver progenitor cell in adult mice. *Genes Dev.* 25, 1193–1203.
- Duncan, A.W., Dorrell, C., and Grompe, M. (2009). Stem cells and liver regeneration. *Gastroenterology* 137, 466–481.
- Francis, H., Glaser, S., Ueno, Y., Lesage, G., Marucci, L., Benedetti, A., Taffetani, S., Marzioni, M., Alvaro, D., Venter, J., et al. (2004). cAMP stimulates the secretory and proliferative capacity of the rat intrahepatic biliary epithelium through changes in the PKA/Src/MEK/ERK1/2 pathway. *J. Hepatol.* 41, 528–537.
- Furuyama, K., Kawaguchi, Y., Akiyama, H., Horiguchi, M., Kodama, S., Kuhara, T., Hosokawa, S., Elbahrawy, A., Soeda, T., Koizumi, M., et al. (2011). Continuous cell supply from a Sox9-expressing progenitor zone in adult liver, exocrine pancreas and intestine. *Nat. Genet.* 43, 34–41.
- Geisler, F., Nagl, F., Mazur, P.K., Lee, M., Zimmer-Strobl, U., Strobl, L.J., Radtke, F., Schmid, R.M., and Siveke, J.T. (2008). Liver-specific inactivation of Notch2, but not Notch1, compromises intrahepatic bile duct development in mice. *Hepatology* 48, 607–616.
- Gore, A., Li, Z., Fung, H.L., Young, J.E., Agarwal, S., Antosiewicz-Bourget, J., Canto, I., Giorgetti, A., Israel, M.A., Kiskinis, E., et al. (2011). Somatic coding mutations in human induced pluripotent stem cells. *Nature* 471, 63–67.
- Gramignoli, R., Green, M.L., Tahan, V., Dorko, K., Skvorak, K.J., Marongiu, F., Zao, W., Venkataramanan, R., Ellis, E.C., Geller, D., et al. (2012). Development and application of purified tissue dissociation enzyme mixtures for human hepatocyte isolation. *Cell Transplant.* 21, 1245–1260.
- Guo, D., Fu, T., Nelson, J.A., Superina, R.A., and Soriano, H.E. (2002). Liver repopulation after cell transplantation in mice treated with retrorsine and carbon tetrachloride. *Transplantation* 73, 1818–1824.
- Hattoum, A., Rubin, E., Orr, A., and Michalopoulos, G.K. (2013). Expression of hepatocyte epidermal growth factor receptor, FAS and glypican 3 in EpCAM-positive regenerative clusters of hepatocytes, cholangiocytes, and progenitor cells in human liver failure. *Hum. Pathol.* 44, 743–749.
- He, Z., Zhang, H., Zhang, X., Xie, D., Chen, Y., Wangenstein, K.J., Ekker, S.C., Firpo, M., Liu, C., Xiang, D., et al. (2010). Liver xeno-repopulation with human hepatocytes in Fah^{-/-}Rag2^{-/-} mice after pharmacological immunosuppression. *Am. J. Pathol.* 177, 1311–1319.
- Heron, M. (2012). Deaths: Leading causes for 2009. National Vital Statistics Reports. October 26, 2012. http://www.cdc.gov/nchs/data/nvsr/nvsr61/nvsr61_07.pdf.
- Huch, M., Bonfanti, P., Boj, S.F., Sato, T., Loomans, C.J., van de Wetering, M., Sojoodi, M., Li, V.S., Schuijers, J., Gracanin, A., et al. (2013a). Unlimited in vitro expansion of adult bi-potent pancreas progenitors through the Lgr5/R-spondin axis. *EMBO J.* 32, 2708–2721.
- Huch, M., Dorrell, C., Boj, S.F., van Es, J.H., Li, V.S., van de Wetering, M., Sato, T., Hamer, K., Sasaki, N., Finegold, M.J., et al. (2013b). In vitro expansion of single Lgr5⁺ liver stem cells induced by Wnt-driven regeneration. *Nature* 494, 247–250.
- Hussein, S.M., Batada, N.N., Vuoristo, S., Ching, R.W., Autio, R., Närvä, E., Ng, S., Sourour, M., Hämmäläinen, R., Olsson, C., et al. (2011). Copy number variation and selection during reprogramming to pluripotency. *Nature* 471, 58–62.
- Jorns, C., Gramignoli, R., Saliem, M., Zemack, H., Mörk, L.M., Isaksson, B., Nowak, G., Ericzon, B.G., Strom, S., and Ellis, E. (2014). Strategies for short-term storage of hepatocytes for repeated clinical infusions. *Cell Transplant.* 23, 1009–1018.
- Jung, P., Sato, T., Merlos-Suárez, A., Barriga, F.M., Iglesias, M., Rossell, D., Auer, H., Gallardo, M., Blasco, M.A., Sancho, E., et al. (2011). Isolation and in vitro expansion of human colonic stem cells. *Nat. Med.* 17, 1225–1227.
- Kamath, B.M., Spinner, N.B., and Rosenblum, N.D. (2013). Renal involvement and the role of Notch signalling in Alagille syndrome. *Nat. Rev. Nephrol.* 9, 409–418.
- Laurent, L.C., Ulitsky, I., Slavin, I., Tran, H., Schork, A., Morey, R., Lynch, C., Harness, J.V., Lee, S., Barrero, M.J., et al. (2011). Dynamic changes in the copy number of pluripotency and cell proliferation genes in human ESCs and iPSCs during reprogramming and time in culture. *Cell Stem Cell* 8, 106–118.
- Lawless, M.W., Mankan, A.K., Gray, S.G., and Norris, S. (2008). Endoplasmic reticulum stress—a double edged sword for Z alpha-1 antitrypsin deficiency hepatotoxicity. *Int. J. Biochem. Cell Biol.* 40, 1403–1414.

- Liang, G., and Zhang, Y. (2013). Genetic and epigenetic variations in iPSCs: potential causes and implications for application. *Cell Stem Cell* 13, 149–159.
- Lund, R.J., Närvä, E., and Lahesmaa, R. (2012). Genetic and epigenetic stability of human pluripotent stem cells. *Nat. Rev. Genet.* 13, 732–744.
- Martins-Taylor, K., Nisler, B.S., Taapken, S.M., Compton, T., Crandall, L., Montgomery, K.D., Lalande, M., and Xu, R.H. (2011). Recurrent copy number variations in human induced pluripotent stem cells. *Nat. Biotechnol.* 29, 488–491.
- Massagué, J., Seoane, J., and Wotton, D. (2005). Smad transcription factors. *Genes Dev.* 19, 2783–2810.
- Mayshar, Y., Ben-David, U., Lavon, N., Biancotti, J.C., Yakir, B., Clark, A.T., Plath, K., Lowry, W.E., and Benvenisty, N. (2010). Identification and classification of chromosomal aberrations in human induced pluripotent stem cells. *Cell Stem Cell* 7, 521–531.
- McCright, B., Lozier, J., and Gridley, T. (2002). A mouse model of Alagille syndrome: Notch2 as a genetic modifier of Jag1 haploinsufficiency. *Development* 129, 1075–1082.
- Michalopoulos, G.K. (2014). The liver is a peculiar organ when it comes to stem cells. *Am. J. Pathol.* 184, 1263–1267.
- Mitaka, T. (1998). The current status of primary hepatocyte culture. *Int. J. Exp. Pathol.* 79, 393–409.
- Pera, M.F. (2011). Stem cells: The dark side of induced pluripotency. *Nature* 471, 46–47.
- Rashid, S.T., Corbineau, S., Hannan, N., Marciniak, S.J., Miranda, E., Alexander, G., Huang-Doran, I., Griffin, J., Ahrlund-Richter, L., Skepper, J., et al. (2010). Modeling inherited metabolic disorders of the liver using human induced pluripotent stem cells. *J. Clin. Invest.* 120, 3127–3136.
- Sato, T., Vries, R.G., Snippert, H.J., van de Wetering, M., Barker, N., Stange, D.E., van Es, J.H., Abo, A., Kujala, P., Peters, P.J., and Clevers, H. (2009). Single Lgr5 stem cells build crypt-villus structures in vitro without a mesenchymal niche. *Nature* 459, 262–265.
- Sato, T., Stange, D.E., Ferrante, M., Vries, R.G., Van Es, J.H., Van den Brink, S., Van Houdt, W.J., Pronk, A., Van Gorp, J., Siersema, P.D., and Clevers, H. (2011). Long-term expansion of epithelial organoids from human colon, adenoma, adenocarcinoma, and Barrett's epithelium. *Gastroenterology* 141, 1762–1772.
- Schaub, J.R., Malato, Y., Gormond, C., and Willenbring, H. (2014). Evidence against a stem cell origin of new hepatocytes in a common mouse model of chronic liver injury. *Cell Rep.* 8, 933–939.
- Schmelzer, E., Zhang, L., Bruce, A., Wauthier, E., Ludlow, J., Yao, H.L., Moss, N., Melhem, A., McClelland, R., Turner, W., et al. (2007). Human hepatic stem cells from fetal and postnatal donors. *J. Exp. Med.* 204, 1973–1987.
- Schwank, G., Koo, B.K., Sasselli, V., Dekkers, J.F., Heo, I., Demircan, T., Sasaki, N., Boymans, S., Cuppen, E., van der Ent, C.K., et al. (2013). Functional repair of CFTR by CRISPR/Cas9 in intestinal stem cell organoids of cystic fibrosis patients. *Cell Stem Cell* 13, 653–658.
- Shan, J., Schwartz, R.E., Ross, N.T., Logan, D.J., Thomas, D., Duncan, S.A., North, T.E., Goessling, W., Carpenter, A.E., and Bhatia, S.N. (2013). Identification of small molecules for human hepatocyte expansion and iPS differentiation. *Nat. Chem. Biol.* 9, 514–520.
- Shin, S., Walton, G., Aoki, R., Brondell, K., Schug, J., Fox, A., Smirnova, O., Dorrell, C., Erker, L., Chu, A.S., et al. (2011). Foxl1-Cre-marked adult hepatic progenitors have clonogenic and bilineage differentiation potential. *Genes Dev.* 25, 1185–1192.
- Stoller, J.K., and Aboussouan, L.S. (2005). Alpha1-antitrypsin deficiency. *Lancet* 365, 2225–2236.
- Sugimoto, H., Yang, C., LeBleu, V.S., Soubasakos, M.A., Giraldo, M., Zeisberg, M., and Kalluri, R. (2007). BMP-7 functions as a novel hormone to facilitate liver regeneration. *FASEB J.* 21, 256–264.
- Vilarinho, S., and Lifton, R.P. (2012). Liver transplantation: from inception to clinical practice. *Cell* 150, 1096–1099.
- Wandel, C., Böcker, R., Böhler, H., Browne, A., Rügheimer, E., and Martin, E. (1994). Midazolam is metabolized by at least three different cytochrome P450 enzymes. *Br. J. Anaesth.* 73, 658–661.
- Wiegerinck, C.L., Janecke, A.R., Schneeberger, K., Vogel, G.F., van Haaften-Visser, D.Y., Escher, J.C., Adam, R., Thöni, C.E., Pfaller, K., Jordan, A.J., et al. (2014). Loss of syntaxin 3 causes variant microvillus inclusion disease. *Gastroenterology* 147, 65, e10. <http://dx.doi.org/10.1053/j.gastro.2014.04.002>.
- Wu, A.L., Coulter, S., Liddle, C., Wong, A., Eastham-Anderson, J., French, D.M., Peterson, A.S., and Sonoda, J. (2011). FGF19 regulates cell proliferation, glucose and bile acid metabolism via FGFR4-dependent and independent pathways. *PLoS ONE* 6, e17868.
- Xu, J., Lamouille, S., and Derynck, R. (2009). TGF-beta-induced epithelial to mesenchymal transition. *Cell Res.* 19, 156–172.
- Yanger, K., Zong, Y., Maggs, L.R., Shapira, S.N., Maddipati, R., Aiello, N.M., Thung, S.N., Wells, R.G., Greenbaum, L.E., and Stanger, B.Z. (2013). Robust cellular reprogramming occurs spontaneously during liver regeneration. *Genes Dev.* 27, 719–724.
- Yanger, K., Knigin, D., Zong, Y., Maggs, L., Gu, G., Akiyama, H., Pikarsky, E., and Stanger, B.Z. (2014). Adult hepatocytes are generated by self-duplication rather than stem cell differentiation. *Cell Stem Cell* 15, 340–349.
- Yoon, S.M., Gerasimidou, D., Kuwahara, R., Hytioglou, P., Yoo, J.E., Park, Y.N., and Theise, N.D. (2011). Epithelial cell adhesion molecule (EpCAM) marks hepatocytes newly derived from stem/progenitor cells in humans. *Hepatology* 53, 964–973.

Subcellular Trafficking of FGF Controls Tracheal Invasion of *Drosophila* Flight Muscle

Soren J. Peterson¹ and Mark A. Krasnow^{1,*}

¹Howard Hughes Medical Institute and Department of Biochemistry, Stanford University School of Medicine, Stanford, CA 94305-5307, USA

*Correspondence: krasnow@stanford.edu

<http://dx.doi.org/10.1016/j.cell.2014.11.043>

SUMMARY

To meet the extreme oxygen demand of insect flight muscle, tracheal (respiratory) tubes ramify not only on its surface, as in other tissues, but also within T-tubules and ultimately surrounding every mitochondrion. Although this remarkable physiological specialization has long been recognized, its cellular and molecular basis is unknown. Here, we show that *Drosophila* tracheoles invade flight muscle T-tubules through transient surface openings. Like other tracheal branching events, invasion requires the Branchless FGF pathway. However, localization of the FGF chemoattractant changes from all muscle membranes to T-tubules as invasion begins. Core regulators of epithelial basolateral membrane identity localize to T-tubules, and knockdown of AP-1 γ , required for basolateral trafficking, redirects FGF from T-tubules to surface, increasing tracheal surface ramification and preventing invasion. We propose that tracheal invasion is controlled by an AP-1-dependent switch in FGF trafficking. Thus, subcellular targeting of a chemoattractant can direct outgrowth to specific domains, including inside the cell.

INTRODUCTION

Insect flight is powered by flight muscles that have the highest known rates of cellular metabolism (Weis-Fogh, 1961, 1964). The oxygen used in aerobic respiration during flight is delivered by an extensive network of air-filled tracheae that ramify not only on the surface of the flight muscle, as in other tissues, but also within muscle plasma membrane invaginations that extend deep inside the myocytes. These fine tracheal branches encircle every mitochondrion of the flight muscle, delivering oxygen directly to where it is used (Smith, 1961a; Weis-Fogh, 1964; Wigglesworth and Lee, 1982; Meyer, 1989). The presence of tracheae within insect flight muscle was first noted over a century ago by Leydig and Ramon y Cajal in the initial descriptions of muscle substructure (Leydig, 1859; Cajal, 1890) and was later elaborated by early electron microscopy (EM) studies (Smith, 1961b). However, the developmental, cellular, and molecular basis of this remarkable structural specialization to accommodate the extreme physiology of flight muscle is unknown.

The Branchless FGF signaling pathway controls tracheal branching throughout development of the fruit fly *Drosophila melanogaster*. In the embryo, tracheal progenitor cells begin to express *breathless* (*btl*) FGF receptor (Glazer and Shilo 1991), while *branchless* (*bnl*) FGF gene turns on in a complex and dynamic pattern in small clusters of cells surrounding the progenitors (Sutherland et al., 1996). Bnl FGF functions as a chemoattractant, activating Btl FGFR and directing branch budding and outgrowth of the stereotyped primary and secondary tracheal branches. *bnl* turns on again later during larval development, its expression now controlled by the oxygen needs of the target tissues (Jarecki et al., 1999). Oxygen starvation induces *bnl* expression, and the secreted FGF induces outgrowth of fine cytoplasmic processes from the tracheal terminal cells toward the hypoxic cell, ultimately forming fine terminal branches (tracheoles) that deliver oxygen to the cell. In this way, the tracheal system provides oxygen directly to most cells of the larva. During metamorphosis, dedifferentiated larval tracheal cells and imaginal tracheal progenitors that remain quiescent during early tracheal development become activated, and here too *bnl* is expressed at specific sites and directs the proliferation and outgrowth of tracheal cells to form pupal and adult branches (Weaver and Krasnow, 2008; Chen and Krasnow 2014) and the adult air sacs that fill much of the adult fly (Sato and Kornberg, 2002).

Here, we describe the development of tracheal branches that supply the indirect flight muscle of *Drosophila*, one of the adult muscles that powers flight. The muscle forms during pupal development and, as we describe below, receives its tracheal supply from progenitors that extend out to the developing flight muscle from a thoracic air sac. However, unlike other tracheal terminal branches, which ramify on the surface of their target cells, we show that flight muscle terminal branches “invade” the T-tubules, plasma membrane invaginations that extend deep within the myocyte interior to facilitate excitation-contraction coupling. We show that the Bnl FGF pathway directs not only tracheal outgrowth to the flight muscle as in other tissues, but also T-tubule invasion, and that invasion is activated by a developmental switch in Bnl trafficking that targets Bnl selectively to T-tubules.

RESULTS

Tracheae Invade Flight Muscle T-Tubules through Transient Surface Openings

Anatomical and ultrastructural studies (Leydig, 1859; Cajal, 1890; Smith, 1961a; Weis-Fogh, 1964) of indirect flight muscle

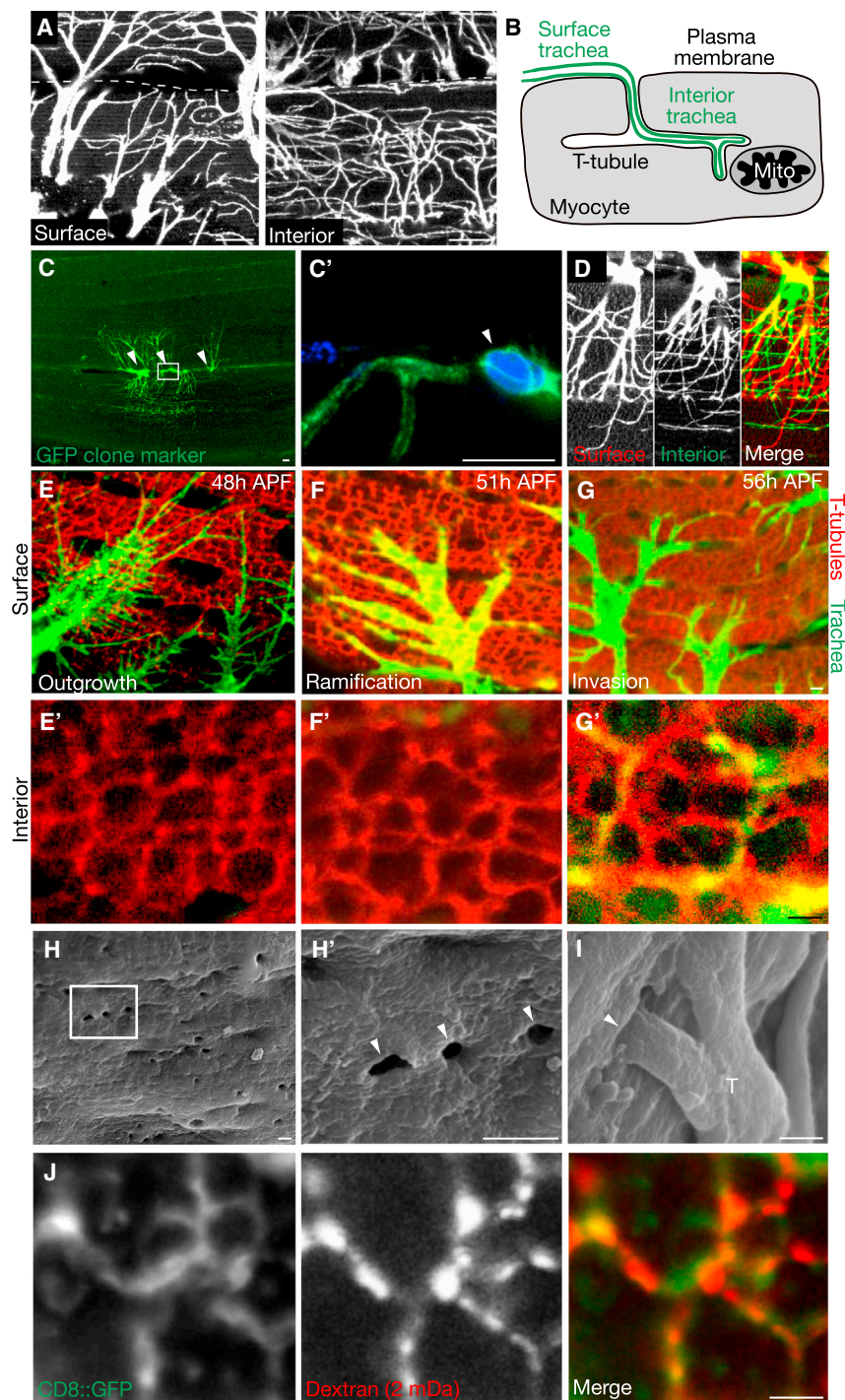


Figure 1. Tracheal Invasion of Flight Muscle T-Tubules

(A) Indirect flight muscle (dorsal longitudinal muscle, DLM) fiber of a *btl-Gal4; UAS-CD8-GFP* adult *Drosophila* showing tracheal branches (CD8-GFP immunostain, white) ramifying on muscle fiber surface (left) or interiorly 5 μm below the surface (right). Dashes, muscle fiber boundary.

(B) Schematic of tracheal branch (green) on surface of flight muscle fiber (Myocyte, gray) and continuing into T-tubule plasma membrane invagination to form internal trachea that terminate at mitochondria (Mito).

(C) Three terminal cells of a GFP-marked tracheal clone (green) generated by MARCM. Nuclei were stained with DAPI (blue); nuclei of the three terminal cells in the clone are indicated (arrowheads); boxed area (C') shows soma of one of the marked cells. Somas of the three terminal cells lie between two fibers and each extends branches onto the surface of and within both neighboring fibers.

(D) Depth-coded confocal stack of single-cell tracheal MARCM clone. Tracheal branches on the muscle surface (red) narrow as they progress within the muscle fiber and become internal branches (green).

(E–G) Time course of tracheal outgrowth to flight muscle and T-tubule invasion. Flight muscle fibers of *btl-Gal4; UAS-CD8-GFP* pupae at the indicated times after puparium formation (APF) immunostained for trachea (GFP, green) and for T-tubules (amphiphysin, red). Upper panels (E–G), muscle fiber surface; lower panels (E'–G'), interior view of same fiber 5 μm below surface. Note tracheae ramifying on fiber surface in (E–G) but invasion of T-tubules only in (G').

(H and I) Scanning electron micrographs of flight muscles 55 hr APF. T-tubule openings (~ 300 nm diameter) are visible at surface of fiber (H', close up of boxed region in H). Trachea (T) enter some of the openings (I).

(J) Close-up of T-tubules (green) of *mef2-Gal4; UAS-CD8::GFP* 55 hr APF flight muscles incubated with 2 mDa fluorescent dextran for 20 min (red). Dextran has entered T-tubules (CD8::GFP, green), indicating that they are open to exterior. Scale bars represent 10 μm (A–D) and 1 μm (E–J).

See also Figure S1.

of *Drosophila* and other insects identified a dense array of tracheal branches (tracheoles) on the muscle surface (plasma membrane or sarcolemma) and within the T-tubule network deep below the surface (Wigglesworth and Lee, 1982) (Figures 1A and 1B). Analysis of *Drosophila* tracheal cell clones marked with CD8::GFP showed that individual tracheal cells formed multiple branches present on both the surface and interior of

btl-Gal4 > CD8::GFP to label tracheal cells and their cytoplasmic extensions and anti-Amphiphysin immunostaining (Razzaq et al., 2001) to label the T-tubule network. We focused our analysis on the dorsal longitudinal muscles (DLM) that are anchored to the thoracic cuticle by tendon cells and, along with the dorsal ventral muscles, are the two sets of nearly perpendicular muscles that comprise the indirect flight muscle (Figure S2A).

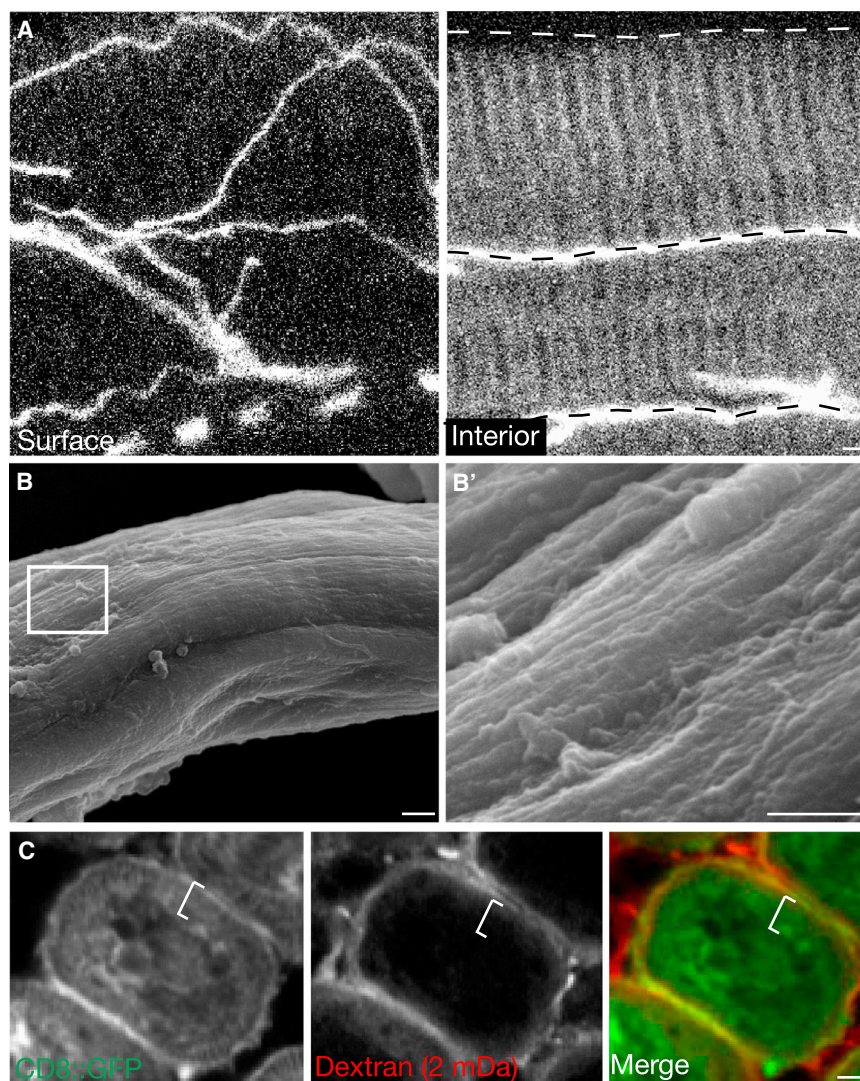


Figure 2. Muscles Not Invaded by Trachea Lack Surface Openings

(A) Surface (left) and interior (right) views of a plural remoter of coxae muscle fiber immunostained for D3 tracheal antigen (white) to show tracheal distribution. Trachea are present on surface and between fibers (dashed lines) but not inside individual fibers.

(B) Scanning electron micrograph of a 68 hr APF leg tubular muscle fiber during tracheal outgrowth. (B') Detail of boxed region in (B). No T-tubule membrane openings are apparent on fiber surface. (C) Cross section of adult leg tubular muscle of *mef2-Gal4; UAS-CD8::GFP* pupa 65 hr APF, after incubation with 2 mDa fluorescent dextran (red) for 20 min. Muscle membranes are marked with CD8::GFP (green). Dextran is detected on fiber surface but not in T-tubule region within fiber (white bracket). Scale bars represent 1 μ m. See also [Figure S2](#).

invaded T-tubules turned off the T-tubule marker amphiphysin while the other T-tubules maintained its expression ([Figure S1A](#) available online). Later, all flight muscle T-tubules constricted ([Figures S1B and S1C](#)) and surface accessibility was lost ([Figure S1D](#)). Thus, tracheal branches invade the flight muscle T-tubule network through large but transient surface openings during a 10–15 hr period of pupal development.

Muscles Not Invaded by Tracheae Lack Surface Openings

The tracheation pattern of other larval and adult thoracic and abdominal muscles was surveyed, and although all showed tracheal branching on their surface, none contained tracheae in their T-tubule

The DLM begin to form at the onset of metamorphosis when a pool of myoblasts from the wing imaginal disc migrate to and fuse with specific “founder” larval myocytes, forming the nascent DLM muscle fibers by 24 hr after puparium formation (APF) ([Dutta et al., 2004](#)). The T-tubule network was present at 48 hr APF, when the medioscutal, lateroscutal, and scutellar air sacs extended tracheal projections that reached the muscle fibers ([Figure 1E](#)). Over the next 6–8 hr, the tracheal projections ramified and formed extensive networks of fine branches on the surface and between flight muscle fibers, but were not detected in the muscle interior ([Figures 1F and 1F'](#)). At ~55 hr APF, fine tracheal branches began to invade the T-tubule network ([Figure 1G'](#)). They entered T-tubules through ~300 nm surface openings that were visualized by scanning electron microscopy ([Figures 1H and 1I](#)) and accessible to 2 mDa (~50 nm diameter) ([Dreher et al., 2006](#)) dextran ([Figure 1J](#)). Tracheae invaded only some of the openings and then extended and ramified within the T-tubule network, ultimately filling just a small portion of the network ([Figure 1G'](#)). By 70 hr APF, invasion appeared complete, and the

networks in internal membrane networks ([Figure 2A](#)). When we examined one of them, the plural remoter of coxa tubular muscle ([Figure S2A](#)), by scanning electron microscopy (SEM) during the time its tracheae develop ([Figure S2B](#)), no openings in the muscle surface were detected ([Figure 2B](#)). Also, T-tubules of the leg muscle were not accessible to large dextrans (2 mDa or 500 kDa) that readily entered the T-tubular network of the indirect flight muscle ([Figures 2C and S2C](#)). Thus, other muscles lack the large surface openings through which trachea invade the indirect flight muscle T-tubule network.

The Branchless FGF Pathway Is Required for Flight Muscle Invasion

Bnl FGF directs tracheal outgrowth during development by activating the Btl FGFR expressed on tracheal cells. To determine if the Bnl pathway is required for flight muscle invasion, we examined the effect of *bni* and *btl* mutations on the number of tracheal branches and branch points within individual flight muscle fibers. Because null mutations in either gene cause early lethality, we

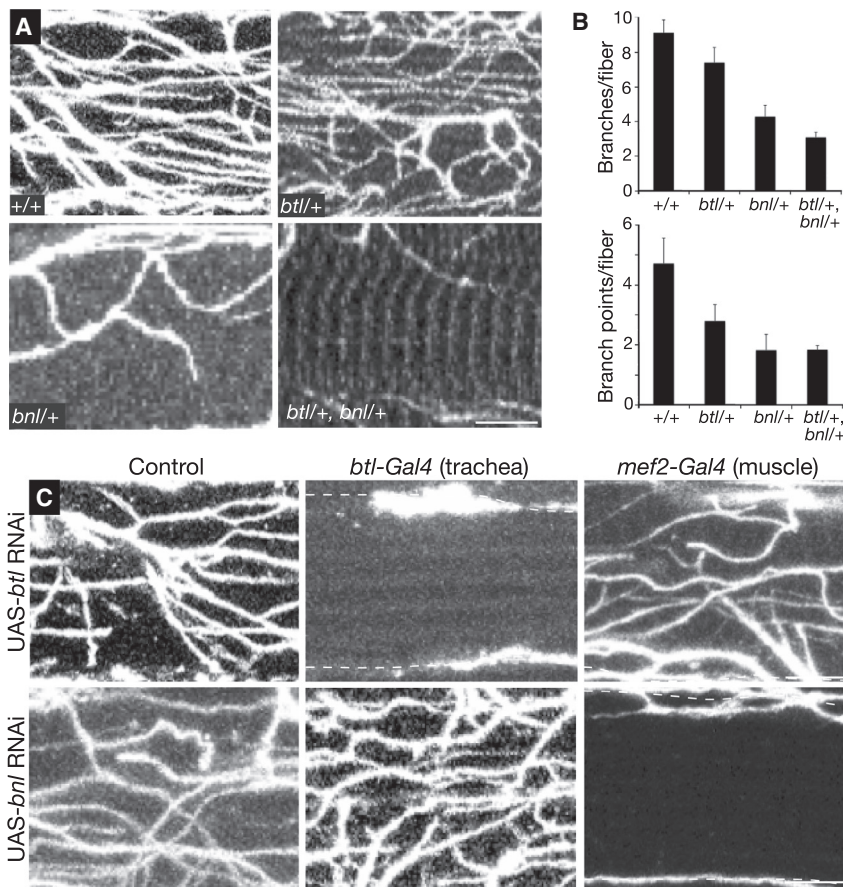


Figure 3. Effect of *breathless* FGFR and *branchless* FGF Mutations on Tracheal Invasion

(A) Interior views of single adult indirect flight muscle fibers of Oregon-R wild-type adult control (+/+) and adults of the indicated genotypes, immunostained for D3 antigen to show invaded trachea. *btl*, *btl*^{L^{G18}} (null allele); *bnl*, *bnl*^{P1} (null allele).

(B) Quantification of tracheal branches and branch points per muscle fiber in genotypes as in (A) (n = 25 fibers scored for each genotype). Error bars represent SEM.

(C) Tissue-specific knockdown of *btl* and *bnl* using Gal4-UAS system. Interior view of single muscle fibers as above from adult controls (no Gal4 driver) or adults with knockdown of *btl* FGFR (UAS-*btl* [RNAi]) or *bnl* FGF (UAS-*bnl* [RNAi]) in the tracheal system (*btl*-Gal4 driver) or flight muscle (*mef2*-Gal4 driver), as indicated. All animals contained a *tubulin*-Gal80ts transgene and were raised at 18°C to inhibit expression of the RNAi transgenes during embryonic and larval development, then shifted to 30°C at 0 hr APF to allow Gal4-mediated induction of the RNAi transgenes during pupal and adult life. Note that although trachea still reach the surface (dashed lines), tracheal invasion is absent in animals with tracheal knockdown of *btl* or muscle knockdown of *bnl*. Scale bars represent 1 μm.

See also Figure S3.

initially evaluated *bnl* and *btl* heterozygotes and a *bnl btl* double heterozygote. All of the mutants showed a reduction in tracheal branches and branch points within muscle fibers, although the effects were most dramatic (60%–75% reduction) in *bnl*^{+/-} heterozygotes and the *bnl*^{+/-} *btl*^{+/-} double heterozygote (Figures 3A and 3B). We also tested the effect of RNAi knockdown of *btl* expression in the tracheal system during pupal development, which completely abrogated flight muscle invasion (Figure 3C). Tracheal expression of a dominant-negative *btl* FGFR construct or the FGF pathway antagonist *sprouty* also reduced flight muscle invasion (Figure S3A), whereas expression of *btl* FGFR RNAi after tracheal invasion (Figure S3B) or using a muscle-specific driver had no effect (Figure 3C). We conclude that Btl FGFR signaling in the trachea is required for flight muscle invasion and is required during the invasion process. Similar experiments with a *bnl* RNAi construct (Figure 3C) demonstrated that Bnl FGF is required in the flight muscle during the same developmental period for tracheal invasion.

Branchless FGF Localizes to T-Tubules during Invasion

Although Bnl FGF can guide outgrowth to individual cells expressing the gene (Jarecki et al., 1999), we sought to understand how it functions in the subcellular targeting of T-tubules during flight muscle invasion. We examined the localization of secreted Bnl FGF protein in flight muscle during pupal development using an antibody staining protocol that detects only extracellular pro-

teins (Figure 4A) (Strigini and Cohen, 2000; Belenkaya et al., 2004). We first validated the specificity of the protocol for Bnl by showing that extracellular immunostaining in flight muscle decreased when endogenous Bnl levels were reduced by RNAi knockdown (Figure S4) and increased when *bnl* was overexpressed (Figures 4D and 4E). Using the validated procedure, we found that there was a developmental shift in Bnl localization. Before invasion, as tracheal branches grew out and ramified on the flight muscle surface, Bnl immunostaining was detected at similar low levels on both the plasma membrane and T-tubules of the flight muscle (Figures 4A and 4B). But as tracheal invasion commenced, Bnl FGF levels increased on the T-tubules and declined on the plasma membrane until they were almost undetectable (Figure 4C). Thus, there is a developmental transition in Bnl FGF localization that coincides with the transition from surface outgrowth to T-tubule invasion.

Bnl Overexpression Leads to Its Surface Accumulation and Increased Surface Branching at Expense of Invasion

Overexpression of Bnl in the flight muscle during tracheal invasion substantially increased the levels of secreted Bnl on both the plasma membrane and the T-tubules, eliminating the normal differential (Figure 4E). Under these conditions, the number of tracheal branches on the muscle surface increased, whereas tracheal invasion of T-tubules was reduced (Figure 4F). By contrast, expression of a constitutively active form of Btl FGFR in trachea during this same period increased both surface branching and invasion (Figure 4F), implying that it was the change in signal distribution and not just increased levels of

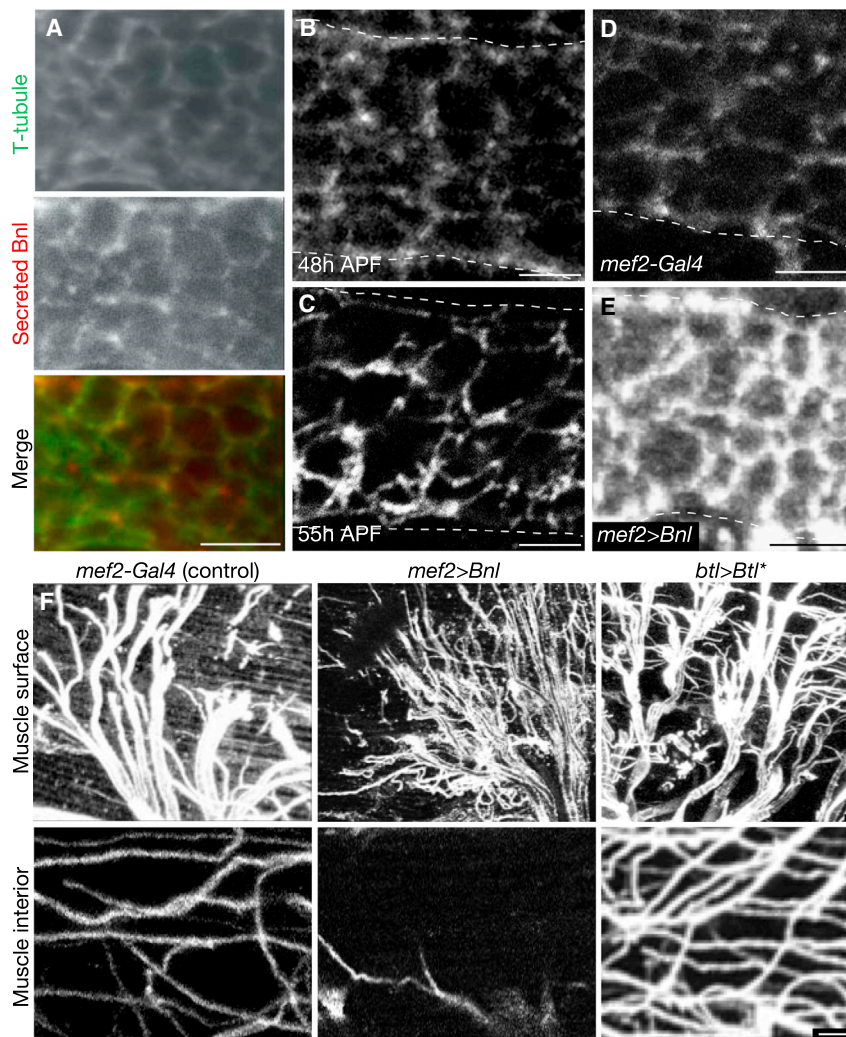


Figure 4. Localized Secretion and Function of Bnl FGF during Tracheal Invasion

(A) Interior view of indirect flight muscle fiber of a *mef2-Gal4; UAS-CD8-GFP* pupa at 55 hr APF with native CD8-GFP fluorescence to show T-tubules (green) and immunostaining for Bnl using an extra-cellular staining protocol to show only secreted Bnl (Secreted Bnl, red). No cytoplasmic staining is detected, unlike standard immunostaining conditions, which detect abundant cytoplasmic Bnl.

(B and C) Secreted Bnl detected as above in indirect flight muscle fiber before (48 hr APF) (B) and during (55 hr APF) (C) tracheal invasion. Animals were prepared and stained in parallel and imaged using identical settings. Note increased levels of secreted Bnl in T-tubules during invasion. Dashed lines, plasma membrane of syncytial muscle fiber.

(D and E) Secreted Bnl detected as above in indirect flight muscle fiber 55 hr APF of control (*mef2-Gal4*) or *mef2-Gal4; UAS-bnlA1-1* that overexpresses Bnl in flight muscle. Dotted lines, plasma membrane of flight muscle fiber. Note overexpression results in increased Bnl on both T-tubule and plasma membrane (E) compared to matched control (D).

(F) Effect of Bnl overexpression on tracheal branching on flight muscle. Surface (upper row) and interior views (bottom row) of single muscle fibers immunostained for D3 antigen to show trachea (white) of control (*mef2-Gal4*), *mef2-Gal4; UAS-bnlA1-1* adult that overexpresses Bnl FGF in muscle, or *btl-Gal4; UAS- λ Btl* (*btl > Btl**) adult that expresses a constitutively-active form of Btl FGFR in the tracheal system. Note extensive tracheal branching on flight muscle surface but reduced tracheal invasion following Bnl overexpression and extensive surface branching and invasion associated with constitutively-active Btl expression. Amphiphsin staining showed normal structure and distribution of T-tubules under these conditions. Scale bars represent 1 μ m.

See also Figure S4.

signaling that was responsible for the difference. We conclude that tracheal invasion depends on the selective localization of Bnl to T-tubules and its depletion from the muscle surface.

Some Basolateral Epithelial Membrane Proteins Localize to T-Tubules

To begin to address the mechanism underlying the transition in Bnl distribution from plasma membrane surface to the T-tubule network, we first molecularly characterized the flight muscle plasma membrane (sarcolemma) and T-tubule membrane domains. Although many functional and molecular differences have been identified between mammalian sarcolemma (e.g., postsynaptic neural specializations and costameres linking to the contractile machinery) (Pardo et al., 1983; Bloch et al., 2004) and T-tubule (e.g., excitation-contraction coupling including the dihydropyrimidine receptor) (Curtis and Catterall, 1983; Fosset et al., 1983; Al-Qusairi and Laporte, 2011) membrane compartments, few markers are known that distinguish these membrane domains in *Drosophila* (marked with * in Figure 5G). One of the two canonical *Drosophila* T-tubule markers

is Discs large (DLG) (Figure 5A) (Thomas et al., 2000; Razaq et al., 2001), the prototypical membrane-associated guanylate kinase (MAGUK), that localizes in polarized epithelia to septate junctions encompassing much of the lateral cell surface and is required for septate junction formation and basolateral membrane identity (Laprise and Tepass, 2011). During tracheal invasion, DLG was broadly localized to both the plasma membrane and T-tubules (Figures 5B–5E), although localization restricts to the T-tubules in mature *Drosophila* flight muscle (Figure 5A) (Razaq et al., 2001).

We examined the expression and distribution in developing flight muscle of septate junction and basolateral identity proteins and found four additional proteins that localized specifically or preferentially to T-tubules during tracheal invasion. These include Scribble (Scrib) (Figure 5E), another key component of the Scribble/Discs large (DLG)/Lethal (2) giant larvae (LGL) basolateral identity complex (Figure 5H, “Scrib module”) and Na^+, K^+ ATPase α (Figure 5F), a component of the other basolateral identity complex in *Drosophila* (Figure 5H, “Yurt/Coracle group”) that also localizes to septate junctions (Laprise and Tepass, 2011), as

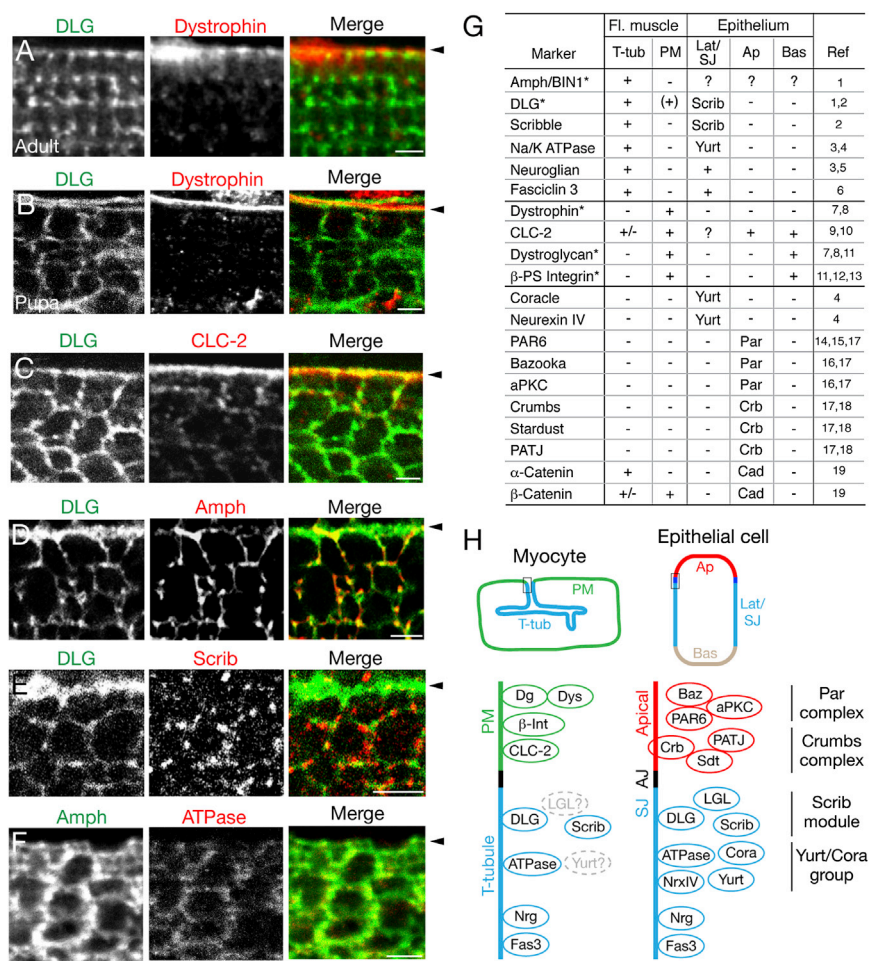


Figure 5. Flight Muscle T-Tubules Express Epithelial Basolateral Markers

(A–F) Interior views of indirect flight muscle fiber of *mefl-Gal4; UAS-CD8-GFP* adult (A) and 55 hr APF pupae (B–F) immunostained for the indicated proteins. Arrowheads, position of fiber plasma membrane. (A) Discs large (DLG), part of Scribble/DLG/LGL epithelial basolateral identity module, localizes to adult flight muscle T-tubules. Dystrophin localizes to plasma membrane. (B) During tracheal invasion, DLG localizes to both plasma membrane and T-tubules. (C) Chloride channel CLC-2 localizes to plasma membrane. (D) Amphiphysin localizes to T-tubules. (E) Scribble, another component of Scribble/DLG/LGL basolateral identity module, localizes to puncta associated with T-tubules but not with plasma membrane. (F), Na^+, K^+ ATPase α (ATPase), a component of Yurt/Coracle basolateral identity group in *Drosophila*, localizes to T-tubules.

(G) Summary of T-tubule and sarcolemma markers during tracheal invasion. *Marker with previously known muscle localization in *Drosophila*. +, marker localizes to the indicated membrane domain (T-tub, T-tubule; PM, plasma membrane [sarcolemma]); +/-, marker localizes to indicated membrane domain at lower levels; (+), marker localizes to indicated membrane domain during pupal development, but not in adult tissue. Localization of marker protein in epithelia (Lat/SJ, basolateral/septate junction; Ap, apical; Bas, basal) are indicated by either a + or the name of the complex they are part of (Scrib, Scribble module; Yurt, Yurt/Coracle group; Par, Par complex; Crb, Crumbs complex; Cad, Cadherin complex). Ref, references for epithelial staining and muscle markers indicated by asterisks. Reference 1, Razaq et al. (2001); 2, Bilder and Perrimon (2000); 3, Laprise et al. (2009); 4, Mohler et al. (2005); 5, Genova and Fehon (2003); 6, Woods et al. (1997); 7, Rybakova et al. (2000); 8, Bogdanik et al. (2008); 9, Peña-Münzenmayer et al. (2005); 10, Blaisdell et al. (2000); 11, Ribeiro et al. (2011); 12, Deng et al. (2003); 13, Fernández-Miñán et al. (2007); 14, Rolls et al. (2003); 15, Petronczki and Knoblich (2001); 16, Schober et al. (1999); 17, Tanentzapf and Tepass (2003); 18, Bulgakova and Knust (2009); 19, McGill et al. (2009).

(H) Schematic comparing localization of membrane domain markers at the indicated region (box) of flight muscle myocyte (left) and polarized epithelial cell (right), focusing on myocyte plasma membrane (sarcolemma [SL], green), T-tubule domain (blue), apical epithelial membrane (red), adherens junction (AJ, black), and septate junction (SJ, blue). Components of epithelial polarity complexes are clustered with names of the complex indicated at right. Proteins in gray, not determined. Scale bars represent 2 μm .

See also Figure S5.

well as Neuroglian (Nrg) (Figure S5A) and Fasciclin 3 (Fas3), transmembrane proteins localized at or near septate junctions that depend on these complexes (Genova and Fehon, 2003; Laprise et al., 2009) for their proper lateral membrane distribution. Thus, the developing flight muscle T-tubule membranes comprise a membrane domain with molecular features in common with lateral epithelial membranes and specifically the septate junction (Figures 5G and 5H). However, T-tubule membranes are not identical to epithelial lateral membranes or septate junctions as several tested members of these complexes were either not expressed in muscle (e.g., Coracle and Neurexin IV) or did not specifically localize to T-tubules (Figures 5G, 5H, and S5B).

We also searched for specific markers of the flight muscle plasma membrane during tracheal invasion. We examined apical

epithelial identity complexes and markers and found that they were either not expressed (members of the Crumbs complex [Crumbs, Stardust, PATJ]) or expressed but not specifically localized to any obvious membrane domain (Par complex [PAR6, Bazooka, and aPKC]) (Figures 5G, 5H, and S5C). Four markers (dystrophin, CLC-2, dystroglycan, β_{PS} -integrin) were found that specifically labeled the flight muscle sarcolemma (Figures 5B, 5C, and 5G), two of which (dystroglycan, β_{PS} -integrin) also label the basal membrane domain of polarized epithelia in *Drosophila* (Ayalon et al., 2011; Ribeiro et al., 2011).

AP-1 Knockdown Reroutes Bnl Secretion and Tracheal Growth to the Myocyte Surface

The T-tubule localization of Bnl observed during invasion might arise from targeted secretion of the protein to T-tubule

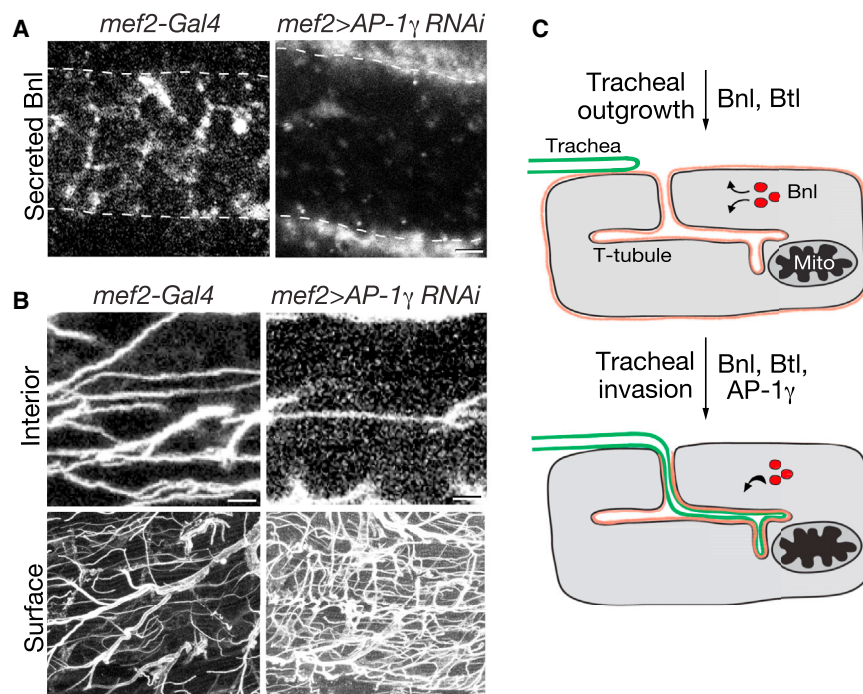


Figure 6. Effect of Knockdown of Clathrin Adaptor AP-1 γ on Bnl Localization and Tracheal Invasion of Flight Muscle

(A and B) Indirect flight muscle fibers of control (left, *mef2-Gal4*) and muscle-specific AP-1 γ knockdown (right, *mef2-Gal4; UAS-CD8::GFP/UAS-AP-1 γ RNAi*) pupal (A) and adult (B) *Drosophila* immunostained as in Figure 4A to show secreted Bnl (A, white) or immunostained for D3 antigen (white) to show tracheal invasion (B). Note severely reduced T-tubule localization and increased surface localization of Bnl (A) and almost complete abrogation of tracheal invasion and increased surface ramification (B) in AP-1 γ knockdown. Dashes, edge of muscle fiber. Scale bars represent 1 μ m (A, upper panel in B), 5 μ m (lower panel in B).

(C) Model of AP-1-dependent Bnl localization and tracheal invasion of flight muscle. Top: Bnl FGF (red) is secreted at similar levels at plasma membrane and T-tubule membranes of flight muscle, attracting tracheal branches to the tissue. Bottom: an AP-1 γ -dependent developmental switch promotes Bnl FGF secretion at T-tubules, causing tracheal invasion.

See also Figure S6.

membranes. Although many markers localize selectively to T-tubule membranes in mammalian myocytes and *Drosophila* flight muscle (see above), it is unclear how cargoes are specifically delivered there. Given the molecular parallels identified above between T-tubules and epithelial lateral domains and septate junctions, we investigated the effect of flight-muscle-specific knockdown of genes implicated in basolateral secretion. Knockdown of one of them, AP-1 γ , a component of the AP-1 clathrin adaptor complex, had a selective and striking effect, as detailed below.

Clathrin and the Clathrin AP-1 adaptor complexes have been implicated in secretion and trafficking to basolateral domains from recycling endosomes and/or the trans-Golgi network (TGN) in mammalian (Gan et al., 2002; Traub and Apodaca, 2003; Icking et al., 2007; Guo et al., 2013; Rodriguez-Boulan et al., 2013) and *Drosophila* epithelia (Peng et al., 2009; Benhra et al., 2011); there is a single AP-1 complex in *Drosophila* and two in mammals. Knockdown of expression of the AP-1 γ subunit in *Drosophila* salivary glands (Peng et al., 2009) or sensory organ precursors (Benhra et al., 2011) leads to rerouting of basolateral-directed cargo to the apical membrane domain. We found that muscle-specific knockdown of the AP-1 γ subunit (*mef2-Gal4 > AP-1 γ [RNAi]*) during pupal development led to a dramatic rerouting of Branchless from the T-tubules, where it specifically accumulated in wild-type flight muscle, to the surface of the developing flight muscle (Figure 6A). The structure of the T-tubules as assayed by membrane GFP and amphiphysin localization during invasion and in the adult flight muscles appeared unaffected by AP-1 γ knockdown (Figure S6A), and T-tubules remained accessible to 2 mDa dextran during tracheal invasion (Figure S6B). Furthermore, T-tubule markers amphiphysin and DLG showed their normal T-tubule localization in adult flight

muscles (Figure S6A). We conclude that the clathrin adaptor AP-1 γ is required for the selective targeting of Bnl FGF to flight muscle T-tubules, and in its absence Bnl FGF is secreted at the plasma membrane.

Under the same knockdown conditions, we observed an equally dramatic effect on tracheal invasion. There were few or no invading trachea in AP-1 γ -depleted flight muscle fibers (Figure 6B), but many more branches than normal on the flight muscle surface (Figure 6B). Thus, although tracheal branches could grow toward and ramify on the flight muscle surface, tracheal projections were unable to invade the T-tubule network. We conclude that AP-1 γ is required for both T-tubule Bnl localization and tracheal invasion.

DISCUSSION

The results presented here on *Drosophila* flight muscle development demonstrate that, in addition to the well-established role of developmental control of *bnl* expression in defining the timing and pattern of tracheal branch budding and outgrowth to target tissues (Sutherland et al., 1996; Jarecki et al., 1999; Sato and Kornberg, 2002; Weaver and Krasnow, 2008; Chen and Krasnow, 2014), developmental control of the specific site of Bnl FGF secretion by a target cell can direct terminal branches to sites within the cell where oxygen is needed. In developing flight muscle, we found that tracheae initially grow out and ramify on its surface, just like in other tissues. Subsequently, fine terminal branches invade the T-tubule network, entering through ~300 nm surface openings. As invasion begins, there is a switch in Bnl FGF distribution from a broad localization across the myocyte membrane, attracting tracheae to the muscle, to a selective T-tubule localization. This developmental switch in

Bnl distribution is critical as knockdown or inhibition of Bnl or its receptor Btl during invasion blocks the process, whereas overexpression of Bnl in flight muscle to restore uniform surface and T-tubule distribution promotes surface branching and inhibits invasion. We further showed that T-tubule membranes are specialized domains distinguished by localization of several core regulators of epithelial basolateral membrane identity, and knockdown of the AP-1 γ clathrin adaptor implicated in basolateral trafficking prevented the T-tubule accumulation of Bnl FGF and shunted it to the surface, promoting surface branching at the expense of tracheal invasion. The results support a model in which tracheal invasion of flight muscle is controlled by a developmental switch in the subcellular localization of Bnl FGF (Figure 6C). This switch is mediated by AP-1-dependent trafficking of Branchless FGF to the T-tubules, where the ligand attracts tracheae from the surface into the T-tubule network and ultimately to the mitochondria where oxygen is utilized.

Targeting Branchless FGF to T-Tubules

Plasma membrane (sarcolemma) and T-tubule membranes of myocytes have long been known to be molecularly and functionally distinct (Al-Qusairi and Laporte, 2011), and studies of viral protein trafficking demonstrate that these membrane domains can be targeted separately (Rahkila et al., 2001). However, how these membrane domains are established and how endogenous proteins are selectively targeted and retained is unknown. Our findings that several core components of the epithelial DLG/Scrib/LGL basolateral polarity module preferentially mark the T-tubule membrane domain (Figure 5G), and the AP-1 γ clathrin adaptor implicated in basolateral trafficking promotes targeting of Bnl to these membranes and away from the sarcolemma provide an entry to these questions. Perhaps AP-1 is involved in sorting Bnl at the trans-Golgi network (TGN) or trafficking or recycling of Bnl-containing vesicles to the T-tubule membrane (Figure 6C), similar to the role proposed for mammalian AP-1 in polarized secretion to epithelial basolateral membrane domains (Gan et al., 2002; Traub and Apodaca, 2003; Icking et al., 2007; Guo et al., 2013; Rodriguez-Boulan et al., 2013). The localization of other T-tubule proteins examined was not affected by AP-1 γ knockdown (Figure S6C), so AP-1-mediated trafficking to T-tubules appears selective and not crucial for maintaining T-tubule identity. Our results also imply that AP-1 γ is dispensable for trafficking Bnl to the sarcolemma, because Bnl selectively accumulates there following AP-1 γ knockdown. It will be important to elucidate the AP-1-dependent T-tubule targeting pathway and other membrane trafficking pathways in myocytes, as well as to identify the developmental signal that activates the AP-1 complex to ensure the timely change in Bnl localization and the switch from surface branching to tracheal invasion before the onset of flight.

Although our results provide only an initial view of the T-tubule targeting pathway, already several parallels are apparent to the well-studied pathway controlling basolateral domains in polarized epithelial cells (Figure 5H). Previous studies of vesicular stomatitis virus glycoprotein showed that this glycoprotein targets both the basolateral domains of mammalian epithelial cells and the T-tubule network of skeletal muscle (Rahkila et al., 2001), suggesting a functional parallel. Our finding that multiple pro-

teins in the core DLG/Scrib/LGL basolateral polarity module preferentially mark the T-tubule membrane provide molecular support for this view, and the parallel functions of AP-1 in T-tubule trafficking and basolateral targeting in polarized epithelia further support this idea. However, a number of key basolateral trafficking proteins are not detectably expressed in flight muscle or do not localize to T-tubules (Figures 5G and 5H), demonstrating important differences as well. We found little, if any, correspondence between sarcolemma and apical epithelial markers, implying a separate mechanism for establishing the sarcolemma domain. Thus, it appears that membrane trafficking in muscle cells has adopted some of the molecules and mechanisms of epithelial basolateral targeting, just as neurons appear to have done for sorting of specific cargos to dendrites (Jareb and Banker, 1998; Margeta et al., 2009).

T-Tubule Transitions during Tracheal Invasion

In addition to the transition in Bnl localization at the time of invasion, we discovered two other notable transitions of flight muscle T-tubules associated with invasion. First, T-tubule surface openings dilate to ~ 30 times their normal size, expanding to 300 nm diameter or more (Figure 1H), large enough to allow entry of filopodia (100–300 nm) (Zhuravlev and Papoian, 2009). This expansion is transient as just 40 hr after tracheal invasion has begun, the large openings are no longer detected and flight muscle T-tubules narrow to a size similar to those in pupal tubular muscles and flight muscle in the adult (Razzaq et al., 2001). T-tubules of other muscles examined did not undergo dilation, implying that T-tubule dilation is a flight-muscle-specific innovation. Second, by 70 hr APF when invasion is complete, the invaded T-tubules show a different marker expression pattern, losing localization of T-tubule molecular markers such as amphiphysin (Figure S1A). Thus, the T-tubule developmental program has apparently specialized to accommodate invasion of tracheal branches that feed the tissue's extreme oxygen demand.

Other Guidance Factors in Tracheal Invasion

Although the results demonstrate that Bnl FGF plays a decisive role in tracheal invasion, it is unlikely to be the only signal. Bnl is distributed rather uniformly across the T-tubule network during invasion, yet tracheae invade only a subset of T-tubules, making dramatic turns (such as abrupt 90° turns immediately after entry) before reaching their targets. We presume that other guidance cues function with Bnl to specify the tracheal outgrowth path within the T-tubule network. A priority for future work is to identify the signal that controls the specific pathway that terminal branches traverse within the T-tubule network that ends in encircling the mitochondria (Wigglesworth and Lee, 1982) and hence oxygen delivery directly to the organelle that uses it. Such targeting would presumably require even more precise subcellular signal localization, to the T-tubules abutting mitochondria.

Although most growth factors and chemoattractants are presumed to be secreted quite generally from the source cells, some that are expressed in polarized epithelial cells have been shown to be selectively secreted from apical or basolateral domains, typically from the domain closest to the receiving cells (Strigini and Cohen, 2000; Rosin et al., 2004). Growth factors

and chemoattractants have also been found to be localized to or secreted from specific membrane domains of neurons, such as dendritic targeting of brain-derived neurotrophic factor (BDNF) and localization of Neurofascin186 at the initial segment of Purkinje cell axons to guide advancing basket cells (Ango et al., 2004). It will be important to explore how broadly important sub-cellular targeting of secretion and accumulation of growth factors and chemoattractants is and whether T-tubule targeting of Bnl FGF and entry into the target cell represents an extreme example of a more general class of regulatory mechanisms, with extravagant morphogenetic consequences serving a critical physiological role.

EXPERIMENTAL PROCEDURES

Drosophila Strains and Genetics

bnl^{P1} (Sutherland et al., 1996) and *btl^{G18}* (Klämbt et al., 1992) are null alleles. The Gal4/UAS system (Brand et al., 1994) was used, with *btl-Gal4* (Ohshiro and Saigo, 1997) used to drive tracheal expression of transgenes and *mef2-Gal4* (Ranganayakulu et al., 1995) used to drive muscle expression. *tubulin-Gal80ts* (McGuire et al., 2004) encodes a ubiquitously expressed and temperature-sensitive repressor of Gal4 activity. UAS responders were: *UAS-DNbtI* (dominant-negative Btl) (Reichman-Fried et al., 1994), *UAS-btl-RNAi* (transformant ID 950, Vienna *Drosophila* RNAi Center (VDRC), Dietzl et al., 2007), *UAS- γ btl* (constitutively-active Btl) (Anderson et al., 1996), *UAS-bnl-RNAi* (transformant ID 5730, VDRC), *UAS-bnlA1-1* (wild-type Bnl) (Sutherland et al., 1996), *UAS-spry* (Hacohen et al., 1998), *UAS-AP-1 γ -RNAi* (line ID JF02684, Transgenic RNAi Project [TRiP]), and *UAS-CD8-GFP* (Lee and Luo, 1999). Crosses were done at 25°C unless noted otherwise.

Temporal Expression of Transgenes

The *btl-Gal4* driver was used with *tubulin-Gal80ts*, a Gal80 temperature-sensitive repressor, to temporally restrict tracheal expression of *UAS-spry*, *UAS-DNbtI*, *UAS- γ btl*, and *UAS-btl-RNAi* responders to the pupal tracheal system: *btl-Gal4*, *UAS-GFP/tubulin-Gal80ts*; *btl-Gal4*, *UAS-GFP/UAS-DNbtI* (or *UAS- γ btl*, *UAS-DNbtI*, *UAS-spry*, or *UAS-btl-RNAi*) flies were grown at 18°C until 0 hr APF, then shifted to 30°C to inactivate Gal80ts and allow Gal4-mediated induction of transgenes. To temporally deplete Bnl FGF by RNAi, *mef2-Gal4/tubulin-Gal80ts/UAS-Bnl-RNAi* flies were treated in the same way.

Labeling of Tracheal Clones

For clonal marking of tracheal cells, the MARCM system (Lee and Luo, 1999) was used. Two- to 6-hour-old *y w hs-flp¹²²; FRT40A, FRTG13, btl-Gal4, UAS-GFP/FRTG13 tubulin-Gal80* embryos raised at 25°C were placed at 38°C for 45 min to induce sporadic GFP-labeled tracheal cells. Animals were returned to 25°C to continue development and analyzed as described below.

Immunostaining and Fluorescence Microscopy

Animals were examined during pupal development for staging and then analyzed at the indicated time after puparium formation (APF). Pupae were immersed in chilled PBS (pH 7.4) and then mounted with pins and dissected along the ventral midline with transverse cuts at the anterior and posterior to allow access to the flight muscles. Muscles were then fixed for 25 min at room temperature in 4% paraformaldehyde (PFA)/PBS and washed in PBS. Adults were dissected 1–3 days following eclosion. Animals were flash frozen in liquid nitrogen and then bisected at the dorsal midline with a blade. Hemithoraces were placed directly into chilled 4% PFA/PBS and fixed for 25 min at room temperature.

For both pupal and adult preparations, antigen blocking was done at room temperature for 30 min in PBS with 0.1% Triton X-100 (PBST), and subsequent incubations were conducted in PBST. Primary antibody incubations were done at 4°C overnight. Antibodies were: chicken anti-GFP (Abcam; 1:500), mouse anti-Complex 5, alpha subunit (Mitosciences, 1:250), rabbit anti-amphiphysin (1:500) (Razzaq et al., 2001), mouse mAb68G5D3 (abbreviated “D3”) (1:10) (Giniger et al., 1993), mouse anti-Discs large (4F3, Developmental

Studies Hybridoma Bank [DSHB]; 1:10), mouse anti-ATPase, (Na⁺, K⁺ alpha subunit) (a5, DSHB; 1:100), rabbit anti-Scribble (1:500) (Bilder and Perrimon, 2000), rat anti-alpha-Catenin (DCAT-1, DSHB; 1:100), rabbit anti-dystrophin CO2H (1:1,000) (van der Plas et al., 2006), mouse anti-Armadillo (N2 7A1, DSHB; 1:100), rat anti-PAR6 (1:200) (Rolls et al., 2003), mouse anti-Neuroglian (BP 104, DSHB; 1:100), and mouse anti-Syntaxin (8C3, DSHB; 1:100). Fluorescent secondary antibodies (Jackson ImmunoResearch) were used at 1:250. DAPI (100 ng/ml) was used to stain nuclei.

To detect extracellular Bnl FGF, we used an extracellular immunostaining protocol in which the specimen is incubated with primary antiserum and washed before fixation (Strigini and Cohen, 2000; Belenkaya et al., 2004). Pupae were dissected on ice in chilled Schneider's M3 media (Sigma) and then incubated with preabsorbed, protein A-purified rabbit anti-Bnl antiserum (Sutherland et al., 1996; Jarecki et al., 1999) (1:20 in M3) for 45 min on ice. After washing with ice cold PBS three times for 90 s, preparations were fixed for 30 min in ice cold 4% PFA/PBS, washed, then processed for immunostaining as above. Experimental specimens were dissected and stained in parallel with control pupae.

Stained specimens were analyzed by confocal fluorescence microscopy (Leica SP2 AOBs). All images shown of individual flight muscle fibers are 10 μ m compressed stacks taken ~20–50 μ m below the flight muscle surface, except when noted as “muscle surface” images. Boundaries of individual muscle fibers were identified by immunostaining of amphiphysin and the localization of F-actin filaments as visualized by phalloidin (Molecular Probes) staining. The number of branches and branch points per muscle fiber was assessed by counts of invaded D3-labeled tracheal branches, or branch points, in randomly selected 10 μ m compressed stacks of adult flight muscle fibers.

Scanning Electron Microscopy

mef2-Gal4 leg tubular and flight muscles were dissected at the indicated times and fixed overnight at 4°C in 4% paraformaldehyde in PBS (pH 7.4). Muscles were then postfixed in 1% osmium tetroxide and stained with 2% uranyl acetate in deionized water for 15 min. Muscles were critical-point dried and sputter-coated with gold by standard methods (Stanford Electron Microscopy Core) and imaged with a scanning electron microscope (Hitachi S-3400N VP-SEM).

T-Tubule Accessibility Assay

Accessibility of T-tubules in AP-1 γ knockdown and in wild-type pupae was evaluated by incubating freshly dissected *mef2-Gal4/UAS-CD8-GFP*; *UAS-AP-1 γ* pupa with 2 mg/ml lysine-fixable 2,000,000 MW or 500,000 MW dextran conjugated to tetramethylrhodamine in ice cold PBS (Molecular Probes) for 20 min. Preparations were immediately fixed for 30 min at room temperature, washed three times in PBS for 5 min, and immediately imaged by confocal microscopy. All steps after addition of dextran were protected from light.

SUPPLEMENTAL INFORMATION

Supplemental Information includes six figures and can be found with this article online at <http://dx.doi.org/10.1016/j.cell.2014.11.043>.

ACKNOWLEDGMENTS

We thank Drs. Suzanne Pfeffer, Nipam Patel, James Nelson, and laboratory members for helpful discussions and Drs. Eric Olson, Cahir O’Kane, David Bilder, Jasprien Noordermeer, and Chris Doe for reagents. Figure S2 and the Graphical Abstract were adapted from Hartenstein (1993). This work was supported by a Stanford Graduate Fellowship and an American Heart Association Predoctoral Fellowship (S.J.P.) and the Howard Hughes Medical Institute.

Received: July 24, 2014

Revised: October 7, 2014

Accepted: November 15, 2014

Published: December 31, 2014

REFERENCES

- Al-Qusairi, L., and Laporte, J. (2011). T-tubule biogenesis and triad formation in skeletal muscle and implication in human diseases. *Skelet Muscle* 1, 26.
- Anderson, M.G., Certel, S.J., Certel, K., Lee, T., Montell, D.J., and Johnson, W.A. (1996). Function of the *Drosophila* POU domain transcription factor *drifter* as an upstream regulator of *breathless* receptor tyrosine kinase expression in developing trachea. *Development* 122, 4169–4178.
- Ango, F., di Cristo, G., Higashiyama, H., Bennett, V., Wu, P., and Huang, Z.J. (2004). Ankyrin-based subcellular gradient of neurofascin, an immunoglobulin family protein, directs GABAergic innervation at Purkinje axon initial segment. *Cell* 119, 257–272.
- Ayalon, G., Hostettler, J.D., Hoffman, J., Kizhatil, K., Davis, J.Q., and Bennett, V. (2011). Ankyrin-B interactions with spectrin and dynactin-4 are required for dystrophin-based protection of skeletal muscle from exercise injury. *J. Biol. Chem.* 286, 7370–7378.
- Belenkaya, T.Y., Han, C., Yan, D., Opoka, R.J., Khodoun, M., Liu, H., and Lin, X. (2004). *Drosophila* Dpp morphogen movement is independent of dynamin-mediated endocytosis but regulated by the glypican members of heparan sulfate proteoglycans. *Cell* 119, 231–244.
- Benhra, N., Lallet, S., Cotton, M., Le Bras, S., Dussert, A., and Le Borgne, R. (2011). AP-1 controls the trafficking of Notch and Sanpodo toward E-cadherin junctions in sensory organ precursors. *Curr. Biol.* 21, 87–95.
- Bilder, D., and Perrimon, N. (2000). Localization of apical epithelial determinants by the basolateral PDZ protein Scribble. *Nature* 403, 676–680.
- Blaisdell, C.J., Edmonds, R.D., Wang, X.T., Guggino, S., and Zeitlin, P.L. (2000). pH-regulated chloride secretion in fetal lung epithelia. *Am. J. Physiol. Lung Cell. Mol. Physiol.* 278, L1248–L1255.
- Bloch, R.J., Reed, P., O'Neill, A., Strong, J., Williams, M., Porter, N., and González-Serratos, H. (2004). Costameres mediate force transduction in healthy skeletal muscle and are altered in muscular dystrophies. *J. Muscle Res. Cell Motil.* 25, 590–592.
- Bogdanik, L., Framery, B., Frölich, A., Franco, B., Mornet, D., Bockaert, J., Sigrist, S.J., Grau, Y., and Parmentier, M.L. (2008). Muscle dystroglycan organizes the postsynapse and regulates presynaptic neurotransmitter release at the *Drosophila* neuromuscular junction. *PLoS ONE* 3, e2084.
- Brand, A.H., Manoukian, A.S., and Perrimon, N. (1994). Ectopic expression in *Drosophila*. *Methods Cell Biol.* 44, 635–654.
- Bulgakova, N.A., and Knust, E. (2009). The Crumbs complex: from epithelial-cell polarity to retinal degeneration. *J. Cell Sci.* 122, 2587–2596.
- Cajal, S.R.y. (1890). Coloration par la méthode de Golgi des terminaisons des trachées et des nerfs dans les muscles des ailes des insectes. *Z. Wissensch. Mikr.* (7), 332–342.
- Chen, F., and Krasnow, M.A. (2014). Progenitor outgrowth from the niche in *Drosophila* trachea is guided by FGF from decaying branches. *Science* 343, 186–189.
- Curtis, B.M., and Catterall, W.A. (1983). Solubilization of the calcium antagonist receptor from rat brain. *J. Biol. Chem.* 258, 7280–7283.
- Deng, W.M., Schneider, M., Frock, R., Castillejo-Lopez, C., Gaman, E.A., Baumgartner, S., and Ruohola-Baker, H. (2003). Dystroglycan is required for polarizing the epithelial cells and the oocyte in *Drosophila*. *Development* 130, 173–184.
- Dietzl, G., Chen, D., Schnorrer, F., Su, K.C., Barinova, Y., Fellner, M., Gasser, B., Kinsey, K., Oppel, S., Scheiblaue, S., et al. (2007). A genome-wide transgenic RNAi library for conditional gene inactivation in *Drosophila*. *Nature* 448, 151–156.
- Dreher, M.R., Liu, W., Michelich, C.R., Dewhirst, M.W., Yuan, F., and Chilkoti, A. (2006). Tumor vascular permeability, accumulation, and penetration of macromolecular drug carriers. *J. Natl. Cancer Inst.* 98, 335–344.
- Dutta, D., Anant, S., Ruiz-Gomez, M., Bate, M., and VijayRaghavan, K. (2004). Founder myoblasts and fibre number during adult myogenesis in *Drosophila*. *Development* 131, 3761–3772.
- Fernández-Miñán, A., Martín-Bermudo, M.D., and González-Reyes, A. (2007). Integrin signaling regulates spindle orientation in *Drosophila* to preserve the follicular-epithelium monolayer. *Curr. Biol.* 17, 683–688.
- Fosset, M., Jaimovich, E., Delpont, E., and Lazdunski, M. (1983). [³H]nitrendipine receptors in skeletal muscle. *J. Biol. Chem.* 258, 6086–6092.
- Gan, Y., McGraw, T.E., and Rodriguez-Boulton, E. (2002). The epithelial-specific adaptor AP1B mediates post-endocytic recycling to the basolateral membrane. *Nat. Cell Biol.* 4, 605–609.
- Genova, J.L., and Fehon, R.G. (2003). Neuroglian, Gliotactin, and the Na⁺/K⁺ ATPase are essential for septate junction function in *Drosophila*. *J. Cell Biol.* 161, 979–989.
- Giniger, E., Jan, L.Y., and Jan, Y.N. (1993). Specifying the path of the intersegmental nerve of the *Drosophila* embryo: a role for Delta and Notch. *Development* 117, 431–440.
- Glazer, L., and Shilo, B.Z. (1991). The *Drosophila* FGF-R homolog is expressed in the embryonic tracheal system and appears to be required for directed tracheal cell extension. *Genes Dev.* 5, 697–705.
- Guo, X., Mattera, R., Ren, X., Chen, Y., Retamal, C., González, A., and Bonifacino, J.S. (2013). The adaptor protein-1 μ 1B subunit expands the repertoire of basolateral sorting signal recognition in epithelial cells. *Dev. Cell* 27, 353–366.
- Hacohen, N., Kramer, S., Sutherland, D., Hiromi, Y., and Krasnow, M.A. (1998). sprouty encodes a novel antagonist of FGF signaling that patterns apical branching of the *Drosophila* airways. *Cell* 92, 253–263.
- Hartenstein, V. (1993). The Atlas of *Drosophila* Development (Cold Spring Harbor, NY: Cold Spring Harbor Laboratory Press).
- Icking, A., Amadii, M., Ruonala, M., Höning, S., and Tikkanen, R. (2007). Polarized transport of Alzheimer amyloid precursor protein is mediated by adaptor protein complex AP1-1B. *Traffic* 8, 285–296.
- Jareb, M., and Banker, G. (1998). The polarized sorting of membrane proteins expressed in cultured hippocampal neurons using viral vectors. *Neuron* 20, 855–867.
- Jarecki, J., Johnson, E., and Krasnow, M.A. (1999). Oxygen regulation of airway branching in *Drosophila* is mediated by branchless FGF. *Cell* 99, 211–220.
- Klämbt, C., Glazer, L., and Shilo, B.Z. (1992). *Breathless*, a *Drosophila* FGF receptor homolog, is essential for migration of tracheal and specific midline glial cells. *Genes Dev.* 6, 1668–1678.
- Laprise, P., and Tepass, U. (2011). Novel insights into epithelial polarity proteins in *Drosophila*. *Trends Cell Biol.* 21, 401–408.
- Laprise, P., Lau, K.M., Harris, K.P., Silva-Gagliardi, N.F., Paul, S.M., Beronja, S., Beitel, G.J., McGlade, C.J., and Tepass, U. (2009). Yurt, Coracle, Neurexin IV and the Na(+),K(+)ATPase form a novel group of epithelial polarity proteins. *Nature* 459, 1141–1145.
- Lee, T., and Luo, L. (1999). Mosaic analysis with a repressible cell marker for studies of gene function in neuronal morphogenesis. *Neuron* 22, 451–461.
- Leydig, F. (1859). Zur Anatomie der Insecten (part 2), section 9. Zum Bau der Tracheen. *Arch. Anat. Physiol. u. Wissensch. Med.*, 160–162.
- Margeta, M.A., Wang, G.J., and Shen, K. (2009). Clathrin adaptor AP-1 complex excludes multiple postsynaptic receptors from axons in *C. elegans*. *Proc. Natl. Acad. Sci. USA* 106, 1632–1637.
- McGill, M.A., McKinley, R.F., and Harris, T.J. (2009). Independent cadherin-catenin and Bazooka clusters interact to assemble adherens junctions. *J. Cell Biol.* 185, 787–796.
- McGuire, S.E., Mao, Z., and Davis, R.L. (2004). Spatiotemporal gene expression targeting with the TARGET and gene-switch systems in *Drosophila*. *Sci. STKE* 2004, pl6.
- Meyer, E.P. (1989). Corrosion casts as a method for investigation of the insect tracheal system. *Cell Tissue Res.* 256, 1–6.
- Mohler, P.J., Davis, J.Q., and Bennett, V. (2005). Ankyrin-B coordinates the Na/K ATPase, Na/Ca exchanger, and InsP₃ receptor in a cardiac T-tubule/SR microdomain. *PLoS Biol.* 3, e423.

- Ohshiro, T., and Saigo, K. (1997). Transcriptional regulation of breathless FGF receptor gene by binding of TRACHEALESS/dARNT heterodimers to three central midline elements in *Drosophila* developing trachea. *Development* 124, 3975–3986.
- Pardo, J.V., Siliciano, J.D., and Craig, S.W. (1983). A vinculin-containing cortical lattice in skeletal muscle: transverse lattice elements ("costameres") mark sites of attachment between myofibrils and sarcolemma. *Proc. Natl. Acad. Sci. USA* 80, 1008–1012.
- Peña-Münzenmayer, G., Catalán, M., Comejo, I., Figueroa, C.D., Melvin, J.E., Niemeyer, M.I., Cid, L.P., and Sepúlveda, F.V. (2005). Basolateral localization of native CIC-2 chloride channels in absorptive intestinal epithelial cells and basolateral sorting encoded by a CBS-2 domain di-leucine motif. *J. Cell Sci.* 118, 4243–4252.
- Peng, Y.H., Yang, W.K., Lin, W.H., Lai, T.T., and Chien, C.T. (2009). Nak regulates Dlg basal localization in *Drosophila* salivary gland cells. *Biochem. Biophys. Res. Commun.* 382, 108–113.
- Petronczki, M., and Knoblich, J.A. (2001). DmPAR-6 directs epithelial polarity and asymmetric cell division of neuroblasts in *Drosophila*. *Nat. Cell Biol.* 3, 43–49.
- Rahkila, P., Takala, T.E., Parton, R.G., and Metsikkö, K. (2001). Protein targeting to the plasma membrane of adult skeletal muscle fiber: an organized mosaic of functional domains. *Exp. Cell Res.* 267, 61–72.
- Ranganayakulu, G., Zhao, B., Dokidis, A., Molkentin, J.D., Olson, E.N., and Schulz, R.A. (1995). A series of mutations in the D-MEF2 transcription factor reveal multiple functions in larval and adult myogenesis in *Drosophila*. *Dev. Biol.* 171, 169–181.
- Razzaq, A., Robinson, I.M., McMahon, H.T., Skepper, J.N., Su, Y., Zelfhof, A.C., Jackson, A.P., Gay, N.J., and O'Kane, C.J. (2001). Amphiphysin is necessary for organization of the excitation-contraction coupling machinery of muscles, but not for synaptic vesicle endocytosis in *Drosophila*. *Genes Dev.* 15, 2967–2979.
- Reichman-Fried, M., Dickson, B., Hafen, E., and Shilo, B.Z. (1994). Elucidation of the role of breathless, a *Drosophila* FGF receptor homolog, in tracheal cell migration. *Genes Dev.* 8, 428–439.
- Ribeiro, I., Yuan, L., Tanentzapf, G., Dowling, J.J., and Kiger, A. (2011). Phosphoinositide regulation of integrin trafficking required for muscle attachment and maintenance. *PLoS Genet.* 7, e1001295.
- Rodriguez-Boulán, E., Perez-Bay, A., Schreiner, R., and Gravotta, D. (2013). Response: the "tail" of the twin adaptors. *Dev. Cell* 27, 247–248.
- Rolls, M.M., Albertson, R., Shih, H.P., Lee, C.Y., and Doe, C.Q. (2003). *Drosophila* aPKC regulates cell polarity and cell proliferation in neuroblasts and epithelia. *J. Cell Biol.* 163, 1089–1098.
- Rosin, D., Schejter, E., Volk, T., and Shilo, B.Z. (2004). Apical accumulation of the *Drosophila* PDGF/VEGF receptor ligands provides a mechanism for triggering localized actin polymerization. *Development* 131, 1939–1948.
- Rybakova, I.N., Patel, J.R., and Ervasti, J.M. (2000). The dystrophin complex forms a mechanically strong link between the sarcolemma and costameric actin. *J. Cell Biol.* 150, 1209–1214.
- Sato, M., and Kornberg, T.B. (2002). FGF is an essential mitogen and chemo-attractant for the air sacs of the *Drosophila* tracheal system. *Dev. Cell* 3, 195–207.
- Schober, M., Schaefer, M., and Knoblich, J.A. (1999). Bazooka recruits In-scuteable to orient asymmetric cell divisions in *Drosophila* neuroblasts. *Nature* 402, 548–551.
- Smith, D.S. (1961a). Reticular organizations within the striated muscle cell: an historical survey of light microscopic studies. *J. Biophys. Biochem. Cytol.* 10, 61–87.
- Smith, D.S. (1961b). The structure of insect fibrillar flight muscle: a study made with special reference to the membrane systems of the fiber. *J. Biophys. Biochem. Cytol.* 10, 123–158.
- Strigini, M., and Cohen, S.M. (2000). Wingless gradient formation in the *Drosophila* wing. *Curr. Biol.* 10, 293–300.
- Sutherland, D., Samakovlis, C., and Krasnow, M.A. (1996). branchless encodes a *Drosophila* FGF homolog that controls tracheal cell migration and the pattern of branching. *Cell* 87, 1091–1101.
- Tanentzapf, G., and Tepass, U. (2003). Interactions between the crumbs, lethal giant larvae and bazooka pathways in epithelial polarization. *Nat. Cell Biol.* 5, 46–52.
- Thomas, U., Ebitsch, S., Gorczyca, M., Koh, Y.H., Hough, C.D., Woods, D., Gundelfinger, E.D., and Budnik, V. (2000). Synaptic targeting and localization of discs-large is a stepwise process controlled by different domains of the protein. *Curr. Biol.* 10, 1108–1117.
- Traub, L.M., and Apodaca, G. (2003). AP-1B: polarized sorting at the endosome. *Nat. Cell Biol.* 5, 1045–1047.
- van der Plas, M.C., Pilgram, G.S., Plomp, J.J., de Jong, A., Fradkin, L.G., and Noordermeer, J.N. (2006). Dystrophin is required for appropriate retrograde control of neurotransmitter release at the *Drosophila* neuromuscular junction. *J. Neurosci.* 26, 333–344.
- Weaver, M., and Krasnow, M.A. (2008). Dual origin of tissue-specific progenitor cells in *Drosophila* tracheal remodeling. *Science* 321, 1496–1499.
- Weis-Fogh, T. (1961). Power in flapping flight. In *The Cell and the Organism*, J.A. Ramsay and V.B. Wigglesworth, eds. (London: Cambridge University Press), pp. 283–300.
- Weis-Fogh, T. (1964). Diffusion in insect wing muscle, the most active tissue known. *J. Exp. Biol.* 41, 229–256.
- Wigglesworth, V.B., and Lee, W.M. (1982). The supply of oxygen to the flight muscles of insects: a theory of tracheole physiology. *Tissue Cell* 14, 501–518.
- Woods, D.F., Wu, J.W., and Bryant, P.J. (1997). Localization of proteins to the apico-lateral junctions of *Drosophila* epithelia. *Dev. Genet.* 20, 111–118.
- Zhuravlev, P.I., and Papoian, G.A. (2009). Molecular noise of capping protein binding induces macroscopic instability in filopodial dynamics. *Proc. Natl. Acad. Sci. USA* 106, 11570–11575.

Organoid Models of Human and Mouse Ductal Pancreatic Cancer

Sylvia F. Boj,^{1,2,14} Chang-Il Hwang,^{3,4,14} Lindsey A. Baker,^{3,4,14} Iok In Christine Chio,^{3,4,14} Dannielle D. Engle,^{3,4,14} Vincenzo Corbo,^{3,4,14} Myrthe Jager,^{1,14} Mariano Ponz-Sarvisé,^{3,4} Hervé Tiriác,^{3,4} Mona S. Spector,^{3,4} Ana Gracani,^{1,2} Tobiloba Oni,^{3,4,5} Kenneth H. Yu,^{3,4,6,7} Ruben van Boxtel,¹ Meritxell Huch,^{1,15} Keith D. Rivera,³ John P. Wilson,³ Michael E. Feigin,^{3,4} Daniel Öhlund,^{3,4} Abram Handly-Santana,^{4,8} Christine M. Ardito-Abraham,^{3,4} Michael Ludwig,^{3,4} Ela Elyada,^{3,4} Brinda Alagesan,^{3,4,9} Giulia Biffi,^{3,4} Georgi N. Yordanov,^{4,8} Bethany Delcuze,^{3,4} Brianna Creighton,^{3,4} Kevin Wright,^{3,4} Youngkyu Park,^{3,4} Folkert H.M. Morsink,¹⁰ I. Quintus Molenaar,¹¹ Inne H. Borel Rinkes,¹¹ Edwin Cuppen,¹ Yuan Hao,³ Ying Jin,³ Isaac J. Nijman,¹ Christine Iacobuzio-Donahue,⁶ Steven D. Leach,⁶ Darryl J. Pappin,³ Molly Hammell,³ David S. Klimstra,¹² Olca Basturk,¹² Ralph H. Hruban,¹³ George Johan Offerhaus,¹⁰ Robert G.J. Vries,^{1,2} Hans Clevers,^{1,*} and David A. Tuveson^{3,4,6,*}

¹Hubrecht Institute, Royal Netherlands Academy of Arts and Sciences (KNAW), University Medical Centre Utrecht and CancerGenomics.nl, 3584 CT Utrecht, the Netherlands

²Foundation Hubrecht Organoid Technology (HUB), 3584 CT Utrecht, the Netherlands

³Cold Spring Harbor Laboratory, Cold Spring Harbor, NY 11724, USA

⁴Lustgarten Foundation Pancreatic Cancer Research Laboratory, Cold Spring Harbor, NY 11724, USA

⁵Graduate Program in Molecular and Cellular Biology, Stony Brook University, Stony Brook, NY 11794, USA

⁶Rubenstein Center for Pancreatic Cancer Research, Memorial Sloan Kettering Cancer Center, New York, NY 10065, USA

⁷Weill Medical College at Cornell University, New York, NY 10065, USA

⁸Watson School of Biological Sciences, Cold Spring Harbor Laboratory, Cold Spring Harbor, NY 11724, USA

⁹Graduate Program in Genetics, Stony Brook University, Stony Brook, NY 11794, USA

¹⁰Department of Pathology, University Medical Centre Utrecht, 3584 CX Utrecht, the Netherlands

¹¹Department of Surgery, University Medical Center Utrecht, 3584 CX Utrecht, the Netherlands

¹²Department of Pathology, Memorial Sloan Kettering Cancer Center, New York, NY 10065, USA

¹³The Sol Goldman Pancreatic Cancer Research Center, Johns Hopkins University School of Medicine, Baltimore, MD 21231, USA

¹⁴Co-first author

¹⁵Present address: Gurdon Institute-University of Cambridge, Tennis Court Road, Cambridge CB2 1QN, UK

*Correspondence: h.clevers@hubrecht.eu (H.C.), dtuveson@cshl.edu (D.A.T.)

<http://dx.doi.org/10.1016/j.cell.2014.12.021>

SUMMARY

Pancreatic cancer is one of the most lethal malignancies due to its late diagnosis and limited response to treatment. Tractable methods to identify and interrogate pathways involved in pancreatic tumorigenesis are urgently needed. We established organoid models from normal and neoplastic murine and human pancreas tissues. Pancreatic organoids can be rapidly generated from resected tumors and biopsies, survive cryopreservation, and exhibit ductal- and disease-stage-specific characteristics. Orthotopically transplanted neoplastic organoids recapitulate the full spectrum of tumor development by forming early-grade neoplasms that progress to locally invasive and metastatic carcinomas. Due to their ability to be genetically manipulated, organoids are a platform to probe genetic cooperation. Comprehensive transcriptional and proteomic analyses of murine pancreatic organoids revealed genes and pathways altered during disease progression. The confirmation of many of these protein changes in human tissues demonstrates that organoids are a facile model

system to discover characteristics of this deadly malignancy.

INTRODUCTION

Mortality due to pancreatic cancer is projected to surpass that of breast and colorectal cancer by 2030 in the United States (Rahib et al., 2014; Siegel et al., 2013). This dire scenario reflects an aging population, the improvement of outcomes for breast and colorectal cancer patients, the advanced stage at which most patients with pancreatic cancer are diagnosed, and the lack of durable treatment responses in pancreatic cancer patients. Indeed, effective therapeutic strategies for patients with pancreatic ductal adenocarcinoma (PDA) have been difficult to identify (Abbruzzese and Hess, 2014).

The therapeutic resistance of PDA has been explored in a variety of cell culture and animal model systems, with clinically actionable findings encountered only occasionally (Villarroel et al., 2011). Patient-derived xenografts (PDXs) have yielded insights into PDA, but their generation requires a large amount of tissue, and they take multiple months to establish (Kim et al., 2009; Rubio-Viqueira et al., 2006). Genetically engineered mouse models (GEMMs) of PDA have also been generated as a parallel system for fundamental biological investigation and preclinical studies (Pérez-Mancera et al., 2012). These GEMMs

accurately mimic the pathophysiological features of human PDA, including disease initiation from preinvasive pancreatic intraepithelial neoplasms (PanINs) (Hingorani et al., 2003; Pérez-Mancera et al., 2012) and were used to discover that PDA possesses a deficient vasculature that impairs drug delivery (Erkan et al., 2009; Jacobetz et al., 2013; Koong et al., 2000; Olive et al., 2009; Provenzano et al., 2012). Although GEMMs have informed PDA therapeutic development (Beatty et al., 2011; Frese et al., 2012; Neesse et al., 2014), they are expensive and time consuming (Pérez-Mancera et al., 2012). In addition, both human PDA and GEMMs exhibit an extensive stromal component that decreases the neoplastic cellularity, making it difficult to isolate and characterize the epithelium-derived malignant cells in pancreatic neoplastic tissues.

To study neoplastic cells, dissociated human tumors are often grown in two-dimensional (2D) culture conditions (Sharma et al., 2010), which do not support growth of untransformed, nonneoplastic pancreatic cells. Three-dimensional (3D) culture strategies have been developed to study normal, untransformed cells but so far have only allowed minimal propagation (Agbunag and Bar-Sagi, 2004; Lee et al., 2013; Means et al., 2005; Rovira et al., 2010; Seaberg et al., 2004). A comprehensive 3D cell culture model of murine and human PDA progression would facilitate investigation of genetic drivers, therapeutic targets, and diagnostics for PDA.

To address this deficiency, we sought to generate normal and neoplastic pancreatic organoids by modifying approaches we previously pioneered to culture intestinal (Sato et al., 2009), gastric (Barker et al., 2010), colon carcinoma (Sato et al., 2011), hepatic (Huch et al., 2013b), pancreatic (Huch et al., 2013a), and prostatic organoids (Gao et al., 2014; Karthaus et al., 2014). We developed 3D organoids from normal and malignant murine pancreatic tissues and used this model system to investigate PDA pathogenesis. Pancreatic organoids derived from wild-type mice and PDA GEMMs accurately recapitulate physiologically relevant aspects of disease progression in vitro. Following orthotopic transplantation, organoids from wild-type mouse normal pancreata are capable of regenerating normal ductal architecture, unlike other 3D model systems. We further developed methods to generate pancreatic organoids from normal and diseased human tissues, as well as from endoscopic needle biopsies. Following transplantation, organoids derived from murine and human PDA generate lesions reminiscent of PanIN and progress to invasive PDA. Finally, we demonstrate the utility of organoids to identify molecular pathways that correlate with disease progression and that represent therapeutic and diagnostic opportunities.

RESULTS

Murine Pancreatic Ductal Organoids Expressing Oncogenic *Kras* Recapitulate Features of PanINs

Recently, we derived continuously proliferating, normal pancreatic organoids from adult murine ductal cells (Huch et al., 2013a). We optimized this approach to generate models of PDA progression. We manually isolated small intralobular ducts and established organoid cultures from C57Bl/6 mouse normal pancreata and pancreatic tissues that contained low-grade murine PanIN

(mPanIN-1a/b) from *Kras*^{+/-LSL-G12D}; *Pdx1-Cre* ("KC") mice (Figure 1A). KC mice develop a spectrum of preinvasive ductal lesions that mirror human PanINs and, upon aging, stochastically develop primary and metastatic PDA (Hingorani et al., 2003). Ducts from KC pancreata were often larger and exhibited higher grades of dysplasia compared to those from wild-type mice (Figure 1A). After 1–3 days in culture, organoid growth was observed from isolated ducts (Figure 1A). We created a collection of 10 murine normal (mN) and 9 PanIN (mP) organoid cultures that we have continuously propagated for over 20 passages and successfully cryopreserved (Table S1A available online). mP organoids exhibited recombination of the conditional *Kras*^{LSL-G12D} allele and higher levels of *Kras*-GTP when compared to mN organoids (Figure 1B).

To determine the contribution of different pancreatic lineages to the organoids, we evaluated the expression of pancreatic lineage markers in these cultures. Genes associated with the ductal lineage (*Ck19* and *Sox9*) (Cleveland et al., 2012) were enriched in the mN and mP organoids compared to total pancreatic tissues, which contain relatively few ductal cells (Figure 1C). In addition, the mP organoids upregulated genes indicative of a PanIN disease state (*Muc5ac*, *Muc6*, and *Tff1*) relative to mN, with no difference in *Klf4* (Figure 1D) (Prasad et al., 2005). GFP-transduced mN and mP organoids were orthotopically transplanted into syngeneic C57Bl/6 or *Nu/Nu* mice. mN organoids quickly formed ductal structures comprised of simple cuboidal cells that persisted for up to 1 month (*n* = 9/27 transplants) but were not observed after 2 months (*n* = 0/13 transplants) (Figure 1E and Table S1B). In comparison, mP organoids formed small cysts lined with a single layer of simple cuboidal ductal cells interspersed with mucin-containing columnar epithelial cells. Although we could not demonstrate that the mP transplants were contiguous with the native ductal system, they resembled preinvasive mPanIN (Figure S1C). These dysplastic epithelial cells persisted for 2 months or longer (*n* = 16/18 transplants), were GFP and *Ck19* positive, expressed the mPanIN-associated mucin *Muc5ac*, and stained prominently with Alcian blue (Figure 1E and Table S1C). In addition, when compared to mN transplants, mP transplants had increased proliferation and a robust stromal response, which are characteristics of autochthonous mPanIN tissue (Figures S1A–S1C). The ability of transplanted mP organoids to form lesions with many of the features of mPanINs demonstrates the utility of this system as a model for early pancreatic neoplasia.

Multiple cellular origins have been proposed for the development of PDA, with the pancreatic acinar cell hypothesized to be a major contributor to PDA initiation (De La O et al., 2008; Gidekel Friedlander et al., 2009; Guerra et al., 2003; Habbe et al., 2008; Kopp et al., 2012; Morris et al., 2010; Sawey et al., 2007). However, recent studies have suggested that translocation of pancreatic ductal cells can also give rise to PDA (Pylayeva-Gupta et al., 2012; Ray et al., 2011; von Figura et al., 2014). Acinar cells isolated from wild-type pancreata are unable to form organoids in our conditions (Huch et al., 2013a). Therefore, our pancreatic ductal organoid system offers a unique opportunity to determine whether ductal cells can give rise to mPanIN. To assess whether expression of oncogenic *Kras* in pancreatic ductal organoids is sufficient to induce mPanIN formation in vivo, we derived

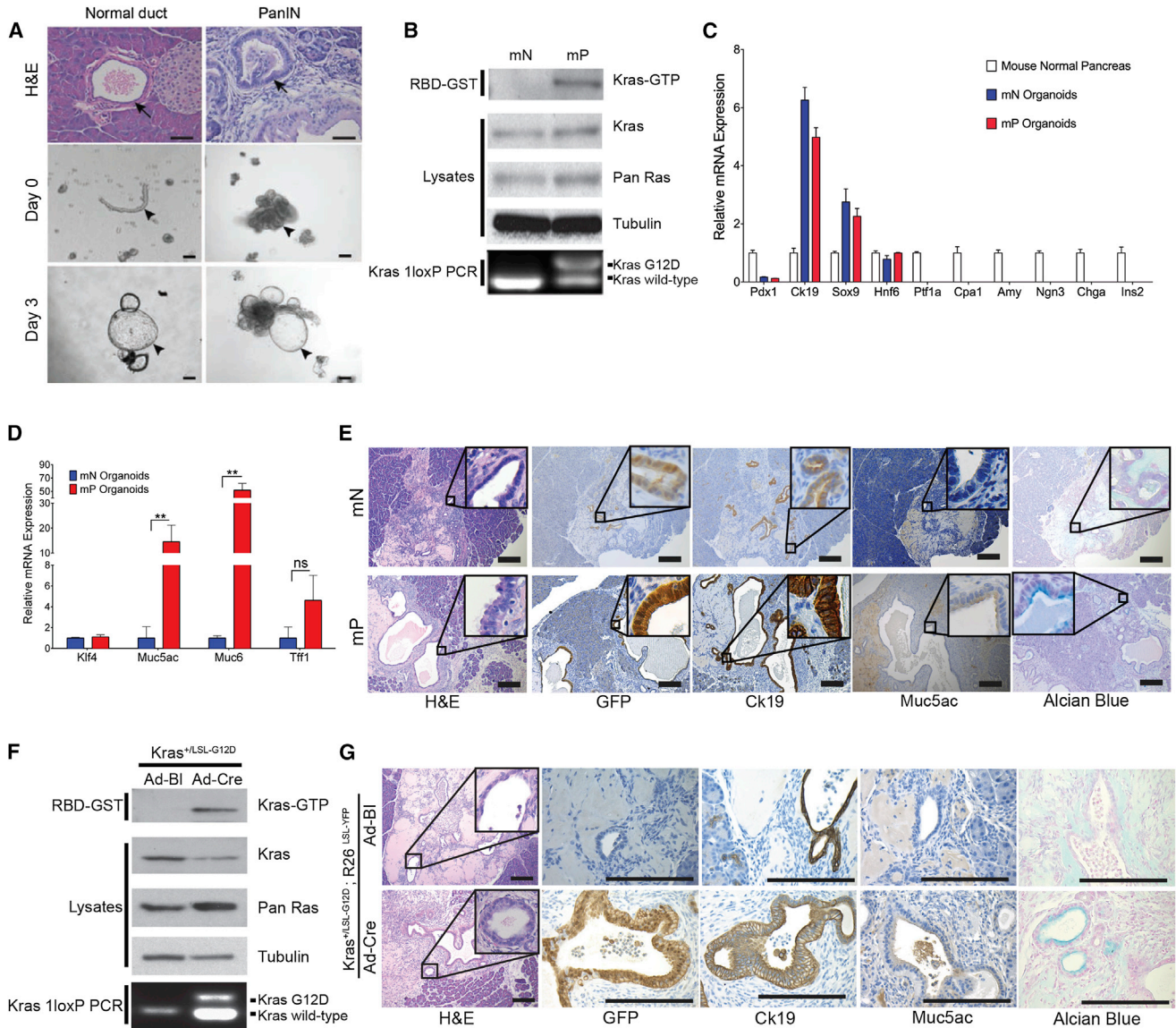


Figure 1. Oncogenic *Kras*^{G12D} Expression in Pancreatic Ductal Organoids Is Sufficient to Induce Preinvasive Neoplasms

(A) Hematoxylin and eosin (H&E) staining of murine pancreatic tissue used to prepare organoids (top). Arrows indicate mouse normal or PanIN ductal structures. Ducts embedded in Matrigel immediately following isolation (middle) and organoids 3 days postisolation (bottom). Arrowheads mark isolated ducts and growing organoids. Scale bars, 50 μ m.

(B) Immunoblots for Kras, pan Ras, Kras-GTP by RBD-GST pull-down, and Tubulin in mN and mPanIN (mP) organoids. PCR confirmation of Cre-mediated recombination of the *Kras*^{LSL-G12D} allele (bottom).

(C) qRT-PCR of ductal (*Pdx1*, *Ck19*, *Sox9*, and *Hnf6*), acinar (*Ptf1a*, *Cpa1*, and *Amy*), and endocrine (*Ngn3*, *Chga*, and *Ins2*) lineage markers in mN and mP organoids. Means of three biological replicates are shown. Error bars indicate SEMs. Values were normalized to mouse normal pancreas.

(D) qRT-PCR of genes indicative of PanIN lesions (*Muc5ac*, *Muc6*, *Tff1*, and *Klf4*) in mN and mP organoids. Values were normalized to mN organoids. Means of three biological replicates are shown. Error bars indicate SEMs. ***p* < 0.01 by two-tailed Student's *t* test.

(E) H&E, Alcian blue staining, and immunohistochemistry (IHC) of orthotopic, syngeneic transplants of GFP-transduced mN and mP organoids. Scale bars, 200 μ m.

(F) Immunoblots for Kras, pan Ras, Kras-GTP by RBD-GST pull-down, and tubulin in *Kras*^{+/LSL-G12D} organoids transduced with adenoviral-Cre (Ad-Cre) or adenoviral-blank (Ad-BI). PCR confirmation of Cre-mediated recombination of the *Kras*^{LSL-G12D} allele (bottom).

(G) H&E, Alcian blue staining, and IHC of orthotopic syngeneic transplants of organoids transduced with Ad-BI (*Kras*^{+/LSL-G12D}; *R26*^{LSL-YFP}) and Ad-Cre (*Kras*^{+/G12D}; *R26*^{YFP}) 2 weeks posttransplant. Scale bars, 200 μ m.

See also Figure S1 and Table S1.

organoids from ducts harboring the conditional *Kras*^{LSL-G12D} allele (Hingorani et al., 2003). Following activation of *Kras* by adenoviral-*Cre* (Ad-*Cre*) infection, *Kras*^{G12D} organoids maintained expression of genes specific to ductal cells and not acinar or endocrine lineages (Figures S1D and S1E). Recombination of the *Kras*^{LSL-G12D} allele was confirmed by PCR, and levels of GTP-bound *Kras* were increased relative to control-infected organoids (Figure 1F). In addition, expression of *Kras*^{G12D} resulted in the upregulation of genes associated with human PanIN (Figure S1F). The *Kras*^{G12D}-expressing organoids demonstrated increased proliferation relative to control organoids (Figure S1G). Finally, *Kras*^{G12D} organoids formed mPanIN-like structures with columnar cell morphology when implanted orthotopically into syngeneic mice (Figure 1G). This morphology contrasted with the normal-appearing ductal architecture formed by transplanting *Kras*^{+/LSL-G12D} organoids or wild-type mN (Figures 1E and 1G). The ability of mPanIN-like structures to develop from *Kras*^{G12D}-expressing ductal organoids following transplantation demonstrates that ductal cells are also competent to form mPanINs.

Tumor-Derived Organoids Provide a Model for Murine PDA Progression

We prepared pancreatic ductal organoids from multiple murine primary tumors (mT) and metastases (mM) from KC and *Kras*^{+/LSL-G12D}; *Trp53*^{+/LSL-R172H}; *Pdx1-Cre* (“KPC”) mice, which develop mPDA more rapidly than KC mice (Figures 2A and Table S2A) (Hingorani et al., 2005). mT and mM organoids exhibited recombination of the *Kras*^{LSL-G12D} allele, as well as increased levels of *Kras*-GTP and *Kras* protein (Figure 2B). mT and mM organoids had increased levels of S6 phosphorylation, but not of Erk or Akt phosphorylation (Figure 2B).

Orthotopic transplantation of mT organoids initially generated low- and high-grade lesions that resembled mPanIN (Figure 2C and Table S2B). Over longer periods of time (1–6 months), transplants developed into invasive primary and metastatic mPDA (Figure 2C and Table S2B). mT organoids engrafted with a similar efficiency upon orthotopic transplantation in *Nu/Nu* mice (91.7%) compared to C57Bl/6 mice (85%), but disease progression was accelerated in *Nu/Nu* hosts (Table S2B). Although most mT organoid transplants required several months to progress from early mPanIN-like lesions to invasive and metastatic cancer (Figure 2C and Table S2B), mM organoids rapidly formed invasive mPDA within 1 month (Table S2C). The ability of organoid transplants to reproduce the discrete stages of disease progression contrasts with the rapid formation of advanced mPDA following transplantation of 2D cell lines (Figures S2A–S2C) (Olive et al., 2009).

Tumors derived from transplanted mT and mM organoids exhibited prominent stromal responses and resembled autochthonous tumors from KPC mice (Figure S2A) (Olive et al., 2009). This stromal response is often absent in tumors formed from 2D cell lines (Figure S2A) (Olive et al., 2009). Low vascular density and high vessel-to-tumor distance were also observed, demonstrating the close resemblance of the organoid transplantation models to autochthonous mPDA, in contrast to transplanted 2D cell lines (Figures S2A–S2C) (Olive et al., 2009).

Loss of heterozygosity (LOH) for *Trp53* has been reported as a common feature of mPDA based on studies of 2D cell lines (Hin-

gorani et al., 2005). Therefore, we assayed for *Trp53* LOH in our murine 3D organoids. All mT organoids prepared from KPC tumors maintained expression of p16, did not exhibit *Trp53* LOH, and maintained a stable karyotype, whereas most mM organoids lost the wild-type *Trp53* allele and were aneuploid (Figures 2D, 2E, and S2D). We generated 2D cell lines from mT and mM organoids but found that mN and mP organoids were unable to propagate in 2D. mT1 was derived from a KC mouse PDA, lacks the mutant *Trp53* allele, and was also unable to propagate in 2D. All mT-derived 2D cell lines exhibited *Trp53* LOH and were aneuploid (Figures 2E and S2D).

To determine whether organoids are suitable for genetic cooperation experiments, shRNAs targeting p53 and p16/p19 were introduced into mP organoids (Figure S2E). Although the proliferation of mP organoids increased upon knockdown of either p53 or p16/p19 (Figure S2G), only p53 knockdown enabled 2D growth and colony formation (Figure S2F; data not shown). Also, only p53 knockdown promoted progression of mP organoid transplants to invasive carcinoma within 3 months (Figure S2H). This contrasts with a previous report that *Kras* mutation and biallelic loss of p16/p19 promoted mPDA (Aguirre et al., 2003; Bardeesy et al., 2006) and may reflect differences in the genetic system or the initiating cellular compartment. Nevertheless, the cooperation between p53 depletion and oncogenic *Kras* demonstrates that organoids are a facile system to evaluate genetic mediators of PDA progression.

Human Pancreatic Organoids Model PanIN to PDA Progression

We modified our culture conditions to support the propagation of human normal and malignant pancreatic tissues. Isolation of ductal fragments was not always feasible because some normal pancreatic tissue samples were predigested in preparation for islet transplantation. Therefore, we directly embedded digested material into Matrigel. This approach achieved an isolation efficiency of 75%–80% for human normal (hN) organoids (Figures 3A and S3 and Table S3). hN organoids require transforming growth factor β (TGF- β) pathway inhibitors (A83-01 and Noggin), R-Spondin1 and Wnt3a-conditioned media, EGF, and PGE2 for propagation (Figures 3B and 3C). Unlike mN organoids, which have unlimited propagation in culture, hN organoids ceased proliferating after 20 passages or ~6 months but could be cryopreserved.

We adapted the methods described above to accommodate the extensive desmoplastic reaction in freshly resected PDA specimens and generated human tumor-derived organoids (hT) (Figures 3A and S3 and Table S3). hT organoids could be passaged indefinitely and cryopreserved (Figure 3C). The establishment of hT organoids had efficiencies of 75% ($n = 3/4$) and 83% ($n = 5/6$) in the Netherlands and USA, respectively (Table S3). The first specimen that failed to generate an organoid culture was obtained from a patient that had undergone neo-adjuvant chemotherapy, and histologic examination of this specimen revealed extensive necrosis. The second specimen that did not generate an organoid culture was predominantly composed of stromal cells, without sufficient viable tumor cells to establish a culture. Although the hN organoids had a simple, cuboidal morphology, the hT organoids had differing degrees of

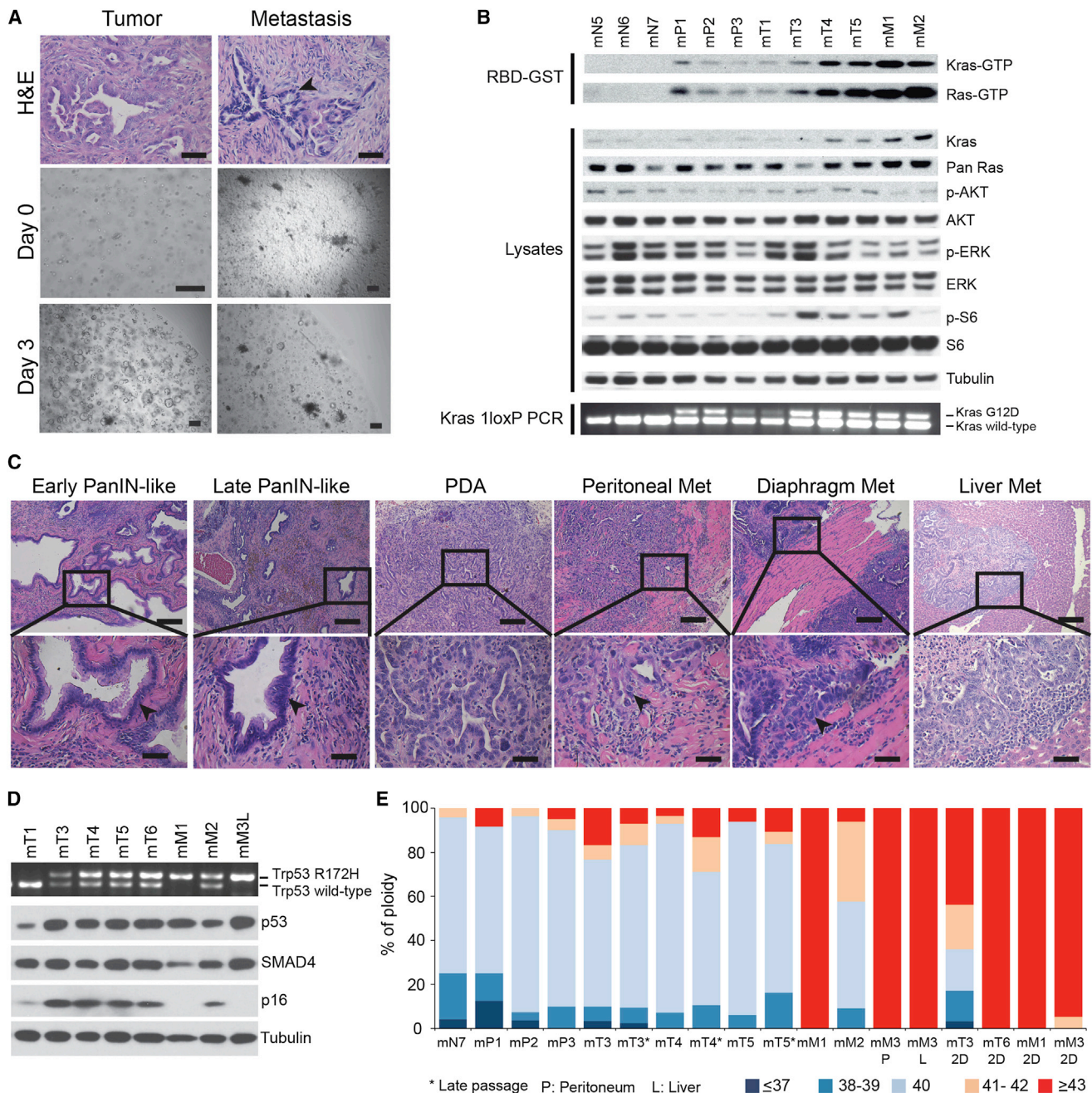


Figure 2. Modeling Murine PDA Progression with Tumor- and Metastasis-Derived Organoids

(A) H&E staining of murine tissue from which tumor and metastasis organoids were derived (top). Arrowhead indicates metastasis. Scale bars, 50 μ m. Digested murine tissues embedded in Matrigel immediately following isolation (middle) and organoids 3 days postisolation (bottom). Scale bars, 200 μ m.

(B) Immunoblots of selected signaling effectors, Kras-GTP and Ras-GTP by RBD-GST pull-down, and tubulin. PCR confirmation of *Kras*^{LSL-G12D} recombination in mP, mT, and mM organoids (bottom).

(C) H&E staining of tumors and metastases (Met) derived from mT organoid orthotopic transplants. Scale bars, 200 μ m (top) and 50 μ m (bottom).

(D) Loss of heterozygosity of the wild-type *Trp53* allele determined by PCR (top) and immunoblot analysis of Trp53, Smad4, p16, and Tubulin. mM3L, derived from a liver metastasis.

(E) Karyotypes of organoids and monolayer (2D) cell lines.

See also Figure S2 and Table S2.

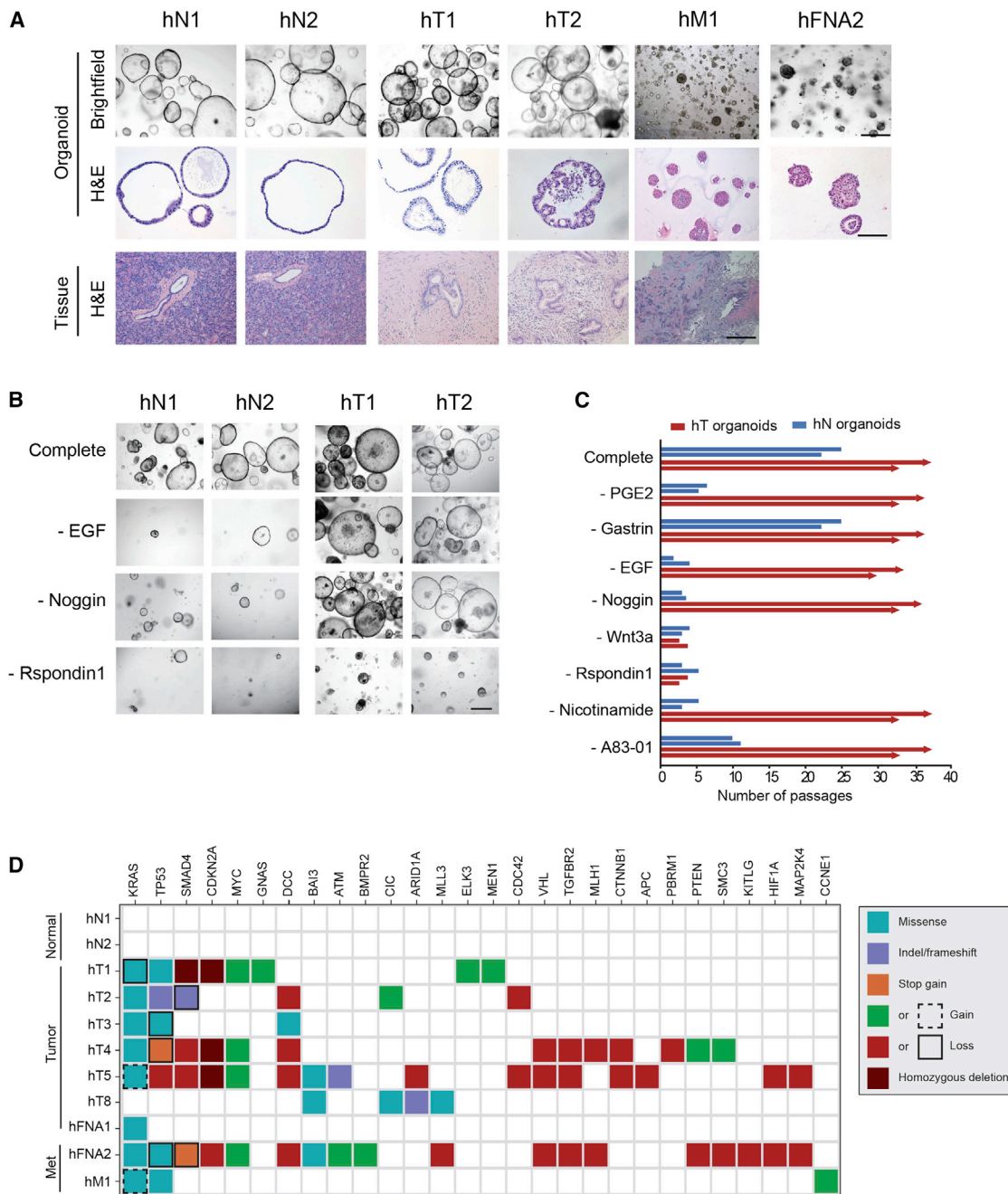


Figure 3. Human Pancreatic Ductal Organoids Recapitulate Features of Normal and Neoplastic Ducts

(A) Representative images (top) and H&E staining (middle) of human organoid cultures established from normal tissues (hN1-2), resected primary tumors (hT1-2), a resected metastatic lung lesion (hM1), and a fine-needle aspiration biopsy of a metastatic lesion (hFNA2). H&E staining of the resected tissues from which the organoids were derived (bottom). Scale bars, 500 μ m (top), 250 μ m (middle), and 500 μ m (bottom).

(B) Representative images of hN and hT organoids cultured for 2 weeks (1 passage) in human complete media or in human complete media lacking the indicated factors. Scale bars, 500 μ m.

(C) Number of passages hN and hT organoids could be propagated in the absence of the indicated factors.

(D) Targeted sequencing analysis of human organoids. Genes altered in more than one sample and/or known to be mutated in PDA are shown. If multiple mutations were found in a gene, only one mutation per gene is shown. Color key for the type of genetic alterations is shown. Met indicates organoids derived from metastatic samples.

See also [Figure S3](#) and [Tables S3](#) and [S4](#).

dysplastic tall columnar cells, resembling low-grade PanINs (Figures 3A). hT organoids tolerated the withdrawal of certain growth factors from the media (Figures 3B and 3C).

85% of pancreatic cancer patients are ineligible for surgical resection of their tumors (Ryan et al., 2014). Therefore, we determined whether hT organoids could be generated from the limited amount of cellular material provided by endoscopic biopsies using fine needle aspirations (FNA). Initial attempts to generate organoids from FNA biopsies were hampered by loss of cellular material during digestion. Upon optimization of these conditions, human FNA biopsy organoids (hFNA) were generated from two specimens that were not dissociated prior to suspension in Matrigel (Figures 3A and S3 and Table S3). This approach is broadly applicable to PDA patients and enables serial sampling.

Targeted sequencing of 2,000 cancer-associated genes was performed on hN and hT organoids. As expected, no mutations were detected in the hN organoid cultures. These analyses identified oncogenic *KRAS* mutations in the majority of tumor-derived samples ($n = 8$), as well as mutations in *TP53* ($n = 7$), *SMAD4* ($n = 5$), and *CDKN2A* ($n = 4$) (Figure 3D and Table S4). We also noted amplification of known oncogenes, such as *MYC* ($n = 4$), and loss of tumor suppressors, including *TGFBR2* ($n = 3$) and *DCC* ($n = 5$). Importantly, the same *KRAS* mutations observed in several hT organoids were confirmed in the primary PDA from which they were derived (Table S4). The allele frequency of oncogenic *KRAS* variants in hT1–hT5 and hFNA2 ranged from ~50–100%. In contrast, the *KRAS*^{G12V} allele frequency in hFNA1 was only 1% (Table S4), which may result from coexistence of wild-type ductal cells. Although *KRAS* mutations were not detected in hT8 (Figure 3D and Table S4), the presence of mutations in known PDA genes (*ARID1A* and *MLL3*) suggests that hT8 contains malignant cells (Table S4).

To further characterize the cell types present in primary PDA organoids, we evaluated the expression of pancreatic lineage markers. hN and hT organoids expressed markers of ductal cells, but not other pancreatic lineages (Figure 4A). The karyotypes of hT organoids were highly aneuploid, whereas the hN organoids were predominantly and stably diploid (Figure 4B). The PDA-associated biomarker CA19-9 (Makovitzky, 1986) was also elevated in hT relative to hN organoids (Figure 4C). The hN and hT organoids are therefore reflective of normal and neoplastic human pancreatic ductal cells and offer a model system to explore pancreatic cancer biology in the more genetically complex background of human cancer.

Following orthotopic transplantation into *Nu/Nu* mice, hN organoids produced normal ductal structures at low efficiency ($n = 2/23$), whereas hT organoids efficiently generated a spectrum of low- and high-grade, extraductal PanIN-like lesions within 1 month ($n = 9/12$) (Figures 4D and S4A and Table S4D). The hT-derived transplants initially formed well-defined hollow lesions lined by a single layer of columnar epithelial cells with apical mucin and basally located, relatively uniform nuclei. The nuclei were small and lacked the pleomorphism and hyperchromasia often seen in invasive PDA. These lesions progressed over several months to infiltrative carcinoma comprised of poorly defined and invasive glands (Figures 4D and S4A and Table S4). A prominent desmoplastic reaction was present in hT-derived PanIN-like structures and PDA, including the deposition

of a collagen-rich stroma and the recruitment of α SMA-positive cells (Figure S4B). The mutation or loss of *TP53* or *SMAD4* in hT1 and hT2 was also detected by IHC in these tumors (Figure S4C and Table S4). Overall, hT organoids represent a transplantable model of human pancreatic cancer progression.

Gene Expression Analysis of Murine Pancreatic Ductal Organoids Implicates Candidate Genes in PDA Progression

The mouse organoids were prepared from syngeneic mice, offering the ability to discern gene expression changes in organoids and determine whether these changes correlate with PDA progression. We harvested RNA from mN ($n = 7$), mP ($n = 6$), and mT ($n = 6$) organoids and generated strand-specific RNA-sequencing (RNA-seq) libraries. Sequences were mapped to the mm9 version of the mouse genome, and relative transcript abundances (transcripts per million) of 29,777 mouse genes were determined (Table S5). Principal component analysis revealed that mN organoids were distinct from mP and mT organoids (Figure 5A and Table S5).

Genes whose levels differed significantly among mN, mP, and mT organoids were identified. 772 genes were found downregulated and 863 genes upregulated in mP relative to mN organoids (Figure 5B and Table S5). When mT organoids were compared to mN organoids, 2,721 genes were downregulated and 2,695 were upregulated. In addition, 823 genes were downregulated and 640 genes were upregulated in mT relative to mP organoids. Distinct patterns of gene expression were found in the data set (Figure 5C). The majority of genes differentially expressed in mP relative to mN organoids changed in a similar manner in mT relative to mN organoids (Figure 5D). However, a much larger cohort of genes changed in expression in mT relative to mN than in mP relative to mN organoids (Figure 5D), suggesting that mP organoids represent an intermediate state between mN and mT organoids.

The glycosyltransferase *Gcnt3* and putative protein disulfide isomerase *Agr2* were among the most upregulated genes in both mP and mT organoids and have been demonstrated to be elevated in human PDA (Figure 5E) (Dumartin et al., 2011; Zhao et al., 2014). The most upregulated gene in both mP and mT relative to mN organoids was the acyl-CoA synthetase *Acsm3* (Figure 5E). RNA-seq results were confirmed by qRT-PCR for 35 out of 40 genes (Table S5), including the upregulation of *Agr2*, *Acsm3*, *Gcnt1*, *Gcnt3*, and *Ugdh* and the downregulation of *Ptprd* in mP and mT organoids (Figure 5F and Table S5). Among the genes upregulated in mP and mT relative to mN organoids, *Gcnt1*, *Gcnt3*, *Acsm3*, *Agr2*, *Syt16*, *Nt5e*, and *Ugdh* were upregulated following the Ad-Cre-induced expression of oncogenic *Kras*^{G12D}, suggesting that these genes are activated downstream of mutant *Kras*^{G12D} (Figure S5A). To determine whether organoid RNA-seq profiles resembled gene expression patterns in vivo, we compared our organoid RNA-seq data to a published transcription profile of murine pancreatic tumors upon *Kras*^{G12D} inactivation (Ying et al., 2012). Genes differentially expressed upon inactivation of oncogenic *Kras* overlapped significantly with those up or downregulated in mP or mT relative to mN organoids (Figure S5B). These analyses demonstrate the ability of the organoid system to identify molecular alterations associated with PDA progression.

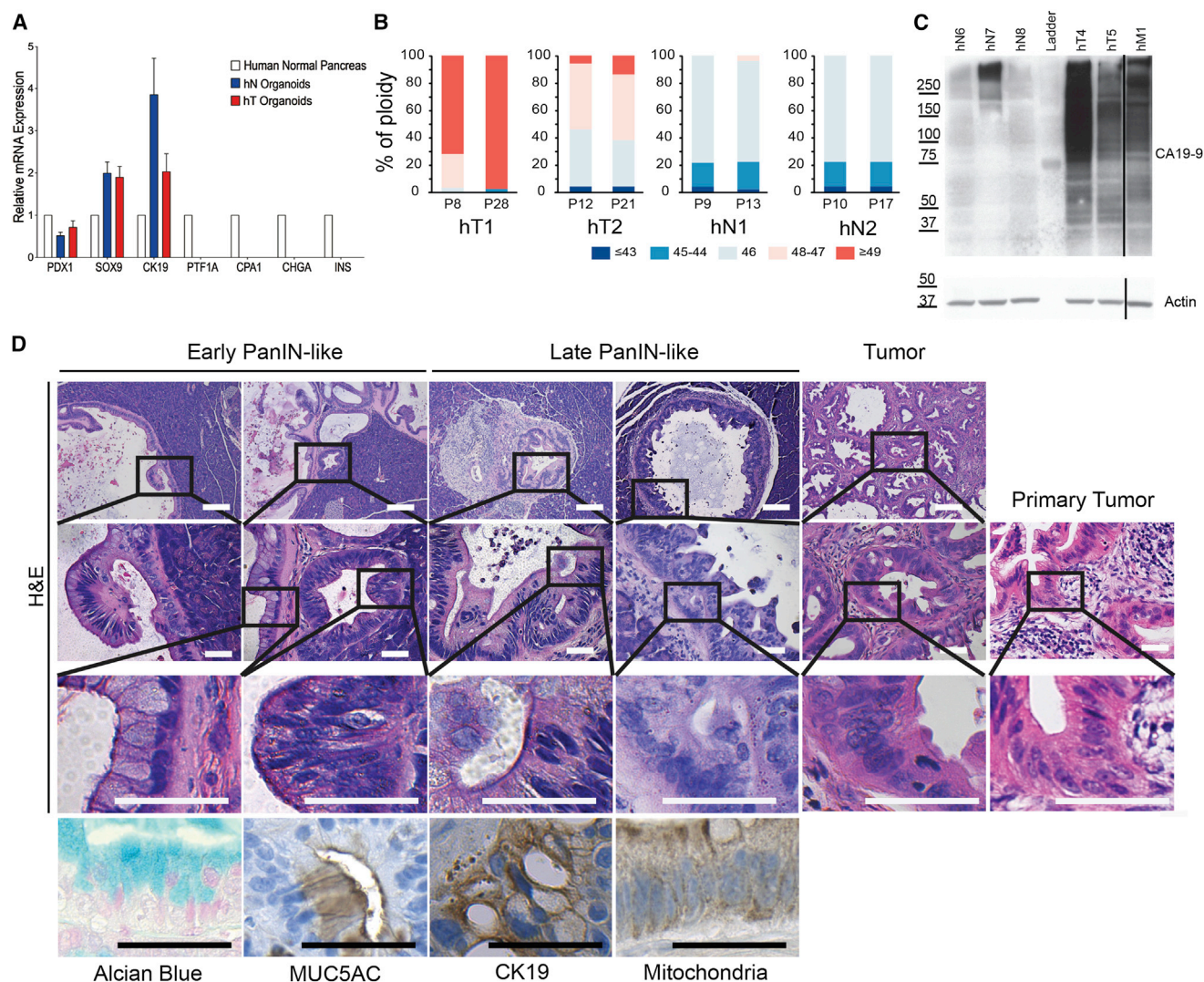


Figure 4. Molecular Characterization and Orthotopic Transplantation of Human Organoids

(A) qRT-PCR of pancreas lineage markers in hN (n = 3) and hT (n = 4) organoids. Mean expression levels were normalized to total pancreas. Error bars indicate SEMs.

(B) Karyotyping of human organoids (2 hN, 2hT) at the indicated passages (P).

(C) CA19-9 and actin levels in hN, hT, or hM organoids. The solid line indicates noncongruent lanes.

(D) H&E, Alcian blue staining, and IHC of orthotopic hT2 transplants and the primary tumor. Scale bars, 200 μ m (top two panels) and 50 μ m (bottom two panels). See also Figure S4 and Table S4D.

Proteomic Alterations in Murine Pancreatic Ductal Organoids Predict Pathways Associated with PDA Progression

As an orthogonal method to investigate molecular alterations in murine pancreatic organoids, we characterized the global proteomes of mN (n = 5), mP (n = 4), and mT (n = 5) organoids. Protein lysates were processed using amine-reactive isobaric tags for relative and absolute quantification (iTRAQ) mass spectrometry (Wiese et al., 2007). Samples were run in four 8-plex experiments and merged using an approach that normalizes the data to common samples included across all experiments (Extended Experimental Procedures). Upon merging, 6,051 unique protein

isoforms were quantified in all samples. We applied linear regression modeling on the normalized intensity peak values and identified 710 protein isoform expression changes between mN and mP organoids (Figure 6A). 1,047 protein isoforms changed expression between mN and mT organoids, and 63 differentially expressed proteins were identified between mP and mT (Figure 6A). The relatively small number of protein expression changes identified between mP and mT organoids reflects their biological similarity (Figure S6A).

mN organoids showed unique proteomic profiles from their mP and mT counterparts (Figures 6B and 6C). To compare the proteomic and RNA-seq data, we collapsed the unique protein

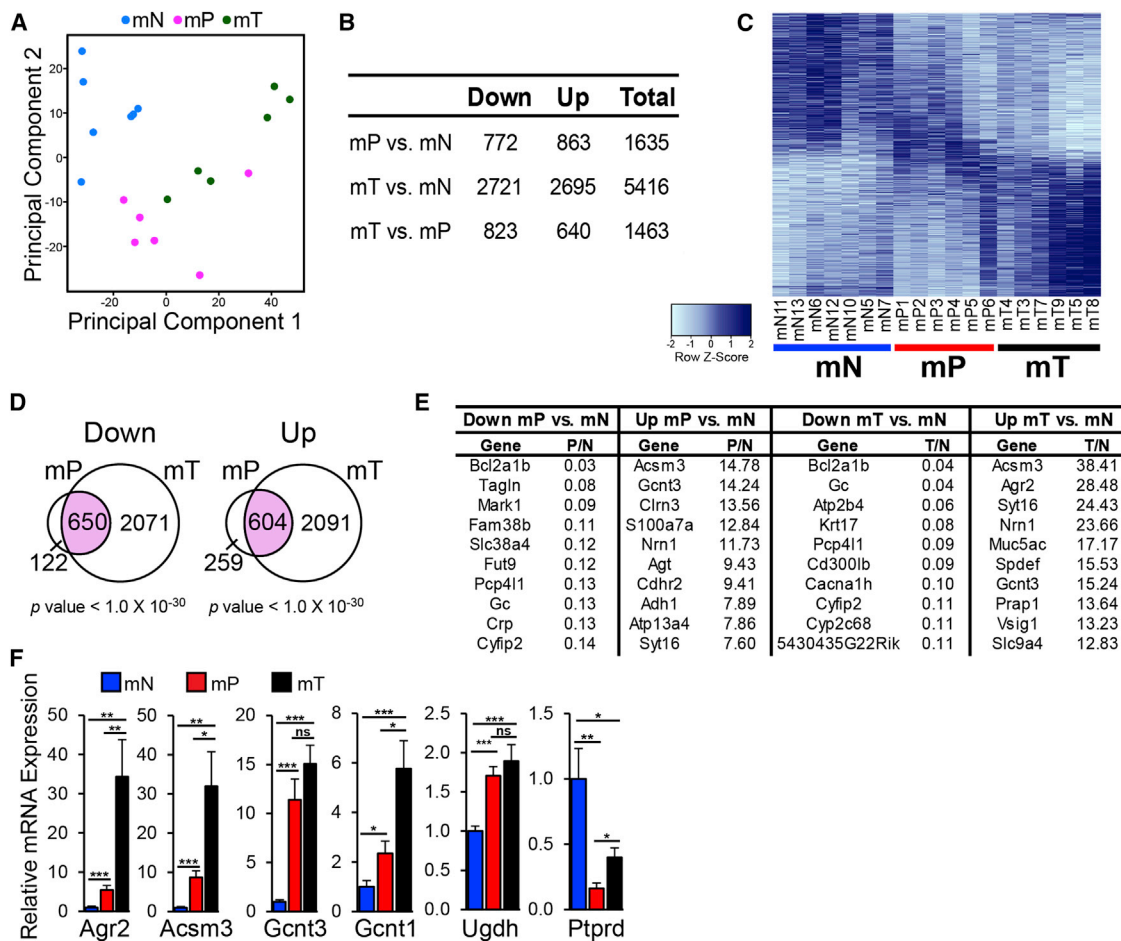


Figure 5. Gene Expression Analysis of Murine Organoids Reveals Genetic Changes Correlated with Pancreatic Cancer Progression
(A) Principal component analysis of gene expression data for mN, mP, and mT organoids.
(B) The number of genes differentially expressed (DESeq adjusted p value < 0.05) among mN ($n = 7$), mP ($n = 6$), and mT ($n = 6$) organoids.
(C) Heatmap showing relative expression levels using Z score normalization among mN, mP, and mT organoids. Color key of Z score is shown.
(D) Venn diagrams show overlap of genes significantly differentially expressed in mP and mT relative to mN organoids. The p values for overlaps were determined by two-tailed Fisher's exact test.
(E) Genes with the largest fold changes in mP or mT relative to mN organoids.
(F) qRT-PCR validation of mN, mP and mT organoid gene expression changes. Values were normalized to mean levels in mN organoids. $n = 8$ mN, 7 mP, and 8 mT organoid cultures. Error bars indicate SEMs. * $p < 0.05$, ** $p < 0.01$, *** $p < 0.001$, and ns, not significant by two-tailed Student's t test.
See also [Figure S5](#) and [Table S5](#).

isoforms into their corresponding 4,155 genes. Some protein expression changes (e.g., 123/150 for downregulated and 96/151 for upregulated mP proteins) did not reflect corresponding transcriptional changes, indicating that protein stability may play a role in cancer progression, particularly in mP organoids ([Figure 6D](#)). Nonetheless, the proteomic data validated many of the expression changes identified by RNA-seq ([Figure 6D](#)), including upregulation of Gcnt3, Agr2, and Ugdh ([Table S6](#)). Additionally, of the 1,599 genes whose expression levels changed in mT relative to mN organoids that were measured by mass spectrometry, 301 (19%) showed corresponding protein changes ([Figure 6D](#)).

Gene Set Enrichment Analysis (GSEA) on the RNA-seq and proteomic data ([Subramanian et al., 2005](#)) revealed elevated

expression of genes and proteins involved in glutathione metabolism and biological oxidations in mP relative to mN organoids ([Figures 6E, S6B, and S6C](#) and [Table S7](#)), which is consistent with elevations in reactive oxygen species metabolism previously reported in *Kras*^{G12D} cells ([DeNicola et al., 2011; Ying et al., 2012](#)). Enrichment of proteins involved in glutathione metabolism was also found in mT relative to mN organoids ([Table S7](#)). Additionally, we identified a significant positive enrichment of proteins involved in the steroid biosynthesis, cholesterol biosynthesis, one carbon pool by folate, and pyrimidine metabolism pathways ([Figures 6E, S6B, and S6C](#) and [Table S7](#)), which is consistent with an earlier report ([Ying et al., 2012](#)). Similar pathways were enriched in mP relative to mN organoids (cholesterol biosynthesis, one carbon pool by folate, and pyrimidine

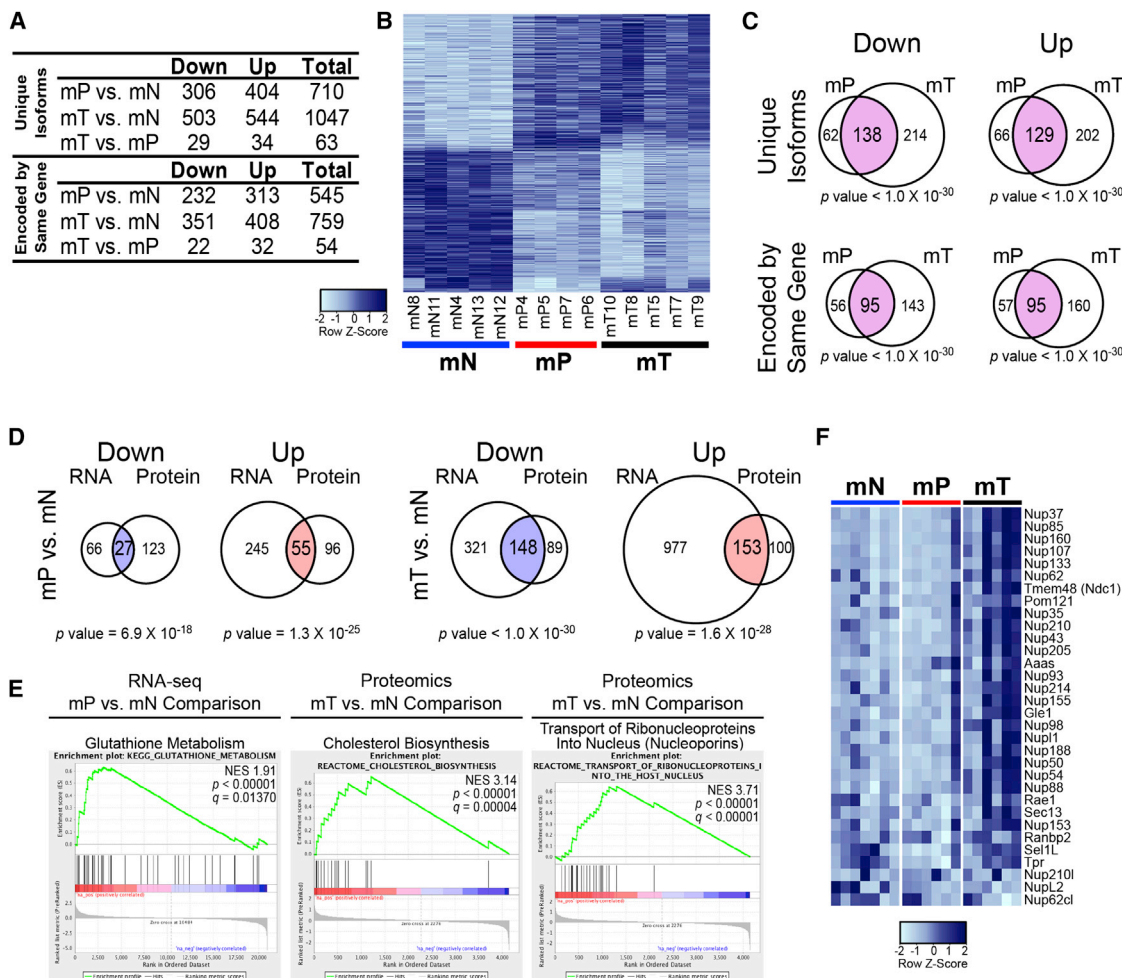


Figure 6. Proteomic Profiling of Murine Organoids Uncovers Molecular Pathways Linked to Pancreatic Cancer Progression

(A) Protein expression changes by iTRAQ proteomic analysis of murine organoids. Both unique protein isoforms and protein isoforms encoded by the same gene are included (adjusted p value < 0.1 by linear regression analysis).

(B) Heatmap of unique protein isoforms that differ (adjusted p value < 0.05) among mN, mP, and mT organoids. Color key of the Z score is shown.

(C) Venn diagrams showing overlaps between proteins differentially expressed (p < 0.05) in mP and mT relative to mN organoids. p values for overlaps were determined by two-tailed Fisher's exact test.

(D) Venn diagrams showing overlaps between genes and proteins found differentially expressed by RNA-seq and proteomic analyses (adjusted p < 0.05). p values for the overlaps were determined by two-tailed Fisher's exact test.

(E) Molecular pathways found enriched by GSEA analysis of RNA-seq and proteomic data. Normalized enrichment scores (NESs), p and q values are shown.

(F) Heatmap showing relative gene expression levels of nucleoporins in mN, mP, and mT organoids determined by RNA-seq. Color key of the Z score is shown. See also [Figure S6](#) and [Tables S6](#) and [S7](#).

metabolism) ([Figures S6B](#) and [S6C](#) and [Table S7](#)), whereas fatty acid metabolism and TCA cycle/respiratory electron transport pathways were downregulated ([Figure S6C](#) and [Table S7](#)). The increase in anabolic and decrease in catabolic pathways suggest that complex alterations in fatty acid and nucleotide metabolism occur during PDA progression.

Interestingly, we also found broad upregulation of the nucleoporin family at both the RNA and protein levels in the mT relative to mN organoids ([Figures 6E](#) and [6F](#) and [Table S6](#)). The individual nucleoporins NUP214, NUP153, and NUPL1 were previously identified in shRNA dropout screens in PDA cell lines ([Cheung et al., 2011; Shain et al., 2013](#)). Furthermore, amplification of

NUP153 was detected in one human PDA cancer cell line, and elevation of NUP88 was detected in human primary PDA ([Cheung et al., 2011; Gould et al., 2000; Shain et al., 2013](#)). This systematic analysis of molecular alterations in pancreatic organoids implicates nuclear transport as a pathway correlated with pancreatic cancer progression.

In Vivo Mouse and Human Validation of Candidates Associated with PDA Progression in Organoids

To demonstrate that the mouse organoid culture system represents a biological resource for the accurate discovery of genes associated with PDA progression, we selected 16 genes

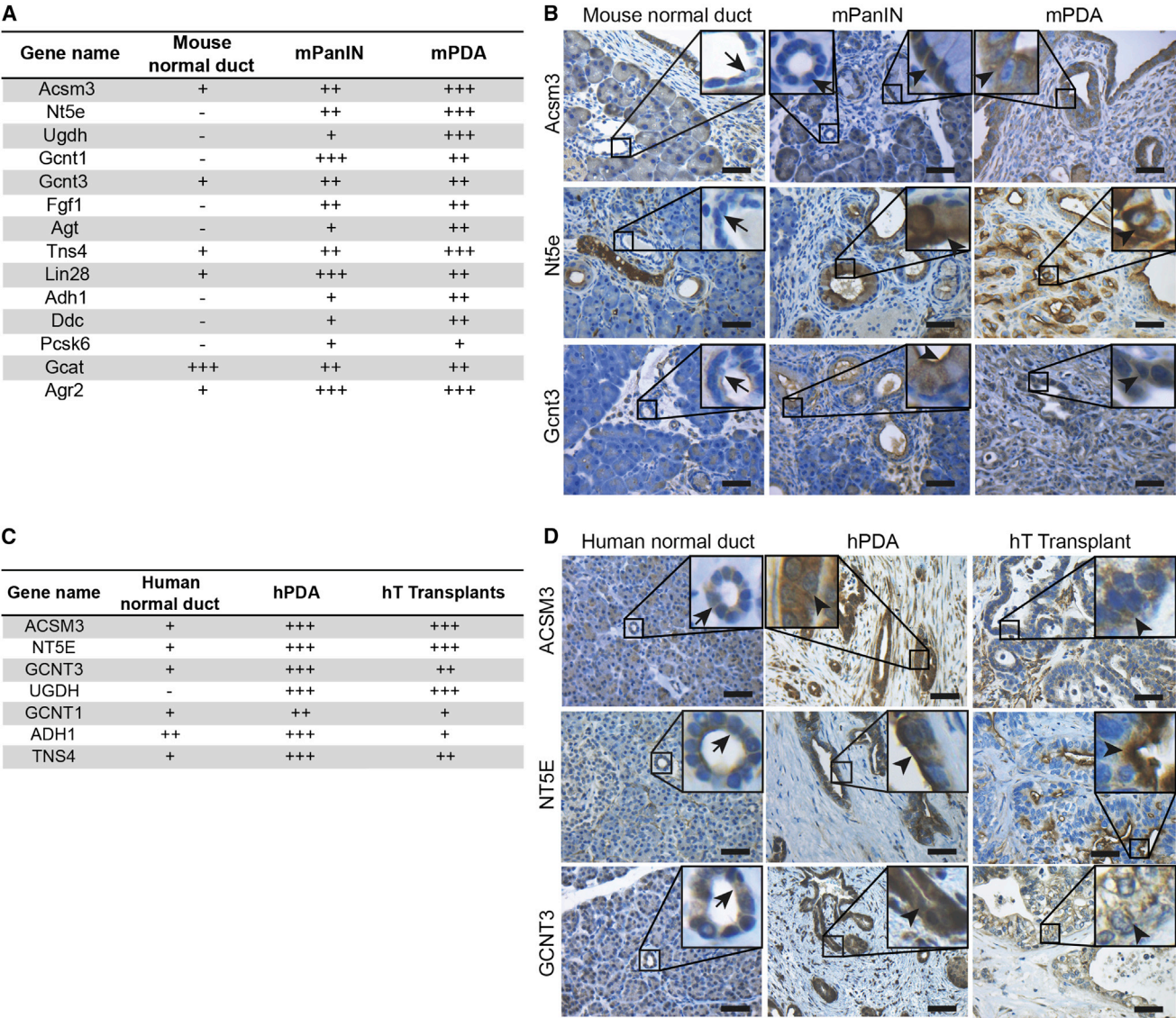


Figure 7. Increased Levels of ACSM3, NT5E, and GCNT3 Correlate with Mouse and Human PDA Progression

(A) IHC analysis of 14 candidate genes in mouse adjacent normal ducts, mPanIN and mPDA. Differential expression is indicated as – (negative), + (weak), ++ (moderate), or +++ (strong). Only the ductal component of the normal pancreas was scored.

(B) IHC analysis of Acsm3, Nt5e, and Gcnt3 in mouse normal ducts, mPanIN and mPDA tissues. Arrow indicates adjacent normal ducts in mPanIN tissues. Arrowhead indicates mPanIN or mPDA. Scale bars, 50 μ m.

(C) IHC analysis of seven candidate genes in human normal pancreas, hT orthotopic transplants, and PDA tissues. Differential expression is indicated as – (negative), + (weak), ++ (moderate), or +++ (strong). Only the ductal component of the normal pancreas was scored.

(D) IHC analysis of ACSM3, NT5E, and GCNT3 in human normal pancreas and PDA tissues. Arrow indicates normal ducts, and arrowhead indicates PDA. Scale bars, 50 μ m.

See also [Figure S7](#).

upregulated in mT organoids for validation in primary tissue specimens by IHC and immunofluorescence (IF) ([Figure 7A](#)). These 16 genes included enzymes, membrane proteins, structural proteins, and secreted ligands, which could represent candidate biomarkers and therapeutic targets. Of the 14 antibodies that generated a detectable signal on murine pancreatic tissue sections, 13 antibodies confirmed the increased expres-

sion of the candidate protein in mPanIN and mPDA lesions in concordance with the RNA-seq and proteomic data ([Figures 7A, 7B, and S7A](#)). 11 of the 13 candidate antibodies were compatible for evaluation in human tissues, and 7 of these candidates were upregulated in human PDA when compared to normal pancreatic ductal tissues ([Figures 7C, 7D, and S7B](#)). The high expression of many of these markers was recapitulated

in orthotopic transplants of hT organoids into *Nu/Nu* mice (Figure 7C). These results indicate that the organoid culture system accurately models PDA progression and can serve as a resource for the discovery and genetic dissection of pathways driving human pancreatic tumorigenesis.

DISCUSSION

We have established pancreatic organoids as a tractable and transplantable system to probe the molecular and cellular properties of neoplastic progression in mice and humans. In contrast to prior reports (Agbunag and Bar-Sagi, 2004; Rovira et al., 2010; Seaberg et al., 2004), our culture conditions prevent the rapid exhaustion of normal ductal cells in vitro and generate a normal ductal architecture following orthotopic transplantation. Importantly, the ability to passage and transplant both normal and neoplastic ductal cells enables a detailed analysis of molecular pathways and cellular biology that is not possible when neonatal pancreatic fragments are propagated in air-liquid interfaces or when induced pluripotent cells are employed (Agbunag and Bar-Sagi, 2004; Kim et al., 2013; Li et al., 2014). Our finding that nucleoporins are broadly upregulated in the neoplastic murine organoids, coupled with the known associations of nucleoporins to cell proliferation and cell transformation, presents a class of proteins to investigate in pancreatic cancer progression (Gould et al., 2000; Köhler and Hurt, 2010). Furthermore, the ability to systematically characterize human pancreatic cancer organoids that lack KRAS mutations, such as hT8, will reveal driver genes for PDA. Finally, because organoids can be readily established from small patient biopsies, they should hasten the development of personalized approaches for pancreatic cancer patients.

EXPERIMENTAL PROCEDURES

Animals

Trp53^{+/LSL-R172H}, *Kras^{+/LSL-G12D}*, and *Pdx1-Cre* strains in C57Bl/6 background were interbred to obtain *Pdx1-Cre; Kras^{+/LSL-G12D}* (KC) and *Pdx1-Cre; Kras^{+/LSL-G12D}; Trp53^{+/LSL-R172H}* (KPC) mice (Hingorani et al., 2005). The *R26^{LSL-YFP}* strain was interbred to get the desired genotype. C57Bl/6 and athymic *Nu/Nu* mice were purchased from Charles River Laboratory and Jackson Laboratory. All animal experiments were conducted in accordance with procedures approved by the IACUC at Cold Spring Harbor Laboratory (CSHL).

Murine Pancreatic Ductal Organoid Culture

Detailed procedures to isolate normal pancreatic ducts have been described previously (Huch et al., 2013a). In brief, normal and preneoplastic pancreatic ducts were manually picked after enzymatic digestion of pancreas with 0.012% (w/v) collagenase XI (Sigma) and 0.012% (w/v) dispase (GIBCO) in DMEM media containing 1% FBS (GIBCO) and were seeded in growth-factor-reduced (GFR) Matrigel (BD). For tumors and metastases, bulk tissues were minced and digested overnight with collagenase XI and dispase and embedded in GFR Matrigel.

Human Specimens

Pancreatic cancer tissues and adjacent normal pancreas were obtained from patients undergoing surgical resection at the University Medical Centre Utrecht Hospital, Memorial Sloan-Kettering Cancer Center (MSKCC), MD Anderson Cancer Center (MDACC), and Weill Cornell Medical College (WCMC). Normal pancreatic tissue was also obtained from islet transplant programs at

the University of Illinois at Chicago and University of Miami Miller School of Medicine. All human experiments were approved by the ethical committees of the University Medical Centre Utrecht or the IRBs of MSKCC, MDACC, WCMC, and CSHL. Written informed consent from the donors for research use of tissue in this study was obtained prior to acquisition of the specimen. Samples were confirmed to be tumor or normal based on pathological assessment.

Human Pancreatic Tumor and Normal Organoid Culture

Tumor tissue was minced and digested with collagenase II (5 mg/ml, GIBCO) in human complete medium (see below) at 37°C for a maximum of 16 hr. The material was further digested with TrypLE (GIBCO) for 15 min at 37°C, embedded in GFR Matrigel, and cultured in human complete medium (AddMEM/F12 medium supplemented with HEPES [1×, Invitrogen], Glutamax [1×, Invitrogen], penicillin/streptomycin [1×, Invitrogen], B27 [1×, Invitrogen], Primocin [1 mg/ml, InvivoGen], N-acetyl-L-cysteine [1 mM, Sigma], Wnt3a-conditioned medium [50% v/v], RSP01-conditioned medium [10% v/v, Calvin Kuo], Noggin-conditioned medium [10% v/v] or recombinant protein [0.1 μg/ml, Peprotech], epidermal growth factor [EGF, 50 ng/ml, Peprotech], Gastrin [10 nM, Sigma], fibroblast growth factor 10 [FGF10, 100 ng/ml, Peprotech], Nicotinamide [10 mM, Sigma], and A83-01 [0.5 μM, Tocris]).

Normal samples were processed as above, except that the collagenase digestion was done for a maximum of 2 hr in the presence of soybean trypsin inhibitor (1 mg/ml, Sigma). Following digestion, cells were embedded in GFR Matrigel and cultured in human complete medium with the addition of PGE2 (1 μM, Tocris).

Additional experimental details and methods can be found in the Extended Experimental Procedures.

ACCESSION NUMBERS

All RNA-seq data are available at Gene Expression Omnibus (GEO) under accession number GSE63348. The proteomic raw data are available at PeptideAtlas under accession number PASS00625. The targeted DNA-sequencing data are available at EMBL European Nucleotide Archive under the accession number ERP006373.

SUPPLEMENTAL INFORMATION

Supplemental Information includes Extended Experimental Procedures, seven figures, and seven tables and can be found with this article online at <http://dx.doi.org/10.1016/j.cell.2014.12.021>.

AUTHOR CONTRIBUTIONS

S.F.B. initiated the project, developed the methods for isolating mouse and human organoids, and characterized human organoids (Figures 1A, 3, 4B, 4D, and S4C and Tables S3 and S4). C.-I.H. developed transplantation models for organoids and performed shRNA knockdown and histological and karyotypic analyses (Figures 1A, 1E, 1G, 2A, 2C–2E, 4D, 7, S1A–S1C, S2A–S2F, S2H, S4A, S4B, S7A, and S7B and Tables S1, S2, and S4). L.A.B. performed RNA-seq on mouse organoids and analyzed RNA-seq and proteomic data (Figures 5, 6, S5B, and S6 and Tables S5, S6, and S7). I.I.C.C. conducted proteomic evaluation of mouse organoids and analyzed proteomic data (Figures 6 and S6C). D.D.E. developed mouse organoid methods and evaluated CA19-9 levels in human organoids (Figures 1A, 2A, 4C, S3, and S6 and Table S6). V.C. developed human organoid methods, performed molecular analyses of organoids, and prepared material for DNA-sequencing and sequencing of *Kras* (Figures 1C, 1D, 3A, 3D, 4A, S1D–S1F, and S5A and Tables S3, S4, and S5). M.J. performed and analyzed the DNA sequencing of human organoids (Figure 3D and Table S4). Mouse and human organoid preparation and characterization was performed by M.P.-S., H.T., M.S.S., T.O., D.Ö., A.H.-S., C.M.A.-A., M.L., E.E., B.A., M.E.F., G.N.Y., G.B., B.D., B.C., K.W., K.H.Y., Y.P., M. Huch, A.G., F.H.M.M., and S.D.L. Sequencing analyses were performed by Y.H., Y.J., M. Hammell, I.J.N., E.C., and R.v.B. Pathological analyses were

performed by G.J.O., R.H.H., D.S.K., O.B., and C.I.-D. Surgical resections and tissue dissection were performed by I.Q.M. and I.H.B.R. Proteomic development was performed by D.J.P., K.D.R., and J.P.W. Overall study management was conducted by D.A.T., H.C., and R.G.J.V. S.F.B., D.D.E., L.A.B., M.E.F., C.H., H.T., V.C., M.P.S., R.G.J.V., H.C., I.I.C.C., and D.A.T. contributed to manuscript writing.

ACKNOWLEDGMENTS

We thank Peter Kapitein and Jan Schuurman from Inspire 2 Live for helping to establish the collaboration between D.A.T. and H.C. We also thank H. Begthel and J. Korving for technical assistance. This work was performed with assistance from the CSHL Proteomic, Histology, DNA Sequencing, Antibody, and Bioinformatics Shared Resources, which are supported by the Cancer Center Support Grant 5P30CA045508. D.A.T. is a distinguished scholar of the Lustgarten Foundation and Director of the Lustgarten Foundation-designated Laboratory of Pancreatic Cancer Research. D.A.T. is also supported by the Cold Spring Harbor Laboratory Association, the Carcinoid Foundation, PCUK, and the David Rubinstein Center for Pancreatic Cancer Research at MSKCC. In addition, we are grateful for support from the following: Stand Up to Cancer/KWF (H.C.), the STARR foundation (I7-A718 for D.A.T.), DOD (W81XWH-13-PRCRP-IA for D.A.T.), the Sol Goldman Pancreatic Cancer Research Center (R.H.H.), the Italian Ministry of Health (FIRB - RBAP10AHJ for V.C.), Sociedad Española de Oncología Médica (SEOM for M.P.S.), Louis Morin Charitable Trust (M.E.F.), the Swedish Research Council (537-2013-7277 for D.Ö.), The Kempe Foundations (JCK-1301 for D.Ö.) and the Swedish Society of Medicine (SLS-326921, SLS-250831 for D.Ö.), the Damon Runyon Cancer Research Foundation (DRG-2165-13 for I.I.C.C.), the Human Frontiers Science Program (LT000403/2014 for E.E.), the Weizmann Institute of Science Women in Science Award (E.E.), the American Cancer Society (PF-13-317-01-CSM for C.M.A.A.), the Hearst Foundation (A.H.S.), and the NIH (5P30CA45508-26, 5P50CA101955-07, 1U10CA180944-01, 5U01CA168409-3, and 1R01CA190092-01 for D.A.T.; CA62924 for R.H.H.; CA134292 for S.D.L.; 5T32CA148056 for L.A.B. and D.D.E.; and CA101955 UAB/UMN SPORE for L.A.B.). In addition, S.F.B. and M.H. are supported by KWF/PF-HUBR 2007-3956, A.G. is supported by EU/232814-StemCellMark, and R.G.J.V. is supported by GenomiCs.nl (CGC). M.J., R.B., and E.C. are supported by the CancerGenomics.nl (NWO Gravitation) program. Ralph Hruban receives royalty payments from Myriad Genetics for the PalB2 inventions. Hans Clevers and Meritxell Huch have patents pending and granted on the organoid technology.

Received: August 1, 2014

Revised: November 24, 2014

Accepted: December 10, 2014

Published: December 31, 2014

REFERENCES

- Abbruzzese, J.L., and Hess, K.R. (2014). New option for the initial management of metastatic pancreatic cancer? *J. Clin. Oncol.* 32, 2405–2407.
- Agbunag, C., and Bar-Sagi, D. (2004). Oncogenic K-ras drives cell cycle progression and phenotypic conversion of primary pancreatic duct epithelial cells. *Cancer Res.* 64, 5659–5663.
- Aguirre, A.J., Bardeesy, N., Sinha, M., Lopez, L., Tuveson, D.A., Horner, J., Redston, M.S., and DePinho, R.A. (2003). Activated Kras and Ink4a/Arf deficiency cooperate to produce metastatic pancreatic ductal adenocarcinoma. *Genes Dev.* 17, 3112–3126.
- Bardeesy, N., Aguirre, A.J., Chu, G.C., Cheng, K.H., Lopez, L.V., Hezel, A.F., Feng, B., Brennan, C., Weissleder, R., Mahmood, U., et al. (2006). Both p16(Ink4a) and the p19(Arf)-p53 pathway constrain progression of pancreatic adenocarcinoma in the mouse. *Proc. Natl. Acad. Sci. USA* 103, 5947–5952.
- Barker, N., Huch, M., Kujala, P., van de Wetering, M., Snippert, H.J., van Es, J.H., Sato, T., Stange, D.E., Begthel, H., van den Born, M., et al. (2010). Lgr5(+ve) stem cells drive self-renewal in the stomach and build long-lived gastric units in vitro. *Cell Stem Cell* 6, 25–36.
- Beatty, G.L., Chiorean, E.G., Fishman, M.P., Saboury, B., Teitelbaum, U.R., Sun, W., Huhn, R.D., Song, W., Li, D., Sharp, L.L., et al. (2011). CD40 agonists alter tumor stroma and show efficacy against pancreatic carcinoma in mice and humans. *Science* 331, 1612–1616.
- Cheung, H.W., Cowley, G.S., Weir, B.A., Boehm, J.S., Rusin, S., Scott, J.A., East, A., Ali, L.D., Lizotte, P.H., Wong, T.C., et al. (2011). Systematic investigation of genetic vulnerabilities across cancer cell lines reveals lineage-specific dependencies in ovarian cancer. *Proc. Natl. Acad. Sci. USA* 108, 12372–12377.
- Cleveland, M.H., Sawyer, J.M., Afelik, S., Jensen, J., and Leach, S.D. (2012). Exocrine ontogenies: on the development of pancreatic acinar, ductal and centroacinar cells. *Semin. Cell Dev. Biol.* 23, 711–719.
- De La O, J.P., Emerson, L.L., Goodman, J.L., Froebe, S.C., Illum, B.E., Curtis, A.B., and Murtaugh, L.C. (2008). Notch and Kras reprogram pancreatic acinar cells to ductal intraepithelial neoplasia. *Proc. Natl. Acad. Sci. USA* 105, 18907–18912.
- DeNicola, G.M., Karreth, F.A., Humpton, T.J., Gopinathan, A., Wei, C., Frese, K., Mangal, D., Yu, K.H., Yeo, C.J., Calhoun, E.S., et al. (2011). Oncogene-induced Nrf2 transcription promotes ROS detoxification and tumorigenesis. *Nature* 475, 106–109.
- Dumartin, L., Whiteman, H.J., Weeks, M.E., Hariharan, D., Dmitrovic, B., Iacobuzio-Donahue, C.A., Brentnall, T.A., Bronner, M.P., Feakins, R.M., Timms, J.F., et al. (2011). AGR2 is a novel surface antigen that promotes the dissemination of pancreatic cancer cells through regulation of cathepsins B and D. *Cancer Res.* 71, 7091–7102.
- Erkan, M., Reiser-Erkan, C., Michalski, C.W., Deucker, S., Sauliunaite, D., Streit, S., Esposito, I., Friess, H., and Kleeff, J. (2009). Cancer-stellate cell interactions perpetuate the hypoxia-fibrosis cycle in pancreatic ductal adenocarcinoma. *Neoplasia* 11, 497–508.
- Frese, K.K., Neesse, A., Cook, N., Bapiro, T.E., Lolkema, M.P., Jodrell, D.I., and Tuveson, D.A. (2012). nab-Paclitaxel potentiates gemcitabine activity by reducing cytidine deaminase levels in a mouse model of pancreatic cancer. *Cancer Discov.* 2, 260–269.
- Gao, D., Vela, I., Sboner, A., Iaquina, P.J., Karthaus, W.R., Gopalan, A., Downing, C., Wanjala, J.N., Undvall, E.A., Arora, V.K., et al. (2014). Organoid cultures derived from patients with advanced prostate cancer. *Cell* 159, 176–187.
- Gidekel Friedlander, S.Y., Chu, G.C., Snyder, E.L., Girnius, N., Dibelius, G., Crowley, D., Vasile, E., DePinho, R.A., and Jacks, T. (2009). Context-dependent transformation of adult pancreatic cells by oncogenic K-Ras. *Cancer Cell* 16, 379–389.
- Gould, V.E., Martinez, N., Orucevic, A., Schneider, J., and Alonso, A. (2000). A novel, nuclear pore-associated, widely distributed molecule overexpressed in oncogenesis and development. *Am. J. Pathol.* 157, 1605–1613.
- Guerra, C., Mijimolle, N., Dhawahir, A., Dubus, P., Barradas, M., Serrano, M., Campuzano, V., and Barbacid, M. (2003). Tumor induction by an endogenous K-ras oncogene is highly dependent on cellular context. *Cancer Cell* 4, 111–120.
- Habbe, N., Shi, G., Meguid, R.A., Fendrich, V., Esni, F., Chen, H., Feldmann, G., Stoffers, D.A., Konieczny, S.F., Leach, S.D., and Maitra, A. (2008). Spontaneous induction of murine pancreatic intraepithelial neoplasia (mPanIN) by acinar cell targeting of oncogenic Kras in adult mice. *Proc. Natl. Acad. Sci. USA* 105, 18913–18918.
- Hingorani, S.R., Petricoin, E.F., Maitra, A., Rajapakse, V., King, C., Jacobetz, M.A., Ross, S., Conrads, T.P., Veenstra, T.D., Hitt, B.A., et al. (2003). Preinvasive and invasive ductal pancreatic cancer and its early detection in the mouse. *Cancer Cell* 4, 437–450.
- Hingorani, S.R., Wang, L., Multani, A.S., Combs, C., Deramandt, T.B., Hruban, R.H., Rustgi, A.K., Chang, S., and Tuveson, D.A. (2005). Trp53R172H and KrasG12D cooperate to promote chromosomal instability and widely metastatic pancreatic ductal adenocarcinoma in mice. *Cancer Cell* 7, 469–483.
- Huch, M., Bonfanti, P., Boj, S.F., Sato, T., Loomans, C.J., van de Wetering, M., Sojoodi, M., Li, V.S., Schuijers, J., Gracanin, A., et al. (2013a). Unlimited in vitro

expansion of adult bi-potent pancreas progenitors through the Lgr5/R-spondin axis. *EMBO J.* 32, 2708–2721.

Huch, M., Dorrell, C., Boj, S.F., van Es, J.H., Li, V.S., van de Wetering, M., Sato, T., Hamer, K., Sasaki, N., Finegold, M.J., et al. (2013b). In vitro expansion of single Lgr5+ liver stem cells induced by Wnt-driven regeneration. *Nature* 494, 247–250.

Jacobetz, M.A., Chan, D.S., Neesse, A., Bapiro, T.E., Cook, N., Frese, K.K., Feig, C., Nakagawa, T., Caldwell, M.E., Zecchini, H.I., et al. (2013). Hyaluronan impairs vascular function and drug delivery in a mouse model of pancreatic cancer. *Gut* 62, 112–120.

Karthauss, W.R., Iaquina, P.J., Drost, J., Gracanin, A., van Boxtel, R., Wongvipat, J., Dowling, C.M., Gao, D., Begthel, H., Sachs, N., et al. (2014). Identification of multipotent luminal progenitor cells in human prostate organoid cultures. *Cell* 159, 163–175.

Kim, M.P., Evans, D.B., Wang, H., Abbruzzese, J.L., Fleming, J.B., and Gallick, G.E. (2009). Generation of orthotopic and heterotopic human pancreatic cancer xenografts in immunodeficient mice. *Nat. Protoc.* 4, 1670–1680.

Kim, J., Hoffman, J.P., Alpaugh, R.K., Rhim, A.D., Reichert, M., Stanger, B.Z., Furth, E.E., Sepulveda, A.R., Yuan, C.X., Won, K.J., et al. (2013). An iPSC line from human pancreatic ductal adenocarcinoma undergoes early to invasive stages of pancreatic cancer progression. *Cell Rep.* 3, 2088–2099.

Köhler, A., and Hurt, E. (2010). Gene regulation by nucleoporins and links to cancer. *Mol. Cell* 38, 6–15.

Koong, A.C., Mehta, V.K., Le, Q.T., Fisher, G.A., Terris, D.J., Brown, J.M., Bastidas, A.J., and Vierra, M. (2000). Pancreatic tumors show high levels of hypoxia. *Int. J. Radiat. Oncol. Biol. Phys.* 48, 919–922.

Kopp, J.L., von Figura, G., Mayes, E., Liu, F.F., Dubois, C.L., Morris, J.P., 4th, Pan, F.C., Akiyama, H., Wright, C.V., Jensen, K., et al. (2012). Identification of Sox9-dependent acinar-to-ductal reprogramming as the principal mechanism for initiation of pancreatic ductal adenocarcinoma. *Cancer Cell* 22, 737–750.

Lee, J., Sugiyama, T., Liu, Y., Wang, J., Gu, X., Lei, J., Markmann, J.F., Miyazaki, S., Miyazaki, J., Szot, G.L., et al. (2013). Expansion and conversion of human pancreatic ductal cells into insulin-secreting endocrine cells. *eLife* 2, e00940.

Li, X., Nadauld, L., Ootani, A., Corney, D.C., Pai, R.K., Gevaert, O., Cantrell, M.A., Rack, P.G., Neal, J.T., Chan, C.W., et al. (2014). Oncogenic transformation of diverse gastrointestinal tissues in primary organoid culture. *Nat. Med.* 20, 769–777.

Makovitzky, J. (1986). The distribution and localization of the monoclonal antibody-defined antigen 19-9 (CA19-9) in chronic pancreatitis and pancreatic carcinoma. An immunohistochemical study. *Virchows Arch. B Cell Pathol. Incl. Mol. Pathol.* 51, 535–544.

Means, A.L., Meszoely, I.M., Suzuki, K., Miyamoto, Y., Rustgi, A.K., Coffey, R.J., Jr., Wright, C.V.E., Stoffers, D.A., and Leach, S.D. (2005). Pancreatic epithelial plasticity mediated by acinar cell transdifferentiation and generation of nestin-positive intermediates. *Development* 132, 3767–3776.

Morris, J.P., 4th, Cano, D.A., Sekine, S., Wang, S.C., and Hebrok, M. (2010). Beta-catenin blocks Kras-dependent reprogramming of acini into pancreatic cancer precursor lesions in mice. *J. Clin. Invest.* 120, 508–520.

Neesse, A., Frese, K.K., Chan, D.S., Bapiro, T.E., Howat, W.J., Richards, F.M., Ellenrieder, V., Jodrell, D.I., and Tuveson, D.A. (2014). SPARC independent drug delivery and antitumour effects of nab-paclitaxel in genetically engineered mice. *Gut* 63, 974–983.

Olive, K.P., Jacobetz, M.A., Davidson, C.J., Gopinathan, A., McIntyre, D., Honess, D., Madhu, B., Goldgraben, M.A., Caldwell, M.E., Allard, D., et al. (2009). Inhibition of Hedgehog signaling enhances delivery of chemotherapy in a mouse model of pancreatic cancer. *Science* 324, 1457–1461.

Pérez-Mancera, P.A., Guerra, C., Barbacid, M., and Tuveson, D.A. (2012). What we have learned about pancreatic cancer from mouse models. *Gastroenterology* 142, 1079–1092.

Prasad, N.B., Biankin, A.V., Fukushima, N., Maitra, A., Dhara, S., Elkahoul, A.G., Hruban, R.H., Goggins, M., and Leach, S.D. (2005). Gene expression

profiles in pancreatic intraepithelial neoplasia reflect the effects of Hedgehog signaling on pancreatic ductal epithelial cells. *Cancer Res.* 65, 1619–1626.

Provenzano, P.P., Cuevas, C., Chang, A.E., Goel, V.K., Von Hoff, D.D., and Hingorani, S.R. (2012). Enzymatic targeting of the stroma ablates physical barriers to treatment of pancreatic ductal adenocarcinoma. *Cancer Cell* 21, 418–429.

Pylayeva-Gupta, Y., Lee, K.E., Hajdu, C.H., Miller, G., and Bar-Sagi, D. (2012). Oncogenic Kras-induced GM-CSF production promotes the development of pancreatic neoplasia. *Cancer Cell* 21, 836–847.

Rahib, L., Smith, B.D., Aizenberg, R., Rosenzweig, A.B., Fleshman, J.M., and Matrisian, L.M. (2014). Projecting cancer incidence and deaths to 2030: the unexpected burden of thyroid, liver, and pancreas cancers in the United States. *Cancer Res.* 74, 2913–2921.

Ray, K.C., Bell, K.M., Yan, J., Gu, G., Chung, C.H., Washington, M.K., and Means, A.L. (2011). Epithelial tissues have varying degrees of susceptibility to Kras(G12D)-initiated tumorigenesis in a mouse model. *PLoS ONE* 6, e16786.

Rovira, M., Scott, S.G., Liss, A.S., Jensen, J., Thayer, S.P., and Leach, S.D. (2010). Isolation and characterization of centroacinar/terminal ductal progenitor cells in adult mouse pancreas. *Proc. Natl. Acad. Sci. USA* 107, 75–80.

Rubio-Viqueira, B., Jimeno, A., Cusatis, G., Zhang, X., Iacobuzio-Donahue, C., Karikari, C., Shi, C., Danenberg, K., Danenberg, P.V., Kuramochi, H., et al. (2006). An in vivo platform for translational drug development in pancreatic cancer. *Clin. Cancer Res.* 12, 4652–4661.

Ryan, D.P., Hong, T.S., and Bardeesy, N. (2014). Pancreatic adenocarcinoma. *N. Engl. J. Med.* 371, 1039–1049.

Sato, T., Vries, R.G., Snippert, H.J., van de Wetering, M., Barker, N., Stange, D.E., van Es, J.H., Abo, A., Kujala, P., Peters, P.J., and Clevers, H. (2009). Single Lgr5 stem cells build crypt-villus structures in vitro without a mesenchymal niche. *Nature* 459, 262–265.

Sato, T., Stange, D.E., Ferrante, M., Vries, R.G., Van Es, J.H., Van den Brink, S., Van Houdt, W.J., Pronk, A., Van Gorp, J., Siersema, P.D., and Clevers, H. (2011). Long-term expansion of epithelial organoids from human colon, adenoma, adenocarcinoma, and Barrett's epithelium. *Gastroenterology* 141, 1762–1772.

Sawey, E.T., Johnson, J.A., and Crawford, H.C. (2007). Matrix metalloproteinase 7 controls pancreatic acinar cell transdifferentiation by activating the Notch signaling pathway. *Proc. Natl. Acad. Sci. USA* 104, 19327–19332.

Seaberg, R.M., Smukler, S.R., Kieffer, T.J., Enikolopov, G., Asghar, Z., Wheeler, M.B., Korbitt, G., and van der Kooy, D. (2004). Clonal identification of multipotent precursors from adult mouse pancreas that generate neural and pancreatic lineages. *Nat. Biotechnol.* 22, 1115–1124.

Shain, A.H., Salari, K., Giacomini, C.P., and Pollack, J.R. (2013). Integrative genomic and functional profiling of the pancreatic cancer genome. *BMC Genomics* 14, 624.

Sharma, S.V., Haber, D.A., and Settleman, J. (2010). Cell line-based platforms to evaluate the therapeutic efficacy of candidate anticancer agents. *Nat. Rev. Cancer* 10, 241–253.

Siegel, R., Naishadham, D., and Jemal, A. (2013). Cancer statistics, 2013. *CA Cancer J. Clin.* 63, 11–30.

Subramanian, A., Tamayo, P., Mootha, V.K., Mukherjee, S., Ebert, B.L., Gillette, M.A., Paulovich, A., Pomeroy, S.L., Golub, T.R., Lander, E.S., and Mesirov, J.P. (2005). Gene set enrichment analysis: a knowledge-based approach for interpreting genome-wide expression profiles. *Proc. Natl. Acad. Sci. USA* 102, 15545–15550.

Villarroel, M.C., Rajeshkumar, N.V., Garrido-Laguna, I., De Jesus-Acosta, A., Jones, S., Maitra, A., Hruban, R.H., Eshleman, J.R., Klein, A., Laheru, D., et al. (2011). Personalizing cancer treatment in the age of global genomic analyses: PALB2 gene mutations and the response to DNA damaging agents in pancreatic cancer. *Mol. Cancer Ther.* 10, 3–8.

- von Figura, G., Fukuda, A., Roy, N., Liku, M.E., Morris Iv, J.P., Kim, G.E., Russ, H.A., Firpo, M.A., Mulvihill, S.J., Dawson, D.W., et al. (2014). The chromatin regulator Brg1 suppresses formation of intraductal papillary mucinous neoplasm and pancreatic ductal adenocarcinoma. *Nat. Cell Biol.* **16**, 255–267.
- Wiese, S., Reidegeld, K.A., Meyer, H.E., and Warscheid, B. (2007). Protein labeling by iTRAQ: a new tool for quantitative mass spectrometry in proteome research. *Proteomics* **7**, 340–350.
- Ying, H., Kimmelman, A.C., Lyssiotis, C.A., Hua, S., Chu, G.C., Fletcher-Sanikone, E., Locasale, J.W., Son, J., Zhang, H., Coloff, J.L., et al. (2012). Oncogenic Kras maintains pancreatic tumors through regulation of anabolic glucose metabolism. *Cell* **149**, 656–670.
- Zhao, L.L., Zhang, T., Liu, B.R., Liu, T.F., Tao, N., and Zhuang, L.W. (2014). Construction of pancreatic cancer double-factor regulatory network based on chip data on the transcriptional level. *Mol. Biol. Rep.* **41**, 2875–2883.

Engineering Complex Synthetic Transcriptional Programs with CRISPR RNA Scaffolds

Jesse G. Zalatan,^{1,2,9} Michael E. Lee,^{5,6} Ricardo Almeida,^{1,2} Luke A. Gilbert,^{1,2,7} Evan H. Whitehead,^{1,3,10} Marie La Russa,^{1,3,4,10} Jordan C. Tsai,^{1,2} Jonathan S. Weissman,^{1,2,7,8} John E. Dueber,^{5,6} Lei S. Qi,^{1,3,8,10,*} and Wendell A. Lim^{1,2,3,8,*}

¹Department of Cellular and Molecular Pharmacology

²Howard Hughes Medical Institute

³UCSF Center for Systems and Synthetic Biology

⁴Biomedical Sciences Graduate Program

University of California San Francisco, San Francisco, CA 94158, USA

⁵Department of Bioengineering

⁶Energy Biosciences Institute

⁷Center for RNA Systems Biology

University of California, Berkeley, Berkeley, CA 94720, USA

⁸California Institute for Quantitative Biomedical Research, San Francisco, CA 94158, USA

⁹Present address: Department of Chemistry, University of Washington, Seattle, WA 98195, USA

¹⁰Present address: Department of Bioengineering, Department of Chemical and Systems Biology and ChEM-H, Stanford University, Stanford, CA 94305, USA

*Correspondence: slqi@stanford.edu (L.S.Q.), wendell.lim@ucsf.edu (W.A.L.)

<http://dx.doi.org/10.1016/j.cell.2014.11.052>

SUMMARY

Eukaryotic cells execute complex transcriptional programs in which specific loci throughout the genome are regulated in distinct ways by targeted regulatory assemblies. We have applied this principle to generate synthetic CRISPR-based transcriptional programs in yeast and human cells. By extending guide RNAs to include effector protein recruitment sites, we construct modular scaffold RNAs that encode both target locus and regulatory action. Sets of scaffold RNAs can be used to generate synthetic multigene transcriptional programs in which some genes are activated and others are repressed. We apply this approach to flexibly redirect flux through a complex branched metabolic pathway in yeast. Moreover, these programs can be executed by inducing expression of the dCas9 protein, which acts as a single master regulatory control point. CRISPR-associated RNA scaffolds provide a powerful way to construct synthetic gene expression programs for a wide range of applications, including rewiring cell fates or engineering metabolic pathways.

INTRODUCTION

Eukaryotic cells achieve many different states by executing complex transcriptional programs that allow a single genome to be interpreted in numerous, distinct ways. In these programs, specific loci throughout the genome must be regulated independently. For example, during development, it is often critical to activate sets of genes associated with a new cell fate while

simultaneously repressing sets of genes associated with a prior or alternative fate. Similarly, environmental conditions often trigger shifts in metabolic state, which requires activating a new set of enzymes and repressing other previously expressed enzymes, leading to new metabolic fluxes. These complex multi-locus, multi-directional expression programs are encoded largely by the pattern of transcriptional activators, repressors, or other regulators that assemble at distinct sites in the genome. Reprogramming these instructions to produce a different cell type or state thus requires precisely targeted changes in gene expression over a broad set of genes.

How might we engineer novel gene expression programs that match the sophistication of natural programs? Such capabilities would provide powerful tools to probe how changes in gene expression programs lead to diverse cell types. These tools would also provide the ability to engineer more sophisticated designer cell types for therapeutic or biotechnological applications. Although a number of transcriptional engineering platforms have been developed, there are major constraints for constructing complex transcriptional programs. For example, synthetic transcription factors (such as designed zinc fingers or transcription activator-like [TAL] effectors) can target a specific regulatory action to a key genomic locus, but it is challenging to simultaneously target many loci in parallel because each DNA-binding protein must be individually designed and tested (Gaj et al., 2013). The bacterial type II CRISPR (clustered regularly interspaced short palindromic repeats) interference system (CRISPRi) provides an alternative suite of tools for genome regulation (Qi et al., 2013). In particular, a catalytically inactive Cas9 (dCas9) protein, which lacks endonuclease activity, can be used to flexibly target many loci in parallel by using Cas9-binding guide RNAs that recognize target DNA sequences based only on predictable Watson-Crick base pairing. CRISPRi regulation can be used to achieve activation or repression by fusing dCas9 to

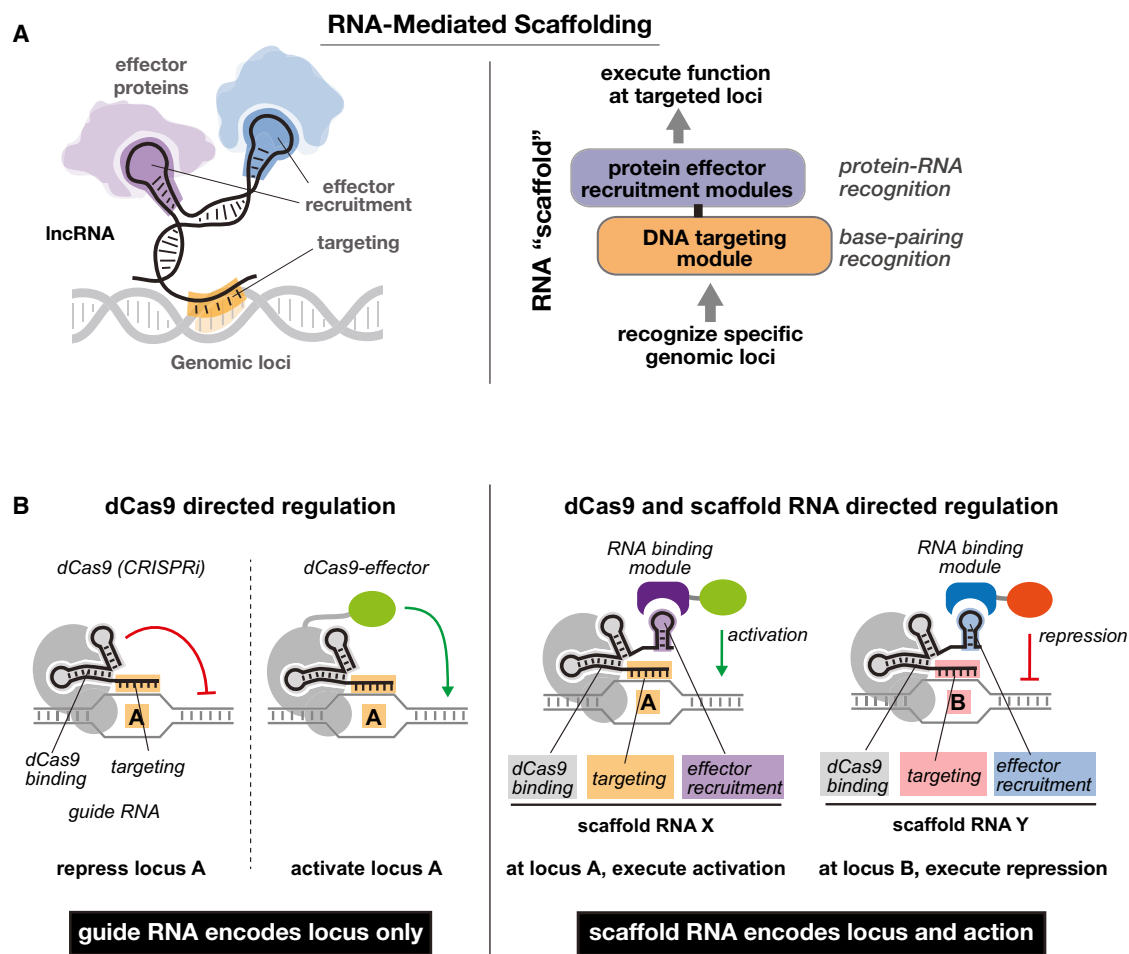


Figure 1. Genomic Regulatory Programming Using CRISPR and Multi-Domain Scaffolding RNAs

(A) lncRNA molecules may act as scaffolds to physically assemble epigenetic modifiers at their genomic targets. Modular RNA structures can encode domains for protein binding and DNA targeting to colocalize proteins to genomic loci.

(B) CRISPR RNA scaffold-based recruitment allows simultaneous regulation of independent gene targets. The minimal CRISPRi system silences target genes when dCas9 and an sgRNA assemble to physically block transcription. Fusing dCas9 to transcriptional activators or repressors provides additional functionality. When function is encoded in dCas9 (CRISPRi) or dCas9-effector fusion proteins, the sgRNA recruits the same function to every target site. To encode both target and function in a scaffold RNA, sgRNA molecules are extended with additional domains to recruit RNA-binding proteins that are fused to functional effectors. This approach allows distinct types of regulation to be executed at individual target loci, thus allowing simultaneous activation and repression.

activator or repressor modules (Gilbert et al., 2013; Mali et al., 2013a), but these direct protein fusions are constrained to only one direction of regulation. Thus, it remains challenging to engineer regulatory programs in which many loci are targeted simultaneously but with distinct types of regulation at each locus.

To develop a platform for synthetic genome regulation that allows locus-specific action, we took inspiration from natural regulatory systems that encode both target specificity and regulatory function in the same molecule. In cell-signaling pathways, scaffold proteins act to physically assemble interacting components so that functional outcomes can be precisely controlled in time and space (Good et al., 2011). Similar scaffolding principles apply in genome organization, wherein, for example, long non-coding RNA (lncRNA) molecules are proposed to act as assembly scaffolds that recruit key epigenetic modifiers to specific genomic loci (Figure 1A) (Rinn and Chang, 2012; Spitale et al.,

2011). The idea that RNA can be used to coordinate biological assemblies has important implications for engineering. RNA is inherently modular and programmable: DNA targets can be recognized by base pairing, and modular RNA-protein interaction domains can be used to recruit specific proteins (Figure 1A). The ability of engineered RNA scaffolds to coordinate functional protein assemblies has already been elegantly demonstrated (Delebecque et al., 2011).

To implement a synthetic, modular RNA-based system for locus-specific transcriptional programming, we can extend the CRISPR single-guide RNA (sgRNA) sequence with modular RNA domains that recruit RNA-binding proteins. This approach converts the sgRNA into a scaffold RNA (scRNA) that physically links DNA binding and protein recruitment activities (Figure 1B). Critically, a single scRNA molecule encodes both information about the target locus and instructions about what regulatory

function to execute at that locus. This approach allows multidirectional regulation (i.e., simultaneous activation and repression) of different target genes as part of the same regulatory program. Engineering multivalent RNA recruitment sites on each scRNA offers the further possibility of independently tuning the strength of activation or repression at each target site. The potential viability of this approach is supported by a recent report showing that a sgRNA extended with MS2 hairpins can recruit activators to a reporter gene in human cells (Mali et al., 2013a).

Here, we demonstrate that CRISPR sgRNAs can be repurposed as scaffolding molecules to recruit transcriptional activators or repressors, thus enabling flexible and parallel programmable locus-specific regulation. We use the budding yeast *S. cerevisiae* as a testbed to identify three orthogonal RNA-protein binding modules and to optimize scRNA designs for single and multivalent recruitment sites. We show that the system developed in yeast also functions efficiently in human cells to regulate reporter and endogenous target genes, and we extend its scope to include recruitment of chromatin modifiers for gene repression. We then demonstrate the use of CRISPR scaffold RNA molecules to construct synthetic multigene expression programs. Specifically, we are able to regulate multiple genes in a highly branched biosynthetic pathway in yeast to express key enzymes in alternative combinations. These synthetic transcriptional programs, by combinatorially altering metabolic organization, allow us to flexibly redirect the pathway between five distinct possible product output states. Finally, we show that dCas9 can act as a master regulator of these gene expression programs, receiving input signals and acting as a single control point to execute a multigene response encompassing simultaneous activation and repression of downstream target genes.

RESULTS

CRISPR RNA Scaffolds Efficiently Activate Gene Expression in Yeast

The minimal sgRNA previously used in CRISPR engineering consists of several modular domains: a 20 nucleotide variable DNA-targeting sequence and two structured RNA domains—dCas9-binding and 3' tracrRNA—which are necessary for proper structure formation and binding to Cas9 (Jinek et al., 2012; 2014; Nishimasu et al., 2014). Here, to generate scaffold RNA (scRNA) constructs with additional protein recruitment capabilities, we first introduced a single RNA hairpin domain to the 3' end of the sgRNA, connected by a two-base linker. For these recruitment RNA modules, we used the well-characterized viral RNA sequences MS2, PP7, and com, which are recognized by the MCP, PCP, and Com RNA-binding proteins, respectively. We fused the transcriptional activation domain VP64 to each of the corresponding RNA-binding proteins.

We first tested the CRISPR scRNA platform in yeast. A strain with a tet promoter driving a fluorescent protein reporter was transformed to express dCas9, scRNAs targeting the tet operator, and the corresponding VP64 fusion proteins. We observed significant reporter gene expression using each of the three RNA-binding recruitment modules (Figure 2A). scRNA constructs with recruitment hairpin domains connected to the sgRNA by linkers longer than two bases (up to 20 bases) gave

weaker reporter gene expression (Figure S1A available online). scRNA designs with recruitment sequences attached to the 5' end of the sgRNA gave no significant activation (Figure S1B). Northern blot analysis indicated that the 5' extended sequence was degraded (Figure S2).

Gene activation mediated by scRNA recruitment of VP64 was substantially greater than that for the direct dCas9-VP64 fusion protein. Both MCP and PCP bind to their RNA targets as dimers (Chao et al., 2008), which may account for some of the difference. The oligomerization state of the Com protein has not been directly determined, but functional data consistent with a monomer has been reported (Wulczyn and Kahmann, 1991).

Three RNA-Protein Recruitment Modules Act in an Orthogonal Manner

To determine whether there is crosstalk between RNA hairpins and non-cognate-binding proteins (e.g., MS2 RNA recruiting the PCP protein), we expressed all three RNA hairpin designs (MS2, PP7, and com) in yeast strains containing either the MCP, PCP, or Com fusion proteins. We used a 7× tetO reporter to maximize sensitivity for detecting any weak cross-activation. No significant crosstalk was detected between mismatched pairs of scRNA sequences and binding proteins (Figure 2B). The strong activation of reporter gene expression only with cognate scRNA- and RNA-binding protein pairs demonstrates the potential for simultaneous, independent regulation of multiple target genes.

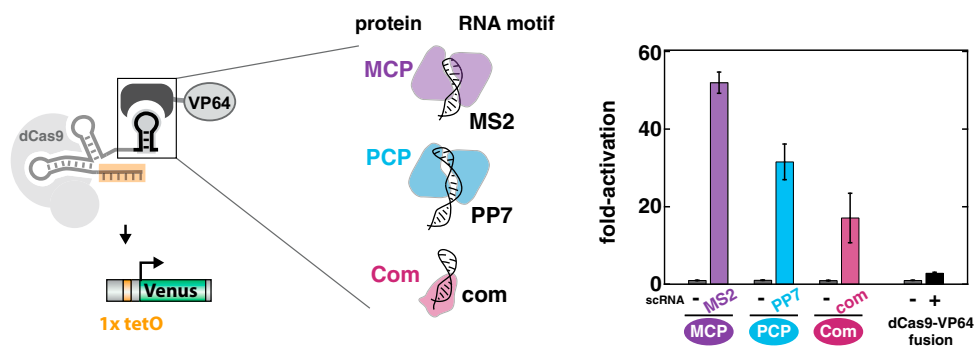
Multivalent Recruitment to scRNAs

To tune the valency of effectors recruited to each gene target, we introduced one, two, or three MS2 RNA hairpins to the 3' end of the sgRNA. Surprisingly, reporter gene expression decreased with increasing numbers of MS2 hairpins (Figure S1C). Northern blot analysis indicated that steady-state RNA levels decreased with two or three MS2 hairpins, suggesting that RNA expression or stability is limiting for these constructs (Figure S2A).

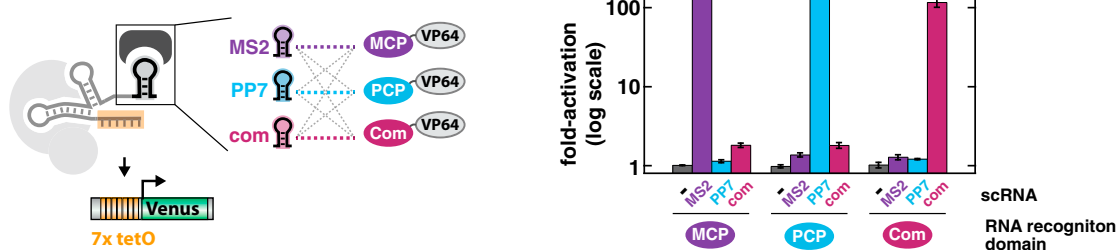
To address the apparent stability problem of multi-hairpin scRNAs, we constructed an alternative RNA design in which double-stranded linkers were inserted between the two repeats of the recruitment hairpins to enforce stable, local hairpin formation. These alternative designs produced stronger reporter gene activation for both MS2 and PP7 modules relative to the analogous single-hairpin scRNAs (Figure 2C). Northern blot analysis of the 2× constructs with double-stranded linkers indicated steady-state RNA levels comparable to single-hairpin scRNA and unmodified sgRNA constructs (Figure S2A).

The strongest activation for a single scRNA construct was obtained with a mixed hairpin construct containing two different recruitment motifs for the MCP-VP64 effector protein (2× MS2 [WT + f6])—this construct contained one MS2 hairpin and a second aptamer hairpin (f6) that had been selected to bind to the MCP protein (Hirao et al., 1998–1999). Attempts to design 2× constructs with double-stranded linkers using the com RNA module were unsuccessful, possibly because the cognate Com protein binds to single-stranded RNA at the base of the com hairpin (Hattman, 1999). RNA constructs with three MS2 hairpins connected by double-stranded linkers did not improve reporter gene expression beyond that obtained with the 2× MS2 scRNA. Northern blot analysis suggests that these constructs are stably

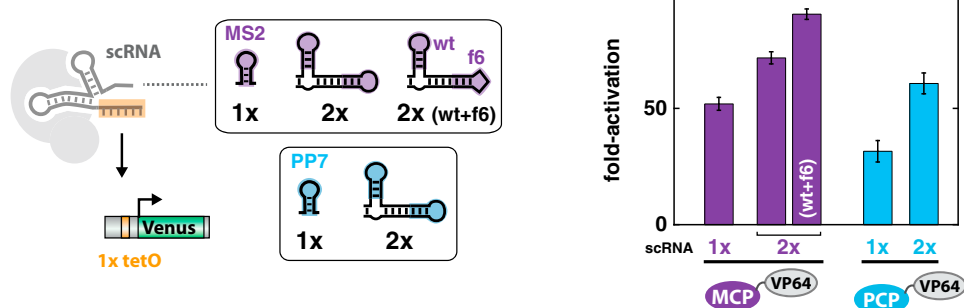
A RNA binding modules recruit activators



B no crosstalk between binding pairs



C multivalent recruitment



D heterologous recruitment

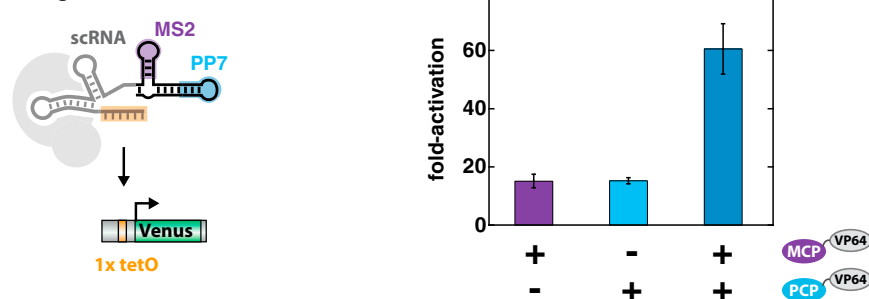


Figure 2. Multiple Orthogonal RNA-Binding Modules Can Be Used to Construct CRISPR Scaffolding RNAs

(A) scRNA constructs with MS2, PP7, or com RNA hairpins recruit their cognate RNA-binding proteins fused to VP64 to activate reporter gene expression in yeast. A yeast strain with an unmodified sgRNA and the dCas9-VP64 fusion protein gives comparatively weaker reporter gene activation. The MS2 and PP7 RNA hairpins bind at a dimer interface on their corresponding MCP- and PCP-binding partner proteins (Chao et al., 2008), potentially recruiting two VP64 effectors to each RNA hairpin. The structure of the com RNA hairpin in complex with its binding protein has not been reported, but functional data suggest that a single Com

(legend continued on next page)

expressed, so the lack of increased expression may be a result of misfolding or steric constraints.

To develop a platform for recruitment of more complex protein assemblies, we designed a heterologous MS2-PP7 scRNA sequence using the 2× double-stranded linker structure. Reporter gene activation was substantially stronger in yeast cells with both MCP-VP64 and PCP-VP64 effector proteins compared to cells with only a single type of effector protein, indicating that distinct RNA-binding proteins can be recruited to the same target site (Figure 2D). This provides an effective approach to combinatorially recruit multiple effectors for the logical control of target genes.

scRNAs Can Mediate Activation of Reporter and Endogenous Genes in Human Cells

To test the efficacy of scRNA-based protein effector recruitment in human cells, we ported the system from yeast to HEK293T cells. The dCas9-binding hairpin of the sgRNA was modified as described previously to improve activity in human cells (see Extended Experimental Procedures) (Chen et al., 2013). In HEK293T cells expressing dCas9, expression of an scRNA with the corresponding VP64 fusion protein effector produced substantial activation of a 7× tet-driven GFP reporter gene for all three RNA-binding modules (Figure 3A), although there are some quantitative differences from the activity trends observed in yeast. GFP activation with 1× MS2 and 1× PP7 scRNA constructs was relatively weak compared to both corresponding multivalent 2× scRNA constructs and the dCas9-VP64 fusion protein.

To determine whether endogenous genes could be activated by targeting a single site upstream of the coding sequence, we designed ten target sequences for the C-X-C chemokine receptor type 4 (*CXCR4*) (Table S3). *CXCR4* expression is low in HEK293T cells, and changes in gene expression can be quantified at the single-cell level by antibody staining. *CXCR4* has previously been a target for CRISPR-based gene silencing in cell types with high basal expression levels (Gilbert et al., 2013). We used the divalent 2× MS2 (WT + f6) scRNA design to recruit the MCP-VP64 protein, and we observed increases in *CXCR4* protein levels for nine of the ten target sites (Figure S3). For the three strongest target sites, we compared *CXCR4* activation mediated by scRNA to that with dCas9-VP64 and observed consistently stronger output with scRNA (Figure 3B).

scRNAs Recruit Chromatin Modifiers to Enhance Gene Silencing in Human Cells

In human cells, CRISPRi-mediated repression is relatively modest but can be enhanced by fusing dCas9 to the KRAB

domain (Gilbert et al., 2013), a potent transcriptional repressor that recruits chromatin modifiers to silence target genes (Gröner et al., 2010). To determine whether scRNAs could recruit KRAB to enhance CRISPR-based gene silencing, we fused KRAB to RNA-binding domains and designed scRNA constructs to target an SV40 promoter driving GFP expression. We targeted one site (P1) upstream of the transcriptional start site (TSS) and another site (NT1) that overlaps the TSS. Recruitment of a Com-KRAB fusion protein to either site by a com scRNA represses the GFP reporter beyond that obtained by CRISPRi alone (there is no significant CRISPRi effect at the P1 site upstream of the TSS) (Figure 3C). The behavior of the KRAB domain recruited by scRNA was similar to that obtained with a direct dCas9-KRAB fusion protein. MCP-KRAB and PCP-KRAB fusion proteins were ineffective at mediating repression, potentially because MCP and PCP form dimers (Chao et al., 2008), which could interfere with KRAB function.

Simultaneous ON/OFF Gene Regulation in Human Cells

The successful application of scRNA-mediated transcriptional control in human cells opens the way toward simultaneous ON/OFF gene regulatory switches mediated by orthogonal RNA-binding proteins fused to transcriptional activators (VP64) or repressors (KRAB). To test this possibility, we targeted endogenous *CXCR4* for activation with MCP-VP64 while simultaneously targeting an additional endogenous gene for repression with COM-KRAB in HEK293T cells. We selected the β -1,4-N-acetyl-galactosaminyl transferase (*B4GALNT1*) gene from a set of target sites previously validated for repression with the dCas9-KRAB fusion protein (Gilbert et al., 2014). We observe simultaneous activation of *CXCR4* and repression of *B4GALNT1* measured by RT-qPCR, and these changes in gene expression are similar to that observed when single genes were targeted (Figure 3D). Importantly, activation and repression are mediated by a single scRNA for each target gene. Thus, this platform could, in principle, be used for large-scale screening of pairwise combinations of genes that yield a target phenotype when one gene is activated and the other is repressed.

Harnessing scRNA Multigene ON/OFF Transcriptional Programs to Redirect Metabolic Pathway Output in Yeast

The complex multigene transcriptional programs that can be generated using scRNAs and dCas9 have the potential to rewire and control diverse cellular networks. One particularly

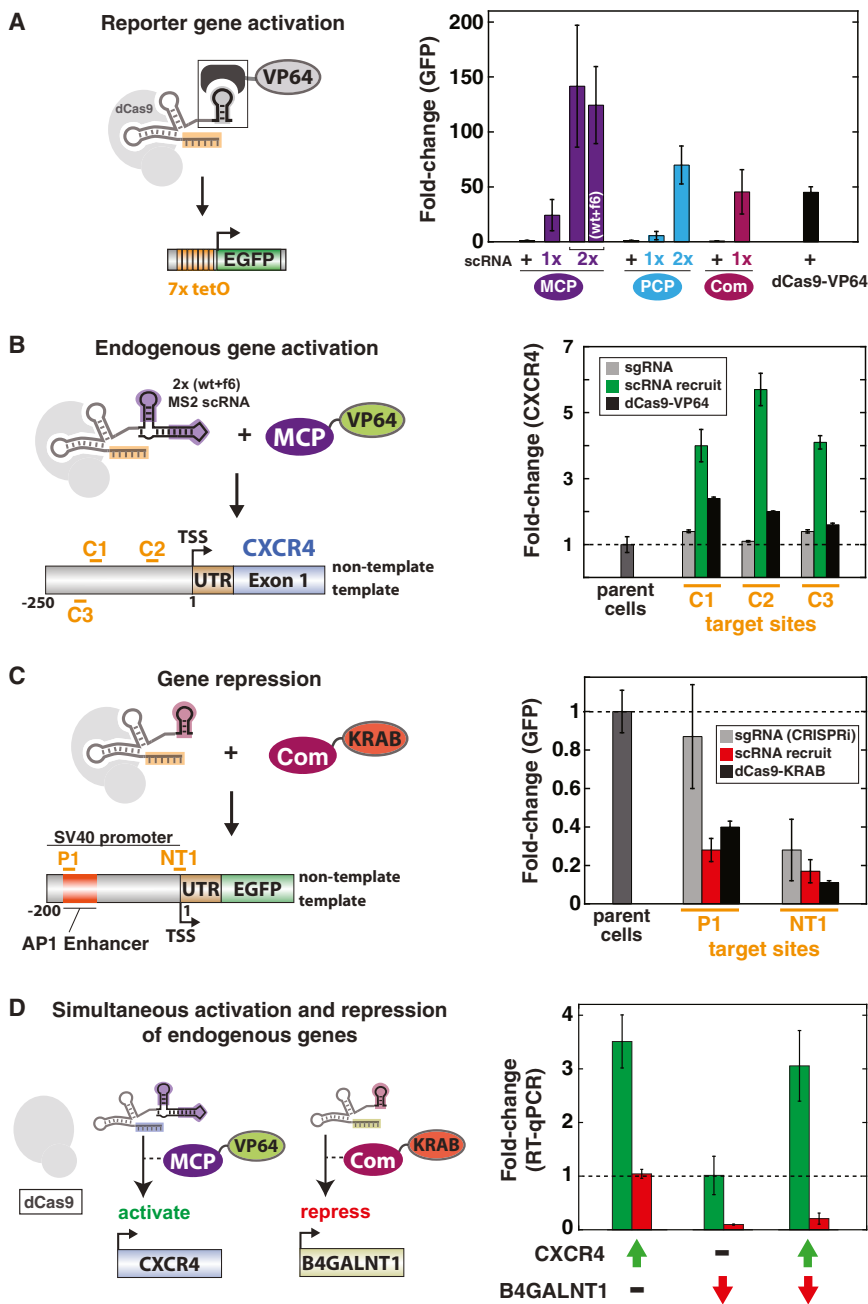
monomer protein binds at the base of the com RNA hairpin (Wulczyn and Kahmann, 1991). scRNA constructs and corresponding RNA-binding proteins were expressed in yeast with dCas9 and a 1× tetO-VENUS reporter gene. Representative flow cytometry data are presented in Figure S1.

(B) There is no significant crosstalk between mismatched pairs of scRNA sequences and non-cognate binding proteins. scRNA constructs and RNA-binding proteins were expressed in yeast with dCas9, using a 7× tetO-VENUS reporter gene to detect any potential weak crosstalk between mismatched pairs. The y axis is on a log scale, and activity with cognate scRNA-binding protein pairs is significantly greater with the 7× tet reporter compared to the 1× reporter.

(C) Multivalent recruitment with two RNA hairpins connected by a double-stranded linker produces stronger reporter gene activation compared to single RNA hairpin recruitment domains. The 2× MS2 (WT + f6) construct was designed with an aptamer sequence (f6) selected to bind to the MCP protein (Hirao et al., 1998–1999). This construct has two distinct sequences to recruit the same protein, which may help to prevent misfolding between hairpin domains that can occur when two identical hairpins are linked on the same RNA.

(D) A mixed MS2-PP7 scRNA constructed using the 2× double-stranded linker architecture recruits both MCP and PCP.

Fold change values in A–D are fluorescence levels relative to parent yeast strains lacking scRNA. Values are median \pm SD for at least three measurements. RNA sequences are reported in Table S1.



interesting application is metabolic control. In biotechnology production strains, there is often competition between pathways required for cell growth versus production of the desired product. In these cases, being able to facilitate control the expression of sets of metabolic enzymes, especially with bidirectional (ON/OFF) control, is essential to optimizing new flux patterns and, thereby, production of the desired product (Paddon et al., 2013; Ro et al., 2006). There is a notable lack of approaches to flexibly increase the expression of enzymes in a desired pathway branch while simultaneously downregulating the expression of enzymes in a competing branch.

To test the ability of our scRNA programs to redirect metabolic pathway outputs, we turned to the highly branched bacterial violacein biosynthetic pathway (Hoshino, 2011). The complete five-gene pathway (*VioABEDC*) produces the violet pigment violacein, and branch points at the last two enzymatic steps (*VioD* and *VioC*) can direct pathway output among four distinctly colored products (Figure 4A). The five-gene pathway can be reconstituted in yeast, and tuning the promoter strength for expression of *VioD* and *VioC* redirects pathway output to different products in a predictable manner (Lee et al., 2013). The four product states are visually distinguishable in yeast

colonies and easily quantified by HPLC, making this pathway an ideal model system to simultaneously tune expression levels of multiple independent target genes to control functional output states.

We designed a yeast reporter strain with two key control points: the first (*VioA*) regulates total precursor flux into the pathway, and the second regulates flow at the *VioC/VioD* branch point. The *VioBED* genes are expressed by strong promoters, and *VioAC* genes are under the control of weak promoters (Figure 4B and Table S4), so that turning *VioA* ON will drive flux into the pathway, and flipping the ON/OFF expression states of *VioC* and *VioD* will redirect the product output. The eight possible pairwise ON/OFF combinations of these three genes lead to five distinct output states: one state with complete pathway output off and four alternative product states when the pathway is on. To access all five states, we designed an scRNA program to target *VioA* and *VioC* with independent activators (2× PP7 and 1× MS2, respectively) and to target *VioD* with CRISPRi-mediated repression (Figure 4B and Table S2). Activation of *VioA* routes pathway flux to the proviolacein product (PV) (Figure 4C). Once *VioA* is activated, activation of *VioC* or repression of *VioD* reroutes flux in a predictable manner. Expressing all three scRNA constructs simultaneously activates *VioA* and *VioC* and represses *VioD* to route flux into the pathway and toward the deoxyviolacein (DV) product. The scRNA/dCas9 platform flexibly and efficiently generates each of the multigene transcriptional states necessary to yield all possible metabolic outputs of the violacein pathway.

Importantly, competition for a fixed pool of dCas9 is not limiting when multiple scRNA constructs are expressed; we observe no significant differences in scRNA-mediated effects at individual gene targets when up to four scRNA constructs are expressed (Figure S4). This result suggests that a large-scale scRNA program can be implemented, as intracellular dCas9 concentration is not a limiting factor, although it remains possible that effects from limiting dCas9 will be observed with different expression levels or if greater numbers of scRNAs are expressed.

dCas9 Acts as a Master Regulator to Execute Expression Programs

The dCas9 protein is a central regulatory node in the execution of scRNA-mediated gene expression programs, raising the possibility that it could act as a single synthetic master regulator, controlling expression levels for multiple downstream genes (Figure 5A). We designed a system in which expression of dCas9 controls a switch from a cell type that produces the PV metabolic product to one that produces DV. Expression of dCas9 was controlled by an inducible pGal10-dCas9 construct. The starting yeast strain contained the *VioABED* genes under the control of strong promoters and *VioC* under the control of a weak promoter (Table S4). We introduced a two-scRNA program to switch *VioC/VioD* from OFF/ON to ON/OFF, redirecting output from PV to DV. When all components are present in yeast but Gal inducer is absent, PV is the dominant product. When the Gal inducer is present, dCas9 is expressed to execute the simultaneous switch of *VioC* ON and *VioD* OFF such that pathway output is routed to DV (Figure 5B). Thus, multiple scRNAs can be regulated using expression of the dCas9 protein as a single control point.

DISCUSSION

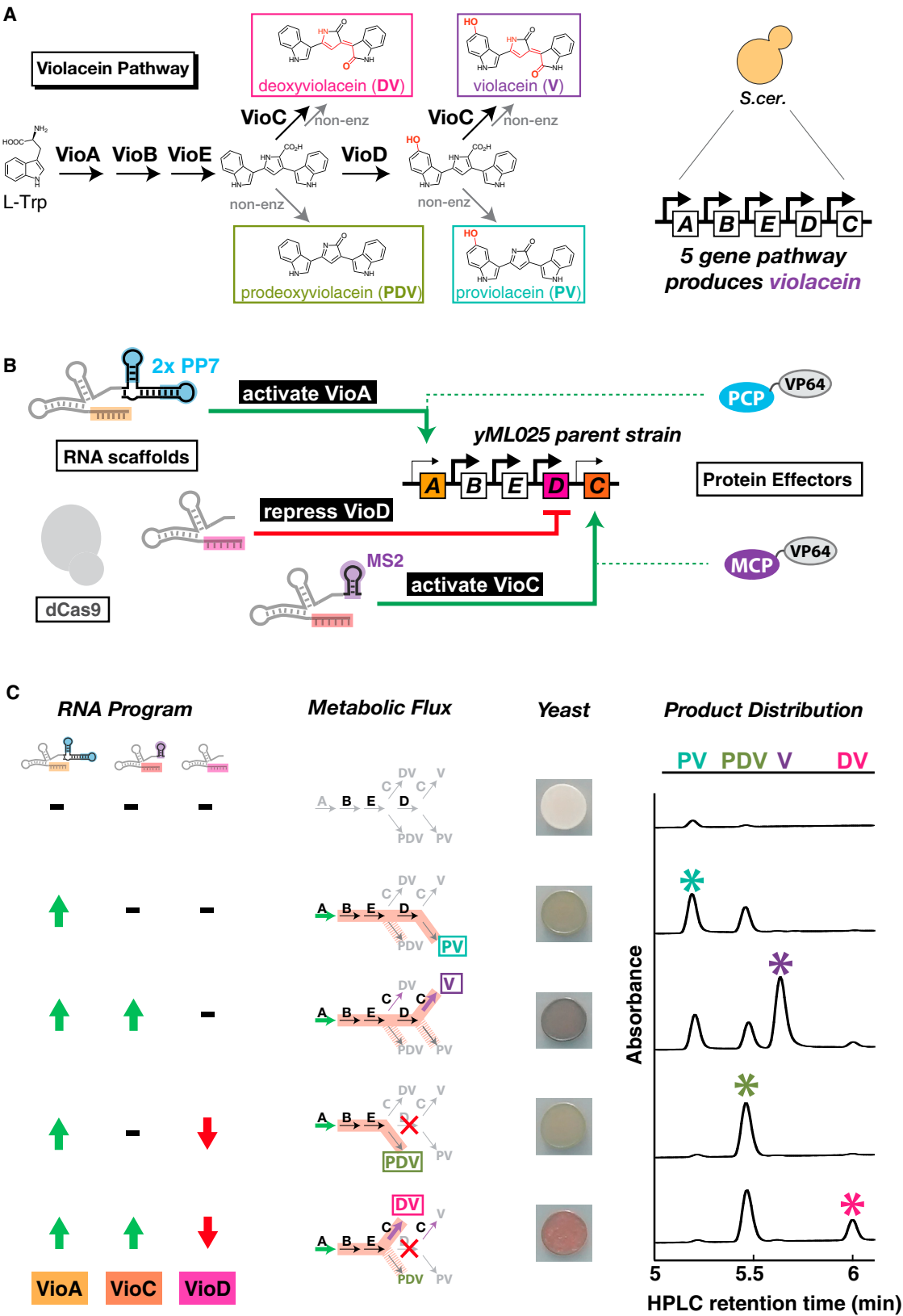
CRISPR Toolkit Enables Construction of Complex Regulatory Circuits

A wide range of CRISPR-related technologies have recently emerged for editing and manipulating target genomes (Mali et al., 2013b; Sander and Joung, 2014). A key advantage of these tools is that they interface with core biological mechanisms, thus allowing the system to be easily ported between different organisms. Watson-Crick base-pairing rules specify target site selection, and synthetic effector proteins interface with conserved features of the transcriptional machinery to control gene expression. Here, we have expanded the scope of the CRISPR toolkit further by adding another basic feature of biological systems, spatial organization mediated by scaffolding molecules, to link functional effector domains to specific genomic target sites. A modular scaffold RNA encodes, within a single molecule, the information specifying the target site in the genome and the particular regulatory function to be executed at that site. scRNAs encode this information using a 5' 20 base targeting sequence, a common dCas9-binding domain, and a 3' protein recruitment domain. Expression of multiple RNA scaffolds simultaneously permits independent, programmable control of multiple genes in parallel. Most simply, this approach provides a straightforward method to implement simultaneous multigene ON/OFF regulatory switching programs.

scRNAs also allow straightforward fine-tuning of output levels in a more analog fashion by altering the valency of effector proteins recruited to an individual target site. Although not explored here, an additional layer of expression control could come from the choice of scRNA target site. In this work, we screened several candidate target sites to identify those that produced maximal output for further analysis (Figure S3 and Tables S2 and S3). To access a range of intermediate output levels, target sites that are less effective could also be selected. More systematic screening approaches will provide general rules to select target sites for varying output levels (Gilbert et al., 2014).

Finally, there are many different classes of protein effectors and epigenetic modifiers that could be recruited via scRNAs to produce different levels and types of gene activation or repression. Qualitatively different regulatory strategies could be implemented, such as regulators that can produce stable, long-lived chromatin states that persist well after an input stimulus is removed. Recent progress toward recruiting a library of epigenetic modifiers with zinc finger proteins (Keung et al., 2014) suggests that a similar range of functionality could be achieved by recruitment via scRNAs. Thus, it may be possible to construct even more nuanced and sophisticated gene expression programs by using a variety of regulators with CRISPR scRNAs and by recruiting these regulators in a combinatorial fashion.

These scRNA-encoded transcriptional programs have several advantages that are lacking in other platforms. First, they are easily programmable using Watson-Crick base pairing to target desired endogenous loci in the genome. TAL effectors can be used to generate complex programs, and these effectors can produce larger effects on gene expression than CRISPR-based approaches, but this requires the custom design of many distinct



(legend on next page)

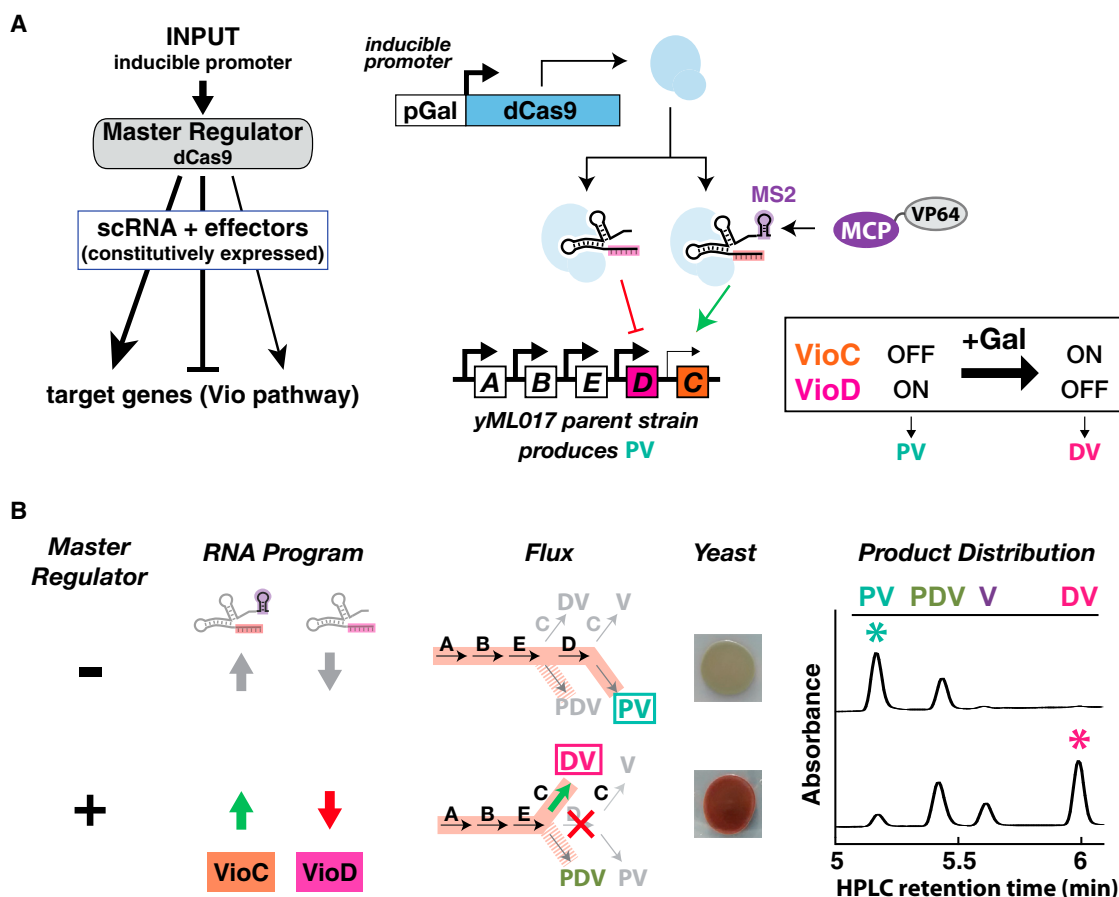


Figure 5. The dCas9 Master Regulator Inducibly Executes scRNA-Encoded Programs

(A) dCas9 can act as a synthetic master regulator of scRNA-encoded circuits. We placed dCas9 under the control of an inducible Gal10 promoter. The yML017 yeast strain (Table S4) has *VioABED* genes strongly expressed (ON) and *VioC* weakly expressed (OFF). A 1× MS2 scRNA targets *VioC* for activation. An unmodified sgRNA targets *VioD* for repression by CRISPRi.

(B) The presence of the master regulator dCas9 controls execution of the scRNA program. Yeast expressing a two-component scRNA program and MCP-VP64 were grown on agar plates in the presence or absence of galactose to control dCas9 expression. When the dCas9 master regulator is not present (-Gal), *VioC* pathway gene expression remains in the basal state and pathway flux proceeds to the PV product. When dCas9 is present (+Gal), *VioC* switches ON, *VioD* switches OFF, and pathway flux diverts to the DV product.

TAL specificities (Kabadi and Gersbach, 2014). Second, scRNA programs allow for distinct regulatory actions to take place at each target locus. Though CRISPRi programs can be targeted to many distinct sites in the genome, fusing or tethering a regulatory effector directly to the Cas9 protein allows only one type of regulatory event (e.g., activation or repression) to take place at all

targets. By tethering effectors to binding motifs in the scRNA, which also encodes the target, we have created single RNA molecules that modularly specify both a target loci and regulatory outcome in their sequence. Third, although multiple scRNAs can be expressed to target many genes, they can still be controlled by a single master regulatory event, the expression

Figure 4. Reprogramming the Output of a Branched Metabolic Pathway with a Three-Gene scRNA CRISPR ON/OFF Switch

(A) Heterologous expression of the bacterial violacein biosynthesis pathway in yeast produces violacein from L-Trp with five enzymatic steps and one non-enzymatic step. Branch points at the last two enzymatic transformations catalyzed by *VioD* and *VioC* produce four possible pathway outputs.

(B) An scRNA program regulates three genes simultaneously to control flux into the pathway and to direct the choice of product. The yML025 yeast strain (Table S4) has *VioBED* genes strongly expressed (ON) and *VioAC* genes weakly expressed (OFF). A 2× PP7 scRNA targets *VioA*, and a 1× MS2 scRNA targets *VioC* for activation. An unmodified sgRNA targets *VioD* for repression by CRISPRi.

(C) scRNA programs flexibly redirect the output of the violacein pathway. The yML025 yeast strain expressing dCas9, MCP-VP64, and PCP-VP64 was transformed with an empty parent vector (pRS316) or with a plasmid containing one, two, or three scRNA constructs to route the pathway to all four product output states (Table S6). Yeast strains were grown on SD -Ura agar plates. Product distribution was analyzed by HPLC. Stars on the chromatograms indicate the expected product of the engineered pathway. Quantitative values for changes in gene expression (by RT-qPCR) and product distributions are reported in Figure S4B.

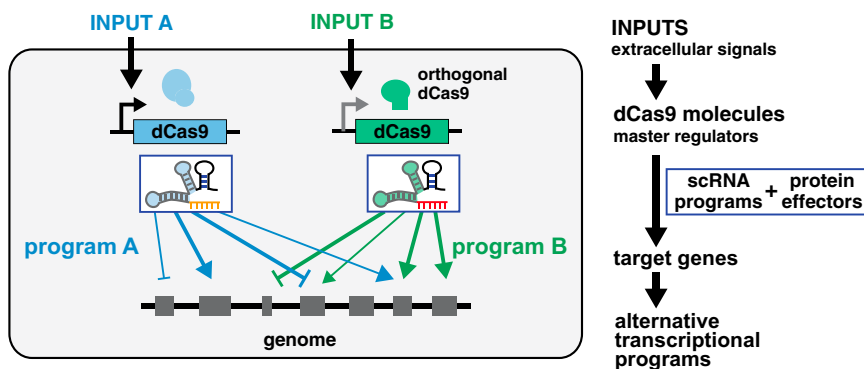


Figure 6. Encoding Complex dCas9/scRNA Regulatory Programs

scRNAs can be combined with dCas9 to construct designer transcriptional programs in which distinct target genes can be simultaneously activated or repressed or subject to other types of regulation. Temporal control of the synthetic program can be achieved by inducing the dCas9 protein as a master regulator. Alternative scRNA gene expression programs could be achieved in the same cell by harnessing orthogonal dCas9 proteins that recognize their guide RNAs through distinct sequences (Esvelt et al., 2013). Each orthogonal dCas9 protein could control a distinct set of scRNAs, allowing independent control over distinct gene expression programs. Each scRNA, in turn, allows independent control at the level of an individual gene. Distinct dCas9 proteins could be placed under the control of different extracellular signals or inducible promoters.

of the dCas9 protein, allowing temporal control over the entire multigene program.

Orthogonal dCas9 proteins from other species (besides *S. pyogenes*) can recognize guide RNAs with different dCas9-binding modules (Esvelt et al., 2013) and thus can provide another potential layer for modular control in CRISPR-engineered transcriptional circuits that is complementary to the scaffold RNAs explored here (Figure 6). For example, one could create, in a single cell, alternative sets of scRNA programs, each executed by an orthogonal dCas9 ortholog. In such a case, one could switch between distinct programs by controlling the expression of the dCas9 master regulators.

Applications: Reprogramming Complex Networks Controlling Cell Function and Fate

scRNA-encoded transcriptional programs provide powerful tools for manipulating complex cellular behaviors, such as differentiation or metabolism. In metabolic engineering, microorganisms can be engineered for biosynthesis by heterologous expression of the desired metabolic pathway. Designing these microbial production factories requires careful engineering to prevent detrimental effects on host growth and metabolism, to avoid buildup of toxic intermediates, and to coordinate the expression of multiple genes to switch from growth to production phase (Keasling, 2012). Often optimizing production requires a coordinated increase in the expression of enzymes that convert precursors into the desired product, as well as simultaneous repression of enzymes that direct these precursors toward alternative products. Because these alternative products are often necessary for growth, optimized production requires precise and coordinated temporal control. It is difficult to construct complex programs of this type with only a handful of well-characterized inducible promoters.

A CRISPR RNA-encoded gene expression program can address these challenges by activating multiple target pathway genes while simultaneously repressing branch points that divert metabolites to cell growth. Execution of the program can be controlled by a dCas9 master regulator that is induced at the appropriate time. To avoid toxic intermediate buildup, expression levels of target pathway genes can be tuned to different

levels, using differential multivalent recruitment of activators, to prevent bottlenecks. One potential limitation of the CRISPR-mediated approach, however, is that metabolic flux is often regulated by mechanisms that act posttranscriptionally (Daran-Lapujade et al., 2007). Nevertheless, there are many situations in which selectively altering transcription levels of pathway enzymes can optimize metabolic flux (Ajikumar et al., 2010; Du et al., 2012; Latimer et al., 2014; Yuan and Zhao, 2013).

To improve metabolite production, CRISPR RNA-based scaffolds could also be used as a rapid prototyping strategy to screen gene expression programs that simultaneously alter the expression levels of multiple metabolic enzymes. The regions of expression space that are identified by such screens could then be custom constructed with specific promoters to achieve finer control. CRISPR tools can also be combined with other approaches to optimize metabolic networks. Global transcription machinery engineering (gTME) screens mutations in general transcription factors or coactivators to modify the expression of many genes simultaneously (Alper et al., 2006). gTME could be used to identify potential target genes for control by scRNA-encoded programs and a dCas9 master regulator. Alternatively, a dCas9 master regulator could be used to switch between global transcription programs by activating and repressing modified general transcription factors that elicit global changes in gene expression.

Finally, scRNA/CRISPR programs are easily transferable to different hosts. Most metabolic engineering efforts use well-characterized and genetically tractable hosts like *E. coli* or *S. cerevisiae*, which offer many desirable industrial characteristics. CRISPR-based tools to modify and regulate host genomes may dramatically expand the space of microorganisms that can be engineered for biosynthesis. Microbial strains or plants that have desirable industrial characteristics or metabolic precursors but lack good tools for genome manipulation may now be accessible for engineering. CRISPR-based tools could also be used to optimize target molecule production in the native host organism for a desired pathway rather than in a heterologous host.

Another broad area of applications for customized expression programs is in controlling cell fate decisions. During development, master regulators specify cell fates by directly or indirectly regulating multiple downstream target genes, and their presence

or absence can determine the outcome of a developmental lineage (Chan and Kyba, 2013). A CRISPR-based multidirectional ON/OFF switch program could provide a straightforward method for genetic reprogramming by synthetically mimicking the behavior of master regulators. scRNA programs could be used to simultaneously activate and repress different master regulators or to bypass master regulators and directly engage the next layer of target genes to specify cell fates. scRNA programs could also be used to create customized hybrid cell fate states that are not generated by natural master regulators but that might still be useful in a therapeutic or research context. In either scenario, the ability of dCas9 itself to act as a synthetic master regulator will be a useful tool for controlling the timing of differentiation. Synthetic control of cell fate reprogramming could provide powerful new tools for regenerative medicine or other cell-based therapeutics.

CRISPR scRNAs as Screening Tools for Biology

High-throughput synthetic lethal screens have proven extremely powerful in analyzing complex biological systems and shedding light on strategies for treating disease networks. Such screens, however, whether they utilize siRNAs or CRISPRi sgRNAs, rely on perturbing the expression of multiple genes in one direction (usually repression). It is equally likely that we can learn new features of networks by simultaneously activating and repressing different combinations of genes. This is particularly true in cases in which a particular cellular outcome requires both activation of that response but also simultaneous inactivation of genes involved in driving competing, alternative responses (Rais et al., 2013). The multi-directional but high-throughput regulation that can be achieved with the scRNA/CRISPR platform is ideal for this type of exploration.

EXPERIMENTAL PROCEDURES

scRNA Sequence Design

sgRNA sequences were extended to include hairpin sequences for MS2 (C5 variant) (Lowary and Uhlenbeck, 1987), PP7 (Lim et al., 2001), or com (Hattman, 1999). Sequences for linkers to the guide RNA and between hairpins were generated by RNA Designer (Andronescu et al., 2004). Candidate sequences were linked to the complete sgRNA sequence and evaluated in NUPACK (Zadeh et al., 2011) to confirm that the extended hairpins were compatible with sgRNA folding. Successful candidates were then evaluated for function in yeast as described below. The 2× MS2 (WT + f6) scRNA design uses the SELEX f6 aptamer, which was selected to bind the MCP protein (Hirao et al., 1998–1999). Sequences of the minimal sgRNA, extended scRNAs, and RNA-binding modules are described in the Extended Experimental Procedures and in Table S1.

Construct Design for CRISPR in Yeast

Mammalian codon-optimized *S. pyogenes* dCas9 (Qi et al., 2013) with three C-terminal SV40 NLSs was expressed from a constitutive Tdh3 or inducible Gal10 promoter. The dCas9-VP64 fusion protein was constructed with two C-terminal SV40 NLSs, the VP64 domain (Beerli et al., 1998), and an additional SV40 NLS. RNA-binding proteins MCP (Δ FG/V29I mutant) (Lim and Peabody, 1994), PCP (Δ FG mutant) (Chao et al., 2008), and Com (Hattman, 1999) were expressed with an N-terminal SV40 NLS and a C-terminal VP64 fusion domain. All protein expression constructs were integrated in single copy into the yeast genome. Complete descriptions of these constructs are provided in Table S5. sgRNA constructs were expressed from the pRS316 CEN/ARS plasmid (*ura3* marker) with the SNR52 promoter and SUP4 terminator (DiCarlo et al., 2013).

sgRNA target sites are listed in Table S2. Twenty base guide sequences upstream of an appropriate PAM motif for *S. pyogenes* dCas9 (Qi et al., 2013) were selected. For genes that had not been previously targeted for CRISPR-based transcriptional regulation, we screened eight candidate sites upstream of the gene and tested each site independently for the desired output (Table S2). The target site with the strongest effect on output was used for subsequent experiments. Methods for manipulation and analysis of yeast strains are described in the Extended Experimental Procedures.

Construct Design for CRISPR in Human Cells

Plasmids for expression of *S. pyogenes* dCas9, dCas9 fusion proteins, and sgRNA constructs were described previously (Gilbert et al., 2013). dCas9 constructs were expressed from an SFFV promoter with two C-terminal SV40 NLSs and a tagBFP. The dCas9-KRAB fusion protein was constructed with a KRAB domain (Margolin et al., 1994) fused to the C terminus of the tagBFP. The dCas9-VP64 fusion protein was constructed with two C-terminal SV40 NLSs, the VP64 domain, an additional SV40 NLS, and a tagBFP. sgRNA sequences were modified as described previously for expression in human cells (see Extended Experimental Procedures) (Chen et al., 2013). sgRNAs were expressed using a lentiviral U6-based expression vector derived from pSico that expresses mCherry from a CMV promoter. To simultaneously express sgRNAs and RNA-binding protein effectors, the mCherry cassette was modified to express the protein effector followed by an IRES and mCherry. RNA-binding proteins (MCP, PCP, and Com) were expressed with an N-terminal SV40 NLS and a C-terminal VP64 or KRAB fusion domain. Complete descriptions of these constructs are provided in Table S7. sgRNA target site sequences are listed in Table S3. To simultaneously target two genes in human cells, we designed a pSico-derived construct with a U6 promoter driving expression of sgRNAs and a CMV promoter driving expression of a protein effector followed by a p2A sequence and tagBFP (Table S7 and Figure S3C). Methods for manipulation and analysis of human cells are described in the Extended Experimental Procedures.

SUPPLEMENTAL INFORMATION

Supplemental Information includes Extended Experimental Procedures, four figures, and eight tables and can be found with this article online at <http://dx.doi.org/10.1016/j.cell.2014.11.052>.

ACKNOWLEDGMENTS

The authors thank J. Park, K. McNally, T. Hsu, M. Larson, S. Torres, M. Horlbeck, W. DeLoache, and members of the Lim lab for technical assistance, advice, and helpful discussions. This work was supported by a Career Award at the Scientific Interface from the Burroughs Wellcome Fund (J.G.Z.), NIH P50 GM081879 (L.S.Q. and W.A.L.), NIH R01 DA036858 (J.S.W., L.S.Q., and W.A.L.), Howard Hughes Medical Institute (J.S.W. and W.A.L.), Leukemia and Lymphoma Society Postdoctoral Fellowship (L.A.G.), NSF SynBERC EEC-0540879 (W.A.L.), Energy Biosciences Institute (J.E.D.), National Defense Science & Engineering Graduate Fellowship Program (M.E.L.), Genentech Pre-doctoral Fellowship (M.L.), and NIH DP5 OD017887 (L.S.Q.).

Received: July 16, 2014

Revised: October 27, 2014

Accepted: November 19, 2014

Published: December 18, 2014

REFERENCES

- Ajikumar, P.K., Xiao, W.-H., Tyo, K.E.J., Wang, Y., Simeon, F., Leonard, E., Mucha, O., Phon, T.H., Pfeifer, B., and Stephanopoulos, G. (2010). Isoprenoid pathway optimization for Taxol precursor overproduction in *Escherichia coli*. *Science* 330, 70–74.
- Alper, H., Moxley, J., Nevoigt, E., Fink, G.R., and Stephanopoulos, G. (2006). Engineering yeast transcription machinery for improved ethanol tolerance and production. *Science* 314, 1565–1568.

- Andronesco, M., Fejes, A.P., Hutter, F., Hoos, H.H., and Condon, A. (2004). A new algorithm for RNA secondary structure design. *J. Mol. Biol.* 336, 607–624.
- Beerli, R.R., Segal, D.J., Dreier, B., and Barbas, C.F., 3rd. (1998). Toward controlling gene expression at will: specific regulation of the erbB-2/HER-2 promoter by using polydactyl zinc finger proteins constructed from modular building blocks. *Proc. Natl. Acad. Sci. USA* 95, 14628–14633.
- Chan, S.S.-K., and Kyba, M. (2013). What is a Master Regulator? *J. Stem Cell Res. Ther.* 3, 114.
- Chao, J.A., Patskovsky, Y., Almo, S.C., and Singer, R.H. (2008). Structural basis for the coevolution of a viral RNA-protein complex. *Nat. Struct. Mol. Biol.* 15, 103–105.
- Chen, B., Gilbert, L.A., Cimini, B.A., Schnitzbauer, J., Zhang, W., Li, G.-W., Park, J., Blackburn, E.H., Weissman, J.S., Qi, L.S., and Huang, B. (2013). Dynamic imaging of genomic loci in living human cells by an optimized CRISPR/Cas system. *Cell* 155, 1479–1491.
- Daran-Lapujade, P., Rossell, S., van Gulik, W.M., Luttk, M.A.H., de Groot, M.J.L., Slijper, M., Heck, A.J.R., Daran, J.-M., de Winde, J.H., Westerhoff, H.V., et al. (2007). The fluxes through glycolytic enzymes in *Saccharomyces cerevisiae* are predominantly regulated at posttranscriptional levels. *Proc. Natl. Acad. Sci. USA* 104, 15753–15758.
- Delebecque, C.J., Lindner, A.B., Silver, P.A., and Aldaye, F.A. (2011). Organization of intracellular reactions with rationally designed RNA assemblies. *Science* 333, 470–474.
- DiCarlo, J.E., Norville, J.E., Mali, P., Rios, X., Aach, J., and Church, G.M. (2013). Genome engineering in *Saccharomyces cerevisiae* using CRISPR-Cas systems. *Nucleic Acids Res.* 41, 4336–4343.
- Du, J., Yuan, Y., Si, T., Lian, J., and Zhao, H. (2012). Customized optimization of metabolic pathways by combinatorial transcriptional engineering. *Nucleic Acids Res.* 40, e142.
- Esvelt, K.M., Mali, P., Braff, J.L., Moosburner, M., Yaung, S.J., and Church, G.M. (2013). Orthogonal Cas9 proteins for RNA-guided gene regulation and editing. *Nat. Methods* 10, 1116–1121.
- Gaj, T., Gersbach, C.A., and Barbas, C.F., 3rd. (2013). ZFN, TALEN, and CRISPR/Cas-based methods for genome engineering. *Trends Biotechnol.* 31, 397–405.
- Gilbert, L.A., Larson, M.H., Morsut, L., Liu, Z., Brar, G.A., Torres, S.E., Stern-Ginossar, N., Brandman, O., Whitehead, E.H., Doudna, J.A., et al. (2013). CRISPR-mediated modular RNA-guided regulation of transcription in eukaryotes. *Cell* 154, 442–451.
- Gilbert, L.A., Horlbeck, M.A., Adamson, B., Villalta, J.E., Chen, Y., Whitehead, E.H., Guimaraes, C., Panning, B., Ploegh, H.L., Bassik, M.C., et al. (2014). Genome-Scale CRISPR-Mediated Control of Gene Repression and Activation. *Cell* 159, 647–661.
- Good, M.C., Zalatan, J.G., and Lim, W.A. (2011). Scaffold proteins: hubs for controlling the flow of cellular information. *Science* 332, 680–686.
- Groner, A.C., Meylan, S., Ciuffi, A., Zangger, N., Ambrosini, G., Dénervaud, N., Bucher, P., and Trono, D. (2010). KRAB-zinc finger proteins and KAP1 can mediate long-range transcriptional repression through heterochromatin spreading. *PLoS Genet.* 6, e1000869.
- Hattman, S. (1999). Unusual transcriptional and translational regulation of the bacteriophage Mu mom operon. *Pharmacol. Ther.* 84, 367–388.
- Hirao, I., Spingola, M., Peabody, D., and Ellington, A.D. (1998–1999). The limits of specificity: an experimental analysis with RNA aptamers to MS2 coat protein variants. *Mol. Divers.* 4, 75–89.
- Hoshino, T. (2011). Violacein and related tryptophan metabolites produced by *Chromobacterium violaceum*: biosynthetic mechanism and pathway for construction of violacein core. *Appl. Microbiol. Biotechnol.* 91, 1463–1475.
- Jinek, M., Chylinski, K., Fonfara, I., Hauer, M., Doudna, J.A., and Charpentier, E. (2012). A programmable dual-RNA-guided DNA endonuclease in adaptive bacterial immunity. *Science* 337, 816–821.
- Jinek, M., Jiang, F., Taylor, D.W., Sternberg, S.H., Kaya, E., Ma, E., Anders, C., Hauer, M., Zhou, K., Lin, S., et al. (2014). Structures of Cas9 endonucleases reveal RNA-mediated conformational activation. *Science* 343, 1247997.
- Kabadi, A.M., and Gersbach, C.A. (2014). Engineering synthetic TALE and CRISPR/Cas9 transcription factors for regulating gene expression. *Methods* 69, 188–197.
- Keasling, J.D. (2012). Synthetic biology and the development of tools for metabolic engineering. *Metab. Eng.* 14, 189–195.
- Keung, A.J., Bashor, C.J., Kiriakov, S., Collins, J.J., and Khalil, A.S. (2014). Using targeted chromatin regulators to engineer combinatorial and spatial transcriptional regulation. *Cell* 158, 110–120.
- Latimer, L.N., Lee, M.E., Medina-Cleghorn, D., Kohnz, R.A., Nomura, D.K., and Dueber, J.E. (2014). Employing a combinatorial expression approach to characterize xylose utilization in *Saccharomyces cerevisiae*. *Metab. Eng.* 25, 20–29.
- Lee, M.E., Aswani, A., Han, A.S., Tomlin, C.J., and Dueber, J.E. (2013). Expression-level optimization of a multi-enzyme pathway in the absence of a high-throughput assay. *Nucleic Acids Res.* 41, 10668–10678.
- Lim, F., and Peabody, D.S. (1994). Mutations that increase the affinity of a translational repressor for RNA. *Nucleic Acids Res.* 22, 3748–3752.
- Lim, F., Downey, T.P., and Peabody, D.S. (2001). Translational repression and specific RNA binding by the coat protein of the *Pseudomonas* phage PP7. *J. Biol. Chem.* 276, 22507–22513.
- Lowary, P.T., and Uhlenbeck, O.C. (1987). An RNA mutation that increases the affinity of an RNA-protein interaction. *Nucleic Acids Res.* 15, 10483–10493.
- Mali, P., Aach, J., Stranges, P.B., Esvelt, K.M., Moosburner, M., Kosuri, S., Yang, L., and Church, G.M. (2013a). CAS9 transcriptional activators for target specificity screening and paired nickases for cooperative genome engineering. *Nat. Biotechnol.* 31, 833–838.
- Mali, P., Esvelt, K.M., and Church, G.M. (2013b). Cas9 as a versatile tool for engineering biology. *Nat. Methods* 10, 957–963.
- Margolin, J.F., Friedman, J.R., Meyer, W.K., Vissing, H., Thiesen, H.J., and Rauscher, F.J., 3rd. (1994). Krüppel-associated boxes are potent transcriptional repression domains. *Proc. Natl. Acad. Sci. USA* 91, 4509–4513.
- Nishimasu, H., Ran, F.A., Hsu, P.D., Konermann, S., Shehata, S.I., Dohmae, N., Ishitani, R., Zhang, F., and Nureki, O. (2014). Crystal structure of Cas9 in complex with guide RNA and target DNA. *Cell* 156, 935–949.
- Paddon, C.J., Westfall, P.J., Pitera, D.J., Benjamin, K., Fisher, K., McPhee, D., Leavell, M.D., Tai, A., Main, A., Eng, D., et al. (2013). High-level semi-synthetic production of the potent antimalarial artemisinin. *Nature* 496, 528–532.
- Qi, L.S., Larson, M.H., Gilbert, L.A., Doudna, J.A., Weissman, J.S., Arkin, A.P., and Lim, W.A. (2013). Repurposing CRISPR as an RNA-guided platform for sequence-specific control of gene expression. *Cell* 152, 1173–1183.
- Rais, Y., Zviran, A., Geula, S., Gafni, O., Chomsky, E., Viukov, S., Mansour, A.A., Caspi, I., Krupalnik, V., Zerbib, M., et al. (2013). Deterministic direct reprogramming of somatic cells to pluripotency. *Nature* 502, 65–70.
- Rinn, J.L., and Chang, H.Y. (2012). Genome regulation by long noncoding RNAs. *Annu. Rev. Biochem.* 81, 145–166.
- Ro, D.-K., Paradise, E.M., Ouellet, M., Fisher, K.J., Newman, K.L., Ndungu, J.M., Ho, K.A., Eachus, R.A., Ham, T.S., Kirby, J., et al. (2006). Production of the antimalarial drug precursor artemisinic acid in engineered yeast. *Nature* 440, 940–943.
- Sander, J.D., and Joung, J.K. (2014). CRISPR-Cas systems for editing, regulating and targeting genomes. *Nat. Biotechnol.* 32, 347–355.
- Spitale, R.C., Tsai, M.-C., and Chang, H.Y. (2011). RNA templating the epigenome: long noncoding RNAs as molecular scaffolds. *Epigenetics* 6, 539–543.
- Wulczyn, F.G., and Kahmann, R. (1991). Translational stimulation: RNA sequence and structure requirements for binding of Com protein. *Cell* 65, 259–269.
- Yuan, Y., and Zhao, H. (2013). Directed evolution of a highly efficient cellobiose utilizing pathway in an industrial *Saccharomyces cerevisiae* strain. *Biotechnol. Bioeng.* 110, 2874–2881.
- Zadeh, J.N., Steenberg, C.D., Bois, J.S., Wolfe, B.R., Pierce, M.B., Khan, A.R., Dirks, R.M., and Pierce, N.A. (2011). NUPACK: Analysis and design of nucleic acid systems. *J. Comput. Chem.* 32, 170–173.

Skeletal Muscle PGC-1 α 1 Modulates Kynurenine Metabolism and Mediates Resilience to Stress-Induced Depression

Leandro Z. Agudelo, Teresa Femenía, Funda Orhan, Margareta Porsmyr-Palmertz, Michel Goiny, Vicente Martinez-Redondo, Jorge C. Correia, Manizheh Izadi, Maria Bhat, Ina Schuppe-Koistinen, Amanda Pettersson, Duarte M.S. Ferreira, Anna Krook, Romain Barres, Juleen R. Zierath, Sophie Erhardt, Maria Lindskog,* and Jorge L. Ruas*

*Correspondence: mia.lindskog@ki.se (M.L.), jorge.ruas@ki.se (J.L.R.)
<http://dx.doi.org/10.1016/j.cell.2014.12.025>

(Cell 159, 33–45; September 25, 2014)

During the preparation of Figure 1 in the article above, we inadvertently included lines separating the lanes in the western blot shown in Figure 1E. In that panel, the Vinculin control for ARC should not display separating lines, as all samples were loaded on consecutive lanes. We would like to clarify that the legends of Figures 1 and 2 should have indicated that the separating lines demarcate bands that come from nonconsecutive lanes of the same gel. Finally, in the legend of Figure 1, we did not mention that the Vinculin loading control for ARC and CamKII α shown in Figure 1E is the same, as these proteins were detected in the same membrane. The errors do not in any way affect the results or interpretation of the figure. We apologize for any confusion that these errors may have caused.

Environment Drives Selection and Function of Enhancers Controlling Tissue-Specific Macrophage Identities

David Gosselin, Verena M. Link, Casey E. Romanoski, Gregory J. Fonseca, Dawn Z. Eichenfield, Nathanael J. Spann, Joshua D. Stender, Hyun B. Chun, Hannah Garner, Frederic Geissmann, and Christopher K. Glass*

*Correspondence: ckg@ucsd.edu
<http://dx.doi.org/10.1016/j.cell.2014.12.024>

(Cell 159, 1327–1340; December 4, 2014)

During the preparation of Figure 2 of the above article, the scatterplot data comparing histone modifications in microglia and large peritoneal macrophages (LPM), shown in the left panel of Figure 2C, was inadvertently inserted also into the adjacent scatterplot for comparison of thioglycollate-elicited macrophages (TGEM) and LPM. In the same left panel of Figure 2C, we also mistakenly labeled “MG-spec” as “TGEM-spec.” In addition, in Figure S2, the base of the log scale for analyzing data of replicate ChIP-seq peaks should have been presented in the same way as what is depicted in Figure 2A. These mistakes do not affect the results in the paper or the interpretation of the data. The corrected version of Figure 2 appears below, and Figures 2 and S2 have both been corrected online. We apologize for any confusion that these errors may have caused.

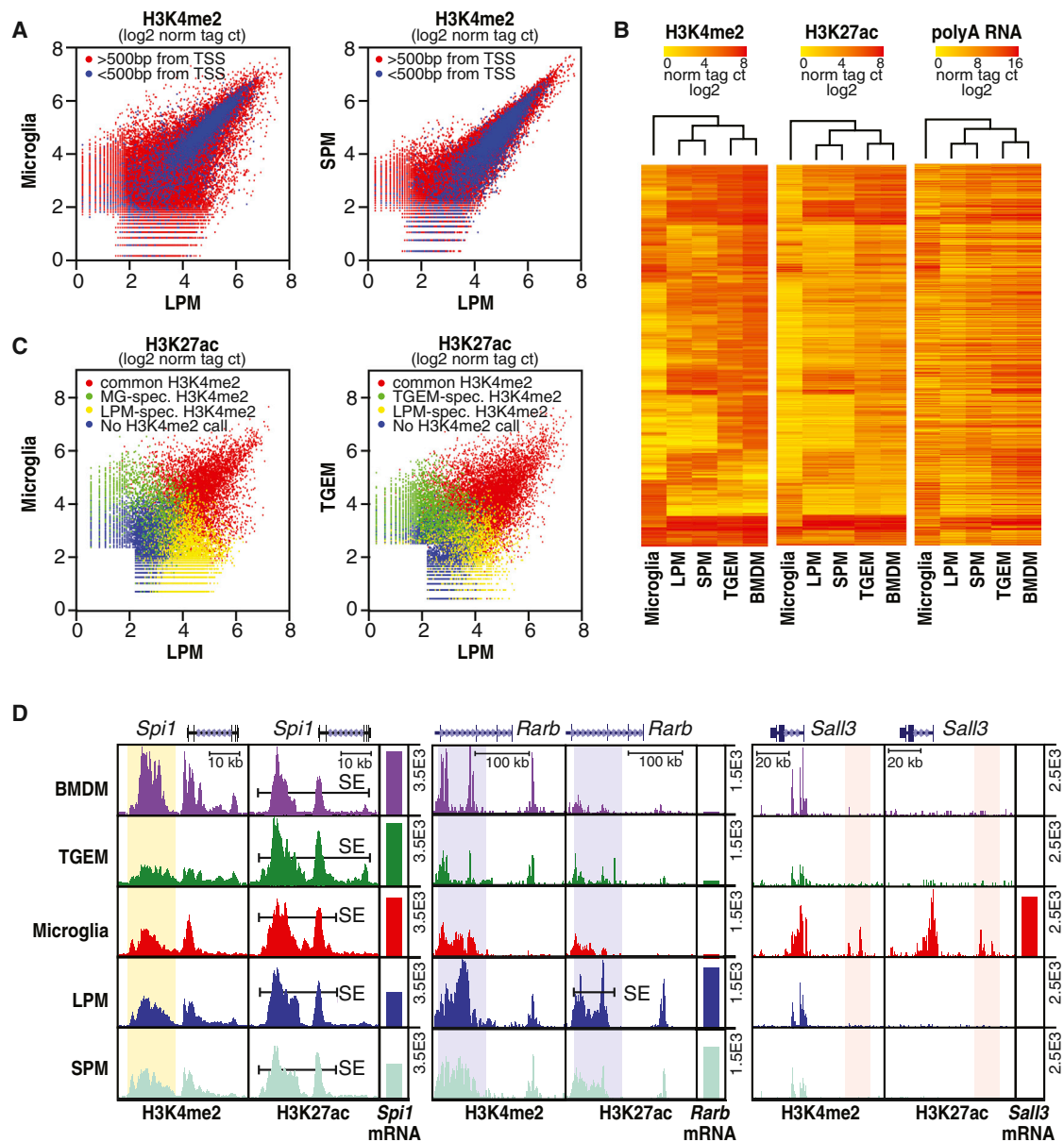
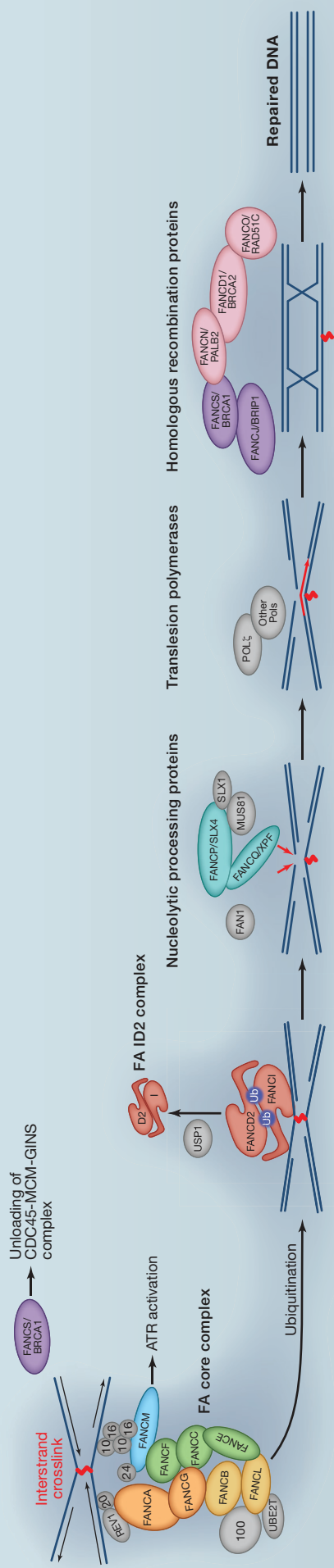


Figure 2. Variation in Enhancer Landscapes in Different Macrophage Subsets

Anderson T. Wang¹ and Agata Smogorzewska¹

¹Laboratory of Genome Maintenance, The Rockefeller University, New York, NY 10065, USA



Genes mutated in FA patients									
Gene	Name (alias)	S. cerevisiae	S. pombe	D. melanogaster	C. elegans	D. rerio	X. laevis	Patient frequency	Protein Function
FANCA	-	-	-	-	-	fanca	fanca	64%	FA core complex
FANCB	-	-	-	-	-	fancb	fancb	2%	FA core complex
FANCC	-	-	-	-	-	fancb	fancb	12%	FA core complex
FANCD1	BRCA2	-	-	Brca2	brc-2	brca2	brca2	2%	Homologous recombination
FANCD2	-	-	-	Fancd2	fcd-2	fancd2	fancd2	4%	FA ID2 complex, gets ubiquitinated by FANCL (in the core complex), directs downstream events
FANCE	-	-	-	-	-	fance	fance	1%	FA core complex
FANCF	-	-	-	-	-	fancf	fancf	2%	FA core complex
FANG	-	-	-	-	-	fancg	fancg	8%	FA core complex
FANCI	-	-	-	Fanci	fnci-1	fanci	fanci	1%	FA ID2 complex, gets ubiquitinated by FANCL (in the core complex), directs downstream events
FANCL	BRIP1 (BACH1)	CHL1 ¹	-	-	dog-1	brp1	brp1	2%	Homologous recombination; 5' - 3' helicase
FANCL	-	-	-	Fancl	ml-113?	fancl	fancl	0.4%	FA core complex, E3 ubiquitin ligase
FANCM	-	MPH1	fml1	Fancm (CG7922)	dfrh-3	fancm	fancm	0.1%	FA core complex; DNA translocase, important for ATR activation during ICL repair, participates in DNA repair in other contexts
FANCN	PALB2	-	-	-	-	palb2	palb2	0.7%	Homologous recombination
FANCO	RAD51C	-	-	Rad51C	rfs-1 ²	rad51c	rad51c	0.1%	Homologous recombination
FANCP	SLX4 (BTBD12)	SLX4	slx4	mus312	him-18	slx4	slx4	0.5%	Scaffold/regulator of XPF-ERCC1, MUS81-EME1/2, and SLX1 nucleases
FANCCQ	ERCC4 (XPF)	RAD1	rad16	rml-9	xpt-1	ercc4	ercc4	0.1%	Associates with ERCC1 to form a FANCP/SLX4-dependent ICL unhooking nuclease; also participates in nucleotide excision repair independently of FANCP
FANCS	BRCA1	-	-	-	brc-1	brca1	brca1	0.1%	Homologous recombination; inhibition of NHEJ; removal of CMG (CDC45-MCM-GINS) complex during ICL repair
UBE2T	-	-	?	?	ube2t	ube2t	ube2t		E2 ubiquitin-conjugating enzyme; works with FANCL
FAAP100 ⁴	C17orf70	-	-	-	sidkey-57h18.1	MGC83104	MGC83104		Subunit of FA core complex
FAAP2 ⁴	C19orf40	-	-	-	zgc:162267	C19orf40	C19orf40		Subunit of FA core complex
FAAP20 ⁴	C1orf86	-	-	-	sich73-70k4.1?	LOC101733463 ³	LOC101733463 ³		Subunit of FA core complex
FAAP16 ⁴	APITD1 (MHF1, CENPS)	MHF1	mhf1	-	?	apitd1	apitd1		FA core complex; histone-fold containing protein
FAAP10 ⁴	STR13 (MHF2, CENPX)	MHF2	mhf2	-	F35H10.5	stra13	stra13		FA core complex; histone-fold containing protein
FAN1	(MTMR15, KIAA1018)	-	fan1	-	fan-1	fan1	fan1		ICL repair nuclease, interacts with monoubiquitinated FANCD2

¹. *CHL1* has similarity to *FANCL* and to *DDX11*; ². *rfs-1* is the sole RAD51 paralog identified so far in *C. elegans*; ³. *X.tropicalis* gene; ? Indicates that the identity of the ortholog is uncertain; ⁴. FAAP proteins are indicated as numbers (10, 16, 20, 24, 100).

SnapShot: Fanconi Anemia and Associated Proteins

Cell

Anderson T. Wang¹ and Agata Smogorzewska¹

¹Laboratory of Genome Maintenance, The Rockefeller University, New York, NY 10065, USA

Fanconi anemia (FA) is a genetic disorder of chromosomal instability caused by mutations in at least 17 different genes (*FANCA* to *FANCS*). Patients with mutations in one of the *FANCA* genes constitute a complementation group (FA-A to FA-S) (reviewed in Kottemann and Smogorzewska, 2013; Sawyer et al., 2014; LOVD database: <http://www.rockefeller.edu/fanconi/mutate/>). A minority of patients are not assigned to any complementation group, and their causative mutations still await identification. FA is inherited in an autosomal-recessive fashion with the exception of the FA-B complementation group with mutations in *FANCB*, which is an X-linked gene. Clinically, FA is a heterogeneous disease. Patients may display diverse congenital abnormalities, including growth restriction, skeletal, and other organ malformations (reviewed in Auerbach, 2009). Most FA patients develop bone marrow failure (at a median age of 7 years) that may affect any of the blood lineages. However, patients with mutations in *FANCO/RAD51C* or *FANCS/BRCA1* show no development of bone marrow failure to date and are therefore termed to have FA-like syndrome. FA patients are cancer prone. Patients with biallelic mutations in *FANCD1 (BRCA2)* and *FANCN (PALB2)* develop acute myelogenous leukemia (AML) and embryonal tumors (medulloblastoma, neuroblastoma, and Wilms tumors), usually in the first few years of life. Patients in other complementation groups have a greatly increased risk of AML and squamous cell carcinoma, especially of the head, neck, and genital regions. Cells derived from FA patients show increased genomic instability and cellular hypersensitivity to DNA crosslinking agents, a characteristic that has also been used as a diagnostic marker for FA (reviewed in Auerbach, 2009).

The proteins encoded by the 17 genes identified to be mutated in FA patients (colored in the schematic) are implicated in a common pathway important for the repair of DNA interstrand crosslink (ICL) lesions that covalently link two strands of DNA together (reviewed in Deans and West, 2011; Kim and D'Andrea, 2012; Kottemann and Smogorzewska, 2013). The pathway also involves other associated proteins (gray in the schematic) that have not yet been shown to be mutated in FA patients. ICL lesions may be formed by endogenous metabolites, such as reactive aldehydes (from alcohol detoxification, histone demethylation, or lipid peroxidation) or exogenous chemotherapeutic drugs, including cisplatin (reviewed in Clauson et al., 2013; Garaycochea and Patel, 2014). This pathway is activated following replication fork stalling at an ICL during S phase, with the FA core complex (*FANCA*, *B*, *C*, *E*, *F*, *G*, *L*, and *M*) recruited through multiple mechanisms. Components of the core complex (including *FANCM*) have additional functions in activating ATR, the DNA damage response kinase, which phosphorylates multiple substrates to facilitate cell-cycle arrest, replication fork stability, and proper repair.

Once the core complex is recruited to the ICL-induced stalled replication fork, *FANCL*, the catalytic E3 ligase subunit of the core complex, in concert with *UBE2T* (ubiquitin-conjugating enzyme), ubiquitinates the *FANCD2-FANCI (ID2)* complex. Patient cell lines with mutations in the genes coding for the core complex components show lack of *FANCD2* or *FANCI* ubiquitination following DNA interstrand crosslink-inducing agents like DEB or mitomycin C (MMC). The ubiquitinated ID2 complex is essential for downstream nucleolytic incisions and translesion synthesis repair events. The deubiquitinating enzyme, *USP1*, is required to deubiquitinate the ID2 complex, and this event has been shown to be important for ICL repair. Two of the FA proteins, *FANCP/SLX4* and *FANCO/XPF*, form a complex in which the endonuclease *XPF* makes incisions to “unhook” the ICL. Other nucleases, including *FAN1 (FANCD2/FANCI-associated nuclease)*, *MUS81*, and *SLX1* might act redundantly to make incisions at the ICL (reviewed in Zhang and Walter, 2014). Unhooking allows for translesion polymerases to repair one duplex, which can then be used for repair of the other strand using homologous recombination. The remaining FA proteins, *FANCD1/BRCA2*, *FANCI/BRIP1*, *FANCN/PALB2*, *FANCO/RAD51C*, and *FANCS/BRCA1*, are all implicated in homologous recombination repair that acts following the unhooking step to resolve resulting double strand breaks. In addition, *FANCS/BRCA1* has been most recently implicated in unloading the replicative CMG helicase at stalled replication forks (Long et al., 2014).

All components of the FA pathways are conserved in vertebrates, including frogs and zebrafish. In invertebrates, such as flies and worms, *FANCL* is the only conserved component of the core complex, whereas the ID2 complex and the rest of the other FA components linked to other repair pathways are present. It remains debatable whether the FA pathway is conserved in lower eukaryotes, including budding yeast and fission yeast as the ID2 complex, the pivotal component of the FA pathway, is not conserved. However, it has been suggested that the orthologs of the most conserved components, *FANCM*, *FAAP10/FAAP16*, *FANCI*, *FANCP*, and *FANCO*, operate during ICL repair in yeast when the predominant repair pathways are inactivated (McHugh et al., 2012).

REFERENCES

Auerbach, A.D. (2009). *Mutat. Res.* 668, 4–10.

Clauson, C., Schärer, O.D., and Niedernhofer, L. (2013). *Cold Spring Harb. Perspect. Med.* 3, a012732.

Deans, A.J., and West, S.C. (2011). *Nat. Rev. Cancer* 11, 467–480.

Garaycochea, J.I., and Patel, K.J. (2014). *Blood* 123, 26–34.

Kim, H., and D'Andrea, A.D. (2012). *Genes Dev.* 26, 1393–1408.

Kottemann, M.C., and Smogorzewska, A. (2013). *Nature* 493, 356–363.

Long, D.T., Joukov, V., Budzowska, M., and Walter, J.C. (2014). *Mol. Cell* 56, 174–185.

McHugh, P.J., Ward, T.A., and Chovanec, M. (2012). *Cell Cycle* 11, 3739–3744.

Sawyer, S.L., Tian, L., Kahkonen, M., Schwartzentruber, J., Kircher, M., Majewski, J., Dymant, D.A., Innes, A.M., Boycott, K.M., Moreau, L.A., et al. (2014). *Cancer Discov.* Published online December 3, 2014. <http://dx.doi.org/10.1158/2159-8290.CD-14-1156>.

Zhang, J., and Walter, J.C. (2014). *DNA Repair (Amst.)* 19, 135–142.